



Proceedings of The 7th Asian Aerosol Conference

August 17-20, 2011, Xi'an, China

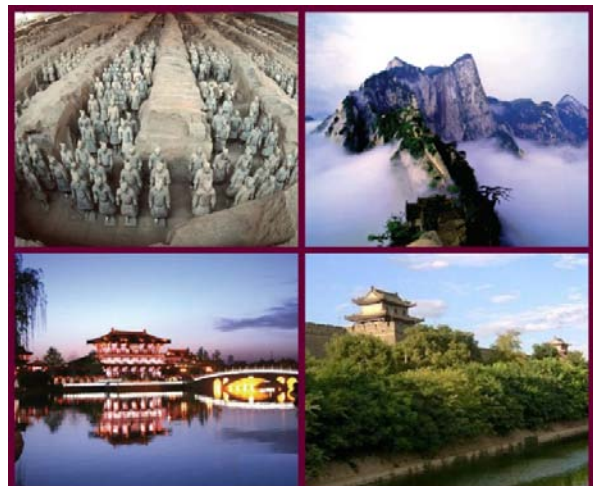
Edited by:

Dr. Junji Cao,

Key Lab of Aerosol,

Institute of Earth Environment,

Chinese Academy of Sciences



Organized by:

Asian Aerosol Research Assembly

Chinese Association of Aerosol Science & Technology

Institute of Earth Environment, Chinese Academy of Sciences

Xi'an Jiaotong University

Institute of Atmospheric Physics, Chinese Academy of Sciences

Preface

Welcome to the seventh Asian Aerosol Conference (AAC 2011) under the auspices of Asian Aerosol Research Assembly (AARA, <http://www.aaraonline.org/>). Beginning in 1999, the successive Asian Aerosol Conferences (AACs) have grown in terms of the spectrum of international participation and the depth of the specialized topics covering every aspects of aerosol science. The AAC2011 continues its tradition in providing an essential and outstanding forum for the latest achievements and future developments in the fields of Aerosol Science and Technology.

With the increasing public awareness and knowledge in different aspects of environment, climate, health and energy, the research of aerosol science has grown rapidly in recent years. In most Asian countries, the management strategies and investments are still in the explorative stage. Therefore, it is of great importance to host this international conference for our intimate communication in order to make us understand the advanced technology more effectively and efficiently.

The 433 abstracts/extended abstracts from 22 countries included in these *Proceedings* provide original and recent information on five major topics:

- Ambient Measurements
- Aerosol Instrumentation
- Aerosol Modeling
- Effects on Climate, Health, Visibility, and Ecosystems
- Pollution Control and Management

On behalf of the Scientific Steering Committee, we warmly welcome all participants and representatives from scientific communities, governmental agencies, and enterprises to share and exchange our experiences at multiple scales and disciplines of Aerosol Science and Technology in the historic city Xi'an.

Finally, we are indebted to Mr. Eric Tian, Ms. Jing Zhao, Ms. Jiamao Zhou of Institute of Earth Environment, Chinese Academy of Sciences for their efforts in categorizing and compilation of abstracts for this proceeding.

Junji Cao, Ph. D.
Technical Program Chair

Tawatchai Charinpanitkul, Ph. D.
Scientific Steering Committee Chair

Renjian Zhang, Ph. D.
General Conference Chair

Committees

General Conference Chairs

Prof. Renjian Zhang, Institute of Atmospheric Physics, Chinese Academy of Sciences, China

Prof. Xiaodong Liu, Institute of Earth Environment, Chinese Academy of Sciences , China

Technical Program Chairs

Prof. Junji Cao, Institute of Earth Environment, Chinese Academy of Sciences, China

Academician Zhisheng An , Chinese Academy of Sciences, China

Scientific Steering Committee

Chair: Prof. Tawatchai Charinpanitkul, President, Asian Aerosol Research Assembly, Thailand

Co-chair: Prof. Chuen-Jinn Tsai, Chiao Tung University, Taiwan

Prof. Mark Adams, University of Sydney, Australia

Dr. Shankar G. Aggarwal, National Physical Laboratory(NPL), CSIR, India

Prof. Kang Ho Ahn, Hanyang University, Korea

Dr. May Antoniette Ajero, CAI-Asia Center, Philippines

Prof. Zhipeng Bai, Naikai University, China

Prof. Helene Cachier, CEA-CNRS, France

Prof. Catherine F. Cahill, University of Alaska Fairbanks, USA

Prof. C.K. Chan, Hong Kong University of Science & Technology, Hong Kong

Prof. Jianmin Chen, Fudan University, China

Prof. Judith C. Chow, Desert Research Institute, USA

Prof. P.C.S. Devara, Indian Institute of Tropical Meteorology, India

Academician Congbin Fu, Nanjing University, China

Prof. Kaarle Hameri, University of Helsinki, Finland

Prof. Masahiko Hayashi, Fukuoka University, Japan

Prof. Kebin He, Tsinghua University, China

Prof. Min Hu, Peking University, China

Prof. Jung Ho Hwang, Yonsei University, Korea

Prof. S. Gerard Jennings, National University of Ireland, Ireland
Prof. Sang-Soo Kim, Korea Advanced Institute of Science and Technology,
South Korea
Dr. Yong Jin Kim, Korea Institute of Machinery & Materials, Korea
Dr. Eladio Knipping, Electric Power Research Institute, USA
Prof. Shuncheng Lee, The Hong Kong Polytechnic University, Hong Kong
Prof. Wen-Jhy Lee, Cheng Kung University, Taiwan
Dr. Wuled Lenggoro, Tokyo University of Agriculture and Technology, Japan
Prof. Neng-Huei Lin, Central University, Taiwan
Prof. Ching-Ho Lin, Fooyin University, Taiwan
Prof. Shaw Liu, Institute of Earth Sciences, Taiwan
Prof. Y.S. Mayya, Bhabha Atomic Research Centre, India
Prof. Lidia Morawska, Queensland University of Technology, Australia
Prof. Varong Pavarajarn, Chulalongkorn University, Thailand
Prof. Olga Popovicheva, Moscow State University, Russia
Prof. Ulrich Poschl, Max Planck Institute for Chemistry, Germany
Prof. David YH Pui, University of Minnesota, USA
Prof. Hiromu Sakurai, National Institute of Advanced Industrial Science and
Technology, Japan
Prof. Takashi Shibata, Nagoya University, Japan
Dr. Xuexi Tie, National Center of Atmospheric Research, USA
Dr. Wladyslaw W. Szymanski, University of Vienna, Austria
Prof. Nattaporn Tonanon, Chulalongkorn University, Thailand
Prof. Mingxing Wang, Institute of Atmospheric Physics, Chinese Academy of
Sciences, China
Prof. Tao Wang, The Hong Kong Polytechnic University, Hong Kong
Prof. John G. Watson, Desert Research Institute, USA
Dr. Liya E. Yu, National University of Singapore, Singapore
Prof. Chung-Shin Yuan, Sun Yat-sen University, Taiwan
Prof. Chandra Venkataraman, Indian Institute of Technology, India
Prof. Xiao-Ye Zhang, Chinese Academy of Meteorological Sciences, China

Local Organizing Committee

Chair: Prof. Zhaolin Gu, Xi'an Jiaotong University, China
Prof. Zhenxing Shen, Xi'an Jiaotong University, China
Mr. Jun Tao, South China Institute of Environmental Sciences, MEP, China

Prof. Gehui Wang, Institute of Earth Environment, Chinese Academy of Sciences, China

Prof. Meigen Zhang, Institute of Atmospheric Physics, Chinese Academy of Sciences, China

Conference Secretariat

Ms. Jiamao Zhou, Email: zjm@ieecas.cn

Mr. Eric Tian, Email: aac2011@ieecas.cn

No. 10 Fenghui South Road, High-Tech Zone, Xi'an 710075, China

Telephone:+86-29-88326128

Fax:+86-29-88320456

Contents

PLENARY LECTURES

Recent Developments in Nanoparticle Filtration Research	1
David Y.H. Pui	
Weight of Evidence Approach for Source Apportionment Studies	3
John G. Watson and Judith C. Chow	
The present and potential future atmospheric environment issues in China	4
Xuexi Tie	
Estimation of the impact of natural and anthropogenic aerosols on air quality and climate change in East Asia using a regional model.....	5
Masayuki Takigawa	
Application of Electrical Means to Aerosol Technologies	10
Jungho Hwang	
Aerosol-Cloud-Precipitation-Climate Interactions:Evidences and Challenges ...	11
Panuganti C.S. Devara	
Aerosol-based Process Technologies for Nano-Materials	18
Bernd Sachweh	

PLATFORM SESSION Ia: Aerosol Chemistry: Field Measurements

I

Ambient Aerosols in Iraq and Afghanistan: Size, Concentration and Elemental and Biological Composition	19
Catherine F Cahill, Thomas A Cahill, Linda S Powers and Walther R Ellis	
Chemical Composition of Precipitation in the Lake Qinghai Area, China.....	27
Kun Zhang, Zhenxing Shen and Junji Cao	
Characterization of Diesel Particulates and Metal Nano-Agglomerates Using the Universal Nanoparticle Analyzer.....	28
Jing Wang, Zhun Liu, Seong Chan Kim, Jacob Swanson and David Pui	
Ambient Ammonia and Ammonium Aerosol in the Urban Area of Beijing.....	34
Zhaoyang Meng, Xiaobin Xu, Weili Lin, Yangmei Zhang, Xiaolan Yu and Xiaofang Jia	
Measurements of Gaseous NH ₃ and HNO ₃ and Particulate Ions Collected over 4 Years in the Upper Green River Basin, Wyoming	35

Table of Contents

Yi Li, Jeffrey L. Collett, Jr., H. James Sewell, Cassie Archuleta, Mark Tigges, Florian M. Schwandner, Lincoln Sherman, Taehyoung Lee, Stephen Holcomb, John V. Molenar and Suresh Raja	
Aerosol Measurements at the Nanjing Xianlin Station.....	36
Erik Herrmann and Aijun Ding	
PLATFORM SESSION IIa:Aerosol Modelling I	
PM2.5 Real-time Forecasting over the Southeastern United States with WRF/Chem-MADRID	41
Ming-Tung Chuang and Yang Zhang	
Model Analysis of Aerosol Impacts on Atmospheric Visibility in China	42
Meigen Zhang, Xiao Han and Renjian Zhang	
A Numerical Simulation of Windblown Sand Movement over a Slope Surface	43
Ning Huang ,Hong Jiang and Ding Tong	
Aerosol-cloud-precipitation Interactions in Numerical Models-a New Perspective	50
Xiaoning Xie and Xiaodong Liu	
Carbonaceous Aerosols in China: Top-down Constraints on Primary Sources and Estimation of Secondary Contribution	51
Tzung-May Fu, Xiaoye Zhang, Junji Cao, Shuncheng Lee, Kin Fai Ho, Wenjun Qu, Qiang Zhang, Zhiwei Han and Renjian Zhang	
Pole-to-Pole Observations of Black Carbon Aerosol and Their Applications to Diagnosis of Long-Range Transport and Model Performance.....	53
R. S. Gao, J. P. Schwarz, J. R. Spackman, A. E. Perring, L. A. Watts, S. C. Wofsy and D. W. Fahey	
PLATFORM SESSION IIIa: Aerosol Instrumentation I	
Enhanced Aerosols Appeared at the Tropical Tropopause over Biak Indonesia in January 2011	54
Takashi Shibata, Masahiko Hayashi, Kei-ichirou Hara, Ayumi Naganuma, Naoko Hara, Suginori Iwasaki, Youichi Inai, Kensaku Shimizu, Fumio Hasebe and Saipul Hamdi	
Development of Optical Aerosol Sensor Based on Polypyrrole Nanofilm	59
Hong-Yi Qin, Hang Zhang, Atul Kulkarni and Taesung Kim	
Develop a Mixing-Type Electrocyclone for Removing Submicron Particulate Matter	64

Table of Contents

Ta-Chih Hsiao	
Application of the Polarization-Raman-Mie Lidar in Automatic and Continuous Observation of Aerosol and Cloud	65
Chenbo Xie, Bangxin Wang, Fudi Qi, Zhiqing Zhong, Zhenzhu Wang, Guangyu Bo and Dong Liu	
Comparative Studies of Instruments That Measure Black Carbon Properties in Mexico City.....	66
Ping Chen, Darrel Baumgardner and Armando Retama	
Mixing height detection with Vaisala LIDAR ceilometer	67
Mark Ma	
PLATFORM SESSION IVa: Advanced Measurement Methods I	
New SMPS for Measurement of Aerosol Size Distributions Down to 1 nm	68
Jingkun Jiang, Modi Chen, Chongai Kuang, Michel Attoui and Peter McMurry	
Development of a Lightweight Simple and Efficient Exhaled Breath Condensate Collection Device and Method.....	69
Zhenqiang Xu and Maosheng Yao	
Use of Electrostatic Sampling and ELISA Method in Studying Charge Distributions of Airborne Allergens	70
Yan Wu and Maosheng Yao	
An Iodine Vapor Filter Based Mobile High-Spectral-Resolution Lidar for Atmosphere and Aerosol	71
Xiaoquan Song, Jinjia Guo, Kailin Zhang, Zhigang Li, Bingyi Liu, Songhua Wu, Decang Bi, Zhangjun Wang and Zhishen Liu	
Effect of Nanoparticle Morphology on the Detection Efficiency of Condensation Particle Counters(CPCs).....	78
Markus Pesch, Xiaoai Guo, Stephan Rennecke, Alfred Weber2, Matthias Richter1 and Lothar Keck	
A Dual-wavelength Lidar Analysis of Dust Aerosol Pproperties	80
Zhiting Wang and Lei Zhang	
PLATFORM SESSION Va: Aerosol Optical Properties	
Optical Characteristics of Aerosols over the Arid-area in Hexi-Corridor.....	86
Wu Zhang, Jinsen Shi, Jianrong Bi, Jianping Huang, Songtao Song, Lei Tian and Tao Xiang	
Aerosol Light Extinction Measurements of Urban and Regional Particulates	

Table of Contents

Using a Cavity Attenuated Phase Shift-Based Monitor	87
Paola Massoli, Paul L. Kebabian, Timothy B. Onasch and Andrew Freedman	
Quantitative Analysis of Aerosol Optical Properties in Summer in Beijing	94
Junshan Jing and Renjian Zhang	
Source Evaluation of the Seasonal Variation in Aerosol Optical Depth	
Distribution over the Indian Subcontinent from Combined Measurement and Modeling Platforms	104
S. Verma, M. Schulz, Y. Balkanski, S. N. Bhanja and S. K. Pani	
Climatology of Aerosol Properties at Mountaintop Sites.....	105
E. Andrews, J.A. Ogren, P. Bonasoni, A. Marinoni, E. Cuevas, S. Rodriguez, J.Y. Sun, D. Jaffe, E. Fischer, U. Baltensperger, E. Weingartner, M. Collaud Coen, S. Sharma, A. Macdonald, W.R. Leaitch, N.-H. Lin, P. Laj, T. Arsov, I. Kalapov, A. Jefferson and P. Sheridan	
Study of Columnar Aerosol Size Spectra at Pune.....	112
G. R. Aher and S. D. More	
PLATFORM SESSION Ib: Aerosol Chemistry: Field Measurements	
II	
Mercury Species in Atmospheric Particles and Their Dependent Conditions ...	113
Guangli Xiu, Yanyan Zhang, Ji Cai, Meigen Zhang, Renjian Zhang, Donald Lucas and Danian Zhang	
Size Distributions of Water Soluble Ions in Atmospheric Aerosol at Lin'an Regional Background Station.....	114
Honghui Xu, Jie Liu, Chunxiao Ji and Minjuan Mao	
Characteristics of Polybrominated Diphenyl Ether in the Air of Southern Taiwan	119
Long-Full Lin, Shin-Hsiung Lin, and Guo-Ping Chang-Chien	
The Physicochemical Characteristics and Fractal Analysis of PM2.5 in the Atmosphere around the Campus of Beijing Forestry University.....	120
Yili Wang and Jiong Li and Yuan Chen	
Aerosol Composition at Gosan, Korea: Measurement Data of TSP, PM10, and PM2.5 between March 1992 and June 2008	121
Na Kyung Kim, Yong Pyo Kim and Chang-Hee Kang	
Distribution Characteristics of Aromatic Acids in Fine Aerosol Particles in Beijing, China.....	125

Table of Contents

Hong Li, Fahe Chai, Xinming Wang, Liqun Deng, Runxiang Ni, Xiaoxiu Lun and Yizhen Chen

PLATFORM SESSION IIb: Black Carbon

Characteristics of Black Carbon Deposition in a Forest.....	129
Kyo kitayama, Yuuki Kimura, Takeshi Mouri, Takumi Kashiwakura, Shogo Ota, Sonoko Drothea Kimura, Masao Takayanagi, Hiroshi Okochi, Akira Takahashi, Sadamu Yamagata, Naoto Murao and Hiroshi Hara	
Proposed Terminology for Black Carbon, as well as Different Forms of Carbon Fractions Used in Different Fields	136
Yongming Han	
Sensitivity Studies for Lagrangian Inversion of Black Carbon Sources in Continental Asia Based on Measurements at Huangshan	137
Ignacio Pisso, Pan Xiaole Takigawa Masayuki, Kanaya Yugo and Prabir Patra	
Variation in Wintertime Black Carbon Aerosols at an Urban Center in the Eastern India.....	138
S. K. Pani, S. Verma, and S. N. Bhanja	
Characteristics of Light Absorbing Carbon in Jiangsu, China	139
Zijuan Lan, Xiaofeng Huang, Lingyan He and Min Hu	
Observational Study of Black Carbon in Urumqi During Summer and Autumn of 2009	144
Yuting Zhang, Xinchun Liu and Qing He	

PLATFORM SESSION IIIb: Aerosol Instrumentation II

A New Stand-alone Wide-range Aerosol Instrument for Automatic Environmental Monitoring.....	145
Xiaoai Guo, Markus Pesch, Hans Grimm and Lothar Keck	
Design and Performance of a Three-wavelength LED-based Total Scatter and Backscatter Integrating Nephelometer	147
Marie Laborde, Thomas Mueller, Grant Kassell and Alfred Wiedensohler	
Two New Fast Response Water-based CPCs for Research Applications.....	154
Kathleen A. Erickson, Fred R. Quant, Sean Morell, Susanne Hering and Robert Caldow	
Performance Evaluation of a Portable Nanoparticle Sizer Under Various Relative Humidity Environments	155
Siqin He and Da-Ren Chen	

Table of Contents

Experimental Evaluation of a Compact Electrostatic Nanoparticle Sampler.....	161
He Jing, Qisheng Ou and Da-Ren Chen	
Single Particle Analysis of Hygroscopic Property of Ambient Aerosol in Shanghai.....	167
Xinning Wang, Xingnan Ye, Hong Chen, Jianmin Chen and Xin Yang	
PLATFORM SESSION IVb: Advanced Measurement Methods II	
Analysis and Handling of Bio-nanoparticles and Intact Viruses using Electrostatic Aerosol Mobility	168
Peter Kallinger, Anne Maißer, Günter Allmaier and Wladyslaw W. Szymanski	
Application of an Ambient Ion Monitor in Northeastern Alberta, Canada.....	173
Yu-Mei Hsu and Kevin Percy	
Aerosol number fluxes measured by eddy covariance method above short vegetation	180
Atsuyuki Sorimachi, Shinji Tokonami, Masaru Haraguchi and Kazuhiko Sakamoto	
Boundary layer top detection from lidar dataset using a Haar wavelet method over Wuhan, China	181
Shalei Song, Feiyue Mao and Wei Gong	
On-line and Off-line Applications of Ion Chromatography in Atmospheric Environment.....	182
Jing Wang	
Decomposition Efficiency of Polycyclic Aromatic Hydrocarbons (PAHs) in Nanoparticles from Rubber-wood Combustion Using Soft X-rays.....	183
J. Chomanee, S. Tekasakul, P. Tekasakul, M. Hata and M. Furuuchi	
PLATFORM SESSION Vb: AMS I	
Carbonaceous Aerosols at Various UK Locations: Source Attribution, Composition and Evolution	190
Dantong Liu, James Allan, Michael Flynn, Gerard Capes, Gavin McMeeking and Hugh Coe	
Measurement of Organic Aerosol Using a High-Resolution Aerosol Mass Spectrometer at a Forest Site in Japan.....	204
Yuemei Han, Yoko Iwamoto, Tomoki Nakayama and Michihiro Mochida	
Overview of Submicron Aerosol Characterization in China Using an Aerodyne	

Table of Contents

High-resolution Aerosol Mass Spectrometer	210
Xiaofeng Huang, Lingyan He, Lian Xue, Min Hu and Yuanhang Zhang	
Comprehensive Characterization of Atmospheric Particles Using Complementary Methods of Chemical Analysis	218
Alexander Laskin	
Laboratory Studies of Organic Aerosol Aging.....	219
Jesse H. Kroll, Kevin R. Wilson, Sean H. Kessler, Theodora Nah, Kelly E. Daumit, Anthony J. Carrasquillo, Eben S. Cross, and Douglas R. Worsnop	
An Aerosol Chemical Speciation Monitor (ACSM) for Routine Monitoring of the Composition and Mass Concentrations of Ambient Aerosol.....	220
Nga L. Ng, Scott C. Herndon, Achim Trimborn, Manjula R. Canagaratna, Philip Croteau, Timothy B. Onasch, Donna Sueper, Douglas R. Worsnop, Qi Zhang, Yele Sun and John T. Jayne	
PLATFORM SESSION Ic: CCN and new particle formation	
Cirrus Cloud Measurement Uusing Lidar over Semi-arid Areas.....	227
Ruijin Liu and Lei Zhang	
Long Term Measurement of Aerosol Size Distribution and CCN Concentration in Seoul, Korea.....	228
Seong-Soo Yum, Woo-Jae Kim, Jong Hwan Kim and Sungbo Shim	
The Relationship between Aerosol and CCN measured on a High Mountain in Southeast China.....	234
Yan Yin, Kui Chen, Chen Chen and Wen Tan	
PLATFORM SESSION IIc: Aeorosol Modelling II	
On the Correlation of Air and Pollutant Exchange for Non-uniform Street Canyons.....	242
Yun-Wei Zhang, Zhao-Lin Gu and Jian-Ying Jiao	
Advanced Remote Sensing and Multi-scale Modeling of Severe Aerosol Episodes	250
R.-M. Hu, R. S. Sokhi and other colleagues	
Simulation of Direct Radiative Forcing of Aerosols and Their Effects on East Asian Climate Using an Interactive AGCM-Aerosol Coupled System.....	251
Hua Zhang and Zhili Wang	
The Turbulent Exchange Characteristics of Typical Pollution Processes over Guangzhou Region	259
Xuejiao Deng, Fei Li, Dui Wu, Hao-bo Tan, Tao Deng	

PLATFORM SESSION IIIc: Pollution Control Technology

Study on Non-steady Collection Theory for Dust of Electrostatic Precipitator	260
Wenge Hao, Electrostatic Precipitator , Mengcheng Li and Yan Li	
Effect of Pleat Shape on the Pressure Drop of Clean Pleated Filter Panels	276
Qisheng Ou and Da-Ren Chen	
Development of the Electro-physical Method of Aero-ion Cleaning	281
Andrey Grishin, Ivan Yagodkin, Andrey Posagennikov and Valerii Melnikov	
Study on Collection Efficiency of 2-layered Electrostatic Filters with Different Gaps	290
Soohyun Ha, Jong-Bum Kim, Soon-Bark Kwon, Seok Namgoong, Kwanhyun Cho and Taesung Kim	

PLATFORM SESSION IVC: Aerosol and Climate Change

Direct Radiative and Climatic Effects of Aerosols in East Asia	295
Zhiwei Han	
A Modeling Study on the Climatic Effects of Aerosols in China	296
Shu Li, Tijian Wang, Bingliang Zhuang and Fanhui Shen	
Semi-direct and Indirect Climate Effects of Fossil Fuel Black Carbon Aerosol over China	302
Bingliang Zhuang, Tijian Wang, Shu Li and Fanhui Shen	
Observational Study of Aerosol Optical Properties over the Cruise during the Third Chinese National Arctic Research Expedition	303
Jie Tang, Peng Yan, Lingen Bian and Changgui Lu	

PLATFORM SESSION Vc: AMS II

Chemical Characterization of Sub-micrometer Aerosol in Beijing.....	304
Junying Sun, Yangmei Zhang, Xiaojing Shen, Xiaochun Zhang and Xiaoye Zhang	
Source Signatures of Submicron Particle-phase Organic Components at Coastal and Inland California.....	305
Shang Liu, Douglas A. Day and Lynn M. Russell	
Changes in Aerosol Mass Spectra during the Photochemical Aging of Organic Aerosols	310
Nga L. Ng, Manjula R. Canagaratna, Jose L. Jimenez, Puneet S. Chhabra, John H. Seinfeld and Douglas R. Worsnop	
Mixing State of Particles by Single Particle Aerosol Mass Spectrometer in Urban	

Table of Contents

Area of PRD 318

Xinhui Bi , Guohua Zhang, Lei Li , Xinming Wang , Guoying Sheng , Jiamo Fu and Zhen Zhou

PLATFORM SESSION Id: Urban Air Pollution I

Inorganic Species of Airborne Particulate Matter and Their Gases Precursors in the Episode Event-A Case Study in Taiwan 320

Jiun-Horng Tsai, Ting Ke Tseng, and Jian-Horng Lin

Humic-like Substances in Ambient Aerosols in the Pearl River Delta Region, China..... 321

Jianzhen Yu and Peng Lin

Chemical Composition of Fine and Coarse Particles at Wuqing during the HaChi Summer Campaign 322

Qian Tang, Min Hu, Zhibin Wang and Binyu Kuang

Chemical Characterization of Water-soluble Species in PM10 of Baoji: a Case Study of a Mid-scale City in Inland China 331

Gehui Wang, Shuyuan Hu, Mingjie Xie, Bianhong Zhou, Jianjun Li and Junji Cao

The Aerosol Characteristics in Different Air Pollution Events over Nanjing 333

Bin Zhu, Honglei Wang, Qiucheng Zhang and Tijian Wang

How Similar are The Aerosols of Beijing and Delhi?..... 334

Kenneth A. Rahn and Manju Mohan

PLATFORM SESSION IIId: Air Pollution Health Effects I

Use of Six-stage Andersen Sampler in Investigating Bioaerosol Inhalation Risks in Different Environments..... 342

Zhenqiang Xu and Maosheng Yao

Real-time Detection of Airborne Influenza A Viruses Using Silicon Nanowire Field Effect Transistor 343

Fangxia Shen, Miaomiao Tan, Zhenxing Wang, Maosheng Yao, Zhenqiang Xu, Yan Wu, Jindong Wang, Xuefeng Guo and Tong Zhu

Traffic Related Particles Induced Pro-inflammatory Cytokine mRNA Expression in Vitro: Importance of Organic Matter and Quinones 344

Yu Shang, Jialiang Feng and Wei Zhao

Moving Boundary Study of Micro-Particle Deposition in Human Oropharynx Airway Model under Steady Inspiration..... 345

Jianhua Huang and Lianzhong Zhang

Table of Contents

Inhibitory Effects on Lung Carcinogenesis in A/J Mice by Aerosolized NSAIDs	346
Jingjie Zhang, Huijing Fu and Da-Ren Chen	
Physicochemical and Toxicological Assessment of Commuter Exposure to Coarse and Fine Particulate Matter (PM) in Subway and Light-Rail Systems of the Los Angeles Metro.....	347
Zhi Ning, Winnie Kam1, James J. Schauer3, Martin M. Shafer and Constantinos Sioutas	
PLATFORM SESSION IIId: Carbonaceous Aerosol	
Characteristics of Carbonaceous Aerosols in Yangtze River Delta Region, China	354
Guanghua Wang, Wei Liu, Jian Yao, Xuebo Fan, Yanhong Geng, Nanan Wei and Jun Lin	
Carbonaceous Aerosols at a High Altitude Location in Central Himalayas	360
Zhiyuan Cong, Shichang Kang and Junji Cao	
Characteristics and the Origins of the Carbonaceous Aerosol at a Rural Site of PRD in Summer 2006	361
Weiwei Hu, Min Hu, Peng Lin, Zhiqiang Deng, Y. Kondo, N. Takegawa, Han, Sunghee and Yongjing Zhao	
Harmonizing Aerosol Carbon Measurements between Two Conventional Thermal/Optical Analysis Methods	368
Guorui Zhi and Yingjun Chen	
Precautions for In-injection Port Thermal Desorption-Gas Chromatography/Mass Spectrometry (TD-GC/MS) as Applied to Aerosol Filter Samples	369
Steven Sai Hang Ho, Judith C. Chow, John G. Watson, Louisa Pan Ting Ng, Yuk Kwok, K.F. Ho, Junji Cao	
Interaction of Minerals with Black Carbon in Thermal Optical Techniques	370
Kochy K. Fung, Judith C. Chow, Jerome Robles, Xiaoliang Wang, Lung-Wen A. Chen and John G. Watson	
PLATFORM SESSION IVd: Aircraft and Satellite Measurement	
Estimation of Aerosol Black Carbon at the Tropopause by Measurements in Commercial Aircraft Cabins.....	371
Anthony D. A. Hansen and Griša Močnik	
Aerosols and Gases Measured by Aircraft during a Dust Storm Event over North China.....	376

Table of Contents

Jianzhong Ma, Wei Wang, Yue Chen and Hongjie Liu	
Asian Dust Detection from Satellite Imagers	377
Xuepeng Zhao	
Aircraft Measurements of Gaseous Pollutants and Particles during CAREBEIJING: Classification and Distribution Analysis.....	386
Wenjie Zhang, Tong Zhu, Jianhua Chen, Lihong Ren, Wen Yang and Baohui Yin	
Direct and Remote Sensing Methods for Chemical Pollution Studies	387
Panuganti C.S. Devara	
Aerosol Variability over East Asia as Seen by Polder Space-borne Sensors.....	395
X. Su, I. Chiapello, P. Goloub, H. Chen, F. Ducos and Z. Li	
PLATFORM SESSION Vd: Source Apportionment I	
Physicochemical Character and Source Appointment of Ambient Coarse/Fine/Ultrafine Particles in Shanghai Atmosphere.....	396
Senlin Lu, Rui Zhang, Man Feng, Zhenkun Yao, Jingjing Re, Fei Yi, Jialiang Feng, Minghong Wu and Qingyue Wang	
Pollution Situation and Possible Markers of Different Sources in the Ordos Region, Inner Mongolia, China	403
Wenjie Zhang, Jianhua Chen, Zhipeng Bai, Wen Yang, Baohui Yin and Wei Wang	
Chemical Composition and Source Apportionment of PM10 in Xi'an and Surrounding Areas	404
Juan Qiang, Wentao Li and Hongmei Xu	
Composition of Fine Particles at Lin'an, a Background Rural Site in the Yangtze River Delta Region	405
Jialiang Feng, Wu Wang, Minghong Wu and Jiamo Fu	
Diurnal Variation and Source Apportionment of Atmospheric Aerosols (PM10) at Xiamen Bay	406
Tsung-Chang, Li, Chung-Yi Wu, Chung-Shin Yuan, Shuei-Ping Wu and Xin-Hong Wang	
Characteristics and Sources of Ionic Species and Metallic Elements in Airborne PM2.5 in Busan, Korea.....	407
Gee-Hyeong Park, Jeong-Gu Cho, Byeong-Kyu Lee and Atilla Mutlu	
PLATFORM SESSION Ie: Secondary Organic Aerosol	
Global In-Cloud Production of Secondary Organic Aerosols Based on Detailed	

Table of Contents

Aqueous-Phase Chemistry	413
Junfeng Liu, Larry W. Horowitz, Songmiao Fan and Hiram Levy II	
Effects of FeSO ₄ Seeds on Secondary Organic Aerosol Formation from Photooxidation of α -Pinene/NO _x and Toluene/Nox.....	414
Biwu Chu, Junhua Li, Jiming Hao, Hideto Takekawa and Kun Wang	
Nationwide Impacts by Fire Emissions in the United Sates in Summer 2002.....	422
Tao Zeng and Yuhang Wang	
Contribution of Aqueous Oxidation of Biogenic VOCs to SOA Production	423
Zhongming Chen, Xuan Zhang, Dao Huang, Hongli Wang, Yue Zhao and Xiaoli Shen	
Characterization of New Particle and Secondary Aerosol Formation during Summertime in Beijing, China.....	424
Y. M. Zhang and X.Y. Zhang	
PLATFORM SESSION IIe: Air Pollution Health Effects II	
A Time-stratified Case-crossover Study of Fine Particulate Matter Air Pollution and Mortality in Guangzhou, China.....	425
Haidong Kan	
CFD Study of Transport and Deposition of Asbestos Fibers in Human Upper Tracheobronchial Airways	426
Lin Tian and Goodarz Ahmadi	
A Study of Mutagenic Index in PM10 of Residential Areas in Bangkok.....	433
Siwatt Pongpiachan, Chomsri Choochuay, Charnwit Kositanone, Kin Fai Ho, and Junji Cao	
Detection of Influenza Virus in Human Exhaled Air	434
Pei-Chun Yen, Pei-Shih Chen and Wan-Chi Kuo	
Problem with Radon Action Level due to the Unattached Radon Decay Products	436
Norbert Kavasi, Tamás Vígh, Tibor Kovács, Janja Vaupotič, Viktor Jobbág, Tetsuo Ishikawa	
Effects of Inhalation Profiles on Particle Deposition in Human Upper Airway	437
Zheng Li and Lujie Cao	
PLATFORM SESSION IIIe: Bio-aerosols, biodefense, inactivation of bioagents I	

Table of Contents

Bioaerosol Science, Technology and Engineering: Past, Current and Beyond	438
Maosheng Yao	
Performance of a Button Inhalable Sampler with Modified MCE Filter Method in Enumerating Culturable Bacterial and Fungal Aerosol Concentration and Diversity	439
Zhenqiang Xu and Maosheng Yao	
Characteristics of Removal of Bioaerosols by Dielectric Barrier Discharge	440
Chul Woo Park, Jae Hong Park and Jungho Hwang	
Ecophysiological Responses of Winter Wheat Seedling to Aerosol Wet Deposition of Xi'an Area	447
Yiping Chen	
Influences of Air Volume, DNA Template, and Dilution Factor on the Performance of qPCR Coupled with a Modified BioStage Sampling Method in Quantifying Bioaerosols	448
Zhenqiang Xu and Maosheng Yao	
Effects of Single-walled Carbon Nanotube Filter on Culturability and Diversity of Environmental Bioaerosols	449
Zhenqiang Xu and Maosheng Yao	
PLATFORM SESSION IVe: Upper air measurements by UAV, balloon, remote sensor, and microsensor	
Boundary Layer Evolution and Soot Aging: a Case Study with Tethered Balloon Observation	450
Daizhou Zhang, Guangyu Shi, Biao Wang, Bin Chen, Maromu Yamada and Hongya Niu	
Unmanned Aircraft System-Based Aerosol Concentration, Size, and Composition Measurements	451
Catherine F Cahill and Gregory W. Walker	
Vertical Distributions of Ozone and Nitrogen Dioxide Observed in a Polluted Marine Boundary Layer around Kaohsiung City	458
Ching-Ho Lin, Chin-Hsing Lai and Yee-Lin Wu	
Monitoring of NO _x by a Sensor Made of Tungsten Oxide multiwalled Carbon Nanotube Composite	459
S. Monchayapisut, M. Sriyudthsak and T. Charinpanitku	
Monitoring of the Atmosphere using Unmanned Aerial Vehicles (UAV)	460

Table of Contents

N.M.Sitnikov, D.V.Akmulin, I.I.Chekulaev, O.B.Popovicheva, A.O.Sokolov, A.E.Ulanovsky and V.I.Sitnikova	
O3/NO ₂ /NMHC Air Pollutants Monitoring Through an Unmanned Aerial Vehicle	466
Char, Jir-Ming, Lin, Chin-Ho, Chu, Harry, Chen and Tan-Chen	
PLATFORM SESSION Ve: Aerosol Emissions	
Large Fire Emissions in Summer over the Southeastern US: Satellite Measurements and Modeling Analysis	467
Tao Zeng, Yuhang Wang, Di Tian and Amistead G. Russell	
Characteristics of Sized-resolved Anhydrosugars and Pollutants Derived from Rice Straw Burning in Controlled Chamber	468
Chih-Jen Chuang, James J. Lee and Jian-Li Lin	
New Methodology for Evaluating Construction Yard Contribution to a PM10 Dust in Shanghai	469
Francesco Petracchini, Michela Sinesi and Ivo Allegrini	
Measurement of PM Emissions and Electrostatic Precipitator Charging Efficiency from Coal Combustion.....	470
Erkki Lamminen and Jukka Kujanpaa	
Characteristics of Particles Emissions and Polycyclic Aromatic Hydrocarbons from IDI-Turbo Diesel Engine Fueled with Palm Oil Blend Diesel.....	471
K. Phoungthong, S. Tekasakul, P. Tekasakul, G. Prateepchaikul, M. Furuuchi and M.Hata	
The Development and Application of Single Particle Aerosol Mass Spectrometer	472
Mei Li, Zhengxu Huang, Lei Li, Zhong Fu, Ping Cheng and Zhen Zhou	
PLATFORM SESSION If: Indoor pollution and air quality I	
Monitoring the Particulate Matter Pollution in an Underground Car Park in Wuhan	473
Rongbiao Xiang and He Wang	
Design and Validation of a Personal Nanoparticle Sampler	474
Chun-Nan Liu, Shao-Ming Hung, Sheng-Chieh Chen, Shi-Nian Uang and Chuen-Jinn Tsai	
Influence of Convection on Diffusion Induced by Inlet Wind Velocity in a Tunnel	476
Jia-Twu Lee and Hsing-Nan Wu	

Table of Contents

Indoor Air Quality in University	489
Yu-Ju Ke, Chia Yu Chen and Pei-Shih Chen	
Numerical Simulation in the Micro Environment in Han Yang Mausoleum Museum.....	491
Nanying Cao	
Ultrafine Particles Counts in Elementary School.....	492
Yi-Chieh Chen and Pei-Shih Chen	
PLATFORM SESSION IIIf: Haze and dust storm	
Assessment of Dust Concentration and Sediment Load of Dust Storms in the Sistan Region of Iran.....	493
A.R. Rashki, D.G. Kaskaoutis, C.J.deW. Rautenbach, P.G. Eriksson and P.Gupta	
Integrated Evaluation of Aerosols from Regional Brown Hazes over Northern China in Winter: Concentrations, Sources, Transformation, and Mixing States	502
Weijun Li, Shengzhen Zhou, Xinfeng Wang, Zheng Xu, Chao Yuan, Yangchun Yu, Qingzhu Zhang and Wenxing Wang	
Discussion on the Haze Pollution Decision Criteria for Shanghai.....	503
Yusen Duan	
The Association of Carbonaceous Species with Haze Pollution.....	504
Guangli Xiu, Mengya Zhu, Jun Tao Junji Cao and Danian Zhang	
Regional Fine Particle Pollution and Haze Problem	505
Min Hu, Xiaofeng Huang, Lingyan He and Yuanhang Zhang	
An Auto-Detection Algorithm for Asian Dust Aerosols over China Seas based on Satellite Observations and Model Simulations.....	506
Zengzhou Hao, Qianguang Tu and Fang Gong	
PLATFORM SESSION IIIIf: Urban Air Pollution II	
Comprehensive Physical and Chemical Characterization of Urban Aerosols in Vienna, Austria.....	507
Nayla Sabbagh-Kupelwieser, Kazuhiko Sekiguchi, Kyung Hwan Kim, Hidehiro Kamiya and Wladyslaw W. Szymanski	
Study of Conditioning System Inside the Temperature of the Flow Field of EMU Air	512
Jia-Twu Lee, Wu-Chou Yu, Wen-Long Yu and Chih-Hung Huang	
Assessment of Traffic Control Measures during the Beijing Olympic Games Based on Particle Number Size Distributions.....	513

Table of Contents

Z.B. Wang, M. Hu1, D. L. Yue, Z. J. Wu, A. Nowak, B. Wehner and A.Wiedensohler	
Chemical characteristics of aerosols in high air pollution episode during autumn of Shanghai, China.....	514
Changhong Chen, Min Zhou, Hongli Wang, Leiyuan Su and Yiran Chen	
Ultrafine, Fine and Coarse Particles in the Ambient Air of Beijing, China.....	515
Dane Westerdahl, Xing Wang, Xiao-chuan Pan and K. Max Zhang	
Evolution of Aerosol Properties Before, During After Fog Events Near Paris, France	516
Darrel Baumgardner, Neda Boyouk and Ping Chen	
PLATFORM SESSION IVf: Ambient Measurement	
Atmospheric Behavior of the Bifunctional Carbonyls Partitioning on <i>SPM</i> and <i>NRPM1</i>	517
Ricardo Ortiz, Satoru Shimada and Kazuhiko Sakamoto	
Iodine Speciation in Marine Aerosols: the Spatial Variation from Shanghai, China to Prydz Bay, Antarctica	524
Senchao Lai, Zhouqing Xie and Thorsten Hoffmann	
Characteristics of Surface Ozone at an Urban Site in Xi'an, China.....	525
Xin Wang and Zhenxing Shen	
Characteristics of Ozone and Fine Particle Observed in Urban and Suburban of Nanjing, China.....	526
Tijian Wang, Ziqiang Jiang, Xiaoxian Huang, Yi Shen and Fanhui Shen	
A Supersite Program for Real-time Characterization of Particulate Matter (PM) in Hong Kong	527
Chak K Chan, NT Lau, Arthur PS Lau, Alexis KH Lau, Jimmy CH Fung, Jian Z Yu, Frank Lee, Christopher YH Chao and Peter Louie	
PLATFORM SESSION Vf: Fundamentals of aerosol physics and chemistry I	
Investigation of Factors Affecting the Mass Size Distribution of Ambient Particulates	529
Jim Juimin Lin, Mon-Shi Lin, and Kuan-Lun Pan	
Quantification of Indirect Combustion Aerosol Impacts on Cirrus Clouds	530
Olga Popovicheva, Yuxing Yu and Joyce E. Penner	
Fabrication of Fibers of Resorcinol/Formaldehyde Gel by Electrospinning toward the Formation of Mesoporous Carbon Fibers	537

Table of Contents

Panitnart Ubollers, Pitt Supaphol and Varong Pavarajarn	
Studies on Sodium Aerosol Characteristics in the Presence of Gamma Radiation Field.....	545
Subramanian V., Baskaran R. and Venkatraman B	
Better Understanding on Particulate Iodine in the Marine Boundary Layer.....	552
Ru-Jin Huang, Michael Kundel, Christopher Kampf, Harald Berresheim, Colin D.O'dowd and Thorsten Hoffmann	
Encapsulation of Menthol with PEG6000 by Aerosol Spraying of Supercritical CO ₂ Suspension.....	553
N. Suankaew, Y. Matsumura and T. Charinpanitkul	
PLATFORM SESSION Ig: Indoor pollution and air quality II	
Chemistry Components in PM2.5 and PM10 for Ambient and Indoor Airs in Campus of Nanchang University, Nanchang City, China.....	554
Hong Huang, Junji Cao and Changwei Zou	
Ionic Components of Indoor Aerosols at Emperor Qin's Terra-Cotta Museum, Xi'an, China.....	555
Jungang Dong, Junji Cao, Ting Zhang	
The Influence of Children Jumping on the Bed on PM10PM2.5PM1 Concentration Profile	556
Wei-Che Houng and Pei-shih Chen	
Concentration of Enterovirus in Air Samples and Exhaled Samples.....	557
Pei-Chun Yen, Pei-Shih Chen and Wan-Chi Kuo	
Physical Parameters Effect on Ozone Initiated Formation of Indoor Secondary Organic Aerosols with Emission from Cleaning Products.....	558
Yu Huang, Kin Fai Ho, Steven Sai Hang Ho and Shun Cheng Lee	
Identification of Volatile Organic Compounds Emitted from Consumer Products	559
Sun-Hwa Kim, Thai Phoung Vu, Seung-Bok Lee, Gwi-Nam Bae and Jong-Ryeul Sohn	
PLATFORM SESSION IIg: Nanoparticle and nanoaerosol technology	
Nano Particle Inhalation System with Electron Spray Generator.....	560
Y. Matsui, S. Kimoto, M. Adachi, A. Tsuda, M. Yoneda	
Numerical Modeling of Nanoparticle Charging Efficiency of Corona-Wire Unipolar Aerosol Charger	561

Table of Contents

Chuen-Jinn Tsai, Chih-Liang Chien, Hui-Lin Chen, Guan-Yu Lin and Jong-Shinn Wu	
Study of Heterogeneous Nucleation upon Nanoparticles in Condensation Particle Counters Effects of Particle and Vapor Composition.....	562
Modi Chen, Michel Attou and Peter McMurry	
Morphological Control of Carbon Nanoparticles Generated by Laser Ablation.....	568
Ayumi Inoue, Masato Takebayashi, Takafumi Seto and Yoshio Otani.	
Quenching of Zinc Vapor for the Generation of Zinc Oxide Nanoparticles ...	572
Chuen-Jinn Tsai and Rodrigo Blanco	
Controlling the Glass Protective Layer on Copper Powders via Spray Pyrolysis.....	573
Dae-Soo Jung, Yun-Chan Kang and Seung-Bin Park	
PLATFORM SESSION IIIg: Urban Air Pollution III	
Regional Pollution Characteristics and Sources of PM10 for Five Northern Cities in China.....	574
Yinchang Feng, Yingze Tian, Guoliang Shi, Zhimei Xiao, Xiaohui Bi, Jianhui Wu, Yufen Zhang	
The Study on Vertical and Temporal Variation of PM10 of Yantaqu in Xi'an during Winter.....	575
Jingbo Zhao, Zhenzhen Mu, Na Xu, Lan Yao, Yuxia Li and Jingjing Meng	
Characterization of Volatile Organic Compounds (VOCs) around the Chinese Spring Festival and International Labour Day in the Urban Area of Shanghai, China	576
Hongli Wang, Changhong Chen, Cheng Huang, Li Li and Minghua Chen	
PM2.5 Speciation and Chemical Extinction during the 2008 Beijing Olympics	578
F. Yang, X. Li, C. Li, Q. Zhao, K. He, Y. Ma, J. Tan, F. Duan and H. Liu	
Influence of Intersection in Chemical Composition of Atmospheric Particulate Matters Observed at Roadside Environment in Urban Area.....	579
Kyung-Hwan Kim, Kazuhiko Sekiguchi, Shinji Kudo, Masatoshi Kinoshita and Kazuhiko Sakamoto	
Characteristics on Air Quality during the 2010 Shanghai Expo	587
Qingyan Fu, Haiping Wei, Yanmin Huang, Song Gao, Yusen Duan and Yihua Zhang	
Chemical Characterization of Aerosol Collected at Mt. Yulong in Winter Time,	

Table of Contents

Southeastern Tibetan Plateau.....	588
Ningning Zhang, Junji Cao and Yuanqing He	
PLATFORM SESSION IVg: Aerosol Radiative Properties and visibility studies	
Determination of Direct Aerosol Radiative Forcing at Pune.....	589
G. R. Aher, G. V. Pawar and P. C. S Devara	
Aerosol Optical and Radiative Properties Observed by Lidar and Sky-radiometer during a Haze Episode over Hefei.....	590
Zhenzhu Wang, Dong Liu, Decheng Wu and Chenbo Xie	
Visual Range Trends in the Yangtze River Delta Region of China during 1981-2005.....	591
Lina Gao, Gensuo Jia, Renjian Zhang, Huizheng Che, Congbin Fu, Tijian Wang, Meigen Zhang, Hong Jiang and Peng Yan	
Simulation of Aerosol Optical Properties and Direct Radiative Forcing with RAMS-CMAQ in East Asia.....	604
Xiao Han, Meigen Zhang and Cui Ge	
Reconstructed Light Extinction Coefficient by Chemical Compositions of PM2.5 in Winter in Urban Guangzhou, China	618
Jun Tao, Renjian Zhang, Junji Cao, Lihua Zhu, Tao Zhang and Si Shi	
Characteristics of Carbon Aerosol Spectrum and Water Soluble Components Spectral in South China during 1988-2010 Period	619
Dui Wu and Biting Liao	
PLATFORM SESSION Vg: Fundamentals of aerosol physics and chemistry II	
Mixing and Water-soluble Characteristics of Particulate Organic Compounds in Individual Urban Aerosol Particles	627
Weijun Li and Longyi Shao	
Experimental Set-up for Particle Deposition Measurements from Turbulent Flow in Large Ventilation Ducts: Application to Food Industries.....	628
Guillaume Da, Evelyne Gehin, Mourad Ben-Othmane, Michel Havet and Camille Solliec	
Numerical Study on Seasalt Depositions in Niigata Prefecture, Japan	635
Naoto Kihara, Hiromaru Hirakuchi, Akira Takahashi, Shin Ohara and Shin-ichi Fujita	

Table of Contents

Spatial and Seasonal Variability of Aerosol Organic Mass-to-Organic Carbon Ratios in Chinese Cities.....	641
Li Xing, Tzung-May Fu, Junji Cao, Gehui Wang, Kin Fai Ho, Shun-cheng Lee and Tijian Wang	
Effects of Gel Network on the Formation of Mesoporous Titania Assisted by Resorcinol/Formaldehyde Gel.....	650
Mananya Thovicha and Varong Pavarajarn	
Polluted Dust Optics: Case of Semi-external Mixing	659
S. K. Mishra, S. N. Tripathi, S. G. Aggarwal and A. Arola	
PLATFORM SESSION I_h: Aerosol Metrology	
Modeling of the Influence of Aerosol Processes for the Dispersion of Traffic Exhaust in a Street Canyon.....	660
Xinling Li, Wei Liu and Zhen Huang	
The Method to Control the Size of Generated Particles from a Spark Discharger by the Ion Bombardment with the Multi-Ionizing	661
Kyu-Tae Park and Jungho Hwang	
Utilization of Three Plutonium Aerosol Monitoring Techniques for Continuous Monitoring of the Filtered Exhaust Gas in a Plutonium Reprocessing Facility	668
Yongyang Su, Zhiming Li, Jiang Xu, Xiangjun Ren, Guoqing Zhou, Lihua Zhai, Longbo Liu, Mei Li and Xiaowei Yi	
Overlooking Aerosol Metrology: A Big Hole in Atmospheric Aerosol Measurement Studies	674
Shankar G. Aggarwal and Prabhat K. Gupta	
PLATFORM SESSION II_h: Ultrafine Particle and Nanoparticle	
Nanoparticle Characteristics at Lulin Site, Taiwan.....	675
Sheng-Chieh Chen, Yi-Hong Hong and Chuen-Jinn Tsai	
Diurnal Variation of Chemical Composition in Ultrafine and Fine Particles in Urban Area, Japan.....	676
Kyung-Hwan Kim, Takayoshi Okamoto, Shimpei Sato, Ortiz Ricardo1, Kazuhiko Sekiguchi, Satoru Chatani, Tazuko Morikawa, Hiroaki Minoura and Kazuhiko Sakamoto	
PLATFORM SESSION III_h: Bio-aerosols, biodefense, inactivation of bioagents II	

Table of Contents

A Different Model for Estimating Monoterpene Emissions over Boreal Pine Forest.....	691
Qingyang He, Michael Boy, Jaana Bäck, Janne Rinne, Hannele Hakola, Alex Guenther, Sampo Smolander and Markku Kulmala	
Effects of Microwave Irradiation on Culturability and Diversity of Biological Aerosols of Different Sizes in Different Environments.....	695
Yan Wu and Maosheng Yao	
Differences in Positively and Negatively Charged Bacterial Aerosol Diversity in Indoor and Outdoor Environments.....	696
Fangxia Shen and Maosheng Yao	
How Combustion of Energetic Materials Affects Viability of Aerosolized Bio-agents.....	697
Sergey A. Grinshpun, Michael Yermakov, Reshma Indugula, Atin Adhikari, Tiina Reponen, Shasha Zhang, Vern Hoffmann, Mirko Schoenitz and Edward Dreizin	
PLATFORM SESSION IVh: Biomass Burning and Biofuels	
Modifications in Physicochemical Properties of Wood Combustion Aerosols Due to Chemical Aging	698
Zhijun Wu, L. Poulaing, O. Böge, R. Gräfe, H. Herrmann, A. Wiedensohler, K. Helbig, T. Schröder, J. von Sonntag, I. Hartmann, Min Hu	
Polybrominated Diphenyl Esters in the Ambient Air of Southern Taiwan during the Biomass Burning Periods	699
Shun-Shiang Chang, Wen-Jhy Lee, Lin-Chi Wang, Kuo-Ping and Chang-Chien	
Injection Heights of Springtime Biomass Burning Plumes in Southeast Asia...	701
Yue Jian and Tzung-May Fu	
Emission Inventory of Air Pollutants from Biomass Burning in the Pearl River Delta Region, China	715
Yisheng Zhang and Min Shao	
PLATFORM SESSION Vh: Source Apportionment II	
Source Apportionment of Primary and Secondary Organic Aerosols at Urban and Rural Locations of Beijing.....	716
Song Guo, Min Hu, Weiwei Hu, Qingfeng Guo and Xin Zhang	
Sources of Carbonaceous Aerosol in the Pearl River Delta Region and Hong Kong	724

Table of Contents

Mei Zheng, James Schauer, Peter K.K. Louie, Limin Zeng, and Yuanhang Zhang	
Application of PMF to AMS Data Observed at Fukue Island, Japan	725
Satoshi Irei, Akinori Takami, Toshihide Hikida and Akio Shimono	
Multivariate Analysis of Particulate Polycyclic Aromatic Hydrocarbons in Bangkok Atmosphere.....	729
Siwatt Pongpiachan, Mattanawadee Hattayanone, Charnwit Kositanone, Kin Fai Ho and Junji Cao	
POSTER SESSION 1	
Lung Generated Aerosols	730
Wan-Ting Lin, Sheng-Hsiu Huang, Yu-Mei Kuo, Chun-Wan Chen, Shih-Wei Tsai and Chih-Chieh Chen	
Control of Indoor Fungal Bioaerosols by Using Ozone	731
Hsiao-Lin Huang and Jen-Hsuan Tai	
A Case Study of the Impacts of Dust Aerosols on Surface Atmospheric Variables and Energy Budgets in a Semi-Arid Region of China.....	737
Xiaolu Ling, Weidong Guo, Lei Zhang and Renjian Zhang	
Contamination Assessment of Copper, Lead, Zinc and Chromium in Dust Fall of Jinan, NE China	743
Suping Feng, Nannan Zhang, Hanchao Liu, Xiaolin Du and Yongli Liu	
Chemical Characteristics of Inhalable Atmospheric Aerosols in Urumqi During Winter	753
DILNUR Talip, YALKUNJAN Tursun, IGAWA Manabu and Abulizi Yimit	
Analysis of the Diurnal Variation of Oxalic Acid in Aerosols by Desorption Electrospray Ionization Mass Spectrometry	754
Xiu Wu, Juntao Huo, Hong Chen and Xin Yang	
Characterization of Optical Properties and Chemical Compositions of Ambient Aerosols in Shanghai	755
Yong Tang, Hong Chen and Xin Yang	
The Impact of the Pollution Control Measures for the 2008 Beijing Olympic Games on the Chemical Composition of Aerosols	756
Tomoaki Okuda, Shinichiro Matsuura, Daisuke Yamaguchi, Tomoaki Umemura, Eriko Hanada, Hiroki Orihara, Shigeru Tanaka, Kebin He, Yongliang Ma, Yuan Cheng and Linlin Liang	
The Measurement of the Size Distribution of Cigarette Mainstream Smoke by ELPI	764

Table of Contents

Yong Jin, Shitai Wang, Jinyun Liu, Ke Li, Hongmei Fan, Haifeng Tan, Xinliang Tan and Xiaochun Qian	
From the Risk/Benefit Aspect to Determine the Optimal Operation Condition for Simultaneously Controlling the Emissions of PCDD/Fs and PAHs from the Iron Ore Sintering Proces	772
Perng-Jy Tsai,Yu-Cheng Chen, Jin-Luh Mou, Yu-Chieh Kuo and Shih-Min Wang	
Single-particle Characterization of Wintertime Atmospheric Particles Collected at Taiyuan City, China on Haze and Non-haze Days	775
Hong Geng, Shila Maskey and Chul-Un Ro	
Comparison of Source Contributions to Urban Ultrafine Particles and other Pollutants.....	776
Yungang Wang, Philip K. Hopke, David C. Chalupa and Mark J. Utell	
Characterization of Particles from Residential Coal Combustion	777
Kun Wang, Junhua Li, Jiming Hao, Chunmei Geng and Hongjie Liu	
Impact of Air Pollution from North Korea to Seoul	784
In Sun Kim, Ji Yi Lee and Yong Pyo Kim	
Elemental Composition of Atmospheric Particles during Periods with and without Traffic Restriction in Beijing: The Effectiveness of Traffic Restriction Measure.....	785
Renjian Zhang, Zhenxing Shen, Leiming Zhang and Meigen Zhang	
Characteristics of Volatile Organic Compounds in Seoul, Korea	793
H.J. Shin, J.C. Kim and Y.P. Kim	
Size Distributions of Polycyclic Aromatic Hydrocarbons in Diesel Exhaust Particles Collected by Newly Developed Ultrafine Particles Sampler	794
Keiko Shibata, Nobuhiro Yanagisawa, Kenji Enya, Kaoru Satou and Kazuhiko Sakamoto	
Characterization and Source Apportionment of Submicron Aerosols at a Regional Site in Pearl River Delta of China Using an Aerodyne High-Resolution Aerosol Mass Spectrometer	801
Z.-H. Gong, L.-Y. He, X.-F. Huang, Z.-J. Lan, L. Xue1 and L.-W. Zeng	
Modification of Dust Particles through Heterogeneous Reactions Uptake of SO ₂ over Chinese Continent during Dust Storm Episodes.....	809
Weijun Li and Longyi Shao	
On-line Analysis and Mass Concentration Characters of Nitrate in Aerosol PM ₁₀ in Beijing.....	810
Kai Zhang, Yuesi Wang, Tianxue Wen, Fahe Chai1 and Guangren Liu	

Table of Contents

An Improved Thermal Oxidation Method for the Quantification of Organic and Black Carbon in Soot Based on the Difference of Pyrolytic Behavior.....	815
Mingyu Jiang, Zhuling Chen, Xinmei Wang and Fengfu Fu	
The Emission Factor and Chemical Characteristics of Particulate N-alkanes Originated from the Combustion of Different Fossil Fuel and Biomass	820
Yiqing Wu, Gongshi Lin and Fengfu Fu	
Investigation about the Association of Children's Lung Function and Air Pollution in Kaohsiung City	824
Yu-Ju Ke, Chih-Sean Ou and Pei-Shih Chen	
Indoor Air Monitoring in Day-care Centers	826
Yu-Ju Ke , Yi-Lien Lee and Pei-Shih Chen	
Real-time Monitoring of PM _{2.5} in Primary School.....	828
Yi-Chieh Chen and Pei-Shih Chen	
The Distribution of PM ₁₀ , PM _{2.5} , and PM ₁ Concentrations in Primary School in Kaohsiung City	829
Yi-Chieh Chen and Pei-Shih Chen	
Airborne Mycobacterium Tuberculosis Profiles in a Hospital with a Nosocomial TB Outbreak.....	830
Wei-Che Houng and Pei-shih Chen	
Exposure Assessment of Ozone in elementary school in Kaohsiung,Taiwan ...	831
Wei-Che Houng and Pei-shih Chen	
Characterization of the Bacterial and Fungal Bioaerosols in three Elementary School in Kaohsiung	832
Pei-Chun Yen, Pei-Shih Chen and Chih-Sean Ou	
Characterization of Organic Particles from Incense Burning Using a High-resolution Time-of-flight Aerosol Mass Spectrometer.....	834
Yong Jie Li and Chak Keung Chan	
Physicochemical Fingerprints of Particulate Matter Emitted from Various Sources in Kin-Xia Region	835
Chung-Yi Wu, Tsung-Chang Li, Chung-Shin Yuan, Shuei-Ping Wu and Xin-Hong Wang	
Field Test for Fine Dust Collection in an MVAC of Metro Subway.....	836
Dong Ki Lee, Yun-Hui Lim and Young Min Jo	
Method for Combining Electrical Mobility and Optical Size Distributions for Wide Range Particle Size Distribution Measurement	837
Hee-Siew Han, Avula Sreenath, Nathan T. Birkeland and George J. Chancellor	

Table of Contents

The Properties of Water-soluble Ions in the Asian Brown Cloud: Observation over the Mountain Lulin Site in Taiwan	840
Ming-Tung Chuang, Chuang-Te Lee and Neng-Huei Lin	
Quantifying the Black Carbon Reduction during the 2008 Olympic Games in Beijing, China	841
Yang Yu, Kuang Cen, Stefan Norra, Nina Schleicher and Mathieu Fricker	
The Research on the CCN Activation of Aerosols in Shanghai	842
Chunpeng Leng and Tiantao Cheng	
Strong Absorption Associated with Coarse Mode Particles over CTCZ Region: Results from Aircraft Experiment 2009.....	846
J. Jai Devi, Priya Choudhry, Marykutty Michael, S.N. Tripathi and Tarun Gupta	
Particulate Mercury and Gas-solid Partition of Gaseous Elemental Mercury in Kaohsiung Area	847
Yi-Shiu Jen, Chung-Shin Yuan and Chang-Gai Lee	
Numerical Investigation of Electrostatic Effect on Indoor Particle Resuspension Due to Human Activity	848
Xinyu Zhang, Goodarz Ahmadi, Jing Qian, Andrea Ferro and Lin Tian	
Aircraft Measurements of Aerosol Composition over Eastern Coastal, Yangtze River Areas and Pearl River Delta of China	854
Lihong Ren, Wei Wang, Jianhua Chen, Hongjie Liu and Renjian Zhang	
Investigation of Indoor Air Quality in Children's Day Care Centers in Korea	855
Hyeun Jun Moon and Soo Hyeun Yang	
Characteristics and Sources of Elements in Atmospheric Particles before and in Heating Period of Beijing	862
Lingda Yu, Guangfu Wang, Guanghua Zhu and Renjiang Zhang	
Emission of Particulate Polycyclic Aromatic Hydrocarbons from Various Combustion Sources in China.....	868
Xinghua Li, Shuxiao Wang, Duan Lei and Jiming Hao	
Components of PM _{2.5} and its Source Apportionment by PFA from 2000 to 2001 in Shanghai.....	869
Guangli Xiu, Qi Ying, Donald Lucas, Koshland and Danian Zhang	
Different Characteristics of Carbonaceous Components in Size-Segregated Particles between a Roadside and a Suburban Site.....	870
Linfa Bao, Masami Furuuchi, Mitsuhiro Hata and Kazuhiko Sakamoto	
Size Distribution and Chemical Composition of PM _{1.0} , PM _{2.5} and PM ₁₀ in the	

Table of Contents

Industrial City in Korea	871
Minkyun Kim	
Carbonaceous, Inorganic, some Molecular Markers and Stable Isotopic Compositions in the Mumbai Aerosols for the Implications of their Sources and Atmospheric Processing.....	872
Shankar G. Aggarwal, Kimitaka Kawamura, Govindraj S. Umarji, Eri Tachibana, Rashmi S. Patil and Prabhat K. Gupta	
Metals in Aerosol as Potential Tracers for Waste, Fossil Fuel, Biomass/Biofuel Burning and Dust Sources	873
Shankar G. Aggarwal, Sudhanshu Kumar, Rajeev K. Saxena, Khem Singh, and Prabhat K. Gupta	
Fine and Coarse Particle Mass Distributions in New Delhi	874
Khem Singh, Arvind K. Jha, Shankar G. Aggarwal, Z. H. Khan and Prabhat K. Gupta	
Characteristics and Source Regions of the Biomass Burning Tracer Levoglucosan in Spring at four Background Sites in South China	875
Zhisheng Zhang, Chuen-Yu Chan, Guenter Engling, Xuefang Sang and Ting Zhang	
Characterization of Water-soluble Organic Carbon in Ash Samples from a Coal Combustion Boiler	876
Seung Shik Park, Ja-Hyun Kim and Jae-Uk Jeong	
Characterization of Hydrophilic and Hydrophobic Fractions of Water-soluble Organic Carbon in PM _{2.5} at an Urban Site	877
Seung Shik Park, Jae-Uk Jeong and Ja-Hyun Kim	
The Study for Inorganic Compounds in Ambient Aerosols by FTIR in Hefei..	878
Xiuli Wei, Minguang Gao, Jianguo Liu, Yihuai Lu, Wenqing Liu, Bei Wang, Liang Xu and Tianshu Zhang	
Observational Study of Black Carbon in Urumqi in Winter of 2009	879
Xin-chun Liu, Yu-ting Zhong, Qing He, Mamtimin Ali, Zhi-zhong Guo	
The Features of Ionic Components of TSP and Factors Analysis in Urumqi....	880
Qing He, Hao Yang, Xinchun Liu and Yuting Zhong	
Characteristics of Chemical Compositions and Sources of PM ₁₀ in Resuspended Dust in Taiyuan, Changzhi and Jincheng City.....	881
Pengjiu Zhang, Lin Peng, Ling Mu, Ying Wang and Haodong Ji	
Chemical Characterization of Water-soluble Organic Carbon Aerosol by Group Separation Method of a XAD Resin	889
Jae-Uk Jeong, Ja-Hyun Kim, Seung Shik Park, K.-J. Moon and Seok Jo Lee	

Table of Contents

Insights into Summer Haze Pollutants over Shanghai Based on Aerosol Water-soluble Ionic Composition.....	890
Huanhuan Du, Lingdong Kong, Tiantao Cheng, Jianmin Chen, Ling Li and Jianfei Du	
Particulate Matter Source Apportionment Based on a Back Trajectory Model during the Episodes in Central Taiwan	891
Chien-Lung Chen, San-Fu Lee, Feng-Chao Chung, Su-Ching Kuo, Jeng-Lin Tsai, Pei-Hsuan Kuo, Li-Ying Hsieh and Ying I. Tsai	
Relationship between Aerosol and Visibility at an Urban Area in Southern Taiwan.....	892
Chien-Lung Chen, Feng-Chao Chung, San-Fu Lee, Li-Ying Hsieh and Ying I. Tsai	
Seasonal Characteristics of Dust Aerosol in three Cities of Northern China	893
Youbin Sun, Yan Yan, Lianji Liang, Hongyun Chen, Jianbo Zhao	
Sources, Solubility, and Deposition Fluxes of Trace Elements in Atmospheric Aerosols over the Yellow Sea.....	894
Tianran Zhang, Jinhui Shi, Xiaohong Yao and Huiwang Gao	
ESR Signal Intensity and Crystallinity of Quartz in Desert Surface Samples from three Major Asian Dust Sources	899
Hongyun Chen, Youbin Sun, Ryuji Tada, Dominik Weiss, Min Lin, Shin Toyoda and Yuko Isozaki	
Numerical Simulation of Nanoparticle Pattern Fabricated by Electrostatic Spray Deposition	900
Wei Wei, Sheng Wang, Zhaolin Gu, Takeshi Fukuda, Kiwamu Kase, Jungmyoung Ju, Yutaka Yamagata and Yusuke Tajima	
Size Distributions of Ambient Aerosol in the Vicinity of Semiconductor Plants	907
Chih-Chung Lin, Shui-Jen Chen, Jen-Hsiung Tsai, Kuo-Lin Huang and Chun-Li Chou	
Rare Earth Composite Materials for the Reduction of Ammonia in Biomass Gasification. Part 1. Synthesis and Structure Properties of the Catalyst	911
Chang-Mao Hung	
Emission Source of Atmospheric Ultrafine Particles Clarified by Simultaneous Sampling and Data Comparison with PM _{2.5}	916
Kazuhiko Sekiguchi, Masatoshi Kinoshita, Shinji Kudo, Kyung Hwan Kim, Seiyo O and Kazuhiko Sakamoto	
Chemical and Physical Characterization of Marine Aerosols on Board RV	

Table of Contents

Polarstern	923
Zhijun Wu, Katrin Mildenberger, Shan Huang, Friederike Höpne, Julia Wenzel, Susanne Fuchs, Laurent Poulain, Hartmut Herrmann, Alfred Wiedensohler and Min Hu	
Rare Earth Composite Materials for the Reduction of Ammonia in Biomass Gasification. Part 2. Reactivity and Characterization in Selective Catalytic Oxidation Processes	924
Chang-Mao Hung	
POSTER SESSION 2	
Structural Design Optimum of the Compound Electrostatic-bag Filter	930
Wenge Hao, Mengcheng Li and Yan Li	
A Facile One-Step Route to BiOBr-Graphene Composites and Their Enhanced Visible Light Photocatalytic Removal of Gaseous NO	941
Zhihui Ai, Lizhi Zhang and Shuncheng Lee	
The Effect of Atmospheric Parameters on Fine Particulate Concentration in the Suburbs of Shanghai	942
Jian Yao, Wei Liu, Wangkun Chen, Guanghua Wang, Xuebo Fan, Yanhong Geng, Nannan Wei, Youshi Zeng, Yu Huang and Jun Lin	
The Variation of PM2.5 Concentration under Different Weather Systems in Hangzhou Urban	949
Hong Shengmao and Jiao Li	
Energy Saving and CO ₂ Emission Reduction in the Refinery Furnace	950
Chien-li Lee, Yu-Shan Wang and Chih-Ju G. Jou	
The Influence of Aerosol Particles Emitted from Smoking and Candle Burning on the indoor Radon and Thoron Progeny Concentration	951
Jin Wang, Juan Liu and Yongheng Chen	
Mixing State Variations of Fine Dust Particles in Atmospheric Boundary Layer of Yellow Sea in Spring	952
Chengming Pang and Zifa Wang	
Simultaneous Measurement of Particle Optical Extinction and Scattering Using the CAPS PMSSA (Single Scattering Albedo) Monitor	953
Timothy B. Onasch, Paola Massoli, Paul L. Kebabian and Andrew Freedman	
Study on Collection Characteristic of Impactor with Single Nozzle for Different Particle Collecting Directions	960
C.H. Huang and S.W. Shen	

Table of Contents

Estimate of Air Exchange Rate Based on Aerosol Concentration Curve	961
Jin Wang, Oliver Meisenberg, Jochen Tschiersch, Juan Liu and Yongheng Chen	
Influence of Turbulent Diffusion in an Electrical Mobility Spectrometer	962
Jaan Salm, Panich Intra, Artit Yawootti and Nakorn Tippayawong	
Effects of Biodiesel and Engine Load on Nanoparticle Emissions from a Heavy-Duty Diesel Engine	967
Yi-Jyun Liou, Li-Hao Young, Man-Ting Cheng, Hsi-Hsien Yang, Ying I. Tsai and Lin-Chi Wang	
Sand Emission Rate Study in Wind Tunnel by Particle Image Velocimetry	973
Xiaohui Lv, Lei Guo and Ning Huang	
Wind Tunnel Study on Aeolian Farmland Soil Movement	980
Ning Huang and Lei Guo	
Environmental Benefit to Enhance the Dust Filtration in a Subway Ventilation Chamber	987
Huang shan, Hyun Hee Lim, Ju Yeol Lee and Young Min Jo	
Field Observation of the Hygroscopic Properties of the Ambient Aerosols in Beijing.....	993
Jian-hua Chen, Xuan Wang, Wenjie Zhang, Jianmin Chen, Xingnan Ye, Hongjie Liu, Wen Yang, Wei Wang and Jianguo Deng	
Unsteady SO ₂ Absorption by a Moving Water Aerosol with Chemical Dissociation.....	994
Ke-Miao Lu, Wei-Hsin Chen, Yuan-Yi Chen, Chen-I Hung, Wen-Jhy Lee and Ta-Chang Lin	
Long-range Transport of Aerosols to the Central Tibet, China, a Case Study Using Ground and Satellite Remote Sensing Data	1001
Xiangao Xia	
An Experiment on Energy Reduction of an Exhaust Air Heat Recovery Type Outdoor Air Conditioning System for Semiconductor Manufacturing Clean Rooms	1002
Kyung-Hoon Yoo, Gen-Soo Song, Hyung-Tae Kim, Seung-Woo Son and Dug-Jun Park	
Particle Deposition on a Semiconductor Wafer Larger than 300 mm	1009
Kyung-Hoon Yoo, Gen-Soo Song, Hyung-Tae Kim and Kun-Hyung Lee	
Particle-Free Atomic Layer Deposition of Transparent Conductive Oxide on Flexible Substrate.....	1015
Kyung-Hoon Yoo, Gen-Soo Song and Hyung-Tae Kim	

Table of Contents

Comparative Study on Steam Humidification Type and Water Spray Humidification Type Outdoor Air Conditioning Systems for Semiconductor Manufacturing Clean Rooms	1019
Kyung-Hoon Yoo, Hyung-Tae Kim, Gen-Soo Song, Seung-Woo Son and Dug-Jun Park	
Scavenging of Sea-salt Aerosol by Snow in Niigata Prefecture, Japan.....	1024
Shin Ohara, Shin-ichi Fujita, Soichiro Sugimoto, Gaku Sakata and Akira Takahashi	
Heterogeneous Nucleation of Water Vapor onto Nanoparticles.....	1031
Shusuke Nakajima, Yusuke Kuromiya, Yoshio Otani and Takafumi Seto	
Durability Investigation of Carbon Supported Platinum Electrocatalysts Synthesized by Microwave Polyol Method	1036
Yu-Chun Chiang, Jinxiao Zhao, Jhao-Ruei Ciou, Zhaoping Zhong and Shih-Yu Lin	
A Dynamic Aerosol Generation System for Aerosol Sensor Calibration.....	1043
Qiaoling Liu and Da-Ren Chen	
The Advanced Aerosol Neutralizer	1047
Markus Gaelli, Stan Kaufman, Philip Poeschl and Rob Caldow	
Experimental Study of Axial-flow Cyclone in the Air Handing Unit	1048
Seyoung Kim, Soon-Bark Kwon, Duck-Shin Park, Youngmin Cho, Joon-Goo Kang, Chang-Heon Shin, Myungjoon Kim and Taesung Kim	
Exhaust of Air Flow and Fine Particles from a Tunnel using an Air Curtain near a Ventilation Opening	1054
Bangwoo Han, Hak-Joon Kim, Yong-Jin Kim, Sang-Hyeon Jeong, Yong-Min Kim and Jong-Ryul Kim	
Reactions of CaCO ₃ Sorbent Particles at an O ₂ /CO ₂ Atmosphere	1055
Seongha Jeong, Kang Soo Lee, Sang In Keel and Sang Soo Kim	
Surface Area and Size Distribution Measurements for Nanoparticles Generated from Nanopowders by a Small-Scale Powder Disperser	1063
Chi-En He, Chun-Nan Liu, Sheng-Chieh Chen, Cheng-Yu Huang, Chun-Wan Chen, Cheng-Ping Chang and Chuen-Jinn Tsai	
The Influence of Various Sorbent Properties to Remove SO ₂ in Fluidized Bed Reactor	1065
Young-Ok Park, Jei-Pil Wang and Yong-Ha Kim	
Simultaneous Removal Characteristics of Fine Particulate and Elemental Mercury in Integrated Particulate Collector	1071
Young-Ok Park and Ju-Yeong Jeong	

Table of Contents

Characteristics of Aerosol Droplets Generated by Cough Simulator	1076
Soon-Bark Kwon, Jae-Hyoung Park, Youngmin Cho, Wotae Jeong, Duck-Shin Park and Gwi-Nam Bae	
Dry Adsorption of CO ₂ by Granular Sorbents	1083
Yun Hui Lim, Huang Shan, Hyun Hee Lim and Young Min Jo	
Evaluation of Filtration Performance for Depth Filter Media using Different Standard Test Dusts	1090
Young-Ok Park and Naim Hasolli	
Removal Characteristics of SO ₂ in Absorbents Internal Circulating Desulfurization Equipment	1094
Young-ok Park and Hyun-Jin Park	
Formation of Non-Aggglomerated Titania Nanoparticles in a Flame Reactor	1099
Akihiro Ishibashi, Hirofumi Ozaki and Yoshiki Okada	
Numerical Analysis of Multi Axial-Flow Cyclone for AHU Pre-Filter in Subway Station	1100
Myungjoon Kim, Hojoong Kim, Soon-Bark Kwon, Seyoung Kim, Jin-Kwan Kim and Taesung Kim	
Submicron Diesel PM Removal Performance of an Electrostatic Filtration Device Combined with a Metallic Foam Filter.....	1106
Hak-Joon Kim, Bang- Woo Han, Yong-Jin Kim, Gyu-Baek Cho, Sang-Hyen Jung, Sung-Hoon Sim, Won-Suk Hong, Wan-Ho Shin and Tetsuji Oda	
Particle size control using flame spray pyrolysis with Emulsion	1107
Shin Ae Song, Dae Soo Jung and Seung Bin Park	
Fracturing of Nanoparticle Agglomerates by Supersonic Flow Impaction with a Laval Nozzle	1108
Masaki Yabuhana, Takeshi Kawabata and Yoshiki Okada	
Study of Aerosol Optical Properties over Shanghai	1111
Xuan Jia, Tiantao Cheng, Jianmin Chen and Yonghang Chen	
Electrostatic Collection of Fine Particles at High Temperature and High Pressure for Wastes Gasification.....	1115
Bangwoo Han, Hak-Joon Kim, Dong-Keun Song, Won-Seok Hong, Wan-Ho Shin, Han-Seok Kim and Yong-Jin Kim	
Efficiency of Dust Removal Device in Subway Cabin.....	1116
Jong Bum Kim, Soon-Bark Kwon, Duck-Shin Park, Youngmin Cho, Seok Namgoong, Tae-Woo Han, Kwanhyun Cho and Taesung Kim	
Fabrication of Polyurethane Nano Fibers by Electrospinning.....	1121

Table of Contents

Hyun-Jin Choi, Sang Bum Kim, Sung Hyun Kim and Myong-Hwa Lee	
Filter Cleaning of PTFE Coated Composite Filter	1122
Byung Hyun Park, Sang Bum Kim, Young Min Jo and Myong-Hwa Lee	
Deposition of Submicron Aerosols on both Sides of a Substrate Derived from Charged Droplets of Aqueous Suspension	1123
Masao Gen, Shin-ichi Sagawa, Hidehiro Kamiya and Wuled Lenggoro	
Capture of Particulate Matters and Odorous Species by In-flight Adsorbents	1124
Myong-Hwa Lee, Byung Hyun Park, Seong-Kyu Park and Sang-Jin Choi	
Reduction in Nanoparticle Formation by Ventilation for Ozonolysis of Volatile Organic Compounds Emitted from a Commercial Air Freshener	1125
Thai Phuong Vu, Sun-Hwa Kim, Seung-Bok Lee and Gwi-Nam Bae	
An Aerosol Generator System for Long-duration Exposures of Plants to Submicrometer-sized Particles.....	1126
W. Lenggoro, M. Gen, F.-Z. Lim, S. Ikawa, M. Yamaguchi and T. Izuta	
Diffuser Design for the Particulate Filter of Diesel Engine.....	1127
Jau-Huai Lu, Wei-Hsin Chang, Jhih-Wei Liao, and Hong-Jin Lin	
An Efficient Wetted-wall Venturi Scrubber with a Two Stage Throat	1128
Shin-You Chen, Hau-Chieh Lin, Fang-Tang Chang, Hung-Min Chein and Chuen-Jinn Tsai	
Hydrothermal Synthesis of TiO ₂ Nanostructured Arrays and Their Photocatalytic Activity for Methylene Blue Degradation in Microreactor	1130
N. Dech-rat, N. Viriya-empikul, K. Faungnawakij and V. Pavarajarn	
Fabrication of Core-Sheath Fibers by Electrospinning for the Formation of Flexible Carbon Nanofibers.....	1138
Chanwit Apibanborirak, Chinarat Tongtaow, Farkfun Duriyasart and Varong Pavarajarn	
The Feasibility Study for Silicon Determination in Airborne Particulate Matter using an Electrical Low Pressure Impactor and Laser Ablation/Inductively Coupled Plasma Mass Spectrometry	1144
Chu-Fang Wang , Yi-Kong Hsieh and Bing-Shen Yang	
Reactions of Calcium Carbonate Particles: Effect of Temperature, Residence Time, and Atmospheric Condition.....	1145
Kang Soo Lee, Jae Hee Jung, Seongha Jeong, Sang In Keel, Jin Han Yun and Sang Soo Kim	
Hygroscopicity of Benzoic acid Aerosol Particles at Room Temperature: Setup and First Applications of H-TDMA system.....	1146

Table of Contents

Yajun Shi, Maofa Ge and Weigang Wang	
Wind Speed Enhancement of Marine Aerosol Optical Depth	1147
S. Gerard Jennings, Jane P. Mulcahy, Claire Scannell, Darius Ceburnis and Colin O'Dowd	
Distribution Characteristics of nano-TiO ₂ Aerosol at Work Place	1155
Yi Yang, Ping Mao, Chun-lan Xu, Shou-wen Chen, Zheng-ping Wang and Jin-hua Zhang	
Skyradiometer Measurements for Monitoring Columnar Aerosol Properties in the Antarctic Research Program of Japan	1156
Masataka Shiobara, Hiroshi Kobayashi, Masanori Yabuki, Maki Yamano and Yoshitaka Muraji	
The Preliminary Study of Aerosol Leakage at Low Gas Leakage Situation ...	1157
Zhihong Zhang, Haijun Dang and Longbo Liu	
The Evaluation of Aerosol Monte Carlo Simulation undergoing Simultaneous Coagulation and Settling.....	1161
Longbo Liu and Lixing Zhang	
Uniform Coating of Multiple Layers on Particles by PCVD Process	1166
Hung-Cuong Pham and Kyo-Seon Kim	
Preparation of Nanostructured TiO ₂ Thin Films with Controlled Morphology by Aerosol Flame Deposition Process	1167
Jinrui Ding and Kyo-Seon Kim	
Synthesis of Multifunctional Nanoparticles with Tunable Magnetic and Optical Properties	1168
Kyo-Seon Kim and Dung T. Nguyen	
Plasma Chemical Vapor Deposition Method to Prepare Nano TiO ₂ Thin Films	1169
Kyo-Seon Kim and Nguyen Hoang Hai	
Modeling Study of Aerosol Indirect Effects on Climate with an AGCM-aerosol Coupled System	1170
Zhili Wang, Hua Zhang, Zaizhi Wang, Xiaoye Zhang and Sunling Gong	
Numerical Studies of Slip Correction in Low-pressure Impactor	1176
Junho Hyun, Yunhaeng Joe and Jungho Hwang	
Performance Test of a Two-staged Impactor for Morphology Analysis of Diesel Exhaust Particles.....	1180
Sang-Gu Lee, Junho Hyun and Jungho Hwang	
Preparation of PCBM Micro- and Nanoparticles via Electrohydordynamic Spray Route for Organic Photovoltaic Applications.....	1184

Table of Contents

Sung-Eun Park, Ji-woon Park, Sang-Yoon Kim and Jungho Hwang	
Characteristic of Charged Particle at Ansan Atmosphere.....	1191
Kang Ho Ahn and Hong Ku Lee	
Development and performance evaluation of Single Fiber MWCNT Generator	1192
Kang-ho Ahn, Sun-man Kim, Gun-ho Lee, Ji-hyun Lee and Il-je Yu	
The Measurement of Atmospheric Aerosol at Ansan, Korea	1193
Ha-Gue Chung, Kang-Ho Ahn and Young-Jun Yoon	
The Study of Number Concentration Measurement Method of Particles Generated by Laser Printer	1194
Ha-Gue Chung, Sun-Man Kim and Kang-Ho Ahn	
OTHERS	
Behavior of Inorganic Secondary Aerosols and Precursors during a Typical Haze Episode in Shanghai.....	1196
Yihua Zhang, Yusen Duan, Song Gao, Qingyan Fu, Haiping Wei, Fei Sha, Yan Cai	
Daytime Variation of PM2.5 Concentration in Street Canyons on Weak-Wind Summer Days.....	1197
Yun-Wei Zhang, Zhao-Lin Gu, Yan Cheng, Zhen-Xing Shen, Jun-Gang Dong and Shun-Cheng Lee	
Analysis of the PM10 concentration difference by different sampling methods at Gosan, Korea.....	1205
So Eun Shin, Jung Chang Hoonand Yong Pyo Kim	
Variability of Blowing Dust Weather Frequency over Semi-arid Areas of China (Baicheng, Jilin Province) and Relationships with Climatic Factors during 1951-2006	1206
Yun-Fei Wu, Ren-Jian Zhang, Cong-Bin Fu and Zong-Ting Gao	
Single Particle Analysis of Ambient Aerosols in Shanghai during World EXPO, 2010: Two Case Studies.....	1207
Shikang Tao, Hong Chen and Xin Yang	
Simulation of the Brownian Coagulation of Smoke Agglomerates in the Entire Size Regime using a Nodal Method.....	1208
Jae-Hark Goo	
Fuel based Emission Factors for Carbonaceous Particles from Commercial Ship Emissions	1209
Shao-Meng Li, Katherine Hayden, Ibraheem Nuemann, Eric Williams and	

Table of Contents

Robert McLaren

- The Long-term Variation of Haze Weather in Zhejiang Urban Areas 1210
Yu-wen Niu, Jun-qiang Gu, Jing-jiao Pu, Wen-juan Li and Jin-sheng Wu
Characterization of Individual Atmospheric Fine and Coarse Particles during Winter in Xi'an, China..... 1211

Tafeng Hu, Junji Cao and Zhenxing Shen

- The Chemical Composition of PM2.5 in Rural Areas of Shannxi, China 1212
Chongshu Zhu, Junji Cao and Ting Zhang
Optical, Microphysical and Chemical Properties of Aerosols: a Comparison between Foggy and Non-foggy Days over a Typical Location in Indo-Gangetic Plains 1213

D. S. Kaul, S. N. Tripathi and Tarun Gupta

- Correlation of Black Carbon Aerosol and Carbon Monoxide Concentrations Measured in the High-altitude Environment of Mt. Huangshan, Eastern China 1214

X.L.Pan , Y.Kanaya, Z.F.Wang, Y.Liu, P.Pochanart, H.Akimoto, H.B.Dong and J.Li

- Graphite Particle Generation in Steel Piles..... 1215

Zhipeng Chen and Suyuan Yu

- Particulate Matters and Associated Polycyclic Aromatic Hydrocarbons in Atmospheric Environment of Songkhla, Thailand in Relation to Rubber-wood Combustion..... 1216

P. Chaichana, S. Tekasakul, P. Tekasakul, M. Furuuchi and M. Hata

- Estimation of selected heavy metals in respirable size range particulates at New Delhi (India) 1222

Monika J Kulshrestha, Subhash Chandra and Nahar Singh

- Suzhou: Air Quality Real-time Monitoring System..... 1223

Francesco Petracchini, Catia Atturo, Marco Panunzi and Andrea Ceolin

- Gas-Particle Distribution of Polycyclic Aromatic Hydrocarbons (PAHs) from Rubber-wood Combustion 1224

J. Chomanee, M. Furuuchi, M. Hata, S. Tekasakul and P. Tekasakul

- Formation of Non-Agglomerated Titania Nanoparticles in a Flame Reactor.. 1225

Akihiro Ishibashi, Hirofumi Ozaki and Yoshiki Okada

- Particulate Pollutants Generated from Co-combustion of Biomass and Coal Fuels 1230

P. Saetiew, A. Suriyawong, M. Hata and M. Furuuchi

- Temperature Response of the Submicron Organic Aerosol from Temperate Forests..... 1231

Table of Contents

Richard Leaitch, Anne Marie Macdonald, Peter C. Brickell, John Liggio, Steve J. Sjostedt, Alexander Vlasenko, Jan W. Bottenheim, Lin Huang, Shao-Meng Li, Peter S.K. Liu, Desiree Toom-Sauntry, Katherine A. Hayden, Sangeeta Sharma, Nicole C. Shantz, H. Allan Wiebe, Wendy Zhang, Jonathan P.D. Abbatt, Jay G. Slowik, Rachel Y.-W. Chang, Lynn M. Russell, Rachel E. Schwartz, Satoshi Takahama, John T. Jayne and Nga Lee Ng	
On-road Emission Factor Distributions of Individual Diesel Vehicles in Beijing and Chongqing, China	1232
Xing Wang, Dane Westerdahl, Ye Wu and K Max Zhang	
The Evaluation of PM _{2.5} by Filter Based and Continuous Measurements in Cincinnati, Ohio	1233
Carlos Pacas, Xianlie Wan, Mingming Lu, and Anna Kelley	
Dry Deposition of Sulfate on Actual Foliar of Quercus Serrata	1234
Hiroshi Hara, Shogo Ota, Yuki Kimura, Kyo Kitayama, and Sonoko Drothea Kimura	
Contribution of New Particle Formation to Cloud Condensation Nuclei in the Beijing Megacity.....	1235
D.L. Yue, M. Hu, R.Y. Zhang, Z.J. Wu, H. Su, Z.B. Wang, J.F. Peng, L.Y. He, X.F. Huang, Y. G. Gong and A. Wiedensohler	
Experimental Investigation of Transient CaCO ₃ Scale Formation in Commercial 90/10 Cu/Ni Tubes	1240
M. IZADI, D.K. AIDUN, P. MARZOCCA and L. TIAN	
Are Volatile Organic Components Responsible for Driving the Oxidative Capacity of Combustion Generated Particles	1241
Zoran Ristovski, Branka Miljevic, Nicholas Surawski, Svetlana Stevanovic, Steve Bottle and Richard Brown	
The Study on Vertical and Temporal Variation of PM10 of Yantaqu in Xi'an During Spring.....	1242
Jingbo Zhao, Lan Yao, Na Xu, Zhenzhen Mu and Yuxia Li	
Emission and transport of carbonaceous aerosol in coastal and urban areas in China	1243
Bing Chen, Ke Du, Yang Wang and Jinsheng Chen	
Observational and Modeling Studies of the Impacts of Indian Summer Monsoon Circulation on Spatiotemporal Distributions of East Asian Aerosols	1245
Xiaodong Liu, Libin Yan, Ping Yang, Zhi-Yong Yin and Gerald R. North	
A Significant Contribution of Aerosol and Dust to Lake Qinghai, NE Tibetan Plateau.....	1246

Table of Contents

Zhangdong Jin and Fei Zhang	
Parameters Influencing Analytical Reliability of Sulfur Speciations in Aerosol Samples Using Sulfur K-Edge X-Ray Absorption Near-Edge Structure (XANES)	1247
Siwatt Pongpiachan, Warangkana Na Phatthalung, Wantana Klysubun, Kanjana Thumanu, Kin Fai Ho and Junji Cao	
Carbonaceous and Ionic Components of Atmospheric Fine Particles in Beijing and its Impacts on Atmospheric Visibility	1248
Jiamao Zhou, Renjian Zhang and Junji Cao	
Contrastion and Investigation of Air Quality in Winter and Summer in the Portary Storage-room of Museum of Terra-Cotta Army of Qin Dynasty	1249
Hua Li, Junji Cao, Yuan Gao and Bo Rong	
Characterization of Carbonaceous Aerosol and Gaseous Pollutants over Urban Air, India	1250
S. Tiwari, D.S. Bisht, A.K. Srivastava, P. Pragya and P.D. Safai	
Community Composition and Granularity Distribution of Airborne Bacteria in Summer in Guangzhou	1251
Chaojie Song, Qiming Tan, Xianliang Chen, Rongjie Shi and Xinyu Chen	
Emission of Primary Carbonaceous Aerosol and Formation Pathways of Secondary Organic Aerosol in the PRD.....	1252
Nan Li, Tzung-May Fu, Junji Cao, Nanying Cao, Shuncheng Lee and Junyu Zheng	
Elemental Characteristics of Fine-grained (<16 µm) Surficial Samples from Major Asian Dust Source Regions	1253
Feng Wu, Youbin Sun, Ryuji Tada, Junji Cao, Yuko Isozaki, Hongyun Chen	
Characterization and Conditioning of Fly Ashes Collected from Petroleum Coke Circulating Fluidized Bed Combustor	1254
Li-Chi Liu, Hong-Ying Tseng and Hsiu-Po Kuo	
3-dimensional Simulation of Micro Virtual Impactor.....	1255
Y.H. Joe and J. Hwang	
Characteristics and Cytotoxicity of Coarse, Fine and Ultrafine Particles Exhausted from the Stack Gas of a Municipal Solid Waste Incinerator	1263
Yu-Feng Kuo, Yuh-Jeen Huang, Ting-Shin Fan and Yi-Siou Chen	
Characteristics of Sized-resolved Anhydrosugars and Pollutants Derived from Rice Straw Burning in Controlled Chamber	1264
Chih-Jen Chuang, James J. Lee and Jian-Li Lin	
Variation and Key Reactive Species of Ambient VOCs in the Urban Area of	

Table of Contents

Shanghai, China	1266
Leiyan Su, Hongli Wang, Changhong Chen, Cheng Huang, Li Li, Min Zhou, Yuezhen Qiao and Yiran Chen	
Real-time Characterization of Particle-bound Polycyclic Aromatic Hydrocarbons at a Heavily Trafficked Roadside Site	1267
Y. Cheng, K. F. Ho, S. C. Lee, Y. B. Peng, Y. M. Han, G. H. Wang, F. Wu, Y. Huang, Y. W. Zhang and P. S. Yau	
Atmospheric Organic Carbon and Elemental Carbon in a Typical Semi-arid Area of Northeastern China in Spring	1268
Renjian Zhang, Jun Tao, K. F. Ho, Junji Cao, Suixin Liu and Zhenxing Shen	
The Observational Characteristic of Aerosol Number Concentration and Size Distribution at Shijiazhuang in Spring Season	1271
Lianji Jin and Qingfei Zhai	
Chemical Composition of TSP at Qinghai Lake Atmospheric Background Site in Summer, 2010	1272
Zhuzi Zhao, Junji Cao, Suixin Liu and Jiamao Zhou	
Measurement of Carbonyl Compounds in PM2.5 in Xi'an, China.....	1279
W.T. Dai, K.F. Ho, S.S.H. Ho and J.J. Cao	
Quantitive Role of INA Bacterial Aerosol in Initiating Heterogeneous Nucleation	1280
Yaling Wang, Rui Du and Ziming Li	
Analysis of the Diurnal Variation of Oxalic Acid in Aerosols by Desorption Electrospray Ionization Mass Spectrometry	1286
Xiu Wu, Juntao Huo, Hong Chen and Xin Yang	
Comparison of Key Air Pollutant (PM2.5) Sources and Their Source Strength over Two Consecutive Winter Seasons in Kanpur (India) Region.....	1287
Soumabha Chakraborty, Anil Kumar Mandariya and Tarun Gupta	
Chemical Composition and Seasonal Variation of PM2.5 Aerosols at Hyderabad (India)	1288
L.A.K. REDDY, J. SATYANARAYANA, MONIKA J KULSHRESRHA , R N RAO I and U C KULSHRESTHA	
Direct & Indirect Radiative Forcing Simulation Study using WRF_Chem Model	1289
Fenjuan Wang and Hua Zhang	
Climate Influences on Optical Characteristics of Aerosols Over The Arabian Gulf	1290

Table of Contents

Fatma Hasan, Hala K.Al-Jassar and Kota S. Rao	
Sampling Method Evaluation for Measurement of Solid Particle Number	
Distributions from Marine Diesel Engines and Fuels.....	1291
Jørgen B. Nielsen and Sergey Ushakov	
Characteristics of Ultrafine Particles Emitted from Compression Ignition Engines	
.....	1292
Xinling Li, Wei Liu and Zhen Huang	
Source Apportionment of Ambient PM10 using Linear Regression and Chemical	
Mass Balance	1293
Shamsh Pervez, Neha Dubey and Yasmeen Pervez	
Source Apportionment of Particulate Toxic Load and their Biomarkers among	
Workers of Steel Re-rolling and Rice Mills	1294
Yasmeen Pervez, James Methew and Shamsh Pervez	
Characteristics, Sources and Long-range Transport of Heavy Metals of Aerosols	
over China	1295
Rong Zhang, Guoshun Zhuang, Juan Li, Kan Huang, Qiongzenh Wang,	
Chang Xu, Yilun Jiang and Ying Chen	
Vertical Structures of PM10 and PM 2.5 and their Dynamical Characters in Low	
Atmosphere in Beijing Urban Area	1296
Guoan Ding, Zhenyu Chen, Zhiqiu Gao, Wenqing Yao and Xinghong Cheng	
An Overview of the Measurements of the Scattering, Absorption and	
Hygroscopic Growth of Aerosols in the Rural Areas of Eastern China	1298
Peng Yan and Xiuji Zhou	
An Aerosol Dipole Event over the Tropical Indian Ocean during 2006	1299
P.R.C.Rahul, P.S.Salvekar and P.C.S.Devara	
Concentrations and Composition of PAHs in Urban Environment of Hong Kong	
.....	1306
Kin Fai Ho, Yan Cheng, Steven Sai Hang Ho, Shun Cheng Lee and Linwei	
Tian	
Relationship between PM Concentrations and Visibility at an Urban Area in	
Southern Taiwan	1307
Chien-Lung Chen, Feng-Chao Chung, San-Fu Lee, Li-Ying Hsieh, Su-Ching	
Kuo and Ying I.Tsai	
Particulate Matter Source Apportionment based on a Back Trajectory Model	
during Episode Days in Central Taiwan	1311
Chien-Lung Chen, San-Fu Lee, Feng-Chao Chung, Su-Ching Kuo, Jeng-Lin	
Tsai, Pei-Hsuan Kuo, Li-Ying Hsieh and Ying I. Tsai	

Table of Contents

Measurement of Near-road Black Carbon Emissions in an Urban Setting in Midwestern US	1316
Jiangchuan Hu, Shuang Liang, Mingming Lu, Tim C. Keener, Zhuo Yao and Heng Wei	
Pollutant Emissions from a Non-road Source with a B20 Biodiesel Blend	1317
Lora Monti , Zifei Liu and Mingming Lu	

Recent Developments in Nanoparticle Filtration Research

David Y.H. Pui

University of Minnesota

Principal Contact: David Y.H. Pui, Distinguished McKnight University Professor, University of Minnesota

Abstract

Filtrations is key to providing clean air, clear water and clean high-tech products, which will advance global well-being by protecting human health and the environment. Filtration is one of the principal means to mitigate nanotech workers' exposure to the accidental release of nanoparticles, and is also used to collect valuable nanoparticle products from reactors. It is therefore a cornerstone toward the sustainable nanotechnology. Baghouse filters are used in collecting particulate emissions from coal-fire power plants. High purity filters are used in the semiconductor and pharmaceutical clean rooms to protect sophisticated and high-value products. New challenges emerge for developing filters for protecting health care workers and the public in episodes of pandemic influenza. New composite filters that incorporate nanofiber, electret fiber, and membrane technologies are developed to meet these challenges. Aerosol scientists can contribute by developing advanced models to facilitate novel filter designs and experimental systems to evaluate filters for these novel applications.

Integrative approach to filtration research is needed to meet the demand of modern filtration requirements. At the Center for Filtration Research (CFR), consisting of ten filter manufacturers and end users, we combine knowledge from several interdisciplinary fields, e.g., powder, aerosol and liquid filtration technologies, to meet the challenges in the filtration of vehicle emissions, biological particles, engineered nanoparticles, and the removal of volatile organic compounds. Examples will be given to show how we apply knowledge in powder technology to model aerosol soot loading, how we apply aerosol technique to evaluate liquid-borne particle filtration, how we disperse liquid-borne engineered nanoparticles and bioparticles using aerosol technique for filtration efficiency evaluations. We will present several topics of nanoscale filtration performed in CFR. Numerical models have been established to simulate the performance of the nanofiber composite filters and the filtration of carbon nanotubes (CNTs)and nanoparticle agglomerates. New methodologies have been developed to disperse airborne CNTs for challenging filters and for evaluating their toxicities. A new instrument, the Universal Nanoparticle Analyzer (UNPA), has been developed to perform fast and online measurement of gas-borne nanoparticle agglomerates. New model and experimental schemes have been developed to evaluate nanoparticle penetration through garment fabrics at zero/finite flow conditions.

David Y. H. Pui, a Distinguished McKnight University Professor, is the L.M. Fingerson/TSI Inc Chair in Mechanical Engineering and the Director of the Particle Technology Laboratory and of the Center for Filtration Research, University of Minnesota. He has a broad range of research experience in aerosol science and technology and has over 205 journal papers and 20 patents. He has developed/co-developed several widely used commercial aerosol instruments. He organized several successful international aerosol conferences/symposia to promote research cooperation especially among young scientists. Dr. Pui is a fellow of the American Society of Mechanical Engineers (ASME) and an inaugural fellow of the American Association for Aerosol Research (AAAR), and is a recipient of the Smoluchowski Award (1992), the Max Planck Research Award (1993), the International Aerosol Fellow Award (1998), the Humboldt Research Award for Senior U.S. Scientists (2000), and the David Sinclair Award (2002). He received the Fuchs Memorial Award (2010) at the International Aerosol Conference in Helsinki, conferred jointly by the American, German and Japanese aerosol associations.

Weight of Evidence Approach for Source Apportionment Studies

John G. Watson and Judith C. Chow

Desert Research Institute, 2215 Raggio Pkwy, Reno, NV 89512 USA

Principal Contact: John G. Watson, Research Professor, Desert Research Institute, 2215 Raggio Pkwy, Reno, NV 89512, USA.

Tel: +1 775 674 7046 Fax: +1 775 674 7009 Email: john.watson@dri.edu

Abstract

Since software became available for effective variance (EV), Positive Matrix Factorization (PMF), and UnMIX solutions to the Chemical Mass Balance (CMB) equations, many articles and reports have been issued on source contributions to high particulate matter (PM) and volatile organic compound (VOC) concentrations in Asian cities. Many of these studies omit the process of stressing the model results. In particular, few comparisons are made between PMF- and UnMIX-derived source factors and measured source profiles. Influential species that are not recognized markers often provide a mathematical solution, but one that is at odds with real-world source contributions. Examples are given of these results, and suggestions are made concerning how a modeler should build a “weight of evidence” that uses all of the solutions to the CMB equations as well as reconciling results with pollutant transport patterns and emission inventories. An iterative process is outlined that demonstrates how the evidence can be improved to formulate more accurate emission reduction strategies.

Keywords: Receptor Model, Weight of Evidence, Source Apportionment, VOC, PM

The present and potential future atmospheric environment issues in China

Xuexi Tie

Institute of Earth Environment, Chinese Academy of Sciences, Xi'an, Shaanxi, 710075, China

Principal Contact: Xuexi Tie, Prof., Institute of Earth Environment, Chinese Academy of Sciences, Xi'an, Shaanxi, 710075, China.

Tel:

Abstract

The key issues of the present environmental issues are illustrated in the talk. The main concerns are the high aerosol particle concentrations and their impacts on atmospheric environment, including poor visibility, human's health, and ecosystem in China. There are several key issues related to the aerosol pollution, such as (1) the interaction between natural (mineral dust, biomass burning, biogenic emissions) and anthropogenic aerosols (industrial, automobiles, and human activities, etc); (2) the different aerosol impacts between eastern (high urbanization area) and western China (large mountain glaciers)

Estimation of the impact of natural and anthropogenic aerosols on air quality and climate change in East Asia using a regional model

Masayuki Takigawa

Japan Agency for Marine-Earth Science and Technology, 3173-25 Showa-machi, Kanazawa-ku, Yokohama, Kanagawa 236-0001, JAPAN.

ABSTRACT

We have developed a one-way nested global regional chemical transport model (CTM) to estimate the radiative and chemical impact of natural and anthropogenic aerosols in East Asia. The global CTM is based on the CHASER (chemical atmospheric global general circulation model for study of atmospheric environment and radiative forcing) model, while the regional part is based on the WRF (weather research and forecasting) / Chem model. The model is online model, that means feedbacks among gaseous chemical species, aerosols, radiation, and dynamics are taken into account in the model. Emissions of mineral dusts and sea-salt aerosols are estimated by using the ground-level wind fields and land-surface temperature and moisture calculated at each time step of the model. Temporal variation of PM 10 calculated by the model is qualitatively reproduced the observed variation at Beijing, and shows clear increase following to the dust event in April 2006. The source region of dust aerosol event in this period was estimated to be Gobi and Taklimakan desert. The radiative impact of aerosols on shortwave radiation at surface and the top of atmosphere is also estimated, and it is found that the impact of BC is quite large to the shortwave radiation at the surface.

KEYWORDS

Aerosol, mineral dust, surface ozone, regional chemical transport model

Introduction

East Asia is a region in which anthropogenic emissions are considered to be rapidly increasing and are predicted to increase further^{[1],[2]}. Thus, it is quite important to estimate the concentration of ozone and aerosols and their impact on the regional climate over East Asia for the prediction of air quality over downstream region such as Japan, and such an outflux from East Asia can affect to the ozone concentration on a global scale^[3]. For this purpose, we have developed a one-way nested global-regional CTM and conducted one-year simulation.

Model description

A global–regional CTM has been developed based on the CHASER^[4] and the WRF/Chem^[5]. The global CTM part is based on the CHASER model, which is based on CCSR/NIES/FRCGC atmospheric general circulation model (AGCM) version 5.7b. The basic physical and dynamical features of the model has been described by Hasumi et al. (2004)^[6], and modifications of the chemical and dynamical features have been described in Takigawa et al. (2005)^[7]. Spectral coefficients are triangularly truncated at wavenumber 42 (T42), equivalent to a horizontal grid spacing of about 2.8°. The model has 32 vertical layers that are spaced at approximately 1-km intervals in the free troposphere and lower stratosphere. The regional CTM part is based on WRF/Chem. The gas–phase chemistry in the model followed the Regional Acid Deposition Model version 2 (RADM2) method^[8]. The aerosol chemistry is based on Modal Aerosol Dynamics Model for Europe (MADE) / Secondary Organic Aerosol Model (SORGAM)^[9,10]. Emission of mineral dust is based on Shaw et al., (2008)^[11] with small modifications of aerosol properties based on observations in East Asia. Anthropogenic surface emissions over East Asia were taken from the Regional Emission Inventory in Asia (REAS)^[2] with 0.5°×0.5° resolution, and surface emissions over Russia were obtained from the Emission Database for Global Atmospheric Research (EDGAR)^[12] 2000 with 1°×1° resolution. Biomass burning emissions, especially those from crop residues burning, are very important as sources of ozone precursors in China^[12]. We therefore also took monthly–mean biomass burning emissions data from EDGAR2000. The diurnal variations of anthropogenic surface emissions are parameterized in emissions from REAS and EDGAR2000 following the averaged variations of the Japan Clean Air Program (JCAP; K. Murano, personal communication). The horizontal resolution for regional CTM is 40 km over East Asia. The regional CTM had 31 vertical layers up to 100 hPa, with 11–12 layers at a height of 0–2 km from the surface. We note here that both the regional and global CTMs are “online” models. This means that the transport of chemical species is performed using the same vertical and horizontal coordinates with the meteorological part of the model, and the same physics parameterization with no interpolation in time. The system was driven by meteorological data from the National Centers for Environmental Prediction (NCEP). The lateral boundary of the regional CTM part was taken from the output of the global CTM with the horizontal resolution of approximately 2.8°. The maximum height of the global CTM was approximately 45 km, and the intrusion of airmass from the stratosphere could be captured by the model. The lateral boundary was updated every 6 hours and linearly interpolated for each time step. We did not take feedback from the regional CTM to the global CTM part. In other words, we performed a one–way nesting calculation between the global and regional CTMs.

Results

To estimate the chemical and radiative impact of aerosols, a one-month calculation has been conducted for April 2006. Figure 1 shows the temporal variation of PM 10 at Beijing in April 2006. Eventual increase of PM10 can be found from 17 to 19 and 22 to 24 April in the observation. Especially on 18 April, PM 10 concentration exceeded 1200 $\mu\text{g}/\text{m}^3$. The model quantitatively reproduced these eventual increases, and it was found that there was corresponding increase of soil aerosols during these periods. It was estimated that over 90% of PM 10 on 19, 22, 23, and 24

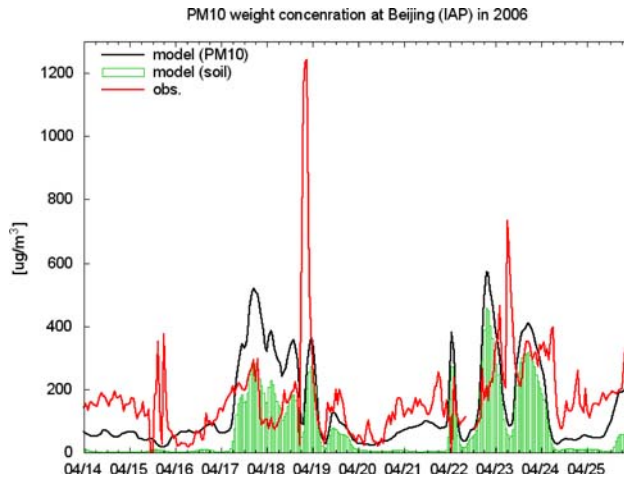


Figure 1 : Temporal variation of PM10 at Beijing in April 2006. Observed PM10 (red line), modeled PM10 (black line), and modeled mineral dust (green bars) are shown. Units are g/m³.

April was

mineral dust. The model showed large emission of mineral dust on 18-19 April at Taklimakan desert, and it was estimated that 0.2 Tg of mineral dust was released. For the later event, the model showed 0.3 Tg was emitted at Taklimakan on 22 April, and 0.2 Tg was emitted at Gobi on 23 April. The model failed to reproduce the eventual increase on 18 April. The possible cause of this increase was the local dust around Beijing, not from the desert area.

The radiative impact of aerosols was estimated by using the offline model based on radiative module of WRF/Chem. The effect of each kind of aerosols was estimated, but the effect of mixture is not taken into account for this estimation. Figure 2 shows the shortwave radiation change at the surface caused by each aerosol in April 2006, averaged over the North China Plain. It was found that the largest change was caused by black carbon, and it was estimated the maximum value was 20 W/m². The impact of sulfate and nitrate on shortwave radiation at the surface was estimated around 5 W/m². Soil dust showed large impact when dust event was occurred. For example, the maximum value was estimated to be 20 W/m² on 18 April, when a large dust event was occurred.

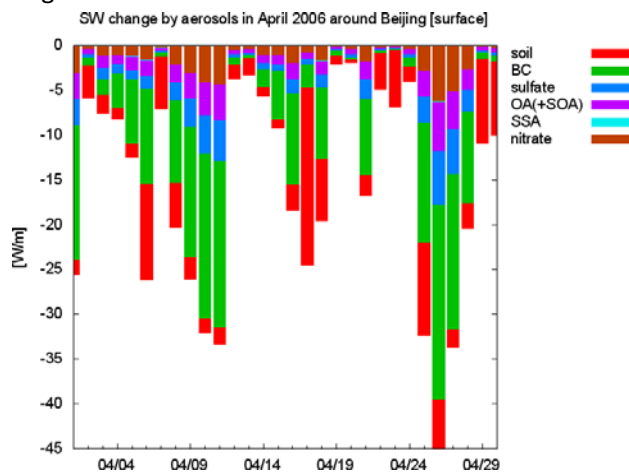


Figure 2: Estimated change of shortwave radiation caused by aerosols, averaged in the North China Plain. Units are W/m².

SUMMARY

We have developed a one-way nested global-regional CTM to estimate the radiative and chemical impact of natural and anthropogenic aerosols in East Asia. Temporal variation of PM 2.5 calculated by the model is qualitatively reproduced the observed variation at Beijing, and shows clear increase following to the dust event in April 2006. The source region of dust aerosol event in this period was estimated to be Gobi and Taklimakan desert. The radiative impact of aerosols on shortwave radiation at surface and the top of atmosphere is also estimated, and it is found that the impact of BC is quite large to the shortwave radiation at the surface.

ACKNOWLEDGMENTS

The author would like to thank Prof. Zhang for offering observational data of PM 10 at Beijing.

REFERENCES

- [1] Akimoto, H., 2003: Global air quality and pollution. *Science*, 302, 1716–1719.
- [2] Ohara, T., H. Akimoto, J. Kurokawa, et al., 2007: Asian emission inventory for anthropogenic emission sources during the period 1980–2020. *Atmos. Chem. Phys.*, 7, 4419–4444.
- [3] Wild, O., M. J. Prather, H. Akimoto, et al., 2004: Chemical transport model ozone simulations for spring 2001 over the western Pacific: Regional ozone production and its global impacts. *J. Geophys. Res.*, 109, doi:10.1029/2003JD004041.
- [4] Sudo, K., M. Takahashi, J. Kurokawa, et al., 2002: CHASER: A global chemical model of the troposphere 1. Model description. *J. Geophys. Res.*, 107, doi:10.1029/2001JD001113.
- [5] Grell, G. A., S. E. Peckham, R. Schmitz, et al., 2005: Fully coupled "online" chemistry within the WRF model. *Atmos. Environ.*, 39, 6957–6975.
- [6] Hasumi, H., S. Emori, A. Abe-Ouchi, et al., 2004: *K-1 Coupled GCM (MIROC) Description*. Technical report, CCSR, Kashiwa, Chiba, Japan.
- [7] Takigawa, M., K. Sudo, H. Akimoto, et al., 2005: Estimation of the contribution of intercontinental transport during PEACE campaign by using a global model. *J. Geophys. Res.*, 110, doi:10.1029/2005JD006226.
- [8] Stockwell, W., P. Middleton, J. Chang, et al., 1990: The second-generation regional acid deposition model chemical mechanism for regional air quality modeling. *J. Geophys. Res.*, 95, 16343–16367.
- [9] Ackermann, I.J., H. Hass, M. Memmesheimer, A. Ebel, F.S. Binkowski, and U. Shankar, 1998: Modal aerosol dynamics model for Europe: Development and first applications, *Atmos. Environ.*, 32, 17, 2981–2999.
- [10] Schell B., I.J. Ackermann, H. Hass, F.S. Binkowski, and A. Ebel, 2001: Modeling the formation of secondary organic aerosol within a comprehensive air quality model system, *J. Geophys. Res.*, 106, 28275–28293.[10]
- [11] Shaw, W.J., K.J. Allwine, B.G. Fritz, F.C. Rutz, J.P. Rishel, and E.G. Chapman, 2008: An evaluation of the wind erosion module in DUSTTRAN, *Atmos. Environ.*, 42,

Doi:10.1016/j.atmosenv.2007.11.022.

- [12] Olivier, J. G. J., A. F. Bouwman, C. W. M. Van der Maas, et al., 1996: Description of EDGAR Version 2.0. A set of global emission inventories of greenhouse gases and ozone-depleting substances for all anthropogenic and most natural sources on a per country basis and on $1^\circ \times 1^\circ$ grid. *RIVM/TNO rep.*, RIVM, Bilthoven, number nr. 711060 002, 1006.
- [13] Yang, S., H. He, S. Lu, et al., 2008: Global air quality and pollution. *Atmos. Environ.*, 42, 1961–1969, doi:10.1016/j.atmosenv.2007.12.007.

Application of Electrical Means to Aerosol Technologies

Jungho Hwang

School of Mechanical Engineering, College of Engineering, Yonsei University, 134 Sinchon-dong, Seodaemun-gu, Seoul 120-749, Korea

Principal Contact: Jungho Hwang, Professor, School of Mechanical Engineering, College of Engineering, Yonsei University, 134 Sinchon-dong, Seodaemun-gu, Seoul 120-749, Korea.

E-mail: hwangjh@yonsei.ac.kr.

Abstract

Electrical gas discharges have been widely used in aerosol technologies. In this talk, fundamentals of corona discharge and its applications are introduced. At atmospheric pressure and temperature, air can be partially ionized when a high electric field is present. Once generated, air ions are utilized to charge contaminant aerosol particles for the increase of aerosol filtration efficiency and also to inactivate bioaerosol particles suspended in air or captured in a filter. Aerosol charging by air ions and measurement of electrical current carried by charged aerosol particles can be applied to real-time measurement of ambient aerosol particles or particulate matter emitted from diesel engine particles. The charged aerosol particles can also be introduced into a coaxial nozzle where a particle-laden jet is formed with being shielded by sheath air flow and directed toward a substrate for aerosol printing. Spark discharge, one of electrical gas discharges, has been used to generate metallic aerosol nano particles, if a spark channel is formed when the applied voltage is beyond a critical value. The metallic particles can be used as catalyst for synthesis of carbon nanotubes and, antimicrobial agent for filter coating. In electrohydrodynamic atomization (EHDA) process, also referred to as electrospray process, highly charged, relatively monodisperse droplets of controlled size can be produced from various conditions of liquid solution material. Utilizing a coaxial nozzle and the cone jet mode of electrospray, a process for the synthesis of encapsulated particles is discussed. In addition, examples of printing metal and ceramic nanoparticles, which are contained in the liquid solution, onto a substrate for application to patterning of conductive line and insulator, respectively, will be stated.

Keywords: Corona discharge, spark discharge, electrohydrodynamic atomization

Aerosol-Cloud-Precipitation-Climate Interactions: Evidences and Challenges

Panuganti C.S. Devara

Indian Institute of Tropical Meteorology, Pune, Maharashtra, 411 008, India

ABSTRACT

Atmospheric aerosols scatter and absorb solar radiation and hence affect weather and climate. Certain aerosols act as cloud condensation nuclei (CCN) and ice-nuclei (IN), and contribute to the cloud formation and development and thus affecting the cloud cycling mechanisms. Present knowledge concerning impact of aerosols on clouds, monsoon activity and climate is incomplete and needs to be studied by collecting systematic observational evidence. In addition, the complex role of aerosols in the climate system in influencing the atmospheric radiation budget is not clear. Impact of anthropogenic pollution on natural clouds is not understood. Aerosols affect clouds in two broad ways: (i) Presence of more number of aerosols lead to formation of more smaller droplets, reduce coalescence, resulting in brighter clouds that reflect more solar energy back to space, hence they contribute to cooling of the Earth's surface, and (ii) Numerous smaller cloud droplets tend to reduce precipitation and change the extent of cloud cover and increases cloud life time and albedo. One of our recent studies on aerosols over the Indo Gangetic Plains (IGP) relative to the pristine oceans to the south of Indian Ocean showed that highly absorbing aerosols could potentially lead to the revival of active condition preceded by long break. The absorption of solar radiation by aerosols such as black carbon and desert dust also produces surface cooling and local stabilization of lower atmosphere. This stability effect is overcome by the enhanced moisture convergence due to the meridional gradient of aerosol-induced heating. In some other studies, we showed association between cloud to sub-cloud ratio, aerosol variability (in terms of aerosol optical depth and aerosol index) and monsoon precipitation and climate over regional scale.

KEYWORDS

Aerosols, Clouds, Lidar, Solar Radiometry, Radiation, Satellites

Introduction

The boundary layer aerosol system is different from that of the troposphere, which implies that the processes responsible for the seasonal and long-term changes in these two regions are quite different. Although the parameters such as total column aerosol optical depth etc. are useful for the study of seasonal and long-term trends, the radiative effects of aerosols on regional scale can be understood better only by accounting for the local influences separately. In order to have a clear understanding of the tropospheric aerosol system it is necessary to separate out the boundary layer component from the total column aerosol parameters and examine the changes and trends. Separation of these two components also provides better understanding of aerosol physical, chemical, radiative and dynamical processes taking place in these two important regions of the atmosphere.

Certain aerosols act as cloud condensation nuclei (CCN) and ice-nuclei (IN), and contribute to the formation and development, and thus cloud cycling mechanisms modifying aerosol properties in the troposphere. Therefore, besides the direct radiative effects of aerosols, it is important to consider aerosols as a sub-system of clouds, because of the interaction between aerosols and clouds. Also, aerosols have a major, and perhaps overwhelming role in determining cloud and precipitation chemistry, and the removal of aerosols from the air via clouds and precipitation is a major part of the cycling of materials in the atmosphere. Specific attention is given to sulphate aerosols, they being the dominant species influencing the acidity and most likely to be involved in providing an aerosol-cloud-climate link^[2].

Albeit numerous aerosol measurement techniques have been applied for the past more than four decades, conventional/direct/in-situ as well as remote sensing methods have been refined recently. Also, a number of new techniques have been developed to monitor and characterize the atmospheric aerosols. Of these, optical remote sensing techniques have been realized to contribute significantly to the studies in the field of ‘Aerosol Science’. While passive optical remote sensing instruments such as solar radiometers have a longer history of operation for atmospheric aerosol studies, including operation in space for a number of years, active lidar (light detection and ranging) system are playing an increasing role in these studies. Existing ground-based and airborne lidar systems yield measurements with range (distance) resolution. Present satellite-borne sensors are passive techniques and, hence, cannot provide data that are as finely resolved in time or space as lidar measurements, but

they provide an unparalleled capability to monitor stratospheric aerosols on a global scale for long time periods. Future satellite based active (lidar) and next-generation passive sensors will extend this capability. This paper deals with aerosol-cloud-monsoon relationship, and reports some sample results from recently installed Doppler wind lidar, Raman lidar and GPS Radiosonde that determine simultaneous aerosol-cloud structures and feedback processes.

Aerosol and Cloud Monitoring Techniques

Monitoring of atmospheric aerosols and clouds can be accomplished by either experimental or theoretical modeling techniques. Both these techniques are highly desirable and need to go hand-in-hand because experimental observations are needed to validate the model outputs which involve many assumptions. Such validations provide a basis for estimating the uncertainty of the model simulations. Model results sometimes provide direction in which the experiments need to be conducted in determining certain critical aerosol and cloud parameters.

Remote Sensing Techniques Developed at IITM, Pune, India

Passive remote sensors are best suited for deployment on satellites but they work only when the Sun is shining on the area under the satellite. Active remote sensors allow mapping of aerosol parameters over large atmospheric volumes with spatial resolution of the order of a few meters both during day and night by following several energy source-atmosphere interaction processes^[3]. Albeit Radars have long history for studying convective systems, of which clouds/precipitation constitute a part, as optical wavelengths are more suitable for aerosol measurements, optical remote sensing techniques such as radiometers (passive) and lidar (active) are widely used for studying aerosol features. Radiometers provide the

unparalleled capability to monitor atmospheric aerosol features over larger area for long period. Because of excellent spatial resolution, unattainable with any other remote sensor, lidar technique attracted many scientists for the study of atmospheric aerosols in the vicinity of environments^[3]. The future satellite-based lidar and next generation passive sensors will extend this capability. Some of the active and passive remote sensing techniques have been in use for monitoring of aerosols and pre-cursor gases, clouds and also for validation of satellite data at IITM, Pune for the past more than two decades.

In recent years, spectro-radiometers, with interchangeable multiple gratings (poly-chromators) have been found to yield more useful information on aerosol physical and chemical characteristic (Devara et al., 1996). More advanced version of sun-sky radiometer (Figure 2) which measures more parameters that better characterizes aerosols are also being operated at IITM, Pune. These radiometers, besides the more general parameters like aerosol optical depth, Angstrom parameters etc., they determine parameters such as phase / asymmetry function (represent particle refractive index and shape), single scattering albedo (represent radiative efficiency) of aerosols^[4].

In recent years, the lidars have been made more compact and associated data acquisition / processing techniques have been far improved for obtaining aerosol information both during day and night at ultra-high spatial and temporal resolution. In this context, an autonomous, dual polarization micro pulse lidar, unique so far in Asia (shown in Figure 1) has been in operation at IITM, Pune for the study of aerosol and cloud extinction and phase profiles and super-fine structures^[5].

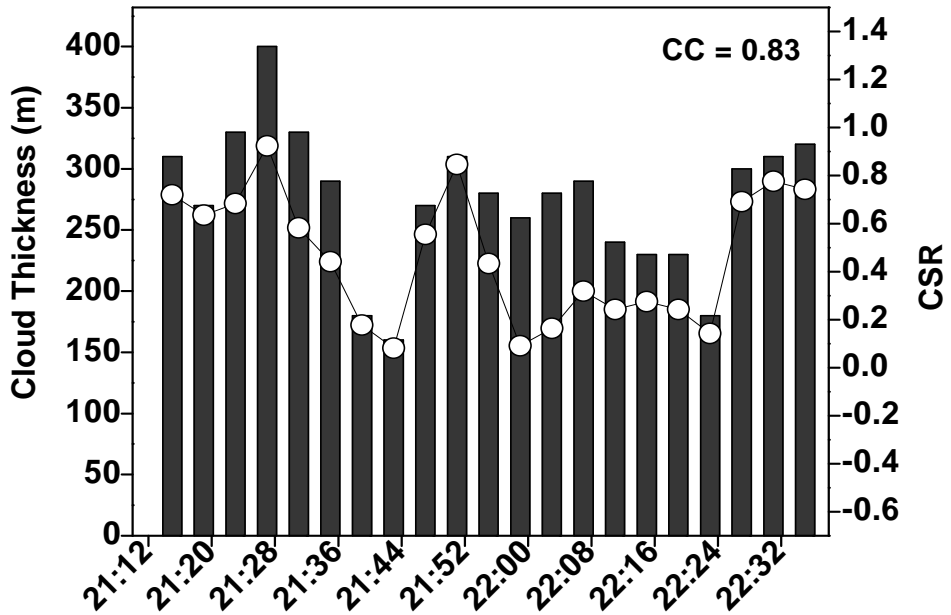


Figure 1: Time evolution of cloud thickness versus CSR observed with DPMPL on 09 June 2008.

Figure 1 depicts the association between cloud thickness (histogram) and cloud to sub-cloud ratio (CSR) (solid curve), recorded on 09 June 2008. The correlation coefficient (CC) between these two parameters is also indicated in the figure. It is evident from the figure that higher the CSR, more is the cloud thickness. The higher and significant CC observed in this case indicates CCN enhancement in the cloud cover at the expense of decrease of CCN concentration in the sub-cloud

region. This finding has a direct bearing on the growth process and persistence of cloud cover which supplements the cloud dissipation due to scavenging by wet deposition or rain-out. The cloud droplet number density depends predominantly on the relationship between the updraft velocity, availability of moisture, the critical activation radius, collision-coalescence etc. The impact of all these environmental parameters on the ratio of sub-cloud and in-cloud air mass is assumed to be negligible.

Interlace between Aerosol, Monsoon and Climate

The climatic effects of aerosols and their interaction with clouds and precipitation are controversial^[6,7]. Tropospheric aerosol research deserves special attention because of its multi-functional role in the aerosol-cloud-precipitation-climate interaction, deriving various feedback mechanisms. The sensitivity of clouds and precipitation to changes in the aerosol is regime dependent^[8,9]. Although the main component of atmospheric aerosol that is responsible for the generation and maintenance of the hydrological cycle is not yet clear, it is evident that aerosols are effective agents^[10] and hence, reliable data as well as, systematic study is needed to understand these complex processes^[6]. Depolarization lidars are widely used for the study of aerosols and clouds because of their ability to discriminate not only ice from water but also spherical particles from particles of irregular shape^[5].

Much of aerosol-cloud-precipitation-climate interaction processes, particularly the second indirect effect and its association with environment, are still not well understood. Albeit some rudimentary evidences of rain inhibition by forest fires etc. exist in the literature, the impact of anthropogenic pollution on natural clouds is not clear yet. While scattering aerosols cool the atmosphere, absorbing aerosols enhance lower-level heating and intensify the Indian monsoon precipitation. The suppression of coalescence and precipitation processes by aerosols remains inconclusive today. Air pollution also either suppresses or delays the precipitation. Among the absorbing aerosols such as carbonaceous particles, containing both elemental and organic fractions, and dust particles coated with organic/inorganic materials (internal and external mixing) exert complex forcing on Earth-atmosphere radiation balance and hydrological cycle. These complex processes, particularly the aerosol indirect effects, are poorly represented in weather and climate models; and have been recognized as major sources of uncertainty in any attempt on future climate projections and seamless predictions.

Very recently, we have reported such an association between aerosol index data from TOMS/OMI satellite and monsoon activity in terms of its season total rainfall^[9]. We have also reported a study indicating an inter-play between aerosols over Arabian Sea and Indian monsoon activity using the MODIS satellite aerosol optical depth and NCEP/NCAR reanalyzed wind field and TRMM rainfall data^[11]. One of our recent studies on aerosols over the Indo Gangetic Plains (IGP) relative to the pristine oceans to the south of Indian ocean showed that highly absorbing aerosols could potentially lead to the revival of active condition preceded by long break^[12].

CONCLUSIONS

The aerosol-cloud interaction studies undertaken recently with an autonomous dual polarization micro-pulse lidar show an interlace between aerosols in the sub-cloud layer and cloud layer aloft. These results suggest better data assimilation and sensitivity techniques which may allow compatibility between the available models and existing data sets. Added, development of boundary layer cloud parameterization schemes with available and planned observations will further help improving the weather and climate understanding, attribution and prediction techniques.

ACKNOWLEDGEMENTS

I am thankful to Director, IITM, Pune for his encouragement and support. I also appreciate the help and cooperation from the Members of “Aerosol and Cloud Physics Laboratory for Weather and Climate Studies”.

REFERENCES

- [1] Twomey, S., 1991, *Atmospheric Environment*, 25A, 2435-2442.
- [2] IPCC (Intergovernmental Panel for Climate Change), 1997, Stabilization of atmospheric greenhouse gases: physical, biological and socioeconomic implications, J.T. Houghton, L.G. Meira Filho, J.T. Griggs and K. Maskell (Eds), IPCC, Geneva, Switzerland, pp 52.
- [3] Devara, P.C.S., 1989, *Journal of Scientific and Industrial Research*, 48, 71-83.
- [4] Sumit, K. and Devara, P.C.S., 2011, *Journal of Geophysical Research* (In Press).

- [5] Devara, P.C.S., Raj, P.E., Dani, K.K., Pandithurai, G., Kalapureddy, M.C.R., Sonbawne, S.M., Rao, Y.J. and Saha, S.K., 2008, *Journal of Atmospheric and Oceanic Technology*, 25, 1288-1295.
- [6] Rosenfeld, D., Lohmann, U., Raga, G.B., O'Dowd, C.D., Kulmala, M., Fuzzi, S., Reissel, A. and Andrae, M.O., 2008, *Science*, 321, 1309-1313.
- [7] Lau, K. M. and Kim, K.M., 2006, *Geophysical Research Letters*, 33, 121810, doi:10.1029/2006GL027546.
- [8] Stevens, B. and Feingold, G., 2009, *Nature*, 46, 607-613.
- [9] Bhawar, R.L. and Devara, P.C.S., 2010, *Atmospheric Chemistry and Physics*, 10, 29-37.
- [10] Sue, W., Schuster, G.L., Loeb, N.G., Rogers, R.R., Ferrare, R.A., Hostetler, C.A., Hair, J.W., and Obland, M.D., 2008, *Journal of Geophysical Research.*, 13, doi:10.1029/2008JD010588.
- [11] Rahul, P.R.C., Salvekar, P.S. and Devara, P.C.S., 2008, *Geophysical Research Letters*, 35, L22812, doi:10.1029/2008GL035573.
- [12] Manoj, M.G., Devara, P.C.S., Safai, P.D. and Goswami, B.N., 2010, Climate Dynamics, doi: 10.1007/s00382-010-0971-3.

Aerosol-based Process Technologies for Nano-Materials

Bernd Sachweh

BASF SE, 67056 Ludwigshafen, Germany

Principal Contact: Bernd Sachweh, Professor, BASF SE, Carl-Bosch-Str.38, 67056 Ludwigshafen, Germany.

Tel: +49 621 60 51732 Email: bernd.sachweh@basf.com

Abstract

Many mass products already use tailor-made particles for improvement of specific product properties, e.g. for printing inks, automotive coatings, UV sun-block creams and polymer materials. The more special the desired function is the smaller and more complex (in terms of shape, number of materials, crystallinity) the particles have to be. Only few materials are in the market featuring completely new product properties only occurring if a characteristic dimension of the particles is below 100 or even 10nm.

For innovative nano-based high-tech materials new process technologies have to be developed. Due to an often very fast building kinetics during synthesis of particulate materials the key process parameters cannot be controlled within the required precision to uniformly deliver the targeted properties. In addition, the key mechanisms (e.g. crystal growth, morphology change and agglomeration) tend to occur simultaneously with complex interaction kinetics. Thus, multiple process steps have to be integrated into a complex process scheme. Aerosol processes can advantageously be used for building structures on a single-digit nano-scale. This is the key for optimum functionality which then has to be further modified for incorporation into bulk material. The transfer of the nanomaterials to the liquid phase can be one route, which allows for an individual optimization of the gas phase process with respect to functionality and the liquid phase process with respect to processability. The complex interaction of the key process parameters has to be thoroughly understood for the entire process to efficiently control the desired product properties. Therefore new measurement techniques are required which allow for particle characterization beyond size preferably with online capability. In this presentation the complexity of integrated processes for synthesis of particle-enhanced materials is demonstrated for various applications.

Keywords: Nanoparticles, Aerosol process, Integrated process UNPA

Ambient Aerosols in Iraq and Afghanistan: Size, Concentration and Elemental and Biological Composition

Catherine F Cahill¹, Thomas A Cahill², Linda S Powers³ and Walther R Ellis⁴

1 Geophysical Institute and Department of Chemistry, University of Alaska Fairbanks, Fairbanks, AK 99775, USA

2 DELTA Group, Department of Chemical Engineering and Materials Science, University of California, Davis, Davis, CA 95616, USA

3 Department of Electrical and Computer Engineering, University of Arizona, Tucson, AZ 85721, USA

4 Department of Biomedical Engineering, University of Arizona, Tucson, AZ 85721, USA

ABSTRACT

Air in Iraq and Afghanistan has high concentrations of ambient aerosols. An ongoing study, started in February 2008 in Baghdad, Iraq, and later expanded to two sites in Afghanistan, is continuously collecting aerosols in eight size fractions less than 10 microns in aerodynamic diameter to quantify human exposure to the respirable fraction of these aerosols. These samples are being collected using an eight-stage DRUM aerosol impactor. The samples are analyzed with 1.5-hour resolution for aerosol mass concentration by beta gauge and elemental composition for 28 specific elements between sodium and uranium by synchrotron x-ray fluorescence. Also, select samples have been analyzed for the presence of markers for live cells, dead cells, and spores using a spectrofluorometer and viable biological species through culturing and identification. The results of these analyses show high concentrations of elements such as lead, aluminum and magnesium and the presence of pathogenic bacteria, such as *bacillus cereus* and *paenibacillus thiaminolyticus*, in the ambient aerosol.

KEYWORDS

Bioaerosol, Human Health, Aerosol Impactor, Composition

BODY

Introduction

Short and long-term aerosol exposures cause a variety of adverse human health impacts including increased morbidity (e.g. asthma, chronic obstructive pulmonary disorder, etc.) and premature mortality^[1]. On September 28, 2006, the United States (U.S.) Environmental Protection Agency (EPA) tightened ambient fine particulate (particulate matter with aerodynamic diameters less than 2.5 μm and also known as PM_{2.5}) 24-hour averaged mass-based standards to protect the health of the public^[2]. The aerosol concentrations observed in many areas where soldiers are deployed are higher than those experienced in the U.S.^[3,4,5] and known to cause adverse human health impacts. The concentrations of PM_{2.5} observed in Iraq exceed the 24-hour average EPA National Ambient Air Quality Standard (NAAQS) and Military Exposure Guidelines (MEGs)^[6]. These aerosols need to be characterized by size, concentration, chemical composition and biological activity to determine their sources and potential impacts on the health of the people in the region. The size of the aerosols determines where in the respiratory track the aerosols might deposit and the concentration of the aerosols provides an estimate of the total aerosol exposure and when that exposure occurred. In addition to size, the composition of the aerosols is essential for determining the health effects associated with a specific aerosol exposure. For example, aerosols may contain components from natural and anthropogenic sources, biological components such as bacteria and viruses, and inorganic components such as heavy metals or radioactive species. The U.S. Army Center for Health Promotion and Preventative Medicine has placed a priority on obtaining aerosol samples suitable for conducting studies on the impacts of aerosols on human health^[5]. However, current instrumentation and studies aimed at obtaining the required aerosol information for use in medical and environmental health determinations are limited in number and scope in most places soldiers are deployed^[7].

Historically, large, non-mobile, filter-based aerosol samplers provide the basis for determining if the 24-hour or annual-average mass concentrations are in compliance with the EPA regulations. These sampling systems have been used in areas where soldiers have been deployed^[3,6] to obtain preliminary information on the size, concentration and composition of aerosols in the region. Engelbrecht et al.^[9] describe one of the most comprehensive studies done on aerosol composition in the Middle East. However, this study had a limited number of sites, 15 sites total, with only one site in the Baghdad area. The study also did not address the issue of biological aerosols. The study did address the inorganic and elemental and organic carbon composition and concentration of the aerosols in the region. The personnel involved in this study collected 24-hour total suspended particulate (TSP), particulate matter less than 10 μm in aerodynamic diameter (PM₁₀), and particulate matter less than 2.5 μm in aerodynamic diameter (PM_{2.5}) samples once every six days. These samplers are not appropriate for long-term use in an area with deployed soldiers due to their limited aerosol size information, requirement for frequent human interaction, and low time resolution (1 day in 6 for mass, and 2 days in 30 for metals such as lead). Weese^[7]

demonstrated that this time resolution, and lack of sub-PM_{2.5} size information, prevents medical and environmental health professionals from obtaining clear correlations between particulate matter exposure and potential health impacts. Therefore, aerosol measurements with higher time resolution and measurements of smaller aerosol particles are needed to assess the potential impacts of these aerosols. The effort described in this paper focuses on a study started in February 2008 in Baghdad, Iraq, of the use a DRUM aerosol impactor to collect higher resolution, time and size-resolved aerosol composition data in Iraq and Afghanistan for use in epidemiological studies. The results of these efforts will lead to aerosol characterization data suitable for use in medical and environmental health assessments, aerosol environment characterization and monitoring studies where military personnel are deployed.

Experimental Methods

Aerosol sampling using ground-based, eight-stage DRUM impactors commenced in Baghdad, Iraq, on February 14, 2008, and at Bagram Air Force Base (AFB), Afghanistan, on February 6, 2010. DRUM impactors, cascade aerosol impactors, have been successfully used to collect size- and time-resolved aerosol elemental composition and mass concentration in remote regions and with minimal human intervention^[8, 9, 10, 11]. These impactors continuously collect aerosols in eight size fractions (10.0-5.0, 5.0-2.5, 2.5-1.15, 1.15-0.75, 0.75-0.56, 0.56-0.34, 0.34-0.26 and 0.26-0.09 μm in aerodynamic diameter) on Apiezon™ coated Mylar™ strips. The time resolution of the sampler is set by the research needs, currently 1.5 hours due to the high mass loading observed at the sites. The initial samples were collected with 3 hour resolution, but were overloaded with mass during dust storms, leading to sample flaking off the sample strips during handling in the lab. Most of the samples collected by the samplers were returned to the University of Alaska Fairbanks for analysis by beta-gauge for aerosol mass, ultraviolet-visible spectroscopy for optical absorption as a function of wavelength and synchrotron x-ray fluorescence for elemental composition for 28 specific elements between sodium and uranium at the Advanced Light Source at Lawrence Berkeley National Laboratory^[12,13]. A few samples were selected for analysis by fluorescence using a Horiba-Jobin Yvon Fluorolog-3 instrument to identify the presence of markers for live cells, dead cells and spores on the Mylar™ strips. Material from these samples was extracted from the sample strip and cultured on Luria-Bertani or blood agar plates under aerobic conditions at 37 °C. The colonies that grew were then subjected to PCR amplification using SybrGreen I and DNA sequenced.

Results and Discussion

This aerosol data show high aerosol mass and component concentrations (Figures 1). These mass concentrations exceed the U.S. EPA's NAAQSs and the MEGs for fine particulate matter. Individual elemental aerosol components, especially those associated with soils, can exceed these mass-based standards by themselves. This frequently occurs during the dust storms that occur in the region. Specific aerosol concentrations also violate other EPA standards. For example, lead frequently exceeds the 150 nanogram per cubic meter EPA standard (Figure 2).

The need for high temporal resolution is seen in figure 2. The study by Engelbrecht et al.^[6] identified the lead observed at the site as coming from the same source as the zinc. The higher resolution data shown in figure 3 shows that the peaks in lead and zinc concentrations occur during similar periods, but with differing lead to zinc ratios and not always at the same time. This implies that these elements are being emitted from different sources.

The concentrations of markers for live cells, dead cells and spores were observable in year-old samples; although the age of the sample may have limited the concentration of live cell markers observed in the sample (Figure 3). It is not surprising that the markers for live cells (e.g., 370nm/440nm and 370nm/480nm markers for the bound and free reduced pyridine [RPN] nucleotides, respectively) were absent as the strips were a year old. In only two samples was the 370nm/480nm free RPN marker seen. Also, none of the sections showed the markers for spores (e.g., 635nm/770nm for Ca²⁺-dipicolinic acid complex) indicating that if spores were present, they were either lacking the fluorescent marker or that it was not possible to measure these markers with this instrumental configuration. The markers for dead cells (e.g., oxidized flavins, porphyrins, collagen, and elastin) were present. The surprise was that there was a large amount

Figure 1. Aerosol mass concentration at Bagram, Afghanistan, from February 6-28, 2010.

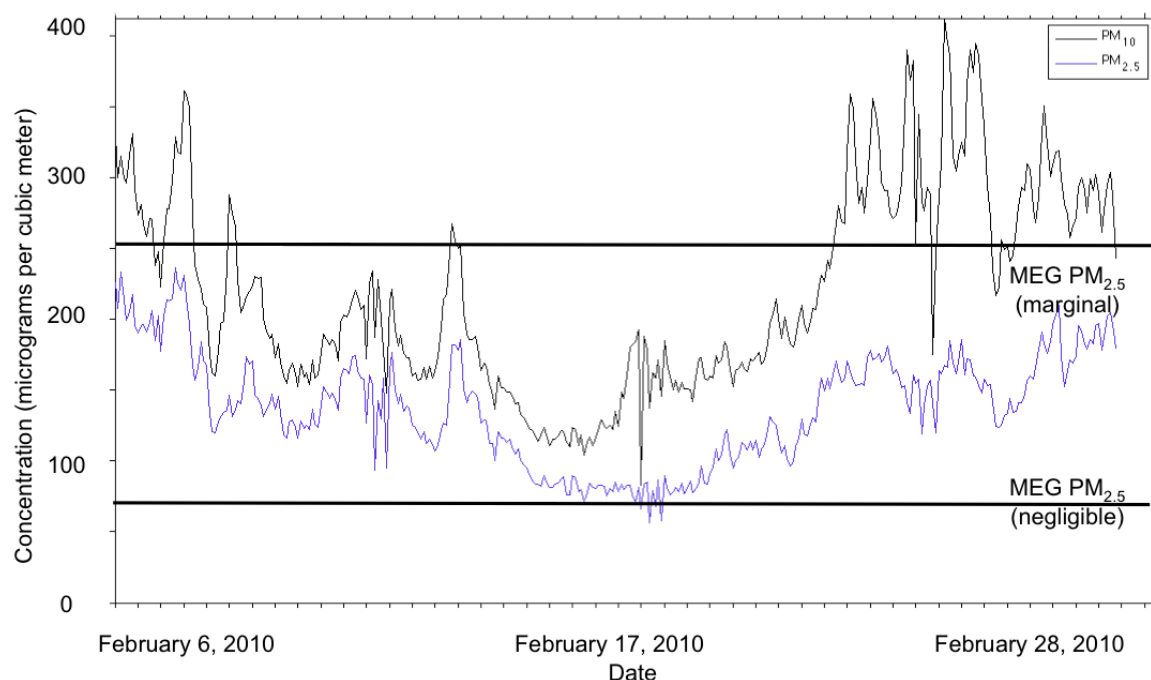


Figure 2. Lead and zinc concentrations in Baghdad, Iraq, from March 16-April 27, 2008.

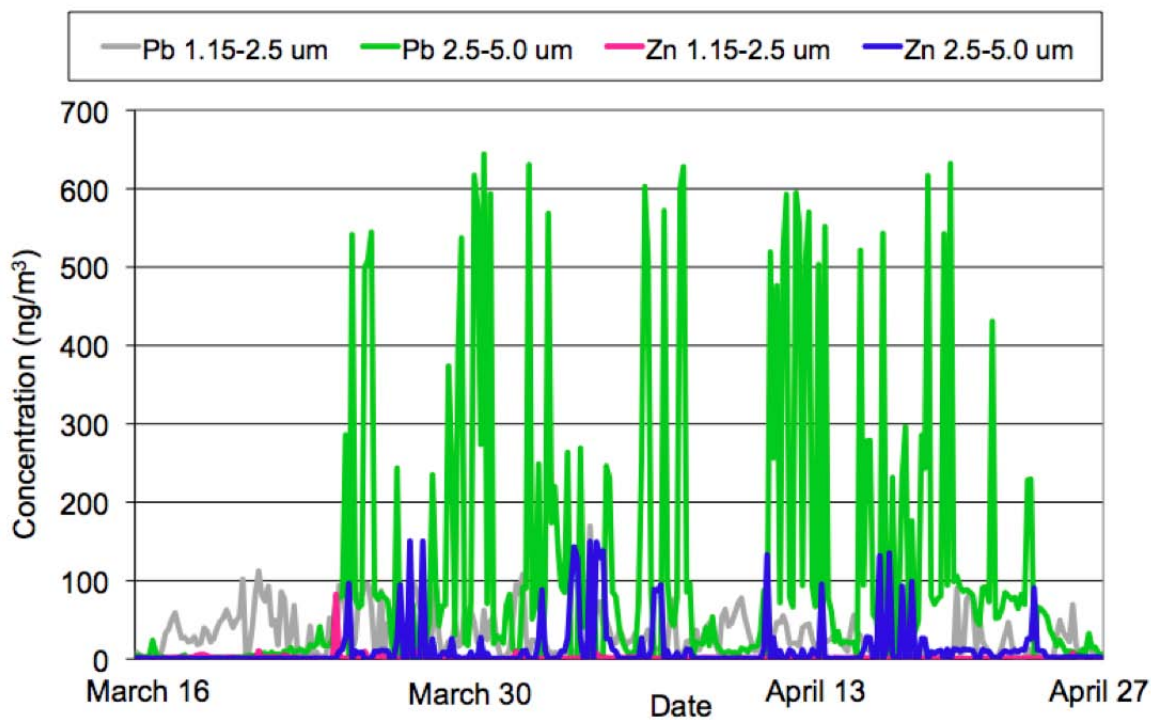


Figure 3. The size-resolved results of the fluorescence measurements.

Fluorescence (in arbitrary units)						Microscopy
Ex/Em	370/480	370/540	450/540	370/585	480/585	
Fluorophore	'free' RPN	Flavins/porphyrins collagen/elastin		Flavins/porphyrins		Stained cells adhering to abiotic particles
Size						
inlet-5 µm			10,500	1000	1500	Large amount
2.5-5 µm		100	300			Large amount
1.15-2.5 µm	550			450	700	Some
0.75-1.15 µm		175	375		40	Many
0.56-0.34 µm			60			Few
0.34-0.26 µm			100			Some
0.26-0.09 µm	325	2000	4800	450	600	Many tiny cells

of these markers in the smallest size range and that this was the only sample to have all the markers except the 370nm/440nm marker for bound RPN. In order to ensure that the source of these markers was actually cells, the samples were stained with crystal violet and viewed under a microscope. Cells were observed.

The result of the culturing and DNA analysis of the viable biological components of the aerosol is a list of bacteria that includes both pathogenic and benign species. These species include *paenibacillus thiaminolyticus*, among others, which were observed in previous studies in the region^[4]. Some of the alpha and beta hemolytic bacteria observed in the samples include: *Bacillus amyloliquifaciens*, *Bacillus simplex*, *Bacillus sp.*, *Bacillus cereus* (a human pathogen), *Paenibacillus thiaminolyticus* (a human pathogen), and *Brevibacterium sp.* (cause a variety of human infections or simply colonize skin, causing noxious odors). Fresher samples found many more species including: *Bacillus endophyticus*, *Bacillus sp.* (cereus/thuringiensis group), *Bacillus subtilis*, *Bacillus pumilus*, *Kocuria sp.*, *Bacillus niacini*, *Bacillus foraminis*, *Lysinibacillus sp.*, *Staphylococcus hominis* and *Bacillus megaterium*.

SUMMARY

This paper describes an ongoing study conducted using DRUM aerosol samplers in Baghdad, Iraq, and at Bagram AFB, Afghanistan. The initial results of the study show that the concentrations of fine particulates in the air at these sites frequently exceeds U.S. EPA ambient air quality standards and military exposure guidelines designed to protect human health. Also,

the lead concentrations in Baghdad in respirable particles exceed the EPA's standards for lead. These results imply that there may be future observable health effects in the populations exposed to these aerosols.

The results of these analyses also show that the DRUM sampler was successful in collecting size-resolved aerosol samples suitable for determining the presence of biological material such as live cells, dead cells and spores in ambient aerosol. The presence of pathogenic bacteria, such as *bacillus cereus* and *paenibacillus thiaminolyticus*, in the ambient aerosol is consistent with the observations of Lyles^[4]. This size-resolved biological activity of the aerosols is vital to determining where in the human respiratory track, e.g. nasal, pharyngeal, bronchial and upper lung and deep lung, a biological pathogen can lodge and grow. This data is unavailable from filter sampling.

The data collected during this project will be useful in future epidemiological studies and retrospective analyses to determine the cause of any potential health effects observed in U.S. military personnel in the future.

ACKNOWLEDGMENTS

The authors wish to thank the United States Army Research Laboratory for its financial support of this work through grants: W911NF-07-1-0346, W911NF-08-1-0318, W911NF-09-1-0543.

REFERENCES

- [1] Environmental Protection Agency
See http://www.epa.gov/particles/pdfs/20060921_factsheet.pdf (accessed April 2011).
- [2] Federal Register, Vol. 71, No. 200, Tuesday, October 17, 2006, *Rules and Regulations*, 2006, pp 61236-61328.
- [3] Engelbrecht, J.P.; McDonald, E.V.; Gillies, J.A.; Jayanty, R.K.M.; Casuccio, G.; Gertler, A.W. *Inhalation Toxicology*, 2009, 21 (4), pp 297-326.
- [4] Lyles, M.B. Technical Report prepared for the Office of Naval Research. Prepared by the Naval Institute for Dental and Biomedical Research Great Lakes, IL 60088, April 1, 2005.
- [5] Sheehy. Presentation #6077. Presented at the 11th Annual Force Health Protection Conference, Albuquerque, New Mexico, August 9-15, 2008.
- [6] Engelbrecht, J.P.; McDonald, E.V.; Gillies, J.A.; Gertler, A.W.; Jayanty, R.K.M.; Casuccio, G. Final Report: Department of Defense Enhanced Particulate Matter Surveillance Program (EPMSP). Prepared by the Desert Research Institute (DRI), Reno, NV 89512-1095. 2008.

- [7] Weese, C. Presentation #6082. Presented at the 11th Annual Force Health Protection Conference, Albuquerque, New Mexico, August 9-15, 2008.
- [8] Cahill, T.A.; Goodart, C.; Nelson, J.W.; Eldred, R.A.; Nasstrom J.S.; Feeney, P.J. In *Proceedings of the International Symposium on Particulate and Multiphase Processes*; Ariman, T.; Veziroglu T. Eds.; Hemisphere Publishing Corporation, 2, 1985; pp 319-325.
- [9] Raabe, O.G.; Braaten, D.A.; Axelbaum, R.L; Teague, S.V.; Cahill, T.A., *J. Aerosol Sci.* 1988, 19(2): 183-195.
- [10] Cahill, T.A.; Wakabayashi, P. In *Measurement Challenges in Atmospheric Chemistry*; L. Newman, Ed.; Amer. Chem. Soc., 1993; pp 211-228.
- [11] Collins, R.L.; Fochesatto,J.; Sassen, K.; Webley, P.W.; Atkinson, D.E.; Dean, K.; Cahill, C.F.; Mizutani, K. *J. of the National Inst. of Inform. and Comm. Tech*, 2007, 54(1/2): 17-28.
- [12] Cahill, T.A.; Cliff, S.S.; Perry, K.D.; Jimenez-Cruz, M.P.; McHugo, S.A. In *Abstracts, Amer. Geophys. Union 1999 Fall Mtg, December 13-17, 1999, San Francisco, California*; published by the American Geophysical Union, 1999.
- [13] Cahill, C.F. *J. Geophys. Res.*, 2003, 108 (D23), 8664, doi:10.1029/2002JD003271.

Chemical composition of precipitation in the Lake Qinghai area, China

Kun Zhang¹, Zhenxing Shen^{1,2*} and Junji Cao^{2,1}

1 Department of Environmental Science and Engineering, Xi'an Jiaotong University, Xi'an 710049, China;

2 SKLLQG, Institute of Earth Environment, Chinese Academy of Sciences, Xi'an 710075, China

Principal Contact: Zhenxing Shen, Dr., Department of Environmental Science and

Engineering, Xi'an Jiaotong University, XianNing West Road 28#,Xi'an, 710049, China.

E-mail: zxshen@mail.xjtu.edu.cn

Abstract

Precipitation samples have been collected at Qinghai Lake area ($36^{\circ}32' - 37^{\circ}15'N$, $99^{\circ}36' - 100^{\circ}16'E$; 3200 m a.s.l) in the northwest of Tibetan Plateau from June to August 2010. Ion Chromatography and Total Organic Carbon Analyzer were used to determine the mass levels of water-soluble inorganic ions (NH_4^+ , Na^+ , K^+ , Ca^{2+} , Mg^{2+} , F^- , Cl^- , NO_3^- , and SO_4^{2-}) and dissolved organic carbon (DOC). The pH values of precipitation samples ranged from 6.05 to 8.19 with an average value of 7.13. The mean concentrations of total ions and DOC were $255.31 \mu\text{eqL}^{-1}$ and $2.61 \text{ mg}\cdot\text{L}^{-1}$, respectively. Ca^{2+} , with a mean value of $65.58 \mu\text{eqL}^{-1}$ ranging from 4.91 to $301.41 \mu\text{eqL}^{-1}$, was the dominant cation in precipitation, accounting for 18% of the total cations in precipitation. The high pH was mainly due to large inputs of crustal components (such as Ca^{2+}) in the atmosphere. Cl^- was the major anion in precipitation samples, accounting for 20.46% of the total anions. Enrichment factor were used to identify the sources of chemical composition of precipitation samples. The results revealed that regional crustal aerosols and anthropogenic species from combustion emissions of residents were the major sources for precipitation components. In addition, sea salt was another important contributor to rainwater in Qinghai Lake areas.

Keywords: Qinghai Lake area; water-soluble components; enrichment factor; source identification

Characterization of Diesel Particulates and Metal Nano-agglomerates using the Universal Nanoparticle Analyzer

Jing Wang^{1,2} , Zhun Liu³ , Seong Chan Kim³ , Jacob Swanson³ and David Pui³

1 Institute of Environmental Engineering, ETH Zurich, Zurich, 8093, Switzerland

2 Empa, Analytical Chemistry, 8600 Dübendorf, Switzerland

3 Particle Technology Laboratory, University of Minnesota, 55414, USA

ABSTRACT

Nanoparticle agglomerates play an essential role in the manufacturing of many nanomaterials and are commonly found in combustion products. Conventional aerosol instruments based on equivalent spheres are not directly applicable to the measurement of nanoparticle agglomerates. The increasing interest in real-time assessment of diesel soot mass makes it highly desirable to develop an online instrument for airborne agglomerates. A recently developed instrument, Universal Nanoparticle Analyzer (UNPA), was used in this study to characterize *in situ* the structure of diesel particulates and metal nanoparticle agglomerates generated by spark discharge. The primary particles sizes measured by UNPA for the soot and metal agglomerates are in reasonable agreement with the TEM sizing results. With regard to the mass concentration of silver agglomerates at room temperature, excellent agreement was found under our experimental conditions between the value calculated by UNPA, the prediction given by the effective density, and the gravimetric result whereas the SMPS gives a mass prediction larger by almost one order of magnitude.

KEYWORDS

Diesel particulates, nanoparticle agglomerates, spark discharge, mass concentration

Introduction

Many nanomaterials are manufactured in the form of nanoparticle agglomerates, which are made up of clusters or chains of nanosize spheres referred to as primary particles. Combustion processes are used to manufacture a variety of materials in agglomerate form including fumed silica, titanium dioxide, and carbon black (Pratsinis 1998^[1], Wang et al. 2011^[2]). Diesel particulate and soot from building fires are also known to be in agglomerated form (Kim et al. 2009^[3]). Agglomerates may possess complicated structures, which makes measurement a difficult task. One of the most common methods for agglomerate measurement is electron microscopy, which can provide direct measurement of the structural properties (Koylu et al.

1995^[4], Rogak et al. 1993^[5], Shin et al. 2009^[6] among many others). However, taking electrical micrographs and performing image analysis can be time consuming and expensive. In addition, interpretation of the 2D images for 3D results may rely on assumptions and cause inaccuracy. Fast and online measurement for agglomerates is required in many scenarios including measuring fast changing agglomerates, quality control for material manufacturing, monitoring toxic airborne agglomerates, etc. Most of the current aerosol instruments are designed for spherical particles. Therefore, there is a need for instruments capable of fast and online measurement of gas-borne nanoparticle agglomerates.

We have developed an instrument, Universal NanoParticle Analyzer (UNPA), for online measurement of gas-borne nanoparticle agglomerates (Wang et al. 2010^[7], Shin et al. 2010^[8]). It is based on combined measurement of electrical mobility and unipolar charging properties. The UNPA can provide morphology information of airborne nanoparticles, and determine the primary sphere size if the agglomerates are composed of primary spheres with a fractal dimension less than two (loose agglomerates). Operated under the scanning mode, the UNPA can provide the number, surface area and volume distributions of loose agglomerates in the range of 50 to several hundred nanometers in several minutes. We have used the UNPA to measure metal nanoparticle agglomerates and diesel exhaust particulates and the results are described here.

UNPA utilizes Differential Mobility Analyzer (DMA), Condensation Particle Counter (CPC) and Nanoparticle Surface Area Monitor (NSAM) to characterize airborne nanoparticle morphology and measure the number, surface area and volume distributions of airborne nanoparticles. The key parameter measured is the UNPA sensitivity, which is defined as the current I (fA) measured by the NSAM divided by the number concentration N (#/cm³) measured by the CPC

$$S = I/N \text{ (fA cm}^3\text{).} \quad (1)$$

Charging theories of Chang (1981^[9]) for aerosol particles of arbitrary shape indicate that the geometric surface area and electrical capacitance of the particles are two important parameters to determine the mean charge of non-spherical particles. The electrical capacitance of agglomerates may be computed using a variational method proposed by Brown and Hemingway (1995^[10]). The surface area of loose agglomerates may be calculated using a mobility analysis developed by Lall and Friedlander (2006^[11]). Shin et al. (2010^[8]) combined the above analyses to show that the electrical capacitance of loose agglomerates is larger than that of spherical particles with the same mobility, and loose agglomerates can gain more charges from unipolar charging.

The primary particle size plays an important role in determination of the surface area and

electrical capacitance, thus the charges on agglomerates. The UNPA sensitivity is related to the primary particle diameter d_p . We found that the UNPA sensitivity can be correlated to the primary particle size through a power law relation (Wang et al. 2010^[7])

$$S = c_2 \left(\frac{12\pi\lambda}{c^* d_p^2 C_c} \frac{d_m}{C} \right)^k c_1 (d_p)^h \quad (2)$$

where c^* is a constant regarding particle orientation, λ is the mean gas free path, c_1 , c_2 , k and h are constants which can be determined from the experimental data. Then the sensitivity data from the experiments can be fitted into (2) to determine the primary particle diameter d_p . Once the primary particle size is determined, surface area and volume of the agglomerates can be calculated.

Experimental Methods

Diesel engine exhaust has profound impact on environment and ecosystem. Diesel aerosols are mainly agglomerates with open structures and composed of primary particles. We measured diesel aerosols generated from a 4045 John Deere Diesel Engine using UNPA. A schematic of the experiment is shown in Fig. 1. Diesel aerosols were sampled from the exhaust pipe and mixed with dilution air in the residence chamber. Then the diesel aerosols were sent to Nanometer Aerosol Sampler (NAS) for collection of electron micrograph samples, and to UNPA for agglomerate measurement.

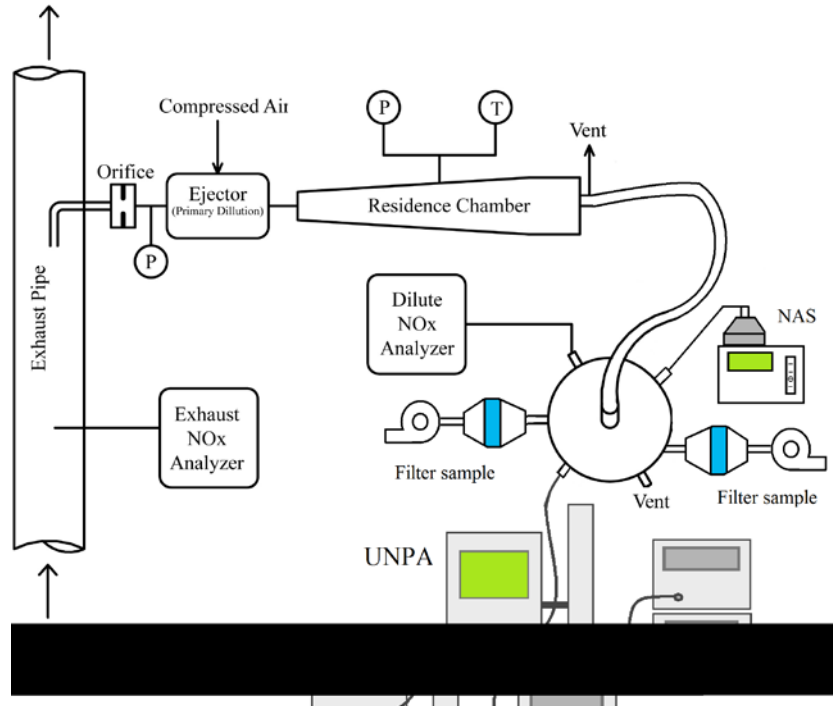


Figure 1. A schematic of the setup for diesel aerosol sampling and measurement.

Periodic spark discharge can vaporize electrode materials and the subsequent nucleation/condensation leads to nanoparticle formation (Schwyn et al. 1988^[12]). The metal nanoparticles in our study were generated by a Palas spark generator (Model GFG-1000). Its design and operating principle can be found in the paper of Helsper et al. (1993^[13]). The following electrodes for the spark generator have been used: gold (ESPI Metals, 0.125" diameter, 99.999%), silver (ESPI Metals, 0.125" diameter, 99.999%) and nickel (ESPI Metals, 0.125" diameter, 99.995%). The generated nanoparticle agglomerates were neutralized and sampled by the UNPA.

Results and Discussion

We sampled the diesel aerosols under two engine conditions: light load and heavy load. The engine speed, torque and exhaust temperature increased with the load. A catalytic stripper was used to remove sulfur compounds and the soluble organic fraction by passing the diluted diesel exhaust over two heated catalysts. The primary particle sizes of diesel particles measured by UNPA are listed in Table 1. The primary sizes were also measured using a large number of TEM images (Fig. 2). A total of 212 primary particles were analyzed in the case of heavy load, and 189 primary particles in the case of light load. The primary particle size from TEM agreed well with UNPA measurement for the heavy load case. In the case of light load, there was about 6 nm difference between UNPA and TEM results, which was still within the standard deviation of the TEM result.

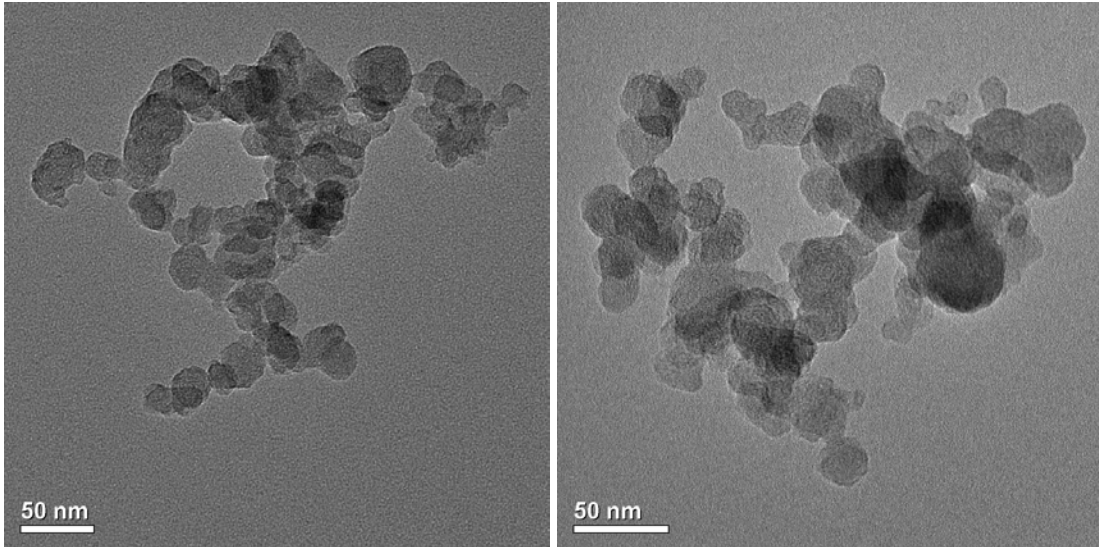


Figure 2. TEM images of diesel particles under the following conditions (a) light load, (b) heavy load.

Table 1. Comparison of the primary particle size in diesel agglomerates measured by UNPA and TEM.

Engine load	Primary particle sizes from UNPA (nm)	Primary particle size from TEM (nm)
Light	29.5	23.2 ± 6.6
Heavy	24.2	23.9 ± 6.8

For the metal nanoparticle agglomerates from the spark discharge generator, we determined the primary particle sizes for agglomerates using the sensitivity data and equation (2). We also analyzed electron micrographs and obtained the primary particle sizes. A comparison of the primary particle sizes from the two methods is shown in Table 2. It can be seen that the agreement for the primary particle size is good and UNPA can measure primary particles in a rather wide size range.

Table 2. Comparison of primary particle sizes measured by UNPA with those by TEM.

Particle	d_p , nm (UNPA)	d_p , nm (TEM)
Au	6.0	7.9 ± 1.5
Ag	8.4	11.8 ± 3.2
Ni	4.1	6.6 ± 1.0

SUMMARY

Nanoparticle agglomerates possess different electrical charging properties than spherical particles, which is the basis of our instrument UNPA. UNPA can measure the primary particle size in open-structured agglomerates and compute the number, surface area and volume distributions. UNPA measurement results for metal nanoparticles agglomerates and diesel exhaust particulates agreed well with offline measurements.

ACKNOWLEDGMENTS

This work was supported by the NSF grant (Award ID: 1056479) on "Real Time Measurement of Agglomerated or Aggregated Airborne Nanoparticles Released from a Manufacturing Process and Their Transport Characteristics".

REFERENCES

- [1] Pratsinis, S. E. (1998). *Prog. Energy Combust. Sci.* 24:197-219.
- [2] Wang, J., Asbach, C., Fissan, H., Hülser, T., Kuhlbusch, T.A.J., Thompson, D. and Pui, D.Y.H. (2011), *In press, J. Nanoparticle Research*, DOI 10.1007/s11051-011-0236-z.
- [3] Kim, S. C., Wang, J., Emery, M. S., Shin, W. G., Mulholland, G. W., and Pui, D. Y. H. (2009). *Aerosol Sci. & Technol.* 43:344-355.
- [4] Koylu, U. O., Faeth, G. M., Farias, T. L., and Carvalho, M. G. (1995). *Combust. Flame*. 100:621-633.
- [5] Rogak S.N., Flagan R.C., Nguyen H.V. (1993) *Aerosol Sci Technol* 18:25-47.
- [6] Shin, W-G, Wang, J., Mertler, M., Sachweh, B., Fissan, H., Pui, D.Y.H. (2009) *J. Nanoparticle Research*. 11, 163 – 173.
- [7] Wang, J., Shin, W. G., Mertler, M., Sachweh, B., Fissan, H., and Pui, D. Y. H. (2010). *Aerosol Sci. & Technol.* 44:97-108.
- [8] Shin, W. G., Wang, J., Mertler, M., Sachweh, B., Fissan, H., and Pui, D. Y. H. (2010) *J. Aerosol Sci.* 41:975-986.
- [9] Chang, J. S. (1981). *J. Aerosol Sci.* 12:19-26.
- [10] Brown, R. C., and Hemingway, M. A. (1995). *J. Aerosol Sci.* 26 (8):1197-1206.
- [11] Lall A.A., Friedlander S.K. (2006) *J. Aerosol Sci* 37: 260-271.
- [12] Schwyn, S., Garwin, E., and Schmidt-Ott, A. (1988). *J. Aerosol Sci.* 19 (5):639-642.
- [13] Helsper, C., Molter, W., Loffler, F., Wadenpohl, C., Kaufmann, S., and Wenninger, G. (1993). *Atmospheric Environ.* 27A (8):1271-1275.

Ambient ammonia and ammonium aerosol in the urban area of Beijing

Zhaoyang Meng¹, Xiaobin Xu¹, Weili Lin¹, Yangmei Zhang¹, Xiaolan Yu¹, and Xiaofang Jia²

1 Key Laboratory for Atmospheric Chemistry of CMA, Center for Atmospheric Watch and Services of CMA, Chinese Academy of Meteorological Sciences, Beijing, 100081 China

2 Department of Environmental Engineering, School of Civil and Environmental Engineering, University of Science and Technology Beijing, Beijing, 100083 China

Principal Contact: Zhaoyang Meng, Professor, Chinese Academy of Meteorological Sciences, Beijing, 100081, China.

Tel: 010-58995263 Email: mengzy@cams.cma.gov.cn

Abstract

Continuous measurements of atmospheric ammonia were conducted using Ogawa passive samplers from February 2008 to July 2010 at a site of China Meteorological Administration (CMA) in Beijing, China. NH₃ was parallel measured by a NOx/NH₃ analyzer (EC9842, Ecotech, Australia) for inter-comparison with passive sampler from June 2009 to June 2010. The hourly concentrations of NH₄⁺ in PM_{2.5} were also measured with the Ambient Ion Monitor (URG 9000 Series, USA) during 2009-2010. The concentrations of NH₃ ranged from 0.7 to 85.1 ppb, with the annual average of 18.5±13.8 ppb and 23.5±18.0 ppb in 2008 and 2009. The NH₃ concentrations were higher than NH₄⁺ in PM_{2.5} in spring, summer and autumn, while were less than NH₄⁺ in winter. Higher NH₄⁺ concentrations also were seen in summer. The diurnal variations of NH₄⁺ in summer displayed that the concentration of NH₄⁺ increased gradually from the early morning to the noon, and then decreased. For spring, autumn and winter, the slight diurnal patterns of NH₄⁺ were noted. NH₃ and NH₄⁺ aerosol concentrations were weakly correlated, while average daily NH₃/NH₄⁺ ratios were higher in summer.

Keywords: NH₃, passive and active sampling, NH₄⁺, Beijing

Measurements of gaseous NH₃ and HNO₃ and particulate ions collected over 4 years in the Upper Green River Basin, Wyoming

Yi Li¹, Jeffrey L. Collett, Jr.¹, H. James Sewell², Cassie Archuleta³, Mark Tigges³, Florian M. Schwandner^{1,4}, Lincoln Sherman³, Taehyoung Lee¹, Stephen Holcomb³, John V. Molenar³, and Suresh Raja^{1,5}

1 Colorado State University, Department of Atmospheric Sciences, Fort Collins, CO 80523 1371

2 Shell Exploration & Production Company, 4582 S. Ulster Street Parkway, Suite 500, Denver, CO 80237

3 Air Resource Specialists, Inc., 1901 Sharp Point Drive Suite E, Fort Collins, CO 80525

4 now at Earth Observatory of Singapore (EOS), Nanyang Technological University, 50 Nanyang Avenue, Singapore, SGP 639798

5 now at Center for Air Resources Engineering and Science and Department of Chemical Engineering, Clarkson University, Potsdam, NY, USA

Principal Contact: Jeffrey L. Collett, Jr., Atmospheric Science Department, Colorado State University, Fort Collins, CO 80523 USA.

E-mail: collett@atmos.colostate.edu

Abstract

A multi-year Ammonia Air Monitoring Project is being conducted at Boulder, Wyoming, USA, a fossil fuel-rich area in the Upper Green River Basin. The aim of this project is to characterize the local nitrogen budget and, specifically, ammonia concentrations and concentrations of related gases and particles by using a URG (University Research Glassware, Incorporated) annular denuder/filter system. Ambient samples were collected twice a week, and then analyzed by ion chromatography at Colorado State University's Atmospheric Science Department.

The four year mean concentrations of NH₃, HNO₃, NH₄⁺, NO₃⁻ and SO₄²⁻ were 0.18, 0.19, 0.25, 0.31 and 0.51 μgm^{-3} , respectively, and a clear seasonality was observed. The concentration of NH₃ was higher in the summer than other seasons, consistent with increased NH₃ emissions and a shift in ammonium nitrate equilibrium toward the gas phase at higher temperatures. High HNO₃ concentrations were observed both in summer and winter. The unusual winter HNO₃ peak appears to be due to active local photochemistry in a shallow boundary layer over a reflective, snow-covered surface. High winter ozone concentrations are also observed at this rural site. The measured aerosol ion balance is generally close to 1:1 except in summer when an anion deficit is apparent. The presence of water soluble organic acidic ions, such as oxalic acid, is being examined.

Keywords: Nitric acid, Ammonia, Ammonium nitrate, Ammonium sulfate, Seasonal variations, Ion balance, Annular denuder system(ADS)

Aerosol Measurements at the Nanjing Xianlin Station

Erik Herrmann^{1,2} and Aijun Ding¹

1 Institute for Climate and Global Change Research & School of Atmospheric Sciences, Nanjing University, Nanjing 210093, P. R. China

2 Department of Physics, Division of Atmospheric Sciences, 00014 University of Helsinki, Finland

ABSTRACT

The Nanjing Xianlin Station for Multi-Process Studies of Earth System is a new site to conduct comprehensive long-term measurements in order to improve our understanding of atmospheric processes and, ultimately, climate. Taking up operation in the Summer of 2011, it will monitor a number of trace gases, gas fluxes, and various meteorological parameters. One focus of the station is on atmospheric aerosols and especially new particle formation. Aerosol size distributions will be measured with DMPS system (6-800nm). Additionally, an Air Ion Spectrometer (AIS, Airel Ltd.) monitors ion concentrations in the size range from 0.8 to 42nm, thus allowing us a direct look at atmospheric nucleation.

KEYWORDS

Aerosol, Atmospheric, Nucleation, Air ions, Size distribution

Introduction

The IPCC report 2007^[1] has identified aerosols as a major unknown factor affecting the global radiation balance. Most recent estimates see atmospheric new particle formation (nucleation) as the source for 20 to 80% of the global aerosol load. Thus, in order to understand climate and predict its future development, one needs to understand atmospheric nucleation. The process has been observed all over the globe, but the exact mechanism and some of the involved vapors are still unclear. It is also an open question if the process is the same all over the world or if there are local or regional differences in terms of the mechanism itself or the species participating in it.

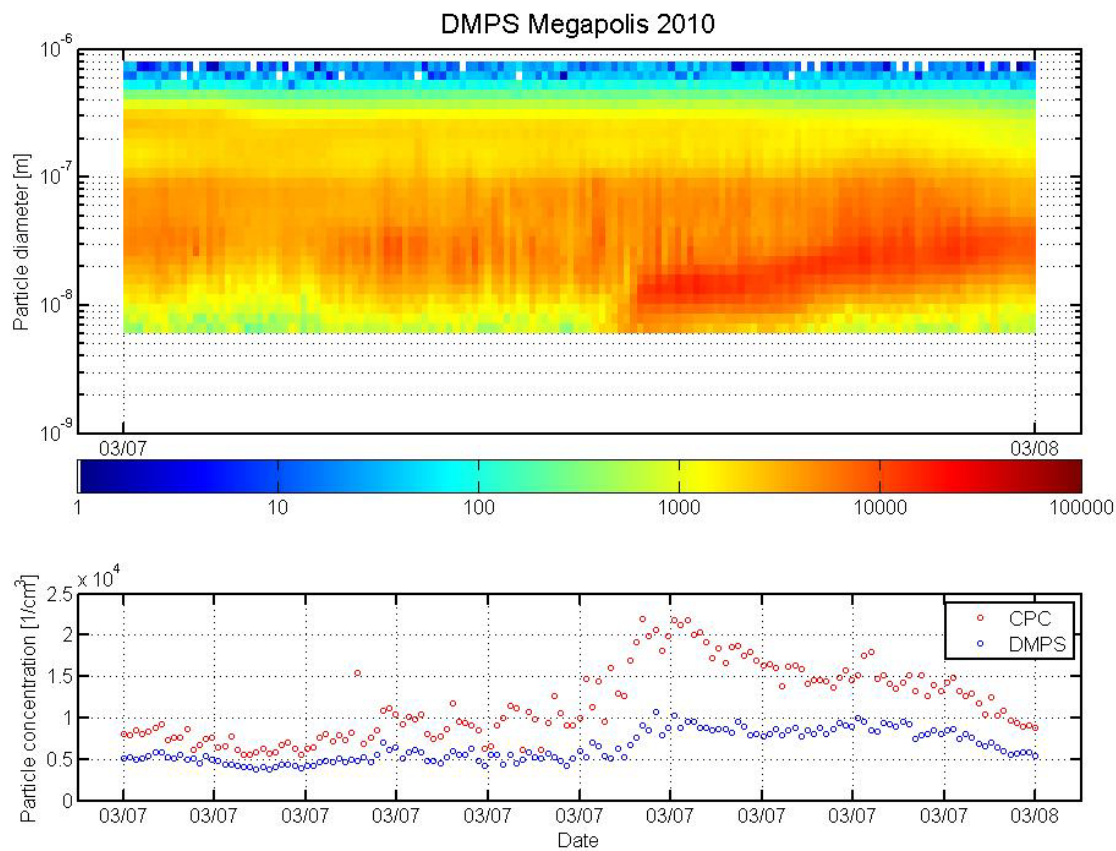
One approach to solve the question of atmospheric nucleation are ambient measurements:

- over long periods of time
- in as many different locations as possible and
- with comprehensive additional measurements of fluxes, trace gases etc.

Despite more than 15 years of observing atmospheric nucleation, such measurements are rare and far from covering the different environments on Earth. The Nanjing Xianlin Station for Multi-

Processes Studies of Earth System will (besides other objectives) provide valuable insight into atmospheric new particle formation. With its state-of-the-art combination of a differential mobility particle sizer (DMPS) and an air ion spectrometer (AIS)^[2], it is possible to measure particle size distributions between 0.8 and 800nm. This well-tested approach allows the identification and characterization of particle formation events which can then be related to a variety of other measurements in order to identify under which circumstances nucleation occurs. Moreover, the station is located at a unique regional background site in the Yangtze River Delta, one of the most developed and polluted areas in China, and will as such give insight into nucleation under these specific conditions.

Figure 1. New particle formation as seen through a DMPS.



The measurement station

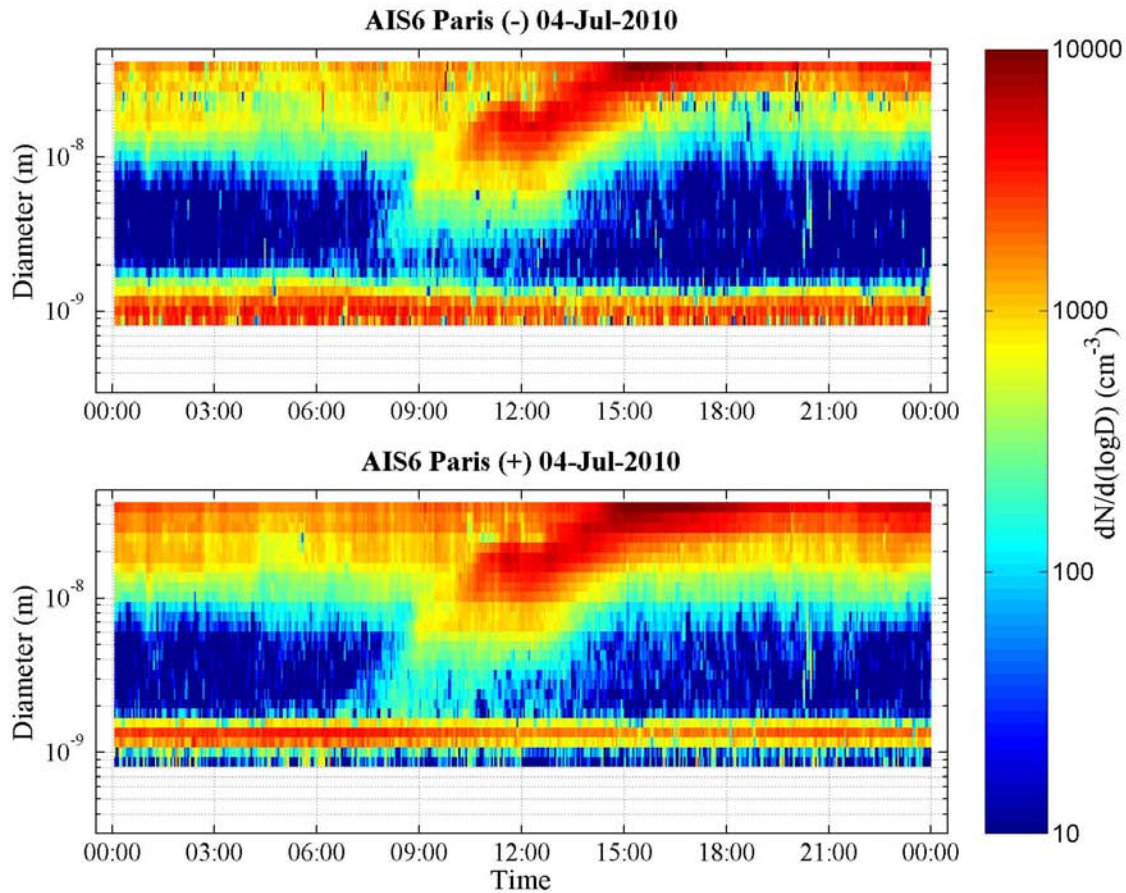
The Station is located about 30km northeast of the Nanjing city center on a hill overlooking the Xianlin campus area. It features a mast to measure temperature, wind, and relative humidity at 6 heights as well as fluxes of water and CO₂. In addition to this, the station houses measurements

of trace gases (O_3 , CO, CO_2 , NO, NO_x , NH_3) and a number of instruments to determine the surface energy balance. Various PM filters (1, 2.5, 10) and a Nephelometer complete the aerosol instrumentation whose core comprises of a DMPS and AIS combination to determine aerosol concentrations from cluster size all the way to the accumulation mode. The pairing of DMPS and AIS has proven to be powerful tool in various measurement campaigns.^[3] A special feature of the station is its location just outside a major city. Depending on wind directions it is so possible to determine the effects of urban air pollution or to measure background aerosol behavior.

Central aerosol instrumentation

The Differential Mobility Particle Sizer (DMPS) has become a standard in atmospheric aerosol research in the last twenty something years.^[4] Combining classification based on electrical mobility in a DMA (differential mobility analyzer)^[5] and subsequent counting of particles in a CNC (condensation nuclei counter)^[6], a DMPS provides information about the aerosol size distribution and its evolution in time. At the Nanjing station, we use a Helsinki-built DMPS that consists of one DMA tube and a TSI model 3772 CPC. With this design, aerosol particles in the size range from 6 to 800nm can be detected. Figure 1 shows an example of a DMPS measurement, in this case originating from the Megapolis campaign in Paris, France. In the plot, one can observe an increase in the number of small particles in the early afternoon and their subsequent growth. In order to see below the DMPS limit of 6nm we use the

Figure 2. New particle formation as seen through an AIS



Air Ion Spectrometer (AIS) which has greatly improved scientific understanding of atmospheric new particle formation during the last years. Very much like the DMPS, the AIS classifies air ions by their electrical mobility. However, the AIS does not require the ions to grow for optical detection. Instead, the charge of the ions is registered. With this technique, air ions as small as 0.8nm can be detected. The upper limit of the AIS size range is at 42nm. Figure 2 shows an example of an AIS data set, once again a nucleation event from the Megapolis campaign. Very typical for AIS spectra is the constant band of air ions around 1.5nm. This band has also been found for neutral particles; its existence supports the cluster activation theory^[7] as a possible explanation for nucleation in the atmosphere.

OUTLOOK

The first phase of Nanjing University's Xianlin station will become fully operational during Summer 2011. After an initial measuring period, the station will be extended by additional

instrument, either permanently or on the basis of intensive campaigns with partners from China and abroad. Ultimately, the research at the station will (from an aerosol point of view) bring us one step closer to understanding atmospheric nucleation.

ACKNOWLEDGMENTS

This work was supported by China National Basic Research Program ('973 Project 2010CB428500) and MOE '985 Project at Nanjing University. Also the financial support by the Academy of Finland Centre of Excellence program (project no 1118615) is gratefully acknowledged.

REFERENCES

- [1] Climate Change 2007: The Physical Science Basis. Cambridge University Press: Cambridge, United Kingdom and New York, NY, USA, 2007.
- [2] Mirme, A. et al.. *Boreal Env. Res.* 2007, *12*, 247-264.
- [3] Manninen, H. E. et al.. *Atmos. Chem. Phys.* 2010, *10*, 7907-7927.
- [4] Kulmala, M. et al.. *J. Aerosol Sci.* 2004, *35*, 143-176.
- [5] Knutson, E. O.; Whitby, K. T.. *J. Aerosol Sci.* 1975, *6*, 443–451.
- [6] Agarwal, J. K.; Sem, G. J.. (1980). *J. Aerosol Sci.* 1980, *11*, 343–357.
- [7] Kulmala, M. et al.. *Atmos. Chem. Phys.* 2006, *6*, 787-793.

PM_{2.5} Real-time Forecasting over the Southeastern United States with WRF/Chem-MADRID

Ming-Tung Chuang^{1, 2} and Yang Zhang¹

1 Air Quality Forecasting Lab, North Carolina State University, Raleigh, NC 27695, USA

2 currently at Department of Environmental Engineering, Air Quality Research Lab, National Central University, Jhung-Li, Taoyuan 32001, Taiwan

Principal Contact: Ming-Tung Chuang, Postdoctoral Researcher, Department of Environmental Engineering, National Central University, No. 300. ChuangDa Road, Jhung-Li, Taoyuan, 32001, Taiwan.

Tel: +886-983932906 Fax: (886)-3-4226551 E-mail: mtchuang100@gmail.com

Abstract

Real-Time Air Quality Forecasting (RT-AQF) provides useful information to the public, in particular, sensitive people, to minimize risks to human health and to take preventive actions to protect welfare such as crops and animals. Such information can also guide air quality agencies to take necessary steps to temporarily shut off major sources of air pollutions. In this work, the Weather Research and Forecasting model with Chemistry with the Model of Aerosol Dynamics, Reaction, Ionization, and Dissolution (WRF/Chem-MADRID) is applied for RT-AQF at a horizontal grid resolution of 12-km over the southeastern United States. Our objectives are to develop an RT-AQF system that can accurately forecast air quality under changing weather and real-time emissions. The National Centers for Environmental Prediction (NCEP)'s meteorological forecast is downloaded at 7 PM (LST) every other day to start a simulation for 60 hours, which is used to provide a two-day forecast. The AQF products are post-processed and evaluated using available observations on a daily basis and as monthly means. The forecasting skills are evaluated for two episodes: 3-10 (6 full days from 4 to 9) August 2008 and May 1 to September 30 in 2009. The AIRNow (<http://www.airnow.gov/>) database is used to assess the model's capabilities in replicating the observations for both episodes. For the first episode, the performance of WRF (Advanced Research WRF (ARW))/Chem-MADRID is also intercompared with that of the NOAA's WRF (Nonhydrostatic Mesoscale Model (NMM))/CMAQ for RT-AQF.

Keywords: real-time forecast, PM_{2.5}, WRF/Chem-MADRID.

Model Analysis of Aerosol Impacts on Atmospheric Visibility in China

Meigen Zhang¹, Xiao Han¹ and Renjian Zhang²

1 LAPC, Institute of Atmospheric Physics, Chinese Academy of Sciences, Beijing 100029.

2 RCE-TEA, Institute of Atmospheric Physics, Chinese Academy of Sciences, Beijing 100029.

Principal Contact: Meigen Zhang, Prof., LAPC, Institute of Atmospheric Physics, Chinese Academy of Sciences, Beijing 100029.

Tel: 86-10-62379620 Fax: 86-10-62379620 E-mail: mgzhang@mail.iap.ac.cn.

Abstract

The air quality modeling system RAMS-CMAQ is implemented to simulate visibility degradation due to aerosol extinction by linking simulated meteorological parameters and aerosol mass concentrations with an aerosol optical properties module in this study. The module is capable to take into account of important factors affecting aerosol optical properties, such as incident wave length, aerosol size distribution, water uptake, internal mixture, etc. Visibility observations, covering the Yangze River Delta region in 2005 are compared against CMAQ visibility parameters. Then several sensitivities runs are performed to analyze the impacts of relatively humidity and aerosol mixing state on aerosol optical properties, Aerosol Impacts on Atmospheric Visibility.

Keywords: haze, aerosol, extinction coefficient

A Numerical Simulation of Windblown Sand Movement over a Slope Surface

Ning Huang¹, Hong Jiang¹ and Ding Tong¹

1 Key Laboratory of Mechanics on Disaster and Environment in Western China, The Ministry of Education of China, Lanzhou, 730000

ABSTRACT

Current theoretical studies and numerical simulations of windblown sand movement concentrate on ideal circumstances, such as steady wind velocity, flat sand surface, etc. However, environment of windblown sand movement is complex in natural, such as complex landform, turbulence structure of wind flow. Actually gradient of windward slope of sand dune and sand ripple etc. which are basic form of desert landscape, have great influence on the initiation and transportation of sand particles. Wind velocity over slope surface is measured by using PDPA technique in wind tunnel to analyze characteristics of wind flow at windward slope and leeward slope. Here established a model of sand saltation movement where wind is coupled with sand particles to simulate windblown sand movement over a slope surface. The SIMPLE algorithm is applied to calculate wind flow and sands transportation is simulated by tracking every particle moving over slope. The results have shown that there is a reversed flow region in leeward slope, and the area become larger when the coupling effect of wind and sand particles is taken into consideration, which implies that particles have obvious effect on wind flow, especially at the leeward slope. At the windward slope, mass flux of sand particles gradually increase along the slope and change regularity of mass flux along height is different from that on flat surface although mass flux of sand particles gradually decreases with height at the windward slope. At the leeward slope, mass flux of sand particles increases first and then decrease with height at leeward slope, which is different from that at windward slope. The maximum of mass flux gradually reduces as sand flux moves away from the top of slope. This work is a preliminary study for sand flow in a complex terrain and is basic importance for study the real sand flow.

KEYWORDS

slope, numerical simulation, mass flux, PDPA

Introduction

The complex interactions between dune morphology, wind flow and sand transport have been

increasingly concerned recently. The research focus on the dynamics of dune windward slopes and sediment dynamics in the turbulent lee-side eddies downwind of transverse dune crests have been made up by similar field and wind tunnel studies. The measurement of wind velocity profile is determined not log-linear on windward slope (Lancaster,1996; Frank and Kocurek,1996). This conclusion has been validated by the wind tunnel experiment (Wiggs,1996) and in the mass the wind tunnel experiment demonstrate a progression increase in shear stress along the windward slope with a maxima at the crest. Streamline curvature lead to the increase of turbulence intensity and shear stress , thereby, sand sediment is restrained at the slope bottom (Wiggs,1996). By measuring the flow velocities of 15 sand leeward slopes at various positions and heights, it presented a model of leeward slopes' flow field which was consist of three flow regions: reflow vortex region, wake current region and a new formed inner boundary layer (Frank and Kocurek,1996). Dong(2009) measured the turbulence and the velocities in the lee of transverse dunes in a wind tunnel. However, the advanced research is prevented by the short of field measurement station and the geometry limit of wind tunnel experiment. The even more worse truth is that the high speed turbulence and backflow cannot be quantified accurately in wind tunnel experiment, because of the design limitation of equipments, for example: Walker and Nickling (2002, 2003) had to neglect the reversed flow survey of leeward slopes. All these elements result that we can neither quantificationally describe the flow field of sand hills nor understand its structure, and meantime the geometry changes influence in sensitivity, the structure of flow region and the coupled dynamic equations. After the international windblown sand physics academy in 1985, the numerical model for description of coupled motion of air stream and sand developed rapidly and it can be divided as two parts: one of them is the model of launch-development-equilibrium on behalf of Anderson, who presented the thesis named Simulation of windblown sand in famous academy journal of science in 1988. It simulate the whole process of windblown sand saltation from the beginning to equilibrium, considering the react force of sand to wind field, which was consistent with the experiment qualitatively yet had a great gap between the experiment and the numerical result in exact number. The other one was brought up to focus on finding a keep state balance model of wind-blown sand based on the self-balanced equilibrium, brought up by Ungar and Haff (Sorensen and McEwan ,1996; Werner,1990). Nevertheless, these simulation were set in even sand bed, failing to consider the effect of rugged surface on wind-blown sand. Although Parson (2004) applied CFD in numerical calculate the wind field under the slope surface, it didn't calculate sand particles movement, nor coupling the relationship among sand particles, wind field and the landform. To make up the respective deficiencies of wind tunnel experiment and numerical simulation, this thesis builds up the coupling wind-blown sand model. Adopting the simple algorithm to calculate the air flow zone and by means of tracking single particle trajectory, it works out the wind-blown sand flow region under slope landform, and also investigates the sand particle entrainment both at upwind

and downwind slope wind field in detail, aiming to mature the wind tunnel test as well as the numerical simulation considering landform and coupling motion for wind flow and sand particles.

Experimental Methods

In order to verify the feasibility and accuracy of numerical simulation model, PDPA was used in wind tunnel experiment to measure wind field velocity over slope. In order to assist the numerical simulation better, the fitting curve is obtained. The fitted wind speed profile is used as the initial wind speed value of entrance in simulation.

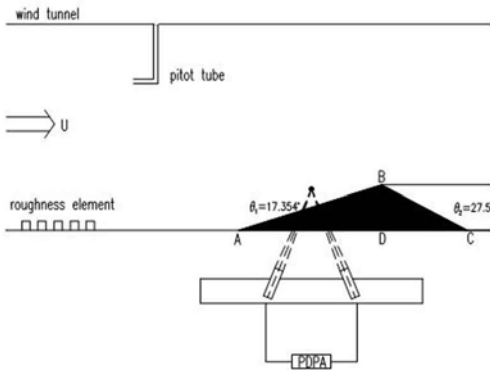


Figure.1. Schematic drawing of the experimental apparatus

The Numerical Model

Equations of one sand particle saltation

$$m \ddot{x} = -\frac{\rho \pi D^2}{8} \left[\frac{24v}{D \sqrt{(\dot{x}-u)^2 + (\dot{y}-v)^2}} + \frac{6}{1 + \sqrt{\frac{D}{v \sqrt{(\dot{x}-u)^2 + (\dot{y}-v)^2}}}} + 0.4 \right] \times (\dot{x}-u) \sqrt{(\dot{x}-u)^2 + (\dot{y}-v)^2} \quad (\text{Eq.1})$$

$$m \ddot{y} = -\frac{\rho \pi D^2}{8} \left[\frac{24v}{D \sqrt{(\dot{x}-u)^2 + (\dot{y}-v)^2}} + \frac{6}{1 + \sqrt{\frac{D}{v \sqrt{(\dot{x}-u)^2 + (\dot{y}-v)^2}}}} + 0.4 \right] \times (\dot{y}-v) \sqrt{(\dot{x}-u)^2 + (\dot{y}-v)^2} - mg \quad (\text{Eq.2})$$

initial condition: $t = 0, x = x_0, y = y_0, \dot{x} = u_0, \dot{y} = v_0$

Equations of wind flow field

$$\text{mass conseravation equation: } \frac{\partial \rho}{\partial t} + \text{div}(\rho \mathbf{u}) = 0 \quad (\text{Eq.3})$$

$$x \text{ momentum conservation equation: } \frac{\partial(\rho u)}{\partial t} + \text{div}(\rho u \mathbf{u}) = \text{div}(\mu \text{grad} u) - \frac{\partial p}{\partial x} + S_u \quad (\text{Eq.4})$$

$$y \text{ momentum conservation equation: } \frac{\partial(\rho v)}{\partial t} + \text{div}(\rho v \mathbf{u}) = \text{div}(\mu \text{grad} v) - \frac{\partial p}{\partial y} + S_v \quad (\text{Eq.5})$$

boundary condition:

- (1) entrance wind velocity is the fit of velocity in the wind tunnel experiment
- (2) export boundary condition is the full development flow.
- (3) top and sides of the field boundary condition are symmetrical.
- (4) bottom of the field boundary condition is no-slip.

computation of wind flow field:

- (1) calculate discretization of conservation equations by finite volume method.
- (2) the coupling of velocity and pressure is calculated by SIMPLE algorithm.
- (3) the resistance $F_x(i, j)$ and $F_y(i, j)$ on wind flow due to saltating sand grains is included in S (generalized source term). S reflect the coupling of sands and wind flow field.

Sand-bed splash process

In wind-blown sand flow, the particle which leaves off the bed surface ,up into saltation layer would finally drop down to the surface by the act of gravity and impact the bed then rebound itself, ejecting other particles on the bed, or neither of them happens, and this process is defined as sand-bed impact. Since it takes place close to surface, the unknown random influence on the impact velocity and angle by the turbulent flow and the various shapes of sand particle in nature which means no definite uniform diameter even homotactic diameter, the particle range in surface is complicated, leading to different sand-bed impact model and also the impact position is indefinable besides the very various material ingredient of nature sand particles. Adopting splash function by Werner(1990), the thesis modifies part of the ejected angle and velocity according to different positions (flat position, downwind slope and upwind slope) and based on these elements it simulates the sand-bed impact process.

Results and Discussion

Wind field over slope

Compared with the flat surface the velocities of wind flow field are accelerated over the slope surface. Wind flow structure changed over slope surface. In addition, Numerical simulation results and measurement results are well anastomotic. It can be seen that horizontal velocity accelerate at windward slope. And there is a region of reversed flow at the leeward slope. Reversed flow vortex can be seen intuitively through streamlines. Vertical velocity is positive at windward slope because of slope and the maximum is at the slope surface. Wind velocity gradually decrease with height increase. With the gradually away from leeward slope, there will be a new inner boundary area. The whole wind flow structure and patterns are similar although the axis wind speed is different.

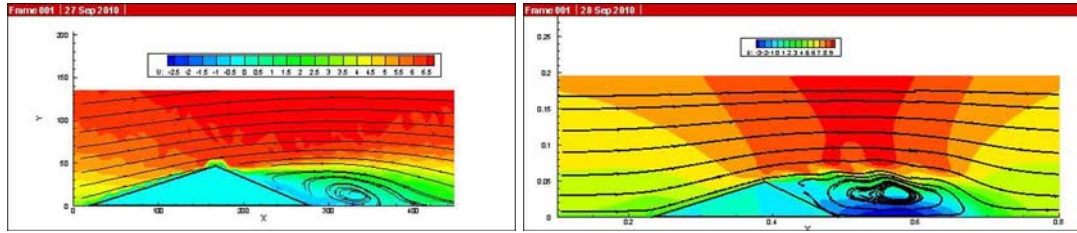


Figure.2. Observation and Simulation of wind field velocity at 8.43m/s Comparisons of coupled and uncoupled windblown sand

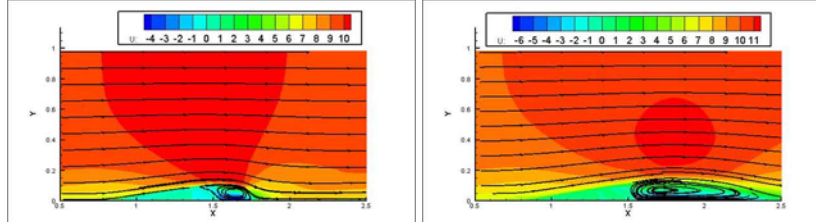


Figure.3. Simulation of wind field velocity of uncoupled and coupled windblown sand

It can see that velocities of wind field change great under the coupling over a slope surface. The windblown sand over the slope surface is different from it over the flat surface. Compared with the flat surface the velocities of wind flow field are accelerated over the slope surface. There is a region of reversed flow at the leeward slope and then the region of reversed flow changes is larger in the coupled windblown sand than uncoupled wind flow field. Re-attachment distance is on the order of 4 times the triangle slope height while there is uncoupled wind flow field. However, in the coupled windblown sand field re-attachment distance is on the order of 9 times the triangle slope height. It documents that the coupling effect is significant in the numerical simulation. This phenomenon is discussed in Frank and Kocurek (1996) and Walker(2000). They estimated this distance to be on average 4-8 dune heights downwind. From this phenomenon, it documents that lee-side secondary flow pattern and re-attachment depend on wind speed and direct as well as dune geometry, incident flow angle and atmospheric stability, what's more, the coupling effect may be main reason.

Comparisons of mass flux profiles at different positions of slope surface

From Figure4 it can be seen that the mass flux profiles over a slope surface are different from flat bed surface. The mass flux is no longer exponential distribution with height. From Figure5 it can be seen mass flux of sand particles gradually decreases with height at the windward slope. Besides that, at the windward slope the gradient of the mass flux-height increase with the slope-point location raise up. From Figure6, all the mass flux profiles increase first and then decrease with height at the leeward slope. In addition, the maximum of the mass flux gradually reduce as it away from the top of the slope.

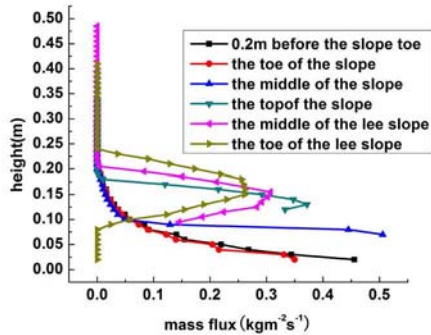


Figure 4. simulated mass flux profiles at different positions of slope

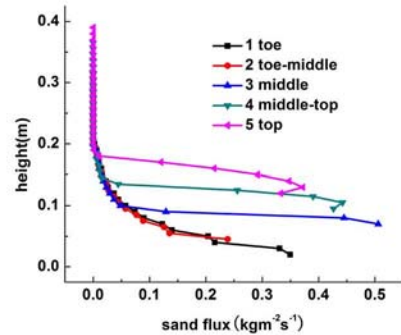


Figure 6. simulated mass flux profiles at different positions of windward slope

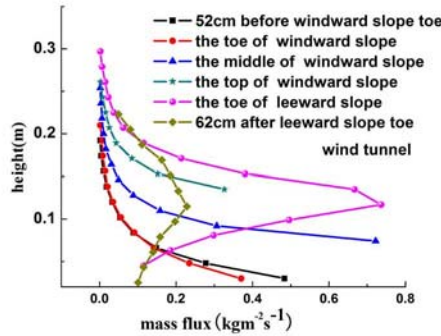


Figure 5. observation mass flux profiles at different positions of slope in wind tunnel

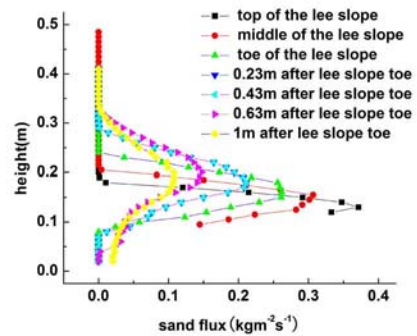


Figure 7. simulated mass flux profiles at different positions of leeward slope

In Figure 7, At the windward slope, the mass flux of sand particles gradually decreases with height , and the gradients of the mass flux of sand grains gradually increase along the slope . At the leeward slope, the mass flux of sand particles increases first and then decrease with height which is different from that at the windward slope. The maximum of the mass flux gradually reduces as sand flux moves away from the toe of the leeward slope.

The deficiency of the numerical simulation is that there are also a little different from wind tunnel experiment at the quantification although the numerical model can describes primary patterns of sands transport over the slope surface. It is related to Splash function is not suitable at the slope surface which is applied in the simulation of windblown sand over flat bed surface.

CONCLUSION

Compared with the flat surface the velocities of wind flow field are accelerated over the slope surface. There is a reversed flow region in the leeward slope and the area become larger along with sand coupling; flow re-attachment distance depend on the coupling effect. At the windward slope, the gradients of both the wind velocity and the mass flux of sand particles gradually

increase along the slope and the change regularity of mass flux along height is different from that on flat surface although the mass flux of sand particles gradually decreases with height at the windward slope. At the leeward slope, the gradient of the wind velocity increase as wind flows down the slope and it becomes slow down as wind flows away from the toe of the slope. The mass flux of sand particles increases first and then decrease with height at the leeward slope, which is different from that at the windward slope. The maximum of the mass flux gradually reduces as sand flux moves away from the top of the slope.

However there is quantification contrast compared with wind tunnel observation. The splash function of the flat surface is the important reason result the contrast. We expect to investigate sand-bed splash process and then obtain the sand-bed splash function of slope. The splash function of slope is the decisive factor to exactly describe the sands saltation over the slope surface.

REFERENCES

- Lancaster N., Nickling W.G., McKenna Neuman, C.K. and Wyatt, V.E. Geomorphology, 1996, 17(1-3):55-62.
- Frank,A.J. and Kocurek,G. Geomorphology,1996, 17(1-3):47-54.
- Frank, A.J. and Kocurek, G. Sedimentology,1996,43(3):451-458.
- Wiggs, G.F.S., Livingstone, I. and Warren, A. Geomorphology,1996, 17:29-46.
- Wiggs, G.F.S. 1993. Geological Society of London, Special Publication 72, pp. 37-46.
- Wiggs, G.F.S. Progress in Physical Geography, 2001, 25(1):53-79.
- Qian Guangqiang, Dong Zhibao, Luo Wanyin and Wang Hongtao. Journal of Arid Environments, 2009, 73(12):1109-1116.
- Dong Zhibao, Qian Guangqiang, Lu Ping, Luo Wanyin and Wang Hongtao. Earth Surface Processes and Landforms, 2009, 34(2):204-216. doi:10.1002/esp.1704
- Walker, I.J. and Nickling, W.G. 2002. Progress in Physical Geography,2002, 26(1):47-75.
- Walker, I.J. and Nickling, W.G. Earth Surface Processes and Landforms,2003, 28(10):1111-1124.
- Anderson, R.S. and Haff, P.K. Science,1988,241(4867):820-823.
- Sørensen, M. and McEwan, I. Sedimentology,1996,43(1):65-76.
- Werner, B.T. 1990. The Journal of Geology,1990, 98(1):1-17.
- Parsons, D.R., Walker, I.J. and Wiggs, G.F.S. 2004. Geomorphology,2004,59(1-4):149-164.
- Nickling, W.G. and McKenna Neuman, C. 1997. Geomorphology 18(3-4):333-345.

Aerosol-cloud-precipitation interactions in numerical models - a new perspective

Xiaoning Xie and Xiaodong Liu

Institute of Earth Environment, Chinese Academy of Sciences, Xi'an, 710075, China

Principal Contact: Xiaoning Xie, Doctor, Institute of Earth Environment, Chinese Academy of Sciences, Xi'an, 710075, China.

Tel: 029-88327411 Email: xnxie@ieecas.cn

Abstract

The impact of aerosols on surface precipitation represents one of the most important issues of anthropogenic climate change, which remains highly uncertain. Whether atmosphere aerosols restrain or enhance precipitation has long been a controversial issue. Liu and Daum (2002, *Nature*, 419, 580–581) indicated that spectral dispersion (spectral dispersion represents the relative dispersion of cloud droplet size distribution which is a measure of size distribution of cloud droplets) can be affected by anthropogenic aerosols, is closely related to the aerosol indirect effects. However, the cloud microphysics parameterization, especially the autoconversion parameterization doesn't consider spectral dispersion in most models. In this study, numerical simulations were performed to investigate the effects of aerosols on clouds and precipitation, using the autoconversion parameterization with spectral dispersion. The Weather Research and Forecast model (WRF) with the different relationships between spectral dispersion ε and cloud droplet number concentration N_c (the Martin, Rotstayn-Liu, and Grabowski relationships) was used with either the Maritime (“clean”) or Continental (“dirty”) backgrounds. Numerical experiments indicate that the response of the accumulative precipitation to aerosols is dependent on the $\varepsilon - N_c$ relationships, suggesting that the variation of the autocoversion processes induced by spectral dispersion can change the effects of aerosols on precipitation. When spectral dispersion is an increasing function of N_c (the Martin relationship or the Rotstayn-Liu relationship), the accumulative precipitation increases from the clean maritime background to the polluted continental background; however, it is evidently reduced with increasing concentrations of aerosol particles when spectral dispersion is a decreasing function of N_c (the Grabowski relationship). Owing to the importance of spectral dispersion on clouds and precipitation, in-depth explorations of the relationships between spectral dispersion and cloud microphysical properties will help further the knowledge on aerosol-cloud-precipitation interactions.

Carbonaceous Aerosols in China: Top-down Constraints on Primary Sources and Estimation of Secondary Contribution

Tzung-May Fu¹, Xiaoye Zhang², Junji Cao³, Shuncheng Lee⁴, Kin Fai Ho⁴, Wenjun Qu⁵, Qiang Zhang⁶, Zhiwei Han⁷ and Renjian Zhang⁷

1 Department of Atmospheric and Oceanic Sciences and Laboratory for Climate and Ocean-Atmosphere Studies, School of Physics, Peking University, Beijing, China, 100871

2 Key Laboratory of Atmospheric Chemistry, Chinese Academy of Metrological Sciences, China Meteorological Administration, Beijing, China, 100081

3 State Key Laboratory of Loess and Quaternary Geology, Institute of Earth Environment, Chinese Academy of Sciences, Xi'an, China, 710075

4 Department of Civil and Structural Engineering, Hong Kong Polytechnic University, Hung Hom, Kowloon, Hong Kong

5 Key Laboratory of Physical Oceanography, Department of Marine Meteorology, College of Physical and Environmental Oceanography, Ocean University of China, Qingdao, China, 266100

6 Center for Earth System Science, Tsinghua University, Beijing, China, 100084

7 Key Laboratory of Regional Climate-Environment Research for Temperate East Asia, Institute of Atmospheric Physics, Chinese Academy of Sciences, Beijing, China, 100029

Principal Contact: Tzung-May Fu, Professor, Peking University, No. 9 Chengfu Road, Haidian District, Beijing, 100871, China.

Tel: +86-10-62753221 Fax: +86-10-62751094 E-mail: tmfu@pku.edu.cn

Abstract

We simulate elemental carbon (EC) and organic carbon (OC) aerosols in China and compare model results to measurements at Chinese rural and background sites, with the goal of deriving “top-down” emission estimates of EC and OC, as well as better quantifying the secondary source of OC. We include in the model the current best Chinese “bottom-up” emission inventories for EC (1.92 Tg/yr) and OC (3.95 Tg/yr), as well as updated secondary organic aerosol formation mechanisms. The model underestimates surface monthly mean EC concentrations at rural and background sites by 46% year-round ($R = 0.48$), with largest discrepancies in fall. The model is unable to reproduce both the magnitudes and the spatial patterns of observed surface monthly mean OC concentrations in any season ($R = 0.16$). We conduct sensitivity tests to calculate the individual contributions to surface EC from the following three Chinese source sectors: (1) power generation, industry, and transportation (PIT), (2) residential activities, and (3) biomass burning activities. Multiple linear regression to fit surface monthly mean EC observations yields best estimates of Chinese EC source of 3.05 Tg/yr, including 2.30 Tg from PIT sources, 0.64 Tg from residential sources, and 0.11 Tg from biomass burning sources. Based on the above best estimate of EC sources and observed seasonal lowest OC/EC ratios, we estimate Chinese OC total emissions to be 6.67

Tg/yr, including 4.96 Tg, 1.46 Tg, and 0.25 Tg from PIT, residential, and biomass burning sources, respectively. The model's performance in reproducing OC observations is only slightly improved when our best estimates of OC sources is applied ($R = 0.24$), indicating poor representation of primary OC sources, as well as secondary formation mechanisms, in the model.

Keywords: carbonaceous aerosol, EC, OC, secondary organic aerosol, emission inventory.

Pole-to-Pole Observations of Black Carbon Aerosol and Their Applications to Diagnosis of Long-Range Transport and Model Performance

R. S. Gao¹, J. P. Schwarz^{1,2}, J. R. Spackman^{1,2}, A. E. Perring^{1,2}, L. A. Watts^{1,2}, S. C. Wofsy³, and D. W. Fahey^{1,2}

1 National Oceanic and Atmospheric Administration, Earth System Research Laboratory, Chemical Sciences Division, Boulder, Colorado, USA

2 Cooperative Institute for Research in Environmental Sciences, University of Colorado, Boulder, Colorado, USA

3 Department of Earth and Planetary Sciences, Harvard University, Cambridge, Massachusetts, USA

Principal Contact: Dr. Ru-Shan Gao, Research physicist, NOAA ESRL CSD, 325 Broadway R/CSD6, Boulder, CO 80305, USA.

Tel: 1-303-497-5431 Fax: 1-303-497-5373 E-mail: rushan.gao@noaa.gov

Abstract

Atmospheric black carbon (BC) plays an important role in global climate change. Climate change might be slowed in the short-term by reductions of atmospheric BC. BC affects climate radiative forcing directly via strong solar radiation absorption and indirectly through cloud effects. There are still large uncertainties in the estimates of BC forcing terms. One source of such uncertainty lies in the large differences that exist between model estimates of BC spatio-temporal loadings and observations. Since early 2009, the NSF/NCAR GV research aircraft has carried the NOAA Single-Particle Soot Photometer (SP2) and other instruments on three HIAPER Pole-to-Pole Observations (HIPPO 1, 2, 3) campaigns to sample the remote atmosphere over global scales in three seasons. On each campaign, lasting only three weeks, the aircraft covered latitudes from ~85°N to ~67°S, primarily in the vicinity of the dateline. Over one hundred vertical profiles from near the surface to 14 km altitude per campaign ensured both high vertical and horizontal resolution. These flight series have produced an unprecedented dataset including BC concentration, size distribution, mixing state, and dry optical size. The dataset provides striking, and previously unobtainable, pole-to-pole snapshots of BC mass loadings showing long-range transport and large interhemispheric gradients of BC that allow us to constrain trans-pacific transport of BC. The vertical profiles averaged in five latitude zones were compared to an ensemble of AEROCOM aerosol model fields. The comparisons suggest that BC removal in global models may need to be evaluated separately in different latitude regions and perhaps enhanced.

Keywords: Black carbon, AEROCOM aerosol model, long-range transport.

Enhanced Aerosols Appeared at the Tropical Tropopause over Biak Indonesia in January 2011

Takashi Shibata¹, Masahiko Hayashi², Kei-ichirou Hara², Ayumi Naganuma², Naoko Hara², Suginori Iwasaki³, Youichi Inai¹, Kensaku Shimizu⁴, Fumio Hasebe⁴ and Saipul Hamdi⁵

1 Nagoya University, Furo-cho, Chikusa-ku, Nagoya 465-8601, Japan

2 Fukuoka University, Nanakuma, Jonan-ku, Fukuoka 814-0180, Japan

3 National Defence Academy of Japan, Hashirimizu, Yokosuka, 239-8686, Japan

4 Hokkaido University, Kita-ku, Sapporo 060-0810, Japan

5 LAPAN, Jalan Dr. Djundjunan 133, Bandung 40173, Indonesia

ABSTRACT

Enhanced aerosols have been found just above the tropical cold point tropopause by observations using lidar and balloon borne optical particle counter (OPC) in January 2011. The aerosols have one or two layers structure within the campaign period from 6th to 13th January. The width of the layer was 1-2 km. The depolarization ratio of the layer was very small (or nearly zero), and the wavelength dependence of the backscattering coefficients were similar to that of the stratospheric aerosols. The backscattering coefficient of the layer was about five times larger than the background aerosols. Cirrus cloud appeared within this aerosol layer. The estimated number concentration of the cloud particles is $\sim 1000 / \text{m}^3$. The relative humidity over ice before the ice formation is estimated to be about 110%. These microphysical characteristics of the cloud are consistent with the recent formation studies of the cirrus cloud particles nucleating on the solid aerosol particles like ammonium sulfate particles.

KEYWORDS

tropical stratosphere, aerosols, ice formation, volcanic aerosols

Introduction

Lower stratospheric water vapor has a crucial contribution to the global climate^[1]. However, the cause of the observed long term temporal variation of the mixing ratio in the lower stratospheric water vapor is not understood well. The main origin of the lower stratospheric water vapor is tropospheric water vapor transported by general circulation (Brewer-Dobson circulation), or by tropical strong convective activity. In the both dynamical processes, the air mass including water vapor passes through the tropical tropopause. Since the temperature at the low latitude tropopause is very low ($\sim 180\text{K}$), the water vapor forms ice clouds and is removed from the air

mass by gravitational sedimentation. This transport from the troposphere to the stratosphere and the freeze drying at the tropopause determine the water vapor flux to the stratosphere. Therefore, the ice cloud formation is a key process to estimate the influence of stratospheric water vapor to the global climate^[2].

Thin cirrus clouds are often observed just below the tropical tropopause. The clouds are frequently having only sub-visible optical depth, and are called sub-visible cirrus clouds (SVC). These ice particles are nucleated from vapor phase with the aerosol particles as the ice nuclei (IN) at the altitude range. But it is still not clear which kind of aerosol particles are working as IN. This uncertainty makes it difficult to estimate the tropical dehydration and the variation of the lower stratospheric water vapor.

We have conducted observational campaign to observe tropical upper tropospheric and lower stratospheric aerosols, cirrus clouds and water vapor in January 2011 at Biak (-1°S, 136°E), Indonesia. The campaign is intended to get the key information on the cirrus formation and resulting dehydration processes. Enhanced aerosols were incidentally observed at the tropical tropopause height level in this campaign. We will report the characteristics of the aerosol layer observed at the tropopause height level and a cirrus cloud layer appeared in this aerosol layer.

Methods of Observation

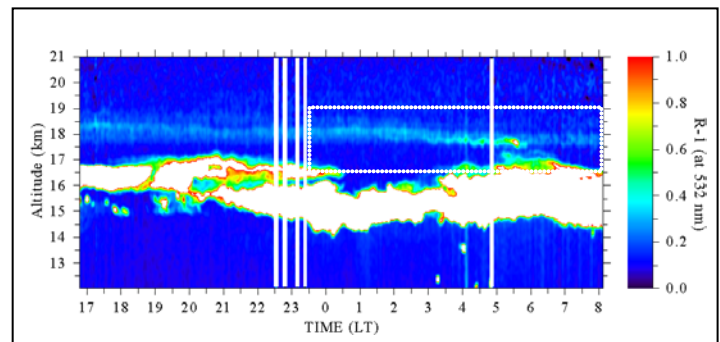
Aerosols were observed by Mie scattering depolarization lidar and balloon borne optical particle counter (OPC)^{[3], [4]}. We use two wavelengths at 1064 nm and 532 nm for the lidar to observe Mie scattering backscattering coefficient by aerosols and cirrus clouds. Depolarization ratio is also observed at 532 nm. The lidar was operated continuously through the campaign period.

OPC was launched by latex balloon up to about 30 km by the ascending speed of 5 m/sec. The minimum detection diameter range is 3 to 10 μm , and the number of interval is ten. OPC observation is also used to measure the heated inlet air to observe the evaporation property of the aerosols. The temperature was set at 200°C.

Water vapor frost point temperature (or partial pressure calculated by using it) was observed by Colorado University, cryogenic frost point hygrometer (CU-CFH)^[5]. CU-CFH is optimized to observe low temperature and very dry condition of tropical tropopause and stratosphere.

Results and Discussion

Figure 1 shows the lidar-observed backscatter ratio (R ; the ratio of total [molecular plus particle] backscattering to molecular backscattering) minus one



observed from January 11 to 12, 2011. The scaled out (white) region at around 14 to 17 km in altitude is by strong backscattering from cirrus clouds.

An aerosol layer was observed at around 18 km in altitude just above the cirrus. Note that denser cirrus cloud was observed within the aerosol layer at the local time around 3 to 6 on 12th and at the altitude between 17.5 and 18 km. The following Figure 2 shows the plots of the R-1, depolarization ratio by particles (DP), and ratio of backscattering coefficients at wavelength 1064 nm to at 532 nm (color ratio, CR)

Figure 1 R-1 at the wavelength of 532 nm observed from January 11 to 12, 2011. Aerosol layer was seen at around 18 km in altitude above cirrus cloud layer that is almost scaled out by the used range of the color scale. At the local time around 3 to 6, cirrus cloud was observed within the aerosol layer. The periods with low data quality are masked by white bars. Rectangular by the dotted line is the expanded area of the next Figures 2 and 3.

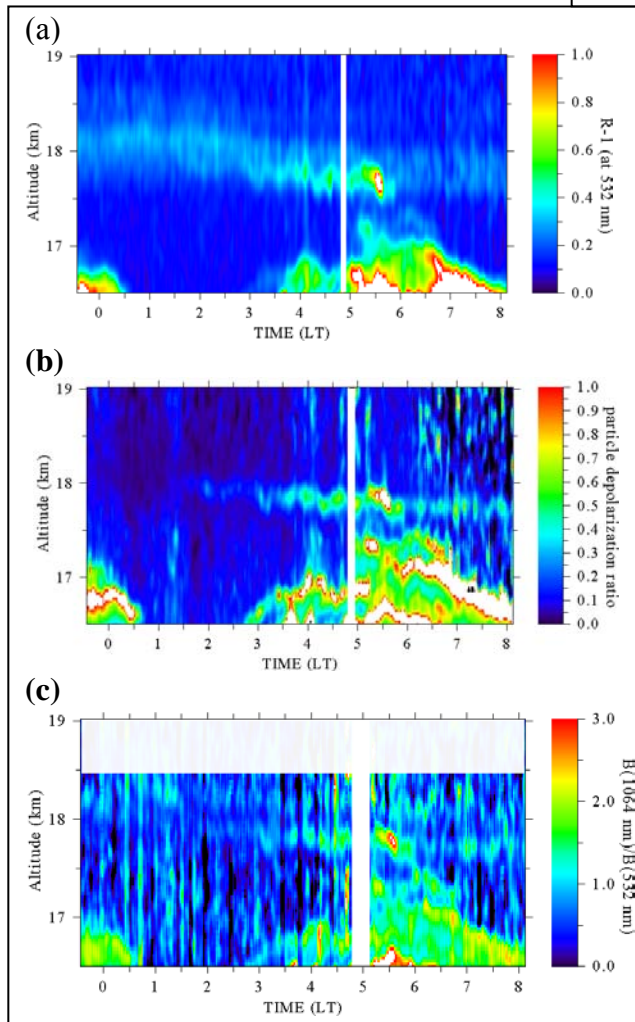


Figure 2

(a) The R-1 for the expanded time-height region on January 12th in the Figure 1.

(b) Depolarization ratio at the wavelength of 532 nm for the same time-height region of (a). The depolarization by aerosol layer was not detectable, or very small, and is indicating that the aerosol particles are spherical shape. Enhancement of depolarization was seen at the local time around 3 to 6 and at the altitude between 17.5 and 18 km. The value of the depolarization is as large as 0.5 at this enhanced layer. This is the typical value for the cirrus clouds.

(c) Color ratio of the backscattering coefficient by the particles between at the wavelength of 1064 nm and of 532 nm. The enhanced layer shows the similar value of the lower cirrus clouds. The color ratio at the aerosol layer is smaller than 1, and is typical value for aerosols. Upper noisy area is masked.

for the same expanded time height region.

The depolarization ratio began to increase at 18 km in altitude and at around 1 AM, and took maximum value at 5:30 AM on 12th (Figure 2 (b)). The time-height region of the increase in DP was just the same region of increase in R-1 (Figure 2 (a)). The increased value of DP is the typical value for the cirrus clouds particles ^[3]. The similar increase was observed in the color ratio, CR (Figure 2 (c)). The value of increased CR, again, is the typical value for the cirrus clouds particles ^[6]. The CR values around the increased CR of cirrus clouds took smaller values smaller than 1. This smaller CR region correspond to the aerosol region (Figure 2 (a)), and the smaller CR is consistent with the CR by aerosol.

The scattering property of the enhanced backscattering layer observed from 1 to 8AM on January 12th, 2011 at the altitude around 18 km shows the property of cirrus clouds. This event can probably be interpreted as the cirrus layer appeared within the aerosol layer that was almost continuously observed over Biak for the campaign period from 6th to 12th January, 2011. This cirrus cloud appearance probably indicates that the aerosol particles within the aerosol layer worked as the ice nuclei for the cirrus cloud particles formation.

Roughly estimated number concentration of cirrus cloud particles from backscattering coefficient by assuming 10 μm for the mode radius of cirrus cloud particles is $\sim 1000 \text{ /m}^3$. This number is two orders smaller than the number concentration of aerosols at the layer observed by the balloon borne OPC, but agrees well with the values by the recent studies ^[2]. Similarly estimated ratio of the ice water content to the saturation water vapor concentration (ISR) is several percent. The estimated ISR suggests that if the ice particles were formed in situ, the saturation ratio before the ice formation is less than 110% at around 5:30AM. This saturation ratio is several ten percents smaller than the experimentally estimated critical saturation ratio of the ice formation in solution liquid aerosol particles ^[7], but again agrees well with the value by the results of recent experimental study ^[8]. The relative humidity over ice 101-105% was observed by balloon borne CU-CFH at the bottom of the aerosol layer. This is supporting the estimated saturation ratio for the ice nucleation.

SUMMARY

Aerosols, cirrus clouds and relative humidity around the tropical tropopause were observed by lidar, balloon borne OPC and CU-CFH. The stable aerosol layer was observed just above the tropopause through the campaign, and an event was observed that cirrus cloud was formed within the aerosol layer. The estimated microphysical characteristics of cirrus clouds are consistent with recently proposed formation mechanism of the tropical cirrus clouds.

References

- [1] Solomon, S.; Rosenlof, K.; Portmann, R.; Daniel, J.; Davis, S.; Sanford, T.; Plattner, G.-K. Science 2010, 327, 1219-1223.

- [2] *e.g.* Jensen, E. J.; Pfister, L.; Bui, T.-P.; Lawson, P.; Baumgardner, D. *Atmos. Chem. Phys.* 2010, 10, 1369-1384.
- [3] Shibata, T.; Voemel, H.; Hamdi, S.; Kaloka, S.; Hasebe, F.; Fujiwara, M.; Shiotani, M. *J. Geophys. Res.* 2007, 112, D03210, doi:10.1029/2006JD007361.
- [4] Hayashi, M. *Earozoru Kenkyu* 2001, 16, 118-124.
- [5] Hasebe, F.; Fujiwara, M.; Shiotani, M.; Voemel, H.; Oltmans, S.; Takashima, H.; Saraspriya, S.; Komala, N.; Inai, Y. *Atmos. Chem. Phys.* 2007, 7, 803-813.
- [6] Vaughan, M. A.; Liu, Z.; McGill, M. J.; Hu, Y.; Obland, M. D. *J. Geophys. Res.*, 2010, 115, D14206, doi:10.1029/2009JD013086.
- [7] Koop, T.; Luo, B.; Tsias, A.; Peter, T. *Nature*, 2000, 406, 611-614.
- [8] Wise, M. E.; Baustian, K. J.; Tolbert, M. A. *PNAS*, 2010, 107, 6693-6698.

Development of Optical Aerosol Sensor Based on Polypyrrole Nanofilm

Hongyi Qin¹, Hang Zhang², Atul Kulkarni¹ and Taesung Kim^{1,2}

1 School of Mechanical Engineering, Sungkyunkwan University, Suwon 440-746, Korea

2 SKKU Advanced Institute of Nano Technology (SAINT), Sungkyunkwan university, Suwon 440-746, Korea

ABSTRACT

Atmospheric aerosol nanoparticles are becoming important in many areas such as environmental science, occupational medicine, semiconductor industry, material science and forensic sciences. In this paper, we propose the use of conductive polymer, polypyrrole (PPy) nanofilm, as an sensitive material for aerosol sensing. The PPy nanofilm is deposited on the distal end of the end face of the optical fiber to form the PPy-fiber optic fiber reflectance probe. The sensor principle relies on the change of the light scattered by the aerosol adsorbed on PPy nanofilm. The sensor performance was encouraging towards NH₄Cl and NaCl aerosols for various concentration and size.

KEYWORDS

Aerosol sensor, Polypyrrole nanofilm, Polymer optical fiber, Scattering

Introduction

Atmospheric aerosol particles refer to microscopic solid or liquid phase material suspended into air. They are primary products of combustion and of industrial or natural processes, and secondary products of gas to particle conversion in the atmosphere. The environmental monitoring for aerosol particles are of great importance because they can greatly affect the human health, the industrial safety, and the climate system^[1, 2].

Various detection methods have been developed for atmospheric aerosol detection^[3-7], however, almost all detection methods depend on mass spectroscopic techniques which is costly and time-consuming. For this reason, there is a need to develop accurate, inexpensive, subminiature sensor. Optical fiber sensor based on the change of absorbance, reflectance, luminescence, reflective index and scattered light is an ideal candidate for the mass production and application. Usually,

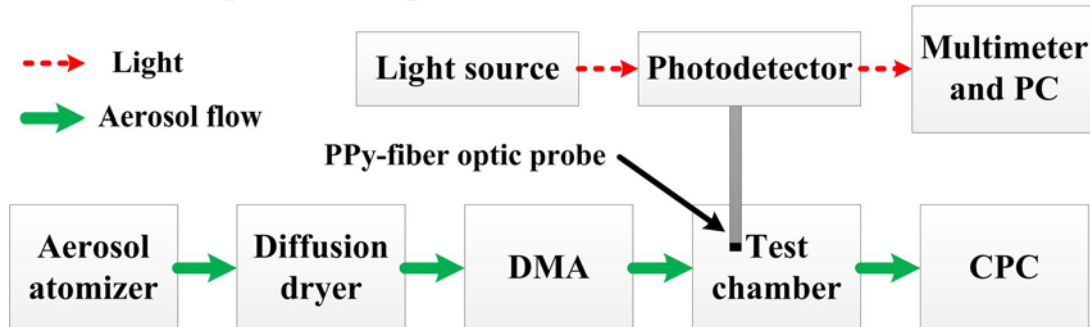
the sensitive thin membrane materials are used as a key part of optical fiber sensor, whose optical properties can change with the detecting environment.

In our present work, the PPy nanofilm based on the interfacial polymerization technique was used as an ideal sensitive membrane material for particle aerosol detection. PPy is a well known conducting polymer because pyrrole (Py) monomer is water soluble, commercially available and can easily oxidized. Usually, almost all the PPy sensor was based on its electrical properties^[8-10], and to our knowledge, no previous work has been reported on the optical fiber sensor based on the PPy nanofilm for atmospheric aerosol detection. The detected aerosols, NaCl and NH₄Cl, were characterized using standard aerosol characterization equipment such as Scanning Mobility Particle Sizer (SMPS) system.

Experimental Methods

The interfacial polymerization technique is utilized to synthesis the sensitive PPy nanofilm^[11]. Here the 70 ml FeCl₃ (0.04 M) water solution is added into the 70 ml Pyrrole (Py) monomer (0.093 M) chloroform solution to achieve the Py/Fe³⁺ ratio to 2.33, and all the chemicals were of reagent grade and purchased from Sigma Aldrich, Korea. After 4 hours, a thin PPy nanofilm is formed at the interface between chloroform and water at room temperature and without stirring. Further the polymerization is quenched via removing the solutions over and below the film. then the PPy nanofilm is transferred to ethanol/DI water mixed solution and immersed for 2 hours, and then, the clean PPy nanofilm is carefully deposited on the end face of the optical fiber to obtain a PPy-fiber optic probe.

Figure 1. Schematic presentation of PPy nanofilm fiber optical sensor evaluation setup for aerosol particles detection.



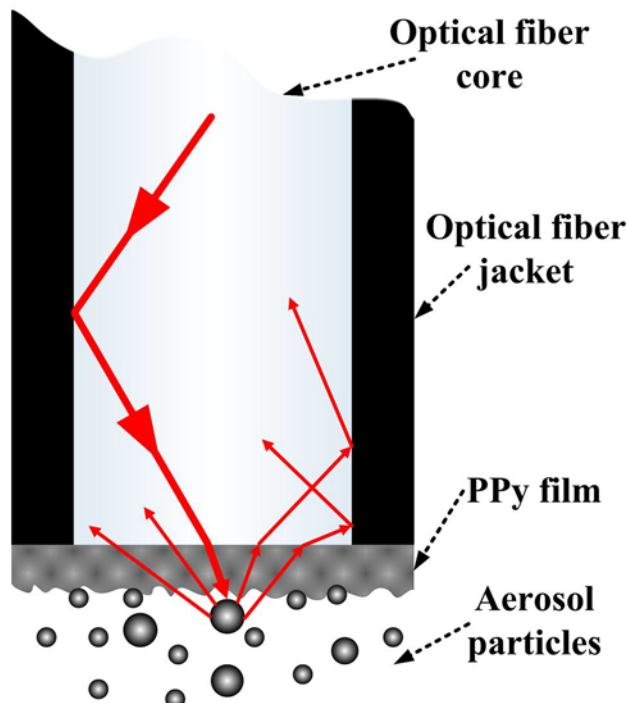
The schematic illustration of the experimental setup used to detect particles aerosol is shown in the Fig. 1. The aerosol flow generated by the aerosol atomizer passed through the diffusion dryer

to remove the water. And then, the polydisperse aerosol flow is injected into the differential mobility analyzer (DMA) (Model 2081, TSI Inc.) to obtain monodisperse aerosol flow which is delivered to the test chamber. The PPy-fiber optic probe of detection system is inserted into the test chamber, this detection system consist of a white light source, a Si photodiode detector (PDA36A, Thorlab) and a computer interfaced digital multimeter (2700, Keighley). Moreover, condensation particle counter (CPC) (Model 3025A, TSI Inc.) is utilized to measure the aerosol particles size distribution. All experiments are carried out in the dark room at room temperature.

Results and Discussion

The detection mechanism of PPy-fiber optic probe for the aerosol is by monitoring the change in scattered light due to the aerosol, as shown in the Fig. 2. In the process of detection, the scattered light travel through the polymer optical fiber and is detected by the photodetector. The key role of PPy nanofilm is that the adsorption effect for the aerosol is greatly increased due to the structure and irregular surface of PPy nanofilm. Therefore, the scattering effect of aerosol particles trapped by the PPy nanofilm is more pronounced, and also the better detection sensitivity is obtained.

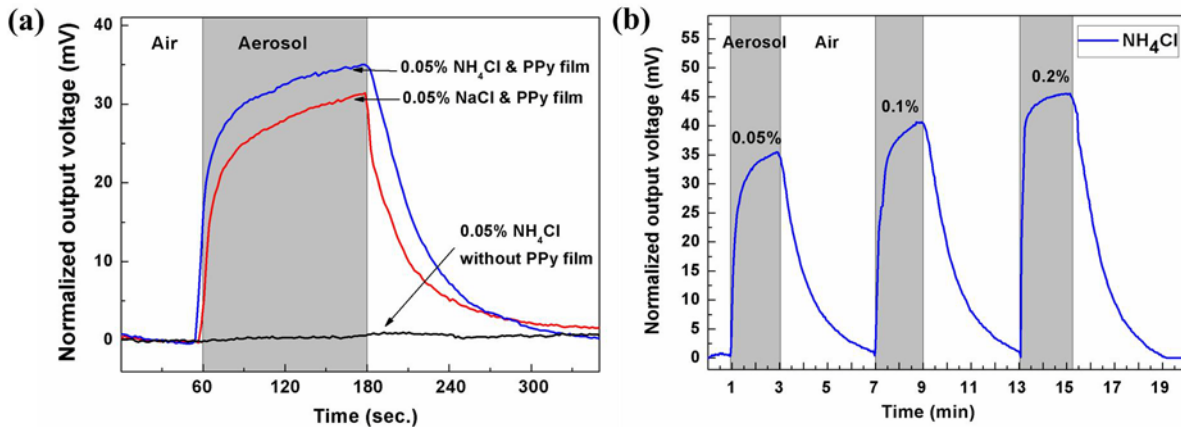
Figure 2 . Schematic of PPy-fiber optic probe and the detecting mechanism.



The synthesis time is an important parameter because it can greatly affects the transmittance of PPy nanofilm. According to the light scattering mechanism, the intensity of light scattered by aerosol particles directly affects the detecting result, therefore, the PPy film with good light transmission is necessary. In our study, the longer synthesis time, the lower transmittance of PPy film. However, the film with shorter than 4 hours synthesis time is easily broken in drying, hence, the 4 hours synthesis time PPy film with 50% transmittance is selected as the ideal sensitive film. The 4 hours film thickness is about 155 nm.

The PPy thin film optical fiber sensor response for the aerosols, NH₄Cl and NaCl, was evaluated using white light and shown in the Fig.3a. A optical fiber without PPy nanofilm was designed to be comparative experiment. Obviously, it shows no response for NH₄Cl aerosol particles. However, comparing with the detection probe without PPy nanofilm, the PPy-fiber optic probe has a excellent response for the aerosol particles detection. The increase of photodetector output voltage demonstrates that the transmitted light has been scattered and reflected by aerosol. Moreover, the response time of PPy-fiber optic probe is approximately 10 second, which is comparable with similar aerosol sensors.

Figure 3. (a) Sensor response with PPy and without PPy for 0.05% aerosol particles detection, (b) sensor response for different mass percent particles detection.



The effects of particle size and concentration are also investigated using the CPC, the particles aerosol with different particle size distribution is obtained by injecting different mass percent salt water solution into the atomizer. The distribution modes of aerosol particles generated from 0.2%, 0.1% and 0.05% salt solution are about 76 nm, 88 nm and 105 nm, respectively. The detection response is enhanced as the particles concentration and size are increased (Fig. 3b). Those detection results have be explained well by the Rayleigh scattering theory^[12], and the particle size and concentration are the key factors to affect the light scattering.

CONCLUSION

PPy nanofilm synthesized by the interfacial polymerization technique and optical fiber sensor based on the PPy nanofilm for the atmospheric aerosol detection were developed. The synthesis procedure of PPy nanofilm is simple, moreover, the structure and rough surface of the PPy nanofilm are greatly advantaged to trap aerosol particles. The PPy nanofilm optical fiber sensor based on the light scattering principle shows a good response for the NH₄Cl and NaCl particles aerosol detection. This technique has many advantages over conventional aerosol sensors and broadens the application fields of conductive polymer, PPy. In a conclusion, the reported sensing technique for atmospheric aerosol nanoparticles has a great potential application.

ACKNOWLEDGMENTS

This research was supported by Basic Science Research Program through the National Research Foundation of Korea (NRF) funded by the Ministry of Education, Science and Technology (2011-0006268).

REFERENCES

- [1] Lohmann, U.; Feichter, J. *Atmos Chem Phys* 2005, 5, 715-737.
- [2] Poschl, U. *Angew Chem Int Edit* 2005, 44, 7520-7540.
- [3] Kalberer, M.; Paulsen, D.; Sax, M.; Steinbacher, M.; Dommen, J.; Prevot, A.S.H.; Fisseha, R. Weingartner, E.; Frankevich, V.; Zenobi, R. et al. *Science* 2004, 303, 1659-1662.12-45.
- [4] Rattigan, O.V.; Hogrefe, O.; Felton, H.D.; Schwab, J.J.; Roychowdhury, U.K.; Husain, L.; Dutkiewicz, V.A.; Demerjian, K.L. *Atmos Environ* 2006, 40, 192-205.
- [5] Stolzenburg, M.R.; Hering, S.V. *Environ Sci Technol* 2000, 34, 907-914.
- [6] Surratt, J.D.; Lewandowski, M.; Offenberg, J.H.; Jaoui, M.; Kleindienst, T.E.; Edney, E.O.; Seinfeld, J.H. *Environ Sci Technol* 2007, 41, 5363-5369.
- [7] Yu, J.Z.; Cocker, D.R.; Griffin, R.J.; Flagan, R.C. *J Atmos Chem* 1999, 34, 207-258.
- [8] Jeon, S.S.; An, H.H.; Yoon, C.S.; Im, S.S. *Polymer* 2011, 52, 652-657.
- [9] Shoa, T.N.; Madden, J.D.W.; Mirfakhrai, T.; Alici, G.; Spinks, G.M.; Wallace, G.G. *Sensor Actuat A* 2010, 161, 127-133.
- [10] Waghuley, S.A.; Yenorkar, S.M.; Yawale, S.S. *Sensor Actuat B* 2008, 128, 366-373.
- [11] Sree, U.; Yamamoto, Y.; Deore, B.; Shiigi, H. *Synthetic Met* 2002, 131, 161-165.
- [12] Sneep, M.; Ubachs, W. *J Quant Spectrosc Ra* 2005, 92, 293-310.

Develop a Mixing-Type Electrocyclone for Removing Submicron Particulate Matter

Ta-Chih Hsiao¹

1 National Central University, No.300, Jhongda Rd., Jhongli City, Taoyuan County 32001, Taiwan (R.O.C.)

Principal Contact: Ta-Chih Hsiao, Assistant Professor, National Central University, No.300, Jhongda Rd., Jhongli City, Taoyuan County 32001, Taiwan (R.O.C.).

Tel: 886-3-4227151#34682 Fax: 886-3-4262163 E-mail: tchsiao@ncu.edu.tw

Abstract

Cyclones are widely used in a variety of industrial sectors, as well as in academic studies, because of the low cost of manufacturing, operating, and maintaining costs. In addition, due to their simple and robust design, cyclones have the potential to treat high volumes and could be employed under high temperature or extreme pressure conditions. However, cyclones are normally used to separate particles in the supermicron size range. To either improve the cyclone collection efficiency (having a smaller cutoff size) or lessen the energy consumption (reducing the pressure drop), the electrostatic force was introduced as an additional mechanism for capturing particles in electrocyclones. Although electrocyclones have these advantages, the performance of traditional electrocyclones will be easily degraded due to the particle contamination on the corona wire. In addition, comparing to the extensive studies on tangential cyclones, only a few literatures were published on electrocyclones. The performance of electrocyclones have not been fully explored and optimized.

In this study, a prototype mixing-type electrocyclone is proposed and the detail particle collection mechanisms will be experimentally characterized. The device combines a cyclone with an air-jet corona ionizer to prevent the corona wire directly exposing to challenging particles. Two different configures of mixing corona ion flow and aerosol stream are proposed. The detail of this experimental work will be presented in the conference.

Keywords: aerosol cyclone, corona charger, particle remover.

Application of the Polarization-Raman-Mie Lidar in Automatic and Continuous Observation of Aerosol and Cloud

Chenbo Xie, Bangxin Wang, Fudi Qi, Zhiqing Zhong, Zhenzhu Wang, Guangyu Bo and Dong Liu

Key Laboratory of Atmospheric Composition and Optical Radiation, Anhui Institute of Optics and Fine Mechanics, Chinese Academy of Sciences, P.O. box 1125, Hefei, Anhui 230031, China

Principal Contact: Chenbo Xie, Dr., Key Laboratory of Atmospheric Composition and Optical Radiation, Anhui Institute of Optics and Fine Mechanics, Chinese Academy of Sciences, P.O. box 1125, Hefei, Anhui 230031, China.

Tel: +86-551-5591007 Fax: +86-551-5591521 Email: cbxie@aiofm.ac.cn.

Abstract

The Polarization-Raman-Mie Lidar (PRML) developed for Chinese Academy of Meteorological Sciences is introduced. The PRML lidar have the three detection channels for detecting the Raman scattering signal, the parallel and perpendicular polarization signals of aerosol and cloud, simultaneously. The use of Raman scattering is a well established method to determine the vertical profile of the aerosol and cloud extinction and backscatter coefficients independently, resulting in a dramatic reduction to the associated uncertainties than the traditional Mie scattering lidar observation. Another advantage of Raman scattering detection is to provide the lidar ratio of aerosol and cloud, which is an important parameter for characterizing microphysical properties of them. The parallel and perpendicular polarization signals are useful indicator of nonspehricity for identifying ice clouds and dust layers. For convenience, the PRML lidar is specially designed to be a compact, turn-key and unattended one-box instrument that are rugged, run from a standard AC power outlet. No specialist knowledge is required for installation and maintenance and the software provides real-time data processing. The PRML lidar can be operated in a continuous mode through a window on the roof of the observation room, regardless of weather. It's very useful to monitor the spatial and temporal properties of aerosols and clouds.

Keywords: Polarization Lidar, Raman Lidar, Aerosol, Cloud

Comparative Studies of Instruments That Measure Black Carbon Properties in Mexico City

Ping Chen¹, Darrel Baumgardner² and Armando Retama³

1 Handix Corporation, Boulder, Colorado, 80301

2 Universidad Nacional Autonoma de Mexico, Ciudad Universitaria, Mexico City, DF, 04510

3 LMD - Ecole Polytechnique, Palaiseau, France

Principal Contact: Darrel Baumgardner, Scientist, Universidad Nacional Autonoma de Mexico, Ciudad Universitaria, Mexico City, DF, 04510, Mexico.

Tel: (52) 555-622-4067 Email: Darrel.baumgardner@gmail.com

Abstract

A new instrument, the Photoacoustic Extinctiometer (PAX), was operated in Mexico City during a four week period to measure the light absorption and scattering coefficients of black carbon (BC) and to estimate the relative mass concentration of BC. The PAX was installed in the mobile laboratory of Mexico City's air quality network, Red Automático de Monitoreo Atmosférica (RAMA), along with a suite of gas analyzers, a TEOM, an Aethalometer and a Sunset Laboratory semi-continuous analyzer for elemental and organic carbon (EC/OC). The measurements were made at four locations with the city area, each representing distinctly different sources of BC: 1) a primarily residential area with limited traffic, 2) an industrial region with emissions from diesel trucks, 3) a central market area with heavy automotive traffic and 4) a transportation hub with concentrated emissions from buses and mini-buses. The results indicate that the differences between the aethalometer and PAX are sensitive to the emission sources as are the differences in the BC mass concentrations derived from the absorption measurements made by the aethalometer and the PAX and those measured by the Sunset EC/OC analyzer.

Keywords: black carbon properties, aethalometer, photoacoustic, light absorption.

Mixing height detection with Vaisala LIDAR ceilometer

Mark Ma

Vaisala China Ltd., 2nd Fl. EAS Building, No. 21 Xiaoyun Rd., Beijing 100027, China.

Principal Contact: Mark Ma, Sales Manager, Vaisala China Ltd., 2nd Fl. EAS Building, No. 21 Xiaoyun Rd., Beijing 100027, China.

Email: mark.ma@vaisala.com

Abstract

As haze problem is becoming more significant in many Chinese cities, there's obvious trend to study the mixing height and the atmospheric vertical aerosol distribution.

In this presentation, a LIDAR-based instrument is introduced, which is not only able to detect the cloud height, but also calculate mixing height and the boundary aerosol structure from laser backscatter profile.

The author will introduce the operational theory of Vaisala CL31 ceilometer and mixing height algorithem intergrated with abroad and domestic application. Comparison between CL31 and other boundary detection instrument is also made.

Keywords: Ceilometer boundary layer Vaisala

New SMPS for Measurement of Aerosol Size Distributions Down to 1 nm

Jingkun Jiang¹, Modi Chen², Chongai Kuang³, Michel Attoui⁴ and Peter McMurry⁵

1 School of Environment, Tsinghua University, Beijing, China

2 Department of Mechanical Engineering, University of Minnesota, Minneapolis, USA

3 Atmospheric Science Division, Brookhaven National Laboratory, New York, USA

4 University of Paris XII, Paris, France

Principal Contact: Jingkun Jiang, Associate Professor, School of Environment, Tsinghua University, Beijing, 100084, China.

Tel: +86-10-62781512 Email: jiangjk@tsinghua.edu.cn

Abstract

The measurement of sub-2 nm particles has applications to different aerosol fields including atmospheric research, nanoscale analytical chemistry, nanomaterial synthesis, and nanoparticle health effects. We report a new scanning mobility particle spectrometer (SMPS) for measuring number size distributions of particles down to ~1 nm mobility diameter. This SMPS includes an aerosol charger, a TSI 3085 nano differential mobility analyzer (nanoDMA), an ultrafine condensation particle counter (UCPC) using diethylene glycol (DEG) as the working fluid, and a conventional butanol CPC (the “booster”) to detect the small droplets leaving the DEG UCPC. The response of the DEG UCPC to negatively charged sodium chloride particles with mobility diameters ranging from 1-6 nm was measured. The sensitivity of the DEG UCPC to particle composition was also studied by comparing its response to positively charged 1.47 and 1.70 nm tetra-alkyl ammonium ions, sodium chloride, and silver particles. These results show that the response of this UCPC to sub-2 nm particles is sensitive to particle composition. The transfer function of the TSI nanoDMA for sub-2 nm particle classification was also evaluated. The applicability of the new SMPS for atmospheric field measurement and laboratory photochemical chamber experiments was demonstrated.

Keywords: Condensation particle counter, scanning mobility particle spectrometer, size distribution, atmospheric nucleation

Development of a Lightweight, Simple and Efficient Exhaled Breath Condensate Collection Device and Method

Zhenqiang Xu and Maosheng Yao

State Key Joint Laboratory for Environmental Simulation and Pollution Control, College of Environmental Sciences and Engineering, Peking University, Beijing 100871, China

Principal Contact: Maosheng Yao, Professor, State Key Joint Laboratory for Environmental Simulation and Pollution Control, College of Environmental Sciences and Engineering, Peking University, Beijing 100871, China.

Tel: +86 010 6276 7282 Email: yao@pku.edu.cn

Abstract

Exhaled breath condensate (EBC) is increasingly being used as a non-invasive method for disease diagnosis in clinical settings. However, current available collectors often appear to be heavy, complex and to take longer time to get adequate amount of EBC. Here, a portable EBC collection device and method were developed and tested. The device consists four major parts: a trapezoidal cover with a round air inlet, a cuboid box, ultra-low temperature treated hydrophobic parafilm, and a layer of ice. During the EBC collection, the layer of ice was first placed onto the bottom of the cuboid box, followed by the hydrophobic parafilm, then tightly covered with the trapezoidal cover. In this study, seven volunteers were selected to exhale toward the device using a sterilized straw inserted into the air inlet of the trapezoidal cover for 5 min. The collected EBC appeared to be small water droplets formed on the surface of hydrophobic parafilm. When collecting the EBC, the trapezoidal cover was removed, and 10 µl of deionized water was pipetted onto the parafilm surface. Using a pipette tip, the deionized water drop was dragged over entire parafilm surface.

Due to the hydrophobic nature of the surface, the collected EBC on the surface was scavenged into the deionized water droplet, finally forming a droplet of 40-80 µl. The collected EBC was then analyzed using both culturing method and polymerase chain reaction (PCR) for culturable and total bacterial concentrations, respectively. Results indicated that the culturable bacterial concentrations ranged from 400 to 4000 CFU/ml with an average of 1452 CFU/ml of the EBC collected. Preliminary PCR tests showed that the EBC collected from some volunteers appeared to be bacteria positive with cycle threshold values of 20-26 with a bacterial DNA concentration of 0.5 to 1.5 ng/µl. While, for some volunteers the EBC was tested not positive, which was likely due to the inhibition problems. In this study, a simple and fast EBC collection device and method were developed and demonstrated. However, sample purification method needs to be developed for post-sample analysis using a variety of techniques for different bio-markers in diverse clinical settings. The developed EBC collection device and method would have great application potentials in early disease screening and diagnosis.

Keywords: Exhaled Breath Condensate, Hydrophobic Parafilm, Bacteria, Culturing, PCR

Use of Electrostatic Sampling and ELISA method in Studying Charge Distributions of Airborne Allergens

Yan Wu and Maosheng Yao

State Key Joint Laboratory for Environmental Simulation and Pollution Control, College of Environmental Sciences and Engineering, Peking University, Beijing 100871, China

Principal Contact: Maosheng Yao, Professor, State Key Joint Laboratory for Environmental Simulation and Pollution Control, College of Environmental Sciences and Engineering, Peking University, Beijing 100871, China.

Tel: +86 010 6276 7282 Email: yao@pku.edu.cn

Abstract

It was shown that exposure to airborne allergens has caused various respiratory problems. Among others factors, their charge levels play an important role in their sampling and deposition of human lung system. Previously, we have developed a method of using electrostatic sampling coupled with qPCR for measuring lab-prepared bacterial aerosol charge levels, preventing the problem of counting non-biologicals if an optical counter is used otherwise. Here, we have investigated the airborne allergen charge distribution in a natural environment using a similar method. The electrostatic sampler with two 96-well plates inside was operated at a flow rate of 3 L/min at an electrostatic field strength of 1.2 kV/cm for 2 h in a hotel environment. The sampling was conducted twice from morning to afternoon. The two 96-well plates were grouped into six regions, and air samples collected into each of the regions were pipetted out for airborne Alt a 1, Der p 1, Der f 1 and Bla g 1 allergens analysis using enzyme-linked immunosorbent assay (ELISA). The airborne allergen charge distributions were calculated using an aerosol calculator.

Results indicated that high levels of airborne allergens (Alt a 1, Der p1, Der f 1 and Bla g 1) were detected in hotel environment. The concentrations for dust mite Der p1 and Der f 1 allergens ranged were 209.4 ng/m³ and 61 ng/m³, respectively. For fungal allergen Alt a 1, its concentration was shown about 23 ng/m³, and airborne Bla g 1 was observed to have a concentration of 2.2 U/m³. For fungal allergen Alt a 1, the charge level ranged from about 60 to 600 units of elementary charge with about 50% of them carrying a charge of 200 or 80 units. For dust mite allergens, their charge levels ranged from 500 to 5000 units of elementary charge with about 20-30% of them carrying a charge level of 1000 units. Due to lack of its aerodynamic size, the charge distribution for Bla g 1 was not calculated, but most of the allergens were collected into the last region of the six regions classified. The results from this study indicated that for carpeted hotel room those common allergens could present an important source of the respiratory problems, and the information obtained here might be used in improving their electrostatic control.

Keywords: Allergens, charge distribution, electrostatic sampling, ELISA, hotel environment

An Iodine Vapor Filter Based Mobile High-Spectral-Resolution Lidar for Atmosphere and Aerosol

Xiaoquan Song^{1,2}, Jinjia Guo¹, Kailin Zhang¹, Zhigang Li¹, Bingyi Liu¹, Songhua Wu¹, Decang Bi^{1,3}, Zhangjun Wang¹ and Zhishen Liu¹

1 Ocean Remote Sensing Institute, Ocean University of China, Qingdao, Shandong 266003, China

2 State Key Laboratory of Severe Weather, Chinese Academy of Meteorological Sciences, Beijing 100081, China

3 Shanghai Institute of Optics and Fine Mechanics, Chinese Academy of Sciences, Shanghai 201800, China

ABSTRACT

A mobile High-Spectral-Resolution Lidar (HSRL) system based on Iodine filter has been demonstrated in Ocean University of China. The HSRL system mainly consists of a tunable seeder-injection Nd:YAG laser, two Iodine vapor filters, a 300mm aperture Cassagrain telescope and a three-dimension optical scanner, which are all installed in a van and transportable. Atmospheric aerosol and molecular backscatterings of the laser pulse are discriminated spectrally with an Iodine vapor filter. Then aerosol backscatter ratio and extinction coefficients are induced with the standard atmospheric model calculations. Since the anti-vibrator and recording meter for van attitude are equipped, aerosol backscatter ratio, extinction coefficients, temperature and even the wind speed have been experimentally measured as the van moving, not just as stationary.

KEYWORDS

High-Spectral-Resolution Lidar, Iodine vapor filter, mobile, aerosol

Introduction

Atmospheric temperature, wind, humidity are all basic but essential parameters for atmosphere science and research. Aerosol acts another important fact in the atmosphere and its absorption and scattering influence the earth radiation equilibrium directly. Aerosol optical properties measurement is important considerably for the atmosphere and flux research [1].

Generally, lidar technique can acquire these atmosphere parameters, including troposphere temperature, wind, humidity and aerosol backscatter ratio etc. Standard lidar systems, or the backscatter lidar, provide profiles of the attenuated backscatter signal. However, the attenuated backscatter signal is a quantity that is composed of different atmospheric properties. [2] As shown in general lidar equation, two unknown profiles, aerosol extinction coefficient α_a and backscattering coefficient β_a , to be determined from one profile of measured data. In another word, the lidar ratio or extinction-to-backscatter ratio is a key parameter in backscatter-lidar inversions, which is required to retrieve the extinction and backscatter coefficients of aerosols and clouds [3,4,5].

Essentially two methods have been in use to solve the problem. One, known as the Klett method, is the assumption of a functional dependency of α_a and β_a . Another is the measurement of two lidar profiles in one of which $\beta_a = 0$. This is the case in Raman lidar. Comparing with Rayleigh-Mie scattering lidar, Raman scattering technique has relative low signal to noise ratio (SNR), especially for daytime operation [2].

Another idea based on the use of two measured profiles instead of just one is high spectral resolution lidar, or HSRL. Fabry - Perot interferometer and atomic and molecular absorption filters are two kinds of discriminators or optical filters to distinguish between photons scattered from molecules and those scattered by aerosol or cloud particles.

Previous study presents an instrument design that can be used as a basis for a design of simple and robust lidar for the measurements of the optical properties of the atmosphere. HSRL using Iodine absorption came into being, to separate the aerosol backscatter return from molecular return and detect atmospheric parameters [6, 7, 8]. Since 2000, a HSRL system in a container has been built by Ocean University of China and began to measure the troposphere aerosol at Qingdao (36.06N/120.3E) , which was based on Iodine vapor filters. After that, wind profiles, atmospheric temperature profiles were successfully observed with the same system [9, 10]. During 2008 Beijing Olympic Games, the upgraded mobile lidar in a van was demonstrated

and operated to measure the wind field for the Qingdao Olympic sailing regatta[11]. Here the paper describes the mobile HSRL system and data processing methods of aerosol backscatter ratio.

Experimental Instrument and Methods

The mobile HSRL system consists of four subsystems: laser transmitter, optoelectronic receiver, data digitalizer and signal processor, and optical scanner. (Fig. 1). The laser transmitter is a tunable pulsed Nd:YAG laser injection seeded by the fundamental output at 1064 nm of a cw diode-pumped Nd:YAG laser. The pulsed laser operates at 2.8 kHz and its pulse energy is ~ 2 mJ at 532 nm. A Cassegrain telescope of $\Phi 300$ mm collects the backscattering from atmosphere aerosol and molecular. At the focus of the telescope, a pinhole is placed to suppress the field-of-view and the background light. The backscattering is collimated with lens and filtered by a narrow band interference filter. Then the backscattering is divided into two channels by a beam splitter: one detects filtered backscattering after passing through the Iodine vapor filter and the other detects the backscattering directly by two photomultiplier tubes respectively. The outputs of the photomultiplier tubes are digitalized by 20 MHz, 12 bit A/D converters and 250MHz photon counter simultaneously. All the key instruments and their specifications are listed in Table 1.

Fig. 1 Photo (left) and Schematic (Right) of The Mobile High-Spectral-Resolution Lidar

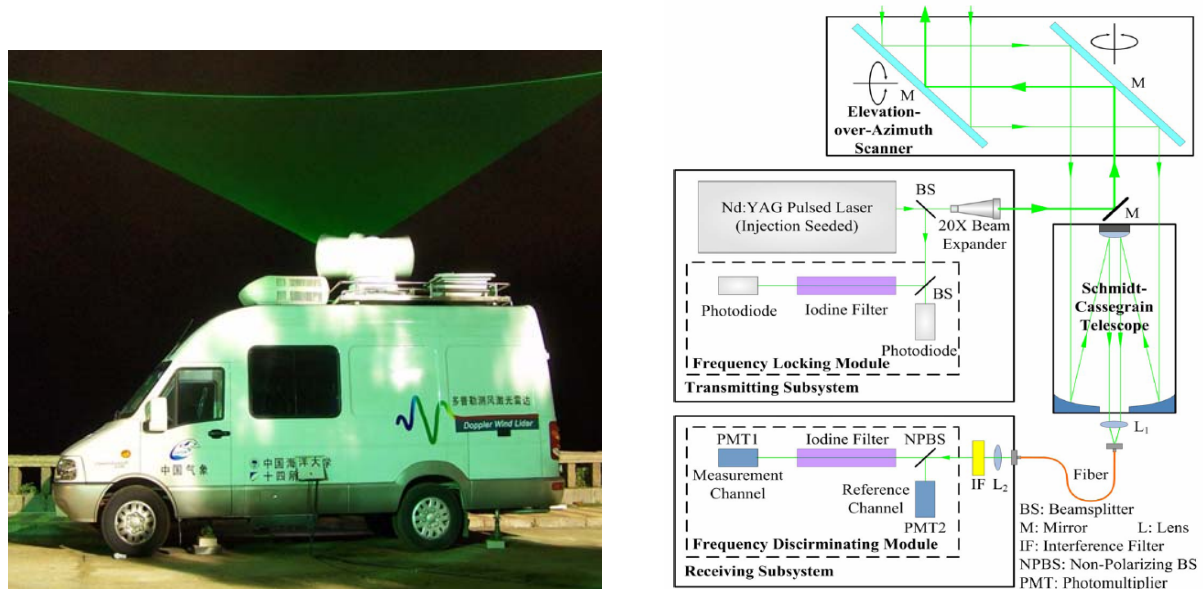
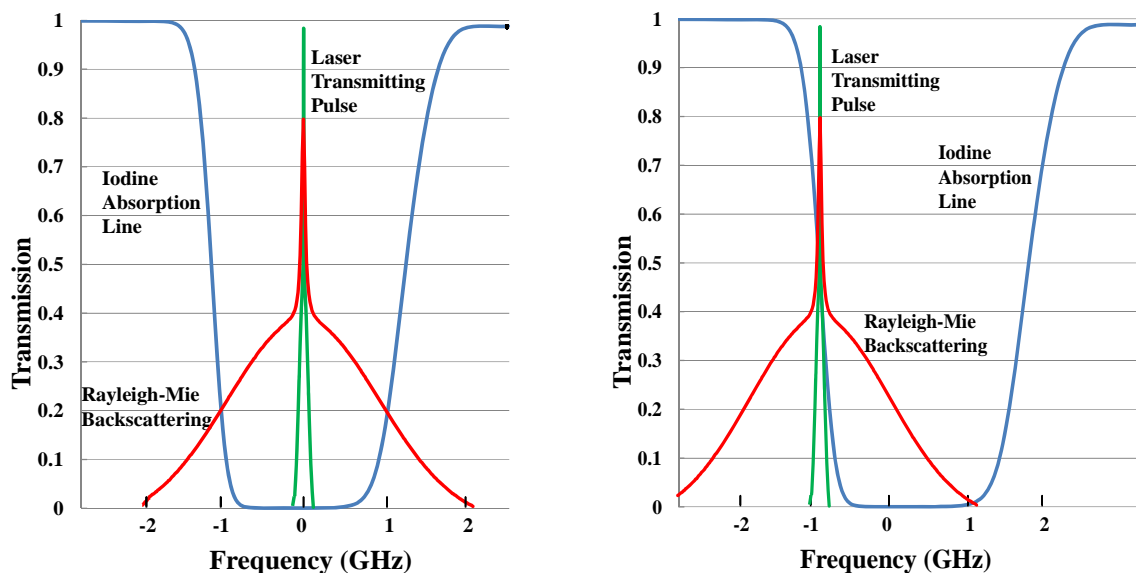


Table 1. Key Specifications of HSRL System

System Parameters	Specifications
Laser Transmitter Wavelength	532nm
Laser Transmitter Power	6W@2.8kHz pulse repetition
Far-field Full-angle Divergence	75 μ rad
Receiving Telescope Aperture	300 mm
Field of View	120 μ rad
Interference Filter Bandwidth	0.1 nm
Transient Recorder	12 bit-20 MHz A/D and 250 MHz photon counter

Iodine vapor has many absorption lines and each has a unique number. In our system, the 1109# Iodine absorption line is chosen as the filter to distinguish between molecular and aerosol backscattering. Transmitted frequency of the seeder-injection pulsed laser is locked at different positions of 1109# Iodine absorption line. In the case of wind measurement, laser frequency is locked at the middle point of the wing, while at the middle point of the valley bottom for aerosol or temperature measurement (Fig.2).

Fig. 2 Spectrum relations between laser pulse, Iodine absorption line and Rayleigh-Mie backscattering at aerosol/temperature measurement mode (left) and wind observation mode (right)



Since the return signal received by HSRL system is divided into two channels, one as the energy monitor detected with photomultiplier tube directly (M channel), the other detected with photomultiplier tube after through the Iodine vapor filter (F channel), signals of the two channels can be written as:

$$N_M(z) = C_M [\beta_a(z) + \beta_m(z)] T^2(z)$$

$$N_F(z) = C_F [f_a(z)\beta_a(z) + f_m(z)\beta_m(z)] T^2(z) \quad (\text{Eq. 1})$$

Here N_M and N_F are photon number received by M and F channels respectively; C_M and C_F are channels' system constants, including laser emission energy, optical efficiency, overlap function of lidar, distance resolution and quantum efficiency of detectors etc.; β_a and β_m (α_a and α_m) are aerosol and atmosphere molecular backscattering (extinction) coefficients; f_a and f_m are the convolution results of laser, aerosol with Iodine spectrum and laser, molecular with Iodine spectrum respectively; T is the transmission in the atmosphere.

The aerosol backscatter ratio R_b can be induced after the transform of Eq. 1:

$$R_b(z) = [\beta_a(z) + \beta_m(z)] / \beta_m(z)$$

$$= \frac{C_F N_M(z)[f_m(z) - f_a(z)]}{C_M N_F(z) - C_F N_M(z)f_a(z)} \quad (\text{Eq. 2})$$

Iodine vapor filter has sharp restrain ability at the valley bottom of the absorption line. When the laser emits vertically and its frequency is locked at the valley bottom, aerosol backscattering signal can be filtered or removed from the molecular backscattering, i.e. $f_a=0$. Then from Eq. 2, we have:

$$R_b(z) = \frac{C_F f_m N_M(z)}{C_M N_F(z)} \quad (\text{Eq. 3})$$

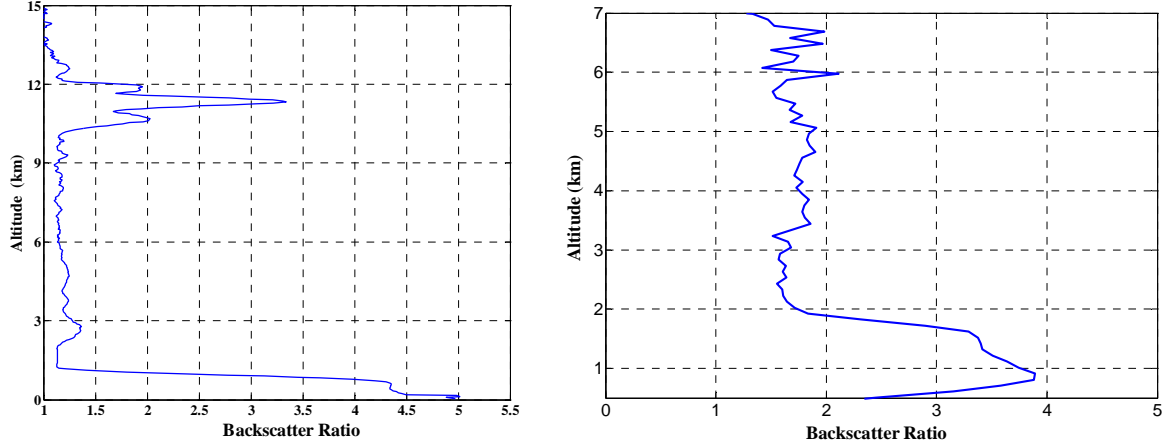
Doppler broaden frequency is small because of the relative low atmosphere vertical wind speed. Consequently, f_m can be acquired with theoretical calculation. In the procedure of system calibration, C_M and C_F can be measured and determined. Finally $R_b(z)$ may get. Since molecular backscatter coefficient β_m is obtained from standard atmosphere model and sounding balloon data, aerosol backscatter coefficient is $\beta_a=(R_b-1)\beta_m$.

Results and Discussion

Figure 3 are two sample results of the aerosol backscatter ratio over Qingdao. The left panel shows two layers with large backscattering, one at 0~1.5km caused by the aerosols in the atmospheric boundary layer and the other at 10~12km probably caused by cirrus clouds. The

right panel shows a thicker atmospheric boundary layer from 0 to 2km high also indicated with large backscatter ratio, but without any obvious clouds exist from 2km to 7km.

Fig. 3 Sample Results of Aerosol Backscatter Ratio



In the case of wind measurement, laser frequency is locked at the middle point of the wing. Then the transmission change of the laser backscattering through the Iodine vapor filter can be monitored to retrieve the Doppler frequency shift by the wind blown aerosol and moleculars. A Single Iodine vapro filter can also be used to make atmospheric temperature measurements. This work is described in Zhi-Shen Liu et al. [11]

SUMMARY

A mobile High-Spectral-Resolution Lidar system based on an Iodine vapor filter is demonstrated at Qingdao, China. Now it can be operated to profile aerosol backscatter ratio, wind and temperature, usually till the tropopause or even higher. Since the anti-vibrator and recording meter for van attitude are equipped, those atmospheric parameters have been experimentally measured as the van moving, not just as stationary.

ACKNOWLEDGMENTS

This work is jointly supported by the Basic Research Project of the State Key Laboratory of Severe Weather, Chinese Academy of Meteorological Sciences (Grant No. 2010LASW-A07) and the National Natural Science Foundation of China (Grant No. 40405005).

REFERENCES

- [1] W. Baker, G. D. Emmitt, F. Robertson, R. Atlas etc., *Bull. Amer. Meteor. Soc.* 1995, **76**, 869
- [2] *Lidar: Range-Resolved Optical Remote Sensing of the Atmosphere*, Claus Weitkamp, Spring Street: New York, 2005
- [3] F. G. Fernald, B. M. Herman, and J. A. Reagan, *J. Appl. Meteorol.* 1972, **11**, 482
- [4] J. D. Klett, *Appl. Opt.* 1985, **24**, 1638
- [5] Y. Sasano and H. Nakane, *Appl. Opt.* 1984, **23**, 11
- [6] H. Shimizu, S.A. Lee and C.Y. She, *Appl. Opt.* 1983, **22**, 1373
- [7] P. Piironen and E.W. Eloranta, *Opt. Lett.* 1994, **19**, 234
- [8] Z. Liu, I. Matsui and N. Sugimoto, *Opt. Eng.* 1999, **38**, 1661
- [9] Z. Liu, D. Wu, J. Liu, K. Zhang, W. Chen, X. Song, J. W. Hair, and C.Y. She, *Appl. Opt.* 2002, **41**, 7079
- [10] Z. Liu, B. Liu, S. Wu, Z. Li, and Z. Wang, *Opt. Lett.* 2008, **33**, 1485
- [11] Z. Liu, D. Bi, X. Song, J. Xia, R. Li, Z. Wang, and C.Y. She, *Opt. Lett.* 2009, **34**, 2712

Effect of Nanoparticle Morphology on the Detection Efficiency of Condensation Particle Counters (CPCs)

Markus Pesch¹, Xiaoai Guo¹, Stephan Rennecke², Alfred Weber², Matthias Richter¹ and Lothar Keck¹

1 GRIMM Aerosol Technik GmbH & Co. KG, Dorfstrasse 9, D-83404 Ainring, Germany

2 Institute of Particle Technology, TU Clausthal, D-38678 Clausthal-Zellerfeld, Germany

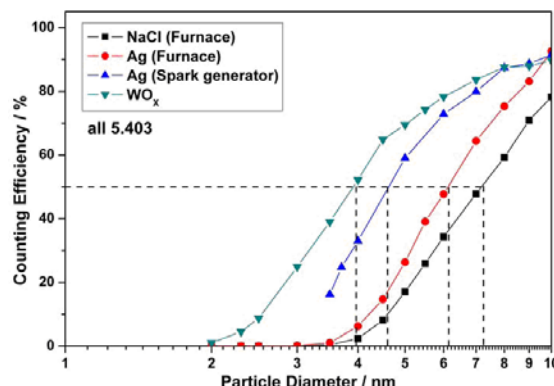
Principal Contact: Xiaoai Guo, Dr., GRIMM Aerosol Technik GmbH & Co. KG, Dorfstrasse 9, D-83404 Ainring, Germany.

Tel: +49-8654 578-0 Fax: +49-8654 578-35 E-mail: guo@grimm-aerosol.com

Abstract

Inhaled nanoparticles are a major concern for the health impact of nanomaterials. Condensation particle counters (CPCs) are the common instruments for measuring the concentration of airborne nanoparticles, and also for measuring nanoparticle size distributions in combination with a Differential Mobility Analyzer (DMA). A well-known characteristic of such instruments, particularly for water-based counters, is the effect of the particle composition on the detection efficiency as a function of particle size [1]. The effect of particle morphology on the detection efficiency, however, was hardly investigated.

The counting efficiency of the GRIMM CPCs model 5.403, 5.414, and 5.416 was measured for Ag particles of two different morphologies, following the ISO 27891 standard. Spherical Ag and NaCl nanoparticles were generated by sublimation and condensation of bulk material, agglomerated Ag particles were produced with a spark generator and a partial sintering was achieved with a quartz furnace. Tungsten oxide nanoparticles were also investigated. Monodisperse size fractions were selected using a DMA and an aerosol electrometer (GRIMM 5.705) served as a reference for the efficiency measurements. Figure 1 shows that the counting efficiency is significantly higher for the Ag agglomerates than for the spherical Ag particles. The 50% detection efficiency for Ag agglomerates was measured at 4.1 nm for the CPC 5.414 (4.5 nm for 5.403), the corresponding values for the spherical particles were 5.0 nm and 6.2 nm [2].



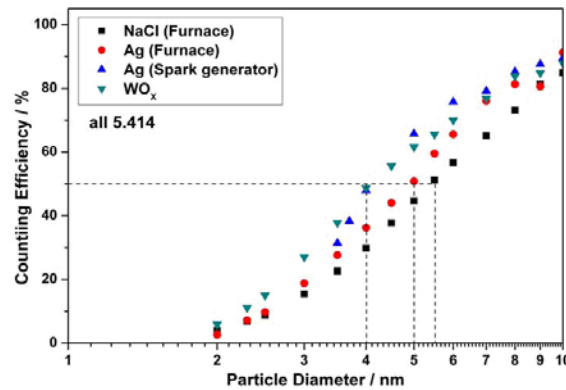


Figure 1: Counting efficiency of the CPCs model 5.403 and 5.414 for different particle compositions and morphology .

Keywords: Nanoparticle, Morphology, Condensation particle counter, Detection efficiency

- [1] Hering, S. V. et al. 2005. A Laminar-Flow, Water-Based Condensation Particle Counter (WCPC). *Aerosol Science and Technology*, 39:659–672.
- [2] Rennecke, A. and Weber, A. 2010. Characterisation of the efficiency of condensation particle counters. Report of the Institute of Particle Technology, TU Clausthal.

A Dual-wavelength Lidar Analysis of Dust Aerosol Properties

Zhitong Wang and Lei Zhang

Key Laboratory for Semi-Arid Climate Change of the Ministry of Education, College of Atmospheric Sciences, Lanzhou University, Lanzhou, 730000, China

ABSTRACT

It is rather difficult to illustrate the dust aerosol optical properties due to the extremely irregular shape of dust particles. Such irregularity often brings about difficulty in transforming their physical properties (size distribution) into optical properties (scattering phase function) in remote sensing retrieval and atmospheric radiation transfer model. Some recent researches reveal that homogeneous spheroids seem to be an applicable approximate model when particles are not much bigger than the wavelength. However, spheroids in reasonable shape distribution can simulate the scattering matrix of dust particles quite well. The paper attempts to introduce such spheroid model into dual-wavelength lidar retrieval of dust aerosol properties. When the size distribution of dust aerosol is modeled by mono-modal lognormal function with a known complex refractive index, the standard deviation, median radius of the size distribution and lidar ratio of dust aerosol at two wavelengths can be derived from dual-wavelength lidar signal. By applying this method to dual-wavelength lidar at Semi-Arid Climate and Environment Observatory of Lanzhou University (SACOL), preliminary results show that the derived size distributions agree with observed ones by Aerodynamic Particle Size when observed size distributions are close to lognormal distributions. The method is also applied to CALIPSO data and six dust storm cases in Saharan and Taklimakan deserts are explored. When complex refractive indexes of dust aerosol are assumed as mean values, lidar ratios of 532 nm and 1064 nm are respectively 41.4 ± 6.7 and 45.0 ± 3.3 .

KEYWORDS

Dust aerosol, Size distribution, Dual-wavelength lidar, Lidar ratio

Introduction

The impact of mineral dust aerosol in the Earth's system depends mainly on particle characteristics such as size, shape and refractive index, which are highly inhomogeneous and variable, due to the variability remote sensing is a necessary method to characterize dust. Through lidar system vertical profiles of aerosol extinction and backscattering can be determine, and several researches have contribute to inversion of aerosol size distribution from lidar measurements of extinction and backscatter^[1-4]. But due to irregularity of dust particle, some difficulties occur when trying deriving size information of dust aerosol from lidar measurements, recent studies reveal that spheroids with certain shape distribution may be a applicable approximate model when dust particles are not much larger than wavelength^[5-9], lidar ratios (extinction-to-backscatter ratio) at 532 nm calculated by Cattrall et al.^[10] based on spheroid model agree with literature values from direct measurements, results by Wiegner et al.^[11] reveal lidar parameters from spheroid model are comparable with in situ measurements.

Accurate retrieval of aerosol extinction and backscatter coefficients from lidar requires knowledge about aerosol lidar ratio which is unknown for elastic backscatter lidar, dual-wavelength lidar can provide additional information about aerosol properties compared with single-wavelength lidar. Lidar ratio can be derived under assumption that aerosol properties do not vary over solution layer when employing aerosol models which associate spectral ratios of extinction, backscatter, and lidar ratio of various aerosol types^[12, 13].

This paper try to derive size information of dust aerosol from dual-wavelength lidar, because inversion of particle properties from lidar measurements of backscatter and extinction requires the solution of Fredholm integral equations of the first kind and leads to ill-posed inverse problem, it is impossible to derive detailed size distribution of dust aerosol from dual-wavelength lidar. The size distributions of pure desert dust are strongly dominated by large particles^[14], and can be modeled by mono-modal lognormal function, under this assumption and applying spheroid parameterization to model scattering properties of dust particles dust aerosol's size distribution can be derived from dual-wavelength lidar measurements, at the same time lidar ratios of dust aerosol at two wavelength can also be attained. This method is applied to dual-wavelength lidar at Semi-Arid Climate and Environment Observatory of Lanzhou University (SACOL), and derived size distributions are compared with results measured by Aerodynamic Particle Size (APS), also CALIPSO data from several dust storm cases are analyzed by this method.

Experimental Methods

The size distributions of dust are bimodal and dominated by large particles, they can be approximate by mono-modal lognormal function especially in pure dust case. So this article models size distributions of dust by lognormal function defined as:

$$\frac{dV(r)}{d \ln r} = \frac{C_v}{\sqrt{2\pi}\sigma} \exp\left[-\frac{(\ln r - \ln r_v)^2}{2\sigma^2}\right] \quad (\text{Eq.1})$$

where C_v - volume concentration, σ - standard deviation and r_v - median radius.

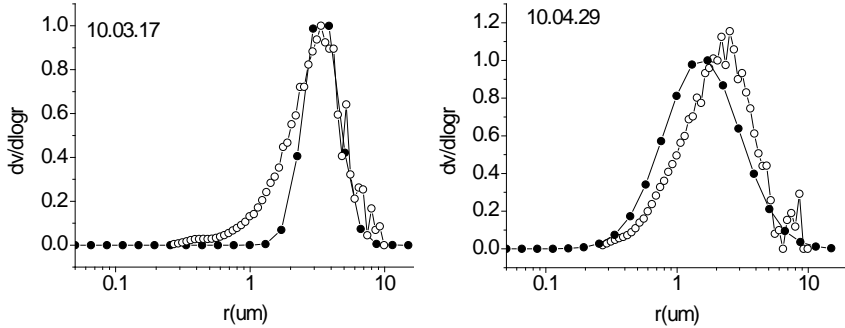
To simulate single-scattering properties of dust aerosol one should use correct shape distribution for an ensemble of spheroids with various shape, Nousiainen et al. ^[6] recommend the so-called $n = 3$ shape distribution, Dubovik et al. ^[5] inverted aspect ratio distribution based on scattering matrix of Feldspar. In this study the latter is used.

In current method the refractive index of dust is assumed to be known, the value at 532nm is fixed at $1.56 + i0.003$, the refractive index at 1064nm is artificially assumed same as one at 532nm to attain more reasonable lidar ratios at 1064nm while in situ measurements reveal imaginary part of dust refractive index decreases as wavelength increases ^[14-16].

To derive size distributions of dust from dual-wavelength lidar measurements, a pair of σ and r_v is given initially, then lidar ratios at 532 and 1064nm, spectral ratios of extinction and backscatter coefficients (532-1064nm) can be calculated. To solve lidar equation the lidar ratio and boundary value must be known, in this study the forward algorithm ^[17] is applied to dual-wavelength lidar at SACOL and boundary value is also assumed initially, then dust extinction and backscatter profiles can be derived from lidar measurements at both wavelengths, yielding another pair of spectral ratios of extinction and backscatter coefficients. Then compare spectral ratios of extinction and backscatter coefficients derived from lidar measurements with ones calculated from assumed size distributions, and adjust boundary value, σ and r_v to minimize the difference, parameters that minimize difference are accepted finally.

Results and Discussion

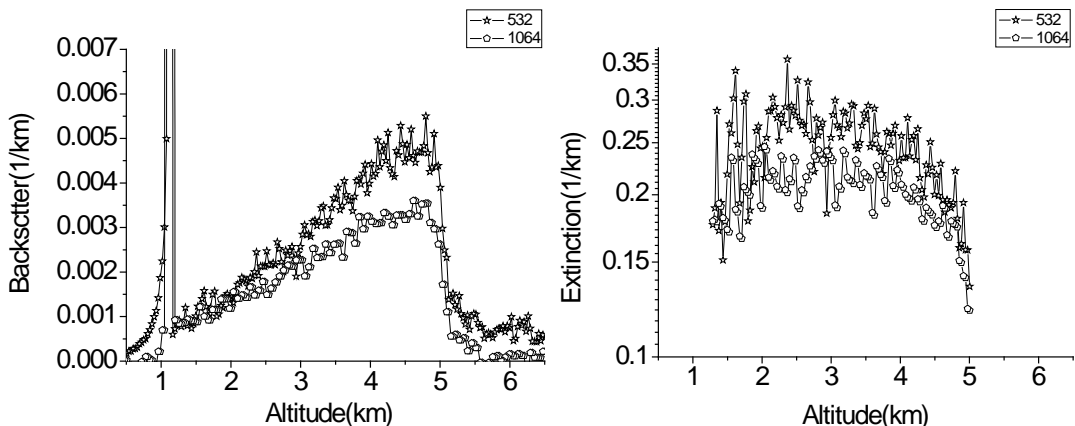
Figure 1. Dust size distributions derived from lidar measurements (dot) and measured by APS (circle), distributions are normalized by their largest dv/dlogr values.



Several dust events are observed at SACOL during March and April, 2010, the lidar measurements are analyzed by current method, Figure 1. displays some cases.

Compared with results from APS both size distributions agree with each other when real dust size distributions are close to lognormal distributions, not in other cases, it is reasonable since solutions have been limited to set of lognormal functions. To simulate dust size distributions more realistically, more parameters are needed and mean more wavelengths which are not available in this study, however these results at least reveal spheroids may be applicable model to account irregularity in lidar remote sensing.

Figure 2. CALIPSO attenuated backscatter profiles from a dust event occurring at Taklimakan desert on July 30. 2006 (left), and derived extinction profiles (right), in this case retrieved lidar ratios are 43.0 at 532 and 47.3 at 1064.



Also this method is applied to measurements from CALISPO, and six dust storm cases that occur at Sahara and Taklimakan deserts are studied, Figure 2. present an example of Taklimakan desert. The derived average lidar ratios are 41.4 ± 6.7 at 532nm and 45.0 ± 3.3 at 1064nm and appear to be reasonable at 532 and lower at 1064 compared with literature values of $43^{[10,13,18,19]}$ and $55^{[18,20]}$, because lidar ratio is very sensitive to refractive index of dust ^[11], which is fixed at $1.56 + i0.003$ for two wavelengths in our study, and in situ measurements of dust refractive index appear scattered largely, further studies are need about refractive index.

SUMMARY

In this paper, through applying spheroids model to account dust particle's irregularity, size distributions of dust aerosol is derived from dual-wavelength lidar measurements when assuming the size distributions belong to set of lognormal functions, results reveal that spheroids approximation may be a feasible approach to deal with irregularity of dust particles in lidar remote sensing. Lidar ratios derived from CALIPSO measurements in dust events are comparable with literature values, several methods have been developed to derived lidar ratios using dual-wavelength lidar, such as transmittance method ^[18, 20] and CRAM technique ^[12, 13], unlike restricting spectral ratios of dust aerosol extinction, backscatter and lidar ratio in CRAM, size distribution shape is constrained in our study and comparing these methods with current method is further work.

ACKNOWLEDGMENTS

The authors are grateful to Semi-Arid Climate Observatory & Laboratory of Lanzhou University and the CLIPSO team at NASA Langley Research Centre for providing data. We would like to thank Oleg Dubovik for his kernels and software package.

REFERENCES

- [1] Muller, D.; Wandinger, U.; Ansmann, A. *Applied Optics*. 1999, 38, 2346-2357.
- [2] Bockmann, C. *Applied Optics*. 2001, 40, 1329-1342.
- [3] Rajeev, K.; Parameswaran, K. *Applied Optics*. 1998, 21, 4690-4700.
- [4] Donovan, D.P.; Carswell, A.I. *Applied Optics*. 1997, 36, 9406-9424.
- [5] Dubovik, O.; et al. *J. Geophys. Res.* 2006, 111, D11208.
- [6] Nousiainen, T.; Kahnert, M.; Veihelmann, B. *Journal of Quantitative Spectroscopy*

& Radative Transfer. 2006, *101*, 471-487.

- [7] Nousiainen, T. *Journal of Quantitative Spectroscopy & Radiative Transfer.* 2009, *110*, 1261-1279.
- [8] Nousiainen, T.; Munoz, O.; Lindqvist, H. *Journal of Quantitative Spectroscopy & Radiative Transfer.* 2011, *112*, 420-433.
- [9] Mishchenko, M.; Travis, L.; Kahn, R.; et al. *J. Geophys. Res.* 1997, *102*(D14), 16831-16847.
- [10] Cattrall, C.; Reagan, J.; Thome, K. and Dubovik, O. *J. Geophys. Res.* 2005, *110*, D10S11.
- [11] Wiegner, M.; et al. *Tellus.* 2008, *61B*, 180-194.
- [12] Reagan, J.; X. Wang.; Cattrall, C. and Thome, K. *IEEE IGARSS'04.* 2004, 1940-1943.
- [13] McPherson, C.; Reagan, J. *IEEE GEOSCIENCE AND REMOTE SENSING LETTERS.* 2010, *7*, 98-102.
- [14] Dubovik, O.; Holben, B.N.; Thomas, F.E.; et al. *J. Atmos. Sci.* 2002, *59*, 590-608.
- [15] Anderas, Petzold.; et al. *Tellus.* 2009, *61B*, 118-130.
- [16] Todd, M.C.; Washington, R.; Martins, J.; et al. *J. Geophys. Res.* 2007, *112*, 1-12.
- [17] Fernald, F.G. *Applied Optics.* 1984, *23*, 652.
- [18] Liu, Z.; Omar, A.; Vaughan, M.; et al. *J. Geophys. Res.* 2008, *113*, D07207.
- [19] Liu, Z.; Sugimoto, N.; Murayama, T. *Applied Optics.* 2002, *41*, 2760-2767.
- [20] Omar, A.; Liu, Z.; Vaughan, M.; et al. *J. Geophys. Res.* 2010, *115*, D24217.

Optical Characteristics of Aerosols over the Arid-area in Hexi-Corridor

Wu Zhang, Jinsen Shi, Jianrong Bi, Jianping Huang, Songtao Song, Lei Tian and Tao Xiang
Key-Laboratory of Semi-Arid Climate Change, Ministry of Education. College of Atmospheric Sciences, Lanzhou University, Lanzhou, Gansu 730000, China

Principal Contact: Wu Zhang, Prof., Key-Laboratory of Semi-Arid Climate Change, Ministry of Education. College of Atmospheric Sciences, Lanzhou University, Tianshui South Road 222, Lanzhou, Gansu 730000, China.

Tel: 86+931+8915695 Phone: 13893281338

Fax: 86+931+8914278 E-mail. wzhang@lzu.edu.cn

Abstract

Both the scattering and absorption characteristics of atmospheric aerosols are analyzed, measured during the Sino-US joint experiment of dust aerosol in the Spring of 2008 in Hexi Corridor, China. Diurnal variation of the atmospheric aerosol scattering coefficient (550nm) and the absorption coefficient (520nm) and the ratio of backscatter to total scattering during dust event and no dust period were discussed, as well as the evolution of dust aerosol scattering and absorption properties during typical dust event. The results show that, the daily variation of total scattering coefficients present a bi-peaks type during both kinds of weather conditions, but the time the peaks occurred and the magnitudes of peaks were different. The daily ranges of the proportion of fine particles on no dust days are wider than that on dust days. The total scattering coefficients were increasing rapidly when dust-storm occurred. The mean value of total scattering coefficients at 550nm is 103 Mm^{-1} and the absorption coefficients at 520nm (σ_{ap}) is 21.7 Mm^{-1} with two peaks at 8:00 and 21:00 (BST) respectively. The diurnal variation of wind direction was one of the main impact factors caused the change of σ_{ap} . The mass absorption efficiency of dust aerosol was $0.033 \text{ m}^2/\text{g}$.

Keywords: aerosol, scattering, absorption, dust event, Hexi Corridor

Aerosol Light Extinction Measurements of Urban and Regional Particulates Using a Cavity Attenuated Phase Shift-Based (CAPS PM_{ex}) Monitor

Paola Massoli, Paul L. Kebabian, Timothy B. Onasch and Andrew Freedman

Center for Sensor Systems and Technology, Aerodyne Research, Inc., Billerica, MA 01821, U.S.A.

ABSTRACT

We present results of optical property characterization of ambient particulates during field deployments where measurements of aerosol light extinction are obtained by using a cavity attenuated phase shift-based particle extinction monitor (the CAPS PM_{ex}). The CAPS PM_{ex} is a light-weight, compact instrument able to perform precise and accurate extinction measurements (3- σ detection limit of $<3\text{ Mm}^{-1}$ for 1s integration time) of ambient aerosol. Two CAPS PM_{ex} instruments (operating at wavelengths of 530 and 630 nm) were deployed during the CalNex 2010 study (May 14 – June 16, 2010) in Pasadena, CA. A very strong diurnal variation in the particle extinction was detected at both wavelengths, with peak extinctions reaching 200 Mm^{-1} . In addition, a CAPS PM_{ex} monitor operating at a wavelength of 530 nm was deployed in a remote rural location, the IMPROVE/CASTNET site (Estes Park, CO) at an altitude of $\sim 3000\text{ m}$ from mid-August through September 2010. Ambient levels of particle extinction generally varied between 0 and 5 Mm^{-1} except for a short period during which a biomass burning plume emanating from a site located 40 km southeast of the measurement site passed through the area.

KEY WORDS

extinction, aerosol, optical properties, cavity attenuated phase shift, cavity enhanced

Introduction

Aerosol particles can affect the energy budget of the earth by scattering and absorbing solar and terrestrial radiation; they also have an indirect influence on cloud formation and properties. It is now thought that the direct radiative effect of anthropogenic aerosols is comparable in magnitude with that exerted by greenhouse gases.^[1] Accurate measurement of aerosol optical properties (i.e., scattering, absorption, extinction) can be problematic because of their low magnitude in many environments.^[2,3] In non-urban areas, particle extinction can be a fraction of that of Rayleigh scattering coefficient of the air itself [~ 6 to 30 Mm^{-1} ($\text{Mm}^{-1} = 10^6\text{ m}^{-1}$) at STP as the wavelength of light shifts

from red to blue]. Furthermore, the extinction can be a strong function of temperature and relative humidity for aerosols which adsorb and desorb water vapor.^[4] Adsorption of water vapor will cause a hygroscopic aerosol to swell, thus increasing its size and scattering cross section as well as causing its shape to become more spherical. Instruments which heat or cool the incoming aerosols even by a couple of degrees can provide erroneous measurements. While recent advances in total extinction measurements through the use of low-loss optical cavities have dramatically improved the state of the art for measurement of this parameter,^[5,6] accurate routine measurement of particle optical extinction still poses a problem because of the lack of suitable commercially available equipment. The user must employ two different instruments, one to measure particle scattering (typically a nephelometer)^[7] and one to measure particle absorption (typically using a filter-based monitor such as a multi-angle absorption photometer)^[8], each having distinct limitations.^[9,10]

To meet this need for accurate and robust instrumentation for the measurement of particle optical extinction, we have developed the CAPS PM_{ex} Particle Extinction Monitor. The monitor, which samples ambient air, employs the cavity attenuated phase shift (**CAPS**) technique^[11,12] to produce measurement pathlengths on the order of 2 km, allowing it to accurately measure atmospheric visibility levels for PM_{2.5} ranging from the Rayleigh limit to as high as 1 km with 1 second time resolution.^[13-15] It comprises a light emitting diode (LED), an optical cavity that acts as the sample cell, and a vacuum photodiode for light detection. The particle-induced optical extinction (which is inversely proportional to the visibility) is determined from changes in the phase shift of the distorted waveform of the square-wave modulated LED light that is transmitted through the cavity. The monitor can be outfitted to operate at one of three wavelengths (450 nm, 530 nm or 630 nm). We present below a brief overview of the operation of the monitor as well as two examples of field measurements, one in a remote rural location, the IMPROVE/CASTNET site, just outside of Rocky Mountain National Park (Estes Park, CO) and the other at an urban ground site located on the campus of the California Institute of Technology in Pasadena, CA.

Experimental Methods

The singular aspect of the CAPS approach is that extinction is measured by determining shifts in the phase angle of a modulated light beam instead of changes in the intensity of the transmitted light caused by the presence of particulates.^[11,11²] As shown in Figure 1, square wave modulated light from a broadband LED enters the optical cavity through one mirror, and exits at the other mirror as a ‘distorted’ wave with respect to the original waveform. The light exiting the cavity is collected by a vacuum photodiode detector. A 10 nm wide band-pass filter, located in front of the detector, is used to define the spectral range of the measurement. The relationship between the measured phase shift and light extinction, ϵ , is described in Equation 1:

$$\varepsilon = [\cot(\theta) - \cot(\theta_0)] [2\pi f/c] \quad (1)$$

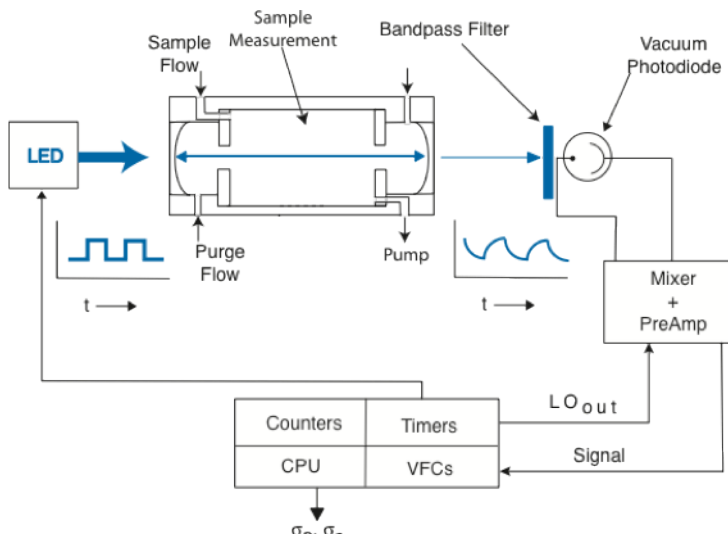


Figure 1 Schematic of CAPS PM_{ex} monitor.

where $\cot(\cdot)$ is the cotangent of the measured phase shift with particles present, θ_0 is the phase shift under particle-free conditions, c is the speed of light and f is the modulation frequency. The phase shift is maintained at 35-40° by setting the modulation frequency at an appropriate value. Note that this is an absolute measurement requiring no calibration. As can be seen in the schematic, a small purge flow is required to prevent particles from contaminating the mirrors.

mirrors; a small correction to the measured value must be made to reflect this fact. In order to maintain proper performance, baseline measurements with particle-free air must be periodically made to correct for drifts in the electronics or changes in the reflectivity of the mirrors. This task is handled automatically by the monitor. Pressure and temperature of the air sample must also be measured in order to correct for short term changes (i.e., in between baseline measurements) in the contribution to the total extinction from air Rayleigh scattering. Complete details and operating specifications including sensitivity (LOD= 2 Mm⁻¹, $\tau=1$ s), baseline stability and accuracy are presented in Reference 13. The monitor response is completely linear over its entire operating range, which is limited at the upper end (~4000 Mm⁻¹ or a range of ~ 1 km) by the severe loss of light at this high an extinction level.

Measurements over the period of a month using a CAPS PM_{ex} monitor operating at 530 nm were conducted at a National Park Service IMPROVE/CASTNET monitoring site located approximately 15 km from Estes Park, CO, just outside the perimeter of Rocky Mountain National Park at an altitude of ~3000 meters. These measurements, conducted from mid-August through September of 2010, were taken with the cooperation of the National Park Service and Colorado State University. An impactor with a nominal cutoff of 2.5 microns was employed, although no attempt to control the relative humidity was made. The monitor was located within a temperature controlled trailer and operated autonomously for the entire period of the campaign without user intervention. Another set of measurements were taken at a site located on the campus of the California Institute of Technology in

Pasadena, CA using two monitors operating at 530 and 630 nm respectively as part of the CalNex 2010 study (May 14 – June 16, 2010). For this study, an impactor with a nominal cutoff of 1 micron was used and the particles were dried to below 30% relative humidity.

Results and Discussion

The left panel of Figure 2 shows a histogram of the probability distribution obtained

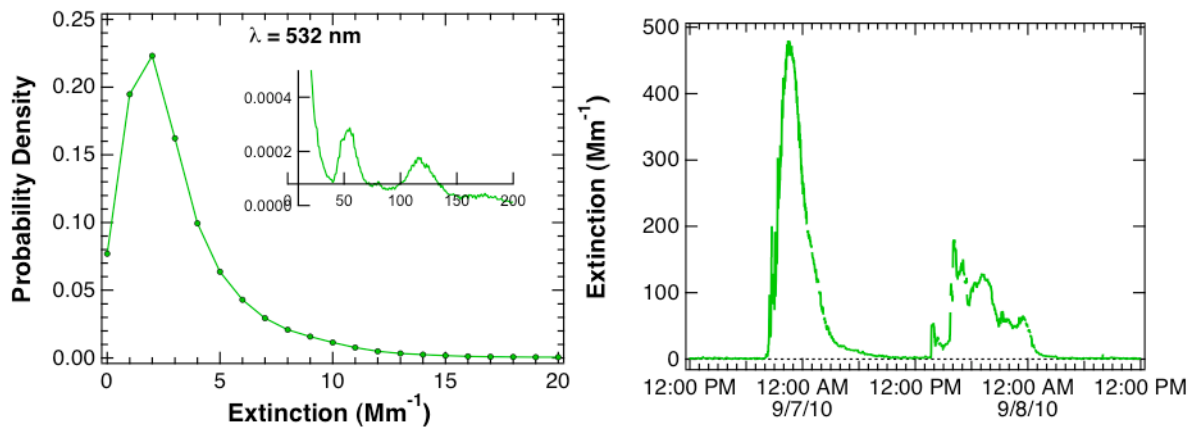


Fig. 3 Left: Probability distribution of aerosol light extinction measurements at high altitude rural site presented as 1 minute averages. Right: Observation of high aerosol extinction caused by biomass burning plume.

from 1 minute averages of the data taken over a period of a month from the site at the Improve Site taken using a CAPS PM_{ex} extinction monitor operating at 530 nm (green). The values of particle optical extinction obtained using the PMex monitor at 530 nm at the high altitude Improve site in Colorado typically vary from 0-10 Mm^{-1} . Periodically, prolonged (> 1 hour) elevated levels of the particle extinction are observed because of updrafts of particles from the urban centers on the lower altitude plains to the east of the site. Short term (< 1 minute) events can be assigned to exhaust plumes from motor vehicles passing by the area. As befits this remote relatively pristine site, the particle extinction probability peaks at only 2 Mm^{-1} , but contains a long tail that reflects both long-term and short-term events mentioned above. However, the data presented in the panel at right coincides with the Boulder, CO (a city ~ 40 km SE of the measurement sites) forest fires which began on September 6 and continued for several days. Extremely high extinction values ($>450 Mm^{-1}$) were reached even at this high altitude site. This dramatic increase in particle light extinction was accompanied by an increase in NO_2 concentrations from <1 ppbv to greater than 10 ppbv.

Data obtained during the CalNex campaign in Pasadena, CA is shown as 1-hour averages for both the green and red monitors in Figure 4. The site, located on the CalTech campus, is located within the Los Angles basin and thus strongly reflects a highly congested urban environment. Note the strong diurnal variation in particle extinction levels measured during much of the campaign. The extinction levels build up overnight and peak in the mid-morning period before declining. It is believed that this cycle reflects the local meteorological conditions where off-ocean winds increase during the day and subside in the evening. The average single scatter albedo, obtained using absorption data from an aethalometer, is >0.95 , indicating that there is comparatively little black carbon present in the ambient aerosol. This result suggests that these aerosols are mainly of secondary nature, i.e., photochemically produced. During “haze” events (May19-21 and June 3-8), extinction levels surpassed 100 Mm^{-1} and coincided with morning hour peaks of particles composed primarily of inorganic material (sulfate and nitrate, according to results by a co-located High Resolution Aerosol Mass Spectrometer). Organic material peaked in the afternoons and was

highly oxidized.^[16] These events were associated to light winds with a dominant south to southeast component, which allowed transport of air masses from the Los Angeles basin to the Pasadena area.

SUMMARY

In summary, we have presented data demonstrating the performance of a newly developed particle optical extinction monitor (CAPS PM_{ex}) capable of providing accurate and precise measurements of optical extinction caused by the presence of ambient particles in both pristine and heavily particle-laden conditions. The rack mounted instrument, which can be outfitted to operate at 450, 530 or 630 nm (blue, green or red) weighs 11 kg and utilizes less than 50W of electrical power. The monitor operates in a completely autonomous fashion, requiring no user interaction or expendables such as zero gas, and can

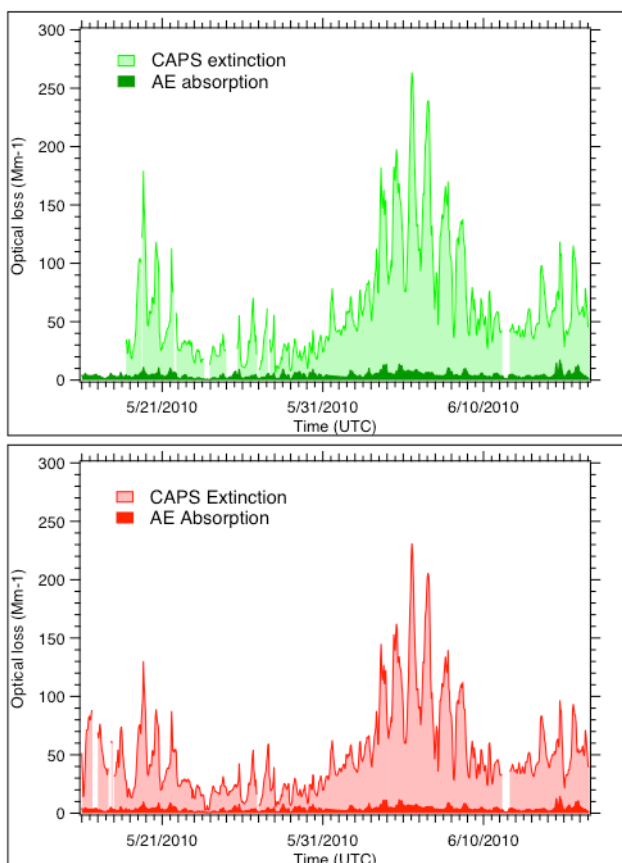


Fig. 4 Data obtained from PMex monitor at both 530 and 630 nm during the Cal-Nex campaign conducted in the Los Angles basin. Note the strong diurnal variation in the extinction levels.

be remotely controlled.

ACKNOWLEDGMENTS

We acknowledge financial support for our participation in the studies presented here from NASA and the National Institutes of Health through the Small Business Innovation Research program. We also acknowledge the cooperation of Dr. Christian Carrico and colleagues at Colorado State University and scientists from the U.S. National Park Service for the studies in Colorado. We also thank the California Institute of Technology for hosting the CalNex ground site and the California Air Resources Board for providing the financial support for this site.

REFERENCES

- [1] IPCC (2007) Climate Change 2007: the physical science basis - contributions of working group I to the fourth assessment report of the intergovernmental panel on climate change, available at <http://www.ipcc.ch/SPM2feb07.pdf>
- [2] Seinfeld, J.H.; S.N. Pandis, *Atmospheric chemistry and physics: from air pollution to climate change*, **1998**, New York, Wiley
- [3] Chen, W.T.; H. Liao; J.H. Seinfeld, Future climate impacts of direct radiative forcing of anthropogenic aerosols, tropospheric ozone and long-lived greenhouse gases, *J. Geophys. Res.* **2007** 112, D14209, doi:10.1029/2006JD008051
- [4] Charlson, R.J.; H. Horvath; R.F. Pueschel, Observation of the effect of humidity on light scattering by aerosols, *Hygroscopic Aerosols*, L.H. Ruhnke and A. Deepak, Eds., **1984** 35-44
- [5] Strawa, A.W.; R. Elleman; A.G. Hallar; D. Covert; K. Ricci; R. Provencal; T.W. Owano; H.H. Jonsson; B. Schmid; A.P. Luu; K. Bokarius; E. Andrews, Comparison of in situ aerosol extinction and scattering coefficient measurements made during the Aerosol Intensive Operating Period, *J.Geophys. Res.* **2006** 111, D05S03, doi:10.1029/2005JD006056
- [6] Baynard, T.; Lovejoy, E.R.; Pettersson, A.; Brown, S.S.; Lack, D.; Osthoff, H., Massoli, P.; Ciciora, S.; Dube, W.P.; Ravishankara, A. R., Design and Application of a Pulsed Cavity Ring-Down Aerosol Extinction Spectrometer for Field Measurements', *Aerosol Sci. Technol.*, **2007** 41:447 – 462
- [7] Anderson, T.L. and J.A. Ogren (1998). Determining aerosol radiative properties using the TSI 3563 integrating nephelometer. *Aerosol Science and Technology*, **29**: 57-69.

- [8] Petzold, A.; Kramer, H.; Schönlinner, M., Continuous Measurement of Atmospheric Black Carbon Using a Multi-Angle Absorption Photometer. *Environ. Sci. Poll. Res.* **2002** 4:78–82.
- [9] Massoli, P.; Murphy, D. M.; Lack, D. A.; Baynard, T.; Brock, C. A.; Lovejoy, E. R., Uncertainty in Light Scattering Measurements by TSI Nephelometer: Results from Laboratory Studies and Implications for Ambient Measurements, *Aerosol Sci. Technol.*, **2009** 43:1064-1074
- [10] Lack, D.A., C.D. Cappa, D.S. Covert, T. Baynard, P. Massoli, B. Sierau, T.S. Bates, P.K. Quinn, E.R. Lovejoy, and A.R. Ravishankara (2008). Bias in filter-based aerosol light absorption measurements due to organic aerosol loading: Evidence from ambient measurements. *Aerosol Science and Technology*, **42**(12): 1033-1041
- [11] Herbelin, J.M.; McKay, J.A.; Kwok, M.A.; Ueunten, R.H.; Urevig, D.S.; Spencer, D.; Benard D.J. Sensitive measurement of photon lifetime and true reflectances in an optical cavity by a phase-shift method, *Appl. Opt.* **1980** 19:144-147
- [12] Engeln, R.; von Holden, G.; Berden, G.; Meijer, G., Phase shift cavity ring down absorption spectroscopy, *Chem. Phys. Lett.* **1996** 262:105-109
- [13] Kebabian, P.L.; Freedman, A., System and method for trace species detection using cavity attenuated phase shift spectroscopy with an incoherent light source, U.S. Patent 7301639, 2007
- [14] Kebabian, P.L., W.A. Robinson and A. Freedman, Optical Extinction Monitor Using CW Cavity Enhanced Detection. *Rev. Scien. Instrum.* **2007** 78, 063102
- [15] Massoli, P.; Kebabian, P.L.; Onasch, T.B.; Hills,F; Freedman, A., Aerosol light extinction measurements by Cavity Attenuated Phase Shift Spectroscopy (CAPS): laboratory validation and field deployment of a compact aerosol extinction monitor,” *Aerosol Sci. Technol.* **2010** 44:428–435
- [16] Patrick Hayes, University of Colorado, personal communication

Quantitative Analysis of Aerosol Optical Properties in Summer in Beijing

Junshan Jing^{1,2} and Renjian Zhang¹

1 Key Laboratory of Regional Climate-Environment Research for Temperate East Asia, Institute of Atmospheric Physics, Chinese Academy of Sciences, Beijing, 100029, China,

2 Graduate University, Chinese Academy of Sciences, Beijing, 100049, China,

ABSTRACT

Aethalometer and nephelometer were used to analyze black carbon concentrations (BC), aerosol absorption coefficient (Ab), scattering coefficient (Sc), single scattering albedo (SSA) in Beijing metropolitan areas in May 20 ~ August 30, 2009. The data downloaded from AERONET website were also employed to investigate aerosol optical depth (AOD). The results showed that the average and standard deviation of BC, Ab, Sc, SSA, AOD were $7.02 \pm 4.76 \text{ Mm}^{-1}$, $54.87 \pm 39.17 \text{ Mm}^{-1}$, $340.6 \pm 346.85 \text{ Mm}^{-1}$, 0.8 ± 0.1 和 0.41 ± 0.44 respectively. Ab, Sc, SSA all presented a obviously single peak diurnal variations, while the maximum value of these three parameters appeared at 05 am, 10am and 01 pm. Ab and Sc were well related with Fine Particulate Matter (PM2.5), for correlation coefficients is respectively 0.65 and 0.78. There was a serious fog and haze event on June 18, while the maximum value of Ab and Sc were 341.14 Mm^{-1} and 3152.02 Mm^{-1} . Yellow Sea and the industrial cities on southeast of Beijing contributed the water vapor and particles for the formation of fog and haze weather.

KEYWORDS

Aerosol; optical properties; fog and haze event

BODY

Introduction

Seawater splashing foam, dust or ash can enter the atmosphere and remain in the air. The multiphase system of solid or liquid particles suspended in the air were known as aerosol^[1-2]. As the scattering and absorption properties of these particles, they have a significant impact on atmospheric radiation process, affecting the regional temperature, precipitation and visibility, even associating with human health, plant

growth, ecosystem carbon cycle, acid rain and tropospheric ozone pollution^[3-4]. A moiety of the particulate matter emission into the atmosphere is originated from the combustion process of carbonaceous material, such as automobile exhaust, biomass burning, etc. This sort of aerosol was called as black carbon (Abbrev. BC). BC has a strong effect on regional climate variability and global change by intense absorption of solar radiation. After the industrial revolution, along with economic development and population surge, more and more particles were emitted into the atmosphere, which lead to aerosols turn into one of the most uncertain factor of worldwide climate adjustment^[5].

The several key parameters of aerosol optical properties are black carbon concentration, absorbing coefficient (Abbrev. Ab), scattering coefficient (Abbrev. Sc) and single scattering albedo (Abbrev. SSA). Sc reflects the visibility status of atmosphere, while the higher value means the shorter visual distance. SSA is defined as ratio of aerosol scattering coefficient to total extinction coefficient, which represent the relative magnitude of scattering and absorbing capacity of aerosol, which is one of the most critical factor of the aerosol radiative forcing. Therefore, it is very important to obtain the regional aerosol SSA. The implication of Aerosol optical depth (Abbrev. AOD) is the weakened quantity of the light undermined by all the absorption and scattering material in unit cross-sectional area of the light's transmission path, which is also the important parameter to describe the aerosol optical properties. AOD had a significant increasing trend in the past 25 years^[6].

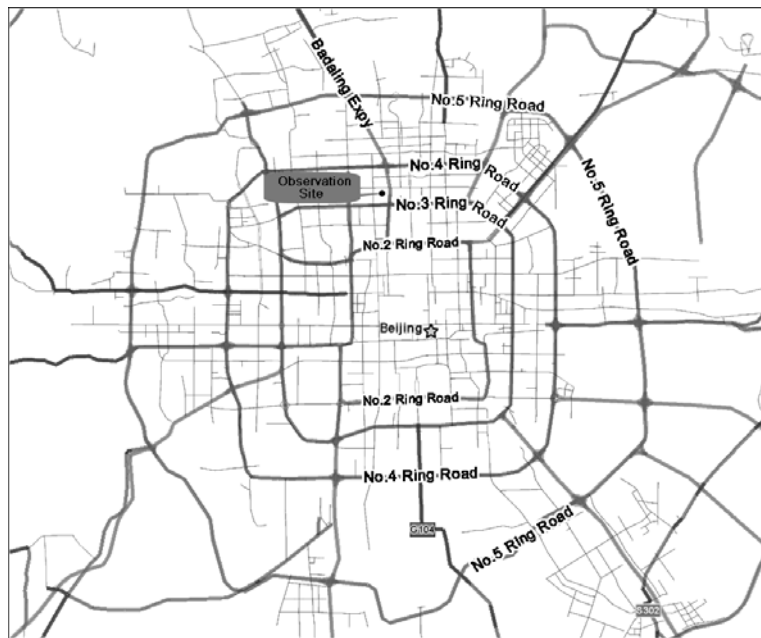
Beijing is one of the most industrialized cities in China, and has attracted a large number of workers to settle in or look for a work due to its economic prosperity, which resulted in dramatic increase in the number of civilian cars. The residents in Beijing reached 17.55 million at the end of 2009, and the total population was more than 22 million if the foreign workers were included, while the amount of motor vehicles exceeded 4 million. Excessive vehicle exhaust and population has brought enormous pressure to living environment. Precipitation plays an important role on the removal of aerosol and the improvement of air quality. Rainfall in Beijing concentrates in summer, so it is of vital significance to understand the importance of aerosol optical properties to regional circumstance by measurement and analysis the aerosol mass concentration, absorption and scattering coefficient during summer in Beijing.

Experiment Methods

Observation time was from May 20, 2009 to August 30, 2009, and this period covered most time of the summer of Beijing because the average threshold of summer and

autumn of historical statistics were in the end of May and in the beginning of September severally. Observation site located at Tower Division of the Institute of Atmospheric Physics, Chinese Academy of Sciences ($39^{\circ}58' N$, $116^{\circ}22' E$) (Figure 1), which situated between the north No.3 ring road and the north No.4 ring road of Beijing and surrounded both living district and traffic main arteries, so the observational results could represent the aerosol concentration and optical characteristics in typical urban zone of Beijing.

Figure 1. Schematic diagram of observation locations



Continuous real-time data of black carbon concentration was obtained by the use of AE-31 type Aethalometer manufactured by American Magee Scientific Corporation. The principle of Aethalometer used to calculate the quality of black carbon is based on the elimination of incident beam caused by the particles in the quartz filter. This instrument has seven channels, and the wavelengths are 370, 470, 520, 590, 660, 880, 950 nanometer while 880 nanometer channel was employed in this article. Hourly or daily average data derived from the every-five-minute data generated by Aethalometer. The absorption of visible light of the other components of aerosol is negligible as compared to the absorption ability of black carbon aerosol, so the absorption coefficient of aerosol can be extrapolated by the concentration of black carbon aerosol. There exists the following relation between them:

$$\sigma_{ab} = a \times [BC], \quad (\text{Eq.1})$$

Where σ_{ab} , $[BC]$ represents aerosol absorption coefficient, the concentration of black carbon aerosol respectively and a is the conversion factor with value of $8.28 \text{ m}^2 \text{g}^{-1}$ here^[7]. Aerosol scattering coefficient was originated from the measurement of

the Aurora-1000 type nephelometer made by Australian Ecotech company. It also had the feature of real-time continuous observation and its operating wavelength is 525 nanometer, while the data resolution is a data every 5 minutes. If aerosol absorption coefficient and scattering coefficient were known, SSA can be calculated by the following formula:

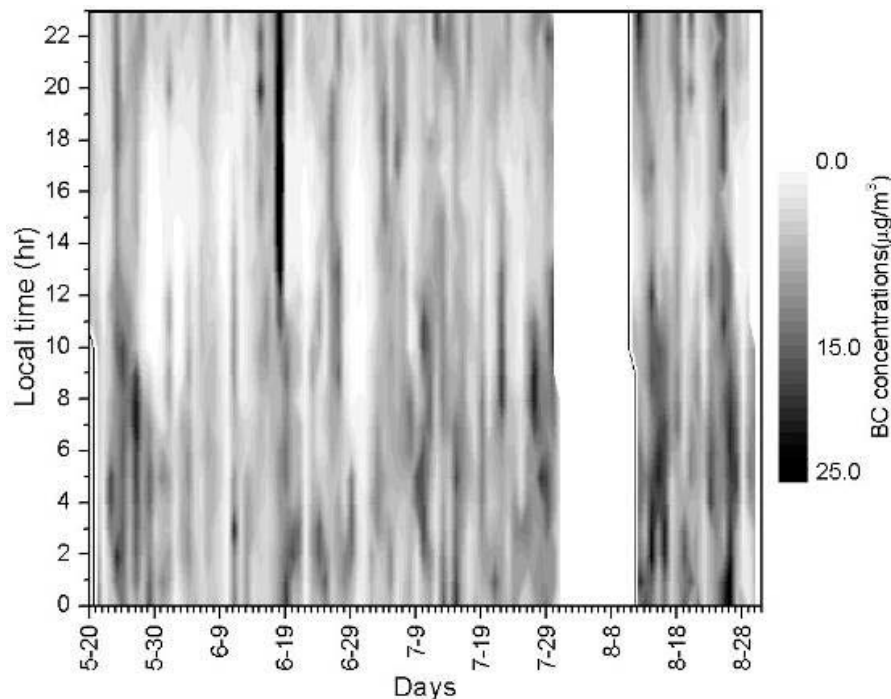
$$SSA = \frac{Sc}{Ab + Sc} \quad (\text{Eq.2})$$

The AOD data was sourced from AEROSOL ROBOTIC NETWORK ([Http://aeronet.gsfc.nasa.gov](http://aeronet.gsfc.nasa.gov)).

QUANTITATIVE ANALYSIS OF AEROSOL OPTICAL PROPERTIES

Variation Time Series of the Black Carbon Concentration

Figure 2 Time Series of the Variety of the black carbon concentration



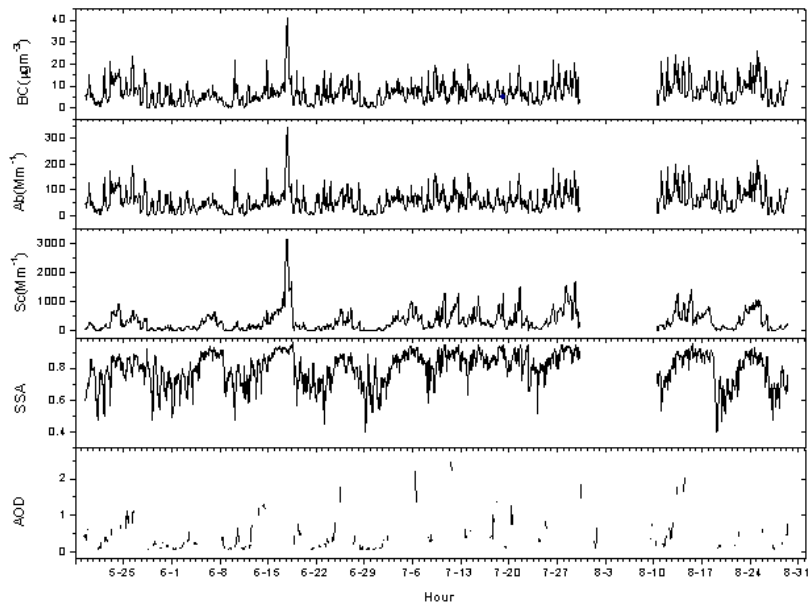
The average black carbon concentration during the observation was $7.02 \pm 4.76 \mu\text{g}\cdot\text{m}^{-3}$, which was closer to the black concentration observed in Guangzhou in China ^[8], but was still higher than Lanzhou, Dunhuang and Tazhong ^[9] and nearly 200 times larger than the value got in Svalbard of Norway, lying in the Arctic Circle ^[10]. This is because the urbanization level in Beijing and Guangzhou is higher than in Lanzhou etc., and more vehicle exhaust will discharge and more urban high-rise building will affect the spread of pollutants. Norway's Svalbard archipelago is close to the Arctic pole, which belongs to nature reserves and less vulnerable to the impact of human activities. The minimum of black carbon aerosol mass concentration during the experiment was $0.29 \mu\text{g}\cdot\text{m}^{-3}$, which appeared at 14 o'clock on the May 29 and was related to the precipitation occurred on May 28 and the strong northerly winds.

emerged on May 29. The maximum value was $41.2 \mu\text{g}\cdot\text{m}^{-3}$, which appear at 17 o'clock on the June 18, it may be caused by heavy fog. Higher black carbon concentration appear at night and in the morning, it can be inferred that it was the sharp increase of motor vehicles during the work and the relatively stable atmospheric stratification at summer night that leaded to this situation. The appearance of lower black carbon concentration was always related to strong wind or precipitation.

Variation Time Series of the Ab, Sc, SSA, AOD

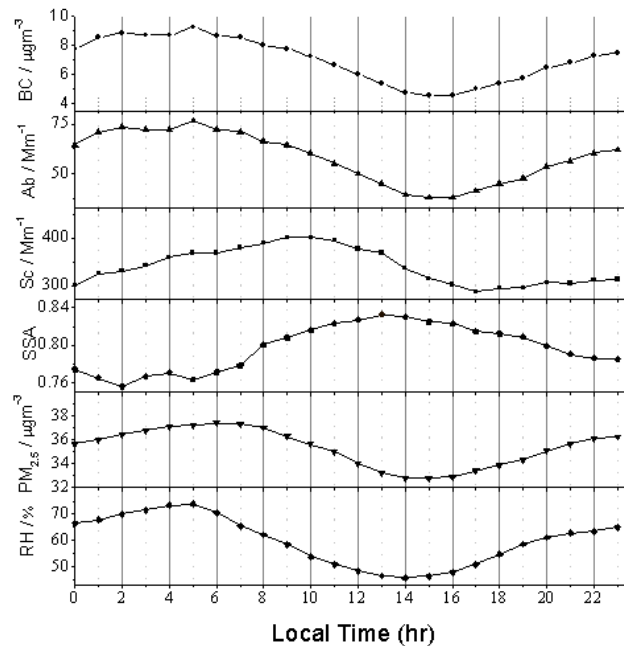
Figure 3 showed the fluctuation of the BC, Ab, Sc, SSA, AOD with the time. There is no difficult to see that the amplitudes were large and they might be caused by the more intense precipitation, wind and other synoptic processes. The average and standard deviation of Ab, Sc, SSA, AOD were $54.87 \pm 39.17 \text{ Mm}^{-1}$, $340.6 \pm 346.85 \text{ Mm}^{-1}$, 0.8 ± 0.1 和 0.41 ± 0.44 respectively, while at the station 30km in the south outskirts of Beijing, The average and standard deviation of Ab, Sc, SSA were $51.8 \pm 36.5 \text{ Mm}^{-1}$, $361 \pm 295 \text{ Mm}^{-1}$, 0.86 ± 0.07 ^[11], indicating that whether in urban or in suburban areas, aerosol absorption and scattering properties were at the same level as the higher level of urbanization. As there had a higher density of motor vehicles in urban areas, which resulted in slightly stronger competence of the aerosol absorption in urban, the value of SSA was appreciably lower, but the value of 0.8 were still comparable with the value published in Mao's article^[12]. The average and standard deviation of Sc, SSA in the Crete island of Greece were $44.2 \pm 17.5 \text{ Mm}^{-1}$ and 0.89 ± 0.04 respectively^[13-14], while the value of SSA was 0.85 ± 0.02 in the southern Africa^[15], so in the whole, the aerosol scattering coefficient was higher and the SSA was lower in the urban area in Beijing during summer.

Figure 3 Time Series of the Variety of BC, Ab, Sc, SSA and AOD



Diurnal Variation Time Series of the Bc, Ab, Sc, SSA

Figure 4 Time Series of the Daily Variety of BC, Ab, Sc, SSA



It can be seen from Figure 4 that, the diurnal variation curves of every element showed obvious single peak structure. The phase of BC, Ab, PM_{2.5}, and RH were consistent with a maximum at 5 am and the minimum at 14 in the afternoon. This distribution result may be due to of the development of mixing layer in the afternoon, which leaded to the increase of boundary layer thickness and the ability of dilution and vertical diffusion of atmosphere to pollutants. The peak of Sc value appeared around 10 am, and this may be due to the humidity control by nephelometer, So that the scattering coefficient was not susceptible by the relative humidity. The occurrence

of the maximum value of SSA is in the afternoon, which might be related to human activities, pollutant emission source sand boundary layer meteorological conditions. The curve of BC, Ab, PM_{2.5} were not have significant bimodal structure as in many other cities, which showed that they mainly affected by weather conditions and atmospheric boundary layer situation.

BC, Ab, Sc and AOD had the best correlation with the PM_{2.5} as can be seen from the correlation analysis table (Table 1). This is because the concentration of particles will directly determine the optical properties of aerosols. As also can be seen from this table, the relative humidity had some effect on aerosol optical properties and the wind speed had a negative relation to PM_{2.5} concentration and the air relative humidity.

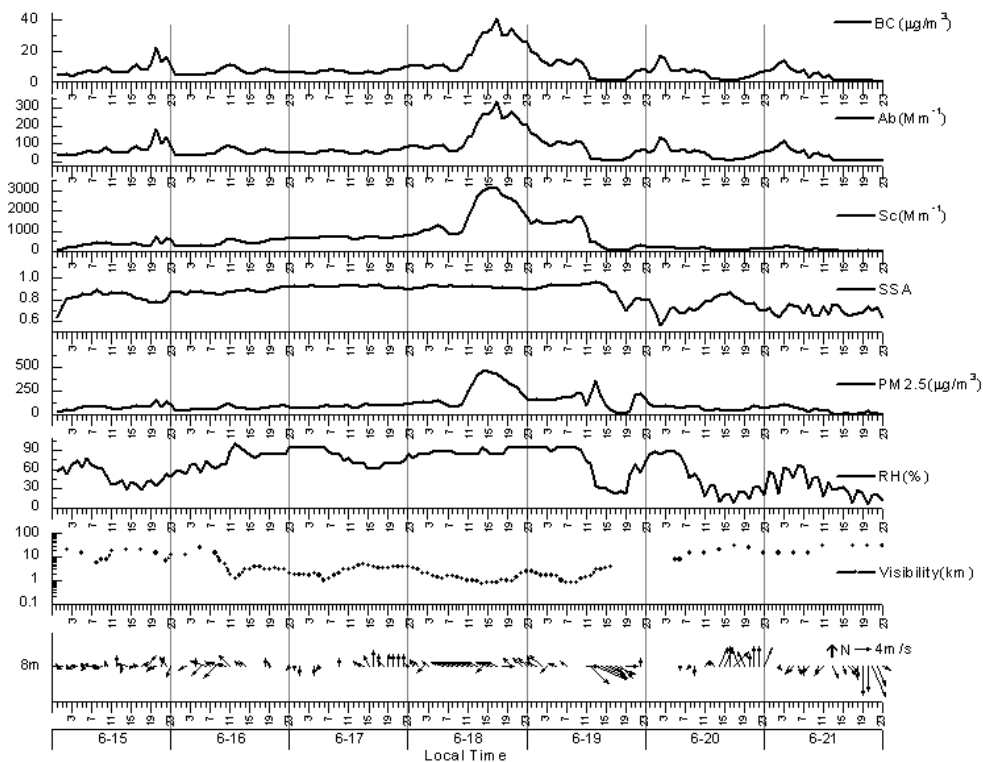
Table 1 The correlation coefficients of aerosol optical parameters and the meteorological conditions

	BC	Ab	Sc	SSA	PM_{2.5}	RH	AOD	Windspeed
BC	1	1	0.72	0.17	0.65	0.50	0.63	-0.22
Ab	1	1	0.72	0.17	0.65	0.50	0.63	-0.22
Sc	0.72	0.72	1	0.61	0.78	0.57	0.84	-0.10
SSA	0.17	0.17	0.61	1	0.46	0.42	0.58	0.01
PM _{2.5}	0.65	0.65	0.78	0.46	1	0.28	0.73	-0.04
RH	0.50	0.50	0.57	0.42	0.28	1	0.52	-0.36
AOD	0.63	0.63	0.84	0.58	0.73	0.52	1	-0.17
Windspeed	-0.22	-0.22	-0.10	0.01	-0.04	-0.36	-0.17	1

ANALYSIS OF AEROSOL OPTICAL PROPERTIES UNDER FOG AND HAZE CONDITIONS ON JUNE 18

A serious fog and haze weather took place in Beijing on June 18, while the minimum visibility dropped to 700 meter and the daily average of BC, PM_{2.5}, Sc were 188%, 447% , 276% higher than the average of the entire observation period, respectively. Maximum of the three parameters were reached 41.2 $\mu\text{g}\cdot\text{m}^{-3}$, 462.92 $\mu\text{g}\cdot\text{m}^{-3}$, 3152.02 Mm^{-1} respectively. Aerosol transport processes often result in dramatic increase in the local aerosol scattering coefficient. The Sc value in Mediterranean region had up to 5000 Mm^{-1} during spring and summer in 2001 -2002 because the dust weather process.

Figure 5. Time Series of the Variety of parameters before and after the fog and haze conditions on June 18



It can be seen from the time series chart (Figure 5) that BC、PM_{2.5}、RH were in the process of a slow increase before June 18 and reached highest value in the afternoon on June 18. On the southeast of Beijing is Baoding, Langfang, Tianjin and other cities with highly developed urban industry, dense population, more motor vehicles, more pollutants and waste, so when the dominant wind direction is southerly wind before June 18, air pollutants in these areas mixed with moist air from the sea caused heavy pollution in Beijing City.

CONCLUSIONS

Aerosol and its optical properties in Beijing city in summer were found to have the following characteristics by continuous monitored: (1) Black carbon aerosol had a seasonal average concentration of $7.02 \pm 4.76 \mu\text{g}\cdot\text{m}^{-3}$, which was higher than other less developed cities or nature reserves. Aerosol absorption coefficient (Ab) and scattering coefficient (Sc) were $54.87 \pm 39.17 \text{ Mm}^{-1}$, $336.6 \pm 346.9 \text{ Mm}^{-1}$, both values higher than the value in the low level industrial region. Single scattering albedo (SSA) was lower than the observation result in the suburb with the value of 0.8 ± 0.1 . (2) The diurnal variations curve of Ab, Sc and SSA showed significant single peak structure due to the conditions of local atmospheric boundary layer. Ab and Sc reached the

minimum in the afternoon when boundary layer flow strongly mixed, and their maximum appeared in early morning and morning respectively while the max value of SSA appeared in the afternoon. Ab, Sc and SSA all had good positive correlation with PM_{2.5} during the observation period, which clarified that aerosol concentration directly determined its scattering and absorption quantity of solar radiation. Ab and Sc had positive correlation with relative humidity. That was when the water vapor content of air increased, the capacity of absorption and scattering of aerosol particles increased, too. PM_{2.5}, Ab, Sc were negatively correlated with wind speed, and it illustrated that wind reduced the concentration of aerosol and thus impact the optical properties of aerosol. (3) It is the sustained but not strong flow mixed with water vapor and air pollutants that cause the strong haze weather in Beijing during summer. The water vapor and air pollutants might aroused from Yellow Sea and the industrial city on the southeastern of Beijing. There was a significant reduction of atmospheric visibility and aerosol concentration and its capabilities of absorption and scattering of sunlight would increase several times when fog and haze weather occurred.

REFERENCES

- [1] Zhang R., Y. Xu, Z. Han. A comparison analysis of chemical composition of aerosols in the dust and non-dust periods in Beijing. 2004, *Advances In Atmospheric Sciences*, 21(2), pp300-305.
- [2] Zhang R., R. Arimoto, J. An, et al.. Ground Observations of a Strong Dust Storm in Beijing in March 2002. *Journal of Geophysical Research*, 2005, 110, D18S06, doi:10.1029/2004JD004589.
- [3] Xia X., Z. Li, B. Holben, et al.. Aerosol optical properties and radiative effects in the Yangtze Delta region of China. *Journal Of Geophysical Research*, 2007, 112, D22S12, doi:10.1029/2007JD008859
- [4] Li Z., X. Xia, M. Cribb, et al.. Aerosol optical properties and their radiative effects in Northern China. *Journal Of Geophysical Research*, 2007, 112, D22S01, doi:10.1029/2006JD007382.
- [5] Cheng Y., A. Wiedensohler, H. Eichlerb, et al.. Aerosol optical properties and related chemical apportionment at Xinken in Pearl River Delta of China. *Atmospheric Environment*. 2008, 42, pp6351-6372.
- [6] Xia X., H. Chen, P. Goloub et al.. A compilation of aerosol optical properties and calculation of direct radiative forcing over an urban region in Northern China. *Journal Of Geophysical Research*, 2007, 112, D12203, doi:10.1029/2006JD008119.

- [7] Schmid, O., D. Chand, and M. Andreae. Aerosol optical properties in urban Guangzhou, PRD workshop, Beijing, January 13–14, 2005.
- [8] Tao J., L. Zhu, J. Han, et al.. Preliminary Study on Characteristics of Black Carbon Aerosol Pollution in Guangzhou during the Spring of 2007. *Climatic and Environmental Research* (in Chinese), 2008, 13(5), pp658-662.
- [9] Gao R., S. Niu, H. Zhang, et al.. An observational study of black carbon aerosol in Northwest China in the spring of 2006. *Journal of Nanjing Institute of Meteorology*, 2008, 31(5), pp 655-661.
- [10] Eleftheriadis K., S. Vratolis, S. Nyeki. Aerosol black carbon in the European Arctic: Measurements at Zeppelin station, Ny-A° lesund, Svalbard from 1998–2007. *Geophysical Research Letters*, 2009, 36, L02809, doi: 10.1029/2008GL035741.
- [11] Garland R., O. Schmid, A. Nowak, et al.. Aerosol optical properties observed during campaign of air quality research in Beijing 2006 (CAREBeijing-2006): Characteristic differences between the inflow and outflow of Beijing city air. *Journal Of Geophysical Research*, 2009, 114, D00G04, doi: 10.1029/2008JD010780.
- [12] Mao J., C. Li. Observation study of aerosol radiative properties over China. *Acta Meteorologica Sinica*, 2006, 20(3), pp 306-321
- [13] Bryanta C., K. Eleftheriadisb, J. Smolikc, et al.. Optical properties of aerosols over the eastern Mediterranean. *Atmospheric Environment*, 2006, 40, pp 6229-6244.
- [14] Vrekoussisa M., E. Liakakoua, M. Koc-akb, et al.. Seasonal Variability of Optical Properties of Aerosols in the Eastern Mediterranean. *Atmospheric Environment*, 2005, 39, pp 7083-7094.
- [15] Leahy L., T. Anderson, T. Eck, et al.. A Synthesis of single scattering albedo of biomass burning aerosol over Southern Africa during SAFARI 2000. *Geophysical Research Letters*, 2007, 34, L12814, doi: 10.1029/2007GL029697,.

Source evaluation of the seasonal variation in aerosol optical depth distribution over the Indian subcontinent from combined measurement and modeling platforms

S. Verma^{1,2}, M. Schulz³, Y. Balkanski³, S. N. Bhanja¹, and S. K. Pani²

1 Department of Civil Engineering, Indian Institute of Technology Kharagpur, 721302, West Bengal, India

2 Centres for Oceans, Rivers, Atmosphere and Land Sciences, Indian Institute of Technology Kharagpur, 721302, West Bengal, India

3 Laboratoire des Sciences du Climat et de l'Environnement, 91191 Gif-sur-Yvette Cedex, France

Principal Contact: S. Verma, Department of Civil Engineering, Indian Institute of Technology Kharagpur, 721302, West Bengal, India.

Fax: +91-3222-255303 Email: shubha@iitkgp.ac.in, shubhaverm@gmail.com

Abstract

Anthropogenic aerosols perturb the radiation energy balance of the earth-atmosphere system and hence impact the earth climate. In contrast to the well-mixed greenhouse gases, which are uniformly mixed around the globe, aerosols exhibit variation in their spatial and temporal characteristics. This could lead to a climate response due to aerosols different on a regional scale than the global. Modeling studies suggest significant link between aerosols and regional climatic effects with a potential to impact large scale circulation and hydrological cycle. Emission fluxes aggregated spatially over India show variation in the regional emission composition, e.g. emission fluxes from the Indo-Gangetic plain (IGP), are mainly composed of sulfate, organic matter, inorganic matter followed by black carbon, while that from northwest India are mainly composed of dust followed by sulfate. On the other hand, the prevalence of different seasonal cycles over Indian subcontinent could further lead to the variation in the chemical and optical characteristic of aerosols. It is therefore, necessary to carryout the source evaluation of chemical and optical characteristics of aerosol during different seasons prevalent over India through integration of measurements and modeling studies. In the present work, we carry out an analysis of aerosol distribution over the Indian subcontinent from aerosol transport simulations in LMDZ-INCA [Schulz *et al.*, 2006] which couples the Laboratoire de Meteorologie Dynamique general circulation model (LMDZ) and the Interaction with Chemistry and Aerosols (INCA) model. Simulations of emissions tagged by region are used to understand the relative influence of emissions on aerosol optical depth (AOD). Model estimates showed the AOD over the IGP to be dominated by dust and sulfate during the southwest monsoon compared to sulphate, organic matter, and BC, during the winter monsoon. Evaluation of GCM simulated aerosol optical depth over the Indian subcontinent with the ground-based measurements during the various campaigns and satellite-based observations will be presented. The chemical constituents to the AOD measured and their probable sources will be evaluated.

Keywords: Anthropogenic aerosols, aerosol optical depth, emission flux, source evaluation

Climatology of Aerosol Properties at Mountaintop Sites

**E. Andrews^{1,2}, J.A. Ogren¹, P. Bonasoni³, A. Marinoni³, E. Cuevas⁴, S. Rodriguez^{4,5},
J.Y. Sun⁶, D. Jaffe⁷, E. Fischer⁷, U. Baltensperger⁸, E. Weingartner⁸, M. Collaud Coen⁹, S.
Sharma¹⁰, A. Macdonald¹⁰, W.R. Leaitch¹⁰, N.-H. Lin¹¹, P. Laj¹², T. Arsov¹³, I. Kalapov¹³, A.
Jefferson^{1,2} and P. Sheridan¹**

¹ NOAA, Earth Systems Research Laboratory, Boulder, CO, 80305, USA

² University of Colorado, CIRES, Boulder, CO, 80305, USA

³ ISAC-CNR, Institute of Atmospheric Sciences and Climate, Bologna I-40129, Italy

⁴ Izaña Atmospheric Research Centre, AEMET, 38071, Sta. Cruz de Tenerife, Canary Isl., Spain

⁶ Key Laboratory for Atmospheric Chemistry, Centre for Atmosphere Watch and Services,
Chinese Academy of Meteorological Sciences, Beijing 100081, China

⁷ University of Washington, Department of Atmospheric Sciences, Seattle, 98195, WA, USA

⁸ Paul Scherrer Institute, Laboratory of Atmos. Chem., Villigen PSI, CH-5232, Switzerland

⁹ Federal Office of Meteorology and Climatology, MeteoSwiss, CH-1530 Payerne, Switzerland

¹⁰ Environment Canada, Toronto, Ontario, M3H 5T4, Canada

¹¹ National Central University, Department of Atmospheric Sciences, Chung-Li 320, Taiwan

¹² University of Grenoble 1 / CNRS, 38 402 Grenoble, France

¹³ Institute for Nuclear Research and Nuclear Energy, Sofia BG-1784, Bulgaria

ABSTRACT

High altitude mountaintop observatories provide the opportunity to make long-term, continuous measurements of aerosol properties in the free troposphere without the added expense and difficulty of operating aircraft. Climatologies of free tropospheric aerosol radiative properties in cloud-free air, including light scattering, light absorption, light extinction, single scattering albedo, Ångström exponent, hemispheric back-scatter fraction and radiative forcing efficiency, from twelve high altitude (2.2-5.1 km) measurement platforms are presented. These climatologies utilize data from ten mountaintop observatories in the 20-50°N latitude band and two multi-year, aircraft vertical profiling programs. The amount of light absorption and scattering observed from these high altitude platforms either peaks in the spring or has a broad spring to summer enhancement. The seasonal variation and systematic relationships among aerosol properties change from site to site but the timing and links among parameters can be related to aerosol sources known to impact the individual sites.

Having first presented an overview of aerosol optical properties for all 12 high altitude sites, we focus on differentiating air masses based on their combined aerosol properties at the three sites in

Asia: Pyramid (Nepal), Mount Waliguan (China), and Lulin Mountain (Taiwan), along with Mauna Loa (USA) in the central Pacific. Specifically we use statistical clustering techniques to identify typical air mass trajectories at these four sites and to determine if the resulting clusters can be related to the characteristics of different aerosol types (e.g., dust, smoke). This allows us to determine the contribution of aerosol events to the aerosol climatology at these locations and to propose site-specific rules for identifying aerosol type. Furthermore, these rules could help to constrain both model parameterizations and remote sensing algorithms that are often based on an assumed aerosol type.

KEYWORDS

Aerosol optical properties, In-situ measurements, Smoke, Dust

Introduction

Atmospheric aerosol particles affect the earth's radiative balance in several ways. They can scatter and absorb radiation, directly changing how much radiation reaches any particular location. Furthermore, aerosol particles indirectly influence the earth's radiative balance by acting as cloud nuclei. The magnitude and sign of the aerosol forcing effect are determined, in part, by both the horizontal and vertical distribution of the aerosol particles^[1]. With lifetimes on the order of days to weeks, aerosols are not distributed homogeneously in the atmosphere. This results in local, regional and global differences in radiative forcing creating an observational challenge. High altitude mountaintop observatories provide the opportunity to make long-term, continuous observations of in-situ aerosol properties in the free troposphere (FT) without the added expense and difficulty of making airborne measurements. Diurnal and synoptic flow patterns can bring varying degrees of boundary-layer or FT air to mountaintop sites. Though segregating boundary layer and FT air can be a challenge, high altitude sites provide a unique opportunity to understand differences and similarities in aerosol properties between these two layers.

Aerosol transport in the free troposphere has important implications for both air quality and climate^[2]. Faster wind speeds in the FT allow aerosols that have been injected into this layer to be transported long distances. Once lofted into the FT, dust, biomass burning smoke and anthropogenic pollution aerosols from surface sources can be transported hemispherically^[3,4,5]. Under favorable meteorological conditions, aerosols that have been redistributed in the FT can be entrained back down to the surface, affecting air quality thousands of kilometers from the aerosol source region^[3,6].

This work presents a climatology of northern hemisphere (20-50° N) FT aerosol optical properties based on continuous, long term in-situ measurements at high altitude observatories. By bringing together measurements from un-related networks and sites we address known knowledge gaps^[2]. Over the last several decades the number of mountaintop observatories continuously measuring in-situ aerosol radiative properties has increased significantly from a single station (Mauna Loa, USA) in the 1970's to at least ten observatories actively making these measurements today (see Table 1). This type of analysis may help constrain chemical transport models, validate satellite measurements, and quantify the influence of smoke, volcanoes and dust episodes on FT aerosol properties.

Using high altitude measurements, screened for both cloud contamination and boundary layer contamination (the screening is described below), the following questions are addressed:

- (1) What are the similarities and differences of free-tropospheric aerosol radiative properties at a wide range of locations?
- (2) Are data clustering techniques based on air mass trajectories useful for identifying aerosol types and events at mountain top sites in Asia?

Experimental Methods

The data used here consist of hourly-averaged, quality-checked light scattering and light absorption (where available) measurements from the ten mountaintop sites and two aircraft platforms. Table 1 presents the sites, their locations and the instruments operated at each site

Table 1. List of observatories included in this study, arranged from west to east.

Station	Lat/long Elev (km) asl	Scat Inst ¹	Abs Inst ¹	size cut (μm)	Sample RH
MLO Mauna Loa, USA	19.54N 155.58W 3.4	T	P	10	controlled <40%
WHI Whistler, Canada	50.01N 122.95W 2.2	T	P	2.5	Typically <40%
MBO Mt Bachelor, USA	43.98N 121.70W 2.8	T,R	P	1	Typically <40%
SGP* Southern Great Plains, USA	36.61N 97.49W 3-5	T	P	7	controlled <40%
BND* Bondville, USA	40.05N 88.37W 3-5	T	P	7	controlled <40%
IZA Izana, Spain	28.47N 16.25W 2.4	T	M	10	Typically <40%

JFJ Jungfraujoch, Switzerland	46.55N 7.99E 3.6	T	A	Whole air	controlled <20%
CMN Mt. Cimone, Italy	44.18N 10.70E 2.2	E	P,M	Whole air	Typically <40%
BEO BEO Moussala, Bulgaria	42.18N 23.59E 2.4	T	--	Whole air	Typically <40%
PYR Pyramid, Nepal	27.57N 86.48E 5.1	T	M	2.5 (σ_{sp}) 10 (σ_{ap})	controlled <30%
WLG Mt. Waliguan, China	36.28N 100.90E 3.8	T	P	10	controlled <40%
LLN Mt. Lulin, Taiwan	23.47N 120.87E 2.9	T	P	10	controlled <40%

[†] T=TSI nephelometer, R=Radiance Research nephelometer, E=Ecotech nephelometer, A=Aethalometer, P=PSAP, M=MAAP

* Multi-year aircraft profile measurements

In all cases light scattering was measured by integrating nephelometers, and at least one channel measured at a green wavelength (in the range 520-550 nm). Light absorption was measured by various filtered-based instruments (i.e., particle soot absorption photometer (PSAP), aethalometer, multi-angle absorption photometer (MAAP)). Most but not all absorption measurements also included a green wavelength channel. Unless otherwise noted, aerosol optical properties are adjusted to and reported at 550 nm.

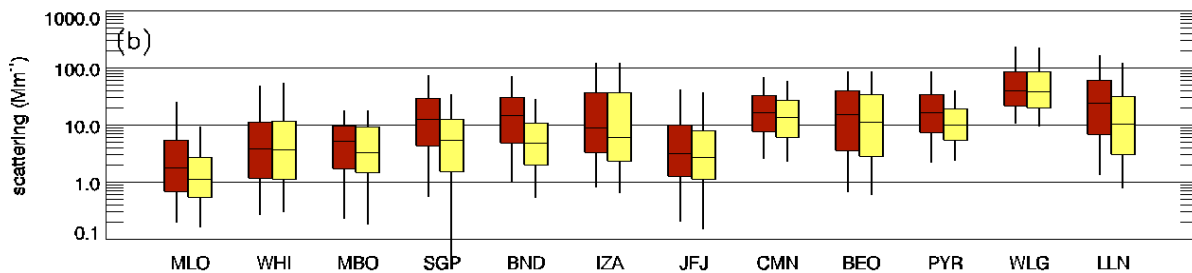
One goal of this paper is to compare and contrast the FT aerosol optical properties observed at various sites, thus measurement consistency is critical. All measurements presented here are adjusted to standard temperature and pressure (STP, $T_{standard}=273.15\text{ K}$ and $P_{standard}=1013.25\text{ hPa}$). The instruments are typically operated at low relative humidity (< 40%). Nephelometer data were adjusted for truncation effects and illumination non-idealities while absorption instrument data were adjusted for scattering artifacts and other instrument non-idealities. Instrument corrections are detailed in Andrews et al.^[7].

Seven day air mass back trajectories were calculated and clustered using the methodology of Harris and Kahl^[8] and the NCEP reanalysis 3D meteorology data. Two sets of trajectory clusters were calculated for each site (1) a daytime group of clusters more likely to correspond to boundary layer-influenced air and (2) a nighttime group of clusters more likely to be representative of FT influences. The time series of aerosol optical properties (AOP) were merged with their corresponding air mass trajectories and AOP statistics were calculated as a function of cluster.

Results and Discussion

Figure 1 shows annual climatological values for aerosol scattering at each site both for ‘all data’ and data that have been identified as being FT aerosol using $3\text{am} \leq \text{FT} \leq 9\text{am}$ local time criterion (for the airplane data from SGP and BND the flight altitude was used to identify FT air – there was no time constraint). The data have been filtered to remove cloud influences. The data in Figure 1 are plotted from west to east so that the six western hemisphere sites are on the left side of the plot and the eastern hemisphere sites are on the right side of the plot.

Figure 1. Aerosol scattering for ‘all data’ and ‘FT data’. Data are reported at 550 nm, except at CMN where light scattering is at 520 nm). Red=‘all data’, Yellow=‘FT data’ (based on time of day). Horizontal line is the median (50th percentile), edges of box are 25th and 75th percentiles, whiskers are 5th and 95th percentiles. Figure from Andrews et al.^[7].

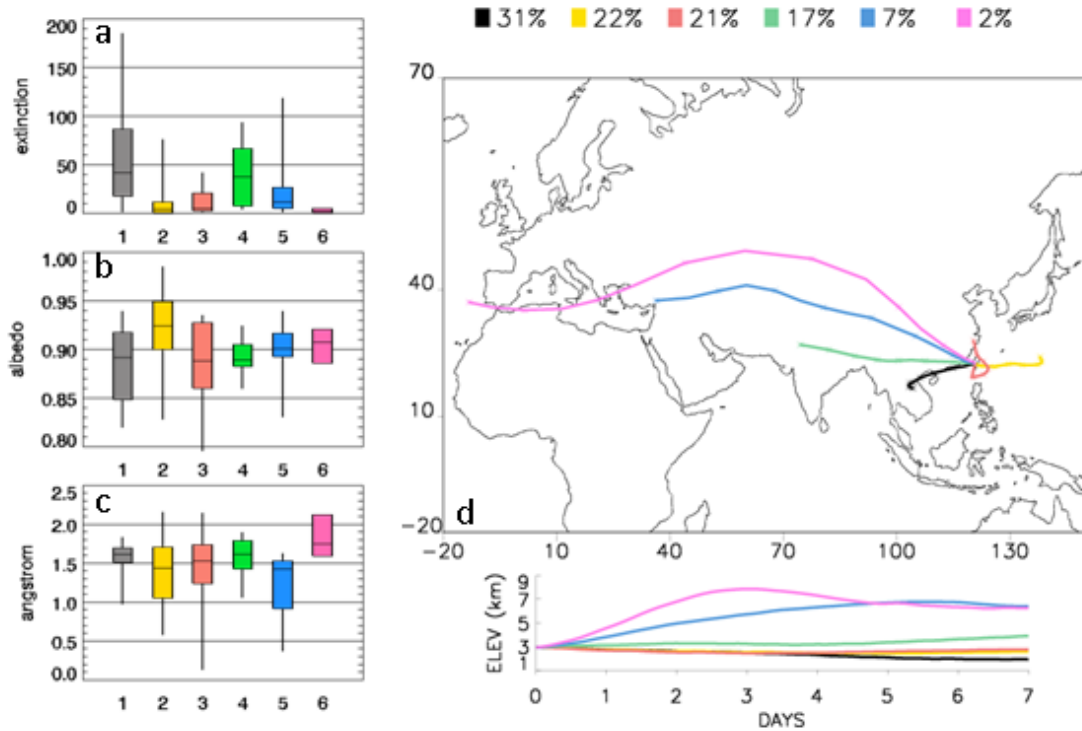


There are several notable features in Figure 1. First, there is an order of magnitude difference in light scattering from the cleanest FT air (MLO) to the FT air with the highest aerosol loading (WLG). In other words there is significant variability in FT aerosol loading depending on location. Second, aerosol light scattering increases from west to east, starting at the International Date Line. This is true for both ‘all data’ and ‘FT data’ and suggests that the BL and FT are coupled and/or that the time of day screening for FT air may not be ideal. This west to east increase in aerosol amount roughly corresponds with increases in population density and estimates of global surface PM2.5 mass concentration^[9]; it may also be related to proximity to aerosol sources such as desert dust or biomass burning. There is no north to south gradient in aerosol amount when all 12 sites are considered, nor is there a consistent pattern in aerosol amount based on observatory altitude. Finally, at most sites, the scattering tends to be lower when air influenced by the boundary layer is excluded.

Figure 2 shows how air mass back trajectories are associated with differences in aerosol extinction, single scattering albedo and Ångström exponent for LLN. This site is strongly impacted by the transport of biomass smoke from southeast Asia in the spring^[10], but may also sample dust, pollution or clean marine air, depending on source region. The aerosol data and

trajectories are for 0200 local time (18 GMT) and thus are likely to be primarily representative of FT air with little influence from upslope flow.

Figure 2. Aerosol extinction (a), single scattering albedo (b) and Ångström exponent (c) as a function of trajectory cluster (d) for Lulin Mountain. Colors of the box plots indicate the associated trajectory cluster. Percentages above the trajectory plot indicate frequency of that trajectory cluster.



In Figure 2, Trajectory 1 is dominated by late winter and springtime transport from SE Asia. It has the highest aerosol loading (as indicated by the high extinction values) and tends to have lower single scattering albedo values than many of the other clustered trajectories. This trajectory is likely to be influenced by biomass burning in the region. Trajectory 2, which is most common in the summer and fall, is likely influenced by clean marine air, consistent with the observed higher single scattering albedo and lower Ångström exponent. Trajectory 3 is the most local trajectory, swirling along the east coast of Taiwan after touching the eastern coast of China. This flow pattern probably includes both regional anthropogenic air pollution and some marine influence, as indicated by lower single scattering albedo values and a wide range of Ångström exponents. Trajectory 4 tends to occur in winter and spring. For this trajectory the main source region is China. The associated aerosol tends to be more absorbing (lower single scattering albedo) and the aerosol loading is higher suggesting this trajectory is likely influenced by

anthropogenic pollution. Trajectory 5 is similar in timing and spatial coverage to Trajectory 6. Trajectory 5 differs from Trajectory 6 in that it has a lower Ångström exponent suggesting a dust influence. Trajectory 6 occurs infrequently, primarily in the winter, and represents long range, high altitude transport. The optical properties suggest air masses of this sort correspond to low loading (i.e., small extinction values) and relatively small aerosol as indicated by the larger Ångström exponent.

SUMMARY

There is significant variability in aerosol optical properties in terms of aerosol loading and intensive properties (single scattering albedo, Ångström exponent and back-scatter fraction) among the 12 sites. Aerosol loading generally moving eastward from the International Date Line, where the western-most site was Mauna Loa (MLO) in Hawaii and the eastern-most site was Mount Lulin (LLN) in Taiwan. Differences in the intensive properties clearly showed the influence of different sources/aerosol types on the different sites. Trajectory clustering suggests that, to some extent, aerosol optical properties can be related to the nominal source regions of the aerosol.

ACKNOWLEDGMENTS

Dan Chao for calculating and clustering trajectories with code developed by J.M. Harris.

REFERENCES

- [1] Haywood, J.M.; Ramaswamy, V. *J. Geophys. Res.*, 1998, 103:6043-6058.
- [2] Laj, P. et al., *Atmos. Environ.*, 2009, 43:5351–5414.
- [3] McKendry, I. G.; Hacker, J. P.; Stull, R.; Sakiyama, S.; Mignacca, D.; and Reid, K. *J. Geophys. Res.*, 2001, 106:18,361–18,370.
- [4] Wandinger, U. et al. *J. Geophys. Res.*, 2001, 107, doi:10.1029/2000JD000202.
- [5] Mattis, I.; Muller, D.; Ansmann, A.; Wandinger, U.; Preißler, J.; Seifert, P.; and Tesche, M. *J. Geophys. Res.*, 2008, 113:doi:10.1029/2007JD009636.
- [6] Colette, A.; Menut, L.; Haeffelin, M.; Morille, Y. *Atmos. Environ.*, 2008, 42:390–402.
- [7] Andrews, E. et al. *Atmos. Res.*, 2011, submitted.
- [8] Harris, J. M.; J. D. Kahl *J. Geophys. Res.*, 1990, 95:13,651–13,667.
- [9] van Donkelaar A; Martin R.V.; Brauer M.; Kahn, R; Levy, R.; Verduzco, C. *Environ Health Perspect.*, 2010, 118:847-855.
- [10] Chi, K.H., Lin, C-Y., Yang, C-F.O., Wang, J-L., Lin, N-H., Sheu, G-R., Lee, C-T., *Environ. Sci. Technol.*, 2010, 44:2954-2960.

Study of Columnar aerosol size spectra at Pune

G. R. Aher¹, S. D. More²

1 Physics Dept., Nowrosjee Wadia College, Pune 411 001, India

2 Dept. of Atmospheric and Space Sciences, University of Pune 411 007, India.

Principal Contact: G. R. Aher, Dr., Physics Dept., Nowrosjee Wadia College, Pune 411 001, India.

Tel: +91(020)26162944 Fax: +91(020)26163108 E-mail: aher.g.r@gmail.com

Abstract

Various properties of atmospheric particles depend on particle size. Their number-size distribution is the most important element describing atmospheric aerosol. Its importance has been increasingly recognized with the concern over the effects of aerosols and clouds on radiation transfer and climate. The Sun-tracking multiple wavelength radiometer in spectral range 400-1020 nm, was operated from Pune University campus to measure the columnar aerosol optical depths (AOD) over Pune city during the years 1998-99, 1999-00 and 2000-01. MICROTOPS- II sun photometer has been operated from Pune University campus during 2008-09 and 2009-10 at spectral channels centered at 440, 500, 675, 870 and 1020 nm wavelengths to measure AOD. The monthly spectral AOD data obtained during these observing seasons forms the subject matter of the present paper and is analyzed to retrieve columnar aerosol size distribution and its variation. Analysis of data reveals that the shape of the monthly size distribution during 1998-99 is mostly bimodal indicating the likelihood of the presence of two groups of aerosol particles with different mode radii values. In 1999-2000, size distribution is found to be either Junge power law or mono-modal type implying the presence of single haze distribution with dominance of small size aerosols. During 2000-01, shape of the size distribution spectrum is mostly monomodal showing the presence of small size aerosols. Columnar aerosol size distribution during 2008-09 and 2009-10 is mostly Junge power law type.

Keywords: Number-size distribution, Aerosol optical depth, Single haze size distribution.

Mercury species in atmospheric particles and their dependent conditions

Guangli Xiu^{1,2}, Yanyan Zhang¹, Ji Cai¹, Meigen Zhang³, Renjian Zhang³, Donald Lucas², Danian Zhang¹

1 East China University of Science & Technology, 130 Meilong Road, Shanghai 200237, China

2 Environmental Energy Technologies Division, Lawrence Berkeley National Laboratory, Berkeley, CA 94702

3 State Key Laboratory of Atmospheric Boundary Layer Physics and Atmospheric Chemistry, Institute of Atmospheric Physics, Chinese Academy of Sciences, Beijing 10029, China

Principal Contact: Guangli Xiu, Professor, East China University of Science & Technology, 130 Meilong Road, Shanghai 200237, China.

Tel: 86-21-64251927 Fax: 86-21-64253113 Email: xiugl@ecust.edu.cn

Abstract

A cascade impactor and PM10 sampler were used to collect atmospheric particles in southern Shanghai. Chemically sequential extraction method was used to take exchangeable particle-phase mercury (ExPM), Hydrochloric particle-phase mercury (HPM), elemental particle-phase mercury (EPM) and residual particle-phase mercury (RPM). Results indicated that averaged Hg concentration in TSP was 0.48 ng/m³ ranging between 0.07 and 1.88 ng/m³, 84.1% of which was in PM8 (particulate matter with diameter $\leq 8\mu\text{m}$) and 47.8% was in PM1.6 (particulate matter with diameter $\leq 1.6\mu\text{m}$). The mean Hg content in particle mass was 1.81 $\mu\text{g/g}$ with a range between 0.35 and 6.89 $\mu\text{g/g}$ which was far higher than those in other emission sources. It implied that atmospheric particle can play a role in enrichment of mercury. Mercury in particles showed distinct seasonal variation and it was higher in winter and spring impaired by dust storm while it was lower in summer. The existing species of mercury were found to be determined by meteorologic conditions and sources distribution. Except spring in 2006, HPM content in particle displayed the similar level to other seasons that HPM was higher in PM1.6. Mercury concentration and content both positively correlated to relative humidity, temperature and visibility whereas have the negative links to SO₂. Higher EPM concentration was observed in winter, 2005 and spring, 2006 and was mainly in fine particles. EPM concentration and content correlated negatively with temperature while positively with SO₂ and NO₂. Residual mercury had a higher content in $<1.6\mu\text{m}$ and $1.6\sim3.7\mu\text{m}$. RPM content and concentration correlated strongly negatively with temperature, daily temperature difference and relative humidity. As for mercury in PM8 mass, residual mercury predominated with 62-72% while HPM and EPM had similar fractions. However, the fractions of HPM and EPM increased in PM1.6 and took more important roles. Based on the gas-particle mechanism analysis, divalent mercury was found to be the important indicator for mercury transformation on particle interface.

Keywords: Particulate matter, atmospheric mercury, speciation, dependence conditions

Size Distributions of Water Soluble Ions in Atmospheric Aerosol at Lin'an Regional Background Station

Honghui Xu¹, Jie Liu², Chunxiao Ji¹ and Minjuan Mao¹

1 Zhejiang Institute of Meteorological Sciences, Hangzhou 310017, China

2 Zhejiang Meteorology Bureau, Hangzhou 310002, China

ABSTRACT

To investigate regional characteristics of aerosol pollution in the area of Changjiang river delta in China, atmospheric aerosol samples were collected with Andersen cascade sampler at Lin'an regional background station during April, July, October of 2008 and January of 2009. The water soluble ionic concentrations were analyzed by IC. Results showed three different size distributions for the ions characterized, including masses in: (i) the accumulation mode, with a peak at 0.43 to 1.1 μm (SO_4^{2-} , NH_4^+ , K^+); (ii) the coarse particle mode, with a peak at 4.7 to 5.8 μm (Ca^{2+} , Mg^{2+}); and (iii) a bimodal distribution, with peaks at 0.43 to 1.1 μm and 4.7 to 5.8 μm (NO_3^- , Na^+ , Cl^-). The measured distributions are believed to result from a combination of processes including regional anthropogenic and natural sources, and long-range transport. The size distributions of the water soluble ions studied were influenced by at least three processes governing their concentrations in fine and coarse particles: (i) primary emissions of ultrafine particles from combustion and industrial processes; (ii) advection of air masses containing aged intermediate size aerosols; (iii) large particles arising mainly from re-suspension.

KEYWORDS

Aerosol, size distribution, Water-soluble ions

Introduction

Atmospheric aerosols consist of complex mixtures of elemental and organic carbon, ammonium, nitrates, sulphates, mineral dust, trace elements, and water. Investigation of the chemical characteristics of these aerosols is important for elucidating particle toxicity and its potential role in climate change^[1]. Atmospheric aerosol size distributions, along with their chemical compositions, sources, and sinks, are key elements in understanding and managing aerosol health effects^[2], visibility, and the climate^[3]. Therefore, it is important to study the chemical characteristics and sources of atmospheric aerosols as well as their spatial and temporal variations.

Rapid urbanization and industrial development in China over the past three decades likely led to significant increases in the emission of particles and their gaseous precursors. In this paper, we

conducted an experimental study to investigate the size distributions of water-soluble ions in atmospheric aerosol using Andersen multi-stage samplers and the field experiment was made at GAW (Global Atmospheric Watch) station of Lin'an regional background station. This location is typical of non-urban regions in Changjiang river delta, which enables the sampling of air masses that are more representative of regional characteristics. Size distributions of water-soluble ions in aerosol were also determined in order to distinguish different aerosol sources.

Experimental Methods

Atmospheric aerosol samples were collected with Andersen cascade sampler at Lin'an regional background station ($30^{\circ}18' N$, $119^{\circ}44' E$, 138.6m ASL) during April, July, October of 2008 and January of 2009. The station is one of the WMO GAW regional background monitoring stations, located on a small hill about 20 km north of Lin'an county town. The distance from the site to Hangzhou City, the capital city of Zhejiang Province, is about 60 km, and is about 200 km northeast to the mega-city Shanghai. About 100 km to the north of the site, there are clusters of industrial and urbanized areas, such as Nanjing, Suzhou, and Wuxi economical zone. To the west of the site are mountainous regions of Anhui Province with relatively less industrial activities.

Aerosol samples were collected with an eight-stage low pressure impactor (Andersen Series 20-800, USA). Mixed cellulose ester filter substrates were employed in all stages, and a flow rate of 28.3 L/min was used. The 50% cut off diameters (D₅₀) were 9.0, 5.8, 4.7, 3.3, 2.1, 1.1, 0.65, and 0.43 μm . Aerosol samples collected from 18:00 p.m. to 17:30 p.m. in the next day. Each sample and a blank were ultrasonically extracted using 50ml of water (deionized H₂O; 18M Ω /cm resistivity). After passing each extracted sample through a microporous membrane (pore size = 0.45 μm ; diameter = 25mm; Ampel Co.), three anions (SO₄²⁻, NO₃⁻, Cl⁻) and five cations (NH₄⁺, Ca²⁺, Na⁺, Mg²⁺, K⁺) were analyzed using ion chromatography (Dionex ICS-90). This system was outfitted with a separation column (Dionex AS14A for anion and CS12A for cation), a guard column (Dionex AG14A for anion and CG12A for cation), and a conductivity detector (Dionex DS5). A gradient weak base eluent (3.5 mmol/L Na₂CO₃; 1 mmol/L NaHCO₃) was used for anion detection, while a weak acid eluent (22 mmol/L MSA) was used for cation detection. Ion recovery was in the range of 80 to 120%. The relative standard deviation (SD) of each ion was less than 3% for the reproducibility test. Limits of detection (S/N=3) were less than 0.03 mg/L for anions and 0.004 mg/L for cations. Quality assurance was routinely carried out using standard reference materials (Merck Co.). Data from blank samples was subtracted from the corresponding sample data after analysis.

Results and Discussion

Size distributions obtained for the water-soluble ions at Lin'an regional background station are illustrated in Figure 1. Three size distributions were found for the water-soluble ions, including

masses within: (i) the accumulation mode, with a peak at 0.43 to 1.1 μm (SO_4^{2-} , NH_4^+ , K^+); (ii) the coarse particle mode, with a peak at 4.7 to 5.8 μm (Ca^{2+} , Mg^{2+}); and (iii) a bimodal distribution, with peaks at 0.43 to 1.1 μm and 4.7 to 5.8 μm (NO_3^- , Na^+ , Cl^-).

SO_4^{2-} was found in the accumulation mode, with 78%~88% of its mass present as fine particles with aerodynamic diameters less than 2.1 μm . SO_4^{2-} and NH_4^+ had a peak between 0.43 to 0.65 μm in summer and fall, while those between 0.43 to 1.1 μm in spring and winter. Sulfate existed mainly in “accumulation mode” states represented by sulfate with aerodynamic diameters by less than 0.43 μm and “droplet mode” states represented with aerodynamic diameters by between 0.43 to 1.1 μm ^[4]. The ratios of “droplet mode” to “accumulation mode” in spring, summer, fall, winter were 2.6, 2.1, 2.0, 2.7 respectively. The ratios of spring and winter were higher due to hygroscopic growth of sulfate during the long-range transport which mainly from the north. This also indicated that more sulfate came from local sources in summer and fall. NH_4^+ was found in the accumulation mode, with 64%~82% of its mass present in fine particles. NH_4^+ and NO_3^- had the same variation of peaks with SO_4^{2-} in the different seasons, indicating that these three ions had the same cumulate process in fine particles.

Concentrations of potassium always had the high value in fall and mainly came from biomass (e.g., straws, leaves) combustion^[5]. Potassium from the combustion mainly presented in fine particles with aerodynamic diameters less than 1 μm . In the study, K^+ was found in the accumulation mode, with 55%~78% of its mass present as fine particles. Concentrations of K^+ reached the highest value in fall and it was $1.6 \mu\text{g m}^{-3}$ in fine particles which was 1.4 times higher than the annual average. And the peak presented between 0.65 to 1.1 μm , further indicating K^+ mainly came from biomass combustion in fall.

The ratios of NO_3^- resided in fine particles were higher in spring and winter, which were 55%, 57% respectively. Because fine particles were easily long-range transported, nitrate in fine particles maybe come from the north. The ratios of NO_3^- resided in coarse particles were higher in summer and fall, which were 61%, 57% respectively. NO_3^- had a peak between 3.3 and 5.8 μm in coarse particles. Ca^{2+} and Mg^{2+} had a peak between 3.3 and 5.8 μm too. Ammonium nitrate was easily decomposed under the higher temperature in summer and fall^[4]. NO_3^- mainly arose from secondary particles formed by NO_x . Nitrate is more easily dissolved in water than sulfate and is thus more easily absorbed to the surface of coarse particles, forming calcium nitrate and magnesium nitrate.

The ratios of Na^+ and Cl^- resided in fine particles were 40%~49% and 40%~52%. Na^+ and Cl^- in fine particles mainly came from coal burning, and Na^+ in coarse particles mainly came from wind-blown soil. Na^+ and Cl^- had similar size distributions, indicating they came from the same sources.

Ca and Mg mainly came from wind-blown soil, and the other important source of Ca was construction source^[5]. The dust from wind-blown soil and construction mainly was coarse

particles. In the study, 62%~68% Ca^{2+} and 55%~61% Mg^{2+} resided in coarse particles, indicating Ca^{2+} and Mg^{2+} mainly came from wind-blown soil and construction.

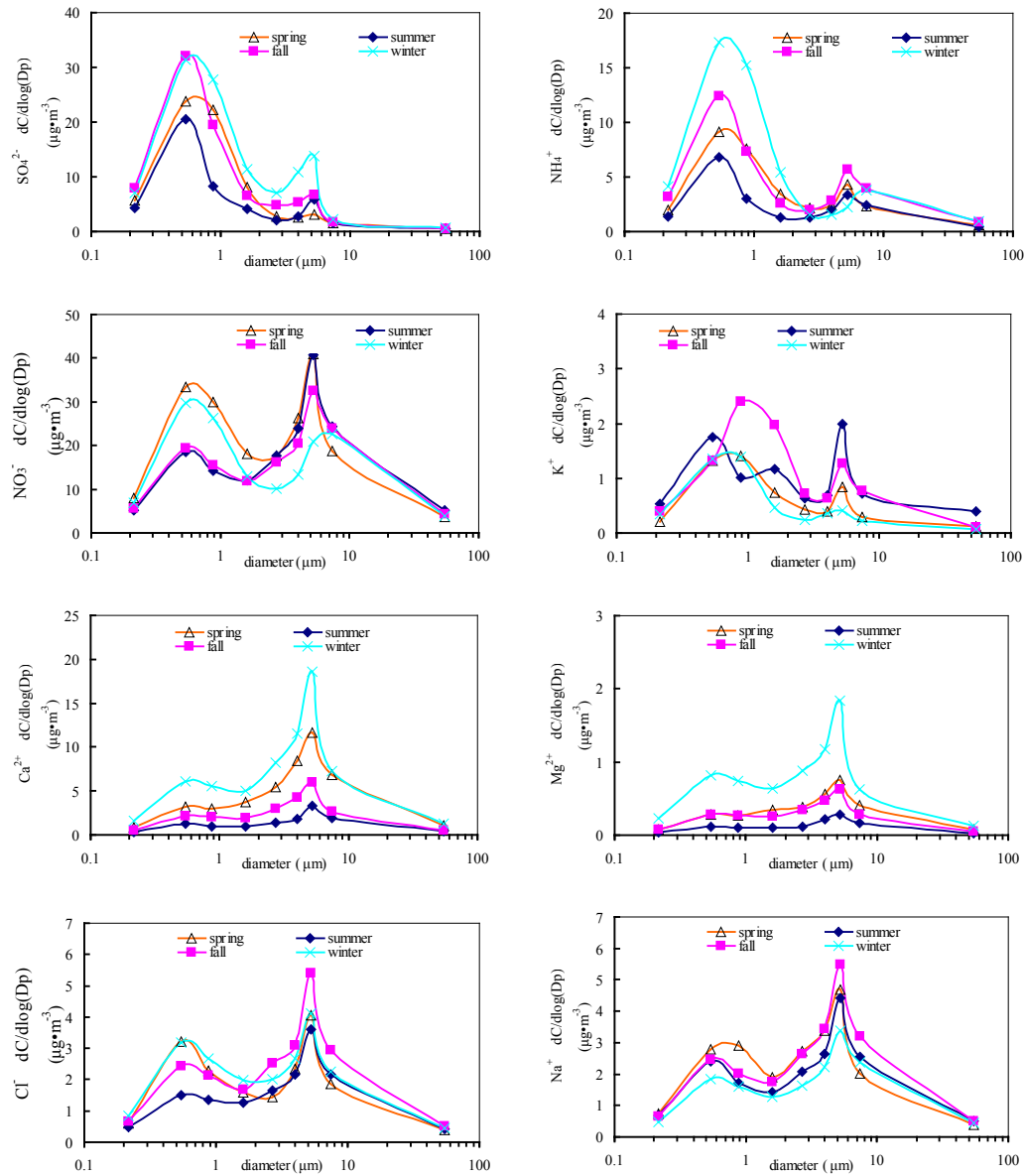


Fig.1 Size distributions of water-soluble ions in atmospheric aerosol in different seasons at Lin'an regional background station

CONCLUSION

The measured distributions at Lin'an regional background station are believed to result from a combination of processes including regional anthropogenic and natural sources, and long-range transport. The size distributions of the water soluble ions studied were influenced by at least three

processes governing their concentrations in fine and coarse particles: (i) primary emissions of ultrafine particles from combustion and industrial processes; (ii) advection of air masses containing aged intermediate size aerosols; (iii) large particles arising mainly from re-suspension.

ACKNOWLEDGMENTS

This work was supported by the National Natural Science Foundation of China under Grant No. 40805054; the Zhejiang Provincial Natural Science Foundation under Grant No.Y5100107.

REFERENCES

- [1] Christoph, H.; Robert, G.; Urs, B.; Martin, G.; Christian, M.; Heinze, V. *Atmospheric Environment*, 2005, 39, 637-651.
- [2] Englert, N. *Toxicology Letters*, 2004, 149, 235-242.
- [3] Seinfeld, J. H.; Pandis, S. N. John Wiley & Sons: New York, 1998.
- [4] Yao, X. H.; Lau, A. P. S.; Fang, M.; Chan, C. K.; Hu, M. *Atmospheric Environment*, 2003, 37, 2991-3000.
- [5] Song, Y.; Tang, X. Y.; Fang, C.; Zhang, Y. H.; Hu, M.; Ceng, L. M. *Environmental Science(in Chinese)*, 2002, 23, 11-16.

Characteristics of polybrominated diphenyl ether in the air of southern Taiwan

Long-Full Lin¹, Shin-Hsiung Lin¹, and Guo-Ping Chang-Chien²

1 Department of Environmental Engineering, Kun Shan University, 949 Da Wan Rd., Tainan, Taiwan 710

2 Department of Chemical and Materials Engineering, Cheng Shiu University, 840 Chengching Rd., Kaohsiung, Taiwan 833

Principal Contact: Long-Full Lin, Associate professor, Department of Environmental Engineering, Kun Shan University, 949 Da Wan Rd., Tainan, Taiwan 710.

Tel: +886-6-2050524 Fax: +886-6-2050540 Email: longfull@mail.ksu.edu.tw

Abstract

Polybrominated diphenyl ethers (PBDEs) are well known hazardous air pollutants (HAPs) and are widely used brominated flame retardants (BFRs) because of their inhibitory effects on the ignition of combustible organic materials. Owing to their adverse health effects and increasing level in the air, their distribution in the air is of great concern to the publics. In this study, three sampling sites situated in industrialized area, metropolitan area as well as rural area which located in southern Taiwan were taken and analyzed for PBDEs. Four samples were taken for each sampling sites, and each sample was taken for a consecutive seven days with a mean sampling size of 4072, 4261, and 3567 Nm³ at the industrialized, metropolitan, and rural sites, respectively. For the industrialized area, the concentrations of PBDEs were in the range of 53.5 to 107 pg/Nm³, with an average of 67.3 pg/Nm³. For the metropolitan area, the concentrations of PBDEs were in the range of 83.5 to 115 pg/Nm³, with an average of 102 pg/Nm³. As for the rural area, the concentrations of PBDEs were in the range of 45.5 to 98.6 pg/Nm³, with an average of 71.7 pg/Nm³. The highest level was found in the metropolitan area. In addition, the particle phase concentrations accounted for 64%, 68% and 55% in the industrialized, metropolitan, and rural area, respectively. The congener profiles of the various bromine substituted congeners showed that BDE #209 (10Br) is the dominant congener. For the industrialized area, BDE #209 account for 63.4% to 82.4% with an average of 73.6%. For the metropolitan area, BDE #209 account for 68.4% to 84.7%, with an average of 76.4%. As for the rural area, BDE #209 account for 64.4% to 81.0%, with an average of 74.2%. The results of this study provide important information for the promotion of air quality.

Keywords: Polybrominated diphenyl ethers, Hazardous air pollutants, Congener profiles

The Physicochemical Characteristics and Fractal Analysis of PM_{2.5} in the Atmosphere around the Campus of Beijing Forestry University

Yili Wang and Jiong Li and Yuan Chen

College of Environmental Science and Engineering, Beijing Forestry University, 25 Qinghua East Road, Haidian District, Beijing 100083, China

Principal Contact: Yili Wang, Professor, College of Environmental Science and Engineering, , Beijing Forestry University, 25 Qinghua East Road, Haidian District, Beijing 100083, China.
Tel: 86-10-62336528 Fax: 86-10-62336596 E-mail.wangyilimail@126.com

Abstract

The morphology and elemental composition of PM_{2.5} in the air around the campus of Beijing Forestry University (BJFU) was investigated. The results showed that soot aggregates, coal fly ash, mineral particles were often observed in the collected particulates, while few biological particles were recognized.

The particle size was in the range of 0.20μm-0.50μm for soot aggregates, 0.20-0.30μm for coal fly ash, 0.25-0.40μm for mineral particles, respectively. Fractal analysis revealed that soot aggregates were fractal, and coal fly ash was not fractal. And soot aggregates collected in spring and winter were looser than those collected in summer and autumn, but the soot aggregates with least irregular boundary were collected in summer, which could be ascribed to reaction and ageing process during soot aggregates suspending in air. The 1-D fractal dimensions of most mineral particles were close to one, which indicated that they had close regular boundary. Comparison with soot aggregates, much higher 2-D fractal dimensions displayed their more compact structure.

The results of EDX detection for these PM_{2.5} particles showed that they were mainly constituted of Si, Al and Ca elements. Cluster analysis of element composition indicated that these mineral particles could be divided into six groups and some typical minerals were recognized, such as: sulphate minerals, calcite, montmorillonite, calcium silicate, silica-alumina salt and little-contained hematite, magnesite and quartz. Then with triangle plots analysis, the most abundant species of silica-alumina salt were identified as: clay minerals, mixture of calcite and dolomite minerals, anorthite and gypsum, and little of quartz. Moreover, many kinds of heavy metals were detected, such as Cr, Au, Ni, Zn, Ti, Cu Cr. In addition, the detected elements of F and P could be the exhaust of burned coal and oil or other industries, then be adsorbed or coagulated on the surface of PM_{2.5} particles.

Keywords: PM_{2.5}, morphology, elements composition, particulate size distribution, fractal dimension

Aerosol Composition at Gosan, Korea: Measurement data of TSP, PM10, and PM2.5 between March 1992 and June 2008

Na Kyung Kim¹, Yong Pyo Kim¹ and Chang-Hee Kang²

¹Dept. of Environmental Science and Engineering, Ewha Womans University, Seoul, 120-750, Korea

²Dept. of Chemistry, Jeju National University, Jeju, 690-756, Korea

ABSTRACT

Northeast Asia is characterized by high energy consumption. China, Japan, and South Korea have consumed 19.5%, 4.2%, and 2.1% of the world total primary energy, respectively in 2009 (BP, 2010). Consequently, there are resultant huge emissions of anthropogenic air pollutants.

Gosan, Jeju Island is located at about 100 km south of Korean Peninsula, about 500 km west of China (Jiangsu province), and about 200 km east of Japanese Islands (Kyushu), and it is one of the cleanest areas in Korea with low emissions of air pollutants. Therefore, it is an excellent location to study the transport and transformation of ambient trace species in Northeast Asia.

In this study, the aerosol composition data measured at Gosan, Jeju, Korea between March 1992 and June 2008 were analyzed to find out the long term concentration variations. Ion composition data of different particle sizes - TSP, PM10, and PM2.5 were compared. The elements data in TSP and PM10, and EC and OC data in PM2.5 were also analyzed.

KEYWORDS

TSP, PM10, PM2.5, ion concentrations, EC, OC

Introduction

Northeast Asia is characterized by high energy consumption. Consequently, there are resultant huge emissions of anthropogenic air pollutants. Based on the satellite observation data of NO_x which is emitted by all combustion processes, significant concentration increase of about 50% over the industrial areas of China was investigated (Richter et al., 2005). The emission of SO₂, another major pollutant emitted by fossil fuel combustion, decreased from 23.7 to 19.3 Mt between 1995 and 2002 in China, but started to increase again since 2003 and reached to 25.9 Mt in 2006 (State Environmental Protection Administration, 2008). Also, organic aerosols are

emitted into the atmosphere through incomplete combustion of biomass and fossil fuel. These emission changes affect directly on the concentrations of ambient aerosols.

In this study, size segregated measurement data between 1992 and 2008 at Gosan, Jeju, Korea were analyzed. Gosan is one of the cleanest areas in Korea and an excellent location to study the ambient aerosols in Northeast Asia (Kim et al., 2009). Long-term trend of aerosol composition changes related to the long term emission changes were analyzed.

Experimental Methods

The measurement site is located on the western tip of Jeju ($126^{\circ} 10' E$, $33^{\circ} 17' N$). A trailer containing the TSP, PM10 and PM2.5 sampler was situated about 10 m inside of cliff, which is about 70 m above sea level.

TSP were collected by a high volume tape sampler, which is an automatic sampling system with roll type PTFE filters. The PM10 sampler consists of a Teflon-coated aluminum cyclone with a cut size $10 \mu m$ at a flow rate of 16.71 LPM, a Teflon filter holder for 47 mm filters, a critical orifice and a pump. The PM2.5 sampler consists of a Teflon-coated aluminum cyclone with a cut size $2.5 \mu m$ at a flow rate of 16.71 LPM, a Teflon filter holder for 47 mm filters, a critical orifice and a pump.

Eight ions in TSP, PM10, and PM2.5 were analyzed. NH_4^+ ion was analyzed by the indophenol method with a UV visible spectrophotometer and Na^+ , K^+ , Ca^{2+} , and Mg^{2+} by atomic absorption spectroscopy. Anions, SO_4^{2-} , NO_3^- , and Cl^- were analyzed by ion chromatography.

Inductively coupled plasma (ICP) spectrophotometer with a polychromator (PMT) detector was used for elemental analysis. Twelve elements in TSP (Cr, Ca, Zn, Cd, Ni, Fe, Al, Cu, Ti, Mn, Pb, and V) were analyzed until 1997, and twenty elements in TSP (Al, Fe, Ca, Mg, Na, K, S, Ti, Mn, Ba, Sr, Zn, V, Cr, Pb, Cu, Ni, Co, Mo, and Cd) were analyzed until 2008. Twenty elements in PM10 (Al, Fe, Ca, Mg, Na, K, S, Ti, Mn, Ba, Sr, Zn, V, Cr, Pb, Cu, Ni, Co, Mo, and Cd) were analyzed until 2006.

Organic aerosols (EC and OC) in PM2.5 were analyzed by three different methods. From 1994 to 2000, they were analyzed by Thermal Manganese dioxide Oxidation (TMO) method. From 2001 to 2004, they were analyzed by thermal conductivity detector, and from 2005, they were analyzed by Thermal optical transmittance (TOT) methods. The data between 2001 and 2004 are removed due to verification problem of the analytical method.

Results and Discussion

Among the ions, the concentration of nss-SO₄²⁻ was the highest, followed by NH₄⁺ and NO₃⁻. The concentrations of sea salt components (Na⁺ and Cl⁻) were high only in TSP because those sea salts are mainly in coarse particles. The concentrations of nss-K⁺, nss-Ca²⁺, nss-Mg²⁺ were low compared to other ions.

The concentrations of nss-SO₄²⁻ decreased continuously till 2003. The nss-SO₄²⁻ concentration in TSP decreased by 60.2 %, that in PM10 decreased by 19.6 %, and that in PM2.5 decreased by 21.2 %. However, after 2003, it started to rapidly increase and showed a peak concentration in 2006 and kept high concentration until 2008 in TSP and PM2.5. The concentration in PM10 also increased since 2003 and showed a peak concentration in 2005.

The concentrations of NO₃⁻ increased continuously at all size particles, and showed the peak concentration in 2006 in TSP and in 2004 in PM10 and PM2.5. The NO₃⁻ concentration in TSP increased by 317 %, that in PM10 increased by 178 %, and that in PM2.5 increased by 307 %. After that, the concentrations of NO₃⁻ slightly decreased at all size.

The concentrations of the elements with natural origin such as Al, Ca, Fe, K, Mg were high both in TSP and PM10. The concentrations of Zn, Mn, Pb, Ti were in the middle and the concentrations of V, Cr, Cu, Cd were very low. The concentrations variations of the elements with natural origin are highly correlated to the frequency of dust storm in this region.

The OC concentrations were 2~4 $\mu\text{g m}^{-3}$ and didn't show any obvious increasing or decreasing trend. The EC concentrations were below 0.5 $\mu\text{g m}^{-3}$ (0.09~0.42 $\mu\text{g m}^{-3}$) before 1999, but they showed continuous increasing trend after the year 2000.

The OC to EC ratio shows a decreasing trend due to steady increase of EC concentrations. OC to EC ratio were 20~30 before the year 1999, but after the year 2000, the ratio decreased to 3~7. The correlations between OC and EC were high throughout all the sampling periods except in spring 1999. Since the relationship between EC and OC concentrations was good, majority of the OC measured at Gosan are considered to be emitted and/or transported along with EC.

SUMMARY

In this study, size segregated measurement data between 1992 and 2008 at Gosan, Jeju, Korea were analyzed. The concentration variations of ion components and organic aerosols were well matched to the emission changes in this region.

The concentrations of nss-SO₄²⁻ showed decreasing trend until 2003, but it started to increase again. The concentrations of NO₃⁻ increased continuously at all size.

The concentrations of the elements with natural origin such as Al, Ca, Fe, K, Mg were high both in TSP and PM10, and the concentrations variations of these elements are highly correlated to the frequency of dust storm in this region.

The OC concentrations didn't show any obvious increasing or decreasing trend. The EC concentrations were below 0.5 μg m⁻³ before 1999, but they showed continuous increasing trend after the year 2000. The OC to EC ratio shows a decreasing trend due to steady increase of EC concentrations. The correlations between OC and EC were high throughout all the sampling periods except in spring 1999. Since the relationship between EC and OC concentrations was good, majority of the OC measured at Gosan are considered to be emitted and/or transported along with EC.

ACKNOWLEDGMENTS

This work was supported by the National Research Foundation of Korea(NRF) grant funded by the Korea government(MEST) (No. 2009-0093459) and the Korea Meteorological Administration Research and Development Program under Grant RACS_2010-3006.

REFERENCES

- [1] British Petroleum, Statistical Review of World Energy June 2010. London, UK.
- [2] Richter, A.; Burrows, J.; Nub, H.; Granier, C.; Niemeier, U., Nature. 2005, 437, 129–132.
- [3] State Environmental Protection Administration,
See http://english.mep.gov.cn/standards_reports/soe/SOE2006/200711/t20071106_112569.htm (accessed March 2011).
- [4] Kim, N.K.; Park, H.-J.; Kim, Y.P., Water, Air, & Soil Pollution, 2009, 204, 165-175.

Distribution Characteristics of Aromatic Acids in Fine Aerosol Particles in Beijing, China

Hong Li¹, Fahe Chai¹, Xinming Wang², Liqun Deng³, Runxiang Ni⁴, Xiaoxiu Lun³ and Yizhen Chen¹

1 Chinese Research Academy of Environmental Science, Beijing 100012, China

2 Guangzhou Institute of Geochemistry, Guangzhou 510640, China

3 Beijing Forestry University, Beijing 100083, China

4 China University of Mining and Technology, Beijing 100083, China

ABSTRACT

Aerosol particles were collected by using a versatile air pollutants sampler (URG-300K) in Beijing in the four seasons from July 2008 to June 2009. A gas chromatography-mass spectrometry method was developed which is able to characterize 20 aromatic acids in the fine aerosol particles. By the application of this method it was found that 19 aromatic acids were detected in the fine aerosol particles in Beijing. The results indicated that the aromatics had the similar distribution pattern in the four seasons, but the daily average values of the concentrations of each aromatic acid showed seasonal variations due to the combined influences of the source emission characteristics, the chemical transformation mechanism and the meteorological factors. In each season, 1, 4-Benzenedicarboxylic acid had the highest concentrations within the 7 groups of aromatic acids; 1, 2-Benzenedicarboxylic acid had close relationship with ozone and sulfate. Further investigation is needed to clarify whether the close relationship between 1, 2-Benzenedicarboxylic acid with ozone and sulfate is caused by new particle formation process or by the secondary formation process.

KEYWORDS

Fine aerosol particles, Aromatic acids, Distribution characteristics, Beijing

Introduction

Aromatic acids are comprised of the benzoic acid type and also similar compounds that have additional substituents on the aromatic ring system which include methyl, hydroxy, methoxy and/or carboxyl groups. Some of aromatic acids are products from photochemical degradation of aromatic hydrocarbons; some of aromatic acids play important roles in the process of atmospheric new particle formation^[1]. The objective of the current study was to investigate the distribution characteristics and the formation mechanism of aromatic acids in aerosols in Beijing.

Experimental Methods

Totally 131 fine aerosol particles(PM_{2.5}) samples were collected by using a versatile air pollutants sampler (URG-300K) in the four seasons in one year from July 2008 to June 2009 in the northeastern urban area of Beijing. A gas chromatography-mass spectrometry method was developed which is able to characterized 20 aromatic acids in the fine aerosol particles, the analytical procedure of the fine aerosol particles included three steps which are pretreatment, derivatization of and analysis by a Agilent 7890A/5975C type GC-MS.

Results and Discussion

Although 20 kinds of aromatic acids were set as the targeted organic compounds in this study^[2], 19 kinds of aromatic acids were detected in the fine aerosol particle samples collected in the four seasons in one year in Beijing since 1,2,4,5-Benzenetetracarboxylic acid was not detected in all the samples. The daily average values of the total mass concentration of the 19 kinds of aromatic acids were lower than those of inorganic acidic components and those of low molecular weight carboxylic acids detected in the samples. The daily average values of the total mass concentration of the 19 kinds of aromatic were 109.05 ng/m³, 44.52 ng/m³, 180.55 ng/m³ and 75.65ng/m³ in the summer, fall, winter and spring, respectively.

Generally speaking, the 19 kinds of aromatics had the similar distribution pattern in the four seasons (Figure 1).

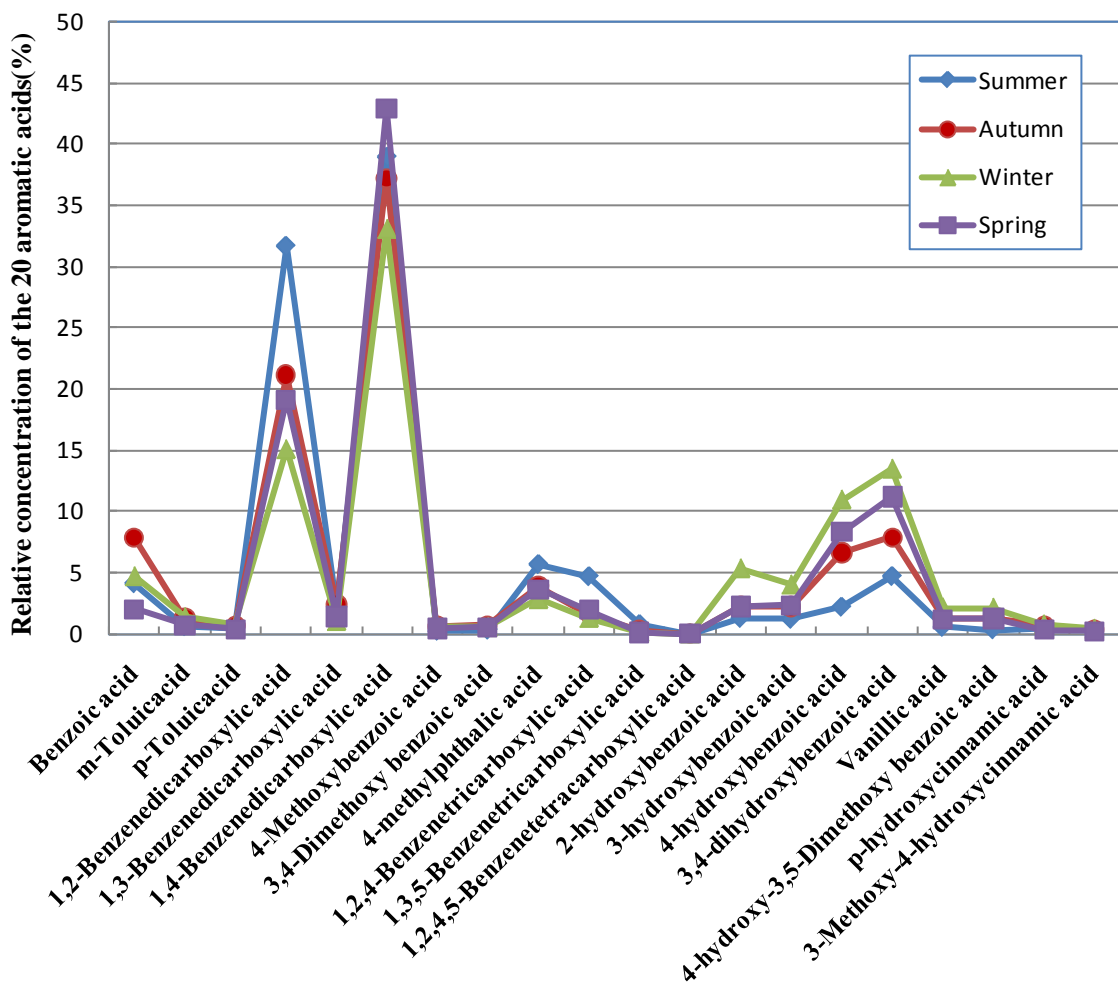


Figure 1 Seasonal distribution profiles of the 20 aromatic acids in PM_{2.5} in Beijing

In each season, 1,4-Benzenedicarboxylic acid had the highest daily average mass concentration followed by 1,2-Benzenedicarboxylic acid, 3,4 - dihydroxybenzoic acid, 4 - hydroxy benzoic acid, 2 - hydroxy benzoic acid, 3 - hydroxy benzoic acid, 4 - methyl - phthalic acid, 1,2,4-Benzenetricarboxylic acid and Benzoic acid. The sum of the mass concentrations of 1,4-Benzenedicarboxylic acid and 1,2-Benzenedicarboxylic acid accounted for 70.65%, 58.36%, 48.06% and 62.08% of the total mass concentrations of the 19 kinds of aromatic acids in summer, autumn, winter and spring, respectively.

The seasonal variation of the daily average values of the total mass concentrations of the 19 kinds of aromatic acids had the characteristics of Autumn < Spring < Summer < Winter. The daily average value of mass concentration of 1,4-Benzenedicarboxylic acid was highest in winter season (59.62 ng/m^3) followed by summer season (42.50 ng/m^3) and spring season (32.47 ng/m^3), it was lowest in autumn season (16.56 ng/m^3); while the daily average value of 1,2-

Benzene dicarboxylic acid was highest in summer (34.54 ng/m^3) followed by winter (27.16 ng/m^3) and spring (14.48 ng/m^3), it was lowest in autumn (9.41 ng/m^3).

The above analysis showed that the daily average values of the concentrations of each aromatic acid showed seasonal variations due to the combined influences of the source emission characteristics, the chemical transformation mechanism and the meteorological factors.

Correlation analysis showed that the total mass concentrations of the aromatic acids in the fine aerosol particles had obvious positive correlation relationship with those of inorganic acids and in the fine aerosol particles in summer, winter and spring, especially in the spring with the correlation coefficient R^2 being 0.81, while they had negative correlation relationship in autumn. The total mass concentrations of the aromatic acids in the fine aerosol particles also had positive correlation relationship with those of low molecular weight carboxylic acids in summer, winter and spring, and egative correlation relationship in autumn.

Correlation analysis also showed that 1, 2-Benzene dicarboxylic acid had close relationship with ozone and sulfate. Further investigation is needed to clarify whether the close relationship between 1, 2-Benzene dicarboxylic acid with ozone and sulfate is caused by new particle formation process or by the secondary formation process.

SUMMARY

This study investigated the seasonal distribution characteristics of aromatic acids in the fine aerosol particles in Beijing, and made the correlation analysis about the relationship between the aromatic acids and inorganic acids, low molecular weight carboxylic acids and ozone, respectively, in order to discuss the formation mechanism of aromatic acids in the fine aerosol particles in Beijing.

ACKNOWLEDGMENTS

This study is funded by the National Natural Science Foundation Committee project (20677054).

REFERENCES

- [1] Zhang R., Suh I., Zhao J., et al., Atmospheric new particle formation enhanced by organic acids. *Science*, 2004. 304: 1487-1490.
- [2] Y. Youkouchi and Y. Ambe. Characterization of polar organics in airborne particulate matter. *Atmospheric Environment*, 1986, 20(9), 1727-1734.

Characteristics of Black Carbon Deposition in a Forest

**Kyo Kitayama¹, Yuuki Kimura¹, Takeshi Mouri¹, Takumi Kashiwakura¹, Shogo Ota¹,
Sonoko Drothea Kimura¹, Masao Takayanagi¹, Hiroshi Okochi², Akira Takahashi³,
Sadamu Yamagata⁴, Naoto Murao⁴ and Hiroshi Hara¹**

1 Tokyo University of Agriculture and Technology, Tokyo 1838509, Japan

2 Waseda University, Tokyo 1698555, Japan

3 Central Research Institute of Electric Power Industry, Chiba 2701194, Japan

4 Hokkaido University, Sapporo 0608628, Japan

ABSTRACT

Black carbon flux in a forest in Japan was estimated by using the gradient method to explore the characteristics of deposition and the dynamics of aerosols. The concentration was measured at three different heights of an observational tower in the forest with a time resolution of ten minutes from February 1 to March 31, 2011. Two types of instruments were employed, absorption photometer and Aethalometer where the photometer had been calibrated against the Aethalometer. The black carbon flux was evaluated by the aerodynamic gradient method with vertical wind measured by an ultrasonic anemometer and the concentration difference between the heights of 25 and 30 m. The average flux over the entire period was $-0.011 \mu\text{g m}^{-2} \text{s}^{-1}$ whereas the averages over daytime (6 a.m. to 6 p.m.) and nighttime (6 p.m. to 6 a.m.) were 0.077 and $-0.11 \mu\text{g m}^{-2} \text{s}^{-1}$, respectively. Diurnal difference in the flux would be attributable to different wind-direction rather than concentration gradient variation. Nocturnal downward wind would be the major factor controlling the black carbon deposition in the forest.

KEYWORDS

black carbon, flux, forest, deposition

Introduction

Black carbon is one of the important factors for climate change and human health^[1]. The characteristics of the deposition will be useful for understanding atmospheric processes of this species, which encourages field measurements of aerosol deposition with gradient methods. For example, Matuda et al.^[2] applied this method to evaluate particulate sulfate flux and deposition velocity in Japan.

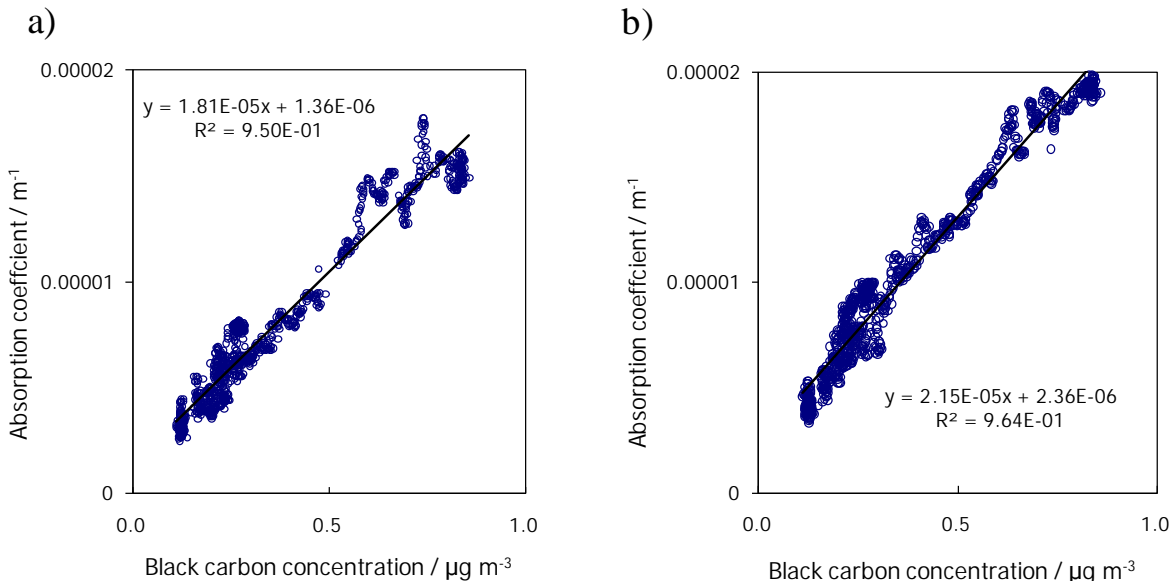
In this study, black carbon concentration was measured in a forest to explore the characteristics of deposition. The flux was evaluated with gradient method in terms of measuring the concentration at two heights and wind speed and direction over the forest crown.

Experimental Methods

The air concentration and meteorological parameters were determined from February 1 to March 31, 2011 in Tamakyuryo, an experimental forest in the suburbs of Tokyo, Japan. The observation was carried out on a 30 m observational tower in a forest with the crown height of 20 m. Black carbon concentration was monitored at three different heights of the tower with two types of instruments: two absorption photometers of tape-filter type^[3] at 25 m and 30 m above the ground and a Aethalometer^[4]. The absorption photometer of tape-filter type detects the absorption coefficient which was calculated by the same principle as Particle Soot/Absorption Photometer^[5]. Black carbon concentration was obtained by linear regression between the absorption coefficient and concentration. The calibration was conducted by simultaneous observations between the absorption photometer and Aethalometer in a laboratory (Fig. 1).

Meteorological parameters were continuously monitored with an ultrasonic anemometer at 30 m, and six multiparameter measuring instruments at 1, 6, 15, 20, 25 and 30 m of the tower.

Fig. 1 Linear regression between black carbon concentrations of Aethalometer and absorption coefficient of the absorption photometers for the height of 30 m (a) and 25 m (b)



Gradient method was applied to evaluate the black carbon flux with Eq. (1).

$$F = -u^* c^*, \quad (\text{Eq.1})$$

where u^* is friction velocity, and c^* is the eddy concentration defined as Eq. (2).

$$c^* = k(C(z_2) - C(z_1)) / [\ln((z_2 - d)/(z_1 - d)) - \psi_h((z_2 - d)/L) + \psi_h((z_1 - d)/L)], \quad (\text{Eq.2})$$

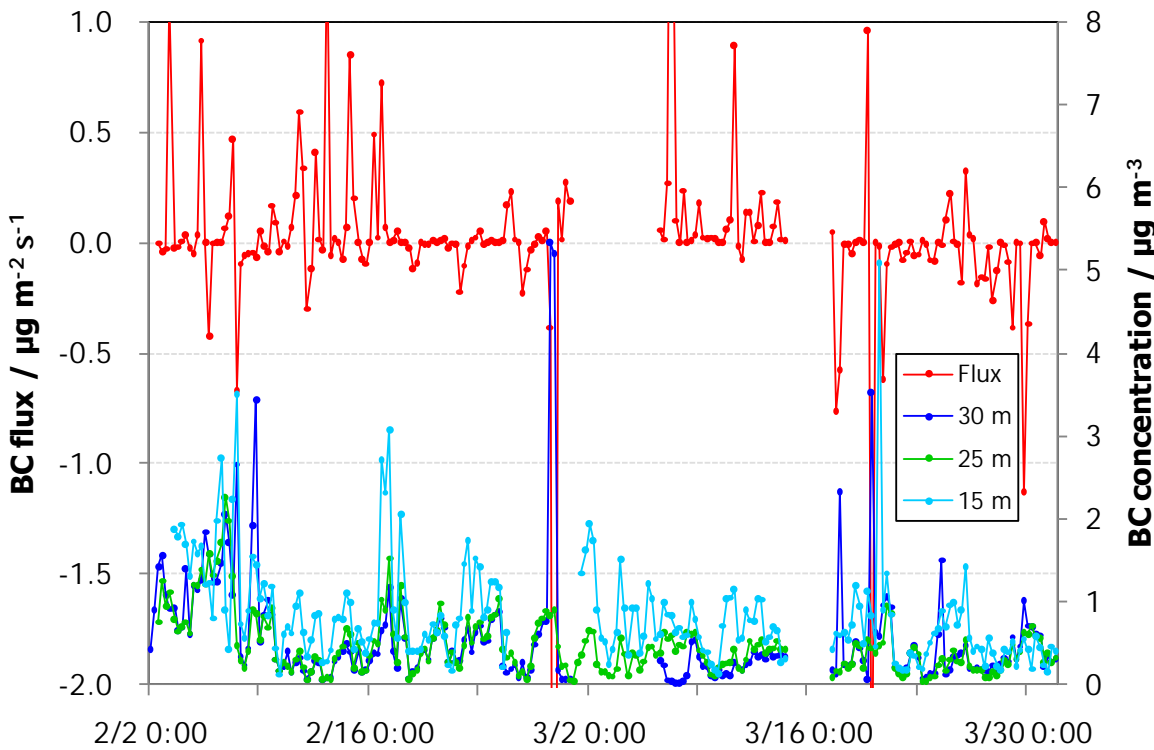
where $C(z_1)$, $C(z_2)$: concentrations for the heights of z_1 and z_2 , k : the von Karman constant, L : the Monin-Obukhov length, ψ_h : the integrated stability correction function for heat and, d : is the zero-plane displacement height.

In this study, z_1 and z_2 were 25 and 30 m, respectively, and d was calculated to be 11 m by the averaged horizontal wind profile.

Results and Discussion

Black carbon concentration and flux were averaged over every 6 hours from February 1 to March 31, 2011 (Fig. 2). The concentration generally ranged from 0 to $3 \mu\text{g m}^{-3}$. High concentrations were observed at the height of 15 m. The averages were 0.84, 0.55 and 0.47 for the height of 15, 25 and 30 m, respectively.

Fig. 2 Black carbon flux (red) and concentrations at the height of 30 m (blue), 25 m (green) and 15 m (sky blue) average every 6 hours.



The flux ranged from -1 to $1 \mu\text{g m}^{-2} \text{s}^{-1}$ with an average of $-0.011 \mu\text{g m}^{-2} \text{s}^{-1}$, which strongly supported the view of that black carbon deposited from the atmosphere to the ground surface during most of the observations in this forest. Figure 2 also demonstrated a discernible diurnal variation of the concentration and flux.

In order to explore this diurnal variation of the flux, daytime and nighttime averages were

calculated for two periods, from 6 a.m. to 6 p.m. of the day and from 6 p.m. to 6 a.m. of the following day (Fig. 3). The daytime flux was actually all positive with a mean of $0.077 \mu\text{g m}^{-2} \text{s}^{-1}$. The nighttime flux, however, fluctuated in two directions, upward and downward, corresponding to the positive and negative values, with an average, $-0.11 \mu\text{g m}^{-2} \text{s}^{-1}$, and further, some significantly large negative fluxes were noted with fairly small daytime flux for the corresponding periods of time (Fig. 3).

The largest upward flux, $1.25 \mu\text{g m}^{-2} \text{s}^{-1}$, took place during daytime on March 7, when the concentration difference between the heights of 25 and 30 m, $\Delta C = C(z_2) - C(z_1)$, marked $-0.47 \mu\text{g m}^{-3}$. It is interesting to note that the other peaks of upward flux in the daytime did not coincide with large concentration differences but with high friction velocity, u^* . The largest and the second largest downward fluxes in the nighttime were $-3.24 \mu\text{g m}^{-2} \text{s}^{-1}$, and $-1.17 \mu\text{g m}^{-2} \text{s}^{-1}$ on February 27 and March 19, respectively (Fig. 3). The corresponding concentration differences were 2.01 and $1.50 \mu\text{g m}^{-3}$ which happened to be the largest and second largest during the period. The large downward flux in the nighttime, therefore, would be due to large concentration differences.

The averaged concentration profiles for daytime and nighttime were similar to each other (Fig. 4). In more detail, however, although the concentration at 15 m was not significantly different, the concentrations at 25 m and 30 m were slightly higher in nighttime than in daytime. The averaged concentration difference was 0.08 and $0.10 \mu\text{g m}^{-3}$ for the daytime and nighttime, respectively. Downward fluxes during the nighttime would be partly attributed to the concentration difference. However, the difference of flux directions between the daytime and nighttime would not be due to the concentration difference.

Fig. 3 Black carbon flux in the daytime (red) and nighttime (blue).

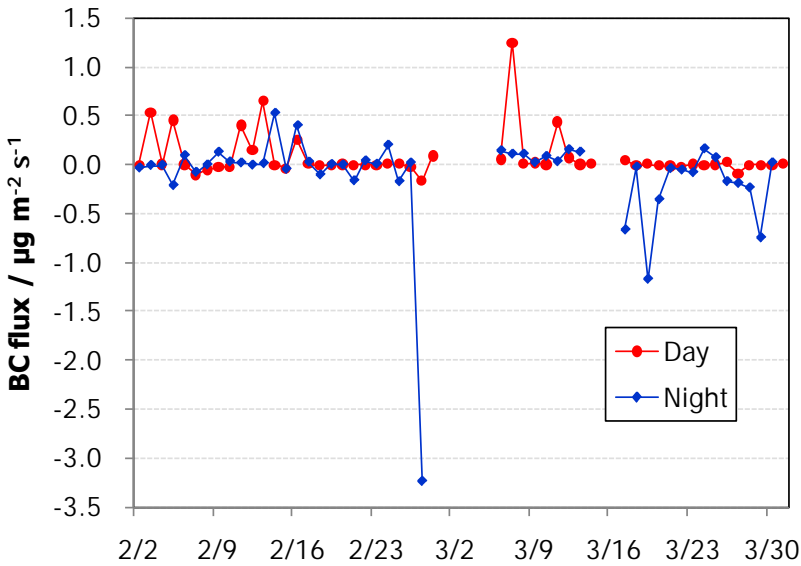
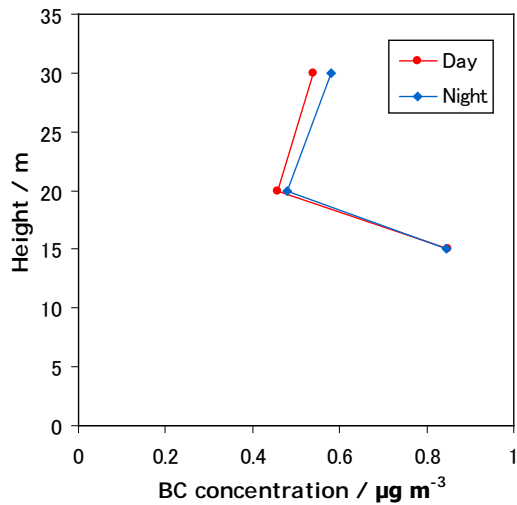


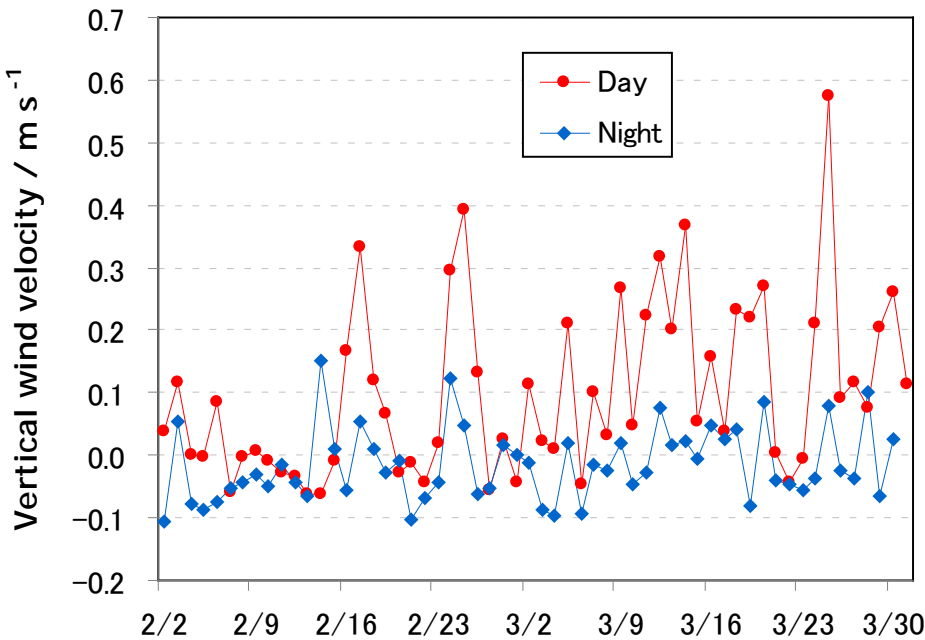
Fig. 4 Black carbon concentrations averaged in the daytime (red) and nighttime (blue).



In relationship with the different flux directions, or specifically with u^* , vertical wind velocity was averaged for the two periods of time, daytime and nighttime (Fig. 5). Generally, the nighttime wind velocity was slightly lower than the daytime. The direction of the averaged wind velocity for the two periods of time was apparently different: 0.10 m s^{-1} and -0.016 m s^{-1} for the daytime and nighttime, respectively. In most cases, the vertical winds were upward during the

daytime whereas downward during the nighttime. These wind differences coincided with the corresponding flux directions, and therefore strongly suggests that the direction of vertical wind is a major controlling factor to the flux direction.

Fig. 5 Vertical wind velocity in the daytime (red) and nighttime (blue).



CONCLUSION

Black carbon concentration and flux was measured in a forest to explore the characteristics of the deposition. Flux of black carbon showed a general diurnal variation that the flux is upward and downward during the day and the night, respectively. The average flux in daytime was $0.077 \mu\text{g m}^{-2} \text{s}^{-1}$ whereas that in nighttime was $-0.11 \mu\text{g m}^{-2} \text{s}^{-1}$. The average concentration in daytime and nighttime was not different, which suggested that flux direction was not due to the concentrations. Vertical wind directions in daytime and nighttime coincided with the flux directions.

REFERENCES

- [1] UNEP; WMO. *Integrated Assessment of Black Carbon and Tropospheric Ozone*, 2011.
- [2] Matuda, K; Fujimura, Y.; Hayashi, K.; Takahashi, A.; Nakaya, K. *Atmospheric Environment*, 2010, 44, 4582-4587.

- [3] Yamagata, S. *Operation Manual for Tape-Filter Type Absorption Photometer*, 2008.
- [4] Hansen, A. D. A. *Aethalometer book*, Magee Scientific Company, Berkeley, California, 2005.
- [5] Bond, T. C.; Anderson, T. L.; Campbell, D. *Aerosol Science and Technology*, 1999, 30, 582-600.
- [6] Erisman, J.W; Draaijers, G.P.J; *Atmospheric Deposition in Relation to Acidification and Eutrophication, Studies in Environmental Science*, vol. 63, 1995, ELSEVIER, pp. 55-75.

Proposed terminology for black carbon, as well as different forms of carbon fractions used in different fields

Yongming Han¹

Institute of Earth Environment Chinese Academy of Sciences

Principal Contact: Yongming Han, Dr., Institute of Earth Environment Chinese Academy of Sciences, 10 Fenghui South Road , Xi'an, Shaanxi, 710075, China.

Tel: 029-88326128 E-mail: yongming@ieecas.cn

Abstract

Within the diverse scientific disciplines interested in fire products (e.g., paleobotany, fire ecology, soils, sediments and atmospheric chemistry) the same term is often used for different materials, and different terms are sometimes used for the same materials. For example, black carbon is the common term that was used in both atmospheric and sediment fields. However, they have inherent discrepancies. In atmospheric science black carbon indicate the particles with light-absorbing characteristics, while in sediment and soil science it indicates its chemical refractivity characteristics. A standard terminology is needed and is proposed in this study applicable to all disciplines. The different materials are defined by optical, chemical, or microscopic characteristics that can be determined using generally available equipment. No new terms are introduced. It is recommended that some terms are comparable in both atmospheric and sediment science; while some terms can only be used specifically in a single field.

Sensitivity studies for Lagrangian inversion of black carbon sources in continental Asia based on measurements at Huangshan

Ignacio Pisso¹, Pan Xiaole² Takigawa Masayuki², Kanaya Yugo² and Prabir Patra²

1 RIGC-JAMSTEC, 3173-25, Showa-machi, Kanazawa-ku, Yokohama-city, Kanagawa, 236-0001, Japan

Principal Contact: Ignacio Pisso, PDR, JAMSTEC, 3173-25, Showa-machi, Kanazawa-ku, Yokohama-city, Kanagawa, 236-0001, Japan.

Tel: +81-45-778-5556 Email: ignacio@jamstec.go.jp

Abstract

Regional inversion models have been recently applied to constrain sources of gases, but the case of aerosols presents specific challenges due to the complexity and non linearity of the process involved during transport. A time series of BC and CO measurements collected at Huangshan (118 E, 31 N 1500 m) and the Lagrangian particle dispersion model FLEXPART are used to assess the sensitivity of BC source inversion to simplified representations of aging and coagulation. Large ensembles of Lagrangian trajectories are initialized at every measurement point, advected backwards driven by the latest ECMWF reanalysis (ERA Interim), and used to assess the interaction of the air with the boundary layer. This yields the influence function (a.k.a. footprint or source receptor relationship, a discretized representation of Green's function for transport) of each measurement. In practice, the actual influence is determined not only for the atmospheric transport as modeled, but also by microphysical processes governing aging and deposition. We focus firstly on the influence of the 3D field of soluble organic compounds (e.g. sulfate, as provided by a regional chemical model) on the evolution of the size distribution, leaving the assessment of wet deposition for future investigations. We study the sensitivity of the influence function to a simplified parametrization of sulfate interaction aiming to asses as well the errors introduced by uncertainty in the transport representation.

Keywords: Black Carbon, source inversion, Lagrangian method.

Variation in Wintertime Black Carbon Aerosols at an Urban Center in the Eastern India

S. K. Pani¹, S. Verma^{1,2}, and S. N. Bhanja¹

1 Department of Civil Engineering, Indian Institute of Technology Kharagpur, India, 721302

2 Centres for Oceans, Rivers, Atmosphere and Land Sciences, Indian Institute of Technology Kharagpur, India, 721302

Principal Contact: S. Verma, Department of Civil Engineering, Indian Institute of Technology Kharagpur, India, 721302.

Tel: +91 3222 281794 Email: shubha@iitkgp.ac.in, shubhaverm@gmail.com

Abstract

Black carbon (BC) are the particulate pollutants emitted primarily from the combustion of the fuel used in residential cooking, industrial, transportation sectors, and from open biomass burning. Black carbon is a primary absorbing aerosol of visible solar radiation in the atmosphere and acts as an important contributor to the atmospheric warming constituting about 55% of the CO₂ forcing on the global scale (Ramanathan and Carmichael, 2008). Modelling studies carried out to understand the origin of BC aerosols over the Indian ocean showed the surface mass concentration of BC to be mainly contributed due to emissions from biofuel use mostly originating from the Indo-Gangetic plain (IGP). However, these modelling studies underestimated the BC surface mass concentration by a factor of 2 to 4 over the Indian Ocean compared to the field measurements. It is therefore, required to have a better representation of BC aerosols in the model through investigation of its characteristics integrating measurements and modelling studies over the Indian subcontinent. There is a lack of studies on black carbon in the eastern India, where the AOD evaluated from satellite-based sensors show the presence of high AOD distribution, specifically during the winter season. In the present study, we present an analysis on surface mass concentration of BC, aerosol optical depth (AOD) due to BC, and its radiative effects at Kolkata (22.57°N, 88.42°E), an urban station, in east India over the IGP, during December 2009 in the winter season through ground based measurements of BC and application of modelling tools. Measurements of BC surface mass concentration exhibited diurnal variation showing higher values and a large variability from evening to early morning hours compared to the daytime. The mean daytime surface mass concentration of BC and the estimated mean AOD due to BC (AOD-BC) at 0.5 μm for the clear days were 12.3±6 μg m⁻³ and 0.22±0.02 respectively. The mean shortwave clear-sky aerosol radiative forcing due to BC at the top-of-atmosphere (TOA) was estimated as +6.5 Wm⁻², which is more than two times the global mean radiative forcing due to greenhouse gases. An analysis on the summary of comparison of BC measurements over different stations in India and evaluation of their probable sources will be presented.

Keywords: Black carbon, Aerosol optical depth, Radiative forcing

Characteristics of Light Absorbing Carbon in Jiangsu Province, China

Zijuan Lan¹, Xiaofeng Huang¹, Lingyan He¹ and Min Hu²

1 Key Laboratory for Urban Habitat Environmental Science and Technology, School of Environment and Energy, Peking University Shenzhen Graduate School, Shenzhen 518055, China

2 State Key Joint Laboratory of Environmental Simulation and Pollution Control, College of Environmental Sciences and Engineering, Peking University, Beijing 100871, China

ABSTRACT

A monitoring campaign was conducted in Hongzehu national wetland park in Jiangsu province in China, a seven-wavelength Aethalometer and a three-wavelength Photo Acoustic Soot Spectrometer (PASS-3) were used to collect the mass concentration and light absorption coefficient of light absorbing carbon from Mar. 22 to Apr. 15. The difference of the mass concentrations among seven wavelengths measured by Aethalometer is slighter than that among three wavelengths measured by PASS-3. The light absorbing carbon absorbed most at blue wavelength measured by PASS-3 but it's not shown clearly from the results measured by Aethalometer.

KEYWORDS

Aethalometer; Photo Acoustic Soot Spectrometer; Light Absorbing Carbon

BODY

Introduction

Carbonaceous materials have strong effect on the radiative balance^[1-3]. Black carbon (BC) can mainly absorb light in a broad visible light spectrum, while the organic carbon is found to have significant absorption at short wavelength, especially at near-ultraviolet^[4-5]. Main methods for BC measurement include filter based method (i.e. Aethalometer, PSAP, MAAP) and insu method (i.e. Photo Acoustic Soot Spectrometer), each instrument has its disadvantages and merits^[6, 7]. In our research, we used both Aethalometer with seven wavelengths and Photo Acoustic Soot Spectrometer with three wavelengths (PASS-3) to measure the concentration and the absorption coefficient simultaneously with the same PM_{2.5} μm size cutter. The purpose of this study is to compare the difference among the different wavelengths and two methods for ambient aerosol in China.

Experimental Methods

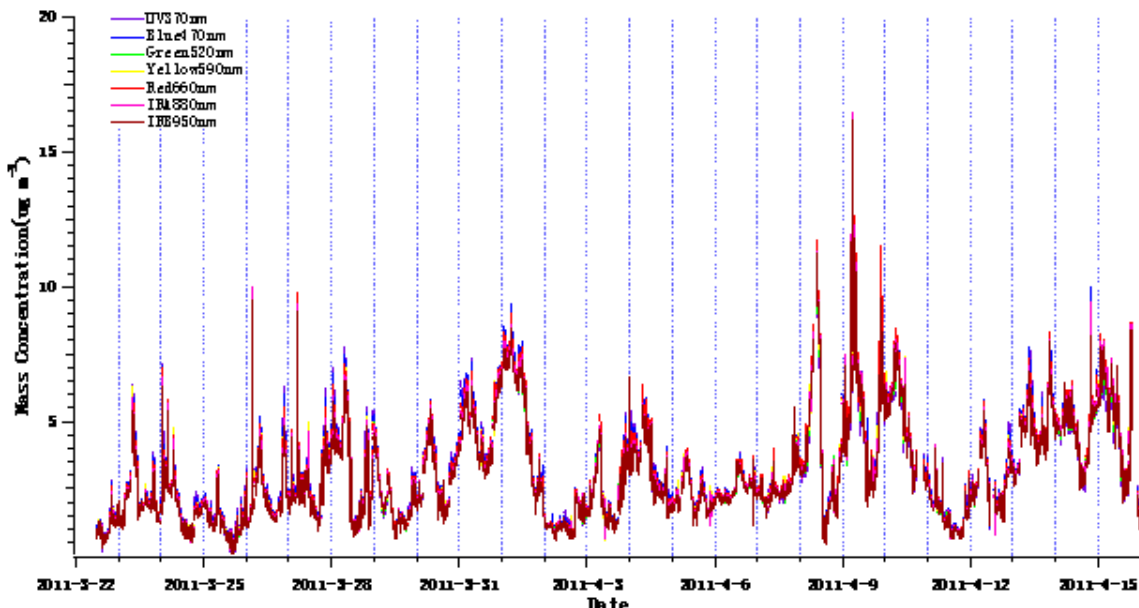
The sampling site located on a 3-floor boat (about 10 m) in Hongzehu national wetland park (118.2° E, 33.2° N) in Jiangsu province, with no significant local pollution sources nearby. It started from Mar. 22 to Apr. 15, a seven-wavelength Aethalometer (370 nm, 470 nm, 520 nm, 590 nm, 660 nm, 880 nm and 950 nm) and a three-wavelength Photo Acoustic Soot Spectrometer (405 nm, 532 nm and 781 nm) were used with the same $\text{PM}_{2.5}$ size cutter. The 5-min average data were collected during the sampling time. Before the experiment, the size cutters were cleaned, the flow rate, laser power, scattering calibration were done carefully.

Results and Discussion

The average mass concentration of the black carbon measured by the Aethalometer is 3.176, 3.236, 3.064, 3.137, 3.193, 3.070, $2.973 \mu\text{g}/\text{m}^3$ at 370 nm, 470 nm, 520 nm, 590 nm, 660 nm, 880 nm and 950 nm separately, and the average absorption coefficient is 47.51, 30.26, 19.71 Mm^{-1} at 405 nm, 532 nm and 781 nm separately.

The time series of mass concentration of the black carbon measured by the Aethalometer at seven wavelengths during the sampling period is shown as Figure 1. The difference among seven wavelengths is so slight that cannot be seen clearly.

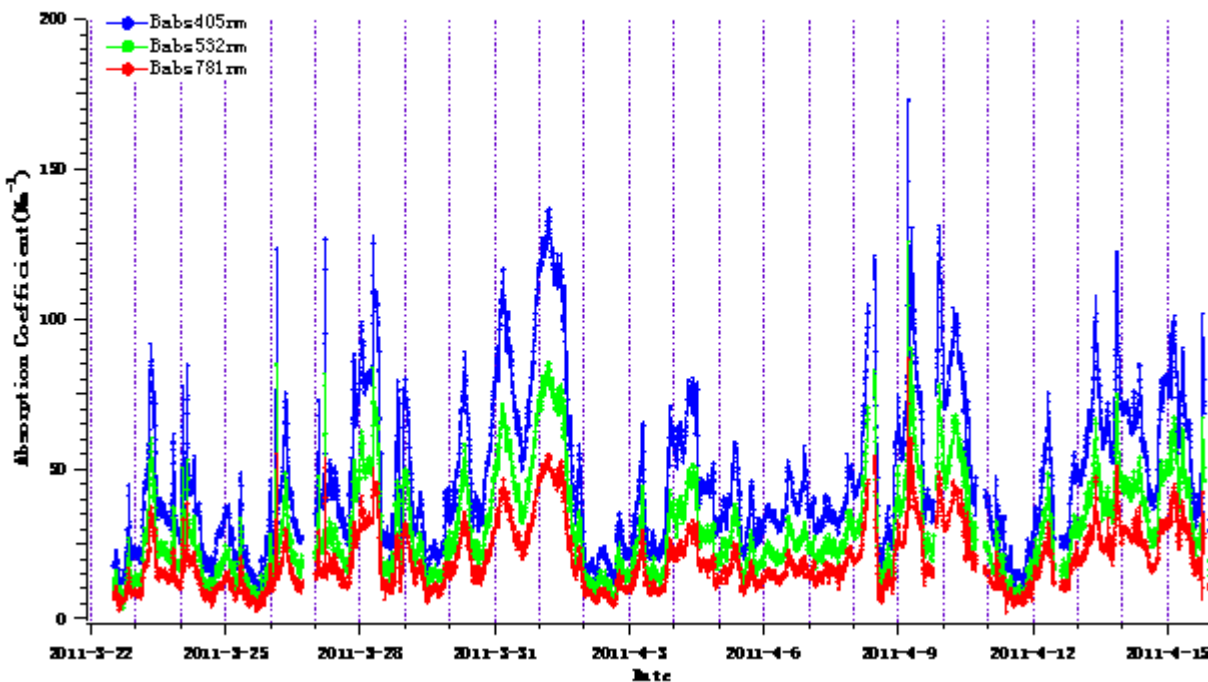
Figure 1. The time series of black carbon measured by Aethalometer at seven wavelengths



The time series of the absorption coefficient measured by PASS at three wavelengths is shown in Figure 2. It can be seen clearly that light absorption is different and it has the strongest absorption

at shortest wavelength, blue wavelength. But the variations are all the same, which indicates there is no significantly special absorption event occurring.

Figure 2. The time series of absorption coefficient measured by PASS at three wavelengths



Comparing to the results measured by PASS at different wavelengths separately, the absorption coefficient at three wavelengths is stable relatively (Figure 3) and R^2 is 0.989 between blue and green wavelength, 0.985 between green and red wavelength and 0.980 between blue and red wavelength, but slope is 1.555, 1.557 and 2.429 separately, shown as Figure 4. The results indicate that results measured by PASS have bigger difference among three wavelengths than Aethalometer, and the variation at three wavelengths is all the same nearly, but the absolute value is different and the difference is different between any two wavelengths. If the span of the wavelength is the bigger, the difference of the absorption value is the bigger. The absorption Angstrom exponent b among three wavelength is $b_{405, 532}=1.67$, $b_{405, 781}=1.33$ and $b_{532, 781}=1.09$, which indicates that the value of b is bigger than 1, especially at shorter wavelength. The stronger absorption at shorter wavelength may be induced by the mixing state of the black carbon or extra absorption by organic carbon, which needs further research.

Figure 3. The absorption coefficient ratio at different wavelength measured by PASS

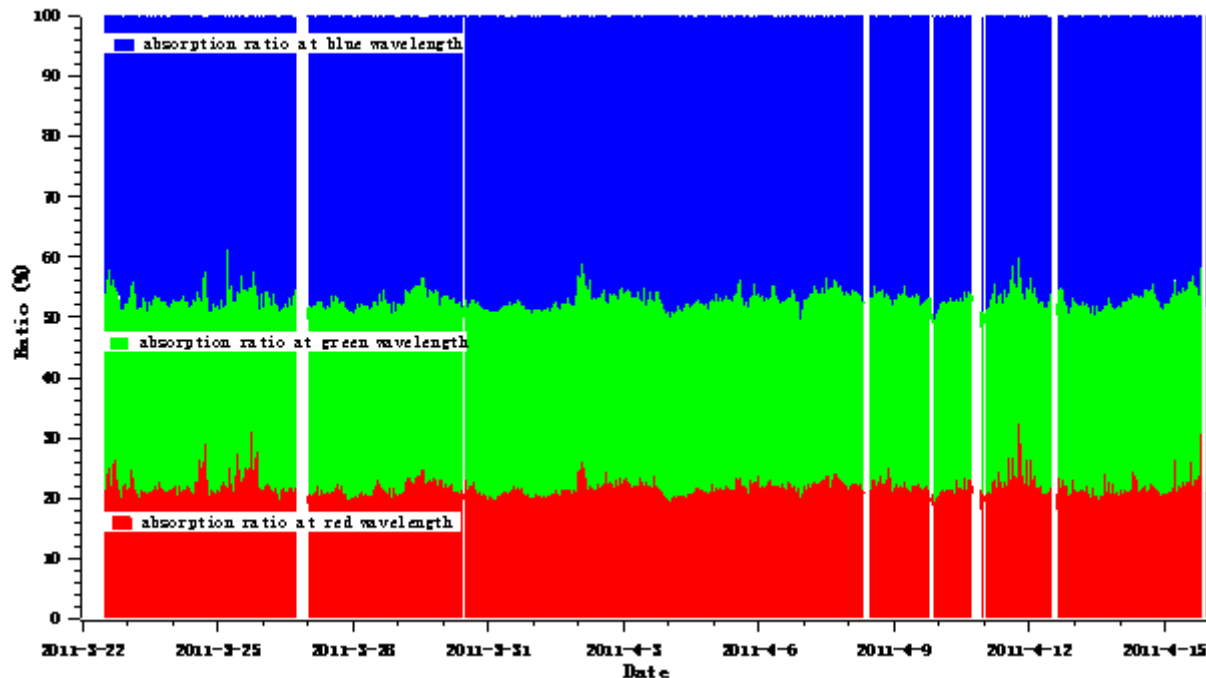
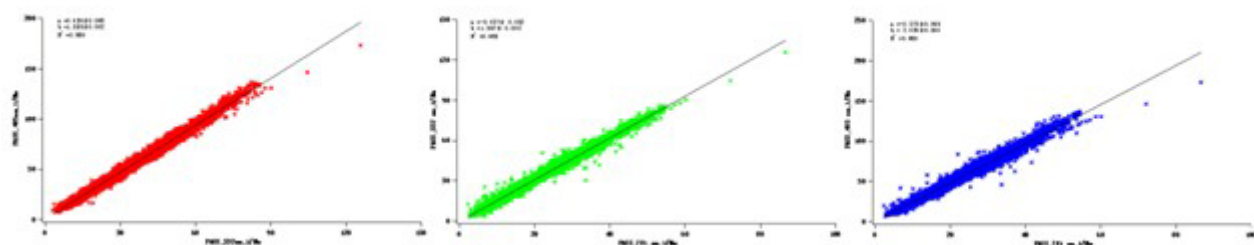


Figure 4. The regression line of results measured by PASS



SUMMARY OR CONCLUSION

The results of the monitoring research indicate that:

1. The difference of the results among seven wavelengths measured by Aethalometer is slight, and there is no clear characteristic at different wavelength;
2. The light absorption coefficient measured by PASS at three wavelength is different from each other, it absorbs most at blue wavelength and least at red wavelength;
3. The absorption ratio at three wavelengths is relatively stable which indicates that there is no special absorption event during the monitoring period.

REFERENCES

- [1] Anderson, T. L., Charlson, R. J., Schwartz, S. E., Knutti, R., Boucher, O., Rodhe, H., Heintzenberg, J.: Climate forcing by aerosols – a hazy picture, *Science*, 300, 1103–1104, 2003.
- [2] McComiskey, A., Schwartz, S. E., Schmid, B., Guan, H., Lewis, E. R., Ricchiazzi, P., and Ogren, J. A.: Direct aerosol forcing: Calculation from observables and sensitivities to inputs, *J. Geophys. Res.*, 113, D09202, doi: 10.1029/2007JD009170, 2008.
- [3] Intergovernmental Panel on Climate Change (IPCC): IPCC Fourth Assessment Report, Working Group I Report “The Physical Science Basis”, <http://www.ipcc.ch>, 2007.
- [4] Lewis, K. A., W. P. Arnott, et al. Strong spectral variation of biomass smoke light absorption and single scattering albedo observed with a novel dual-wavelength photoacoustic instrument. *Journal of Geophysical Research*, vol. 113, d16203, doi: 10.1029/2007jd009699, 2008.
- [5] Lack, D. A. and C. D. Cappa. "Impact of brown and clear carbon on light absorption enhancement, single scatter albedo and absorption wavelength dependence of black carbon." *Atmospheric Chemistry and Physics* **10**(9): 4207-4220, 2010.
- [6] Arnott, W. P., K. Hamasha, et al. "Towards aerosol light-absorption measurements with a 7-wavelength Aethalometer: Evaluation with a photoacoustic instrument and 3-wavelength nephelometer." *Aerosol Science and Technology* **39**(1): 17-29, 2005.
- [7] Arnott, W. P., H. Moosmuller, et al. "Photoacoustic spectrometer for measuring light absorption by aerosol: instrument description." *Atmospheric Environment* **33**(17): 2845-2852, 1999.

Observational Study of Black Carbon in Urumqi During Summer and Autumn of 2009

Yuting Zhong^{1,2}, Xinchun Liu^{1,2} and Qing He^{1,2}

1 Institute of Desert Meteorology, CMA, Urumqi 830002, China;

2 Key Laboratory of Tree-ring Physical and Chemical Research of China Meteorological Administration/ Xinjiang Laboratory of Tree Ring Ecology, *Urumqi 830002, China*

Principal Contact: Yuting Zhong, Research Associate, Institute of Desert Meteorology, CMA, No.46 Jianguo Road Urumqi Xinjiang 830002 China.

Tel: +086 991 2651450 Fax: 0086 991 2621387 E-mail: zhongyuting830@sina.cn

Abstract

This research presents the variational characteristic of Black Carbon aerosol (BC) concentration in Urumqi city within the period from June to November in 2009. The investigation mainly based on the local and international observational data. The results illustrate: 1) the average daily BC concentration in the summer and the autumn of 2009 was $3843 \pm 3095 \text{ ng} \cdot \text{m}^{-3}$ with the distribution range of $688 \sim 15181 \text{ ng} \cdot \text{m}^{-3}$. The maximum daily BC concentration was 22 times as much as the minimum. BC had a similar variational trend with API with a correlation coefficient 0.55. 2) The variationally daily BC concentration had obviously peak and trough periods. The peak value mainly occurred in the morning or at the night; the trough value frequently happened before dawn and in the afternoon. The variational characteristics of average weekly BC concentration were decreased from Monday to Thursday; reached the minimum on Thursday and then increased from Friday with a mild variational range. 3) The share of BC concentration, which were less than $2500 \text{ ng} \cdot \text{m}^{-3}$, were 64% and 36% in summer and autumn respectively. The lowest instantaneous BC concentration in summer was higher than the autumn's which means the pollution in autumn was heavier than summer. 4) The BC concentration in Urumqi city was lower than some Chinese cities as well as some international cities, however it was obviously higher than the rurally clean region. Comparing to Waliguan Global Atmospheric and South Pole, which are both background areas, the BC concentration in Urumqi city were $12.9 \sim 17.2$ times and 6.4×10^3 times higher respectively.

Key words: Black Carbon aerosol; variational characteristic; Urumqi city

A New Stand-alone Wide-range Aerosol Instrument for Automatic Environmental Monitoring

Xiaoai Guo, Markus Pesch, Hans Grimm and Lothar Keck

GRIMM Aerosol Technik GmbH & Co. KG, Dorfstrasse 9, D-83404 A inring, Germany

Principal Contact: Xiaoai Guo, Dr., GRIMM Aerosol Technik GmbH & Co. KG, Dorfstrasse 9, D-83404 A inring, Germany.

Tel: +49-8654 578-0 Fax: +49-8654 578-35 E-mail: guo@grimm-aerosol.com

Keywords: Aerosol size distribution, Wide-range aerosol Instrument, Environmental monitoring

Abstract

The health risk due to environmental particles is most probably not from the total particle mass but from specific toxic fractions of the atmospheric aerosols. Ultrafine particles act more toxically on public health due to their larger specific surface area and hence more probability to carry toxic chemical compounds. One useful parameter is the particle number size distribution, from which various parameters such as particle number, surface area and volume can be derived. Continuous long-term monitoring of complete particle size distribution and number concentrations in the atmosphere helps better understanding of aerosol transport, formation and mixing processes. Therefore, in this work a new stand-alone wide-range aerosol system was introduced for automatic environmental monitoring, seen in Figure 1a. This instrument is an ideal combination of optical and electrical mobility particle sizing, allowing determination of the particle size distribution of all aerosols ranging from 5nm to 32 μ m. In addition, this monitoring system has integrated an automatic sample air dehumidification, moisture extraction system and air-conditioning, and can be run unsupervised for extended time periods with low maintenance. Meteorological and gaseous sensors, GPS and wireless transfer are optionally available for many applications. As illustrated in Figure 1b, the monitoring results show a high time resolution (about 4 minutes) and size resolution (over 70 size channels) with a perfect overlap of both technologies.

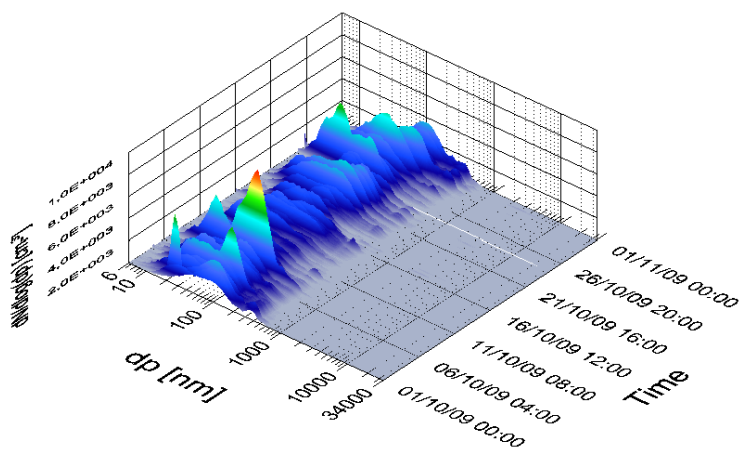


Figure 1: a) Stand-alone wide-range aerosol instrument; b) Continuous one-month monitoring of aerosol size distribution.

Design and Performance of a Three-wavelength LED-based Total Scatter and Backscatter Integrating Nephelometer

Marie Laborde¹, Thomas Müller², Grant Kassell³ and Alfred Wiedensohler²

1 Paul Scherrer Institut, Villigen, Switzerland, 5232

2 Leibniz-Institut für Troposphärenforschung, Permoserstraße 15, Leipzig, Germany, 04318

3 Ecotech Pty, 1492 Ferntree Gully Road, Knoxfield, VIC, 3180

ABSTRACT

Integrating nephelometers are instruments that directly measure a value close to the light scattering coefficient of airborne particles. Different models of nephelometers have been used for decades for monitoring and research applications. Now, a series of nephelometers (Ecotech models M9003, Aurora 1000 and Aurora 3000) with newly designed light sources based on light emitting diodes are available. This presentation reports on the design of the Aurora series of integrating nephelometers and a comparison of the Aurora 3000 to another commercial instrument (TSI model 3563) that uses an incandescent lamp.

Both instruments are three-wavelength, total and backscatter integrating nephelometers.

We present a characterization of the new light source design of the Aurora 3000 and provide parameterizations for its angular sensitivity functions. These parameterizations facilitate to correct for measurement artifacts using Mie-theory. Comparison measurements against the TSI 3563 with laboratory generated white particles and ambient air are shown and discussed. Both instruments agree well within the calibration uncertainties and detection limit for total scattering with differences less than 5%. Differences for backscattering are higher by up to 11%. Highest differences were found for the longest wavelengths, where the signal to noise ratio is lowest. Differences at the blue and green wavelengths are less than 4% and 3%, respectively, for both total and backscattering

KEYWORDS

Nephelometer, parameterization

Introduction

Integrating nephelometers offer a method of measuring the light scattering coefficient of airborne particles^[1]. Because no assumptions about particle composition, size or shape are necessary, the use of integrating nephelometers is widespread for ambient air monitoring as well as for laboratory studies. A scientific review of this type of instrument was given by Heintzenberg and Charlson^[2]. Integrating nephelometers can be calibrated with gases of well known scattering

coefficients, which facilitates quality assurance and maintenance. Radiative transfer calculations of the Earth's atmosphere require the scattering phase function or at least the asymmetry parameter of airborne particles. One method of estimating the asymmetry parameter is to convert the measured backscatter fraction, the ratio of hemispheric backscattering to total scattering, into their corresponding asymmetry parameters. Integrating nephelometry for measuring hemispheric backscattering is described in Charlson et al.^[3] and relationships between backscatter fraction and particle asymmetry parameter were investigated by Marshall et al.^[4] and Andrews et al.^[5]. Several studies on the performance of integrating nephelometers were performed^{[6][7]}. However, previous intercomparisons of instruments of different makes are limited to total scattering only. We present the first intercomparison of two integrating total/backscatter nephelometers. Additionally to the backscatter option both nephelometers are three wavelength instruments. One instrument type TSI 3563 (TSI Inc, St. Paul, MN, USA) was characterized in detail by Anderson et al.^[6]. In the recent years nephelometers (models M9003, Aurora 1000, and Aurora 3000) with light emitting diodes were developed by Ecotech Pty, Ltd, Knoxfield, Australia. We present a comparison of this three wavelength total and backscattering instrument against the TSI model 3563. We discuss the theory of integrating nephelometers and describe the Aurora 3000 instrument. Furthermore, we investigate the characteristic of the angular sensitivity of the new light source design and provide values to parameterize it. Finally, intercomparison experiments between the two integrating nephelometer types are presented and discussed using ammonium sulfate and ambient aerosols.

Experimental Methods

Angular illumination functions for TSI 3563 were measured in a previous study^[7] with a goniometer setup. For this present study, illumination functions for the Aurora 3000 were measured using the same experimental setup with small modifications. We briefly describe here the principle of the angular intensity measurements. Relative emitted intensity was measured with detection optics at the end of a rotating arm at angles $0^\circ < \theta < 180^\circ$ in steps of 5° . The detection optics consists of a lens which couples the light into an optical fibre and a photodiode attached to the other end of the fibre. The overall angular alignment was estimated to be less than one degree. Measured angular intensity functions for the Aurora 3000 are shown in Fig. 1.

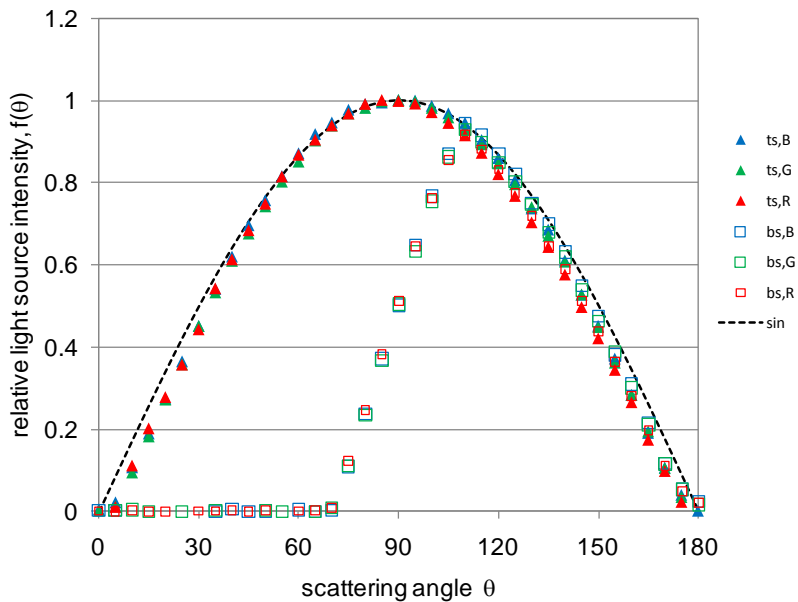


Figure 1: Measured angular intensity functions for nephelometer model Aurora3000

Wavelengths are indicated by B (450 nm), G (525 nm), and R (635 nm), respectively, and total scattering and backscattering are indicated by ts and bs, respectively. Total scattering illumination functions were normalized to unity at a scattering angle of 90° and the backward scattering illumination function was adjusted to match the value of the total scattering illumination function at 110°. Illumination functions for total scattering and for backscattering agree well among each other at large scattering angles ($\theta > 110^\circ$).

Illumination functions of TSI 3563 were measured independently and published^{[6][7]}. The illumination functions for total scattering agreed well for both studies. It also was found, that there is no difference between illumination functions for different nephelometer wavelengths. Besides the non-Lambertian illumination, the angular truncation contributes to the overall angular sensitivity function. Truncation angles for the TSI 3563 and were reported to be 7° and 170°^[6]. From technical drawings truncation angles for the Aurora 3000 were determined to be 10° and 171°. To our knowledge there is currently no method for experimental verification of truncation angles.

In addition to the measurement of the light source illumination function, a comparison of the instruments was performed using ambient sample and an atomized solution of ammonium sulfate. The atomized ammonium sulfate aerosol was fed into a 15 l mixing tank upstream of the Aurora 3000 and TSI 3563 nephelometers. Particle number size spectra were measured with an optical particle size spectrometer (UHSAS, Droplet Measurement Technologies, Boulder, CO, USA) in the size range 0.06 to 1.0 μm .

Results and Discussion

From the measurement of the illumination function, the parameterization of the Aurora 3000 could be developed for total and backscattering sensitivity functions. The parameterizations are modifications of sine-functions with

$$Z_{ts}(\theta) = \begin{cases} 0 & 0^\circ \leq \theta \leq \alpha_1 \\ \beta_1 \cdot \sin(\theta)^{\beta_2} & \alpha_1 < \theta < \alpha_2 \\ 0 & \alpha_2 \leq \theta \leq 180^\circ \end{cases} \quad (1)$$

And

$$Z_{bs}(\theta) = \begin{cases} 0 & 0^\circ \leq \theta \leq \alpha_1 \\ \max\left(0, \beta_1 \cdot \sin(\theta)^{\beta_2} \cdot \min\left(1, \frac{\theta - \gamma_1}{\gamma_2}\right)\right) & \alpha_1 < \theta < \alpha_2 \\ 0 & \alpha_2 \leq \theta \leq 180^\circ \end{cases} \quad (2)$$

where α_1 and α_2 account for the upper and lower truncation and β_2 accounts for the decreased relative illumination at small and large angles. β_1 is a normalization factor which cancels out in Equations 1 and 2. β_1 and β_2 are the same for total and backscattering. These parameters define the shape of the illumination curve for total scattering and that part of the backscatter illumination curve which is not blocked by the shutter. The shadowing of the backscatter shutter is accounted for by parameters γ_1 and γ_2 . Parameters are given in Table 1.

Table 1. Parameters for truncation and non-Lambertian illumination correction functions. Correction functions are given for TSI model 3563 and Aurora 3000 nephelometers.

Nephelometer	α_1	α_2	β_1	β_2	γ_1	γ_2
TSI 3563 ⁽¹⁾	7°	170°	1.005	1.175	73.86	32.84
Aurora 3000	10°	171°	1.01	1.190	70.25	39.99

For both ambient and laboratory comparisons of the instrument, scattering and backscattering coefficients measured by TSI 3563 were adjusted to wavelengths 450, 525 and 635nm using the Ångström exponents defined by

$$\alpha_{ts,\lambda_1,\lambda_2} = -\ln(\sigma_{ts,\lambda_1}/\sigma_{ts,\lambda_2})/\ln(\lambda_1/\lambda_2) \quad (3)$$

and

$$\alpha_{bs,\lambda_1,\lambda_2} = -\ln(\sigma_{bs,\lambda_1}/\sigma_{bs,\lambda_2})/\ln(\lambda_1/\lambda_2) \quad (4)$$

Ångström exponents $\alpha_{ts,\lambda_1,\lambda_2}$ and $\alpha_{bs,\lambda_1,\lambda_2}$ are calculated from scattering coefficients at wavelengths λ_1 and λ_2 .

In addition to the adjustment made for the difference in wavelength, the measurements were corrected for truncation and non lambertian error using the parameterization described in table 1 and using the angstrom exponent measured. Scatter-plots of total and backscattering from the laboratory comparison are shown in Fig. 2.

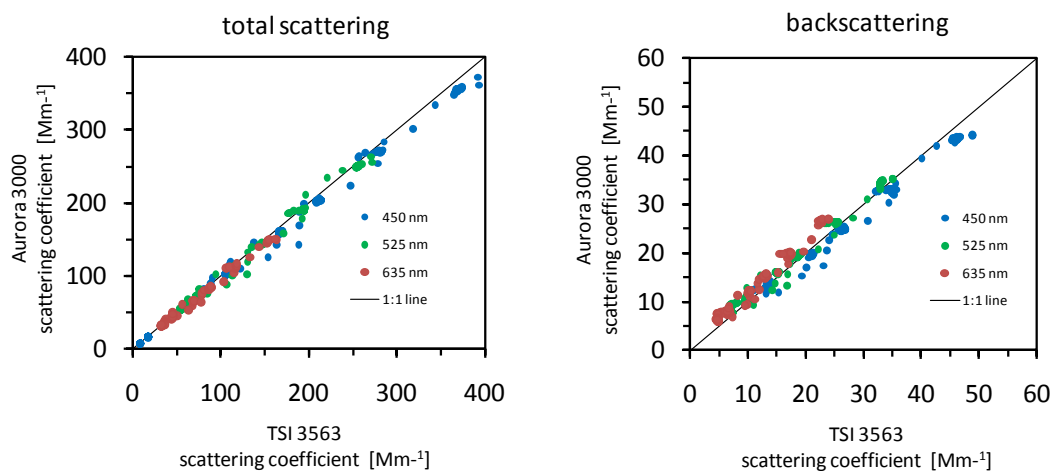


Figure 2. Correlation between total scattering coefficients measured with the TSI 3563 and Aurora 3000

Corrected total scattering coefficients measured by the Ecotech Aurora 3000 and TSI 3563 differ between 2% and 5%. Differences in backscattering are between 1% and 11%. Differences for total scattering are in agreement within the uncertainties of calibration. The highest deviation occurs for the red channels in backscattering mode and can not be explained by calibration uncertainties. Both nephelometers have the lowest signal to noise ratios for this channel. The intercepts of all linear regressions are small and close to the sum of detection limits of both nephelometers.

The comparison done with ambient air performed equally well. There is an excellent agreement between both instruments with a coefficient of determination (R^2) higher than 0.99 for both total scattering and backscattering. Deviations in the slope are small with about 1% and 3% for total scattering and backscattering, respectively. In all cases, the coefficients of determination are better than 0.99. Average slopes after applying angular sensitivity correction corrections are 0.98 and 1.00. Differences in the slopes of the blue and green channels are less than 2%. Differences

in the red wavelength compared to the other wavelengths are about 6%.

CONCLUSION

We presented the performance of the new Ecotech Aurora 3000 integrating nephelometer. The Aurora 3000 is a three-wavelength total and backscatter integrating nephelometer. The light source consists of three LEDs per wavelength. An opal glass diffuser provides a nearly Lambertian angular illumination function, which is cut by the cell geometry at truncation angles of 10° and 171°. An intercomparison of the Ecotech Aurora 3000 and the TSI 3563 three-wavelength total scatter and backscatter integrating nephelometers was performed in this investigation. To correct systematic uncertainties due to angular truncation and non-Lambertian illumination, truncation angles were obtained from technical drawings and angular illumination functions of the Ecotech Aurora 3000 were measured and compared to the TSI model 3563 nephelometer. Parameterizations of angular sensitivities for total scattering and backscattering were derived for both models of nephelometers along with correction factors as a function of Ångstrom exponent.

The Ecotech Aurora 3000 and TSI 3563 integrating nephelometers were compared using ammonium sulphate and ambient air. Scattering and backscattering coefficients at wavelengths 450 and 525 nm agree well within the calibration uncertainties. Calibration uncertainties are less than 3% and 5% for total and backscattering, respectively. Maximum differences in total scattering are 4% (450 nm), 2% (525 nm) and 5% (635 nm) for experiments with ambient air and laboratory generated white particles. For backscattering the differences are higher and amount 7% (450 nm), 3% (525 nm) and 11% (635 nm). Ångström exponents for a large range of volume median diameters were investigated during an ambient air experiment. Ångström exponents derived at the wavelength pair 450 and 525 nm agree well and differ by less than 5% for particle populations with volume median diameter less than 0.3 μm . Ratios of Ångström exponents for both nephelometer models show a slight dependence on volume median diameters. A sound explanation of this size effect is missing. However, values of scattering and backscattering coefficients of both nephelometers agree well.

REFERENCES

- [1] Beuttell, R. G. and Brewer, A. W.: Instruments for the measurement of the visual range. Journal of Scientific Instruments and of Physics in Industry 26:357-359, 1949.
- [2] Heintzenberg, J. and Charlson, R. J.: Design and applications of the integrating nephelometer: A review. J. Atmos. Oceanic Technol. 13:987-1000, 1996.
- [3] Charlson, R. J., Porch, W. M., Waggoner, A. P. and Ahlquist, N. C.: Background aerosol light-scattering characteristics - nephelometric observations at Mauna-Loa-observatory compared with results at other remote locations. Tellus 26:345-360, 1974.

- [4] Marshall, S. F., Covert, D. S. and Charlson, R. J.: Relationship between asymmetry parameter and hemispheric backscatter ratio - implications for climate forcing by aerosols. *Applied Optics* 34:6306-6311, 1995.
- [5] Andrews, E., Sheridan, P. J., Fiebig, M., McComiskey, A., Ogren, J. A., Arnott, P., Covert, D., Elleman, R., Gasparini, R., Collins, D., Jonsson, H., Schmid, B. and Wang, J.: Comparison of methods for deriving aerosol asymmetry parameter. *J. Geophys. Res.-Atmos.* 111, 2006.
- [6] Anderson, T. L., Covert, D. S., Marshall, S. F., Laucks, M. L., Charlson, R. J., Waggoner, A. P., Ogren, J. A., Caldow, R., Holm, R. L., Quant, F. R., Sem, G. J., Wiedensohler, A., Ahlquist, N. A. and Bates, T. S.: Performance characteristics of a high-sensitivity, three-wavelength, total scatter/backscatter nephelometer. *J. Atmos. Oceanic Technol.* 13:967-986, 1996.
- [7] Müller, T., Nowak, A., Wiedensohler, A., Sheridan, P., Laborde, M., Covert, D. S., Marinoni, A., Imre, K., Henzing, B., Roger, J. C., dos Santos, S. M., Wilhelm, R., Wang, Y. Q. and de Leeuw, G.: Angular Illumination and Truncation of Three Different Integrating Nephelometers: Implications for Empirical, Size-Based Corrections. *Aerosol Sci. Tech.* 43:581-586, 2009.

Two New Fast Response Water-based CPCs for Research Applications

Kathleen A. Erickson¹, Fred R. Quant¹, Sean Morell¹, Susanne Hering² and Robert Caldow¹

1 TSI Incorporated, 500 Cardigan Road, Shoreview, MN, 55126

2 Aerosol Dynamics, 935 Grayson Street, Berkeley, CA, 94710

Principal Contact: Kathleen A. Erickson, Particle Instrument Product Specialist, TSI Incorporated, 500 Cardigan Road, Shoreview, MN, 55126.

Tel: 651-765-3784 Fax: 651-490-3824 E-mail: kerickson@tsi.com

Abstract

Two new laminar-flow, water-based condensation particle counters (WCPCs) will be presented: models 3788 Nano Water-based Condensation Particle Counter (N-WCPC) featuring 2.5 nanometer minimum particle detection, and the 3787 General Purpose Water-based Condensation Particle Counter (GP-WCPC) featuring 5 nanometer minimum particle detection. These next generation instruments are based on the Hering design of a differentially diffusive, laminar-flow WCPC (Hering, 2005). The N-WCPC (3788) has the fastest response of any condensation particle counter to date with a time constant of 43 milliseconds and a rise time (10-90%) of <100 milliseconds. The N-WCPC also has the highest activation energy of any WCPC with a temperature differential of 63°C. Optimization of the wick geometry in both instruments leads to more uniform droplet growth as a function of concentration (Lewis and Hering, 2010). This more uniform droplet growth, paired with changes to the optical design and electronics signal detection enable the N-WCPC and GP-WCPC to measure concentrations up to 4×10^5 particles/cm³ and 2.5×10^5 particles/cm³ respective in single-particle count mode. A unique pulse height analyzer tracks the amplitude of the analog pulses to monitor the instrument health and supersaturation rate as a safeguard for measurement accuracy. The basic design of the instruments will be reviewed, and several key performance parameters will be detailed for each WCPC including particle detection efficiency for a variety of particle types, concentration linearity versus a traditional butanol-based CPC and response time.

Keywords: particle counter, condensation particle counter, CPC, WCPC.

Performance Evaluation of a Portable Nanoparticle Sizer under Various Relative Humidity Environments

Siqin He¹ and Da-Ren Chen^{1*}

¹Department of Energy, Environmental and Chemical Engineering, Washington University in St. Louis, Campus Box 1180, One Brookings Drive, St. Louis, MO 63130, USA

ABSTRACT

Nanoparticles (i.e., ultrafine particles, UFPs) are ubiquitous in the ambient. The primary sources for UFPs are traffic-related (i.e., particulate emission from automobile engines). More recent studies show that UFPs may be particularly relevant to pulmonary and cardiovascular diseases, cancer and mortality, as indicated by studies on both acute and long term effects. Epidemiological studies have also evidenced that increased asthma prevalence, including the number of patients diagnosed with the disease as well as asthma-related hospital visits is closely associated with UFP PM levels in the ambient air, the regional motor vehicle traffic density and residential proximity to freeways. As the increased concern of adverse health effect of nanoparticles, a cost-effective portable particle sizer based on the particle electrical mobility technique has been developed to meet the demand of personal monitoring or spatial distribution measurement of nanoparticles. The sizer consists of three key components: a miniature unipolar charger to electrically charge sampled particles, a miniaturized disk-type electrostatic aerosol precipitator to alter charged particle distributions and a TSI P-Trak to measure the concentration of particles exited from the precipitator. In this study we first evaluated the performance of the above sizer in the laboratory setting using the particles produced by various aerosol generation techniques. A humidity chamber had further been constructed for conditioning test aerosol stream at various relative humidity and temperature. The performance of the portable sizer was then evaluated by comparing the measured particle size distribution with that characterized by a Scanning Mobility Particle Sizer (TSI SMPS). The detail results of this study will be discussed in this presentation.

KEYWORDS

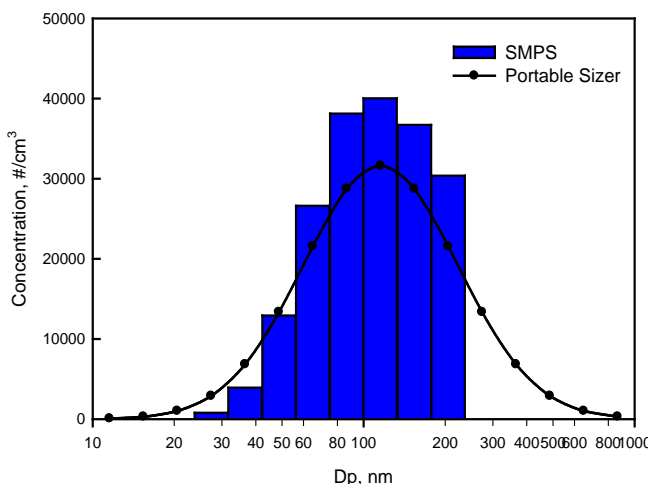
Portable nanoparticle sizer, Personal aerosol exposure, Relative humidity

Introduction

The rising concern with the health effects by personal nanometer-sized aerosol exposure in

working places and ambient environments has led to the urgent demand for miniature nanoparticle sizers. To meet the requirement of personal monitoring or spatial distribution measurement, we have developed a cost-effective portable particle sizer. The prototype sizer developed includes three key components: a miniature unipolar charger^[1] for particle charging a miniaturized disk-type electrostatic aerosol precipitator^[2] for particle distribution alteration and a TSI P-Trak as the particle concentration detector. The basic operational principle of the above sizer is based on the particle electrical mobility technique. The performance of the miniature unipolar charger used thus takes the essential role in the sizer operation. Previous study on the sizer performance has verified that it can provide the reliable size distribution measurement. Shown in Figure 1 is the comparison of particle size distributions measured by both portable sizer and TSI scanning mobility particle sizer. Reasonable agreement between both measurements has been achieved. However, the testing was done at the low relative humidity (RH) environment. The ultimate objective of our study is to investigate the performance of the portable sizer at various RH environments, often encountered in the ambient. To achieve the ultimate goal we first evaluate the performance of miniature particle charger under various RH environments.

Figure 1. Comparison of particle size distributions measured by both prototype Portable Sizer and SMPS.



Experimental Methods

The performance evaluation of a particle charger consists of the measurements of intrinsic charging efficiency, extrinsic charging efficiency and average charges. The experimental setup for the charger evaluation is given in Figure 2. The first part of the experimental setup shown in the figure is the generating system for monodisperse neutral particles. Polydisperse particles were generated by the evaporation-and-condensation method with a high temperature tube furnace for covering the particles with sizes from 20 to 80 nm, and by a custom-made

Collision atomizer for particles with the sizes up to 500 nm. Monodisperse test particles were then selected from generated polydisperse particles by a differential mobility classifier (DMC). A particle neutralizer was used at the downstream of the DMC to establish the stationary charge distribution on classified particles. The charged fraction of particles after the neutralizer was then removed by an electrostatic precipitator, thus resulting in monodisperse neutral particles.

At the downstream of monodisperse particle generation system, a humidity chamber was fused to condition the RH level of test aerosols. For the measurement of intrinsic and extrinsic charging efficiencies, the particle concentrations at the upstream and downstream of the charger were measured by a TSI UCPG (Model 3025). The intrinsic charging efficiency η_{in} and extrinsic charging efficiency η_{ex} could then be calculated by the equations shown below^[3].

$$\eta_{in} = 1 - \frac{N_1}{N_2} \quad (\text{Eq.1})$$

$$\eta_{ex} = \frac{N_3 - N_1 / P_{cpr}}{N_4} \quad (\text{Eq.2})$$

Figure 2. Generation system for monodisperse neutral particles

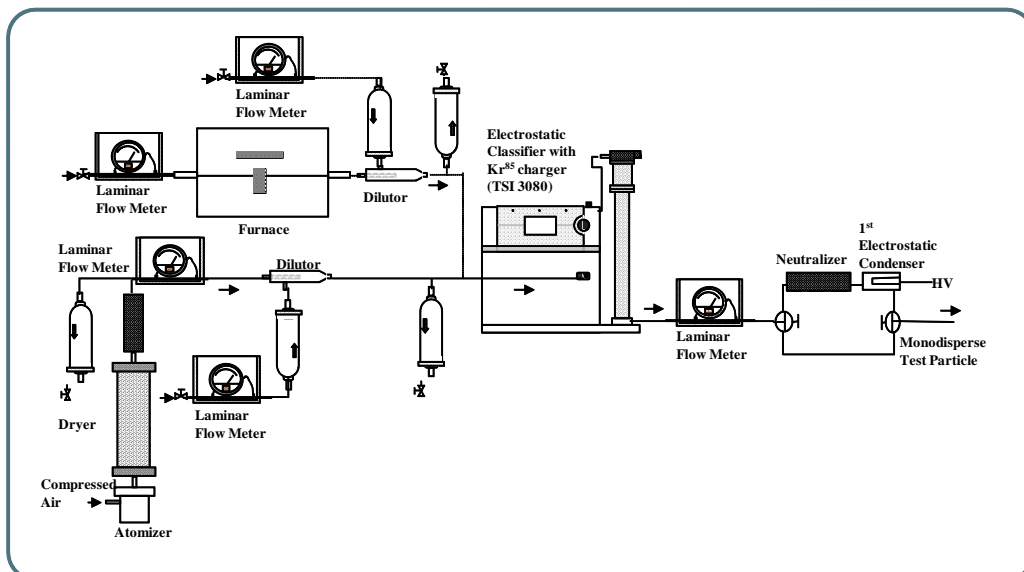
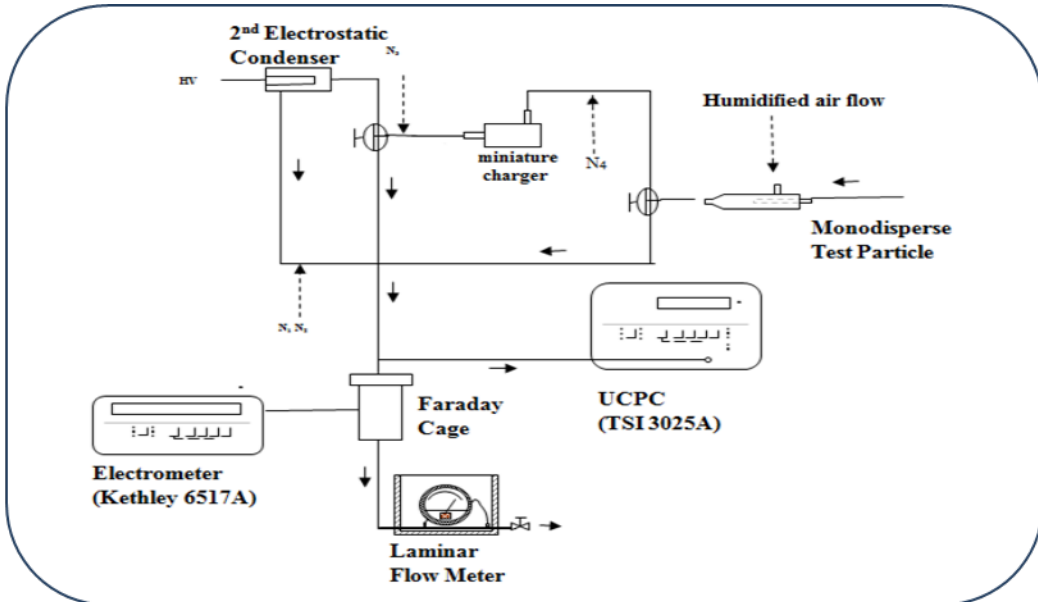


Figure 3. Evaluation measurement system for the miniature charger



Average charges for charged aerosols were measured by splitting the particle stream, and simultaneously measuring the particle number concentration by a UCPC and the charges on particles by the faraday cage and a high sensitive electrometer. In this part of measurement UCPC was operated at the 1.5 lpm flow rate, and the faraday cage at 3.0 lpm. The calculation equation of average charges n is given in Eq. 3.

$$n = \frac{I}{V \cdot C \cdot e} \quad (\text{Eq.3})$$

where, I is the current measured by the aerosol electrometer; V the volume of air passing through the faraday cage during the sampling time; C the concentration reading by UCPC and e the elementary charge as $1.6 \cdot 10^{-19}$ C.

Results and Discussion

Shown in Figures 4 and 5 are both charging efficiencies and average charges for the cases with the relative humidity of 90%, and 10%.

Figure 4a. Intrinsic charging efficiency of the miniature unipolar charger under 10% and 90% RH conditions

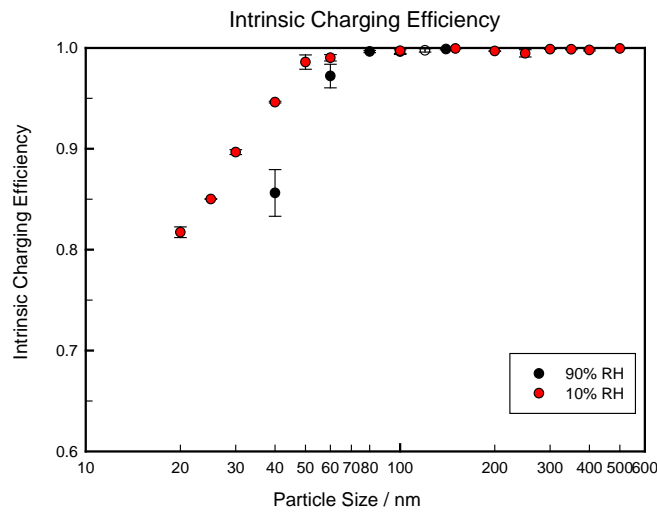


Figure 4b. Extrinsic charging efficiency of the miniature unipolar charger under 10% and 90% RH conditions

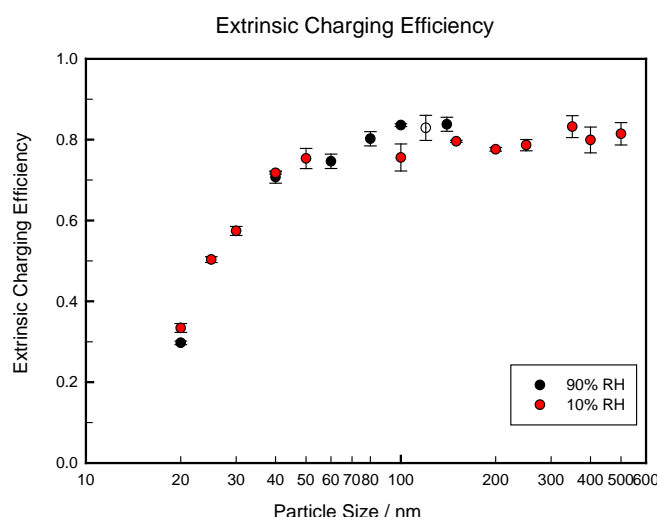
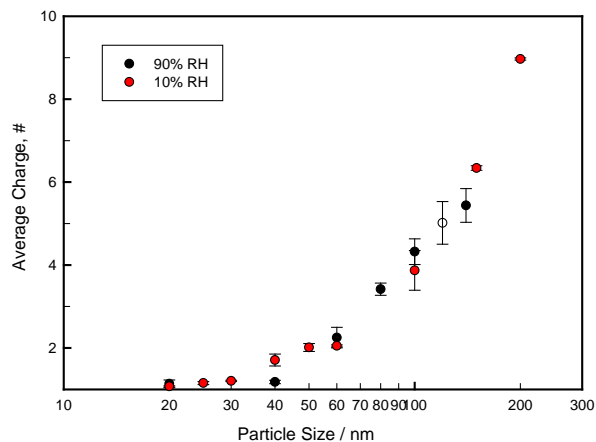


Figure 5. Average charges of the miniature unipolar charger under 10% and 90% RH conditions



CONCLUSION

Based on the experimental result given above, it is evidenced that the performance of miniature unipolar charger was not significantly influenced by the effect of relative humidity. However, a slight decrease on the intrinsic charging efficiency was observed for the particles with the sizes less than 100 nm. More detailed results of this investigation will be discussed in this presentation.

REFERENCES

- [1] Qi, C., Chen, D.-R., and Greenberg, P. Performance study of a unipolar aerosol mini-charger for a personal nanoparticle sizer. *J. Aerosol Sci.*, 39(5):450-459, 2008.
- [2] Qi, C., Chen, D.-R., & Greenberg, P. Fundamental study of a miniaturized disk-type electrostatic aerosol precipitator for a personal nanoparticle sizer. *Aerosol Science and Technology*, 42:505-512, 2008.
- [3] Chen, D.-R., & Pui, D.Y.H. A high efficiency, high throughput unipolar aerosol charger for nanoparticles. *Journal of Nanoparticle Research*, 1: 115-126, 1999.

Experimental Evaluation of a Compact Electrostatic Nanoparticle Sampler

He Jing¹, Qisheng Ou¹ and Da-Ren Chen¹

¹Washington University in St. Louis, St. Louis, Missouri 63130, United States

ABSTRACT

A new compact aerosol sampler for particle SEM/TEM analysis was evaluated. The sampler is based on electrostatic deposition. The sampler consists of two key components: aerosol charging and particle deposition chambers. In this study the performance optimization of the sampler was first carried out by varying the charger voltage, and flow rates of aerosol and ion carry flows. The sampler's performance when operated at the identified operational condition was then evaluated. Collection efficiency of the sampler for solid (potassium chloride), liquid (oleic acid) and PSL particles in the size range from 40 to 480 nm were measured. Fluorescent particles in the sizes ranging from 80 to 480 nm were also used to assess the particle deposition distribution in the sampler via the fluorescence technique. Our study shows that the collection efficiency was 65%-76% and 88%-96% for solid and liquid particles, respectively. The collection efficiency for PSL particles is in par with that for liquid particles. Fluorescent study further showed that 35%-67% of liquid particles were collected on the side wall of particle collection stage installed in the sampler.

KEYWORDS

Electrostatic nanoparticle sampler, Particle collection efficiency, SEM/TEM particle analysis

Introduction

Collection of aerosol particles for offline analysis is the common task for aerosol studies in order to better understand the property of airborne particles, such as the particle size, morphology and even chemical composition. Scanning Electron Microscopy (SEM)^[1] and Transmission Electron Microscope (TEM) are the tools to obtain the above particle information. Various aerosol samplers based on different operational principles have been used in the task of particle collection. Among various particle collection techniques, an electrostatic precipitation sampler is the most efficient one for nanoparticles collection. The operational principle of an electrostatic sampler is similar to that of electrostatic precipitators (ESPs).

Two types of ESPs are existed: single stage and two stage design. Single stage ESPs perform the

above two tasks in one chamber (or stage)^[2,3]. In two stage ESPS, the particle charging and collection are performed in two separate chambers (or stages)^[2-6]. Other configurations of ESPs include the disk-type ESP^[7] and the rod-type one^[8].

The performance of an ESP is characterized by the collection efficiency of particles. It has been evidenced that the particle collection efficiency of an ESP is significantly influenced by the flowrate of sampled aerosol and the voltage exerted on the ESP device^[6,9]. In certain performance condition, the particle collection efficiency of an ESP would further vary with different types and sizes of particles. Two experimental methods were used in the evaluation of collection efficiency of an ESP. One is based on the measurement of particles upstream and downstream of an ESP by two CPCs (Condensation Particle Counters), leading to the number based collection efficiency. The other is based on the fluorescent measurement of particle deposited on collection stage, leading to mass-weighted efficiency. The maximal collection efficiencies of ESPs can be higher than 70% among the literature. It is also shown that the particles size has great influences on the charging of particles in an ESP, thus affecting its particle collection performance.

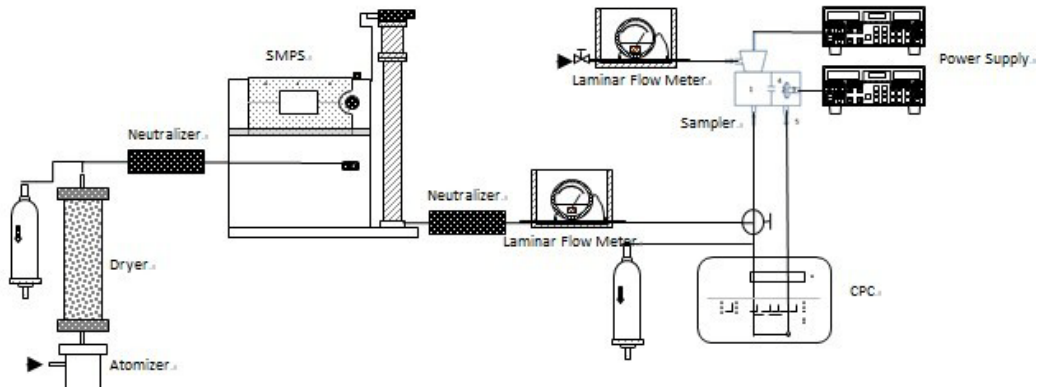
In this study, a new electrostatic particle sampler has been design and its performance has been experimentally evaluated. The studied sampler implemented two-stage design of an ESP. In the sampler the particle charging was done by the mixing of sampled aerosol with unipolar ions produced by corona discharge. Once charged particles were then delivered to the precipitation chamber, in which the precipitation task was accomplished by establishing an electrical field between the aerosol flow orifice and the collection substrate. The objective of this study is to evaluate the performance of this sampler, to be more specific, to investigate the collection efficiency of particles in the flow stream once sampled by the studied sampler.

Experimental Methods

1 Experiment setup

The experimental setup for this study was shown in Figure 1. A custom-made Collison atomizer was used to produce polydisperse particles for obtaining monodisperse KCl particles in the sizes larger than 80 nm. A tube furnace was used to generate polydisperse KCl polydisperse particles by evaporation and condensation technique for obtaining monodisperse KCl particles with the sizes less than 80 nm. A differential mobility classifier was used to classify monodisperse particles of desired sizes. Two Berton Model 205B-10R power supplies were used to operate the studied sampler: one for the corona discharge operation and the other for particle collection. A TSI Model 3022 CPC was used to measure the number concentrations of test particles upstream and downstream the sampler.

Figure 1 Experiment Setup



2 Methods

Two experimental methods were used in this study to evaluate the number-based and mass-weighted collection efficiencies. The number-based efficiency was evaluated by using two CPCs measuring the percentage of particles captured by the sampler. The mass-weighted efficiency was measured by performing the fluorescent experiment to determine the proportion of particles depositing on the the substrate in the sampler.

In the two-CPC experiment, the particle number concentrations at the upstream and the downstream were measured while the sampler was in working. The collection efficiency can be calculated by:

$$\eta = (n_u - n_d) / n_u \quad (\text{Eq.1})$$

in which, η is the collection efficiency, n_u and n_d are particle number concentrations at upstream and downstream of the sampler, respectively.

In the fluorescent experiment^[10], the fluorescent salt was first dissolved in the solution to be used for test particle generation. After deposited on different locations in the sampler, the salt particles were then recovered by washing them down into the prepared solution. The fluorescence amount in the solution was then measured by a fluorescence meter. The value of fluorescence signal obtained from the meter is proportional to the mass of salt particles in the solution. The percentage of particles deposited on the collection substrate was then obtained using the fluorescent values of solutions used to recover salt particles deposited in various parts of the sampler:

$$\delta = m_2 / (m_1 + m_2 + m_3 + m_4 + m_5) \quad (\text{Eq.2})$$

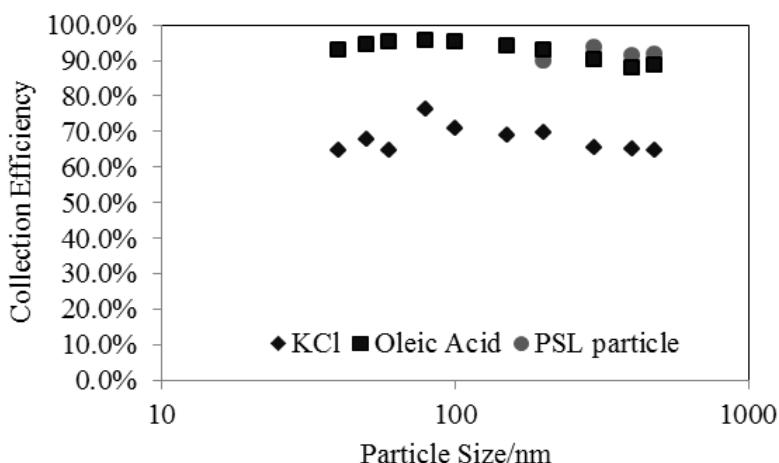
in which, δ is the percentage of particles that deposit on the substrate in the sampler. m_1, m_2, m_3, m_4, m_5 are the fluorescent value of the solutions used to recover salt particles deposited in the particle charging chamber, the upside surface of the substrate, other surface of the substrate and the rod, the collection chamber, and the downstream filter collecting all the particles in the exhaust flow, respectively.

Results and Discussion

1 Results based on particle number concentrations

Figure 2 shows the results of number-based collection efficiencies. In general the particle collection efficiency of the studied sampler is above 65%. The collection efficiency of solid KCl particles ranges from 65%~85%, while that of the liquid oleic acid particles is from 88%~96%. The lower collection efficiency for solid particles as compared with that for liquid particles may be due to the bounce off of solid particles when colliding on the collection substrate. The collection efficiency for PSL particles is similar with that for oleic acid liquid particles.

Figure 2 Collection Efficiencies of The Sampler Measured by Two CPCs Methods

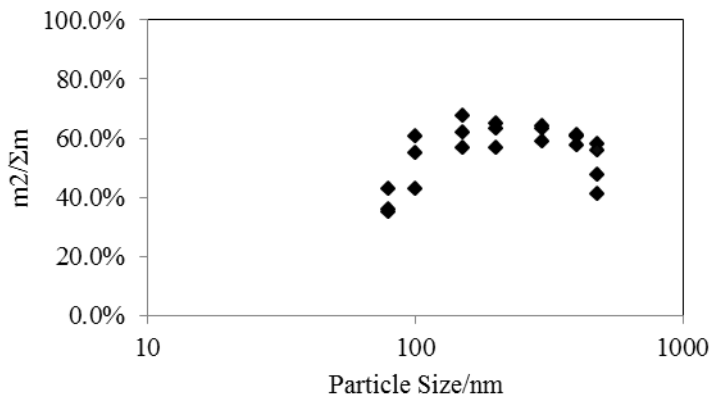


2 Results of the fluorescent experiment

Figure 3 shows the result of fluorescent experiment. From the figure, 35%~67% particles can be collected on the particle collection substrate of the sampler. Triplicate was done in this part of the study and the result was repeated very well. The collection efficiencies are relatively low for particles in the sizes of 80, 100 and 480 nm. The possible reason for the above observation is given in the following: in the experiment for small sized particles, the particle mass collected was rather low, resulting in increased experimental error. For the case of 480 nm particles, the particle

number concentration measured was very low, resulting again the increased errors in the calculation.

Figure 3 Percentages of Particles That Were Collected on The Upside Surface of The Substrate



SUMMARY

The number-based collection efficiency of the studied sampler was 65%-76% and 88%-96% for solid and liquid particles, respectively. The collection efficiency for PSL particles is in par with that for liquid particles. Fluorescence study further showed that 35%-67% of liquid particles were collected on the side wall of particle collection stage.

REFERENCES

- [1] Germani M, Buseck P. Automated scanning electron-microscopy for atmospheric particle analysis. *Analytical chemistry*, 1991, 63(20), 2232-2237
- [2] Zhuang Y, Kim Y, Lee T, Biswas P. Experimental and theoretical studies of ultra-fine particle behavior in electrostatic precipitators. *Journal of Electrostatics*, 2000, 48, 245-260
- [3] Haque, M, Rasul M, Khan M. Fine particulate emission control by optimizing process parameters of an electrostatic precipitator. *Recent Advances in energy & environment*, Cambridge, UK, 2010, 223-228
- [4] Li M, Christofides P. Collection Efficiency of Nanosize Particles in a Two-Stage Electrostatic Precipitator. *Ind. Eng. Chem. Res.* 2006, 45, 8484-8491
- [5] Sillanpää, M, Geller M, Phuleria H, Sioutas C. High collection efficiency electrostatic precipitator for in vitro cell exposure to concentrated ambient particulate matter (PM). *Aerosol Science*, 2008, 39, 335-347
- [6] Han B, Hudda N, Ning Z, Kim Y, Sioutas C. Efficient Collection of Atmospheric Aerosols with a Particle Concentrator—Electrostatic Precipitator Sampler. *Aerosol Science and*

Technology, 2009, 43, 757-766

- [7] Qi C, Chen D, Greenberg P. Fundamental Study of a Miniaturized Disk-Type Electrostatic Aerosol Precipitator for a Personal Nanoparticle Sizer. *Aerosol Science and Technology*, 2008, 42, 505~512
- [8] Fierz, M. Kaegi, R. Burtscher, H. Theoretical and Experimental Evaluation of a Portable Electrostatic TEM Sampler. *Aerosol Science and Technology*, 2007, 41, 520-528
- [9] Li C, Liu S, Zhu Y. Determining Ultrafine Particle Collection Efficiency in a Nanometer Aerosol Sampler. *Aerosol Science and Technology*, 2010, 44, 1027-1041
- [10] Chen D, Pui D. Numerical and experimental studies of particle deposition in a tube with a conical contraction-laminar flow regime. *J. Aerosol Sci.*, 1995, 26(4), 563-574

Single particle analysis of hygroscopic property of ambient aerosol in Shanghai

Xinning Wang, Xingnan Ye, Hong Chen, Jianmin Chen and Xin Yang*

Department of Environmental Science and Engineering, Fudan University, 220 Handan Road, Shanghai, 200433

Principal Contact: Xin Yang, Professor, Department of Environmental Science and Engineering, Fudan University, 220 Handan Road, Shanghai, 200433

Tel: 021-55665272 Fax: 021-65640082 E-mail: yangxin@fudan.edu.cn.

Abstract

Aerosol's ability to absorb water is a function of its chemical composition, diameter, as well as ambient conditions such as relative humidity. Hygroscopic Tandem Differential Mobility Analyzer (HTDMA) and Aerosol Time-of-Flight Mass Spectrometer (ATOFMS) were deployed to investigate aerosol chemical composition and its impacts on the hygroscopic behavior at single particle level. 200 nm diameter particles were sampled directly from ambient environment and particles with preset hygroscopic growth factor (GF) were selected by HTDMA system. The selected particles then entered ATOFMS to have chemical composition analyzed. By scanning the GFs in HTDMA, connections between aerosol hygroscopic property and the origins of particles, their atmospheric aging histories, and presence of certain chemical species can be established. In this study, aged biomass burning particles were observed enriched in the hygroscopic mode ($GF > 1.3$), which accounts for ~50% in particle counts. Meanwhile, in the hydrophobic mode ($GF = 1.0$), dominant particle types included organic carbon, PAH-rich, and fresh biomass burning particles. Hygroscopic particles contained more nitrate than hydrophobic particles. Hygroscopic distribution of aged and fresh biomass burning particle highlights the importance of aging history of aerosol in determining its hygroscopic properties. Dust particles displayed a median hygroscopic behavior. Sea salt particle were of minor importance because of the small size we selected.

Keywords: aerosol, hygroscopic growth, HTDMA, ATOFMS

Analysis and Handling of Bio-nanoparticles and Intact Viruses using Electrostatic Aerosol Mobility

Peter Kallinger¹, Anne Maißer¹, Günter Allmaier² and Wladyslaw W. Szymanski¹

¹University of Vienna, Faculty of Physics, Boltzmanngasse 5, A-1090 Vienna, Austria

²Vienna University of Technology, Institute of Chemical Technologies and Analytics, Getreidemarkt 9, A-1060 Vienna, Austria

ABSTRACT

The utilization of differential mobility analysis for the separation of singly charged particles by their electrophoretic mobility diameter at atmospheric pressure together an appropriate detection instrument allows measurement of the individual electrostatically separated singly charged nanoparticles (ions). A direct relationship between molecular mass and equivalent diameter was obtained yielding a possibility of determination of molecular masses of high molecular weight proteins and non-covalent protein complexes and observation of influence of different environmental conditions on the stability of the selected protein complexes. The study of human rhinoviruses has demonstrated the capability of the technique to analyze the intact infectious human-pathogenic viruses and corresponding antibodies along with the monitoring of the dissociation of these supra-molecular structures by means of heat.

KEYWORDS

Nanoparticles, Bio-macromolecules, Virus detection, Protein stability, PDMA, GEMMA

Introduction

Real-time analysis and handling of airborne nanoparticles based on the utilization of the electrophoretic mobility of a charged particle in a defined electrostatic field appears to be one of the best approaches currently available. Electrophoretic mobility analysis is a technique not only well suited for size analysis but also for preparative collection of nanosized airborne particles [1-3]. The beauty of this technique is its principal simplicity. The usual arrangement is a co-axial placement of a larger outer cylindrical and thinner inner electrode with an electrostatic field between them, which is well-defined by the voltage applied to the inner electrode. The recent extension of the working range of the electrostatic size classification of aerosols into the sub-10 nm size range where it merges with chemical analytical methods opens new fields of applications. Combined with an aerosol generation from nanoparticle solutions and suspensions using nano-

electrospray (nano-ES) electrostatic methods (GEMMA - Gas phase Electrophoretic Mobility Molecular Analyser (TSI, Inc.) and PDMA – Parallel Differential Mobility Analyzer) has been recently proven very useful to characterize proteins, functional protein complexes or intact viruses with attached antibodies. Due to the fact that this electrostatic technique functions at ambient pressure it offers an opportunity for a real-time measurement, sampling and enrichment of airborne nanoparticles or bio-macromolecules (viruses) and complements analytical tools such as e.g. mass spectrometry, or size exclusion chromatography.

Experimental Methods

The GEMMA system is a commercial experimental arrangement (TSI, Inc.) consisting in the case of this study of an electrospray unit, nanoDMA and a condensation particle counter.

The PDMA system used here is combined with an electrical aerosol detection device working on the Faraday cup principle. Parallel with the scanning n(nano)DMA1 which scans and delivers the complete size spectrum of the original suspended particles, an identical separation unit nDMA2 is in operation at one given voltage setting (separation) and used for sampling or enrichment (collection) of the selected size class of nano-particles, hence the acronym PDMA. The most recent engineering solutions extended the lower detection limit of the PDMA system even below 1 nm in terms of the electrical mobility diameter. The prerequisite for this detection method is the necessity of a certain minimum number of charged particles (concentration) needed to achieve measurable electrical signal. The detection limit of this system is currently in the order of 10^2 charged particles per cm^3 .

Results and Discussion

A variety of particles were measured with both PDMA and GEMMA systems. Fig. 1 shows size spectra of globular nanoaerosol particles summarized in Table 1.

Table 1. Electrosprayed materials and the modal values (EM-Diameter) of the measured size distribution with the PDMA system

	Material	Symbol	EM-Diameter (nm)
Proteins	Bovine Serum Albumin	△	6.3
	Enolase	□	7.2
	Gamma-Globulin	□	8.2
	Ferritin	○	12.8
	Thyroglobulin	★	13.3
Silica Particles	HS-40	▽	18.2
	AS-40	◇	27.2

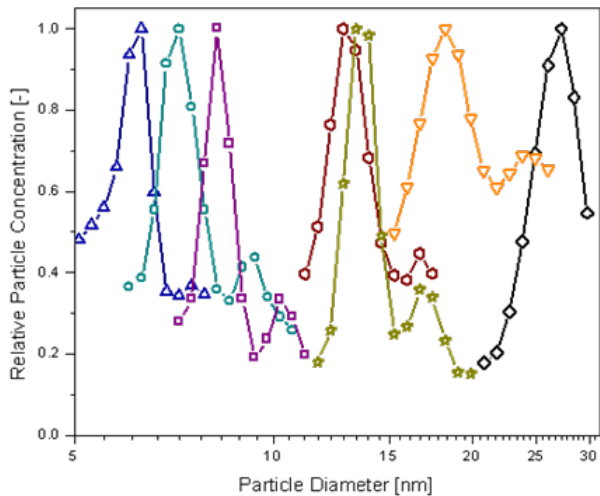


Fig. 1. Size distribution obtained with the PDMA system for materials listed in Table 1.

A result of a measurement of bio-nanoparticles obtained with the GEMMA system is shown in Fig. 2. The size distribution of parvalbumin isolated from Cyprinus Carpio was measured in terms of aerosol concentration as a function of electromobility (EM) diameter (upper diagram). The conversion of the measured data to data showing the size distribution as a function of molecular weight is shown in the lower diagram and shown good agreement with the well-known molecular weight of this compound (11478 Da) [1].

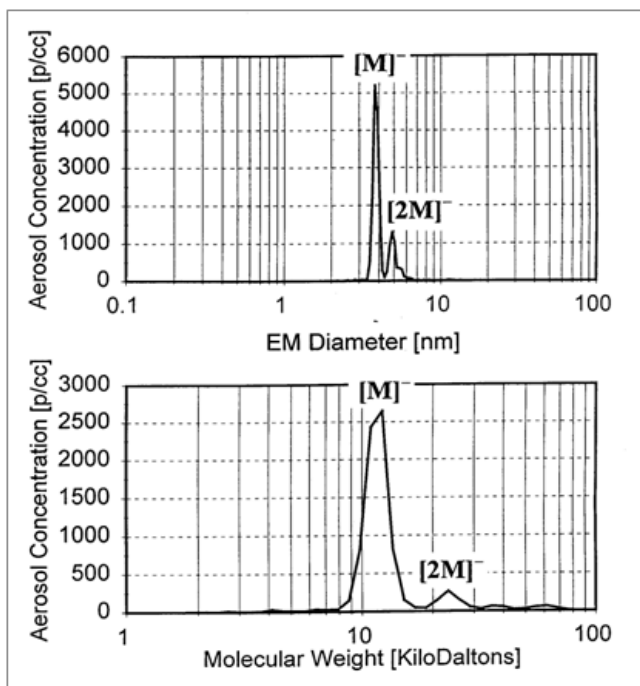


Fig. 2. Measured spectra of the parvalbumin (Cyprinus Carpio) vs. EM diameter and the conversion to spectra providing concentration vs. molecular mass

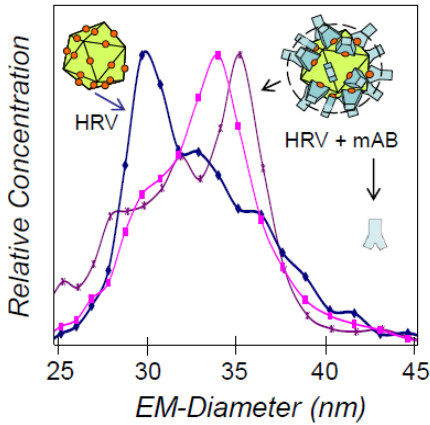


Fig. 3. Size spectra (GEMMA) of the human rhinovirus (HRV) showing the increasing antibody attachments indicated by the size changes from the plain virus to a virus with a complete surface coverage by the virus-specific antibody (mAB-8F5).

The possibility of direct transformation from the measured nanoparticle size (at least for globular particles and molecules) offers the opportunity to calibrate a DMA system in terms of molecular weight and characterize macromolecular complexes in the mega-Dalton molecular weight range. Many viruses and its complexes with antibodies or receptors possess approximately globular shape. This fact allows a conversion from a measured EM-diameter (EMD) to the volume equivalent diameter [4]. Measuring the EM-diameter of the antibodies and assuming that the volume of the complex (HRV (Human rhino virus) and monoclonal antibody (mAB-8F5) is the sum of the volume of “plain”, antibody-free viruses and that of the attached mABs, one can calculate from the increase in the measured EM-diameter of the virus the number of attached antibodies [5]. This can be done assuming that no significant conformational changes – that might change the volume or density during the attachment process – would occur. Consequently, the experimentally-determined maximum number of attached antibodies can be obtained and is in agreement with the theoretical prediction of 30 antibodies [5].

CONCLUSIONS

The electrostatic methods of aerosol science have proven to be an extremely useful tool for a number of applications beyond the original field of research. One could say that electrostatic size classification of airborne nanoparticles was born in aerosol science, but matures in analytical chemistry. The analysis of macromolecules and nanobioparticles by electrical means discussed here seems to offer not only a possibility to complement mass spectrometric and liquid-phase separation techniques, but due to the fact that measurements are performed at ambient pressure, it

opens a wide spectrum of new applications. Of importance is also to realize that non-volatile contaminants have to be avoided or may only be present in the sample at low concentrations. Otherwise, the determined particle size is too high. What still limits this technique today are the low charging efficiency processes for nanoparticles available to date. Once better charging methods in the nanosize particle range are accessible, electrophoretic mobility could also be a major preparative tool for nanotechnological applications.

ACKNOWLEDGMENTS

This work was supported in part by grants of the Austrian Science Foundation (P16185 to W.W.S. and TRP 29-N20 to W.W.S and G.A.).

REFERENCES

- [1] G. Bacher, W.W. Szymanski, S.L. Kaufman, P. Zöllner, D. Blaas, G. Allmaier, *J. Mass Spectrom.* 36 (2001) 1038.
- [2] G. Allmaier, C. Laschober, W.W. Szymanski, *J. Am. Soc. Mass Spectrom.* 19 (2008) 1062.
- [3] J.F. de la Mora, L. de Juan, T. Eichler, J. Rosell, *Trends Anal. Chem.* 17 (1998) 328.
- [4] A.A. Lall, S.K. Friedlander, *J. Aerosol Sci.* 37 (2006) 271.
- [5] G. Allmaier, A. Maißer, C. Laschober, P. Messner, W.W. Szymanski, *Trends Anal. Chem.* 30 (2011) 123.

Application of an Ambient Ion Monitor in Northeastern Alberta, Canada

Yu-Mei Hsu and Kevin Percy

Wood Buffalo Environmental Association, #100-330 Thickwood Blvd, Fort McMurray, AB T9K 1Y1, Canada

ABSTRACT

A semi-continuous ambient ion monitor (AIM) has been used to monitor low, ambient concentrations of inorganic gases (NH_3 , HCl , HNO_2 , HNO_3 and SO_2), and water-soluble inorganic aerosol species (Na^+ , NH_4^+ , K^+ , Mg^{2+} , Ca^{2+} , Cl^- , NO_3^- , and SO_4^{2-}) in the Athabasca Oil Sands Region (AOSR) of northeastern Alberta. The URG Corporation (Chapel Hill, NC) Model 9000D AIM is configured with two Dionex Corporation (Sunnyvale, CA) Model ICS-2000 ion chromatography (IC) systems for cation and anion analyses, a parallel plate membrane denuder with H_2O_2 solution for absorbing gases, a steam injection chamber to nucleate aerosols, and a slurry sample collection cyclone. The AIM system was optimized for our application by adding: (1) a pressurized N_2 system to control the flow rate of H_2O_2 solution through the denuder and allow precise control of membrane position; and (2) a Dionex model 200 carbonate removal device in the anion IC to minimize its peak interference.

The AIM is currently collecting hourly integrated data at the Fort McKay air monitoring station ($57^\circ 11'21.88'' \text{ N}$; $111^\circ 38'25.75'' \text{ W}$). The station is situated in a First Nation's community that is located between oil production operations 15 km to the south and 15 km to the northeast. Advantages of the AIM for this application are its low detection limit, and its semi-continuous mode of operation, thus, allowing for better investigation of transient pollution events and for informing on atmospheric chemistry.

Comparison of the URG AIM system to continuous pulsed fluorescence gas instruments (SO_2), and integrated manual annular denuder samplers indicates good agreement for SO_2 concentrations which demonstrates the AIM is a reliable monitor.

KEYWORDS

Ambient ion monitor, Athabasca Oil Sands, Northeastern Alberta

Introduction

The Wood Buffalo Environmental Association (WBEA) has monitored air quality in the Athabasca Oil Sands Region (AOSR) in northeastern Alberta since 1998 with continuous monitoring of sulfur dioxide (SO_2), nitric oxide (NO), nitrogen dioxide (NO_2), ozone (O_3), ammonia (NH_3), total hydrocarbon (THC), total reduced sulfur (TRS), hydrogen sulfide (H_2S), and $\text{PM}_{2.5}$. Additional, integrated measurements are conducted and may include: passive samplers for O_3 , SO_2 , NO_2 ; $\text{PM}_{2.5}$ and PM_{10} samplers for mass, water-soluble ionic species, and metal species; polyurethane foam (PUF) samplers for polycyclic aromatic hydrocarbons (PAHs); and an annular denuder sampler for nitric acid (HNO_3), nitrous acid (HNO_2) and NH_3 . In the fall of 2009, WBEA deployed a new semi-continuous ambient ion monitor (AIM) to monitor low ambient concentrations of inorganic gases (NH_3 , hydrogen chloride (HCl), HNO_2 , HNO_3 , and SO_2), and water-soluble $\text{PM}_{2.5}$ aerosol species in the AOSR to understand the atmospheric chemistry in this region. The URG Corporation (Chapel Hill, NC) Model 9000D AIM deployed in the AOSR is configured with two Dionex Corporation (Sunnyvale, CA) Model ICS-2000 ion chromatography (IC) systems for cation and anion analyses, a parallel plate membrane denuder with H_2O_2 solution for absorbing gases, a steam injection chamber to nucleate aerosols, and a slurry sample collection cyclone. This paper reports on the evaluation of performance characteristics of this semi-continuous monitor under the unique conditions of the AOSR.

Experimental Methods

The AIM system was optimized by adding: (1) a pressurized N_2 system to control the flow rate of H_2O_2 solution through the denuder and allow precise control of membrane position; and (2) a Dionex model 200 carbonate removal device in the anion IC to minimize its peak interference. The AIM is currently located at the WBEA's Fort McKay ($57^{\circ} 11'21.88'' \text{ N}$; $111^{\circ} 38'25.75'' \text{ W}$) station and is collecting hourly integrated data. The Fort McKay station is situated in the immediate vicinity of oil production operations in northeastern Alberta.

To verify the AIM data, a Thermo Scientific (Franklin, MA) Model 43A SO_2 monitor, a $\text{PM}_{2.5}$ (URG model 2000-30EN) sampler and one set of annular denuder sampling system (ADSS) are collocated for the performance evaluation of the AIM. Twenty-four hour $\text{PM}_{2.5}$ filter samples and 48-hour ADSS samples were extracted and analyzed by IC for water-soluble ionic species to compare with the high-resolution AIM results.

Results and Discussion

The AIM was installed at Fort McKay in November 2009, and has been operating continuously since that time. In this study, SO_2 concentrations from the 43A monitor and the water soluble ionic extracts from the 24-hour $\text{PM}_{2.5}$ filter samples were used to evaluate the AIM data.

SO₂ Concentration Comparison

SO₂ concentrations from January 2010 to December 2010 are shown in Figure 1 for the AIM and model 43A instruments. The two instruments had a very similar temporal response, ($R= 0.76$; $P<0.05$; $n= 7373$) indicating good agreement. Table 1 lists the SO₂ comparison results between two measurements in 2010. The 2010 hourly mean concentrations (\pm standard deviation) from the AIM and the 43A monitor were 1.38 (± 3.5) and 1.31 (± 3.65) ppb, respectively.

Figure 1. SO₂ Concentrations Measured by the AIM and SO₂ Continuous Monitor (43A).

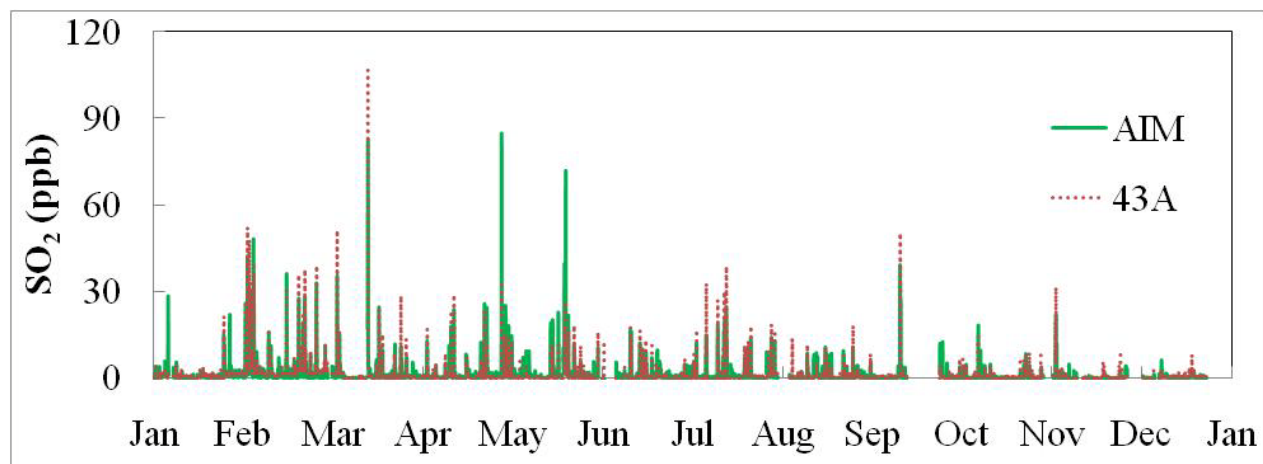


Table 1. SO₂ Concentration Comparison between Two Measurements

	AIM	43A monitor
Sample number	7373	7373
Mean (ppb)	1.38	1.31
Standard deviation	3.50	3.65

PM_{2.5} Concentration Comparison

Water soluble extracts from PM_{2.5} Teflon membrane filter samples collected from January 2010 to December 2010 were acquired for IC analysis and comparison with the AIM. Overall, concentrations were quite low, and only three species (NO₃⁻, SO₄²⁻, and NH₄⁺) were found to be above method detection limit (MDL) for both instruments. The correlations coefficients ($P>0.05$) between the AIM and filter based measurements were 0.17 for NO₃⁻, 0.56 for SO₄²⁻, and 0.13 for

NH_4^+ (See Table 2). Means of NO_3^- and NH_4^+ from the filter samples were lower than those from the AIM, as expected, due to the volatilization of nitrate species from the filter during the sampling^[1, 2].

Table 2. Summary of NO_3^- , SO_4^{2-} , and NH_4^+ Concentrations from Filter Extracts and AIM.

	$\text{NO}_3^- (\mu\text{g m}^{-3})$		$\text{SO}_4^{2-} (\mu\text{g m}^{-3})$		$\text{NH}_4^+ (\mu\text{g m}^{-3})$	
	Filter	AIM	Filter	AIM	Filter	AIM
Correlation Coefficient	0.17		0.56		0.13	
n	40	40	44	44	43	43
Mean	0.14	0.27	1.10	1.53	0.58	1.23
Min	0.02	0.03	0.13	0.15	0.05	0.09
Max	0.39	0.74	3.96	4.47	1.75	2.55
Std Dev	0.10	0.17	6.46	6.44	0.46	0.76

Data Comparison with Annular Denuder Sampling System

Twenty-two sets of annular denuder samples were collected for both gaseous and particulate phases in 2010 for performance evaluation of the AIM. Particulate sulfate concentrations from the ADSS and AIM, as shown in Figure 2, demonstrated an excellent correlation ($r=0.97$, $P<0.05$). However, the sulfate concentrations measured by the AIM were higher than those of ADSS (Table 3). Sulfur dioxide concentrations from the ADSS, the AIM and the continuous monitor (43A) showed good agreement, as displayed in Figure 3. The correlation coefficients were 0.85 for the ADSS and 0.80 for the continuous monitor. Table 3 summarizes the SO_2 concentrations from 3 measurements and the SO_2 mean concentrations were 2.07, 2.10, and 1.81 ppb for the AIM, the ADSS and the continuous monitor, respectively. Overall, particulate sulfate concentrations from the AIM and the ADSS were well correlated, and SO_2 concentrations measured using three methods had good agreement.

Figure 2. Sulfate Concentrations Measured by the ADSS and AIM.

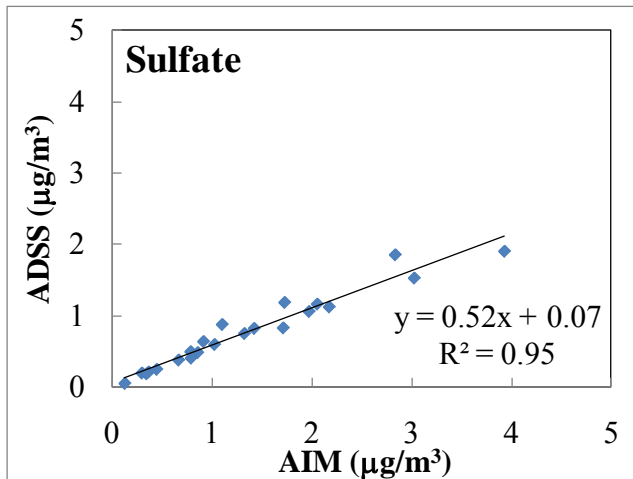
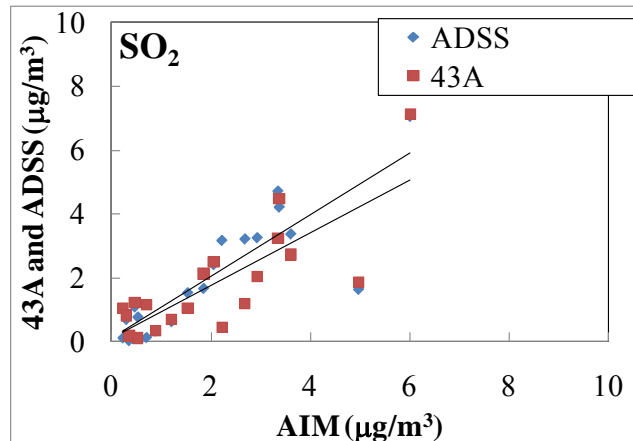


Figure 3. SO₂ Concentrations Measured by the ADSS, AIM and SO₂ Continuous Monitor (43A).



$$\text{ADSS: } [\text{SO}_2]_{\text{ADSS}} = 0.97 \times [\text{SO}_2]_{\text{AIM}} + 0.10 \\ R^2 = 0.72$$

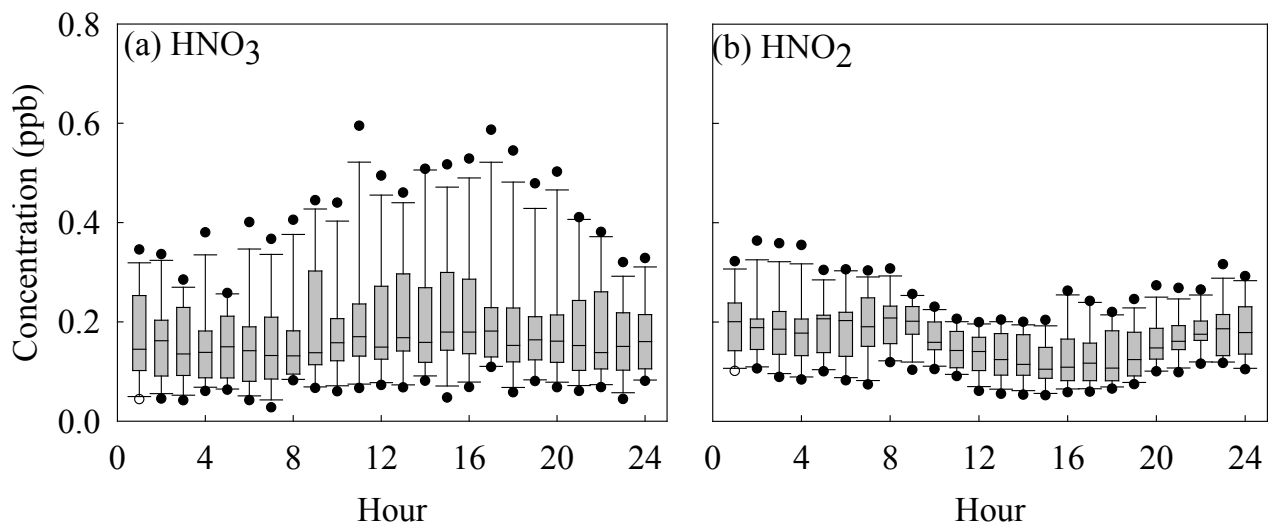
$$43A: \quad [\text{SO}_2]_{43A} = 0.82 \times [\text{SO}_2]_{\text{AIM}} + 0.11 \\ R^2 = 0.63$$

Table 3. Summary of SO_4^{2-} and SO_2 Concentrations Measured Using Three Methodologies.

	$\text{SO}_4^{2-} (\mu\text{g m}^{-3})$		$\text{SO}_2 (\text{ppb})$		
	AIM	ADSS	AIM	ADSS	43A
Correlation Coefficient	0.97		-	0.85	0.80
N	22	22	19	19	19
Mean	1.36	0.78	2.07	2.10	1.81
Min	0.13	0.05	0.23	0.02	0.12
Max	3.93	1.91	6.01	7.05	7.14
Std Dev	0.99	0.53	1.66	1.89	1.72

2010 Daily HNO_2 and HNO_3 Concentrations

Yearly hourly concentrations of HNO_2 and HNO_3 in 2010 are presented in Figure 4. Overall, HNO_3 concentrations were higher during the day and had high variation in the afternoon. HNO_3 concentrations were higher than HNO_2 concentrations in this region. HNO_2 concentrations were significantly ($P=0.05$) higher in the early morning, and decreased during the day due to photolysis. The 57 degree N latitude of the AOSR results in relatively short day light periods in winter, and long day light in summer which could impact the photochemistry in the region significantly. In general, the HNO_2 and HNO_3 concentrations were low during winter.

Figure 4. Yearly Hourly Average Concentrations of HNO_2 and HNO_3 .

SUMMARY

The AIM 9000D has been deployed at WBEA's Fort McKay monitoring station in the AOSR since November 2009. Overall, the SO₂ concentrations from the AIM, the ADSS and the Model 43A SO₂ continuous monitor had good agreement, and sulfate concentrations from the AIM and the ADSS were well correlated. We are hopeful that the AIM's hourly time resolution of inorganic species for both aerosols and gases will aid our understanding of atmospheric chemistry in the region. Long-term measurements are planned to further investigate the concentrations of NH₃, HNO₂, and HNO₃ and to examine acidification and eutrophication potential.

REFERENCES

- [1] Rodes, C. E.; Evans, G. F. *Summary of LACS Integrated Measurements*; U.S. Environmental Protection Agency; Research Triangle Park, NC, 1977; EPA-600/4-77-034.
- [2] Lee, K. W.; Mukund, R. In *Aerosol Measurement: Principle, Techniques, and Applications*; Baron, P.A.; Willeke, K., Ed.; John Wiley and Sons, Inc.: New York, NY, 2001; pp197-228.

Aerosol number fluxes measured by eddy covariance method above short vegetation

Atsuyuki Sorimachi¹, Shinji Tokonami¹, Masaru Haraguchi², and Kazuhiko Sakamoto³

¹ Hirosaki University, 66-1 Hon-cho, Hirosaki City, Aomori 036-8564, Japan

² Saitama Prefectural Comprehensive Education Center (Konan Branch), 1355-1, Kumagaya City, Saitama 360-0113, Japan

³ Saitama University, 255 Shimo-Okubo, Sakura-ku, Saitama City, Saitama 338-8570, Japan

Principal Contact: Atsuyuki Sorimachi, Ph.D., Hirosaki University,
66-1 Hon-cho, Hirosaki City, Aomori 036-8564, Japan.

Tel.: +81 172 39 5502; fax: +81 172 39 5502. E-mail address: sorimac@cc.hirosaki-u.ac.jp

Abstract

This study describes measurement for number fluxes of particles with diameter larger than 15 nm using the eddy covariance method in laboratory and field experiments. The main component of flux measurement system consists of a 3-D-ultrasonic anemometer and a condensation particle counter (CPC). In the laboratory experiments the CPC instrument response was tested using a walk-in chamber (about 25-m³ inner volume). In the field measurement with the prototype system, the diurnal number particle fluxes over the short vegetation were measured in April and June 2010 in Saitama prefecture, Japan. According to the initial analysis, only data with a sufficient and uniform upwind fetch were used. As a result, both the upward and downward particle fluxes were observed in this study.

Keywords : CPC, Dry deposition, Eddy covariance, Number particle flux

Boundary layer top detection from lidar dataset using a Haar wavelet method over Wuhan, China

Shalei Song¹, Feiyue Mao², and Wei Gong²

1 Wuhan Institute of Physics and Mathematics, Chinese Academy of Sciences, P.O. Box 71010, Wuhan 430071, China

2 The State Key Laboratory of Information Engineering in Surveying, Mapping and Remote Sensing, Wuhan University, Wuhan 430079, China

Principal Contact: Shalei Song, Wuhan Institute of Physics and Mathematics, Chinese Academy of Sciences, P.O. Box 71010, Wuhan 430071, China.

Tel: +86 13476082677 Email: songshalei@gmail.com

Abstract

A Mie light detection and ranging (lidar) system was utilized to measure the boundary layer height over Wuhan, China. Recent studies have used a Haar wavelet covariance transform to detect the boundary layer top from lidar dataset. This wavelet method can detect boundary layer top from lidar backscatter profiles by locating the maximum in the covariance profiles. Thus we utilized the Haar wavelet covariance transform method to found the boundary layer top to our lidar dataset. The primary results show that the method can detect the boundary layer top effectively. Therefore, a general pattern can be concluded after a long-term monitoring is completed. Also the detected results of boundary layer top can be used to improve the existing atmospheric model and Meteorological forecast system.

Keywords: Lidar, boundary layer

On-line and Off-line Applications of Ion Chromatography in Atmospheric Environment

Jing Wang

Chromatography and Mass Spectrometry, Dionex Product, Thermo Fisher Scientific, 100029, Beijing

Principal Contact: Jing Wang, Engineer, Chromatography and Mass Spectrometry, Dionex Product, Thermo Fisher Scientific, 100029, Beijing.

Tel: 13401108793 Email: xiwei.yue@thermofisher.com

Abstract

Dionex Ion Chromatography has been applied successfully to on-line continuous measurements and off-line analysis in atmospheric environment. On-line Ion Chromatography is an ambient ion monitor (AIM). It aims to characterize atmospheric pollutants in the gaseous and the particulate phases, including common water-soluble inorganic ions in both the particulate phase (F^- , Cl^- , NO_2^- , NO_3^- , Br^- , SO_4^{2-} , PO_4^{3-} , Li^+ , Na^+ , NH_4^+ , K^+ , Mg^{2+} , Ca^{2+}) and the gas phase (HF, HCl, HNO_2 , HNO_3 , SO_2 , NH_3), and water-soluble organic acids. High time resolution pollutant concentration measurements are provided for further studying the formation mechanism and sources of heavy pollution with meteorological conditions. Especially, AIM samplers are employed for air quality monitoring during some important international and domestic events. In addition, off-line analysis of ion chromatography in the laboratory is also widely used to detect common water-soluble inorganic ions, carboxylic acid compounds (formate, acetate, methylsulfonate, malate, malonate, maleate, succinate, oxalate and tartrate), and saccharides(sugar alcohols, monosaccharides and monosaccharide anhydride).

Keywords: On-line; Off-line; Ion Chromatography; Water-soluble inorganic ions; organic acids; saccharides

Decomposition Efficiency of Polycyclic Aromatic Hydrocarbons (PAHs) in Nanoparticles from Rubber-wood Combustion Using Soft X-rays

J. Chomanee¹, S. Tekasakul¹, P. Tekasakul², M. Hata³ and M. Furuuchi³

¹Department of Chemistry and Center of Excellence for Innovation in Chemistry (PERCH-CIC), Faculty of Science, Prince of Songkla University, Hat Yai, Songkhla 90112, THAILAND

²Department of Mechanical Engineering, Faculty of Engineering, Prince of Songkla University, Hat Yai, Songkhla 90112, THAILAND

³Graduate School of Natural Science and Technology, Kanazawa University, Kakuma-machi, Kanazawa 920-1162, JAPAN

ABSTRACT

Soft X-rays with a wave length of 1.3×10^{-4} – 4.1×10^{-4} μm was used to investigate the characteristics of decomposition of particle-bound polycyclic aromatic hydrocarbons (PAHs) in smoke particles emitted from biomass (Rubber-wood) combustion in a laboratory scale tube furnace. The smoke particles irradiated and not irradiated by the soft x-rays were collected using a 10-stage Andersen sampler equipped with an inertial-filter stage (ANIF) simultaneously, which can collect sized particles down to ~70 nm. Particle-bound PAHs were analyzed to determine the decomposition efficiency of PAHs in relation to particle size and irradiation time of soft X-rays. The results showed that smoke particles in nano-size range (<100 nm) have a major mass fraction more than 20% of total smoke particles as well as their large contribution to PAHs. 4-6 rings PAHs in nano-particles (<70 nm) were decomposed by soft X-rays irradiation up to about 90% at the longest irradiation time. The decomposition efficiency of PAHs was shown to increase as the particle size decreases, while the soft X-rays could not decompose gaseous PAHs.

KEYWORDS

Soft X-rays, PAHs decomposition, Rubber wood, Nanoparticles

Introduction

Soft X-rays have recently been used as an effective neutralizer or charge inducer of aerosol particles^[1], because soft X-rays have a high radiation energy which may degrade some chemical components. From another point of view, if soft X-rays can degrade some hazardous air

pollutants, it is possible that they can be used to degrade pollutants, similar to UV^[2]. Polycyclic aromatic hydrocarbons (PAHs) are carcinogenic pollutants that are emitted during biomass burning. The Benzo(a)pyrene-toxic equivalent factor(BaP-TEQ) emitted from biomass burning correlate with smoke particle size range, especially in nanoparticles (<100 nm)^[3]. Previous research investigated the decomposition of polycyclic aromatic hydrocarbons (PAHs) and found that Soft X-rays were shown to be potentially useful as an effective device for pollution control^[4]. However, current understanding of PAHs decomposition by soft X-rays have not been examined extensively on degradation characteristic of nanoparticle-bound PAHs, which have significant health risk.

In this study, soft X-rays with a wave length of 1.3×10^{-4} – 4.1×10^{-4} μm, emitted from a commercially available soft X-ray bulb, was applied to decomposition of smoke particle-bound polycyclic aromatic hydrocarbons (PAHs) emitted from the combustion of rubber wood in laboratory scale electric tube furnace. Particle-bound PAHs were analyzed to discuss the decomposition efficiency of PAHs in relation to particle size down to nanosize range (<70 nm) and irradiation time of soft X-rays.

Experimental Methods

Experiment setup and procedure

Fig. 1 shows a schematic of the experimental setup, which consists of an electric tube furnace, a soft X-ray irradiation chamber and the smoke particle sampler. A selected amount of biomass fuel were dosed in quartz combustion boat put in middle of an electric tube furnace. While fuel sample was heated up from room temperature to the maximum temperature (550°C) by controlled heating rate at 20°C /min, air cleaned by HEPA filter and dried packed silica gel was fed at a constant flow rate via a mass flow controller (MFC3650, KOFLOC) into the furnace using an air pump. The flue gas from the furnace was diluted by mixing with clean and dried nitrogen gas (25 L/min) in a dilutor to reduce temperature and moisture content. In order to obtain a uniform dispersion of gas and smoke particles before the measurement, a φ15-mm and 750-mm-long stainless steel tube was used to downstream the dilutor as a post mixer before it is introduced into the irradiation chamber at a constant flow rate. The smoke particles irradiated and not irradiated by the soft x-rays were collected using an Andersen cascade impactor with an inertial filter stage (ANIF) attached between 0.43 μm stage and backup filter^[5,6]. The inertial filter has a cutoff size of ~70 nm. Binder-less quartz fiber filters (Pallflex, 2500QAT-UP, φ 80), prepared 48 hours in a desiccator at room temperature (~25 °C) and ~50%RH, were used for the particle sampling through impactor stages. The inertial filter used was a similar one for Nanosampler^[6]: ca. 4 mg of webbed SUS fibers (φ 9.6 μm diameter) was packed into a cassette with a circular nozzle

(ϕ 3x4.5 mm). As test fuels, cut pieces of rubber wood (\sim 5x5x5 mm³) were used. Fed amounts were \sim 0.2 g. The moisture content of biomass fuel was measured by a moisture analyzer (Mettler Toledo, HB43). The irradiations of soft x-ray chamber were designed for evaluated PAHs decomposition efficiency by varying irradiation time and irradiation energy to compare with non irradiation samples. The irradiation time and irradiation energy were study at 0.04s and 0.07s at the average energy level of 90% and 94% of source energy by adjusting the spaces of S and L as shown in **Fig.2**. Experimental conditions are summarized in **Table 1**.

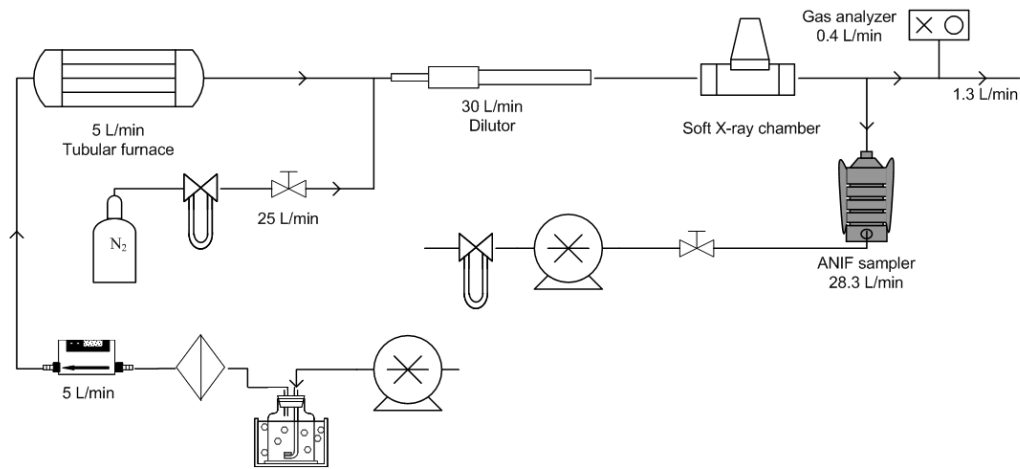


Figure 1. Schematic diagram of the experimental set up

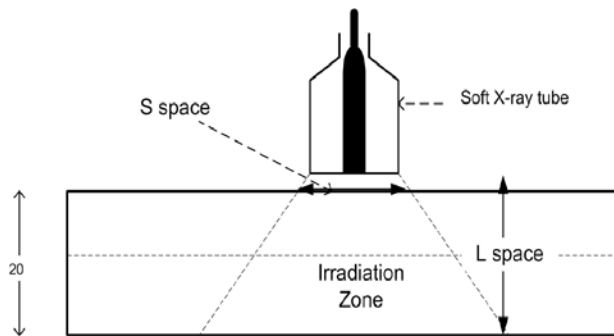


Figure 2. Details of the irradiation chamber and specification of the irradiation zone
(unit in millimeters)

Table 1. Experimental conditions used to study the influent of residence time and irradiation energy on PAHs decomposition efficiency.

Combustion operating			Soft X-ray Irradiation operating		
Combustion temperature (°C)	Heating rate (°C min ⁻¹)	Air flow rate (L min ⁻¹)	Soft X-ray	Residence time (Secound), (S space, mm)	Irradiation Energy (Kev), (L space, mm)
550	20	5	OFF	-	-
ON				0.04s, (S = 20 mm)	4.93 Kev,94.8%,(L=13 mm)
					4.73 Kev,90.9%,(L=23 mm)
				0.07s, (S = 30 mm)	4.93 Kev,94.8%,(L=13 mm)

PAHs analysis

Following the same procedure with the previous report^[7], particle-bound 16 PAH compounds were analyzed: Naphthalene (Nap), Acenaphthene (Ace), Phenanthrene (Phe), Anthracene (Ant), Fluorene (Fle), Fluoranthene (Flu), Pyrene (Pyr), Benzo[a]anthracene (BaA), Chrysene (Chr), Benzo[e]pyrene (BeP), Benzo[a]pyrene (BaP), Benzo[b]fluoranthene (BbF), Benzo[k]fluoranthene (BkF), Dibenz[a,h]anthracene (DBA), Indeno[1,2,3-cd]pyrene (IDP) and Benzo[g,h,i]perylene (BghiPe). Filter samples cut into small pieces were ultrasonically extracted in ethanol: benzene (1:3 v/v) for 15 min. After adding 50 µL of dimethyl sulfoxide (DMSO), the extracted solution was concentrated using a rotary evaporator (EYELA, NVC-2000). Extracted PAHs were analyzed using high-performance liquid chromatography (HPLC) (HITACHI, L-2130/2200/2300/2485) with a fluorescence detector and a Inertsil ODS-P reversed phase column (5 µm, φ 4.6-mm diameter, 250-mm length). The recovery efficiency was confirmed to be 0.82 ± 0.12 ($n = 3$) by adding a standard reagent (Accustandard, 0.2 mg/mL in CH₂Cl₂: MeOH (1:1)) to dissolved samples following previous reports^[6]. Filter blank values of PAHs were confirmed to be small enough then they were subtracted from analyzed values.

Results and Discussion

Characteristics of smoke particle

Fig. 3 shows the cumulative under size fraction of smoke particles in relation to irradiation time and irradiation energy level. Nanoparticles (< 70 nm) and ultrafine particles (0.07-0.43 µm) shows large fractions. Nanoparticles (<100 nm) are estimated by interpolating the distributions to be 20-30%, indicating an important contribution of nanoparticles from biomass burning. In addition the size distributions of smoke particle shows a single-model behavior in the

accumulation mode. However, irradiation of Soft X-ray does not have significant influence on both amount of smoke particle emission and particle size distribution.

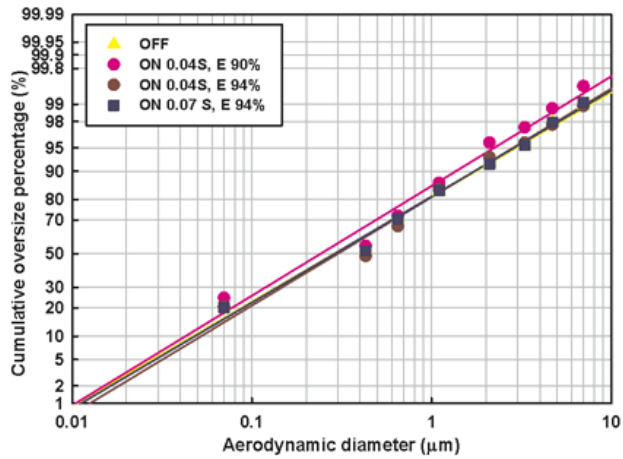


Figure 3. Shows the cumulative under size fraction of smoke particles in relation to irradiation time and irradiation energy level.

Characteristics of smoke particle-bound PAHs

Fig.4. Comparison of the emitted mass of particle-bound 4-6 ring PAHs per unit fuel mass from irradiated and not irradiated smoke particles for different particle size range. 4-6 rings PAHs emissions from smoke particle samples are reduced after irradiated with soft x-ray for all irradiation conditions. The emitted amount is rather constant for coarser particles ($>\sim 1 \mu\text{m}$) while it decreases more than 50% for particles smaller than $<\sim 1 \mu\text{m}$.

The PAHs decomposition efficiency for all conditions were calculated by comparison with the case of non irradiation. **Fig.5.** Comparison of the decomposition efficiency of PAHs in each particle size range at different irradiation conditions of soft X-ray. The decomposition efficiency of PAHs increases as the particle size decreases. In addition PAHs decomposition efficiency for nanoparticle ($< 70 \text{ nm}$) is more than 50% for all experimental conditions. The maximum of PAHs decomposition is more than 90% for nanoparticles at longest irradiation time and highest irradiation energy. This is because ultra-fine smoke particles contain more PAHs, especially smoke particles in nano-size range as shown in Fig.4^[8,9,10]. In addition, it is possible that soft X-ray irradiation is more effective for nanoparticles because of its limited permittivity deep inside the particles.

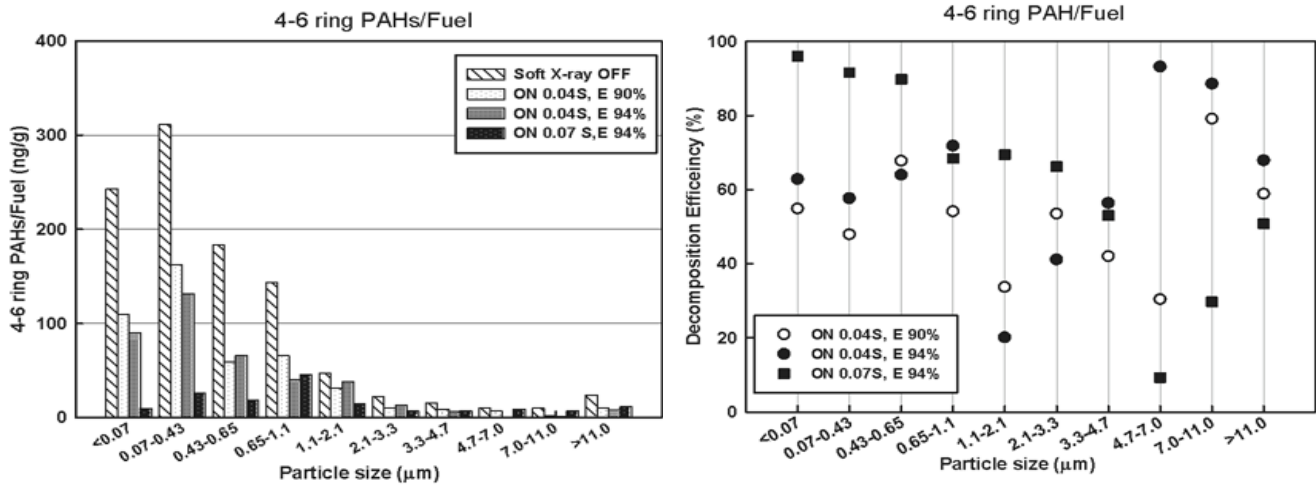


Figure 4. 4-6 rings PAH Mass per unit fuel mass in each size range at difference condition of soft X-ray irradiation

Figure 5. Decomposition Efficiency of 4-6 rings PAHs per smoke particle mass at difference conditions of soft X-ray irradiation in each particle size range.

CONCLUSION

The smoke particles from the rubber-wood burning in laboratory scale were shown to have a single modal. The smoke particles in nano-size range (<100 nm) have a major mass fraction more than 20% of total smoke particles as well as their large contribution to PAHs. Irradiation of Soft X-ray does not have significant influence on both amount of smoke particle emissions and particle size distributions. The decomposition efficiency of PAHs increases as the particle size decreases, especially for nanoparticles and with a slight dependent on irradiation time and irradiation energy. Soft X-ray irradiation is more effective for nanoparticles because of its limited permittivity deep inside the particles. Soft X-rays were shown to be potentially useful as an effective device for pollution control.

ACKNOWLEDGMENTS

The authors gratefully acknowledge, The Japan Society for the Promotion of Science (JSPS) and Center of Excellence for Innovation in Chemistry (PERCH-CIC).

REFERRENCES

- [1] Han, B., Shimada, M., Okuyama, K. and Choi, M. *Powder Technology*. 2003, 39, 336-344.
- [2] Sekikuchi, K., Juyoung, J. and Sakamoto, J. *Aerosols Res.* 2004, 19, 188-195.
- [3] Furuuchi, M., Chomanee, J., Thongyen, T., Hata, M., Tekasakul, P., Tekasakul, S., Limpaseni, W., Ikemoto, R. and Otani, Y. *International Symposium on contamination control (ISCC2010)*, Tokyo, A27.
- [4] Bai, Y., Furuuchi, M., Tekasakul, P., Tekasakul, S., Choosong, T. Aizawai, M., Hata, M. and Otani, Y. *Aerosol and air Quality Research*. 2007, 7, 79-94.
- [5] Hata, M., Fukumoto, M., Otani, Y., Yunhe, B., Sekiguchi, K., Tajima, N. and Furuuchi, M. *Proc. 6th Asian Aerosol Conference (AAC2009)*, Bangkok, AM-P-03.
- [6] Furuuchi, M., Eryu, K., Nagura, M., Hata, M., Kato, T., Tajima, N., Sekiguchi, K., Ehara, K., Seto, T. and Otani, Y. *Aerosol and air Quality Research*. 2010, 10, 185–192.
- [7] Furuuchi, M., Murase, T., Tsukawaki, Hang, P., Sieng, S. and Hata, M. *Aerosol and air Quality Research*. 2007, 7(2), 221-238.
- [8] Tekasakul, P., Furuuchi, M., Tekasakul, S., Chomanee, J. and Otani, Y. *Aerosol Air Qual. Res.* 2009, 8, 265-278.
- [9] Furuuchi, M., Tekasakul, P., Murase, T., Otani, Y., Tekasakul, S. and Bai, Y. *J. Ecotechnol. Res.* 2006, 12, 135-139.
- [10] Chomanee, J., Tekasakul, S., Tekasakul, P., Furuuchi, M. and Otani, Y. *Aerosol and air Quality Research*. 2009, 9, 404-411.

Carbonaceous Aerosols at Various UK Locations: Source Attribution, Composition and Evolution

Dantong Liu¹, James Allan^{1,2}, Michael Flynn¹, Gerard Capes¹, Gavin McMeeking^{1,*} and Hugh Coe¹

1School of Earth, Atmospheric and Environmental Sciences,
The University of Manchester, Oxford Road, Manchester, M13 9PL, UK

2National Centre for Atmospheric Science,
The University of Manchester, Oxford Road, Manchester, M13 9PL, UK

*now at Dept. of Atmospheric Science, Colorado State University, Fort Collins, Colorado, 80523
US

Principal Contact: Dantong Liu, Dr., School of Earth, Atmospheric and Environmental Sciences,
The University of Manchester, Oxford Road, Manchester, M13 9PL, UK,
Tel: +44 161 306 3914, Fax: +44 161 306 3951, Email: Dantong.liu@manchester.ac.uk

ABSTRACT

Carbonaceous aerosols contribute a significant amount to the submicron aerosol burden. Both black carbon (BC) and brown carbon, from absorbing organic material (OM), have been shown to be important absorbers of solar radiation, with important implications for the climate impacts of human activity. The results presented here are representative of urban, urban downwind and rural background environments in the UK. The chemical composition of aerosols and their atmospheric possessing across spatial and temporal scales are investigated. We examine the extent to which we are able to probe the physiochemical evolution of carbonaceous aerosol particles.

A suite of novel instruments were deployed to characterize the aerosol properties. Specifically, an Aerodyne Time-of-Flight Aerosol Mass Spectrometer (ToF-AMS) measured the chemical composition of submicron non-refractory particulate matter, such as organic matter (OM), sulfate and nitrate as a function of size and a Droplet Measurement Technologies single particle soot photometer (SP2) measured the mass, size distribution and mixing state of refractory BC particles.

Positive Matrix Factorization (PMF) analysis is applied to the mass spectra of OM to classify key types of organic particulate matter: Oxygenated organic aerosol (OOA) is a ubiquitous component in all environments; the emission of primary organic aerosol (POA) can be linked to types of identified sources, such as hydrocarbon-like OA (HOA) from vehicle emissions, solid fuel burning (SFOA) or cooking (COA) depending on anthropogenic activities. The emission of BC was correlated with POA linking to various sources. The experimental locations relative to pollutant sources and local meteorology influenced the constituents of carbonaceous aerosols and their diurnal patterns. Solid fuel burning was revealed to be an important contributing source under all types of environments during the winter time. The combined investigations under different environments suggest the OOA fraction and BC mixing state could indicate the extent of aerosol ageing.

KEYWORDS

CARBONACEOUS AEROSOL, OM, BC, AMS, SP2, PMF, SOURCE ATTRIBUTION

Introduction

Particles have long been known to significantly influence air quality and climate and to originate from a variety of sources. Primary aerosols are emitted directly into the atmosphere but undergo transformation in the atmosphere during transport. Secondary material is added both as additional mass to existing particles and through the formation of secondary aerosols. Recent studies on the source attribution of sub-micron aerosols have been primarily focused on the investigation of the organic fraction as individual organic compounds can be used as markers for certain sources^[1]. The Aerodyne Time of Flight Aerosol Mass Spectrometer (ToF-AMS) provides detailed information on the mass spectra of aerosols with high time resolution^[2]. The organic aerosol (OA) mass spectra obtained from AMS measurements is often incorporated into analysis mechanisms to identify the general classes of OA. Positive matrix factorization (PMF)^[3] has been applied to the time series of organic mass spectra obtained from the ToF-AMS in a variety of polluted environments to identify key types of OA^[4,5], for example, separating the measured signal as the oxygenated organic aerosol (OOA) that is mostly characteristics of secondary organic aerosol (SOA), and some classes of primary organic aerosol (POA) relating to different source sectors, such as hydrocarbon-like organic aerosol (HOA) or biomass burning organic aerosol (BBOA).

Besides OA, black carbon aerosol (BC) also contributes to carbonaceous particulate mass. The relationship between BC and OA has been widely used to diagnose the ageing of sources as BC

is conserved after emission other than through wet removal, whilst SOA greatly increases the OA mass with time [6 and references therein]. The emission of BC is concurrent with other combustion species, such as HOA and trace gases (e.g. CO, NOx). However, fresh OA undergoes gas phase repartitioning and is photochemically processed becoming more oxidized with time as distance from the source increases [7]. Ageing of aerosol often changes the hygroscopicity of the particles, thus affecting their atmospheric lifetime by modifying the efficiency of wet removal. Recently, studies on the evolution and ageing time of BC in the atmosphere became possible by examining its mixing state utilizing the single particle photometer instrument (SP2, manufactured by Droplet Measurement Technologies, Boulder, USA) [e.g. 8]. A better understanding of the BC mixing state is of great importance for modeling its lifetime in the atmosphere.

This article summarizes the results from our several recent campaigns conducted at ground stations, representative of urban, urban downwind and rural background environments in the UK. These experiments were all conducted in the late autumn-winter time, when the ambient temperature was low and localized residential heating sources were prevalent. In addition, the influence of urban sources such as vehicle emissions will depend on the locations of the sites and prevailing meteorological conditions. PMF analysis is applied to the mass spectra of organic aerosols measured by the AMS to attribute the OA from different sources at these sites. The refractory BC (rBC) mass and mixing state were measured by the Manchester SP2 instrument [9]. The physiochemical evolution of carbonaceous aerosol particles across spatial and temporal scales is investigated. The main sources of carbonaceous aerosols in Europe are emissions from traffic and residential combustion of solid fuels [10] and it is their emission and spatial and temporal variation that lead to the largest uncertainties [11]. Our results will therefore provide important constraints on modelling carbonaceous aerosols in northwestern Europe.

Experimental Methods

Site Description and Meteorological Conditions

A brief description of the experimental sites in this study is summarized in Tab.1, and their geographical locations are shown in Fig.1. The detailed description for each site is given in the corresponding reference.

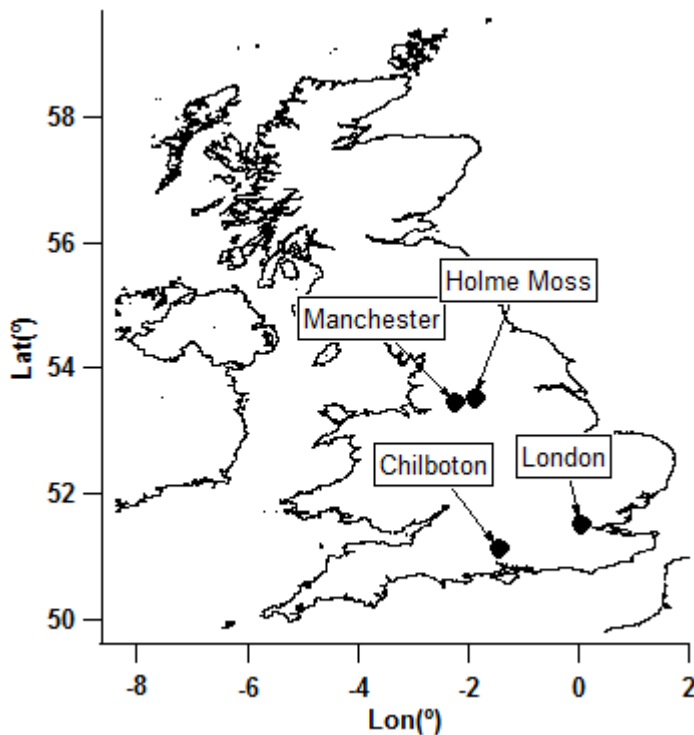


Fig.1. The geographical locations of experimental sites

For the urban studies^[12]: The London measurements were conducted in the “Inner Circle” of the Regent’s park (51.53°N , -0.153°E), which is a 300m diameter area surrounded by a park road and at a minimum distance of 500m from urban street traffic. Given that the park road is not used intensively by motor vehicles, it is assumed that at this location, the measurements are representative of the urban background atmosphere in an inner city location. In Manchester, the measurements were performed at roof level on the Sackville Street Building at The University of Manchester (53.476°N , -2.234°E). The aerosols were sub-sampled from the flow through a standard PM10 inlet, located on the northeastern side of the building at a height of approximately 35 m, above a street canyon and with no significantly taller buildings in the immediate vicinity.

For the urban downwind study^[13]: The Holme Moss site is positioned in the rural southern Pennines of Northern England at an altitude of 525m a.s.l. (53.53°N , 1.86°W), approximately 30km to the northeast of the city of Manchester. The experimental period lasted from 7 November 2006 to 4 April 2006, during which time the locally monitored wind speed was 10 to 15ms^{-1} , and the wind direction was from the southwest for 90% of the time. This led to efficient transport of urban pollutants from the Greater Manchester conurbation to the site. In addition, the site is in close proximity to several small towns, where the burning of wood, coke, coal and anthracite for domestic space heating is widespread in the winter^[15]. This meant the site was

significantly influenced by primary pollutants from combined sources.

For the rural background study^[14]: The measurements were taken at the Chilbolton Observatory (51.15°N, 1.44°W) in central southern England. The experimental site is on the outskirts of the village remote from the major urban centers. The typical local wind speed was below 6ms⁻¹ during the experiment, thus lack of efficient transport of pollutants from nearby sources.

Non-refractory Particle Composition

For all of the campaigns, the time resolved chemical mass loadings and distributions of key submicron non-refractory components of the aerosol (such as organic, nitrate and sulfate) were measured by an Aerodyne compact Time of Flight Aerosol Mass Spectrometer (cToF-AMS)^[2]. In addition, the cToF-AMS delivers time series of component mass spectra. Positive matrix factorization (PMF) was used to investigate the organic mass spectral profiles. PMF seeks to represent the measured data by a linear superposition of a number of unchanging mass spectral profiles as factors, and the contribution from each profile to the measured data as a function of time can be determined^[3,4]. The profiles of factors represent mass spectra and the changing contributions capture the variation of mass loadings to determine the varying relative contributions from each type which may be linked to a source. PMF analysis was performed on the data from all of the campaigns mentioned in this article.

Refractory BC Particles (rBC)

The physical properties of single refractory BC particles (rBC) were characterized by the single particle soot photometer (SP2). This instrument uses an intra-cavity Nd:YAG laser at 1064 nm to determine the size of a single particle by light scattering and quantify its rBC mass by detection of the incandescence radiation if the particle absorbs at the laser wavelength. The SP2 measurement was conducted at both Holme Moss and Chilbolton sites. The operation, calibration and data analysis methods for the Manchester SP2 instrument during the experiments are described elsewhere^[9,16]. The SP2 is capable of providing information on the mixing state of rBC by measurement of the delay time between the scattering and incandescence signals that is commonly referred to as the coating evaporation time. The SP2 can also be used to estimate the rBC mass fraction within a single particle for a coated rBC^[9]. A thicker coating on an rBC particle tends to increase the time delay and decrease the rBC mass fraction. The mixing efficiency of BC is defined as the number fraction of thickly coated BC particles.

Results and Discussion

Classification of PMF Factors

The PMF analyses are performed on all the urban ^[12], urban downwind ^[13], and rural data ^[14]. Given the PMF analysis for each project has been described in detailed in the corresponding references, this article will mainly summarize. In all three environmental locations, the Oxygenated Organic Aerosol (OOA) is consistently identified with a strong peak at m/z 44. This type of organic aerosol has been widely reported to represent aged secondary organic aerosols (SOA) ^[4,17]. The Hydrocarbon-like Organic Aerosol (HOA) is consistent with previously reported mass spectra associated with vehicle exhaust emissions ^[2,18], showing the largest peak at m/z 43 and 57, in addition to the characteristic peaks at 41, 43, 55 and 57 with a weak signal at 44. Another consistently resolved factor, Solid Fuel Organic Aerosol (SFOA), has some m/z signals similar to HOA (55, 57, 69, 71) and a notable signal at m/z 60, a typical indicator of levoglucosan, which is often a typical tracer for the organic aerosol from biomass burning as has been evidenced via the AMS measurement in both ambient and laboratory spectra ^[18,19]. The sum of HOA and SFOA is considered to constitute the majority of primary organic aerosols (POA=HOA+SFOA) at the urban downwind and rural locations. In the urban studies ^[12] a further factor was attributed to cooking organic aerosol (COA) in addition to HOA and SFOA (POA=HOA+SFOA+COA). There is little evidence of COA at the Holme Moss or Chilbolton sites. It is possible that there are other minor contributions to primary organic aerosol (POA) but these were not resolved by the PMF analysis.

The Source Attributions Under Different Environments

In common with other studies ^[20 and references therein], the POA should be correlated with other primary combustion emissions, such as BC; whereas the OOA has a signature of secondary aerosols, which has been revealed to have correlations with aerosol attributed to secondary species, such as sulphate and nitrate. Figure 2 shows the time series for the three PMF factors and identifies species that temporally correlate with the organic factors under both urban downwind and rural environments. The rBC loadings have both urban transport pollution and solid fuel burning sources, therefore at the Holme Moss or Chilbolton site, rBC was observed to have a closer correlation with POA rather than if solely correlated with HOA or SFOA. The OOA represents the contribution of aged, oxidized secondary organic material to the particulate mass, and, consistent with previous studies ^[4,20], is shown to be correlated with nitrate and sulfate. However, correlations between OOA and inorganic secondary species will depend on the relative similarities of the distributions of precursor emissions and formation processes.

The PMF mass fractions within total OM during experiments are summarized in Tab.2, and the averaged results are compared in Fig.2. The urban downwind and rural sites contain higher fraction of OOA compared to urban sites, indicative of the ageing process of organic aerosols and the formation of SOA when remote from sources^[20]. The OOA shows no obvious diurnal variability for all of these campaigns, indicating that it represents the regional background as has been observed in other studies^[4,5].

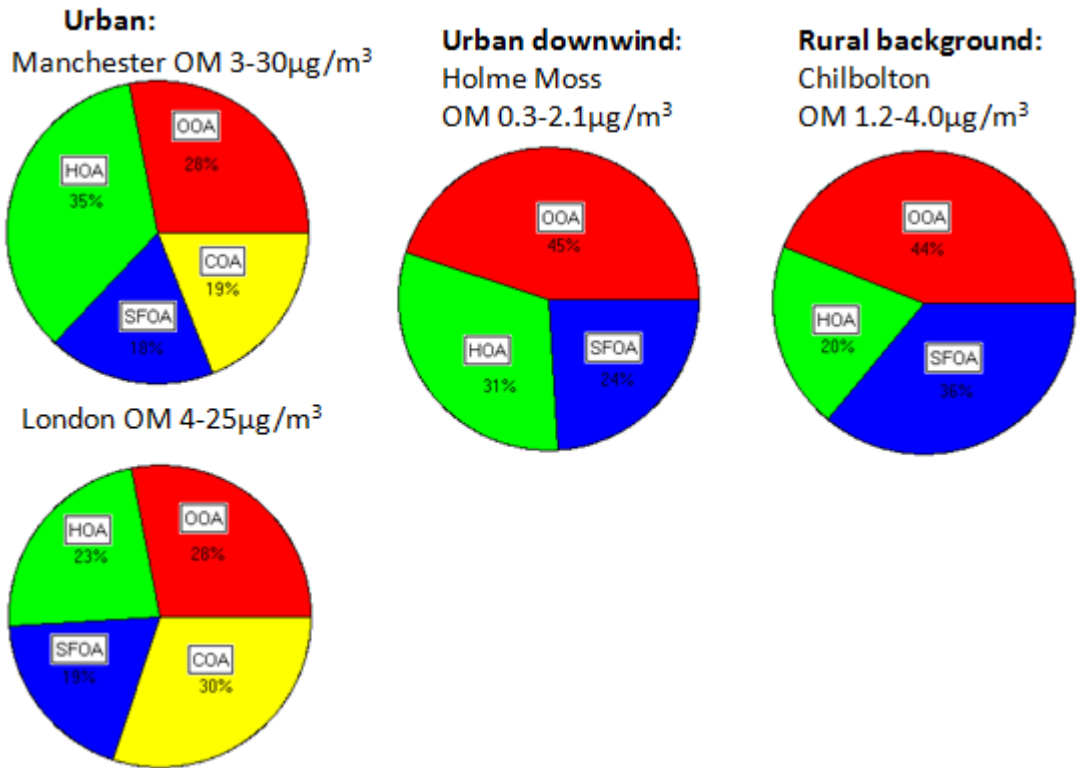


Fig.2. The averaged organic contributions from sources as analyzed by PMF during different campaigns.

OA at both urban and urban downwind locations is composed of a significant fraction of HOA as vehicle emissions are one of the primary sources in the urban environment. The location and meteorological conditions during the Chilbolton experiment mean that this site was less influenced by the urban vehicle emission sources, therefore the HOA at this rural site has a slightly lower fraction of HOA. Both the urban and urban downwind environments exhibited clear diurnal variations of HOA. In urban studies, the HOA peaked in the morning between 07:00 and 09:00 (Fig.3), coinciding with the traffic rush hour. Compared to the Manchester urban results, the HOA peak loading at the Holme Moss site was considerably lower and the morning occurrence of the peak urban pollution at the Holme Moss site, was delayed for about 1–2 hours. This is consistent with advection times from Manchester urban centre (~25 km) based on the

average local wind speeds ($10\text{--}13\text{ms}^{-1}$) and direction during the experiment^[13]. The average mass loading and the morning peak of HOA are both significantly reduced at weekends, which would be expected given the reduced traffic. At the Chilbolton rural site, HOA only showed a slight increase in the morning in the mean and 75% percentile value but displayed no apparent trend in the median. The weaker diurnal variation suggests the relatively minor influences from significant traffic sources, consistent with the lower wind speed at this site during the experimental period.

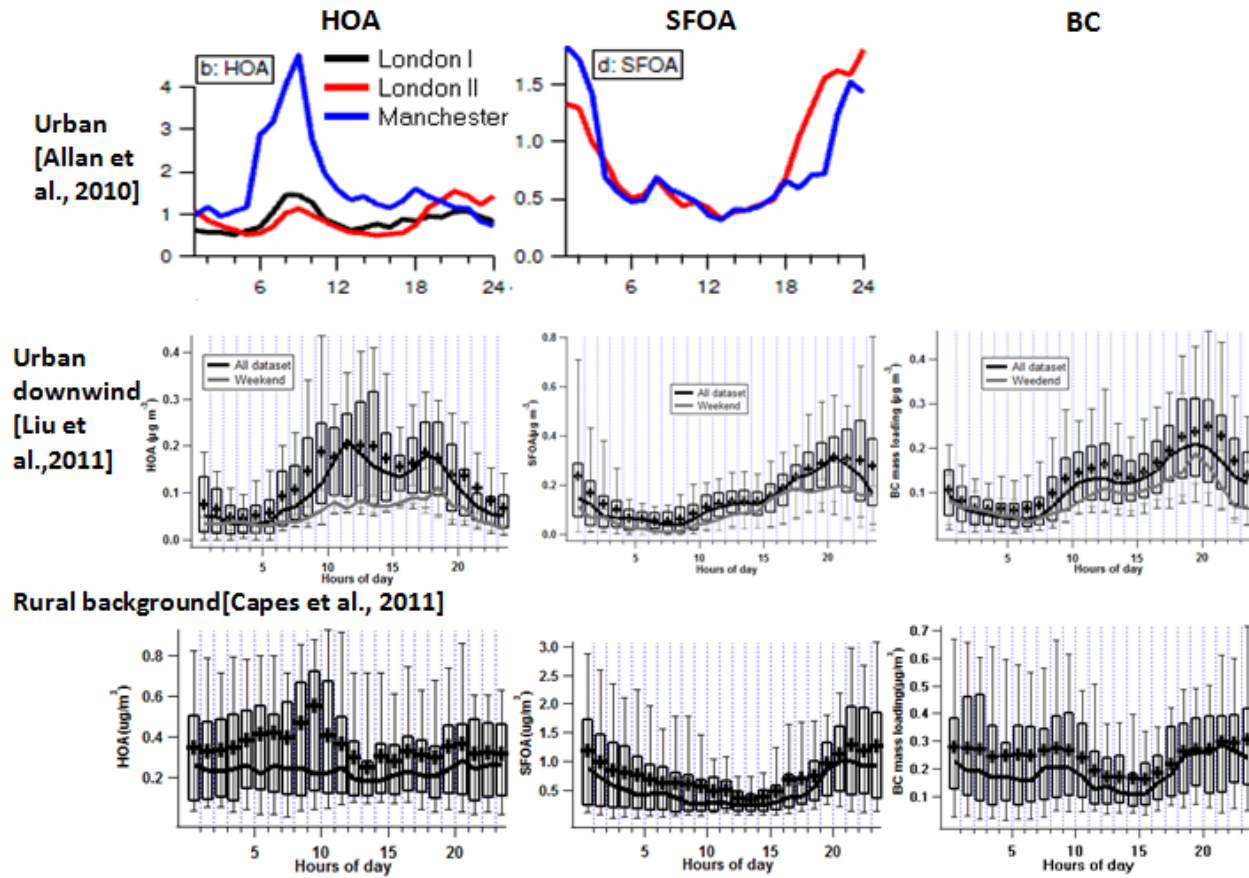


Fig.3. Diurnal variations of HOA, SFOA and BC for urban, urban downwind and rural background environments. The upper and lower edges of the box denote the 25% and 75% percentiles respectively. The lines in the middle of box and cross markers indicate the median and average values respectively, with error bars explaining the 10% and 90% percentiles.

SFOA serves as an important organic aerosol source for all types of UK sites during the winter seasons when the experiments were conducted. The SFOA constitutes a more important fraction at the non-urban sites as shown in Fig.2. Diurnal trends of SFOA have great similarities for all of the sites (Fig.3): tending to rise significantly from late afternoon and peaking in the evening. A UK national survey has shown that wood is commonly used as a space heating fuel in the UK^[15]. Although solid fuel burning that produces smoke is legislated against in most metropolitan areas

in the UK^[21], the practice of seasonal burning of smoking fuels such as wood in open fires is still widespread in the rural areas. Other solid fuels such as coal, anthracite and smokeless fuels are also strong contributors^[15]. In the winter, most burning for domestic space heating occurs in the late evening, which explains the observed occurrence of SFOA peak loadings for all of the experiments.

The diurnal peaks of rBC mass coincided with the peak loadings of either HOA or SFOA, because both traffic and solid fuel burning are important sources of BC aerosol.

Evolution of Aerosol Properties Related to Ageing

The BC mixing efficiency, defined as the number fraction of thickly coated BC particles as measured by the SP2, is a parameter to examine the mixing state of BC^[9] and the ageing of primary aerosols. At the urban downwind Holme Moss site, the minimum BC mixing efficiency was observed around 10:00 as shown in Fig.4, indicating a less atmospheric processing of BC particles. This time coincides with the HOA peak influenced by fresher urban outflow. The BC mixing state maintained an increasing trend throughout the average diurnal cycle, and reached a maximum at midnight when the surface temperature was low. However, at the rural background Chilbolton site, the BC mixing efficiency showed little diurnal variation and was higher than the fresher BC in Holme Moss when contributed by urban outflow. The lack of variability in the BC mixing state at Chilbolton suggests the BC at that local is characteristic of the regional background.

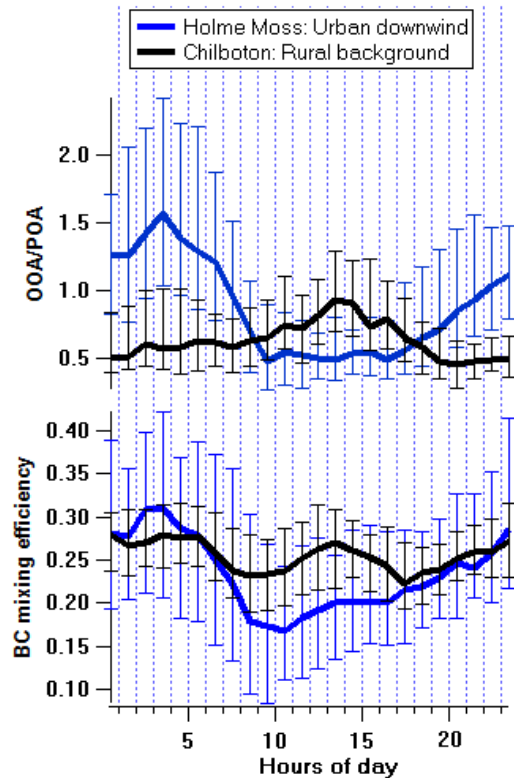


Fig.4. The diurnal variations of BC mixing efficiency and OOA/POA for Holme Moss and Chilbolton. The line is median value with error bars denoting 25% and 75% percentiles.

Given the OOA is mostly representative of secondary organic aerosol and the OOA fraction has been observed to increase with distance from sources as aerosols become aged^[20], the OOA/POA ratio is an important indicator of organic aerosol ageing. At the Holme Moss site, the OOA/POA had a strong positive correlation with BC mixing efficiency. This relationship describes a picture at this site of how the atmospheric processing on carbonaceous aerosols had developed: the BC and organic aerosol became eventually mixed and the latter becomes more oxygenated after emission. The regional background organic aerosols at Chilbolton showed a higher OOA/POA compared the fresher particles observed at Holme Moss corresponding to the BC mixing efficiency, however the organic aerosol was observed to be less oxygenated at night.

Tables

Table 1. The brief information of experimental sites mentioned in this study.

Site name	Site type	Geographical coordinates	Period	References
London	Urban	51.53°N, 0.15°W	Oct.-Nov.07	Allan et al., 2010[12]
Manchester	Urban	53.48°N, 2.23°W	Jan.-Feb.07	Allan et al., 2010[12]
Holme Moss	Urban downwind	53.53° N, 1.86°W	Nov.-Dec.06	Liu et al., 2011[13]
Chilbolton	Rural background	51.15°N, 1.44°W	Feb.-Mar.09	Capes et al., 2011[14]

Table 2. Summary of attributed mass fractions of organic species from sources analyzed by PMF during different campaigns.

Campaign	Site type	OOA	HOA	SFOA	COA
Manchester	urban	28%(24-28%)	35%(33-37%)	18%(13-23%)	19%(17-27%)
London	urban	28%(28-29%)	23%(15-23%)	19%(19-28%)	30%(29-30%)
Holme Moss	Urban downwind	45%(30-60%)	31%(18-42%)	24%(15-35%)	N/A
Chilbolton	Rural background	44%(35-47%)	20%(13-26%)	36%(28-55%)	N/A

SUMMARY

This article summarizes and compares our current and ongoing studies on the carbonaceous aerosols from the urban, urban downwind and rural sites in the UK. The AMS and SP2 are the key instruments we deployed to characterize the non-refractory compositions (such as organic, sulfate and nitrate) and refractory black carbon (BC) respectively. Particularly, the deconvolution of organic mass spectra is performed by PMF analysis to attribute sources, and the mixing state of BC is investigated by the fraction of thickly coated BC particles. Under all types of environments, the identified class oxygenated organic aerosol (OOA) represents the signature of secondary particles, though urban environments have a lower fraction of OOA due to the fresher contributing sources. The primary organic aerosols (POA) linked to different sources exhibited diurnal variations due to reproducible anthropogenic daily activities. For example, the urban and urban downwind environments showed strong influence from the traffic sector, as tracked by the hydrocarbon-like organic aerosol (HOA). The solid fuel organic aerosol (SFOA) emitted from solid fuel burning used for domestic space heating during the cold season, peaked consistently in the evening under all types of environments. This suggests the importance of solid fuel burning in contributing carbonaceous aerosols in the UK during the winter season. The emission of BC was correlated with POA linked to various sources. The carbonaceous aerosols influenced by fresher sources were associated with a lower extent of BC mixing and lower OOA/POA ratio, with BC mixing enhanced and organic aerosol oxygenated when particles became aged.

The traffic and residential combustion of solid fuels provide the main sources of carbonaceous aerosols in Europe, and their spatiotemporal emission rates are subject to large uncertainties^[10]. Our results provide the source-specific information on chemical compositions and emission rates of carbonaceous aerosols across spatial and temporal scales. Besides the urban emission, the domestic solid fuel burning was revealed to be a significant source during the cold season in the UK. The particle ageing after emission will influence their optical properties, i.e. the absorption enhancement due to BC internal mixing, and the affinity of water uptake, leading to climate impacts via direct and indirect radiative forcing effects. The regional modelling on the carbonaceous aerosols in the northwestern Europe will benefit from these results and ongoing studies.

REFERENCES

- [1] Rogge, W. F., Hildemann, L. M., Mazurek, M. A., Cass, G. R., and Simoneit, B. R. T.: Sources of fine organic aerosol, Environ. Sci. Technol., 27(4), 636–651, doi:10.1021/es00041a007, 1993.
- [2] Canagaratna, M. R. et al.: Chemical and microphysical characterization of ambient aerosols with the

- aerodyne aerosol mass spectrometer, *Mass Spectrom. Rev.*, 26, 185–222, 2007.
- [3] Paatero, P.: Least squares formulation of robust non-negative factor analysis, *Chemometr. Intell. Lab.*, 37, 23–35, 1997.
- [4] Lanz, V. A., Alfarra, M. R., Baltensperger, U., Buchmann, B., Hueglin, C., and Préevot, A. S. H.: Source apportionment of submicron organic aerosols at an urban site by factor analytical modelling of aerosol mass spectra, *Atmos. Chem. Phys.*, 7, 1503–1522, doi:10.5194/acp-7-1503-2007, 2007.
- [5] Ulbrich, I. M., Canagaratna, M. R., Zhang, Q., Worsnop, D. R., and Jimenez, J. L.: Interpretation of organic components from Positive Matrix Factorization of aerosol mass spectrometric data, *Atmos. Chem. Phys.*, 9, 2891–2918, doi:10.5194/acp-9-2891-2009, 2009.
- [6] Chu, S.: Stable estimate of primary OC/EC ratios in the EC tracer method, *Atmos. Environ.*, 39, 8, 1383–1392, 2005.
- [7] Jimenez, J. L. et al.: Evolution of Organic Aerosols in the Atmosphere, *Science*, 326, 1525–1529, doi:10.1126/science.1180353, 2009.
- [8] Schwarz, J. P. et al.: Single-particle measurements of midlatitude black carbon and light-scattering aerosols from the boundary layer to the lower stratosphere, *J. Geophys. Res.*, 111, D16207, doi:10.1029/2006JD007076, 2006.
- [9] Liu, D., Flynn, M., Gysel, M., Targino, A., Crawford, I., Bower, K., Choularton, T., Jurányi, Z., Steinbacher, M., Hüglin, C., Curtius, J., Kampus, M., Petzold, A., Weingartner, E., Baltensperger, U., and Coe, H.: Single particle characterization of black carbon aerosols at a tropospheric alpine site in Switzerland, *Atmos. Chem. Phys.*, 10, 7389–7407, doi:10.5194/acp-10-7389-2010, 2010.
- [10] Kupiainen, K. and Klimont, Z.: Primary emissions of fine carbonaceous particles in Europe, *Atmos. Environ.*, 41, 2156–2170, 2007.
- [11] Tsyro, S., Simpson, D., Tarrason, L., Klimont, Z., Kupiainen, K., Pio, C., and Yttri, K. E.: Modeling of elemental carbon over Europe, *J. Geophys. Res.-Atmos.*, 112, D23S19, doi:10.1029/2006JD008164, 2007.
- [12] Allan, J. D., Williams, P. I., Morgan, W. T., Martin, C. L., Flynn, M. J., Lee, J., Nemitz, E., Phillips, G. J., Gallagher, M. W., and Coe, H.: Contributions from transport, solid fuel burning and cooking to primary organic aerosols in two UK cities, *Atmos. Chem. Phys.*, 10, 647–668, doi:10.5194/acp-10-647-2010, 2010.
- [13] Liu, D., Allan, J., Corris, B., Flynn, M., Andrews, E., Ogren, J., Beswick, K., Bower, K., Burgess, R., Choularton, T., Dorsey, J., Morgan, W., Williams, P. I., and Coe, H.: Carbonaceous aerosols contributed by traffic and solid fuel burning at a polluted rural site in Northwestern England, *Atmos. Chem. Phys.*, 11, 1603–1619, doi:10.5194/acp-11-1603-2011, 2011.
- [14] G.L. Capes, P.I. Williams, M.J. Flynn, K.N. Bower and T. W. Choularton: Composition and hygroscopic properties of background aerosols at a rural U.K. site. European Aerosol Conference, Manchester, 2011.
- [15] National atmospheric emissions inventory (NAEI): available at: <http://www.naei.org.uk>, last access: 4 August 2009.
- [16] McMeeking, G. R., Hamburger, T., Liu, D., Flynn, M., Morgan, W. T., Northway, M., Highwood, E. J., Krejci, R., Allan, J. D., Minikin, A., and Coe, H.: Black carbon measurements in the

boundary layer over western and northern Europe, *Atmos. Chem. Phys.*, 10, 9393–9414, doi:10.5194/acp-10-9393-2010, 2010.

[17] McFiggans, G., Alfarra, M. R., Allan, J., Bower, K., Coe, H., Cubison, M., Topping, D., Williams, P., Decesari, S., Facchini, C., and Fuzzi, S.: Simplification of the representation of the organic component of atmospheric particulates, *Faraday Discuss.*, 130, 341–362, 2005.

[18] Schneider, J., Hock, N., Weimer, S., and Borrmann, S.: Nucleation particles in diesel exhaust: Composition inferred from in situ mass spectrometric analysis, *Environ. Sci. Technol.*, 39, 6153–6161, 2005.

[19] Alfarra, M. R., Prevot, A. S. H., Szidat, S., Sandradewi, J., Weimer, S., Lanz, V. A., Schreiber, D., Mohr, M., and Baltensperger, U.: Identification of the mass spectral signature of organic aerosols from wood burning emissions, *Environ. Sci. Technol.*, 41, 5770–5777, doi:10.1021/Es062289b, 2007.

[20] Zhang, Q. et al.: Ubiquity and dominance of oxygenated species in organic aerosols in anthropogenically-influenced Northern Hemisphere midlatitudes, *Geophys. Res. Lett.*, 34, L13801, doi:10.1029/2007GL029979, 2007.

[21] Smoke control areas: <http://www.uksmokecontrolareas.co.uk>, last access: 6 April 2009.

Measurement of Organic Aerosol Using a High-Resolution Aerosol Mass Spectrometer at a Forest Site in Japan

Yuemei Han¹, Yoko Iwamoto¹, Tomoki Nakayama² and Michihiro Mochida¹

1 Graduate School of Environmental Studies, Nagoya University, Nagoya, 464-8601, Japan

2 Solar-Terrestrial Environment Laboratory, Nagoya University, Nagoya, 464-8601, Japan

ABSTRACT

The physical and chemical properties of atmospheric aerosols were studied at a remote forest site, Wakayama, Japan, from 20 to 30 August, 2010. An Aerodyne high-resolution time-of-flight aerosol mass spectrometer (HR-ToF-AMS) was deployed to measure non-refractory species in submicron particles, including sulphate, nitrate, ammonium and organics. The number-size distributions of aerosols were measured using a scanning mobility particle sizer (SMPS). The temporal variations of aerosol properties and the results from backward air mass trajectory analysis (HYSPPLIT) suggests that aerosols in the first six days were under the influence of long-range transported anthropogenic aerosols and that the influence was smaller in the next four days. The events of new particle formation and the subsequent growth, which were evidenced by the substantial increase in the number concentrations of particles with the mobility diameter below ~150 nm, were frequently observed in the last four days of the observation period. Organic component was abundant even below 100 nm in vacuum aerodynamic diameter during this period. These characteristics can be explained by the transport of clean air masses from the North Pacific, which probably lead to lower aerosol concentrations and resulted in the dominance of secondary organic aerosol (SOA) formed from biogenic volatile organic compounds (VOCs). Two organic components, low-volatile oxygenated organic aerosol (LV-OOA) and semivolatile OOA (SV-OOA) were resolved by Positive Matrix Factorization (PMF) analysis. LV-OOA, which correlated well with sulfate and nitrate, was probably composed of long-range transported aerosols from anthropogenic sources and some biogenic SOA. SV-OOA may have mainly been composed of the biogenic SOA; its mass fraction increased substantially in the new particle formation and growth periods.

KEYWORDS

HR-ToF-AMS, Biogenic aerosol, Particle growth, PMF analysis

Introduction

Organic species generated from anthropogenic and natural sources constitute a substantial mass

fraction of submicron aerosols in the atmosphere^[1,2]. Recent laboratory and field studies indicate that biogenic volatile organic compounds (BVOCs), which are emitted mainly from terrestrial vegetation, such as isoprene, monoterpene, and sesquiterpenes, form large amounts of secondary organic aerosol (SOA). Model studies estimated global budget of biogenic SOA (12-70 Tg yr⁻¹) to be an order of magnitude higher than that of anthropogenic SOA (2-12 Tg yr⁻¹)^[3,4,5]. However, significant uncertainties exist in quantification of biogenic SOA in worldwide areas.

Here, we present results from a field observation using an Aerodyne high-resolution time-of-flight aerosol mass spectrometer (HR-ToF-AMS) and other instruments at a forest site of Japan, in the summer of 2010. The main objective is to characterize the properties of aerosols at the forest site and to identify their sources.

Experimental Methods

Field measurement of atmospheric aerosols was conducted from 20 to 30 August, 2010 at Wakayama Forest Research Station (WFRS, 34.07° N, 135.52° E, as shown in Fig.1), Field Science Education and Research Center of Kyoto University, Japan.

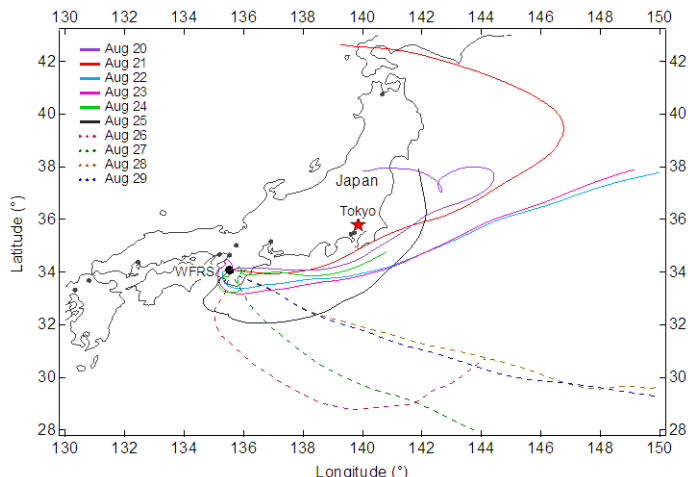


Fig.1. Location of the measurement site and backward air mass trajectories for the days during the observation period.

An Aerodyne HR-ToF-AMS and a TSI 3936 scanning mobility particle sizer (SMPS) were operated to measure the non-refractory (NR) chemical species and number-size distributions of submicron aerosol particles, respectively. The ToF-AMS software of SQUIRREL (version 1.51B) was used to generate the mass spectra and P-ToF size distribution in unit mass resolution; PIKA (version 1.10B) was used to generate high resolution mass spectra. The HR organic mass spectra were resolved using Positive Matrix Factorization (PMF) Evaluation Tool (PET, version 2.03A)^[6]. The collection efficiency of 0.5 was used for the AMS data processing. However, the absolute mass concentrations of chemical species measured using the AMS were not reported

here, because CE lower than 0.5 is suggested from the comparison of AMS and SMPS data. Backward trajectories of air masses were calculated by the Hybrid Single Particle Lagrangian Integrated Trajectory Model (HYSPLIT 4)^[7]. The HYSPLIT 4 model was performed in the duration of 96 hours at 500m above ground level every day (start at 0900 LT) in the observation period.

Results and Discussion

Backward Trajectory of Air Masses

The backward trajectories of air masses arrived at WFRS during the observation period are presented in Fig.1. The trajectories show two distinct origins and transport pathways of the air masses. The air masses trajectories for the first six days (from 0600 LT, 20 Aug to 0600 LT, 26 Aug) mainly pass near the coastal areas in Japan (around some megacities, such as Tokyo). The passage of air masses over other anthropogenic source regions further in the past is possible, which is however not studied yet. The trajectories for the following four days (from 0600 LT, 26 Aug to 0600 LT, 30 Aug) are from the area apart from Japan over the North Pacific.

Aerosol Chemical Composition

The time series of the AMS-derived composition of NR-PM₁ species are presented in Fig.2. Organics, sulfate, and ammonium were three dominant components, which accounted for, respectively, 43%, 40%, and 14% of the total NR-PM₁ mass on average.

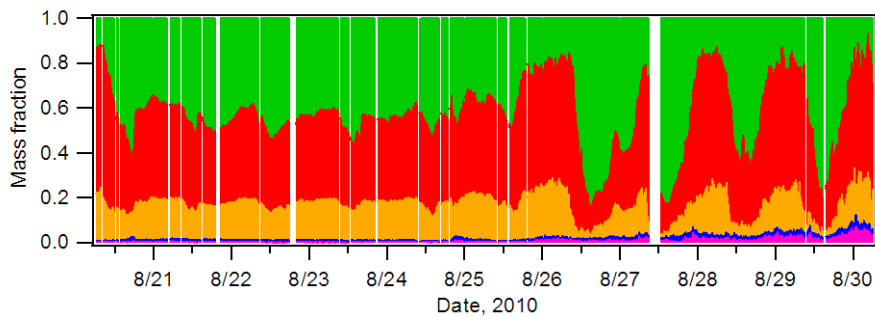


Fig.2. Time series of mass fractions of NR-PM₁ chemical species

Whereas the mass fractions of five chemical components did not change significantly in the first six days, they showed pronounced diurnal variations in the next four days. From the chemical composition and the backward air mass trajectories, it can be deduced that air mass origin was a significant factor that influenced on the total aerosol burden at WFRS. This result is similar to those from previous studies at other forest sites^[8,9]. The air masses from the coastal areas probably transported anthropogenic pollutants that would contribute to the aerosol mass in the first six days. The air masses from the area apart from Japan (i.e., the North Pacific) may be cleaner, because of which biogenic aerosols generated from the local forest vegetation were

presumably the dominant contributor to the organic aerosol mass. The AMS-derived size distribution data show that sulfate was abundant in the vacuum aerodynamic diameter (d_{va}) of ~600 nm in the first six days and ~400 nm in the next four days. Organics distributed in the smaller size range and even extended to below 100 nm in the last four days.

Aerosol Number-Size Distribution

As shown in Fig.3, the number-size distributions of aerosol particles in the first six days have the maximum at the mobility diameters (d_m) of ~100 nm. The size distributions in the next four days were characterized by the dramatically increased number concentrations of ultrafine particles at ~1000 LT every morning, and the subsequent particle growth that lasted several hours. This phenomenon is very similar to that of the typical new particle formation and growth events observed in a variety of environments^[10].

The estimated air mass origins and the number-size distributions of aerosol particles suggest that new particle formation and growth events at WFRS mainly occurred when the clean air masses from the North Pacific arrived at the area. This is probably because the surface areas of pre-existing particles were quite low in the clean air, which would provide a favorable condition for particle nucleation. Secondary organic aerosols formed from the biogenic VOCs are probably the dominant sources of new particles in this forest environment. In addition, other environmental factors, such as temperature, humidity, and wind, may also affect the aerosol processing.

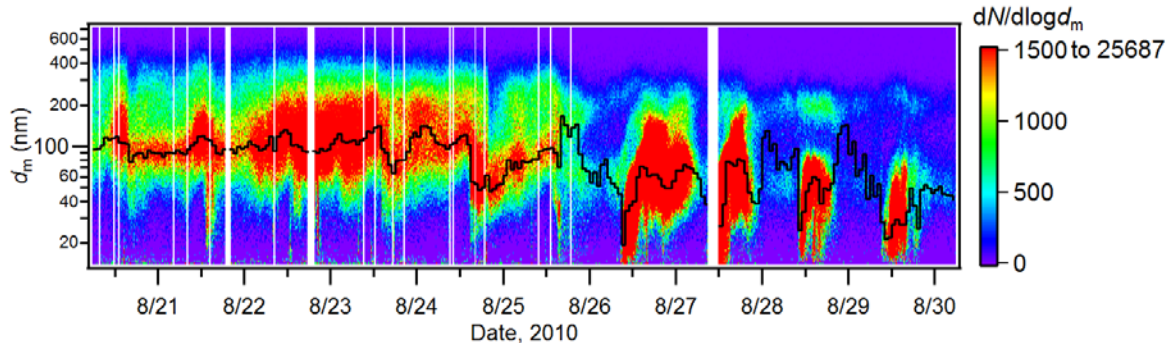


Fig.3. SMPS-derived particle number-size distributions. The solid black line represents the diameters at which the concentrations were the highest.

PMF Analysis

Two oxygenated organic aerosol (OOA) components, low volatile OOA (LV-OOA) and semivolatile OOA (SV-OOA), were retrieved from the PMF analysis. The mass spectra of two OOA components are both dominated by the $C_xH_yO_z$ ion family, that is CO_2^+ (m/z 44) for LV-OOA and $C_2H_3O^+$ (m/z 43) for SV-OOA. LV-OOA has a higher O/C ratio (0.63) and lower H/C ratio (1.20), comparing with O/C 0.35 and H/C 1.38 for SV-OOA. The temporal variation of LV-OOA correlated well with sulfate ($r^2= 0.85$) and nitrate ($r^2= 0.63$); while SV-OOA did not

correlate strongly with sulfate and nitrate (r^2 were 0.40 and 0.53, respectively). LV-OOA was the dominant organic component in the first six days, which accounted for 66% of the total organic mass on average. The mass fraction of SV-OOA increased in the last four days, which account for 50% of the total organic mass. The mass concentrations of LV-OOA in the first six days were much higher than those in the next four days. Unlike LV-OOA, a strong diurnal variation pattern was observed for SV-OOA throughout the measurement period.

CONCLUSIONS

The chemical compositions, size distributions, and sources of submicron aerosols have been characterized by using the HR-ToF-AMS and other instruments at Wakayama Forest Research Station (WFRS) of Japan in the summer of 2010. Organics, sulfate, and ammonium were three dominant components of NR-PM₁. Air mass origin was probably an important factor influencing on the total aerosol burden. The particle size distribution patterns in the first six days were different from those in the next four days. The temporal variations of aerosol properties and the results from backward air mass trajectory analysis suggest that aerosols in the first six days were under the influence of long-range transported anthropogenic aerosols and that the influence was smaller in the next four days. New particle formation and growth events were occurred repeatedly when air masses from the area apart from Japan over the North Pacific arrived, which is presumably due to the favorable environmental condition of the lower surface area of pre-existing particles. LV-OOA and SV-OOA were retrieved from the HR organic mass spectra by the PMF analysis. LV-OOA positively correlated with sulfate and nitrate, suggesting that they were composed of long-range transported organic aerosols from anthropogenic sources as well as some biogenic SOA. SV-OOA had a strong diurnal variation pattern and probably related to the biogenic SOA.

ACKNOWLEDGMENTS

This study was supported in part by JSPS KAKENHI 20671001 and the Program for Improvement of Research Environment for Young Researchers from Special Coordination Funds for Promoting Science and Technology (SCF) commissioned by MEXT. The authors greatly appreciate the assistance from Wakayama Forest Research Station (WFRS), Field Science Education and Research Center of Kyoto University, Japan. We acknowledge the NOAA Air Resources Laboratory (ARL) for the provision of the HYSPLIT transport and dispersion model and/or READY website (<http://www.arl.noaa.gov/ready.php>).

REFERENCES

- [1] Kanakidou, M.; Seinfeld, J. H.; Pandis, S. N., et al. *Atmos. Chem. Phys.* 2005, 5, 1053-1123.

- [2] Zhang, Q.; Jimenez, J. L.; Canagaratna, M. R., et al. *Geophys. Res. Lett.* 2007, **34** (13), doi:10.1029/2007GL029979.
- [3] Hallquist, M.; Wenger, J. C.; Baltensperger, U., et al. *Atmos. Chem. Phys.* 2009, **9** (14), 5155-5236.
- [4] Carlton, A. G.; Wiedinmyer, C.; Kroll, J. H. *Atmos. Chem. Phys.* 2009, **9** (14), 4987-5005.
- [5] Kesselmeier, J.; Staudt, M. *J Atmos Chem* 1999, **33** (1), 23-88.
- [6] Ulbrich, I. M.; Canagaratna, M. R.; Zhang, Q., et al. *Atmos. Chem. Phys.* 2009, **9** (9), 2891-2918.
- [7] Draxler, R. R.; Rolph, G. D. HYSPLIT (<http://www.arl.noaa.gov/ready/hysplit4.html>), NOAA Air Resources Laboratory, Silver Spring, MD, USA 2003.
- [8] Allan, J. D.; Alfarra, M. R.; Bower, K. N., et al. *Atmos. Chem. Phys.* 2006, **6**, 315-327.
- [9] Raatikainen, T.; Vaattovaara, P.; Tiitta, P., et al. *Atmos. Chem. Phys.* 2010, **10** (4), 2063-2077.
- [10] Holmes, N. S. *Atmos Environ* 2007, **41** (10), 2183-2201.

Overview of Submicron Aerosol Characterization in China Using an Aerodyne High-resolution Aerosol Mass Spectrometer

Xiaofeng Huang¹, Lingyan He¹, Lian Xue¹, Min Hu² and Yuanhang Zhang²

1 Key Laboratory for Urban Habitat Environmental Science and Technology, School of Environment and Energy, Peking University Shenzhen Graduate School, Shenzhen, China

2 State Key Joint Laboratory of Environmental Simulation and Pollution Control, College of Environmental Sciences and Engineering, Peking University, Beijing, China

ABSTRACT

China is one of the most rapidly developing countries in the world, but in the meantime it is suffering from severe air pollution due to heavy industrial/metropolitan emissions. Most previous aerosol studies in China were based on filter sampling followed by laboratory analysis, which provided datasets at a coarse time resolution like a day. The coarse time resolution of the aerosol datasets cannot match the actual faster variation of aerosol properties in the real atmosphere, which strongly favors highly time-resolved on-line measurement techniques. In recent years, our group deployed an Aerodyne high-resolution aerosol mass spectrometer (AMS) in different ambient atmospheres in China. In this presentation, we will overview these on-line AMS measurement results to characterize the properties of submicron particles in China atmosphere, with an emphasis for the Pearl River Delta region.

KEYWORDS

AMS, aerosol characterization

1. Introduction

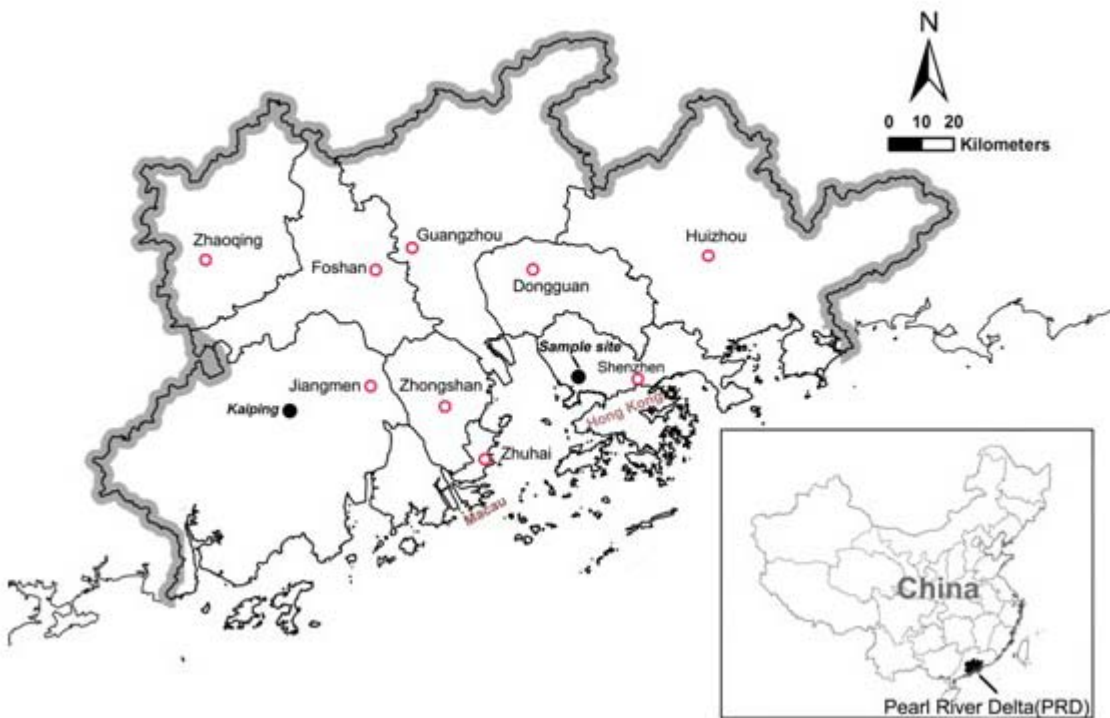
The Pearl River Delta (PRD) region is one of the most developed regions in China and noted for its rapid economic development due to manufacturing and export industries, which comes with the consequence of fast deterioration of its atmospheric environment from urban to regional scales^[1, 2]. The most apparent phenomenon of air pollution in PRD is the regional hazy days due to high concentrations of airborne fine particles in the ambient air^[3, 2]. Most of previous aerosol studies in PRD have been based on filter sampling, which offers measurement results with low time-resolution, such as 24 h^[4-6], although the chemical complexity and labile nature of aerosols as well as fast variation of meteorological conditions necessitate highly time-resolved on-line

analysis. In order to understand in depth the chemical and physical processes causing fine particle pollution in PRD, we deployed an Aerodyne high-resolution time-of-flight aerosol mass spectrometer (HR-ToF-AMS) at a rural site (Kaiping) during fall 2008 and at an urban site (Shenzhen) during fall 2009 to measure PM₁ chemical composition with high time-resolution. This presentation reports the highly time-resolved measurement results of HR-ToF-AMS in the campaigns and the results of factor analysis for OA source apportionment based on high-resolution mass spectrometry.

2. Experimental Methods

2.1. Sampling site and period

The Kaiping rural site was located at a patriotic educational base (22.32° N, 112.53° E), about 120 km away from Guangzhou. This site was surrounded by shrubs and eucalyptus forest and was free of any significant local pollution emissions. The Kaiping campaign lasted from October 12 to November 18, 2008. Shenzhen (113.9° E, 22.6° N) is located in the subtropics along the southeast coast of China, as shown in Figure 1. The sampling site was on the campus of Shenzhen Graduate School, Peking University in the western urban area of Shenzhen. The Shenzhen campaign was conducted between 25 October and 2 December 2009.

Figure 1. The location of the sampling sites. 

2.2. Operation of HR-ToF-AMS and other instruments

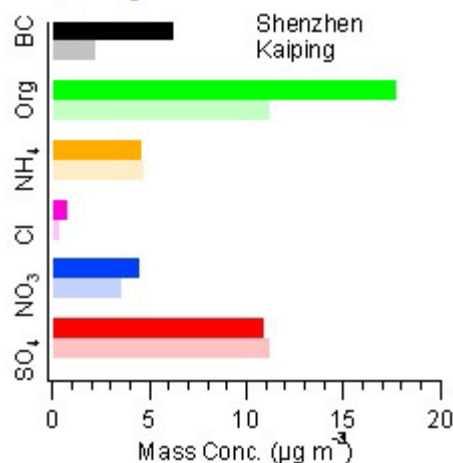
An Aerodyne high-resolution time-of-flight aerosol mass spectrometer was deployed in the campaigns. A PM_{2.5} cyclone inlet was set up on the roof of the building to remove coarse particles and introduce air stream into the room through a copper tube with a flow rate of 10 l min⁻¹. The HR-ToF-AMS sampled isokinetically from the center of the copper tube without drying at a flow rate of 80 cc min⁻¹. The detailed instrumental description of HR-ToF-AMS was shown by DeCarlo et al. [7]. Mass concentrations and size distributions of the aerosol species measured with the HR-ToF-AMS were calculated using the methods outlined by DeCarlo et al. . Standard ToF-AMS data analysis software packages (SQUIRREL v1.49 and PIKA v1.08) downloaded from the ToF-AMS-Resources webpage (<http://cires.colorado.edu/jimenez-group/ToFAMSResources/ToFSoftware/index.html>) were used to generate unit and high-resolution mass spectra from the V-mode and W-mode data, respectively.

3. Results and Discussion

3.1. PM₁ composition

Figure 2 compares the mean concentrations of individual PM₁ species observed in Shenzhen and at Kaiping. It is found that sulfate and ammonium had almost the same mean concentrations in Shenzhen and at Kaiping, strongly indicating they are mainly a regional pollutant in PRD. In contrast, the mean concentrations of organics, chloride, and BC in Shenzhen are much higher than at Kaiping, suggesting there are more local emissions of them in Shenzhen. Nitrate has a little higher mean concentration in Shenzhen than at Kaiping, implying it has some fresh local formation. The mean non-refractory PM₁ mass concentration in Shenzhen (38.3 µg m⁻³, without BC) is also higher than those observed in urban atmospheres in developed countries (below 20 µg m⁻³) [8], but lower than that during summertime in urban Beijing (61 µg m⁻³) [9].

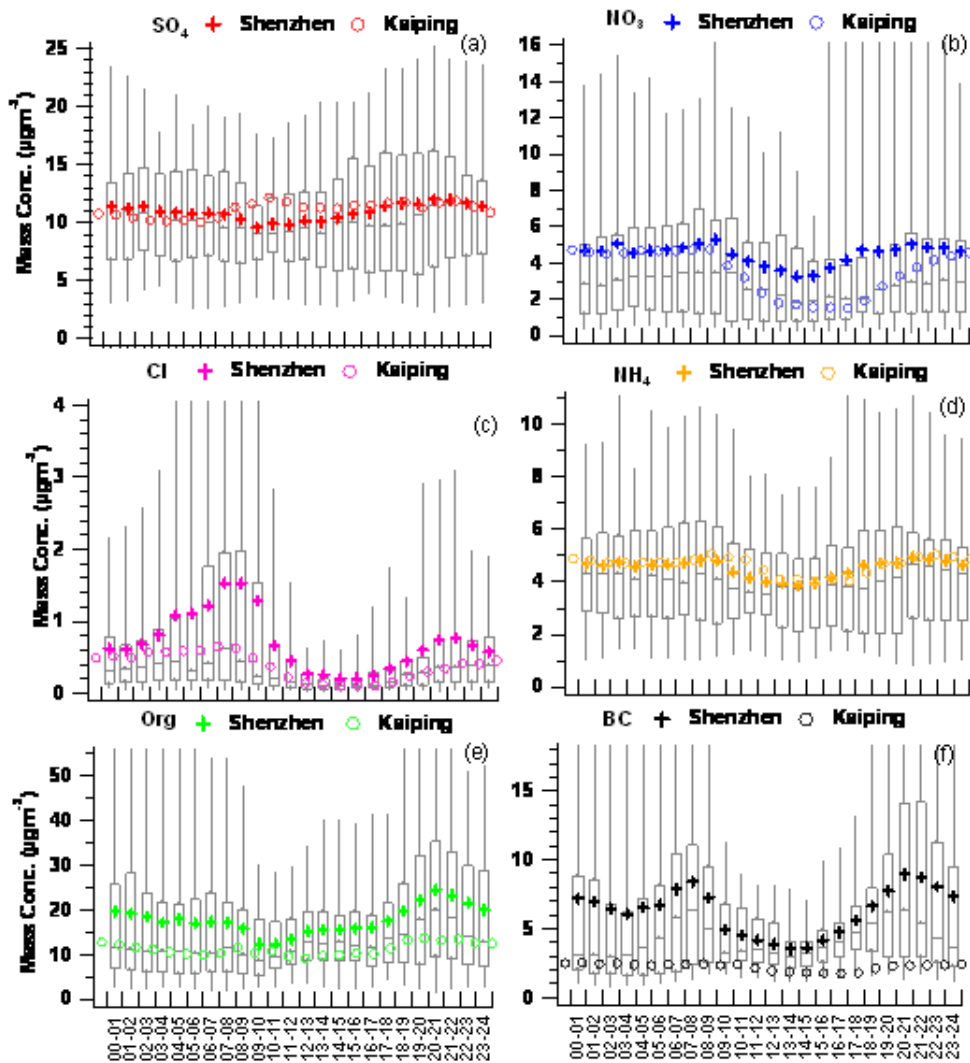
Figure 2. The comparison of PM₁ component concentrations in Shenzhen and at Kaiping.



3.2. Diurnal patterns of PM₁ species

Figure 3 presents the mean diurnal variations of different PM₁ species during the two campaigns. In terms of hourly mean concentrations, sulfate showed small diurnal variation. A slight concentration growth of sulfate in the daytime suggests significant photochemical production of (NH₄)₂SO₄ in the campaigns. Nitrate showed lower concentrations in the afternoon, suggesting that gas-aerosol partitioning was the dominant control mechanism^[10]. The higher and earlier lowest hourly concentration of nitrate in Shenzhen compared to at Kaiping implies more active photochemical formation of nitrate in Shenzhen, which is consistent with large emissions of NO_x from vehicles in urban areas. Due to the semi-volatile nature of NH₄Cl and the variation of PBL, chloride showed much lower concentrations in the afternoon. Ammonium showed lower concentrations in the afternoon, which was the combined result of the variations of (NH₄)₂SO₄, NH₄NO₃ and NH₄Cl. As organic matter has both large primary and secondary sources and is also influenced by semi-volatile compounds, the observed diurnal variation of organic matter was a complicated result. In comparison with the stable BC concentrations during the whole day at Kaiping, BC showed two peaks in Shenzhen in the early morning and early evening due to the effects of both lower PBL and rush hour traffic.

Figure 3. Diurnal variation box plots of PM₁ species in Shenzhen (as well as those at Kaiping).



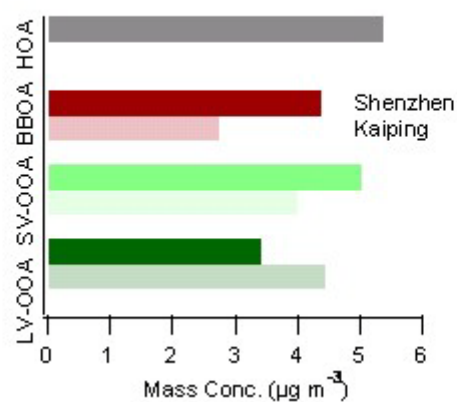
3.3. Organic aerosol source apportionment

Positive matrix factorization (PMF) analysis^[11] was conducted on the high-resolution mass spectra measured with HR-ToF-AMS to identify major organic components. Four organic components was identified in the Shenzhen campaign included a hydrocarbon-like (HOA), a biomass burning (BBOA) and two oxygenated (LV-OOA and SV-OOA) OA components, while only BBOA, LV-OOA and SV-OOA were identified in the Kaiping campaign.

Figure 4 compares the mean concentrations of the OA components observed in Shenzhen and at Kaiping. It is seen that the mean concentration of BBOA in Shenzhen is higher than at Kaiping,

possibly due to different intensities of crop residue burning events in rural areas during the two campaigns. The mean concentration of SV-OOA is some higher in Shenzhen while the mean concentration of LV-OOA is higher at Kaiping. This may implies that the formation of SV-OOA is more active in Shenzhen while the formation of LV-OOA is more active at Kaiping, which is supported by their diurnal variations as discussed later. In terms of the sum of LV-OOA and SV-OOA concentrations, it is the same in Shenzhen ($8.4 \mu\text{g m}^{-3}$) and at Kaiping ($8.4 \mu\text{g m}^{-3}$), indicating SOA is mostly a regional pollutant in PRD. There was no component like HOA identified by PMF analysis at Kaiping, which was mainly attributed to the dilution and oxidation of HOA during the pollutant transport from source areas^[12].

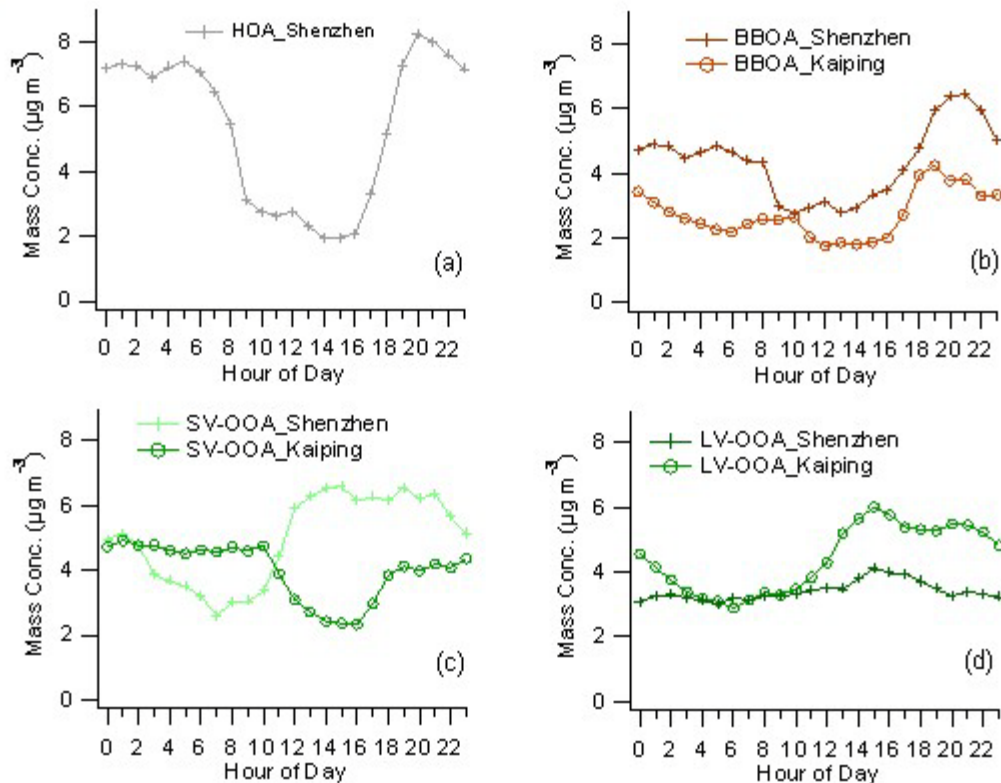
Figure 4. The comparison of component concentrations in Shenzhen and at Kaiping.



The average diurnal patterns of the four organic components were shown in Figures 5. Both of the HOA and the BBOA showed lower concentrations in the daytime but higher concentrations at night, which should be mainly attributed to the diurnal variation of PBL. The SV-OOA in Shenzhen showed a quick concentration increase from 9 am to 3 pm, indicating that its secondary photochemical formation in the daytime could be great enough to overwhelm both the dilution by higher PBL and its partial evaporation into the gas phase. In contrast, the diurnal pattern of SV-OOA showed a decreasing trend during the similar period at Kaiping, indicating that SV-OOA formation at Kaiping was not as active as in Shenzhen. This difference is most likely due to more emissions of SV-OOA precursors in urban areas, which lead to more photochemical production of SV-OOA during the daytime. This contrast is something like the contrast of the diurnal patterns of nitrate between in Shenzhen and at Kaiping, as discussed in section 3.2. The LV-OOA concentration in Shenzhen showed a slight continuous increase in the daytime in Shenzhen, indicating its significant photochemical production that can offset the elevation of PBL. However, this daytime LV-OOA increase is much shallower than that observed at Kaiping, indicating that the formation of LV-OOA was more active at Kaiping. As the aging of OA is a continuum in the atmosphere^[13], the above discussion suggests that the formation process from precursors to SV-

OOA is dominant in urban atmospheres in PRD while the formation process from SV-OOA to LV-OOA is dominant in rural atmospheres.

Figure 5. The comparison of diurnal variations of the OA components in Shenzhen and at Kaiping.



REFERENCES

- [1] Streets, D. G., C. Yu, M. H. Bergin, X. Wang, and G. R. Carmichael. Modeling study of air pollution due to the manufacture of export goods in China's Pearl River Delta, Environmental Science and Technology, 40, 2099-2107, 2006.
- [2] Zhang, Y. H., M. Hu, L. J. Zhong, A. Wiedensohler, S. C. Liu, M. O. Andreae, W. Wang, and S. J. Fan. Regional Integrated Experiments on Air Quality over Pearl River Delta 2004 (PRIDE-PRD2004): Overview, Atmospheric Environment, 42, 6157-6173, 2008.
- [3] Cheung, H.-C., T. Wang, K. Baumann, and H. Guo. Influence of regional pollution outflow on the concentrations of fine particulate matter and visibility in the coastal area of southern China, Atmospheric Environment, 39, 6463-6474, 2005.

- [4] Louie, P. K. K., J. G. Watson, J. C. Chow, A. Chen, D. W. M. Sin, and A. K. H. Lau. Seasonal characteristics and regional transport of PM_{2.5} in Hong Kong, *Atmospheric Environment*, 39, 1695-1710, 2005.
- [5] Hagler, G. S. W., et al. . Source areas and chemical composition of fine particulate matter in the Pearl River Delta region of China, *Atmospheric Environment*, 40, 3802-3815, 2006.
- [6] Yuan, Z. B., J. Z. Yu, A. K. H. Lau, P. K. K. Louie, and J. C. H. Fung. Application of positive matrix factorization in estimating aerosol secondary organic carbon in Hong Kong and its relationship with secondary sulfate, *Atmos. Chem. Phys.*, 6, 25–34, 2006.
- [7] DeCarlo, P. F., et al. . Field-Deployable, High-Resolution, Time-of-Flight Aerosol Mass Spectrometer, *Analytical Chemistry*, 78, 8281-8289, 2006.
- [8] Zhang, Q., J. L. Jimenez, D. R. Worsnop, and M. Canagaratna. A case study of urban particle acidity and its influence on secondary organic aerosol, *Environ. Sci. Technol.*, 41, 3213-3219, 2007.
- [9] Huang, X.-F., L.-Y. He, M. Hu, M. R. Canagaratna, Y. Sun, Q. Zhang, T. Zhu, L. Xue, L.-W. Zeng, X.-G. Liu, Y.-H. Zhang, J. T. Jayne, N. L. Ng, and D. R. Worsnop. Highly time-resolved chemical characterization of atmospheric submicron particles during 2008 Beijing Olympic Games using an Aerodyne High-Resolution Aerosol Mass Spectrometer, *Atmos. Chem. Phys.*, 10, 8933–8945, 2010.
- [10] Zheng, J., R. Zhang, E. C. Fortner, R. M. Volkamer, L. Molina, A. C. Aiken, J. L. Jimenez, K. Gaeggeler, J. Dommen, S. Dusander, P. S. Stevens, and X. Tie. Measurements of HNO₃ and N₂O₅ using ion drift-chemical ionization mass spectrometry during the MILAGRO/MCMA-2006 campaign, *Atmos. Chem. Phys.*, 8, 6823-6838, 2008.
- [11] Paatero, P., and U. Tapper. Positive matrix factorization: A non-negative factor model with optimal utilization of error estimates of data values, *Environmetrics*, 5, 111-126, 1994.
- [12] Huang, X. F., L. Y. He, M. Hu, M. R. Canagaratna, J. H. Kroll, N. L. Ng, Y. H. Zhang, Y. Lin, L. Xue, T. L. Sun, X. G. Liu, M. Shao, J. T. Jayne, and D. R. Worsnop. Characterization of submicron aerosols at a rural site in Pearl River Delta of China using an Aerodyne High-Resolution Aerosol Mass Spectrometer, *Atmos. Chem. Phys.*, 11, 1865–1877, 2011.
- [13] Jimenez, J. L., et al. . Evolution of Organic Aerosols in the Atmosphere, *Science*, 326, 1525-1529, doi: 10.1126/science.1180353, 2009.

Comprehensive Characterization of Atmospheric Particles Using Complementary Methods of Chemical Analysis

Alexander Laskin

Environmental Molecular Science Laboratory, Pacific Northwest National Laboratory,
Richland, WA, 99354, USA

Principal Contact: Alexander Laskin, Senior Research Scientist, Environmental Molecular
Science Laboratory, Pacific Northwest National Laboratory, Richland, WA, 99354, USA.

Tel: 509-371-6129 Fax: 509-371-6139 E-mail: Alexander.laskin@pnl.gov

Abstract

Fundamental understanding of the complex chemistry of aerosols and their environmental impacts is a challenging task because no single method of analytical chemistry is capable of providing the full range of analytical chemistry information. Electron microscopy and micro-spectroscopy approaches can visualize individual particles and their internal structures; however, they largely exclude molecular-level information, and are limited to elemental and chemical bonding characterization. In contrast, contemporary methods of high resolution mass spectrometry can provide detailed information on the molecular content of organic aerosol (OA), but these methods use bulk particle samples and provide no knowledge of the individual particle composition. Therefore, application of complementary analytical methods of chemical analysis is necessary for comprehensive characterization of aerosol properties ranging from bulk molecular composition of complex OA mixtures to microscopy level details of individual particles. Combined assessment of the results provided by complementary analytical chemistry techniques offers unique insights to understand the composition and environmental chemistry of atmospheric particles. This presentation will review our recent field and laboratory studies of atmospheric aerosols, and explain how the information obtained from complementary analytical methods can be translated into an improved understanding of aerosol chemistry.

Keywords: Particle analysis, microscopy, micro-spectroscopy, high-resolution mass spectrometry

Laboratory studies of organic aerosol aging

Jesse H. Kroll¹, Kevin R. Wilson², Sean H. Kessler¹, Theodora Nah², Kelly E. Daumit¹, Anthony J. Carrasquillo¹, Eben S. Cross¹, and Douglas R. Worsnop³

1 Massachusetts Institute of Technology, Cambridge, MA 02139, U.S.A

2 Lawrence Berkeley National Laboratory, Berkeley CA 94720, U.S.A

3 Aerodyne Research, Inc., Billerica, MA 01821, U.S.A

Principal Contact: Jesse H. Kroll, Assistant Professor, Massachusetts Institute of Technology, 15 Vassar St. 48-323, Cambridge, MA 02139.

Tel: (617) 253-2409 Email: jhkroll@mit.edu

Abstract

The multigenerational oxidative processing (“aging”) of atmospheric organic aerosol (OA) is likely to have a major influence on OA loadings and properties. However, due to the difficulty in simulating such processes in the laboratory, these aging processes are poorly understood, limiting our ability to accurately predict effects of atmospheric aerosol on climate. Here we describe laboratory experiments aimed at better constraining the key chemical changes that organics undergo upon multigenerational aging. Two sets of experiments are carried out: chamber studies of the gas-phase oxidation of simple alkanes and flow-tube studies of the heterogeneous oxidation of single-component particulate organics. In both cases, organics are exposed to elevated levels of OH, in order to access the equivalent of several days’ worth of atmospheric oxidation. A scanning mobility particle sizer (SMPS) and an Aerodyne high-resolution aerosol mass spectrometer (HR-AMS) are used to measure the mass and elemental composition of the particles as a function of OH exposure. These enable the accurate determination of two key quantities, the absolute abundance and the average oxidation state of particulate organic carbon. Changes in these quantities observed in both the chamber experiments and the flow-tube experiments provide strong evidence for the increasingly important role of fragmentation (C-C bond-breaking) reactions with oxidation; such reactions are generally not included in most current models of aerosol aging. Implications of these results for our understanding of the lifecycle of organic compounds in the atmosphere will be discussed.

Keywords: organic aerosol, photochemical aging, SOA, heterogeneous oxidation

An Aerosol Chemical Speciation Monitor (ACSM) for Routine Monitoring of the Composition and Mass Concentrations of Ambient Aerosol

Nga L. Ng¹, Scott C. Herndon¹, Achim Trimborn¹, Manjula R. Canagaratna¹, Philip Croteau¹, Timothy B. Onasch¹, Donna Sueper^{1,2}, Douglas R. Worsnop¹, Qi Zhang³, Yele Sun³ and John T. Jayne¹

1 Aerodyne Research, Inc. Billerica, MA, USA

2 CIRES, University of Colorado, Boulder, CO, USA

3 Department of Environmental Toxicology, University of California, Davis, CA, USA

ABSTRACT

Ambient particles are known to play a significant role in altering the chemistry and the radiative balance of the Earth's atmosphere, reducing visibility, and adversely affecting human health. In order to address aerosol effects on health and the environment, there is a need for instrumentation which is capable of reporting the chemical and microphysical properties of ambient particles. We present here results on the development and demonstration of a compact aerosol mass spectrometer system, the Aerosol Chemical Speciation Monitor (ACSM) which measures aerosol mass and chemical composition of non-refractory submicron aerosol particles in real-time. The ACSM provides composition information for particulate ammonium, nitrate, sulfate, chloride, and organics and is designed and built around the same technology as our larger research grade Aerosol Mass Spectrometer (AMS) in which an aerodynamic particle focusing lens is combined with high vacuum thermal particle vaporization and mass spectrometry. The ACSM system is smaller, uses lower cost components and thus operates with lower performance than the research grade AMS. It is simpler to operate and maintain and is stable for long periods of time (months). The ACSM is designed for routine monitoring of PM with sufficient sensitivity to provide chemically speciated mass loadings and aerosol mass spectra at data rates up to 15 min for typical urban aerosol loadings. Results are presented from recent field deployments which compare the ACSM performance with AMS systems. Data quality and data analysis methods will be presented and areas of current development will also be discussed.

KEYWORDS

Aerosol mass spectrometry, organic aerosols, aerosol composition, real time measurements

Introduction

In order to address aerosol effects on the environment and health, instrumentation capable of reporting the chemical and microphysical properties of ambient particles is needed. From an air quality monitoring standpoint, aerosol instrumentation that is simple to operate, capable of long-term, autonomous and stable operation with real time results is also desired.

In recent years the Aerodyne Aerosol Mass Spectrometer (AMS) [1]; [2] equipped with quadrupole (Q-AMS) and time-of-flight (C-ToF-AMS and HR-ToF-AMS) [3]; [4] mass spectrometers provides quantitative measurements of sub-micron non-refractory particle mass and composition (organics, ammonium, nitrate, sulfate, and chloride). Positive matrix factorization (PMF) of AMS organic aerosol mass spectra [5], [6] has been used to further characterize the sources and evolution of ambient organic aerosol (OA) [7]; [8]. Two types of OA groups are observed at most sites: hydrocarbon-like organic aerosol (HOA) and oxygenated organic aerosol (OOA)^[9]. The HOA and OOA components are surrogates of primary combustion OA (POA) and secondary OA (SOA), respectively.

In this work we introduce the Aerodyne Aerosol Chemical Speciation Monitor (ACSM), a new instrument that has many of the capabilities of the AMS but is better suited for monitoring applications. The ACSM is designed and built around the same sampling and detection technology as the state-of-the art research grade AMS systems, but it has lower size, weight, cost, and power requirements than the AMS and is specifically designed to be a stand-alone monitor that is more easily transportable and can operate with minimal user intervention. The ACSM has been successfully deployed in three field campaigns: DAURE in Montseny, Spain (March 2009, 3 weeks attended operation), SHARP in Houston, TX (April 2009, 6 weeks unattended operation) and Queens College, NY (July 2009, 8 weeks unattended operation). Since the Queens campaign involved more co-located monitoring and research-grade instruments for comparing the ACSM data with, the Queens dataset is used to demonstrate the performance and capabilities of the ACSM.

Instrument Description

The ACSM measures 19" D x 21" W x 33" H, weighs 140 pounds, and requires approximately 300W of power to operate. It consists of three vacuum chambers that are differentially pumped by turbo pumps and backed by a small diaphragm pump. During operation, an aerodynamic lens [10]; [11] is used to efficiently sample and focus submicron particles into the ACSM. The 50% transmission range of the lens is 75 – 650 nm [12]. The sample flow into the instrument, which is fixed by a 100 µm diameter critical aperture mounted at the entrance of the aerodynamic lens, is approximately 85 cc/min. The focused particle beam is transmitted through the first two chambers into the final detection chamber where particles impact and flash vaporize on a hot

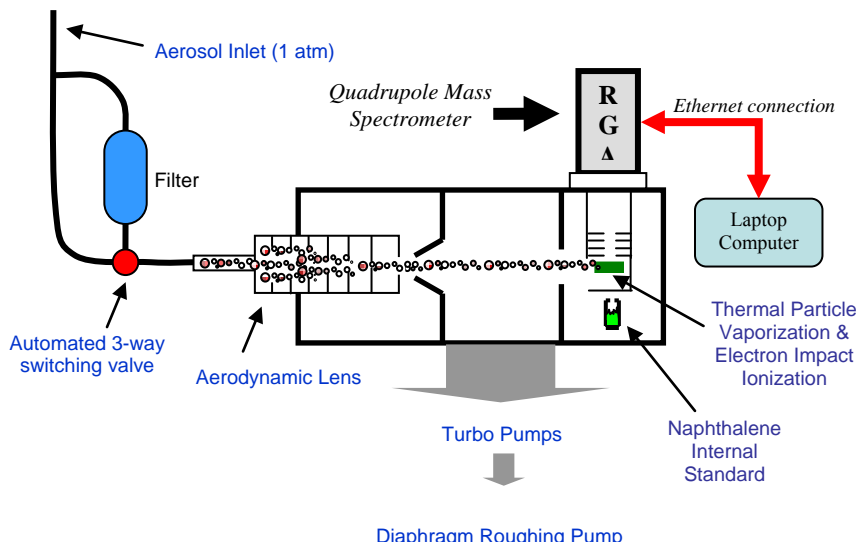
oven; non-refractory particulate material that vaporizes at the oven temperature (typically 600 °C) is subsequently detected and chemically characterized with 70eV electron impact quadrupole mass spectrometry.

The particle lens and particle vaporizer used in the ACSM are identical to those used in the research grade AMS^{[11];[10];[1];[12]}. The electron impact ion source used in the ACSM is smaller, but otherwise identical to that used in the AMS^[1]. Several design features make the ACSM a simpler, smaller, and less expensive stand-alone instrument. Two key design differences include: 1) The use of a lower cost residual gas analyzer (RGA) type quadrupole mass analyzer instead of the high-performance quadrupole and time-of-flight spectrometers used on AMS systems, and 2) the lack of a fast data acquisition and particle beam chopper system for measuring particle time-of-flight to obtain particle size information. These modifications result in a more compact and less costly instrument compared to the AMS at the expense of lower sensitivity and time resolution. The ACSM has sufficient sensitivity to operate as a monitoring instrument providing chemically speciated mass loadings and aerosol mass spectra at data rates up to 30 min for typical urban aerosol loadings (several $\mu\text{g}/\text{m}^3$). For 30 min of averaging time (t_{30}), the 3σ detection limits for ammonium, organics, sulfate, nitrate, and chloride are $0.284 \mu\text{g}/\text{m}^3$, $0.148 \mu\text{g}/\text{m}^3$, $0.024 \mu\text{g}/\text{m}^3$, $0.012 \mu\text{g}/\text{m}^3$, and $0.011 \mu\text{g}/\text{m}^3$, respectively.

The detection chamber contains an internal calibration standard that consists of an effusive source of naphthalene. The parent peak for naphthalene at m/z 128 provides an internal standard for calibrating the mass to charge ratios of the measured ions. Since this source is placed inside the detection chamber, naphthalene is always present in the mass spectra (both background and ambient mass spectra). The naphthalene source also allows for in-situ measurement of the m/z dependent ion transmission efficiency of the RGA quadrupole system and allows for routine monitoring of the performance of the instrument and simplified calibration of the ionization efficiency of the mass spectrometer.

The ACSM ion signal must be corrected for contributions from background gases in the detection region of the instrument, including naphthalene from the calibration source. Instrument zeroing is done by a 3-way valve system that automatically switches between filter mode and sample mode. In the filter mode, ambient particles are removed from sampled air and the resulting particle-free sample is sent to the ACSM. In the sample mode, ambient aerosol particles are unperturbed and directly sampled into the ACSM. Particle signal is obtain as the difference between the sample and filter mode measurements.

Figure 1. ACSM schematic.

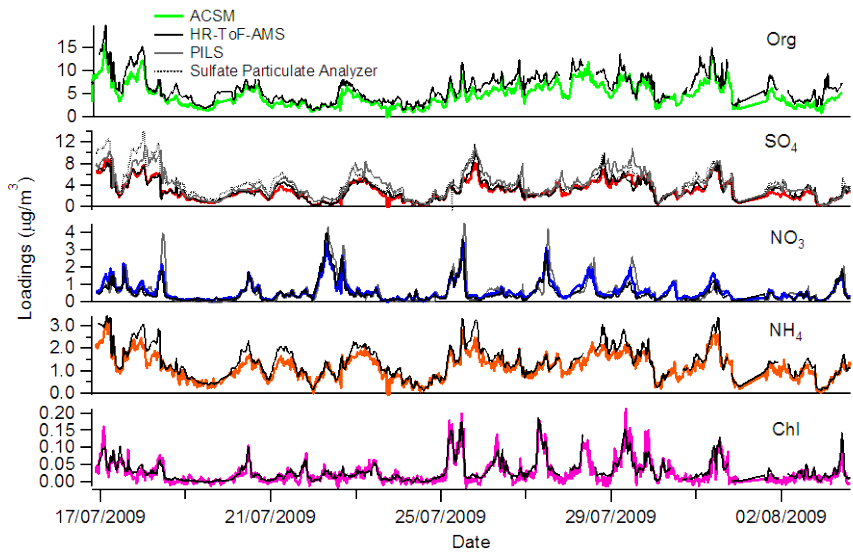


Field measurement results and discussion

AEROSOL MASS CONCENTRATIONS AND TIME SERIES

The ACSM ran unattended continuously for 8 weeks with a 30 min sampling time interval during the Queens New York field campaign. Shown in Fig. 2 are the time series of organics, sulfate, nitrate, ammonium, and chloride as well as the average mass fraction of each species measured by the ACSM. The average total loading is $7.2 \mu\text{g}/\text{m}^3$; the aerosol is dominated by organics and sulfate species throughout the campaign, with organics accounting for more than 50% of the aerosol. The concentrations of the different species measured by the ACSM are compared to those measured by HR-ToF-AMS in Sun et al^[13]. In general, there is very good correlation between the ACSM and HR-ToF-AMS data ($R^2=0.81-0.91$, slope = 0.76-1.01). For sulfate, other than the HR-ToF-AMS, two other comparison instruments are present at the shelter: PILS-IC and Thermo Scientific Sulfate Particulate Analyzer. The sulfate aerosol mass measured by the ACSM agrees well with measurements from these three independent instruments ($R^2=0.91, 0.77, 0.85$, slope=0.95, 0.69, 0.69, for HR-ToF-AMS, PILS-IC, and Sulfate Particulate Analyzer, respectively). The ACSM nitrate data also agree with the PILS-IC data ($R^2=0.65$, slope=0.75). The ACSM sulfate and nitrate account for ~70% of those in $\text{PM}_{2.5}$ measured by PILS-IC and Sulfate Particulate Analyzer.

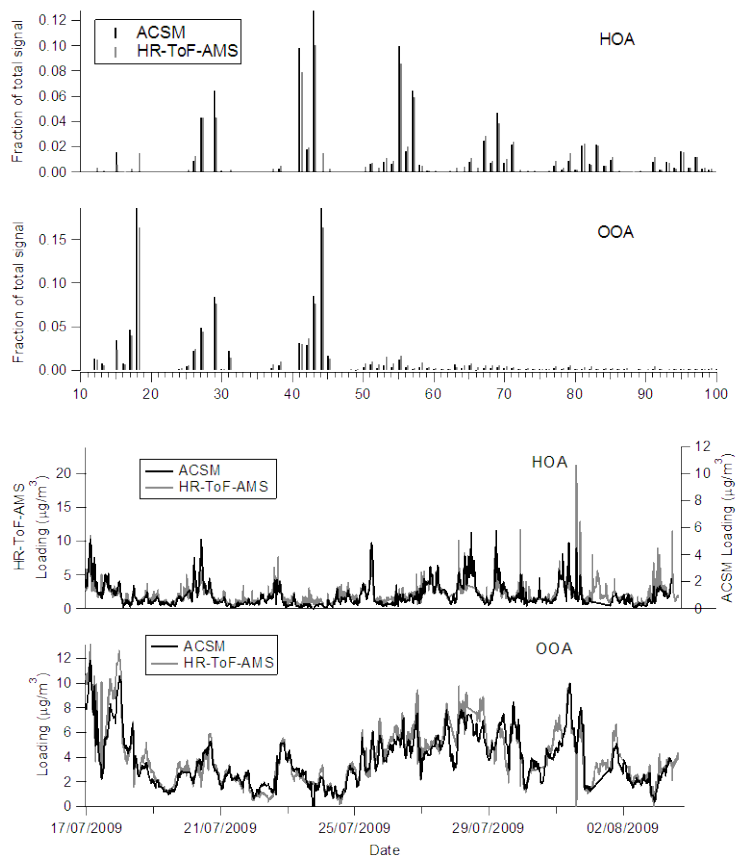
Figure 2. ACSM time trends for the Queens study.



INVESTIGATING OA COMPONENTS WITH POSITIVE MATRIX FACTORIZATION (PMF)

We apply PMF analysis to the ACSM Queens dataset. The PMF2 executable version 4.2 is used in robust mode together with a custom software tool for solution comparison and analysis, the PMF Evaluation Tool (PET)^[6]. The analysis and input error matrix calculations are performed following the procedures described in Ulbrich et al.^[6]. The mass spectra and times series of each component are shown in Fig. 3. The HOA component is distinguished by the clear hydrocarbon signatures in its spectrum, which are dominated by the ion series $C_nH_{2n+1}^+$ and $C_nH_{2n-1}^+$ (m/z 27, 29, 41, 43, 55, 57, 69, 71, 83, 85, 97, 99...) that are typical of hydrocarbons. The OOA component is distinguished by the prominent m/z 44 (CO_2^+) in its spectrum and the lower relative intensity of higher mass fragments. The f_{44} (ratio of m/z 44 to total signal in the component mass spectrum) in the OOA spectrum is 19%, which is at the high end of the f_{44} observed in the OOA components observed across multiple sites around the world^{[7];[8]}. The unit mass resolution PMF results for the HR-ToF-AMS data^[13] are also shown in Fig. 3. There is good agreement between the mass spectra and time series of both the HOA and OOA components determined from the ACSM and HR-ToF-AMS data. The OOA loading agrees well between the two instruments, but the HOA loading determined from the ACSM data is approximately half of that determined from the HR-ToF-AMS data. These observations are consistent with the hypothesis that externally mixed HOA particles have a collection efficiency (CE) of ~0.5 because they remain dry in the humid sampling inlet, while OOA, which is internally mixed with inorganic species, has a CE of 1 because it is more hygroscopic and takes up enough water in the sampling line to become liquid.

Figure 3. HOA and OOA component mass spectra and time series.



SUMMARY

This work introduces the Aerodyne Aerosol Chemical Speciation Monitor (ACSM), an instrument that is designed for long-term, autonomous and stable field measurements of ambient aerosol. The ACSM operates by sampling ambient aerosol through an aerodynamic inlet, vaporizing them on a hot oven, and then analyzing the resulting vapor with electron impact ionization quadrupole mass spectrometry. The ACSM is based on the widely used Aerodyne aerosol mass spectrometer (AMS), but key changes in the detection electronics and mass spectrometer allow the ACSM to be smaller, lower cost, and simpler to operate. Although these changes lower the relative sensitivity of the ACSM, it still has a detection limit of $< 0.2 \mu\text{g}/\text{m}^3$ for 30 minutes of averaging, which is suitable for measuring typical urban aerosol loadings of several $\mu\text{g}/\text{m}^3$. The ACSM has been deployed in 3 different field campaigns. Results from the Queens campaign are used to demonstrate the performance and capabilities of the ACSM. During the campaign the ACSM provided real-time (30 min resolution) chemically resolved mass concentrations of particulate ammonium, nitrate, sulfate, chloride, and organic species. The

inorganic measurements agree well with those obtained from other aerosol mass instrumentation (PILS-IC, Thermo Scientific Sulfate Particulate Analyzer). The speciated inorganic aerosol time trends and organic aerosol components also compare well with results from a co-located HR-ToF-AMS instrument. PMF analysis of ACSM organic spectra is used to further speciate the observed organic aerosol material into HOA and OOA components. These components compare well with those obtained from HR-ToF-AMS measurements.

REFERENCES

- [1] Jayne, J. T.; Leard, D. C.; Zhang, X. F.; Davidovits, P.; Smith, K. A.; Kolb, C. E.; Worsnop, D. R. *Aerosol Sci. Technol.* **2000**, *33*, 49-70.
- [2] Canagaratna, M. R.; Jayne, J. T.; Jimenez, J. L.; Allan, J. D.; Alfarra, M. R.; Zhang, Q.; Onasch, T. B.; Drewnick, F. et al. *Mass Spectrometry Reviews.* **2007**, *26*, 185-222.
- [3] Drewnick, F.; Hings, S. S.; DeCarlo, P.; Jayne, J. T.; Gonin, M.; Fuhrer, K.; Weimer, S.; Jimenez, J. L. et al. *Aerosol Sci. Technol.* **2005**, *39*, 637-658.
- [4] DeCarlo, P. F.; Kimmel, J. R.; Trimborn, A.; Northway, M. J.; Jayne, J. T.; Aiken, A. C.; Gonin, M.; Fuhrer, K. et al. *Anal. Chem.* **2006**, *78*, 8281-8289.
- [5] Lanz, V. A.; Alfarra, M. R.; Baltensperger, U.; Buchmann, B.; Hueglin, C.; Prévôt, A. S. H. *Atmos. Chem. Phys.* **2007**, *7*, 1503-1522.
- [6] Ulbrich, I. M.; Canagaratna, M. R.; Zhang, Q.; Worsnop, D. R.; Jimenez, J. L. *Atmos. Chem. Phys.* **2009**, *9*, 2891-2918.
- [7] Jimenez, J. L.; Canagaratna, M. R.; Donahue, N. M.; Prevot, A. S. H.; Zhang, Q.; Kroll, J. H.; DeCarlo, P. F.; Allan, J. D. et al. *Science.* **2009**, *326*, 1525-1529.
- [8] Ng, N. L.; Canagaratna, M. R.; Zhang, Q.; Jimenez, J. L.; Tian, J.; Ulbrich, I. M.; Kroll, J. H.; Docherty, K. S. et al. *Atmos. Chem. Phys.* **2010**, *10*, 4625-4641.
- [9] Zhang, Q.; Jimenez, J. L.; Canagaratna, M. R.; Allan, J. D.; Coe, H.; Ulbrich, I.; Alfarra, M. R.; Takami, A. et al. *Geophys. Res. Lett.* **2007**, *34*, L13801, doi:10.1029/2007GL029979.
- [10] Liu, P.; Ziemann, P. J.; Kittelson, D. B.; McMurry, P. H. *Aerosol Sci. Technol.* **1995**, *22*, 293-313.
- [11] Liu, P.; Ziemann, P. J.; Kittelson, D. B.; McMurry, P. H. *Aerosol Sci. Technol.* **1995**, *22*, 314-324.
- [12] Liu, P. S. K.; Deng, R.; Smith, K. A.; Williams, L. R.; Jayne, J. T.; Canagaratna, M. R.; Moore, K.; Onasch, T. B. et al. *Aerosol Sci. Technol.* **2007**, *41*, 721-733.
- [13] Sun, Y. L.; Zhang, Q.; Schwab, J. J.; Demerjian, K. L.; Chen, W. N.; Bae, M. S.; Hung, H. M.; Hogrefe, O. et al. *Atmos. Chem. Phys. Discuss.* **2010**, *10*, 22669–22723.

Cirrus cloud measurement using lidar over semi-arid areas

Ruijin Liu and Lei Zhang

Key Laboratory for Semi-Arid Climate Change of the Ministry of Education, College of Atmospheric Sciences, Lanzhou University, Lanzhou, 730000, China

Principal Contact: Lei Zhang, Professor, College of Atmospheric Sciences, Lanzhou University, Lanzhou, 730000.

Tel: 0931-8915610 Email: zhanglei@lzu.edu.cn

Abstract

By using cirrus measurements with a Micro Pulse Lidar (MPL-4B) at Semi-Arid Climate and Environment Observatory of Lanzhou University (SACOL) from April to November in 2007, a statistical analysis is made of cirrus height and thickness. The cirrus optical depth is derived in the transmittance method, and then the Correlations of cirrus optical depth, cirrus thickness and cirrus base height. The results show that the mean value of the cirrus height at SACOL is 10.16 ± 1.32 km above sea level. Cirrus thickness is often between 0.3 and 2.8 km, and the mean value is 1.10 ± 0.49 km. Cirrus optical depth varies between 0.003 and 1.057, and the mean value tends to be 0.17 ± 0.16 . Most cirrus observed at SACOL is rather thin whose optical depth is less than 0.3. The cirrus height is higher and the optical depth and thickness is often lower than in other months from June to August. The cirrus optical depth and cirrus thickness appears to be in a positive linear relation, while the cirrus optical depth and cirrus base height in a negative linear relation.

Keywords: cirrus height, cirrus thickness, optical depth, transmittance method, lidar

Long Term (2004-2010) Measurement of Submicron Aerosol Size Distribution and CCN Concentration in the Mega City of Seoul, Korea

Seong Soo Yum, Woo-Jae Kim, Jong Hwan Kim and Sungbo Shim

Dept. of Atmospheric Sciences, Yonsei University, 50 Yonsei-ro, Seodaemun-gu, Seoul 120-749, Korea

ABSTRACT

As an effort to characterize the physical properties of anthropogenic aerosols, we measured total aerosol(CN) number concentration, cloud condensation nuclei(CCN) number concentration and aerosol size distribution($10\text{NM} < \text{particle diameter} < 500\text{ NM}$) in the mega city of Seoul, Korea for the period of 2004-2010. The average CN number concentration was $18517 \pm 8880\text{ cm}^{-3}$ while CCN number concentration at 0.6 % supersaturation was $5227 \pm 3142\text{ cm}^{-3}$. The average of CCN/CN ratio was approximately 0.30 ± 0.15 . The diurnal variation of CN number concentration in Seoul showed minima around 4 a.m. and the highest peaks around 8 ~ 10 a.m. regardless of the season of the year. The average CN and CCN number concentrations were higher in winter than in summer. The correlation between CN number concentration and traffic was high ($R^2=0.84$). Out of the 891days of size distribution measurement particle formation and growth (PFG) events were observed in 83days. Thus the PFG events occurred during 10 % of the measurement days and appeared to be associated with cloudiness and precipitation.

KEYWORDS

Aerosol size distribution, CN and CCN concentrations, Particle formation and growth events, Seoul

Introduction

The effects of atmospheric aerosols on climate change are among the most uncertain and are of low scientific understanding^[1]. Particularly, Asian regions of rapid industrialization are well-known for emitting enormous air pollution aerosols and transporting them throughout the pacific. Nevertheless, efforts to measure and characterize the physical, chemical and optical properties of aerosols in this region have been relatively weak, compared to other parts of the world until recently. These properties are important in the assessment of aerosol effects on climate. For example, the basic physical property of aerosol number concentration is the most important factor that determines the droplet concentration of the clouds formed on these aerosols. The aerosols that can act as the nucleus of cloud droplets are called cloud condensation nuclei (CCN) and they

constitute a subset of the total aerosol population. In this study we present total aerosol (i.e., condensation nuclei, CN) number concentration (N_{CN}) and CCN concentration (N_{CCN}) measured in the mega-city of Seoul, the capital of South Korea, for the 7 year period of 2004-2010. Diurnal and seasonal variations are presented that may characterize a typical large city environment. Particle formation and growth (PFG) events are observed occasionally and their statistical characteristics are shown. Lastly, comparisons with the measurements at coastal sites in South Korea or over the sea around the Korean Peninsula^{[2][3][4]} are made.

Experimental Methods

Measurements were made at a room (drawing air from outside) on the 6th (~ 20 m height from the ground) floor of a building in the Yonsei University campus, located near the city center of Seoul, and therefore the measurement location is safely away from immediate emission sources like car exhaust. Measurements were interrupted due to malfunctioning, repair and deployment for field measurements in other places but otherwise the measurements were continuously made. The instruments were TSI CPC3010 for total aerosol concentration, N_{CN} (particle diameter, $d_p > 10$ nm) and TSI SMPS for aerosol size distribution ($10 \text{ nm} < d_p < 500 \text{ nm}$). A DMT CCN Counter was used for N_{CCN} measurement at five supersaturations (S) of 0.2, 0.4, 0.6, 0.8 and 1.0%.

Results and Discussion

Overall statistics

The overall statistics are shown in Table 1. For the entire measurement period, the average N_{CN} was 18517 cm^{-3} while N_{CCN} at 0.6% S was 5227 cm^{-3} . The average geometric mean diameter of the size distributions (D_g) was 49.2 nm. The average of the ratio of N_{CCN}/N_{CN} , a measure of CCN capability of aerosol population, was approximately 0.30. The average N_{CN} and N_{CCN} were lower with precipitation than without it.

Table 1. Overall statistics of the measured CN and CCN concentrations.

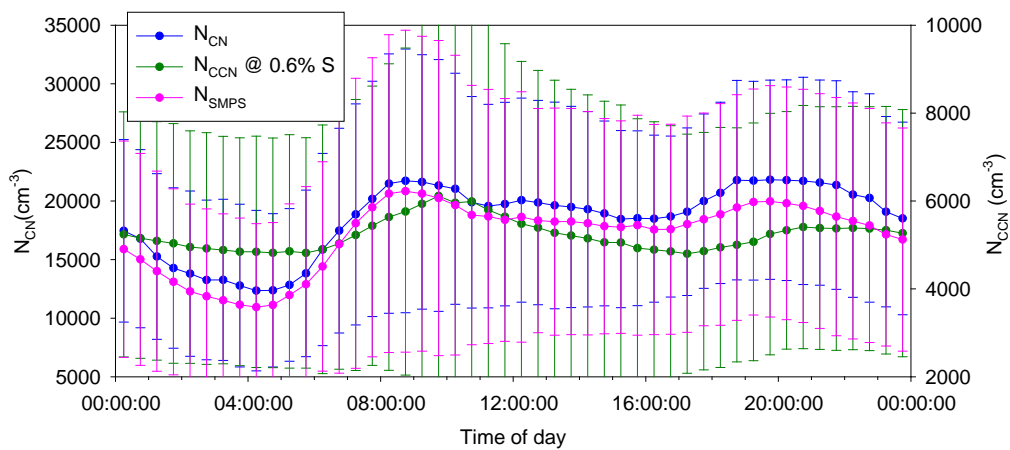
	Total period	No Precipitation	Precipitation
$N_{CN} (\text{cm}^{-3})$	18517 ± 8880	19185 ± 7354	15546 ± 5920
$N_{CCN} (\text{cm}^{-3}) @ 0.6\% \text{ S}$	5227 ± 3142	5793 ± 2631	3973 ± 2189
N_{CCN}/N_{CN}	0.30 ± 0.15	0.30 ± 0.11	0.27 ± 0.12

Diurnal variation

The diurnal variation of N_{CN} and N_{SMPS} (aerosol concentration obtained by integration of the SMPS size distribution) showed minima around 4 a.m. and the high peaks around 8 ~ 10 a.m. and

6 ~ 8 p.m. (Figure 1), which is similar to that of traffic volume (not shown). Contrastingly, N_{CCN} showed less impact from traffic volume than N_{CN} did. Consistently, the linear regression between N_{CN} and traffic volume showed $r^2 = 0.84$ while r^2 for N_{CCN} vs. traffic volume was only 0.20. N_{CCN} / N_{CN} and D_g showed an opposite diurnal variation to those of aerosol concentrations, showing maxima around 4 a.m but no clear minima. This means that CCN concentration was relatively higher when particles were larger, demonstrating that larger particles were easier to act as CCN.

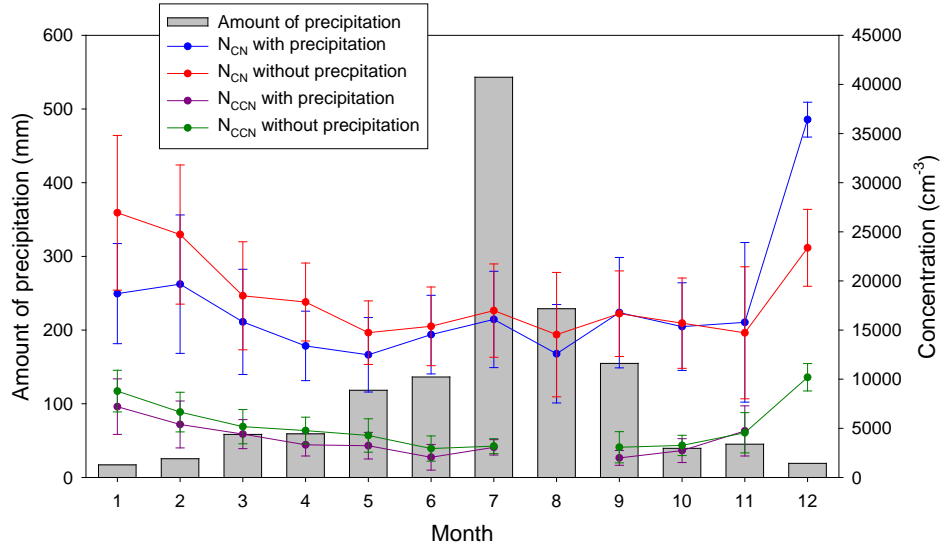
Figure 1. The average diurnal variation of N_{CN} , N_{SMPS} and N_{CCN} at 06% S.



Seasonal variation

Figure 2 shows the seasonal trends. The monthly average N_{CN} and N_{CCN} were higher in winter months than those in summer months. Larger precipitation amount during the summer months may seem related to the lower concentrations but the concentrations with and without precipitation showed smaller difference during these months than other months. N_{CN} ($20 < D_p < 200$ nm) was the highest in winter but N_{CN} ($D_p < 20$ nm) was the highest in summer. This seems to be because particle formation and growth events occurred more frequently in spring and summer than it did in fall and winter as described below.

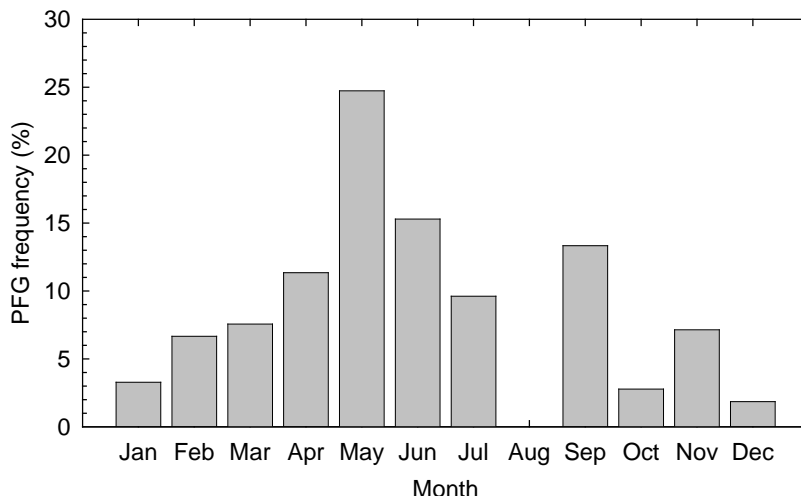
Figure 2. Monthly average N_{CN} , N_{CCN} and the amount of precipitation during 2004-2010.



Particle formation and growth (PFG) events

PFG events were observed in roughly 10% of the measurement days and their monthly occurrence frequencies only for the measurement days are shown in Figure 3. PFG events were found to be associated with meteorological condition when the sky was clear and had no precipitation or one or two days after precipitation. PFG events occurred mostly in spring and summer.

Figure 3. Monthly PFG event frequency only for the measurement days.



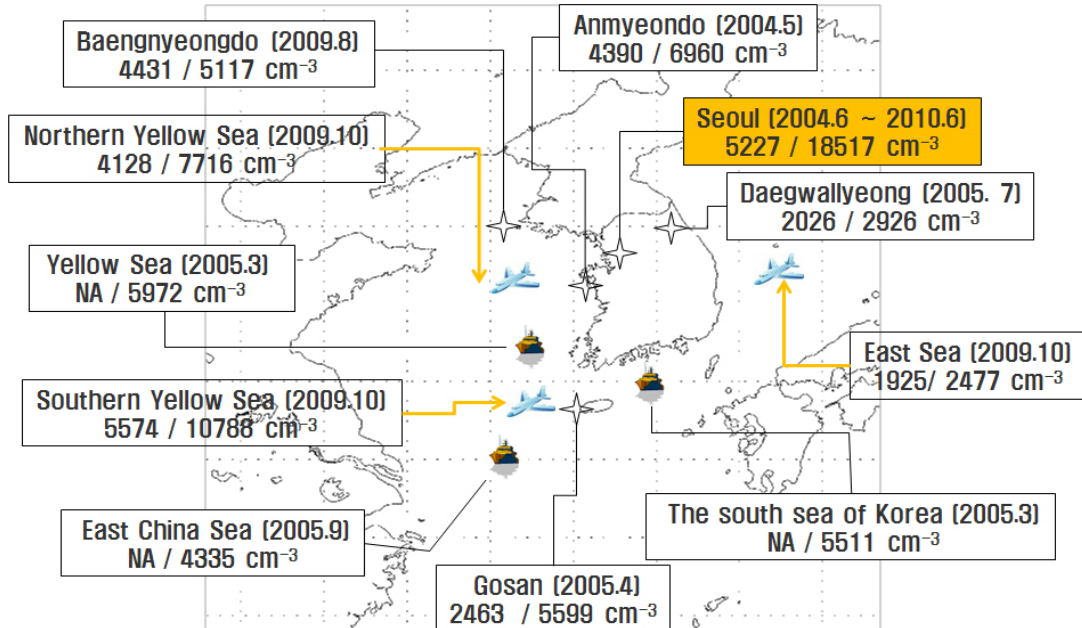
Comparision with other measurements

Figure 4 shows the comparison of the Seoul N_{CCN} and N_{CN} with other measurements in and around the Korean Peninsula^{[2][3][4]}. The N_{CN} in Seoul was much higher than those at other places in and around the Korean Peninsula but the N_{CCN} in Seoul was comparable to or somewhat higher than coastal or marine measurements. N_{CN} and N_{CCN} were higher over the Yellow Sea than over the East Sea of Korea probably because of the heavier pollution sources to the west of the Korean Peninsula.

SUMMARY OR CONCLUSION

The size and number concentration of aerosols measured in Seoul during 2004 – 2010 show characteristics that may be typical of a megacity measurement, i.e., early morning (~4 a.m.) minima and morning (8~10 a.m.) and evening (6~8 p.m.) peaks that seemed associated with the traffic volume. The N_{CN} and N_{CCN} were generally higher in winter, probably due to increased particle emissions (e.g. from heating). Particle formation and growth events occurred about 10% of the measurement days and mostly in spring and summer. The N_{CCN} measured in Seoul was comparable to or somewhat higher than coastal or marine measurements in and around the Korean Peninsula, although N_{CN} was much higher. These long term measurement data can be used in the assessment of the aerosol effects on climate change as representative values of mega-cities in East Asia.

Figure 4. Average N_{CCN} and N_{CN} values measured in and around the Korean Peninsula^{[2][3][4]} in comparison to the average for the Seoul measurement during 2004 ~ 2010.



ACKNOWLEDGMENTS

This work was funded by the Korea Meteorological Administration Research and Development Program under Grant RACS_2010-5001.

REFERENCES

- [1] *Climate Change 2007: the physical science basis*; IPCC, 2007.
- [2] Yum, S. S.; Hudson, J. G.; Song, K.; Choi, B.-C. *Geophys. Res. Lett.*, 2005, 32, doi:10.1029/2005GL022641.
- [3] Yum, S.S.; Roberts, G.; Kim, J.H.; Song, K.; Kim D. *J. Geophys. Res.*, 2007, 112, doi:10.1029/2006JD008212.
- [4] Kim, J.H.; Yum, S.S.; Lee, Y.-G.; Choi, B.-C. *Atmos. Res.*, 2009, 93, 700-714.

The Relationship between Aerosol and CCN Measured on a High Mountain in Southeast China

Yan Yin, Kui Chen, Chen Chen and Wen Tan

Open Key Laboratory for Atmospheric Physic and Environment of China Meteorological Administration, Nanjing University of Information Science & Technology, Nanjing 210044, China

ABSTRACT

Based on observing data of atmospheric aerosols measured on the top of Mts. Huang, southeast China, the physical characteristics of aerosol particles, such as number concentration, size distribution were analyzed. The results show that the mean number concentration reached $3.14 \times 10^3 \text{ cm}^{-3}$ in spring, $1.80 \times 10^3 \text{ cm}^{-3}$ in summer, and ultra fine particles ($<0.1 \mu\text{m}$) account for 79% in spring and 68% in summer, respectively. The number concentration distributions in spring and summer all present a single peak, the peak value appears in $0.04\text{--}0.12 \mu\text{m}$ size range. The accumulation mode particles dominate in volume and surface concentration distributions. The CCN concentration can be expressed with the formula: $N=CS^k$, the results of parameters C and k show that there is a continental characteristic of CCN in spring, while maritime characteristic in summer. A parameterization scheme for describing aerosol-cloud relationships is proposed.

KEYWORDS

Aerosol, CCN, Cloud-fog droplet, Size distribution, Relationship

Introduction

Atmospheric aerosol is ubiquitously suspended in the air. The radiation budget of earth-atmosphere system might directly influenced by the process of absorption and scattering of aerosols, this is called the direct effect of aerosols. Meanwhile, the aerosol particles might act as Cloud Condensation Nuclei (CCN) to influence the optical properties, cloud cover, and the lifetime of Cloud, which leads to the indirect effect, such as, Twomey Effect^[1], Cloud Life Span Effect or the Second Indirect Effect^[2], Half Direct Effect^[3]. In addition, the decrease of the scale of cloud droplets might postpone the congelation of Cloud droplets, which might be caused by the increase of aerosol concentration. Some researches indicate that the particles with the diameter larger than $0.05 \mu\text{m}$ contribute to a large part of the Condensation Nuclei (CN) and IN to the formation of the Cloud Droplet and Ice Crystal (IC)^[4], especially to the sulphate aerosol particles. However, the organic aerosol also plays a significance role in the formation of the

cloud as well as sulphate aerosols^[5]. Therefore, if we want to fully understand and estimate the indirect effect caused by artificial aerosols, we need to know more information about the space-time distribution characteristics, number concentration, and chemical composition of atmosphere aerosol, and we also need to build the relationship between Aerosol, CCN (IN) and Cloud Droplet. Nevertheless, there is a much uncertain to estimate the direct and indirect radiation force due to the deficiency of understanding the characteristics such as the geological, vertical distribution, and the transfer process of the artificial aerosols^[6]. So it is important to develop more research on observation of Atmosphere Aerosol, Cloud and CCN for its significance to the weather and climate research.

Experimental Methods

1. Instrumentation

Aerosol was measured by using the Wide-Range Particle Spectrometer (WPS), made in USA, MSP Corporation. WPS is a general purpose, high-resolution aerosol spectrometer to measure the diameter and number concentration of aerosol particles in the 0.01~10 μm particle diameter range. There is a detailed description about this instrument by Benjamin^[7]. The temporal resolution is 7 minutes. The WPS was maintained and calibrated regularly by engineers before and during the experimental cycle; CCN was measured by DMT CCN counter, made by Droplet Measurement Technologies (DMT), USA. The main structure of DMT CCN counter is a cylindrical column continuous-flow streamwise thermal gradient chamber with 50 cm height and 2.3 cm inner diameter. A diode laser at a wavelength of 660 nm is used as the light source, and detective particle size is 0.75~10 μm in diameter, the supersaturation between 0.1~2.0%, the airflow is about 500 cm^3/min . More information about this instrument can be seen in reference^[8]; Cloud-fog Droplets was measured by DMT's Fog Particle Spectrometer (FM-100), the Fog Monitor relies on light scattering to determine particle size. Particles scatter light from a laser diode of approximately 50 mW, and collecting optics guide the light from 5~14° into forward and masked (qualifier) detectors, the peak scattering value is digitized and categorized into one of 10, 20, 30, or 40 bins. The particles in the range of 2~50 μm can be measured with 1 S precision.

2. Observation

The in-situ ground observation was carried out in Mts. Huang (30°10' N, 118°09' E), located in south of Anhui province. There are about 183 rain days through the year, and the averaged annual rainfall is about 2395 mm. The sampling site located in the meteorological station at Bright Summit of Mts. Huang (about 1840m over sea level). The campaign was starting in April, till June, 2008, with uninterruptedly observation a day. During the sampling period, conventional meteorological data and weather condition were recorded by an automatic weather station.

Results and Discussion

1. Characteristics of Aerosol Number Concentration

There is a directly relationship between the particle size and the formation, transport, transform, the process of precipitation, and the physical and chemical properties. The ultrafine particles ($0.01\text{--}0.1\text{ }\mu\text{m}$) were mainly formed through the process of complicated multiphase chemical reaction or the condensation of super saturated gases which emitted under the high temperature condition; and a small amount of them come from the nature and artificial source. These particles are instability and easily to growth through collision-coalescence process, or transform into the nuclei of the cloud or fog droplets, the life time of the ultrafine particles is almost less than one hour.

Table 1 shows the particles number concentration during spring and summer. The results showed that the number concentration of particles in size of $0.01\text{--}0.05\text{ }\mu\text{m}$ was higher than other size range, and the number concentration of the particles in the size of $1\text{--}2.5\text{ }\mu\text{m}$ and $2.5\text{--}10\text{ }\mu\text{m}$ was about three magnitudes less than the others size range in spring,. The mean value of the particles was about 3135 cm^{-3} , and the ultrafine particles ($0.01\text{--}0.05\mu\text{m}$) was accounted for about 79%. In summer, the particles in the size of $0.01\text{--}0.05\text{ }\mu\text{m}$, $0.05\text{--}0.1\text{ }\mu\text{m}$ and $0.1\text{--}1.0\text{ }\mu\text{m}$ were account for 33.8%, 34.08% and 32.09%, respectively; and the ultrafine particles ($0.01\text{--}0.05\mu\text{m}$) was accounted for about 68%. The particles ($0.01\text{--}0.05\mu\text{m}$) in summer took about 14% less than in spring. The average aerosol number concentration in summer was about 1798 cm^{-3} . Whether in spring or in summer, the ultrafine particles take account for a large proportion in aerosols. Both Buzorius et al. ^[9] and Peters et al. ^[10] indicated that the number concentration of air pollutions might be a factor more important to impact on human health, rather than the mass concentration.

Table 1. The aerosol number concentration in Spring and Summer (cm^{-3})

	Size range (μm)	Mean	Maximize	Minimize	Standard Deviation	Proportion of Mean (%)
Spring	0.01~0.05	1498	11480	92.00	615.42	47.80
	0.05~0.1	987	3940	78.00	114.04	31.50
	0.1~1.0	655	1783	12.00	49.42	20.90
	1.0~2.5	0.23	1.04	0.00	0.03	0.009
	2.5~10	0.03	0.14	0.00	0.00	0.001
Summer	0.01~0.05	607	1239	185	285	33.8
	0.05~0.1	612	636	332	76	34.08
	0.1~1.0	576	470	341	37	32.09
	1.0~2.5	0.32	0.47	0.22	0.06	0.03
	2.5~10	0.03	0.10	0.01	0.02	0.002

2. Size Distribution of Aerosol

There are two categories of aerosol sources^[11], one is the particles ($\geq 1.0 \mu\text{m}$) generated by the processes of mechanical fragmentation of solid and liquid substances; the other is the particles ($\leq 2.0 \mu\text{m}$) produced through the process of gas-particle transformation. Figure 1 shows averaged size distribution of aerosol at Mts. Huang during spring and summer, the results showed that the size spectrum profiles at Mts. Huang were similar, the peak area mainly concentrated at $0.04\sim 0.12 \mu\text{m}$ size interval, and in this size range the number concentration in spring is probably twice that in summer. In addition, there is a smaller peak area at the $0.5\sim 0.7 \mu\text{m}$ size interval, this was mainly caused by the different measurement principles of the instrument.

Figure 1. The size distribution of aerosol number concentration

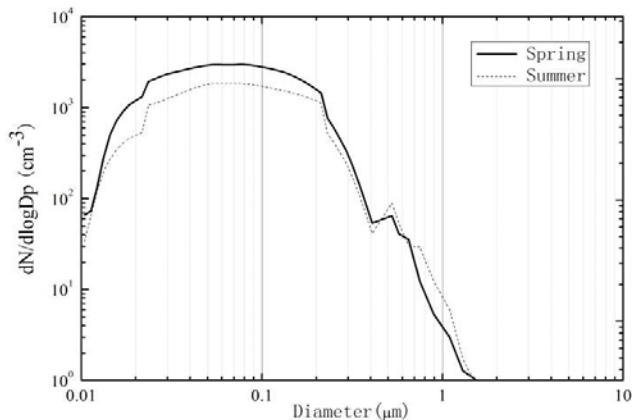


Table 2 shows the proportion of volume and surface area concentration of the particles in different size range and sampling period. In spring, the accumulation mode ($0.1\sim 1.0 \mu\text{m}$) is account for about 86% of the particles, and the particles in the range of $0.5\sim 1.0 \mu\text{m}$ take account for about 50.61%. However, in summer, the particles in the range of $0.5\sim 1.0 \mu\text{m}$ takes about 62.22% higher than that in spring, this was mainly due to the higher relative humidity in summer, nucleation mode particles might easily through the process of aggregation, adsorption, and growth into the accumulation mode particles. Aerosol surface area concentration is a significant parameter to atmospheric heterogeneous chemistry^[12]. The surface area of the particles in the range of $0.1\sim 1.0 \mu\text{m}$ take account for 82% and 86% in spring and summer. However, the particles in size of $0.1\sim 0.2 \mu\text{m}$ takes about 33.7% in spring, and the particles in size of $0.5\sim 1.0 \mu\text{m}$ takes about 41.41% in summer, which showed a different characteristic during the observation period.

Table 2. The proportion of the particles in spring and summer

Size range	Volume concentration		Surface concentration	
	Spring (%)	Summer (%)	Spring (%)	Summer (%)
0.01~0.02	0.07	0.002	0.10	0.11

0.02~0.05	0.28	0.14	2.47	1.58
0.05~0.1	3.32	1.90	13.08	9.31
0.1~0.2	16.21	9.80	33.40	25.10
0.2~0.5	18.95	14.12	21.40	19.93
0.5~1.0	50.61	62.22	27.25	41.41
1.0~2.5	7.90	8.08	1.57	2.09
2.5~10	2.70	3.70	0.32	0.46

3. Characteristic of Aerosol, Cloud Droplet and CCN

Finally, the activation spectrum of CCN in different supersaturation can be expressed by the following equation:

$$N = CS^k \quad (\text{Eq.1})$$

Where N is the CCN concentration under a special supersaturation; S is the supersaturation (taking a percentage of numerical representation); C and k are parameters that include the information of the size and chemical composition of aerosol particles. Figure 2 shows the CCN Activation spectrum at Mts. Huang in spring (a) and summer (b), the activation spectrum can be expressed as $N=2688S^{0.80}$ in spring and $N=1659S^{0.52}$ in summer. The study showed the $N=1830S^{0.84}$ in South-central region of Henan province by Shi et al. [13].

In spring, the C and k are higher than in summer and Shi's study. Twomey [14] studied the CCN activation spectrum in different regions, his research indicated that the typically k value over the ocean is 0.5, which is smaller than continent ($k=0.7$); and the C value in continent is significantly higher than ocean. The results in Mts. Huang showed that there is a larger C and k value in spring, which indicated that the climate in spring might be continental climate in spring. However, the smaller C and k value in summer, which indicated that there might be maritime climate in summer.

Figure 2. The CCN Activation spectrum at Mts. Huang in spring (a) and summer (b)

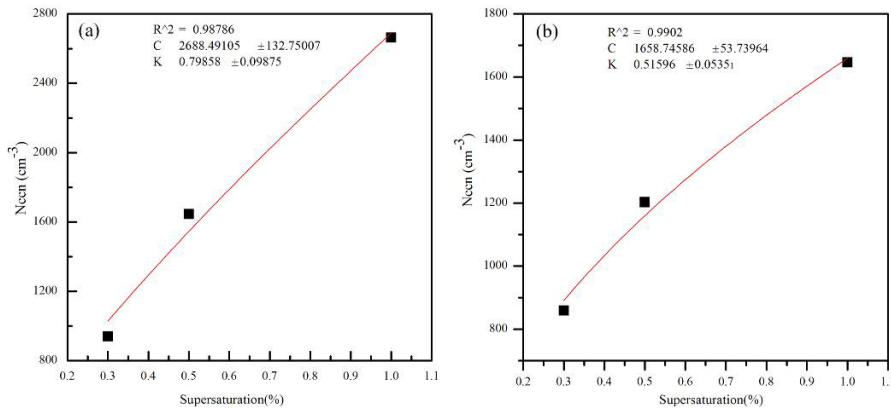
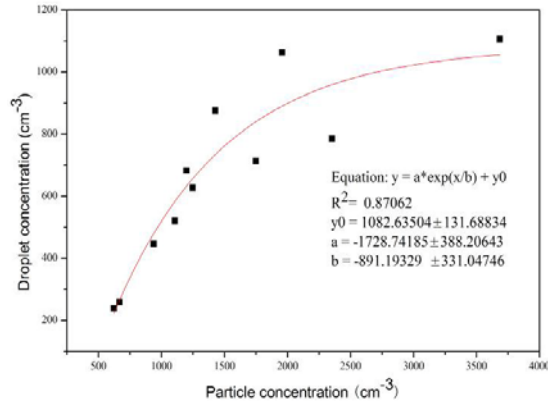


Figure 3. The relationship between cloud droplet and CCN



In the case of constant relative humidity conditions, when the aerosol particle size greater than the activation diameter, aerosol particles can be activated as CCN, and the activation diameter is determined by the curvature of particles and solute, only after acted as the nuclei of water droplets and being activated, the soluble condensation nuclei can be formed into cloud droplets. Figure 3 shows the relationship between cloud droplet and CCN concentration, it notes that there is an negative exponential function relationship between aerosol and CCN, which can be expressed as

$$N_{Cloud} = (-1829 \pm 388)e^{N_{CCN}/(-891 \pm 331)} + 1083 \quad (\text{Eq.2})$$

SUMMARY OR CONCLUSION

In this study, the aerosol, CCN and Cloud droplet was investigated on the Mts. Huang during April to June, 2008. In this campaign, the aerosol number concentration and size distribution was analyzed, the result indicates that the averaged number concentration reached $3.14 \times 10^3 \text{ cm}^{-3}$ in spring, and $1.80 \times 10^3 \text{ cm}^{-3}$ in summer, and ultrafine particles ($<0.1 \mu\text{m}$) account for 79% and 68%, respectively. The number size distributions in spring and summer all presests a single peak, with

the peak value in 0.04~0.12 μm size range. The accumulation mode particles dominate in volume concentration and surface concentration distributions. The CCN concentration can be expressed with formula: $N=CS^k$, the fitted result show that C is 2688 cm^{-3} and k is 0.80 in spring, and C is 1659 cm^{-3} and k is 0.52 in summer. According to Twomey's research, the C and k value indicates that the climate feature in Mts. Huang is continental characteristic in spring and maritime characteristic in summer. A parameterization scheme for describing aerosol-cloud relationships is proposed, which can be expressed as: $N_{\text{Cloud}} = (-1829 \pm 388)e^{N_{\text{CCN}}/(-891 \pm 331)} + 1083$.

ACKNOWLEDGMENTS

This study is jointly sponsored by the National Science Foundation of China (grant No. 41030962), and the Program for "Excellent Creative Research Team in Universities of Jiangsu".

REFERENCES

- [1] Twomey, S. A.; The Nuclei of Natural Cloud Formation. Part II: The Super saturation in Natural Clouds and the Variation of Cloud Droplet Concentrations, Geofis. Pure Appl., 1959, 43, 227–242.
- [2] Albrecht, B.; Aerosols, Cloud Microphysics, and Fractional Cloudiness, Science, 1989, 245, 1227-1230.
- [3] Graßl, H.; Possible changes of planetary albedo due to aerosol particles, in Man's Impact on Climate, edited by: W. Bach, J. Pankrath, and W. Kellogg, Elsevier, New York, 1979.
- [4] Twomey S.; Pollution and the planetary albedo, Atmospheric Environment, 1974, 8:1251-1256.
- [5] Novakov T.; Penner J. E.; Larger contribution of organic aerosols to cloud-condensation-nuclei concentrations, Nature, 1993, 365, 823-826.
- [6] Penner J. E.; Charlson R. J.; Hales J. M.; et al.; Quantifying and minimizing uncertainty of climate forcing by anthropogenic aerosols, U S Department of Energy, 1993.
- [7] Benjamin Y.H.L.; Francisco J. Romay J.R.; William D.D.; Woo K.S.; Chiruta M.; A Wide-Range Particle Spectrometer for Aerosol Measurement from $0.010\mu\text{m}$ to $10\mu\text{m}$, Aerosol and Air Quality Research, 2010, 10(2):125-139.
- [8] Roberts G. C.; Nenes A.; A continuous-flow streamwise thermal-gradient CCN chamber for atmospheric measurements, Aeros. Sci. Tech., 2005, 39, 206-221.
- [9] Buzorius G, Hameri K, Pekkanen J, et al. Spatial variation of aerosol number concentration in Helsinki city, Atmospheric Environment, 1999, 33(4): 553- 565.
- [10] Peters A.; Wichmann H. E.; Tuch T.; et al.; Respiratory effects are associated with the number of ultra fine particles, American Journal of Respiratory and Critical Care Medicine, 1997, 155 (4):1376 - 1383.
- [11] Wang M.X.; Atmospheric Chemistry (the 2nd issue), China Meteorological Press, 178, 1999.
- [12] Zhu B.; Ma L.; Yang J.; Zeng X. P.; Physical and chemical properties of winter aerosols particles in Chongqing, Journal of Nanjing Institute of Meteorology, 2006, 29(5), 662-668.

- [13] Shi L. X.; Duan Y.; Observations of cloud condensation nuclei in north China, *Acta Meteorological Sinica*, 2007, 65(4):644-652.
- [14] Twomey S.; Wojciechowski T. A.; Observations of the geographical variation off cloud nuclei, *Journal of Atmospheric Science*, 1969, 26(4),684-688.

On the Correlation of Air and Pollutant Exchange for Non-uniform Street Canyons

Yun-Wei Zhang¹, Zhao-Lin Gu² and Jian-Ying Jiao³

¹ School of Energy and Power Engineering, Xi'an Jiaotong University, Xi'an, 710049

² Department of Environmental Science and Technology, School of Human Settlements and Civil Engineering, Xi'an Jiaotong University, Xi'an, 710049

³ School of Mechanical Engineering, Xi'an Jiaotong University, Xi'an 710049, P.R. China

Principal Contact: Zhao-Lin Gu, Dr.

Department of Environmental Science and Technology, School of Human Settlements and Civil Engineering, Xi'an Jiaotong University, Xi'an, 710049,

+86-29-8339-5100, guzhaoln@mail.xjtu.edu.cn.

ABSTRACT

Air flow and pollutant dispersion in idealized non-uniform street canyons, composed of separated stepup and stepdown notches and a uniform notch in the middle, are investigated with Large-eddy Simulations (LES). Pollutant exchange rate is calculated at the roof level of the low buildings. Large scale vertical air movements are found in non-uniform street canyons, resulting of the increase of average velocity influence on pollutant exchange rate and the enhancement of pollutant escaping efficiency from the canyon to the aloft air. Sensitive analysis of average pollutant concentration at the pedestrian level to the height differences of buildings in the stepup and/or stepdown notches is conducted. Results show that even if only one floor of the buildings on the opposite sides of the canyon of the height difference, but also can cause differences in the average concentration at the pedestrian level of 20% compared to the uniform case.

KEYWORDS

Street canyon, Building layout, Air exchange rate, Pollutant exchange rate, Large eddy simulation

Introduction

Street canyons are basic geometric units of urban areas, composed of buildings and streams of people and public transportation. However, poor air quality is often observed at the pedestrian level inside these street canyons since the air recirculation there will stop pollutants from dispersing to the layer aloft^[1, 2].

The flow pattern inside a street canyon is mainly determined by the aspect ratio (AR), free wind velocity, building roof shape, building layout, atmospheric instabilities and so on^[3-7]. AR is defined as the building-height-to-street-width (H/W , where H is the building height and W is the street width). Dispersion behavior of pollutants from vehicles is closely linked to the flow pattern

inside street canyons.

However, most previous studies, where uniform street canyon models were used, focus on the effects of free wind velocity, aspect ratio, building roof shape and urban planting. In uniform street canyon models, the buildings are assumed to be of the same height, and the effect of the layout with different height buildings is neglected. But in actual street canyons, buildings are usually of different heights. Simulation results of uniform street canyon models may produce air flow patterns much different from those in non-uniform street canyons with different height buildings. Thus, studies based on uniform street canyon models cannot reveal the effects of the building layouts of actual street canyons.

A few studies have already focused on non-uniform street canyons. Nelson et al.^[8] measured the wind field within the Oklahoma City Park Avenue street canyon. Based on their measurements, a hypothetical flow structure inside the street canyon was proposed, illustrating the wind downdraft and horizontal divergence resulted from non-uniform building arrangement. With laboratory scale experiments and numerical simulations, Baik and Park^[6] investigated the flow patterns in stepup notch or stepdown notch street canyons, where unilateral buildings have the same height but the heights of buildings on the upwind side are lower (or higher) than those on the downwind side. Baik and Park's simulation of the stepdown notch flow demonstrated two counter-rotating vortices inside the street canyon. Klein et al.^[9] studied the wind and turbulence characteristics in an urban roughness layer in a wind tunnel model where buildings were arranged by blocks with different heights, and measured the vertical wind distributions at different points. However, they did not analyze the effects of building layouts along the street in details. Hu and Wang^[10], using a CFD approach, studied the effect of single high-rise building on the street level wind structure in a built-up area, and demonstrated the amplification of wind velocities in the vicinity of the building. However, actual street canyons are usually composed of multiple high-rise buildings, and it is necessary to investigate the interactions between the air flows and the layout of multiple high-rise buildings.

The motivation of this work is to study the air and pollutant exchange in non-uniform street canyons by large eddy simulations on ideally non-uniform street canyon models, and analyze the effect of building height difference on pollutant exchange rate.

Model Description

Non-uniform Street Canyon Model

Actual street canyons usually take on uneven building layouts, which, in urban roughness layer, result in difficulty in the modeling of a non-uniform street canyon and the formation of boundary conditions. Gu et al.^[11] used the ideal non-uniform street canyon models to investigate the effects of building layout on air flow and pollutant dispersion in urban street canyons, where buildings in urban roughness layer are assumed in regular arrangement, i.e., tall and low building

existing alternatively. Thus, when the ambient wind flows perpendicularly to the street, the computational domain boundaries can be set in the middle sections of the bilaterally laid buildings^[10].

In the current simulations, the length of the computational domain in the lateral direction is $L=40$ m, and that in the longitudinal direction, x , is 90 m, which is three times of the street width ($W=30$ m). The low building height (H_1) is set to be 30 m, while the tall building height (H_2) is varied from 33 to 45 m in different cases. The computational domain in the vertical direction, z , is 2.5 times of H_1 . For all the simulations, ambient winds are assumed flow perpendicularly to the street.

Mathematical Equations and Algorithms

The large eddy simulation (LES) method is used in solving the turbulence flow. Detail descriptions of governing equations and subgrid scale scheme were given in a former work^[12].

The modified periodic conditions are used in the longitudinal direction boundaries. The resolved-scale dynamic equations of the mathematical model are solved by the Finite Volume Method (FVM), with the SIMPLE algorithm used to deal with the implicit dependence of velocity and pressure. Self-developed software is used.

Results and Discussion

Pollutant concentrations are normalized by

$$C^* = \frac{C \cdot U_{ref} \cdot H_1}{Q/L} \quad (\text{Eq. 1}),$$

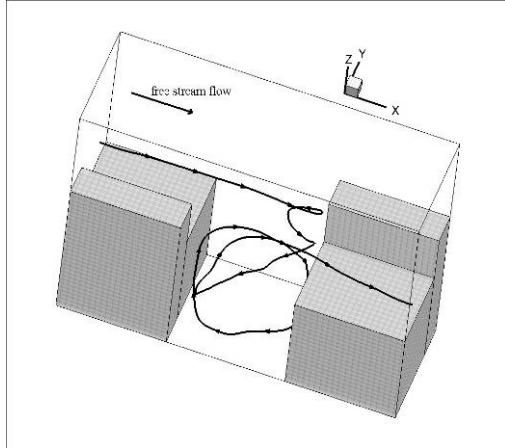
where C^* is the normalized pollutant concentration, C is the resolved pollutant concentration, U_{ref} is the reference wind velocity, Q is the pollutant emission rate (in $\mu\text{g} \cdot \text{s}^{-1}$), and L is the street length in the computational domain.

Statistical averages on wind velocities and pollutant concentrations are collected for 200 s after the flow has fully developed. Hereafter, statistically-averaged results are shown.

Air Flow Structures

Air flow structures simulated in case the tall building height (H_2) is 45 m are shown in Figure 1. Figure 1 shows a typical stream line in case $H_2=45$ m, which clearly illustrates the wind flow structures in the non-uniform street canyon. Spiral circulations dominate the air flow inside the street canyon, and it can be clearly seen that the wind direction tilts near the leeward wall, near the windward wall and near the road surface. The air flows on the top of the upwind low building which go down to the street canyon experience several re-circulations and eventually go out of the canyon over the top of the downwind low building. This air flow feature reveals that there are large scale air flows going down or going up in the non-uniform street canyon.

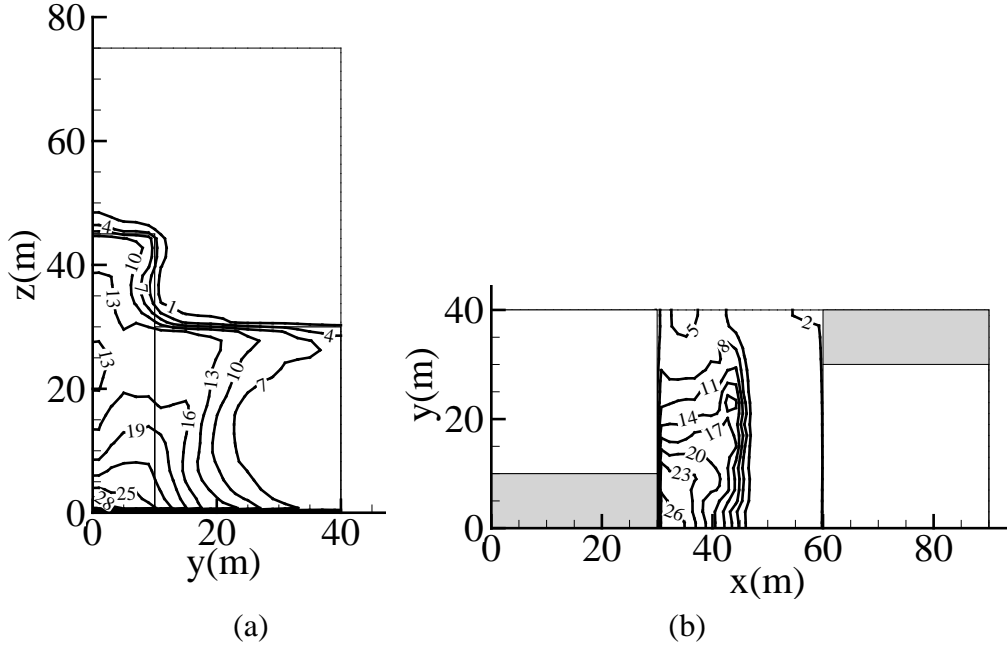
Figure 1. A typical stream line in the non-uniform street canyon for case $H_2=45$ m.



Pollutant Distributions

The simulated pollutant concentrations for case $H_2=45$ m are illustrated in Figure 2. Figure 2 (a) is the contours of pollutant concentrations in the lateral vertical plane at $x=32$ m (2 m from the leeward wall), and Figure 2 (b) are that in the horizontal plane at the pedestrian level 1.5 m from the road surface. Compared to the pollutant distribution in the uniform street canyon, where pollutants emitted from vehicles are transported to the leeward wall and then to the top areas along the leeward wall^[7, 13, 14], the pollutant concentration in the non-uniform street canyons has an evident non-uniform distribution, affected by the non-uniform wind field. In the current simulation, after pollutants are transported to the leeward wall, the lateral accumulation of pollutants occurs behind the upwind high building due to the horizontal convergence of air flow.

Figure 2. Contours of the simulated normalized pollutant concentrations in case $H_2=45$ m in planes 2 m from the leeward walls (a) and at the pedestrian level 1.5 m above the road surface (b).



Pollutant Exchange Rate and Building Height Effect

The pollutant exchange rate (PER) represents the rate of pollutant removal from the street canyon and can be calculated as,

$$PER = \overline{PER} + PER' = \int_{\Gamma_{roof}} wcdx + \int_{\Gamma_{roof}} w'c'dx \quad (\text{Eq. 2}),$$

where \overline{PER} and PER' are the average and fluctuation parts of PER, respectively^[15, 16].

Figure 3 shows the PER profiles on top of the street canyons. PER values near the leeward walls are positive, which means that pollutants are transported to the upper layers. PER values near the windward walls are negative, which means that pollutants are circulated down to the street canyons. The fluctuation parts always transport the pollutants to the upper air and occupied the most of the total PER value, as shown in Table 1. In case the tall building $H_2=39$ m, the average part (\overline{PER}) show large positive values near the leeward wall and occupied the most of the total PER value, as shown in Figure 3 and Table 1. Even in case $H_2=33$ m, i. e. the tall building is about one floor higher than the low building, the \overline{PER} occupied the most of the total PER value, see Table 1. These large positive \overline{PER} values near the leeward wall should be result from the large scale air flows going down or going up in the non-uniform street canyons (see Figure 1).

Figure3. Pollutant exchange rate (PER) on top of the street canyon.

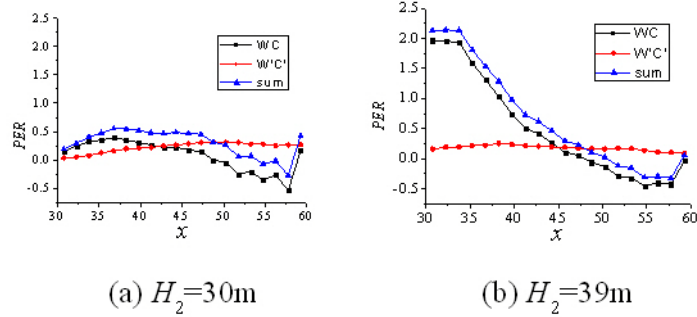
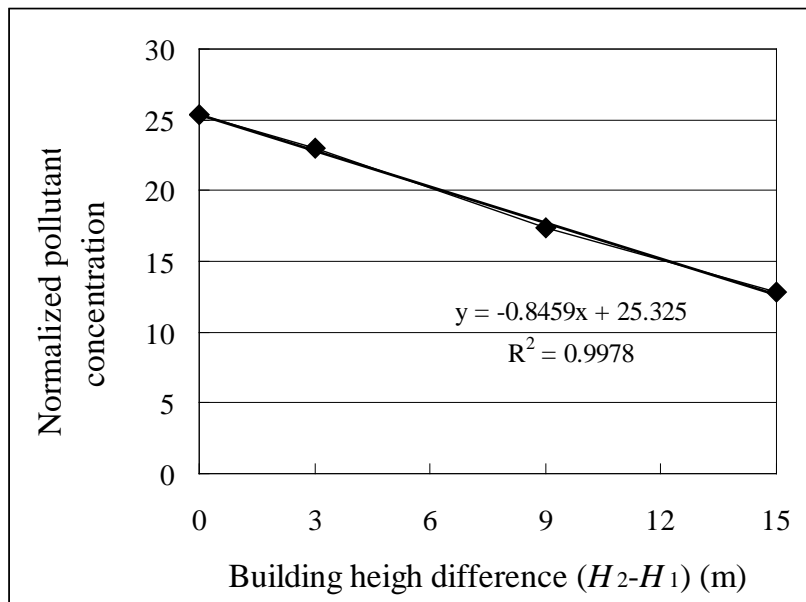


Table 1. PER simulated with different tall building height (H_2).

H_2 (m)	30	33	39	45
\overline{PER}	1.650	3.019	9.753	16.810
PER'	4.439	2.375	3.547	3.103
PER	6.089	5.394	13.300	19.913

Figure 4 shows the average normalized pollutant concentration at the pedestrian level ($z = 1.5$ m). The average normalized pollutant concentration at the pedestrian level decrease with the tall building height increasing almost linearly. Figure 3 shows that even if only one floor of the buildings on the opposite sides of the canyon of the height difference can also cause differences in the average concentration of 20% compared to the uniform case.

Figure4. Average normalized pollutant concentration at the pedestrian level.



CONCLUSIONS

In non-uniform street canyons, air flows on the top of the upwind low building which go down to the street canyon experience several re-circulations and eventually go out of the canyon over the top of the downwind low building. This air flow feature reveals that there are large scale air flows going down or going up in the non-uniform street canyon. The pollutant concentration in the non-uniform street canyons has an evident non-uniform distribution, affected by the non-uniform wind field.

In the current simulation of non-uniform street canyons, after pollutants are transported to the leeward wall, the lateral accumulation of pollutants occurs behind the upwind high building due to the horizontal convergence of air flow.

In case the tall building $H_2=39$ m, the average part (\overline{PER}) show large positive values near the leeward wall and occupied the most of the total PER value. Even in case $H_2=33$ m, i. e. the tall building is about one floor higher than the low building, the \overline{PER} occupied the most of the total PER value. Sensitive analysis of average pollutant concentration at the pedestrian level show that, even if only one floor of the buildings on the opposite sides of the canyon of the height difference can also cause differences in the average concentration of 20% compared to the uniform case.

ACKNOWLEDGMENTS

This work was supported by the National Natural Science Foundation of China (No.

40675011 & 10872159).

REFERENCES

- [1] Depaul, F.T.; Sheih, C.M. *Atmospheric Environment*. 1986, 20, 455-459.
- [2] Oke, T.R. *Energy Biult*. 1988, 11, 103-113.
- [3] Xie, X.M.; Huang, Z.; Wang, J.S.; Xie, Z. *Building and Environment*. 2005, 40, 201-212.
- [4] Niachou, K.; Livada, I.; Santamouris, M. *Building and Environment*. 2008, 43, 1383-1392.
- [5] Hang, J.; Li, Y.; Sandberg, M.; Claesson, L. *Building and Environment*. 2010, 45, 1353-1365.
- [6] Baik, J.J.; Park, R.S.; Chun, H.Y.; Kim, J.J. *Journal of Applied Meteorology*. 2000, 39, 1592-1600.
- [7] Ahmad, K.; Khare, M.; Chaudhry, K.K. *Journal of Wind Engineering and Industrial Aerodynamics*. 2005, 93, 697-717.
- [8] Nelson, M.A.; Pardyjak, E.R.; Klewicki, J.C.; Pol, S.U.; Brown, M.J. *Journal of Applied Meteorology and Climatology*. 2007, 46, 2038-2054.
- [9] Klein, P.; Rotach, M.W. *Boundary-Layer Meteorology*. 2004, 111, 55-84.
- [10] Hu, C.-H.; Wang, F. *Building and Environment*. 2005, 40, 617-631.
- [11] Gu, Z.L.; Zhang, Y.W. In *The A&WMA International Specialty Conference: Leapfrogging Opportunities for Air Quality Improvement*; Chow, J.C.; Watson, J.G.; Cao, J.J., Ed. Xi'an, China, 2010; pp 785-792.
- [12] Zhang, Y.W.; Gu, Z.L.; Lee, S.C.; Fu, T.M.; Ho, K.F. *Indoor and Built Environment*. 2011, Inpress.
- [13] Walton, A.; Cheng, A.Y.S. *Atmospheric Environment*. 2002, 36, 3615-3627.
- [14] Vardoulakis, S.; Fisher, B.E.A.; Pericleous, K.; Gonzalez-Flesca, N. *Atmospheric Environment*. 2003, 37, 155-182.
- [15] Cheng, W.C.; Liu, C.H.; Leung, D.Y.C. *Atmospheric Environment*. 2008, 42, 9041-9051.
- [16] Gu, Z.L.; Zhang, Y.W.; Lei, K.B. *SCIENCE CHINA Technological Sciences*. 2010, 53, 1928-1937.

Advanced Remote Sensing and Multi-scale Modeling of Severe Aerosol Episodes

R.-M. Hu (1), R. S. Sokhi (1), and other colleagues

(1) Centre for Atmospheric and Instrumentation Research (CAIR),

University of Hertfordshire, Hatfield, UK

Principal Contact: R.-M. Hu, Dr., Centre for Atmospheric and Instrumentation Research (CAIR), University of Hertfordshire, Hatfield, UK, TEL +44(0)1707 284052, FAX +44(0)1707 284185, r.hu@herts.ac.uk

Abstract

Despite the great environmental and social impacts of the aerosol episodes such as volcano eruption, forest fire, megacity haze and dust storm, the detailed information relative to the origin, transport and dissipation of these aerosol episodes is still limited. These incidents represent a unique opportunity to examine the dynamics and transport characteristics of the aerosol plume over regional scales through the use of advanced air quality models and monitoring data. In this study, we use regional (WRF-CMAQ) and global (GEOS-Chem) air quality models to simulate the aerosol plume in order to improve our understanding of the dynamical, dispersion and removal processes affecting the aerosol optical and microphysical properties. The combined ground-based, airborne and satellite measurements are also used to evaluate the performance of this integrated modeling approach providing an insight into the strengths and weaknesses of the models and their potential for emergency response.

Simulation of Direct Radiative Forcing of Aerosols and Their Effects on East Asian Climate Using an Interactive AGCM-aerosol Coupled System

Hua Zhang¹ and Zhili Wang²

1 National Climate Center, China Meteorological Administration, No. 46 Zhongguancun Nandajie Haidian District, Beijing, China, 100081

2 Chinese Academy of Meteorological Sciences, No. 46 Zhongguancun Nandajie Haidian District, Beijing, China, 100081

ABSTRACT

An interactive system coupling the Beijing Climate Center atmospheric general circulation model (BCC_AGCM2.0.1) and the Canadian Aerosol Module (CAM) was developed to investigate the global distributions of optical properties and direct radiative forcing (DRF) of typical aerosols and their impacts on East Asian climate. Under all-sky conditions, the simulated global annual means of sulfate, BC, and OC DRF at the TOA were -0.19 W m^{-2} , $+0.1 \text{ W m}^{-2}$, and -0.15 W m^{-2} , respectively. The sulfate, BC, and OC aerosols led to decreases of 0.58°C and 0.14 mm day^{-1} in the JJA means of surface temperature and precipitation rate in East Asia. The differences of land-sea surface temperature and surface pressure were reduced in East Asian monsoon region due to these aerosols, thus leading to the weakening of East Asian summer monsoon.

Atmospheric dynamic and thermodynamic were affected due to the three types of aerosol, and the southward motion between 15°N and 30°N in lower troposphere was increased, which slowed down the northward transport of moist air carried by the East Asian summer monsoon, and moreover decreased the summer monsoon precipitation in south and east China.

KEYWORDS

AGCM, Aerosol, Radiative forcing, Climate effects, East Asian monsoon

Introduction

Both natural processes and anthropogenic activities contribute to global climate change. The latter have played an important role in significant changes in atmospheric components since the beginning of industrialization. Currently, the aerosol climate effect (especially the interactions among aerosols, radiation, and clouds) remains one of the largest uncertainties in model simulation and climate change assessment (IPCC, 2007). Aerosols can affect climate in several

ways. First, aerosol particles can directly scatter or absorb infrared and solar radiation, thereby disturbing the energy budget of the earth-atmosphere system (Houghton et al., 1996). Second, aerosol particles acting as cloud condensation or ice nuclei can change cloud microphysical and radiative properties and cloud lifetimes, and hence indirectly affect the climate (Twomey, 1977; Albrecht, 1989).

Some field studies, such as the Cloud Indirect Forcing Experiment (CIFEX) (Wilcox et al., 2006), the Aerosols over China and their Climate Effect (Zhang, 2007), have investigated aerosol properties and radiative effects. Quantitatively understanding the different aerosol effects on climate through observation is very difficult due to the large spatial variations in aerosol concentrations. An atmospheric general circulation model (AGCM) coupled with an aerosol chemical and transport model is therefore a useful tool with which to study aerosol climate effects. The feedback between climate and aerosols can be considered using an interactively-coupled system (Kristjansson et al., 2005; Bauer et al., 2010).

To more accurately estimate the DRF due to aerosols and understand their climatic response, we coupled an AGCM developed by the National Climate Center of the China Meteorological Administration [NCC/CMA; the Beijing Climate Center (BCC) BCC_AGCM2.0.1; Wu et al. 2008] to a size-segregated multi-component aerosol module [the Canadian Aerosol Module (CAM)] developed by Gong et al. (2002; 2003). Five aerosol species were taken into account, including sulfate, BC, OC, soil dust, and sea salt. Please refer to Zhang et al. (2010) about the description of the models in detail. The DRF of aerosols and their effects on East Asian climate are investigated based on the above coupled model.

Experimental Methods

Our aim was to explore the effects of aerosols mainly produced by human activities (including sulfate, BC, and OC) on East Asian summer climate, including both direct and semi-direct effects. To this end, two experiments were conducted: (i) all five species of aerosol were considered (EXP1); (ii) only soil dust and sea salt aerosols were included (EXP2). The differences between the results of EXP1 and EXP2 (EXP1 minus EXP2) were regarded as the effects of sulfate, BC and OC aerosols on the climate. In each experiment, the interactive system coupling the BCC_AGCM2.0.1 and CAM had run for 60 years. There was a spin-up period covering the first 30 years, during this period the climate gradually changes. But after that, the simulated climatology had reached a new equilibrium, and we consequently analyzed the last 30 years of each 60-year simulation.

Results and Discussion

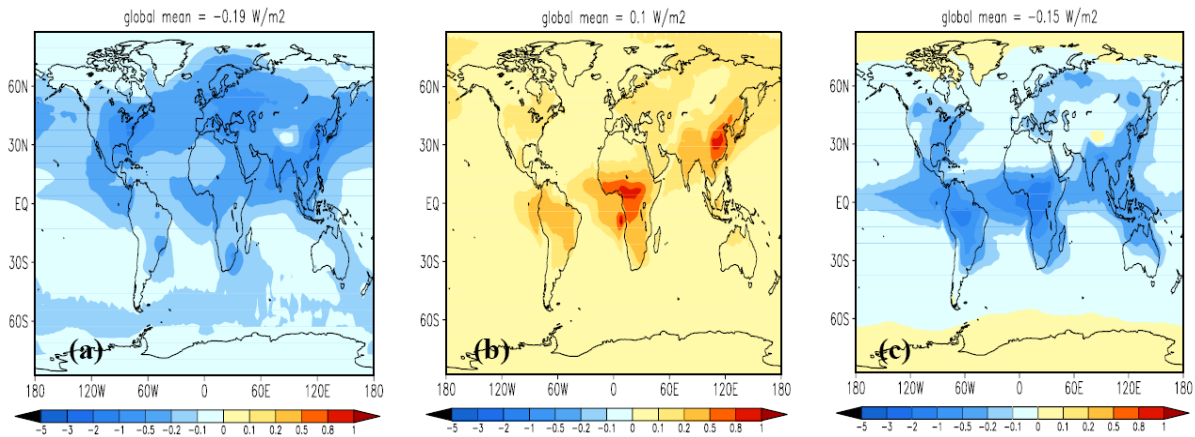
- *Direct radiative forcing of aerosols*

Instantaneous radiative forcing calculations were performed online with the AGCM-aerosol coupled system. Figure 1 shows the annual mean distributions of the simulated DRF of each aerosol species at the TOA under all-sky. Generally, sulfate aerosols caused negative radiative forcing at the TOA due to their strong scattering under all sky condition (Fig. 1a). The highest DRFs of sulfate, with a maximum value exceeding -1.0 W m^{-2} , occurred in East Asia and North America due to large industrial emissions of SO_2 and sulfate particles. The second strongest DRFs were about -0.5 W m^{-2} in India and western Europe. Long-distance transport of sulfate aerosols from the continent and the oxidation of DMS in the ocean caused negative forcing over the ocean. The simulated global annual mean of sulfate DRF at the TOA was -0.19 W m^{-2} .

BC can absorb solar radiation, generating positive radiative forcing at the TOA under all sky conditions (Fig. 1b). The region with the largest DRF was East Asia, especially south and east China, where the maximum value reached approximately $+1.0 \text{ W m}^{-2}$. The large DRF of BC in that region was mainly caused by local fossil fuel and biomass burning. The DRFs exceeded $+0.5 \text{ W m}^{-2}$ in most of central Africa and were attributable to the natural burning of carbonaceous materials. BC DRFs were mainly above $+0.1 \text{ W m}^{-2}$ in western Europe, eastern U.S., and South America. There was also positive forcing at the high latitudes of more than 60°N , resulting from long-distance transport of BC emitted at lower latitudes. The simulated global annual mean of BC DRF at the TOA was $+0.1 \text{ W m}^{-2}$.

The main optical property of OC is its scattering of solar radiation. This results in negative DRF at the TOA under all sky conditions (Fig. 1c). The distributions of the DRF of OC were basically consistent with those of BC but with negative values. The largest DRFs of OC occurred in central Africa, where maximum values exceeded -1.0 W m^{-2} . Other regions with large OC DRF included South America, Southeast Asia, North America, and Europe. DRFs in these regions were generally between -0.2 W m^{-2} and -1.0 W m^{-2} . The transport distance of OC is generally much farther than that of BC because of the strongly hydrophilic properties of OC. This implies that the spatial extent of the forcing due to OC is larger than that of BC. The simulated global annual mean of OC DRF at the TOA was -0.15 W m^{-2} .

Figure 1. Annual mean distributions of the simulated DRF due to (a) sulfate, (b) BC and (c) OC at the TOA under all sky conditions (W m^{-2}).

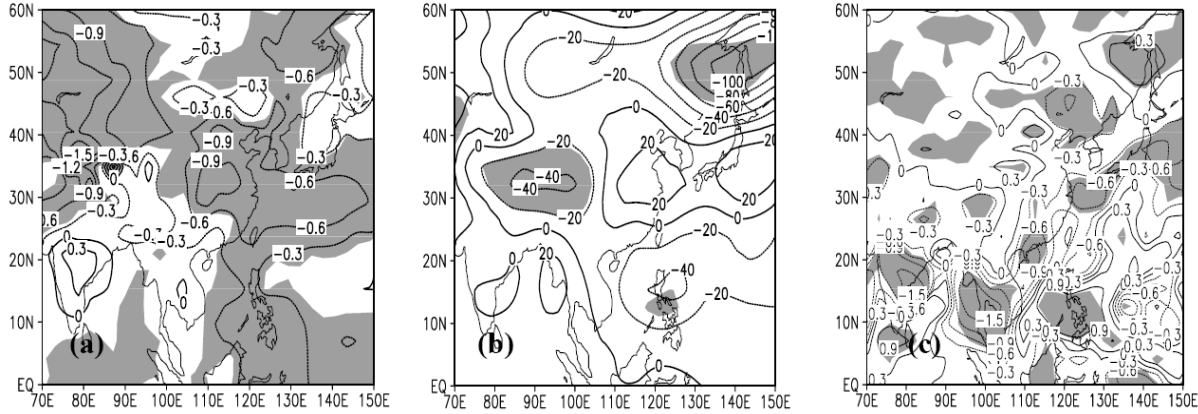


- ***Effect of sulfate, BC and OC aerosols on the East Asian summer monsoon***

The East Asian summer monsoon plays a controlling role in the summer climate in East Asia, where the emissions of sulfate, BC and OC aerosols mainly produced by human activities are the highest in the world. The large aerosol burden inevitably affects the temperature structure and atmospheric circulation by changing the radiation fields and thereby also affects the East Asian summer monsoon and regional climate. The results obtained in this work showed that the summer season (June, July, August: JJA) average DRFs due to the aforementioned three types of aerosol in East Asia ($20^{\circ}\text{--}40^{\circ}\text{N}$, $100^{\circ}\text{--}140^{\circ}\text{E}$) at the TOA and surface were -1.4 W m^{-2} and -3.3 W m^{-2} , respectively, leading to decreases of 0.58°C and 0.14 mm d^{-1} in the JJA means of surface temperature and precipitation rate in this area, respectively.

Figure 2 shows the changes of the JJA mean surface temperature, surface pressure and precipitation in East Asian monsoon region due to sulfate, BC and OC aerosols. A decrease of surface temperature was seen almost everywhere in East Asian monsoon region, but the decrease of surface temperature over land was obviously stronger than that over sea (Fig. 2a). The cooling over land at most areas of East Asia exceeded -0.6°C , especially in north China and central and east China with a magnitude of -0.9°C or so due to the huge loading of aerosols. The cooling in the west Pacific was below -0.6°C . As can be seen from the change of surface pressure in JJA (Fig. 2b), surface pressure was increased dramatically in the central and east China due to cooling over land, whereas surface pressure over the ocean on the south of China was reduced. The differences of land-sea surface temperature and pressure were weakened in East Asian monsoon region due to the effect of aerosols, thus leading to the weakening of East Asian summer monsoon.

Figure 2. The differences of JJA mean (a) surface temperature ($^{\circ}\text{C}$), (b) surface pressure (Pa) and (c) precipitation (mm day^{-1}) between EXP1 and EXP2. The shade indicates a confidence level of 90% from the T -test.



As can be seen from the change of wind field at 850 hPa in JJA (Fig. 3), the enhanced northeasterly flow in south and east China due to sulfate, BC and OC aerosols distinctly weakened the intensity of the southwest summer monsoon, and moreover the moisture flux divergence in lower atmosphere was strengthened. Thus, the monsoon precipitation is suppressed in most areas of south and east China and over the nearby oceans (Fig. 2c).

Figure 3. The differences of JJA mean wind field at 850 hPa (vector) between EXP1 and EXP2. The shade shows the differences of moisture flux divergence between EXP1 and EXP2 are negative integrated from 850 to 700 hPa.

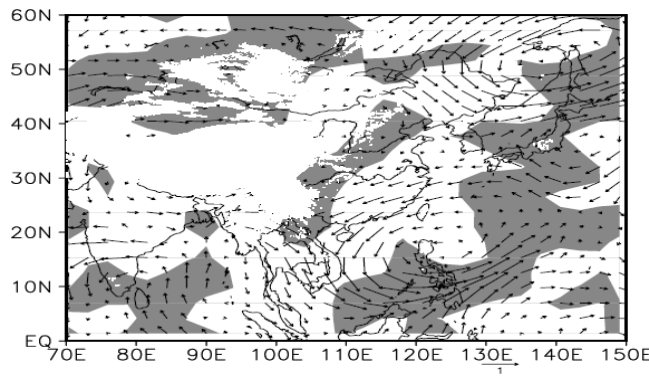
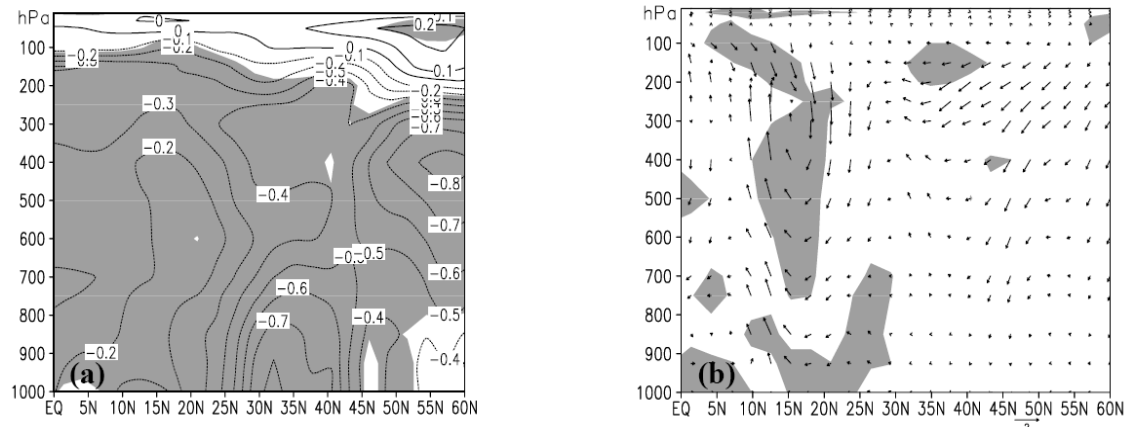


Figure 4 shows the changes of JJA mean temperature and vertical meridional circulation zonally averaged between 105°E and 120°E due to the aerosols. Aforementioned three species of aerosol led to the decrease of temperature in whole troposphere, which indicated the total feature of these aerosols was scattering over China. The reduce of temperature in the lower atmosphere

was smaller than that in mid- and high atmosphere to the south of 15°N which was beneficial to the enhancing of vertical ascending motion, whereas the contrary changes occurred between 15°N and 30°N which enhanced the atmospheric stability and suppressed convective motions (Fig. 4a). The local meridional circulation was changed with the atmospheric temperature changes (Fig. 4b). A clockwise rotation appeared between 10°N and 30°N. The increased subsidence between 15°N and 30°N strengthened the southward motion in lower troposphere, which weakened the northward transport of warm and moist air carried by the East Asian summer monsoon. Ultimately, the decrease of moist air and increase of subsidence led to the decrease of monsoon precipitation between 15°N and 30°N in south and east China.

Figure 4. The differences of JJA mean (a) temperature (°C) and (b) vertical meridional circulation zonally averaged between 105°E and 120°E between EXP1 and EXP2. The shade indicates a confidence level of 90% from the *T*-test.



CONCLUSION

An interactive coupled climate-aerosol model consisting of the BCC_AGCM2.0.1 and the Canadian Aerosol Module (CAM) was developed at the NCC/CMA. The simulated global annual means of sulfate, BC, and OC DRF at the TOA under all sky condition were -0.19 W m^{-2} , $+0.1 \text{ W m}^{-2}$, and -0.15 W m^{-2} , respectively. The summer seasonal average DRFs due to three types of aerosol (sulfate, BC, and OC) in East Asia at the TOA and surface were -1.4 W m^{-2} and -3.3 W m^{-2} , respectively, leading to decreases of 0.58°C and 0.14 mm d^{-1} in the JJA means of surface temperature and precipitation rate in this area, respectively. The differences of land-sea surface temperature and surface pressure were reduced in East Asian monsoon region due to the effect of these aerosols, thus leading to the weakening of East Asian summer monsoon. The enhanced northeasterly flow in south and east China at 850 hPa due to sulfate, BC and OC aerosols distinctly weakened the intensity of the southwest summer monsoon, and suppressed the monsoon precipitation in most areas of south and east China and over the nearby oceans. The

local meridional circulation was also affected due to these aerosols, and a clockwise rotation appeared between 10°N and 30°N. The increased subsidence between 15°N and 30°N strengthened the southward motion in lower troposphere, which weakened the northward transport of warm and moist air carried by the East Asian summer monsoon, and moreover decreased the summer monsoon precipitation in south and east China.

ACKNOWLEDGMENTS

This work is financially supported by National Basic Research Program of China (Grants No. 2011CB403405 and 2006CB403707), the Public Meteorology Special Foundation of MOST (Grant No. GYHY200906020), and the National Key Technology R & D Program (Grant No. 2007BAC03A01&2008BAC40B02).

REFERENCES

- [1] Albrecht, B. Aerosols, cloud microphysics, and fractional cloudiness, *Science*, 1989, *245*, 1227-1230.
- [2] Bauer, S.E.; Menon, S.; Koch, D.; et al. A global modeling study on carbonaceous aerosol microphysical characteristics and radiative effects, *Atmos. Chem. Phys.*, 2010, *10*, 7439-7456.
- [3] Gong, S.L.; Barrie, L.A.; Lazare, M. Canadian Aerosol Module: A size-segregated simulation of atmospheric aerosol processes for climate and air quality models 2. Global sea-salt aerosol and its budgets, *J. Geophys. Res.*, 2002, *107*. doi:10.1029/2001JD002004.
- [4] Gong, S.L.; et al. Canadian Aerosol Module: A size-segregated simulation of atmospheric aerosol processes for climate and air quality models 1. Module development, *J. Geophys. Res.*, 2003, *108*, doi:10.1029/2001JD002002.
- [5] Houghton, J.T.; et al. *Climate Change 1995: The Science of Climate Change*. Cambridge University Press, 1996, 572 pp.
- [6] IPCC, *Climate Change 2007: The Physical Science Basis. Contribution of Working Group I to the Fourth Assessment Report of the Intergovernmental Panel on Climate Change*, S. Solomon, D. Qin, M. Manning, Z. Chen, M. Marquis, K. B. Averyt, M. Tignor, and H. L. Miller, Ed.; Cambridge University Press, Cambridge, 2007, 131-217.
- [7] Kristjansson, J.E.; Iversen, T.; Kirkevag, A.; Seland, Ø.; Debernard, J. Response of the climate system to aerosol direct and indirect forcing: Role of cloud feedbacks, *J. Geophys. Res.*, 2005, *110*, D24206, doi:10.1029/2005JD006299.
- [8] Twomey, S.A. The influence of pollution on the shortwave albedo of clouds. *J. Atmos. Sci.*, 1977, *34*, 1149-1152.

- [9] Wilcox, E.M.; Roberts, G.; Ramanathan, V. Influence of aerosols on the shortwave cloud radiative forcing from North Pacific oceanic clouds: Results from the Cloud Indirect Forcing Experiment (CIFEX), *Geophys. Res. Lett.*, 2006, 33, doi:10.1029/2006GL027150.
- [10] Wu TW et al (2008) The Beijing Climate Center atmospheric general circulation model: description and its performance for the present-day. *Climate Dyn* 34:123–147. doi:10.1007/s00382-008-0487-2
- [11] Zhang, Hua; Zhili Wang; ZaiZhi Wang; Coauthors. Simulation of direct radiative forcing of typical aerosols and their effects on global climate using an online AGCM-aerosol coupled model system, Submitted to *Climate Dynamic*, 2010.
- [12] Zhang, X.Y. Aerosol over China and their climate effects. *Advances in Earth Science*, 2007, 22(1), 12-16.

The Turbulent Exchange Characteristics of Typical Pollution Processes over Guangzhou Region

Xuejiao Deng, Fei Li, Dui Wu, Hao-bo Tan, Tao Deng

Institute of Tropical and Marine Meteorology , China Meteorological Administration, Guangzhou 510080,China

Principal Contact: DENG Xue-jiao, Associate professor, Institute of Tropical and Marine Meteorology , China Meteorological Administration, Guangzhou 510080,China.

Phone: 13622893007 Fax: 020-87775231 E-mail: dxj@grmc.gov.cn

Abstract

The turbulent exchange characteristics of pollution and clean processes over Guangzhou region are analysed by combined pollutants data with land-air interaction data observed in the periods from May 2004 to August 2005. The analyses focus on the relationship between the surface stability, wind, turbulent energy, mass flux with the pollutants. The analyses show that the relation coefficient between mean wind and mean turbulent energy reach up to 0.9, the larger wind the larger turbulent energy. The relation coefficients between pollutants and mean wind, mean turbulent energy are higher, following by the relation coefficient between pollutants and vapor flux, those above relationships are obvious anti-correlations. The mean wind, turbulent energy and vapor flux in the pollution process are just 0.48, 0.59, 0.51 times as high as that with clean process, indicating the reduction of unfavourable meteorological condition for the advection and diffusion of pollutants by a half, can result in the pollutants cumulation up to 3-6 times. The relations among the pollutants are better in the pollution process, especially the relativity between PM_{10} and NO_2 is higher compared with that in the clean process, in which the relations among the pollutants are obvious weaker, the relativity between PM_{10} and NO_2 is inexistence.

Keywords: pollution process and clean process, turbulent exchange characteristics, Guangzhou region.

Study on Non-steady Collection Theory for Dust of Electrostatic Precipitator

Wenge Hao¹, Mengcheng Li¹ and Yan Li¹

¹College of Resources and Civil Engineering, Northeastern University, Shenyang, Liaoning 110819, China.

ABSTRACT

The traditional electrostatic collection theory lacked quantitative description for the effect to collection efficiency from dust layer deposited on the collection plates of ESP. To further improve the collection efficiency of ESP especially for high-resistivity dust and perfect electrostatic collection theory, the dust layer how effect collection efficiency should be revealed more accurately. Taking dust layer as research object and theoretically analyzing the charge distribution of dust layer used basic principles of electrostatics and Ohm's Law, the formula of the amount of accumulated charge in dust layer was deduced. The formula of electric-field strength formed by accumulated charges in collection space was deduced according to the principle of constant voltage between electrodes and plates and the potential continuity principle of phase boundary, and the formulas to calculate the effective collecting electric-field and the effective theory migration velocity of charged particles when superimposed this electric-field strength with depolarization electric-field strength of dust layer and initial electric-field strength when had no dust layer were obtained. The theoretical criterion of occurring anti-corona was proposed by theoretical analysis of distribution characteristics of electric-field strength in dust layer. Many phenomena appeared in operating practice of ESP, which contradicted with traditional electrostatic collection theory were explained successfully using theoretical research results. The scientific elaborations in non-steady electrostatic collection theory, which were about dust layer deposited on surface of collection plates how affected operating status of collection space electric-field and collection efficiency, enriched and developed the traditional electrostatic collection theory. These have theoretical guidance for structure designing and the selection of operating parameters of ESP and point out the direction to explore the new ways of improving collection efficiency of high-resistivity dust.

KEYWORDS

Electrostatic precipitator(ESP); Non-steady collection theory; Accumulated charges of dust

layer; Effective theory migration velocity; Anti-corona; Collection efficiency

1 Introduction

Electrostatic precipitator, a high efficiency dust collection device, has played an important role in improving atmospheric quality^[1], which is widely used in many industrial production processes. To the theory of electrostatic precipitator, the efficiency formula is still in use which was obtained by Deutsch basing one-dimensional model of electrostatic collection in 1922, while the theory has a larger deviation with the reality because of the complexity of the electrostatic collection mechanism^[2]. Many scholars proposed different collection theory models to overcome the shortage of the Deutsch theory, the dimensional diffusion model of Cooperman and the three-dimensional diffusion model of Leonard were typical^[3-5]. Guoquan Zhang, who introduced the electric Reynolds number into turbulent mixing coefficient, established the particle transporting equation basing on turbulent mass transfer theory and identified the new formula to calculated collection efficiency^[6]. Furthermore, he also proposed the theory of non-steady of electrostatic precipitator for the effect to collection efficiency of particles from dust layer deposited on collecting plates in early nineties of last century, which generalized the fact that the change of the thickness of dust layer and resistivity affected the collection efficiency^[7]. Therefore, there is no doubt that the changes of dust layer deposited on surface of collecting plates and resistivity and other important properties affect electric-field between electrodes and plates, operating parameters and collection efficiency during ESP collecting dust. This paper, used the basic principles of electrostatics, theoretically described the changing rules of accumulated charges in dust layer with changes of thickness of dust layer and resistivity during collecting of ESP, and described the effect to original collecting electric-field and even to migration velocity of charged particles from the electric-field formed by accumulated charges themselves. Meanwhile, the anti-corona and many phenomena of non-Deutsch were interpreted theoretically. So it has enriched and developed the existing electrostatic collection theory, and will provide theoretical basis for improvement of the collecting technology of ESP.

2 Theoretical Study on Non-steady Collection Process

2.1 Depolarization Electric-field

There is no doubt that the changes of dust layer deposited on surface of collecting plates and resistivity and other important properties affect electric-field between electrodes and plates, operating parameters and collection efficiency during ESP collecting dust. The dust layer deposited on surface of collecting plates induces polarization under the function of space

electric-field when ESP collected dust. According to the principle of voltage stability, the polarization electric-field induced by dust layer's polarization would produce depolarization electric-field in outer space^[8]. The depolarization electric-field is calculated as follows.

$$E_t(b-L) = (E_{p0} - \frac{E_{p0} + E_t}{\varepsilon})L$$

$$E_t = \frac{L(\varepsilon-1)}{\varepsilon b - L(\varepsilon-1)} E_{p0} \quad (\text{Eq.1})$$

E_t is strength of depolarization electric-field, $V \bullet m^{-1}$; b is distance between electrodes and plates, m ; L is thickness of dust layer, m ; ε is relative permittivity of dust layer, $C^2 \bullet N^{-1} \bullet m^{-2}$; E_{p0} is strength of electric-field on surface of collecting plates when deposited no dust, $V \bullet m^{-1}$.

Analyze formula(1), we find that, generally L is much smaller than b , and the strength of depolarization electric-field is very small which compensates the potential difference shared by the polarization electric-field of dust layer.

From the theory of ESP we know that^[2]:

$$E_{p0} = \sqrt{\frac{4j_0b}{\pi\varepsilon_0 k}} \quad (\text{Eq.2})$$

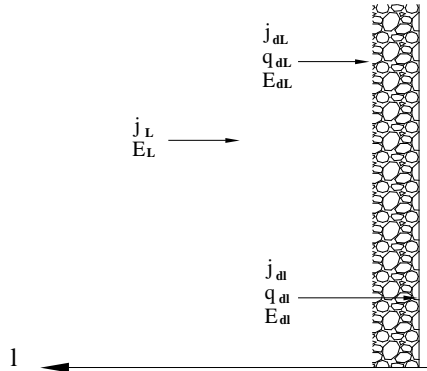
j_0 is the corona current density of space electric-field, $A \bullet m^{-2}$; ε_0 is vacuum permittivity, $\varepsilon_0 = 8.85 \times 10^{-12} C^2 \bullet N^{-1} \bullet m^{-2}$; k is ion mobility, $m^2 \bullet V^{-1} \bullet s^{-1}$.

2.2 Accumulated Charges of Dust Layer

With the deposition of charged particles on collecting plate surface, the corona current formed certain amount of charges accumulation in dust layer when corona current passed through it during ESP collecting dust.

2.2.1 Charge Density in Deposited Dust Layer

Figure.1 Schematic Diagram of the Electric-field of the Dust Layer



See figure.1, the thickness of deposited dust layer on surface of collecting plates is L at one time of the process of collecting, to a thin layer of dust l away from plate surface, we analyzed the electric-field strength, current areal density and charge density in the thin layer using Poisson equation and charge continuity equation and Ohm's Law.

$$\frac{dE_{dl}}{dl} = -\frac{q_{dl}}{\epsilon_0 \epsilon} \quad (\text{Eq.3})$$

$$\frac{dq_{dl}}{dl} = \frac{dq_{dl}}{dt} \quad (\text{Eq.4})$$

$$\frac{E_{dl}}{\rho_d} = j_{dl} \quad (\text{Eq.5})$$

Integrate the above three formulas: $\frac{dq_{dl}}{dt} = -\frac{q_{dl}}{\rho_d \epsilon_0 \epsilon} \quad (\text{Eq.6})$

E_{dl} is electric-field strength in dust layer l away from plate surface, $V \bullet m^{-1}$; l is distance of dust layer away from plate, m ; j_{dl} is current density in dust layer l away from the plate surface, $A \bullet m^{-2}$; q_{dl} is charge density in dust layer l away from the plate surface, $C \bullet m^{-3}$; ρ_d is dust layer resistivity, $\Omega \bullet m$.

The needed time when the thickness of dust layer increased from l to L is $\Delta t = \frac{L-l}{\alpha}$ if the increasing speed is $\alpha (m \bullet s^{-1})$. The charge density of dust layer l away from the plate surface develops from q_{dl0} to q_{dl} during this time. Integrate the formula(6) with collecting time, we obtain the value of charge density l

away from the plate surface when dust layer is $L^{[9]}$.

$$\int_{q_{dl0}}^{q_{dl}} \frac{dq_{dl}}{q_{dl}} = \int_{t-\Delta t}^t -\frac{1}{\epsilon_0 \epsilon \rho_d} dt \quad (\text{Eq.7})$$

$$q_{dl} = q_{dl0} \exp \frac{-\Delta t}{\epsilon_0 \epsilon \rho_d} = q_{dl0} \exp \frac{-(L-l)}{\epsilon_0 \epsilon \rho_d \alpha} \quad (\text{Eq.8})$$

The charge density (q_{dl0}) of inside of outer surface of dust layer when the thickness is l can be calculated based on charge continuity principle:

$$q_{dl0} = \frac{j_{l0}}{\alpha} - \frac{E_{dl0}}{\alpha \rho_d} \quad (\text{Eq.9})$$

j_{l0} is the current areal density flowed into dust layer, $A \bullet m^{-2}$; E_{dl0} is electric-field strength of

inside of outer surface of dust layer when dust layer is l , $V \bullet m^{-1}$.

The formula (9) can be rewritten according to the potential continuity principle of phase boundary.

$$q_{dl0} = \frac{1}{\alpha} \left(j_{l0} - \frac{E_{l0}}{\epsilon \rho_d} \right) \quad (\text{Eq.10})$$

E_{l0} is space electric-field strength near the outer surface of dust layer $V \bullet m^{-1}$.

2.2.2 Accumulated Charge of Dust Layer

Firstly, assume that the space electric-field strength near the outer surface of dust layer (E_{l0}) is unchanged when dust layer increases different thickness during collecting dust.

The electric-field strength of inside of outer surface of dust layer $E_{dl0} = \frac{E_{l0}}{\epsilon}$ is unchanged according to the potential continuity principle of phase boundary.

Meanwhile, assume that the current areal density (j_{l0}) is unchanged. Integrate the formula(8), we obtain the amount of charge accumulated by unit area of dust layer when the thickness of dust layer is L .

$$Q = \int_0^L q_{dl} dl = (\epsilon_0 \epsilon \rho_d j_{l0} - \epsilon_0 E_{l0}) \left(1 - \exp \frac{-L}{\epsilon_0 \epsilon \rho_d \alpha} \right) \quad (\text{Eq.11})$$

Firstly, we should emphasize that j_{l0} is the current areal density flowing into the outer surface of dust layer from space electric-field when dust layer is in different thicknesses, which is

different from the current density($j_{dl0} = \frac{E_{l0}}{\epsilon\rho_d}$) flowing out from dust layer surface to plate that

is driven by electric-field strength. Analyze the formula(9) and formula(11), both the value of q_{dl0} and Q are in appropriate range when the dust resistivity is moderate. However, to the low-resistivity dust, the value of q_{dl0} and Q will be negative. It says that the accumulated charges are positive ions. The formation mechanism is that the moved amount of charge promoted by the strong electric-field in dust layer is bigger than the amount compensated to dust layer by the corona current of space electric-field, so dust layer gets positive charge under the electrostatic induction force. Conversely, when the dust resistivity is high, the charges flew into the dust layer release to plate surface slowly because of the resistance effect dust layer($j_{l0} > j_{dl0}$), so the value of q_{dl0} and Q are bigger. However, the charge density of other thickness of dust layer is at small value generally in addition to the thin layer of inside of outer surface of dust layer. The reason is that the charges flowing through dust layer are quickly and almost unreservedly pushed into the collecting plate surface under the joint action of space electric-field and accumulated charges electric-field. This fact can be known from formula(8).

2.3 Back Electric-field

The electric-field formed by accumulated charges in dust layer will superimpose original electric-field and forms distribution of new electric-field strength, and spread to distribution of electric-field strength of interelectrode space through the phase boundary. Based on the fact that voltage between electrodes and plates is constant and the characteristic that accumulated charges almost all concentrate in thin layer of outer surface of dust layer, we can infer that two dropped voltage values should be equal numerically, and both are generated by additional electric-field, one additional electric-field is formed by accumulated charges in space between electrodes and plates, and the other additional electric-field is formed by accumulated charges in dust layer.

$$(b - L)E_{ea} = LE_{ed} \quad (\text{Eq.12})$$

E_{ea} is additional electric-field formed by accumulated charges in space between electrodes and plates, $V \bullet m^{-1}$; E_{ed} is additional electric-field formed by accumulated charges in dust layer, $V \bullet m^{-1}$.

Assumed that accumulated charges almost all concentrate in thin layer of outer surface of dust

layer, the electric-field strength of inside of outer surface of dust layer is $E_{dL0} - \frac{E_{ea}}{\epsilon}$, and the electric-field strength of dust layer near collecting plate is $E_{dL0} + E_{ed}$, so from Gauss theorem we obtain:

$$E_{dL0} + E_{ed} - E_{dL0} + \frac{E_{ea}}{\epsilon} = \frac{Q}{\epsilon_0 \epsilon} \quad (\text{Eq.13})$$

E_{dL0} is the electric-field strength of inside of outer surface of dust layer when dust layer is L , $V \bullet m^{-1}$.

Combine the formulas from (11) to (13), we get:

$$E_{ea} = \frac{L}{\epsilon b - L(\epsilon - 1)} (\epsilon j_{l0} \rho_d - E_{l0}) (1 - \exp \frac{-L}{\epsilon_0 \epsilon \rho_d}) \quad (\text{Eq.14})$$

According to the continuous distribution of electric-field strength in dust layer, the formula (13) indicate that there is a critical position in thin layer of dust layer where accumulates many accumulated charges, and here the electric-field strength is E_{dL0} . Correspondingly, the electric-field strength of inside of outer surface of dust layer declines to $E_{dL0} - \frac{E_{ea}}{\epsilon}$, which is caused by the combination of accumulated charges electric-field and original electric-field. So the electric-field strength of outside of outer surface of dust layer is $E_{L0} - E_{ea}$.

E_{dL0} and j_{l0} are regards as certain value not changing with increase of thickness of dust layer in above derivation. Obviously, this approach will make some errors to derived result.

Actually, with formation and development of dust layer in process of collecting middle-resistivity dust and high-resistivity dust, electric-field formed by accumulated charges will cause weaken of electric-field strength of inside of outer surface of dust layer, and this weaken causes reduction of corona current. Conversely, the reduction of corona current causes decrease of accumulated charges, and prompts electric-field strength of outside of outer surface of dust layer recover slightly. The compensating correction cycles until a balance appears. It is difficult to get result on math if taking this correction relationship into above derivation. When we use this formula practically, we can replace j_{l0} and E_{l0} with j_L and E_L as dust layer is L , the E_L can be got when taking instant current (j_L) into formula (2). The formula (14) can be rewritten as follows.

$$E_{ea} = \frac{L}{\epsilon b} (\epsilon j_L \rho_d - E_L) (1 - \exp \frac{-t}{\epsilon_0 \epsilon \rho_d}) \quad (\text{Eq.15})$$

E_{ea} is electric-field strength formed by accumulated charges in space between electrodes and plates. To middle-resistivity dust and high-resistivity dust, the direction of

this additional electric-field is opposite to original electric-field's which is formed between two poles. Therefore, superimpose this additional electric-field with the depolarization electric-field, we get back electric-field, E_a is the strength.

$$E_a = E_{ea} - E_t = \frac{L}{\varepsilon b - L(\varepsilon - 1)} [\varepsilon j_L \rho_d - \varepsilon E_L - (\varepsilon j_L \rho_d - E_L) \exp \frac{-t}{\varepsilon_0 \varepsilon \rho_d}] \quad (\text{Eq.16})$$

Formula (16) indicates the relationship between back electric-field strength and corona current areal density (j_L), collecting electric-field strength (E_L), dust layer resistivity(ρ_d), collecting time(t), relative thickness of dust layer($\frac{L}{b}$) and relative permittivity of dust layer(ε). What is important E_a is positive correlation with j_L , and collecting time also promotes E_a slightly, and dust layer resistivity and relative thickness of dust layer all have positive correlation relation with back electric-field.

2.4 Effective Electric-field Strength

2.4.1 Effective Collecting Electric-field Strength

In process of collecting dust, the distribution of space electric-field strength takes place new adjustment when superimposing the electric-field formed by accumulated charges and depolarization electric-field with original electric-field. We can obtain effective collecting electric-field strength corresponding to one thickness of dust layer.

$$\begin{aligned} E_p &= E_{p0} - E_a = E_L - E_a \\ &= E_L - \frac{L}{\varepsilon b - L(\varepsilon - 1)} [\varepsilon j_L \rho_d - \varepsilon E_L - (\varepsilon j_L \rho_d - E_L) \exp \frac{-t}{\varepsilon_0 \varepsilon \rho_d}] \end{aligned} \quad (\text{Eq.17})$$

$$\approx E_L - \frac{L}{b} (j_L \rho_d - E_L) + \frac{L}{\varepsilon b} (\varepsilon j_L \rho_d - E_L) \exp \frac{-t}{\varepsilon_0 \varepsilon \rho_d} \quad (\text{Eq.18})$$

The j_L adopts instant value when dust layer is L , and the E_L adopts the value calculated by j_L . Undoubtedly, there is error if doing like this. While it is difficult to achieve accurate calculation, j_L is less than j_{l0} , and E_L calculated by j_{l0} is less than E_{p0} , the errors formed by two values have the role of mutual compensation and amendment objectively, so the error of final calculated result of E_p can be ignored.

2.4.2 Effective Charged Electric-field Strength

It is difficult to estimate the back electric-field how affects charged electric-field accurately, because that the method calculated average electric-field strength to

calculate charged electric-field lacks of theoretical basis. Adopting the method of averaging back electric-field to space electric-field of two poles, the effective charged electric-field strength can be calculated as follows.

$$E_h = \frac{U_0}{b} - E_a \approx \frac{U_0}{b} - \frac{L}{\epsilon b} [\epsilon j_L \rho_d - \epsilon E_L - (\epsilon j_L \rho_d - E_L) \exp \frac{-t}{\epsilon_0 \epsilon \rho_d}] \quad (\text{Eq.19})$$

U_0 is voltage between two poles, V.

2.5 Electric-field Strength in Dust Layer and Theoretical Criterion of Anti-corona

2.5.1 Electric-field Strength in Dust Layer

From the Gauss theorem we obtain:

$$\begin{aligned} \int E_{dl} dA &= \int_l^L \frac{q_{dl} dl}{\epsilon_0 \epsilon A} \\ E_{dl} &= E_{dL} + (j_L \rho_d - \frac{E_L}{\epsilon}) [1 - \exp \frac{-(L-l)}{\alpha \epsilon_0 \epsilon \rho_d}] \\ &= j_L \rho_d - \frac{L}{\epsilon b} (j_L \rho_d - E_L) + \frac{L}{\epsilon^2 b} (\epsilon j_L \rho_d - E_L) \exp \frac{-L}{\alpha \epsilon_0 \epsilon \rho_d} - (j_L \rho_d - \frac{E_L}{\epsilon}) \exp \frac{-(L-l)}{\alpha \epsilon_0 \epsilon \rho_d} \end{aligned} \quad (\text{Eq.20})$$

The electric-field strength (E_{dl}) of dust layer near collecting plate is the maximum value of dust layer when $l=0$.

$$E_{d0} = j_L \rho_d - \frac{L}{\epsilon b} (j_L \rho_d - E_L) + \left(\frac{L}{\epsilon b} - 1 \right) (j_L \rho_d - \frac{E_L}{\epsilon}) \exp \frac{-L}{\alpha \epsilon_0 \epsilon \rho_d} \quad (\text{Eq.21})$$

See from formula(21), the maximum electric-field strength is very close to the electric-field strength formed by corona current when the whole corona current passes through dust layer. This fact is the same as the substance that of q_{dl} expressed by the formula to calculate Q . It says that, when dust layer has certain thickness(collecting time arrives certain value), all current flew into dust layer releases out from plates under the joint action of outer electric-field and accumulated charges.

2.5.2 Theoretical Criterion of Anti-corona

See from formula(21), anti-corona will happen when the maximum electric-field strength(E_{d0}) in dust layer is bigger than breakdown electric-field strength (E_{dc}) of dust layer. So the following formula can be theoretical criterion of anti-corona.

$$E_{d0} \geq E_{dc} \quad (\text{Eq.22})$$

Actually, the more accurate criterion should be expressed by breakdown electric-field strength

of air gap in dust layer.

$$E_{d0} \geq \frac{E_{ac}}{\epsilon} \quad (\text{Eq.23})$$

E_{ac} is breakdown electric-field strength of air, $V \bullet m^{-1}$; usually, $E_{dc} = 1 \times 10^4 V \bullet cm^{-1}$,

$$E_{ac} = 3 \times 10^4 V \bullet cm^{-1}.$$

The maximum electric-field strength in dust layer appears in the level contacting with the plate as above analysis. It says that anti-corona happens in the bottom of dust layer near plate. However, the observed anti-corona seems to happen on the outer surface of dust layer. This contradiction is not hard to explain, because that almost all accumulated charges stay in charged layer of outer surface, and the electric-field strengths of other levels are same under this level and all are nearly equal to the electric-field strength of bottom layer. Simplify formula (21), we obtain another criterion which is easy to use from formula (23).

$$\epsilon j_L \rho_d \geq E_{ac} \quad (\text{Eq.24})$$

2.5.3 Extreme Thickness

We can get that there is a maximum value for E_{d0} to thickness of dust layer through analyzing formula (21). The reason is that, with increase of thickness of dust layer, space electric-field strength, corona current density and accumulated charges all have increasing trend, which helps electric-field strength in dust layer increase. The other aspect is that, with increase of thickness of dust layer, electric-field strength of inside of dust layer tends to reduce. The maximum electric-field strength has an extreme value when dust layer increases to a certain thickness. This thesis was also confirmed by other researchers^[10]. This thickness is defined as extreme thickness.

$$\frac{\partial E_{d0}}{\partial L} = 0$$

$$(\epsilon b - L)(\epsilon j_L \rho_d - E_L) + \alpha \epsilon_0 \epsilon \rho_d (\epsilon j_L \rho_d - E_L) - \alpha \epsilon_0 \epsilon^2 \rho_d (j_L \rho_d - E_L) \exp \frac{L}{\alpha \epsilon_0 \epsilon \rho_d} \quad (\text{Eq.25})$$

2.6 Electrostatic Adhesion of Dust Layer

The electrostatic adhesion strength between dust layer and plate determines the dust cleaning effect of plate directly. Electrostatic adhesion contacts electrostatic Coulomb force, polarization electric-field force, capillary force and so on, and electrostatic force is the main force suffered by accumulated charges. Multiply electric-field strength in dust layer by corresponding charges density, and then integrate it with thickness of dust layer from l to L ,

we get the electrostatic adhesion between unit area dust layer and plate.

$$F = \int_0^L q_{dl} E_{dl} dl \quad (\text{Eq.26})$$

Multiplying the amount of accumulated charges by electric-field strength of inside of outer surface of dust layer can represent the electrostatic adhesion.

$$F = QE_{dl}$$

$$\begin{aligned} &= (\varepsilon_0 \varepsilon j_L \rho_d - \varepsilon_0 E_L) (1 - \exp \frac{-t}{\varepsilon_0 \varepsilon \rho_d}) \left\{ \left(1 + \frac{L}{b}\right) \frac{E_L}{\varepsilon} - \frac{L}{\varepsilon b} [j_L \rho_d - (j_L \rho_d - \frac{E_L}{\varepsilon}) \exp \frac{-t}{\varepsilon_0 \varepsilon \rho_d}] \right\} \\ &\approx (\varepsilon_0 \varepsilon j_L \rho_d - \varepsilon_0 E_L) \left[\left(1 + \frac{L}{b}\right) \frac{E_L}{\varepsilon} - \frac{L j_L \rho_d}{\varepsilon b} \right] \end{aligned} \quad (\text{Eq.27})$$

Analyzing formula(27) we know that positive or negative and big of small of electrostatic force depends on that of accumulated charges. If resistivity of dust is moderate, electrostatic adhesion is more appropriate. And if resistivity is too big, the larger electrostatic adhesion will create difficulties for cleaning. And if resistivity is too samll, dust layer will charge the same charge as plate, and the formed electrostatic adhesion may exclude plate, which can create second flying of dust and lead transmittance of dust increase substantially. For low-resistivity dust, adopting specific technical measures to delay the release speed of charge can effectively avoid the phenomenon that particles separate from plate themselves because of too small electrostatic adhesion or repulsive force^[11].

2.7 Voltage drop of dust layer and V-j characteristics of space electric-field

2.7.1 Voltage Drop of Dust Layer

Integrating the thickness into electric-field strength in dust layer, the formula to calculate the voltage drop of dust layer is got.

$$\begin{aligned} \Delta U &= \int_0^L E_{dl} dl \\ &= j_L \rho_d L - \frac{L^2}{2 \varepsilon b} (j_L \rho_d - E_L) + \frac{L^2}{2 \varepsilon^2 b} (\varepsilon j_L \rho_d - E_L) \exp \frac{-L}{\alpha \varepsilon_0 \varepsilon \rho_d} - \alpha \varepsilon_0 \rho_d (\varepsilon j_L \rho_d - E_L) (1 - \exp \frac{-L}{\alpha \varepsilon_0 \varepsilon \rho_d}) \\ &\approx j_L \rho_d L - \varepsilon_0 \alpha \rho_d (\varepsilon j_L \rho_d - E_L) \end{aligned} \quad (\text{Eq.28})$$

See formula(28), the voltage drop of dust layer is not equal to $j_L \rho_d L$ normally, but it has a correction according to the value of dust layer resistivity. This correction reflects the fact that corona current doesn't cross the dust layer equivalently and the electric-field strength of dust layer in the thickness is not a fixed value comprehensively.

2.7.2 V-j Characteristics of Space Electric-field

The voltage drop of dust layer is different with the voltage drop of this space thickness with no dust, and this difference will change the shared effective voltage of voltage between two poles in space and accompanied the corona current.

$$j_L = \frac{2\epsilon_0 k}{b^3} (U_0 - \Delta U)(U_0 - \Delta U - U_c) \quad (\text{Eq.29})$$

U_c is initial corona voltage, V.

The voltage between electrodes which corresponds to instant current (j_L) has increased one voltage drop of dust layer. It is said that the voltage which is shared in the space between electrodes needs to subtract the voltage drop of dust layer, and then call the remaining voltage as effective voltage(U_L)^[12].

$$U_0 = \frac{1}{2} [2j_L \rho_d L - 2\epsilon_0 \alpha \rho_d (\epsilon j_L \rho_d - E_L) + U_c + \sqrt{U_c^2 + \frac{2j_L b^3}{\epsilon_0 k}}] \quad (\text{Eq.30})$$

$$U_L = U_0 - \Delta U = \frac{1}{2} (U_c + \sqrt{U_c^2 + \frac{2j_L b^3}{\epsilon_0 k}}) \quad (\text{Eq.31})$$

At this time, the charged electric-field strength can be expressed as follows.

$$E_h = \frac{U_L}{b - L} \quad (\text{Eq.32})$$

2.8 Effective Theory Migration Velocity

The charged amount of particles is q , and these particles move to collecting plate in the original electric-field(E_{p0}), so the theoretical migration velocity is calculated as follows^[2].

$$\omega_0 = \frac{qE_{p0}}{3\pi\mu d} = \frac{\epsilon_0 \epsilon d U_0 E_{p0}}{(2 + \epsilon) \mu b} \quad (\text{Eq.33})$$

μ is air viscosity coefficient, $\text{Pa} \bullet \text{s}$; d is diameter of particles, m .

Analyzing the experimental studies and testing data of ESP in practical operation, both the results reflect that the effective theory migration velocity calculated by formula(33) are often much larger than that calculated by actual data. The reason is very hard to understand.

Taking collecting electric-field strength in practice (formula(18)) and effective charged collecting electric-field strength (formula(32)) into formula(33), the formula to calculated the effective theory migration velocity of charged particles when there has dust layer on plate is got.

$$\begin{aligned}
 \omega &= \frac{\varepsilon_0 \varepsilon d (U_0 - \Delta U)}{\mu(2 + \varepsilon)(b - L)} (E_{p0} - E_a) \\
 &= \frac{\varepsilon_0 \varepsilon d}{2\mu(2 + \varepsilon)(b - L)} (U_c + \sqrt{U_c^2 + \frac{2j_L b^3}{\varepsilon_0 k}}) \left\{ (1 + \frac{L}{b}) E_L - \frac{L}{\varepsilon b} [\varepsilon j_L \rho_d - (\varepsilon j_L \rho_d - E_L) \exp \frac{-t}{\varepsilon_0 \varepsilon \rho_d}] \right\} \\
 &= \frac{\varepsilon_0 \varepsilon d}{2\mu(2 + \varepsilon)(b - L)} (U_c + \sqrt{U_c^2 + \frac{2j_L b^3}{\varepsilon_0 k}}) \left[(1 + \frac{L}{b}) \sqrt{\frac{4j_L b}{\pi \varepsilon_0 k}} - \frac{L}{b} j_L \rho_d \right] \quad (\text{Eq.34})
 \end{aligned}$$

As is known to us, the collection efficiency of ESP largely depends on the migration velocity of charged particles. Comparing formula(34) with formula(1), charged electric-field strength and collecting electric-field strength reduce $\frac{b\Delta U - LU_0}{b(b-L)}$ and E_a respectively because of the

effect of accumulated charges, and the named effective theory migration velocity must have considerable gap comparing with traditional theoretical migration velocity. The formula(16) indicated that the difference between them is depends on resistivity value of dust layer and the relative thickness of deposited dust layer. The electric-field strength formed in dust layer ($j_L \rho_d L$) is very big when collecting high-resistivity dust, and leads the voltage drop in the dust layer thickness increase which is equal to reduce the effective voltage between two poles. Meanwhile, it also leads accumulated charges increase and cause electric-field strength formed by accumulated charges increase. The former reduces the charged electric-field strength and the latter decreases the collecting electric-field strength. So the two function make the effective theory migration velocity a little smaller than the traditional theoretical migration velocity when collecting high-resistivity dust.

Widening plate distance is benefit to reduce current areal density and improve the uniformity of its distribution, which avoid charge releasing poorly and happening anti-corona. So far, it is the reason why wide plate distance can improve the collection efficiency of high-resistivity dust in the traditional electrostatic collection theory. We can know that from formula(29) clearly. However, the comprehensive effect from the joint action of decline of current intensity and widening of plate distance needs further mathematical analysis. While the relative thickness of dust layer how affect migration velocity is very clear. Reducing the value of relative thickness of dust layer as much as possible is benefit to improve the effective

theory migration velocity. Certainly, the selection of the width of plate distance should take into account the effect to the corona current and air flowing state.

The formula(34) also indicates that corona current areal density has close relationship with the effective theory migration velocity of charged particles. Laying aside the effect to particles charging, in order to consider the corona current density how affects the effective theory migration velocity of charged particles comprehensively, we should firstly insure that the corona current not exceed restricted current of occurring anti-corona.

3 Optimization of Electric-field Parameters

The back electric-field formed by accumulated charges makes both charged electric-field and collecting electric-field decline, which reduces the migration velocity of charged particles. That is the fundamental reason that affects collection efficiency of high-resistivity dust. Therefore, we may minimize the effect to collection efficiency maximally through adjusting the operating parameters of electric-field to make back electric-field strength achieve the minimum. We can calculate j_L and b when the electric-field strength is 0 from formula(16).

$$j_L = \frac{4b}{\pi \epsilon_0 k \rho_d^2} \quad (\text{Eq.35})$$

$$b = \frac{\pi \epsilon_0 k j \rho_d^2}{4} \quad (\text{Eq.36})$$

The above two formulas indicate that both the optimized current and plate distance have no relationship with the thickness dust layer. And also indicate that the current areal density reduces and plate distance increases with increase of dust resistivity. The supply voltage (U_0) between poles is got when taking formula(35) into formula(30). It is through adjusting supply voltage to ensure that the operation of ESP is always in good condition.

$$U_0 = \frac{Lb}{\pi \epsilon_0 k \rho_d} - \alpha \epsilon_0 \rho_d \left(\frac{4 \epsilon b}{\pi \epsilon_0 k \rho_d} - E_L \right) + \frac{1}{2} U_c + \frac{1}{2} \sqrt{U_c^2 + \frac{8b^3}{\pi \epsilon_0^2 k^2 \rho_d^2}} \quad (\text{Eq.37})$$

Calculating the extreme value of the effective theory migration velocity may be the more reasonable optimization method^[12].

$$\frac{\partial \omega}{\partial b} = 0, \quad \frac{\partial \omega}{\partial j_L} = 0, \quad (\text{Eq.38})$$

Only through numerical method can the above two formulas be calculated. Emphasize again, we should insure that the corona current(j) not exceed restricted current of occurring anti-corona no matter how we calculate it.

CONCLUSIONS

In non-steady collection process of ESP, taking dust layer deposited on collecting plate as study object and using the basic principles of electrostatics, the distribution of charge density of dust layer, the total amount of accumulated charges, the back electric-field formed by electric-field generated by accumulated charges of dust layer and depolarization electric-field in space, distribution of electric-field strength in dust layer were analyzed theoretically and systematically. The formulas to calculate the effective charged electric-field strength, the effective collecting electric-field strength and the effective theory migration velocity of charged particles, and theoretical criterion of anti-corona were proposed. There was an extreme value for electric-field strength in dust layer with increase of thickness of dust layer. The completed non-steady electrostatic collection theory reveals the mechanism that dust resistivity, relative thickness of dust layer, and corona current strength and other factors how affect collection efficiency of particles. Meanwhile, the non-steady electrostatic collection theory has made rational and theoretical interpretation to many phenomena that the traditional electrostatic collection theory can't explain.

REFERENCES

- [1] Lixian Gong. The Application of ESP in Domestic Thermal Power Plant and the Outline of Designing ESP. *ESP and Purify of Air*, 2001, 7 (3):10-14.
- [2] White H J. *Industrial Electrostatic Precipitation*. Massachusetts, Andison-Wesley, Reading, 1963, 95-293.
- [3] Cooperman P. A New Theory of Precipitator Efficiency. *Atorm Environ*. 1971, 5: 541-551.
- [4] G. L. Leonard, M. Mitchner and S. A. Self. Experimental Study of the Effect of Turbulent Diffusion on Precipitator Efficiency. *Journal of Aerosol Science*, 1982, 13: 271-284.
- [5].G. L. Leonard, M. Mitchner and S. A. Self. An Experimental Study of the Electro hydrodynamic Flow in Electrostatic Precipitators. *J. Fluid Mech*, 1983, 127: 123-140.
- [6] Zhibin Zhao, Guoquan Zhang. New Model of Electrostatic Precipitation Efficiency Accounting for Turbulent Mixing. *Journal of Aerosol Science*, 1992, 23(2):115-121.
- [7] Zhibin Zhao, Guoquan Zhang. Theory of Non-Steady Electrostatic Precipitation. *Journal of Northeastern University*, 1992, 13(4): 325-329.
- [8]Muzhen Sun. *Physical Basis of Dielectric*. Guanzhou: South China University of Technology Press, 2000, 17-18.
- [9]Chongguang Bao. *Theory of Electric Technique*. Beijing: Beijing University of Technology Press, 1983, 53-54.

- [10] Wangsheng Chen, Xiaodong Xiang, Jidong Lu. Charged Dust Layer Thickness at Back CoronaBreakdown Point in Electrostatic Precipitation. *Environmental Science and Technology*, 2006, 29(10):32-33.
- [11] Wenge Hao, Yaping Hou, Guangling Zhao, et al. Effect of a Conductive Anticorrosion Coating on Collection Efficiency in an Electrostatic Precipitator. *Acta Scientiae Circumstantiae*, 2008, 28(5): 956-959.
- [12] Wenge Hao, Yaping Hou, Haowang Xiong. Study on Operation Parameters of Electrostatic Precipitator Based on Non-steady Electrostatic Collection Theory. *Chinese Journal of Environmental Engineering*, 2008, 2 (3):378 - 382.

Effect of Pleat Shape on the Pressure Drop of Clean Pleated Filter Panels

Qisheng Ou¹ and Da-Ren Chen¹

¹Department of Energy, Environmental and Chemical Engineering, Washington University in St. Louis, Campus Box 1180, One Brookings Drive, St. Louis, MO 63130, USA

ABSTRACT

A numerical model has been developed to model the flow field and pressure drop of the pleat filter panel. In this model, the fluid flow in free flow channel is modeled by steady laminar flow and by modified Navier-Stokes equation using Darcy-Brinkman equation in filter media. A finite element method is used to solve the model numerically. It is shown that under certain pleat shape, the pressure drop can be minimized at an optimal pleat count, above which the pressure drop is dominated by viscous drag in pleat spacing, while below which, by resistance in filter media. Curved pleat shape will reduce the pressure drop in media-dominated regime while increase pressure drop in viscosity-dominated regime.

KEYWORDS

Pleated filter panel, Pleat shape, Pressure drop

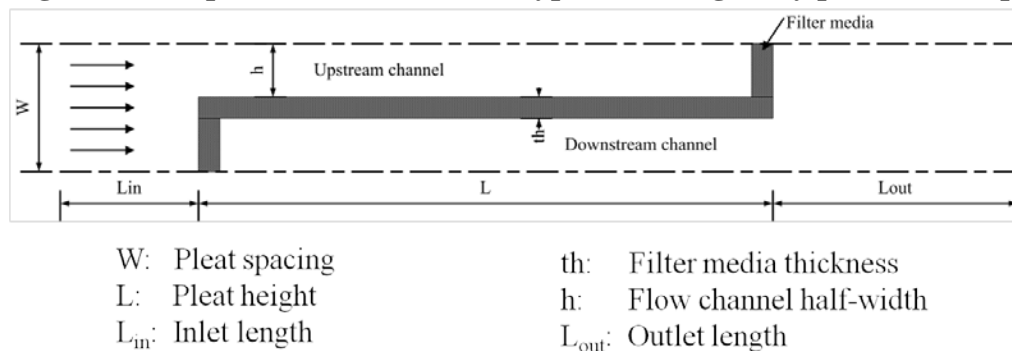
Introduction

Pleated filter panels have been used in a variety of filtration systems in industrial warehouses, office building and residential houses. Different from the cases of flat filter media, the performance of pleated filter panels is affected by the parameters such as the pleat count, pleat height, and pleat shape in addition to the properties of filter media. The design optimization of pleated filter panels to meet the application requirement thus becomes important. Numerical work has been conducted to investigate and optimize the pressure drop of clean pleated filter panels. However, the former studies mostly focused on the regular rectangular and triangular pleat shapes. In this study, a finite-element-based model was constructed to predict the pressure drop of pleated filter panels of various pleat shapes, e.g., a waved shape configuration.

Numerical Modeling

A typical computational domain of a rectangular-pleated filter panel is shown in Figure 1. Gas flow entered the domain from the left and exited from the right. The domain consists of upper flow channel, filter media and lower flow channel. Gas flow was moved in the upper flow channel upon entering the domain, passed through the filter media to the lower flow channel and exited the domain from the outlet on the right. The total pressure drop across the filter panel is the sum of that due to the flow contraction in the upstream region, the viscous drag in both flow channels, the pressure drop across filter media as well as the flow expansion in the downstream region^[1]. To predict the total pressure drop resulted by a pleated filter panel a detailed flow field modeling is prerequisite.

Figure 1. Computational domain of a typical rectangularly pleated filter panel.



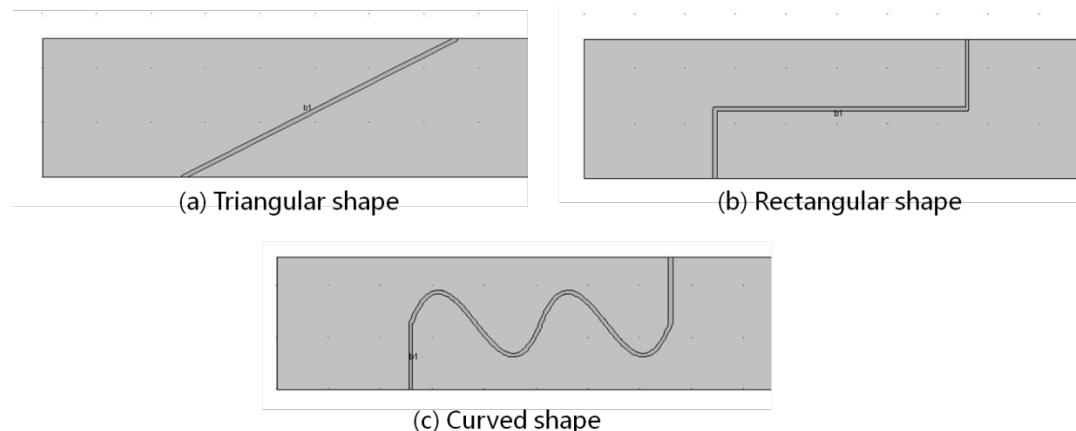
In our study, a finite-element based model was developed to calculate the flow field in both air channel and filter media. Due to the panel design and pleat repetition a two-dimensional computation domain was used. The flow in the air channel was modeled by the Navier-Stokes equation with the assumptions that (1) the flow is incompressible and steady-state; (2) the fluid is isotropic and homogeneous; (3) a uniform velocity profile at the upstream. For modeling the flow inside the filter media, the media was assumed to be a porous media. Then the Darcy-Brinkman equation was incorporated into the classical Navier-Stokes equation as shown in Eq. 1^[2]. The continuity equation (Eq. 2) was applied for both domains.

$$\frac{\rho}{\varepsilon^2}(\bar{u} \cdot \nabla \bar{u}) = -\nabla p + \frac{\mu}{\varepsilon} \nabla^2 \bar{u} - \frac{\mu}{\kappa} \bar{u} \quad (\text{Eq.1})$$

$$\nabla \cdot \bar{u} = 0 \quad (\text{Eq.2})$$

For the boundary conditions, the inlet boundary on the left was set as uniform velocity profile. Symmetrical boundary conditions were imposed on the top and bottom of the computational domain. For the outlet boundary condition, only the absolute pressure of one point on the boundary was set as zero for reference. The shape functions of the elements for the finite element computation are in the second for velocity and the first order for pressure.

Figure 2. Schematic diagram of the computational domain of different pleat shapes



Results and Discussion

Several pleat shapes were studied, as illustrated in Figure 2. Additional to rectangularly and triangularly pleated shapes, curved pleat shapes with various variations was also investigated in this study.

Figure 3. Pressure drop as a function of pleat count of rectangular pleat shape and curved shape with opposite bend directions

$\epsilon=0.99$, $\kappa=1.03\text{e-}12\text{m}^2$, $U_0=0.5\text{ m/s}$, PleatHeight=1 inch

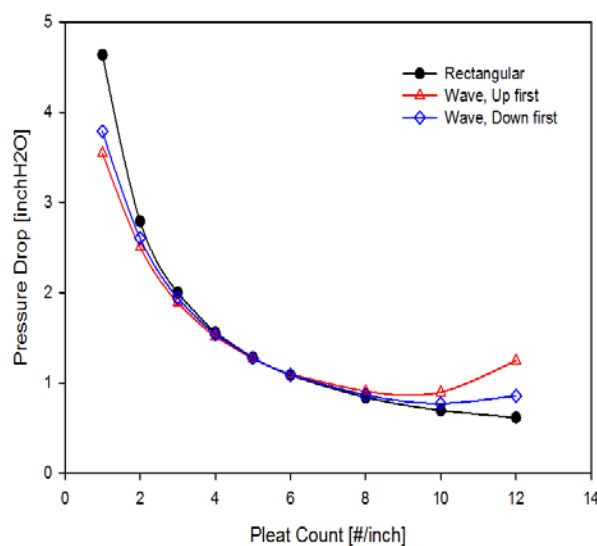
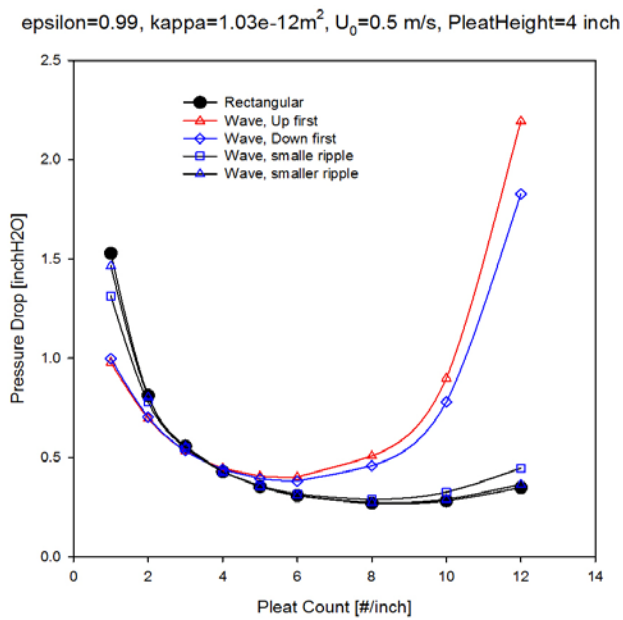


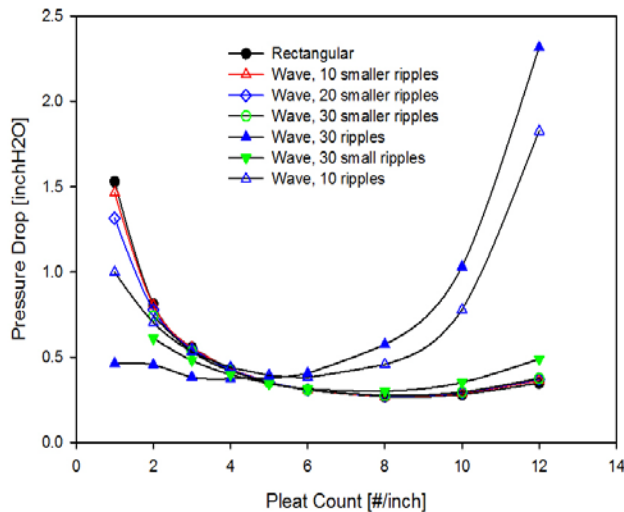
Figure 4. Pressure drop as a function of pleat count of curved shape pleat with different ripple size



As shown in Figure 3, 4 and 5, for certain pleat shape, the pressure drop cross the filter panel is a function of pleat count, which is defined as number of pleats per unit length. Generally speaking, there is an optimal pleat count corresponding to the minimum pressure drop across the filter panel. At a low pleat count, the flow face velocity in the filter media will be high, resulting in a high pressure drop cross the media (i.e., medium dominated regime). At a high pleat count, the pressure drop due to the viscous drag in the air channel between pleat spacing becomes more significant, resulting in a high total pressure drop (i.e., viscosity-dominated regime). Comparing with rectangularly pleated shape, curved pleat shape will have a lower pressure drop in media-dominated regime. It is because curved surface increases the total surface area of filter media. However, in the viscosity-dominated regime, a higher total pressure drop is expected as curved surface narrows the air flow channels between pleat spacing,. It is thus concluded that using the pleats with large ripple size or large number of ripples if the panel design was in media-dominated regime will further reduce the panel pressure but result in an even high pressure drop if the panel was in viscosity-dominated regime.

Figure 5. Pressure drop as a function of pleat count of curved shape pleat with different number of ripples

$\epsilon=0.99$, $\kappa=1.03 \text{e-}12 \text{m}^2$, $U_0=0.5 \text{ m/s}$, PleatHeight=4 inch



CONCLUSION

Based on the computational results given above, an optimal pleat counts for a filter panel with a certain pleat shape, pleat height and given filter medium properties, corresponding to a minimum pressure drop, is existed. Comparing with regular pleat shape, curved pleat shape tends to reduce the total pressure drop when the filter panel was designed to operate in media-dominated domain but results in higher pressure drop if the panel was operated in viscosity-dominated domain. Ripple size and number in curved pleat shapes will affect the total pressure drop. More detailed discussion and data resulted from this study will be given in this presentation.

REFERENCES

- [1] Chen, D.-R., D.Y.H. Pui, and B.Y.H. Liu, Optimization of Pleated Filter Designs Using a Finite-Element Numerical Model. *Aerosol Science and Technology*, 23:579-590, 1995.
- [2] Katto, Y. and T. Masuoka, Criterion for the onset of convective flow in a fluid in a porous medium. *International journal of heat and mass transfer*, 10:297-309, 1967.

Development of the Electro-physical Method of Aero-ion Cleaning

Andrey Grishin, Ivan Yagodkin, Andrey Posagennikov and Valerii Melnikov

Institute for Physics and Power Engineering, Obninsk 249034, Russia

ABSTRACT

Cleaning of gas-air flows in different branches of industry remains one of the most important directions in the field of technologies of environmental protection from aerosols of the different origin, including radioactive and toxic ones.

High-efficient aerosol filters being used today at NPP are the source of large volumes of radioactive waste subject to burial. They have a limited lifetime, and their fabrication and operation are costly.

The situation arisen with gas cleaning from radioactive and toxic aerosol particles at NPP requires, on the one hand, updating of traditional approaches and, on the other hand, development of fundamentally new methods and aids of air cleaning, namely, the principle of combined cleaning based on the fact that particles take up specific properties in ionized gas and then are to be caught on filters.

The problems of experimental investigation of the effect of intensive aeronization on catching of aerosol particles from the air flow using combined filtering systems is the subject of this paper.

KEYWORDS

Aero-Ion Cleaning, Aerosols, Electro-physical Method, Cleaning of Gas-Air Flows, Filters

Introduction

Cleaning of gas-air flows in different branches of industry remains one of the most important directions in the development of technologies used to protect the environment from aerosols of different origin, including radioactive and toxic ones.

The environmental safety, including the radiation one, which is associated with operation of the equipment being used at plants of radiochemical, nuclear, instrument engineering industry and others is governed by the surrounding atmosphere to a large extent. Therefore quality of filtering equipment, in particular, aerosol filters capable of ensuring high-efficient decontamination of air from radioactive and toxic aerosols of the different origin becomes especially important.

High-efficiency aerosol filters being used today at NPPs are the source of large volumes of

radioactive waste subject to burial. They have a limited lifetime and a rather high cost of fabrication and operation.

Such situation with gas cleaning from radioactive and toxic aerosol particles at NPPs requires, on the one hand, improvement of traditional approaches to creation of filtering equipment and, on the other hand, development of fundamentally new methods and means for air cleaning, namely, the principle of combined cleaning, which lies in the fact that particles acquire specific properties in ionized gas and subsequently are caught by filters.

The method of electophysical action on the disperse medium is based on the charge which appears at particles with the aim of their subsequent more efficient trapping by high-porous filtering medium with opposite surface charge. The gain in decontamination efficiency (by particles), being achieved in multi-stage filters at the stage of rough cleaning, can markedly reduce the concentration of aerosols arriving at the final expensive stage of high-efficient decontamination, thereby extending service time of the high-efficient section and the whole filter. Charging of aerosol particles of the different origin and disperse composition is widely used in a number of processes and units such as electric filtration of air and electric filters of the various purpose and electric separation. The physical processes accompanying formation of charged aerosols and their interaction with other materials are varied and complicated. Among them are charging of aerosol particles of different size and composition, motion of charged particles in own and external electric fields, interaction of charged aerosol particles with each other and other aerosol particles (electric coagulation), deposition and interaction of charged aerosol particles with various objects and other processes.

The investigation of possible physical mechanisms, conditions and trends of the impact of aeroionization on aerosol particles with a view to provide their more efficient trapping by different filtering systems is of special interest, since all this could have considerable promise in a number of processes and devices.

Experimental Methods

To carry out a comprehensive investigation of the effect of aeroionization parameters (corona discharge intensity, electric field strength) and filtering system performance on the efficiency of aerosol particles filtration, a test facility was developed and manufactured. The schematic diagram of the test facility is shown in Fig.1.

The basic components of the test facility are aerosol plenum (1) with aerosol generator of the condensation type; ionizer (2); universal portable aeroion counter UT-8401 (3); computer-monitored laser aerosol spectrometer (4) provided with data processing system (5); test section (6), modeling air pipeline; flow rate inducer – ventilator with voltage regulator (7); Shch-300 combined digital instrument (8); filter holder (9).

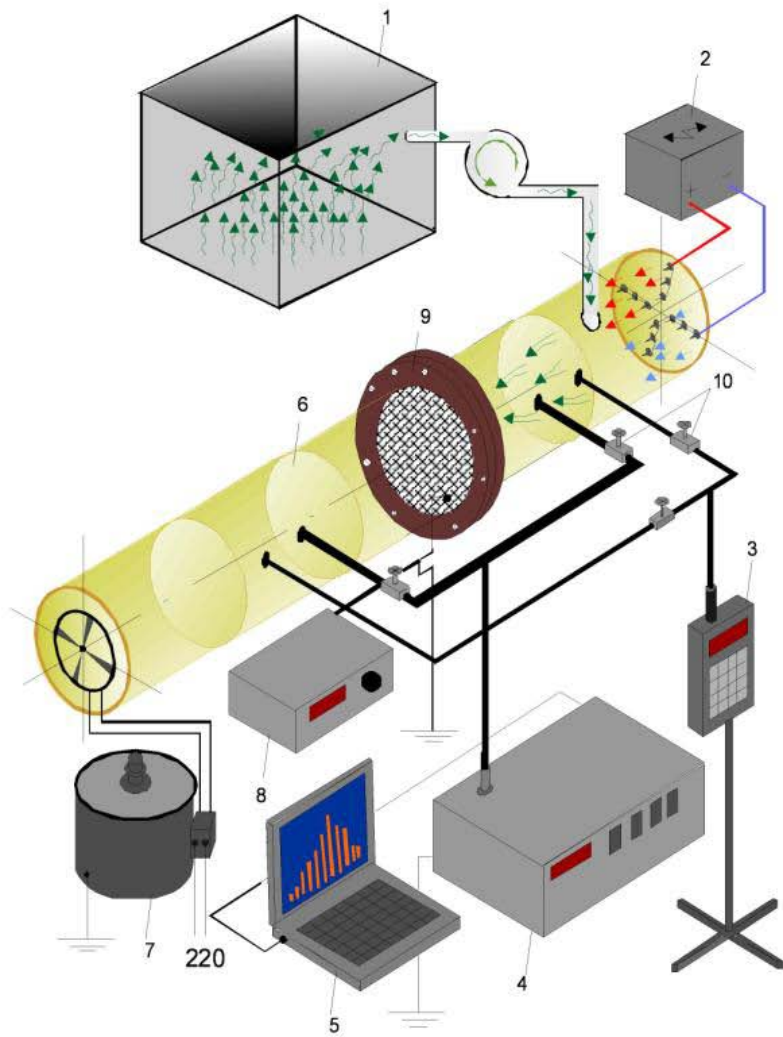
The test section represents a 200 mm-d. 1500 mm-long cylindrical tube successively

accommodating coronating electrodes, filtering materials and flow rate inducer. The filtromaterial under investigation is fastened in filter holder.

Three electrode systems were used as coronating electrodes in tests:

1. eight needles distributed over the dielectric holder which is positioned over the air pipeline cross-section;
2. a number of smooth coronating wires put normally to the air flow (wire diameter being 300 µm, interwire spacing being 35 mm);
3. a number of saw-shaped electrodes set normally to the air flow and forwarded by their points towards deposition electrodes.

Figure 1. – Schematic Diagram of Test Facility.



- 1 – aerosol plenum with aerosol generator of the condensation type;
2 – ionizer for generation of aeroions; 3 – UT-8401 universal portable counter of aeroions; 4 – laser aerosol spectrometer; 5 – computer monitoring and data processing system; 6 – test section modeling air pipeline; 7 – flow rate inducer – ventilator with voltage regulator; 8 - Shch-300 combined digital instrument;
9 – filter holder; 10 – valve.

Materials of three types were used as filtering elements: metallic fine-cellular (160 μm) mesh (FS6); FL- 150 dielectric polyester (FS2); metal-felt (needle-punchable cloth fabricated of metal fibers) (FS1). In the majority of cases a combination of several conducting and dielectric filtromaterials was used: FL-150 + metal mesh (FS3); FL 150 + metal-felt (FS4); FL 150 + metal mesh + metal-felt (FS5), metal-felt + mesh (FS7).

To run investigations under the different operating conditions, provision was made for the possibility of variation of interelectrode spacing (IS) between filtering material and coronating electrodes.

Aerosol plenum was not connected; while ambient air containing aerosol particles of various sizes in relatively small concentrations was tapped from a large 250 m^3 - volume aerosol room. In different days of test investigations the total concentration of aerosol particles in surrounding room air could vary from $\sim 107 \text{ 1/m}^3$ to $\sim 109 \text{ 1/m}^3$. The concentration of aerosol particles in air was periodically controlled throughout the whole period of test performance.

Measurement of concentration of aerosol particles was taken by laser spectrometer; air being tapped behind the filtering element at a distance of 30 cm from it. In testing four options of air flow rate (flow velocity) through aerosol plenum were used: 1 – 5,5 m^3/h (4 cm/s); 2 – 16 m^3/h (14 cm/s); 3 – 26 m^3/h (23 cm/s); 4 – 36 m^3/h (31 cm/s). In the majority of tests one and the same air flow rate 16 m^3/h (14 cm/s) through the filtering system was maintained.

Voltage of negative polarity was applied to coronating electrodes from high-voltage power source with max voltage not exceeding 16 kV.

The problems of experimental study of the impact of intense aeroionization on catching of aerosol particles from the air flow using combined filtering systems are the subject of this investigation.

The objective to be pursued by the investigation of the impact of aeroionization on the efficiency of aerosol catching from the air flow is to identify the physical processes which may play a significant role in deposition of charged aerosol particles, including their travel and interaction with dielectric and conducting materials of filtering systems. Such physical processes are the charging of aerosol particles of various size and composition in the field of corona discharge and at the cost of triboelectrification at interaction of particles with materials of filtering systems, the motion of charged particles in own and external electric fields in the presence of the main gasodynamic flow, and the interaction of charged aerosol particles between each other.

Experimental and theoretic research of the impact of intense aeroionization on catching of aerosol particles from the air flow using combined filtering systems enable one to determine the factors exerting effect on deposition of aerosol particles from the air flow, reveal the optimal parameter ranges of electrode and filtering systems using which the maximum efficient deposition of particles is assured. The results as obtained provide a basis for advanced combined

gas cleaning systems of different purpose.

Results

Experimental investigations of aeroionization parameters (of systems of coronating electrodes and intensity of corona discharge being created by them) and response of filtering systems for variation of concentration and disperse composition of model aerosols in the air flow are carried out.

The investigations as performed demonstrated that the efficiency of catching of aerosol particles from the air flow by the combined filter consisting of a system of coronating electrodes and a filtering system which is installed across the air flow is governed by the simultaneous action of the following factors: intensity of corona discharge, magnitude of electric field strength in the gap, air flow rate and characteristics of the filtering system.

Intensity of corona discharge is dependent upon the type of the coronating system, the applied voltage and the electrode gap.

In the course of investigations three types of electrode systems (1 – “needles – plane”, 2 – “wires – plane”, and 3 – “saw-like electrodes – plane”) typical of electric filtration of gas-aerosol flows were considered. The experiments demonstrated that the highest efficiency of catching is observed for saw-like coronating electrodes. In this case, the system of saw-like coronating electrodes creates low hydrodynamic resistance to the gas flow and assures a rather intense corona discharge. Besides, it is mechanically very strong and assures reliable operation in the conditions typical of NPP ventsystems.

The limiting charge (which aerosol particles can acquire in the corona discharge field) is governed by corona discharge intensity which is dependent on the applied voltage, the type of coronating electrodes and the electrode gap. For particles in a size range of 0.1-3.0 μm the magnitude of the limiting charge of aerosol particles is governed by the impact and diffusive mechanisms of charging and depends on the field strength E in the gap as follows.

$$q_{\max} = q_{\max_{\text{o}\ddot{\alpha}}} + q_{\max_{\dot{\alpha}\check{\alpha}}} = 4\pi\varepsilon_0 k_\varepsilon E a^2 + \frac{4\pi\varepsilon_0 A_{\max} Da}{K}, \quad (\text{Eq.1})$$

where $A_{\max} \approx 6,7$ is the parameter of diffusive charge; a is the particle radius; ε is the relative dielectric constant of particle material; $K \approx 2,2 \text{ cm}^2/(\text{B}\cdot\text{c})$ is the ion mobility; and D is the coefficient of ion diffusion ($D \approx 0,025 \cdot K$).

The charging of aerosol particles in the corona discharge field as a function of time in the case of the impact mechanism of charge is given by

$$q(t) = q_{\max_{\text{o}\ddot{\alpha}}} \cdot \frac{e \cdot n \cdot K \cdot t}{4\varepsilon_0 + e \cdot n \cdot K \cdot t}, \quad (\text{Eq.2})$$

where e is the elementary charge, n is the ion concentration in the electrode gap, K is the ion mobility, and t is the time of stay of aerosol particle in the zone of action of corona discharge. For diffusive mechanism of charge of aerosol particles in the field of corona discharge the kinetics of charge in time is taken into account by the following relationship:

$$t = \frac{\varepsilon_0}{enK} \left[Ei\left(\frac{K}{D} \frac{q}{4\pi\varepsilon_0 a}\right) - C_0 - \ln\left(\frac{K}{D} \frac{q}{4\pi\varepsilon_0 a}\right) \right], \quad (\text{Eq.3})$$

where $C_0 = 0,577$ is the Euler constant; $Ei(y)$ is the exponential integral function

$$(\text{at } y > 1: Ei(y) \approx \frac{e^y}{y});$$

K is the ion mobility; a is the particle radius; n is the ion concentration in the electrode gap; D is the coefficient of ion diffusion; t is the time of stay of aerosol particle in the zone of action of corona discharge (in the electrode gap).

According to the above relationships, the larger the time of aerosol particle stay in the electrode gap in the zone of corona discharge action, the closer its charge to the maximum possible value. Thus, the maximum charges, the aerosol particles of microne and submicrone size can acquire in the field of corona discharge, are in the range 10-17 – 10-15 C.

The higher the strength of the electric field in the discharge gap and, correspondingly, the charge of aerosol particles, the more efficient is the catching of aerosol particles by the filtering deposition system.

It was established by experiments that with air velocities lower than 0,5 m/s and electric field strength (in the gap) exceeding 5,3 kW/cm the efficiency of catching of aerosol particles by the filtering system practically ceases to build up. Under the action of the electric field forces the velocities of aerosol particles motion achieve values equal to dozens centimeters per second, become comparable and even exceed air velocities. As a result, taking into account the velocity of the passing gas-dynamic flow, aerosol particles “enter” in the filtering system at high velocity, and the efficiency of their catching does not increase with rise of the field strength in the gap and even starts decreasing in spite of the growth of the own charge of the particle and its electric interaction with materials of the filtering system.

It was established by experiments that with air flow velocities lower than 1 m/s an essential reduction of aerosol particle concentration can be provided by combined filtering systems where fibrous dielectric and conducting elements are placed in series.

This makes it possible to set in action the maximum number of physical mechanisms of catching of charged aerosol particles and catch both negatively and positively charged aerosol particles.

In using a combination of dielectric and conducting filtering materials one can observe that overshoot of aerosol particles (0.3 μm in size) through the filtering system is reduced by 10-30%

at air flow velocities not higher than 1 m/s and the average strength of the field of corona discharge (in the discharge gap) equal to 4-6kW/cm.

Thus, the experiments as conducted made it possible to determine the optimal characteristics of the electrode and filtering system, at which efficient catching of aerosol particles from air flow can be assured.

Discussion

Test investigations of the effect of aeroionization parameters (systems of coronating electrodes and intensity of corona discharge being created by them) and characteristics of the filtering systems on variation of counting concentration and disperse composition of the model aerosols in the air flow are carried out.

Based on the analysis of the test results as obtained one can single out the following ranges of best parameters at which the most efficient trapping of aerosol particles from air flow is provided, given aeroionization.

1. Electrode system: a number of saw-shaped electrodes - plane.

The application of this system makes it possible to ensure maximum efficiency of deposition in the field of corona discharge, manufacturability, sufficient mechanical strength and low hydrodynamic resistance.

The optimal electrode-to-electrode spacing ranges from 23 to 27 mm.

Spacing between coronating saw-shaped electrodes is 24-26 mm.

2. Filtering system: FS5 (dielectric cloth FL-150 + metal fine-cellular mesh + metal-felt behind it).

Maximum efficiency of trapping of aerosol particles from the air flow is provided at the cost of the multilateral action of dielectric and conducting components constituting it.

3. Voltage of electrode system power supply: negative polarity at coronating electrodes, the optimal range is 13-15 kV.

Negative polarity enables one to ensure avalanche corona conditions in a wide range of applied voltages without break-down of discharge gap, high intensity of coronating discharge and sufficiently high average electric field strength in the gap where deposition of charged aerosol particles takes place.

The power supply voltage range 13-15 kV for the above-cited parameters of electrode and filtering systems is the best one, since it provides the superiority of positive factors of aeroionization (high charge of aerosol particles, sufficient velocity of their motion towards the filtering system and minimum outgo to channel walls, maximum efficient interaction of charged aerosol particle with dielectric and conducting materials of the filtering system) over the negative factors (first of all, high initial velocity of income of charged aerosol particle into the filtering system).

CONCLUSIONS

During the tests as performed the optimal electrode and filtering system characteristics ensuring efficient trapping of aerosol particles from the air flow are determined. The maximum efficiency is provided by FS5 filtering system (FL 150 + metal mesh + metal-felt) where successive accommodation of dielectric and conducting components enables the maximum number of physical mechanisms of trapping of charged aerosol particles to be put into action. Among the electrode systems which are considered saw-shaped electrodes enable the maximum efficiency (reduction of falling-through to 10%) to be achieved. The optimum inter-electrode spacing 23-27 mm and the power supply voltage range 13-15 kV are found to be best to run efficient trapping of aerosol particles.

Study on Collection Efficiency of 2-layered Electrostatic Filters with Different Gaps

Soohyun Ha¹, Jong-Bum Kim², Soon-Bark Kwon², Seok Namgoong³, Kwanhyun Cho⁴ and Taesung Kim^{1,5}

1 SKKU Advanced Institute of Nanotechnology, Sungkyunkwan University, 300 ChunChun-dong Jangan-gu, Suwon-si, Gyeonggi-do, 440-746, Korea

2 Railroad Environment Research Department, Korea Railroad Research Institute, Woram-dong, Uiwang-si, Gyeonggi-do, 437-757, Korea

3 R&D System Team, Seungchang Airtek, Naegachoen-ri Wongok-myeon, Anseong-si, Gyeonggi-do, 456-811, Korea

4 R&D center, Seoulmetro, Dongjak-dong, Dongjak-gu, Seoul, 137-712, Korea

5 School of Mechanical Engineering, Sungkyunkwan University, 300 ChunChun-dong Jangan-gu, Suwon-si, Gyeonggi-do, 440-746, Korea

ABSTRACT

In this paper, we study to analyze the effect of the gap between two filters on particle collection efficiency of electrostatic filter system which is applied to subway cabin. Two sheets of electrostatic filter with different gap size (2 mm, 5 mm, 8 mm) and no gap are used and compared. The particle collection efficiency of four cases is different. In the case of filter with 8 mm gap has the highest particle collection efficiency. The result shows that filter with gap has better particle collection efficiency than filters with no gap and gap size between two filters is significant factor to affect the particle collection efficiency of electrostatic filter system.

KEYWORDS

Electrostatic filter, Efficiency improvement, Different gap

Introduction

Poor indoor air quality is regarded as a significant problem of health, environment and economy. As indoor human activity is continuously increased, the importance of air quality management for the public transportation has been highlighted. Especially the pollution level of dust in the subway cabin is higher than Korea standard guideline on public transportation air quality. Therefore the technique for contamination control of subway cabin is necessary, so the air-cleaner with roll filter system for subway cabin has been developed by Korea railroad research institute. This roll filter system consists of 2-layered electrostatic filters with gaps. The

electrostatic filter is composed of permanently charged electrostatic fibers highly capable of collecting charged and uncharged nanosize particles. It was reported that using 2-layered woven filter shows twenty percent better efficiency than 1-layered woven filter^[1]. Furthermore, 2-layered woven filter with different gaps shows different particle collection efficiency. So in this study, we analyze the effect of the gap between two filters on particle collection efficiency of electrostatic filter and find out optimal distance.

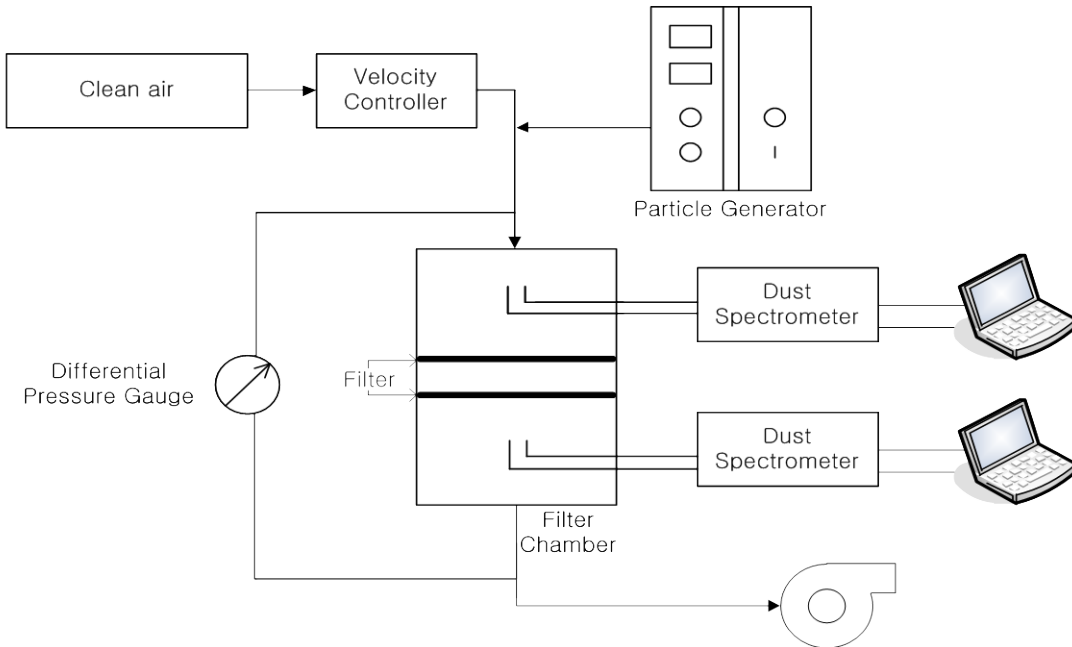
Experimental Methods

In our study, electrostatic filter(370 mm(W) x 220 mm(H)) is used and table 1 shows the specification of this filter. Figure 1 shows schematic diagram of experimental setup for filter test. Solid particles have sizes ranging from 0.3 μm to 3.5 μm are generated by particle generator(TOPAS, SAG 410) which is using A2 fine test dust(ISO 12103-1). Particle counters(Grimm, Dust spectrometer) are used for measuring the particle number concentration. Sampling ports are installed at the front and the back of filter^[2]. Ventilation resistance is measured by differential pressure gauge. The Experiment is carried out under 1.5 m/s face velocity condition. The gap sizes of two electrostatic filters are 2 mm, 5 mm, 8 mm and 0 mm(no gap). When flow become stable, measurement of particle number concentration is started. Comparing with particle number concentration of front and back of filter, particle collection efficiency is calculated.

Table 1. Specification of Electrostatic filter

ITEMS	Electrostatic Filter
Basis weight	35 g/m ²
Thickness	0.25 mm
Media	Polypropylene (PP)

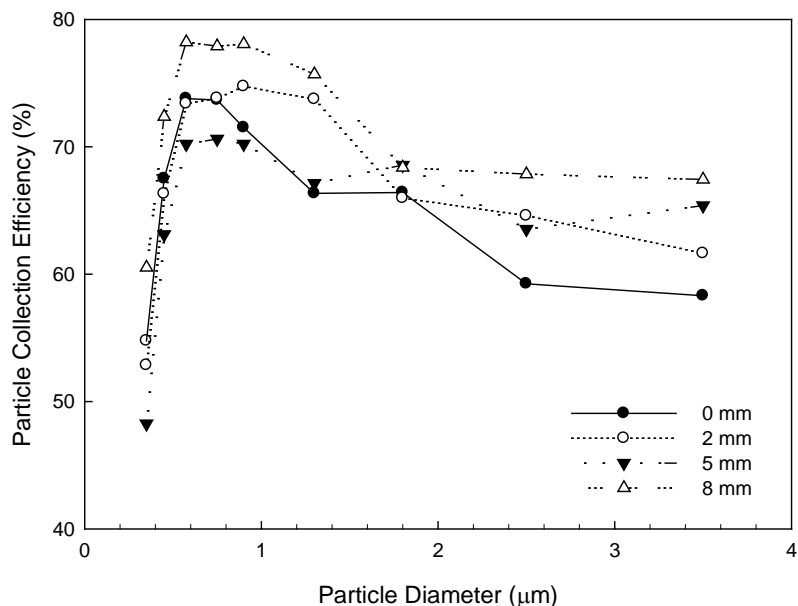
Figure 1. Schematic diagram of experimental setup for filter test.



Results and Discussion

Figure 2. shows the particle collection efficiency of 2-layered electrostatic filter. Two sheets of electrostatic filter with different gap size (2 mm, 5 mm, 8 mm) and no gap are used and compared. In the case of filter with 8 mm gap has the highest particle collection efficiency. The result shows that filter with gap has generally better particle collection efficiency than filter with no gap. And 2-layered electrostatic filter with different gaps shows different particle collection efficiency.

Figure 2. Particle collection efficiency curves of 2-layered electrostatic filter.



CONCLUSION

To increase particle collection efficiency of 2-layered filter system, we study about the effect of gap size between 2-layered filter to particle collection efficiency. Using dust spectrometer, we can get the particle number concentration and calculate efficiency. Our experimental result shows 2-layered electrostatic filter with different gaps shows different particle collection efficiency and 2-layered electrostatic filter with gap has generally better particle collection efficiency than filter with no gap. Therefore, the gap size between two filters is one of the significant factor can affect the particle collection efficiency of 2-layered electrostatic filter system.

ACKNOWLEDGMENTS

This work was supported by a grant (11 Urban Railroad A-01) from Urban Railroad Technology Development Program funded by Ministry of Land, Transport and Maritime Affairs of Korean government.

REFERENCES

- [1] Benesse, M., Le Coq, L., & Soliec., *Collection efficiency of a woven filter made of multifiber yarn : Experimental characterization during loading and clean filter modeling based on a two-tier single fiber approach*; *Aerosol Science*, 2006, 37, 974-989. Carson, M.A.; Atkinson, K.D.; Waechter, C.J. *J. Biol Chem.* 1982, 257, 8115-8121.

[2] J.H. Ji, G.N. Bae, S.H. Kang, J. Hwang, *Effect of particle loading on the collection performance of an electret cabin air filter for submicron aerosols*; Aerosol Science, 2003, 34, 1493-1504.

Direct radiative and climatic effects of aerosols in East Asia

Zhiwei Han¹

1 Key Laboratory of Regional Climate-Environment for East Asia (RCE-TEA), Institute of Atmospheric Physics (IAP), Chinese Academy of Sciences, Beijing, P. R.China, 100029.

Principal Contact: Zhiwei Han, Prof., Institute of Atmospheric Physics, Chinese Academy of Sciences, P.O.Box 9804, Beijing, 100029, China.

Tel: 86-10-82995158 Fax: 86-10-82995135 E-mail: hzw@mail.iap.ac.cn

Abstract

A regional climate model RIEMS was developed by incorporating tropospheric chemistry and aerosol processes in order to investigate the radiative and climatic effects of aerosols over East Asia, which include soil dust, sea salt, sulfate, black carbon and organic carbon. Direct radiative effects by all these aerosols exhibit a strong seasonal variation, with maximum surface cooling in March and minimum surface cooling in winter, but maximum TOA cooling in July and minimum TOA cooling in winter. At the surface, for all-sky condition, the direct radiative effect of aerosols in March is much larger than that in other months, with a range of -10 to -45 W m^{-2} over wide areas of China and the western Pacific rim, and a maximum around the Chongqing district. The surface cooling by the direct radiative effect of aerosols is more obvious in winter than that in summer, with mean ground temperatures decreasing by $0.1\text{--}0.7^\circ\text{C}$ over most of east China, whereas little changes in precipitation was found in winter. In summer, alternating bands of ground temperature and precipitation increasing and decreasing occur in east China from south to north, due to a combined effect of changes in temperature and water vapor gradients by aerosol direct radiative effects.

Keywords: aerosols, radiative effect, climatic effect, regional model, east Asia.

A Modeling Study on the Climatic Effects of Aerosols in China

Shu Li¹, Tijian Wang¹, Bingliang Zhuang¹ and Fanhui Shen¹

1 School of Atmospheric Science, Nanjing University, Nanjing 210093, China

ABSTRACT

A coupled modeling system (RegCCMS) which consists of a regional climate model (RegCM3) and a tropospheric atmosphere chemistry model (TACM) is applied to investigate the distribution, radiative forcing as well as the climatic effects of aerosols in China. In this study, parameterizations for cloud droplet number concentration and precipitation autoconversion rate are introduced into RegCCMS to investigate the indirect effect of aerosols. Modeling results show that sulfate, nitrate, BC and OC aerosols are mainly distributed in East and North China as well as Sichuan basin because of industrial distribution and terrain, while dust is mainly distributed in Northwest China. Annual averages of direct, indirect and total radiative forcing of aerosols at the top of atmosphere are -2.77 W/m², -2.42 W/m² and -4.43 W/m², respectively. Indirect radiative forcing is close to direct radiative forcing and can not be ignored. Owing to the total effects of aerosols, the countrywide annual average changes of surface air temperature and precipitation are -0.59K and -0.31 mm/d, respectively, showing significant differences in seasons and regions.

KEYWORDS

Aerosol, Climatic effects, Radiative forcing, China

Introduction

Aerosols are not only pollutants in atmosphere, but also the essential constituent influencing radiation of atmosphere. Aerosols affect climate through the scattering and absorption of solar radiation and through their influence on cloud formation (Twomey, 1974; Albrecht, 1989)^[1,2]. During the past several years, emissions of aerosols and their precursors in China have increased markedly, following the dramatic growth of economy. Many studies on radiative forcing and climatic effects of aerosols in China have been carried out in recent years (Qian *et al.*, 2003; Wu *et al.*, 2004; Huang *et al.*, 2007; Li *et al.*, 2009; Zhang *et al.*, 2009)^[3-7]. However, aerosol species considered in these works are not comprehensive and most works are conducted concerning sulfate and carbonaceous aerosols. Therefore, it is necessary to perform quantitative studies to understand the environmental and climatic effects of tropospheric aerosols in China. In this study,

a coupled regional climate-chemistry modeling system (RegCCMS) which consists of a regional climate model (RegCM3) and a tropospheric atmosphere chemistry model (TACM)^[8] is applied to simulate the spatial distribution, radiative forcing as well as the climatic effects of aerosols in China.

Experimental Methods

In this study, parameterizations for cloud droplet number concentration (Gultepe and Isaac, 1999)^[9] and precipitation autoconversion rate (Chen and Cotton, 1987)^[10] are introduced into RegCCMS to investigate the first and second indirect effects of aerosols. The emission inventory is based on Zhang et al.'s (2009) work^[11]. The horizontal resolution is set as 50 km with 120×89 grid points and the vertical resolution is set as 18 levels. The pressure at the model top is 50 hPa. The model domain, covering the mainland China and its surrounding regions, is on a Lambert map projection. Holtslag's planetary boundary layer scheme, relaxation boundary condition and Grell's cumulus convection parameterization were selected in this study. To investigate the direct and indirect effect of aerosols on climate, five numerical experiments were conducted spanning a period from November 2005 to November 2006, with the first month serving as spin-up for the subsequent 1 year simulation. The control run Experiment 1 uses the standard model in which the climatic effects of aerosols are not included. In Experiment 2, Experiment 3 and Experiment 4, direct, first indirect and second indirect effect of aerosols, respectively, is taken into account. The direct, first and second indirect effect of aerosols are all included in Experiment 5.

Results and Discussion

Figure 1 shows the annual average surface concentrations of sulfate (a), nitrate (b), BC (c), OC (d) and dust (e). Results show that anthropogenic aerosols are mainly distributed in East and North China as well as Sichuan basin, while dust is mainly distributed in Northwest China. Maximums of sulfate, nitrate, BC, OC and dust are $48 \mu\text{g}/\text{m}^3$, $12 \mu\text{g}/\text{m}^3$, $6 \mu\text{g}/\text{m}^3$, $8 \mu\text{g}/\text{m}^3$ and $1500 \mu\text{g}/\text{m}^3$, respectively.

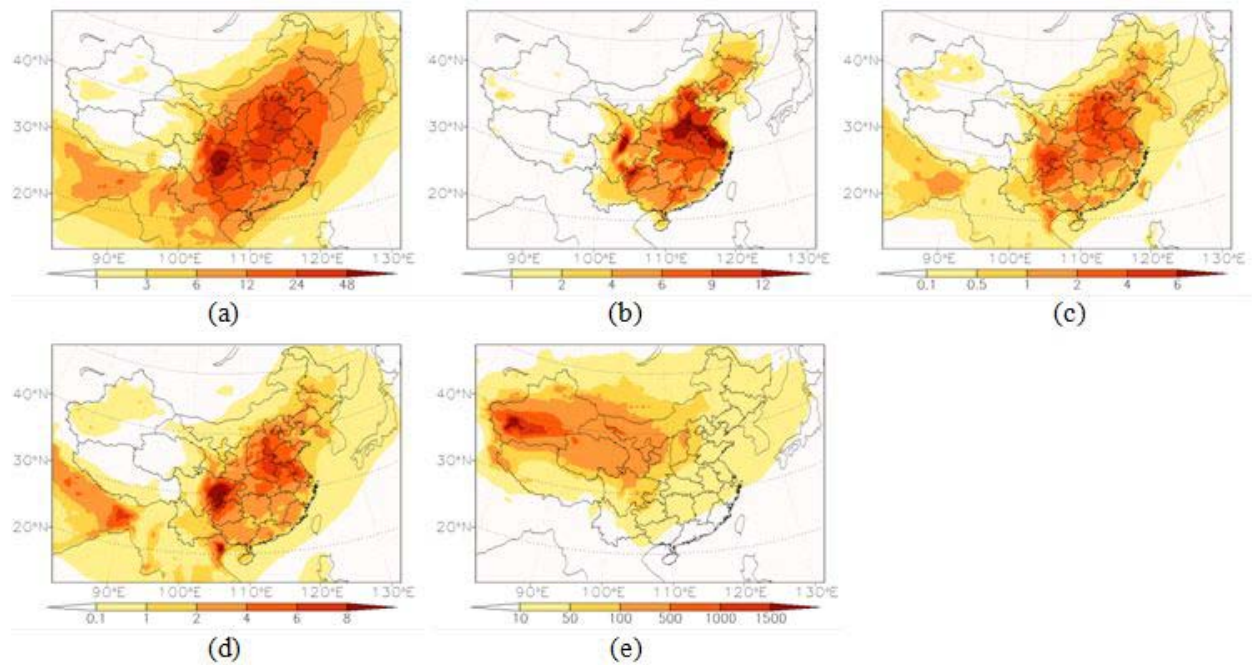


Figure 1 Annual average surface concentrations of sulfate (a), nitrate (b), BC (c), OC (d) and dust (e)

Figure 2 shows the annual average direct radiative forcing of aerosols at TOA (a), the annual average changes of surface air temperature (b) and precipitation (c) due to direct effect. The annual average of direct radiative forcing is -2.77 W/m^2 , in some region it can reach -12 W/m^2 . Spatial distribution of direct radiative forcing is influenced by surface concentration of aerosols. Besides, it is also influenced by cloud cover, surface albedo and other factors. Owing to the direct effect, the countrywide annual average changes of surface air temperature and precipitation are -0.34K and -0.12 mm/d , respectively.

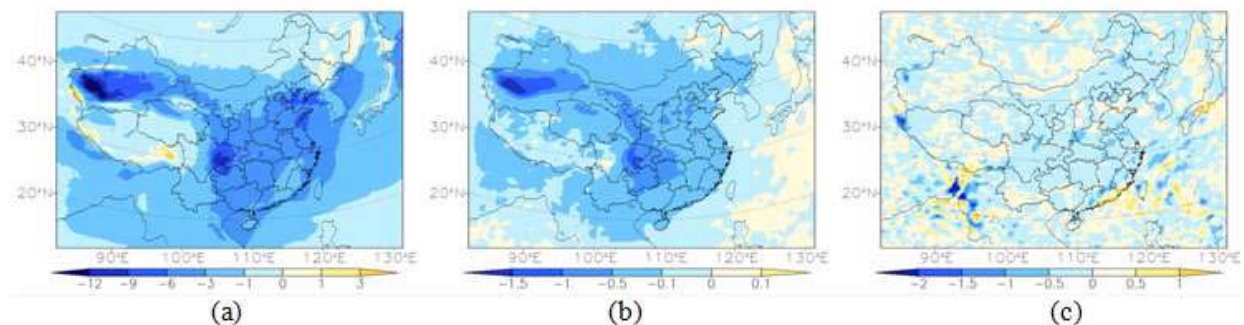


Figure 2 Annual average direct radiative forcing of aerosols at TOA (a), the annual average changes of surface air temperature (b) and precipitation (c) due to direct effect.

Figure 3 shows the annual average first indirect radiative forcing of aerosols at TOA (a), the annual average changes of surface air temperature (b) and precipitation (c) due to first indirect effect. Annual average of the first indirect radiative forcing of aerosols at TOA is -2.42 W/m^2 ; it

reaches -7 W/m^2 in some regions. Spatial distribution of indirect radiative forcing is related to that of aerosol concentrations as well as cloud amount. Because of the first indirect effect, the countrywide annual average changes of surface air temperature and precipitation are -0.12K and -0.08 mm/d , respectively.

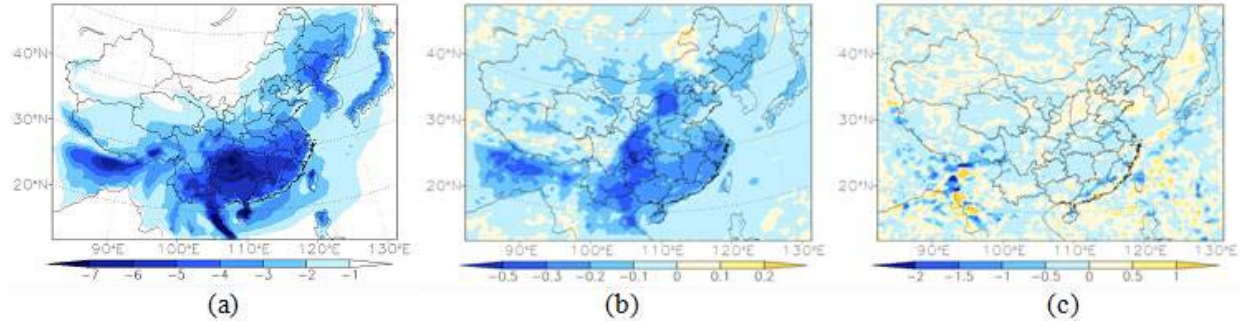


Figure 3 Annual average first indirect radiative forcing of aerosols at TOA (a), the annual average changes of surface air temperature (b) and precipitation (c) due to first indirect effect.

Figure 4 shows Annual average changes of surface air temperature (a), precipitation (b) and cloud amount(c) due to second indirect effect. The second indirect effect of aerosols would increase cloud amount, thus reducing solar radiation, decreasing surface air temperature and precipitation. Annual average changes of surface air temperature and precipitation due to the second indirect effect are -0.17K and -0.16 mm/d . The second indirect effect is stronger than the first indirect effect.

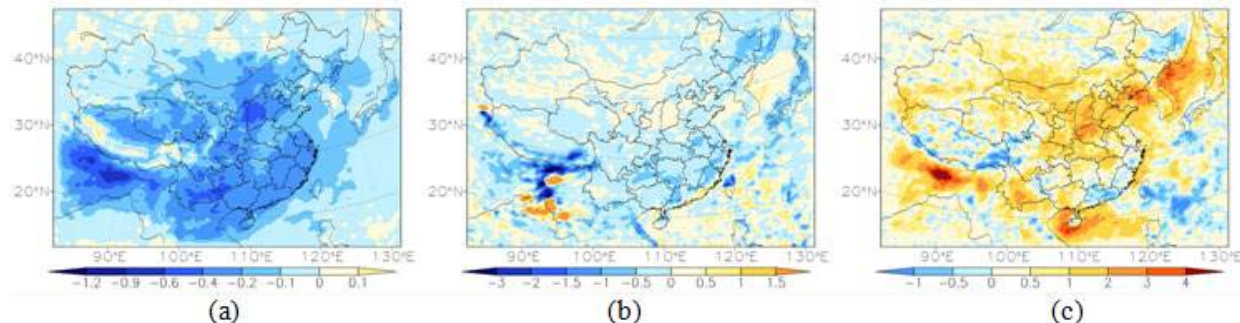


Figure 4 Annual average changes of surface air temperature (a), precipitation (b) and cloud amount(c) due to second indirect effect.

Figure 5 shows the annual average total radiative forcing of aerosols at TOA (a), the annual average changes of surface air temperature (b) and precipitation (c) due to total effect. The annual average of total radiative forcing of aerosols at TOA is -4.43 W/m^2 . Owing to the total effect, the regional annual average changes of surface air temperature and precipitation are -0.59°C and -0.31 mm/d , respectively. The changes of surface temperature and precipitation due to the total effect are less than the sum of each individual effect, showing a strong nonlinearity between climate change and radiative forcing. The preliminary results in this study suggest that the impact

of aerosols on regional climate change in China is very significant and complex. More emphasis should be concentrated on the improvements on parameterization of cloud condensation nuclei and autoconversion rate of rainwater, thus to reduce the uncertainty in estimation of indirect effect of aerosols. In addition, the performance of regional climate model need to be improved to reduce uncertainties associated with simulated cloud and precipitation which could influence radiative forcing and climate response significantly.

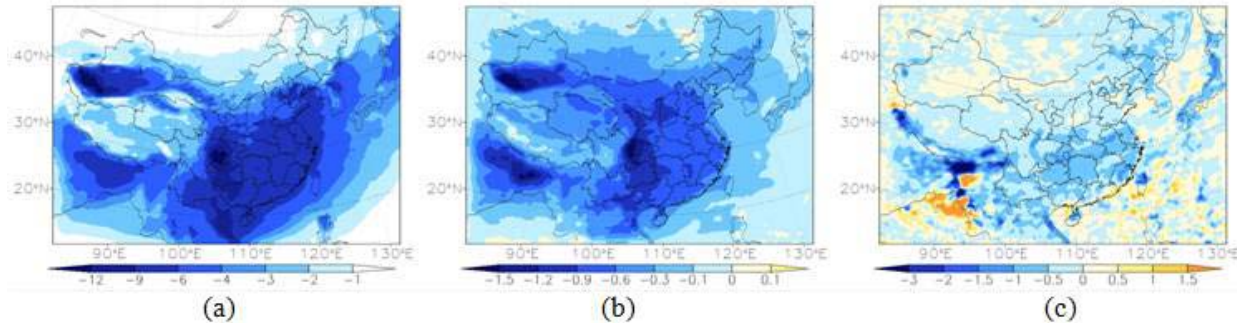


Figure 5 Annual average total radiative forcing of aerosols at TOA (a), the annual average changes of surface air temperature (b) and precipitation (c) due to total effect.

SUMMARY OR CONCLUSION

Anthropogenic aerosols are mainly distributed in East and North China as well as Sichuan basin, while dust is mainly distributed in Northwest China.

The annual average of direct radiative forcing is -2.77 W/m^2 . Spatial distribution of direct radiative forcing is influenced by surface concentration of aerosols and other factors. Owing to the direct effect, the countrywide annual average changes of surface air temperature and precipitation are -0.34K and -0.12 mm/d , respectively.

Annual average of the first indirect radiative forcing of aerosols at TOA is -2.42 W/m^2 . Spatial distribution of indirect radiative forcing is related to that of aerosol concentrations as well as cloud amount. Because of the first indirect effect, the countrywide annual average changes of surface air temperature and precipitation are -0.12K and -0.08 mm/d , respectively.

The second indirect effect of aerosols would increase cloud amount, thus reducing solar radiation, decreasing surface air temperature and precipitation. Annual average changes of surface air temperature and precipitation due to the second indirect effect are -0.17K and -0.16 mm/d . The second indirect effect is stronger than the first indirect effect.

The annual average of total radiative forcing of aerosols at TOA is -4.43 W/m^2 . Owing to the total effect, the regional annual average changes of surface air temperature and precipitation are -0.59°C and -0.31 mm/d , respectively. The preliminary results in this study suggest that the impact of aerosols on regional climate change in China is very significant and complex.

ACKNOWLEDGMENTS

This work was supported by the National Key Basic Research Development Program of China (2011CB403406, 2010CB428503), and the National Special Fund for the Weather Industry (GYHY200806001, GYHY200706036).

REFERENCES

- [1]Twomey, S. *Atmos. Environ.*, 1974, 8, 1251-1256.
- [2]Albrecht, B. A. *Science*, 1989, 245(4923): 1227-1230.
- [3]Qian, Y.; Leung, L. R.; Ghan, S. J.; Giorgi, F. *Tellus, Ser. B*, 2003, 55, 914-934.
- [4]Wu, J.; Jiang, W.; Fu, C.; Su, B.; Liu, H.; Tang, J. *Adv. Atmos. Sci.*, 2004, 21(4), 637-649.
- [5]Huang, Y.; Chameides, W. L.; Dickinson, R. E. *J. Geophys. Res.*, 2007, 112, D03212, doi: 10.1029/2006JD007114.
- [6]Li, S.; Wang T. J.; Zhuang, B. L.; Han, Y. *Adv. Atmos. Sci.*, 2009, 26(3), 543-552.
- [7]Zhang, H.; Wang, Z. L.; Guo, P. W.; Wang, Z. Z. *Adv. Atmos. Sci.*, 2009, 26(1), 57-66.
- [8]Wang, T. J.; Li, S.; Shen, Y.; Deng, J. J.; Xie, M. *J. Geophys. Res.*, 2010, 115, D00K26, doi: 10.1029/2009JD013264.
- [9]Gultepe, I.; Isaac, G. A. *J. Clim.* 1999, 12, 1268-1279.
- [10]Chen, C.; Cotton, W. R. *J. Atmos. Sci.* 1987, 44, 2951-2977.
- [11]Zhang, Q.; Streets, D. G.; Carmichael, G. R.; He, K.; Huo, H. *Atmos. Chem. Phys.* 2009, 9, 5131-5153.

Semi-direct and indirect climate effects of fossil fuel black carbon aerosol over China

Bingliang Zhuang, Tijian Wang, Shu Li and Fanhui Shen

School of Atmospheric Sciences, Nanjing University, Hankou Rd. 22, Nanjing 210093, China

Principal Contact: Bingliang Zhuang, Ph. D Candidate, School of Atmospheric Sciences, Nanjing University, Hankou Rd. 22, Nanjing 210093, China.

Tel: 86+13913993513 E-mail: dzhblyzh@yahoo.com.cn

Abstract

A regional climate chemistry modeling system was applied to investigate spatial distribution of black carbon (BC) loading, radiative forcing (RF) as well as its climatic effects over China. Results show that high levels of BC distribute in southwest and central to eastern China. Simulated aerosol optical depth is large with maximum of 0.11. Annual mean cloud droplet number concentration, effective radius and auto conversion rate changed by $+70.89 \text{ cm}^{-3}$, $-0.154 \mu\text{m}$ and $-7.51 \times 10^{-6} \text{ g kg}^{-1} \text{ s}^{-1}$ due to BC indirect effects. Owing to the absorption, BC exerts a positive RF at the top of atmosphere (TOA) with the regional mean of $+0.81 \text{ W m}^{-2}$. Strong BC first indirect RF distributes in south, northeast China and north India, with the regional averaged value of -0.95 W m^{-2} . Combined (direct plus first indirect) RF at TOA over the region is -0.15 W m^{-2} . Climate responses to BC direct effect show significant decreases of low level cloud amount and liquid water path in whole east China, with regional average of -0.017% and -0.104 g m^{-2} . Since more solar radiation was absorbed ($+1.223 \text{ W m}^{-2}$), surface became warming and drying (Changed by 0.042 K and -0.003 mm d^{-1}). For total indirect effects, annual mean cloud amount, liquid water path, and total absorbed solar radiation over the region changed by 0.114% , 1.42 g m^{-2} and -2.02 W m^{-2} . Second indirect effect is more significant compared to BC first indirect effect. Surface cooling and drying appear in north India and south to east China, yielding regional averaged changes of -0.135 K for surface temperature and -0.06 mm d^{-1} for rainfall. Due to the combined effects of BC, annual mean cloud amount, cloud liquid water path and the radiative fluxes are changed by -0.025% , 1.28 g m^{-2} , -0.733 W m^{-2} . Considerable annual mean surface air temperature decrease in center and south China, with the maximum of -0.7 K . Total precipitation is inhibited in most parts of China (regional mean of -0.09 mm d^{-1}).

Keywords: Black carbon, Radiative forcing, Climate effects, Regional climate and chemistry model

Observational study of aerosol optical properties over the cruise during the Third Chinese National Arctic Research Expedition

Jie Tang¹, Peng Yan¹, Lingen Bian², Changgui Lu²

1 Meteorological Observation Center of CMA, Beijing 100081, China

2 Chinese Academy of Meteorological Sciences, Beijing 100081, China

Principal Contact: Jie Tang, Research Prof., Meteorological Observation Center of CMA,
Zhongguancun South Street 46, Beijing, 100081, China.

Tel: 010-58995262 Email: Tangj@cams.cma.gov.cn

Abstract

This paper presents the measurement results of aerosol optical properties obtained at deck level on board the R/V Xuelong, with aethalometer and nephometer, during the cruise of the Third Chinese National Arctic Research Expedition from July 12 to September 22, 2008. The cruise starts from and ends up at Shanghai, with the north-most point of $85^{\circ} 13.57' N$. Both of absorption coefficient and scattering coefficient in Arctic Ocean are the lowest throughout the course, while both of those are highest in the Yellow sea and Japan sea. There is little meridional gradient of absorption coefficient and scattering coefficient observed in Arctic Ocean north of $70^{\circ}N$. Back trajectory analysis indicated that the transportation from low latitude to Arctic Ocean north of $70^{\circ}N$ in summer, resulting in not only low values of absorption coefficient and scattering coefficient, but also a small variation and a very weak meridional gradient of black carbon concentration. The single scattering albedo coefficient (SSA) is calculated and the result shows the SSA is lowest in surfaces of Yellow Sea and Japan Sea and highest in Arctic Ocean. The terrestrial transport from northeast Asia land and Alaska is a crucial factor to influence the levels of absorption coefficient and scattering coefficient, and as well as the SSA.

Keywords: the Third Chinese National Arctic Research Expedition, aerosol optical properties, observation

Chemical Characterization of Sub-micrometer Aerosol in Beijing

Junying Sun¹, Yangmei Zhang¹, Xiaojing Shen^{1,2}, Xiaochun Zhang¹, and Xiaoye Zhang¹

1 Key Laboratory for Atmospheric Chemistry of CMA, Center for Atmosphere Watch and Services, Chinese Academy of Meteorological Sciences, No.46, Zhongguancun Nandajie, Beijing 100081, China

2 Graduate University of Chinese Academy of Sciences, Beijing, 100049, China

Principal Contact: Junying Sun, Dr., Chinese Academy of Meteorological Sciences, No.46, Zhongguancun Nandajie, Beijing 100081, China.

Tel: 010-68407943 Fax: 010-62176414 Email: jysun@cams.cma.gov.cn

Abstract

Atmospheric aerosols are receiving increasing attention because of their effect on human health, visibility, acid deposition and global/regional climate. It is well known that unlike the major long-lived gases, aerosols are not distributed uniformly in the atmosphere. Regions downwind of major particulate sources such as deserts, biomass burning areas and large cities often have heavy atmospheric aerosol burdens while other areas in cleaner regions have relatively low aerosol loadings. The composition and size distribution of these particles, and thus their optical properties, vary widely from place to place and over time.

To achieve a better understanding of the characteristics, sources and processes of aerosols in Beijing, an Aerodyne Aerosol Mass Spectrometer (AMS) was deployed to obtain size-resolved chemical composition of non-refractory submicron particles (NR-PM1), while SMPS (Scanning Mobility Particle Sizer) and TDMPS (Twin Differential Mobility Particle Sizer) was used to obtain the particle number size distribution in Beijing region. The particle loading and chemical composition, chemical-resolved size distributions, number size distribution was discussed. Surface-based measurements of aerosol properties such as size distribution, chemical composition, etc, either at long-term monitoring sites, or specifically as part of intensive field campaigns, could provide essential validation for satellite retrieval, and thus to provide near-global retrievals of aerosol properties.

Keywords: Beijing, Submicron aerosol, Particle Number size distribution

Source Signatures of Submicron Particle-phase Organic Components at Coastal and Inland California

Shang Liu¹, Douglas A. Day² and Lynn M. Russell¹

(Affiliation, Times New Roman 12-pt., left-justified)

1 Scripps Institution of Oceanography, University of California, San Diego, La Jolla, California, 92037, USA

2 Cooperative Institute for Research in the Environmental Sciences, University of Colorado, Boulder, Colorado, 80309, USA

ABSTRACT

Atmospheric submicron particles were collected at a coastal site (La Jolla; 32.87° N, 117.25° W) and an inland site (Bakersfield; 35.35° N, 118.97° W) in California during August 15 - October 1 2009 and May 15 - June 29 2010, respectively. Organic functional group concentrations were quantified by Fourier Transform Infrared (FTIR) spectroscopy and organic fragments were measured using Aerosol Mass Spectrometry (AMS). At the coastal site, organic mass (OM) was dominated (60% of the OM) by fossil fuel combustion sources originating from a heavily polluted area upwind of the site (near the Los Angeles and Long Beach port region), which resulted in a mixture of alkane and carboxylic acid functional groups. The two functional groups varied diurnally in mass and the daytime profiles followed the variations of O₃, indicating carboxylic acid groups were formed from ozone-driven reactions. Gas-phase oxidation of alkanes by OH radicals to form dihyfrofuran followed by further ozone reaction of dihydrofuran is the likely acid formation mechanism. Using the multi-day average of the daytime increase of carboxylic acid group concentrations and m/z 44-based AMS Aged Combustion factor, we estimated the lower-bound contributions of secondary organic aerosol (SOA) formed in 12-h daytime of processing in a single day to be 30% of the carboxylic acid groups and 25-50% of the Aged Combustion factor concentration at the coastal site. In contrast, at the inland site, Positive Matrix Factorization (PMF) analyses on the mass-weighed FTIR spectra and the AMS fragment concentrations suggest that the OM consisted primarily of oxygenated organic components, which were also of secondary origin. The inland site also had influence from primary particles from motor vehicular emissions, petroleum operation, and vegetation detritus, which accounted for less than one third of submicron OM.

KEYWORDS

AMS, organic aerosol, functional groups, SOA

Introduction

Organic compounds typically account for 10-70% of dry particle mass. Understanding the chemistry of particle-phase organic compounds is important for assessing the effects of aerosol particles on air quality, human health, and climate change. The major organic components identified in ambient particles include alkane, carboxylic acid, hydroxyl, amine, and non-acid carbonyl functional groups. Alkane groups, a large component of ambient organic compounds, are typically associated with primary gas and particle-phase emissions that originate from fossil fuel combustion emissions, including vehicular exhaust and coal burning. Carboxylic acid groups are observed in urban, rural, and remote atmospheric particles and sometimes account for more than 30% of OM. Because many carboxylic acids are highly soluble and tend to absorb water under high relative humidity (RH), they could affect physical (e.g. light scattering) and chemical (e.g. aqueous-phase reaction) properties of ambient particles. Carboxylic acid groups are generally SOA components. To date, there is no conclusive formation mechanism of formation of carboxylic acids.

Large uncertainty in SOA formation mechanisms makes identification of ambient SOA controversial. Organic carbon (OC) to elemental carbon (EC) ratio has been used to estimate SOA by assuming an average OC/EC from emission source measurements. OC/EC exceeding the average OC/EC is assumed to be SOA. The SOA mass estimated from this method is highly uncertain, since OC/EC is highly variable from source to source and the average OC/EC is dependent on meteorological conditions. Another approach is to identify SOA products from individual precursors. This method requires detection of SOA by molecular level speciation and known SOA formation mechanisms, which are often not available.

In this work, organic functional groups are quantified using Fourier Transform Infrared spectroscopy (FTIR) and organic mass fragments are measured using Aerosol Mass Spectrometry (AMS). The measurements provide an opportunity to use the diurnal trend in aerosol composition to evaluate the contribution of SOA. The formation mechanism of carboxylic acid groups and other oxygenated organic aerosol (OOA) is also considered based on the recurrence of diurnal cycles.

Experimental Methods

37 mm Teflon filters (Teflo, Pall Inc., Ann Arbor, MI) were used for the FTIR analysis performed using a Bruker Tensor 27 FTIR Spectrometer with a DTGS detector (Bruker, Waltham, MA). The typical time resolution is 3-6 hours. Concentrations of non-refractory organics, sulfate, ammonium, nitrate, and chloride in submicron particles were measured using a quadrupole/high

resolution AMS (Aerodyne, Billerica, MA). The time resolution is about 5 min.

Results and Discussion

1. Carboxylic acid groups are formed from ozone-driven oxidation of alkane groups.
2. Gas-phase alkane oxidation by OH radicals to form dihyfrofuran followed by further oxidation of dihydrofuran by O₃ is the likely acid formation mechanism.
3. The formation is likely volume-limited.
4. Lower-bound contributions of secondary organic aerosol (SOA) formed in 12-h daytime of processing in a single day to be 30% of the carboxylic acid groups and 25-45% of the Combustion factor concentration.

Figures

Figure 1. Daytime profiles of carboxylic acid functional groups and aged combustion factors from PMF analyses.

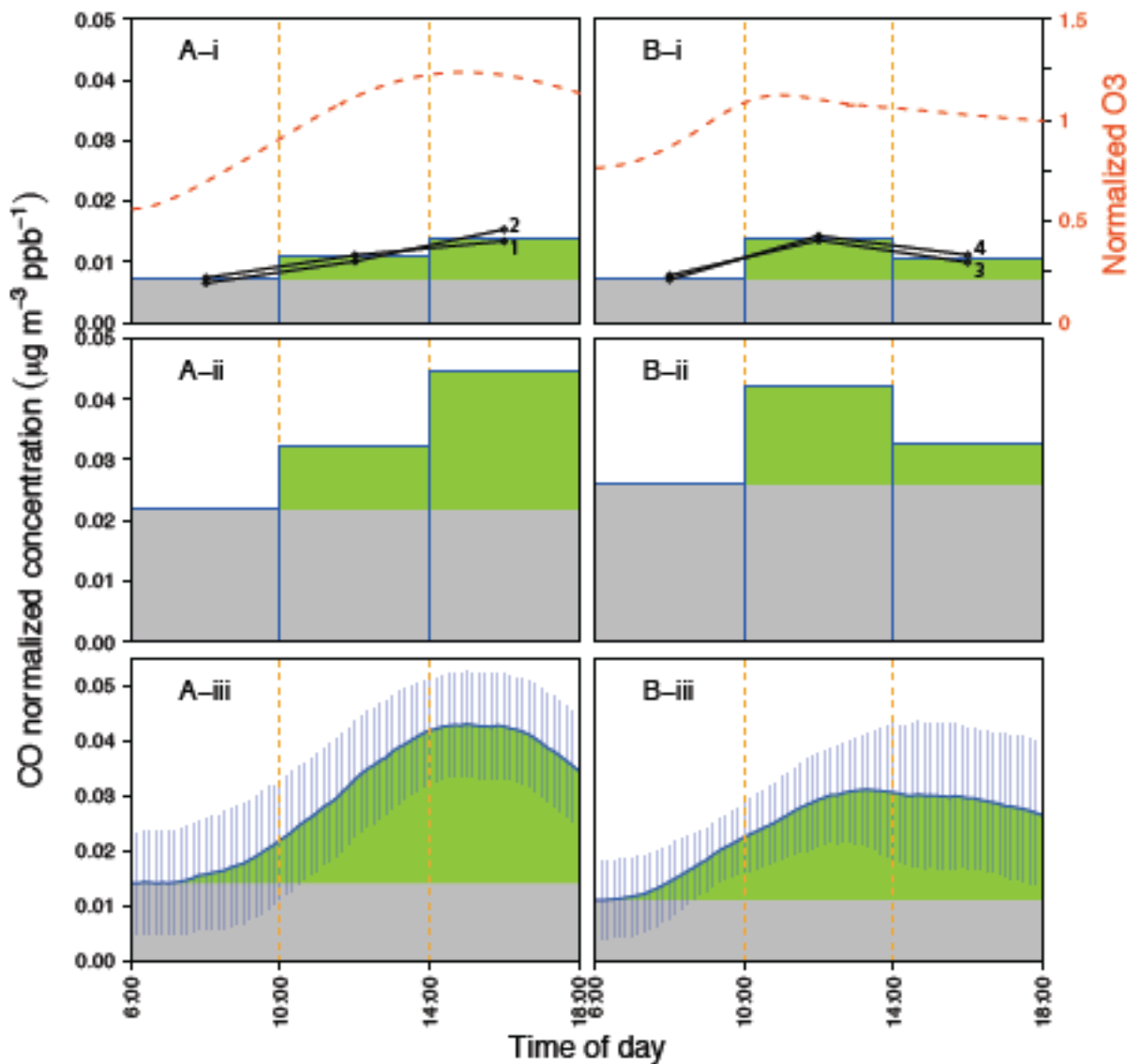


Figure 1. Daytime profiles of A (“Afternoon High” days) and B (“Noon High” days) for (i) carboxylic acid group, (ii) the FTIR Combustion factor, and (iii) the AMS Aged Combustion factor concentration. Colors indicate POA (grey) and SOA (green), respectively. Red dashed lines in panels A-i and B-I represent average daytime profiles of normalized O₃. Black lines in panels A-i and B-i are the average diurnal carboxylic acid group profiles. Vertical blue bars in panels A-iii and B-iii show standard deviations of the averaged diurnal cycles.

SUMMARY OR CONCLUSION

Measurements at the Scripps Pier showed that OM accounted for nearly 50% of ambient submicron particle mass. The OM was dominated by fossil fuel combustion type sources, which resulted in a mixture of alkane and carboxylic acid functional groups. In this mixture, the abundances of these two functional groups changed diurnally, with the carboxylic acid group concentration increasing significantly during the daytime, indicating photochemical formation of carboxylic acid groups, consistent with past studies that have argued carboxylic acids are secondary. This daytime increase was tightly correlated with O₃ mixing ratios, suggesting O₃ played an important role in acid formation. A two-step alkane oxidation mechanism is consistent with the observed diurnal variation of carboxylic acid groups and the composition of the Combustion factor resulted from the PMF analysis. In this mechanism, gas-phase alkane molecules are oxidized by OH radicals, forming dihydrofuran in the particle phase, followed by evaporation of dihydrofuran and further gas-phase oxidation by O₃. The O₃ peaked both at noon and in the afternoon, likely caused by different NO_x or VOC conditions upstream, resulting in two classes of carboxylic acid group and alkane group daytime profiles (the “Afternoon High” and the “Noon High” days) under comparable meteorological conditions. In both cases, the size distribution of m/z 44/nrOM and nrOM/PM1 revealed that the newly formed nrOM condensed onto existing particles, while m/z 44 may undergo further reactions in the particle phase under high RH at the sampling site.

The fraction of OM that is contributed by secondary carboxylic acid groups is estimated to be 10%. This number represents a lower-bound of the SOA contribution to OM, as other groups are also present in photochemically-generated molecules (i.e. alkane groups). Another estimate is to consider the fraction of OOA that is formed each day as secondary, which is 15-30% of OM. These measurements account for only the SOA formed during an approximately 12-hr period, yet it contributes a large fraction of the combustion-associated OM factors (50% for FTIR) and a significant fraction of OM at the Scripps Pier during this study. This large contribution of alkane-derived SOA is not surprising given their large contributions to VOC emissions in the LA/LB source region and the relative absence of significant additional organic precursors during transit in the coastal marine boundary layer. Our study reinforces the importance of gas-phase alkane photochemistry for the air quality of regions downwind of emission sources.

ACKNOWLEDGMENTS

We appreciate the fundings from UCSD-PNNL ACCI and NSF grant ATM-0744636. We also thank Kimberly Prather and Cassandra Gaston for providing the O₃ data.

Changes in Aerosol Mass Spectra during the Photochemical Aging of Organic Aerosols

Nga L. Ng¹, Manjula R. Canagaratna¹, Jose L. Jimenez^{2,3}, Puneet S. Chhabra⁴, John H. Seinfeld⁴ and Douglas R. Worsnop¹

1 Aerodyne Research, Inc. Billerica, MA, USA

2 Department of Chemistry and Biochemistry, University of Colorado, Boulder, CO, USA

3 CIRES, University of Colorado, Boulder, CO, USA

4 Department of Chemical Engineering, California Institute of Technology, Pasadena, CA, USA

ABSTRACT

The Aerosol Mass Spectrometer (AMS) provides real-time quantitative mass concentrations of non-refractory species in ambient aerosols. Factor analysis of the AMS organic aerosols (OA) data showed that the oxygenated OA (OOA) can be deconvolved into two broad subtypes differ in volatility and degree of oxidation: low-volatility OOA (LV-OOA) and semi-volatile OOA (SV-OOA). Differences in the mass spectra of these components are characterized in terms of the two main ions m/z 44 (mostly CO_2^+ , likely from acid groups) and m/z 43 (mostly $\text{C}_2\text{H}_3\text{O}^+$, likely from non-acid oxygenates). The OOA components from all sites cluster within a well defined triangular region in the f_{44} (ratio of m/z 44 to total signal in the component spectrum) vs. f_{43} space (defined similarly) (“triangle plot”), which can be used as a standardized means of comparing and characterizing any OOA components (laboratory or ambient) observed with the AMS. The OOA components become increasingly similar with atmospheric photochemical aging^[1].

We develop a method to parameterize H:C of OOA in terms of f_{43} . Such parameterization allows the transformation of large database of ambient OOA components from “triangle plot”^[1] into the Van Krevelen diagram (H:C vs. O:C). Heald et al.^[2] suggested that the bulk composition of OA line up in the Van Krevelen diagram with a slope ~ -1 ; such slope can potentially arise from the physical mixing of HOA and OOA, and/or from chemical aging of these components. In this study, we find that the OOA components from all sites occupy an area in the Van Krevelen space, with the evolution of OOA following a shallower slope of ~ -0.5 , consistent with the additions of both acid *and* alcohol functional groups without fragmentation, and/or the addition of acid groups with C-C bond breakage. The importance of acid formation in OOA evolution is consistent with increasing f_{44} in the triangle plot with photochemical age.

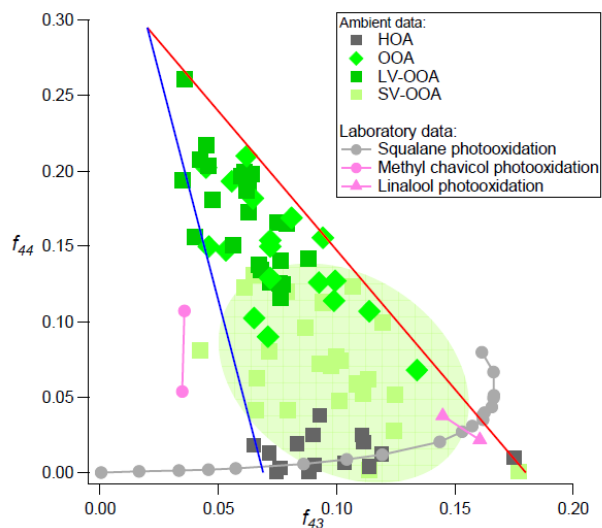
KEYWORDS

Aerosol mass spectrometry, organic aerosols, functional groups

Introduction

Recently, simplified ways of characterizing the aging of organic aerosols (OA) in the atmosphere from aerosol mass spectrometer (AMS) datasets have been identified^{[1]; [2]}. Ng et al.^[1] analyzed OA components determined from positive matrix factorization (PMF) analysis of 43 AMS datasets in the Northern hemisphere (unit mass resolution mass spectra UMR, and high resolution HR). At most sites, OA could be separated into hydrocarbon-like OA (HOA) and oxygenated OA (OOA), and sometimes other primary components. OOA is a good surrogate for SOA under most conditions^[3] and can be further deconvolved into semi-volatile OOA (SV-OOA) and low-volatility OOA (LV-OOA). OA evolution is characterized in terms of the changing intensities of the two most dominant oxygen-containing ions in the OOA spectra, m/z 44 (mostly CO_2^+ in ambient data) and m/z 43 (mostly $\text{C}_2\text{H}_3\text{O}^+$). The m/z 44 is thought to be due mostly to acids^[4] or acid-derived species, such as esters. The m/z 43 ion is predominantly due to non-acid oxygenates. Both acid and non-acid oxygenates have been observed in ambient OA^{[5], [6]}. When f_{44} (ratio of m/z 44 to total signal in the component spectrum) is plotted against f_{43} (defined similarly), all OA components fall within a triangular space (Fig. 1, hereafter referred to as the “triangle plot”). The HOA components have $f_{44} < 0.05$; SV-OOA and LV-OOA components concentrate in the lower and upper halves of the triangle, respectively. The m/z 43 fragment is mainly $\text{C}_2\text{H}_3\text{O}^+$ for the OOA components, and C_3H_7^+ for the HOA components. The base of the triangle encompasses the variability in HOA and SV-OOA composition. This range decreases with increasing f_{44} (O:C ratio), suggesting that the aerosols become more chemically similar with increasing aging, largely independent of the initial source of the material^{[3]; [1]}. Most SOA produced in the laboratory cluster on the lower half of the triangle, indicating that they are not as oxidized as ambient LV-OOA^[1].

Figure 1. “Triangle plot” of all OOA components. The light green area indicates the region where most laboratory data fall into.



Heald et al. [2] characterized the evolution of bulk OA composition using the Van Krevelen diagram (H:C vs. O:C)^[7]. In this approach high resolution mass spectra were analyzed to obtain bulk H:C and O:C values^{[8], [9]}. HR-AMS field datasets and laboratory studies occupy a narrow range when plotted in the Van Krevelen diagram. The authors reported that all the data cluster along a line with slope ~ -1 , consistent with simultaneous increases in carbonyl and alcohol moieties, either in separate carbons or due to the addition of carboxylic acid groups. It is suggested that the aerosol composition moves along this line with increased aging^[2].

In this work, we link the complementary information of the triangle plot and the Van Krevelen diagram to provide further understanding of atmospheric OA evolution. The triangle plot provides an empirical way of viewing all new AMS data in the context of available data for characterizing aerosol aging; data obtained from both UMR (such as the Q-AMS and the recently developed Aerosol Chemical Speciation Monitor, ACSM^[10]) and HR instruments can be readily plotted in real time in this space. With detailed data processing of HR-AMS data, the added chemical insight contained in the Van Krevelen diagram provides information on the mechanism of evolution of OA composition.

Methods

In order to map data from the triangle plot (f_{44} vs. f_{43}) onto the Van Krevelen diagram (H:C vs. O:C), both H:C and O:C must be parameterized using UMR data. Aiken et al.^[9] showed that O:C of ambient OA can be estimated from f_{44} through a linear parameterization. In this work, we obtain an analogous parameterization of H:C in terms of f_{43} for SOA/OOA, using OOA

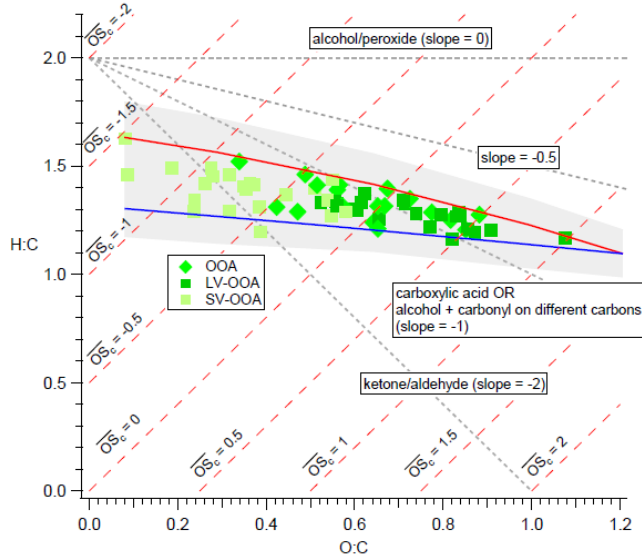
components obtained from PMF analysis of HR-AMS ambient datasets [11]; [12]; [13]; [14]; [15]; [16] and SOA formed in laboratory studies^{[17]; [18]}.

Results and Discussion

The OOA components in the triangle plot are transformed into the Van Krevelen diagram using the parameterization, and the results are shown in Fig. 2. The left and right sides of the triangle plot become the bottom and top lines in the Van Krevelen diagram, respectively. The light green points are SV-OOA which has lower O:C, while the dark green data are LV-OOA which has higher O:C. We refer to Fig. 2 as the “VK-triangle” diagram. The variation in f_{43} of the SV-OOA components in the triangle plot is still preserved in the VK-triangle diagram, with SV-OOA components spanning a range of H:C ratios. Possible reasons for the range of observed H:C ratios include the different SOA precursor mixes and chemical pathways of SOA formation. For instance, the chamber data from photooxidation of methyl chavicol ($C_{10}H_{12}O$) and linalool ($C_{10}H_{18}O$) span the base of the triangle plot (Fig. 1); these data roughly define the intercepts of the two lines that made up the VK-triangle, which is consistent with the H:C ratios of the precursor hydrocarbon (i.e. H:C = 1.2 for methyl chavicol, H:C = 1.8 for linalool).

There are two observations from this VK-triangle diagram that differ from those in Heald et al. ^[2]: (1) Most data points in Heald et al. ^[2] cluster around the line with the -1 slope, with only some points at high ages showing a lower slope of ~ -0.8 . In Fig. 2, however, the data points span a larger region in the diagram; (2) On average, the transition from SV-OOA to LV-OOA follows a line with a slope that is shallower than -1 (~ -0.5). Only four HR OOA components were available at the time of Heald et al. ^[2], which may explain why these features are not clear in that study.

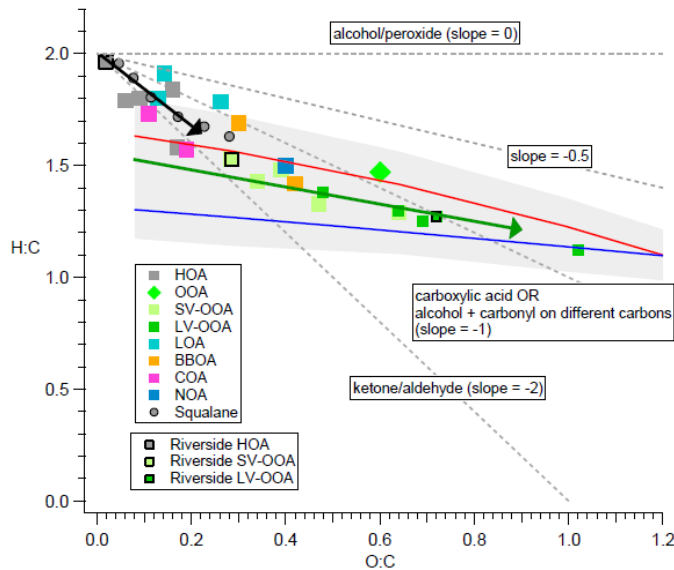
Figure 2. Representation of all the OOA components into the VK-triangle diagram. The left and right sides of the triangle plot become the bottom and top lines in the Van Krevelen diagram, respectively. The light gray shaded region denotes the $\pm 10\%$ uncertainty in the parameterization. The estimated carbon oxidation states (OSC _2 O/C–H/C) are shown with the red dotted lines.



Other than Mexico City (flight and ground)^{[12]; [13]}, the OA components from other HR datasets (Riverside, Queens NY, China PRD, Beijing)^{[11], [16]; [14]; [15]} have also become available recently. The OA components from all these sites and the results from the heterogeneous oxidation of squalane^[19] are shown in Fig. 3. The OOA components from these HR datasets mostly fall into the VK-triangle region defined by the UMR data while the HOA components and the squalane data are outside the VK-triangle region. As most data in Heald et al.^[2] represent the average OA composition at each site, the observed slope of ~ -1 in their study can arise from a combination of physical mixing of HOA and OOA components, and/or chemical evolution of these components. The HOA, SV-OOA, and LV-OOA components from Riverside are highlighted in Fig. 3. It is clear that once the total OA is deconvolved into these components, the evolution of SV-OOA to LV-OOA follows a shallower slope. The differences in primary OA components (HOA, LOA, BBOA, COA) likely reflect some atmospheric evolution, but are not easily interpreted since they also likely represent differences in the initially emitted POA. However, the squalane data suggest that the initial heterogeneous oxidation of POA species may follow a steeper slope, consistent with carbonyl group addition. This corresponds to the horizontal movement of the squalane data across the triangle plot (Fig. 1), with larger increase in f_{43} due to non-acid oxygenates (such as carbonyls) and relatively smaller increase in f_{44} (acids). Freshly formed SOA, represented by SV-OOA, evolves in a different way, with a shallower slope of ~ -0.5 . It is possible that further aging of aged HOA which has reached the SV-OOA region of the VK-triangle may also proceed

with the shallower slope, as hinted by the change in slope of the evolution of squalane oxidation products in Fig. 3. However, this is not definitive from the available ambient data.

Figure 3. VK-triangle diagram for the OA components from all sites with HR-AMS data and results from the heterogeneous oxidation of squalane. The light gray shaded region denotes the $\pm 10\%$ uncertainty in the parameterization. (Note: LOA=local OA; BBOA=biomass burning OA; COA=cooking OA; NOA=nitrogen-enriched OA)



A slope of ~ -0.5 in the Van Krevelen diagram can be explained by at least two systematic OA chemical transformations mechanisms. If the functional group addition occurs on a CH_2 group without C-C bond breakage, this slope can be caused by e.g., the addition of 3 OH groups and 1 $\text{C}=\text{O}$ group, or the addition of 2 OH groups and 1 COOH group. A movement to the right (increase in O:C) with the gentler slope (~ -0.5) in the Van Krevelen diagram is equivalent to a movement up the triangle plot (increase in f_{44}). Since m/z 44 is found to be proportional to the acid content of standard compounds [4], it is likely that acid group formation plays an important role in the aging of SOA. Therefore, an OOA aging mechanism that is consistent with measurements (laboratory + field data) is that the ensemble average of the transformation involves both the net addition of COOH and OH functional groups. An alternative explanation for a slope of -0.5 is due to COOH group addition to the site of a C-C bond cleavage. Fragmentation is thought to become increasingly important for already oxidized material such as fresh SOA [19]; [20].

CONCLUSION

By parameterizing organic aerosol H:C of SOA/OOA in terms of f_{43} , we are able to transform data in the triangle plot (f_{44} vs. f_{43}) into the Van Krevelen diagram (H:C vs. O:C). Ambient OOA components in the triangle plot map out a triangular space in Van Krevelen diagram, showing a range of H:C at lower oxidization; such variation decreases with increasing oxidation. Taking all the UMR and HR-AMS data together, it is found that on average, the change in the bulk composition of OOA as oxidation progresses follows a line with a slope ~ -0.5 , which is shallower than the -1 slope proposed by Heald et al.^[2] and indicates that aging of OA likely involves the addition of both COOH and OH functional groups without fragmentation, and/or the addition of COOH groups with C-C bond cleavage. This simplified view of bulk OOA aging can provide a useful guide for modeling the complex oxidation pathways and changes in OA chemical and physical properties with increased oxidation, and needs to be investigated in detail with molecular-level studies.

REFERENCES

- [1] Ng, N. L.; Canagaratna, M. R.; Zhang, Q.; Jimenez, J. L.; Tian, J.; Ulbrich, I. M.; Kroll, J. H.; Docherty, K. S. et al. *Atmos. Chem. Phys.* **2010**, *10*, 4625-4641.
- [2] Heald, C. L.; Kroll, J. H.; Jimenez, J. L.; Docherty, K. S.; DeCarlo, P. F.; Aiken, A. C.; Chen, Q.; Martin, S. T. et al. *Geophys. Res. Lett.* **2010**, *37*.
- [3] Jimenez, J. L.; Canagaratna, M. R.; Donahue, N. M.; Prevot, A. S. H.; Zhang, Q.; Kroll, J. H.; DeCarlo, P. F.; Allan, J. D. et al. *Science*. **2009**, *326*, 1525-1529.
- [4] Duplissy, J.; DeCarlo, P. F.; Dommen, J.; Alfarra, M. R.; Metzger, A.; Barmpadimos, I.; Prevot, A. S. H.; Weingartner, E. et al. *Atmos. Chem. Phys. Discuss.* **2010**, *10*, 19309–19341.
- [5] Russell, L. M.; Bahadur , R.; Ziemann, P. J. *Proc. Natl. Acad. Sci. U. S. A.* **2011**, doi/10.1073/pnas.1006461108.
- [6] Decesari, S.; Mircea, M.; Cavalli, F.; Fuzzi, S.; Moretti, F.; Tagliavini, E.; Facchini, M. C. *Environ. Sci. Technol.* **2007**, *41*, 2479-2484.
- [7] Van Krevelen, D. W. *Fuel*. **1950**, *24*, 269-284.
- [8] Aiken, A. C.; DeCarlo, P. F.; Jimenez, J. L. *Anal. Chem.* **2007**, *79*, 8350-8358, doi:8310.1021/ac071150w.
- [9] Aiken, A. C.; DeCarlo, P. F.; Kroll, J. H.; Worsnop, D. R.; Huffman, J. A.; Docherty, K. S.; Ulbrich, I. M.; Mohr, C. et al. *Environ. Sci. Technol.* **2008**, *42*, 4478-4485.
- [10] Ng, N. L.; Herndon, S. C.; Trimborn, A.; Canagaratna, M. R.; Croteau, P.; Onasch, T. M.; Sueper, D.; Worsnop, D. R. et al. *Aerosol Sci. Technol.* **2011**, in print.
- [11] Docherty, K. S.; Stone, E. A.; Ulbrich, I. M.; DeCarlo, P. F.; Snyder, D. C.; Schauer, J. J.; Peltier, R. E.; Weber, R. J. et al. *Environ. Sci. Technol.* **2008**, *42*, 7655-7662.

- [12] Aiken, A. C.; Salcedo, D.; Cubison, M. J.; Huffman, J. A.; DeCarlo, P. F.; Ulbrich, I. M.; Docherty, K. S.; Sueper, D. et al. *Atmos. Chem. Phys.* **2009**, *9*, 6633-6653.
- [13] DeCarlo, P. F.; Ulbrich, I. M.; Crounse, J.; de Foy, B.; Dunlea, E. J.; Aiken, A. C.; Knapp, D.; Weinheimer, A. J. et al. *Atmos. Chem. Phys.* **2010**, *10*, 5257-5280.
- [14] Huang, X. F.; He, L. Y.; Hu, M.; Canagaratna, M. R.; Kroll, J. H.; Ng, N. L.; Zhang, Y. H.; Lin, Y. et al. *Atmos. Chem. Phys. Discuss.* **2010**, 25841-25869.
- [15] Huang, X. F.; He, L. Y.; Hu, M.; Canagaratna, M. R.; Y., S.; Q., Z.; Zhu, T.; Xue, L. et al. *Atmos. Chem. Phys.* **2010**, 8933-8945.
- [16] Sun, Y. L.; Zhang, Q.; Schwab, J. J.; Demerjian, K. L.; Chen, W. N.; Bae, M. S.; Hung, H. M.; Hogrefe, O. et al. *Atmos. Chem. Phys. Discuss.* **2010**, *10*, 22669-22723.
- [17] Chhabra, P. S.; Flagan, R. C.; Seinfeld, J. H. *Atmos. Chem. Phys.* **2010**, *10*, 4111-4131.
- [18] Massoli, P.; Lambe, A. T.; Ahern, A. T.; Williams, L. R.; Ehn, M.; Mikkila, J.; Canagaratna, M. R.; Brune, W. H. et al. *Geophys. Res. Lett.* **2010**, *37*.
- [19] Kroll, J. H.; Smith, J. D.; Che, D. L.; Kessler, S. H.; Worsnop, D. R.; Wilson, K. R. *Phys. Chem. Chem. Phys.* **2009**, *11*, 8005-8014.
- [20] Kroll, J. H.; Donahue, N. M.; Jimenez, J. L.; Kessler, S. H.; Canagaratna, M. R.; Wilson, K. R.; Altieri, K. E.; Mazzoleni, L. R. et al. *Nature Chemistry*. **2011**, DOI: 10.1038/NCHEM.1948.

Mixing State of Particles by Single Particle Aerosol Mass Spectrometer in Urban Area of PRD

Xinhui Bi¹, Guohua Zhang¹, Lei Li², Xinming Wang¹, Guoying Sheng¹, Jiamo Fu^{1,2} and Zhen Zhou²

1 State Key Laboratory of Organic Geochemistry, Guangdong Province Key Laboratory of Utilization and Protection of Environmental Resource, Guangzhou Institute of Geochemistry, Chinese Academy of Sciences, Guangzhou, 510640, P.R. China

2 School of Environmental and Chemical Engineering, Shanghai University, Shanghai 200444, P. R. China

Principal Contact: Xinhui Bi, SKLOG, Chinese Academy of Sciences.

Tel: +86-20-85290195 Fax: +86-20-85290288 E-mail: bixh@gig.ac.cn

Abstract

Single particle aerosol mass spectrometer (SPAMS) was used to characterize the single particle size and chemical composition of submicron aerosols in the urban area of the Pearl River Delta (PRD) region, China, for the period April 30 through May 22, 2010. This is the first study for the mixing state of aerosols by direct observation in this region. 696,465 particles were sized and chemical analyzed with both positive and negative ion spectra, in which 141,338 biomass burning particles were identified representing a significant source of submicron particles ~20.3% by number, and carbonaceous particles accounted for as much as ~85% of submicron particles by number. Up to 98% carbonaceous particles were found to internally mix with secondary inorganic species. Carbonaceous particles were clustered into three distinct particle groups, comprised of organic carbon (OC), elemental carbon (EC) and the mixture of both (OCEC). The OC specie was the most abundant, with concentrations of 43%. EC and OCEC followed with 32% and 25%, respectively. Nitrate and ammonium traces between particle groups had negligible variance, while sulfate was found to prefer to associate with OC and OCEC rather than EC. The influence of aerodynamic diameter was substantial for mixing states with nitrate and ammonium, with ratios lower in the condensation mode than droplet mode; whereas sulfate mixing ratios were nearly constant within 0.2-1.2 μm . Biomass burning particles were clustered into six distinct particle groups, comprising of Ca-rich, Na-rich, organic carbon (OC), elemental carbon (EC), the mixture of OC and EC (OCEC) and Secondary. OC was the largest contributor with a fraction of 22.9%, followed by Secondary type (21.4%) and OCEC (19.0%). Na-rich type was observed in 11.9% of the particles and 90% internally mixed with EC. The fraction of nitrate in biomass burning particles was higher 10% than in carbonaceous particles, which could be explained by the fact that the rich sodium and potassium in biomass burning particles exhibited high affinity for nitrate gases during neutralization reactions and thus facilitated the particulate nitrate formation. The results added appreciably to the knowledge of aerosol characteristics in the PRD region atmosphere and can be applied to the climate models.

Keywords: Biomass burning, carbonaceous aerosol, mixing state, single particle, nitrate, sulfate, SPAMS, ATOFMS, aerosol, PRD.

Inorganic species of airborne particulate matter and their gases precursors in the episode event-A case study in Taiwan

Jiun-Horng Tsai, Ting Ke Tseng, and Jian-Horng Lin

Department of Environmental Engineering, 1 University Road, Tainan City, Taiwan 70101

Principal Contact: Jiun-Horng Tsai, Professor, Department of Environmental Engineering, National Cheng-Kung University, 1 University Road, Tainan City, Taiwan 70101.

Tel: +886-6-2751084 Fax: +886-6-2083152 E-mail: jhtsai@mail.ncku.edu.tw

Abstract

This study investigated the relationship between concentrations of airborne particulate matter and water-soluble ionic species and meteorological parameters (temperature, relative humidity and wind velocity) during air pollution episode events in southern Taiwan. The airborne particulate matter and their precursor gases were sampled by MOUDI/Nano-MOUDI and ADS (Annular Denuder System) at the ambient air quality monitoring station in southern Taiwan. The content of water-soluble ion species and precursor gases was detected by ion chromatography. All samples were categorized as four groups: non-episode daytime, non-episode nighttime, episode daytime, and episode nighttime in this study. Aerosol mass size distributions showed a tri-model distribution and the concentrations of coarse particles and fine particles were increasing in episode event. The mass concentration of aerosol during episode daytime ($85\mu\text{g}/\text{m}^3$) and nighttime ($104\mu\text{g}/\text{m}^3$) were 3.0 and 3.9 times higher than that on non-episode daytime ($28\mu\text{g}/\text{m}^3$) and at nighttime ($27\mu\text{g}/\text{m}^3$) diameters ranging from $0.1\text{-}2.5\mu\text{m}$. Results of multi-way analysis of variance (ANOVA) showed that the $\text{PM}_{0.1\text{-}2.5}$ mass was influenced by temperature and relative humidity. NH_4^+ , SO_4^{2-} , and NO_3^- were the dominant particulate components which appeared in the accumulation mode of $\text{PM}_{2.5}$ on the episode and non-episode daytime and nighttime. The concentrations of water-soluble ions showed a significant difference in $\text{PM}_{0.1\text{-}2.5}$ during episode daytime, increasing by 1.8 (NO_3^-), 1.4 (SO_4^{2-}) and 1.3 (NH_4^+) times over those on non-episode daytime. The observation data also indicated that the concentration of precursor gases (HCl, HNO_3 , and SO_2) during episodes were higher than those in non-episodes. The gas-to-particle conversion ratio of NO_2 and SO_2 were high during episode days.

Keywords: Episode day, water soluble ion, precursor gas

Humic-like Substances in Ambient Aerosols in the Pearl River Delta Region, China

Jian Zhen Yu¹ and Peng Lin²

1 Division of Environment & Department of Chemistry, Hong Kong University of Science & Technology, Hong Kong, China

2 Division of Environment, Hong Kong University of Science & Technology, Hong Kong, China

Principal Contact: J. Z. Yu, Associate Professor, Division of Environment & Department of Chemistry, Hong Kong University of Science & Technology, Hong Kong, China.

Tel: 852-2358-7389 Fax: 852-2358-1594 E-mail: chjanyu@ust.hk

Abstract

HUMIC-LIKE Substances (HULIS) are an abundant unresolved mixture of organic compounds present in atmospheric samples. In this work, we investigate the spatial and temporal variation of HULIS in ambient PM_{2.5} samples collected at an urban and a suburban location in the Pearl River Delta (PRD), China over a period of one year. The annual average HULIS concentrations were 4.9 µg m⁻³ at the urban site and 7.1 µg m⁻³ at the suburban site while the annual average concentrations of elemental carbon were 3.3 µg m⁻³ and 2.4 µg m⁻³, respectively. The urban-suburban spatial gradient of HULIS was opposite to that of elemental carbon, negating vehicular emissions as a significant source of HULIS. The HULIS concentrations in the ambient PM_{2.5} were significantly higher in air masses originating from regions influenced by biomass burning. Significant correlations between HULIS and water-soluble K⁺ concentrations at both sites further support that biomass burning was an important source of HULIS. Ambient concentrations of HULIS also correlated well with those of sulfate, oxalate, and oxidant (the sum of O₃ and NO₂), suggesting that secondary formation is a significant source of HULIS in the PRD region. The ambient HULIS was also studied for its potential in generating reactive oxygen species using a chemical assay and the health impact of HULIS will be discussed.

Keywords: Humic-like substances, organic aerosols, water-soluble aerosols, biomass burning emissions, chemical characterization of ambient aerosols

Chemical Composition of Fine and Coarse Particles at Wuqing during the HaChi Summer Campaign

Qian Tang, Min Hu*, Zhibin Wang and Binyu Kuang

State Key Joint laboratory of Environmental Simulation and Pollution Control, College of Environmental Sciences and Engineering, Peking University, Beijing 10871, China

ABSTRACT

To characterize regional aerosol pollution of North China Plain (NCP), fine ($PM_{2.5}$) and coarse particle ($PM_{2.5-10}$, between 2.5 and 10 microns in size) samples were collected during the HaChi (Haze in China) field campaign in the summer of 2009, at a suburban site Wuqing which located between two important mega-cities Beijing and Tianjin at the northern edge of NCP. The average mass concentrations of $PM_{2.5}$ and PM_{10} were 74.90 ± 38.53 and $97.47 \pm 47.52 \mu\text{g}/\text{m}^3$, respectively, with $PM_{2.5}/PM_{10}$ ratio of $76\% \pm 7\%$. Secondary inorganic compounds (sulfate, nitrite and ammonium) accounts for 57% in fine particles, indicating the serious secondary pollution. Particle pollution during the campaign showed meteorological dependent. When the weather was stagnant, fine particle concentration, especially secondary components, accumulated steadily. On the contrary, when heavy rain combined with northern strong wind occurred pollution was scavenged with great efficiency. Back trajectory cluster analysis was applied to classifying air mass trajectories and the weather situations governing the receptor site, yielding three trajectory clusters, arrived at Wuqing from the northwest (13%), northeast (15%) and south (72%). Wuqing was mostly influence by regional secondary pollution of the North China Plain in the summer, while occasionally strong wind bring air mass from the northwest and primary pollution would be obvious.

KEYWORDS

Water-soluble ions; EC/OC; fine and coarse particles; North China Plain

1. Introduction

Since the economic reforms in 1978, China's economic growth has resulted in increasing energy consumption, air pollution and associated health effects (HEI International Scientific Oversight Committee, 2004). PM_{10} is reported to be the major air pollutant on about 90% of the days during 1999-2005 (Beijing Environmental Bulletin), and on 30% of the days in each year,

* Corresponding author: Tel: 86-(0)10-62759880, Fax: 86-(0)10-62759880, email: minhu@pku.edu.cn

the daily average PM₁₀ concentration exceeded the Grade II standard. PM_{2.5} concentrations in most Chinese cities are far above the World Health Organization Air Quality Guidelines of 10 µg/m³ (annual average) and 25 µg/m³ (24h average) (WHO, 2005). With an increasing number of air pollution episodes and low visibility days reported by the media, the air pollution problems in mega cities will continue to be one of the top environmental concerns in the next decade in China [1].

North China Plain (NCP) region, in which there are two of the most heavily populated mega-cities in China, Beijing and Tianjin, suffered severe air pollution these years, and it has become a serious environmental challenge for China to solve these problems [2][3]. Wuqing is a suburban district, situated between Beijing and Tianjin. Compared to the neighboring mega-cities, Wuqing lies inside the polluted region, but is relatively clean. The special characteristic of geographic location make it highly representative of the overall pollution level of the polluted NCP region and a favorable spot for observing transport of air pollutants. In this study, fine (PM_{2.5}) and coarse particle (PM_{2.5-10}, between 2.5 and 10 microns in size) samples were collected within the HaChi (Haze in China) project at Wuqing Meteorology Station, from 18th July to 25th August 2009. Mass concentration and chemical compositions (major ions, organic and elemental carbon) were analyzed. Trajectories and significant concentration differences for fine/coarse particles were discussed in detail to characterize regional transport of aerosol pollution.

2. Experimental Methods

2.1 Sample collection

The Dichotomous Partisol-Plus Sequential Air Sampler (Model 2025, Thermo Electron Corporation, rp Products, USA) was used to collect fine (PM_{2.5}) and coarse particle (PM_{2.5-10}, between 2.5 and 10 microns in size) sample at Wuqing District Meteorological Bureau (39°22'58.8"N, 117°01'1.2"E). The site was located in the rural area in Wuqing, to the west of it were large areas of farm land, and to the east were groups of small factories. A rural road lied about 100 m away from the site in the south. Traffic flow near the site was low and there were no large emission sources in the surrounding areas.

Totally 39 sets of 24-hour aerosol samples and 1 set of field blank were collected from 18th July to 25th August 2009 during the HaChi (Haze in China) field campaign, each set of samples included two quartz filters for fine and coarse particles, respectively. One paper filter for each set was to correct the loss of semi-volatile compounds such as NO₃⁻ and NH₄⁺.

2.2 Sample analysis

Mass concentrations were calculated as the difference in weight of each quartz filter before and after sampling divided by the recorded sampling volume, the method was the same as Liu^[4].

A punch with the dimensions of 1 cm x 1.45 cm was used to remove an accurately defined part of the exposed area of the sample filter. A slice of quartz filter was cut from each quartz filter for EC and OC analysis by thermal/optical method (Sunset OC/EC analyzer) using NIOSH

temperature protocol^[5].

Another punch of quartz filter was extracted with 20 ml de-ionized water, by using ultrasonic in water bath for 30 minutes at controlled temperature (below 30°C). Then the extraction was filtered using 0.45 mm PTFE filters (Gelman Sciences), and transferred to two 10 mL clean plastic covered tubes. The tubes were stored in a refrigerator (4 °C) before analysis.

Ionic compounds were analyzed by ion-chromatograph (DIONEX, ICS-2500 for cations and ICS-2000 for anions)^[6]. An AS11 column (4 mm) with an AG11-HC (4×50 mm) guard column were used for anion with an eluent of 2.5–20 mM/L KOH (1.2 mL/min, gradient). Cations were analyzed by using CS-12A Column, with a CG-12A (4×50 mm) guard column, CSRS-I suppressor. The eluent was 20 mM/L MSA with a flow rate of 1.0 mL/min. Totally 5 kinds of cations (Na^+ , NH_4^+ , K^+ , Mg^{2+} and Ca^{2+}), 3 kinds of anions (Cl^- , NO_3^- and SO_4^{2-}) were analyzed with the detection limits of 0.003, 0.04, 0.05, 0.006, 0.009, 0.002, 0.007, and 0.004 mg/L in liquid.

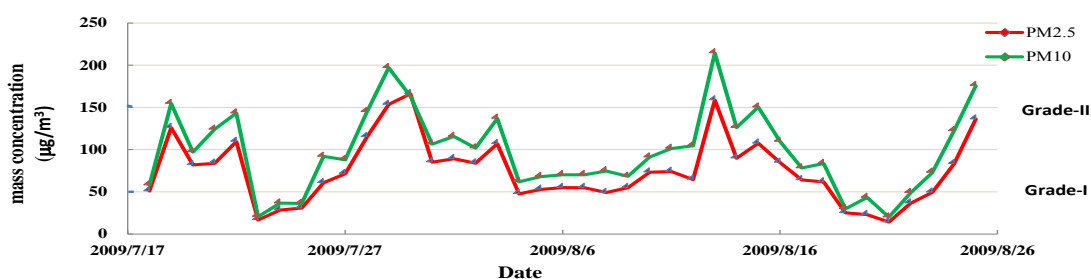
Field blanks and lab blanks were treated as the real samples and all samples were revised by using the blank results.

3. Results and Discussion

3.1 Mass concentration

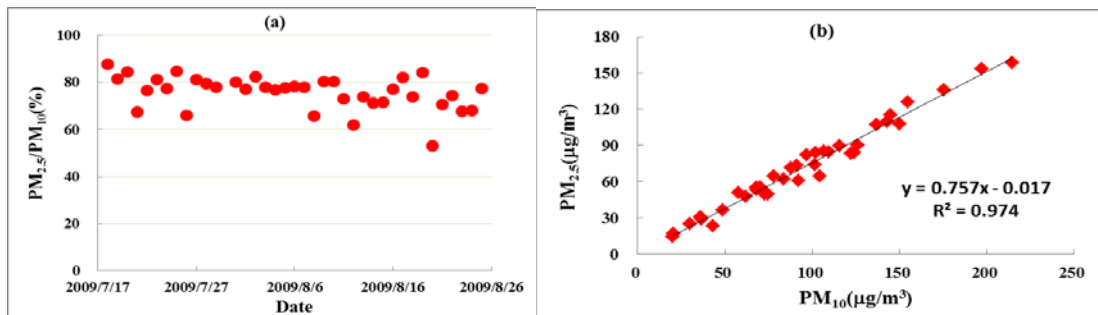
From 18th July to 25th August 2009, totally thirty-nine sets of 24-hour aerosol samples were collected. The average mass concentration of $\text{PM}_{2.5}$ and PM_{10} was 74.90 ± 38.53 and $97.47 \pm 47.52 \mu\text{g}/\text{m}^3$, respectively. Figure 1 showed the particle mass concentration during the campaign. The large day-to-day variations were observed with the $\text{PM}_{2.5}$ range of $14.19\text{--}166.07 \mu\text{g}/\text{m}^3$ and PM_{10} of $20.08\text{--}214.44 \mu\text{g}/\text{m}^3$. The ratio of $\text{PM}_{2.5}/\text{PM}_{10}$ (see figure 2a) was between 53- 88%, with the average ratio of $76\% \pm 7\%$. The mass concentration of $\text{PM}_{2.5}$ and PM_{10} show good correlation (see figure 2b) and showed high ratios of $\text{PM}_{2.5}/\text{PM}_{10}$, indicating the fine particles were the major component of PM_{10} , and determined the fluctuation of PM_{10} ^[7]. The mass concentration of $\text{PM}_{2.5}$ ($166.07 \mu\text{g}/\text{m}^3$) was larger than PM_{10} ($163.19 \mu\text{g}/\text{m}^3$) on July 30th due to the error of sampling and weighing, and this data was not included in figure 2.

Figure 1. Mass concentration of $\text{PM}_{2.5}$ and PM_{10} at Wuqing



Grade I and Grade II : daily concentration limits for PM_{10} in Chinese National Ambient Air Quality Standards (CNAQS), Grade I $50 \mu\text{g}/\text{m}^3$; Grade II $150 \mu\text{g}/\text{m}^3$.

Figure 2. The ratio of PM_{2.5}/PM₁₀ (a) and correlation between the mass concentration of PM_{2.5} and PM₁₀ (b).



3.2 Chemical compositions

3.2.1 Average concentration and fraction of chemical compositions

Table 1 and figure 3 show the concentrations and fractions of the chemical compounds of fine (PM_{2.5}) and coarse particles (PM_{2.5-10}). OM and SO₄²⁻, NO₃⁻, EC consisted of the major fraction in both PM_{2.5} and PM_{2.5-10}. SO₄²⁻ was the largest fraction in PM_{2.5}, accounting for 27.6 %, followed by OM (22.3 %), NH₄⁺ (14.6 %), NO₃⁻ (13.3 %) and EC (4.5 %). In coarse particles, OM accounted the largest fraction, which was 17.4 %, followed by NO₃⁻ (12.6 %), SO₄²⁻ (11.5 %), EC (5.0 %) and Ca²⁺ (4.7 %).

The sum of secondary ions (sulfate, nitrite and ammonium) accounted for 55.5 % of the fine particles, indicating that strong secondary transformation occurred in summer because of active photochemical process, high temperature and humidity. As an indicator of dust source, Ca²⁺ accounts for large fraction in coarse particles. Nearly a half of other chemical compositions in coarse particles were mainly mineral dust.

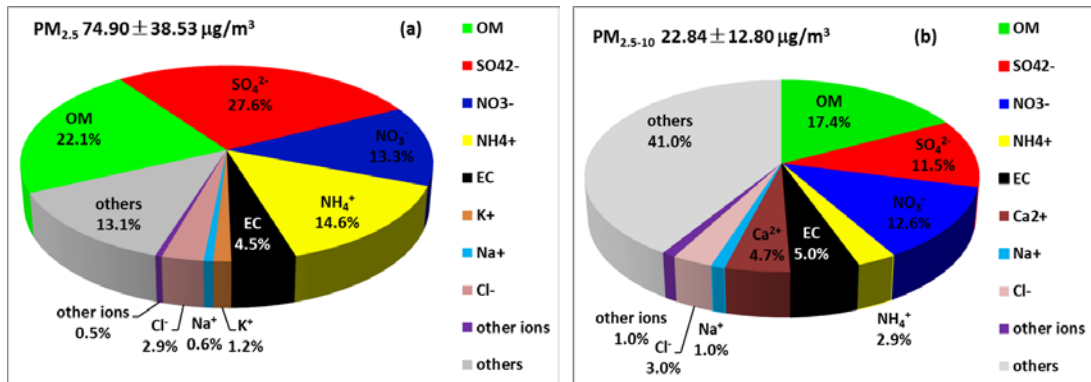
Table 1. Concentration and fraction of chemical compositions of PM_{2.5} and PM_{2.5-10}

	Concentration (µg/m ³)	Percentage (%)		Concentration (µg/m ³)	Percentage (%)
PM_{2.5}	74.90±38.53		PM_{2.5-10}	22.84±12.80	
OM	14.38±6.03	22.24±8.37	OM	3.18±1.69	17.55±11.65
EC	2.74±1.16	4.46±2.29	EC	0.88±0.38	4.97±3.49
SO₄²⁻	21.39±12.88	27.64±5.62	SO₄²⁻	2.46±1.69	11.55±5.71
NO₃⁻	9.95±6.14	13.30±4.16	NO₃⁻	2.84±1.73	12.71±4.57
NH₄⁺	11.13±6.41	14.55±2.19	NH₄⁺	0.68±0.67	2.88±2.24
Na⁺	0.42±0.40	0.64±0.51	Na⁺	0.17±0.18	0.98±1.66
K⁺	0.83±0.39	1.24±0.59	K⁺	0.08±0.12	0.55±1.39
Cl⁻	1.86±1.00	2.92±1.75	Cl⁻	0.58±0.33	2.99±2.29
Mg²⁺	0.03±0.02	0.04±0.04	Mg²⁺	0.10±0.06	0.44±0.25

Ca^{2+}	0.25 ± 0.15	0.41 ± 0.35	Ca^{2+}	1.03 ± 0.62	4.78 ± 1.61
others	11.67 ± 11.65	12.51 ± 8.84	others	10.96 ± 7.65	41.21 ± 18.75

OM= OC*1.4

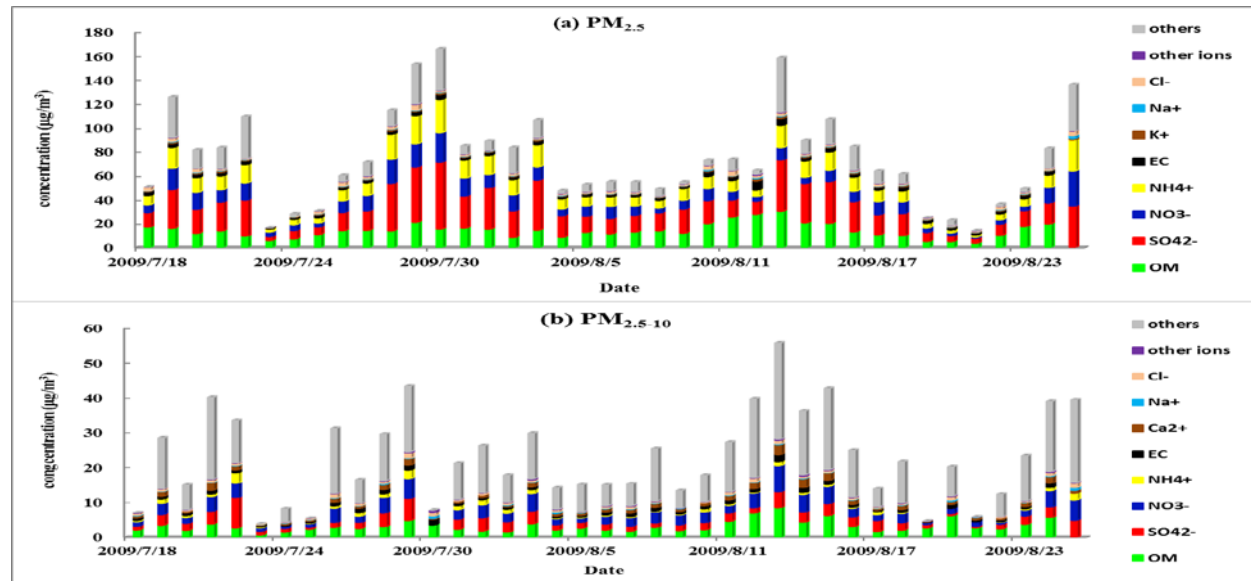
Figure 3. Chemical compositions of PM_{2.5} (OM= OC*1.4, other ions= $\text{Ca}^{2+} + \text{Mg}^{2+}$) (a) and PM_{2.5-10} (OM= OC*1.4, other ions= $\text{K}^+ + \text{Mg}^{2+}$) (b).



3.2.2 Day-to-day variations of chemical compositions

Figure 4 shows day-to-day variations of chemical compositions in fine and coarse particles from 18th July to 25th August 2009 at Wuqing. Four pollution episodes occurred during this period; they were 19th-22nd July, 26th July- 3rd August, 10th -19th and 24th -25th August. The highest 24h concentration of PM_{2.5} reached $125.93 \mu\text{g}/\text{m}^3$ (19th July), $166.07 \mu\text{g}/\text{m}^3$ (30th July), $158.65 \mu\text{g}/\text{m}^3$ (13th August) and $136.15 \mu\text{g}/\text{m}^3$ (25th August), respectively.

Figure 4. Day-to-day variations of chemical compositions in PM_{2.5} (OM= OC*1.4, other ions= $\text{Ca}^{2+} + \text{Mg}^{2+}$) (a) and PM_{2.5-10} (OM= OC*1.4, other ions= $\text{K}^+ + \text{Mg}^{2+}$) (b)

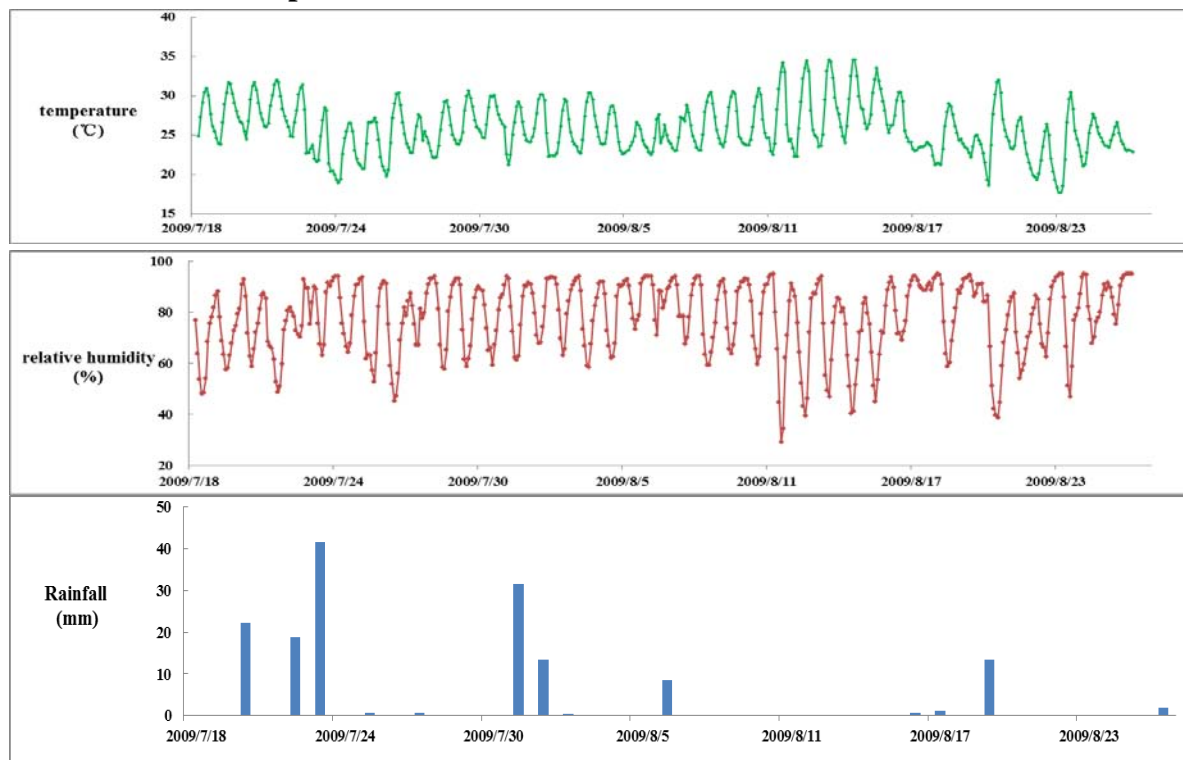


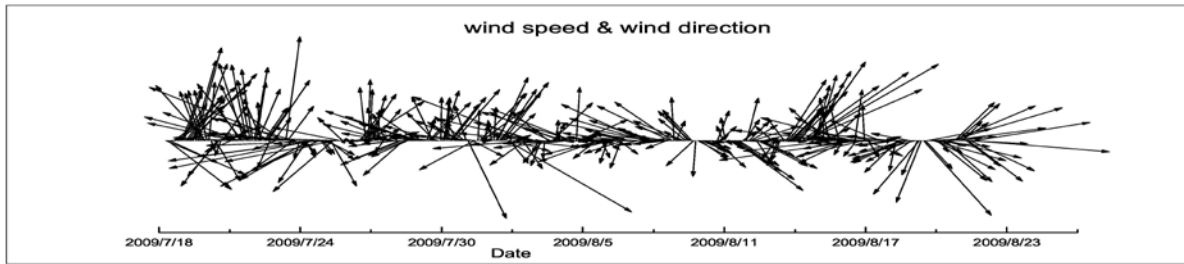
As shown in Figure 5, the meteorological condition was mostly stagnant with high relative humidity ($78 \pm 14\%$), high temperature ($25 \pm 3^\circ\text{C}$) and low south or southwest wind . During the

stagnant days, which were suitable for secondary transformation, particle pollution accumulated steadily, which resulted in high fine particle concentrations, especially secondary components (sulfate, nitrite, ammonium). For example, in a pollution accumulation process between 23rd and 30th July 2009, the mass concentration of fine particles increased from $16.77\mu\text{g}/\text{m}^3$ to $166.07\mu\text{g}/\text{m}^3$ in eight days, with sulfate from $3.22\mu\text{g}/\text{m}^3$ to $55.92\mu\text{g}/\text{m}^3$, nitrite from $3.87\mu\text{g}/\text{m}^3$ to $24.59\mu\text{g}/\text{m}^3$, and ammonium from $2.38\mu\text{g}/\text{m}^3$ to $27.90\mu\text{g}/\text{m}^3$. If define the increasing rate roughly as the difference between the initial and final concentration divided by duration, the increasing rate of sulfate ($0.27\mu\text{g m}^{-3}\text{ h}^{-1}$), nitrate ($0.11\mu\text{g m}^{-3}\text{ h}^{-1}$) and ammonium ($0.13\mu\text{g m}^{-3}\text{ h}^{-1}$) accounts for 66% of the increasing rate of $\text{PM}_{2.5}$ ($0.78\mu\text{g m}^{-3}\text{ h}^{-1}$).

When the wind changed to north or precipitation process occurred, particles were removed or diluted, so that the particle concentrations decreased rapidly. Heavy rain combined with northern strong wind scavenged particles with great efficiency, resulting in very clean days, such as 23rd-25th July and 19th- 21st August. But on 20th and 31st July, 1st and 6th August, when wind direction didn't change much before and after precipitation process, rain eased the pollution but didn't remove fine and coarse particles completely.

Figure 5. Meteorological conditions during the campaign: Temperature, RH, rainfall, wind direction and wind speed





3.2.3 Back trajectory cluster analysis

The concentration of particles was highly related to meteorological conditions. In order to get a better insight into the relationship of pollution processes and their meteorological air masses, back trajectories are used to follow the history of an air mass. The 36h back trajectories for Wuqing were calculated using the NOAA HYSPLIT_4 Model, and a back trajectory cluster analysis was applied to classifying and separating air mass trajectories, which were good indicates of the weather situations governing the receptor site. The trajectories terminated on a height of 200m above ground level, and one trajectory per day has been used, arriving at 12:00 (local time) in Wuqing, when ground based and elevated air masses are assumed to be well mixed because of the boundary layer development^[8]. The trajectories were classified into three clusters (see figure 6). The mean back trajectories show significant differences in both direction and length, and could represent the main classes of atmospheric flow conditions over the North China Plain (NCP) in the summer. Cluster 3 arrived from the northwest and was much longer than cluster 2 and 3, representing higher mean transportation speed along the trajectory. While cluster 2 arrived from the south and was the shortest, representing air masses from the surrounding places, mostly from North China Plain. Most of days (72%) were classified to cluster 2, indicating the air quality of Wuqing was mostly influenced by North China Plain.

Figure 6. Mean back trajectories for 3 trajectory clusters arriving at Wuqing.

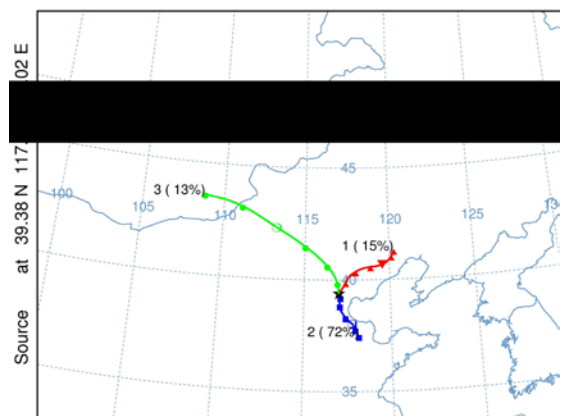
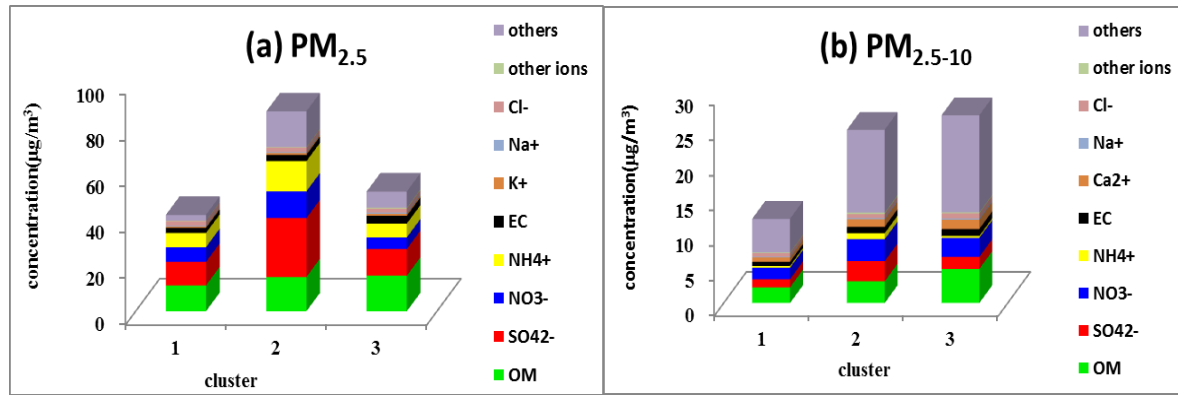


Figure 7 shows the mean chemical compositions of fine and coarse particles for each cluster. The mass concentration of both fine and coarse particles of cluster 1 was the lowest, indicating the air mass from the northeast was relatively clean. Comparing cluster 2 and 3, cluster 2 had higher concentration of fine particles, and the chemical composition was dominated by secondary

ions (sulfate, nitrite, and ammonium), while cluster 3 had higher concentration of coarse particles and the chemical composition was dominated by organic matter. This indicates that Wuqing was mostly influence by regional secondary pollution of the North China Plain in the summer, while occasionally strong wind bring air mass from the northwest and primary pollution would be obvious.

Figure 7. Averaged chemical compositions of PM_{2.5} (OM= OC*1.4, other ions= Ca²⁺ + Mg²⁺) (a) and PM_{2.5-10} (OM= OC*1.4, other ions= K⁺ + Mg²⁺) (b) belonging to the same cluster



SUMMARY

During the HaChi campaign, the average mass concentration of PM_{2.5} and PM₁₀ at Wuqing was 74.90 ± 38.53 and $97.47 \pm 47.52 \mu\text{g}/\text{m}^3$, with the average ratio of PM_{2.5}/PM₁₀ 76% ± 7%, indicating that fine particles was the main problem of particle pollution. SO₄²⁻ (27.6 %) was the largest fraction in PM_{2.5}, followed by OM (22.3 %), NH₄⁺ (14.6 %), NO₃⁻ (13.3 %) and EC (4.5 %). In coarse particles, OM (17.4 %) accounted the largest fraction, followed by NO₃⁻ (12.6 %), SO₄²⁻ (11.5 %), EC (5.0 %) and Ca²⁺ (4.7 %). The sum of secondary ions (sulfate + nitrite + ammonium), accounted for 55.5 % in fine particles, indicated strong secondary transformation occurred in summer. The concentration of particles was highly related to meteorological conditions, when the weather was stagnant, fine particles, especially secondary components, accumulated steadily; while heavy rain combined with northern strong wind scavenged particles with great efficiency and speed. The air mass trajectories could be classified to three clusters, arrived at Wuqing from the northwest (13%), northeast(15%) and south(72%). Wuqing was mostly influence by regional secondary pollution of the North China Plain in the summer, while occasionally strong wind bring air mass from the northwest and primary pollution would be obvious.

ACKNOWLEDGMENTS

European Integrated project on Aerosol Cloud Climate and Air Quality interactions (EUCAARI, No.036833). It is also supported by the National Natural Science Foundation of China (20977001, 21025728).

REFERENCES

- [1] Chak K. Chan, et al., Air pollution in mega cities in China, *Atmospheric Environment*, 42, 1-42, 2008.
- [2] Shao, M., et al., City Clusters in China: Air and Surface Water Pollution, *Front Ecol. Environ.*, 4(7), 353–361, 2006.
- [3] Van Donkelaar, A., et al., Global estimates of ambient fine particulate matter concentrations from satellite-based aerosol optical depth: Development and application, *Environ Health Perspect*, 118, 2010.
- [4] Liu, S., et al., Size distribution and source analysis of ionic compositions of aerosols in polluted periods at Xinken in Pearl River Delta(PRD) of China, *Atmospheric Environment*, 42, 6284-6295,2008.
- [5] Birch, M.E., Analysis of carbonaceous aerosols: interlaboratory comparison. *Analyst* 123, 851–857,1998.
- [6] Hu, M., et al., Chemical compositions of precipitation and scavenging of particles in Beijing, *Sci. China. Ser B*, 48(3), 265–272, 2005.
- [7] Guo, S. et al., Size-resolved aerosol water-soluble ionic compositions in the summer of Beijing: implication of regional secondary formation. *Atmos. Chem. Phys.*, 10, 947-959, 2010.
- [8] Wehner, B., et al.,Relationships between submicrometer particulate air pollution and air mass history in Beijing, China, 2004-2006. *Atmos. Chem. Phys.*, 8, 6155–6168, 2008.

Chemical characterization of water-soluble species in PM₁₀ of Baoji: a case study of a mid-scale city in inland China

Gehui Wang¹, Shuyuan Hu², Mingjie Xie², Bianhong Zhou³, Jianjun Li¹, and Junji Cao¹

1 State Key Laboratory of Loess and Quaternary Geology, Institute of Earth Environment, Chinese Academy of Sciences, Xi'an 710075, China

2 State Key Laboratory of Pollution Control and Resources Reuse, Nanjing University, Nanjing 210093, China

3 Department of Geographical Science and Environmental Engineering, Baoji University of Arts and Sciences, Baoji 721007, China

Principal Contact: Gehui Wang, Professor of Atmospheric Chemistry, State Key Laboratory of Loess and Quaternary Geology, Institute of Earth Environment, Chinese Academy of Sciences, Xi'an 710075, China.

Tel: 86-29-8832-9320 Fax: 86-29-8832-0456 Email: wanggh@ieecas.cn

Abstract

PM₁₀ aerosols at four sites and 8-stage size resolved particles at one site in Baoji, an inland city in China, were collected during 2008 winter and spring. Water-soluble organic carbon (WSOC), water-soluble inorganic carbon (WSIC), and inorganic ions in the samples together with pH of the extracts were measured. A bimodal size distribution was found for the particles in the winter and spring urban atmosphere with geometric mean diameters (GMDs) for the total range of the impactor sampler being 1.47 ± 0.07 m in winter and 1.85 ± 0.12 m in spring. The enhancements of coarse mode (>2.5 m) particle concentrations and the bigger GMDs indicate more fugitive dust in the spring air. WSOC (31 ± 7 g m⁻³), SO₄²⁻ (47 ± 23 g m⁻³), NO₃⁻ (41 ± 19 g m⁻³) and NH₄⁺ (29 ± 11 g m⁻³) are major components in the water-soluble fraction during winter, being 20-80% more abundant than in spring. No significant spatial difference in the concentrations of the water-soluble species was observed among the four locations, although slightly higher concentrations of WSOC and SO₄²⁻ were obtained in the residential and downtown areas due to coal burning for house heating and cooking. Concentrations of SO₄²⁻, levoglucosan, and PAHs well correlated each other, further demonstrating emission from coal burning as the major sources of the water-soluble species. Abundances of WSOC, sulfate, nitrate and ammonium in the city are comparable and even higher than those in heavily polluted mega-cities in China, probably suggesting a serious air pollution problem in mid-scale cities in the country.

Keywords: Atmospheric aerosols, Water-soluble species, Abundances and sources, Mid-scale

cities

The aerosol characteristics in different air pollution events over Nanjing

Bin Zhu¹, Honglei Wang¹, Qiucheng Zhang and Tijian Wang²

1 Nanjing University of Information Science & Technology, Nanjing China, 210044

2 Nanjing University, Nanjing China, 210093

Principal Contact: Bin Zhu, Dr., Nanjing University of Information Science & Technology, 219 Ningliu Road, Nanjing China, 210044.

Tel: 025-58699785 E-mail: binzhu@nuist.edu.cn

Abstract

By using the field observation data, which collected in 2 sites located at downtown and suburb of Nanjing during the period of autumn and winter of 2009, summer of 2010. The air pollution events in Nanjing can be sorted into three categories: local emission by anthropogenic sources (vehicle, industry emission etc.) within Yangtze river delta, crop residual biomass burning around Nanjing during harvest season and long range transport of air pollutants (eg. dust in spring) outside of Yangtze delta. The characteristics of aerosol number concentration, mass concentration ions concentration (Ca^{2+} , NH_4^+ , SO_4^{2-} , NO_3^- , etc.) are analyzed in these different air pollution events. We found that there were some distinct features of aerosol in different categories events, for example the number and mass concentration of coarse mode aerosol are highest in dust pollution events and fine mode aerosol are highest in local pollution. The differences of aerosol characteristics among that of the downtown, suburb and beside highway are also presented in this study. The seasonal variations of aerosol and the relation of aerosol-visibility-meteorology will be discussed.

Keywords: aerosol, air pollution, Nanjing.

How Similar Are The Aerosols Of Beijing And Delhi?

Kenneth A. Rahn¹ and Manju Mohan²

1 School of Environmental Science and Engineering, Tsinghua University, Beijing 100084, China

2 Centre for Atmospheric Sciences, Indian Institute of Technology Delhi, Hauz Khas, New Delhi 110016, India

ABSTRACT

More than you might think. Both have the strong daily variations of megacities. Both contain multiday cycles with raised baselines that mean transport from surrounding regions. Both are affected by mountain/valley (upslope/downslope) breezes created by sloping ground near mountain ranges. Both can show solenoidal flow and oscillating flow during stagnant conditions that can return air and pollutants the next day. Regional aerosol seems to be less important to Delhi than to Beijing. Delhi's mountain/valley circulation is stronger than Beijing's. Delhi may have a mild valley effect created by the surrounding Aravali Mountains and the Delhi Ridge to the west (receding foothills), whereas Beijing has no valleys nearby. Delhi's mountain/valley breezes often run perpendicular to the mountains, whereas Beijing's usually run nearly parallel to the mountains. Regional contributions to Delhi's aerosol can come from the NW or SE, whereas regional contributions to Beijing's aerosol come from the south.

KEYWORDS: Beijing, Delhi, aerosol, transport

Introduction

This work was undertaken purely for curiosity, when M. Mohan gave a set of PM measurements from Delhi to K. Rahn, and he noticed that they had daily and weekly cycles that reminded him of Beijing's. He then generated some back-trajectories for them, and found abundant looping, which he attributed to mountain-valley effects. This reminded him that Beijing sits near mountain ranges, too, to its west and north. Trajectories for Beijing under certain conditions also revealed looping similar to that of Delhi, so the authors decided to pursue the matter for their own enlightenment.

Experimental methods

Back air-mass trajectories were calculated with the Web-based version of ARL/NOAA's HYSPLIT program (<http://ready.arl.noaa.gov/HYSPLIT.php>). Short- and long-term contributions to the cycles of PM were calculated with the method of Jia et al. (2008). PM data were provided from TEOMs.

Results and discussion

The first clear result was that both Delhi and Beijing showed the strong daily variations of megacities (Figures 1,2).

Figure 1. Beijing PM_{2.5} Sep-Dec 2004

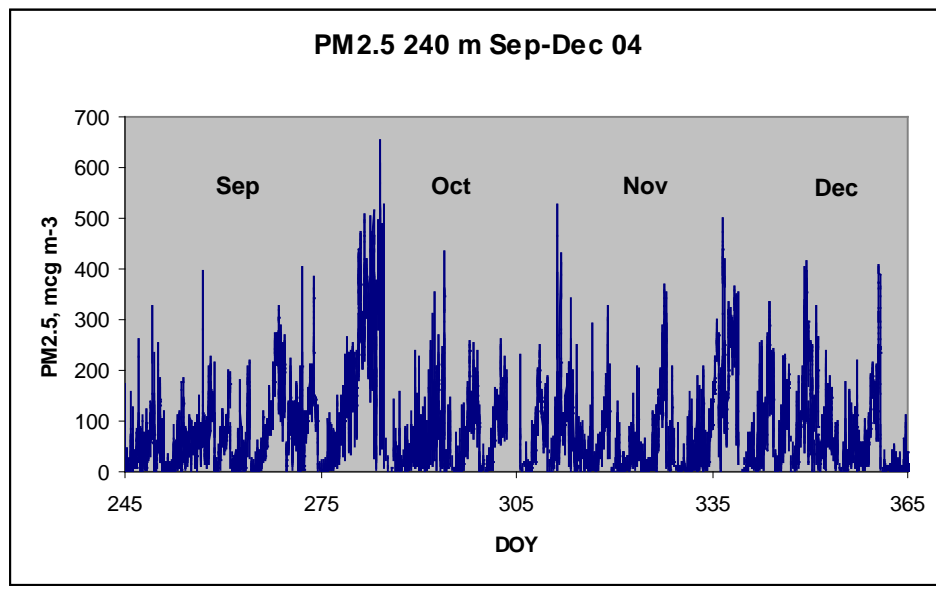
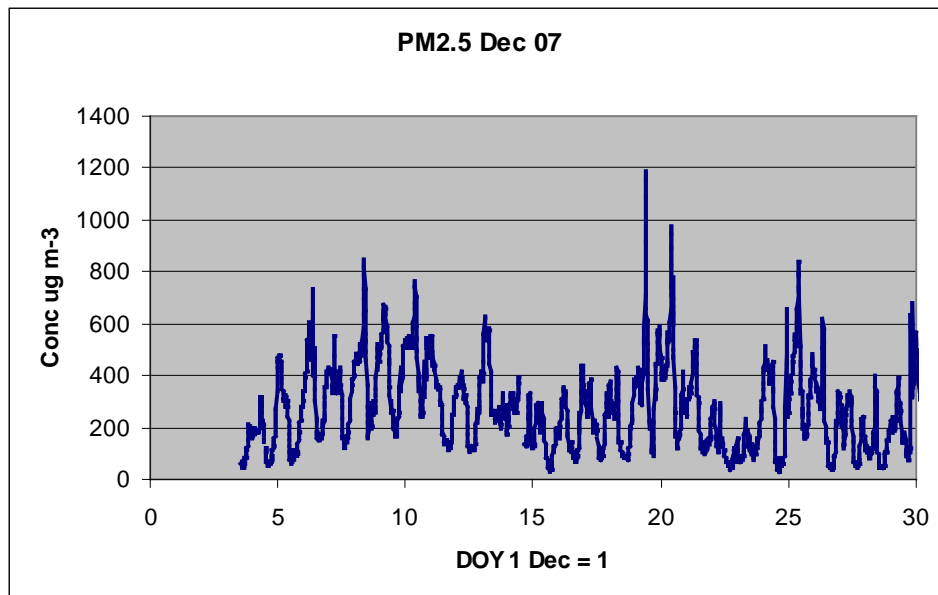
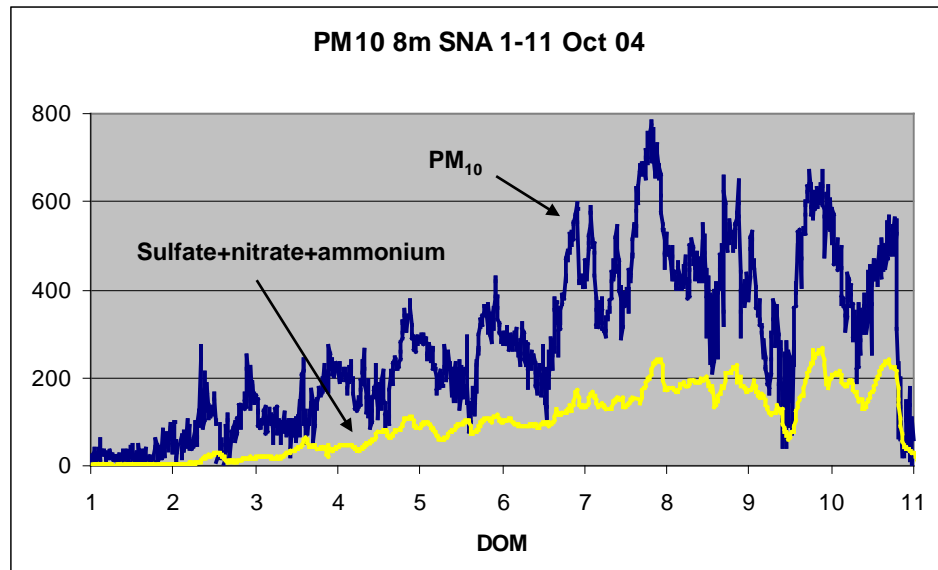


Figure 2. Delhi PM_{2.5} Dec 2007



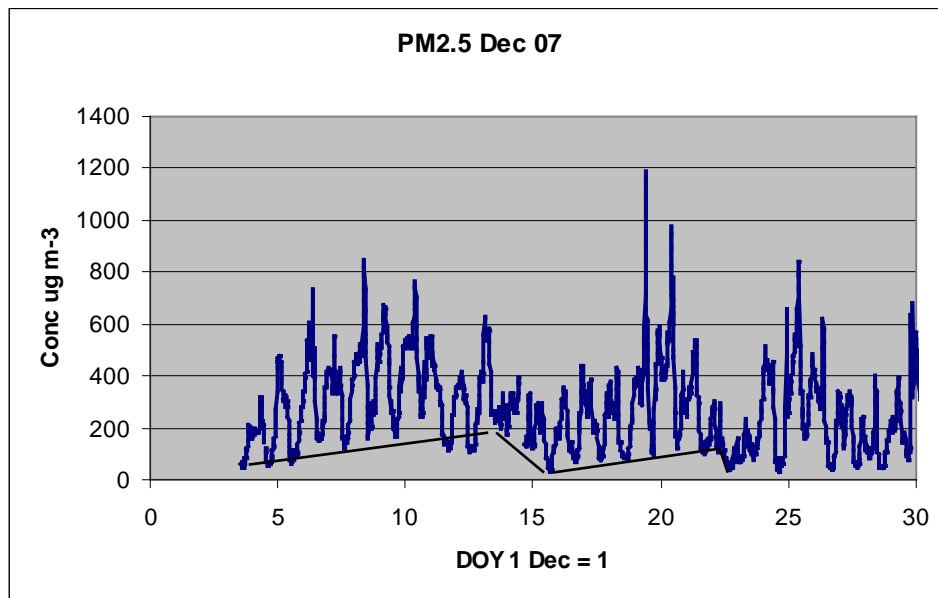
Both sites show multiday cycles with raised baselines that mean transport from surrounding areas (Figures 3,4).

Figure 3. Multiday cycle in Beijing, 1–11 October 2004.



From JGR paper Dec 08

Figure 4. Multiday cycles in Delhi, December 2007. Concentrations in $\mu\text{g m}^{-3}$.

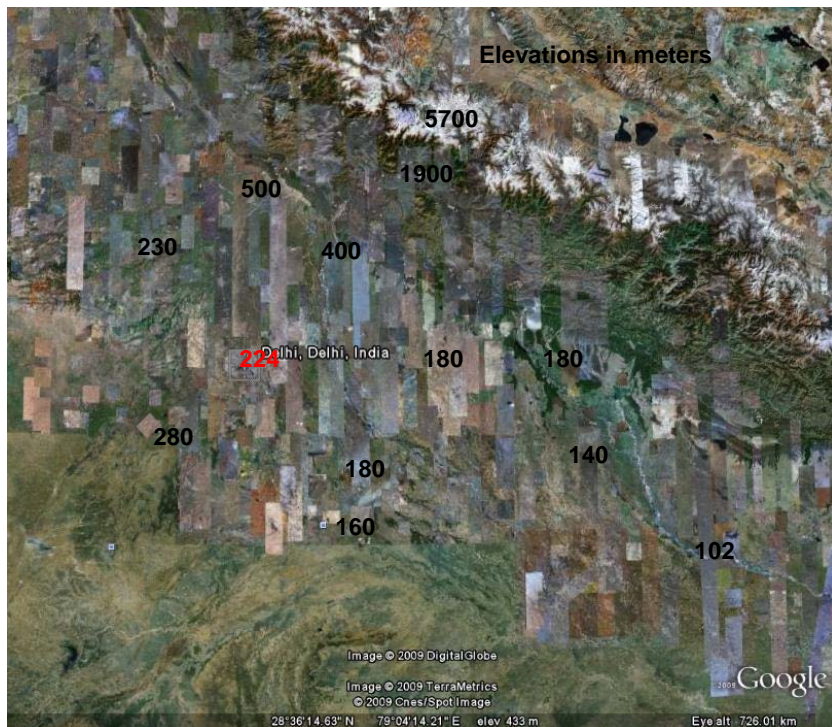


Both cities are affected by mountain/valley (upslope/downslope) breezes created by sloping ground near mountain ranges (Figure 5,6).

Figure 5. Topography near Beijing. Elevations in meters.



Figure 6. Topography near Delhi. Elevations in meters.



Mountain/valley breezes near both sites are shown clearly by the looping and oscillating of some of their back-trajectories (Figures 7,8).

Figure 7. Looping and oscillating near Beijing.

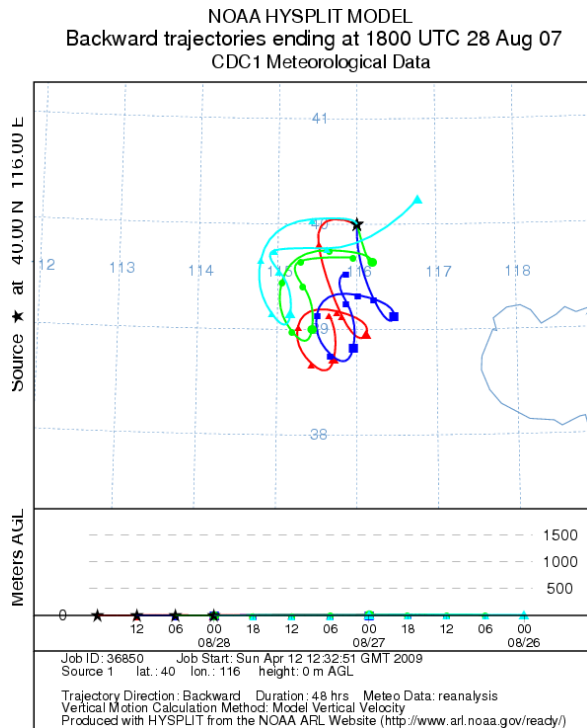
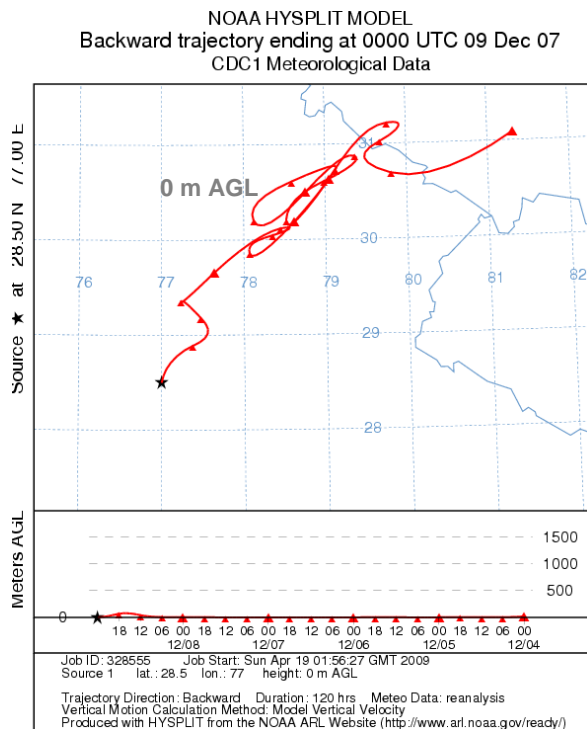
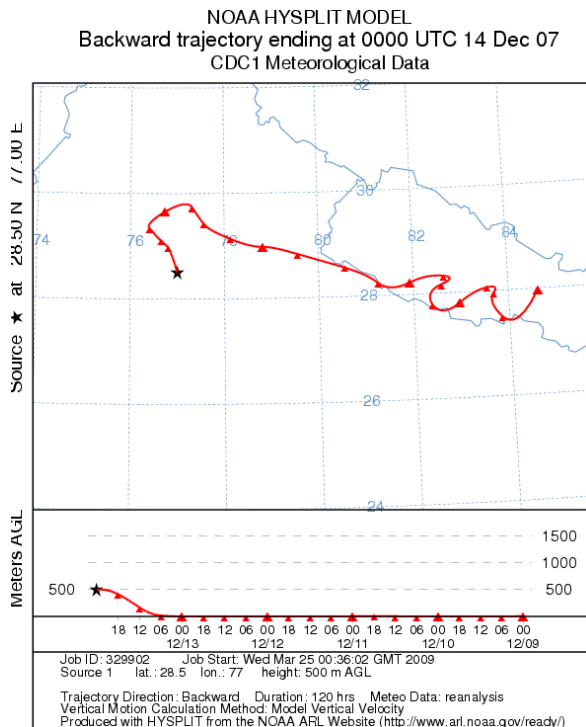


Figure 8. Looping and oscillating near Delhi.



Westerly winds superimposed on oscillations near Delhi create a solenoidal pattern:

Figure 9. Solenoidal flow near Delhi.



Regional aerosol seems to be less important to Delhi than to Beijing. At Beijing, the regional contributions are 40% annually, whereas at Delhi they seem to be closer to 20%. Delhi's mountain/valley circulation is stronger than Beijing's, in spite of Delhi's greater distance from the mountains (200 km, vs. 30 km for Beijing). Presumably this is because of the much greater height of the Himalayas (7000 m vs. 1500 m) and the stronger solar radiation at Delhi.

Delhi's mountain/valley breeze layer is thicker than Beijing's (1000 m vs. 300 m at Beijing). The heights are roughly proportional to the heights of the nearby mountains. Delhi may have a mild valley effect created by the surrounding Aravali Mountains and the Delhi Ridge to the west (receding foothills), whereas Beijing has no valleys nearby.

Delhi's mountain/valley breezes often run perpendicular to the mountains. Beijing's usually run nearly parallel to the mountains.

Regional contributions to Delhi's aerosol can come from the NW or SE, because the foothills of the mountains in either direction have relatively great population density. By contrast, regional contributions to Beijing's regional contributions come from the south, because the strongest sources lie in that direction.

REFERENCE

Jia Y., Rahn K., He K., Wen T. and Wang Y. (2008) A novel technique for quantifying the regional component of urban aerosol solely from its sawtooth cycles. *J. Geophys. Res.* **113**, D21309, doi: 10.1029/2008JD010389.

Use of six-stage Andersen Sampler in Investigating Bioaerosol Inhalation Risks in Different Environments

Zhenqiang Xu and Maosheng Yao

State Key Joint Laboratory for Environmental Simulation and Pollution Control, College of Environmental Sciences and Engineering, Peking University, Beijing 100871, China

Principal Contact: Maosheng Yao, Professor, State Key Joint Laboratory for Environmental Simulation and Pollution Control, College of Environmental Sciences and Engineering, Peking University, Beijing 100871, China.

Tel: +86 010 6276 7282 Email: yao@pku.edu.cn

Abstract

Increasing evidences show that inhalation of indoor bioaerosols has caused numerous adverse health effects and diseases. However, the bioaerosol size distribution, composition and concentration level could vary with human environments, thus representing different inhalation risks. The six-stage Andersen sampler is designed to simulate the sampling of different human lung regions. Here, the sampler was thus used in investigating culturable bacterial and fungal aerosols collected onto different stages in six different environments (student dormitory, hospital, office lab, hotel, student dining hall, and outdoor environment) in this study. During the sampling, the Andersen sampler was operated for 30 min and three independent experiments were performed for each of the environments. The air samples collected onto each of the six stages were incubated on agar plates directly at room temperature, and the colony forming units were manually counted and statistically corrected.

Results revealed that for most environments investigated the culturable bacterial aerosol concentrations were higher than those of culturable fungal aerosols. The culturable concentration of fungal aerosols were shown to be in comparable levels, while office lab, student dorm and hotel room appeared to have higher culturable bacterial concentrations. For most environments tested, larger ($>3 \mu\text{m}$) culturable bacterial aerosols were shown to dominate, while for culturable fungal aerosols those $2.1\text{-}4.7\mu\text{m}$ dominated. Comparisons of the air samples collected by different stages of the Andersen sampler indicated that the outdoor environment might represent more fungal inhalation risks to human alveoli region, and the hotel room was shown to have highest culturable bacterial aerosol concentrations collected by the six stage of the sampler. The results from this study suggested that different environments even with similar levels of total microbial cuturable aerosols concentrations could present different inhalation risks due to different size distribution and composition.

Keywords: six-stage Andersen sampler, Bacterial and fungal aerosols, Inhalation

Real-time Detection of Airborne Influenza A Viruses Using Silicon Nanowire Field Effect Transistor

Fangxia Shen¹, Miaoqiao Tan¹, Zhenxing Wang², Maosheng Yao^{1,*}, Zhenqiang Xu¹, Yan Wu¹, Jindong Wang², Xuefeng Guo^{2,*} and Tong Zhu¹

1 State Key Joint Laboratory for Environmental Simulation and Pollution Control, College of Environmental Sciences and Engineering, Peking University, Beijing 100871, China

2 College of Chemistry and Molecular Engineering, Peking University, Beijing 100871, China

***Principal Contact:** Maosheng Yao, Professor, State Key Joint Laboratory for Environmental Simulation and Pollution Control, College of Environmental Sciences and Engineering, Peking University, Beijing 100871, China.

Tel: +86 010 6276 7282 Email: yao@pku.edu.cn

Abstract

Numerous threats from biological aerosol exposures, such as H1N1 influenza, SARS, bird flu, and bio-terrorism necessitate the development of a real-time bioaerosol sensing system, which however is a long standing challenge in the field. Here, we reported real-time detection of airborne influenza H3N2 viruses by integrating electrically addressable silicon nanowire (SiNW) sensor devices with microfluidics and a bioaerosol-to-hydrosol air sampling system. Influenza A viruses were aerosolized into exposure chamber, and collected by an automated electrostatic sampler (AES) at a sampling flow rate of 5 L/min and transported onto the SiNW sensor device via microfluidic channel via a peristaltic pump at a flow rate of 0.4 L/min in a real-time manner. The electrical conductance of the SiNW device was monitored using a pre-amplifier and a lock-in amplifier.

Results show that when airborne influenza H3N2 virus samples were collected and delivered to antibody-modified SiNW devices, discrete nanowire conductance changes were observed within seconds. However, the conductance levels remained relatively unchanged when indoor air or clean air samples were delivered. Quantitative polymerase chain reaction (qPCR) tests indicated that higher virus concentrations in the air samples corresponded to higher conductance levels in the SiNW devices. The sensing system here has been demonstrated to have the capability to monitor the airborne presence of influenza A viruses in a real-time manner, typically from 1 to 2 minutes. This response time scale exceeds many of those available bioaerosol sensing systems. The work here opens a new arena for real-time monitoring of biological aerosols by integrating the technologies in different disciplines, holding great promise in the combat of fighting both infectious diseases and bio-terrorism.

Keywords: Influenza A H3N2 virus, bioaerosol, Silicon Nanowire, aerosol-to-hydrosol, qPCR, real-time detection

Traffic Related Particles Induced Pro-inflammatory Cytokine mRNA Expression *in vitro*: Importance of Organic Matter and Quinones

Yu Shang, Jialiang Feng, and Wei Zhao

School of Environmental and Chemical Engineering, Shanghai University, Shanghai, China, 200444

Principal Contact: Yu Shang, Dr., School of Environmental and Chemical Engineering, Shanghai University, Shanghai, China, 200444.

Tel: 021-66137734 Email: yushang@shu.edu.cn

Abstract

Traffic related particles (TRP), one major source of PM_{2.5} in urban areas, are demonstrated to induce cytokine production both *in vitro* and *in vivo*, but the biological mechanisms and attributable chemical components behind are not fully understood. In present study, we investigated the impacts of organic extracts of TRP (oTRP) and 1, 4-naphthoquinone on gene expressions in human alveolar epithelial cells (A549).

TRP was collected in Dapu road, a main road in Shanghai, China. Organic matter were extracted by dichloromethane, dried under nitrogen atmosphere and re-suspended in DMSO for cell exposure. Real time reverse transcription polymerase chain reaction (RT-PCR) was performed to quantify the mRNA level in cells. Briefly, total RNA was extracted by TRIZOL reagent then reverse transcribed to cDNA and quantified by RT-PCR using TOYOBO (Japan) ReverTra Ace®qPCR RT Kit and THUNDERBIRD SYBR qPCR Mix respectively.

oTRP showed a stimulatory impacts on IL-6, IL-8, TNF- α , CYP1A1 and CYP1B1 mRNA levels with a dose-dependent manner ($p<0.01$), but not MCP-1 or RANTES (Fig. 1A). IL-6, TNF- α , CYP1A1 and CYP1B1 were also up-regulated by 1,4-NP, but MCP-1, RANTES or IL-8 was not (Fig. 1B). Our results indicated organic components of TRP induced cytokine and metabolic enzyme mRNA up-expression, and quinines may be important components. Our previous research found 1,4-NQ generated ROS through redox reaction, thus 1,4-NQ may induce inflammatory cytokine through oxidative stress, and ultimately leading to airway inflammation and diseases.

Keywords: Traffic related particles, cytokine, RT-PCRs

Moving boundary study of micro-particle deposition in human oropharynx airway model under steady inspiration

Jianhua Huang¹ and Lianzhong Zhang^{1,2}

1 School of Physics, Nankai University, Tianjin 300071, China,

2 State Key Laboratory of Loess and Quaternary Geology, Institute of Earth Environment, Chinese Academy of Sciences, Xi'an 710075, China,

Principal Contact: Lianzhong Zhang, Professor, School of Physics, Nankai University, Weijin Road No. 94, Tianjin 300071, China.

Tel: +86-22-23503454 Fax: +86-22-23503454 E-mail: zhanglz@nankai.edu.cn

Abstract

Airflow into the lung is the result of negative alveolar pressure caused by the simultaneous action of diaphragm contraction and rib cage expansion. In this study the expansion of pleural cavity was simulated by a moving boundary setting at the end of bell-mouthed bronchial cavity. The steady airflow and micro-particle transport in the oropharynx airway model were investigated using the movable boundary under normal breath condition (30 l/min). The pressure drop, turbulence intensity and particle deposition efficiencies were compared with the numerical results in the immovable-boundary model under three different boundary condition assumptions, including a) uniform airflow velocity profile inlet and zero pressure outlet, b) axial-symmetrical airflow profile inlet with no-slip boundary and zero pressure outlet, c) zero airflow velocity inlet and negative pressure outlet.

Keywords: Moving boundary, Micro-particle deposition, Human oropharynx airway model,

Inhibitory Effects on Lung Carcinogenesis in A/J Mice by Aerosolized NSAIDs

Jingjie Zhang, Huijing Fu and Da-Ren Chen

Washington University in St. Louis, Brauer Hall, One Brookings Drive Campus Box 1180, St. Louis, Missouri 63130

Principal Contact: Da-Ren Chen, Doctor, Washington University in St. Louis, One Brookings Drive Campus Box 1180, St. Louis, Missouri 63130.

Tel:314-935-4983 Fax: 314-935-7211 Email: chen@seas.wustl.edu

Abstract

Chemoprevention of lung carcinogenesis is one of the approaches to control the epidemic of lung cancer attributed to cigarette smoking. Many agents, both synthesized and naturally occurring, have been tested and showed preventive effect in well-established animal model. Since lung cancer is usually accompanied by inflammation, anti-inflammatory drugs can potentially be used as candidates of chemopreventive agents for lung carcinogenesis. Meanwhile, the means of agent administration is also important to ensure the delivery efficiency and efficacy of testing agents in the lung. Aerosol delivery has shown significant advantages over other means of administration (i.e., intravenous, oral, intraperitoneal) at lowering the dose level and reducing the systemic toxicity of agents. The aim of this study is to appraise the inhibitory effects of aerosolized Non-Steroids Anti-Inflammatory Drugs (NSAIDs) on lung carcinogenesis.

In this study, chemopreventive agents were dissolved in the solvent (ethanol and DMSO, 1:1 by volume) and then atomized by a home-made atomizer. Solvents in the atomized droplets evaporated and absorbed via an activated carbon column. The resulting particles were introduced into a nose-only mouse exposure system, custom-built for this animal exposure study. Female A/J mice were given a single intraperitoneal dose of B(a)P carcinogen two weeks prior to the experiment. Mice were treated by aerosolized chemopreventive agents at the schedule of 5 days per week for 18 weeks. Treated mice were then sacrificed after 20 weeks, and their lungs were harvested and evaluated to obtain the data of tumor count and tumor load. The detail result of this study will be given in this presentation.

Keywords: aerosol delivery, chemoprevention, lung carcinogenesis, NSAIDs

Physicochemical and Toxicological Assessment of Commuter Exposure to Coarse and Fine Particulate Matter (PM) in Subway and Light-rail Systems of the Los Angeles Metro

Zhi Ning^{1,2}, Winnie Kam¹, James J. Schauer³, Martin M. Shafer³ and Constantinos Sioutas¹

1 University of Southern California, Los Angeles, CA, USA

2 City University of Hong Kong, Hong Kong, China

3 University of Wisconsin, Madison, WI, USA

ABSTRACT

Elevated concentrations of particulate matter (PM) have been found in a number of worldwide underground transit systems, with major implications regarding exposure of commuters to PM and its associated health effects. An extensive sampling campaign was conducted in May - August 2010 to assess personal exposure of coarse ($2.5\mu\text{m} < d_{\text{p}} < 10\mu\text{m}$) and fine ($d_{\text{p}} < 2.5\mu\text{m}$) particulate matter (PM) in two lines of the Los Angeles Metro system – an underground subway line (Metro red line) and a ground-level light-rail line (Metro gold line). Concurrent measurements were taken at downtown Los Angeles to represent urban ambient conditions. Considering that a commuter typically spent 75% of time inside the train and 25% of time waiting at a station, subway commuters were exposed on average to PM_{10} and $\text{PM}_{2.5}$ concentrations that were 1.9 and 1.8 times greater than the light-rail commuters. The average PM_{10} concentrations for the subway line at station platforms and inside the train were 78.0 and $31.5 \mu\text{g}/\text{m}^3$, respectively; for the light-rail line, corresponding PM_{10} concentrations were 38.2 and $16.2 \mu\text{g}/\text{m}^3$. A comprehensive chemical analysis was also performed including total and water-soluble metals, inorganic ions, and elemental and organic carbon. Mass balance showed that in coarse PM, iron makes up 27%, 6%, and 2% of gravimetric mass for red line, gold line, and urban background, respectively; in fine PM, iron makes up 32%, 3%, and 1%. Ambient air is the primary source of inorganic ions for both lines. Non-crustal metals, particularly Cr, Mn, Co, Ni, Mo, Cd, and Eu were elevated for the red line and, to a lesser degree, the gold line. Mo exhibited the greatest crustal enrichment factors. The enriched species were less water-soluble on red line than corresponding species on gold line. Reactive oxygen species (ROS) activity results suggest that one unit of PM from gold line may be as toxic as one unit of PM from red line; however, PM from red line generates greater ROS activity per volume than PM from gold line and urban background.

KEYWORDS

Subway systems, commuter exposure, particulate matter, $\text{PM}_{2.5}$, PM_{10} , reactive oxygen species

Introduction

Metro systems are an important transportation mode in megacities across the world that commuters take on a daily basis. However, recent measurements in cities across the world indicate that subway systems may present a unique microenvironment with particulate matter (PM) concentrations subject to different influences than ground-level sources. Studies have shown that respirable subway air can be substantially different than corresponding street-level air in terms of PM number and mass concentration and chemical composition. Earlier studies have documented elevated PM levels in major subway systems across the world. Mean exposure levels in the London Underground rail system were 3-8 times higher than street-level transportation modes^[1]; mean PM_{2.5} and PM₁₀ concentrations on station platforms in the Seoul Metropolitan Subway System were significantly higher than corresponding ambient levels^[2]. On the other hand, studies have also reported lower PM levels for the Hong Kong^[3] and Guangzhou^[4] subway systems than compared to other transport modes. Therefore, differences between subway ventilation methods, braking systems, wheel type, air conditioning, system age, and train motive source make it impossible to directly extrapolate results from previous studies to other subway systems. In addition, elevated concentrations of elements especially Fe, Mn, Cu, Ni, Cr have been observed in numerous subway systems relative to ambient urban concentrations^[5]. Although passengers spend a relatively short amount of time in subway systems, exposures to high concentrations of PM with enriched levels of certain elements may have significant health implications. This study focuses on the personal exposure assessment of PM for two lines of the Los Angeles Metro system including underground subway line (red line) and ground-level light-rail line (gold line).

Experimental Methods

The sampling campaign was carried out in the Los Angeles Metro red line and gold line. Both lines cover key parts of the Los Angeles area (Hollywood, Downtown L.A., and Pasadena) and are heavily trafficked especially during commute hours.

Sampling took place on May 3 -August 13, 2010 on weekdays from 9:30am to 1:00pm. To assess the personal exposure of a typical commuter, the subjects carried suitcases equipped with portable devices to measure the real-time pollutants concentrations including a Q-Trak Monitor Model 7565 (TSI Inc., Shoreview, MN) and two DustTrak Aerosol Monitors (TSI Inc., Shoreview, MN) to measure continuous PM_{2.5} and PM₁₀ concentrations. The subjects spent 25% of the time at stations and 75% of the time riding inside the train and carried a suitcase equipped with 3 Personal Cascade Impactor Samplers (PCIS) operated individually with a battery-powered Leland Legacy pump (SKC Inc., Eighty-Four, PA) at a flow rate of 9 liters per minute (lpm) to collect time-integrated filter samples in coarse ($2.5\mu\text{m} < d_p < 10\mu\text{m}$) and fine ($d_p < 2.5\mu\text{m}$) mode.

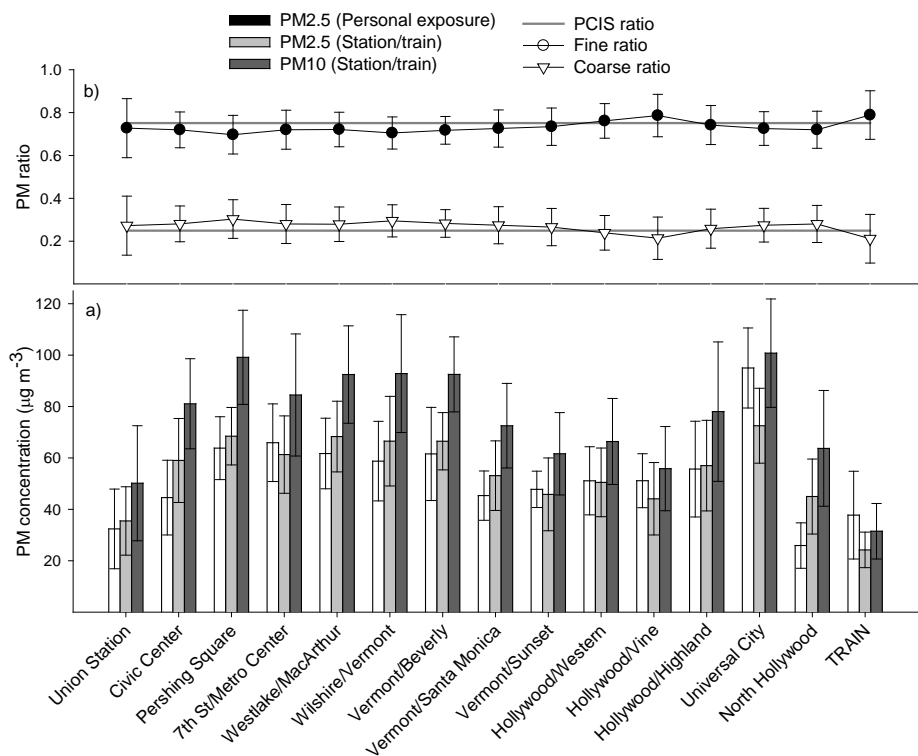
Both Teflon and Quartz filters were used. The Teflon filters were analyzed by magnetic-sector Inductively Coupled Plasma Mass Spectroscopy (SF-ICPMS) to determine total elemental composition^[6] and by SF-ICPMS analysis to determine water-soluble elemental composition and for ion chromatography (IC) analysis to determine the concentrations of inorganic ions. The IC methodology is fully described in Kerr et al.^[7]. A sensitive macrophage-based in-vitro assay was used to determine the reactive oxygen species (ROS) activity^[8]. Elemental and organic carbon (ECOC) was analyzed by Thermal Evolution/Optical Transmittance^[9] on the quartz filters.

Results and Discussion

PM Concentrations at Platforms and inside Trains

Figure 1 shows the average PM₁₀ and PM_{2.5} concentrations from the subway station and train. In general, the subway's platforms and train have PM₁₀ and PM_{2.5} concentrations that are approximately double those of the light-rail's platforms and train levels; however, coarse PM levels for the subway platforms and trains are 2.4 and 2.9 times greater than the light-rail platforms and train levels, likely a result of the enclosed tunnel environment of the subway line. The light-rail platform PM concentrations are comparable to the USC fixed site concentrations, while the subway stations have PM₁₀, PM_{2.5}, and coarse PM levels that are 2.5, 2.8, and 2.0 times greater than those at USC. For the underground subway stations, the concentrations vary (i.e. PM₁₀ values range from 50 to 100 µg/m³) while the ground-level, light-rail station PM₁₀ concentrations are distributed in a narrower range (31 to 48 µg/m³). It is possible that the ventilation system installed at some stations along the subway line may be more efficient at removing PM than at other stations.

Figure 1. Particulate matter (PM) concentrations for subway stations and inside the train.



Mass Balance

To reconstruct PM mass concentration for the red line, gold line, and USC ambient site, chemical species were grouped into six categories: organic matter (OM), elemental carbon (EC), inorganic ions, crustal metals less Fe (CM), elemental Fe, and trace metals. Inorganic ions are the sum of Cl^- , NO_3^- , SO_4^{2-} , PO_4^{3-} , Na^+ , K^+ , and NH_4^+ . The CM category represents the sum of Al, K, Ca, Mg, Ti, and Si, each of which were multiplied by appropriate factors to convert to oxide mass (19). For the purpose of this study, all Fe data is presented as total elemental Fe. Figure 2 shows mass reconstruction based on the six identified categories along with total gravimetric mass concentration for the gold line, red line, and ambient site for (a) coarse and (b) fine PM.

In coarse PM, the gravimetric mass concentration of the gold line is approximately 40% of USC ambient site, while mass concentration for red line is almost equivalent to USC ambient site. In fine PM, the red line gravimetric mass concentration is approximately 70% greater than both the gold line and USC ambient site concentrations, while concentrations for gold line are only 5% less than USC ambient site. The most significant difference between the three sites is the abundance of Fe in the subway environment in both PM modes. This significant presence of Fe in the subway air has major implications in terms of personal exposure of subway passengers.

Figure 2. Mass reconstruction of the 6 identified categories for the gold line, red line, and USC ambient site in (a) coarse PM and (b) fine PM.

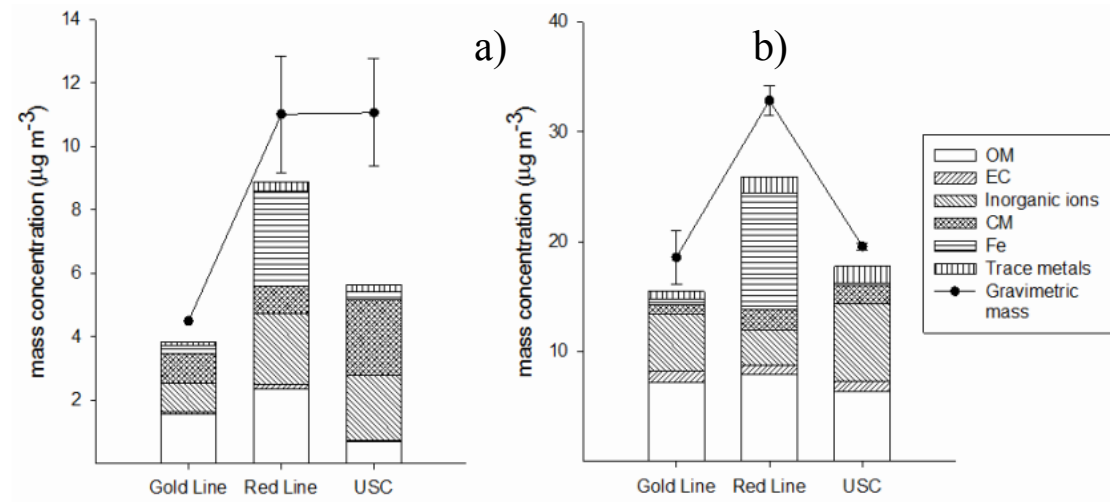
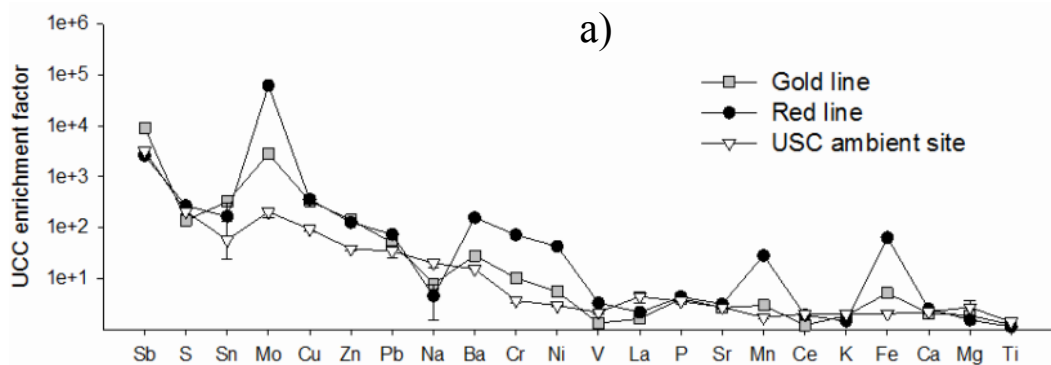
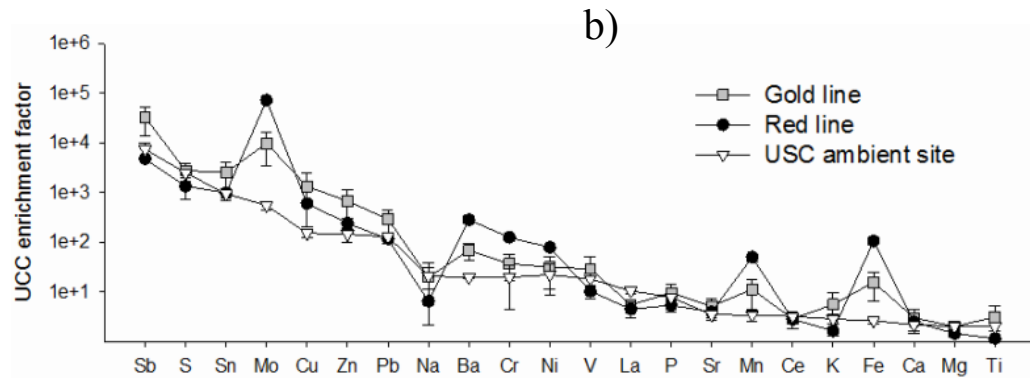


Figure 3 shows the crustal enrichment factors (EF) for 22 elements for the three sites in (a) coarse and (b) fine mode. A much higher crustal EF indicates anthropogenic origin for a given element, while an EF approaching 1 indicates crustal origin. The pattern in fine and coarse mode crustal EFs are remarkably similar to each other. In both modes, Mo has the highest crustal EF for the gold and red lines, followed by Fe, Mn, Ba, Cr, and Ni. It is evident that the source of these enriched elements is substantially greater on the red line than on the gold line.

Figure 3. Upper Continental Crustal (UCC) enrichment factors (EFs).

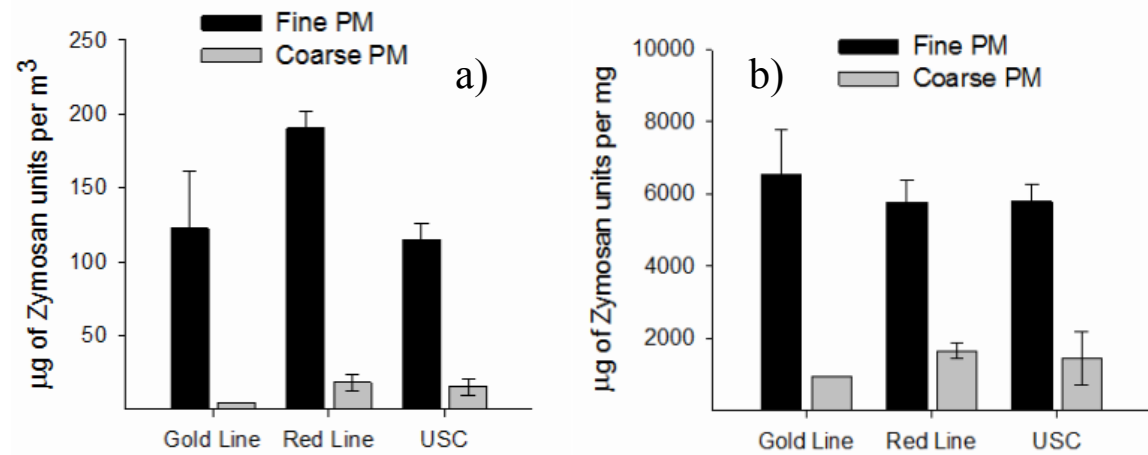




Particle Redox Activity

Figure 4 shows the ROS activity of particles for the gold line, red line, and USC ambient site in ng of Zymosan units (a) per volume (m^3) and (b) per mass (mg). The per volume basis is relevant for the personal exposure assessment of passengers, while the per mass basis is a measure of the intrinsic properties of the particles collected. On a per volume basis, fine PM accounts for 90-98% of total ROS activity. In addition, ROS activity observed on the red line is greater than USC ambient site and gold line activity by 65% and 55%, respectively.

Figure 5. Reactive oxygen species (ROS) activity.



Even though total concentrations of ROS-active metals (Fe, Ni, and Cr) in both modes are 4-44 times greater on the red line than at USC ambient site, ROS activity differs by less than 2 times. On a per mg basis, gold line ROS activity in fine mode is 13% greater than red line and USC ambient site activity, while red line and USC ambient site ROS activity are comparable. Our results suggest that one unit of PM mass on the gold line may be as intrinsically toxic as one

unit of PM mass from the red line, however, from a personal exposure perspective, PM originating from the red line generates greater ROS activity on a per volume basis than PM from the gold line and at USC ambient site.

SUMMARY OR CONCLUSION

The present study evaluated the physicochemical and toxicological properties of the fine and coarse PM exposure of the commuters in subway and light rail in Los Angeles Metro system. The PM mass concentrations are significantly higher in subway system due to the limited ventilation, associated with high levels of transition metals, such as Fe, Mn, Mo etc. The redox activity of the PM collected in subway also showed higher levels than urban background and ground level light rails implicating the potential health impact to the commuters.

ACKNOWLEDGMENTS

This study was supported by METRANS Transportation Center through grant 53-4507-5382.

References

- [1] Adams, H.S., Nieuwenhuijsen, M.J., Colvile, R.N., McMullen, M.A.S., and Khandelwal, P., *Science of the Total Environment*, 2001. 279: p. 29-44.
- [2] Kim, K.Y., Kim, Y.S., Roh, Y.M., Lee, C.M., and Kim, C.N., *Journal of Hazardous Materials*, 2008. 154: p. 440-443.
- [3] Chan, L.Y., Lau, W.L., Lee, S.C., and Chan, C.Y., *Atmospheric Environment*, 2002. 36: p. 3363-3373.
- [4] Chan, L.Y., Lau, W.L., Zou, S.C., Cao, Z.X., and Lai, S.C., *Atmospheric Environment*, 2002. 36: p. 5831-5840.
- [5] Aarnio, P., Yli-Tuomi, T., Kousa, A., Makela, T., Hirsikko, A., Hameri, K., Raisanen, M., Hillamo, R., Koskentalo, T., and Jantunen, M., *Atmospheric Environment*, 2005. 39: p. 5059-5066.
- [6] Zhang, Y.X., Schauer, J.J., Shafer, M.M., Hannigan, M.P., and Dutton, S.J., *Environmental Science & Technology*, 2008. 42: p. 7502-7509.
- [7] Kerr, S.C., Schauer, J.J., and Rodger, B., *Journal of Environmental Engineering and Science*, 2004. 3: p. 213-222.
- [8] Landreman, A.P., Shafer, M.M., Hemming, J.C., Hannigan, M.P., and Schauer, J.J., *Aerosol Science and Technology*, 2008. 42: p. 946-957.
- [9] Schauer, J.J., Mader, B.T., Deminter, J.T., Heidemann, G., Bae, M.S., Seinfeld, J.H., Flagan, R.C., Cary, R.A., Smith, D., Huebert, B.J., Bertram, T., Howell, S., Kline, J.T., Quinn, P., Bates, T., Turpin, B., Lim, H.J., Yu, J.Z., Yang, H., and Keywood, M.D., *Environmental Science & Technology*, 2003. 37: p. 993-1001.

Characteristics of Carbonaceous Aerosols in Yangtze River Delta Region, China

Guanghua Wang¹, Wei Liu^{1*}, Jian Yao¹, Xuebo Fan¹, Yanhong Geng¹, Nanan Wei^{1,2} and Jun Lin¹

1 Key Laboratory of Nuclear Analysis Techniques, Shanghai Institute of Applied Physics, Chinese Academy of Sciences, Shanghai 201800, China.

2 School of Nuclear Science and Technology, University of South China, Hengyang, Hunan 421001, China

ABSTRACT

Mass concentrations of organic carbon (OC) and elemental carbon (EC) in both PM_{2.5} and size-resolved aerosols collected in five cities (Jiading District of Shanghai, Hangzhou, Nanjing, Zhoushan and Taicang) of Yangtze River Delta Region (YRDR), China, in the period of April 25th to May 19th and October 19th to November 2nd, 2009, with size range of <0.49 μm, 0.49-0.95 μm, 0.95-1.5 μm, 1.5-3.0 μm, 3.0-7.2 μm, >7.2 μm were determined. The secondary organic carbon (SOC) was also estimated based on the EC tracer method. Average mass concentrations of OC and EC in the PM_{2.5} were 15.9 and 4.0 μg·m⁻³ while those in the total size-resolved aerosols were 19.2 and 3.4 μg·m⁻³, respectively. Mass concentrations of OC and EC accounted for 18.7% and 4.8% of the PM_{2.5}, as well as they accounted for 12.5% and 2.2% of the total size-resolved aerosols, respectively. Concentrations of OC and EC in the size-resolved aerosols showed a typical bio-modal with peaks in size ranges of < 0.49 μm and >3.0 μm respectively. Mass concentration of SOC in the PM_{2.5} was 6.6 μg·m⁻³, accounting for 42% of OC in the PM_{2.5}. Size distribution of SOC in the size-resolved aerosols collected in Jiading district of Shanghai indicated the abundance of SOC in both fine and coarse aerosols.

KEYWORDS

Organic Carbon, Elemental Carbon, PM_{2.5}, Size-resolved Aerosol, YRDR

Introduction

Carbonaceous matters, organic carbon plus elemental carbon, are important components of ambient aerosols^[1]. They comprise 20%-60% of fine particulate mass in the United States and 10%-50% in Europe, respectively. In China they cover a range from 20% to more than 50%^[2, 3].

Carbonaceous aerosols have drawn wide concern due to their significant impacts on global and regional climate changes, visibility reduction and negative effects on both environment and human health [4, 5, 6].

Accompanied with the rapid development of economic, both increasing of industry and variations of urban construction lead to tremendous energy consumption. Consequently, elevated particulate matter level and poor visibility have already become a serious problem YRDR. In the present study, OC and EC in PM_{2.5} collected in five representative cities of YRDR were determined as well as SOC. Size distributions of OC and EC were also determined in four cities of YRDR. Comparing with those in other cities, the characteristics of carbonaceous matters in YRDR were presented.

Experimental Methods

1.1 Sampling sites

Five representative cities of YRDR were selected for sampling. They include one rural site-Jiading District in Shanghai, two developed cities with large pollution-Nanjing in Jiangsu Province and Hangzhou in Zhejiang Province, one satellite city around the large city Shanghai-Taicang in Jiangsu Province, and an island city with fishing, shipping and tourism as its main industry-Zhoushan in Zhejiang Province [7].

1.2 Sampling and processing

PM_{2.5} and size-resolved aerosols were collected with two kinds of samplers respectively during the periods of April 25th to May 19th and October 19th to November 2nd, 2009. The PM_{2.5} aerosols were collected simultaneously in the five sampling sites on quartz-fiber filters with medium-volume samplers for 24 h. The size-resolved aerosols were performed using six-stage cascade impactors (M235 TFIA-2, Staplex, USA) with aerodynamic equivalent diameter in size ranges of <0.49 μm, 0.49-0.95 μm, 0.95 μm-1.5 μm, 1.5-3.0 μm, 3.0-7.2 μm and >7.2 μm in those four sampling sites except for the one in Taicang. The sampling time was 48 h and nominal flow rate through the impactors were 1.13 m³·min⁻¹. All valuable samples are shown in Table 1.

Table 1 Samples in five cities of YRDR

Cities	Samples	
	PM _{2.5}	Size-resolved
Shanghai	22	10
Hangzhou	32	4
Nanjing	34	4
Zhoushan	36	1
Taicang	27	—

* one set of size-resolved sample includes 6 quartz filters

1.3 Analysis for OC and EC

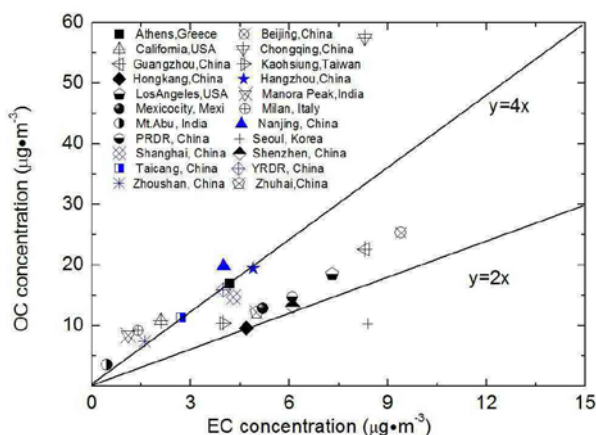
Samples were analyzed for OC and EC using the Interagency Monitoring of Protected Visual Environments (IMPROVE) protocol by a thermal and optical carbon analyzer (DRI Model 2001A).

Results and Discussion

2.1 Concentrations of OC and EC

2.1.1 OC and EC in PM_{2.5}

Fig. 1 OC and EC for PM_{2.5} in cities around the world.



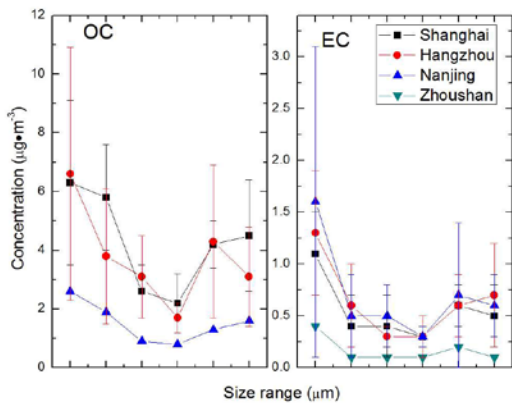
The largest concentration of OC appears in Nanjing, followed by Hangzhou with the same level and the maximum EC concentration is in Hangzhou. The least concentrations of OC and EC are shown in Zhoushan. Among the five cities, OC and EC account for the largest fraction of PM_{2.5} collected in Hangzhou while the least in Zhoushan. Based on these results of the five cities, concentrations of OC and EC in PM_{2.5} in YRDR could be suggested to be $15.9 \pm 10.4 \mu\text{g}\cdot\text{m}^{-3}$ and $4.0 \pm 2.1 \mu\text{g}\cdot\text{m}^{-3}$, contributing to 18.7% and 4.8% of the PM_{2.5}, respectively. Figure 1 shows the

comparisons of OC and EC concentrations in this study with those in other cities over the world. The OC /EC value is larger than 4 in any of the five cities. This may be explained as the more SOC or the higher OC/EC ratio of particles from primary sources in YRDR than in other cities.

2.1.2 OC and EC in Size-resolved aerosols

Figure 2 illustrates the overall results for the size distribution of OC and EC in the four cities, respectively.

Figure 2 Size distributions of OC (a) and EC (b) concentrations in four cities of YRDR



The concentrations of both OC and EC show a bio-modal with peaks in size ranges of <0.49 µm and > 3 µm. As a whole part, approximately 69% of OC and 68% of EC are located in the fine aerosols, indicating that the OC and EC mainly exist in fine aerosols in this area. The highest concentrations of OC and EC in each size segment appear in Hangzhou and Nanjing while the lowest appear in Zhoushan.

2.2 SOC in PM_{2.5} and size-resolved aerosols

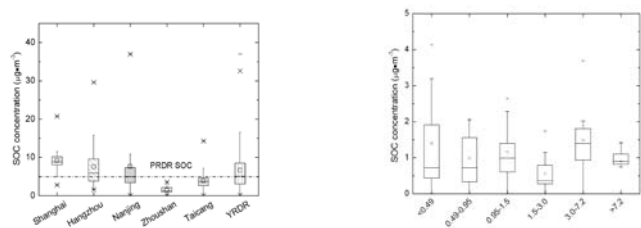
An EC tracer method [8] was used to estimate the SOC in PM_{2.5} and size-resolved aerosols with the following equation:

$$\rho(\text{SOC})_{ij} = \rho(\text{OC})_{ij} - \rho(\text{EC})_{ij} \left(\frac{\text{OC}}{\text{EC}} \right)_{\min - ij} \quad (1)$$

Where, $\rho(\text{SOC})$, $\rho(\text{OC})$ and $\rho(\text{EC})$ stand for mass concentrations of SOC, OC and EC, respectively, $(\text{OC}/\text{EC})_{\min}$ is the minimal value of OC/EC, subscripts of i and j represent the different city and aerosol size, respectively. The $(\text{OC}/\text{EC})_{\min}$ for PM_{2.5} was determined based on

the present PM_{2.5} samples. Since the number of size-resolved aerosol samples is less in three cities except for that in Jiading of Shanghai, the (OC/EC)_{min} of size-resolved aerosols in Jiading of Shanghai could be representative. For this reason, only the SOC for the size-resolved aerosols in Jiading was estimated.

Fig 3 Box plots of SOC concentrations in PM_{2.5} (a) and size-resolved aerosols (b) of YRDR cities



Average SOC concentrations in PM_{2.5} follow an order as below: Jiading of Shanghai ($9.2 \mu\text{g}\cdot\text{m}^{-3}$) $>$ Nanjing ($7.6 \mu\text{g}\cdot\text{m}^{-3}$) $>$ Hangzhou ($7.5 \mu\text{g}\cdot\text{m}^{-3}$) $>$ Taicang ($3.8 \mu\text{g}\cdot\text{m}^{-3}$) $>$ Zhoushan ($1.5 \mu\text{g}\cdot\text{m}^{-3}$). The average SOC abundance of YRDR is $6.6 \mu\text{g}\cdot\text{m}^{-3}$, accounting for 42% of OC in PM_{2.5}. Comparing with those in PRDR, it can be found that the average SOC in YRDR is 34.7% higher than that of PRDR. This may be caused by the better environment provided by YRDR than PRDR for the formation of secondary aerosols such as higher concentration of precursor, plenty of sunshine and lower temperature or the higher OC/EC ratio in particulates emitted directly from the sources.

For size-fractionated aerosols in Jiading of Shanghai, the average concentrations of SOC are $1.4, 1.0, 1.2, 0.6, 1.5$ and $0.9 \mu\text{g}\cdot\text{m}^{-3}$ for aerosols with size range of $<0.49 \mu\text{m}$, $0.49-0.95 \mu\text{m}$, $0.95-1.5 \mu\text{m}$, $1.5-3.0 \mu\text{m}$, $3.0-7.2 \mu\text{m}$, $>7.2 \mu\text{m}$, respectively. Approximately 64% of SOC locates in the fine aerosols, indicating that the SOC mainly exists in fine aerosols. SOC accounts for 31.2%, 26.4%, 49.8%, 44.0%, 65.4% and 40.6% of OC in each size range above, respectively, suggesting that the large fraction of SOC exists in coarse aerosols. As the photo-chemistry proceeds after the primary aerosols in small size emitted from the sources, the organic aerosols converge towards highly aged aerosols with low-volatile regardless of original sources. In this procession, the newly born particulates grow larger according to colliding with each or absorbing semi-volatile organic matters and water. With larger surface area and higher hygroscopicity coefficient, the aged aerosols absorb more semi-volatile matters and water-soluted organic species.

CONCLUSION

OC and EC were determined for PM_{2.5} and size-resolved aerosols in five representative cities of YRDR. SOC in the PM_{2.5} and size-resolved aerosols was also estimated with an EC tracer method. Average mass concentrations of OC and EC in the PM_{2.5} are 15.9 $\mu\text{g}\cdot\text{m}^{-3}$ and 4.0 $\mu\text{g}\cdot\text{m}^{-3}$ while those in the sum of size-resolved aerosols are 19.3 $\mu\text{g}\cdot\text{m}^{-3}$ and 3.4 $\mu\text{g}\cdot\text{m}^{-3}$. The OC and EC account for 18.7% and 4.8% of the PM_{2.5}, 12.5% and 2.2% of the total size-resolved aerosols, respectively. OC and EC in the size-resolved aerosols show a bio-modal with peaks in size ranges of < 0.49 μm and > 3.0 μm , respectively, and the EC is relatively more enriched in the particles with size range of < 0.49 μm . The SOC concentration in PM_{2.5} is 6.6 $\mu\text{g}\cdot\text{m}^{-3}$. The large fraction of SOC accounts for OC in coarse aerosols is demonstrated according to the size distributions of SOC in the size-resolved aerosols collected in Jiading district of Shanghai. Comparing with previous studies of other cities around the world, the concentrations of OC and EC are at the same level while SOC is larger than that in other cities.

ACKNOWLEDGMENTS

This research was supported by Knowledge Innovation Project of Chinese Academy of Sciences (KJCX-3SYW-N3), the National Natural Science Foundation of China (10775174) and Shanghai Natural Science Foundation (3109ZR1438200). The authors would like to thank Prof. Shi Jiyan in Zhejiang University, Prof. Wang Tijian in Nanjing University as well as researchers of Zhoushan and Taicang Environmental Protection Bureau for their help during the field campaign.

REFERENCES

- [1] Saylor, R. D.; Edgerton, E.S.; Hartsell, B.E.; *Atmospheric Environment* , 2006,40, 7546-7556.
- [2] Cao, J.J.; Lee, S.C.; Ho, F.O.; *Atmospheric Environment*, 2003, 37,1451–1460.
- [3] Ye, D.; Zhao, Q.; Jiang, C. *China Particuology*, 2007, 5, 255-260.
- [4] Gustafsson, O.; Krusa, M.; Zencak, Z.; *Science* ,2009,323, 495-498.
- [5] Nel, A.; *Science*, 2005, 308, 804-806
- [6] Rosenfeld, D.; Lohmann, U.; Raga, G.B.; *Science*, 2008, 321, 1309-1313
- [7] <http://en.wikipedia.org/wiki/Zhoushan>,<http://www.zhoushan.gov.cn/en/about/about.htm>
- [8] Dan, M.; *Atmospheric Environment*, 2004, 38, 3443-3452.

Carbonaceous aerosols at a high altitude location in central Himalayas

Zhiyuan Cong¹, Shichang Kang^{1, 2}, and Junji Cao³

1 Key Laboratory of Tibetan Environment Changes and Land Surface Processes,
Institute of Tibetan Plateau Research, Chinese Academy of Sciences, Beijing 100085, China

2 State Key Laboratory of Cryospheric Sciences, Chinese Academy of Sciences, Lanzhou
730000, China

3 SKLLQG, Institute of Earth Environment, Chinese Academy of Sciences, Xi'an 710075,
China

Principal Contact: Zhiyuan Cong, Institute of Tibetan Plateau Research, Chinese Academy
of Sciences, Beijing 100085, China.

Email: zhiyuancong@itpcas.ac.cn

Abstract

Atmospheric aerosols receive increasing attention due to their role in many atmospheric processes. Especially, the carbonaceous aerosols may result in global climate change through scattering/absorbing the solar radiation. In the Himalayan region, the carbonaceous aerosols at high elevations may act as the major reason causing the melting of snow packs and glaciers, posing negative effects on water resources of millions of people. Nevertheless, large uncertainties still exist to evaluate the impact of aerosols in this area, primarily due to the scarcity of adequate information on the aerosol properties.

In the study, total suspended particle samples were collected weekly from Aug. 2009 to Jul. 2010 at the north slope of Mt. Qomolangma (Mt. Everest), the summit of the world. Organic carbon (OC) and elemental carbon (EC) were analyzed using the thermal/optical reflectance (TOR) method. EC varied from below detection to $1.12 \mu\text{g m}^{-3}$ with the average of $0.26 \mu\text{g m}^{-3}$, while OC ranged from $0.23 \mu\text{g m}^{-3}$ to $7.22 \mu\text{g m}^{-3}$ with the average of $1.58 \mu\text{g m}^{-3}$. The OC and EC concentrations at Mt. Qomolangma are generally comparable to other remote sites like McMurdo in Antarctica, representing a regional background.

Finally the source region and the warming effect of the carbonaceous aerosols are discussed.

Keywords: Aerosol, Elemental carbon, Organic carbon, Himalayas, Climate change.

Characteristics and the Origins of the Carbonaceous Aerosol at a Rural Site of PRD in Summer 2006

**Weiwei Hu¹, Min Hu^{1,*}, Peng Lin¹, Zhiqiang Deng¹, Y. Kondo², N. Takegawa², Han,
Sunghee² and Yongjing Zhao³**

1 State Key Joint Laboratory of Environmental Simulation and Pollution Control, College of Environmental Sciences, Peking University, Beijing 100871, China;

2 Research Center for Advanced Science and Technology, University of Tokyo, 4-6-1 Komaba, Meguro, Tokyo 153-8904, Japan,

3 Mechanical and Aeronautical Engineering, University of California, USA

ABSTRACT

Carbonaceous aerosol including organic carbon (OC) and elemental carbon (EC) was measured at a sub-urban site near Guangzhou City in July 2006 during PRIDE-PRD campaign, using a semi-continuous thermal-optical analyzer. The average OC concentrations for three type periods during the campaign (local emission, typhoon and normal days) were $28.1\mu\text{gC}/\text{m}^3$, $4.0\mu\text{gC}/\text{m}^3$ and $5.7\mu\text{gC}/\text{m}^3$, respectively, and EC were $11.6\mu\text{gC}/\text{m}^3$, $1.8\mu\text{gC}/\text{m}^3$, and $3.3\mu\text{gC}/\text{m}^3$ orderly. Compared to the constant diurnal enhancement ratios of primary EC, the enhancement ratio of OC (OC versus CO-CO_{background}) remained n a relative high level in the afternoon which showed similar diurnal variation to oxygenated organic aerosol (OOA), indicating the strong photochemical formation of OC in the afternoon. We modified the traditional EC tracer method and used this modified approach to estimate the daily secondary organic carbon formation, which showed that the average SOC concentration in BG site was about $2.0\pm2.3\mu\text{gC}/\text{m}^3$, accounting for about 47 % mass value of OC.

KEYWORDS

Carbonaceous aerosol, Secondary formation, SOC estimation, Modified EC tracer method

1. Introduction

Carbonaceous aerosol is the main constituent (20-80% of fine particle) in the particulate matter¹. Recently, carbonaceous aerosol has been one of the most hot research spots due to its important roles on climate and healthy effects, together with its extremely complex properties. However, the classification of carbonaceous aerosol is still not clear due to the various detection methods². It is common to divide carbonaceous aerosol into two main fractions: organic carbon

* Corresponding author: Tel: 86-(0)10-62759880, Fax: 86-(0)10-62759880, email: minhu@pku.edu.cn

(OC) and element carbon (EC), which could be measured by the thermal/optical method. In general, the OC can be ascribed to primary organic carbon (POC) which is emitted by combustion sources similar to the EC sources or the primary biogenic sources, and secondary organic carbon (SOC) that is caused by the oxidation of volatile organic compounds. High-time resolved indirect estimation on POC and SOC contributions become an important and useful way to understand the secondary organic formation process. At present, one of the widely applied SOA estimation methods is the EC tracer method owing to its simplicity and reliance on ambient measurements alone³.

2. Experimental Methods

At the BG site of PRD campaign, a number of instruments were used to measure aerosol and gas pollutants. The observation period of different instruments is shown in Figure 1 and brief descriptions of these instruments used are given below.

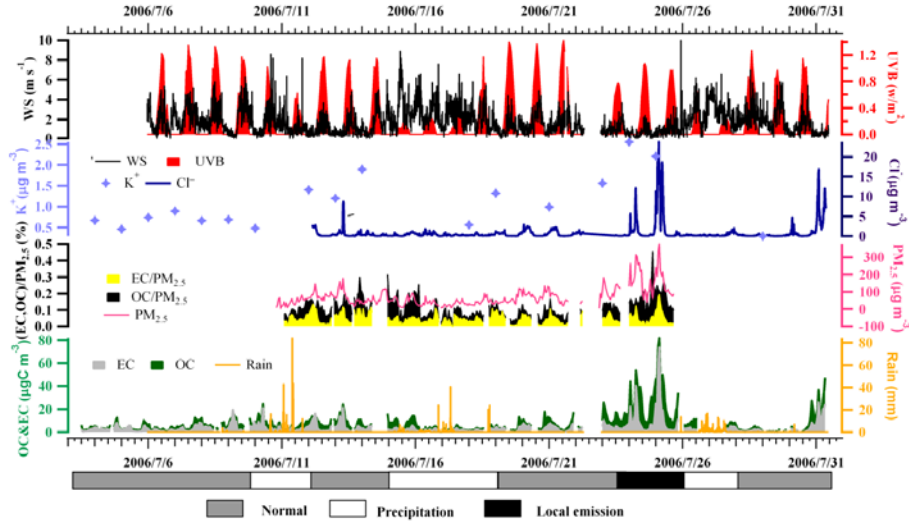
OC and EC concentrations in particle were measured hourly with an in situ semi-continuous OC and EC analyzer manufactured by Sunset Laboratory Inc². The ambient aerosol was collected on a 1.03 cm² Quartz filter through an 8L/min cyclone at the cut size of PM_{2.5} (from July 3 to July 16) and PM₁ (from July 17 to July 31), then analyzed by using improved NOISH 5040 protocol. More detailed description about OC and EC data can be obtained in Lin et al².

3. Results and Discussion

3.1 The time series of carbonaceous aerosol

The time series of the mass concentrations for carbonaceous aerosol and the meteorological parameters are shown in Figure 1.

Figure 1. The time series mass concentration of PM_{2.5}, EC, OC, Cl⁻, K⁺ and meteorology conditions during PRIDE-PRD 2006 campaign. The whole campaign was divided into tree periods: normal days (grey bar), typhoon days (white bar) and local emission days (black bar)

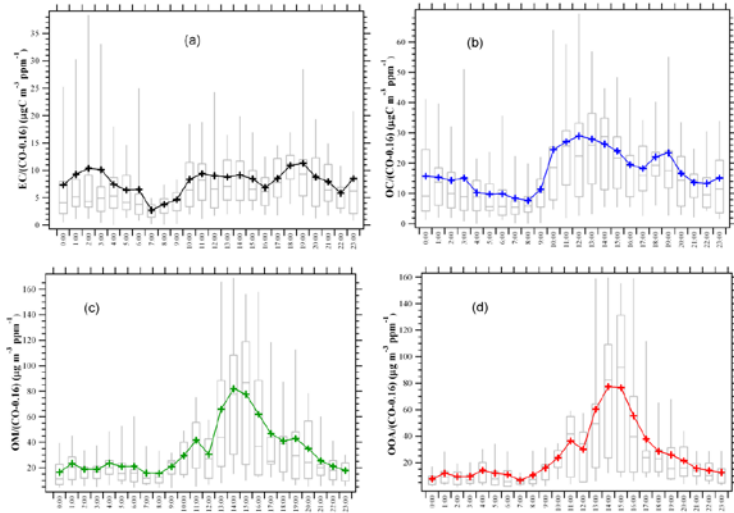


3.2 Daytime formation of organic aerosol

To evaluate the SOA formation, the diurnal profiles of different aerosol species versus CO are done in Figure 2. CO is used to exclude the dilution and boundary layer height influence on aerosol concentrations. In consider that CO is relative long -lived tracer of primary emissions, about one month in the troposphere⁴, CO background is considered here and calculated as the lowest 5 percentile of the CO mixing ratios observed during the study periods, 160 ppb⁵.

In the Figure 2, the enhancement ratio of EC is scaled from round 2.5 to 12.5 $\mu\text{g}\cdot\text{m}^{-3}$ ppm⁻¹, respectively. The profile of enhancement ratio of EC is relative constant, indicating the similar profiles between EC and CO emission sources. The EC profile here is also similar to the result in Mexico suburban T1⁶.

Figure 2. Diurnal variations of different aerosol species versus (CO-0.16). The value of 0.16 ppm was CO background concentration. The grey shaded areas show the uncertainty of the diurnal variation during the whole campaign



OOA is formed in the oxygenated process and is the typical secondary production. The diurnal variation of OOA shows clearly variations with an extreme high enhancement ratio in the afternoon indicating the strong secondary formation in the afternoon. OC and OM enhancement ratios displays very similar to OOA, implying secondary formations plays an important role in OC and OM. It is interesting to compare OC in BG site to urban plumes in the US⁷ and is found the OC enhancement ratio in the morning at BG site is similar to the OC direct emissions ratio (red solid line) in US plumes, as well as enhancement ratios in the afternoon in the BG Site agrees well with emission ratio from secondary formation after 0.5 day of processing. Different from consistence of OC enhancement ratio between BG and US, the OM enhancement ratio in BG is much higher than the urban plumes in US as showed in Figure 2. The difference between OC and OM comparison is probably caused by the other chemical composition in the OM. On the whole, the secondary formation contributes a lot to OC and OM, especially in the afternoon when the photochemical activity was strong.

3.3 Estimation of secondary organic carbon by modified EC tracer method

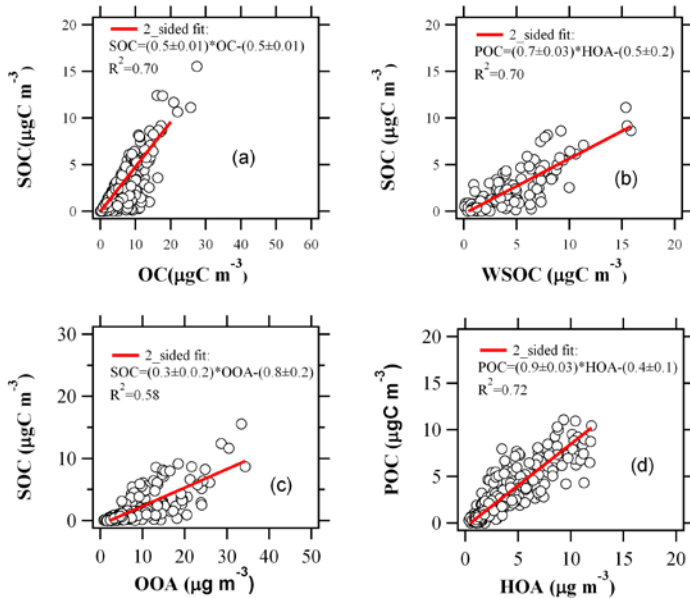
EC tracer method is usually adopted to estimate the SOC concentration. The EC tracer method assumes EC is a tracer for primary emission, since the primary OC and EC almost comes from the same combustion sources. The determination of emission ratio of primary OC to EC that is $(OC/EC)_{pri}$ is the key step in EC tracer method.

To improve the accuracy of SOC estimation, modification on traditional EC tracer method is done here to obtain a more specific $(OC/EC)_{pri}$. That is to combine traditional EC tracer method with source tracer ratio method which is firstly introduced by Millet et al⁸. The good agreement of

source tracer ratio method has been confirmed in Zhang et al⁴. Detailed description about source tracer ratio method can be obtained in the Millet et al⁸.

Then the SOC concentration is calculated by estimating $(OC/EC)_{pri}$ is 1.57 and 1.42 during the day and night.. Overall, the average SOC concentration is scaled from 0 to $15.6 \mu\text{g}/\text{m}^3$ and average concentration is about $2.0 \pm 2.3 \mu\text{g}/\text{m}^3$ (average \pm stdev).SOC fraction of OC is about 47% as the figure 3 shows. WSOC correlated well with SOC which shows the correlation coefficient is about 0.7 and regression slop 0.7 ± 0.03 .The good linear correlation ship confirms that WSOC and SOC mainly come from the same source. The regression coefficient between SOC and OOA is fine that is about 0.6. The regression slope between them is 0.31 which a little lower than the result in Pittsburgh ~ 0.45 ⁴, which may be caused by the differential of non-carbon fraction in OOA. However the HOA correlated POC very well. The regression coefficient between POC and HOA is about 0.76. And the regression slope between POC and HOA is about 0.9 indicating that most or all HOA is POC .The POC and HOA ratio is similar to result ~ 0.8 in Mexico city T0 site and ~ 0.8 in Pittsburgh⁴.

Figure 3. Scatter plots of SOC versusOC(a), SOC versus WSOC(b), SOC versus OOA(c) and POC versus HOA(d) at BG site.



CONCLUSION

Carbonaceous aerosol was measured at a sub-rural Back Garden site during PRIDE-PRD-campaign in July, 2006. According to the potential sources of carbonaceous aerosol and meteorology condition, we defined three typical days to reflect the carbonaceous concentration level in BG site: normal days, typhoon days and local emission days with the OC concentrations

were $28.1\mu\text{gC}/\text{m}^3$, $4.0\mu\text{gC}/\text{m}^3$ and $5.7\mu\text{gC}/\text{m}^3$ respectively and EC were $11.6\mu\text{gC}/\text{m}^3$, $1.8\mu\text{gC}/\text{m}^3$, and $3.3\mu\text{gC}/\text{m}^3$ orderly. It is found that the carbonaceous aerosol in BG was influenced by the oxygenated aerosol of PRD region by the high ratios between OM and OC, WSOC and OC.

CO minus background CO was used to normalize carbonaceous aerosol to exclude the meteorology influence. Compare to the constant diurnal variation of primary species EC enhancement ratio, the OC showed similar diurnal variation to oxygenated organic aerosol (OOA) which dominated a relative high peak in the afternoon indicating the strong photochemical formation in OC. We modified traditional EC tracer method by combining the source tracer ratio method to estimate the secondary organic carbon formation. Average SOC concentration in BG site is about $2.0\pm2.3\mu\text{gC}/\text{m}^3$ accounting for about 47% mass value of OC. Good correlation ships between OOA, WSOC versus SOC and POC versus HOA are observed.

ACKNOWLEDGMENTS

This work is supported by Beijing Council of Science and Technology. It is also supported by the National Natural Science Foundation of China (20977001, 21025728).

REFERENCES

1. Lim, H.-J.; Turpin, B. J., Origins of Primary and Secondary Organic Aerosol in Atlanta: Results of Time-Resolved Measurements during the Atlanta Supersite Experiment. *Environmental Science & Technology* **2002**, *36* (21), 4489-4496.
2. Lin, P.; Hu, M.; Deng, Z.; Slanina, J.; Han, S.; Kondo, Y.; Takegawa, N.; Miyazaki, Y.; Zhao, Y.; Sugimoto, N., Seasonal and diurnal variations of organic carbon in PM_{2.5} in Beijing and the estimation of secondary organic carbon. *J. Geophys. Res.* **2009**, *114* (D2), D00G11.
3. Cabada, J. C.; Pandis, S. N.; Subramanian, R.; Robinson, A. L.; Polidori, A.; Turpin, B., Estimating the Secondary Organic Aerosol Contribution to PM_{2.5} Using the EC Tracer Method
Special Issue of <i>Aerosol Science and Technology</i> on Findings from the Fine Particulate Matter Supersites Program. *Aerosol Science and Technology* **2004**, *38* (12 supp 1), 140 - 155.
4. Zhang, Q.; Worsnop, D. R.; Canagaratna, M. R.; Jimenez, J. L., Hydrocarbon-like and oxygenated organic aerosols in Pittsburgh: insights into sources and processes of organic aerosols. *Atmos. Chem. Phys.* **2005**, *5* (12), 3289-3311.
5. Miyazaki, Y.; Kondo, Y.; Shiraiwa, M.; Takegawa, N.; Miyakawa, T.; Han, S.; Kita, K.; Hu, M.; Deng, Z. Q.; Zhao, Y.; Sugimoto, N.; Blake, D. R.; Weber, R. J., Chemical characterization of water-soluble organic carbon aerosols at a rural site in the Pearl River Delta, China, in the summer of 2006. *J. Geophys. Res.* **2009**, *114* (D14), D14208.

6. de Gouw, J. A.; Welsh-Bon, D.; Warneke, C.; Kuster, W. C.; Alexander, L.; Baker, A. K.; Beyersdorf, A. J.; Blake, D. R.; Canagaratna, M.; Celada, A. T.; Huey, L. G.; Junkermann, W.; Onasch, T. B.; Salcido, A.; Sjostedt, S. J.; Sullivan, A. P.; Tanner, D. J.; Vargas, O.; Weber, R. J.; Worsnop, D. R.; Yu, X. Y.; Zaveri, R., Emission and chemistry of organic carbon in the gas and aerosol phase at a sub-urban site near Mexico City in March 2006 during the MILAGRO study. *Atmos. Chem. Phys.* **2009**, *9* (10), 3425-3442.
7. de Gouw, J. A.; Brock, C. A.; Atlas, E. L.; Bates, T. S.; Fehsenfeld, F. C.; Goldan, P. D.; Holloway, J. S.; Kuster, W. C.; Lerner, B. M.; Matthew, B. M.; Middlebrook, A. M.; Onasch, T. B.; Peltier, R. E.; Quinn, P. K.; Senff, C. J.; Stohl, A.; Sullivan, A. P.; Trainer, M.; Warneke, C.; Weber, R. J.; Williams, E. J., Sources of particulate matter in the northeastern United States in summer: 1. Direct emissions and secondary formation of organic matter in urban plumes. *J. Geophys. Res.* **2008**, *113* (D8), D08301.
8. Millet, D. B.; Donahue, N. M.; Pandis, S. N.; Polidori, A.; Stanier, C. O.; Turpin, B. J.; Goldstein, A. H., Atmospheric volatile organic compound measurements during the Pittsburgh Air Quality Study: Results, interpretation, and quantification of primary and secondary contributions. *J. Geophys. Res.* **2005**, *110* (D7), D07S07.

Harmonizing Aerosol Carbon Measurements between Two Conventional Thermal/Optical Analysis Methods

Guorui Zhi and Yingjun Chen

Yantai Institute of Coastal Zone Research, CAS, 17 Chunhui Road, Laishan District, Yantai, Shandong 264003, P. R. China

Principal Contact: Yingjun Chen, Dr., Yantai Institute of Coastal Zone Research, CAS, 17 Chunhui Road, Laishan District, Yantai, Shandong 264003, China.

Tel: 0535-2109159 Fax: 0535-2109000 Email: yjchen@yic.ac.cn

Abstract

Although total carbon (TC) can be consistently quantified by various aerosol carbon measurement methods, the demarcation of TC into organic carbon (OC) and elemental carbon (EC) has long been inconsistent. The NIOSH and IMPROVE protocols are most widely used for thermal/optical analysis (TOA), but current knowledge rests in the description that the NIOSH protocol usually gives lower EC values than does the IMPROVE protocol. This study seeks to explore the possibility of quantitatively linking the difference between the two TOA protocols. Residential coal-burning samples that had been collected and analyzed following the NIOSH protocol in previous studies were directly reanalyzed following the IMPROVE protocol for this study. A comparison of each pair of NIOSH and IMPROVE EC values reveals the dynamic relation between the two protocols, which can be expressed as a regression equation, $y = (1-x)/(1+4.86x^2)$ ($R^2 = 0.96$), where the independent x is the EC/TC ratio ($R_{EC/TC}$) for the IMPROVE protocol, and the dependent y is the share of difference between IMPROVE and NIOSH $R_{EC/TC}$ relative to IMPROVE $R_{EC/TC}$. This regression equation may be the first effort in formulating the relationship between the two TOA protocols, and it is very helpful in harmonizing inconsistent TOA measurements for source characterization, ambient monitoring and atmospheric modeling.

Keywords: TOA protocols, organic carbon, elemental carbon, source emissions.

Precautions for In-injection Port Thermal Desorption-Gas Chromatography/Mass Spectrometry (TD-GC/MS) as Applied to Aerosol Filter Samples

Steven Sai Hang Ho ^{1,2,3}, Judith C. Chow ^{1,2}, John G. Watson ^{1,2}, Louisa Pan Ting Ng ³, Yuk Kwok ³, K.F. Ho ¹, Junji Cao ¹

1 SKLLQG, Institute of Earth Environment, Chinese Academy of Sciences, Xi'an, 710075, China

2 Division of Atmospheric Sciences, Desert Research Institute, 2215 Raggio Pathway, Reno, NV 89512, United States

3 Hong Kong Premium Services and Research Laboratory, Chai Wan, Hong Kong, China

Principal Contact: Steven Sai Hang Ho, Prof., Chief Executive Officer, Hong Kong Premium Services and Research Laboratory, Chai Wan, Hong Kong, China.

Tel.: +00-852-51990005 Fax: +00-852-35220157 E-mail: stevenho@hkpsrl.org.

Abstract

In-injection port thermal desorption-gas chromatography/mass spectrometry (TD-GC/MS) allows for analysis for >130 non-polar organic compounds on small quartz-fiber filter samples without extraction chemicals. TD-GC/MS has been applied to samples from long-term U.S. networks since it is cost effective and less labor intensive. However, analysis of large numbers of samples results in sensitivity reductions over time. Instrument sensitivity and reproducibility were examined after 100, 200, and 500 sample analyses. Analyses of standards between batches of heavily loaded samples from China and Japan showed signal decreases of 28 – 78% for major organic classes. In the GC injection port, residues can accumulate on the gold-plated seal resulting in analyte adsorption as well as elevating signal background. Decreases in signal response were 28 – 43% for *n*-alkanes, 33 – 45% for hopanes and steranes, 28 – 56% for PAHs, and 38 – 78% for phthalates when the gold-plated seal was not replaced after 500 TD-GC/MS sample analyses. Limits of detection (LODs) also increased by 14 – 76% for the targeted non-polar organic compounds. Residues trapped in the capillary column head can cause peak broadening and overlap. The GC/MS system, including the injection port and gold seal, the column head (where the eluted sample is pre-concentrated), and the ion source should be cleaned after every batch of 50 to 100 samples.

Keywords: Thermal desorption; In-injection port; GC/MS; non-polar organic; PAHs; alkanes; phthalates.

INTERACTION OF MINERALS WITH BLACK CARBON IN THERMAL OPTICAL TECHNIQUES

Kochy K. Fung¹, Judith C. Chow², Jerome Robles², Xiaoliang Wang², Lung-Wen A. Chen² and John G. Watson²

1 AtmAA, Inc. 23917 Craftsman Rd., Calabasas, CA 91302

2 Desert Research Institute, 2215 Raggio Pkwy, Reno, NV 89512

Principal Contact: Kochy K. Fung, Doctor, AtmAA Inc., 23917 Craftsman Rd., Calabasas, CA 91302, USA.

E-mail: kochy@sbcglobal.net

Abstract

Measurement of particulate carbon is essential to the assessment of its impacts and formulation of control strategies. Quartz fiber filter samples are routinely analyzed for organic and elemental carbon (OC/EC) using thermal volatilization-pyrolysis correction methods, as the *Interagency Monitoring of PROtected Visual Environments* (IMPROVE) with correction by reflectance (TOR), or the National Institute of Occupational Safety and Health (NIOSH) Method 5040 using transmittance (TOT). In both methods, the filter is heated stepwise at specified temperatures, rates of temperature increase, and residence times at each temperature, first in He to volatilize the OC, then in O₂/He for EC combustion. The resulting CO₂ is converted to methane for detection by a flame ionization detector.

These techniques may include some inorganic carbonate carbon (ICC) if present in the sample. Interaction with other constituents is also assumed to be negligible. However, these normally small errors may become significant when samples are impacted by dust storm or certain industrial emissions. Metal oxides, such as those of iron, manganese, and copper can oxidize EC when the temperature is at or above 700°C without the addition of external O₂. Naturally occurring carbonates were found to decompose at much lower temperatures than their respective pure chemical forms. Thus in contrast to previous thinking, ICC's impact can be either on the OC or EC fractions depending on the analytical protocol used. Details of the experiments, findings, and implications will be presented.

Estimation of Aerosol Black Carbon at the Tropopause by Measurements in Commercial Aircraft Cabins

Anthony D. A. Hansen ⁽¹⁾ and Griša Močnik ⁽²⁾

(1) Magee Scientific, 1101 Cowper Street, Berkeley, CA 94702 USA

(2) Aerosol d.o.o., Kamniška 41, Ljubljana, SI-1000 Slovenia

ABSTRACT

Aerosol Black Carbon (BC) is emitted during combustion of all carbonaceous fuels. It absorbs sunlight and interacts with cloud nucleation processes, leading to direct and indirect climate forcing. Widespread measurements demonstrate the extreme variability of BC concentrations at ground level. Knowledge of the vertical distribution of BC in the atmosphere is essential for calculations of its contribution to climate change, but measurements from research aircraft are complex, expensive, and only occasional.

Black carbon is a significant component of aircraft engine exhaust. Most long-range aircraft cruise at altitudes in the range of 10 to 12 km, and release BC into this layer of the atmosphere from which the rate of removal may be slow. There may therefore be a significant enhancement or accumulation of BC in this vertical range of the atmosphere.

We have used the “micro Aethalometer” to measure BC concentrations in the passenger cabin of commercial aircraft during conventional travel. There are no combustion sources of BC within the aircraft: air is drawn from the outside at high altitude, compressed, and pumped into the aircraft to provide ventilation for the passengers. The measured concentrations therefore represent a lower limit estimate for BC in the atmosphere at the airplane’s cruising altitude.

We present data from measurements made during many long-distance flights. The results may be used to estimate the concentration of BC near the tropopause.

KEYWORDS

Aerosol Black Carbon; Vertical Profile; Upper Troposphere, Lower Stratosphere

Introduction

Aerosol Black Carbon (BC) is emitted from combustion of carbonaceous fuels and has important interactions with radiative transfer and cloud nucleation processes in the atmosphere. Most sources are located at ground level: but aircraft operating at cruise altitudes in the range of 10 km. to 12 km. may represent a significant source of emissions. The residence time of aerosols at these altitudes may be long, due to slow removal processes.

It is therefore important to measure the concentration of BC throughout the vertical column of the atmosphere, and especially in the layers heavily impacted by commercial air traffic.

Experimental Methods

We use the Magee Scientific Model AE51 “micro” Aethalometer to measure Black Carbon in real time in the cabin of a passenger aircraft. The instrument is battery operated; self-contained; and small enough to be taken on board in a passenger’s hand luggage and switched on during flight. It reports BC concentration data on a 1-minute or 5-minute timebase with high sensitivity. The data is stored internally for subsequent download. The noise on the data is inversely proportional to the integrating time: consequently, it is possible to recover statistically-meaningful data at BC concentration levels of a few tens of nanograms per cubic meter (ng/m^3) if the data is averaged over effective timebase periods of tens of minutes.

BC concentrations in the cabin of a passenger aircraft in flight are not affected by internal activity, because combustion sources are not permitted on the aircraft. The air supplied to the passengers is drawn from the outside atmosphere; compressed; cooled; possibly filtered; and then injected into the passenger cabin to provide fresh air. Typical operating conditions keep the passenger cabin at approximately 80% of ground-level pressure. Stale air is released from the cabin to the outside atmosphere to provide an Air Exchange Rate that is typically claimed to be equal to 1 exchange per every few minutes. However, the energy used by the compression and cooling of the fresh air supply is drawn from the aircraft’s engines: anecdotally, it is believed that the rate of exchange of fresh air is reduced in order to reduce fuel consumption.

Nevertheless, since there are no sources of BC within the passenger cabin; and since the compression, filtration and injection processes can only reduce the BC content of the outside air; a measurement of BC within the passenger cabin after a long duration of stabilization and flushing of the air must necessarily represent a lower limit on the BC content of the outside air at the cruising altitude.

The experimental method is to switch on the “micro” Aethalometer after the cabin crew has permitted the use of electronic devices; and to place it in the seat pocket with its sampling hose protruding into the general cabin atmosphere. It is switched off at the end of the flight. The data analysis usually shows an initial decay from high



BC values representing the initial atmosphere in the aircraft cabin including BC-loaded air from the airport runway area; followed by a long period of relatively steady concentrations at low levels of BC, after the cabin air equilibrates with the BC concentration of the outside atmosphere.

Prof. J. Turner, Washington University

Results

On every flight, BC concentrations at the levels of tens to hundreds of ng/m³ were measured. This demonstrates that BC concentrations in the atmosphere outside the aircraft, when operating at this altitude, must have a minimum level of tens to hundreds of ng/m³. Concentrations over the Pacific Ocean (on flights from the USA to Asia) generally increased when approaching Asia. Concentrations over the Atlantic Ocean (on flights from Europe to North America) generally increased when approaching the United States.

One particularly interesting result is shown in Figure 1.

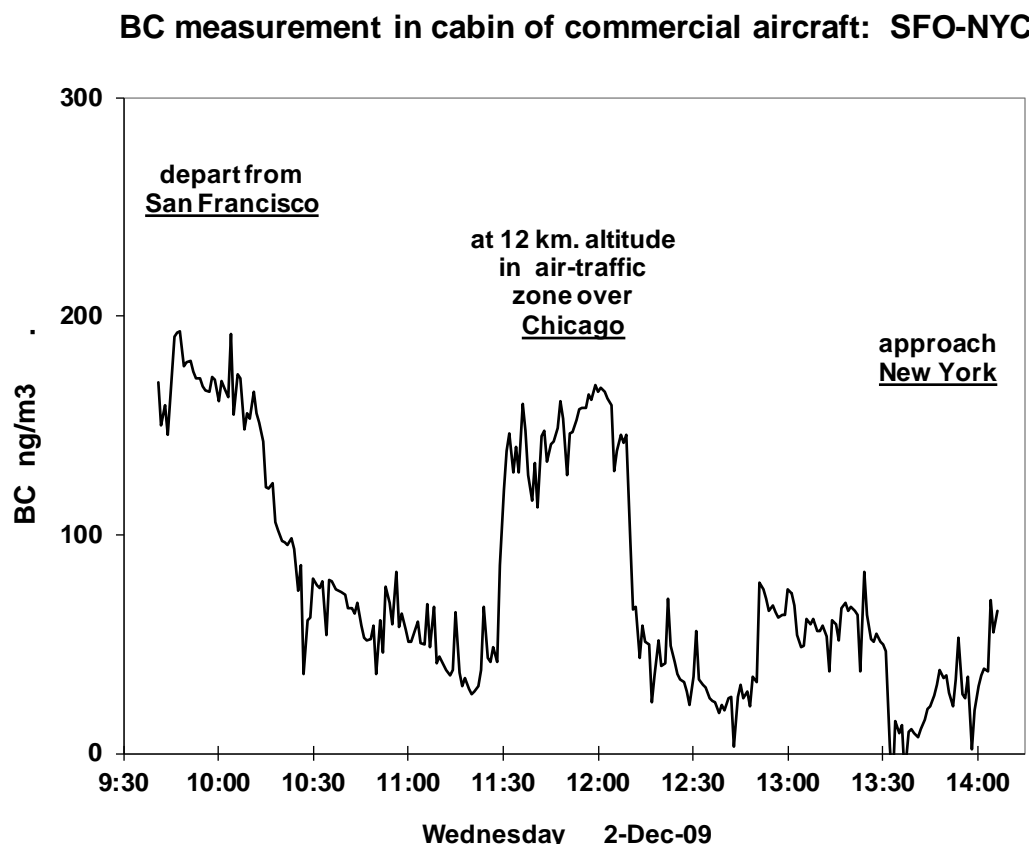


Figure 1. BC data from “micro” Aethalometer in passenger aircraft cabin while flying from San Francisco to New York.

This result shows a notable increase in BC concentrations when the aircraft flight track passed near to Chicago. Chicago is one of the busiest air-traffic hubs in the United States and there are a very large number of aircraft flight routes that begin or end in Chicago. Consequently, the upper atmosphere has a high local density of operating aircraft in this region, and a high local density of aircraft exhaust emissions. It is our belief that the increase in BC concentrations seen in this data represents the fact that the aircraft, on which we were travelling, passed through a densely-trafficked portion of the stratosphere which was “locally” polluted by aircraft emissions.

The concentrations measured at 12 km. altitude over Chicago were almost 200 ng/m³. This implies that BC concentrations in the outside atmosphere at this altitude were certainly greater than 200 ng/m³. This is a BC concentration level that is comparable to measurements in ‘clean’ urban areas of cities on the West Coast of the USA (such as San Francisco).

We shall present a number of similar results, including measurements taken during flights from the USA to Asia, showing strong increases when approaching the coast of Asia; flights to and over Europe; flights within and over Asia; etc.

CONCLUSIONS

In all cases, it is abundantly clear that the atmosphere at 10 km. to 12 km. altitude contains concentrations of Black Carbon that are easily measurable. Although the measurement method can only provide a lower estimate, the ability to measure 100 ng/m³ in an aircraft cabin must necessarily imply that the concentration outside the cabin must be higher.

The measurement technique is extremely simple, and data on a long-distance flight of many hours’ duration can be accomplished at essentially zero incremental cost. The instrument may be used by non-technical participants with minimum training required. Any commercial passenger flight traveling over any air route anywhere in the world can provide baseline data for that portion of the atmosphere. This method therefore provides an opportunity to make a “pollution survey of the tropopause” in a quick and accessible manner.

REFERENCES

- Babu, S. S. et al. (2011), “Free tropospheric black carbon aerosol measurements using high altitude balloon: Do BC layers build “their own homes” up in the atmosphere?”, *Geophys. Res. Lett.* **38**, L08803, DOI:10.1029/2011GL046654.

Ban-Weiss GA., Long Cao, G. Bala and K. Caldeira, (2011), “Dependence of climate forcing and response on the altitude of black carbon aerosols”, *Climate Dynamics*, DOI: 10.1007/s00382-011-1052-y

Schwarz, J.P., et al. (2006), “Single-Particle Measurements of Mid-latitude Black Carbon and Light-Scattering Aerosols from the Boundary Layer to the Lower Stratosphere”, *J. Geophys. Res. Atmospheres* **111** (D16). DOI: 10.1029/2006jd007076.

Ziguang Han et al., (2003), “Airborne measurements of aerosol extinction in the lower and middle troposphere over Wyoming, USA”, *Atmospheric Environment* **37**, 789.

Pueschel, R.F., A.D.A. Hansen et al., (1992), “Black carbon (soot) aerosol in the lower stratosphere and upper troposphere,” *Geophys. Res. Lett.* **19**, 1659.

Hansen, A.D.A. and H. Rosen, (1984), “Vertical distributions of particulate carbon, sulfur, and bromine in the Arctic haze and comparison with ground-level measurements at Barrow, Alaska,” *Geophys. Res. Lett.* **11**, 381.

Aerosols and Gases Measured by Aircraft during a Dust Storm Event over North China

Jianzhong Ma¹, Wei Wang², Yue Chen¹, and Hongjie Liu²

1 Chinese Academy of Meteorological Sciences, Beijing 100081, China

2 Chinese Research Academy of Environmental Sciences, Beijing 100012, China

Principal Contact: Jianzhong Ma, Dr., Chinese Academy of Meteorological Sciences, Beijing 100081, China.

Tel: +86 10 58995270 Fax: +86 10 62176414 E-mail: mjz@cams.cma.gov.cn

Abstract

North China is a region strongly affected by both natural desert dust and pollution smog. During the field campaign of IPAC-NC (Influence of Pollution on Aerosols and Cloud Microphysics in North China) in spring 2006, we performed 17 aircraft research flights to concurrently measure atmospheric trace gases, aerosols and clouds over this part of China. The detail items measured were condensation nuclei concentrations, the number size distributions of particles in diameters ranging from 5.6 nm to 47 μm (by EEPS 3090, APS 3310A, PCASP-100X, and FSSP-100), PM₁₀ mass concentrations and chemical components, and trace gases including O₃, NO_x, SO₂, CO, and NMHCs. One of these research flights took place over the Bohai Gulf on 17 April 2006 when a severe dust storm occurred. Our measurements provide a unique data set for in-depth investigation of the interactions between atmospheric chemistry and aerosols in polluted and semi-arid regions.

Keywords: Dust, Pollution, Aerosols, Gases, Atmospheric chemistry

Asian Dust Detection from Satellite Imagers

Xuepeng Zhao

National Climate Data Center, NOAA/NESDIS, 151 Patton Ave., Asheville, NC, 28801, USA

ABSTRACT

Aerosols, including those with large spatial and temporal variability, such as dust, exert large influences on climate, weather, air quality, hydrological cycles, and ecosystems. Detection of these highly variable aerosols is challenging because of their episodic features, such as short lifetime, multi-scales, and strong interactions with local and regional surface and meteorological conditions. Since dust particles can directly alter solar and earth radiation in both visible and infrared (IR) spectral regions through scattering and absorption processes, both visible and IR remote sensing techniques can be used for detection of dust in the atmosphere^[1]. In this paper, we introduce an algorithm for detecting episodic dust storms from satellite imagers considering dust particles display some spectral variations in visible and IR spectral regions different from those of cloud and underlying surface. The detection is based on the analysis of reflectance (or radiance) in visible bands or brightness temperature (BT) in IR bands. The magnitude of the difference in reflectance and/or BTs in selected bands (or channels) is used to infer the signature of dust^[2,3]. Detailed descriptions of the algorithm and its application for Asian dust detection from the MODIS satellite measurements are provided.

KEYWORDS

Aerosol, Asian Dust, Satellite

Introduction

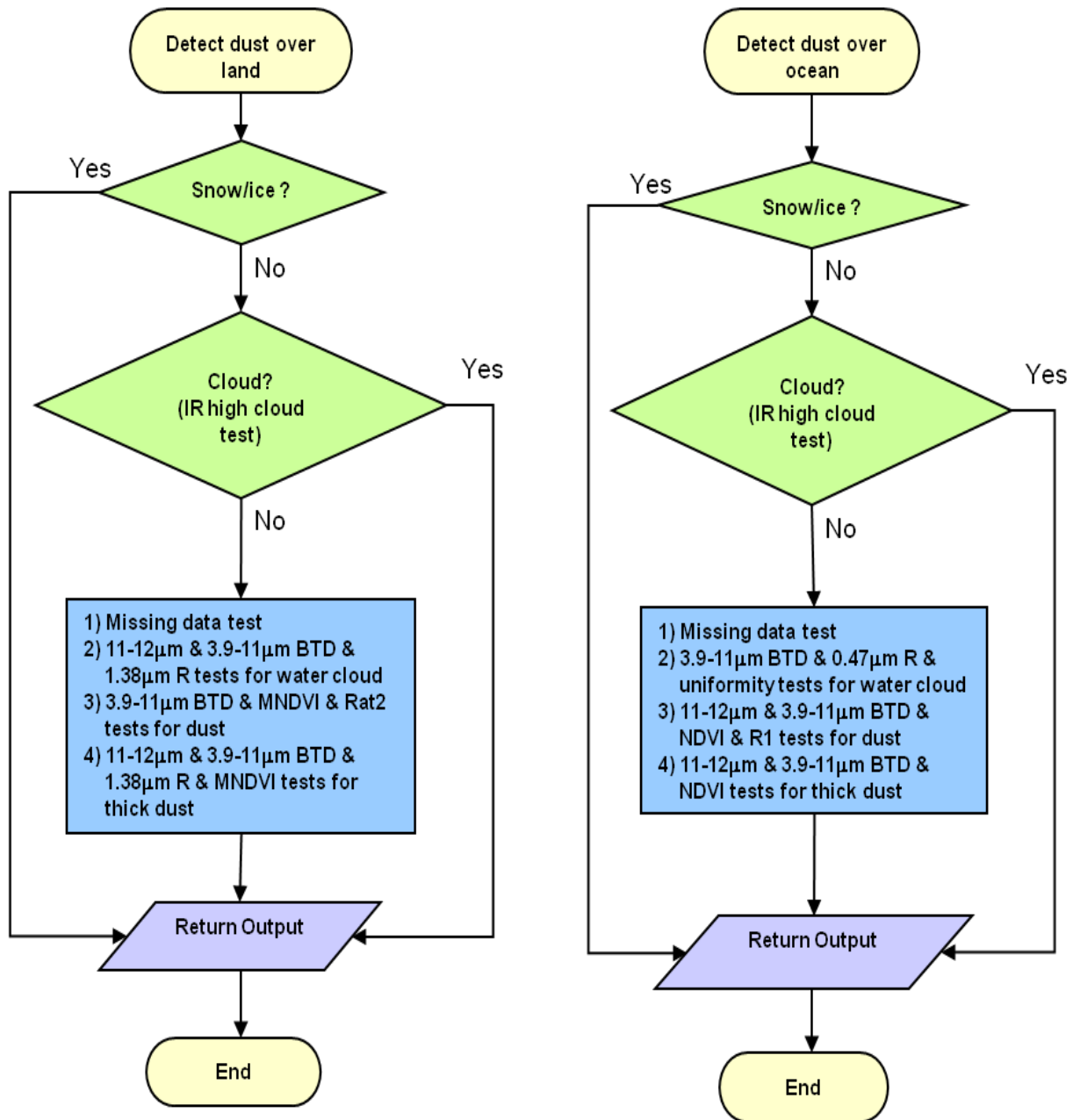
Mineral dust exerts large influences on regional weather, air quality, hydrological cycles, and ecosystems. Detection of these highly variable aerosol events is challenging because of: episodic features, short lifetimes, multiple-scales, and strong impact of local surface and meteorological conditions. Dust particles can directly alter solar and Earth radiation in both visible and infrared (IR) spectral regions through scattering and absorption processes. Due to specific optical properties of dust particles, satellite observed radiances carry the spectral signatures of dust particles that are different from molecular, cloud, and underlying surface. Based on these differences, various detection schemes have been developed to distinguish dust^[1]. In practice, the detection is based on the analysis of reflectance (or radiance) in visible bands or brightness temperature (BT) in IR bands^[2]. The magnitude of the difference in reflectance or BT in selected

bands (or channels) can be used to infer the signature of dust^[3]. This is the essence of aerosol imagery detection algorithms, such as those developed for the detection of volcanic aerosols^[4,5] and dust outbreaks^[6,7,8]. Building upon these previous research results, we introduce a detection algorithm of dust storms for satellite multi-channel imagers by combing visible channel radiances/reflectances with IR channel brightness temperatures. Application to the Asian dust detection is addressed.

Dust Detection Algorithm

Dust detection is performed only for daytime (defined as solar zenith angle < 80 degree) in the current algorithm. Different detecting schemes are developed for land and ocean and they are summarized in Figure 1.

Figure 1. Flow chart for dust detection algorithms over land (left) and ocean (right).



The detection tests are based on the spectral and spatial signatures of dust, cloud, and underlying surfaces in the reflectances (R) or their ratios (Rat) on visible channels and brightness temperature differences (BTD) in IR bands. For examples, the tests of 1) and 2) for dust detection over land are used to remove bad observations and cloudy pixels, respectively. For test 3), if $BT_{3.9\mu m} - BT_{11\mu m} \geq 25K$ is satisfied, then flag the pixel as dust laden. This is because dust

reflects solar energy at 3.9 μm and so increases the brightness temperature difference with $\text{BT}_{11\mu\text{m}}$ during the day. Moreover, $\text{MNDVI} < 0.08$ ($\text{MNDVI} = \text{NDVI}^2 / (\text{R}_{0.64\mu\text{m}} \times \text{R}_{0.64\mu\text{m}})$; $\text{NDVI} = (\text{R}_{0.86\mu\text{m}} - \text{R}_{0.64\mu\text{m}}) / (\text{R}_{0.86\mu\text{m}} + \text{R}_{0.64\mu\text{m}})$) and $\text{Rat}_2 > 0.005$ ($\text{Rat}_2 = (\text{Rat}_1 \times \text{Rat}_1) / (\text{R}_{0.47\mu\text{m}} \times \text{R}_{0.47\mu\text{m}})$; $\text{Rat}_1 = (\text{R}_{0.64\mu\text{m}} - \text{R}_{0.47\mu\text{m}}) / (\text{R}_{0.64\mu\text{m}} + \text{R}_{0.47\mu\text{m}})$) are added to identify dust over some semi-arid surfaces with small amounts of vegetation. This is because dust absorbs at blue wavelengths and appears visually to be brownish in color. Clouds are spectrally neutral and appear white to our eyes. For this reason, the reflectances at 0.86, 0.64 and 0.47 μm have been used to identify dust. This is often done in a ratio of one to another or as a normalized difference index (such as MNDVI or Rat₂). In the ratio tests described here, we square the reflectances trying to take better advantage of the non-linear behavior.

Two tests are used to indicate the presence of optically thick dust in test 4). The first is $\text{BT}_{11\mu\text{m}} - \text{BT}_{12\mu\text{m}} \leq -0.5\text{K}$ and $\text{BT}_{3.9\mu\text{m}} - \text{BT}_{11\mu\text{m}} \geq 25\text{K}$ and $\text{R}_{1.38\mu\text{m}} < 0.035$. The bulk transmittance of many aerosols displays a strong spectral variation in the 8-10 μm and 10-12 μm regions. This is also a spectral region over which the atmosphere is fairly transparent (or window regions). For these reasons, techniques have been developed which successfully employ satellite radiance measurements at 11 and 12 μm to detect aerosols. These split window IR techniques have primarily been applied to the detection of volcanic aerosols, particularly those from sulfur-rich eruptions^[4, 5], and dust outbreaks^[6, 7, 8]. Dust absorbs more radiation at 12 μm than 11 μm , which causes the brightness temperature difference between the two to become negative. Moreover, there is absorption and emission of water vapor in the 11 and 12 μm channels. Because the weighting function for the 11 μm channel peaks lower in the atmosphere (higher in temperature) than the 12 μm channel does, the presence of a dry air mass, often associated with dust events, will tend to reduce the positive $\text{BT}_{11\mu\text{m}} - \text{BT}_{12\mu\text{m}}$ values associated with clear-sky atmospheres. In addition, dust has a larger absorption at 12 μm than at 11 μm , so that dust plumes generally have a higher emissivity and lower transmissivity in the 12 μm channel^[2, 9]. For elevated dust layers, the increased temperature separation between the dust layer and the surface, and the coincident reduction of dry air closer to the peak of the 11 μm weighting function makes the split window brightness temperature difference less positive. This difference has also been observed to be affected by the optical thickness of a given dust plume, so that with thick optical thickness the $\text{BT}_{11\mu\text{m}} - \text{BT}_{12\mu\text{m}}$ difference has a negative value.

Since dust over ocean is more uniformly distributed than cloud and less reflective than cloud, uniformity test ($\text{StdR}_{0.86\mu\text{m}} \leq 0.005$) and reflectance test ($\text{R}_{0.47\mu\text{m}} \leq 0.3$) are added to BTD test ($4\text{K} < \text{BT}_{3.9\mu\text{m}} - \text{BT}_{11\mu\text{m}} \leq 20\text{K}$) to separate better the dust from cloud over ocean. There are three separate tests for dust over water and each is described below. Any pixel that passes any of the

three tests is flagged as dusty, although some of the tests have multiple conditions that must be satisfied.

If $BT_{11\mu m} - BT_{12\mu m} < 0.1K$ and $-0.3 \leq NDVI \leq 0$ then set the pixel as dust contaminated.

Ackerman^[2] studied the possibility of detecting airborne dust using the difference between the $BT_{11\mu m}$ and $BT_{12\mu m}$. He found that airborne dust caused a depression of this value and therefore may be useful in detecting and tracking dust plumes. This split window brightness temperature difference is also the basis for current efforts to use airborne dust in assisting the tracking of the Saharan air layer^[9] using GOES satellite observations. However, the split window difference can also lead to false positive tests, and so it is coupled with a NDVI-type condition of the pixel. The presence of smaller aerosols, like smoke, tends to reduce the values of $R_{0.86\mu m}/R_{0.64\mu m}$ ratio, as smaller particles are more efficient at scattering light at 0.64 μm . Although dust particles are observed to scatter more light at 0.64 μm than at 0.86 μm probably due to their size, they tend to exhibit more uniform scattering across this spectral region^[10]. Thus, the $R_{0.86\mu m}/R_{0.64\mu m}$ ratio test^[8] has been found useful in discriminating pixels containing smoke from those with dust. Rather than directly using the ratio, a modified version (or NDVI test) is employed here.

Another test for examining dust over ocean is the requirement of $R_{0.47\mu m}/R_{0.64\mu m} < 1.2$ since clear-sky ocean surface tends to reflect more in 0.47 μm than 0.64 μm compared with dust particles. Similar to the dust detection over land, low level clouds (often towering cumulus) can also have a negative split window brightness temperature difference. Therefore, the two additional tests ($BT_{3.9\mu m} - BT_{11\mu m} > 10K$ and $BT_{11\mu m} - BT_{12\mu m} < -0.1K$) are applied to attempt reducing cloud contaminated pixels.

Similar to the tests of heavy dust over land, two conditions that indicate the presence of optically thick dust over ocean are employed. The first test, $BT_{3.9\mu m} - BT_{11\mu m} > 20K$, is used to define thick dust regime by separating from thin dust. The second test is $BT_{11\mu m} - BT_{12\mu m} \leq 0K$ and $-0.3 \leq NDVI \leq 0.05$. The first part of the test associated with BTD is the ocean version of the split window IR detection technique for heavy dust. The second part of the test associated with NDVI is similar to the detection of non-thick dust, which is used to reduce the false detection in the split window test.

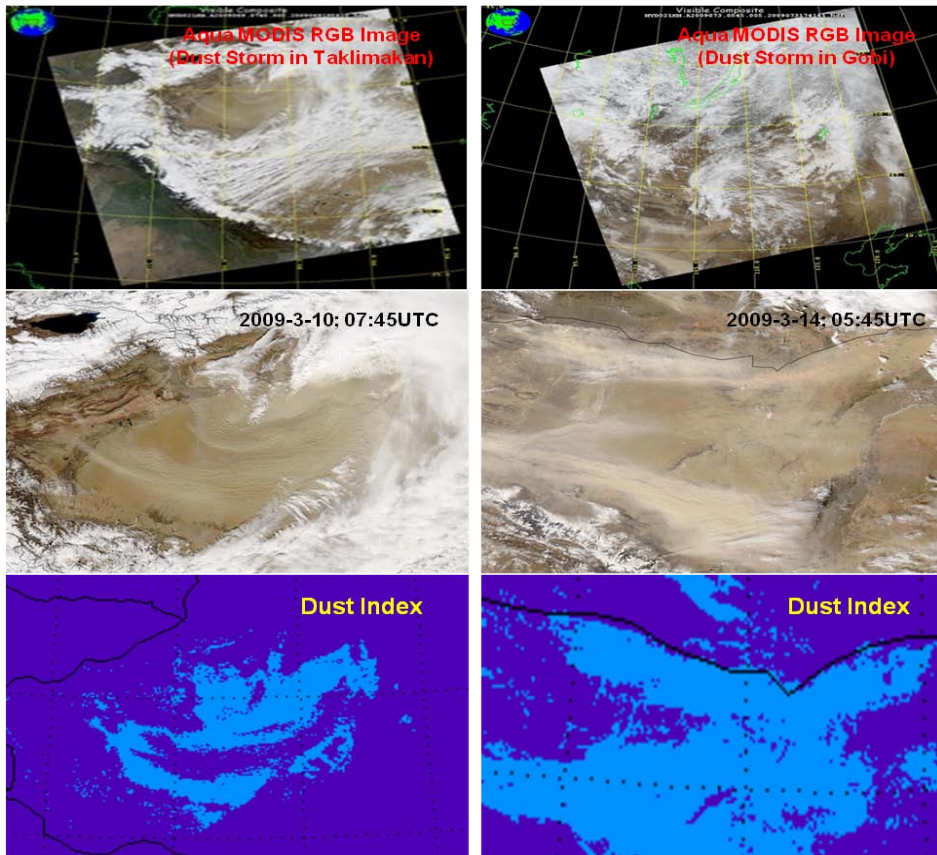
The threshold values for the tests discussed above were obtained through analysis of many training images over the globe^[11]. First, a set of initial test threshold values were selected with our sight. This selection is somewhat subjective but selected values can reasonably separate dust from clouds and underlying surface for these training cases. Then, these initial thresholds were further refined by applying to more sample images mainly through try-and-error check. The

current thresholds may need to be further adjusted in the future practical operational applications.

Results

One detection example for the dust storms over Chinese Taklimakan and Gobi deserts is shown in Figure 2. The dust plumes in the red-green-blue (RGB) false color images for both cases (top and middle panels) are captured by the detection algorithm (dust index) very well (bottom panels). Other detection practices (not shown here) indicate our detection algorithm can successfully capture small dust outbreak as well as dust plumes transported to down-wind oceanic regions and above broken clouds. Aside from the comparison of the detection results from MODIS observation with the corresponding MODIS RGB images (such as Figure 2), our detection results are also compared with the aerosol optical thicknesses (AOT) retrieved from the MODIS radiances using a physically based algorithm by the official MODIS aerosol team^[12]. The comparison indicates our dust detection algorithm performs reasonably well and can be applied to global dust detection.

Figure 2. Top and middle panels: Red-green-blue (RGB) false color images of Aqua MODIS observation of dust storms in Chinese Taklimakan (left) and Gobi (right) deserts. The middle panels are enlarged images of the corresponding top panels. Bottom panels: the results of the dust detection where pixels flagged as dusty are in bright blue color.



SUMMARY AND CONCLUSIONS

A dust detection algorithm and its application to Asian dust detection are presented in this paper. The detection product (dust index) is produced for each pixel observed by a satellite multi-channel imager. The detection relies on spectral and spatial threshold tests along with some uniformity texture examinations by using radiances (or reflectances) and brightness temperatures from a multi-channel radiometric imager. The algorithm makes detection for all satellite pixels during daytime. It can capture heavy dust plumes over both land and ocean so that can be used as a global detection algorithm. Due to the relatively weak aerosol signal and large uncertainties associated with a bright surface, the current algorithm has difficulty capturing thinner or dispersed dust plumes. It also does not work for the snow/ice surface due to associated strong surface perturbation on the dust signal. The algorithm can be applied to any multi-channel

imagers with proper detection channels at (or close to) 0.47, 0.64, 0.86, 1.38, 3.9, 11.0, 12.0 μm used by the algorithm (such as current EOS/MODIS and future JPSS/VIIRS and GOES-R/ABI).

There are some improvement of the algorithm that can be explored in the future, including 1) refining test thresholds based on vigorous operational applications and validations, 2) developing alternative detection approach for thinner or dispersed dust (such as the neural networks approach), 3) exploring dust detection at night using brightness temperature only.

ACKNOWLEDGMENTS

The author would like to acknowledge the climate data record (CDR) project at the National Climate Data Center (NCDC) of NOAA for providing the funding support. Collaborations with Dr. Steve Ackerman at CIMSS of University of Wisconsin, Madison, USA and Dr. Wei Guo at I. M. System Group, INC. in Maryland of USA are greatly appreciated.

REFERENCES

- [1] Tanré, D.; Legrand, M. On the Satellite Retrieval of Saharan Dust Optical Thickness Over Land: Two Different Approaches. *J. Geophys. Res.*; 96, 5221-5227, 1991.
- [2] Ackerman, S.A. Using the radiative temperature difference at 3.7 and 11-mm to track dust outbreaks. *Remote Sensing of Environment*; 27, 129-133, 1989.
- [3] Verge-Depre, G.; Legrand, M.; Moulin, C.; Alias, A.; Francois, P. Improvement of the detection of desert dust over the Sahel using METEOSAT IR imagery. *Annales Geophysicae*; 24, 2065-2073, 2006.
- [4] Prata, A.J. Observations of volcanic ash clouds in the 10-12 μm window using AVHRR/2 data. *International Journal of Remote Sensing*; 10, 751 – 761, 1989.
- [5] Barton, I.J.; Prata, A.J.; Watterson, I.G.; Young, S.A. Identification of the Mount Hudson Volcanic Cloud over Se Australia. *Geophysical Research Letters*; 19, 1211-1214, 1992.
- [6] Legrand, M.; Cautenet, G.; Buriez, J.C. Thermal Impact of Saharan Dust over Land. Part II: Application to Satellite IR Remote Sensing. *Journal of Applied Meteorology*; 31, 181-193, 1992.
- [7] Legrand, M.; Plana-Fattori, A.; N'Doumé, C. Satellite detection of dust using the IR imagery of Meteosat 1. Infrared difference dust index. *J. Geophys. Res.*; 106, 18251-18274., 2001.
- [8] Evan, A.T.; Heidinger, A.K.; Pavolonis, M.J. Development of a new over-water Advanced Very High Resolution Radiometer dust detection algorithm. *International Journal of Remote Sensing*; 27, 3903 – 3924, 2006.
- [9] Dunion, J.P.; Velden, C.S. The impact of the Saharan air layer on Atlantic tropical cyclone activity. *Bulletin of the American Meteorological Society*; 85, 353-365, 2004.
- [10] Dubovik, O.; Holben, B.; Eck, T.F.; Smirnov, A.; Kaufman, Y.J.; King, M.D.; Tanré, D.;

- Slutsker, I. Variability of Absorption and Optical Properties of Key Aerosol Types Observed in Worldwide Locations. *Journal of the Atmospheric Sciences*; 59, 590-608, 2002.
- [11] Zhao, T. X.-P.; Ackerman, S.; Guo, W. Dust and smoke detection for multi-channel imagers. *Remote Sensing*; 2(10), 2347-2368; doi:10.3390/rs2102347, 2010.
- [12] Remer, L.A.; Kaufman, Y.J.; Tanre, D.; Mattoo, S.; Chu, D.A.; Martins, J.V.; Li, R.R.; Ichoku, C.; Levy, R.C.; Kleidman, R.G.; et al. The MODIS aerosol algorithm, products, and validation. *Journal of the Atmospheric Sciences*; 62, 947-973, 2005.

Aircraft measurements of gaseous pollutants and particles during CAREBEIJING: classification and distribution analysis

Wenjie Zhang^{1*}, Tong Zhu², Jianhua Chen¹, Lihong Ren¹, Wen Yang¹ and Baohui Yin¹

1 Chinese Research Academy of Environmental Sciences, Beijing, 100012, China

2 State Key Joint Laboratory for Environmental Simulation & Pollution Control, College of Environmental Sciences, Peking University, Beijing, 100871, China

Principal Contact: Wenjie Zhang, Associate Professor, Chinese Research Academy of Environmental Sciences, No. 8, Dayangfang, Anwai, Chaoyang District, Beijing, 100012, China.
Tel: 010-84915246 Fax: 010-84935950 Email: zhangwj@craes.org.cn

Abstract

Measurements of gaseous pollutants, including ozone (O_3), Sulfur dioxide (SO_2), nitrogen oxides ($NO_x = NO + NO_2$), carbon monoxide (CO), particle concentration (5.6-560 nm and 0.47-30 μm), and related meteorological information (T, RH, P) were conducted for the Program of Campaigns of Air Quality Research in Beijing and Surrounding Region (CAREBEIJING) during Aug. 27-Oct. 13 in 2008. Total 18 flights (70 h flight time) from the surface to 2100 m were obtained with a Yun-12 aircraft with a cruising speed of about 180 km h^{-1} during the latitude range of 38°N - 40°N and longitude range of 114°E - 118°E , the southern surrounded area of Beijing city. This measurement was to characterize the regional variation of air pollution during and after the Olympics of 2008, the impacts of different transport direction and possible influencing factors. Results suggested that four different groups of transport sources influenced the pollution level of pollutants with the consideration of the backward trajectory analysis, including: (1) the pollutant transport of the southern direction with higher pollutants level; (2) the cleaner long-range transport of the northern or northwestern direction with lower pollutants level; (3) the transport from the eastern direction with characteristics of sea sources, i.e. middle level of gases pollutants and higher particle concentration; (4) the transport of mixing directions, i.e. lower altitudes from the pollutant transport direction or local pollution but higher altitudes from the clean transport direction. Additionally, the relatively long-lived CO was shown to be a possible transport tracer of long-range transport of northwestern direction especially on the higher altitudes.

Keywords: Aircraft monitoring, Gaseous pollutants, Particles, Back trajectory

Direct and Remote Sensing Methods for Chemical Pollution Studies

Panuganti C.S. Devara

Indian Institute of Tropical Meteorology, Pune, Maharashtra, 411 008, India

ABSTRACT

Efficient observational methods and long-term monitoring of the pollutant levels are of great interest in understanding the source emissions, ambient air quality, atmospheric chemical transformation and long-term transport and removal of aerosol pollutants (wet and dry) and the associated feedback processes. Most quantitative determination of air pollutants such as aerosols and gases have until now been made by point monitors/direct/conventional techniques, which provide reliable information at a specific location. Vertical profiling of any parameter using point monitors involves tedious procedures and analysis of such data is laborious and time consuming. Much more representative values can be obtained with remote sensing techniques, which also provide unique means to study the dynamical, physical and radiative processes influencing directly or indirectly the air quality. Remote sensing schemes, on the other hand, have made considerable progress in the recent past. Of the latest optical remote sensing techniques, the active methods such as lidar and passive methods such as solar radiometry have been recognized to be powerful and versatile tools for environmental diagnostics. Satellites provide an unparalleled capability to monitor atmospheric constituents from higher altitudes on a global scale for longer time periods. The recent satellite-based active (lidar) and hyper-spectral passive sensors extended this capability further.

KEYWORDS

Aerosols, Gases, Direct Techniques, Remote Sensing Methods, Satellites

Introduction

During recent years the subject of environmental monitoring has been drawing worldwide attention. There is a growing body of observational and theoretical evidence which suggests that atmospheric aerosols and trace gases play vital role not only in the thermal state of the Earth-atmosphere system but also in the local / regional air pollution. Emissions and anthropogenic concentrations of several gases important to atmospheric chemistry are known to have increased substantially during the recent decades. Their impact on weather and climate on one hand and on biogeochemical processes on other hand has been recognized to be one of the priority areas for investigations^[1]. Moreover, the closely packed houses, streets and industrial complexes with scarce open spaces, hamper the meteorological processes of

dispersion and dilution of high concentration of pollutants as they are released from the sources into the atmosphere. All these effects prompted numerous efforts to develop a variety of experimental / modeling techniques and systems. These pollutants constitute a threat to public health both directly through inhalation and indirectly through possible long-term influences on the atmospheric environment. Clearly, effective methods of the measurement of atmospheric pollutant concentrations are of great interest in any program for air pollution assessment, forecast and control^[2]. Simultaneous measurements of aerosols and gases, and inter-comparison of their properties by employing multi-instrument approach, consisting of remote sensing as well as point monitors / *in-situ* techniques, have also been reported by many researchers^[3, 4]. This paper delineates different experimental techniques, based on both direct and remote sensing methods that have been used in the past and the state-of-the-art technology currently availability for making measurements of physico-chemical properties of aerosols and gases. It will also highlight the current gap areas in the field and some directions for future research work.

Direct (*in-situ*) Methods

Conventionally, the chemical pollution (aerosol / gas-phase chemistry) or air quality studies are carried out by collecting air samples from different environments and analyzed in the laboratory for their chemical composition^[5]. In these methods, the sensor will interact directly with the measuring media. Impaction technique and particle counters are some examples for this category. The *in-situ* observations, because of their high cost, cannot provide sufficient coverage of the spatial and temporal scales for calculating their effects on environmental pollution, weather and climate. These observations are mostly obtained with impactors and optical counters and are confined to the aerosol characteristics within a few meters of the Earth's surface at one location. The most general instruments that fall in this category include Aitken nuclei counter, multi-stage low volume/pressure impactor, quartz crystal micro-balance, electrical aerosol analyzer. Some details like principle of operation, measuring size range etc. for these instruments are presented in Table 1. In recent years, these instruments

Table 1: Different direct sampling techniques and details

Direct Sampling Techniques

Instrument	Specification	Parameter	Principle of operation	Minimum duration of sampling
Aitken Nuclei Counter	0.001-0.1 μm	Number density	Adiabatic expansion	~ 5 minutes
Andersen Sampler (high & low pressure)	0.08-0.1 μm	Mass-size distribution	Impaction	Few to ~100 hours
High Volume Sampler	Total suspended particulate	Mass-size distribution	Impaction	~ 4 hours
Quartz Crystal Micro Balance	0.08-10 μm	Mass-size distribution	Impaction	~ 40 hours
Electrical Aerosol Analyzer	0.003-1 μm	Number-size distribution	Mobility of charged aerosol	Few minutes
Real-time Gas Analyzers	Up to ppt levels	Concentration	Optical scattering and absorption	Instantaneous

have been made more sophisticated and are available with facilities like self-calibration, on-line data archival and analysis systems. These measurements may not be representative of the mixed aerosol in the total boundary layer. To acquire measurements above ground, i.e. profile information about aerosols, sampling systems need to be mounted on a suitable platform such as balloon, aircraft or rocket. This complicates, many times, the process of relating the measured aerosol properties to that of the actual ones in the atmosphere. Consequently, the utility of *in-situ* observations cannot be fully realized until they are closely coupled with numerical models and satellite observations. Compared to direct measuring techniques which provide reasonably reliable information at a specific location with good temporal but poor spatial resolution, more representative values can be obtained with remote sensing techniques. The basic problem with the direct measuring techniques is that the sensor disturbs the medium in which the measurement is made. Moreover, these techniques are more cumbersome because one has to install the sensors on a platform like tower or balloon or helicopter or aircraft or rocket for obtaining vertical profiles. Compared to them, remote sensing techniques have several advantages. The remote sensing techniques consist of a transmitter, receiver and data acquisition system. The remote sensing techniques are basically of two types. First one is active remote sensing, in which the user will have complete control over the transmitter [(for example, RADAR (Radio Detection And Ranging), LIDAR (Light Detection And Ranging), SODAR (Sound Detection And Ranging)]. The second one is passive remote sensing techniques, in which user will not have control over the transmitter (For example, Solar Radiometer, Lunar Radiometer, Star Photometer). Of the latest optical remote

sensing techniques, optical radar or laser radar or lidar has been recognized to be a powerful and versatile tool for environmental monitoring^[6]. The basic principle involved in the laser sounding of the atmosphere or hydrosphere is that molecules and aerosols cause absorption and scattering of transmitted energy and the small backscattered energy is collected by a suitable optical system, which in turn gives the information about the presence, range and concentration of various scatterers and absorbers.

Laser Remote Sensing Methods

Laser remote sensing for environmental monitoring can be accomplished basically in two ways. One technique involves measurement of long-path absorption employing a tunable laser source and detector are located together and a retro-reflector is placed at a distance of several hundred meters, such a system is useful when the laser source is weak, since the retro-reflector greatly enhances the returned radiation. In the other technique, the laser and the detector are located together and no retro-reflector is used as the target, in this case the returned laser radiation is due to backscatter from aerosols in the atmosphere (in the case of vertical profiling of pollutant concentration) or a topographic target such as a hill or trees (in the case of path-averaged measurements of pollutant levels). In the lidar technique, radiation/energy is transmitted into the atmosphere, some portion of the light is absorbed and / or scattered back into the laser direction, where a telescope with a photo-detector (receiver) produces an electrical signal proportional to the returned intensity. The intensity of the signal indicates the concentration of absorbing or scattering material. The primary influence of the atmosphere on a low-power laser beam is through scattering and absorption. Both processes cause an attenuation of the beam according to Bouguer's or Beer's law as

$$I = I_0 e^{-\alpha R}$$

where I is intensity of laser beam after transmission over a distance R ; α is the atmospheric extinction coefficient; and I_0 is the initial intensity of the beam. It is possible to express α as

$$\alpha = \alpha_{\text{Mie}} + \alpha_{\text{Ray}} + \alpha_{\text{Raman}} + \alpha_{\text{abs}}$$

where α_{Mie} , α_{Ray} and α_{Raman} are the extinction coefficients related to Mie, Rayleigh and Raman scattering, respectively and α_{abs} is the molecular absorption coefficient.

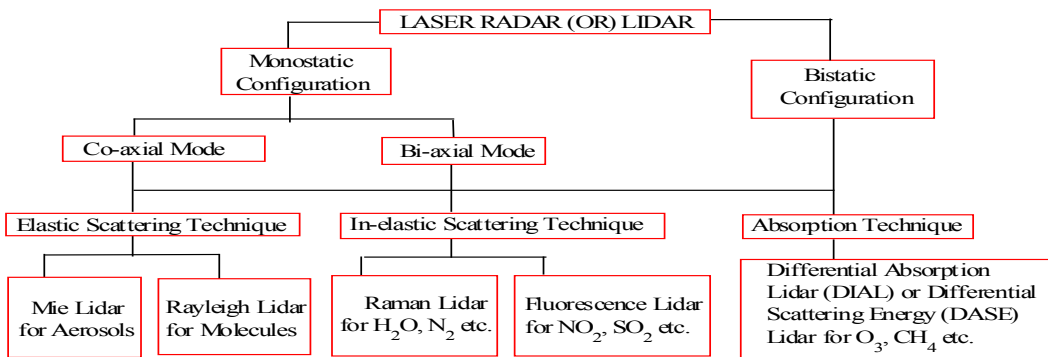


Figure 1: Block diagram showing different types of Lidar Techniques for Environmental Monitoring

The block diagram in Figure 1 shows different lidar techniques that are commonly used for monitoring of aerosols, air molecules and gases in the near Earth's environment. Mie scattering is associated with larger particles such as aerosols whose size is on the order of probing laser wavelength, λ . Rayleigh scattering is due to particles in the atmosphere, such as molecules or fine dust, that are much smaller than λ . Rayleigh and Mie processes are elastic scattering in which the scattered light has the same wavelength (or color) as the incident laser beam. Raman scattering is associated with interaction of the laser beam involving excitation of the energy levels of a molecule and re-radiation at a different wavelength. Absorption of the laser beam is a resonant interaction (direct absorption) leading to excitation of the molecule, followed possibly by fluorescence. Thus the Raman and fluorescence processes are in-elastic scattering in which the wavelength of scattered and that of laser are different. The DIAL (Differential Absorption Lidar) measures the concentration of molecular species in the atmosphere by transmitting two wavelengths, only one of which is absorbed, and detecting the difference in the intensity of the returns at the two wavelengths, the backscattering in the DIAL may be from a hard target or aerosols. By following such approach the Argon ion and Excimer lidars at the IITM have been used for determining vertical distributions of atmospheric NO₂ and O₃ concentration (Devara and Raj, 1999; Devara et al., 2007). Fluorescence lidar uses single wavelength while a DIAL system uses two wavelengths. The fluorescence lidars use spectrometric techniques to separate the wavelength-shifted fluorescence signal from the strong Rayleigh backscatter in the atmosphere. Such a technique has been extensively employed for oceanic and vegetation remote sensing. Raman lidar uses a single wavelength laser and sophisticated spectrometric detection techniques to spectrally resolve the wavelength-shifted signal from the strong background due to Rayleigh or Mie scattering. Thus, unlike, DIAL, with single wavelength, several pollutant concentrations can be determined using the Raman lidar technique. Only drawback with Raman lidar is that measurable shifts are possible only when the concentration of gas under study has sufficiently

high concentration in the medium. The lidar systems developed for the past more than two decades at the IITM, Pune, based on the above laser-atmosphere interaction mechanisms and some results obtained with them have been discussed^[7].

Air Pollution or Air Quality Studies

By using inhomogeneities in aerosol content as tracers, many researchers have studied the atmospheric boundary layer that directly or indirectly affects the air quality. The quantitative retrievals of aerosol features are often used for the study of atmospheric dynamics, physical modeling of the atmosphere, for establishing the criteria for meaningful sampling of air quality and environmental pollution. From the lidar-derived vertical profiles of aerosol concentration, information on mixed layer height (i.e. height up to which the pollutants are thoroughly mixed in the atmosphere) can be derived. The product of mixed layer height and average wind speed up to that height is known as ventilation coefficient, which is an indicator of air pollution or air quality over the place^[8]. In other words, larger ventilation coefficients imply smaller air pollution potential i.e. good air quality and vice-versa. The state of air pollution potential derived from long-term aerosol vertical distribution data from lidars at IITM, for the last 14 years indicated that ventilation coefficients are minimum in monsoon months and winter months (December, January and February) which means more pollution during these months. During monsoon season, most of the pollutants are scavenged by clouds and the precipitation (rainfall) washes out the pollutants, hence it doesn't lead to any pollution problem. However, the smaller ventilation coefficients during winter period really cause serious problem over Pune. Added, the haze formation, close to the ground (hardly few meters above the surface of the Earth) further enhances this pollution problem because these haze layers act as lid to the pollutants emitted on the Earth and hence they are hardly dispersed into the atmosphere.

Lidar Applications to Marine Chemistry and Pollution

Remote sensing of the oceans, lakes and rivers of our Planet is possible with visible, infrared and microwave radiation. Most of this information was derived passively prior to the introduction of lasers into hydrographic work. Lidars have added another dimension to hydrographic research, because it permits a degree of depth resolution and subsurface interrogation that is unattainable with other remote sensing techniques. The primary reason for this is that infrared and microwave radiations have negligible penetration in water. The scattering and absorption processes that occur in the atmosphere are also applicable to ocean research by lidars. The laser induced fluorescence (LIF) is one of the important techniques generally used in lidar remote sensing of oceans.

Passive Remote Sensing of Air Pollutants by Solar Radiometry

Like in the active remote sensing, in passive remote sensing also, the amount of solar radiation transmitted by the atmosphere is given by the Lambert-Beer's law as

$$I(\lambda) = I_0(\lambda) e^{-\alpha(\lambda)m} = I_0(\lambda) e^{-\tau(\lambda)m}$$

where I and I_0 are the transmitted and incident intensities at any wavelength, λ ; α is total extinction coefficient, τ is total atmospheric optical thickness or depth, m is mass of the air through which the transmitted light is passed (which is proportional to $\sec \chi$, where χ is solar zenith angle).

The straight line fitted to the data points by linear regression, slope gives the atmospheric optical thickness or extinction or attenuation. The intercept corresponding to $\sec \chi = 0$ is directly related to the solar flux at the top of the atmosphere (TOA) and it can be used to self calibrate the system. By using the plot between logarithms of $\tau_{a(\lambda)}$ and λ , aerosol size distribution at the experimental site can be determined. Results obtained in this direction, using sun photometers and sun-sky radiometers have been published in the literature.

SOME GAP AREAS FOR FUTURE RESEARCH

- (i) Lidars and solar radiometers have augmented humanity's ability to study aerosols and trace gas pollutants, joining *in-situ* instruments in both complementary and unique ways for chemical pollution studies. There is still much work to be done to bring the field maturity.
- (ii) Besides the stationary lidar and radiometric systems, new generation mobile systems need to be developed for multi-dimensional mapping of aerosols and gases in different environments. Such systems in network mode will play a vital role in the identification of sources/sinks and modeling of the role of aerosols and gases in air pollution / air quality.
- (iii) As the existing air pollution / quality monitoring programs are continuing and new proposals coming in, it is hoped that the complex physico-chemical characteristics of pollutants (aerosols and trace gas species) are better understood in the years to come.

ACKNOWLEDGEMENTS

The author is thankful to all the members of "Aerosol and Cloud Physics Laboratory for Weather and Climate Studies" and "Air Pollution and Precipitation Chemistry Studies". Thanks are also due to Director, IITM, Pune for support.

REFERENCES

- [1] NRC (National Research Council) 1984, *Global Tropospheric Chemistry: A Plan for Action*, U.S. National Research Council, National Academy Press, Washington D.C.
- [2] Beniston, M., Wolf, J.P., Beniston-Rebetez, M., Kolsch, H.J., Rairoux, P., Woste, L., *J. Geophysical Research*, 1990, 95, 9879-9894.
- [3] Takamura, T. and Sasano, Y., 1990, *Journal of Meteorological Society of Japan*, 68, 729-739.
- [4] Maheskumar, R.S., Devara, P.C.S., Raj, P.E., Pandithurai, G., Dani, K.K. and Momin, G.A., 2001, *Atmospheric Environment*, 35, 2895-2905.
- [5] Devara, P.C.S., 2000, *Indian Journal of Environmental Protection*, 20, 15-22.
- [6] Devara, P.C.S., 1989, *Journal of Scientific and Industrial Research*, 48, 71-83.
- [7] Devara, P.C.S., Raj, P.E., Jaya Rao, Y., Pandithurai, G., Dani, K.K., Reddy, K.M.C., Saha S.K. and Sonbawne, S.K., 2007, *The International Society for Optical Engineering (SPIE) Newsroom*, 10.1117/2.1200706-0640, 1-3.
- [8] Devara, P.C.S., Maheskumar, R.S., Raj, P.E., Pandithurai, G. and Dani, K.K., 2002, *International Journal of Climatology*, 22, 435-449.
- [9] Devara, P.C.S., Raj, P.E., Pandithurai, G., Maheskumar, R.S. and Dani, K.K., 1997, *Journal of Indian Society for Remote Sensing*, 25, 225-238.
- [10] Dani, K.K., Raj, P.E., Devara, P.C.S., Pandithurai, G., Sonbawne, S.M., Maheskumar, R.S., Saha, S.K. and Jaya Rao, Y., 2010, *International Journal of Climatology*, DOI: 10.1002/joc.2250.

AEROSOL VARIABILITY OVER EAST ASIA AS SEEN BY POLDER SPACE-BORNE SENSORS

X. Su^{1,2}, I. Chiapello², P. Goloub², H. Chen¹, F. Ducos², and Z. Li^{2,3}

1 Key Laboratory of Middle Atmosphere and Global Environment Observation, Institute of Atmospheric Physics, Chinese Academy of Sciences, Beijing 100029, China

2 Laboratoire d'Optique Atmosphérique, Université Lille 1, Villeneuve d'Ascq 59655, France

3 State Environmental Protection Key Laboratory of Satellite Remote Sensing, Institute of Remote Sensing Applications, Chinese Academy of Sciences, Beijing 100101, China

Principal Contact: X. Su, Dr., Key Laboratory of Middle Atmosphere and Global Environment Observation, Institute of Atmospheric Physics, Chinese Academy of Sciences, Beijing 100029, China.

Tel: +86-29-88326128 Fax: +86-29-88320456 Email:suxl@ieecas.cn

Abstract

This paper is devoted to analyze aerosol distribution and variability over East Asia based on PARASOL/POLDER-3 aerosol products over land. We first compared POLDER-3 Aerosol Optical Depth (AOD) with fine mode AOD (particles radius $< 0.30 \mu\text{m}$) computed from AERONET (Aerosol Robotic Network) inversions over 14 sites. The rather good correlation ($R \approx 0.91$) observed over land demonstrates the remarkable sensitivity of POLDER-3 retrievals to the smaller fraction of fine particles, mostly originating from anthropogenic sources. We analyzed the characteristics and seasonal variation of aerosol distribution over East Asia considering four years of POLDER-3 Level 2 data (March 2005 to February 2009). Our study shows that the spatial distribution of fine-mode aerosols over East Asia, as retrieved from POLDER-3, is highly associated with human activities. Our work also evidenced a strong variability of seasonal fine-mode AOD patterns with geographical locations. Finally, the inter-annual variation during 2003-2009 periods of summer fine-mode AOD over North China, in particular the Beijing City region, was analyzed for the contribution to evaluating the regional impact of emission reduction enforced in Beijing during the 2008 Olympic Summer Games. We found that summer average of fine-mode AOD exhibited relatively higher values in 2003, 2007 and 2008. The inter-annual variation patterns of monthly averaged AOD (June to August) shows that June generally exhibits the strongest variation and varies similar to July, but differs from August. As reference, measured total AOD and fine mode AOD computed from AERONET inversions in summer are also discussed for the Beijing City region.

Keywords: Aerosol; POLDER; AERONET; AOD

Physicochemical Character and Source Appointment of Ambient Coarse/Fine/Ultrafine Particles in Shanghai Atmosphere

Senlin Lu^{1*}, Rui Zhang¹, Man Feng¹, Zhenkun Yao¹, Jingjing Re¹, Fei Yi¹, Jiali Feng¹, Minghong Wu¹ and Qingyue Wang²

1 School of Environmental and Chemical engineering, Shanghai University, Shanghai 201800, China;

2 Graduate School of Science and Engineering, Saitama University, Japan

ABSTRACT

The chemical composition and their source appointment of airborne coarse/fine/ultrafine particles in Shanghai, China were investigated. Ambient size-resolved particles were collected by using of a MOUDI125 sampler in a Shanghai commercial centre (Xujiahui) from 27, August to 10, September, 2008. The size-resolved particles were divided into 3 groups, i.e. coarse (diameter 1.8~10 μm), fine (diameter 0.1~1.8 μm) and ultrafine/nanoparticles (diameter <0.1 μm) fractions. Micro-morphology was investigated by scanning electron microscopy coupled with energy dispersive X-ray detection (SEM/EDX), and 20 chemical elements were quantified using synchrotron radiation X-ray fluorescence (SRXRF). Source appointment of these particles was indicated by enrichment factor. Our results showed that the average mass concentrations of coarse particles, fine particles and ultrafine particles were 46.51 ± 14.38 , 74.63 ± 19.59 , $2.19 \pm 1.24 \mu\text{g} \cdot \text{m}^{-3}$ respectively. The mass ratio of $\text{PM}_{0.1 \sim 1.8}/\text{PM}10$ was 0.62 ± 0.06 , indicating that fine particles dominated the total mass of PM10. The coarse particles were dominated by minerals, fine particles by soot aggregates and fly ashes, and ultrafine particles by soot particles and unidentified particles. Crustal elements, such as Si, Ca and Fe were mainly found in coarse particles. Sulphate, emitted from coal combustion, could be found in different size fractions. The anthropogenic elements (Cr, Mn, Ni, Cu, Zn, Pb) were higher in the fine particle fraction compared with that of coarse particles and ultrafine particles.

KEYWORDS

Shanghai ambient size-resolved particles, chemical elements, source appointment.

Introduction

Epidemiological studies have showed that airborne particulate matters were associated not only with exacerbations of respiratory diseases but also with increased morbidity and mortality

from cardiovascular causes (Dockery et al., 1998; Hetland et al., 2004). Airborne particulate matters can be divided into 3 categories on the base of their aerodynamic meters, i.e., coarse particles, fine particles and ultrafine particles. Many literatures focused on the physicochemical characterization of coarse particles and fine particles. Relative few papers described ultrafine particles. However, owing to higher surface area-to-mass ratio and deposition efficiency of UPF are higher in the alveolar compared with that of coarse particles and fine particles, and the size and chemical composition of ambient particles importantly govern their potential impacts on human health. Therefore, these findings motivate researchers to investigate physicochemical characterization of ultrafine particles in the atmosphere. For example, Wu et al. (2008) conducted two-year measurement on particle number size distribution (3nm-10μm) in Beijing, China. They reported that the annual average particle number concentrations of the nucleation mode (3-20nm), Aitken mode (20-100nm), and accumulation mode (0.1-1μm) were 9000 cm^{-3} , $15,900\text{ cm}^{-3}$, and 7800 cm^{-3} , respectively. Allen et al. (2001) measured the size distributions of Ba, Cd, Co, Cu, Hg, Mn, Ni, Pb, Sn, Se, Sr, Zn and Fe in atmospheric aerosols at three background sites in central England and southern Scotland. They claimed that the size distributions obtained in Scotland which were typically trimodal differed from those in central England where modes were more variable. Lin et al (2005) reported that size distribution of chemical elements in the size-resolved ambient particles near a high-way in Taiwan. Their results showed that anthropogenic elements, such as Zn, Ni, and Pb mainly distributed in the size range of $1.0\text{--}0.56\text{ }\mu\text{m}$. As the biggest commercial city in China, ambient inhalable particles (PM_{10} , $\text{PM}_{2.5}$) in Shanghai atmosphere has been investigated recently (Lu et al., 2008). However, few studies on ultrafine particles in the Shanghai air have been reported.

Herein, this study will focus on comparison of physicochemical characterization of coarse/fine/ultrafine particles in Shanghai atmosphere. Our results will reveal the variety of different chemical elements distributed in the size-resolved particles

Experimental Methods

(1) Field Sampling

The sampling site located in Xujiahui, one of commercial center of Shanghai, a 13-stage MOUDI (Micro-Orifice Uniform Deposit Impactor, MSP) with the flow rate of $10\text{ l}\cdot\text{min}^{-1}$ was employed to collect the size-resolved ambient particles. The sampling campaigns were performed from August 27 to September 10, 2008. Aerodynamic size cuts for the 13-stage impactor are 0.010, 0.018, 0.032, 0.056, 0.10, 0.18, 0.32, 0.56, 1.0, 1.8, 2.5, 5.6 and $10\text{ }\mu\text{m}$. After sampling, the filter samples were stored in desiccators until analysis. These samples were weighed before and after sampling under the same conditions at constant temperature ($20\pm1^\circ\text{C}$) and humidity ($40\%\pm5\%$) with a microbalance (Model CP225D, Sartorius), then, mass concentrations of the size-resolved ambient particles were obtained.

(2) Scanning electronic microscopy

Approximately $1.5 \times 2 \text{ cm}^2$ of the polycarbonate filter was cut off by resin scissors and was attached to the conductive metal pads by using double-sided adhesive. The samples were observed by using scanning electron microscopy (ESEM) (JSM-6700F, JEOL), equipped with an energy dispersive X-ray system (EDX) which was used for the chemical elemental analysis. The detail protocol can be found in the reference (Lu et al., 2011)

(3) Synchrotron radiation X-ray fluorescence analysis

The experiment on the chemical composition analysis of size-segregated particles was carried out at the synchrotron radiation X-ray fluorescence analysis end station (BL-4A) of the photon factory's high energy accelerator research organization in Tsukuba, Japan. The method was described by Li et al. (2007). Briefly, The electron beam energy and ring current of synchrotron radiation are 2.5GeV and 300—450mA respectively, and the X-ray energy ranges from 1 to 20KeV. A double crystal monochromator was regulated, and the monochromatic excitation energy was 19.5KeV. The electronic slot was adjusted to making the beam spot sizes with $5\mu\text{m} \times 5\mu\text{m}$. Measurement time for each sample was set for 100 seconds. The experiments were repeated 3 times. The fluorescence signals acquisitioned by a Si (Li) semiconductor detector and sent into 1024 pulse height analyzer (MCA) to record the XRF spectrum. The spectrum was analyzed and processed by the software AXIL.

Results and Discussion

(1) Mass concentrations

Mass concentration of coarse, fine and ultrafine particles in Shanghai atmosphere was showed in Figure 1. Mass concentration of Shanghai coarse particles from 27 th, Aug. to 10th, Sept., ranged from $21.88 \text{ to } 37.41 \mu\text{g} \cdot \text{m}^{-3}$. The mean average was $28.13 \pm 6.57 \mu\text{g} \cdot \text{m}^{-3}$. Mass level of fine particles ranged from $21.18 \text{ to } 50.28 \mu\text{g} \cdot \text{m}^{-3}$ with average mean $35.27 \pm 14.1 \mu\text{g} \cdot \text{m}^{-3}$. The mass concentration of ultrafine particles ranged from $5.56 \text{ to } 9.70 \mu\text{g} \cdot \text{m}^{-3}$ with average mean $8.09 \pm 1.66 \mu\text{g} \cdot \text{m}^{-3}$. After the size-resolved particles were divided into coarse particles (size diameter $< 3.2 \mu\text{m}$), fine particles (size diameter, $0.1 \sim 1.8 \mu\text{m}$) and ultrafine particles (size diameter $< 0.1 \mu\text{m}$), mass percentage of the fine particles accounted up to 51.47% in the total mass of PM₁₀, while the coarse particles and ultrafine particles accounted up to 37.69% and 10.84% respectively (Figure 2). The ratio of fine particles /coarse particles ranged from 54% to 68% with an average of 62%, indicating that Shanghai ambient particles were dominated by fine particles.

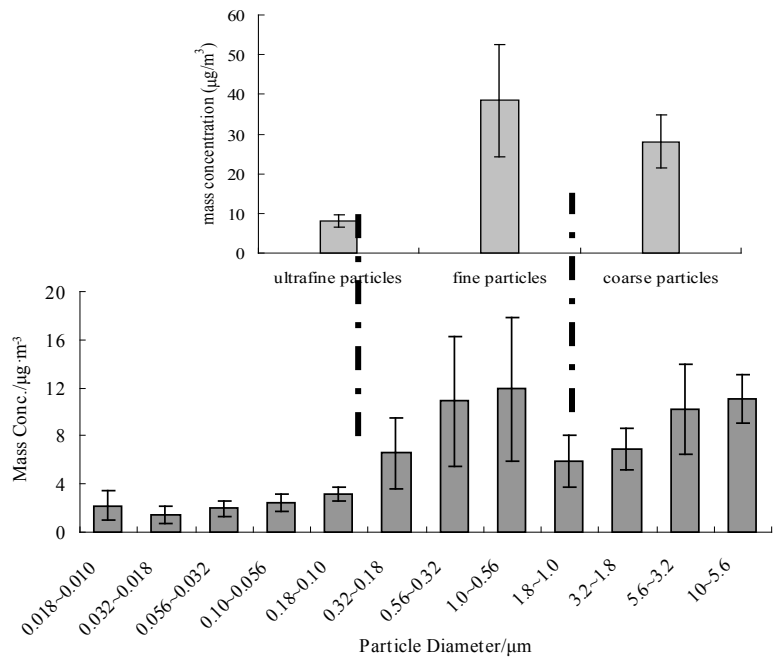


Fig. 1. Mass concentrations of size-segregated particles collected in Shanghai atmosphere

(2) Microscopic character of the ambient size-resolve particles

The SEM results demonstrated that microscopic characterization of Shanghai different size particles showed differently. Based on SEM morphological character (Figure 2) and EDX spectrum (data not show), individual particles in Shanghai atmosphere could be identified as irregular mineral particles (with main chemical elements, Si, Al, K, Na), regular mineral particles (S, O, Cl, Na), fly ash (Si, Al, O), Soot particles (Carbon) and unidentified particles. The Shanghai coarse particles were mainly composed by mineral particles (figure 2-a), fine particles were dominated by mineral particles, soot aggregates, fly ashes and unidentified particles (figure 2-b, 2-d~i), and ultrafine particles composed by soot particles (figure 2-c).

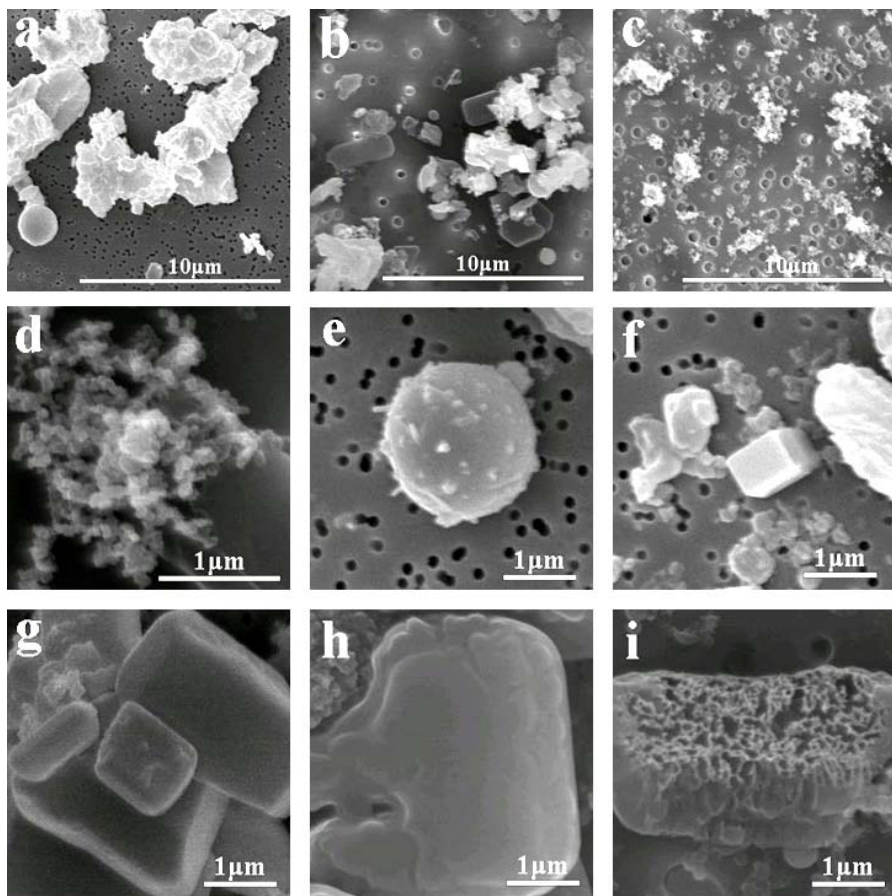


Fig. 2. SEM microphotographs of size-segregated particles: a. coarse particles; b. fine particles; c. ultrafine particles; d. soot aggregates; e. fly ash; f,g. mineral particles; h,i. irregular particles

(3) *Chemical elements analysis*

Our results showed that Si, Ca, Fe, K were the most abundant crustal elements, while S, Zn, Pb were the most rich anthropogenic elements in the Shanghai size-resolved particles (figure 3). Silicon was the richest elements in the measured elements, its highest mass concentration ($892.36 \text{ ng}\cdot\text{m}^{-3}$) was found in the size range of $5.6\sim 3.2\mu\text{m}$ and the lowest mass level ($25.10 \text{ ng}\cdot\text{m}^{-3}$) was in $0.032\sim 0.018\mu\text{m}$ (figure 6), mass concentration of silicon ($1385.84 \text{ ng}\cdot\text{m}^{-3}$) was the highest in the coarse particles, while sulfur ($1124.29 \text{ ng}\cdot\text{m}^{-3}$) was the highest in fine particles with the value of, which attributed to Xujiahui being located in urban centre and coal combustion from thermal power generation and daily life. Mass concentrations of the soil-derived elements K, Ca, Fe were higher in coarse particles, and the mass concentrations of the toxic metal Zn, Pb were higher than those of other trace elements, owing to automobile exhaust emissions in Xujiahui region. All elements in the ultrafine particles were very low.

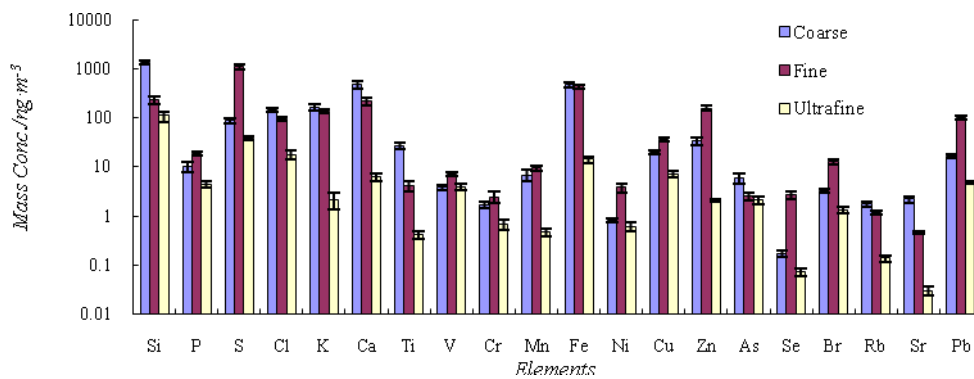


Fig.3. The mass concentrations of 20 elements in coarse, fine and ultrafine particles

(4) Source apportionment

Enrichment factor (EF) is used to analyze source apportionment of the size-resolved particles in Shanghai atmosphere. EF value is calculated by using the following equation:

$$EF_i = \frac{(M_i/M_r)_{PM}}{(M_i/M_r)_{Crust}}$$

Ti was selected as the reference element.

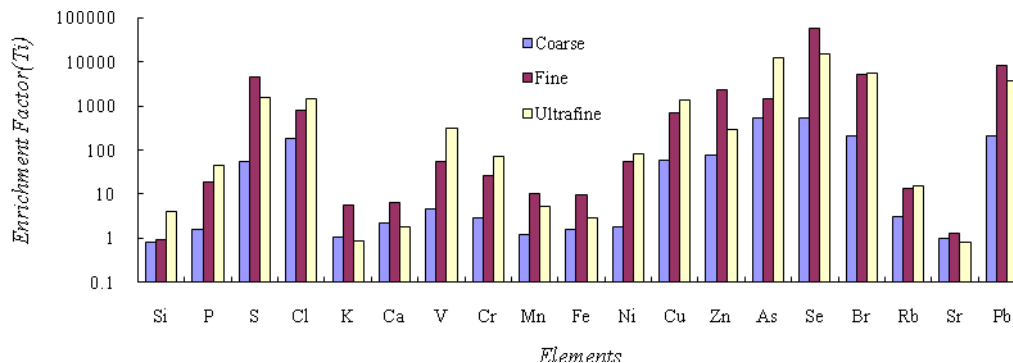


Fig. 4. The enrichment factor of elements in Shanghai ambient coarse, fine ,ultrafine particles. The Fig.4 showed that the enrichment factor values of the coarse, fine and ultrafine particles different. Anthropogenic chemical elements, such as P, S, Cl, V, Cr, Ni, Cu, Zn, As, Se, Br, Pb, were enriched in fine and ultrafine particles. Crustal elements were rich in the coarse particles.

CONCLUSIONS

- (1) Average mass concentrations of coarse particles, fine particles and ultrafine particles in Shanghai summer (from 27, August to 10, September, 2008) atmosphere were 46.51 ± 14.38 , 74.63 ± 19.59 , $2.19 \pm 1.24 \mu\text{g} \cdot \text{m}^{-3}$ respectively. The mass ratio of $\text{PM}_{0.1 \sim 1.8}/\text{PM}_{10}$ was 0.62 ± 0.06 , indicating that fine particles dominated the total mass of PM_{10} .
- (2) The coarse particles were dominated by minerals, fine particles by soot aggregates and fly ashes, and ultrafine particles by soot particles and unidentified particles.

- (3) Crustal elements, such as Si, Ca and Fe were mainly found in coarse particles. Sulphate, emitted from coal combustion, could be found in different size fractions. The anthropogenic elements (Cr, Mn, Ni, Cu, Zn, Pb) were higher in the fine particle fraction compared with that of coarse particles and ultrafine particles.

ACKNOWLEDGMENTS

The research was granted by the NSFC (Grant No. 10775094, 40973072) and by Shanghai Pujiang Talent Program, the Shanghai Committee of Science and Technology (Grant No. 10JC1405500), Innovation Program of Shanghai Municipal Education Commission, Shanghai Leading Academic Discipline Project (No. S30109).

REFERENCES

- [1] Dockery, D.W., Pope, C.A.. Acute respiratory effects of particulate air pollution. Annual Review of Public Health, 1994, 15:107-132.
- [2] Hetland R.B., Cassee F.R. M. Refsnæs,. Release of inflammatory cytokines, cell toxicity and apoptosis in epithelial lung cells after exposure to ambient air particles of different size fractions. Toxicology in Vitro, 2004, 18:203-212.
- [3] Wu Z.J., Hu M., Lin P.. Particle number size distribution in the urban atmosphere of Beijing, China. Atmospheric Environment, 2008, 42:7967-7980
- [4] Allen A.G., Nemitz E., Shi J.P.. Size distributions of trace metals in atmospheric aerosols in the United Kingdom. Atmospheric Environment, 2001, 35:4581-4591
- [5] Lin C., Chen S., Huang K.. Characteristics of metals in nano/ultrafine/fine/coarse particles collected beside a heavily trafficked road. Environmental science and technology, 2005, 39, 21, 8113~8122.
- [6] Lu Senlin, Yao Zhenkun, Chen Xiaohui, Wu Minghong, Sheng Guoying, Fu Jiamo, Daly Paul. Physicochemical characterization and potential toxicity of fine Particulate matter (PM_{2.5}) in Shanghai Atmosphere. Atmospheric Environment, 2008, 42, 7205~7214.
- [7] Li X., Yue W., Iida A.. A study of the origin of individual PM_{2.5} particles in Shanghai air with synchrotron X-ray fluorescence microprobe. Nuclear Instruments and Methods in Physics Research B, 2007, 260:336-342
- [8] Senlin Lu, Man Feng, Zhenkun Yao, An Jing, Zhong Yufang, Minghong Wu, Guoying Sheng, Jiamo Fu, Shinich Yonemochi, Jinping Zhang, Qingyue Wang, Ken Donaldson. Physicochemical characterization and cytotoxicity of ambient coarse,fine, and ultrafine particulate matters in Shanghai atmosphere. Atmospheric Environment, 2011, 45, 736-744

Pollution Situation and Possible Markers of Different Sources in the Ordos Region, Inner Mongolia, China

Wenjie Zhang*, Jianhua Chen, Zhipeng Bai, Wen Yang, Baohui Yin and Wei Wang

Chinese Research Academy of Environmental Sciences, Beijing 100012, China

Principal Contact: Wenjie Zhang, Associate Professor, Chinese Research Academy of Environmental Sciences, No. 8, Dayangfang, Anwai, Chaoyang District, Beijing, 100012, China.
Tel: 010-84915246 Fax: 010-84935950 Email: zhangwj@craes.org.cn

Abstract

A systematic study on the gaseous and particulate pollution in the Ordos Region of Inner Mongolia was performed during 9–24 September 2005, the gaseous pollutants SO₂, NO, NO₂, O₃, and CO, and the particulates PM₁₀ and PM_{2.5} were sampled at five sites in the Ordos Region. Within the aerosol, species measured were 21 elements, 10 ions, organic carbon (OC), elemental carbon (EC), and the acid-buffering capacity of PM₁₀ and PM_{2.5}. The pollution situation in Ordos Region was studied, and possible markers of different sources direction were investigated among the species measured above. None of the gases exceeded the national standards of China. PM_{2.5} contributed most to PM₁₀ at the background site, indicating the greatest contribution of regional transport. Organic matter, crustal material, and sulfate ion were the three dominant species of aerosol, followed by EC, NO₃⁻, NH₄⁺, trace elements, and other ions. The acidity of PM_{2.5} was higher than that of PM₁₀, and the buffering capacity in PM₁₀ was higher than in PM_{2.5}. Four peaks of pollution aerosol (elements and ions) were observed, separated by periods of cleaner air. Back-trajectories revealed that the peaks came from the south and the cleaner air from the north. It is the first time to find different markers for different direction aerosols in Ordos. S and Pb, as well as the secondary ions, SO₄²⁻, NO₃⁻, and NH₄⁺ appeared to be good markers of southern aerosol in the Ordos district, since both showed four clear peaks. Extremely high peaks of Al and Ti on the 16th and 17th, especially at the dust-monitoring site, indicated that they were good markers for soil dust. Ca and Mg showed earlier peaks on the 16th at the western site, indicating possible markers for western aerosol.

Keywords: pollution, acid-buffering capacity, sources direction, back trajectory, markers

Chemical composition and source apportionment of PM₁₀

in Xi'an and surrounding areas

Juan Qiang¹, Wentao Li¹, and Hongmei Xu²

1 Xi'an environmental monitoring station, No.260 Youyi East Road, Xi'an, 710054

2 Institute of Earth Environment, Chinese Academy of Sciences, No.10 Fenghui South Road, Xi'an, 710075

Principal Contact: Hongmei Xu, Postgraduate, Institute of Earth Environment, Chinese Academy of Sciences, No.10 Fenghui South Road, Xi'an, 710075, China.

Tel: +86-29-88326128 Fax: +86-29-88320456 Email: xuhongmei@ieecas.cn

Abstract

The chemical characteristics and source apportionments of PM₁₀ in Xi'an and surrounding areas in 2010 were determined in this study. Totally, six sampling sites were selected in this study: four of them (named as SZF, WDJ, DHS, and CB) represent urban areas of Xi'an, one for surrounding county town (GL) from 48km west by north of Xi'an, and one for rural area in Qinling Mountain (HH) of Xi'an. The annual average concentrations of PM₁₀ were 263.2 and 211.2 $\mu\text{g}/\text{m}^3$ in urban (SZF, WDJ, DHS, CB, and GL) and rural areas (HH), respectively. Significant spatial variations of PM₁₀ in Xi'an and surrounding areas were observed, with the pattern of SZF>WDJ>DHS>GL>CB>HH.

Moreover, source apportionments were performed by EPA PMF 3.0 to identify the possible sources of PM₁₀ and to quantify their contributions in Xi'an and surrounding areas. Secondary transformation, soil dust, building dust, coal combustion, vehicular emissions were the major contributors to PM₁₀. However, the abundance of these major sources also changed with sampling sites. Besides, industrial emissions and biomass burning were the minor sources for PM₁₀ in the atmosphere of Xi'an.

Keywords: PM₁₀, Source apportionment, Xi'an

Composition of Fine Particles at Lin'an, a Background Rural Site in the Yangtze River Delta Region

Jialiang Feng, Wu Wang, Minghong Wu and Jiamo Fu

Institute of Environmental Pollution and Health, Shanghai University, Shanghai, 200444, China

Principal Contact: Jialiang Feng, Institute of Environmental Pollution and Health, Shanghai University, Shanghai, 200444, China.

Tel: 86-21-66137738 E-mail: fengjialiang@shu.edu.cn

Abstract

Fine particles are major air pollutants in China, which cause low atmospheric visibility and are harmful to human health. Lin'an is a rural site representative for the regional air pollution in the Yangtze River Delta Region. Seasonal samples of fine particles were collected in April, July, October and December of 2008 at the background air pollution monitoring station in Lin'an. Concentrations of organic carbon (OC), elemental carbon (EC), and water soluble ions including Cl^- 、 NO_3^- 、 SO_4^{2-} 、 $\text{C}_2\text{O}_4^{2-}$ 、 Na^+ 、 NH_4^+ 、 K^+ 、 Ca^{2+} 、 Mg^{2+} were measured. Compositions of the solvent extractable organic compounds (SEOC, including alkanes, PAHs, fatty acids, alkanols, levoglucosan and sugars) were also analyzed with GC-MS. High loading of fine particles (annual average of $66 \mu\text{g m}^{-3}$) were found, with obvious seasonal variation. Water-soluble ions and carbonaceous matter were the major components of the fine particles, accounting for about 40% and 30% of the mass respectively. More than half of the organic carbon measured was water soluble, indicating that the fine particles at Lin'an were transported and aged. Reasons for the observed seasonal variations of OC, EC, major ions and SEOC were discussed. Positive matrix factorization (PMF) analysis was conducted and the results showed that secondary sulfate, secondary nitrate, vehicle emissions, coal burning and biomass burning were the main sources of the fine particles at Lin'an.

Keywords: fine particles, OC/EC, water-soluble ions, SEOC, sources, PMF.

Diurnal Variation and Source Apportionment of Atmospheric Aerosols (PM₁₀) at Xiamen Bay

Tsung-Chang, Li¹, Chung-Yi Wu¹, Chung-Shin Yuan¹, Shuei-Ping Wu² and Xin-Hong Wang²

1 Institute of Environmental Engineering, National Sun Yat-sen University, Taiwan, R.O.C.

2 State Key Laboratory of Marine Environmental Science, Xiamen University, Xiamen, P.R.C.

Principal Contact: Chung-Shin Yuan, Prof., Institute of Environmental Engineering, National Sun Yat-sen University, No. 70, Lienhai Rd., Kaohsiung 80424, Taiwan, R.O.C.

Tel: 886-7-5252000 ext 4409 Fax: 886-7-5254409 E-mail:ycsngi@mail.nsysu.edu.tw

Abstract

This study characterized the chemical composition of daytime and nighttime atmospheric particles sampled at Xiamen Bay located at the west bank of Taiwan Strait at both air pollution event and background period. Ten particulate matter (PM) sampling sites at Xiamen Bay, including five sites at Kinmen Island and five sites at metro Xiamen, were selected for this particular study. Regular sampling was conducted to collect PM₁₀ with high-volume samplers thrice a month since April 2010 to March 2011, while intensive sampling was conducted to collect PM_{2.5} and PM_{2.5-10} with dichotomous samplers in the spring and winter of 2010-2011. Metallic elements were analyzed with an inductively coupled plasma-atomic emission spectrometry (ICP-AES). Ionic species and carbonaceous contents were analyzed with an ion chromatography (IC) and an elemental analyzer (EA), respectively. Finally, the source identification and apportionment of PM₁₀ were analyzed by principal component analysis (PCA) and receptor modeling (CMB). Results from PM sampling indicated that atmospheric particles had a tendency to be accumulated in Xiamen Bay all year round, particularly in the spring and winter. Regular PM₁₀ sampling results showed a significant diurnal variation with higher PM₁₀ concentrations during the daytime compared to nighttime. Chemical analysis results showed that major chemical components of PM₁₀ were SO₄²⁻, NO₃⁻, NH₄⁺, OC, and EC and crustal elements (Ca, Mg, Fe, and Al), which were also commonly higher in the daytime than those in the nighttime at Xiamen Bay. However, the concentration of anthropogenic metallic elements (e.g. Ni, Cu, As, V) were higher in the nighttime than those in the daytime. Results from CMB receptor modeling showed that the major sources of atmospheric PM₁₀ at Xiamen Bay were soil dusts, secondary aerosols, petroleum industry, motor vehicle exhansts, iron and steel industry, diesel vehicle exhansts, marine aerosols, and biomass at Xiamen Bay.

Keywords: Xiamen Bay, Diurnal variation, CMB.

Characteristics and Sources of Ionic Species and Metallic Elements in Airborne PM_{2.5} in Busan, Korea

Gee-Hyeong Park¹, Jeong-Gu Cho¹, Byeong-Kyu Lee² and Atilla Mutlu²

1 Busan Institute of Health and Environment, Gwangan-4 dong, Suyeong-gu, Busan, Korea

2 Department of Civil and Environmental Engineering, University of Ulsan, 102 Daehak-ro, Nam-gu, Ulsan, Korea (corresponding author).

ABSTRACT

Daily PM_{2.5} samples were collected from March to October in 2010 in Busan, Korea. Ionic species and carbon species, and metallic elements were identified to characterize chemical composition in airborne PM_{2.5} samples. Daily mean concentrations of PM_{2.5} ranged from 6.7 to 59.8 μgm^{-3} and the arithmetic mean concentration over the study period was $23.5 \pm 11.6 \mu\text{gm}^{-3}$. High mass concentrations over $35 \mu\text{gm}^{-3}$ were observed on primarily mist and haze episode days and also under stabilized atmospheric conditions except Asian dust event period. Composition of PM_{2.5} were 41% of ionic species, 2% of metallic elements, 26% of carbonic species and 31% of the others including particle bound water, and etc. Sulfate, ammonium, and nitrate were the most abundant ionic species and nss-SO₄²⁻ (0.44), NO₃⁻ (0.48), Mg²⁺ (0.52), and NH₄⁺ (0.44) showed significant correlations ($p<0.01$) with PM_{2.5} concentrations. Major metallic elements were composed of soil related species like Fe and Al. From a positive matrix factorization (PMF) receptor modelling analysis for source profiles of ionic species and metallic elements in airborne PM_{2.5} samples, seven sources were identified as follows; 1) soil and industry related sources, 2) secondary particle 3) sea-salt related, 4) paved road related, 5) mobile and combustion related, 6) coal combustion, 7) biomass burning.

KEYWORDS

PM_{2.5}, Ionic species, Metallic elements, Mist and haze episode, PMF modeling

Introduction

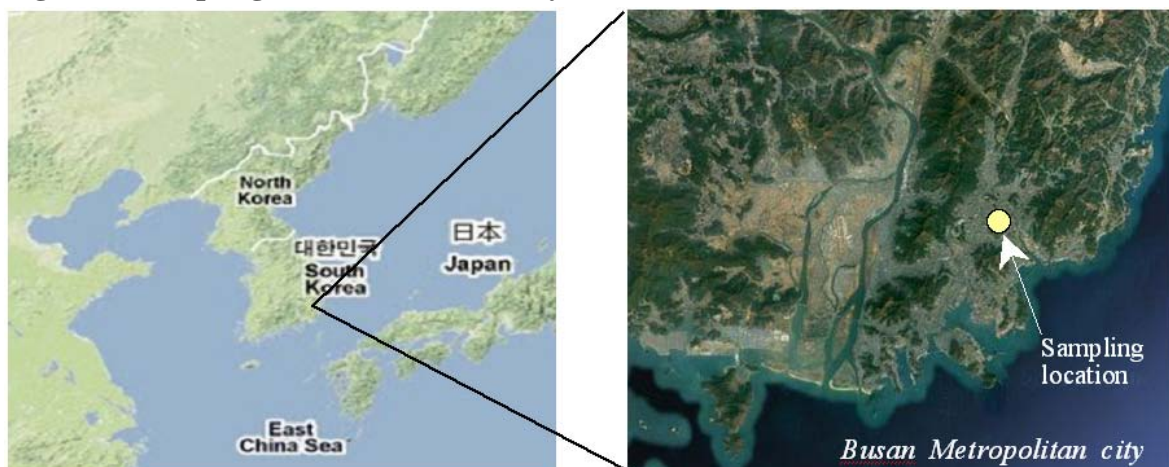
Atmospheric particulate matter (PM) affects climate, environment, visibility and health through a great variety of processes [1-2]. Fine particles (commonly PM_{2.5}), defined as particular matter less than or equal to 2.5 μm in an aerodynamic diameter, are of concern because they can carry toxic substances and have high deposition rates in the lungs. Fine particles in the ambient air are typically composed of complex mixtures of chemical species, originating from a wide range of natural sources and human activities, distributed over transport distances of tens to thousands of kilometers from their origins [3]. The US EPA promulgated new National Ambient Air Quality Standards for particulate matter with PM_{2.5} in 1997 [4], and revised them more strengthen (15 and 35 μgm^{-3} for annual and 24h averages,

respectively) due to its importance in 2006. Ministry of Environment in Korea has been preparing for promulgating new standards for PM_{2.5}. This study summarizes characteristics and sources of ionic species and metallic elements in PM_{2.5} collected regularly at a central area in Busan, the second largest city in Korea, for one year.

Experimental Methods

The location of sampling site as shown in Figure 1 is a representative central area of Busan metropolitan city with a population of about 3.6 millions, Korea. Daily based airborne PM_{2.5} samples were taken from March to October in 2010 every week using a PM_{2.5} sampler. Teflon filters (47 mm Zefluor PTFE) with 2.0 μm pore size and 47 mm diameter were conditioned for 24 h in a controlled-environment chamber maintained at a RH of 50±5% and a temperature of 20±2 °C before and after sampling, and then weighted for gravimetric analysis of PM_{2.5} mass concentrations. 8 water soluble ionic species were extracted from a half portion of the conditioned filter samples in 20 mL ultrapure water (specific resistance: 18.2 MΩ·cm) by using an ultrasonic bath for 2h. The extracted solution was filtered through a micro porous membrane filter (0.45 μm pore size) and stored in a refrigerator at 4 °C until chemical analysis. The analytical instruments used for measurement of the ionic species are as follows; ion chromatograph (Dionex, ICS-3000, USA) for anion species (Cl⁻, NO₃⁻, SO₄²⁻), ICP-OES (Varian, 720-ES) for cation species (Na⁺, K⁺, Ca²⁺, Mg²⁺), and automatic analyzer (BLTEC STAT-2000) for NH₄⁺. The other half portion of filter strips was utilized for measurement of metallic elements in PM_{2.5}. The metallic elements were extracted from the filter strips using 10mL HNO₃ (13%) solution in a Teflon bottle with microwave digestion for 40 min. The extracted solution was filtered and filled in a 15 mL centrifuge tube. The concentrations and components of the metallic elements were analyzed by ICP-OES (Varian, 720-ES). In order to identify sources of PM_{2.5}, this study applied advanced receptor models [5], which mainly use positive matrix factorization (PMF) of the concentration data set of the components in PM_{2.5}.

Figure 1. Sampling location for the study.



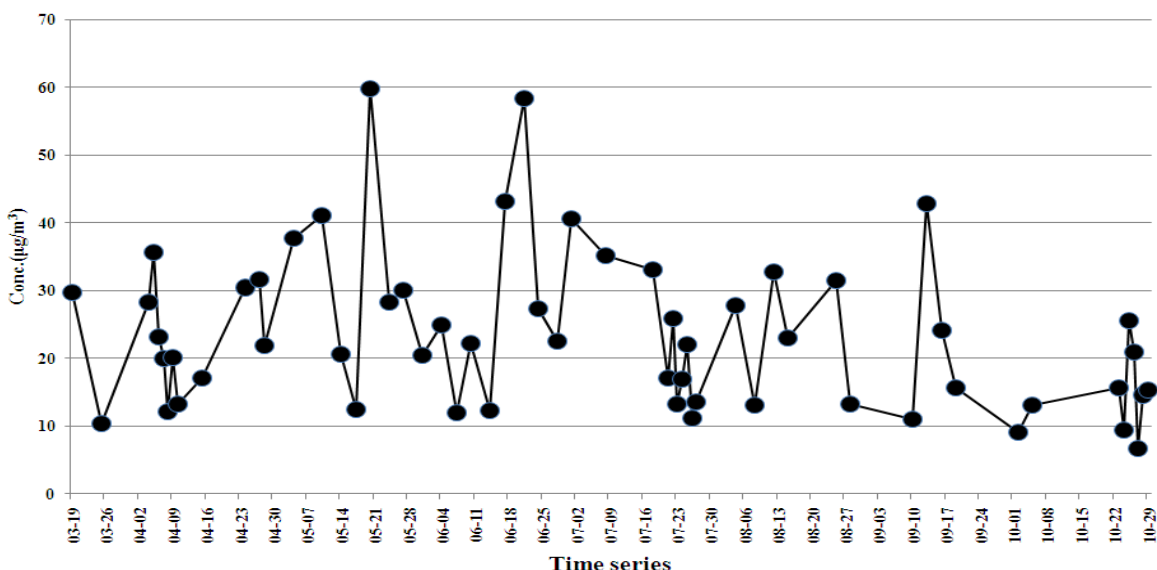
Results and Discussion

PM_{2.5} mass concentration and compositions

Time series concentrations of airborne PM_{2.5} collected from the central area of Busan during the study periods were shown in Figure 2. Daily mean concentrations ranged from 6.7 to 59.8 μgm^{-3} , and the mean and median concentrations of PM_{2.5} were 23.5 and 22.0 μgm^{-3} , respectively. High mass concentrations over 35 μgm^{-3} of PM_{2.5} were mainly observed in mist and haze episode days. Ionic species strongly contributed to the mass of PM_{2.5} with 41%, whereas metallic elements only accounted for 2% of the mass of PM_{2.5}. Carbon species (EC and OC) were 26% of PM_{2.5} mass and the unidentified other species, including particle bound water and pollen, were 31% of the mass of PM_{2.5}.

The statistical results of concentrations of mass and ionic species in PM_{2.5} were presented in Table 1. Total anion and cation concentrations were 6.615 and 3.121 μgm^{-3} , respectively, which account for 28% and 13% of the total mass of PM_{2.5}, respectively. The ratio of identified anions to cations exceeded 2.1, which indicates acidic characteristics of ambient fine particulate. For example, the pHs of the precipitation (rain fall) measured in Kwangan-dong, a downtown area, of Busan during the study period ranged from 4.3 to 5.0 with an average of 4.6 which shows fairly acidic characteristics [6].

Figure 2. A time series variation of ambient PM_{2.5} concentrations.



The identified concentrations of the major ions in PM_{2.5} during the study period followed the order of SO₄²⁻>NO₃⁻>NH₄⁺>Cl⁻>Na⁺>Ca²⁺>Mg²⁺>K⁺. SO₄²⁻, NH₄⁺, and NO₃⁻ were the most prominent ionic species in PM_{2.5} composition and they showed high correlations with PM_{2.5} concentrations. Sulfate concentration which is a major ionic constituent of the PM_{2.5} composition accounted for 35% of the total concentrations of the identified ions. The fraction of the non-sea salt sulfate (nss-sulfate) over the total sulphate concentrations was 96%.

Although Busan is located in near coastal areas, the contribution of sea-salts to the total

sulfates in fine particles was a very small fraction, indicating substantial anthropogenic origins of PM_{2.5} components.

Table 1. Statistical results of concentrations of PM_{2.5} and ionic species (unit : μgm^{-3})

Statistics	PM _{2.5}	Cl ⁻	NO ₃ ⁻	ss-SO ₄ ²⁻	nss-SO ₄ ²⁻	Na ⁺	NH ₄ ⁺	K ⁺	Mg ²⁺	Ca ²⁺
Mean	23.5	0.664	2.569	0.150	3.231	0.598	1.766	0.079	0.103	0.574
Median	22.0	0.479	1.553	0.184	2.398	0.735	0.958	0.070	0.098	0.525
SD	11.6	0.756	2.380	0.082	2.215	0.325	2.008	0.044	0.027	0.173
Max	59.8	3.012	9.583	0.274	9.611	1.091	7.814	0.213	0.195	1.331
Min	6.7	0.001	0.202	0.005	0.157	0.020	0.222	0.000	0.069	0.334

The statistical result of the metallic elements in PM_{2.5} was presented in Table 2. The concentration fractions of the metallic elements are relatively low level as compared those of ionic and carbonic species. High fractions of the metallic elements in ambient fine particles are occupied by the soil related species, such as Fe and Al, followed by the concentration fractions of Zn, Pb, and Mn, which are major metallic components with significant relations to anthropogenic sources. In particular, the identified maximum concentration of As, one of carcinogenic heavy metals, was 21.6 ng/m³ which much exceeds the ambient air quality standard (6 ng/m³) of As proposed as a target value to be effective from the end of 2012 in European Union.

Table 2. Statistical results of metallic species (unit : ng/m³)

	Fe	Al	Zn	Pb	Mn	Cu	V	Ni	As	Cr	Se	Cd	Sr	Co
Mean	133.9	119.4	40.9	26.1	10.8	3.8	2.8	3.1	2.8	0.8	0.7	1.0	0.5	2.0
Median	119.3	74.0	38.8	22.8	9.6	3.6	2.0	2.8	1.4	0.4	0.2	0.9	0.3	1.1
SD	101.4	164.5	22.1	14.9	6.8	2.4	3.2	1.7	4.3	1.0	1.0	0.5	1.0	2.2
Max	522.1	892.5	110.3	61.9	35.9	13.1	17.2	9.0	21.6	4.1	3.5	2.7	6.3	7.5
Min	17.9	0.0	7.5	2.2	1.3	0.2	0.0	0.1	0.0	0.0	0.0	0.1	0.0	0.0

Correlation Analysis

Table 3 shows the correlation analysis result between PM_{2.5} and ionic species and between ionic species. PM_{2.5} concentrations showed significant correlations ($p<0.01$) with Mg²⁺ (.524), NO₃⁻ (.479), nss-SO₄²⁻ (.440), and NH₄⁺ (.437). There were also significant correlations between the ionic species as follows; NO₃⁻ with Cl⁻ (.594), NH₄⁺ with ss-SO₄²⁻ (.403), nss-SO₄²⁻ (.681), and Na⁺ (.403), K⁺ with ss-SO₄²⁻ (.445), nss-SO₄²⁻ (.536), Na⁺ (.444), and NH₄⁺ (.645), Mg²⁺ with Cl⁻ (.362) and NO₃⁻ (.738), and Ca²⁺ with NO₃⁻ (.499), ss-SO₄²⁻ (.471), Na⁺ (.471), NH₄⁺ (.420), K⁺ (.456), and Mg²⁺ (.631).

Table 3. Correlation analysis result of PM_{2.5} and ionic species.

	PM _{2.5}	Cl ⁻	NO ₃ ⁻	nss-SO ₄ ²⁻	ss-SO ₄ ²⁻	Na ⁺	NH ₄ ⁺	K ⁺	Mg ²⁺	Ca ²⁺
PM _{2.5}	1.000									
Cl ⁻	0.316 **	1.000								
NO ₃ ⁻	0.479 **	0.594 **	1.000							
nss-SO ₄ ²⁻	0.440 **	-0.175	0.109	1.000						
ss-SO ₄ ²⁻	0.285 **	0.325 **	0.217 *	0.122	1.000					
Na ⁺	0.285 **	0.325 **	0.217 *	0.122	1.000	1.000				
NH ₄ ⁺	0.437 **	-0.007	0.264 **	0.681 **	0.403 **	0.403 **	1.000			
K ⁺	0.268 **	-0.098	0.249 **	0.536 **	0.445 **	0.444 **	0.645 **	1.000		
Mg ²⁺	0.524 **	0.362 **	0.738 **	0.092	0.250 **	0.250 **	0.255 **	0.210 *	1.000	
Ca ²⁺	0.312 **	0.201 *	0.499 **	0.228 **	0.471 *	0.471 **	0.420 **	0.456 **	0.631 **	1.000

*,** is significant at the confident level of 95, 99%

PMF receptor modeling

PMF analysis was performed using data collected at the study site. From the PMF receptor modelling analysis for source profiles of ionic species and metallic elements in airborne PM_{2.5} samples, seven source factors were identified as follows; 1) soil and industry related sources, 2) secondary particle, 3) sea-salt related, 4) paved road related, 5) mobile and combustion related, 6) coal combustion, 7) biomass burning.

SUMMARY

Arithmetic and median concentrations of PM_{2.5} observed in a central area of Busan, the second largest city in Korea, 23.5 and 22.0 μgm^{-3} , respectively, with a range of 6.7 to 59.8 μgm^{-3} . High mass concentrations over 35 μgm^{-3} of PM_{2.5} were mainly observed in mist and haze episode days. NH₄⁺, SO₄²⁻, and NO₃⁻ were main ionic species in PM_{2.5} and they showed relatively high correlations with PM_{2.5} mass concentrations. PM_{2.5} also have significantly correlated with nss-SO₄²⁻(.440), NO₃⁻(.479), Mg²⁺ (.524), and NH₄⁺(.437). From a PMF receptor modelling analysis, seven sources contributing to PM_{2.5} were identified as soil and industry related sources, secondary particles, sea-salts, paved road related sources, mobile and combustion, coal combustion, and biomass burning.

REFERENCES

- [1] Pope, C.R.; Burnett, R.; Thun, M.J.; Calle, E.; Krewski, D.; Ito, K.; Thurston, G. Lung cancer, cardiopulmonary mortality, and long-term exposure to fine particulate air pollution. *J. Am. Med. Assoc.* 2003, 287, 1132–1141.
- [2] Zhao, X.; Zhang, X.; Xu, X.; Xu, J.; Meng, W.; Pu, W., Seasonal and diurnal variations of ambient PM2.5 concentration in urban and rural environments in Beijing. *Atmos. Environ.* 2009, 43, 2893–2900.

- [3] Seinfeld, J.H.; Pandis, S.N. In *Atmospheric Chemistry and Physics*. John-Wiley & Sons Inc., Toronto, 2006.
- [4] U.S. Environmental Protection Agency (US EPA). *National Air Quality and Emission Trends Report*. EPA-454/R-97-013, Research Triangle Park, NC 27711, 1996.
- [5] U.S. Environmental Protection Agency (US EPA). *Protocol for Applying and Validating the CMB Model for PM2.5 and VOC*. <http://www.epa.gov/scram001>.
- [6] Busan Institute of Public Health and Environment. Acidic deposition of year 2010. http://heis.busan.go.kr/environmental/eair_06_002.aspx?&yearselect=8&year=2010.

Global In-cloud Production of Secondary Organic Aerosols (SOA) based on Detailed Aqueous-Phase Chemistry

Junfeng Liu^{1,2}, Larry W. Horowitz¹, Songmiao Fan¹ and Hiram Levy II¹

1 Geophysical Fluid Dynamics Laboratory, GFDL/NOAA, Princeton, NJ, 08540

2 Atmospheric and Oceanic Sciences Program, Princeton University, Princeton, NJ, 085441

Principal Contact: Junfeng Liu, Associate Research Scholar, Princeton University, 201 Forrestal Road, Princeton, New Jersey, 08540.

Tel: 1-609-452-5346 Email: Junfeng.Liu@noaa.gov

Abstract

Substantial evidence has shown that oxidation of water-soluble volatile organic species in cloud droplets could lead to the formation of secondary organic aerosols (SOA). However, very few studies currently have been made to quantify this SOA source in a global scale. In this study, we estimate global in-cloud SOA production based on the fully coupled chemistry-climate model AM3, recently developed at Geophysical Fluid Dynamics Laboratory (GFDL/NOAA). To quantify in-cloud SOA production, both parameterization (based on cloud parcel model) and a detailed aqueous-phase chemistry mechanism (including sulfur and SOA chemistry) in conjunction with microphysics for gas-liquid transfer are developed. Currently, six cloud SOA species are simulated, including Glycolic acid, Glyoxylic acid, Pyruvic acid, Oxalic acid, as well as two types of oligomers formed from glyoxal and methylglyoxal upon cloud evaporation. Cloud properties (i.e., cloud droplet size, cloud fraction, liquid water content) from large-scale condensation are enhanced coupled into the aqueous-phase chemistry. Cloud PH values are determined on-line by electroneutrality equation.

We find that for years around 2000, global in-cloud SOA production is about 10 Tg/yr if assuming cloud droplet lifetime (τ_{cloud}) is 30 min. Shrinking τ_{cloud} to 10 min will raise this production by 20%, mostly due to the increase in oligomers' formation. This is opposed to the parameterized results which show a 40% reduction. We find that most of the SOA production are distributed in the tropical and mid-latitude regions between 800-600hPa. In DJF, western Amazon and southern Africa are the major source regions. While in JJA (the northern summer), in-cloud SOA is heavily produced over southern China as well as the boreal forest regions over Eurasia and North America. Our estimation indicates that in-cloud SOA production accounts for ~30% of total SOA sources, which could directly and indirectly influence radiation balance and global climate as well.

Keywords: Secondary Organic aerosol, in-cloud production, aqueous phase chemistry, radiative forcing

Effects of FeSO₄ Seeds on Secondary Organic Aerosol Formation from Photooxidation of α -pinene/NO_x and Toluene/NO_x

Biwu Chu¹, Junhua Li¹, Jiming Hao¹, Hideto Takekawa² and Kun Wang¹

1 School of Environment, Tsinghua University, Beijing 100084, China

2 Toyota Central Research and Development Laboratory, Nagakute, Aichi, 480-1192, Japan

ABSTRACT

A series of photooxidation experiments with α -pinene and toluene in the presence of nitric oxides (NO_x) were conducted using a Tsinghua-Toyota smog chamber. Both gas phase compounds and secondary organic aerosol (SOA) concentrations were measured in each experiment. Iron(II) sulfate (FeSO₄) or iron(III) sulfate (Fe₂(SO₄)₃) seeds were introduced to observe their effect on photochemical reactions. FeSO₄ seeds indicate negative effects on SOA formation. However, the effects of FeSO₄ seeds on gas phase compounds, including ozone (O₃), nitrogen oxides (NO_x) and hydrocarbons (HC), are not obvious. Nor are effects of Fe₂(SO₄)₃ seeds on SOA formation observed. Based on the experiment results, a preliminary mechanism for FeSO₄ seeds' effects during the photooxidation process is proposed. The reduction of oxidized products of hydrocarbons is not sufficient for explaining the suppression effects of FeSO₄ seeds on SOA formation and some catalytic action of ferrous iron during SOA formation may be existed.

KEYWORDS

Secondary Organic Aerosol (SOA), FeSO₄ seeds, Fe₂(SO₄)₃ seeds, α -Pinene, Toluene

BODY

Introduction

There are various volatile organic compounds (VOCs) in the atmosphere, including anthropogenic sources VOCs, such as aromatics (1), and biogenic sources VOCs, such as terpenes (2). The photooxidation of these organics and subsequent partition of oxidized products between gas and particulate phases generate secondary organic aerosol (SOA). SOA can significantly contribute to the air particulate burden (3-4) and has a significant influence on human health (5), visibility degradation (6) and climate change (7).

However, the controlling factors, especially the effects of particulate matter (PM) seeds, remain highly uncertain. In order to identify the effects of co-existing inorganic seeds on SOA formation,

a series of smog experiments were conducted by different research groups (8-13). In these studies, $(\text{NH}_4)_2\text{SO}_4$ or H_2SO_4 seed was widely used to study the effect of particle acidity on SOA formation from both biogenic and aromatic hydrocarbons (8-13) and significant increases in SOA yields were observed in the presence of acidic seeds. Most of the research concludes that acid-catalyzed particle phase reactions generate additional aerosol mass by producing oligomeric products with large molecular weight and extremely low volatility (8-9, 11).

Transitional metals have very important applications in the field of catalysis due to their multivalence. Metal-containing aerosols are important components in the atmosphere. Iron has very important catalytic effects on SO_2 oxidation in the atmosphere (14). In addition, it is reported that Fe(II) is a major contributor to total iron at certain atmospheric conditions (15). This study investigated the effects of Fe-containing aerosol seeds on SOA formation and considered its mechanism.

Experimental Methods

The experiments were carried out in a smog chamber which was described in detail in Wu et al. (16). The 2 m^3 cuboid reactor, constructed with $50 \mu\text{m}$ -thick FEP-Teflon film (Toray Industries, Inc. Japan), was located in a temperature controlled room (Escpec SEWT-Z-120) and irradiated by 40 black lights (GE F40T12/BLB, peak intensity at 365 nm). Seed particles were generated by atomizing FeSO_4 and $\text{Fe}_2(\text{SO}_4)_3$ salt solutions using a constant output atomizer (TSI Model 3076). The generated particles were passed through a diffusion dryer (TSI Model 3062) and neutralizer (TSI Model 3077) to remove water and to bring the aerosol to an equilibrium charge distribution, respectively.

Using the smog chamber, a series of experiments were conducted for α -pinene and toluene photooxidation in the presence of NO_x . Experimental conditions were designed with different initial hydrocarbon concentrations (HC_0) or different initial FeSO_4 seeds concentrations (PM_0) for comparative analysis. Since temperature (17), RH (18) and ratio of hydrocarbon to NO_x (19) might have significant influence on SOA formation, all the experiments were carried out with a temperature of $30 \pm 0.5^\circ\text{C}$ and 48.5~50.5%RH. The initial ratio of hydrocarbon to NO_x was fixed to 20 and 70 of the molar ratio of C:N for the system of α -pinene and toluene, respectively. During each experiment, the hydrocarbon, NO_x , O_3 and size distribution (17-1000 nm) of PM were monitored by gas chromatograph (GC, Beifen SP-3420, equipped with a DB-5 column and flame ionization detector), NO_x analyzer (Thermo Environmental Instruments, Model 42C), O_3 analyzer (Thermo Environmental Instruments, Model 49C) and scanning mobility particle sizer (SMPS, TSI 3936), respectively. The volume concentration of aerosols was estimated from the measured size distribution by assuming the particles were geometrically spherical.

Results and Discussion

Estimating the Generated SOA Mass (M_o) and SOA Yields(Y)

Due to deposition of PM on Teflon film, the measured aerosol concentration had to be corrected. Takekawa et al. (17) developed a particle size-dependent correction method, in which the aerosol deposition rate constant ($k(d_p)$, h^{-1}) is a four-parameter function of particle diameter (d_p , nm):

$$k(d_p) = a \bullet d_p^b + c \bullet d_p^d \quad (\text{Eq.1})$$

After deposit correction, SOA mass (M_o) were obtained based the volume concentration of aerosols measured by the SMPS system after deducting initial seeds concentration (PM_0) using a unit density (1.0 g/cm^3) in this work.

The fractional SOA yield (Y) was used to represent aerosol formation potential of the introduced hydrocarbon in the chamber (20). Odum et al. (21) developed a gas/particle absorptive partitioning model to describe the phenomenon that Y largely depended on the amount of organic aerosol mass present:

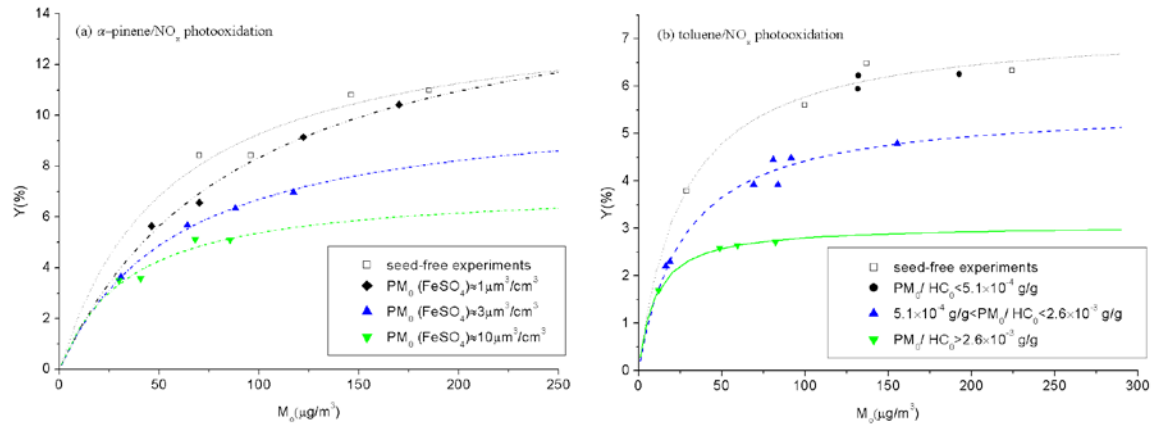
$$Y = \frac{\Delta M_o}{\Delta HC} = \frac{\sum_i A_i}{\Delta HC} = M_o \sum_i \frac{\alpha_i K_{om,i}}{1 + K_{om,i} M_o} \quad (\text{Eq.2})$$

In Eq. 2, i presents the serial number of oxidized products of the hydrocarbon, A_i , α_i and $K_{om,i}$ ($m^3/\mu\text{g}$) are the aerosol mass concentration, the stoichiometric coefficient and the partitioning constant for product i respectively. If we assume that all semi-volatile products can be classified into one or two groups, Eq. 2 can be simplified to a one-product model (i.e. $i=1$) or two-product model (i.e. $i=2$). A one-product model was used to present our experimental SOA yield data.

Effects of $FeSO_4$ Seeds on SOA Formation in α -Pinene/ NO_x Photooxidation

In our experiments, $FeSO_4$ seeds were found to have no significant effect on gas-phase reactions. This result is consistent with the results of the experiments with $CaSO_4$ and $(NH_4)_2SO_4$ seeds using our smog chamber (13, 22) and the findings of Kroll et al.(23) and Cao et al. (9) that $(NH_4)_2SO_4$ and $(NH_4)_2SO_4/H_2SO_4$ seeds had a negligible effect on hydrocarbon oxidation.

Figure 1. SOA yield (Y) variations as a function of generated SOA mass (M_o) from α -pinene/ NO_x (a) and toluene/ NO_x (b) photooxidation



However, in the 16 irradiated toluene/ NO_x /air experiments, it seems that FeSO_4 seeds have very important effects on SOA formation, indicated from the variations of PM with time at similar α -pinene concentrations. The 16 experiments were classified into four groups by the amount of FeSO_4 seeds introduced to draw the SOA yield curves, shown in Figure 1(a). The regression lines for each group were produced by fitting the data of generated SOA mass (M_o) and SOA yield (Y) into a one-product partition model. As indicated in Figure 1(a), the four SOA yield curves had similar shapes, but experiments with higher concentration of FeSO_4 seeds introduced had lower yield curves.

Effects of FeSO_4 Seeds on SOA Formation in Toluene/ NO_x Photooxidation

We conducted 18 irradiated toluene/ NO_x /air experiments, significant suppression effects on SOA formation were also found. The 18 experiments with FeSO_4 seeds were classified into four groups by the ratio of mass concentration of FeSO_4 seeds to initial toluene concentrations ($\text{FeSO}_4/\text{toluene}$) to draw SOA yield variations as a function of generated SOA mass, which is shown in Figure 1(b). Experiments with different ratios of $\text{FeSO}_4/\text{toluene}$ seemed to fall into different yield curves. When the mass ratio of $\text{FeSO}_4/\text{toluene}$ is lower than $5.1 \times 10^{-4} \text{ g/g}$, FeSO_4 seed has a negligible effect. When the mass ratio of $\text{FeSO}_4/\text{toluene}$ is higher than $5.1 \times 10^{-4} \text{ g/g}$, the lower yield curve is obtained from the experimental results with higher mass ratio of $\text{FeSO}_4/\text{toluene}$. This indicates that a higher ratio of Fe/C has more suppression effect on SOA formation from toluene/ NO_x photooxidation.

Effects of $\text{Fe}_2(\text{SO}_4)_3$ Seeds in Toluene/ NO_x Photooxidation

A series of toluene/ NO_x photooxidation experiments with and without $\text{Fe}_2(\text{SO}_4)_3$ seeds were carried out and similar PM profiles were obtained, indicating $\text{Fe}_2(\text{SO}_4)_3$ seeds has no obvious

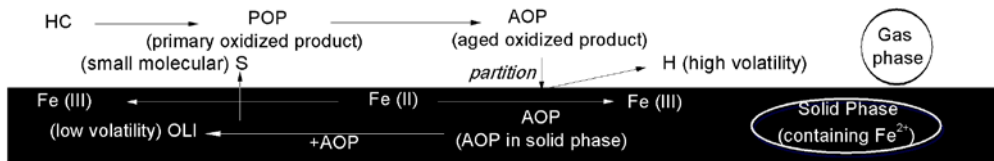
effect on SOA formation from toluene/NO_x photooxidation. The inert effect of Fe₂(SO₄)₃ seeds may also indicate that FeSO₄ seeds are not likely to be a redox catalyst and cause SOA generation reduced.

Hypothesis for FeSO₄ Seeds' Effects

Since that FeSO₄ seeds don't have obvious effects on gas phase compounds it is assumed that FeSO₄ seeds play roles mainly in particulate phase. There are two possible reasons of FeSO₄ seeds' negative effect on SOA formation. One is the strong reducibility of ferrous iron, and the other is the possible catalytic reaction of ferrous iron during the SOA formation process. A possible mechanism is shown in Figure 2.

Figure 2. Hypothesized mechanism for FeSO₄ seeds' negative effect:

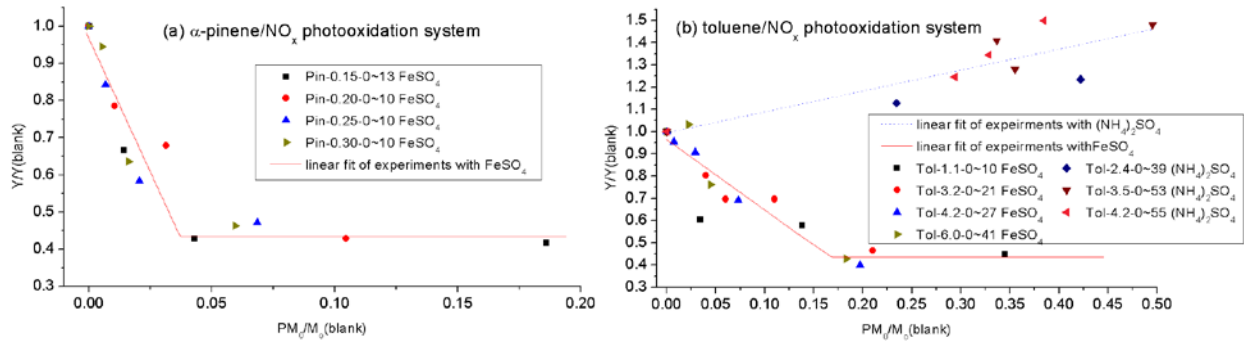
- (1) ferrous iron Fe (II) reduces aged oxidized products (AOP) of precursors, generating high volatility compounds (H);
- (2) ferrous iron Fe (II) reacts with oligomers (OLI), generating small molecular compounds (S)



First, when the oxidized products of precursors with a lower saturation vapor pressure partition between gas and particle and contact ferrous iron with strong reducing properties, they may react and produce ferric iron and reduced organic compounds (H). The reduced organic compounds have a high saturation vapor pressure enough to vaporize into gas phase.

Using the ratio of introduced seeds concentration to the generated SOA mass of the seed-free experiments with a similar initial hydrocarbon concentration, signed as PM₀/M₀(blank), and the ratio of the SOA yields between experiments with FeSO₄ seeds and the seed-free experiment with a similar initial hydrocarbon concentration, signed as Y/Y(blank), some quantitative analyses are possible. As indicated in Figure 3, Y/Y(blank) decreases linearly with increasing PM₀/M₀(blank) at lower PM₀/M₀(blank), and does not varied at high PM₀/M₀(blank). If the negative effects of FeSO₄ seeds are due to the reduction of oxidized products of hydrocarbons by ferrous ion, the fixed Y/Y(blank) value may reflect the proportion of SOA mass which would not evaporate with ferrous iron introduced, and in Figure 5, similar values (0.434 and 0.435) are found for α -pinene and toluene, while slope of the decreasing line (SDL) may be related to the molar ratio of reactants, aged oxidized product (AOP) and ferrous iron. SDLs are 14.36 and 3.17 for α -pinene and toluene, respectively.

Figure 3. The degree of negative effect of FeSO_4 seeds and positive effects of $(\text{NH}_4)_2\text{SO}_4$ seeds on SOA yield $Y/Y(\text{blank})$ as a function of relative concentration of introduced FeSO_4 seeds PM_0/M_0 (blank) in α -pinene/ NO_x (a) and toluene/ NO_x (b) photooxidation



Describing the reduction reaction as: AOP+mFe(II) —— nH+mFe(III), the reaction molar ratio of the products (n/m) and the molecular weight of H (M_H) can be roughly related as follow:

$$\frac{n}{m} \approx \text{SDL} \cdot \frac{M_{\text{FeSO}_4}}{M_H} \quad \text{Eq. 3}$$

Using Eq.3, if molecular weight of 160 g/mol is low enough to evaporate, 1 mol ferrous iron should evaporate about 3 and 13.5 mol organic compounds generated by toluene and α -pinene photooxidation, respectively. This surprisingly high reducing efficiency of ferrous iron is unreasonable, indicating the reducing of oxidized products of hydrocarbons is not sufficient for explaining the suppression effects of FeSO_4 seeds on SOA, especially in α -pinene/ NO_x photooxidation. What's more, compared to $(\text{NH}_4)_2\text{SO}_4$ seeds, the data of which were also obtained in our chamber, a larger absolute value of the SDL for FeSO_4 seeds is indicated in Figure 5(b) in toluene/ NO_x photooxidation. The negative effects of FeSO_4 seeds thus seem to be more significant than the positive effects of $(\text{NH}_4)_2\text{SO}_4$ seeds on SOA, not to mention the surprisingly effective suppression of FeSO_4 seeds in α -pinene / NO_x photooxidation.

A second possible mechanism for the suppression effects is the catalytic action of ferrous iron during SOA formation, which is also displayed in Figure 4. Ferrous iron may react with oligomer (OLI) and make it decompose, generating smaller molecular organic compounds “S” with high volatility and causing SOA reduced.

SUMMARY OR CONCLUSION

FeSO_4 seeds were found to have obvious negative effects on SOA formation in both α -pinene/ NO_x and toluene/ NO_x photooxidation system. And the reducing oxidized products of hydrocarbons by FeSO_4 seeds is not sufficient for explaining their suppression effects on SOA, and it is too difficult to propose the mechanism of the suppression effect without analyzing the components of SOA as well as gas phase products. Possible catalytic action may existed, but FeSO_4 seeds are not likely to have effects before SOA generation and not likely to be a redox

catalyst. Our research indicate that some other seeds may also have very important effects on SOA formation besides acid $(\text{NH}_4)_2\text{SO}_4$ or H_2SO_4 seeds, and it is meaningful to investigate these effects for better understanding the formation of SOA as well as controlling SOA pollution.

ACKNOWLEDGMENTS

This work was financially and technically supported by Toyota Motor Corporation and Toyota Central Research and Development Laboratories Inc.

This work was also supported by the National Natural Science Fundation of China (20937004).

REFERENCES

- (1) Wei, W.; Wang, S. X.; Chatani, S.; Klimont, Z.; Cofala, J.; Hao, J. M. *Atmos. Environ.* **2008**, 42(20), 4976-4988.
- (2) Guenther, A.; Geron, C.; Pierce, T.; Lamb, B.; Harley, P.; Fall, R. *Atmos. Environ.* **2000**, 34(12-14), 2205-2230.
- (3) Turpin, B. J.; Huntzicker, J. J. *Atmos. Environ.* **1995**, 29(23), 3527-3544.
- (4) Duan, F. K.; He, K. B.; Ma, Y. L.; Jia, Y. T.; Yang, F. M.; Lei, Y.; Tanaka, S.; Okuta, T. *Chemosphere*. **2005**, 60(3), 355-364.
- (5) Seaton, A.; Macnee, W.; Donaldson, K.; Godden, D. *Lancet*. **1995**, 345(8943), 176-178.
- (6) Appel, B. R.; Tokiwa, Y.; Hsu, J.; Kothny, E. L.; Hahn, E. *Atmos. Environ.* **1985**, 19(9), 1525-1534.
- (7) Pilinis, C.; Pandis, S. N.; Seinfeld, J. H. *J. Geophys. Res. , [Atmos.]* **1995**, 100(D9), 18739-18754.
- (8) Czoschke, N. M.; Jang, M.; Kamens, R. M. *Atmos. Environ.* **2003**, 37(30), 4287-4299.
- (9) Cao, G.; Jang, M. *Atmos. Environ.* **2007**, 41(35), 7603-7613.
- (10) Jang, M. S.; Czoschke, N. M.; Lee, S.; Kamens, R. M. *Science*. **2002**, 298(5594), 814-817.
- (11) Gao, S.; Ng, N. L.; Keywood, M.; Varutbangkul, V.; Bahreini, R.; Nenes, A.; He, J. W.; Yoo, K. Y.; Beauchamp, J. L.; Hodyss, R. P.; Flagan, R.C.; Seinfeld, J. H. *Environ. Sci. Technol.* **2004**, 38(24), 6582-6589.
- (12) Liggio, J.; Li, S. M. *Atmos. Chem. Phys.* **2008**, 8(7), 2039-2055.
- (13) Lu, Z. F.; Hao, J. M.; Takekawa, H.; Hu, L. H.; Li, J. H. *Atmos. Environ.* **2009**, 43(4), 897-904.
- (14) Freiberg, J. *Environ. Sci. Technol.* **1974**, 8(8), 731-734.
- (15) Zhuang, G. S.; Yi, Z.; Duce, R. A.; Brown, P. R. *Nature*. **1992**, 355(6360), 537-539.
- (16) Wu, S.; Lu, Z. F.; Hao, J. M.; Zhao, Z.; Li, J. H.; Takekawa, H.; Minoura, H.; Yasuda A. *Adv. Atmos. Sci.* **2007**, 24(2), 250-258.
- (17) Takekawa, H.; Minoura, H.; Yamazaki, S. *Atmos. Environ.* **2003**, 37(24), 3413-3424.
- (18) Prisle, N. L.; Engelhart, G. J.; Bilde, M.; Donahue, N. M. *Geophys. Res. Lett.* **2010**, 37.

- (19) Song, C.; Na, K. S.; Cocker, D. R. *Environ. Sci. Technol.* **2005**, 39(9), 3143-3149.
- (20) Pandis, S. N.; Harley, R. A.; Cass, G. R.; Seinfeld, J. H. *Atmos. Environ. Part A: Gen. Top.* **1992**, 26(13), 2269-2282.
- (21) Odum, J. R.; Hoffmann, T.; Bowman, F.; Collins, D.; Flagan, R. C.; Seinfeld, J. H. *Environ. Sci. Technol.* **1996**, 30(8), 2580-2585.
- (22) Lu, Z. F.; Hao, J. M.; Li, J. H.; Wu, S. *Acta Chim. Sinica.* **2008**, 66(4), 419-423.
- (23) Kroll, J. H.; Chan, A. W. H.; Ng, N. L.; Flagan, R. C.; Seinfeld, J. H. *Environ. Sci. Technol.* **2007**, 41(10), 3545-3550.

Nationwide impacts by fire emissions in the United Sates in summer 2002

Tao Zeng^{1,2} and Yuhang Wang¹

1 Georgia Institute of Technology, 311 Ferst Drive, Atlanta, GA, 30332, USA

2 Georgia Department of Natural Resources, 4244 International Parkway, Atlanta, GA, 30354, USA

Principal Contact: Tao Zeng, Research Scientist II, Georgia Institute of Technology, 311 Ferst Drive, Atlanta, GA, 30332, USA.

Tel: 1-404-363-7081 Email: tzeng@gatech.edu

Abstract

The ratios of observed organic carbon (OC) to elemental carbon (EC) from the rural sites of the IMPROVE network are analyzed for the 5-year period from 2000 to 2004. Among these years, nationwide OC/EC peaks are observed most consistently in the summer of 2002. Several potential factors are analyzed, including biomass burning, secondary organic aerosols (SOA) formation from biogenic sources and in-cloud processing, long-range transport from East Asia, and meteorological conditions over the U.S. We find that biomass burning and SOA formation make the most significant contributions using the global GEOS-Chem model simulations. The effect of model estimated in-cloud SOA formation is significant compared to the estimate of (non-cloud) biogenic SOA. The impacts of Canadian and western U.S. fires are larger than fires in Russia or Mexico in summer. The dry meteorological condition of the summer of 2002 tends to promote higher OC/EC ratios by inducing larger fire emissions, SOA formation, and a longer OC lifetime.

Keywords: OC/EC ratio, biomass burning, summer burning, SOA, model evaluation

Contribution of Aqueous Oxidation of Biogenic VOCs to SOA Production

Zhongming Chen, Xuan Zhang, Dao Huang, Hongli Wang, Yue Zhao and Xiaoli Shen
College of Environmental Sciences and Engineering, Peking University, Beijing, China
100871

Principal Contact: Zhongming Chen, Professor, College of Environmental Sciences and Engineering, Peking University, Beijing, China 100871.

Tel/Fax: +86-10-62751920 E-mail: zmchen@pku.edu.cn

Abstract

Increasing evidence suggests that secondary organic aerosol (SOA) is formed through aqueous phase reactions of organic compounds in the atmospheric aqueous-phase including cloud, fog, rain, and aerosol-surface water. However, the knowledge about the aqueous-phase formation mechanism of SOA is limited. We have studied experimentally the aqueous-phase oxidation of isoprene, α -pinene, β -pinene, methyl vinyl ketone and methacrolein. The major products including organic acids, carbonyl compounds and peroxides were quantitatively determined, and the high-molecular-weight compounds (HMCs) were investigated. The reaction mechanisms were discussed. Among these products, the dicarboxylic acids, multifunctional carbonyls and HMCs are important SOA components or precursors. We suggest that the oxidation of volatile organic compounds (VOCs) occurs not only in the bulk but also on the surface of droplets and the latter should be considered into the atmospheric SOA models.

Keywords: aqueous-phase, oxidation, organic compound, aerosol.

Characterization of new particle and secondary aerosol formation during summertime in Beijing, China

Y. M. Zhang^{1,2} and X.Y. Zhang¹

1 Key Laboratory for Atmospheric Chemistry, Centre for Atmosphere Watch and Services, Chinese Academy of Meteorological Sciences, China Meteorological Administration, 46 Zhongguancun S. Ave., Beijing 100081, China

2 Graduate University of Chinese Academy of Sciences, 19A Yuquanlu Shijingshan district, Beijing 100049, China

Principal Contact: Y. M. Zhang, Doctor, 46 Zhongguancun S. Ave., Beijing 100081.

Tel: 58995271 Fax: 62176414 Email: ymzhang@cams.cma.gov.cn

Abstract

Size-resolved aerosol number and mass concentrations and the mixing ratios of O₃ and various trace gases were continuously measured at an urban station before and during the Beijing Olympic and Paralympic Games (June 5 to September 22, 2008). Twenty-three new particle formation (NPF) events were identified; these usually were associated with changes in wind direction and/or rising concentration of gas-phase precursors or after precipitation events. Most of the NPF events started in the morning and continued to noon as particles in the nucleation mode grew into the Aitken mode. From noon to midnight, the aerosol particle size increased into the accumulation mode through condensation and coagulation processes. During this latter period, O₃ experienced a gradual rise reaching its peak around 15:00 local time, and then started to decline as the organics increased. The dominant new particles species were organics (40 to 75% of PM₁) and sulphate, with nitrate and ammonium as minor contributors.

Keywords: Secondary aerosol formation, new particle formation, AMS, Beijing

A time-stratified case-crossover study of fine particulate matter air pollution and mortality in Guangzhou, China

Haidong Kan

School of Public Health, Fudan University, Shanghai 200032, China

Principal Contact: Haidong Kan, Professor, Fudan University, Box 249, 130 Dong-An Rd., Shanghai 200032, China.

Tel: +86-21-54237908 Email: haidongkan@gmail.com

Abstract

Few studies in China investigate health impact of fine particulate matter ($PM_{2.5}$) due to lack of monitoring data and the findings are controversial. In Guangzhou, we measured daily $PM_{2.5}$ concentrations between 2007 and 2008, and conducted a time-stratified case-crossover analysis to explore the association between $PM_{2.5}$ and daily mortality, and examine potential effect modifiers including age, sex, and education. The averaged $PM_{2.5}$ concentration in 2007-2008 was $70.1 \mu\text{g}/\text{m}^3$ in Guangzhou, which was approximately seven times higher than the WHO Air Quality Guidelines for $PM_{2.5}$ (annual average: $10 \mu\text{g}/\text{m}^3$). Regression analysis showed that ambient $PM_{2.5}$ was associated with mortality from all causes and cardiorespiratory diseases. An increase of $10 \mu\text{g}/\text{m}^3$ in 2-day moving average (lag01) concentration of $PM_{2.5}$ corresponds to 0.90% [95% confidence interval (CI): 0.55%, 1.26%] increase of total mortality, 1.22% (95%CI: 0.63%, 1.68%) increase of cardiovascular mortality, and 0.97% (95%CI: 0.16%, 1.79%) increase of respiratory mortality. The associations were stronger in the elderly (aged 65 years or more), in females and in those with low education level, but the differences were statistically insignificant. Conclusively, our findings provided new information for the adverse health effects of $PM_{2.5}$ in China, and may have some implications for environmental policy making and standard setting in Guangzhou.

Keywords: fine particle, $PM_{2.5}$, mortality, case-crossover

CFD Study of Transport and Deposition of Asbestos Fibers in Human Upper Tracheobronchial Airways

Lin Tian¹ and Goodarz Ahmadi²

1 Department of Science and Engineering Technology, State University of New York, Canton NY 13617, U.S.A.

2 Department of Mechanical and Aeronautical Engineering, Clarkson University, 13699, Potsdam, NY, U.S.A.

ABSTRACT

Fate of the inhaled asbestos fibers has attracted considerable research attention during the past few decades due to its malignant pathological response in living beings. Extensive earlier studies have been identified the links between the inhalation of asbestos and the occurrence of lung cancer; however, details of the pathological correlation are still to be uncovered. The understanding is further hampered by the lack of tools to reveal the details of motion of the asbestos fibers and their interaction with the airflow within the tracheobronchial airways. This work is intended to investigate the transport and deposition of elongated fibers in a physiological realistic multi-level lung model using a computational modeling approach. Motions of the inhaled fibers and their interactions with the surrounding environment were reproduced by solving the system of coupled nonlinear equations governing the fibers translational and rotational motions. Correlations between the deposition pattern, fiber characteristics, breathing conditions, and airway morphology in human upper tracheobronchial airways were analyzed. The simulation results were compared with the experimental data, and good agreement was found. The carcinogenicity of these asbestos fibers was also discussed.

KEYWORDS

Asbestos Fibers, Particle Transport and Deposition, Tracheobronchial Tree, Numerical Simulation.

Introduction

Occupational exposure to asbestos fibers has been linked to the occurrence of malignant respiratory diseases such as mesothelioma and lung cancer. Widely accepted, the respiratory pathological response in living being is mainly induced by the retention and deposition of the inhaled asbestos fibers. Measurements of such deposition in human patient tissues as well as in vivo animal studies were reported by many researchers, such as Lippmann et al. (1988, 1990)^{[1][2]},

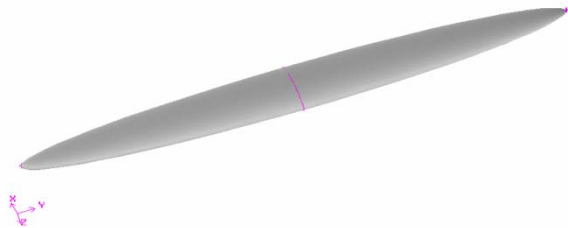
Berman et al. (1995)^[3], and Suzuki et al. (2005)^[4]. Based on the available data EPA (2003)^[5] concluded that fibers with length shorter than 5 μm posed minimum risk, while the threshold for diameter needed further investigation. NIOSH (2008)^[6] concluded that fibers with length smaller than 1.5 μm or greater than 40 μm and diameter thinner than 0.25 μm or thicker than 3 μm , respectively, were at the highest risk to cause lung cancer.

In this study, simulation of the transport and deposition of elongated ellipsoidal fibers in the first generation of human airway model was conducted. Mathematical description of fiber motion was given by system of coupled nonlinear equations accounting for the hydrodynamic drag and torque, shear induced lift, Brownian diffusion, and the gravitational sedimentation. The simulated results provided detailed information for analyzing the contribution of fiber dimensional characteristics (length, diameter, aspect ratio, density) toward deposition. Effects of the airflow pattern and airway morphology were also studied. Results of the study were compared to earlier experimental measurements, and carcinogenicity of the fiber in relation to its dimensional characteristics was discussed.

Computational Model

For the ellipsoidal fiber shown in Figure 1, the governing equations for the coupled translational and rotational motion are:

Figure 1. Ellipsoidal Fiber.



$$m^p \frac{d\mathbf{v}}{dt} = m^p \mathbf{g} + \mathbf{f}^h + \mathbf{f}^L + \mathbf{f}^B, \quad (\text{Eq. 1})$$

$$I_{\hat{x}} \frac{d\omega_{\hat{x}}}{dt} - \omega_{\hat{y}} \omega_{\hat{z}} (I_{\hat{y}} - I_{\hat{z}}) = T_{\hat{x}}^h, \quad (\text{Eq. 2})$$

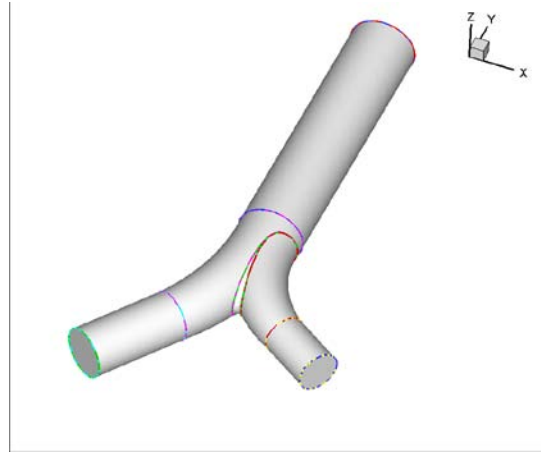
$$I_{\hat{y}} \frac{d\omega_{\hat{y}}}{dt} - \omega_{\hat{z}} \omega_{\hat{x}} (I_{\hat{z}} - I_{\hat{x}}) = T_{\hat{y}}^h, \quad (\text{Eq. 3})$$

$$I_{\hat{z}} \frac{d\omega_{\hat{z}}}{dt} - \omega_{\hat{x}} \omega_{\hat{y}} (I_{\hat{x}} - I_{\hat{y}}) = T_{\hat{z}}^h, \quad (\text{Eq. 4})$$

Here \mathbf{v} is the velocity vector of the fiber particle mass center in the fixed coordinate, and $(\omega_{\hat{x}}, \omega_{\hat{y}}, \omega_{\hat{z}})$ is the angular velocity vector of the fiber in the particle frame (Cartesian coordinate attached to the fiber centroid with its axes parallel to the fiber's principle axis). m^p is the mass of the fiber, \mathbf{g} is the acceleration of gravity, \mathbf{f}^h is the hydrodynamic force, and \mathbf{f}^L is the shear induced lift force. $(I_{\hat{x}}, I_{\hat{y}}, I_{\hat{z}})$ is the moments of inertia of the fiber about the principle axes in the particle frame $(\hat{x}, \hat{y}, \hat{z})$, and $(T_{\hat{x}}^h, T_{\hat{y}}^h, T_{\hat{z}}^h)$ is the hydrodynamic torques acting on the particle with respect to the principle axes in the particle frame.

In the trachea and the first airway generation shown in Figure 2, Tian and Ahmadi (2007)^[7] used the Reynolds stress transport turbulence model to describe the airflow motion.

Figure 2. Trachea and First Bifurcation Airway Model.



Results and Discussion

Figure 3 displays the simulated fiber motion in the trachea and the first bifurcation for a breathing rate of 40 L/min. Diameter of the fiber is 0.1 μm , while lengths of the fiber are, respectively, 0.4 μm , 1.2 μm and 2.4 μm , or aspect ratio of 4, 12 and 24. Throughout the trajectory, fibers illustrate coupled translational and rotational motion. Distinctive Brownian excitation is

observed in Figure 3.a while smoother motion is exhibited for longer fibers (Figure 3.b and 3.c). It is shown in Figure 3.c that longer fibers tend to suppress the rotation, this may have profound effect in predicting fiber deposition rate.

Figure 3. Simulated Fiber Motion.

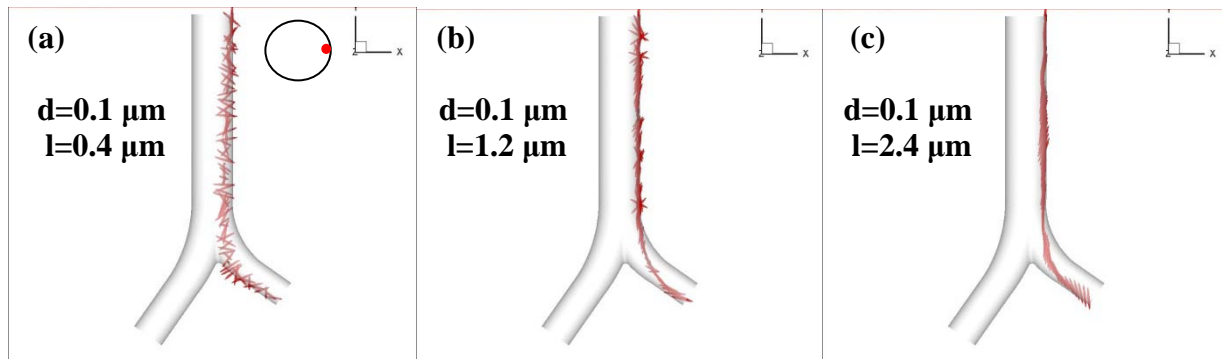


Figure 4 displays the simulated fiber deposition pattern for a breathing rate of 40 L/min. Figure 4.a and 4.b present the result for fibers with diameter being $3.66 \mu\text{m}$ and aspect ratio being 15 and 80, while Figure 4.c and 4.d show the result for fibers with diameter of $0.1 \mu\text{m}$ and aspect ratio of 15 and 80. It is seen from Figure 4.a and 4.b that most of the depositions occur at the bifurcation and the inner ridge of the daughter branches. This indicates that the major deposition mechanism is inertial deposition. However in Figure 4.c and 4.d, the deposition is more uniformly distributed at the bifurcation as well as at the outer wall of the daughter branches. This implies a diffusion deposition mechanism. In summary, fiber deposition pattern in the human upper airways is largely affected by the transport mechanism. For ellipsoidal fibers, the deposition mechanism is determined by its diameter. For fibers with diameter larger than $3.66 \mu\text{m}$, inertial impaction plays the major role, while for fibers with diameter $0.1 \mu\text{m}$ or smaller, diffusion is the major deposition mechanism.

Figure 4. Simulated Fiber Deposition Pattern.

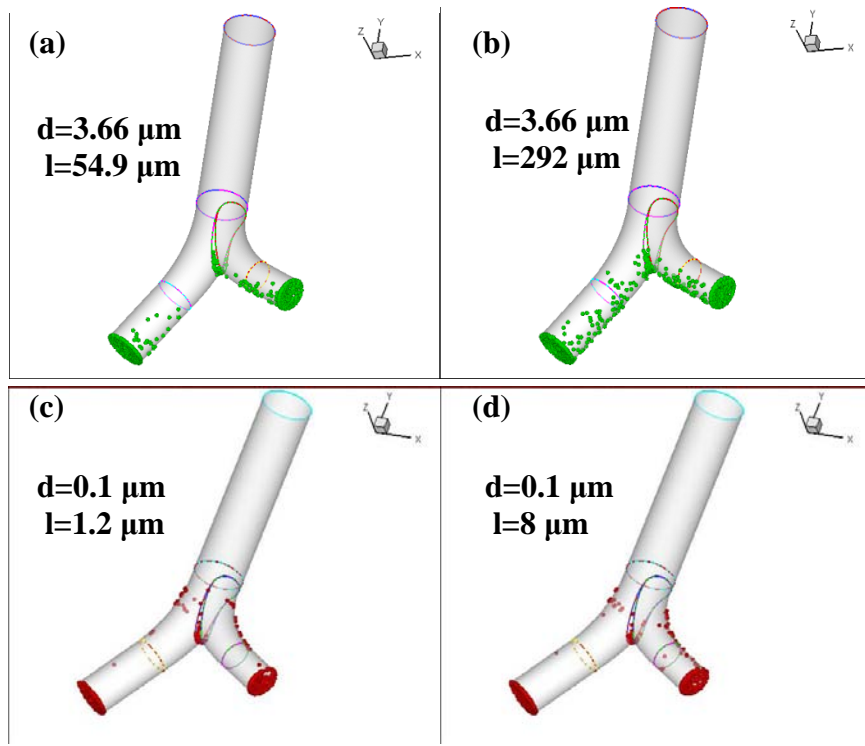
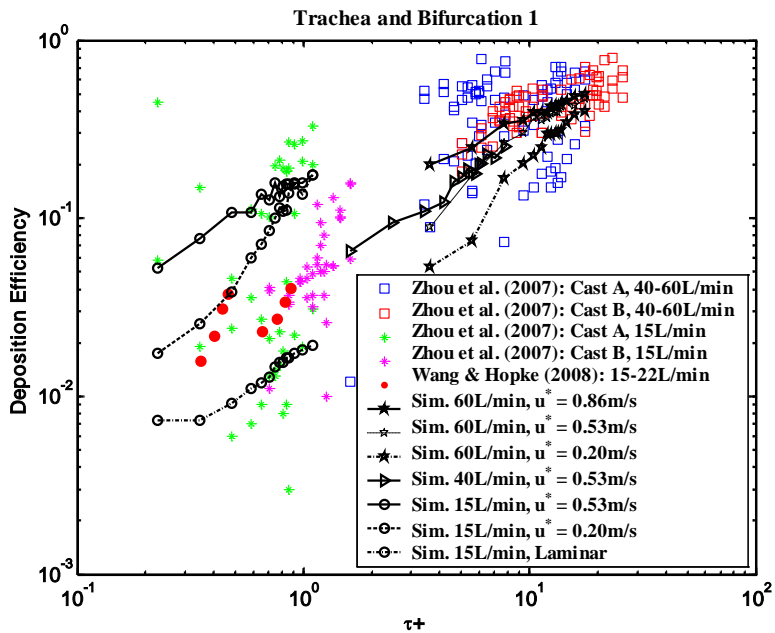


Figure 5 compares the predicted fiber deposition efficiency in the trachea and the first bifurcation. The data are plotted versus the equivalent fiber relaxation time. Experimental measurements of Zhou et al. (2007)^[8] in a human airway replica are plotted in this figure for comparison. Carbon fibers of semi-minor being $3.66 \mu\text{m}$, and aspect ratios from 1 to 80 are included in the simulation study. It is observed from Figure 5 that the measured deposition rates are rather scattered. For the inertial size range considered, in general, as the fiber relaxation time increases, the deposition efficiency increases. The fiber deposition is also enhanced as the breathing rate increases. However, at moderate to intensive breathing rates (40 to 60L/min), the effect of the airflow on the fiber deposition is less important. According to Tian and Ahmadi (2007)^[7], the near wall correction on the turbulence fluctuation near a surface is essential for correct prediction of the particle deposition rates in turbulent flows. The present simulation accounts for this correction by using the turbulence near wall “two-layer zonal model” and the “quadratic variation near wall model”. A series of simulations for wall corrections being made assuming a range of u^* are performed and the results are presented in Figure 5. This figure shows that altering the level of

shear velocity (u^*) for the near wall correction will affect the fiber deposition rates noticeably. Higher values of shear velocity lead to higher values of turbulence fluctuations and leads to higher deposition rate. Figure 5 shows that for the range of u^* considered, the predicted deposition rate are within the range of the experimental measurements. This figure further shows the importance of the turbulence near wall correction in the study of fiber depositions in human lung. Due to the complexity of fiber deposition and the scatter of the experimental data, the applied correction as quantified by the values of u^* appears to be reasonable.

Figure 5. Comparison of Simulated Fiber Deposition Efficiency.



CONCLUSIONS

The computational model is able to reproduce the coupled fiber motion in human upper tracheobronchial airways covering from inertial to Brownian region. Brownian diffusion is successfully simulated and it has profound effect to the movement of fibers with extremely thin diameters ($d < 0.1 \mu\text{m}$). Intensive Brownian excitation is observed for fibers with small aspect ratio (length), however longer fibers of this group tend to overcome the Brownian excitation and align with the flow with less rotation. Inertial and diffusion deposition patterns for large and extra thin fibers are also illustrated. Finally, the simulated deposition efficiency agrees well with the experimental data. This suggests the developed computational model is suitable for simulating the fiber transport and depositions in the human tracheobronchial airways.

ACKNOWLEDGMENTS

This work is supported by National Institute for Occupational Safety and Health (NOISH) and Center for Air Resources Engineering and Science at Clarkson University.

REFERENCES

- [1] Lippmann, M. *Environ Res.* 1988, 46, 86–106.
- [2] Lippmann, M. *Environ Health Perspect.* 1990, 88, 311–317.
- [3] Berman, D.W.; Crump, K.S.; Chatfield, E.J.; Davis, J.M.G.; Jones, A.D. *Risk Anal.* 1995, 15, 188–195.
- [4] Suzuki, Y.; Yuen, S.; Ashley, R. *Int J Hyg Environ Health.* 2005, 208, 201–210.
- [5] EPA (U.S. Environmental Protection Agency). 2003.
- [6] NIOSH (National Institute for Occupational Safety and Health). 2005.
- [7] Tian, L.; Ahmadi, G. *Journal of Aerosol Science.* 2007, 38, 377–397.
- [8] Zhou, Y.; Su, W-C.; Cheng, Y.S. *Inhalation Toxicology.* 2007, 19, 1071–1078.

A Study of Mutagenic Index (MI) in PM₁₀ of Residential Areas in Bangkok

Siwatt Pongpiachan^{1,2}, Chomsri Choochuay³, Charnwit Kositanone⁴, Kin Fai Ho², and Junji Cao²

1 School of Social and Environmental Development, National Institute of Development Administration (NIDA), 118 Moo 3, Sereethai Road, Klong-Chan, Bangkapi, Bangkok 10240, Thailand

2 SKLLQG, Institute of Earth Environment, Chinese Academy of Sciences (IEECAS), Xi'an 710075, China

3 Faculty of Environmental Management, Prince of Songkla University, Hat-Yai, Songkla 90120, Thailand

4 Inter-Department of Environmental Science, Faculty of Graduate Studies, Chulalongkorn University, Bangkok 10330, Thailand

Principal Contact: Dr. Siwatt Pongpiachan, Assist. Prof., School of Social and Environmental Development, National Institute of Development Administration (NIDA), 118 Moo3, Sereethai Road, Klong-Chan, Bangkapi, Bangkok 10240, Thailand.

Tel: +66-89637-2211, +66-27273113 E-mail: pongpiajun@gmail.com

Abstract

To investigate the influence of traffic emissions and industrial activities on the genotoxicity of Bangkok atmosphere, PM₁₀ samples were collected at the Community Housing Klongchan, Nonsi Witthaya School, Singharat Pittayakhom School, Thon Buri Electricity Sub, Chok Chai 4 Police Station, Dindang Community Housing and Bodindecha (Sing Singhaseni). For all monitoring sites, each sample covered a period of 24 hours taken at a normal weekday every month from January-December 2006 forming a database of 84 individual air samples (i.e. 12 x 7 = 84). The mutagenicity of extracts of the samples was compared in the Salmonella according to standard AMES test method. The dependence of the effects on sampling time and on sampling location was investigated with the aid of a calculation of mutagenic index (MI). This MI was used to estimate the increase in mutagenicity above background levels at the seven monitoring sites in urban area of Bangkok due to anthropogenic emissions within that area. Applications of the AMES method showed that the average MI of PM₁₀ collected at all sampling sites were 1.37 ± 0.10 (TA98; +S9), 1.24 ± 0.08 (TA98; -S9), 1.45 ± 0.10 (TA100; +S9) and 1.30 ± 0.09 (TA100; -S9) with relatively less variations. Comparison of the results obtained with the different AMES-test variants (i.e. +S9 and -S9) reconfirms that the particulate mutagenic concentrations measured at residential areas of Bangkok are moderately low in comparison with previous results observed in other countries.

Keywords: Mutagenicity, Bangkok, PM₁₀, Hierarchical Cluster Analysis, Principal Component Analysis, Multiple Linear Regression Analysis

Detection of Influenza Virus in Human Exhaled Air

Pei-Chun Yen², Pei-Shih Chen^{1*}, and Wan-Chi Kuo¹

1 Department of Public Health, Kaohsiung Medical University 100, Shih-Chuan 1st Road, Kaohsiung, 80708, Taiwan

2 Graduate Institute of Occupational Safety and Health, Kaohsiung medical university 100, Shih-Chuan 1st Road, Kaohsiung, 80708, Taiwan

Principal Contact: Pei-Shih Chen, Department of Public Health, Kaohsiung Medical University 100,Shih-Chuan 1st Road,Kaohsiung,80708,Taiwan.

Tel: +886-7-312-1101-2141-34 Fax: +886-7-321-2062 E-mail: pschen@kmu.edu.tw

Abstract

Influenza virus infects at least 5 million people and kills 250 to 500 thousand people every year. It should be one of the most concern infectious bioaerosols. We had successfully quantified influenza virus from the air and exhaled air in the previous study. However, the relation between exhaled influenza virus and the symptoms was not investigated yet. The aims of this study is to investigate the association between exhaled influenza virus and the symptoms of patients as well as the association between exhaled influenza virus and the concentration of influenza virus in throat swab samples of infected patients.

Total of 22 exhaled samples were collected during two periods, 2008/11 and 2009/02. Throat swab specimens also obtained from patients as well as the symptoms records. The exhaled samples were collected by 37mm, 2.0 μ m Teflon filters, and the sampling volume was 10 L. Influenza Virus was quantified by real-time qPCR for all the exhaled and swab samples.

The positive rate influenza virus in exhaled sample and throat swab specimen were 68.2%(15/22)and 72.7%(16/22), respectively. The concentration mean is 1.76×10^5 copies/m³ (5.27×10^3 — 9.26×10^5) for exhaled sample and 1.19×10^4 copies/ml (1.37×10^1 — 1.66×10^5) for throat swab specimen. It was found that a significantly positive correlation between exhaled influenza virus and symptom score, and a significantly positive correlation between exhaled influenza virus and rhinitis. In regard to the flu symptoms, it was demonstrated that the symptoms percentage in positive exhaled samples was higher than that in positive throat swab samples for all symptoms expect abdominal pain. To our knowledge, it is the first study investigating the correlation between the concentration of

exhaled influenza virus and the symptoms. Good correlation implicated that quantifying exhaled influenza virus may be a good indicator for the evaluation of disease severity.

Keywords: Exhaled air, influenza virus, throat swab

Problem with Radon Action Level due to the Unattached Radon Decay Products

Norbert Kávási^{1*}, Tamás Vígh², Tibor Kovács³, Janja Vaupotič⁴, Viktor Jobbág⁵, Tetsuo Ishikawa¹

1 Research Center for Radiation Protection, National Institute of Radiological Sciences, 4-9-1 Anagawa, Chiba 263-8555, Japan

2 Mangán Mining and Processing Ltd., 1 Külterület, Úrkút 8409, Hungary

3 Institute of Radiochemistry and Radioecology, University of Pannonia, 10 Egyetem, Veszprém 8200, Hungary

4 Department of Environmental Sciences, Radon Center, Jožef Stefan Institute, 39 Jamova, 1000 Ljubljana, Slovenia

5 Social Organization for Radio Ecological Cleanliness, 10 Egyetem, Veszprém 8200, Hungary

Principal Contact: Norbert Kávási, National Institute of Radiological Sciences, Research Center for Radiation Protection, Environmental Radiation Effects Research Group, 4-9-1 Anagawa, Chiba 263-8555, Japan.

Tel: +81-43-206-3111 Fax: +81-43-206-4098 E-mail: norbert@fml.nirs.go.jp

Abstract

During the radon surveys of workplaces in Hungary the equilibrium factor measured and the dose conversion factor $7.9 \text{ nSv m}^3 \text{ Bq}^{-1} \text{ h}^{-1}$ recommended by ICRP were used for the dose estimations. After studying the air-quality parameters of workplaces it has become apparent that using the same dose conversion factor – e.g. in case of a deep mine and a medicinal bath – may considerably reduce the reliability of the estimated dose.

In order to study this, the concentration of radon and its progenies, the unattached fraction of radon short-lived progenies-t, the equilibrium factor, the temperature, and relative humidity were measured in a medicinal bath (14 days), in a tourist cave (7 days), in a medicinal cave (7 days), in a manganese deep mine (9 days), and in a deep geological radioactive waste deposit under construction (7 days). With the above data known the possible dose conversion factors were determined taking into consideration respiration through the nose and through the mouth, and then calculating with the annual labour hours related to the given territory the effective dose of the workers was estimated.

For the radon medicinal bath the calculated dose conversion factors, distinguished nose and mouth respiration, were 2.3, and $6.2 \text{ nSv m}^3 \text{ Bq}^{-1} \text{ h}^{-1}$, respectively. For the tourist cave, the medicinal cave, the manganese deep mine and the deep geological radioactive the same data were 6.8 and $19.7 \text{ nSv m}^3 \text{ Bq}^{-1} \text{ h}^{-1}$; 8.6 and $14.8 \text{ nSv m}^3 \text{ Bq}^{-1} \text{ h}^{-1}$; 7.9 and $23.7 \text{ nSv m}^3 \text{ Bq}^{-1} \text{ h}^{-1}$ and 4.7 and $11.0 \text{ nSv m}^3 \text{ Bq}^{-1} \text{ h}^{-1}$, respectively.

Keywords: Effective Dose, Radon, Unattached Fraction, Dose Conversion Factor

Effects of Inhalation Profiles on Particle Deposition in Human Upper Airway

Zheng Li¹ and Lujie Cao²

1 International Biomedical, 8206 Cross Park Dr., Austin, TX 78754 USA

2 Mechatronics Engineering Department, Ocean University of China, QingDao, China

Principal Contact: Zheng Li, Doctor, International Biomedical, 8206 Cross Park Dr., Austin, TX 78754 USA.

Tel: 1-9192720867 Fax: N/A E-mail: grouplzh@hotmail.com

Abstract

Particulate matter is inhaled and deposits in the respiratory tract with every breath. Some of these particles can be harmful depending upon the aerosol material, deposition site, local concentration and individual health status, etc. A well-known example is the deposition of mainstream (MS) cigarette smoke particles on human airways. Currently, millions of adults frequently smoke. Some of them suffer one or several respiratory diseases. Thus, it is important to study the MS cigarette smoke particles characteristics in human respiratory system.

Human respiratory system consists of nose, oral-tracheal airway, bronchial airways and the alveolar region. Particle deposition in the oral-tracheal airway is an important aspect of the study of particle deposition in the respiratory system. Very small and large particles mainly deposit in oral or nasal airways. Additionally, airflow patterns and particle distribution at the outlet of oral-tracheal airway are the inlet conditions for the lower respiratory tract.

In this work, low inhalation flow rates, i.e., 35 cc/2s (1.05 L/min) and 55 cc/2s (1.65 L/min), are studied. Airflow and particles are released in a small region of the mouth inlet to mimic the cigarette smoke inhalation area. Both micro- and nano-particles are studied. Particle depositions in three different oral-tracheal airway models, i.e., circular, elliptic and realistic models, are compared under currently investigated inhalation profiles. It is observed that inhalation profiles greatly influence the particle deposition. The difference could be significant between the currently implemented and normal breathing situations. The geometric influence is still important. For particles with different sizes, the highest deposition fraction could be in either circular or realistic models due to the multiple effect of the Brownian motion, drag force and/or gravity.

Keywords: Particle deposition, human airway, cigarette smoke particle

Bioaerosol Science, Technology and Engineering: Past, Current and Beyond

Maosheng Yao

State Key Joint Laboratory for Environmental Simulation and Pollution Control, College of Environmental Sciences and Engineering, Peking University, Beijing 100871, China

Principal Contact: Maosheng Yao, Professor, State Key Joint Laboratory for Environmental Simulation and Pollution Control, College of Environmental Sciences and Engineering, Peking University, Beijing 100871, China.

Tel: +86 010 6276 7282 Email: yao@pku.edu.cn

Abstract

Poor air hygiene as a result of bioaerosol contamination has caused diverse forms of adverse health effects and diseases. In addition, global bio-security is threatened by purposeful use of bio-warfare agents and vulnerability to the infectious agents. Accordingly, developments in high volume bio-sampling including aerosol-to-hydrosol techniques with low cutoff size, real-time bioaerosol detection, adequate biological quantification and exposure control as well as the investigation of the link between disease outcome and bioaerosol exposure are current areas of the bioaerosol research. Besides, the roles of bioaerosols in climate change are also getting increased attention. Although milestone progress has been achieved both in bioaerosol sampling and analysis techniques since late 1800s, compared to atmospheric chemistry the bioaerosol field is still under-studied. This is partially due to the lack of both bioaerosol scientists and multidisciplinary collaboration. It is becoming necessary to develop a pool of scientists with different expertise, e.g., bioaerosol scientists, environmental engineers, bio-medical engineers, epidemiologists, microbiologists, chemists, physicists as well as researchers in other engineering fields in mitigating bioaerosol related adverse health effects, eliminating diseases, preventing and controlling epidemic outbreaks. This work is conducted to broadly review current state-of-the-art sciences and technologies in bioaerosol field. In tackling the challenges ahead, the review also provides perspectives for bioaerosol research needs, and further reminds the bioaerosol scientists those existing technologies in other fields that can be leveraged. In view of the past, forward-looking hypotheses and revolutionary perspectives need to be formed in order to have the bioaerosol research to have major impacts in the academic community in this new millennium.

Keywords: Bioaerosol, health effects, climate, sampling, detection, exposure assessment, bioaerosol control, biosensor

Performance of a Button Inhalable Sampler with Modified MCE Filter Method in Enumerating Culturable Bacterial and Fungal Aerosol Concentration and Diversity

Zhenqiang Xu and Maosheng Yao

State Key Joint Laboratory for Environmental Simulation and Pollution Control, College of Environmental Sciences and Engineering, Peking University, Beijing 100871, China

Principal Contact: Maosheng Yao, Professor, State Key Joint Laboratory for Environmental Simulation and Pollution Control, College of Environmental Sciences and Engineering, Peking University, Beijing 100871, China.

Tel: +86 010 6276 7282 Email: yao@pku.edu.cn

Abstract

In this study, a modified mixed cellulose ester (MCE) filter culturing method (directly placing filter on agar plate for culturing) was investigated in enumerating airborne culturable bacterial and fungal aerosol concentration and diversity both in indoor and outdoor environments. A Button Inhalable Sampler loaded with MCE filter was operated at a flow rate of 5 L/min to collect indoor and outdoor air samples using different sampling times: 10, 20, and 30 min. As a comparison, a BioStage impactor was operated at a flow rate of 28.3 L/min in parallel for all tests. The air samples collected by the Button Inhalable Sampler were directly placed on agar plates for culturing, and those collected on agar plates by the BioStage impactor were incubated directly. The colony forming units (CFUs) were manually counted and the culturable concentrations were calculated both for bacterial and fungal aerosols. The bacterial CFUs grown were further washed off and subjected to polymerase chain reaction-denaturing gradient gel electrophoresis (PCR-DGGE) for diversity analysis. For fungal CFUs, microscopy method was applied to study the culturable fungal diversity obtained using different methods.

Experimental results showed that the direct MCE filter culturing method performed reasonably well, and in some cases it outperformed the BioStage impactor, in enumerating bacterial and fungal aerosols. For bacterial aerosol sampling, the BioStage impactor was shown to perform better, and in contrast the MCE filter method was demonstrated to enumerate more culturable fungal aerosols. In general, the microbial species richness was observed to increase with increasing collection time. For both methods, the DGGE gel patterns were observed to vary with sampling time and environment despite of their similar species richness. In addition, an increase in sampling time from 20 to 30 min seemed to not significantly alter the species richness. Regardless of the sampling methods, more species richness was observed in outdoor environment than indoor environment. Compared to the BioStage impactor, the direct MCE filter culturing method with the Button Inhalable Sampler described here can be easily adapted to provide better personal biological exposure monitoring protocols.

Keywords: Direct MCE filter culturing method, Button Inhalable Sampler, BioStage impactor, culturable aerosol diversity, bacterial and fungal aerosols, polymerase chain reaction (PCR), denaturing gradient gel electrophoresis (DGGE), phylogenetic similarity

Characteristics of Removal of Bioaerosols by Dielectric Barrier Discharge

Chul Woo Park¹, Jae Hong Park² and Jungho Hwang¹

1 Department of Mechanical Engineering, Yonsei University, Seoul 120-749, Republic of Korea

2 The University of Iowa, Department of Occupational and Environmental Health, USA

ABSTRACT

Bioaerosols (airborne bio-particles) can cause serious health hazards when they contaminate a human environment. In this study, we attempted to remove bioaerosols using a lab-made dielectric barrier discharge (DBD) reactor, and studied characteristics of removal of bioaerosols by DBD reactor. Total removal efficiency, collection efficiency, and sterilization efficiency of bioaerosols were up to 94%, 64%, and 83%, respectively, when 7.5 kV of applied voltage and 0.24 sec of residence time were employed. The performance of a DBD reactor can also be evaluated using specific input energy (SIE). In this study, the SIE susceptibility constant is suggested as a quantitative parameter for the estimation of ability to remove bioaerosols of collection and sterilization process by the DBD reactor. The SIE susceptibility constants of total removal process, collection process, and sterilization process are 0.00737, 0.00306, and 0.00431 L/J, respectively. The paper shows that the DBD reactor was effective in removing bioaerosols in the short time (0.24 sec) and under 12.8 W.

KEYWORDS

Removal, Bioaerosols, Dielectric barrier discharge (DBD), Susceptibility

Introduction

Bioaerosols (airborne bio-particles) can cause serious health hazards when they contaminate a human environment. Diseases from pathogenic bacteria are the major cause of death, accounting for nearly 40% of the total 50 million annual estimated deaths worldwide. It is well known that dielectric barrier discharge (DBD) produces highly non-equilibrium plasmas in a controllable way at atmospheric pressure and temperature. Until recently, DBD has primarily been used as an effective ozone generator. However, researchers are now investigating the feasibility of using DBD for a wide range of fields. Since DBD serves as a chemical reactor that produces active chemical species under various reactions, it has been used to remove various undesired species interesting for environmental applications.

For a long time, researchers have reported that plasma can kill or inhibit the growth of

bacteria. Many sterilization methods such as autoclaving, γ -irradiation, ethylene oxide, and UV sterilization, as well as plasma sterilization are currently being used. However, most means for sterilization, except atmospheric pressure plasma such as DBD, need lengthy sterilization time (~ 30 min) and can be operated only in closed space while other methods are toxic to the human body; these are not easy to apply to air purifiers for germicidal effect. Thus, DBD that can be applied to open space, have very short sterilization time (~ 1 min), have huge merit for application to sterilization systems (Choi et al., 2006).

While sterilization of *E. coli* and *F. oxysporum* with a DBD reactor was reported by Choi et al. (2006) and Takayama et al. (2006), respectively, the studies have not been concerned with the removal of bioaerosols, that is, the studies have not been concerned with collection of bioaerosols on the plates of DBD reactor. In this study, we attempted to remove bioaerosols using a lab-made DBD reactor, and studied characteristics of removal of bioaerosols by DBD reactor.

Experimental Methods

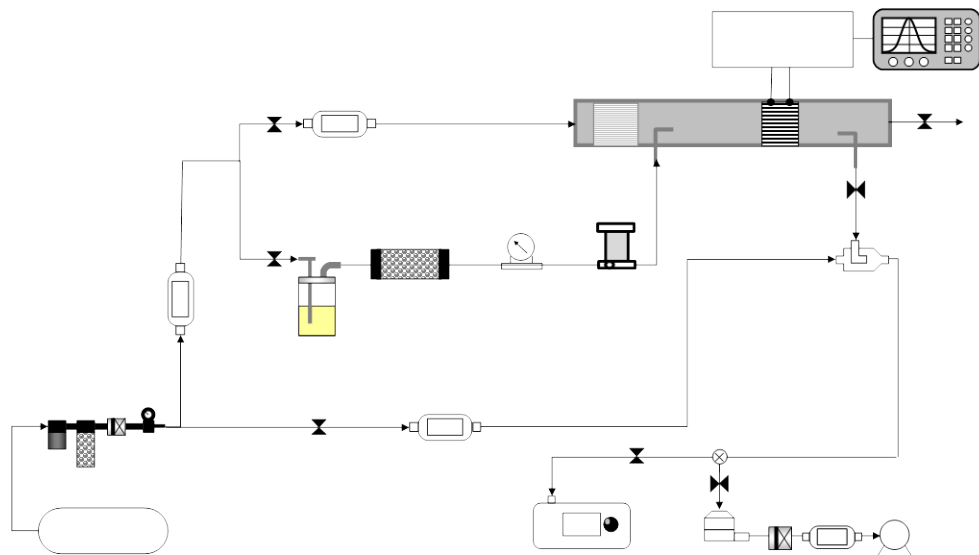


Fig. 1. Schematic diagram of experimental setup.

The DBD reactor installed in an acryl duct ($5 \times 5 \text{ cm}^2$) consisted of nine parallel plate electrodes that were configured in an alternating fashion, with one electrode being grounded and the next one received high AC voltage. The gap spacing between any two electrodes was 5 mm. Each electrode was made from 0.03 mm thick copper foil (5 mm of streamwise length and 40 mm of spanwise length) sandwiched between two 0.25 mm thick dielectric plates (alumina plates, 20 mm streamwise length and 50 mm of spanwise length). Non-thermal plasma was formed in the space between the electrodes. Fig. 2 shows the voltage-current characteristics for frequencies

of 60 Hz. The discharge currents were 0.442 – 1.7 mA. The voltage and current were measured using a two-channel digital oscilloscope (TDS 1012, Tektronix) and their root-mean-square (RMS) amplitude values are indicated in Fig. 2. The transition to arc occurred at voltages slightly higher than 8 kV. The experimental schematic is shown in Fig. 1. *S. epidermidis* bioaerosols were dispersed into air using a nebulizer (1 jet, BGI Inc.) at a flow rate of 2 L/min. The bioaerosols entered the test duct after first passing through diffusion dryer and an aerosol neutralizer (soft X-ray type neutralizer, HCT CO., Ltd. model 4530). The air flow including bioaerosols was diluted with particle-free air that was delivered through the clean air supply system. Next, the diluted mixture was treated by passing it through plasma region formed by DBD reactor at residence times of 0.12, 0.16, 0.24 sec. To determine the total removal efficiencies of bioaerosols, the bioaerosols passed through plasma region sampled on nutrient agar plates by an impactor (TE-10-800, Tisch Environmental Inc.). The cutoff size of the impactor was 500 nm in aerodynamic diameter. For 1.5 min, 1 L/min was sampled from the test duct and 27.3 L/min was filled up from particle-free air that was delivered through the clean air supply system. The bioaerosols sampled on the nutrient agar plates were incubated for 5 days at 37°C. After incubation, the colony forming units (CFU) were estimated by a visual inspection. To determine the collection efficiencies of bioaerosols, size distribution and number concentration of the bioaerosols were measured using APS (Aerodynamic Particle Sizer; model 3321, TSI Inc.). APS measures the aerodynamic diameter of bioaerosols by the time of flight between two laser beams. The measurable range of APS is 0.5 – 20 μm.

The total removal efficiency (η_{total}), collection efficiency ($\eta_{\text{collection}}$), and sterilization efficiency ($\eta_{\text{sterilization}}$) of bioaerosols are defined by

$$\eta_{\text{total}} = 1 - \frac{\text{CFU}_D}{\text{CFU}_0}, \quad (\text{Eq.1})$$

$$\eta_{\text{collection}} = 1 - \frac{C_D}{C_0}, \quad (\text{Eq.2})$$

$$\eta_{\text{sterilization}} = 1 - \frac{\text{CFU}_D}{\text{CFU}_0 \times (1 - \eta_{\text{collection}})} \quad (\text{Eq.3})$$

where CFU_0 and C_0 are the CFU and the number concentration when the power applied to the DBD reactor is turned off, respectively, and CFU_D and C_D are the CFU and the number concentration when the power to the DBD reactor is on, respectively.

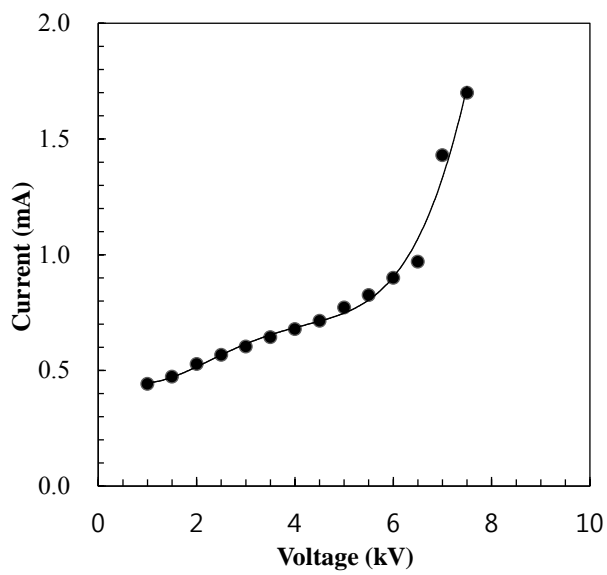


Fig. 2. I-V characteristics of DBD (at 60 Hz).

Results and Discussion

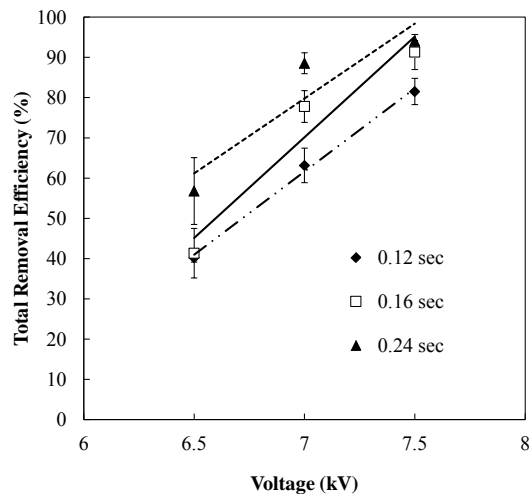


Fig. 3. Total removal efficiency of bioaerosols as a function of voltage and residence time.

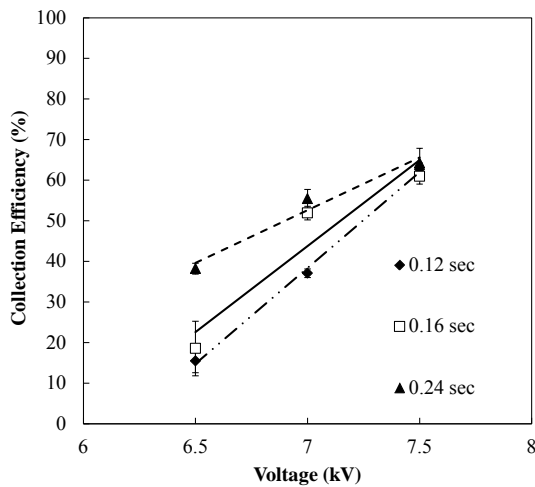


Fig. 4. Collection efficiency of bioaerosols as a function of voltage and residence time.

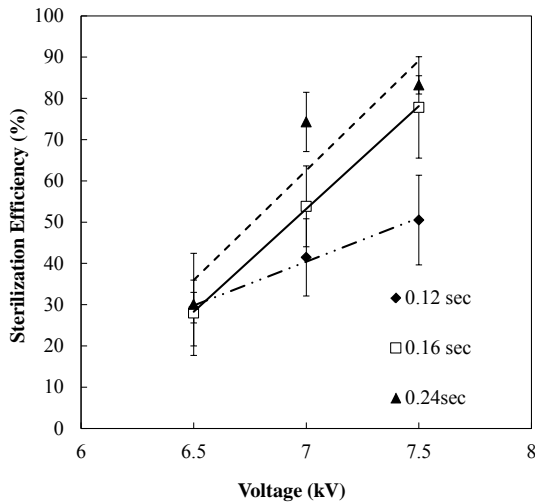


Fig. 5. Sterilization efficiency of bioaerosols as a function of voltage and residence time.

Figs. 3, 4, and 5 show the dependence of total removal efficiency, collection efficiency, and sterilization efficiency, respectively, on applied voltage when residence times were 0.12, 0.16, and 0.24 sec. Total removal efficiency was simultaneously concerned with collection and sterilization of bioaerosols by DBD reactor. These efficiencies increased as the applied voltage or residence time increased. Because the amplitude of oscillation of bioaerosols in a DBD reactor and the particle charging increase as the applied voltage increased, higher applied voltage led to higher collection efficiencies. Longer residence times and higher applied voltages increased the chance of bioaerosols being attacked by ion, ozone, or atomic oxygen, which resulted in higher sterilization efficiencies. The residence time did not have a strong effect on the collection efficiency and sterilization efficiency for the applied voltage of 7.5 kV and 6.5 kV, respectively. Total removal efficiency, collection efficiency, and sterilization efficiency of up to 94%, 64%,

and 83%, respectively, were obtained for applied voltage of 7.5 kV and residence time of 0.24 sec.

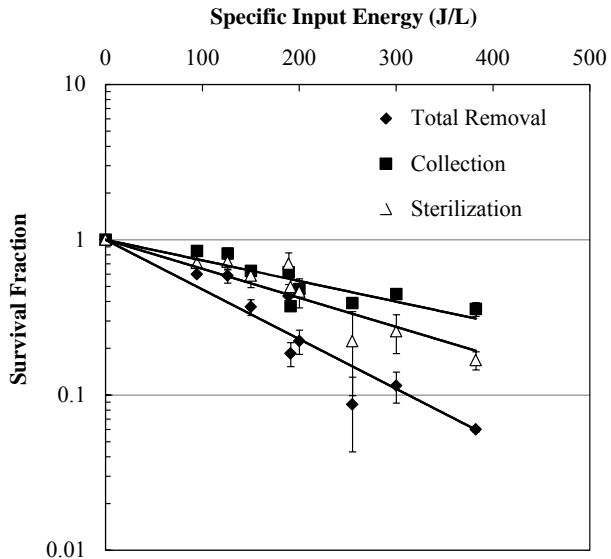


Fig. 6. Survival fraction as a function of specific input energy.

The performance of a DBD reactor can also be evaluated using specific input energy (SIE). SIE was calculated with the following relation:

$$\text{SIE (Specific Input Energy)} = \frac{\text{discharge power (W)}}{\text{gas flow rate (L/min)}} \times 60 \quad (\text{J/L}) \quad (\text{Eq.4})$$

Fig. 6 shows the behavior of survival fraction of bioaerosols with SIE. In this study, the SIE susceptibility constant is suggested as a quantitative parameter for the estimation of ability to remove bioaerosols of collection and sterilization process by the DBD reactor. The SIE susceptibility constants of collection and sterilization processes, $Z_{\text{collection}}$ and $Z_{\text{sterilization}}$, respectively, are defined by the following equation:

$$Z_{\text{collection}} = \frac{-\ln(C_D / C_0)}{\text{SIE}} \quad (\text{L/J}), \quad (\text{Eq.5})$$

$$Z_{\text{sterilization}} = \frac{-\ln[\text{CFU}_D / \{\text{CFU}_0 \times (1 - \eta_{\text{collection}})\}]}{\text{SIE}} \quad (\text{L/J}) \quad (\text{Eq.6})$$

The SIE susceptibility constant simultaneously concerned with collection and sterilization

process, Z_{total} , is defined by the following equation:

$$Z_{\text{total}} = \frac{-\ln(\text{CFU}_D / \text{CFU}_0)}{\text{SIE}} \quad (\text{L/J}) \quad (\text{Eq.7})$$

The values of Z_{total} , $Z_{\text{collection}}$, and $Z_{\text{sterilization}}$ are 0.00737, 0.00306, and 0.00431 L/J, respectively (Fig. 6).

SUMMARY OR CONCLUSION

In this study, we attempted to remove bioaerosols using a lab-made dielectric barrier discharge (DBD) reactor, and studied characteristics of removal of bioaerosols by DBD reactor. Total removal efficiency, collection efficiency, and sterilization efficiency of bioaerosols were up to 94%, 64%, and 83%, respectively, when 7.5 kV of applied voltage and 0.24 sec of residence time were employed. The SIE susceptibility constant is suggested as a quantitative parameter for the estimation of ability to remove bioaerosols of collection and sterilization process by the DBD reactor in this study. The SIE susceptibility constants of total removal process, collection process, and sterilization process are 0.00737, 0.00306, and 0.00431 L/J, respectively. The paper shows that the DBD reactor was effective in removing bioaerosols in the short time (0.24 sec) and under 12.8 W.

ACKNOWLEDGMENTS

This work was supported by the National Research Foundation of Korea Grant funded by the Korean Government (MEST) (grant No. NRF-2010-0029297).

REFERENCES

- [1] Choi, J.H.; Han, I.; Baik, H.K.; Lee, M.H.; Han, D.W.; Park, J.C.; Lee, I.S.; Song, K.M.; Lim, Y.S. *Journal of Electrostatics* 2006, 64, 17-22.
- [2] Takayama, M.; Ebihara, K.; Stryczewska, H.; Ikegami, T.; Gyoutoku, Y.; Kubo, K.; Tachibana, M. *Thin Solid Films* 2006, 506-507, 396-399.

Ecophysiological responses of winter wheat seedling to aerosol wet deposition of Xi'an area

Yiping Chen

SKLLQG, Institute of Earth Environment, Chinese Academy of Science, Xi'an 710075, China.

Principal Contact: Yiping Chen, Prof., SKLLQG, Institute of Earth Environment, Chinese Academy of Science, Xi'an 710075, China.

Tel: 029-88324766 E-mail: lifesci@ieecas.cn

Abstract

Aerosol leads to a 30% reduction in solar radiation reaching the earth's surface, and in crops yield for both wheat and rice. To determine the effect of aerosol wet deposition on crops, aerosol samples were collected in September of 2006 at Xi'an urban suburb ($34^{\circ}44'N$, $109^{\circ}49'E$) using two battery powered mini volume samplers (Airmetrics, Oregon, USA) operating at a flow rate of 5 L/min, then the samples were extracted ultrasonically and diluted to concentrations of 1, 2, 3 and 4 mg/L, wheat seedlings were treated with aerosol of different concentrations in laboratory conditions. Changes in physiological and biochemical parameters of wheat seedlings were measured. In comparison with the control, the activities of superoxide dismutase (SOD) and catalase (CAT) and the concentration malondialdehyde (MDA) and oxidized glutathione (GSSG) of wheat seedlings increased progressively with increasing concentrations of added aerosol, while the opposite trend was seen for the activities of nitric oxide synthase (NOS), the concentrations of glutathione (GSH) and nitric oxide (NO), and the ratio of GSH/GSSG. When the seedlings were treated with the aerosol of 1 and 2 mg/L, the coleoptile elongation, shoot elongation and biomass accumulation were increased, the best effect was at treatment of 2 mg/L. However, aerosol treatments with rates of 3 and 4 mg/L resulted in a decrease in coleoptile elongation, shoot elongation and biomass accumulation in seedlings, significant effect was for the treatment of 4 mg/L. Hence, a lower concentration of aerosol wet deposition was in favor of crops growth, but its higher concentrations resulted in deleterious effects for crops and decreased crops growth.

Key words: aerosol deposition, environment pollution, air pollution, ecotoxicological testing, aerosol risk assessment.

Influences of Air Volume, DNA Template, and Dilution Factor on the Performance of qPCR Coupled with a Modified BioStage Sampling Method in Quantifying Bioaerosols

Zhenqiang Xu and Maosheng Yao

State Key Joint Laboratory for Environmental Simulation and Pollution Control, College of Environmental Sciences and Engineering, Peking University, Beijing 100871, China

Principal Contact: Maosheng Yao, Professor, State Key Joint Laboratory for Environmental Simulation and Pollution Control, College of Environmental Sciences and Engineering, Peking University, Beijing 100871, China.

Tel: +86 010 6276 7282 Email: yao@pku.edu.cn

Abstract

There is an increased interest in integrating polymerase chain reaction (PCR) based technologies with air sampling in investigating airborne microbial community. However, a variety of factors influence the overall performance of such integration. For the sampling method, Andersen type impactors are widely used, but most of them are restricted to the agar culturing method. Here, a BioStage impactor was modified to collect air samples directly into petri dish filled with deionized (DI) water, instead of agar plates. During the sampling, the BioStage impactor was operated at a standard sampling flow rate of 28.3 L/min for 10, 20, 30 min both in indoor and outdoor environments. For each experimental condition, three independent repeats were performed. The collected air samples into the DI water under different experimental conditions were further filtered through a mixed cellulose ester (MCE) filter, and further extracted using DI water. The final sample suspension was subject to qPCR analysis. In addition to the different air sampling volumes, different sample DNA templates (2 or 5 μ l) and dilution factors (10 and 50 times) were investigated on the overall performance of PCR-BioStage integration method.

Results revealed that use of the modified BioStage bioaerosol collection method resulted in successful amplification of bacterial cells. In general, use of 2 μ l resulted in higher PCR product concentrations under all experimental conditions than those obtained using 5 μ l DNA template. This would be helpful for further diversity analysis. Sampling time was also observed to play a role in the overall performance of qPCR, and 10 min sampling time was shown enough to allow the air samples to be efficiently amplified. The effects of dilution factors were shown to be dependent on the sampling time and environments. The results from this study have demonstrated an effective bioaerosol monitoring protocol by integrating qPCR and impaction based air sampling method by choosing an optimal combination sampling time, DNA template and dilution factor.

Keywords: six-stage Andersen sampler, Bacterial aerosols, PCR, BioStage impactor

Effects of single-walled carbon nanotube filter on culturability and diversity of environmental bioaerosols

Zhenqiang Xu and Maosheng Yao

State Key Joint Laboratory for Environmental Simulation and Pollution Control, College of Environmental Sciences and Engineering, Peking University, Beijing 100871, China

Principal Contact: Maosheng Yao, Professor, State Key Joint Laboratory for Environmental Simulation and Pollution Control, College of Environmental Sciences and Engineering, Peking University, Beijing 100871, China.

Tel: +86 010 6276 7282 Email: yao@pku.edu.cn

Abstract

In this study, single-walled carbon nanotube (SWNT) filters were prepared using mixed cellulose ester (MCE) filters and carbon nanotubes with three levels of loading: 0.02, 0.16 and 0.64 mg/cm². Both MCE and SWNT filters were used to collect bacterial and fungal aerosols with a total volume of 200 L air sampled in indoor and outdoor environments. After sampling, the filters were directly placed on agar plates at 26 °C for culturing. The culturable aerosol counts were manually obtained both for MCE and SWNT filters, and the resulting bacterial colony forming units (CFUs) were washed off and subjected to the culturable aerosol diversity analysis using polymerase chain reaction-denaturing gradient gel electrophoresis (PCR-DGGE). For fungal CFUs, microscopy method was used to study the diversity obtained using different filter types.

The results showed that use of SWNT filters with medium and high CNT loadings resulted in significant reduction (up to 2 logs) of culturable bacterial and fungal aerosol counts compared to MCE filters in both environments. For low CNT loading (0.02 mg/cm²), very limited inactivation effects were observed for fungal aerosols, while more bacterial counts were obtained possibly due to the split of the aerosol aggregates. PCR-DGGE analysis revealed that SWNT filters at high CNT loading (0.64 mg/cm²) resulted in lowest culturable diversity, especially pronounced for outdoor bacterial aerosols. For low and medium CNT loading, the culturable bacterial aerosol diversity remained similar. Fungal aerosol analysis showed that use of SWNT filters with medium to high CNT loading also resulted in significant reduction of fungal species diversity. The results here demonstrated great promise of the SWNT hybrid filter in controlling biological aerosols, and suggested its potential to impact current air conditioning system.

Keywords: Single-walled carbon nanotube (SWNT), culturability, culturable bioaerosol diversity, inactivation, denaturing gradient gel electrophoresis (DGGE)

Boundary layer evolution and soot aging: a case study with tethered balloon observation

Daizhou Zhang¹, Guangyu Shi², Biao Wang², Bin Chen², Maromu Yamada³ and Hongya Niu⁴

1 Faculty of Environmental and Symbiotic Sciences, Prefectural University of Kumamoto, Kumamoto 862-8502, Japan

2 Institute of Atmospheric Physics, Chinese Academy of Sciences, Beijing 100029, China

3 Center for Innovation, Kanazawa University, Kanazawa 920-1192, Japan

4 College of Geoscience and Surveying Engineering, China University of Mining & Technology, Beijing 100083, China

Principal Contact: Daizhou Zhang, Dr., Prefectural University of Kumamoto, Kumamoto 862-8502, Japan.

Tel: +81-96-312-6712 Fax: +81-96-384-6765 E-mail:dzzhang@pu-kumamoto.ac.jp

Abstract

A layered structure of aerosol particles from surface to 1080 m was observed in Beijing during daytime on December 8, 2007. Under about 700 m, particles were well mixed vertically. From 700 to 1000 m was an elevated aerosol layer (EAL), in which aerosol concentration was remarkably larger than those in the lower and upper layers. Electron microscopic analysis of particles in the size range of $0.2 \sim 1.3 \mu\text{m}$ at different altitudes revealed that soot particles were predominant in all layers. There were fresh, young and aged soot particles in the lower layer. In contrast, soot particles in the EAL were all well aged, showing the structure of shrunk soot inclusions coated with weak absorbing species (the so-called core-shell structure). The geometric mean equivalent diameter of soot particles in the EAL was approximately $0.4 \sim 0.6 \mu\text{m}$ while that of their soot inclusions was about $0.1 \mu\text{m}$. The EAL coincided with the remaining nocturnal layer aloft, which was the residual left by the daytime upward convective mixing in the boundary layer. The lapse rate in the lower part of the EAL had an obvious decrease in the morning, indicating the absorption effect of soot particles there. These results suggest that the fate of soot particles was closely dependent on the evolution of the boundary layer. While particles emitted from surface were efficiently mixed upward in daytime, residual nocturnal layer as a cap lid produced an EAL abundant in well-aged soot particles, in which the aerosols, as a feedback, enhanced the stability of the layer by absorbing solar radiation.

Keywords: urban atmosphere, vertical distribution, convective mixing, elevated aerosol layer

Unmanned Aircraft System-Based Aerosol Concentration, Size, and Composition Measurements

Catherine F Cahill¹ and Gregory W. Walker¹

1 Geophysical Institute, University of Alaska Fairbanks, 903 Koyukuk Drive, Fairbanks, AK 99775, United States

ABSTRACT

Aerosol plumes with high mass concentrations, such as wildfire smoke, dust storms, or volcanic ash, can have significant adverse effects on human health and aircraft safety. Satellites can locate these plumes if the aerosol concentrations are high while models can predict where the plumes will propagate in the future. However, the thresholds at which the aerosols are visible in a satellite image and how effective the models are at predicting an aerosol concentration at a specific point in time and space are not known. Measurements of aerosol concentration, size, and composition under these high concentration conditions are needed to establish the thresholds and validate the models. Because these high aerosol conditions are often contained in elevated plumes, aircraft sampling is the only way to collect this information. However, these plumes content or concentrations are often too hazardous for manned aircraft, so unmanned aircraft systems (UAS) provide an ideal way to get the needed *in situ* information. Scientists and engineers from the University of Alaska Fairbanks (UAF) have developed a small UAS-based aerosol impactor for use in high concentration aerosol plumes. The sampler can collect aerosols in up to eight size fractions for *ex post facto* analyses, such as beta-gauge for mass concentration, synchrotron x-ray fluorescence for elemental composition, and wavelength-specific fluorescence for bioaerosol content. The UAF UAS this system was designed to operate upon has an endurance of up to 20 hours and a flight ceiling of over 6 km allowing the aircraft to map the plume vertically and horizontally. The aircraft also can follow a plume and monitor the evolution of the plume's aerosol during transport away from the source.

KEYWORDS

Unmanned Aircraft System (UAS), Aerosol Impactor, Wildfire Smoke, Volcanic Ash

BODY

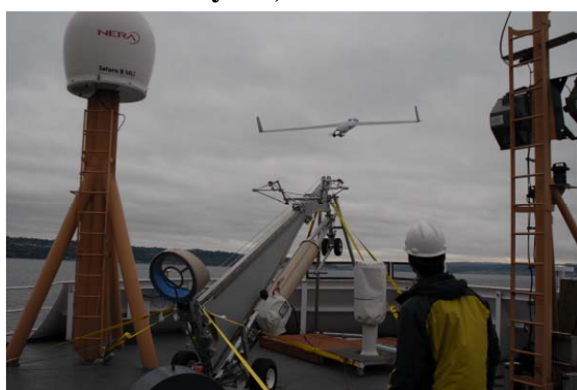
Introduction

Airborne measurements of high concentration aerosols, such as volcanic emissions and dense wildfire smoke are essential for aerosol cloud model development improvement and validation. Space-based remote sensing is routinely used to track aerosol clouds; however, a lack of *in situ* collections limits the reliability of such methods. Measurement techniques for *in situ* collection are limited. Flying manned aircraft through these clouds, although executed, is known to be damaging to the aircraft and considered dangerous for the pilots or scientific crew. Ground based disposable instruments, such as sondes on weather balloons, currently lack some of the aerosol specific observations, such as composition and concentration that are essential for improving the satellite retrieval algorithms. Unmanned aircraft are well suited for *in situ* measurements, such as atmospheric vertical profiles in hazardous environments. Our research addresses tailoring current aerosol sampler designs for small, unmanned aircraft that are suitable for deployment into volcanic plumes. Also, we are investigating the value gained by combining information from *in situ* samples with an existing airborne synthetic aperture radar, visible spectrometer, and thermal imaging payloads all of which the University of Alaska has flown on their small, unmanned aircraft. Together this instrument suite offers a safe method to collect data that has never been collected and should provide insight into the vertical structure of such aerosol plumes.

University of Alaska's Unmanned Aircraft System

The University of Alaska owns four Boeing ScanEagle unmanned aircraft (Figure 1). These 20 kg, 3.1 m wingspan aircraft have long endurance capabilities in excess of 20 hours duration and can operate at altitudes in excess of 6,000 m. The small size of the aircraft sets strict limits on the size of the aerosol-sampling payload.

Figure 1. Launching a University of Alaska ScanEagle from the NOAA Research Vessel Oscar Dyson, October 2009.



The ScanEagle aircraft are well suited for operations in hazardous conditions and have successfully operated in the desert, in the Arctic and over wildfires. The University of Alaska has operated a ScanEagle in wildfire smoke under zero visibility conditions (Figure 2)

and was able to provide imaging data necessary for monitoring an ongoing and evolving incident with image resolutions not available from satellite observations but critical for management decisions. The ability of the ScanEagle to fly in poor visibility conditions and beyond the line of sight of the operators means that the University of Alaska can operate the aircraft from a location of safety away from any aerosol hazard, but still take measurements inside an aerosol plume.

Given that the unmanned aircraft may be operated from ships, the aircraft will be able to follow plumes originating from island volcanoes, such as those in the Aleutian Islands or in Iceland (Figure 3). This is vital for validating model predictions the amount of ash present in the North Pacific or North Atlantic flight lanes that could pose a hazard to aviation.

Figure 2. A University of Alaska ScanEagle approaching recovery after conducting a successful wildfire observation mission in thick smoke while supporting the Alaska Fire Service on the 2009 Crazy Mountain Wildfire Complex.



Figure 3. A University of Alaska ScanEagle approaching recovery on the NOAA Ship MacArthur II along the ice edge in the Bering Sea May 2009. (Photo by NOAA).



Instrument Development

A multi-stage aerosol impactor such as a DRUM (Davis Rotating-drum Unit for Monitoring) can collect size- and time-resolved aerosol samples^[1,2]. After being collected the samples can undergo Proton Induced X-ray Emission (PIXE), Proton Elastic Scattering Analysis (PESA) and Synchrotron X-ray Fluorescence (S-XRF) to determine the sizes and elemental compositions of the collected aerosols.

The University of Alaska has designed and built a compact lightweight aerosol sampler based on the DRUM aerosol impactor concept. The DRUM impactor technology has been used to collect volcanic ash from eruptions in Alaska^[3] and in extremely hot and dusty environments such as Iraq and Afghanistan and is a proven technique in harsh conditions^[3,4].

This eight-stage DRUM aerosol impactor was designed to fit on one of the University's ScanEagle UAS and weighs less than 3 Kg. The sampler technology has been successfully used to collect ground-based, size-and time-resolved aerosol mass concentration and elemental composition in volcanic ash and wildfire plumes^[3,4]. In these studies, the sampler continuously collected aerosol in eight size fractions (0.09-0.26, 0.26-0.34, 0.34-0.56, 0.56-0.75, 0.75-1.15, 1.15-2.5, 2.5-5.0, 5.0-10.0 or 35 μm in aerodynamic diameter), but these size fractions can be changed to collect aerosols in size fractions that would interact with light of the wavelength being used for the satellite analysis. The aerosol is collected on ApiezonTM coated MylarTM strips and analyzed with time resolutions designed to match the small, unmanned aircraft's flight plans. The aerosols will be analyzed for mass using a β -gauge, elemental composition (28 selected elements between sodium and lead) using synchrotron x-ray fluorescence^[5,6], and optical absorption/scattering using ultraviolet/visible spectroscopy. The sampler is sized for the small ScanEagle dimensions (Figures 4-6). By combining the time data with the known aircraft flight track, aerosol loading as a function of location can be determined.

Figure 4. The University of Alaska's Airborne DRUM Sampler (ADS) sitting beside a ScanEagle payload nose.



Figure 5. The eight-stage airborne DRUM sampler design.

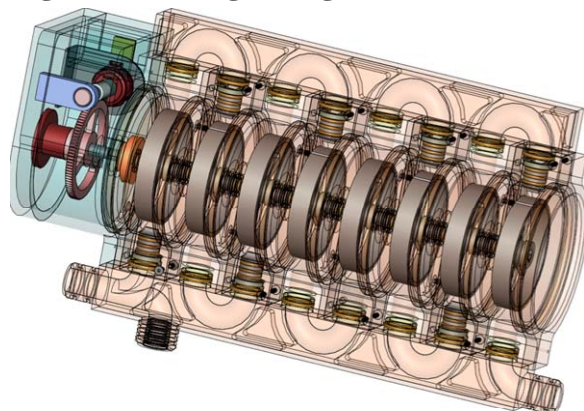
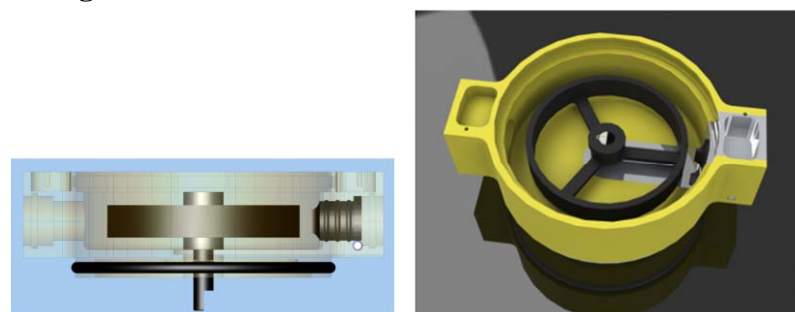


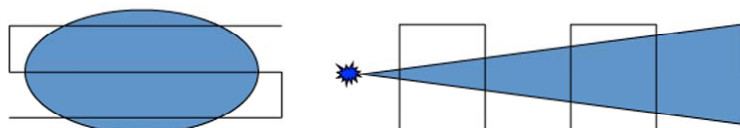
Figure 6. A single stage showing the sampler disk and the accelerating nozzle configuration.



Uses

Flying vertical and horizontal cross-sections through an aerosol plume can provide a three-dimensional picture of the aerosol compositions and concentrations in the plume (Figure 7). Following an air parcel during a Lagrangian flight will also allow scientists to examine the evolution of the aerosols in the plume. These measurements will help validate model predictions of aerosol concentrations, plume chemistry and plume extent as the emission ages.

Figure 7. Proposed cross-sectional and Lagrangian flight paths.



The promise of the three-dimensional picture has not yet been realized. The impactor has not yet flown through dense aerosol plumes. Fabrication of the lighter instrument was recently completed. The utility in the measurements however are evident in published current uses of the aerosol impactor technology in many environments, two of which (Volcanic Eruptions and Wildfire Smoke) are briefly discussed below.

Volcanic Eruptions

DRUM aerosol impactors are being used to collect size-segregated aerosol concentration and/or composition information at sites downwind of volcanic eruptions. For example, during the Augustine Volcano eruption in 2006, an eight stage DRUM impactor was located at the University of Alaska Fairbanks Homer research station 110 km ENE from Augustine Volcano. The sampler continuously collected aerosol in eight size fractions between 35 and 0.09 microns in aerodynamic diameter) from January 13 to February 11, 2006. The aerosol was analyzed with 3-hour resolution. The collected aerosol was analyzed for mass using a beta-gauge and elemental composition (28 selected elements between sodium and lead) using S-XRF^[5,6].

Wildfire Smoke

In wildfire analysis fresh or aged smoke can be isolated and the chemical composition and size distribution of the smoke particles under those conditions studied. For example, samples of aged Siberian wildfire smoke obtained at the Poker Flat Research Range during spring 2008 have been analyzed. The chemical composition of the aerosols showed a peak of mixed wildfire smoke and Asian dust followed by a period of primarily wildfire smoke.

SUMMARY

The University of Alaska operates a research center for small, unmanned aircraft systems that provides integration of unique payloads and supports pathfinder missions within science communities. The promise of the three-dimensional aerosol impactor created by this research center has not yet been realized, as the impactor has not been flown; however, fabrication is complete.

With this instrument the University of Alaska is developing the capability to collect the aerosol and optical measurements required to validate satellite imagery of such events as wildfire and volcanic ash transport and dispersion models predictions. These techniques can be extended and applied to any plumes of concern. When the satellite retrievals and model predictions have been shown effective in describing the environment, we will be better able to estimate the impact of the aerosols on the environment.

ACKNOWLEDGMENTS

To date, the University of Alaska unmanned aircraft flight operations and aerosol cloud instrument development work has been supported by the US Naval Surface Warfare Center Crane Division and the US Army Research Laboratory in Adelphi Maryland.

REFERENCES

- [1] Raabe, O. G., Braaten, D. A., Axelbaum, R. L, Teague, S. V. and Cahill, T. A. (1988), *J. Aerosol Sci.*, 19, 2, 183-195.
- [2] Cahill, T. A., and Wakabayashi, P. (1993), *Measurement Challenges in Atmospheric Chemistry*, L. Newman, ed., American Chemical Society, 211-228.
- [3] Cahill, C. F., Rinkleff, P. G., Dehn J., Webley, P. W., Cahill, T. A., and Barnes D.E. (2010), *J. Vol. Geothermal. Res.*, doi:10.1016/j.jvolgeores.2010.08.012.
- [4] Cahill, C.F., T.A. Cahill and K.D. Perry. (2008), *Atmos. Environ.*, 42, pp. 7553-7559, doi: 10.1016/j.atmosenv.04.034.
- [5] Cahill, T.A., Cliff, S.S., Perry, K.D., Jimenez-Cruz, M.P., McHugo, S.A., 1999, In Abstracts, Amer. Geophysical Union 1999 Fall Meeting, December 13-17, 1999, San Francisco, California, published by the American Geophysical Union.
- [6] Cahill, C.F., 2003, *Journal of Geophysical Research* 108 (D23): 8664-8671, doi:10.1029/2002JD003271.

Vertical Distributions of Ozone and Nitrogen Dioxide Observed in a Polluted Marine Boundary Layer around Kaohsiung City

Ching-Ho Lin¹, Chin-Hsing Lai¹, and Yee-Lin Wu²

1 Department of Environmental Engineering and Science, Fooyin University, Taiwan

2 Department of Environmental Engineering, National Cheng-Kung University, Taiwan

Principal Contact: Ching-Ho Lin, Associate professor, Department of Environmental Engineering and Science, Fooyin University, Kaohsiung 83101, Taiwan.

Tel: 886-7-7821221 Fax: 886-7-7821221 Email:chlin@mail.fy.edu.tw

Abstract

In a coastal region, ozone pollution is usually dominated by a sea-breeze circulation. However, vertical structures of ozone and its precursors within the circulation are seldom observed. Some preliminary results obtained during a 10-day field study are presented in this work. The field study was conducted in October 2009 at a small island, Little Liuqui, 15 km from the nearest coastline of southern Taiwan and 25 km to the Kaohsiung City. A tethered sounding system was installed at the shoreline of the small island to measure vertical features of meteorological parameters, ozone and nitrogen dioxide over polluted marine area. Elevated plumes at 400-800 m over the sea were detected, noticed by low ozone concentrations and high nitrogen dioxide at night. Elevated ozone layers with concentrations more than 100 ppb were observed at day above marine boundary layers with a typical depth at 250-500 m. The results suggested the observed elevated ozone layers were possibly formed by the emission of large point sources around the Kaohsiung City and the ozone within the layers may be brought into the marine boundary layers by the subsidence and the turbulent diffusion.

Keywords: Vertical distribution, ozone, nitrogen dioxide, marine boundary layer, point source

Monitoring of NO_x by a sensor made of tungsten oxide-multiwalled carbon nanotube composite

S. Monchayapisut¹, M. Sriyudthsak² and T. Charinpanitkul^{1,*}

1 Center of Excellence in Particle Technology, Department of Chemical Engineering,
Faculty of Engineering, Chulalongkorn University, Bangkok, 10330, THAILAND

2 Department of Electrical Engineering, Faculty of Engineering, Chulalongkorn University,
Bangkok, 10330, THAILAND

Principal Contact: T. Charinpanitkul, Professor, Center of Excellence in Particle
Technology, Department of Chemical Engineering, Faculty of Engineering, Chulalongkorn
University, Bangkok, 10330, THAILAND.

E-mail: ctawat@chula.ac.th

Abstract

It is well recognized that nitrogen oxides (NO_x: NO and NO₂) are harmful to the environment and human health. NO_x produced during combustion exhibits acute toxicity to human nerves and respiratory organ. Therefore detection and monitoring of these toxic gases dispersing in the surrounding have become a highly important research issue. In this work, tungsten oxide-multiwalled carbon nanotube composite (WO₃-MWCNT) have been prepared by compositing a designated amount of pristine MWCNTs into the precipitated tungstate salt with nitric acid. After synthesis, the WO₃/MWCNT composites are characterized by scanning electron microscopy (SEM), X-ray diffraction spectroscopy (XRD), Fourier Transform Infrared spectroscopy (FT-IR) and BET analysis. The NO_x-sensing properties of hybrid film prepared by simple screen printing of WO₃-MWCNT onto alumina substrate are investigated and discussed in this work.

Keywords: Gas sensor, NO_x, Tungsten oxide, Carbon nanotube.

Monitoring of the Atmosphere using Unmanned Aerial Vehicles (UAV)

**N.M.Sitnikov¹, D.V.Akmulin¹, I.I.Chekulaev¹, O.B.Popovicheva², A.O.Sokolov¹,
A.E.Ulanovsky¹ and V.I.Sitnikova¹**

1 Central Aerological Observatory, Pervomayskaja 3, Dolgoprudny, Moscow region, 141700, Russia

2 SINP MSU, Leninskie gory 1, Moscow, 119991, Russia

ABSTRACT

Instruments for atmospheric measurements on board of unmanned aerial vehicles (UAV) developed in Central Aerological Observatory are presented. Light weight, low power and small size of the instruments permits to use them on board of small and light UAV.

Measurements of horizontal distributions and vertical profiles of atmospheric parameters have been carried out using developed instruments. Some results of field experiments concerning gas species and aerosol investigations using UAV are presented. Overview of perspectives of UAV for solutions of some tasks of atmospheric investigations was made. Some aspects of UAV applications for monitoring of the atmosphere and methods and technique for using on board of UAV are discussed.

KEYWORDS

Unmanned aerial vehicles (UAV), gas species, aerosol, monitoring, atmosphere

Introduction

Unmanned aerial vehicles (UAV) have a lot of applications in different fields of activities. In particular they can be used for environmental monitoring and atmospheric investigations. In fact they can solve the tasks which are usually solved by aircraft laboratories such as:

- Investigations of horizontal and vertical distributions of gas and aerosol composition of the atmosphere,
- Environmental monitoring of natural and anthropogenic disasters regions,
- Monitoring of atmospheric pollutions,
- Biomass burning products monitoring,
- Investigations of gas and aerosol volcanic products,
- Monitoring of radioactive pollutions,
- Investigations of processes in atmospheric boundary layer,
- Control of transboundary pollutions transport

and so on.

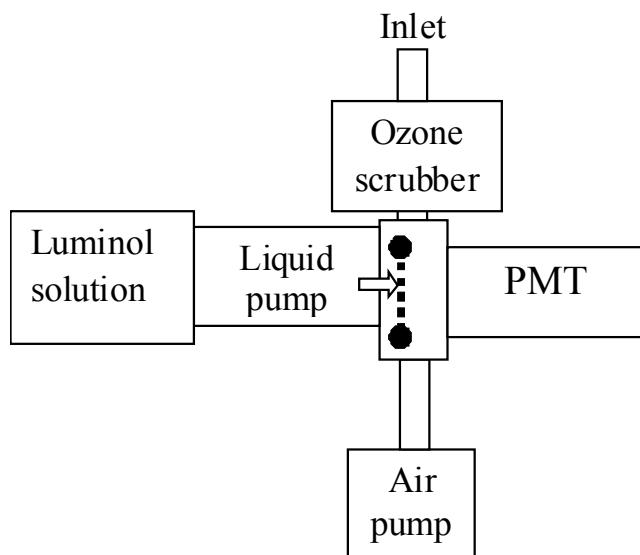
Increasing of number of publications concerning several atmospheric measurements using UAV of different types is observed during the last some years [1-4]. Usually UAV payload

capacity is considerably less than payload capacity of research aircraft. And this is why UAV are not widespread for atmospheric measurements in spite of some advantages of UAV applications in particular comparably low cost of UAV and its operation. The problem of UAV application is pure choice of small, light and low power instruments for UAV especially instruments for atmospheric composition measurements. Most of aircraft instrument are not acceptable for UAV because of their heaviness. Therefore choice, adaptation and development of small, light and low power instruments are very important for UAV applications. Some methods and sensors can be used for development of small and light instruments, such as electrochemical cells, semiconductor and chemiluminescent sensors for gas species measurements, small temperature, pressure and humidity sensors and so on. Particles counters and small aethalometers for mass concentration of black carbon measurements also can be used on board of UAV.

Instrumentation and Experimental Results.

Some instruments for UAV developed in Central Aerological Observatory and testing of the instruments on board of UAV are presented in this paper. Special attention was paid to decreasing of weight and size of the instruments to use them on board of small UAV. Developed instruments for measurements of nitrogen dioxide and ozone are based on heterophase chemiluminescent method that is interaction of determined molecules with chemiluminescent sensitive element with light generation. Main advantages of the method are high sensitivity and time resolution. Two types of sensitive element are usually used. One of them is solid porous element impregnated by chemiluminescent composition and dried. Another type is chemiluminescent solution continuously supplied on surface of porous material in reaction chamber. Sensitive elements of both types are small peace (1 cm^2) of porous material. Photoelectric multiplayer is usually used as photo receiver. Chemiluminescent methods permit to develop small, light and low power instruments suitable for using on board of UAV. These methods are used in atmospheric investigations for ozone ^[5] and NO_2 measurement ^[6]. Chemiluminescent instruments for ozone and nitrogen dioxide measurements on board of aircraft have been developed in Central Aerological Observatory. These instruments are used for atmospheric investigations on board of research aircrafts M55 "Geophysica" (Russia) and "Falcon" (Germany). The weight of the instruments was 5-10 kg. For UAV only sensor elements were used. Another elements and electronics have been developed taking into account the necessity to make them small and light. Block layout of chemiluminescent nitrogen dioxide analyzer for UAV is shown in Fig.1.

Figure 1. Block layout of chemiluminescent nitrogen dioxide analyzer



Main elements of the instrument are:

- Liquid pump,
- Air pump,
- Reaction chamber,
- Photoelectric multiplier with electronic block.

For stable operation of the instrument constant flow of chemiluminescent solution and air flow through the reaction chamber must be provided. Stability of the solution and air flows is very important because the intensity of chemiluminescent radiation depends on them.

Specially developed small syringe pump have been used as a liquid pump. Light radiation as a result of NO₂ reaction with chemiluminescent solution on the surface of porous material is detected by photoelectric multiplier HAMAMATSU H5783-06. To avoid ozone influence special ozone filter is used [6]. High sensitivity and high time resolution are the main advantages of the method. This method can be used also for ozone measurements. Special solution as a chemiluminescent composition has to be used for ozone measurements but construction of the instruments may be the same.

Technical characteristics of the instrument:

- range of measured NO₂ concentration – 0.1 – 100 ppb,
- time resolution – 0.2 sec,
- power – 5 W,
- weight – 200 g.

For ozone measurements another modification of heterophase chemiluminescent method can be used. It is based on reaction of ozone with solid chemiluminescent element. Block layout of the instrument is shown in Fig.2 (a).

Figure 2. Block layout of chemiluminescent ozone analyzer (a) and time dependence of sensor sensitivity during exposition by ozone (b).

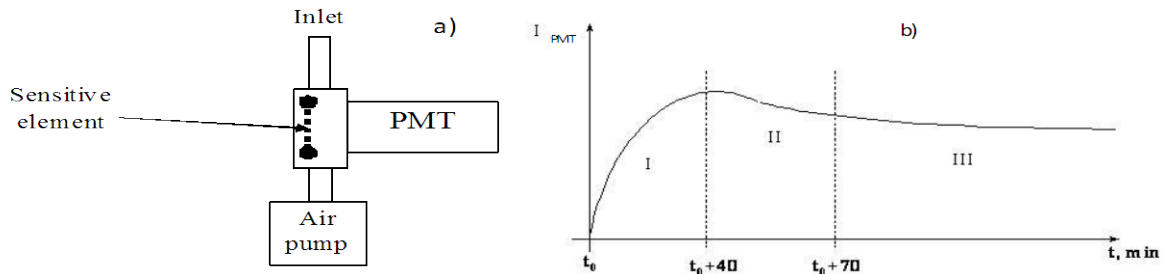


Fig2. Block layout of chemiluminescent ozone analyzer (a) and time dependence of sensor sensitivity during exposition by ozone (b).

This method is used for development of balloon, aircraft and ground based instruments. It is suitable for tropospheric and stratospheric measurements. The main disadvantage of this method is instability of solid chemiluminescent sensor. Usual time dependence of sensitivity during exposition of the sensor by ozone is shown in Fig 2(b). There are three periods of time dependence: activation (I), stabilization (II) and operation (III)^[5]. The best time period of the sensor operation is period 3 with slow decreasing of sensitivity. For aircraft instruments periodical in flight calibration of chemiluminescent sensor is provided. But if duration of a flight is not long (1-2 hours) it is enough to calibrate the sensor before and after the flight. In this case the instrument can be made very small light and simple. The weight of developed instrument is 150 g. For both chemiluminescent instruments temperature and pressure must be carefully controlled.

Technical characteristics of the instrument:

- range of measured NO₂ concentration – 1 – 1000 ppb,
- time resolution – 0.2 sec,
- power – 5 W,
- weight – 150 g.

Microprocessor block with flash memory is based on AT Mega microcontroller. Pressure, humidity and temperature were measured on board of UAV using MPX 4115 (Motorola) pressure sensor, HIH-4000 (Honeywell) humidity sensor and thermistor. Besides some impactors for collection of aerosol particles for further chemical analysis have been tested. Characteristics of UAV which have been used for field experiments are.

- Wingspread – 180 cm,
- Weight - 3 kg,
- Payload - 0.8 kg,
- Flight duration – 30 min.

Video camera and developed instruments have been installed on board of UAV. The distance of flights was about some kilometers. Chemiluminescent instruments, block of sensors and microprocessor block have been tested. Data of measurements during flights have been recorded to flash memory on board of UAV. Maximal altitude of flights was 500 m. Some results of measurements are shown in Fig.3.

Figure 3. Vertical distribution of temperature and relative humidity (a) and NO₂ distribution at the altitude 50 m (b) measured on board of UAV near Moscow.

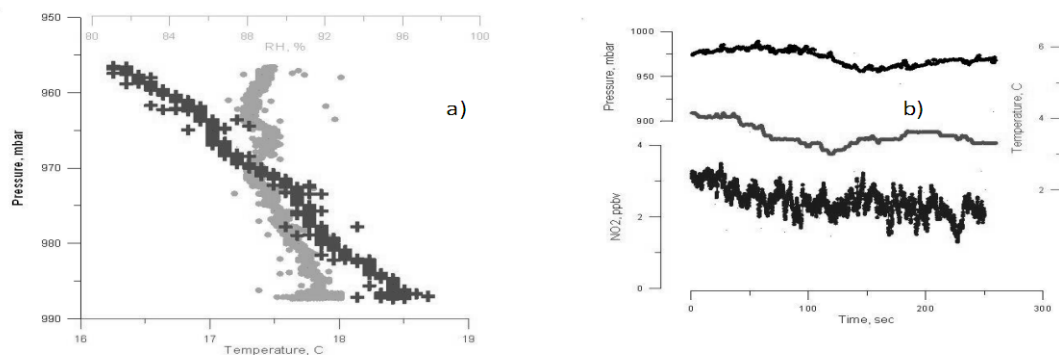


Fig.3. Vertical distribution of temperature and pressure (a) and NO₂ distribution at the altitude 50 m (b) which have been measured on board of UAV near Moscow.

CONCLUSION

Thus application of UAV permits to solve different tasks connected with atmospheric measurements and environmental monitoring. UAV can be used in monitoring system as mobile tools or as additional instrument to mobile tools. They are very actual taking into account increasing of natural and anthropogenic disasters. As analyze show even small, light and not expansive UAV with instrumental equipment permits to make measurements horizontal and vertical distributions of meteo parameters gas and aerosol composition of the atmosphere. Known methods and modified instruments can be used for development of instruments for UAV. In common activity connected with using of UAV for atmospheric investigations and environmental monitoring is very actual and perspective demanding further development. This is promoted by the progress of UAVs, improvement of their flight control, constructions and characteristics.

ACKNOWLEDGMENTS

The work has been carried out by support of Russian Federal Service for Hydrometeorology and Environmental Monitoring.

REFERENCES

- [1] Jonassen, M., The Small Unmanned Meteorological Observer (SUMO) – Characterization and test of a new measurement system for atmospheric boundary layer research. Master thesis, University of Bergen, Norway, 2008.
- [2] Aline van den Kroonenberg A. C., Martin T., Buschmann M., Bange J. and Vørsmann P., Measuring the Wind Vector Using the Autonomous Mini Aerial Vehicle M2AV. *J. Atmos. Oceanic Technol.*, 2008.
- [3] McGonigle A.J.S., Aiuppa A., Giudice G., Tamburello G., Hodson A.J., Gurrieri S., Unmanned aerial vehicle measurements of volcanic carbon dioxide fluxes. *Geophysical research letters*, v. 35, L06303, 4 PP., 2008
- [4] Pereira E., Bencatel R., Correira J., Felix L., Gonsalves G., Morgado J. and Sousa J. Unmanned Air Vehicles for coastal environmental research. *Journal of Coastal Research*, SI 56 (Proceedings of the 10th International Coastal Symposium) 1557 – 1561. Lisbon, Portugal, ISSN 0749-0258, 2009.
- [5] Ulanovsky A.E., Yushkov V.A., Sitnikov N.M., Ravegnani F. Fast chemiluminescent airborne ozone analyzer FOZAN-II. *Instruments and Experimental Techniques*, No.2, pp. 127 – 135, 2001.
- [6] Sitnikov N., Sokolov A., Ravegnani F., Yushkov V., Ulanovsky A. A Chemiluminescent Balloon-Type Nitrogen Dioxide Meter for Tropospheric and Stratospheric Investigations (NaDA). *Instruments and Experimental Techniques*, Vol. 48, No. 3, pp. 400–405, 2005.

O₃/NO₂/NMHC Air Pollutants Monitoring Through an Unmanned Aerial Vehicle

Char, Jir-Ming, Lin, Chin-Ho, Chu, Harry, Chen and Tan-Chen

Department of Environmental Engineering and Science, Fooyin University, Taiwan

Principal Contact: Jir-Ming Char, Prof., Department of Environmental Engineering and Science, Fooyin University, Taiwan.

Tel: 886-921821598 Email: jirmchar@yahoo.com.tw

Abstract

This research adopts a fully self-developed Unmanned Aerial Vehicle (UAV) to measure the variation of O₃/NO₂/NMHC distributions in the air. This carbon-fiber material made UAV uses modulus design to deal with the multiple needs for air pollution detecting instruments in the future. The instrument for examining the variation of ozone in this research uses carried ozone sensor (Model OFM-106) from 2B company, which takes advantage of the theory of ultraviolet ray absorption to monitor the concentration of ozone. This instrument completely conforms to the regulation of NIEA A420.11C for automatically examining ozone in the air in Taiwan. In this research, Ligang in PingTung was chosen as the testing site. First of all, the area and height of navigation is decided between 200 meters and 300 meters. The mean value of ozone is 67.9 ppb; the minimum value is 53.2ppb and the maximum value is 86.8 ppb. Compared with the mean value of 69.5 ppb examined by Air Quality Monitoring Station at that time, the mean value 67.9 measured by UAV is slightly lower by 1.6 ppb. The instruments for measuring the NO₂/NMHC are also adopted and use the same scheme as O₃ system. Hence, these indicate that the UAV equipped with O₃/NO₂/NMHC meteorological sounding instrument is able to accurately examine the variation and distribution of pollutants in the air. Also we couple the flying route of UAV with GPS positioning system. It shows that the corresponding relationship between O₃ and geographical position in detail and which can improve the application of 3D environmental monitoring capability.

Keywords : Ozone, NO₂, Air pollutant measurements, UAV.

Large fire emissions in summer over the southeastern US: Satellite measurements and modeling analysis

Tao Zeng and Yuhang Wang¹, Di Tian^{1,2}, Amistead G. Russell¹

1 Georgia Institute of Technology, 311 Ferst Drive, Atlanta, GA, 30332, USA

2 Georgia Department of Natural Resources, 4244 International Parkway, Atlanta, GA, 30354, USA

Principal Contact: Tao Zeng, Research Scientist II, Georgia Institute of Technology, 311 Ferst Drive, Atlanta, GA, 30332, USA.

Tel: 1-404-363-7081 Email: tzeng@gatech.edu

Abstract

MODIS satellite observed fire products are compared to the ground-based fire inventory in 2002 in the southeastern United States. The correlation coefficient between the monthly totals from Terra MODIS fire products and VISTAS fire inventory is 0.57. The relationship between Terra and Aqua MODIS fire products from 2003 to 2006 are analyzed and then used to predict Aqua MODIS fire counts in the first 7 months in 2002. A better description of ground fire burning in the southeastern US is obtained by combining Terra and Aqua MODIS fire products. Consistent springtime fire maximum are shown in both ground and satellite-based datasets in the southeastern US. The major discrepancy is that the satellite observed fire peak in summer 2002 is not reflected in ground inventories. A new fire emission inventory is therefore constructed by incorporating the satellite detected fire monthly trend into the ground-based fire inventory. It is evaluated by air quality modeling using the newly developed fire emissions. The results show an improved elemental carbon (EC) aerosol simulation against the observations. Further analysis of MODIS AOD changes at fire pixels in the Southeast detected fine AOD increase by 27% due to fire events. Both model study and AOD analysis indirectly confirm the satellite fire observed summertime fire events missed in the current inventory and help reconcile the underestimate of summertime carbonaceous aerosol loading in the southeastern United States.

Keywords: Biomass burning, satellite fire detection, carbonaceous aerosol, model evaluation

Characteristics of Sized-resolved Anhydrosugars and Pollutants

Derived from Rice Straw Burning in Controlled Chamber

Chih-Jen Chuang¹, James J. Lee^{2*}, Jian-Li Lin²

1 Engineering Science and Technology, National Yunlin University of Science and Technology, Yunlin, Taiwan

2 Environmental Health and Safety Engineering, National Yunlin University of Science and Technology, Yunlin, Taiwan

Principal Contact: Chih-Jen Chuang, candidate for doctor's degree, National Yunlin University of Science and Technology, 123 University Road, Section 3, Douliou, 640.

Tel: 05-5342601#4408 Fax 05-5312069 E-mail g9214711@yuntech.edu.tw.

Abstract

This study discusses the particle-sized emission characteristics in three combustion conditions (smoldering, flaming, and mixing conditions). The purpose of this paper is to investigate of characterize particle-sized profiles for the compositions of particulate mass, carbon species (OC and EC), three anhydrosugars (levoglucosan, mannosan, and galactosan) and water-soluble inorganic derived from rice straw burning in a controlled chamber. The results have shown that the smoldering smoke releases the highest particulate mass concentration in three combustion conditions. The particle-size emission of rice straw burning was concentrated in PM_{2.5} particles (66~77% of TSP). Levoglucosan constituent accounts 90% in three anhydrosugars from rice straw burning in the experiment. The ratio range of levoglucosan to mannosan (Levo/Mann) from rice straw burning was approximately 25-40 resulting from cracking cellulose composition in several burning conditions. The carbonaceous composition from rice straw burning was mainly consisted in organic carbon (OC>90%), indicated that rice straw burning belongs to incomplete combustion. Water-soluble ions of particles from rice straw burning significantly abound in splices of Cl⁻, F⁻, SO₄²⁻, K⁺, and NH₄⁺. The higher CO/CO₂ value (>11%) was belong to smoldering condition of rice straw burning. Therefore, the study indicated that levoglucosan might be assigned as a unique molecular tracer and very helpful to identify rice straw burning emission characteristics in the future.

Keywords: Biomass burning, Levoglucosan, Particle-size distribution, Ions, Carbon dioxide

NEW METHODOLOGY FOR EVALUATING CONSTRUCTION YARD CONTRIBUTION TO A PM₁₀ DUST IN SHANGHAI

Francesco Petracchini¹, Michela Sinesi¹, and Ivo Allegrini²

1 CNR-IIA, Via Salaria Km 29.300, Monterotondo (Rome), Italy, 00040

2 Consorzio Coram Via C. Colombo, 37/E, Ferrara 44100

Principal Contact: Francesco Petracchini, Dr., CNR - Institute of Atmospheric Pollution Research, Area della Ricerca di Roma 1, Via Salaria Km 29,300, Monterotondo (RM) 00016.

Tel: +390690672402 Fax: +390690672660 E-mail petracchini@iia.cnr.it

Abstract:

Shanghai is a fast developing city and a conspicuous number of construction yards can affect the air quality in term of PM₁₀ production. A monitoring campaign and air dispersion modelling simulations have been done to evaluate dust emission factor from the constructions sites. The study was conducted by Italian CNR and Chinese EMC of Shanghai in the framework of the APEM project (Air Pollutants Emission Monitoring). A first assessment activity was developed from October to November 2006, in a construction site named Peng Xin Mansion, where 8 PM₁₀ sequential samplers and 2 meteorological towers, were deployed. The data collected were used to improve a new empirical methodology to evaluate the emission factor related to the PM₁₀; also a Gaussian plume model AERMOD was used to test the methodology.

Results from the air dispersion model were obtained using different emission factor calculate from two procedures, one from the known AP-42 (EPA-USA) and the second from the empirical areal emission factor that had to be tested. The first procedure based on the US EPA AP-42 assigns different sources depending on construction activities and in this case no good results were achieved. The reason is a lack of a knowledge regarding the source location depending on schedule time, the specific employed machinery and the detailed construction operations. The second procedure, based on the determination from the measured data of an areal emission factor, gave good results regarding the trends and the values obtained comparing with the measured data. Considering the results obtained we found for the construction site, one emission factor, valid for the month of October and November 2006; this value is 1.8 g/ (m²*sec) of PM₁₀ emitted.

At the end to better understand the role of the construction yards in the air quality budget in a city of Shanghai we use the estimated emission factor as input in the AERMOD model.

Keywords: Shanghai, construction yard, emission factor, modeling

Measurement of PM Emissions and Electrostatic Precipitator Charging Efficiency from Coal Combustion

Erkki Lamminen, Jukka Kujanpää

Dekati Ltd. Osuusmellynkatu 13, Tampere, 33700

Principal Contact: Erkki Lamminen, CEO, Dekati Ltd. Osuusmellynkatu 13, Tampere, 33700, Finland.

Tel: +358-3-3578100 Fax: +358-3-3578140 Email: erkki.lamminen@dekti.fi

Abstract

Particulate matter, PM, is one of the main pollutants in urban environment and especially in developing countries one of its main sources is energy production at power plants.

We have developed a method for particle characterization in different parts of the power plant to understand particle formation and transformation and for optimization of the combustion process and flue gas cleaning systems. This method allows measurements directly from combustion, before and after the cleaning devices and from the actual emission into ambient air. In this work we present a particle measurement and dilution system that is capable of taking samples from most sources and carry out measurements of particle number and mass concentrations and distributions.

All measurements were conducted with the Electrical Low Pressure Impactor+, ELPI+, which measures real-time particle number and mass size distributions and concentrations in the size range between 0.006 and 10 μm . The size range is logarithmically evenly spaced into 14 separate size classes. As a unique feature of the instrument, ELPI+ can also automatically measure charge/particle (Q/N, Q/M) levels with the same size resolution. Sample conditioning was carried out with the Dekati[®] FPS-4000 and DEED systems with suitable accessories.

Particle measurements were conducted at a large scale coal firing power plant at Helsinki, Finland. The power plant is equipped with an electrostatic precipitator (ESP), scrubber with sulfur removal and a final baghouse filter for flue gas cleaning. Electrostatic precipitator charging efficiency was also studied with the automatic charge measurement feature of the ELPI+[®] instrument.

ELPI+ measurement shows the size distribution and concentration of PM before and after the cleaning equipment. ESP size resolved charging efficiency is presented and discussed with additional results from other power plants. The importance of correct measurement location and measurement setup and the pros and cons of the used setup are discussed.

Keywords: Combustion, Electrical Low Pressure Impactor+, ESP

Characteristics of Particles Emissions and Polycyclic Aromatic Hydrocarbons from IDI-Turbo Diesel Engine Fueled with Palm Oil Blend Diesel

K. Phoungthong¹, S. Tekasakul¹, P. Tekasakul², G. Prateepchaikul², M. Furuuchi³, and M. Hata³

1 Department of Chemistry and Center of Excellence for Innovation in Chemistry (PERCH-CIC), Faculty of Science, Prince of Songkla University, Hat Yai, Songkhla 90112, Thailand

2 Department of Mechanical Engineering, Faculty of Engineering, Prince of Songkla University, Hat Yai, Songkhla 90112, Thailand

3 Graduate School of Natural Science and Technology, Kanazawa University, Kakuma-machi, Kanazawa 920-1162, Japan

Principal Contact: Khamphe Phoungthong, Department of Chemistry and Center of Excellence for Innovation in Chemistry (PERCH-CIC), Faculty of Science, Prince of Songkla University, Hat Yai, Songkhla 90112, Thailand.

Email: khamphe@hotmail.com

Abstract

Physical and chemical characteristics of fine- and nano-particles associated polycyclic aromatic hydrocarbons (PAHs) from emission of an indirect injection (IDI)-turbo diesel engines (Toyota, model 2L-T) fueled with diesel and palm oil blends were investigated. In this study, commercial diesel (PB0) and blends of degummed-deacidified mixed crude palm oil in diesel at portions of 20 (PB20), 30 (PB30) and 40 (PB40) vol.% were used in engine testing. Two cascade air samplers of fine- and nano-particles were used to collect particles emitted from the engines. Sixteen PAH compounds were analyzed using a high performance liquid chromatography (HPLC). The particulate matters (PM) size distributions of emission from the engines show a unimodal behavior in the accumulation mode and the mass median aerodynamic diameters (MMAD) were in sub-micron, dependent on the blending ratio and engine hour. Increasing the blending ratio caused a reduction of MMAD while it was increased when the operation time was increased. The total PAH emission patterns associated with fine-particles (<1 μm) indicated a dominance of larger-molecular-weight PAHs (4-6 aromatic rings) especially pyrene (Pyr). In addition PAH concentrations increased when the engine running hours were increased. From the values of carcinogenic potency equivalent (BaP_{eq}), the PB0 gave the highest BaP_{eq} emissions in all size ranges of particles compared to the palm oil blend mixtures. Because, palm oil contains less aromatic constituent and palm oil blend contains more oxygen amount thus most likely enables more completely combustion than commercial petroleum diesel fuel. The results demonstrated clear reduction of PMs, total PAHs and carcinogenic potency emission decreased apparently as the blending percentages of palm oil blend increased.

Keywords: Engine emission, Palm oil blends, PMs, PAHs, BaP_{eq}

The development and application of single particle aerosol mass spectrometer

Mei Li¹, Zhengxu Huang¹, Lei Li¹, Zhong Fu², Ping Cheng¹, Zhen Zhou¹

1 School of Environmental and Chemical Engineering, Shanghai University, Shanghai 200444, China

2 Guangzhou Hexin Analytical Instrument Company Limited, Guangdong Guangzhou 510530, China

Principal Contact: Mei Li, research assistant, School of Environmental and Chemical Engineering, Shanghai University, Shanghai, 200444.

Tel: 021-66137753, 021-66137753 Email: meili@shu.edu.cn

Abstract

Single particle aerosol mass spectrometer (SPAMS), an advanced instrument for aerosol detection, can be on-line and real-time to measure the aerodynamic size and chemical composition of individual aerosol particle. In this presentation, we firstly describe the principle, configuration and features of our newly home-made SPAMS as well as its potential application areas; then the SPAMS study of mixing state of individual aerosol particles(biomass burning, carbon and dust)in the urban area of PRD will be presented and discussed in detail, and also the monitoring results of Shanghai city and Guangdong province during the period of the World Expo 2010 Shanghai China and Guangzhou Asian Games ; finally, SPAMS study of the cigarette smoke aerosol will be presented, and the difference of size distribution and chemical composition between fresh and old cigarette smoke particles will be discussed.

Keywords: SPAMS, home-made, single particle aerosol, on-line and in real time, mixing state, cigarette smoke aerosol analysis;

Monitoring the Particulate Matter Pollution in an Underground Car Park in Wuhan

Rong Biao Xiang and He Wang

School of Resources and Environment, Huazhong Agricultural University, Wuhan 430070, P. R. China

Principal Contact: Rong Biao Xiang, Associate Professor, School of Resources and Environment, Huazhong Agricultural University, Wuhan 430070, P. R. China.

Tel: 86-27-87282137 Fax: 86-27-87288618 E-mail: xiangrb@mail.hzau.edu.cn

Abstract

The rapid growth of automobile population and the limited land resource have led to the significant growth of underground car parks. On the other hand, because of the enclosed nature, most people are concerned about the poor air quality in these car parks. In this study, PM₁₀ and PM_{2.5} concentration were monitored with gravimetric method in an underground car park located in Wuhan, China. Results show that the concentration of PM₁₀ and PM_{2.5} at the entrance ranged from 0.019 mg/m³ to 0.146 mg/m³, 0.032 mg/m³ to 0.263 mg/m³, respectively. At the exit, concentrations of 0.050-0.133 mg/m³, 0.153-0.513 mg/m³ were found for PM₁₀ and PM_{2.5}, respectively. PM_{2.5} concentrations at the entrance and the exit were rather close. On the other hand, PM₁₀ level at the exit was much higher than that at the entrance. Both PM₁₀ and PM_{2.5} concentrations exceeded the reference values set in the related air quality standard.

Keywords: Underground car park, PM₁₀, PM_{2.5}

Design and validation of a personal nanoparticle sampler

Chun-Nan Liu¹, Shao-Ming Hung¹, Sheng-Chieh Chen¹, Shi-Nian Uang², Chuen-Jinn Tsai^{1,*}

¹ Institute of Environmental Engineering, National Chiao-Tung University, No. 1001, University Rd., Hsin Chu, 300 Taiwan.

² Institute of Occupational Safety and Health, Council of Labor Affairs, Executive Yuan, No. 99, Lane 407, Hengke Rd., Sijhih District, New Taipei City, 22413, Taiwan.

Principal Contact: Chun-Nan Liu, PhD Student, National Chiao Tung University, Hsinchu, Taiwan 300.

Tel: +886920950825 Email: gym1986.ev97g@nctu.edu.tw

Abstract

At present, there are no active personal sampling devices to assess the exposure levels of workers to engineered nanoparticles (NPs). To meet the demand, a novel IOSH-NCTU personal nanoparticle sampler (IOSH-NCTU PNS) was designed and tested. The PNS operates at 2 L/min with a pressure drop of 125 cm H₂O by a SKC XR 5000 pump. The PNS consists of a respirable cyclone and a micro-orifice impactor (137, 55 μm nozzles) in series for classifying respirable particulate matter (RPM) and NPs, respectively. The impactor plate is rotated by a stepper motor to deposit particles uniformly on the substrate. A final filter is used to collect NPs. The sampler is light weighted (250 g) and compact (H-10.5 cm, D- 6.3 cm).

Both liquid and solid particles were used to calibrate the sampler for the collection efficiency. The effect of heavy particle mass loading on performance of the PNS was evaluated. For assessing its accuracy, the measured RPM and NPs concentrations by the PNS were compared with those of a collocated MOUDI.

Calibration results show that the cutoff aerodynamic diameter (d_{p50}) of the respirable cyclone and the micro-orifice impactor is 3.98 ± 0.1 μm and 101.4 ± 0.1 nm, respectively, with the S/W of 13.8. A decreasing S/W from 16.2 to 3.13 results in a decreased d_{p50} of impactor from 111 to 72.5 nm. The particle loading tests reveals that the PNS has a maximum loading of 0.65 mg with a less than 5 % shift of d_{p50} and a negligible solid particle bounce. The

change in the pressure drop was less than 5 cm H₂O after heavy particle loading, and the RPM and NPs concentrations agreed well with those of the MOUDI. Therefore, the present IOSH-NCTU PNS sampler is capable of assessing personal exposure levels of RPM and NPs in workplaces.

Keywords: personal nanoparticle sampler, respirable cyclone, micro-orifice impactor

Influence of Convection on Diffusion Induced by Inlet Wind Velocity in a Tunnel

Jia-Twu Lee and Hsing-Nan Wu

Department of Environmental Engineering and Science , National Pingtung University of Science and Technology

ABSTRACT

Diffusion and convection are related. This study demonstrated that only when convection is dominant which be influenced by the convection. This study shows that remains the same as inlet wind velocity which is < 0.02 m/sec.

As the value exceeds this critical velocity, diffusion starts to be influenced by convection. As wind velocity increases, convection increase. And if inlet velocity is assumed > 0.05 m/sec, convection increases. When PE number exceeds 1.05, convection becomes conducive to diffusion. Pulsating inlet flow markedly impact unless the frequency at which the flow pulsates increase.

In this study, the frequency of wind pulsates once every 5-8 times, respectively, and the diffusion cloud is influenced by this frequency. The pulsating flow and non-uniform are conducted using (User's-Defined Functions(UDFs)) that control flow and frequency.

Keywords:

KEYWORDS

CFD, tunnel, pollutant dispersion, finite volume method, numerical integral

Introduction

Simulation or modeling with computers in the field of environmental engineering can be classified as statistical modeling, (e.g. Geographical Information System), information technological applications (e.g.: data mining, neural networks, and fuzzy theory), preliminary operational research (known as linear programming), time series.

Chu (2003)^[1] suggested that dynamic methods can be categorized analytical field measurements, model testing, experimental studies and numerical studies. In this study, the five forces in a tunnel (Chen, 1998; Chen, 2002)^[2] are reduced to only one force that dominates the tunnel pollutant dispersion. Ideally, inlet velocity directly influences on the diffusion. However, in practice, a small breeze velocity does not contribute markedly to changes

in a concentration field. As is widely known, the Peclet number (Pe) is deived

as $Pe = \frac{UL}{D_m}$, where U is characteristic velocity, L is pipe diameter and D_m is diffusivity.

It is generally regarded as the ratio of convection to diffusion. When $Pe \gg 1$, flow velocity is much significantly stronger than diffusion. Diffusion can be negligible under this condition. Conversely, when $Pe \ll 1$, Diffusion is significant and the diffusion cloud moves rapidly, such that the convection can be negligible.

This study attempts to determine the point at which inlet velocity influencing the dispersion pollutants. Ideally, this study applies a similar approach to all diffusion phenomena.

Experimental Methods

The Governing Equations is

$$\frac{\partial \rho}{\partial t} + \nabla \cdot (\rho \vec{V}) = 0 \quad (\text{Eq.1})$$

$$\rho \frac{Du_i}{Dt} = - \frac{\partial P}{\partial x_i} + \frac{\partial \tau_{ji}}{\partial x_j} + \rho f_i \quad (\text{Eq.2})$$

$$\frac{\partial C}{\partial t} + C \cdot \nabla U + U \cdot \nabla C = E_i \nabla^2 C + R \quad (\text{Eq.3})$$

$$\frac{D}{Dt}(\rho \varepsilon) + \frac{\partial}{\partial x_i}(\rho k u_i) = \frac{\partial}{\partial x_j} \left[\left(\mu + \frac{\mu_t}{\sigma_\varepsilon} \right) \frac{\partial \varepsilon}{\partial x_j} \right] +$$

$$C_{\varepsilon 1} \frac{\varepsilon}{k} (G_k + 3C_{3\varepsilon} G_b) - \rho C_{2\varepsilon} \frac{\varepsilon^2}{k} + S_\varepsilon \quad (\text{Eq.4})$$

Where ρ , and P is density and pressure respectively.

τ_{ji} is shear stress in a control volume.

C is concentration.

U has three components μ_x , μ_y and μ_z are the three directional velocities.

And E_i is turbulent diffusivity, or eddy diffusivity.

1. Case Study

Delineation and assumptions

The real tunnel case addressed in this study is complex. To find a rapid solution to the problem, the tunnel characteristics and dynamics are simplified. We assume the tunnel walls are smooth, and the flow remains uniform.

A six-sided experimental car is used to as a substitute for a real car. Five forces in the tunnel are reduced to – tunnel inlet velocity .

2. Grid Generation

The research is categorized into several aspects:

A. The mesh can be tetrahedral or polyhexdral.

Conversion from a tetrahedral mesh into a polyhexdral mesh is in use by the Fluent Corp.

This function has greatly enhances of the efficiency of (CFD) by way of the grid number reduction.

B. Polyhexdral grids cannot be processed by some post-processing programs , such as Tecplot360, and Fieldview. All the data and animation files related to polyhedra are presented using Fluent. The tetrahedral mesh, conversely, can be processed by Tecplot360.

C. A common practice to construct the ideal mesh is a hexahedral base on grid reduction to reduce the number of grids and increase efficiency. Due to the complexity of building mesh, the solution – namely tetrahedral mesh together with polyhedral mesh. The tetrahedral mesh number has more than reached 320,000 grid which does not ideal and run-time may be considerable.

3 Tunnel Profiles

Fig. 1 shows a rough profile of experimental car.

The red plane (right surface in Fig.1) represents the tunnel outlet, while the blue face (red surface in Fig.1) represents the tunnel inlet.

Fig. 2 -5 show diagrams of iso-surfaces or line segments inside the tunnel.

Parameter settings

Case1 A polyhexdral with 62086 meshes

Case2 A polyhexdral with 62086 meshes

Case 2(A) is used to verify the proposed-model. Comparison between semi-analytical numerical approach and Case 2(A) is conducted in subsequent chapters. Case 2(B) to Case 2(F) are utilized to identify the critical inlet wind velocity that starts diffusion within the tunnel. Turbulence models are either laminar or k- ϵ , which is used for Case 2(F).The adoption of either turbulent model is generally based on the Reynolds number. The Reynolds number is derived as $Re = \frac{UL}{v}$, where U is characteristic velocity, L is pipe diameter, and v is kinetic viscosity.The Reynolds

number is generally viewed as the ratio of inertia force acting on viscous force. All mesh profiles are polyhedral and have 62086 meshes, and the diffusivity is (m^2/sec). Case3 is Polyhedral mesh with 62086 meshes.

Most fluid dynamic studies discuss the velocity distribution under any circumstances, such as pulsating flows. Currie (1997)^[3], who focused on particular flow conditions.

Summarized plenty of the flow conditions addresses and solutions obtained over several decades.

In this study, pulsating flows are utilized to simulate wind gusts that influence pollutants concentration distributions. The frequency at which the inlet pulsates in these two cases varies depending on the quotient and time elapsed. Take Case 3(A) for example. Pulsating frequency is derived by dividing time by 8. The quotient is again divided by 8, and to obtain the remainder, ranging of 0 - 7. Likewise, the pulsating frequency in Case 3(B) is similar that in Case 3(A), but has a different quotient (time elapsed divided by 5) and the remainder (quotient divided by 5). In this study, uses UDFs to simulate the pulsating flows. The Pulsating flow frequency (Table 3) in Case 3(A). The Pulsating flow frequency in Case 3(B) appears similar only if the quotient equals 0 and 1.

Results and Discussion

1. Steady Flow

Fig. 6 and Fig. 7 show the velocity and concentration contour for Case 1, inlet velocity between 0.01 and 0.05 (m/s). Fig. 6~7 represent Case 2, while Fig. 8 present a special case use to verify the proposed model. Fig. 6~7 present the distribution of velocity along the line of line segments are presented.

Fig. 6 is classified into three time span domains, which are 20, 200, and 400 seconds, and the concentration distribution along the line segment during three time domains of them, respectively. The first the legend that designates the line of distribution resembles the point source. The latter two legends that designate the line of distribution are resembles the line source with a pollutant emission at the interval of 0 to 10 (m).

The numerical approaches suggest that the concentration distribution should be symmetrical, however, the concentration along line segment ab or cd is asymmetric because the distance to between and the boundaries are not equal, which may result in backflow effects. Conversely, the

concentration along ef is more symmetric than that along line ab and cd. Fig. 6 , 7 ,and 8 show profile of velocity along ef line segment.

Figs. 6 and 7 indicate that the maximum occurs at the point near the car muffler. The total concentration accumulates over time. Notably concentration profile have a perfectly normal concentration distribution. At an inlet velocity of 0.01 (m/s), the both sides of the pollutant distribution increase .

Other cases are neglected, such as those with an inlet velocity of 0.03m/sec, due to the similarity among all cases. That is, addressing two cases, the start and end cases is sufficient.

2. Pe Number

The concentration contour is influenced by the diffusive coefficient(Tables 1 and 2). The concentration contours (Tables 1 and 2) indicate that the influence o convection on diffusion induced by inlet wind velocity is significant.

From Case 2, it conclude that inlet wind velocity influences to the pollutant concentration when inlet velocity 0.03. When inlet velocity is assumed ≥ 0.05 , convection force increases. When Pe as defined , Pe is ≥ 1.05 (or simply rounded off), convection becomes conducive to diffusion.

3. Pulsate Flow

Fig. 9~10 shows the illustrations with respect to Case 3, a more complex case of pulsating inlet velocity flow. Table 3 lists other relevant profile information.In Case 3(A) (Fig.9), the pulsating frequency is based on time divided by 8.

The quotient is then divided by 8, to obtain the remainder, which is in the range of 0-7.

Tables correspond to Cases3-(A) and (B) Figure 10 presents illustrations of pulsating flow in Case3(A) where diffusivity is 1 m/sec. Likewise , is the pulsating frequency in Case 3(B)resembles that in Case3(A), with the quotient (times elapsed divides by 5 and remainder (quotient divided by 5) Figure 10 show the inlet velocity direction. Figure 10 shows more time span changes in terms of both velocity and concentration distribution from 64 seconds to 152 seconds. Sequentially, the first, second, and last column represent the velocity distribution, concentration distribution on a plane, and lastly concentration distribution along -the ef line segment respectively.

Fig 9 and 10 show overall comparisons of different pulsating frequencies, do not significantly impact under different pulsating frequencies.

At an inlet velocity of 0.01 (m/s), the both sides of the pollutant distribution increase (Fig.9). The difference between both sides varies at 0.02; and, thus, is insignificant. The left side of the pollutant distribution is more fat-tailed and the right side is smoother. In comparison with (Fig.9), and (Fig.10), the right side of concentration profile curve is no longer smooth. As inlet velocity increases, the side tail of concentration profile is widens.

4. Grid Verification

Fig 11 and 12 shows all different type results of for different polyhedral mesh at 20 seconds. Fig 6 shows all results for different polyhedral mesh at 20 sec. Notably, 41295, 61635, 89829, 117757 and 136184 meshes, presents in upper-left sides in both figures. The time spans are 20 seconds on the upper-left side of both figures. The different colors are assigned to each mesh number. Sequentially, they are black, scarlet, green, navy, and light blue as a token of #P41295, #P61635, #P89829, #P117757, and lastly #P136184.

Fig.11 and 12 show the comparison of different time span elapsed, using tetrahedral mesh.

The tested numbers of mesh are 227836, 329546, 982369, denoted #227836, #329546, #982369 on the upper-left side of both figure.

A polyhedral mesh can yield similar tetrahedral type results to those obtained with a tetrahedral mesh. A polyhedral mesh is reconstructed from a tetrahedral which is a new function in Fluent 6.3. Clearly, this functionality improved efficiently in terms of accuracy and execution time. Thus , this study focused most on the polyhedral mesh.

CONCLUSION

1. The concentration contour is influenced by the diffusive coefficient.
2. The inlet wind velocity influences to the pollutant concentration when inlet velocity 0.03 m/sec. When inlet velocity is assumed ≥ 0.05 , convection force increases.
When Pe as defined , Pe is ≥ 1.05 (or simply rounded off), convection becomes conducive to diffusion.
3. A polyhedral mesh can yield similar tetrahedral type results to those obtained with a tetrahedral mesh. A polyhedral mesh is reconstructed from a tetrahedral which is a new function

in Fluent 6.3. Clearly, this functionality improved efficiently in terms of accuracy and execution time.

REFERENCES

- [1] J. Chu, *Environmental Fluid Mechanics*, ISBN: 9576553636, 2003 (originally in Chinese)
- [2] K. S. Chen, C. Y. Chung, and S. W. Wang, Measurement and three-dimensional modeling of airflow and pollutant dispersion in an undersea traffic tunnel, *Journal of Air and Waste Management Association*, Vol. 52, p. 349-363, 2002
- [3] I. G. Currie, Fundamental mechanic of fluids, 2nd edition, McGraw-Hill, 1997
- [4] Zhang Zhengxing, Lin Jinxian, Lubo Jian, "Environmental Engineering Laboratory of the indoor air quality simulation ", the Republic of China Environmental Engineering Annual Meeting, Air Pollution Control Technology Conference, 2006.
- [5] Yejun Ming, Cai Youxi, Shi Yang is "open section of highway tunnel study of pollution dispersion model", National Computational Fluid Dynamics Conference, 2006.
- [6] Luo Ting, Xu Yajuan, "valley of diffusion of pollutants CFD method of parallel computing", *Sichuan Environment*, Volume 24, 4, p.77-79, Aug. 2000。
- [7] A. D. Polyanin, *Handbook of linear partial differential equations for engineers and scientists*, Chapman & Hall/CRC, ISBN:1584882999, 2002
- [8] B. Choy and D. D. Reible, "Diffusion Models of Environmental Transport," Lewis Publishers, 2000
- [9] C.S. Chen, The study of the ventilation system of Pinglin tunnel, Tamkang *Journal of Science and Engineering*, p85-92, 1999 (originally in Chinese)
- [10] F. Chen, On the determination of the aerodynamic coefficients of highway tunnels, *Journal of Wind Engineering and Industrial Aerodynamics*, 2002
- [11] Fluent User's Guide, Fluent Corporation, 2006
- [12] H.K. Versteeg and W. Malalasekera, *An introduction to computational fluid dynamics – the finite volume method*, Longman Scientific and Technical, ISBN:0-582-21884-5, 1995
- [13] H. M. Jang and F. Chen, A novel approach to the transient ventilation of road tunnels, *Journal of Wind Engineering and Industrial Aerodynamics*, 86, p15-36, 2000
- [12] I. G. Currie, Fundamental mechanic of fluids, 2nd edition, McGraw-Hill, 1997
- [14] M. Y. Tsai and K. S. Chen, Measurements and three-dimensional modeling of air pollutant dispersion in an Urban Street Canyon, *Atmospheric Environment*, 38, pp5911-5924, 2004
- [15] R. Schmitz, Modelling of air pollution dispersion in Santiago de Chile, *Atmospheric Environment*, 39, p.2035-2047, 2005
- [16] S.M. Lee Jojo and W.K. Chow, Numerical studies on performance evaluation of tunnel

Fig. 1 The profile of the simulated tunnel

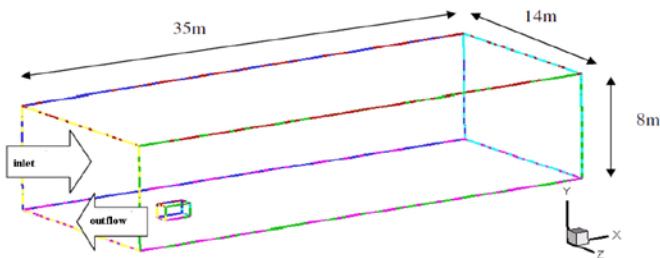


Fig. 2 shows a rough profile of experimental car.

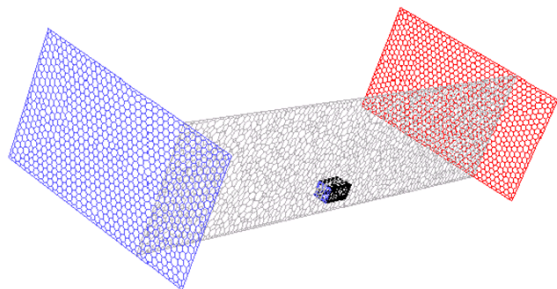


Fig. 3 Overview of the iso-surface along coordinate at z=3.5

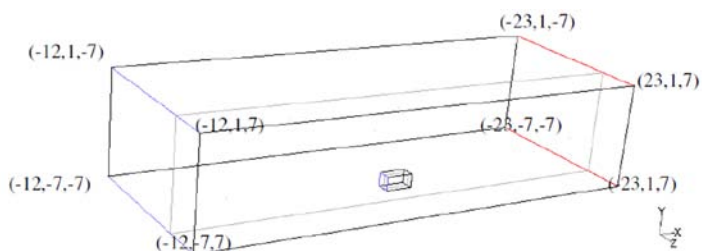


Fig .4 The test lines along ab and cd where a=(3, 1, 3.5), b=(3, -7, 3.5), and c=(4, 1, 3.5), d=(4, -7, 3.5)

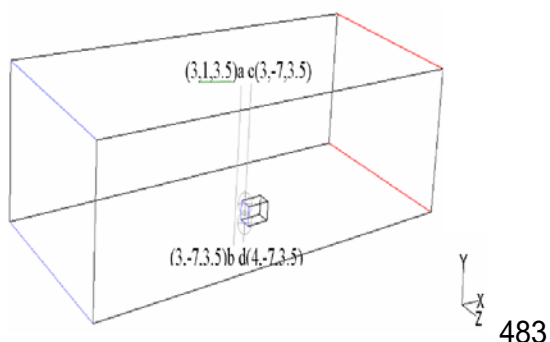


Fig .5 The sample line along e(-12, -3, 3.5) and f(23, -3, 3.5)

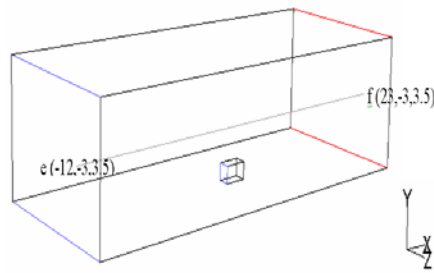


Fig. 6 Illustrations at the inlet velocity of 0.01 m/s

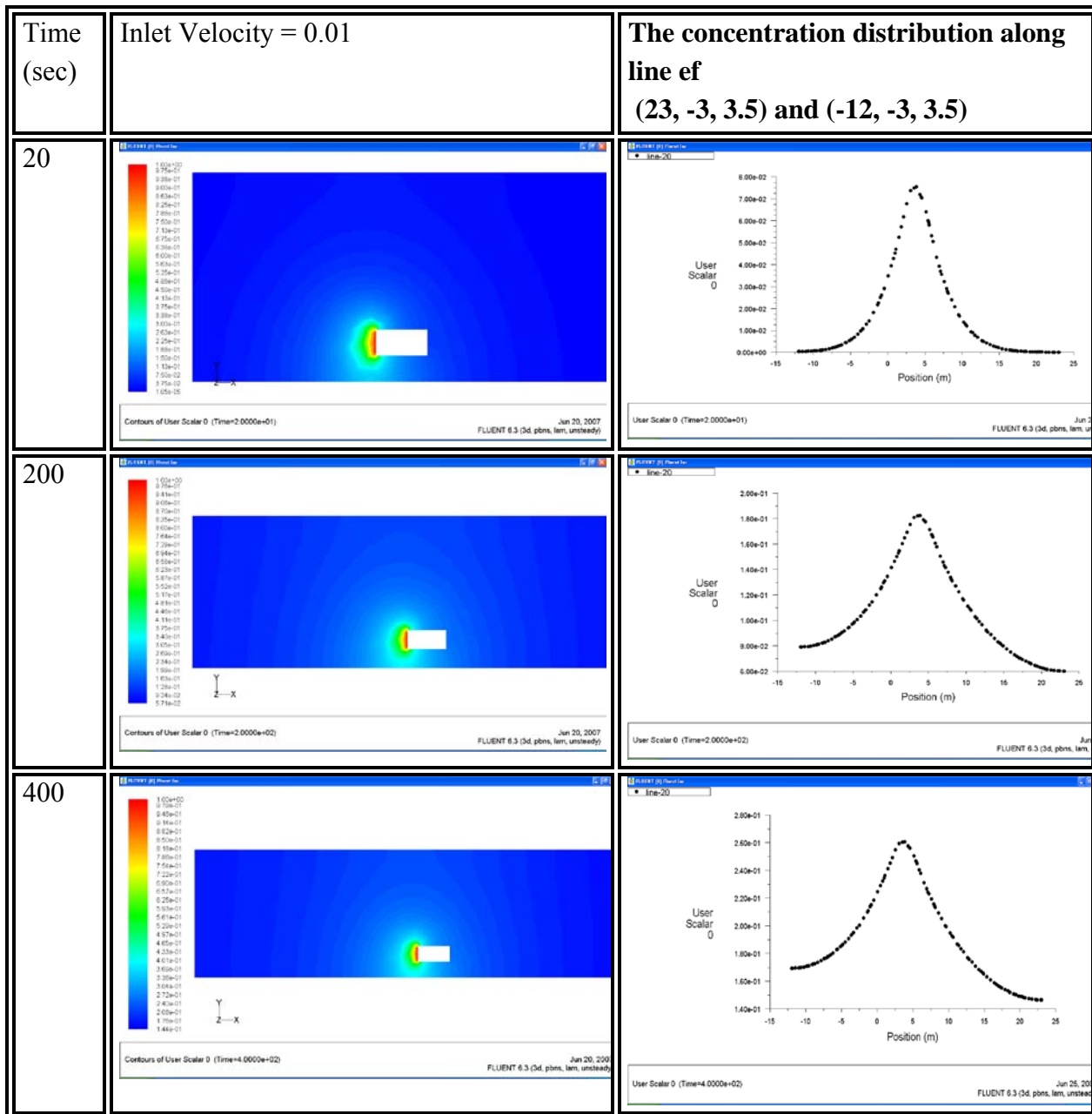


Fig.7 Illustrations at the inlet velocity of 0.05 m/s

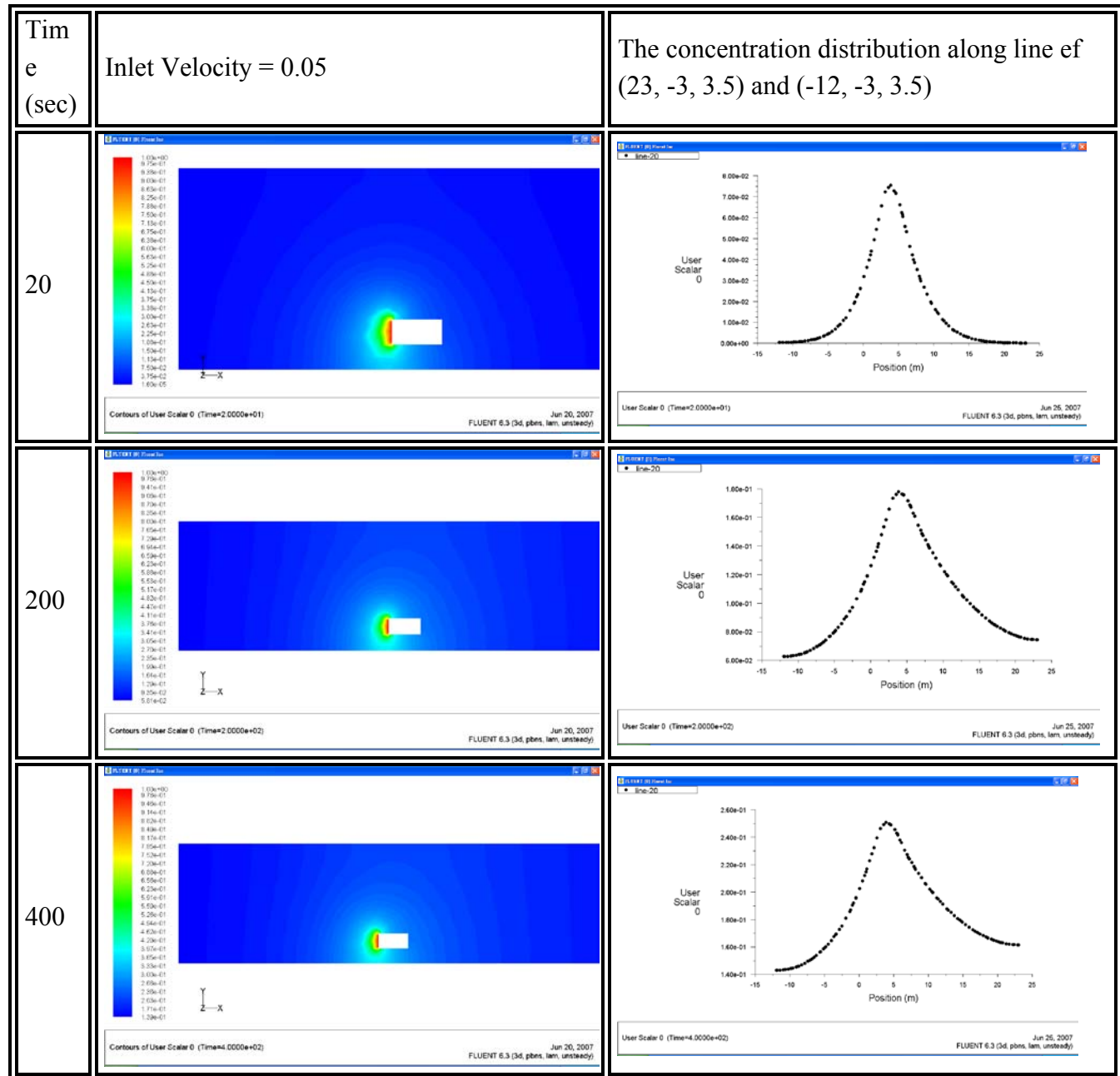


Fig.8 Illustration regard to pulsating flows

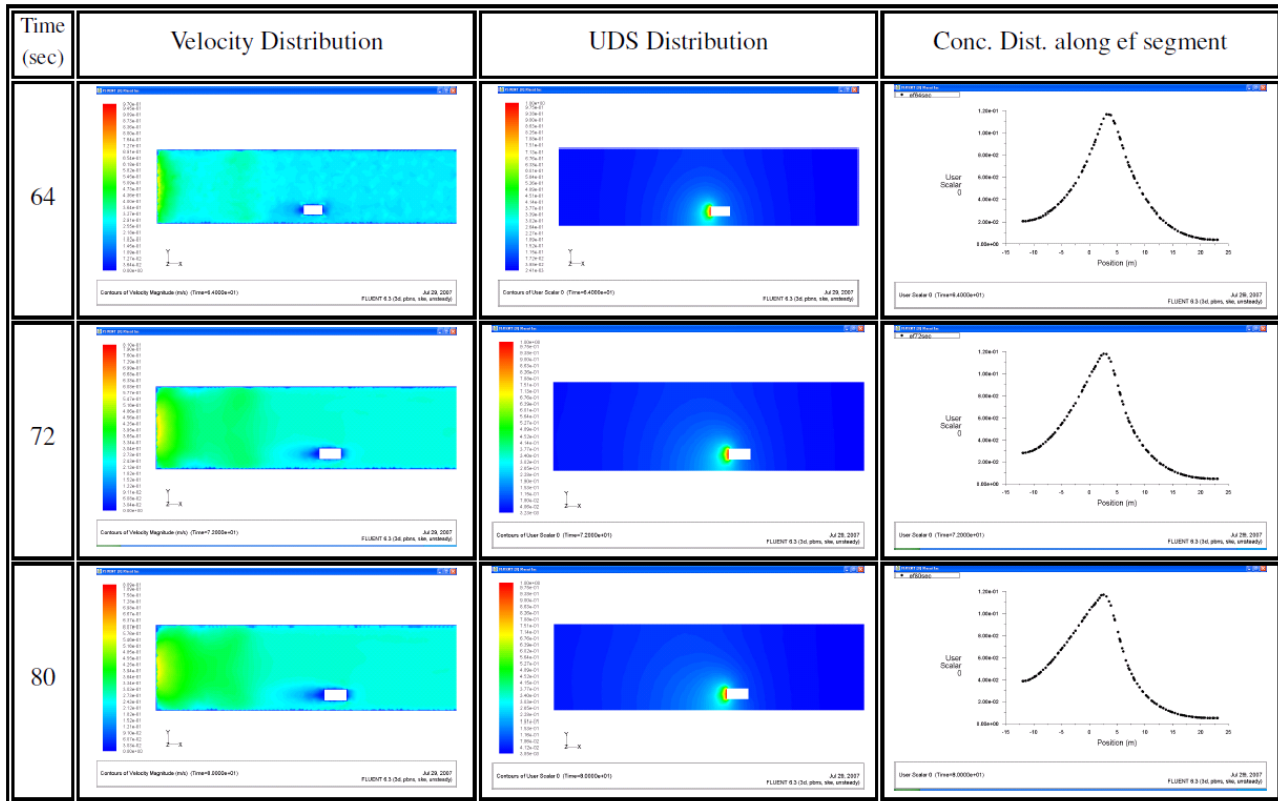


Fig .9 Pulsates three times, Case 3(A)

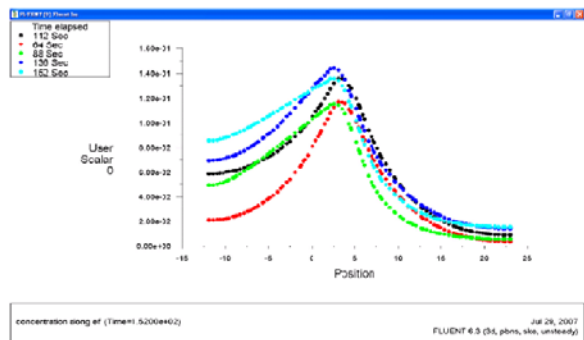


Fig .10 Pulsates twice, Case 3(B)

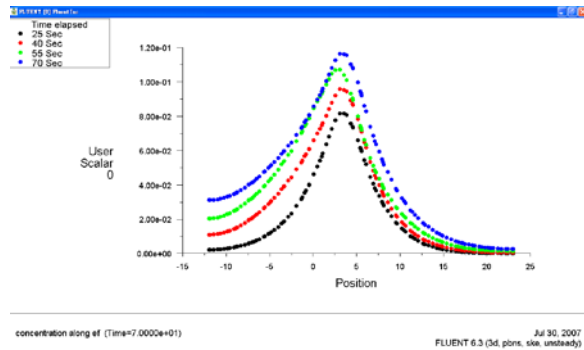


Fig 11 Grid verification at 20 sec mesh (polyhedral)

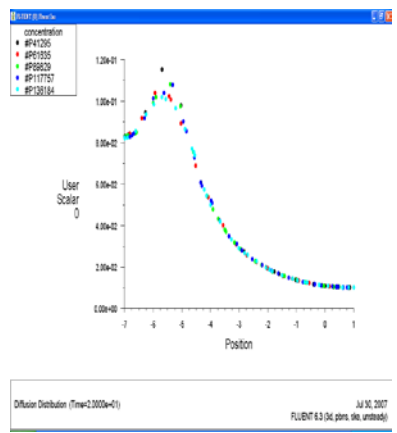


Fig 12 Grid verification at 20 sec mesh (tetrahedral)

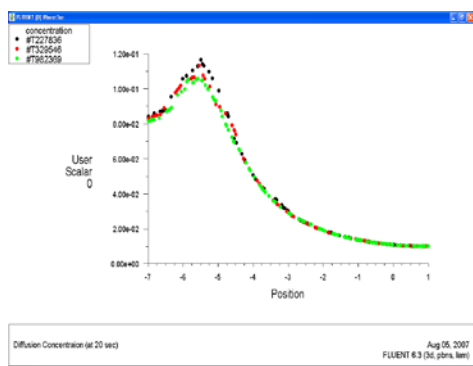


Table 1 Parameter setting, diffusivity=0.01 (m²/sec)

φ	Case 1(A) φ	Case 1(B) φ	Case 1 (C) φ
Rear tunnel- (velocity inlet in m/s) φ	0 φ	0.01 φ	0.05 φ
Rear car(s) φ (velocity inlet) φ	-0.01 (m/sec) φ	-0.01 (m/sec) φ	-0.01 (m/sec) φ
diffusivity φ	0.01 φ	0.01 φ	0.01 φ
Algorithm φ	SIMPLE φ	SIMPLE φ	SIMPLE φ
Momentum / UDS φ Discretization φ	Second Order Upwind φ	Second Order Upwind φ	Second Order Upwind φ
Laminar / Turbulent model φ	laminar φ	laminar φ	k-ε φ
Mesh profiles φ	polyhedron φ	polyhedron φ	polyhedron φ
Peclet Number φ	0 φ	0.35 φ	1.75 φ

Table 2 Parameter settings, diffusivity =1 (m²/sec)

φ	Case 2 (A) φ	Case 2 (B) φ	Case 2 (C) φ	Case 2 (D) φ	Case 2 (E) φ	Case 2 (F) φ
Rear tunnel- (velocity inlet) φ	0 φ	0.01 φ	0.02 φ	0.03 φ	0.04 φ	0.05 φ
Rear car(s) φ (velocity inlet m/s) φ	-0.01 φ	-0.01 φ	-0.01 φ	-0.01 φ	-0.01 φ	-0.01 φ
Diffusivity φ (m ² /sec) φ	1 φ	1 φ	1 φ	1 φ	1 φ	1 φ
Algorithm φ	SIMPLE φ	SIMPLE φ	SIMPLE φ	SIMPLE φ	SIMPLE φ	SIMPLE φ
Momentum / UDS φ Discretization φ	Second Order Upwind φ	Second Order Upwind φ	Second Order Upwind φ	Second Order Upwind φ	Second Order Upwind φ	Second Order Upwind φ
Laminar / Turbulent model φ	laminar φ	laminar φ	laminar φ	laminar φ	laminar φ	k-ε φ
Mesh profiles φ	polyhedron φ	polyhedron φ	polyhedron φ	polyhedron φ	polyhedron φ	polyhedron φ
Number of mesh φ	62086 φ	62086 φ	62086 φ	62086 φ	62086 φ	62086 φ
Peclet Number φ	0 φ	0.35 φ	0.7 φ	1.05 φ	1.4 φ	1.75 φ

Table 3 Pulsating flow parameter settings, diffusivity= 1(m²/sec)

φ	Case 3(A) φ	Case 3(B) φ
Front tunnel- (pressure outlet) φ	**** φ	**** φ
Rear tunnel- (velocity inlet) φ	Pulsating Flow (UDF) φ	Pulsating Flow (UDF) φ
Rear car(s) φ (velocity inlet) φ	-0.01 φ	-0.01 φ
diffusivity φ	1 φ	1 φ
Algorithm φ	SIMPLE φ	SIMPLE φ
Momentum / UDS Discretization φ	Second Order Upwind φ	Second Order Upwind φ
Laminar / Turbulent model φ	k-ε φ	k-ε φ
Mesh profiles φ	Polyhedron φ	Polyhedron φ
Number of mesh φ	62086 φ	62086 φ

Indoor Air Quality in University

Yu-Ju Ke², Chia Yu Chen², and Pei-Shih Chen¹

1 Department of Public Health, Kaohsiung Medical University 100, Shih-Chuan 1st Road, Kaohsiung, 80708, Taiwan

2 Graduate Institute of Occupational Safety and Health, Kaohsiung medical university 100, Shih-Chuan 1st Road, Kaohsiung, 80708, Taiwan

Principal Contact: Pei-Shih Chen, Department of Public Health, Kaohsiung Medical University 100, Shih-Chuan 1st Road, Kaohsiung, 80708, Taiwan.

Tel: +886-7-312-1101-2141-34 Fax: +886-7-321-2062 E-mail: pschen@kmu.edu.tw

Abstract

In the previous studies, indoor air quality in classroom affected learning efficiency and health status of students. Air pollutants and environmental factors such as carbon dioxide (CO), temperature, relative humidity (RH), ozone (O₃), particulate matter (PM), fungi, bacteria and ventilation rate were the factors of concern. It was indicated that poor air quality in office building decreased workers' working efficiency in the range of 6%-9%. The ventilation type of classroom in university is similar to office buildings. Therefore, the purpose of this study is to investigate the indoor air quality in university.

We selected 9 classrooms in 2 academic buildings (Building A, building B) for research from September to December in 2008. CO₂, CO, Relative Humidity, temperature (Indoor Air Quality Meters, TSI INCORPORATED, USA), wind speed, ventilation rate (TSI INCORPORATED, USA), O₃ (Ozone Monitor, BUD INDUSTRIES, USA), PM₁₀, PM₄, PM_{2.5}, PM₁ (Dust Trak, TSI INCORPORATED, USA), and ultrafine particles (P-Trak, TSI INCORPORATED, USA) were measured indoor and outdoor simultaneously before and after mechanical ventilation turning on in the morning and noon. Airborne bacteria and fungi were also sampled by impaction method and cultured in Malt Extract Agar and Tryptic Soy Agar, respectively.

Our results showed that the concentration of PM₁₀, PM₄, PM_{2.5}, PM₁, fungal bioaerosols and bacterial bioaerosols before mechanical ventilation turning on were higher than it turned on. For CO₂ concentration, 9.52% and 33.33% samples in building A and building B, respectively, were exceeded the recommendation of indoor air quality from Taiwan Environmental

Protection. In addition, O₃ concentration of building B was significant higher than building A (p=0.0169). A lot of plants nearby building B might be the reason.

Keywords: Ultrafine, PM, Classroom

Numerical simulation in the micro environment in Han Yang mausoleum museum

Nanying Cao

The Hong Kong Polytechnic University, Flat 11 Floor 11 Block B Ming On Street 20 Hong Hum Kowloon, Hong Kong

Principal Contact: Nanying Cao, Master, The Hong Kong Polytechnic University, Flat 11 Floor 11 Block B Ming On Street Hong Hum Kowloon, Hong Kong.

Tel: (852)63526499 E-mail: lion19851111@sina.com

Abstract

As the first underground museum, Han Yang Mausoleum museum adopts whole sealing glass system to protect relics from destruction while providing visitors a wonderful environment to enjoy the fantastic artwork closely at different angles. But from its open, this method cannot stop relics from destruction and weathering by covering the surface with crystalloid salt.

Following the problems, this study simulated its micro environment including temperature, air movement and relative humidity numerically via CFD software Fluent.

After simulation under the actual heating system, micro-environment did not perform perfectly as expected: Four gas cyclones are found; there are trends that temperature is getting lower from one side to another while relative humidity is in the opposite situation especially at low height near the ground. After estimating the given suggested case, relative humidity distribution is even worse therefore suggested case should not be adopted.

Keywords: CFD, Fluent, numerical simulation, relative humidity, Han Yan Mausoleum, Museum.

Ultrafine particles counts in elementary school

Yi-Chieh Chen¹ and Pei-Shih Chen^{1*}

1 Department of Public Health, Kaohsiung Medical University
100, Shih-Chuan 1st Road, Kaohsiung, 80708, Taiwan.

Principal Contact: Pei-Shih Chen, Department of Public Health, Kaohsiung Medical University, 100,Shih-Chuan 1st Road, Kaohsiung, 80708, Taiwan,
Tel:[+886-7-312-1101~2141-34](#) Fax: +886-7-321-2062 E-mail: pschen@kmu.edu.tw

Abstract

Introduction:

Previous studies showed that exposure to ultrafine particles have adverse health effects in children. Kaohsiung City is a heavy industrial city with high particulate matter concentration. Therefore, it is important to assess children's exposure to ultrafine particles in Kaohsiung City. In this study, we aimed to measure ultrafine particles concentration in the classrooms of elementary schools in Kaohsiung City. In addition, indoor and outdoor concentration was simultaneously measured in the morning and afternoon.

Methods:

Three elementary schools, background, industry and traffic schools, was selected in Kaohsiung City. Nine classrooms were randomly selected in each elementary school with a total sample size of twenty-seven classrooms. Ultrafine particles concentration was monitoring in real-time from 8 am to 4 pm between April 2009 and June 2009 (TSI P-trak model 8525, TSI, USA). We also measured ultrafine particles concentration indoor and outdoor of classroom at 8 am and 4 pm.

Results:

The average concentration for ultrafine particles in background, industry and traffic school was 7.8×10^3 (pt/cc), ranging from 2.9×10^3 (pt/cc) to 1.2×10^4 (pt/cc), 1.7×10^4 (pt/cc), ranging from 4.3×10^3 (pt/cc) to 3.5×10^4 (pt/cc), and 1.7×10^4 (pt/cc), ranging from 2.7×10^3 (pt/cc) to 4.0×10^4 (pt/cc), respectively. Our results showed that the average concentration in industry and traffic school was significantly higher than that of background school ($p < 0.0001$). More sources of pollutants around traffic and industrial school may be the reason. Hourly average concentration of ultrafine particles in background school was all lower than that of industrial and traffic school. Furthermore, the variance was high in industrial and traffic schools. The I/O ratio of ultrafine particles in the three elementary schools was below 1 the range from 0.9 to 1. For the trend of I/O ratio, it was high in the morning and decreased with the time.

Keywords: ultrafine particles, elementary school, I/O ratio.

Assessment of Dust Concentration and Sediment Load of Dust Storms in the Sistan Region of Iran

A.R. Rashki¹, D.G. Kaskaoutis², C.J.deW. Rautenbach¹, P.G. Eriksson³ and P.Gupta^{4,5}

1 Department of Geography, Geoinformatics and Meteorology, Faculty of Natural and Agricultural Sciences, University of Pretoria, Pretoria, 0002, South Africa

2 Research and Technology Development Centre, Sharda University, Greater Noida – 201306, India

3 Department of Geology, Faculty of Natural and Agricultural Sciences, University of Pretoria, Pretoria, 0002, South Africa

4 Goddard Earth Science and Technology Center, University of Maryland Baltimore County

5 NASA Goddard Space Flight Center, Greenbelt, MD 20770

ABSTRACT

The Sistan region in southeast Iran presents a seasonally varied climate. The region is subject to severe winds that blow with speeds occasionally reaching 30 ms^{-1} . After the 1999 drought, because of land-use change and drying-up of the Hamoun Lakes, the frequency and severity of dust storms have been significantly increased. To assess the air quality and sediment load of dust storms, Particulate Matter (PM10) concentrations were measured during September 2010 to January 2011 using Beta Attenuation Monitors model 1020 (BAM-1020). The dust sediment load was also measured using dust traps set at up to 8 meters height (1 meter distance between the traps) during the period August 2009 to August 2010. The results of measuring sediment load up to 8 meters height have shown that, yearly, about 31,000 tons of dust enter the Sistan region. Daily mean PM10 levels are found to be around $437\text{ }\mu\text{gm}^{-3}$, ranging from $66\text{ }\mu\text{gm}^{-3}$ to $2339\text{ }\mu\text{gm}^{-3}$. Analyses of the Air Quality Index (AQI) shows that 17 % of the days are unhealthy for sensitive people and 61% have a high health risk or are even hazardous.

KEYWORDS

Dust storm, PM (particulate matter), wind sediment load, Air Quality Index, Sistan, Levar

Introduction

Dust storms, as a major source of aerosols, frequently occur in the arid and semi-arid regions over the globe and are regarded as a serious environmental hazard [1]. Each year, several billion tons of soil dust are entrained into the atmosphere playing a vital role in solar irradiance attenuation, atmospheric dynamics and weather [2, 3, and 4].

Several studies demonstrated that airborne Particulate Matter (PM) of dust storms has an

impact on climate, biogeochemical cycling in ecosystems, visibility and human health [5,6]. Epidemiological studies have shown that exposure to particulates with aerodynamic diameters of $< 10 \mu\text{m}$ (PM10) induces an increase of lung cancer, morbidity and cardiopulmonary mortality [7,8,9]. The national air quality standards in many countries are currently under review with the aim of including the monitoring of aerosol quantity as well as quality in order to maintain a healthy atmospheric environment. Based on Environmental Protection Agency (EPA) standards, the concentration of PM10 is regarded as an important criterion for determining the Air Quality Index (AQI), which is a measure of quality of the air at a specific location.

In addition, dust is considered to be one of the major components of troposphere aerosols over the globe [10] with global flux estimations of 1500-2600 Tg.yr⁻¹ [11] and constitutes a key parameter in climate aerosol-forcing studies [12, 13].

The aim of this study is to analyze the PM10 concentrations in the arid Sistan region in southeastern Iran. The AQI is used to provide information regarding the status of Sistan's air quality and the associated health concerns for the public when severe air pollution episodes and dust outbreaks occur pursuant to favourable meteorological conditions. It should be noted that such studies are lacking from this region, and the present work is the first that examines the seasonal evolution of PM concentrations and AQI over Sistan.

Experimental Methods

Study area

The Sistan region is in the southeastern part of Iran ($61^{\circ}15' \text{ E}$ and $61^{\circ}50' \text{ E}$ longitude, and $30^{\circ}5' \text{ N}$ and $31^{\circ}28' \text{ N}$ latitude) close to the borders with Pakistan and Afghanistan (Fig 1). The region has 4 cities and 980 villages with a population of more than 400,000. The climate is arid, with a low annual average precipitation of 55 mm occurring mainly in winter (Dec to Feb) and evaporation exceeding $\sim 4000 \text{ mm.year}^{-1}$ [14]. The monthly mean temperature exhibits a clear annual pattern with low values in winter ($9\text{-}12^{\circ}\text{C}$) and high values ($\sim 46^{\circ}\text{C}$) in summer, following the common pattern found in the northern latitudes. RH illustrates an inverse annual variation with larger values in winter (45-57%) and very low values in summer (below 25%), which are indicative of an arid environment. The atmospheric pressure presents generally high values in winter (1020-1024 hPa) from October to March and then decreases significantly during summer ($\sim 996 \text{ hPa}$ in July). The summer low pressure is attributed to the Indian thermal low that extends further to the west over the arid environments of Iran and the Middle East as a consequence of the South Asian monsoon system. These low pressure conditions are the trigger for the development of the Levar northerly wind, commonly known as the “120-day wind”, causing frequent dust and sand storms, especially during the summer (June to September) [3, 15].

The Levar wind circulation is not only an atmospheric system that has a significant environmental impact in the Sistan basin, but is also one of the least studied meteorological phenomena in Iran and its surroundings. Throughout history the Levar has had serious effects on ecosystems, human health and architecture due to its intensity, consistency and duration. The Levar wind is modulated by the intense solar heating of the south Asian landmass, peaking in the summer months. In general, the Levar wind develops pursuant to the formation of an intense surface low-pressure system over south Asia attributed to the strong positive turbulent sensible heat flux [16, 17]. Other studies suggest the Levar might be a limb of the return flow of the Indian monsoon circulation [18]. Despite all of these postulates, the Levar wind remains a phenomenon that contributes significantly to dust storms and air quality over the study region.

The Hirmand River (also known Helmand) is the longest river in Afghanistan and the main watershed for the Sistan basin, since it irrigates the Sistan agricultural region and finally drains into the natural swamp of Hamoun. The Hamoun lake complex (e.g. Hamoun Saburi, Hamoun Puzak) is situated in the north of the Sistan region and is the largest freshwater ecosystem of the Iran Plateau and one of the first wetlands in the Ramsar Convention [14].

Severe droughts in the past decades and especially after the 1999 drought have caused drying of the Hamoun lakes leaving a fine layer of sediment that is easily lifted by the wind. The basin is one of the most active sources of dust in the Iran-Afghanistan-Pakistan basin [15, 19, 20] and seasonal winds blow fine sands off the exposed lake bed. The sand is swirled into huge dunes that may cover a hundred or more villages along the former lakeshore. Thus, wildlife around the lake is negatively impacted, and fisheries are brought to a halt. Middleton (1986) used ground-based observations to explain the frequency and seasonality of dust storms in south-west Asia, highlighting the borders between Iran, Pakistan and Afghanistan as an active dust source region with 81 annual dust storms. Furthermore, he has reported more than 30 dust storms over the Sistan region [3].

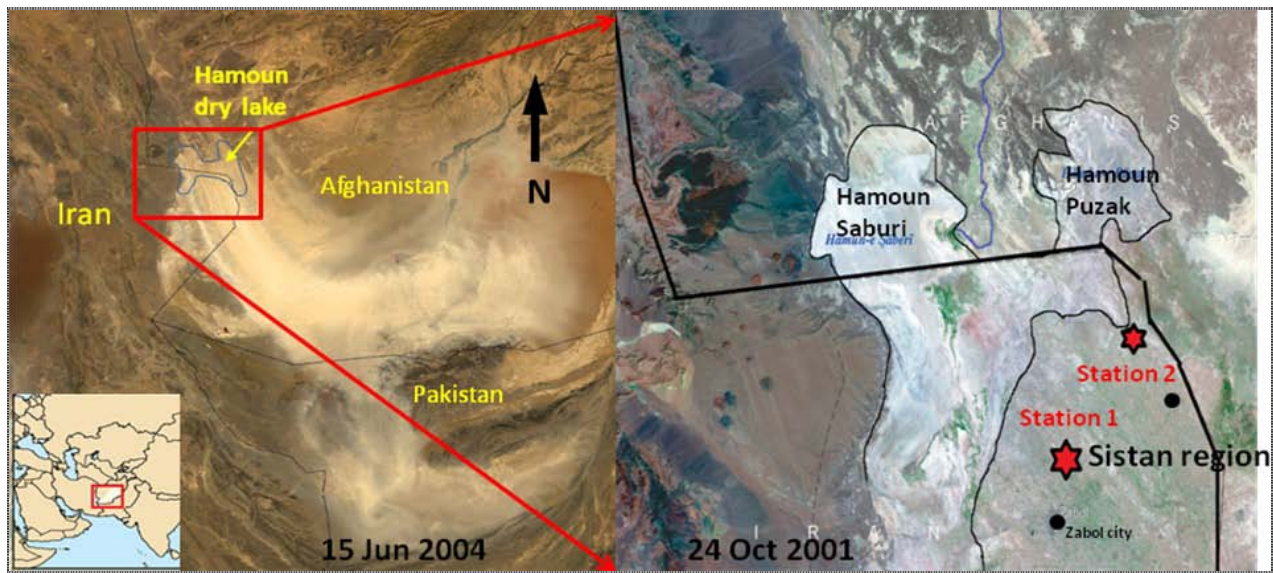


Figure 1 Location of study area. This figure shows severe dust storms over the Sistan region as observed from Terra-MODIS. The dust plumes form a giant U shape that extends from Sistan in Iran into southwestern Pakistan. Some source points for the dust are discernible in this image. Hamoun lakes define the border between Iran and southwestern Afghanistan and some dry lake-bed sediments have contributed to the dust. The dust is blowing off the dry lake beds that become the Hamoun Wetlands during wet years. The Hamoun Wetlands are among the most common sources of dust in southwest Asia and fine, desiccated soil lifts easily when strong winds blow [21].

PM measurements

PM concentrations at the near-surface level were systematically measured using the Environmental Dust Monitor (Bam-120). The BAM-120 measures PM₁₀ concentration (in μgm^{-3}) with a high temporal resolution of one hour. The measurements were carried out at the Environmental Institute in the Sistan region ($31.23^\circ \text{ N}, 61.73^\circ \text{ E}$) during the period September 2010 to January 2011. The recording station is at the outskirts of the city of Zabol, close to Hamoun Lake. This region is placed in the main corridor of dust storms in the Sistan region. The measured PM data were converted to 24-hour averages (daily averages) from which the monthly values and variations were obtained. For assessment of air quality in the Sistan region, the necessary data were sorted according to AQI standards.

Sediment load measurements

The sediment loads of dust storms were measured using passive dust traps (Figure 2a) up to 8 meters in height (one meter distance between the traps) during the period August 2009 to August

2010 at two locations in Hamoun lake (31.2° N, 61.31° E and 31.10° N, 61.41° E). After each measurement the samplers were evacuated to be ready for measuring the next dust events. The samples were weighed with a sensitive scale and were ready for further analysis.

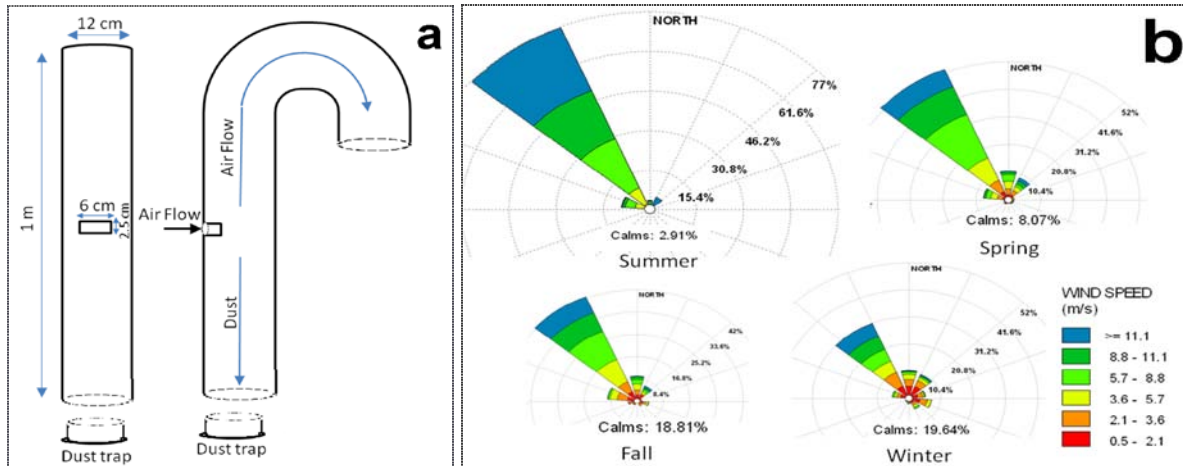


Figure 2. Dust sediment sampler (a) and seasonal wind rose of Zabol meteorological station (b)

Results and Discussion

PM measurements

The results show that PM_{10} concentrations in the Sistan region are much more than the standard concentration ($155 \mu\text{gm}^{-3}$) and are even within dangerous levels as defined by the Environmental Protection Agency ($425 \mu\text{gm}^{-3}$). The daily PM_{10} concentrations during major dust storms were 20 times ($3094 \mu\text{gm}^{-3}$) above the standard level (Table 1). The monthly average PM_{10} concentrations (Table 1) show extremely large values due to frequent severe dust storms, suggesting that the atmospheric conditions are very unhealthy for the people living in this area.

Table 1: Monthly mean, maximum and minimum PM_{10} concentrations (μgm^{-3}) in Sistan during the period September 2010 to January 2011

	Monthly Mean	Daily Maximum	Daily minimum
September	720	2045	22
October	531	2339	100
November	200	737	66
December	476	3094	84
January	196	579	29

Air Quality Index (AQI)

Air pollution indices are commonly used to define the impact of air pollution on human health [22, 23]. In this respect, the AQI is a powerful tool to ensure public health protection [24]. The AQI varies from 0 to 500, is divided into six categories and its health indicators are given in Table 2. The two first AQI categories (good and moderate, $<155 \text{ PM}_{10} \mu\text{g m}^{-3}$) have no impact on health, whereas the last AQI categories ($>355 \text{ PM}_{10} \mu\text{g m}^{-3}$) are associated with serious risk of respiratory symptoms and aggravation of lung disease, such as asthma, for sensitive groups and the whole population [25, 26].

Assessment of air quality during the period of investigation showed that 102 days out of 166 (61%) had air pollution levels of above the air quality standard ($> 155 \mu\text{g m}^{-3}$). Seventeen days were regarded as unhealthy for sensitive people, 17 days were unhealthy or very unhealthy and 54 days were hazardous or dangerous (Table 2). These results, in combination with adverse effects on human health, make clear that environmental conditions in the Sistan region are rather poor for human well-being. The accumulation of ambient air pollutants associated with enhanced values of AQI (>100) can result in an increase in hospital admissions for the treatment of cardiovascular and respiratory problems. Several studies have shown that ambient air pollution is highly correlated with respiratory morbidity among children [8, 27]. The results gathered from hospitals in the Sistan region showed that during the dust storm days, respiratory patients were increased dramatically, mainly those affected by Chronic Obstructive Pulmonary Disease (COPD) and asthma. The percentage of these diseases increases in summer (July and August) because of most severe dust storms occurring then [28].

Table 2: Determination of health quality with AQI, PM_{10} and number of days with severe pollution in Sistan during the period September 2010 to January 2011

Health Quality	AQI	$\text{PM}_{10} (\mu\text{g m}^{-3})$	Days	(%)
Good	0-50	0-54	4	2.4
Moderate	51-100	55-154	60	37.5
Unhealthy for sensitive people	101-150	155-254	17	10.5
Unhealthy	151-200	254-354	13	8
Very unhealthy	201-300	355-424	4	2.4
Hazardous	301-500	425<	54	33.5

Sediment load measurements

The amount of particles passing during dust storms was measured using dust traps up to 8 meters height (1 meter distance between the traps). The amount of particles recorded was different depending on frequency and intensity of dust storms. For example, an event on 5 September 2009 with about eight-hour continuity and an average PM_{10} concentration of

$3000\mu\text{gm}^{-3}$ has passed an average of 2 kg.m^{-2} (Fig. 3). The average of sediment load was calculated at $88 (\text{kg.m}^{-2})$ during August 2009 to August 2010. These values equate to 31680 tons for 8 meters height measurements and the 45 km cross-section of the Sistan residential area abutting against the Hamoun lakes. Note that these values do not include material above 6 meters height nor the sand saltation and sand traction components.

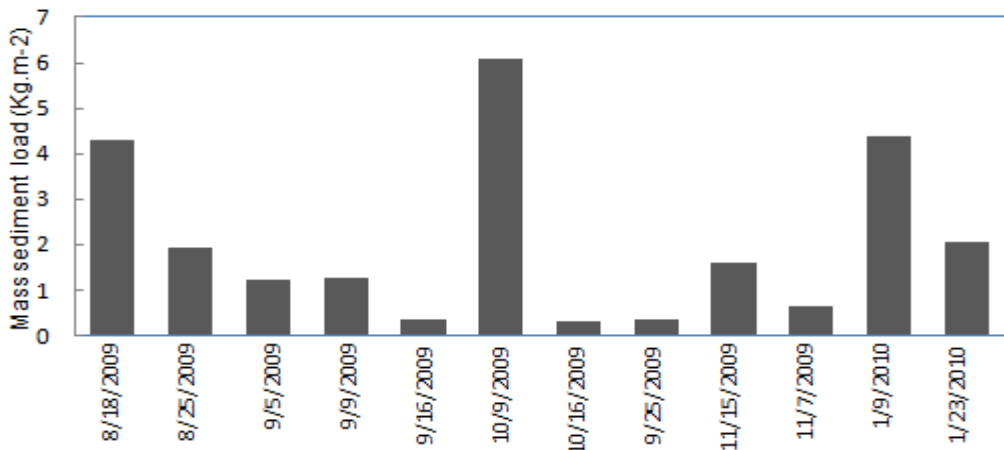


Figure 3- sediment load passing in various events in the Sistan region

CONCLUSION

The Sistan region has been involved in wind erosion and dust storms problems for many years, but lack of adequate and reliable data in the region has meant that most studies, reports and conclusions have lacked a proper scientific basis. The data and information presented here can be suitable for future studies to inhibit or provide for reduction in the harmful effects of these phenomena. PM_{10} concentrations in this region reach 60 times the EPA standard, and this should alarm officials and international institutions and demand more attention. Some residents continuously live in these critical areas and will not enjoy a future of good health. The huge deposits of dust on different levels after each dust storm will settle, disrupting the plant and animal life cycles, even in industrialized areas. Thus the region is not stable. Dust storms remove sediment from the lake's bed, and this keeps the lake sediments unstable. Some sediments deposit in residential areas and water channels. Removal of these deposits incurs large costs and efforts each year.

These results have been collected using the limited facilities and equipments at two sampling points within the Sistan region; we recommend a network of stations for more complete monitoring of dust storms. The sediments measured with the present instruments provide only a first-pass approximation and it is recommended to use more accurate types of measurements to provide better results in future.

REFERENCES

- [1] Prospero, J.M., Ginoux, P., Torres, O., Nicholson, S.E., Gill, T.E., Environmental characterisation of global sources of atmospheric soil dust identified with the Nimbus 7 total ozone mapping spectrometer absorbing aerosol product. *Rev Geophys.* 2002, 40:2–31
- [2] Tegen, I., Fung, I., Modeling of mineral dust in the atmosphere: sources, transport, and optical thickness. *Journal of Geophysical Research.* 1994, 99, 22897–22914.
- [3] Goudie, A.S., Middleton, N.J. Dust storms in south west Asia. *Acta Universitatis Carolinae, Supplement.* 2000, 73-83
- [4] Engelstaedter, S., Tegen, I., Washington, R., North African dust emissions and transport. *Earth-Science Reviews.* 2006, 79, 73-100.
- [5] Dockery D, Pope A. Epidemiology of acute health effects: summary of time-series studies. In: Particles in Our Air: Concentrations and Health Effects (Wilson R, Spengler JD, eds). Cambridge, MA:Harvard University Press, 1996;123-147
- [6] Broecker, W.S., Abrupt climate change: causal constraints provided by the paleoclimate record, *Earth Science Reviews.* 2000, 51, 137–154.
- [7] Pope, C. A., Epidemiology of fine particulate air pollution and human health: Biologic mechanisms and who's at risk?, *Environmental Health Perspectives.* 2000, 108, 713-723
- [8] Schwartz J., Air pollution and children's health, *Pediatrics.* 2004, 113:1037-1043
- [9] Chakra, O.R.A., Joyeux, M., Nerriere, E., Strub, M.P., Zmirou-Navier, D., Genotoxicity of organic extracts of urban airborne particulatematter: an assessment within a personal exposure study, *Chemosphere.* 2007, 66:1375–1381
- [10] Mishchenko, M.I., and I.V. Geogdzhayev. Satellite remote sensing reveals regional tropospheric aerosol trends. *Optics Express.* 2007, 15(12):7423-7438
- [11] IPCC, 2007. Climate Change 2007: Synthesis Report. Contribution of Working Groups I, II and III to the Fourth Assessment Report of the Intergovernmental Panel on Climate Change. In: Core Writing Team, Pachauri, R.K., Reisinger, A.(Eds.). IPCC, Geneva, Switzerland, p. 104.
- [12] Pandithurai, G., R.T. Pinker, P.C.S., Devara, T., Takamura, K.K., Seasonal asymmetry in diurnal variation of aerosol optical characteristics over Pune, western India. *J. Geophys. Res.* 2007, 112, D08208, doi:10.1029/2006JD007803
- [13] Gautam, R., Liu, Z., Singh, R. P., Hsu, N.C., Two contrasting dust-dominant periods over India observed from MODIS and CALIPSO data. *Geophys. Res. Lett.* 2009, 36, L06813, doi:10.1029/2008GL036967
- [14] Moghaddamnia, A., Ghafari, M.b., Piri,J., Amin.S., Han.D., Evaporation estimation using arti.cial neural networks and adaptive neuro-fuzzy inference system techniques, *Advances in Water Resources.* 2009, 32 ,88–97
- [15] Middleton, N. J.'Dust storms in the Middle East', *Journal of Arid Environments.* 1986, 10,

- [16] Hossenzadeh, S.R., One hundred and twenty days winds of Sistan. *Iran J Res Geogr.* 1997, 46, 103–127
- [17] de Wekker, S. F., Zhong, J.S., Fast, J.D., and Whiteman, C.D., A numerical study of the thermally driven plain-to-basin wind over idealized basin topographies. *J. Appl. Meteor.* 1998, 37, 606–622.
- [18] Hahn, D. G., Manabe, S., The role of mountains in the South Asian Monsoon circulation. *J Atmospheric Science.* 1995, 32:1515–1541
- [19] Esmailli,O., Tajrishy, M. Peyman Daneshkar, P., Results of the 50 year ground-based measurements in comparison with satellite remote sensing of two prominent dust emission sources located in Iran, *Remote Sensing of Clouds and the Atmosphere.* 2006, 6362, 77-786
15d.o i: 10.1117/12.692989
- [20] Goudie, A.S., Midleton, N.J., *Desert dust in the global system*, Springer. 2006
- [21] Dust Storm over Afghanistan and Iran .
See <http://earthobservatory.nasa.gov/NaturalHazards/view.php?id=42242>.
- [22] Cogliani, E., Air pollution forecast in cities by an air pollution index highly correlated with meteorological variables, *Atmospheric Environment.* 2001, 35, 2871-2877.
- [23] Nikolaou, K., Basbas, S., Taxiltaris, C., Assessment of air pollution indicators in an urban area using the DPSIR model, *Fresenius Environmental Bulletin.* 2004, 13: 820-830
- [24] Environmental Protection Agency (EPA)., 1999. Guideline for reporting the daily air quality-air quality index (AQI). EPA-1999-454/R-99-010.
- [25] Ozer, P., Bechir, M., Laghdaf, O.M., Gassani, J., Estimation of air quality degradation due to Saharan dust at Nouakchott, Mauritania, from horizontal visibility data, *Water Air Soil Pollut.* 2006, 178:79–87
- [26] Mohan, M., Kandy, A., An Analysis of the Annual and Seasonal Trends of Air Quality Index of Delhi. *Environ. Monit. Assess.* 2007, 131: 267–277
- [27] Jalaludin, B.B., O'Toole, B.I., Leeder, S.R., Acute effects of urban ambient air pollution on respiratory symptoms, asthma medication use, and doctor visits for asthma in a cohort of Australian children. *Environmental Research.* 2004, 95, 32-42.
- [28] Miri, A., Ahmadi, H., Ghanbari, A., Moghaddamnia, A., Dust Storms Impacts on Air Pollution and Public Health under Hot and Dry Climate, *international journal energy and environment.* 2007, 2, 1

Integrated Evaluation of Aerosols from Regional Brown Hazes over Northern China in Winter: Concentrations, Sources, Transformation, and Mixing states

Weijun Li, Shengzhen Zhou, Xinfeng Wang, Zheng Xu, Chao Yuan, Yangchun Yu, Qingzhu Zhang and Wenxing Wang

Environment Research Institute, Shandong University, Jinan, Shandong 250100, China.

Principal Contact: Weijun Li, Ph.D, Shandong University, Shanda Nanlu 27, Jinan, Shandong Province 250100, China.

Phone: 86-531-88364416, Email: liweijun@sdu.edu.cn

Abstract

To evaluate the wintertime regional brown haze in northern China, trace gases and aerosols were measured at an urban site between 9 and 20 November, 2009. Ion chromatography and transmission electron microscopy (TEM) were used to investigate soluble ions in PM_{2.5} and the mixing state of individual particles. The contrasts between clear and hazy days were examined in detail. Concentrations of the primary gases including NO (55.62 ppbv), NO₂ (54.86 ppbv), SO₂ (83.03 ppbv), and CO (2.07 ppmv) on hazy days were two to six times higher than those on clear days. In contrast, concentrations of O₃ remained low (5.71 ppbv) on hazy days. Mass concentrations of PM_{2.5} (135.90 µg m⁻³) and BC (7.85 µg m⁻³) were three times higher on hazy days than on clear days. Based on the estimations from TEM analysis, fractions of both ammoniated sulfate (AS)-soot (20%) and AS-soot/organic matter/fly ash (20%) were larger on hazy days than on clear days (13% and 12%), implying that coagulation is an important mixing process in the polluted air. The SO₂ emissions from coal combustion for power plants, industrial activities, and household heating led to high concentrations. Also, high concentrations of secondary sulfates significantly formed in the haze. Therefore, high concentrations of acidic gases contributed to the increased mass and number of secondary aerosols. Our study indicates that metal-catalyzed oxidation in the aqueous phase is a major pathway of sulfate formation. The mixtures of aerosol particles, together with MODIS images, suggest that the hazes covered not only the industrial cities, but extended into the neighboring rural regions.

Keywords: Transmission electron microscopy, Brown haze, North China plain, metal-catalyzed oxidation

Discussion on the Haze Pollution Decision Criteria for Shanghai

Yusen Duan

Shanghai Environmental Monitoring Center, No.1 Nandan Road, Shanghai, 200030

Principal Contact: Yusen Duan, Engineer, Shanghai Environmental Monitoring Center, No. 1 Nandan Road, Shanghai, 200030.

Tel: 86-21-24011580 Fax: 86-21-64393639 E-mail: duanys@yeah.net

Abstract

With the global warming and the overspreading of industrial pollutant emissions, regional visibility deterioration is becoming a more and more serious problem in the more developed area in eastern China. Regional air quality and visibility become worsen with the large-scale fog and haze which frequently occurred. Based on the theoretic analysis of relative humidity (RH) and air pollutants which affect visibility, we proposed the concept of haze pollution of the environmental category and established the haze pollution criteria for Shanghai which included visibility, particle mass concentration and speciation. The RH factor was parameterized based on the equation among b_{ext} , RH and PM_{2.5} chemical species. Based on the 5-years monitoring data analysis on several sites in Shanghai, the linear correlation was calculated between daily average and hourly average concentration of PM_{2.5}, then the hourly haze PM_{2.5} criteria for Shanghai was created. The haze pollution days calculated from haze pollution criteria had good corresponding relation to meteorological category. The haze pollution criteria of Shanghai was significant to evaluate regional air pollution and establish control strategies.

Keywords: Haze, Brownish Haze, Haze Pollution, Assessment, Criteria.

The association of carbonaceous species with haze pollution

Guangli Xiu¹, Mengya Zhu¹, Jun Tao² Junji Cao³ and Danian Zhang¹

1 East China University of Science & Technology, 130 Meilong Road, Shanghai 200237, China

2 South China Institute of Environmental Sciences, Ministry of Environmental Protection, No.7 West Street, Yuancun, Guangzhou 510655, P. R. China

2 Institute of Earth Environment, China Academy of Science, 10 Fenghui South Road, Xi'an High-Tech Zone, Xi'an, 710075 China

Principal Contact: Guangli Xiu, Professor, East China University of Science & Technology, 130 Meilong Road, Shanghai 200237, China.

Tel: 86-21-64251927 Fax: 86-21-64253113 Email: xiugl@ecust.edu.cn

Abstract

One year round PM_{2.5} samples were collected and chemically measured from 2009 to 2010 in ECUST site in Shanghai in order to reveal the association of PM_{2.5} components with haze pollution. Carbonaceous species including Organic carbon (OC), element carbon (EC), water-soluble organic carbon (WSOC) and water soluble ions were analyzed and compared. Results showed that the PM_{2.5} daily-average mass concentrations in spring, summer, fall and winter were $82.60 \pm 45.73 \mu\text{g}/\text{m}^3$, $54.48 \pm 22.18 \mu\text{g}/\text{m}^3$, $101.18 \pm 47.27 \mu\text{g}/\text{m}^3$ and $127.50 \pm 53.83 \mu\text{g}/\text{m}^3$, respectively. Total carbon took around 21.2%, 27.7%, 18.8% and 16.8% of total PM_{2.5} mass, respectively. The char-EC, soot-EC, Volatile Particulate Organic Carbon (VPOC) and Non-Volatile Particulate Organic Carbon (NVPOC) were defined and correlated to other constituents. It was found that the VPOC/OC ratio changed little in different seasons while WSOC showed a negative correlation to VPOC/OC, which suggests that NVPOC may be the major contributor to WSOC. The OC in summer was the lowest, but OC/PM_{2.5} in summer was the highest, which suggests that secondary aerosol is the major source of particles in summer. The highest EC was found in fall and char-EC/soot-EC ratio was also high in autumn and winter, which might result from the higher contribution of biomass burning in these two seasons. The haze-days were screened out according to meteorological definition. The haze days were classified into four-types with the strong correlation to carbonaceous species.

Keywords: PM_{2.5}; Haze; Carbonaceous Components; Formation Mechanism

Regional Fine Particle Pollution and Haze Problem

Min Hu¹, Xiaofeng Huang², Lingyan He² and Yuanhang Zhang¹

1 State Key Joint Laboratory of Environmental Simulation and Pollution Control, College of Environmental Sciences and Engineering, Peking University, Beijing 100871

2 Key Laboratory for Urban Habitat Environmental Science and Technology, School of Environment and Energy, Peking University Shenzhen Graduate School, Shenzhen 518055

Principal Contact: Min Hu, State Key Joint Laboratory of Environmental Simulation and Pollution Control, College of Environmental Sciences and Engineering, Peking University, Beijing, 100871, China.

Tel: +86-01-62759880 E-mail: minhu@pku.edu.cn

Abstract

Ambient particulate matter has been reported as a dominant pollutant and results in haze problem. Deterioration of visibility is believed strongly depending on particles' size, optical properties, chemical components and mixing states. The integrated measurements were carried out in the Pearl River Delta, as well as Yangtze River Delta to explore the haze formation mechanism. High time resolution measurements of particle size distribution, chemical and optical properties in PM_{2.5} were conducted. It was found that secondary formation of SNA (sulfate, nitrite and ammonium) and SOA (secondary organic aerosol) enhanced both regional particle pollution and haze problem. Local traffic and biomass burning emit soot or element carbon, contribute light absorption of the particles. Source apportionment by the receptor model was introduced to analyze the contribution of sources to extinction coefficient.

Keywords: fine particle, haze, chemical compositions, optical property.

An auto-detection algorithm for Asian dust Aerosols over China Seas based on satellite observations and model simulations

Zengzhou Hao, Qianguang Tu and Fang Gong

State Key Laboratory of Satellite Ocean Environment Dynamics, Second Institute of Oceanography, State Oceanic Administration, Hangzhou, 310012, China

Principal Contact: Zengzhou Hao, Title, State Key Laboratory of Satellite Ocean Environment Dynamics, Second Institute of Oceanography, State Oceanic Administration, Hangzhou, 310012, China.

Tel: 0571-81963119 Fax: 0571-88839374 E-mail: hzyx80@163.com

Abstract

Asian dust storms, which often occur on spring, can long range transport and pass through the China Seas. During this process, it makes some impact on marine ecology and region climate. In this paper, the optical and thermal properties of Asian dust aerosols are firstly presented by combining the satellite observations and radiance transfer model simulations. By compare, the reflectance of dust aerosols over ocean at the visible $0.47\mu\text{m}$ $0.86\mu\text{m}$, and the near-infrared $1.64\mu\text{m}$ have some significant features, it satisfies $R_{0.47} < R_{1.64} < R_{0.86}$ for strong dust aerosol over ocean, the weak dust aerosol meets $R_{1.64} < R_{0.86} < R_{0.47}$, and the dust reflectance may be from 0.1 to 0.3. At the thermal atmospheric windows bands 8.5 , 11 and $12\mu\text{m}$, for cloud and clear water region, the brightness temperature at $12\mu\text{m}$ is highest and the temperature at $11\mu\text{m}$ is close to $12\mu\text{m}$. However, for dust aerosols, the brightness temperature at $12\mu\text{m}$ is much greater than those at $8.5\mu\text{m}$ and $11\mu\text{m}$. The brightness temperature difference between $8.5\mu\text{m}$ and $11\mu\text{m}$ is small and the lower is the difference, the stronger is the dust aerosol. Based on those visible and thermal characteristics, an auto-detection algorithm for dust aerosols over ocean is designed and is conducted for some cases. It can identify the strong and the weak dust regions well and it is nice to study the dust properties deeply.

Keywords: Asian dust, aerosol, remote sensing.

Comprehensive Physical and Chemical Characterization of Urban Aerosols in Vienna, Austria

Nayla Sabbagh-Kupelwieser¹, Kazuhiko Sekiguchi², Kyung Hwan Kim², Hidehiro Kamiya³ and Wladyslaw W. Szymanski¹

¹Faculty of Physics, University of Vienna, Austria

²Graduate School of Science and Engineering, Shimo-Okubo, Saitama University, Japan

³Tokyo University of Science and Technology, Dept. of Chemical Engineering, Tokyo, Japan

ABSTRACT

This contribution presents results of a broad physical and chemical characterization of urban aerosol covering particle size range from nanoparticles to microparticles. PM10, PM2.5 and PM1 size fractions were measured with impactors delivering information about particle mass concentrations. Due to the atmospheric optical relevance of fine particles a telephotometric method was utilized to obtain atmospheric visibility, another quantity providing an insight into the particulate air pollution and linked with the PM1 fraction. The time-resolved detailed size distribution of PM1 was determined using a scanning differential mobility analyzer. A comprehensive post-sampling chemical characterization of the aerosol in question was performed. The data obtained shows that there is a shift of particles from the PM1 size fraction to the PM2.5 size fraction at the expense of about 50% of the mass concentration in the PM1 fraction. Evidently, merely PM filter sampling does not provide an appropriate insight into the actual situation and dynamics in the PM-fractions. Due to the small absolute mass concentration values of the PM1 fraction, its presence in the PM2.5 fraction results in a negligible mass contribution and will likely not be observed by means of the conventional PM measurement.

KEYWORDS

Atmospheric Aerosols, PM-fractions, Nanoparticles, Chemical Composition

Introduction

Aerosol micro- and nanoparticles are abundant in natural and man-made environment. Air quality studies and health impact of those particles, in particular of nanoparticles, are being conducted with an increasing level of interest in the academic and also non-academic community. The potential risks to the health and environment of natural and man-made nanoparticles become increasingly the focus of general attention in recent years [1, 2]. However, so far no standard procedures for measurement of aerosol nanoparticles and their properties were attempted to

invoke. Moreover, even PM2.5, even though recognized as necessary information regarding the quality of ambient air, is not routinely monitored in Europe, although attempts were made to standardize this method [3]. The toxicological evidence provides an indication that aspects of PM other than mass alone determine toxicity [4]. In terms of chemical species, the strongest toxicological consistency is with secondary inorganic PM, namely sulfates and nitrates at above-ambient levels, but this consistency is opposed by a lack of effect in controlled exposure studies within the ambient concentration range. A number of studies have recently addressed the association between ambient ultrafine particle (UFP, $D_p < 100\text{nm}$) concentrations, epidemiological issues and research implications. The results are still rather limited [5, 6].

Experimental Methods

This contribution presents results of a comprehensive physical characterization of urban aerosol covering particle size range from nanoparticles to microparticles. PM10, PM2.5 and PM1 size fractions were measured with virtual impactors delivering information about particle mass concentration. Because of the atmospheric optical relevance of the fine particle mode with sizes below $2.5\mu\text{m}$ a telephotometric method was utilized to obtain data regarding atmospheric particle extinction properties. This real-time measurement was then used to determine the atmospheric visibility, another quantity providing an insight into the particulate air pollution and linked with the PM1 fraction. Simultaneously for measuring of the time-resolved detailed size distribution a differential mobility analyzer in scan mode (SDMA) yielded the data corresponding to the PM1 fraction.

A comprehensive post-sampling chemical characterization of the aerosol in question was performed. Some results are shown in Fig. 3. The organic (OC) and elemental carbon (EC) fractions contained the investigated aerosol were determined with the Desert Research Institute Mod. 2001 Carbon Analyzer (Atmoslytic Inc.) following the IMPROVE_TOR method. The ionic species were analyzed by ion chromatography (DX-100, Dionex, USA). Water soluble organic compounds (WSOC) were analyzed on a total organic compounds analyzer (TOC-V, Shimadzu, Japan). The water insoluble organic compound (WIOC) content was obtained as the difference of the total OC analyzed by DRI carbon analyzer minus WSOC analyzed by TOC-V.

Results and Discussion

Fig. 1 shows the ratio of PM10/PM1, as well between PM2.5/PM1 with reference to the extinction coefficient of the urban aerosol in Vienna measured with the telephotometer [7]. The increase of the extinction coefficient relates to the increase of the PM1 fraction within the PM10. A corresponding effect can be seen for the PM2.5/PM1 ratio. That shows the prevailing influence of particles within the PM1 fraction on the optical properties of atmosphere and the apparent correspondence between this fraction and the extinction coefficient and hence the visual range.

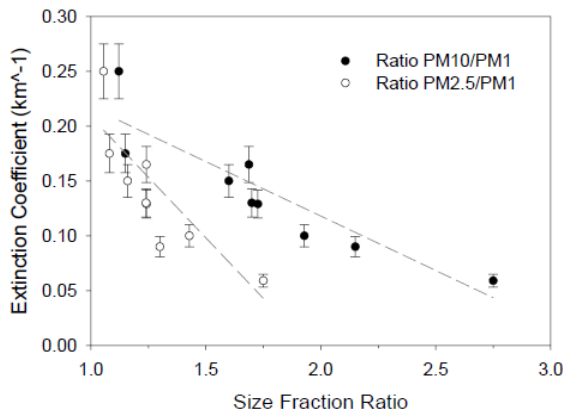


Fig.1. Extinction coefficient vs. PM size fraction ratios obtained from mass concentration measurements with the cascade virtual impactor.

Time-resolved measurement of the particle number concentration with the SDMA i.e. for particles below 1 μm in term of the electrical mobility diameters shows a distinct drop in concentration of the UFP at 18:00 hours. The simultaneous monitoring of the relative humidity indicated at this time a significant increase from about 55 up to 85%. A corresponding behavior was observed around noon of the following day. The lower number concentration during the night time can be explained by the fact that traffic in the night time is substantially reduced. Then at 7 a.m. during morning rush hour, one can clearly see the increase in UFPs.

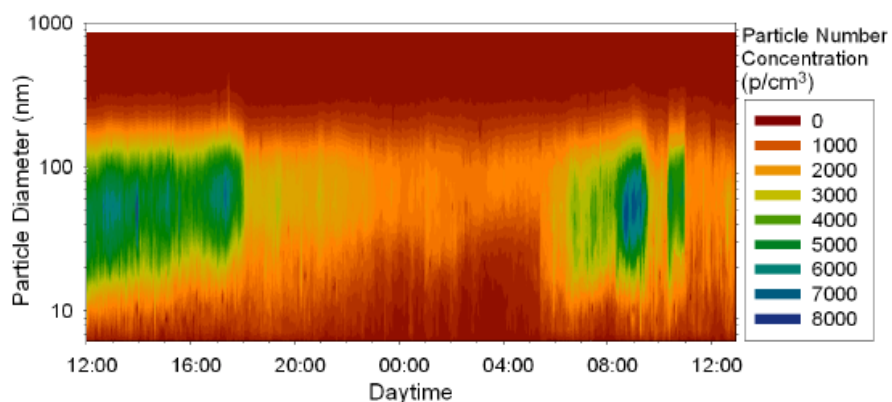


Fig.2. Time resolved distributions of number concentrations measured with the SDMA from 24 November 24, noon, until November 25, 2008, noon.

A possible explanation for the decrease of particles in the PM1 fraction during the higher relative

humidity period is the humidity driven growth and coagulation. The data suggests that there is a shift of particles from the PM1 size fraction to the PM2.5 size fraction at the expense of about 50% of the mass concentration in the PM1 fraction. The likely loss of PM1 particles due to their growth driven by the increased relative humidity will not be observed using the conventional PM measurement.

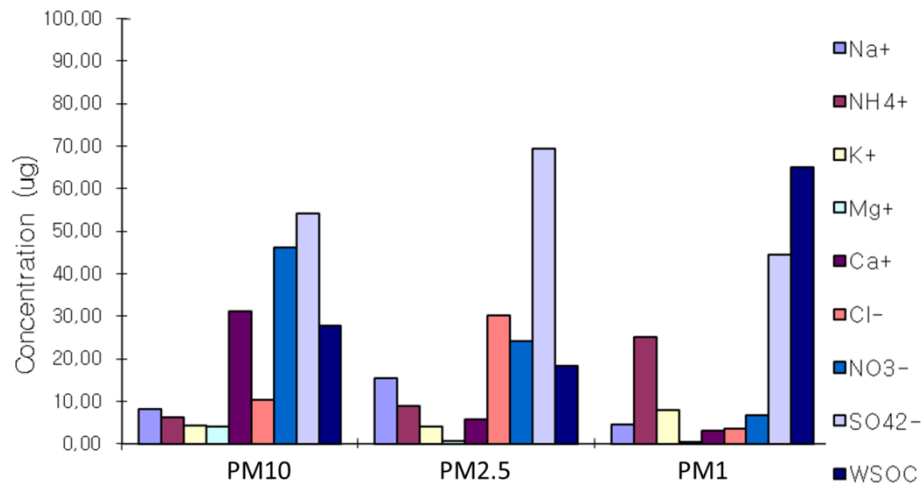


Fig.3. Chemical composition of the ambient aerosol corresponding to data shown in Fig. 2. CONCLUSIONS

UFPs which are generated mainly from combustion, gas to particle conversion, nucleation processes or photochemical processes, with some of them being primary (emitted directly by the source) and some secondary in nature (formed in the air from the precursors emitted by the sources) are an integral part of the ambient aerosol. Due to their negligible mass in comparison with the PM10, or PM 2.5 fraction they cannot be identified my means of mass measurement. Mass measurement of the PM1 fraction seems also to be an insufficient method to judge the actual ambient particle burden. Particle removal from the PM1 fraction due to humidity driven size increase and shift into the larger particle size fraction PM2.5 cannot be determined using time integrated mass sampling. Moreover, such a measurement might lead to erroneous conclusions regarding possible health effects. Evidently only time resolved monitoring of the PM1 and UFP size fraction in combination with chemical analysis delivers comprehensive information regarding the air quality. Obviously PM10 and PM2.5 filter sampling does not provide an appropriate insight into the actual situation and dynamics in the PM-fractions and should be complemented by time resolved particle size measurement for conclusive assessment of the ambient air quality.

ACKNOWLEDGMENTS

A partial support of this research was provided by the University of Vienna, the Austrian Science Foundation Proj. Nr. P16185 and TRP 29-N20 and Grant-in-Aid for Scientific Research on Innovative Areas Japan, "Impacts of Aerosols in East Asia on Plants and Human Health".

REFERENCES

- [1] Pui DYH, Chen DR, Nanometer particles: a new frontier for multidisciplinary research, *J. Aerosol Sci.* 1997; 28: 539-544
- [2] Maynard A, Kumpel ED, Airborne Nanostructured Particles and Occupational Health, *J. Nanoparticle Research* 2005; 7: 587-614
- [3] Hazenkamp-von Arx ME, Goetschi Fellmann T, Oglesby L, Ackermann-Liebrich U, Gislason T, Heinrich J, Jarvis D, Luczynska C, Manzanera AJ, Modig L, Norbäck D, Pfeifer A, Poll A, Ponzio M, Soon A, Vermeire P, Künzli N, PM2.5 assessment in 21 European study centers of ECRHS II: Method and first winter results, *J. Air Waste Manag. Assoc.* 2003; 53(5):617.
- [4] McMurry PH, Shepherd M, Vickery JS, eds. *Particulate matter science for policy makers: a NARSTO assessment.* 2004; Cambridge, Cambridge University Press
- [5] Oberdoerster G, Utell MJ, (2002). Ultrafine Particles in the Urban Air: To the Respiratory Tract - And Beyond; *Environ. Health Perspectives*, 2002; Vol 110 (8): 440-444
- [6] Sioutas C, Delfino RJ, Singh M, Exposure assessment for atmospheric ultrafine particles (UFPs) and implications in epidemiologic research, *Environ. Health Perspectives* 2005,113 (8): 947-955
- [7] Sabbagh-Kupelwieser N, Horvath H, Szymanski WW, Urban Aerosol Studies of PM1 Size Fraction with Reference to Ambient Conditions and Visibility, *Aerosol and Air Quality Research*, 2010; 10: 425–432

Study of Conditioning System Inside the Temperature of the Flow Field of EMU Air

Jia-Twu Lee, Wu-Chou Yu, Wen-Long Yu, and Chih-Hung Huang

National Pingtung University of Science and Technology, 1, Shuefu Road, Neipu, Pingtung 91201, Taiwan

Principal Contact: Jia-Twu Lee, Associate Professor, National Pingtung University of Science and Technology, 1, Shuefu Road, Neipu, Pingtung 91201, Taiwan.

Tel: 08-7703202-7635 Fax: 08-7740256 E-mail: leejia@mail.npu.edu.tw

Abstract

With economic development, urban public transport needs tend to pay attention to safe, fast, stable, coupled with the increasingly important global environmental awareness; government promotion of energy-saving carbon spared no effort, the importance of mass transit systems become more and more. EMU car comfortable or not, have significant impact on passenger travel, especially commuting passengers feel even more evident. Objective of this study make the process of car passengers enjoy a comfortable ride somatosensory, but also improve the EMU energy efficiency of air conditioning systems.

This study used CFD software to simulate the EMU car air-conditioning system, the temperature variations of kinetic energy. Air outlet (inlet) is set to 2, the export (outlet) is set to 4; speed setting range is 0.2m / s, 0.3m / s, 0.4m / s, the body temperature of a fixed set of ITU 30°C; air -conditioning temperature is set to 23°C, 24 °C, 25 °C at three different temperatures, the human body for optimum comfort standards, the temperature set to 28 (301K). After several attempts, the simulation results are as follows: (1) from the outlet closer, the lower the temperature, low temperature compartments on both sides of the outlet extension to form a center compartment lower temperature, higher temperature on both sides of the temperature flow field. (2) In the same wind speed, temperature setting lower temperature lower temperature flow field area will be reduced, the temperature contours of the flow field will be more intensive.

A direct impact on air temperature inside the passenger car comfort; if more than optimum temperature diffusion time, the air conditioning of the system performance. The simulation experimental results, the increased wind speed, can reduce the temperature to speed up the time, better efficiency, not lower the temperature setting.

Keywords: Temperature flow field, CFD, optimum temperature standards, proper temperature diffusion time

Assessment of traffic control measures during the Beijing Olympic Games based on particle number size distributions

Z.B. Wang¹, M. Hu¹, D. L. Yue¹, Z. J. Wu^{1,2}, A. Nowak², B. Wehner² and A. Wiedensohler²

1 State Key Joint laboratory of Environmental Simulation and Pollution Control, College of Environmental Sciences and Engineering, Peking University, Beijing 10871, China

2 Leibniz Institute for Tropospheric Research, Leipzig, Germany

Principal Contact: Zhibin Wang, State Key Joint Laboratory of Environmental Simulation and Pollution Control, College of Environmental Sciences and Engineering, Peking University, Beijing, 100871, China.

Tel: +86-01-62759880 Fax: +86-01-62751920 E-mail: wangzhibinpku@gmail.com

Abstract

In order to investigate the efforts of traffic control measures during the Olympic Games, detailed variations of particle number and volume concentrations are needed. The Aitken mode and accumulation mode were the major contributors to the fine particle ($<1\text{ }\mu\text{m}$) number and volume concentration, respectively. Continuous particle number size distributions were measured in an urban site of Beijing. During the Olympic and Paralympics Games periods total particle number and volume concentrations were reduced by approximately 16% and 41%, respectively, in which number concentrations of Aitken mode and Accumulation mode was reduced 6% and 30%, respectively. Also significant reduction of the total number and volume concentrations was observed in the summer of 2008 compared to last four years. The obvious decline of total particle volume concentration suggested the measures taken during the Olympic Summer Games had a noticeable effect.

Keywords: traffic control, number size distribution, reduction, Olympic Games.

Chemical characteristics of aerosols in high air pollution episode during autumn of Shanghai, China

Changhong Chen^{1,2}, Min Zhou^{2,1}, Hongli Wang¹, Leiyuan Su², Yiran Chen¹

1 Shanghai Academy of Environmental Sciences, Shanghai 200233

2 The School of Resources and Environmental Engineering , East China University of Science and Technology, Shanghai 200237

Pincipal Contact: Changhong Chen, Prof., Shanghai Academy of Environmental Sciences, Shanghai 200233.

E-mail: chench@saes.sh.cn

Abstract

In order to better understanding the chemical characteristics of aerosols in high air pollution episode, a continuous monitoring work was conducted during October 1st to November 30th, 2010 in urban area of Shanghai. The mass concentration of aerosols and their chemical characteristics under three types of pollution episode including haze, fog-haze, and dust days were obtained. The results show that daily maximum mass concentrations of PM₁₀ and PM_{2.5} is 293 $\mu\text{g}\cdot\text{m}^{-3}$ and 204 $\mu\text{g}\cdot\text{m}^{-3}$, 243 $\mu\text{g}\cdot\text{m}^{-3}$ and 158 $\mu\text{g}\cdot\text{m}^{-3}$, 539 $\mu\text{g}\cdot\text{m}^{-3}$ and 133 $\mu\text{g}\cdot\text{m}^{-3}$ in the haze, fog-haze, and dust days, respectively. Fine particles are the dominant aerosols in the haze and fog-haze pollution with SO₄²⁻, NO₃⁻, NH₄⁺ and OC accounting for 14.7%, 17.4%, 9.8%, 19.4% and 16.7%, 19.6%, 11.6%, 19.4% of PM_{2.5} mass concentration, while coarse particle is the main component in dust days, with SO₄²⁻, NO₃⁻, NH₄⁺ and OC accounting only for 7.7%, 5.6%, 1.7%, 10.4% of the total. Meanwhile a significant larg proportion of crust ions (Ca²⁺, Mg²⁺) in PM_{2.5} was found in dust days, leading to higher alkalinity during that period. In addition, High concentrations of secondary ions in haze days were likely to be related with higher sulfur and nitrogen oxidation rate in gas-to-particulate reactions. SOR and NOR reached 0.24±0.10 and 0.15± 0.06, implying a greater transformation of NO₂ and SO₂ to NO₃⁻ and SO₄²⁻ during haze and fog-haze pollution episode.

Keywords: aerosols; water-soluble ions; OC and EC; haze;

Ultrafine, Fine and Coarse Particles in the Ambient Air of Beijing, China

Dane Westerdahl¹, Xing Wang¹, Xiao-chuan Pan² and K. Max Zhang¹

1 Cornell University, Sibley School of Mechanical and Aerospace Engineering, Address, Ithaca, New York, 14853

2 Peking University School of Public Health, Xueyuan Road 38, Beijing, China, 100083

Principal Contact: Dane Westerdahl, Associate Professor (courtesy), Cornell University, Sibley School of Mechanical and Aerospace Engineering, Upson 127, Cornell University, Ithaca NY, 14853.

Tel: (916) 837-4925 Email: danew@jps.net.

Abstract

Beijing is a rapidly growing city with elevated particulate pollution levels. Considerable regulatory effort is focused on attaining the PM10 ambient air standard, the sole metric of particulate pollution currently regulated in Beijing. In preparation for the recent Summer Olympic Games very extensive controls were implemented to reduce PM10. We conducted summertime air monitoring both before (2007) and during the Games (2008) to observe particle phase pollutants in ambient air as well as on roadway where heavy duty diesel truck traffic was present. We also conducted air monitoring during two heating seasons (2009/10 and 2010/11) to assess PM when strong inversions, traffic, and both regional and local coal combustion impact urban air quality. Key metrics evaluated during these campaigns include particle number concentration and size distribution (5.6 nm to 20 microns), black carbon (BC), PM2.5 mass as well as carbon monoxide. PM2.5 and BC mass were of special interest because, while they are yet of regulatory concern in China, they are considered to have important adverse health and environmental impacts. Key summertime findings are that diurnal BC levels reflected truck traffic in 2007 but not during the Olympics when truck traffic was limited, that PM2.5, ultrafine particle (UFP) numbers and BC levels are closely related on polluted summer days, and that PM2.5 levels appear to be uniform at different locations in the city. During heating seasons very high PM2.5 levels were observed, and BC and PM2.5 were observed to follow similar patterns. Concentrations of these pollutants increased during days of stagnation when inversions were strong and fell when inversions broke. Visibility measurements from both summer and heating seasons were studied and found to reflect changes in PM2.5.

Keywords: PM2.5, black carbon, visibility, seasons, PM size

Evolution of Aerosol Properties Before, During After Fog Events Near Paris, France

Darrel Baumgardner¹, Neda Boyouk² and Ping Chen³

1 Universidad Nacional Autonoma de Mexico, Ciudad Universitaria, Mexico City, DF, 04510

2 Laboratoire Meteorologie dynamique (LMD), LMD - Ecole Polytechnique, Palaiseau, France

3 Handix Corporation, Boulder, Colorado, 80301

Principal Contact: Darrel Baumgardner, Scientist, Universidad Nacional Autonoma de Mexico, Ciudad Universitaria, Mexico City, DF, 04510, Mexico.

Tel: (52) 555-622-4067 E-mail: Darrel.baumgardner@gmail.com

Abstract

A new instrument, the Aerosol Particle Spectrometer with Depolarization (APSD), was been deployed during the period from November, 2010 through March, 2011 to measure aerosol particle properties as part of the Paris Fog Experiment. The APSD measures the size and degree of light depolarization of individual particles in the size range from 0.5 to 20 μm . Three detectors measure light scattered as particles pass through a focused laser beam by collecting at side and back angles. These three pieces of information provide a measure of the particle size, composition and shape. Many unexpected results have come from the measurements that were made during fog free periods and when fog formed on aerosols with many different sources. Preliminary analysis shows that immediately proceeding many of the fog events, there was an abrupt increase in depolarization events signaling the possibility of increased biogenic activity. At other times, significant shifts in the size distribution seem linked to processing of the aerosols by the fog. The APSD promises to offer important new information on aerosol properties that were not previously possible.

Keywords: aerosol properties, shape factors, aerosol fog interactions, biogenic aerosols.

Atmospheric Behavior of the Bifunctional Carbonyls Partitioning on *SPM* and *NRPM₁*

Ricardo Ortiz¹, Satoru Shimada² and Kazuhiko Sakamoto^{1, 2, 3*}

1 Institute for Environmental Science and Technology, Saitama University, 255 Shimo-Okubo, Sakura, Saitama 338-8570, Japan

2 Graduate School of Science and Engineering, Saitama University, 255 Shimo-Okubo, Sakura, Saitama 338-8570, Japan

3 Center for Environmental Science in Saitama, 914 Kami-tanadare, Kazo, Saitama 347-0115, Japan

ABSTRACT

Field samples of eight bifunctional carbonyls were taken with a 3 h time resolution at a suburban area (Saitama City) of Tokyo Metropolitan from 29 July to 4 August 2008. It is said that semivolatile compounds distribute mainly in the fine fraction of the aerosols, however our results show that these compounds distribute more uniformly on the particles below 7 μm (*SPM*) than in particles below 1 μm (*NRPM₁*), this fact confirms that in the sampling site an important fraction of the aerosol produced by these species is secondary and not primary in origin. The highest fraction values for *NRPM₁* were shown in the morning with decreasing values during the period. While for *SPM* the fraction values were very similar in all the period, with slightly higher values in the morning, where primary emissions increased and higher radiation made these compounds to decrease in the aerosol phase. This behavior reproduced the effects observed by Kalberer et al.^[1] and Molina et al.^[2] in the aerosol fractions. The partitioning coefficient of a given compound did not show such big differences throughout the period. Furthermore the correlations of other components in the *NRPM₁* fraction, like ammonium and sulfate ions concentrations, which even if they are of basic and acidic character, show the same trend when correlated to the partitioning coefficient of the measured bifunctional carbonyls.

KEYWORDS

Aerosol evolution, suburban pollution, atmospheric sampling, bifunctional carbonyls partitioning

Introduction

Organic carbon is a ubiquitous component in the aerosol, however, its aerosol-phase chemistry is not well understood yet and hence, it is not included in many atmospheric models. Partitioning of semivolatile organics affects the evolution of organic aerosol when photochemical reactions

generate compounds with lower vapor pressure that will be partially adsorbed into particulate material forming secondary organic aerosol (SOA). It is thought that semivolatile organic compounds tend to equilibrium and in terms of that equilibrium the amount of aerosol produced by these species can be determined, and therefore predicted, however there are so many variables that alter this equilibrium that, as demonstrated so far, the models are not able to predict their aerosol production. Kalberer et al.^[1] found compounds with molecular weights up to 700 Da (Da = unified atomic mass unit) in Zurich aerosol, increasing molecular weight with time of absorption of low-molecular oxidized compounds from the gaseous phase. On the other hand, Molina et al.^[2] found that organic layers react with H₂O, NO, NO₂, O₂, HONO, HNO₃ or mixtures of them when OH radical is present, these reactions in the aerosol interface can volatilize the aerosol. These studies illustrate the complexity of the atmospheric aerosol evolution due to the different influences that it undergoes during its lifetime.

Field species-resolved chemical evolution of aerosols is so complicated that reports of it are almost non-existent. Efforts on trying to describe the chemical evolution processes of atmospheric aerosol are mainly based on the development of numerical models. It can be surmised in the fact that, it is necessary to understand the chemical and physical transformations in the atmosphere, but these processes are complicated by the movement of air masses and the presence of multiple sources with variable strengths. Therefore, it is common to find that, compared to actual atmospheric values, models under-predict aerosol formation. This work reports the measurement of concentrations of bifunctional carbonyls in gaseous and particulate phases to determine their partition coefficients in the suburban atmosphere in order to evaluate their variation at a shorter time-resolution than in previous measurements^[3,4,5] and its variation to the existing *SPM* and *NRMP*₁.

Experimental Methods

In order to measure their concentrations in gaseous and particulate phases, seven semivolatile bifunctional carbonyl compounds were sampled at a site located in a suburban c.a. 30 km north-northwest of the center of Tokyo metropolitan area, and between 2 important roads: national road 463 and prefectoral road 57. The sampler was located at the balcony in the 10th floor of the

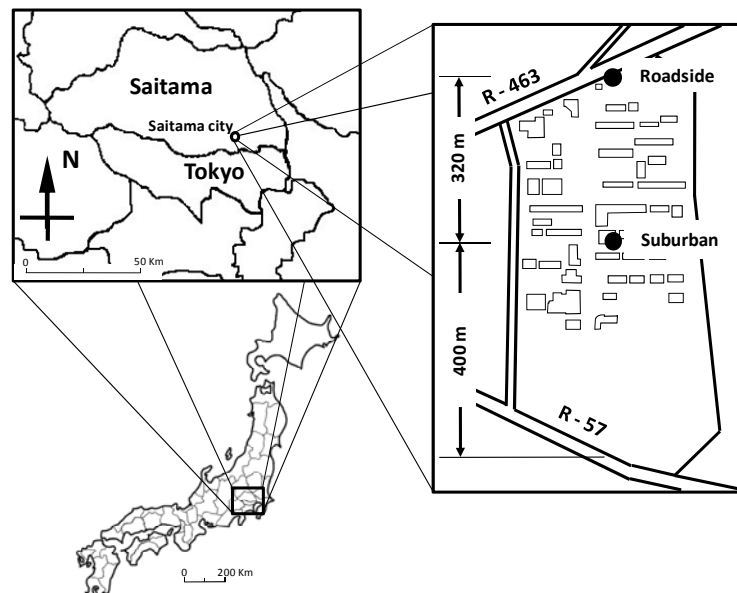


Fig. 1. Sampling site location.

General Research Building at a height of 37 m inside Saitama University. Figure 1 shows the location of the sampling site.

Samples were collected with a set of two low volume denuder and filter pack systems (AD-FP) at a flow rate of 10 L m^{-1} as shown in Fig. 2. The two systems were set to sample in parallel for 5 h 50 min with a delay of 3 h, in order to get concentrations with a 3 h resolution; 10 min were taken to exchange the sampling system, which introduces a total error of 0.02 in the calculations. The samples were taken in summer from 29 July to 4 August 2008. The O -(2,3,4,5,6-pentafluorobenzyl)hydroxylamine hydrochloride (PFBHA) sorbent technique^[3,4,5] was used to collect the carbonyls (Fig. 2). Simultaneously, aerosol composition was monitored with an aerosol mass spectrometer (AMS, Aerodyne Research Inc., Billerica, MA, USA).

Gaseous samples collected in the denuders were immediately extracted in situ by 3 consecutive extractions with 5 mL of dichloromethane in each denuder; the solutions were stored at 4°C in hermetic amber vials. Filter samples were stored at -40°C in petri slides which were put in hermetically sealed aluminum bags. Filters were later ultrasonically extracted with dichloromethane, and after a second derivatization with N,O -bis(trimethylsilyl)trifluoroacetamide (BSTFA) at 75°C , filter and denuder samples were analyzed by gas chromatography-mass spectrometry (GCMS-QP5050, Shimadzu, Kyoto, Japan).

Results and Discussion

Concentrations and their temporal variation

The average results of the concentration of the bifunctional carbonyls in gaseous and particulate phases, as well as their standard deviations are summarized in Table 1. The partitioning coefficient proposed by Pankow (1997)^[6] (originally defined in the referred work as $\log K_p = \log ([F]/[A]) - \log [TSP]$ (where F , A , and TSP represent the particulate concentration of a given compound, its gaseous concentration, and the concentration of the total suspended particles, respectively)). We evaluated an approximation to this partitioning coefficient by using suspended particulate matter (SPM) instead of TSP (SPM is defined in this work as the particulate matter below $7 \mu\text{m}$, and it is measured by the β -ray attenuation method)^[7]. The results are also reported for each compound in Table 1. Additionally to the compounds reported in Table 1, *m*-hydroxybenzaldehyde was also analyzed, however, most of its concentrations were below detectable limits, and hence not reported here.

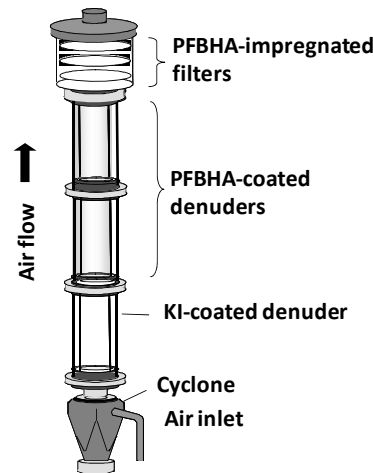


Fig. 2. Sampling system.

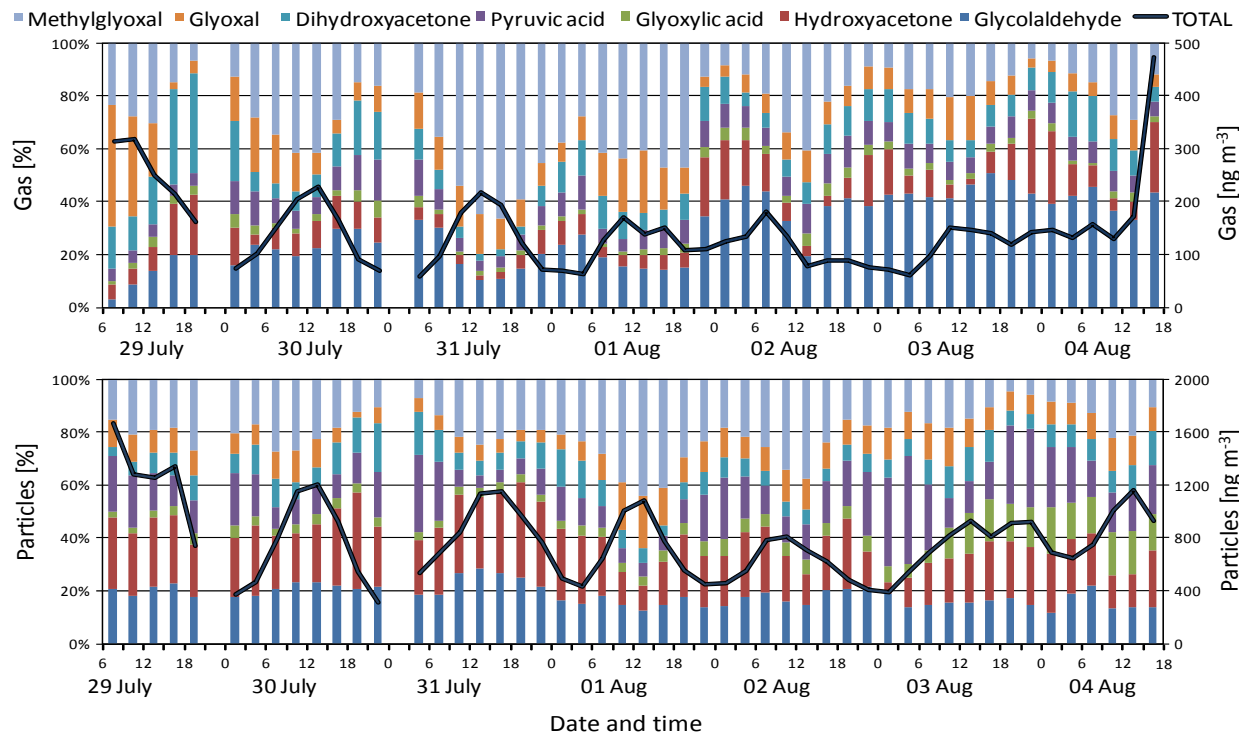
Table 1. Average concentrations

Compound	Gaseous (ng m ⁻³)	Particulate (ng m ⁻³)	Log K _p
Glycolaldehyde	40 ± 30	147 ± 75	-0.974 ± 0.409
Hydroxyacetone	16 ± 19	173 ± 91	-0.421 ± 0.465
Glyoxylic acid	4 ± 2	51 ± 46	-0.523 ± 0.278
Pyruvic acid	10 ± 4	115 ± 67	-0.566 ± 0.254
Dihydroxyacetone	16 ± 15	65 ± 26	-0.899 ± 0.339
Glyoxal	19 ± 25	76 ± 45	-0.875 ± 0.222
Methylglyoxal	40 ± 32	164 ± 100	-0.907 ± 0.210
Total	139 ± 80	761 ± 329	

The average concentration values in particulate phase reported in Table 1 are higher than those measured on previous measurements^[3,4,5], they appear influenced by higher concentrations on oxidants which averaged 38 ppb in the sampling period reported in this work, while on previous measurements averaged 24 ppb and this probably forced a higher oxidation in the gaseous phase, which showed average concentrations of about one fourth in 2008 compared to previous measurements. The variation on the composition is shown in Fig. 3 separately for gaseous and particulate phase.

Among the measured compounds, methylglyoxal and glycolaldehyde were the most abundant in both phases, while in the particulate phase hydroxyacetone and pyruvic acid also showed important percentages, which indicates that in the particulate phase the latter two compounds had a slower decomposition than in gaseous phase where they are more likely protected by the formation of dimers and oligomers^[8].

Fig. 3. Concentrations percentage variation in gas (top) and particle phases (bottom).



SPM and NRPM₁

During the sampling period, *SPM* concentrations averaged $39 \pm 13 \mu\text{g m}^{-3}$ and *NRPM*₁ concentrations averaged $12 \pm 6 \mu\text{g m}^{-3}$. Figure 4 shows the ratios of the total concentrations of bifunctional carbonyls in the particulate phase to the measured concentrations of *SPM* and *NRPM*₁. It is said that semivolatile compounds distribute mainly in the fine fraction of the aerosols, because of the generation mechanism of both fractions. However, results in Fig. 4 show that an increase in the concentrations of the total bifunctional carbonyls does not correspond to an increase in *NRPM*₁,

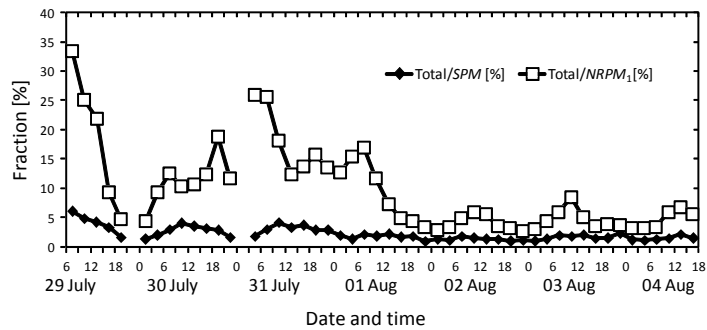


Fig. 4. Total particulated bifunctional carbonyls represented as a fraction of aerosol.

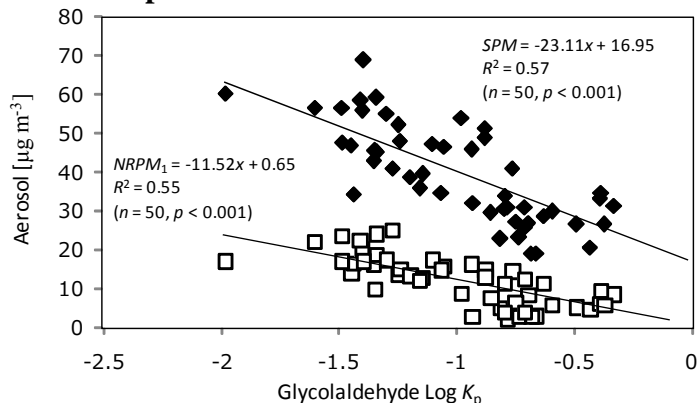


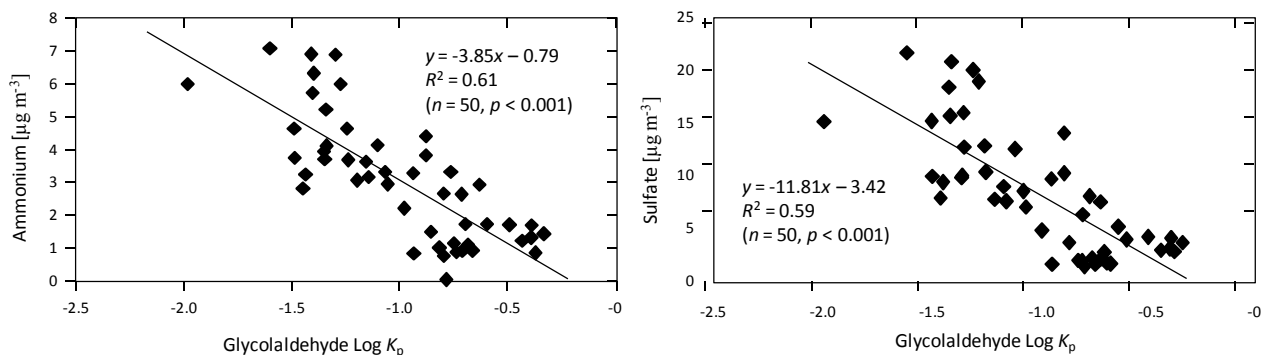
Fig. 5. Log K_p vs. Aerosol concentrations.

nevertheless, it does correspond to an increase in the *SPM*, hence, the ratios show small variations for *SPM* and big variations for *NRPM₁*. This fact reconfirms that an important fraction of the aerosol produced by these species is secondary and not primary in origin. We surmise this distribution on the growth of ultrafine particles emitted or generated in the metropolitan area of Tokyo that reach diameters above 1 μm when they reach the Saitama area, and then include the original bifunctional carbonyls. The ultrafine particles generated in Saitama include bifunctional carbonyls; however, transported particles include them at higher amounts.

The highest fraction values for *NRPM₁* were shown in the morning with decreasing values as time passes during the period. While for *SPM*, the fraction values were very similar all the period, with slightly higher values in the morning, where the more traffic increased primary emissions of these compounds and higher radiation made them decrease, in the aerosol phase. This behavior reproduces once again the effects observed by Kalberer et al.^[1] and Molina et al.^[2], these effects though are seen on the amount of aerosol-phase compounds in the aerosol fractions. While in the partitioning coefficient of a given compound, the amount of a given aerosol fraction through all the period do not seem to have such big differences, as it can be seen in Fig. 5, nevertheless, the correlation coefficient for *SPM* are still slightly higher than for *NRPM₁*, and this effect is corroborated by the effect showed by the correlations values to other components in the *NRPM₁* fraction, like ammonium and sulfate ions concentrations, which even if they are of basic and acidic character, both show a negative slope when correlated to the partitioning coefficient (Fig. 6). These results indicate that these ionic species in the aerosol may neutralize their acidity in the particle and hence not affect considerably the partitioning and even if the correlation values are

Fig. 6. Ammonium and sulfate concentrations in the *NRPM₁* aerosol fraction vs the partitioning coefficient of glycolaldehyde.

still good, they must be affected by the variation showed in Fig. 4.



SUMMARY

The concentrations of seven bifunctional carbonyls were measured at a suburban site with a time resolution of 3 h. Compared to results of previous years; gaseous concentrations were lower due

to higher concentrations of oxidant species. Results showed that concentrations of bifunctional carbonyls on particulate phase do not depend on the concentrations of $NRPM_1$ as they do on SPM , which demonstrate that a fraction of these compounds is transported from other areas. However, when correlated to the partition coefficients, SPM showed only slightly better correlation coefficients than $NRPM_1$, but a more pronounced slope which demonstrate the stronger dependence. Additionally we found that the concentration of ionic species does not affect positively or negatively the partitioning depending on their acidic or basic, since these ionic species are neutralized inside the particle and not affect to that level the acidity of the aerosol.

ACKNOWLEDGMENTS

This work was supported in part by Japan Auto-Oil Program (JATOP) and in part by Grants-in-Aid from Saitama University.

REFERENCES

- [1] Kalberer, M.; Sax, M.; Samburova, V.; *Environ. Sci. Technol.* 2006, 40, 5917–5922.
- [2] Molina, M.J.; Ivanov, A.V.; Trakhtenberg, S.; Molina, L.T.; *Geophys. Res. Lett.* 2004, 31, L22104.
- [3] Ortiz, R.; Hagino, H.; Sekiguchi, K.; Wang, Q.; Sakamoto, K.; *Atmos. Res.* 2006, 82, 709–718.
- [4] Ortiz, R.; Enya, K.; Sekiguchi, K.; Sakamoto, K.; *Atmos. Environ.* 2009, 43, 382–388.
- [5] Ortiz, R.; Yoshida, N.; Sorimachi, A.; Sekiguchi, K.; Sakamoto, K., *Aerosol Air Qual. Res.* (Submitted)
- [6] Pankow, J.F.; *Atmos. Environ.* 1987, 21, 2275–2290.
- [7] Takahashi, K.; Minoura, H.; Sakamoto, K.; *Atmos. Environ.* 2008, 42, 5232–5240.
- [8] Altieri, K.E., Carlton, A.G., Lim, H.J., Turpin, B.J., Seitzinger, S.P., 2006. *Environ. Sci. Technol.* 40, 4956-4960.

Iodine speciation in marine aerosols: the spatial variation from Shanghai, China to Prydz Bay, Antarctica

Senchao Lai^{1,2}, Zhouqing Xie³, and Thorsten Hoffmann²

1 School of Environmental Science and Technology, South China University of Technology, Guangzhou 510006, China

2 Institute of Inorganic and Analytical Chemistry, Johannes Gutenberg University of Mainz, Mainz, Germany

3 Institute of Polar Environment, University of Science and Technology of China, Hefei, China

Principal Contact: Senchao Lai, Associate Professor, School of Environmental Science and Technology, South China University of Technology, Guangzhou, 510006, China.

Email: sclai@scut.edu.cn

Abstract

Iodine chemistry plays an important role in the tropospheric ozone depletion and the new particle formation in the Marine Boundary Layer (MBL). However, the sources, reaction pathways, and sinks of iodine in MBL are not fully understood. Here we present a study on iodine speciation in the marine aerosols collected onboard a round-trip cruise from Shanghai, China to Prydz Bay, Antarctica from November 2005 to March 2006. Water-soluble species were measured by an online coupling technique of ion chromatography coupled to Inductively Coupled Plasma-Mass Spectrometry (IC-ICP-MS). The results reveal that soluble organic iodine (SOI) was the most abundant fraction, accounting for approximately 70 % of total soluble iodine (TSI) on average. The abundance of inorganic iodine species, iodate and iodide, was less than 30% of TSI. Spatial variations of soluble iodine species were observed in different areas of coast and open ocean. In general, the levels of TSI in the coastal region were higher than over the open ocean except Antarctic coast, which had the lowest TSI level. The levels of TSI in the coastal regions decreased by an order of Chinese coast > Southeast Asian coast > Australian coast > Antarctic coast, indicating a decreasing trend from North hemisphere to South hemisphere. The causes for the variation in iodine speciation and concentrations can be assumed to be connected to the flux of iodine from the oceans and cycling processes in the atmosphere.

Keywords: Iodine speciation, marine aerosol, spatial variation

Characteristics of surface ozone at an urban site in Xi'an, China

Xin Wang^{1, 2} and Zhenxing Shen^{1, 2}

1 Department of Environmental Science and Engineering, Xi'an Jiaotong University, Xi'an 710049, China

2 SKLLQG, Institute of Earth Environment, Chinese Academy of Sciences, Xi'an 710075, China

Principal Contact: Zhenxing Shen, Dr., Department of Environmental Science and Engineering, Xi'an Jiaotong University, Xi'an 710049, China.

Tel: 18792765891 E-mail: zxshen@mail.xjtu.edu.cn

Abstract

The surface ozone levels over Xi'an, China were monitored every five minutes using the TE Model 49C ozone analyzer from March 23, 2008 to January 12, 2009. The daily O₃ concentrations ranged from 0.43 ppbv to 64.23 ppbv, averaging a yearly mean value of 16.04 ppbv. Seasonal variation of O₃ levels showed a clear summer maximum and winter minimum pattern. The diurnal variation of surface O₃ typical peaked between 14:00 and 16:00 local standard time (LST), and had the minimum value between 5:00 and 7:00 LST, corresponding with the lowest and the highest temperature periods. The frequency distribution of surface O₃ showed a commonly seasonal pattern except in summer. Significantly positive correlation was found between O₃ concentration and ambient temperature. In contrast, ambient pressure had a negative correlation with O₃ level.

Keywords: surface ozone; temporal characteristics; diurnal variation

CHARACTERISTICS OF OZONE AND FINE PARTICLE OBSERVED IN URBAN AND SUBURBAN OF NANJING, CHINA

Tijian Wang, Ziqiang Jiang, Xiaoxian Huang, Yi Shen and Fanhui Shen

School of Atmospheric Sciences, Nanjing University, Hankou Rd. 22, Nanjing 210093, China

Principal Contact: Tijian Wang, Professor, School of Atmospheric Sciences, Nanjing University, Hankou Rd. 22, Nanjing 210093, China.

Tel: 86+25-83593797 E-mail: tjiang@nju.edu.cn

Abstract

Ozone (O_3) and fine particulate matter ($PM_{2.5}$) are both important species for air quality and climate change. Surface O_3 and $PM_{2.5}$ have been continuously collected for two years during 2008-2009 at Cao Chang Men (CCM) station and Pu Kou (PK) station, representing urban and suburban locations of Nanjing, China. Observations show that the average concentrations of $PM_{2.5}$, O_3 are $64.6 \pm 47.4 \mu g/m^3$ and 24.6 ± 22.8 ppb for CCM station, and $94.1 \pm 63.4 \mu g/m^3$ and 16.9 ± 14.9 ppb for PK station during the study period. A significant diurnal pattern was observed for O_3 with high value in the afternoon and low value at night, while $PM_{2.5}$ shows double peak with one appearing between 7:00 and 9:00 in the morning, and the other between 19:00 and 21:00 in the evening. O_3 also exhibits seasonal variation with spring maximum and winter minimum. $PM_{2.5}$ shows summer maximum in PK station and autumn maximum in CCM station. $PM_{2.5}$ was high in weekdays and low in weekend. Typical case studies suggest that high absorbing aerosols in $PM_{2.5}$ causes decreasing of UV radiation and leads to the decline of O_3 concentration. On the other hand, the scattering particles in the boundary layer accelerate photochemical reactions and smog production, which results in positive-feedback mechanisms between $PM_{2.5}$ and O_3 . Apart from the surface measurements, monthly tropospheric ozone residual (TOR) and aerosol optical depth (AOD) series of Nanjing were constructed from satellite data to understand their trend, periodic and abrupt change characteristics. Investigations show that both TOR and AOD have a rising trend during the period of 1979-2007. The increasing rates for annual mean TOR and AOD were 1.2DU per decade and 0.03 per decade, respectively. Wavelet analysis shows that TOR and AOD have the obvious periodic of one year and two years. By use of the Mann-Kendall technique, the abrupt changes in 1999-2000 for TOR and in 1998-1999 for AOD are resolved.

Keywords: O_3 , $PM_{2.5}$, TOR, AOD, Nanjing

A supersite program for real-time characterization of particulate matter (PM) in Hong Kong

Chak K Chan^{1,2}, NT Lau¹, Arthur PS Lau¹, Alexis KH Lau^{1,3}, Jimmy CH Fung^{1,4}, Jian Z Yu^{1,5}, Frank Lee⁶, Christopher YH Chao⁷, and Peter Louie⁸

1 Division of Environment, The Hong Kong University of Science and Technology, Clear Water Bay, Hong Kong, China

2 Department of Chemical and Biomolecular Engineering, The Hong Kong University of Science and Technology, Clear Water Bay, Hong Kong, China

3 Department of Civil and Environmental Engineering, The Hong Kong University of Science and Technology, Clear Water Bay, Hong Kong, China

4 Department of Mathematics, The Hong Kong University of Science and Technology, Clear Water Bay, Hong Kong, China

5 Department of Chemistry, The Hong Kong University of Science and Technology, Clear Water Bay, Hong Kong, China

6 Department of Civil and Structural Engineering, Hong Kong Polytechnic University, Hong Kong, China

7 Department of Mechanical Engineering, The Hong Kong University of Science and Technology, Clear Water Bay, Hong Kong, China

8 Environmental Protection Department, The Hong Kong Special Administration Region Government, Hong Kong, China

Principal Contact: Chak K. Chan, Head and Professor, Division of Environment, The Hong Kong University of Science and Technology, Clear Water Bay, Hong Kong, China.

Tel: 852 2358 7124 Fax: 852 2358 0054 Email: keckchan@ust.hk

Abstract

Atmospheric particulate matter (PM) is a major air pollutant causing the haze that chokes the citizens in Hong Kong (HK) and the Pearl River Delta (PRD). A “supersite” program has been recently developed to utilize continuous real-time characterization of the physical and chemical properties of PM and VOCs in HK as well as numerical modeling to study the fast evolution processes of PM in the region and how the PM from local anthropogenic sources and regional transport influence the air quality and visibility in HK. It complements the existing compliance measurements conducted in Hong Kong. The supersite has a floor area over 1000 m² on the roof of a structure in the campus of The Hong Kong University of Science and Technology in the eastern part of HK. It is located at the seafront and open to Port Shelter and the Sai Kung West Country Park with no significant anthropogenic sources. It also has 10 plinths for outdoor equipments and an air-conditioned modular house with 10 inlet ports for PM and gaseous instrumentation. The air quality parameters monitored include the chemical composition (high resolution time-of-flight aerosol mass spectrometer, HR-ToF-AMS, Aerodyne Research Inc.), hygroscopic properties (cloud condensation nuclei counter, CCN-200, DMT Inc.; humidified tandem differential mobility analyzer, 2000C,

Brechtel Manufacturing Inc.), number size distribution (fast mobility particle sizer, FMPS, TSI Inc.), EC/OC content (EC/OC analyzer, RT-4, Sunset Laboratory Inc.), ion composition (particle-into-liquid ion chromatograph, PILS-IC, Metrohm AG), and vertical profile of PM in ambient (micro-pulse lidar, MPL-4B-532, Sigma Space Corporation) as well as the concentration of ambient VOCs (ion-molecule reaction mass spectrometer, AIRSENSE, V&F Analyse- und Messtechnik GmbH). Preliminary results will be reported in this paper.

Keywords: Real-time measurement, AMS, PILS, particulate matter, VOC, ozone, supersite, Pearl River Delta

Investigation of Factors Affecting the Mass Size Distribution of Ambient Particulates

Jim Juimin Lin, Mon-Shi Lin, and Kuan-Lun Pan

National Kaohsiung First University of Science and Technology, Taiwan

Principal Contact: Jim Juimin Lin, National Kaohsiung First University of Science and Technology, 2, Jhuoyue Rd., Nanzih Dist., Kaohsiung City, 811, Taiwan.

Tel: +886-7-6011000 ext 2312 Fax: +886-7-6011332 Email: envelin@nkfust.edu.tw

Abstract

In this study, a GRIMM-1.109 sub-micron particle size distribution automatic monitor was applied to measure the concentration and size distribution of atmospheric particles. The results showed that high concentrations in winter and low concentration in summer with the lowest concentration in August, 2009. The concentration increased in September and October to the highest in December, and then gradually decreased. Due to the influence of rainfall in summer, ambient particulates were easily settled by rain, while with the northwest wind blowing during the winter, combined with topographic effects, the suspended particles cumulated, so PM₁₀ maintained high in concentration. In spring, the wind speed increased, atmospheric aerosols dispersed more easily, thus concentrations reduced.

When the wind speed was greater than 3 m/s, the average ratio of PM_{2.5}/TSP concentration was 0.65 ± 0.15 , particle size distribution showed bimodal, the peak size range of fine particles was 0.35-0.45 μm , coarse particles 4.0- 5.0 μm ; while when the wind speed was less than 1 m/s, PM_{2.5}/TSP ratio was 0.59 ± 0.15 , particle size distribution was also bimodal, the peak size range of fine particles was 0.28-0.30 μm , coarse particles 4.0-5.0 μm . When NO_x concentration was greater than 50 ppb, the average ratio of PM_{2.5}/TSP concentration was 0.66 ± 0.10 , particle size distribution was bimodal, the peak size range of fine particles was 0.28-0.30 μm , coarse particles 4.0-5.0 μm . When SO₂ concentration was greater than 30 ppb, the average ratio of PM_{2.5}/TSP was 0.59 ± 0.06 , particle size distribution was bimodal, the peak size range of fine particles was 0.40-0.45 μm , and coarse particles 7.5-8.5 μm . The observed results in this study suggest that meteorological conditions and precursor gases are significant and important affecting factors of ambient particulates.

Keywords: Ambient particulates, mass size distribution, precursor gases, meteorological conditions

Quantification of Indirect Combustion Aerosol Impacts on Cirrus Clouds

Olga Popovicheva¹, Yuxing Yu² and Joyce E. Penner²

1 Institute of Nuclear Physics, Moscow State University, Moscow, 119991, Russia

2 AOSS, University of Michigan, Ann Arbor, MI 48105

ABSTRACT

The goal of our research is to increase the state of scientific understanding of black carbon (BC)/cloud/climate interactions and to provide a realistic assessment of the effects of fossil fuel combustion on climate. The major sources of BC emitted by transport (road, aviation, shipping) are characterized with an emphasis on the key particle properties responsible for interaction with water. The relationship between soot physico-chemistry and the effects of soot on cloud microphysics is proposed based on the concept of the quantification of water uptake which allows the separation of BC aerosols into hydrophobic, hydrophilic, and hygroscopic (3-BC scheme). To better quantify the role of fossil fuel burning BC in climate change, a 3-BC scheme is developed to replace the 1-BC scheme in a coupled climate and aerosol transport model (CAM-IMPACT). The new scheme explicitly calculates the aging of emitted BC aerosols due to condensation of gas phase sulfate and coagulation of pure sulfate aerosols with BC aerosols. The hygroscopicity of BC is determined by the layers of sulfate coating on their surface according to criteria developed in laboratory observations. This approach allows the identification of the range of BC hygroscopicity responsible for heterogeneous ice nucleation in cirrus clouds and the most significant effects of combustion aerosol on climate forcing.

KEYWORDS fossil fuel BC aerosol, water uptake, heterogeneous ice nucleation, cirrus clouds

Introduction

The effects of combustion-generated particles (also known as soot, which is a mixture of black carbon (BC) and organic matter (OM)) is currently acknowledged to be one of the largest sources of uncertainties in understanding of aerosol impacts on global climate. The contribution of fossil fuel from oil fuel combustion and transportation is estimated to be significant part of the global inventory of combustion aerosols.^[1] The first indirect BC effect is related to the increase in cloud droplet concentrations due to aerosols serving as cloud condensation nuclei (CCN) and thereby to the decrease of the cloud effective radius.^[2] The decreased radius may decrease the rate of

precipitation, causing longer cloud lifetime and higher cloud amount (second indirect effect). Global models demonstrate that combustion-derived particulates can significantly increase the CCN concentration and thus the droplet concentration of low clouds and affect by that means the life cycle and radiative properties of stratus clouds at the top of the marine boundary layer.^[3] A major source of uncertainty in assessing the impact of aircraft-emitted soot aerosols on climate change is their secondary effects on cirrus through their potential action as ice nuclei (IN). In all effects the quantification of the CCN/IN ability of combustion-generated aerosols is the key issue that requires an increase in the state of scientific understanding of their behavior in the humid atmosphere. For this reason, we further developed the CAM/IMPACT global climate model by incorporating a new cirrus cloud formulation.^[4]

Fossil fuel combustion emissions are highly uncertain presently due to difficulties in quantifying surface and traffic sources.^[1] A key reason is the wide variety of source-dependent properties of the soot particles emitted from the various engines, boiler, and ovens which burn gaseous, liquid and solid fuels. The lack of a comprehensive characterization of surface, marine, and aircraft emissions led to the general conclusion that exhaust BC/OM particles are insoluble and therefore hydrophobic and poor CCN/IN. However, during transport and aging in the atmosphere BC/OM particles of different origin may change their properties due to condensation of gaseous sulfate and coagulation with pure sulfate particles. Understanding the nature of mixed particles is essential for determining the role of BC in the atmosphere. Therefore, the extent to which the processing causes the BC/OM particles to become hydrophilic is important in evaluating their susceptibility for wet deposition and lifetime.

In laboratory simulations it is found that one monolayer (ML) of sulfuric acid deposited on hydrophobic soot leads to a hydrophilization that is much stronger than that of adding any organic acid.^[5] Upon humidification the H₂SO₄-coated soot particles display distinct hygroscopic growth depending on their initial size and the mass fraction of condensed sulfuric acid. Exposure of soot particles to H₂SO₄ vapor^[6] or coagulation with sulfuric acid aerosols lead to a significant increase of their CCN activity. A few MLs of sulfuric acid on soot particles increases their CCN activity as well as their capability to act as a heterogeneous ice nuclei whereas the high fraction of sulfate found in aircraft engine – generated soot causes ice nucleation near conditions expected for homogeneous freezing of aqueous solutions.^[7] Therefore, in this paper we analyzed the effects of fossil fuel BC emissions and their aging in environment. We developed the characterization of original soot emissions from diesel, aircraft, ship emission sources, and added the effects of the evolution with time in the humid atmosphere due to the aging.

Progress has been achieved by a systematic comparative analysis of the water uptake by soot particles of various physic-chemical properties and by the identification of water-soot interaction mechanisms in relation to the soot composition.^[8] Two mechanisms of water/soot interaction, namely, the bulk dissolution of water into soot due to coverage by soluble

compounds and the water molecule adsorption on surface active sites are identified. The formation of a water film extended over the surface is suggested as a quantification measure which separates hygroscopic from non-hygroscopic (hydrophobic and hydrophilic) soot.

This presentation summarizes the characterization of major sources of soot emitted by transport (road, aviation, shipping) with emphasis on key particle properties responsible for interaction with water. The relationship between soot physico-chemistry and cloud microphysics is proposed on the basis of the amount of water uptake allowing the separation of soot aerosols into hydrophobic, hydrophilic, and hygroscopic (3-BC/OM scheme). This approach allows the identification of the range of BC/OM hygroscopicity responsible for heterogeneous ice nucleation and the most significant combustion aerosol effects on cirrus clouds in the developed coupled climate and aerosol transport model (CAM-IMPACT).

Experimental Methods

Laboratory-made and originally produced soots by an aircraft gas turbine engine combustor, and truck and ship diesel engines are characterized by SEM/EDS, and FTIR with respect to heterogeneous morphological and chemical structure^[8]. Water uptake measurements on well-characterized soots are performed by gravimetry. Comparative analysis of water adsorption isotherms on soots of various compositions allows us to apply the concept of quantification of their behavior in clouds. Initially hydrophobic primary soot particles emitted by diesel and aircraft engines are proposed to be simulated by EC soot with OC coating or a mixture that is typical for such kind of emissions. Deposition of various amount of sulfuric acid on initially hydrophobic soot changes their hygroscopic properties, thus simulating the hygroscopic effects of the soot aging in the atmosphere due to deposition of hygroscopic material.

Theory

The NCAR CAM3 model is updated to include a two-moment microphysics scheme for cloud liquid and cloud ice. A statistical cirrus cloud scheme that accounts for mesoscale temperature perturbations is implemented to better represent both subgrid-scale supersaturation and cloud formation.^[4] Fossil fuel burning, biomass burning, and dust are considered as heterogeneous ice nuclei in mixed-phase clouds. Aircraft BC is treated as having an increase in active sites as a result of processing by contrails and so is treated as heterogeneous ice nuclei in cirrus clouds. The determination of hydrophobic, hydrophilic, and hygroscopic fossil fuel-derived soot is based on the concepts developed in laboratory simulations. Freshly emitted BC/OM particles are assumed in to be hydrophobic, and therefore the amount of hydrophilic and hygroscopic BC/OM particles are set to be zero initially. The effect of aging BC/OM is accounted for by its mixing with sulfate: the three BC/OM categories are defined by the number of monolayers of sulfuric acid coating on these aerosols. At the end of each time step, if the amount of sulfate coating is sufficient to move

the BC/OM to the next category, the mass concentration of the original categories is set to zero. The size distribution of the three BC categories is assumed to be the same. The accommodation coefficients for the condensation of sulfuric acid on hydrophobic and hydrophilic BC particles are assumed to be 0.018, while that for hygroscopic BC particles is assumed to be 0.65.

Results and Discussion

The morphology and chemical composition analysis demonstrates the high heterogeneity of any combustion-derived particles properties, either collected behind an aircraft turbine engine combustor, or in the diesel engine exhaust pipe, or at the end of a ship pipe. Whenever there is an engine, fuel, or operation conditions, soot particles are separated into hydrophobic, hydrophilic, and hygroscopic categories depending on their morphology, content of chemical species and water uptake. Water uptake on initially hydrophobic primary soot particles emitted by diesel and aircraft engines is shown in Fig.1.

The laboratory simulations demonstrate how thick the sulfuric acid coverage on soot particles with a given size needs to be to impact on their hygroscopic quality. Fig.1 shows the water uptake by soot with various H_2SO_4 coatings. Deposition of a small amount of sulfuric acid on initially hydrophobic soot, less than a half of 1ML, provides just a limited number of active sites and low water adsorption, a typical feature for water uptake by hydrophobic soot. Increase of the H_2SO_4 coverage from 0.5 to 1.4 ML leads to increasing the number of active sites that become large enough to produce water clusters which may form a water film extended over the soot surface, a feature of hydrophilic soot. Therefore, we conclude that the transformation of soot particles from hydrophobic to hydrophilic takes place with an H_2SO_4 coverage on the surface in the range from 0.5 up to 1.5 ML, and the threshold value of the monolayers of sulfuric acid to convert each soot type from hydrophobic to hydrophilic is near 0.5 ML. If the sulfuric acid coverage exceeds 1.5- 2.3 ML leading to a change of the mechanism of the water/soot interaction from adsorption on active sites to dissolution, the soot is transformed from non-hygroscopic to hygroscopic soot. Therefore, we conclude that the threshold value of monolayers of sulfuric acid to convert each soot type from hydrophilic to hygroscopic is 2.3 ML.

In the NCAR CAM3/IMPACT model for hydrophobic and hydrophilic BC, if the number of monolayers of sulfuric acid coating exceeds 3ML, then they are partitioned into the hygroscopic BC category. For hydrophobic BC/OM, if the accumulation of sulfuric acid coating is less than 3ML, but more than 1ML, then it is partitioned into the hydrophilic BC category. We choose number of monolayers of sulfuric acid coverage, instead of weight percent, as the selection criteria, because different BC particle densities may result in differences in the calculated weight percent.

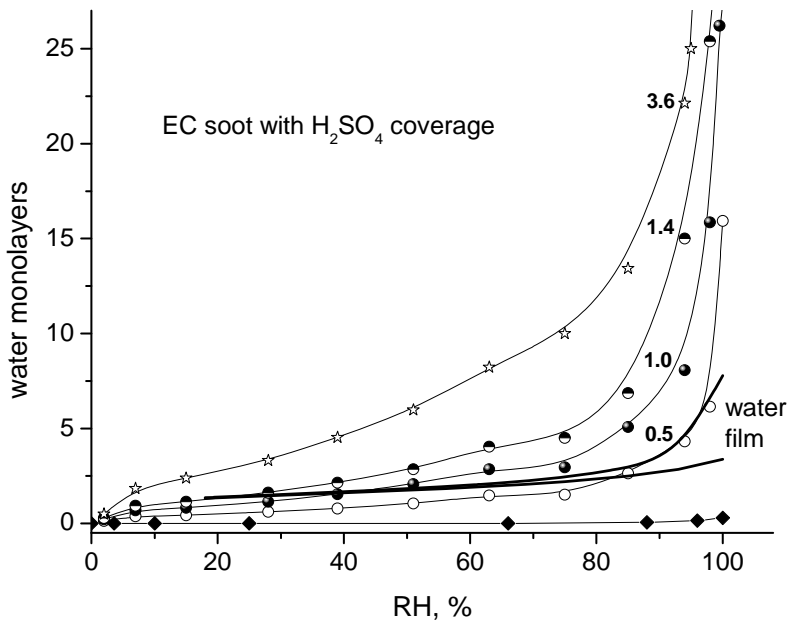


Figure 1. Water uptake on EC soot: without coverage (full diamond), with 0.5, 1., 1.4, and 3.6 ML of H_2SO_4 (indicated by numbers) corresponding to 2.5, 4.9, 6.8, and 15 wt%. The curves are to guide the eye. The area of existence for water film on the surface is marked by thick boundary lines.

The model CAM-IMPACT is used for the quantification of the cloud impacts by BC/OM emissions. In mixed-phase clouds, the hydrophobic fossil fuel plus biofuel BC/OM are assumed to be contact ice nuclei following the contact freezing parametrization^[9] as in the 1 BC/OM scheme. We applied some modifications to the deposition/condensation/immersion freezing parameterization to treat hydrophobic BC/OM and hydrophilic BC/OM. The frozen fraction of the hydrophilic TOS soot in Koehler et al.^[7] at -40C and at water saturation is 2%, and that of the hydrophobic TS soot is 0.02%. However, the deposition/condensation/immersion freezing parameterization predicts only one frozen fraction at the same condition for all soot particles, which is 0.2%. Therefore, to account for the differences in the ice nucleating ability of hydrophilic and hydrophobic BC/OM, we increase the frozen fraction predicted by the deposition/condensation/immersion freezing parameterization by a factor of 10 to represent the freezing ability of hydrophilic BC/OM, while decreasing it by a factor of 10 to represent the freezing ability of hydrophobic BC/OM. By doing so, we also preserve the frozen fractions at different temperatures as it is calculated in Phillips et al.^[8].

Fossil fuel/biofuel burning BC burden is increased in the 3BC scheme. The hygroscopic BC is the most abundant of the three types of BC. The lifetime of hygroscopic BC is larger than

the lifetime of BC in the 1BC scheme. The lifetime of hydrophobic and hydrophilic BC is shorter because they are quickly converted to hygroscopic BC. Hydrophobic BC/OM only exists below 800hPa, near the region where they are emitted. Hydrophilic BC/OM can extend further to above 800hPa before they are converted to the hygroscopic BC/OM group. Hygroscopic BC is the most abundant and can reach high altitudes and extend to the North Pole.

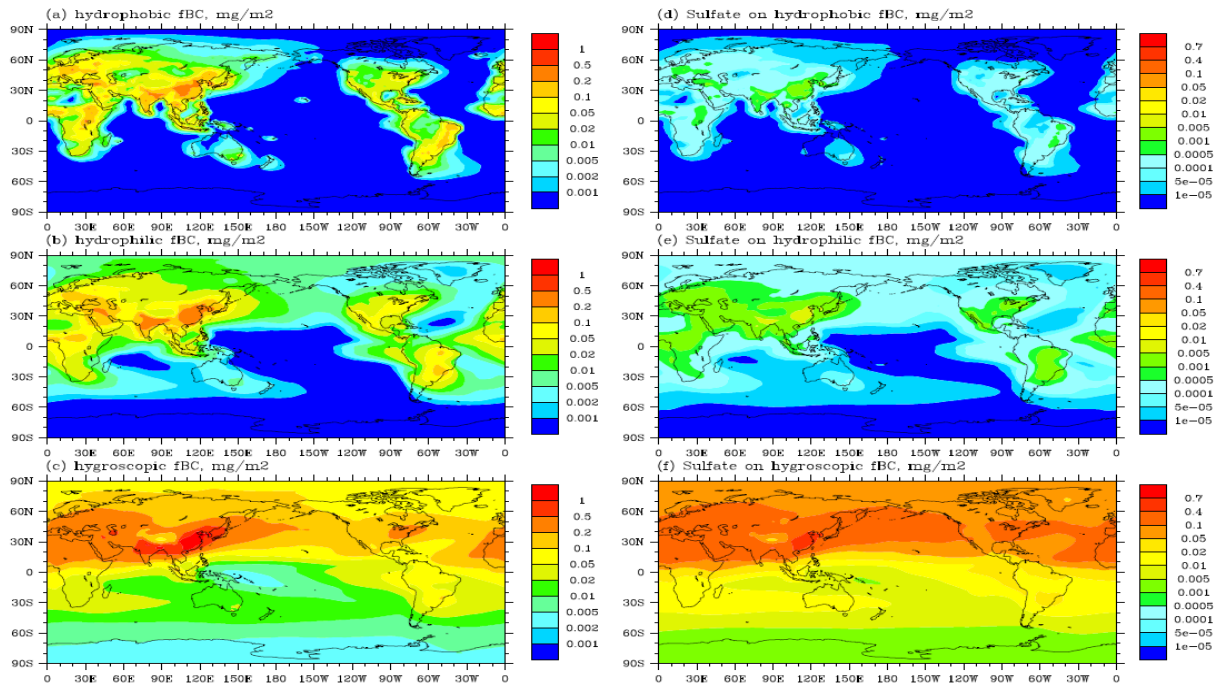


Figure 2. Annual average horizontal distribution of fossil fuel and biofuel BC.

SUMMARY AND CONCLUSION

A laboratory approach for quantification of aging the fossil fuel combustion particles due to mixing with sulfuric acid in the atmosphere is developed^[10]. A version of the numerical code that includes 3 categories (hydrophobic, hydrophilic and hydroscopic) of fossil-fuel BC/OM has been generated. The new scheme explicitly calculates the aging of emitted BC/OM aerosols due to condensation and coagulation of sulfate. All combustion-derived aerosols are assumed to be hydrophobic and converted to hydrophilic and hydroscopic fractions upon deposition/coagulation

of sulfate. Laboratory simulations provide information about how much soluble material needs to be added to a hydrophobic BC/OM particle to define this particle as hydrophilic and is thus capable of being taken up into clouds and wet deposited. The most significant effects of combustion aerosol on climate forcing and the range of BC hygroscopicity responsible for heterogeneous ice nucleation in cirrus clouds are demonstrated.

ACKNOWLEDGMENTS

This work is funded by CRDF/RFBR project 2949/09-05-92506 and by grant of the President of the Russian Federation SS-3322.2010.2.

REFERENCES

- [1] Bond, T.; Streets, D.; Yarber, K.; Nelson, S.; Woo, J-H.; Klimont, Z. *J.Geophys. Res.* 2004, 109,D.14203, doi:10.1029/2003JD00369
- [2] Chen, Y.; Penner, J. *Atmos. Chem. Phys.* 2005, 5, 2935.
- [3] Lauer, A.; Eyring, V.; Hendricks, J.; Jockel, P.; Lohmann, U. *Atmos. Chem. Phys.* 2007, 7, 5061.
- [4] Wang, W.; Penner, Cirrus clouds in a global climate model with a statistical cirrus cloud scheme, *Atmos. Chem. Phys.*, 2010, 10, 5449-5474.
- [5] Popovicheva, O.B.; Kireeva, E.D.; Shonija, N.K.; Khokhlova. T.D. *J.Phys. Chem.A.* 2009, 113, 10503.
- [6] Kotzick, R.; Niessner, R. *Atmos. Environ.* 1999, 33, 2669.
- [7] Koehler, K.; DeMott, P.; Kreidenweis, S.; Popovicheva, O.; Petters, M., Carrico, C.; Kireeva, E.; Khokhlova, T.; Shonija, N. *Phys. Chem. Chem. Phys.* 2009, 11, 7906.
- [8] Popovicheva, O.B.; Persiantseva, N.M.; Tishkova,V.; Shonija, N. K.; Zubareva, N.A. *Environ. Res. Let.* 2008, 3. doi:10.1088/1748-9326/3/2/025009
- [9] Phillips, V.; DeMott, P.; Andronache, C. *J.Atmos. Sci.*, 2008, 65, 2757-2783.
- [10] Kireeva E., Popovicheva O., Persiantseva N., Timofeyev M., Shonija N. *J. Atmos. Chem.*, 2010, 64, 129-147.

Fabrication of Fibers of Resorcinol/Formaldehyde Gel by Electrospinning toward the Formation of Mesoporous Carbon Fibers

Panitnart Ubollers¹, Pitt Supaphol² and Varong Pavarajarn^{1,*}

1 Center of Excellence in Particle Technology, Faculty of Engineering,
Chulalongkorn University, Bangkok, 10330, Thailand

2 The Petroleum and Petrochemical College and The Center for Petroleum, Petrochemical and Advanced Materials, Chulalongkorn University, Bangkok 10330, Thailand

*** Principal Contact:** E-mail: Varong.P@chula.ac.th.

ABSTRACT

Carbon fibers having mesoporous structure is a promising material for several applications, including advanced catalyst support, adsorbent and filtration. Mesoporous carbon with controllable pore size can be formed via the pyrolysis of resorcinol/formaldehyde (RF) gel. In this work, electrospinning technique was applied to fabricate the RF-gel into fibers. The RF-gel was prepared by the sol-gel polycondensation of resorcinol (R) and formaldehyde (F) with sodium carbonate (C) as basic catalyst. Upon the application of high electrical potential, in the range of 10-22 kV, the RF mixture which was supplied to the nozzle at a flow rate of 0.8 ml/h was ejected toward the collector. Morphology and size of the obtained product were found to depend upon the conditions for RF-gel preparation, namely R/F molar ratio, aging period and aging environment, and upon the electrospinning conditions such as the applied potential and nozzle-to-collector distance. The RF-gel prepared by using R/F molar ratio of 0.5 that was aged in 8%-relative humidity (RH) environment was found to produce fibers with the average diameter of 1-3 μm . As the aging period was increased, the average diameter of the fibers was increased. For the RF-gel aged under high humidity (e.g. 75% and 100% RH), the products were found to be mostly spherical particles deposited on the collector. After pyrolysis, all products retained the same morphology yet the RF-gel was converted into carbon.

KEYWORDS

Resorcinol/formaldehyde gel, Fibers, Electrospinning, Mesoporous

Introduction

Carbon fibers having very large surface area-to-volume ratio, flexibility in surface modification and superior mechanical performance have been receiving increasing attention for various applications such as nanocomposites, rechargeable batteries, advanced catalyst support, drug delivery and filtration^[1]. As a source of carbon, resorcinol/formaldehyde (RF) gel has been an attractive choice because the pore size of the pyrolyzed product can be conveniently controlled into micro-, meso- or macro-sized. RF-gel was firstly produced by Pekala via the sol-gel polycondensation of resorcinol (R) and formaldehyde (F) with sodium carbonate (C) as basic catalyst^[2]. Resorcinol reacts with formaldehyde in two steps, i.e., the formation of hydroxymethyl (-CH₂OH) derivatives of resorcinol and the condensation of the hydroxymethyl derivatives to form methylene (-CH₂-) and methylene ether (-CH₂OCH₂-) bridged compounds. The intermediates formed during the reactions further react to form a cross-linked polymer network.

Electrospinning technique is a relatively simple and versatile method for fabricating nanofibers. In typical electrospinning process, a droplet of solution held by its surface tension at the end of a capillary tube is subjected to an electric field. Charge is induced on the liquid surface by electric field. As the intensity of the electric field is increased, the hemispherical surface of the solution at the tip of the capillary tube elongates to form a conical shape known as the Taylor cone. When the electric field reaches a critical value at which the repulsive electric force overcomes the surface tension force, a charged jet of the solution is ejected from the tip of the Taylor cone. Since this jet is charged, its trajectory can be controlled by the electric field. As the jet travels toward a collecting plate, the solvent evaporates, leaving the charged fiber depositing itself randomly as a non-woven mat on the collecting plate^[3].

The aim of this study is to understand the influences of RF-gel synthesis parameters and the electrospinning conditions on the size, size distribution and morphology of the obtained RF-products fabricated via electrospinning technique. The conversion of the RF-products into carbon via pyrolysis was also investigated.

Experimental Methods

Preparation of RF-Gel

RF-gel was synthesized by polycondensation of resorcinol [C₆H₄(OH)₂, 99%, Fluka] and formaldehyde [HCOH, 37% w/v; stabilized by 11-14 wt% methanol, Ajax Fine Chemical], according to the method proposed by Pekala et al^[2]. RF solution was prepared by mixing the required amount of R, F, sodium carbonate (C) and distilled water (W) and stirring for 45 min.

The gel was prepared by using R/F, R/W and R/C molar ratios of 0.5, 0.15 and 86.15, respectively, while the C/W ratio was kept at 10 mol/m³.

Electrospinning

The apparatus for electrospinning was consisted of a high voltage DC power supply (ES30PN, Gamma High Voltage Research Inc., USA), a syringe pump, a plastic syringe equipped with a stainless steel needle (gauge No.18 with the inner diameter of 1.2 mm) and an aluminum foil used as a ground collector. The needle was connected to the negative electrode of the power supply, while the aluminum collector was attached with the grounding electrode. The distance between the tip of the needle and the collector was in the range of 5 to 20 cm. Upon the application of high electrical potential across the electrodes, the jet of electrospinning solution, i.e., the RF-gel, was ejected and collected on the collector. The volumetric flow rate of the gel was fixed at 0.8 ml/h, using a syringe pump, for all experiments. It should be noted that the RF-gel had been aged for predetermined period of time prior to the electrospinning to have suitable viscosity. Unless mentioned otherwise, the aging was done in ambient condition.

Pyrolysis of RF-Products

Right after the electrospinning, the obtained RF products were frozen using liquid nitrogen. The residual solvent in the product was then removed by freeze drying at -54°C for 2 days. After drying, RF-products were subjected to the pyrolysis in a horizontal tubular flow reactor under constant flow of nitrogen (40 ml/min), in a step-wised operation, i.e., at 250°C for 2 h and at 750°C for 4 h. The heating rate was fixed at 10°C/min.

Characterizations

Morphology of the obtained products was studied using a scanning electron microscope (SEM, JEOL JSM-6400). Size of the products was then measured from the micrographs, using image processing software (JEOL SemAfore 5.0). The surface area, pore volume and pore size were measured by a BELSORP-mini nitrogen adsorption analyzer.

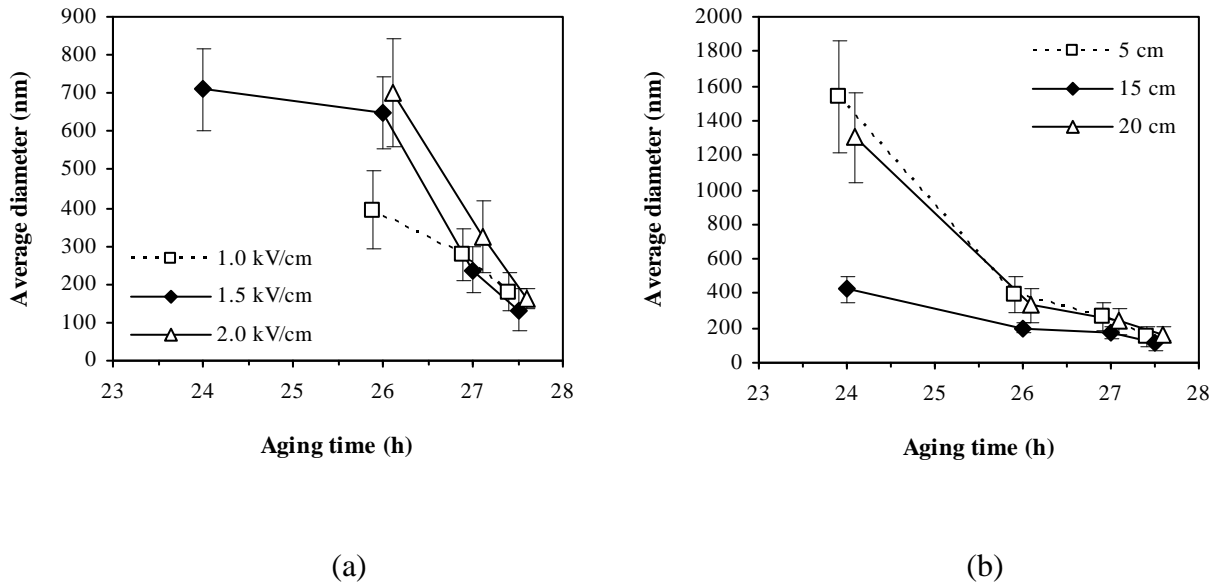
Results and Discussion

Effects of Electrospinning Parameters

A crucial element in the electrospinning is the strength of applied electric field. In this work, the electric potential was applied in the range of 1.0 to 2.0 kV/cm. It was found from SEM micrographs that the products from the electrospinning of RF-gel aged for 26-27.5 h under the electric field strength of 1 kV/cm were dispersed spherical particles. Average diameters of the obtained products are shown in Figure 1a. As the electric potential was increased to 1.5 and 2

kV/cm, the particles tended to agglomerate and merged together to form porous structure, especially when the aging time of the RF-gel was not long enough.

Figure 1. Average diameter of RF-products obtained from electrospinning of RF gel using different electric field strength (a) and different tip-to-collector distance (b), as a function of RF aging time. The data points are intentionally shifted in horizontal direction for clarity of the plot.



Increasing the electric field strength results in an increase in both the electrostatic force, which is responsible for the transport of the charged jet from injection orifice to the collective target, and the Coulombic repulsion force, which is responsible for ejected jet segment^[4, 5]. The increase in electrostatic force gives rise to the increase in mass throughput of the liquid jet from the nozzle, while the increased Coulombic repulsion force results in the increase in the average diameter of the particles. When the electric field strength becomes too high, the spinning jet becomes unstable, and the average diameter of the particles was found to decrease with increasing electric field strength, as shown in Figure 1a.

For the electrospinning of low viscosity RF-gel (e.g. RF-gel that was aged for 24 h) using weak electric field strength, the acceleration of the jet is reduced and the surface tension of the liquid droplet becomes a dominant influence for the electrospinning. The gel is ejected as large droplets, from which the evaporation of solvent becomes ineffective. As a result, the products deposited on the collector merge into a film. On the other hand, for the RF-gel with high viscosity, charges are accumulated on the surface of the gel before being ejected. When the repulsive electrical forces

overcome the surface tension, the jet splits into several mini-jets, which subsequently disintegrate into small droplets. Therefore, the products from RF-gel aged for 27.5 h are very small particles.

The distance between the tip of the needle and the collector is another important factor in the electrospinning. It affects both flight time of the ejected jet and the electric field strength. In this work, the tip-to-collector distance was varied in the range of 5 to 20 cm. The applied voltage was kept constant at 15 kV. When the tip-to-collector distance is decreased, the jet will travel at shorter distance before it reaches the collecting plate, which reduces the time for solvent evaporation from the jet. Nevertheless, the increased electric field strength by the decrease tip-to-collector distance prevents the ejection of RF-gel as very large droplets. According to the results in Figure 1b, the average diameter of the product increases when the tip-to-collector distance is decreased. However, the effect of the tip-to-collector distance is dominant only for the RF-gel that has been aged for short period of time.

Effects of Aging Conditions for RF-Gel

Aging conditions has been known to affect formation of the gel network. In this work, pure water, saturated solution of sodium chloride and silica-gel were used to control the relative humidity (RH) of the aging system to be 100%, 75% and 8% at 25°C, respectively. The aged RF-gel was then electrospun using the electric potential of 15 kV and the tip-to-collector distance of 10 cm.

The products fabricated from RF-gel that was aged under 100% and 75% RH were nanosized spherical particles. The average diameter of the particles decreases when the RF gel is aged in atmosphere with increased the relative humidity. However, prolonged aging time allows more chain entanglement within the gel, which makes the effect of surface tension to be less pronounced and consequently results in the decrease in average diameter of the obtained product^[6]. The results are shown in Figure 2. On the other hand, when the relative humidity of the aging system was adjusted to be 8% RH, it significantly affected morphology of the electrospun RF-product. The product became micro-fibers as shown in Figure 3a-b.

Figure 2. Average diameter of RF-products obtained from electrospinning of RF gel aged under different humidity, as a function of aging time. Noted that the aging time investigated are 24, 26, 27 and 27.5 h. The data points are intentionally shifted in horizontal direction for clarity of the plot.

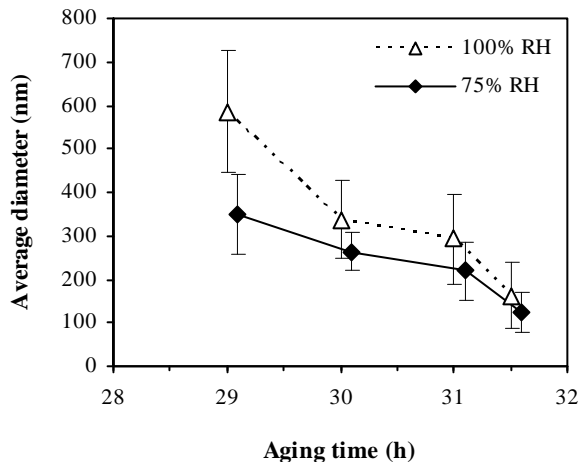
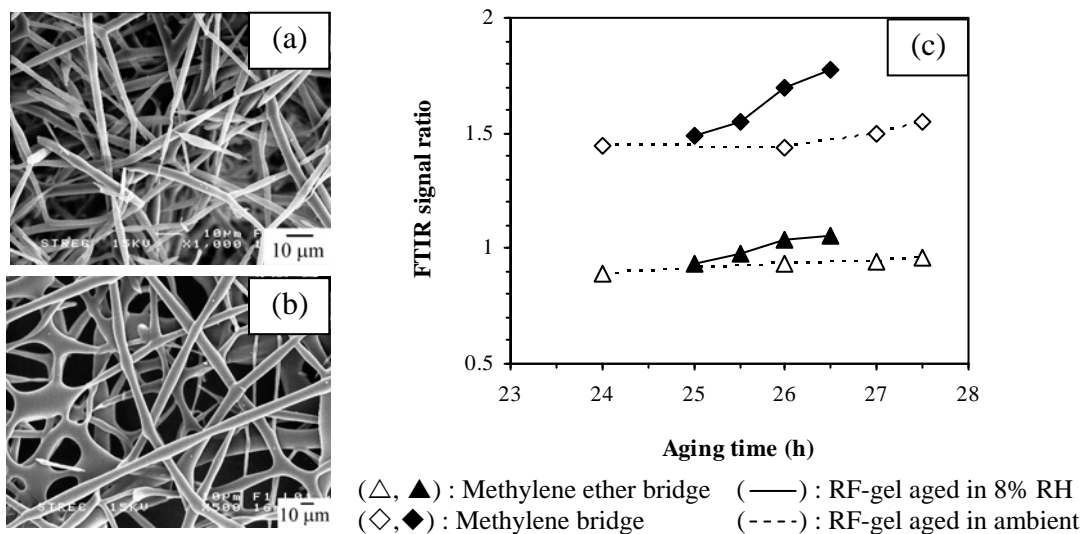


Figure 3. SEM micrographs of products obtained from electrospinning of RF gel aged under the atmosphere of 8% RH for 26 h (a) and 26.5 h (b) and FTIR signal ratio of methylene bridge and methylene ether bridge comparing to that of aromatic rings in RF gel aged in 8% RH (c).

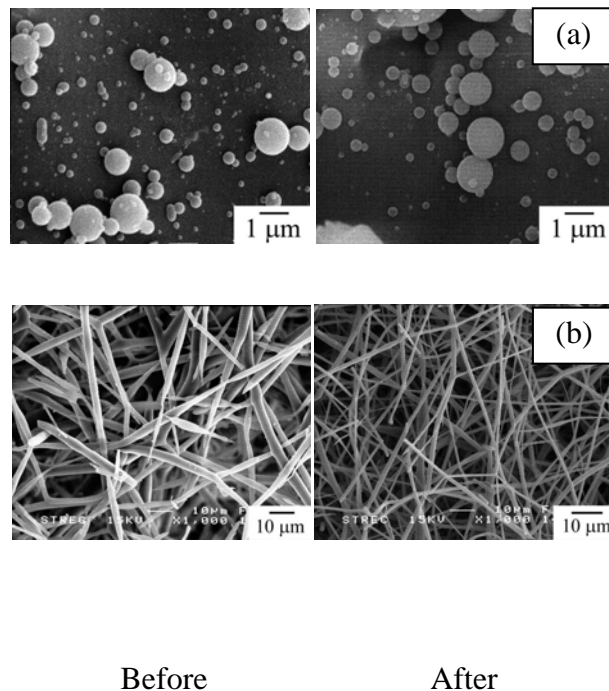


It should be noted that water is a by-product from the condensation or RF-cluster. Therefore, for the RF-gel aged in 8% RH, in which water is continuously removed from the gel during aging, the RF condensation is enhanced. Consequently, the molecular chain entanglement within the RF-gel is increased, as witnessed from the increases in signal from both methylene and methylene ether bridges shown in Figure 3c. Such increase in the entanglement prevents disintegration of the jet during the electrospinning and results in fibers deposited on the collector. The average fiber diameter increases from 2.83 to 4.67 μm when the aging time of RF-gel is increased from 26 to 26.5 h. This is probably due to the increased resistance of the RF-gel to be stretched by the increase in the molecular entanglement.

Pyrolysis of the RF-Products

The products obtained from the electrospinning of RF-gel were subjected to freeze drying prior to being pyrolyzed to form carbon products. It can be seen from Figure 4 that morphology of the products remains unchanged after the pyrolysis. The nitrogen adsorption isotherm suggested that both products are mesoporous. Nevertheless, the specific surface area of the fiber product was found to be higher than that of the spherical particles (i.e., $39.6 \text{ m}^2/\text{g}$ versus $0.6 \text{ m}^2/\text{g}$). This is suggested to be a result from high extent of cross-linking network within the gel that allows the formation of fiber, which also prevents collapses of pores during the pyrolysis.

Figure 7. SEM micrographs of RF-products in form of particles (a) and fibers (b), before and after pyrolysis.



CONCLUSION

RF gel can be used as a precursor for the synthesis of mesoporous structures of carbon fibers and carbon nano-spheres via electrospinning. Several parameters including preparation parameters for RF-gel and electrospinning parameters can be manipulated to control morphology and size of the product. The fibers are formed only from RF-gel containing high cross-linking network, which can be achieved by lowering the humidity of aging atmosphere.

ACKNOWLEDGMENTS

This study is partly supported by the Centennial Fund of Chulalongkorn University to the Center of Excellence in Particle Technology.

REFERENCES

- [1] S. Moon and R. J. Farris, "Strong electrospun nanometer-diameter polyacrylonitrile carbon fiber yarns," *Carbon*, vol. 47, pp. 2829-2839, 2009.
- [2] R. W. Pekala, "Organic aerogels from the polycondensation of resorcinol with formaldehyde," *Journal of Materials Science* vol. 24, pp. 3221-3227, 1989.
- [3] G. Srinivasan, Reneker, "Structure and morphology of small diameter electrospun aramid fibers," *Polymer International*, vol. 36, pp. 195-201, 1995.
- [4] I. S. C. A. Frenot, "Polymer nanofibers assembled by electrospinning," *Current Opinion in Colloid and Interface Science*, vol. 8, pp. 64-75, 2003.
- [5] W. H. T. Jarusuwannapoom, S. Jitjaicham, L. Wannatong, M. Nithitanakul, C. Pattamaprom, P. Koombhongse, R. Rangkupan, P. Supaphol, "Effect of solvents on electro-spinnability of polystyrene solutions and morphological appearance of resulting electrospun polystyrene fibers," *European Polymer Journal*, vol. 41, pp. 409-421, 2005.
- [6] K. F. S. Ramakrishna, W.E. Teo, T.C. Lim, Z. Ma, *An Introduction to Electrospinning and Nanofibers*: World Scienctific Publishing, 2005.

Studies on Sodium Aerosol Characteristics in the Presence of Gamma Radiation Field

Subramanian V., Baskaran R. and Venkatraman B.

Radiological Safety Division, Radiation Safety and Environmental Group,
Indira Gandhi Centre for Atomic Research,
Kalpakkam – 603 102, INDIA.

ABSTRACT

In the case of Core Disruptive Accident (CDA) condition of fast reactor, fuel, fission products and sodium (coolant) aerosols are released into reactor containment building (RCB) and they remain suspended in the containment volume where huge amount of gamma radiation field prevails. To study the aerosol behavior in a confined environment an Aerosol Test Facility (ATF) is designed and constructed in our division. In this study, sodium combustion aerosols were generated, bottled-up in the 1 m³ chamber and exposed to various dose rates using Cs-137 source of strength 60 GBq. The time evolution of suspended mass concentration is studied with and without the presence of gamma radiation field. It is found that, the aerosols mass concentration decreases at faster rate in the presence of gamma radiation field, when compared to no gamma radiation field. In the presence of gamma field, the aerosols acquire bi-polar charges which have a distribution with mean value of $\langle j \rangle$ charges and it is governed by Boltzmann Distribution. When the aerosols undergo Brownian coagulation with additional charges acquired due to gamma radiation, there exists enhanced coagulation of aerosol which is defined as $f = K'/K$ (where K' and K – coagulation kernels for the charged and uncharged particles respectively). In order to understand the process of enhanced coagulation of the aerosols, it is important to know number of charges acquired by the aerosol, which is predicted by Clement and Harrison (steady state charge theory). It is calculated that, for a monodispersed sodium aerosol condition (initial size MMD~1.05μm, GSD=1.2), in order to have the coagulation enhancement factor of 5 times (as per the experimental value), the modest charging required by the aerosol particle is about 8 charges.

KEYWORDS

Sodium aerosol, Bipolar charging by gamma irradiation, Enhanced coagulation, Mass concentration

Introduction

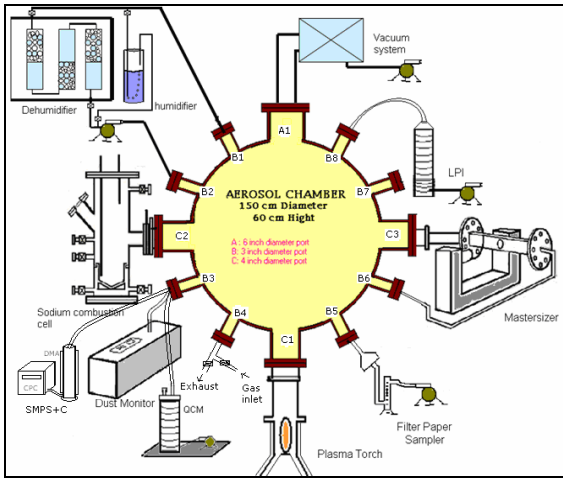
In the context of safety related studies on Sodium cooled Fast Reactor (SFR), a careful understanding of the aerosol sources and its characteristics are very important, in particular during the CDA conditions. It is expected that, during CDA, the RCB is bottled-up with large amount of aerosols of sodium compounds along with fuel and fission products. There exists possibility of release of these aerosols from the RCB resulting exposures to the public in the emergency planning zone. The quantity of radioactive materials released during CDA is defined as environmental source term, which depends on the amount of aerosols remain suspended in the RCB volume from time to time and the leak rate of RCB^[1]. Out of all the above aerosols, the behaviour of sodium compound aerosols eclipses all other aerosols because (i) its mass concentration is high^[2] and (ii) The initial Mass Median Diameter (MMD) of sodium combustion aerosols is found to be 1.0 μm (GSD-1.2) while that of fission products aerosols are in the nanometer range (about 10 of nanometers)^[3], hence, the sodium aerosol behaviour governs the suspended radioactivity inside RCB. In order to assess the behavior of the aerosols, some of the parameters like size distribution, coagulation constants, mobility constants and sedimentation rate are to be known^[4]. At this juncture, it is to be taken into account that, the RCB is associated with large amount of gamma radiation field (in the order of kGys) during CDA. When the aerosols are exposed to additional bi-polar charges (induced by the gamma radiation), the aerosols acquire these charges and the number of aerosol particles carrying a distribution of 'j' charges is governed by Modified Boltzmann Distribution^[5,6]. In our earlier experiments, we found that, when the charged aerosols undergo Brownian coagulation in our experimental condition, the coagulation enhancement factor is reported to be 5-8 times, when compared to no gamma radiation condition^[7] (The coagulation enhancement factor $f = K'/K$, where K' and K – coagulation kernels for the charged and uncharged particles respectively^[8]). This enhanced coagulation is followed by the faster depletion of mass concentration inside the RCB. Hence in this study, sodium aerosols are generated at a mass concentration of about 2 g.m⁻³ and bottled-up in the 1 m⁻³ chamber. The time evolution of suspended mass concentration is studied with and without the presence of gamma radiation field. In order to have enhanced coagulation of aerosols and enhanced depletion rate of suspended mass concentration, the number of charges associated with aerosols have been calculated using Modified Boltzmann Distribution^[8] and these results are presented in this paper.

Experimental Methods

Aerosol Test Facility

The experiments were carried out in the Aerosol Test Facility (ATF)^[9], (Fig.1) which has been designed and commissioned, for the safety analysis of fast reactors.

Figure 1: Aerosol Test Facility



ATF mainly consists of an aerosol chamber of volume one cubic meter (diameter = 1.5m, height = 0.6m), a sodium combustion cell for the production of sodium aerosols, aerosol measurement apparatus (Low pressure impactor, Quartz crystal Microbalance, SMPS, Filter paper sampler, Single particle counter and Ensemble diffraction instrument), humidity and auxiliary systems such as water cooling, air flow, gas flow, pneumatic control, vacuum, material handling systems and on-line data acquisition system for temperature, pressure and Relative Humidity (RH) during experiments.

Sampling

About 5g of sodium was heated up to 550°C, in the sodium combustion cell under argon environment. The hot sodium was ignited by exposing it to compressed air, after letting out the argon gas. By combustion, sodium oxide aerosols were formed in the combustion cell.

Immediately, the valve separating the aerosol chamber and the combustion cell was opened and the aerosols get filled into the chamber. Since the initial pressure at the combustion cell was at 50-70 kPa excess over atmospheric pressure, it helped to fill the aerosols into the chamber and its diagnostic ports immediately. A closed face type filter paper sampler (47 mm) and a non-lubricant rotary vane pump with a capacity of 20 lpm coupled with rotameter were used for the measurement of mass concentration. An analytical balance with an accuracy of 0.1 mg (Model No.GR 200, M/s AND Corporation, Japan) was used for the gravimetric analysis. Aerosol sampling was carried out for 1 minute at a flow rate of 10 lpm. The cumulative experimental errors associated with measurement in time, flow rate and mass is nearly $\pm 10\%$.

A ^{137}Cs source of strength 60 GBq was used for the panoramic gamma exposure of the aerosol chamber. The ^{137}Cs decays into $^{136}\text{Ba}^*$ through beta decay, $^{55}\text{Cs}^{137} \rightarrow {}^{56}\text{Ba}^{137*} + .e^0 + \nu_e$ (514 keV), which in-turn decays through gamma decay, ${}^{56}\text{Ba}^{137*} \rightarrow {}^{56}\text{Ba}^{137} + \gamma$ (662 keV). The source was mounted on top of the chamber on the center axial line and its position was varied to

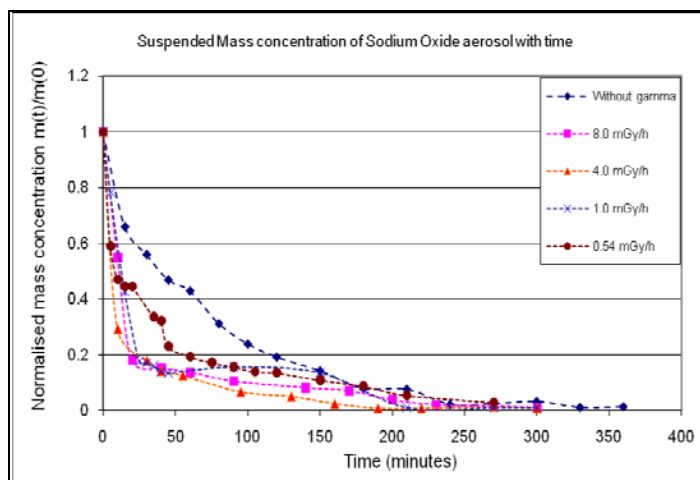
get the desired dose rate inside the chamber. The dose rate inside the chamber was measured using a Teletector (M/s Automation Uno Mentechnik, Germany). Owing to the occupational dose constraints, the experiments were restricted to a maximum dose rate of 8.0 mGy/h. The experiments were carried out for the dose rate starting from 8.0, 4.0, 1.0 and 0.54mGy/h with the same quantity of sodium and by keeping RH at 50%.

The suspended mass concentration of sodium aerosols inside the aerosol chamber is measured for about 5 hours. Figure 2 shows the normalized suspended mass concentration [$m(t)/m(0)$] where, $m(t)$ – mass concentration at a time ‘ t ’ minutes and $m(0)$ – initial mass concentration] of sodium compound aerosols as a function of time for the two cases viz. (i) no gamma field condition and (ii) various gamma dose rate conditions.

Results and Discussion

It is observed from the figure 2, the suspended mass concentration decreases by one order in about two hours and by two orders in five hours when there is no gamma radiation field. While, in the presence of gamma radiation, for the dose rate 8.0, 4.0 and 1.0 mGy/h, the suspended mass concentration decreases by one order in one hour. However, in the case of 0.54 mGy/h, the depletion pattern for the first hour is less steeper compared to other dose rates. Beyond two hours the collected mass variations are insignificant as the collected mass on the filter paper is becoming low. Nevertheless at the at about 5 hours duration, the suspended mass concentration is reduced by two orders in all the cases.

Figure 2. Time evolution of suspended mass concentration of sodium aerosols with and without the presence of gamma radiation field.



It is inferred from Figure 2, that the suspended mass concentration decreases at a faster rate in the presence of gamma radiation, which implies that the particle size grows at a faster rate (due to

enhanced coagulation) and undergo gravitational settling. The enhanced coagulation factor for the particles in the presence of bi-polar ions concentration is calculated by using general theory derived by Zebel^[10] and by Williams and Loyalka^[11].

The coagulation enhancement factor is given as

$$f(Y) = \frac{Y}{\exp(Y) - 1} \quad \text{---(Eq.1)}$$

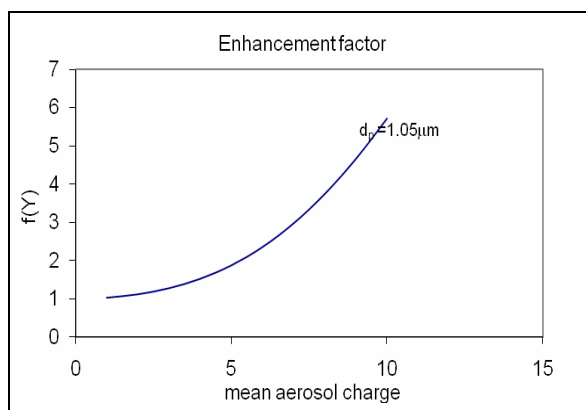
where $Y = \frac{j_1 e j_2 e}{4\pi k T \epsilon_0 (a_1 + a_2)}$ for two particles of radii a_1, a_2 with charges j_1 and j_2 respectively,

and k – Boltzmann's constant, T – Temperature in Kelvin, ϵ_0 – permittivity of the medium.

It is to be noted here from our earlier experiment^[12], the initial particle size distribution of sodium aerosols bottled up in the aerosols chamber is lognormal with initial size (at $t= 20$ s) of the particle (mean value of $\text{Vol.}d_{50}$) was $1.05 \mu\text{m}$ with geometric standard deviation of 1.2.

Let us consider the particle of $1.05 \mu\text{m}$, coagulating with the same sized particles ($a_1 = a_2$), acquired with opposite charges j_1 and $-j_1$ (the mean number of charges acquired by the particle is governed by modified Boltzmann distribution). By choosing various mean charges (j) acquired by the aerosol particles from 1-12, the coagulation enhancement factor $f(Y)$, is calculated using equation (1). Fig.3 shows the variation of $f(Y)$ as a function of mean aerosol charges. It is observed from the Fig.3, in order to have the coagulation enhancement factor of 5 times^[6] (as per the experimental value), the modest charging required by the aerosol particle is about 8 charges.

Figure 3: Variation of Coagulation Enhancement factor Vs particle mean charge for the aerosol $d_p=1.05 \mu\text{m}$



SUMMARY AND CONCLUSION

The result obtained in this experiment is a strong evidence for the faster depletion rate of suspended particle concentration in the presence of gamma field. This is due to enhanced brownian coagulation of particles when they are bi-polarly charged due to induced ionization of gamma radiation. In the presence of gamma field, the aerosols acquire steady state charging due to atomic and nuclear interactions of gamma rays with aerosols, as well as interaction aerosols with ions which are generated by the ionization of air molecules/water vapour by gamma rays. However, in the real scenario, the particle size distribution changes with time and so the charges acquired by the aerosols (real time charging). Hence the number of charges required for the enhanced coagulation of 5 time would change when time progress. Nevertheless, there could be the average effect of charge associated with aerosols as described the Clement and Harrison^[6,8]. By considering mean charge $\langle j \rangle$ for a distribution of number of charges acquired by an aerosols

$$\text{i.e. } \langle j \rangle = \sum_{j=-\infty}^{j=+\infty} jN_j / Z \text{ where } N_j - \text{number of particles having 'j' charges and } Z - \text{total number of}$$

particles, over a certain period of time, which would help to substantiate the enhanced coagulation of aerosols followed by the faster settling.

ACKNOWLEDGEMENT

Director REG is acknowledged for his contant support for this study. The authors acknowledge the associated staffs at ATF for the conduction of the experimental runs.

REFERENCES

- [1] R. Baskaran, V. Subramanian and R. Indira, (2007), "Aerosol Issues in Fast Reactor, IASTA-2007 Nov.2007, NPL, Delhi. *IASTA Bulletin, Vol.18. No.1&2*, p.222.,
- [2] Malet J.C.,(1996), 'Ignition and combustion of sodium–fire consequences extinguishments and prevention', IWGFR/92, *Technical committee meeting on Evaluation of Radioactive materials release and sodium fires in Fast reactors*, November 11-14, O-arai, Ibaraki, JAPAN.
- [3] V. Subramanian, R. Baskaran and R. Indira, "Experimental study on the behaviour of suspended aerosols of Sodium and inactive Fission Products in a closed vessel", in Press Nuclear Technology, September 2011.
- [4] Abbey F., and Silberberg M., (1979), 'Resolving aerosol safety for LMFBR's – An International consensus', *Proc. of International meeting on fast reactor safety technology*, Seattle, Washington.
- [5] Fuchs N.A., (1964), *The Mechanics of Aerosols*, Pergamon, New York.

- [6] Clement C.F. and Harrison R.G., (1991), ‘Charge distribution on aerosols’, *Proceedings of 8th International Electrostatics Conference*, Oxford, Institute of Physics Conference Series 118, p.275.
- [7] V. Subramanian, R. Baskaran and R. Indira, (2008), “Experimental study on enhanced Brownian Coagulation of Sodium Compound Aerosol in the presence of Gamma Field”, *Journal of Aerosol Science*, Vol. 39, p.814.
- [8] Clement C.F. and Harrison R.G., (1990), ‘On the Boltzmann charging equation for aerosols’, *Meeting of the Aerosol Society on Aerosols and Electrostatic Charge*, Sheffield.
- [9] Baskaran R., Selvakumaran T.S. and Subramanian V., (2004), ‘Aerosol Test Facility for Fast Reactor Safety Studies’, *Indian journal of pure and applied physics*, **42**, p.873.
- [10] G. Zebel, “Coagulation of aerosols” In: Davies C.N. (ed) *Aerosol Science*, Academic Press, London, 1966.
- [11] M.M.R. Williams and S.K. Loyalka, “Aerosol Science Theory and Practice”, *Pergamon*, Oxford, 1991.
- [12] V. Subramanian and R.Baskaran, (2007) “Initial size distribution sodium combustion aerosols”, Nuclear Technology, Vol.160, p.308.

Better Understanding on Particulate Iodine in the Marine Boundary Layer

Ru-Jin Huang^{1,2}, Michael Kundel¹, Christopher Kampf¹, Harald Berresheim², Colin D. O'dowd², Thorsten Hoffmann¹

1 Institute of Inorganic and Analytical Chemistry, Johannes Gutenberg University of Mainz, Duesbergweg 10-14, D-55128 Mainz, Germany

2 School of Physics & Centre for Climate and Air Pollution Studies, National University of Ireland, Galway, University Road, Galway, Ireland

Principal Contact: Ru-Jin Huang, Doctor, Johannes Gutenberg University of Mainz, Mainz, D-55128.

Tel: +49 6131 39 25877 Fax: +49 6131 39 25336 E-mail: rujin@uni-mainz.de

Abstract

Especially within the last few years the role of iodine in the lower troposphere has received increasing attention. In addition to the potential to affect the atmospheric oxidation capacity in a variety of ways such as catalytic destruction of ozone, the importance of iodine in the natural new particle formation (via secondary gas-to-particle conversion) in the marine boundary layer (MBL) is responsible for the increased interest and is motivated by the role of marine aerosol particles in the global radiation budget. One goal of current research activities is the identification and quantification of natural particle formation processes in the MBL. Although some progress has been made in recent years, the chemical species, reaction cycling and evolution of particulate iodine are still poorly understood, which in turn hinders our knowledge of the marine new particle formation processes. Here we will present results from recent field campaigns carried out at the Mace Head Atmospheric Research Station (Global Atmosphere Watch site) on the west coast of Ireland. The speciation of particulate iodine is performed by a newly developed precolumn derivatization and solid phase extraction preseparation method in combination with liquid chromatographic/mass spectrometric determination. The diurnal and seasonal variation as well as the reaction cycling of different iodine species in the marine aerosols will be discussed. Furthermore, the linkage between gaseous reactive iodine species and particulate iodine will be presented.

Keywords: Iodine; New particle formation; Marine boundary layer

Encapsulation of menthol with PEG6000 by aerosol spraying of supercritical CO₂ suspension

N. Suankaew¹, Y. Matsumura² and T. Charinpanitkul^{1,*}

1 Center of Excellence in Particle Technology, Department of Chemical Engineering,
Faculty of Engineering, Chulalongkorn University, Bangkok, 10330, THAILAND

2 Department of Mechanical System Engineering, Faculty of Engineering, Hiroshima
University, Hiroshima, JAPAN

Principal Contact: T. Charinpanitkul, Professor, Center of Excellence in Particle
Technology, Department of Chemical Engineering, Faculty of Engineering, Chulalongkorn
University, Bangkok, 10330, THAILAND.

E-mail: ctawat@chula.ac.th

Abstract

Recently the development of pharmaceutical and cosmetic industrial sectors has paid more attentions on novel particulate products with modified size, morphology and surface characteristics. Aerosol spraying method could provide very fine particles of active substance encapsulated within a coating material with a size range of nanometer or micrometer. As a result, it could provide a function of controlled-release of encapsulated materials. It is well recognized that rapid expansion of supercritical suspension (RESS) could provide controllable size and morphology of composite particles by adjusting some operating parameters. In this work, we set an objective to prepare composite particle of menthol and coating material which is PEG6000 by the aerosol spraying method. Specific operating parameters which are initial pressure, temperature, weight ratio of PEG6000 to menthol will be varied for examining their effects on the properties of encapsulated products.

Keywords: Aerosol spraying, supercritical fluid, encapsulation, menthol, PEG.

Chemistry components in PM_{2.5} and PM₁₀ for ambient and indoor airs in Campus of Nanchang University, Nanchang city, China

Hong Huang^{1,2}, Junji Cao² and Changwei Zou¹

1 School of Environmental and Chemical Engineering, Nanchang University, Nanchang, China 330031;

2 State Key Laboratory of Loess and Quaternary Geology, Institute of Earth Environment, Chinese Academy of Sciences, Xi'an, China 710075;

Principal Contact: Hong Huang, Associate Professor, School of Environmental and Chemical Engineering, Nanchang University, No. 999, Xuefu Avenue, Honggutan, Nanchang, 330031, China.

Tel: 86-13755697035 Fax: 86-791-3969594 E-mail: irishhjx@163.com

Abstract

Ambient PM_{2.5}, PM₁₀ samples and PM_{2.5} samples in three different indoor environments (common office, special printing & copying office and student dormitory) in campus of Nanchang university, Nanchang city were collected from 5th to 20th June, 2009 (summer), and from 1st to 14th January, 2010 (winter). The loaded samples were analyzed for organic carbon (OC), elemental carbon (EC), and water-soluble ions (sulfate [SO₄²⁻], nitrate [NO₃⁻] and chloride [Cl⁻], sodium [Na⁺], ammonium[NH₄⁺], potassium [K⁺], magnesium [Mg²⁺], calcium [Ca²⁺]). Spatial (outdoor, different indoor environments) and temporal (daily, semidiurnal and seasonal) distributions of OC, EC, SO₄²⁻, NO₃⁻, Cl⁻, Na⁺, NH₄⁺, K⁺, Mg²⁺, Ca²⁺ were discussed. The contributions of components to PM_{2.5} and mass balance of PM_{2.5} were calculated. Indoor-outdoor relationship of those components, and the correlation among OC, EC, SO₄²⁻, NO₃⁻, Cl⁻, Na⁺, NH₄⁺, K⁺, Mg²⁺ and Ca²⁺ were investigated. Above characteristics of chemistry components were combined to sampling site character and implicated sources, especially for indoor sources.

Keywords: PM_{2.5}, PM₁₀, Water soluble ions, OC, EC, Source, indoor air.

Ionic Components of Indoor Aerosols at Emperor Qin's Terra-Cotta Museum, Xi'an, China

Jungang Dong^{1,2}, Junji Cao², Ting Zhang²

1 Xi'an University of Architecture and Technology, Yanta Rd, Xi'an, P.R. China 710055

2 SKLLQG, Institute of Earth Environment, Address, Xi'an, P.R. China 710075

Principal Contact: Dong Jungang, Lecturer, Xi'an University of Architecture and Technology, Yanta Rd, Xi'an, P.R. China 710055.

Tel: 13060374007 Fax: 029-85518589 E-mail: Jungangdong@ieecas.cn

Abstract

TSP, PM_{2.5}, SO₂, NOx, HNO₃, NH₃ and microclimate are continuously monitored and sampled at Qin's terra-cotta museum during from April 18, 2006 to April 15, 2007. There are high concentrations of aerosol pollution in indoor and outdoor air. The average concentration of TSP is $232.2 \pm 136.8 \mu\text{g}\cdot\text{m}^{-3}$ at Pit No.1, $188.9 \pm 107.9 \mu\text{g}\cdot\text{m}^{-3}$ at Pit No.2 and $364.6 \pm 222.9 \mu\text{g}\cdot\text{m}^{-3}$ at Outdoor air; PM_{2.5} is $118.2 \pm 73.1 \mu\text{g}\cdot\text{m}^{-3}$, $112.0 \pm 64.4 \mu\text{g}\cdot\text{m}^{-3}$ and $154.9 \pm 103.2 \mu\text{g}\cdot\text{m}^{-3}$ respectively. Outdoor aerosol is much higher than indoor and Pit No.1 is higher than Pit No.2. High value occurs in winter and spring and Lower in summer and autumn. The aerosol is mainly composed by fine particle in indoor air and coarse particle in outdoor air. The fine particle PM_{2.5} in summer is much higher than other season indicate that much more particle formation in indoor air. The main water soluable components of PM_{2.5} is SO₄²⁻, NO₃⁻, NH₄⁺. The average concentration of them is $31.11 \pm 21.94 \mu\text{g}\cdot\text{m}^{-3}$, $11.84 \pm 9.88 \mu\text{g}\cdot\text{m}^{-3}$, $9.37 \pm 8.29 \mu\text{g}\cdot\text{m}^{-3}$ in Pit No.1; $28.13 \pm 18.86 \mu\text{g}\cdot\text{m}^{-3}$, $8.8 \mu\text{g}\cdot\text{m}^{-3}$, $8.49 \pm 6.66 \mu\text{g}\cdot\text{m}^{-3}$ in Pit No.2; $35.14 \pm 24.61 \mu\text{g}\cdot\text{m}^{-3}$, $14.63 \pm 12.21 \mu\text{g}\cdot\text{m}^{-3}$, $10.06 \pm 9.72 \mu\text{g}\cdot\text{m}^{-3}$ in outdoor site. Indoor concentration is much higher than outdoor site. Pit No.2 is higher than Pit No.1. The ion equivalent calculation analysis show that acidic in Pit No.2, neutral in Pit No.1 and alkaline in outdoor. The SOR and NOR analysis shows that sulfate and nitrate is formed by secondary aerosol. Indoor SOR is higher than Outdoor suggests that more sulfur transformation in indoor environment.

Keywords: Indoor Air Pollution, Aerosol, PM_{2.5}, Ionic Components.

The influence of children jumping on the bed on PM₁₀/PM_{2.5}/PM₁ concentration profile

Wei-Che Houng¹ and Pei-shih Chen^{1*}

1 Department of Public Health, Kaohsiung Medical University

Principal Contact: Pei-shih Chen, 100, Shih-Chuan 1st Road,Kaohsiung,80708,Taiwan.

Tel: 886-7-312-1101~2141-34 E-mail: cool996862@gmail.com

Abstract

Recently, the harmful effects of suspended particulate matter (PM) on human's respiratory system were observed. When children jump on the bed at home, it may resuspend PM. Therefore, the purpose of the present study was to evaluate the influence of children jumping on the bed on PM₁₀/PM_{2.5}/PM₁ concentration profile at schoolchildren's house.

20 schoolchildren's houses in Kaohsiung city in Taiwan were evaluated. Firstly, PM₁₀/PM_{2.5}/PM₁ concentration was simultaneously monitored over the first five minutes to obtain background concentration profiles. Then, a common cane was used to tap the bed for about one minute, followed by keeping motionless in 7 to 10 minutes to let PM settle down. Then, we made children's bed by raising bed sheets for about one minute, followed by keeping motionless in 7 to 10 minutes. This evaluation was conducted by the same person for consistency of the beating strength, beating frequency, and beating location.

Our results showed that the concentration of PM₁₀, PM_{2.5} and PM₁ were immediately arising when tapping bed was started, and the peak was kept at least one minute. The mean background concentration of PM₁₀, PM_{2.5} and PM₁ was 89, 80, 80 ug/m³, respectively. When tapping bed, the mean concentration of PM₁₀, PM_{2.5} and PM₁ was 1561, 1457, and 1456 ug/m³, respectively. When making bed, the mean concentration of PM₁₀, PM_{2.5} and PM₁ was 179, 156, and 156 ug/m³, respectively. When tapping-bed, PM concentration was 27, 28, and 28 times higher than that of background concentration for PM₁₀, PM_{2.5} and PM₁, respectively. When making bed, PM concentration was 2.6, 2.5, and 2.5 times higher than that of background concentration for PM₁₀, PM_{2.5} and PM₁, respectively.

In conclusion, jumping on the bed and making bed significantly increased PM concentration. Mite may be one of the majority components of these resuspended PM. These actions may increase the risk of respiratory symptoms, especially for asthma children.

Keywords: schoolchildren, suspended particulate matter, PM.

Concentration of enterovirus in air samples and exhaled samples

Pei-Chun Yen², Pei-Shih Chen¹, and Wan-Chi Kuo¹

1 Department of Public Health, Kaohsiung Medical University 100, Shih-Chuan 1st Road, Kaohsiung, 80708, Taiwan

2 Graduate Institute of Occupational Safety and Health, Kaohsiung medical university 100, Shih-Chuan 1st Road, Kaohsiung, 80708, Taiwan

Principal Contact: Pei-Shih Chen, Department of Public Health, Kaohsiung Medical University 100,Shih-Chuan 1st Road,Kaohsiung,80708,Taiwan.

Tel: +886-7-312-1101-2141-34 Fax: +886-7-321-2062 E-mail: pschen@kmu.edu.tw

Abstract

Enterovirus is a common pathogen, responsible for upper and lower respiratory tract infections in adults and infants. In 1998, 78 children died because of enterovirus infection in Taiwan. In 2008, enterovirus attacked Taiwan again leading to 14 children death. It was believed that all enterovirus serotypes except Coxsackievirus A21 (CA21) is fecal-oral transmission. However, high transmission rate among family members implicated the possibility of air transmission. So, the purpose of our study is to exam the hypothesis that enterovirus can be transmitted via air. Air concentration of enterovirus in pediatric department and in the exhaled air from infected children was evaluated.

We collected 14 air samples from June to August 2008 by using Teflon filter (Diameter 37mm, pore 1.0 μ m) at 20L/min. Temperature, relative humidity, CO concentration, CO₂ concentration and ventilation rate of the microenvironment were also collected. For exhaled samples, 24 samples were collected by using Teflon filter (Diameter 37mm, pore 2.0 μ m). All samples were detected by real-time quantitative polymerase chain reaction (qPCR).

Enterovirus was detected in 64.3% (9/14) and 79.2% (19/24) for air samples and exhaled samples, respectively. In air samples, the concentration of enterovirus range from 4.6×10^1 to 1.4×10^8 copies/m³. In exhaled samples, the concentration of enterovirus range from 3.8×10^5 to 1.6×10^{13} copies/m³. To our knowledge, it is the first study to detected enterovirus in air samples and exhaled air from patients. It revealed that enterovirus can be transmitted through the air. Exhaled CO was considered as an indicator of virus infection. By regression analysis, our data showed that exhaled CO concentration increased 1 ppm, air concentration of enterovirus increase 1.01×10^{13} copies/m³. It pointed out that exhaled CO may be the indicator of enterovirus infection. In conclusion, this study confirmed enterovirus other than CA21 can be transported by air.

Keywords: Enterovirus, exhaled air, air

Physical Parameters Effect on Ozone Initiated Formation of Indoor Secondary Organic Aerosols with Emission from Cleaning Products

Yu Huang¹, Kin Fai Ho^{1,2}, Steven Sai Hang Ho¹ and Shun Cheng Lee^{1,*}

1 Department of Civil and Structural Engineering, Research Center for Environmental Technology and Management, The Hong Kong Polytechnic University, Hung Hom, Hong Kong, China

2 SKLLQG, Institute of Earth Environment, Chinese Academy of Sciences, Xi'an, 710075, China

Principal Contact: S. C. Lee, The Hong Kong Polytechnic University, Hung Hom, Hong Kong.

Tel.: +852-27666011 Fax: +852-23346389 E-mail: ceslee@polyu.edu.hk

Abstract

In this study, the effect of physical parameters including air exchange rate (AER), temperature (T), and relative humidity (RH) on the formation of secondary organic aerosols (SOA) from ozonolysis of BVOC emissions from floor cleaner were investigated in a large environmental chamber. The dosage of floor cleaner was 50 mL with the ozone concentration of 5-45 ppb. Our results showed that with AER of 1.08 h⁻¹, the total particle count (with D_p of 6-225 nm) was up to 1.2×10^3 # cm⁻³, and it became much more significant with AER of 0.36 h⁻¹ (1.1×10^4 # cm⁻³). With temperature verifying from 15 to 30 °C, the total particle count firstly increased and then decreased. This was probably because high temperature restrained the condensation of formed semi-volatile compounds and resulted in low yields of SOA. When the RH in the chamber were at 50% and 80%, it was most efficient in producing SOA ($1.1 \sim 1.2 \times 10^4$ # cm⁻³) compared with that at RH of 30% (5.9×10^3 # cm⁻³). The formation of formaldehyde could be ascribed to both the ozonolysis and OH oxidation of BVOCs, while the increase of acetone concentration can be ascribed to the oxidation of α-terpineol by OH radicals.

Keywords: Secondary organic aerosols (SOA); Cleaning products; Physical parameters; Ozone-initiated indoor chemistry; BVOCs; Indoor air quality (IAQ).

Identification of Volatile Organic Compounds Emitted from Consumer Products

Sun-Hwa Kim¹, Thai Phoung Vu¹, Seung-Bok Lee¹, Gwi-Nam Bae¹ and Jong-Ryeul Sohn²

1 Global Environment Center, Korea Institute of Science and Technology, Seoul 136-791, Korea

2 Department of Environmental Health, Korea University, Seoul 136-703, Korea

Principal Contact: Gwi-Nam Bae, Global Environment Center, Korea Institute of Science and Technology, Seoul 136-791, Korea.

Tel: +82-2-958-5676 Fax: +82-2-958-5805 E-mail: gnbae@kist.re.kr

Abstract

Recently, consumer products (air freshener, home cleaner, insecticide, etc.) containing various volatile organic compounds (VOCs) have been used in indoor environments. Some of these volatile organic compounds are known to be toxic or hazardous. Especially, terpenes can react with ozone to form a variety of secondary pollutants including formaldehyde and ultrafine particles. For management of these compounds, we need to identify volatile organic compounds emitted from consumer products and make a list about them. In this study, volatile organic compounds emitted from air fresheners, home cleaners, and insecticides were identified using headspace-SPME (solid phase microextraction) analysis with gas chromatography/mass spectrometry (GC/MS). 2 mL for liquid type or 2 mg for gel type of air freshener of each sample was put into 20 mL glass vial and they were equilibrated for 10 min at room temperature. Headspace in vial was absorbed to 75 µm Carboxen-PDMS fiber and analyzed by a GC/MS. It was found that all air fresheners contained limonene and linalool. In addition, ethanol, pinene and terpinolene were identified with high frequency. Home cleaners including dish cleaners were found to have pinene, limonene and cymene very frequently. Insecticides were identified to contain toluene, tridecane and tetradecane. Limonene and linalool were also detected for products with fragrance. A variety of volatile organic compounds were identified by kind of consumer products and ingredient of fragrance. This information will help to characterize formation of secondary pollutants under ozone reaction.

Keywords: Consumer product, Volatile organic compounds, Terpenes, Headspace-SPME analysis.

Nano Particle Inhalation System with Electron Spray Generator

Y. Matsui¹, S. Kimoto², M. Adachi³, A. Tsuda⁴, M. Yoneda¹

1 Department of Urban Environmental Engineering, Graduate School of Engineering,
Kyoto University, Kyoto, JAPAN

2 Environmental Business Unit, Analytical and Measuring Instruments Division,
Shimadzu Corporation, Kyoto, JAPAN

3 Department of Chemical Engineering, Graduate School of Engineering,
Osaka Prefecture University, Osaka, JAPAN

4 Department of Environmental Health, Harvard University, Boston, USA

Principal Contact: Yasuto Matsui, Lecturer, Kyoto University, Katsura, Nishikyo, Kyoto,
615-8540 Japan.

Tel: +81-75-383-3354 Email: y.matsui@risk.env.kyoto-u.ac.jp

Abstract

It is difficult to inhale nano particles to experimental animals. Once nano particles aggregate each other in solutions or as powder form, they do not easily and fully break up. It is well known that nano particle inhalation assays connect spark or burn generator directly with bulks, powders, etc. Nano sized particles are not made by nebulizer or grinder. The purpose of this paper is to show an easy inhalation system with electron spray generator. We used a Quantum-dot nano colloid solution (15 nm, 8 μM). Three different types of modification (Plane, -COOH, -NH₃) particles were tested because dispersion stability is depend on surface modification. When high concentration Q-dot solution was sprayed, particles were aggregated and mean particle size was roughly 40 nm. On the other hand, dilute Q-dot solution was sprayed and aerosolized to single dispersed particle size, which equaled to primary particle size in colloidal suspension. Particles modified with carboxyl groups were aggregated even when sprayed, but amino modified particles or non-modified particles were well dispersed in aerosol. Additional ghost peak was observed around 10 nm, due to the usage of ammonium acetate for diluting colloidal suspension. We are planning to delete this peak by altering diluting media to other ones.

Keywords: Electron Spray, Nano Particle, Quantum Dot, Inhalation System

Numerical Modeling of Nanoparticle Charging Efficiency of Corona-Wire Unipolar Aerosol Charger

Chuen-Jinn Tsai¹, Chih-Liang Chien¹, Hui-Lin Chen¹, Guan-Yu Lin¹ and Jong-Shinn Wu²

1 Institute of Environmental Engineering, National Chiao Tung University, No. 1001, University Road, Hsin Chu, 300 Taiwan.

2 Department of Mechanical Engineering, National Chiao Tung University, No. 1001, University Road, Hsin Chu, 300 Taiwan.

Principal Contact: Chuen-Jinn Tsai, Professor, Institute of Environmental Engineering, National Chiao Tung University, No. 1001, University Road, Hsin Chu, 300 Taiwan.

Tel: +886-3-5731880 Fax: +886-3-5727835 E-mail: cjtsai@mail.nctu.edu.tw

Abstract

Charging of nanoparticles has been applied in different areas. Numerous corona unipolar chargers were designed to achieve high charging efficiency. However, no detailed numerical model is available to optimize the design to reduce electrostatic loss and predict the extrinsic charging efficiency of the unipolar charger. In this study, a 2-D numerical model was developed to predict nanoparticle charging efficiency in the unipolar charger. Flow field was solved by using the SIMPLER method (Patankar 1980), while electric field and ion concentration distribution were solved based on Poisson and convection-diffusion equations, respectively. The charged particle concentration distribution and charging efficiency were then calculated based on the convection-diffusion equation with particle charging calculated by Fuchs diffusion charging theory (Fuchs 1963). An efficient corona-wire unipolar aerosol charger with sheath air to avoid particle loss was also developed to facilitate the comparison of the numerical results with the experimental data obtained at a fixed aerosol flow of 1 L/min using silver particles of 2.5 to 20 nm in diameter. The charger has a cylindrical casing of 30 mm in diameter in which a gold wire of 50 μm in diameter and 2 mm in length was used as the discharge electrode. Good agreement between the predicted and the experimental extrinsic charging efficiency was obtained. Numerical results indicate the location where the significant amount of the charged particle loss occurred in the present charger, and further show that uniform aerosol stream of the flow field distribution in the charging zone is important to minimize electrostatic loss for the corona-wire unipolar charger with sheath air. Present numerical model has been validated and enables the design of a more efficient corona-wire unipolar charger. Improvement in the charging zone structure and enhancement of $Ni \cdot t$ product are currently being conducted to improve the charger performance.

Keywords: nanoparticles, unipolar charger, charging efficiency, numerical simulation.

Study of Heterogeneous Nucleation upon Nanoparticles in Condensation Particle Counters (CPCs): Effects of Particle and Vapor Composition

Modi Chen¹, Michel Attoui² and Peter McMurry¹

¹ University of Minnesota, 111 Church ST. SE., Minneapolis, MN, 55455

² Faculté des Sciences, UPEC, Paris, France

ABSTRACT

Recent developments have led to significant reduction in the minimum size that can be detected with condensation particle counters (CPCs). While CPCs are widely used as particle detectors due to their high sensitivity and high signal-to-noise ratio, previous laboratory work shows that the activation efficiencies for particles smaller than 3nm are influenced by their chemical compositions and the condensing vapor, which lead to measurement uncertainties that are difficult to quantify. On the other hand, in spite of the work on heterogeneous nucleation in the past decades, discrepancies between measurements and theory still exist.

In this study, we carry out experiments to explore the effects of nanoparticle chemical composition and electrical polarity (+1, 0, -1) on heterogeneous nucleation of several supersaturated vapors. Particle materials studied include (NaCl, W, Ag, and tetra-heptyl ammonium bromide and tetra-dodecyl ammonium bromide ions). Several condensing vapors (water, n-butanol, and diethylene glycol) were investigated. This study not only enriches our knowledge of activation efficiencies of different CPCs, which are essential for aerosol scientists who work with them, but also serves as an attempt to explore the fundamental scientific questions about heterogeneous nucleation.

KEYWORDS

CPC, counting efficiency, chemical composition, electrical charges

Introduction

Aerosol particles are ubiquitous in the nature and range in size over several orders of magnitude. They can affect different aspects of human life, including the health and global climate. While large size particles (>100nm) can be effectively detected by light scattering, detection of nano-scale particles is more challenging. CPCs are widely used for aerosol

particle detection down to several nanometers^[1]. Unlike electric methods^[2], which require particles to be charged, CPCs can also detect neutral particles. Furthermore, because CPCs detect individual particles, exceedingly low concentrations can be accurately measured. Until recently, the minimum 50% cut-off diameter for commercial CPCs has been around 3 nm^[3, 4]. To push the detection limit to lower size, different approaches have been applied to existing CPC designs. In order to activate particles in the 1 nm range, Mordas (2008) and Sipilä (2009) operate their CPCs at saturation ratios that lead to self-nucleation^[5, 6]. Distinguishing between particles that were present in the sampled aerosol (the desired particles) from those formed by self nucleation complicates the analysis of data from such instruments. Iida, on the other hand, discovered that by using diethylene glycol (DEG) as the working fluid, the lowest cut-off diameter can be significantly decreased^[7]. Based on Iida's work, several DEG based CPCs have been developed to detect particles down to 1 nm^[7-9].

While the ability to detect sub-3 nm particles directly by condensational growth provides rich information in studies of, for example, atmospheric nucleation or material synthesis, experiments show that various effects can influence the activation efficiency of particles smaller than 5 nm. These effects include chemical compositions of particles^[7, 8, 10], electrical polarity^[11, 12], and also the composition of the condensing vapor^[7]. Measurement uncertainties are reduced when those effects are understood. This paper describes experimental studies on the effects of these variables on heterogeneous nucleation inside CPCs.

Experimental Methods

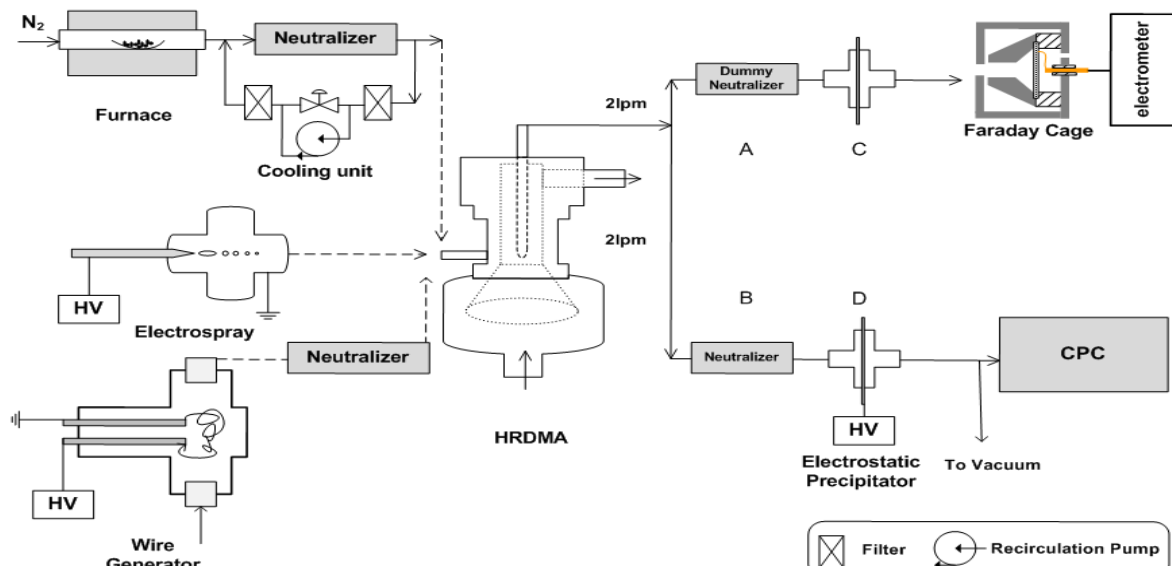


Figure 1. Experimental setup for calibrating CPC activation efficiencies.

For calibrating the counting efficiency of different CPCs, CPC signals are compared with measurements of absolute particle concentrations obtained with an aerosol electrometer.^[13].

The setup is shown in Figure 1. Particles of different compositions are generated by a furnace^[14], glowing wire generator^[15] or electrospray^[16-18]. Afterwards, these particles are classified according to their electrical mobility via a high resolution Hermann-DMA (HRDMA, R>10)^[19]. The resulting size-selected particles are divided into two flows: one to the Faraday cage electrometer (FCE) and the other to the CPC under investigation. For detection efficiencies of neutral particles, neutralizer B is used to adjust the charge distribution of the mobility classified particles to a bipolar equilibrium distribution, and any residual charged particles (which would be a small fraction of the total in this size range) are removed by electrostatic precipitator D. This ensures all the particles detected by the CPC are neutral. Dummy neutralizer A (a neutralizer without a Po-210 chip) and a dummy ESP C (ESP with grounded electrodes) are used to ensure the same diffusion loss to the CPC and electrometer. A B C and D are all removed when detecting charged particles. The fraction of the particles that can be detected by the CPC is defined as the counting efficiency of that CPC. All the chemicals are bought from Sigma Aldrich. Table 1 summarizes experiments done in this study.

Table 1. Summary of Activation Experiments.

	UWCPC 3786	UMN DEG	UCPC 3025
NaCl	+ - 0	+ - 0	+ - 0
Ag		+ - 0	+ - 0
W	+ - 0	+ - 0	+ - 0
Molecular Ions	+	+	+

In this table, UWCPC 3786 is a commercially-available TSI water based ultra-fine CPC (product number 3786); UMN DEG is a diethylene glycol based UCPC developed in University of Minnesota; 3025 is a TSI butanol-based ultra-fine CPC. +, -, and 0 identify the nano-particle charging states that were investigated (positive one, negative one, and neutral, respectively). Molecular ions stand for tetra-heptyl ammonium bromide (THABr) and tetra-dodecyl ammonium bromide (TDDABr) ions.

Results and Discussion

Detection Efficiency for Different Particle Composition

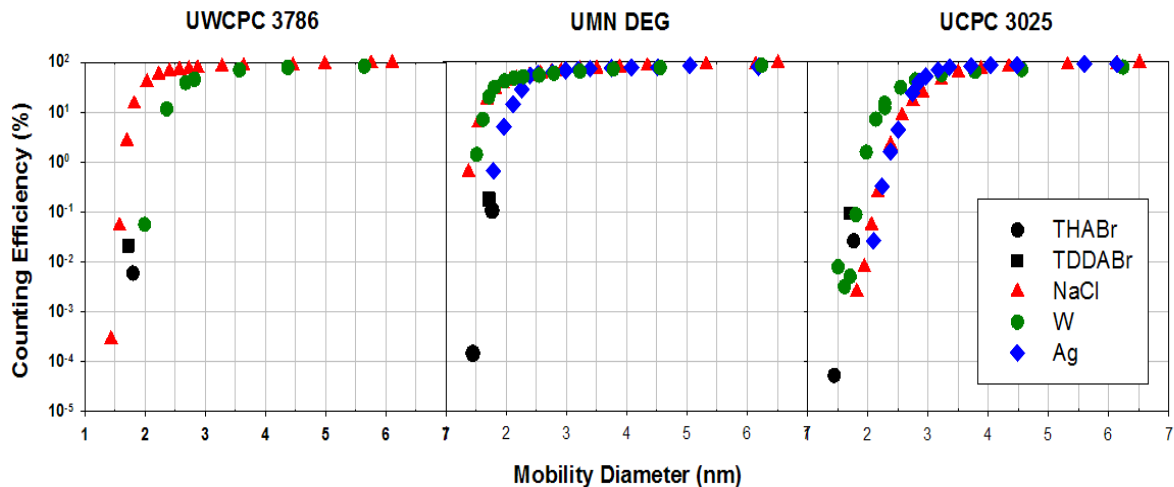


Figure 2. Counting efficiencies of positive charged particles for three CPCs.

Figure 2 shows the counting efficiencies of positively charged particles of different chemical compositions. Three instruments are shown here for comparison. This figure illustrates how different working fluids respond to different materials. Strong dependence on chemical composition is observed by all the instruments for particles smaller than about 2.5 nm. The difference in counting efficiencies between hygroscopic particles (NaCl) and hydrophobic particles (W) is significant for the water based CPC. At the mobility diameter of 2 nm, counting efficiency of NaCl is over 100 times larger than that for W for UWCPC 3786, while, for the UMN DEG, W and NaCl behave almost the same.

Beside particle and working fluid composition, counting efficiency is also determined by the saturation ration and diffusion loss inside the instruments. Since these three CPCs use different temperature configurations and hardware designs, simple comparison of the counting efficiency of the same material between different CPCs cannot provide the effect of the working fluid explicitly. More work is needed to explore it in the future.

Detection Efficiency for Different Charging States

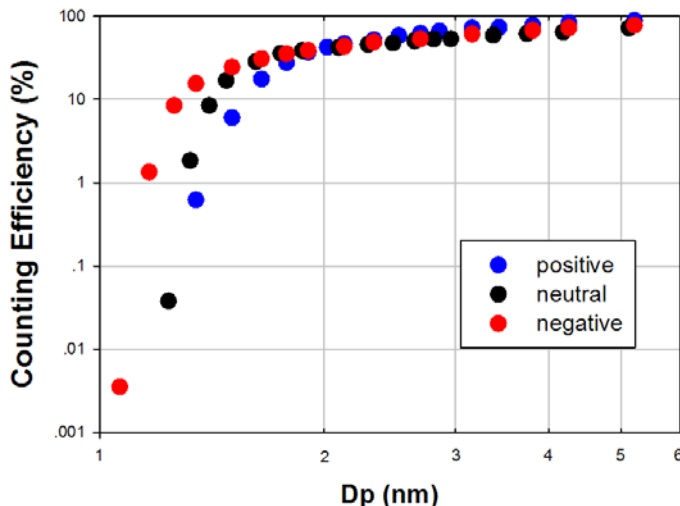


Figure 3. Counting efficiencies of NaCl particles with different polarities for DEG CPC.

Counting efficiencies of particles with different polarities has been studied over one century^[11]. While negative sign preference has been reported in several laboratory studies previously^[7, 11, 12], positive sign preference has also been observed^[6, 9]. In this study, all the negative particles we tested show higher activation efficiency than positive ones. Figure 3 shows a typical result, in which NaCl particles of three charging states are tested with the DEG CPC. One may notice, in the same figure, neutral particles have higher counting efficiency than positive ones, which cannot be explained by any existing theory. This charge dependence needs to be understood, and we are currently carrying out experiments to test various hypotheses that might explain this surprising result.

SUMMARY

We studied the counting efficiency of different CPCs for particles of different chemical composition as well as charging states. Our results show that for particles smaller than 2.5 nm, effects of working fluids and particle composition are significant. We observed that for all the materials studied, negatively charged particles were detected more efficiently than either neutral or positively charged particles. In the future, we will explore further the relative counting efficiency value for neutral particles compared with charged ones. The effect of multiple charging will also be investigated.

ACKNOWLEDGMENTS

This study is supported by Department of Energy, Award No. DE-FG02-05ER63997.

REFERENCES

- [1] P.H. McMurry, *Aerosol Science and Technology*, 33 (2000) 297-322.
- [2] R.C. Flagan, *Aerosol Science and Technology*, 28 (1998) 301-380.
- [3] M.R. Stolzenburg, P.H. McMurry, *Aerosol Science and Technology*, 14 (1991) 48-65.
- [4] G. Mordas, H.E. Manninen, T. Petaja, P.P. Aalto, K. Hameri, M. Kulmala, *Aerosol Science and Technology*, 42 (2008) 152-158.
- [5] G. Mordas, M. Sipila, M. Kulmala, *Aerosol Science and Technology*, 42 (2008) 521-527.
- [6] M. Sipila, K. Lehtipalo, M. Attou, K. Neitola, T. Petaja, P.P. Aalto, C.D. O'Dowd, M. Kulmala, *Aerosol Science and Technology*, 43 (2009) 126-135.
- [7] K. Iida, M.R. Stolzenburg, P.H. McMurry, *Aerosol Science and Technology*, 43 (2009) 81-96.
- [8] J. Jiang, M. Chen, C. Kuang, M. Attou, P. McMurry, *Aerosol Science and Technology*, 45 (2011) 510-521.
- [9] J. Vanhanen, J. Mikkilä, K. Lehtipalo, M. Sipilä, H.E. Manninen, E. Siivola, T. Petäjä, M. Kulmala, *Aerosol Science and Technology*, 45 (2011) 533 - 542.
- [10] C.D. O'Dowd, P. Aalto, K. Hameri, M. Kulmala, T. Hoffmann, *Nature*, 416 (2002) 497-498.
- [11] C.T.R. Wilson, *London Philos. Trans.*, (1899) 289-308.
- [12] P.M. Winkler, G. Steiner, A. Vrtala, H. Vehkamaki, M. Noppel, K.E.J. Lehtinen, G.P. Reischl, P.E. Wagner, M. Kulmala, *Science*, 319 (2008) 1374-1377.
- [13] B.Y.H. Liu, D.Y.H. Pui, *Journal of Colloid and Interface Science*, 47 (1974) 155-171.
- [14] H.G. Scheibel, J. Porstendorfer, *Journal of Aerosol Science*, 14 (1983) 113-&.
- [15] C. Peineke, M.B. Attou, A. Schmidt-Ott, *Journal of Aerosol Science*, 37 (2006) 1651-1661.
- [16] S. Ude, J.F. de la Mora, *Journal of Aerosol Science*, 36 (2005) 1224-1237.
- [17] D.R. Chen, D.Y.H. Pui, S.L. Kaufman, *Journal of Aerosol Science*, 26 (1995) 963-977.
- [18] G. Bacher, W.W. Szymanski, S.L. Kaufman, P. Zollner, D. Blaas, G. Allmaier, *J Mass Spectrom*, 36 (2001) 1038-1052.
- [19] S. Rosser, J.F. de la Mora, *Aerosol Science and Technology*, 39 (2005) 1191-1200.

Morphological Control of Carbon Nanoparticles Generated by Laser Ablation

Ayumi Inoue, Masato Takebayashi, Takafumi Seto and Yoshio Otani

Kanazawa University, Kakuma, Kanazawa, Ishikawa 920-1192, Japan

ABSTRACT

The morphology and nanostructure of carbon nanoparticles are controlled by using pulsed laser ablation of carbon target at the atmospheric pressure and room temperature. The size distribution of gas-borne nanoparticles measured by a scanning mobility particle sizer (SMPS) had the mean mobility diameter of around 100 nm regardless of laser fluence and intensity. The measurements of primary particle size and nanostructure of particles with a transmission electron microscope (TEM) showed that the particles are agglomerates consisting of about 8-nm primary particles. When these particles are irradiated by the multiple shots of pulsed laser beam, they form spherical and unagglomerated nanoparticles with the mobility diameter of around 10 to 20 nm as a result of restructuring of agglomerated particles. High resolution electron micrographs revealed that the generated carbon particles have shell structure composed of multiple graphene sheets. The laser irradiation conditions to control the structure of carbon nanoparticles are discussed.

KEYWORDS

Carbon nanoparticle, Laser ablation, Onion-like carbon

Introduction

Carbon nanoparticles exhibit unique characteristics due to their dimension and crystal structure. They have potential applications in the variety of fields including electronic, chemical, mechanical and medical engineerings. Pulsed laser ablation (PLA) of a carbon target is a conventional method to generate carbon nanoparticles and the allotropes such as fullerenes [1], carbon nanotubes [2]. However, when PLA is used to generate aerosol at the atmospheric pressure and room temperature, the aerosol produced are generally in the form of agglomerates because of rapid nucleation and subsequent Brownian coagulation of highly concentrated primary nanoparticles [3].

In this study, carbon nanoparticles are generated by the pulsed laser ablation of carbon target at the atmospheric pressure and room temperature. The evolution of morphology and nanostructure of gas-borne nanoparticles is measured by a scanning mobility particle sizer (SMPS). Primary particle size distribution and nanostructure of particles are also measured with a transmission

electron microscope (TEM).

Experimental Methods

Figure 1 shows the flow diagram of nanocarbon synthesis. Third harmonic wave of ns-pulsed Nd:YAG laser ($\lambda = 355$ nm, 20 Hz; INDI-40, Spectra physics Inc.) irradiates the carbon target which is placed at the center of quartz tube (ID = 40 mm). Before the experiments, the generator was evacuated by a vacuum pump (VP) and the residual gas was replaced with pure nitrogen. The particle generator was operated at the atmospheric pressure (0.1 MPa) and room temperature (20 degree Celcius). During the particle generation, nitrogen (>99.999%) was continuously fed to the generator and the flow rate was set at 4.0 L/min by a mass flow controller (MFC). With line (a) in Fig. 1, the mobility-based size distributions of generated particles in the gas phase were measured using a Scanning Mobility Particle Sizer (SMPS; model 3080, TSI Inc.). By line (b), particles were collected on microgrids by an electrostatic precipitator (Nanometer Aerosol Sampler; Model 3089, TSI Inc.) for observation by a transmission electron microscope (TEM).

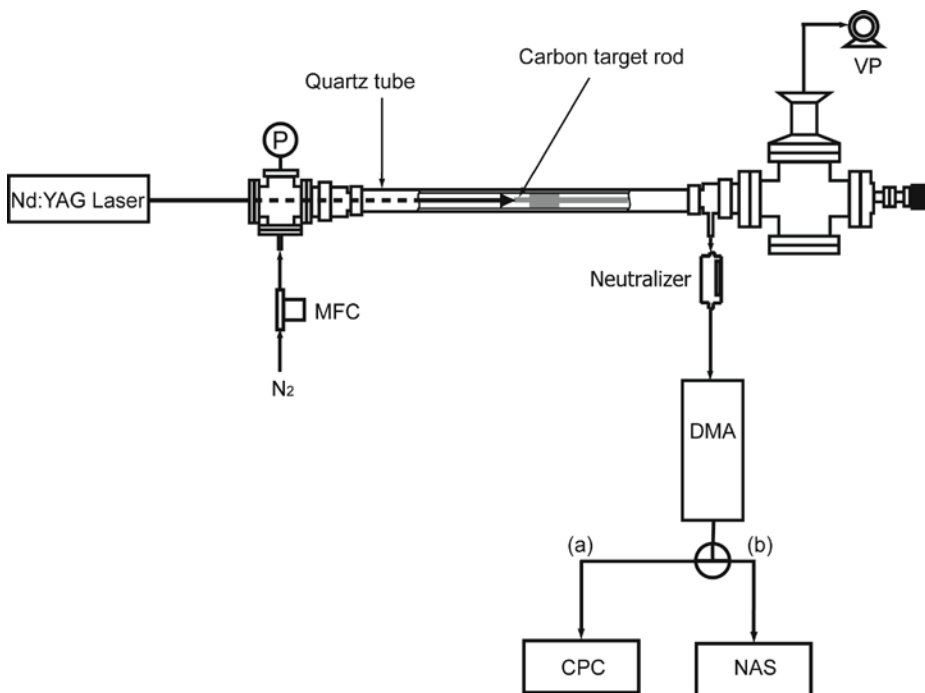


Figure 1 Experimental setup used in this study.

Results and Discussion

Figure 2 shows TEM images of carbon particles generated by laser ablation. The generated particles are agglomerates composed of irregular shaped amorphous carbon nanoparticles with

average primary particle diameter of 7.6 nm. Figure 3 shows the mobility-based size distribution of aerosol particles. As shown in Fig. 3, the average of electrical mobility diameter of particles generated by laser ablation is 83 nm which is much larger than that of primary particles. Therefore the particles generated by normal laser ablation are agglomerates of many primary particles while they are suspended in the gas. Figure 4 shows high resolution TEM image of carbon particle generated by multiple laser irradiations. In this experiment, carbon agglomerates are irradiated by laser beam in the gas phase during the transport by carrier gas. As shown in Fig. 4, polyhedral particle with concentric shell structure is generated by the irradiation of multiple laser shots. Similar structure of carbon nanoparticles has been reported by Ugarte [4], and it is called onion-like carbon.

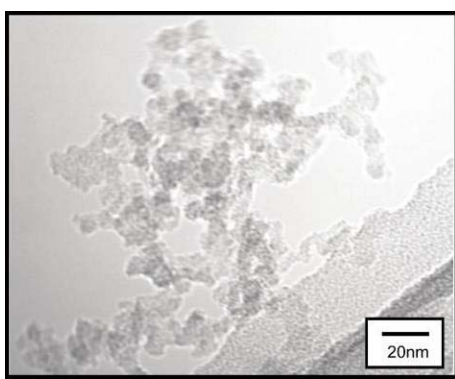


Figure 2. TEM image of carbon agglomerates.

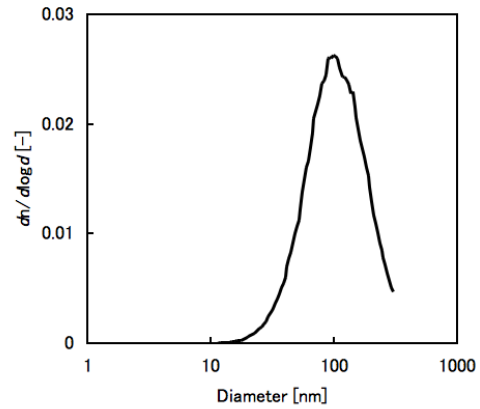


Figure 3. Mobility size distribution of the agglomerate.

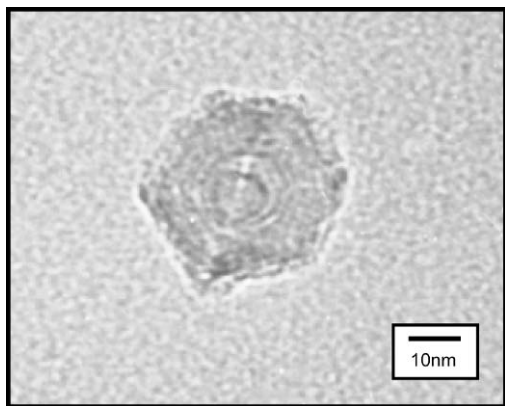


Figure 4. TEM image of polyhedral carbon particle generated by multiple laser irradiations.

SUMMARY

The morphology and nanostructure of carbon nanoparticles are controlled by using the pulsed laser ablation of carbon target at the atmospheric pressure and room temperature. Generated particles are agglomerates and these agglomerates transform to onion-like carbon during the irradiation of multiple laser shots in the gas phase.

REFERENCES

- [1] Oyama, T.; Ishii, T.; Takeuchi, K. *Fullerene Science and Technology*. 1997, vol.5, No.5, 919-933
- [2] Ting, G.; Pavel, N.; Andrew, G.R.; David. T.; Daniel. T.C.;Richard. E.S. *J. Biol Chem.* 1995, 99, 10694-10697.
- [3] Ullmann, M.; Friedlander, S.K.; Schmidt-Ott, A. *Journal of Nanoparticle Research*. 2002, 4, 499-509
- [4] Ugarte, D. *Carbon*. 1995, vol. 33, No. 7, 989-993

Quenching of Zinc Vapor for the Generation of Zinc Oxide Nanoparticles

Chuen-Jinn Tsai¹ and Rodrigo Blanco¹

1 Institute of Environmental Engineering, National Chiao Tung University, Hsinchu, Taiwan 300

Principal Contact: Chuen-Jinn Tsai, Institute of Environmental Engineering, National Chiao Tung University, No. 1001, University Road, Hsin Chu, 300 Taiwan.

Tel : +886-3-5731880 Fax : +886-3-5727835 Email: cjtsai@mail.nctu.edu.tw

Abstract

Zinc Oxide particles find applications as vulcanizing agents and to a lesser extent as semiconductors, catalysts, cosmetics, and food supplements. Note that Zinc Oxide is the third largest aerosol-made commodity by volume produced by the so called French and American processes leading to micron-sized particles. Zinc Oxide nanoparticles can also be dissociated by a solar energy reactor and be used as a precursor for hydrogen production. In this study A battery of experiments were carried out in a tubular furnace at 500°C containing a flow of N₂ that carried Zn(g) throughout the furnace and deliver it to a diluter/condenser that quenched the Zn(g) and mixed it with air for the production of ZnO nanoparticles. The experiments were carried out at different flow rates of carrier gas and dilution air. This changes reflected a change on the average particle normal median diameter of the generated ZnO nanoparticles, the lowest and more stable particle median diameter was obtained at N₂ = 1.5 LPM and dilution air = 5 LPM with the NMD = 9.31 nm. It is yet to be analyzed which setting is the best for this purpose so that a proper particle diameter is obtained to use Zinc Oxide nanoparticles as a precursor for hydrogen production. It is also still undetermined if a different cooling or diluting system design could provide better results for nanoparticle production, for that reason a new diluter/condenser is under investigation.

Keywords: Zinc Oxide, Zinc, Nanoparticles, evaporation-condensation.

Controlling the glass protective layer on copper powders via spray pyrolysis

Dae-Soo Jung¹, Yun-Chan Kang² and Seung-Bin Park¹

1 Dept. of Chemical and Biomolecular Engineering, KAIST, 373-1, Guseong-dong, Yuseong-gu, Daejeon, 305-701, Republic of Korea

2 Department of Chemical Engineering, Konkuk University, 1 Hwayang-dong, Gwangjin-gu, Seoul 143-701, South Korea

Principal Contact: Seung-Bin Park, Dept. of Chemical and Biomolecular Engineering, KAIST.

Tel.: +82-42-869-3928, E-mail address: SeungBinPark@kaist.ac.kr

Abstract

Conducting films were used for various applications, which have been grown with continuous growth of new microelectronic circuit needs. Among the conducting materials, copper is considered as an alternative conducting material, which is cheaper than silver and has a high conductivity (only 6% less than that of silver). Usually, conducting thick films are formed from a conducting paste, consisting of metal powder, glass powder, and an organic vehicle. The metal powders used for fabricating conducting film with high conductivity should have fine-size, spherical shape and high crystallinity and density.

Fine sized copper powders can be easily oxidized under atmosphere condition which hinders its further application, resulting in increasing the required melting temperature and reducing the electrical conductivity. To overcome the oxidation problem, various organic or oxide materials have been studied. However, the protective materials reduce the electrical properties of copper film due to their non-metallic properties.

In this work, we used glass material as a protective layer. The glass materials act as permanent binders and help bind the conducting film to the substrate and improve the sintering of the copper powders. The Cu-glass composite powders with core-shell structure for copper electrode were prepared directly by spray pyrolysis. The effects of the glass content in the composite powders on the oxidation property and electrical property of the copper thick film formed from composite powders were investigated.

Keywords: Spray pyrolysis, Cu electrode, Oxidation resistivity, Core-shell structure, Glass frit

Regional pollution characteristics and sources of PM₁₀ for five northern cities in China

Yinchang Feng, Yingze Tian, Guoliang Shi, Zhimei Xiao, Xiaohui Bi, Jianhui Wu, Yufen Zhang

State Environmental Protection Key Laboratory of Urban Ambient Air Particulate Matter Pollution Prevention and Control, College of Environmental Science and Engineering, Nankai University, Tianjin, 300071, China

Principal Contact: Guoliang Shi, State Environmental Protection Key Laboratory of Urban Ambient Air Particulate Matter Pollution Prevention and Control, College of Environmental Science and Engineering, Nankai University, Tianjin, 300071, China.

Email: fengyc@nankai.edu.cn (Y.C. Feng), nksgl@hotmail.com (G.L. Shi)

Abstract

In order to understand the regional pollutant characteristics of particulate pollution condition in northern China, PM₁₀ samples were collected from five representative cities in northern China, in summer and winter. PM₁₀ and species concentrations in ambient samples were analyzed in order to study the pollutant level. The study of seasonal variation showed that the PM₁₀ and species concentrations got relatively higher level in winter than those in summer for five cities. In addition, the contributions from primary and secondary sources were estimated by nonnegative constrained principal component regression chemical mass balance (NCPCRCMB) model. The results indicate that coal combustion source was the most important source category in winter for five cities, mainly because that coal combustion is used for heating supply in northern Chinese cities; while in summer, the highest contributors were different across cities. In Tianjin, the highest contribution in summer (12.98 μg/m³, 13%) and winter (33.62 μg/m³, 19%) were from soil dust; in addition, coal combustion was also an important source in winter (31.23 μg/m³, 18%). In Anyang, the highest contributor in summer was cement dust (22.60 μg/m³, 18%) and in winter was coal combustion (34.59 μg/m³, 19%). In Ji'nan, soil dust was the highest contributor in seasons, accounting for 18.37 μg/m³ (22%) in summer and 44.97 μg/m³ (24%) in winter respectively. In Kaifeng, cement dust was the highest contributor (12.37 μg/m³, 13%) in summer and coal combustion was the highest (42.66 μg/m³, 25%) in winter. And in Taiyuan coal combustion was the important sources in summer (21.66 μg/m³, 15%) and winter (47.66 μg/m³, 22%).

The Study on Vertical and Temporal Variation of PM₁₀ of Yantaqu in Xi'an During Winter

Jingbo Zhao, Zhenzhen Mu, Na Xu, Lan Yao, Yuxia Li and Jingjing Meng

College of Tourism and Environment, Shanxi Normal University, Xi'an, Shaanxi, China, 710062

Principal Contact: Jingbo Zhao, Professor, College of Tourism and Environment, Shanxi Normal University, Xi'an, Shaanxi, China, 710062.

Email: zhaojb104@126.com

Abstract

In order to ascertain vertical and temporal variation characteristics of PM₁₀ of Yanta area in Xi'an during winter, we observed the PM₁₀ mass concentration for 6 days of the four buildings near Changyanbao in Yanta area during Jan.22 to Jan.29 in 2010, and studied the vertical and temporal variation of PM₁₀ and the influencing factor, evaluated the level of pollution for different height. The results showed that: the PM₁₀ mass concentration was lower at the height of 1 and 45~54 meter; it ranged from 0.005mg/m³ to 0.080mg/m³, 0.037mg/m³ on average at the height of 1 meter; the PM₁₀ mass concentration at the height of 45~54 meter ranged from 0.000mg/m³ to 0.005mg/m³, 0.038mg/m³ on average, while PM₁₀ mass concentration was higher at the height of 3~27 meter; it ranged from 0.030mg/m³ to 0.180mg/m³, 0.076mg/m³ on average. PM₁₀ had a temporal variation with two peaks in the day. The variation of PM₁₀ mass concentration was influenced by the stability of atmosphere, etc. There was a negative correlation between temperature and PM₁₀ mass concentration at the height of 6~27 meter. The average value of PM₁₀ at the height of 1 and 45~54 meter conformed to the national primary standards and that of the rest height conformed to secondary standards. PM₁₀ concentration was high in the morning and at night and low in the afternoon; it increased and decreased and finally increased with the increasing height and showed that the variation of dusk concentration was complex and needed further study.

Keywords: PM₁₀; Vertical variation; Diurnal variation; Pollution level; Influencing factor; Yanta area in Xi'an

Characterization of volatile organic compounds (VOCs) around the Chinese Spring Festival and International Labour Day in the urban area of Shanghai, China

Hongli Wang, Changhong Chen, Cheng Huang, Li Li, Minghua Chen
Shanghai Academy of Environmental Sciences, Shanghai 200233, China

Principal Contact: Hongli Wang, Shanghai Academy of Environmental Sciences,
Shanghai 200233, China.
Email: wanghl@saes.sh.cn

Abstract

Volatile organic compounds (VOCs) have been recognized as one of the most important precursors of the production of tropospheric ozone and secondary organic aerosol. Study on the concentration, speciation, and chemical reactivity of VOCs are necessary to further understand of the formation process of atmospheric pollution. The gas chromatography with flame ionization detector (GC/FID) was employed to monitor VOCs in urban area of Shanghai during Chinese Spring Festival (from Jan. 19th to Feb. 7th, 2009) and the International Labor Day (from Apr. 23rd to Jun. 5th, 2009) and 56 kinds of VOCs were detected. According to the results, there were two peaks in the morning and evening for the diurnal profile of VOCs, which were consistent with the rush hours, suggesting that the atmosphere in the urban area of Shanghai was mainly affected by the vehicle emission. The average mixing ratio of VOCs in the urban area of Shanghai was (28.39±18.35) ppbv. The major compositions of VOCs were alkanes, aromatics, alkenes, and acetylene, which accounted for 46.6%, 27.0%, 15.1%, and 11.2% of the total VOCs, respectively. The OH radical loss rate and the ozone formation potential were applied to access the chemical reactivity of VOCs. Based on the results, there was significantly positive correlation between the mixing ratio and the chemical reactivity. The chemical reactivity of the atmosphere in the urban area of Shanghai was similar to that of ethylene. The alkenes and aromatics were the dominant species for the chemical reactivity. For the OH radical loss rate, the alkenes and aromatics accounted for 51.2% and 31.8%, respectively; and for the ozone formation potential, they accounted for 30.2% and 53.4%, respectively. In the case of compounds, propylene, ethylene, toluene, xylenes, and butenes were the most important contributors to the ozone formation for the atmosphere in the urban area of Shanghai.

Keywords: Volatile organic compounds; Mixing ratio; Chemical reactivity; OH radical loss rate; Ozone formation potential

PM_{2.5} speciation and chemical extinction during the 2008 Beijing Olympics

F. Yang,¹ X. Li,² C. Li,³ Q. Zhao,² K. He,² Y. Ma,² J. Tan,¹ F. Duan,² H. Liu²;

1 Graduate University of Chinese Academy of Sciences, Beijing, China

2 Tsinghua University, Beijing, China

3 Peking University, Beijing, China

Principal contact: Fumo Yang, Professor, College of Earth Science, Graduate University of Chinese Academy of Sciences, Beijing 100049, China.

Tel: 8610-8825-6333 Fax: 8610-8825-6012 Email: fmyang@gucas.ac.cn

Abstract

Distinct contrast of air quality and visibility between the periods during and before the 2008 Beijing Olympics provides a rare opportunity to investigate PM_{2.5} chemical extinction in this megacity. 24-hr integrated PM_{2.5} samples were collected, and light scattering and light absorption coefficients were measured using an integrating nephelometer and a light absorption photometer at urban Beijing from June 24 through September 23, 2008. Major inorganic ions, trace elements, and organic and elemental carbon in analyzed to perform reconstruction of PM_{2.5} speciation. Daily mass concentrations of PM_{2.5} were noticeably associated with scattering coefficients for the study period, indicating light scattering contributed predominantly to visibility impairment in Beijing. It is found that their correlation was significantly strengthened ($r=0.95$) for the Olympics month (August). During the Olympics (August 8-24), sulfate and nitrate experienced maximum (62-65% on average) reduction in their concentrations, followed by ammonium and crustal material compared to those before the Games. These reductions were at least partly due to strict desulphurization and traffic control measurements adopted in the period. Accordingly, visibility improved dramatically as light scattering coefficient decreased by 60% on average. Average concentrations of organic matter and elemental carbon, however decreased in this period by only 23% and 31%, respectively. This comparison implies that secondary inorganic aerosols (i.e., sulfate, nitrate, and ammonium, SNA) in PM_{2.5} likely play predominant role in hazy occurrence and haziness enhancement in Beijing.

Influence of Intersection on Chemical Composition of Atmospheric Particulate Matters Observed at Roadside Environment in Urban Area

Kyung Hwan Kim¹, Kazuhiko Sekiguchi^{1,2*}, Shinji Kudo¹, Masatoshi Kinoshita¹ and Kazuhiko Sakamoto^{1,2,3}

1 Graduate School of Science and Engineering, Saitama University, 255 Shimo-Okubo, Sakura, Saitama, 338-8570, Japan

2 Institute for Environmental Science and Technology, Saitama University, 255 Shimo-Okubo, Sakura, Saitama, 338-8570, Japan

3 Center for Environmental Science in Saitama, 914 Kami-tanadare, Kazo, Saitama 347-0115, Japan

*Corresponding author

Fax & Tel: +81-48-858-9542, E-mail: kseki@mail.saitama-u.ac.jp

ABSTRACT

Atmospheric ultrafine particles (UFPs; $D_p < 0.1 \mu\text{m}$) and fine particles (FPs; $D_p < 2.5 \mu\text{m}$) are simultaneously collected for 11 h (daytime and nighttime) at four sites around one intersection in urban area. 14-day consecutive sampling was carried out to find the influence of intersection on the chemical composition of atmospheric UFPs and FPs, and to provide supportive data for possible emission of char or char-like particles from motor vehicles. Relative contribution of organic carbon (OC) and elemental carbon (EC) for total carbon (TC) in daytime samples accounts for 65 – 86% (UFPs: 83 – 86%, FPs: 65 – 75%) and 14 – 35% (UFPs: 14 – 17%, FPs: 25 – 35%) respectively whereas those in nighttime samples accounts for 71 – 90% (UFPs: 87 – 90%, FPs: 71 – 78%) and 10 – 29% (UFPs: 10 – 13%, FPs: 22 – 29%) respectively indicating high contribution of EC for the two particle sizes during daytime. Decreasing tendency of carbonaceous components was observed as the distance from intersection increases indicating strong influence of motor vehicles emissions around intersection. Furthermore, this study provides supportive data for possible char-EC emissions from motor vehicles around intersection.

KEYWORDS

Roadside, Ultrafine particles, Chemical composition, Intersection, black carbon

Introduction

Motor vehicle exhausts are the main contributors to anthropogenic particulate matters (PM) in urban environment. The amount of PM emitted from motor vehicles is on a declining tendency due to strict regulations on motor vehicle emissions. However, there is a concern that the particle size maybe reduced because of the advanced exhaust-gas management practices of motor vehicle manufacturers related to the factors such as driving conditions which influence the emissions of smaller particles. Information regarding the properties of size divided particles generated from motor vehicles, and the behavior of these particles in the atmosphere surrounding the roadside environment are still unknown. Our previous study revealed that the operation of motor vehicles in various drive modes (i.e., deceleration, idling, acceleration, and constant velocity), which can be observed frequently at an intersection, could significantly influence on the particle emissions around the sampling site¹⁾. Furthermore, this study also discusses about possible emission of char or char-like particles from motor vehicles. Thus, we carried out a field sampling at a roadside intersection for the collection of ultrafine particles (UFPs) size range ($D_p < 0.1 \mu\text{m}$) as well as fine particles (FPs) size rage ($D_p < 2.5 \mu\text{m}$) to find out the influence of intersection in chemical composition of PM. In order to clarify the relationships between chemical components in PM and meteorological data or gaseous pollutants, samples were collected for 11 h (daytime and nighttime). Our seasonal variation study for roadside environment revealed 11 h UFPs collection using an inertial filter (INF) sampler would be possible in fall and winter²⁾.

In the present study, atmospheric UFPs and FPs are simultaneously collected for 11 h (daytime and nighttime) at four sites around one intersection in urban area. 14-day consecutive sampling was carried out to find: 1) the influence of intersection on the chemical composition of atmospheric UFPs and FPs, 2) to provide supportive data for possible emission of char or char-like particles from motor vehicles.

Experimental Methods

Saitama City is located on the Kanto Plain at 35. 867° N, 139.65° E to the northwest of the Tokyo Metropolis (Fig. 1). Field sampling was carried out for 14 days (18th - 31st) in January 2011.

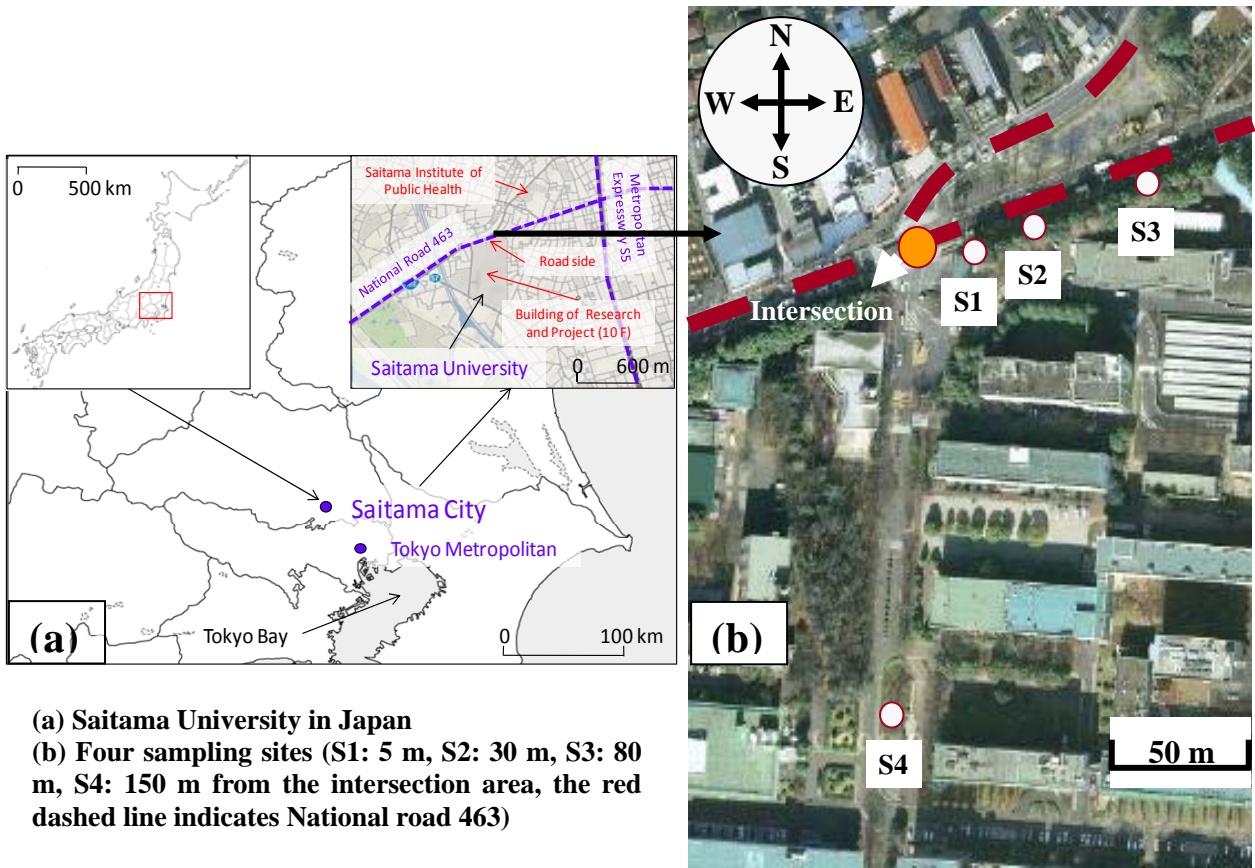


Fig. 1. Sampling locations.

The sampling sites were located on a roadside at the front gate of the Saitama University campus, located near the intersection of two roads. Four sampling spots were selected (S1: 5 m away from an intersection, S2: 30 m away from the intersection, S3: 80 m away from the intersection, S4: 150 m downwind from the intersection) to characterize the influence of an intersection. From S1 to S3 sites are all located 3 m away from roadside while the S4 site is located 150 m away (from north to south) not only from the intersection but also roadside (Fig. 1. (b)). Cyclone PM_{2.5} (URG, Chapel Hill, NC, USA) samplers operated at 16.7 L/min and an INF sampler (Kanomax Japan, Inc., Osaka, Japan) operated at 40 L/min were used for the collection of FPs and UFPs, respectively. The sampling duration was 11 h (daytime: 06:00 a.m. to 05:00 p.m., nighttime: 06:00 to 05:00 a.m.) corresponding to a total sampling volume of 26.4 and 11.5 m³ for the collection of UFPs and FPs, respectively. Quartz fiber (2500 QAT-UP, Pallflex, CT, USA) filters were used to determine carbonaceous components.

Carbon analyses were carried out on a Desert Research Institute (DRI) Model 2001 Carbon Analyzer (Atmoslytic Inc., Calabasas, CA) following the IMPROVE_TOR method. In this study,

the EC fractions were divided into char-EC and soot-EC⁴). Char-EC is defined as EC1 minus pyrolyzed organic carbon (POC), and the soot-EC is defined as the sum of EC2 and EC3. The total OC is defined as the sum of the four OC fractions plus POC, and the total EC is define as the sum of the three EC fractions minus POC.

Results and Discussion

Concentrations of chemical composition

The average concentrations of carbonaceous components for daytime and nighttime samples in UFPs and FPs during our sampling periods are shown in Table 1 and 2 respectively.

Table 1. Average concentrations of carbonaceous components in UFPs during the sampling periods.

UFPs	OC ($\mu\text{g}/\text{m}^3$)	EC ($\mu\text{g}/\text{m}^3$)	Char-EC ($\mu\text{g}/\text{m}^3$)	Soot-EC ($\mu\text{g}/\text{m}^3$)	OC /EC	Char-EC /soot-EC
S1	Daytime	1.18 ± 0.30	0.22 ± 0.06	0.10 ± 0.04	0.12 ± 0.05	5.52 ± 1.39
	Nighttime	1.22 ± 0.44	0.18 ± 0.11	0.08 ± 0.07	0.10 ± 0.05	8.27 ± 3.76
S2	Daytime	1.03 ± 0.29	0.21 ± 0.07	0.09 ± 0.03	0.12 ± 0.06	5.24 ± 1.38
	Nighttime	1.03 ± 0.34	0.14 ± 0.08	0.06 ± 0.05	0.08 ± 0.04	8.83 ± 3.43
S3	Daytime	1.15 ± 0.27	0.20 ± 0.07	0.09 ± 0.04	0.11 ± 0.04	6.15 ± 6.15
	Nighttime	1.15 ± 0.35	0.13 ± 0.07	0.07 ± 0.04	0.06 ± 0.03	10.1 ± 3.84
S4	Daytime	0.86 ± 0.31	0.14 ± 0.07	0.10 ± 0.05	0.04 ± 0.04	6.76 ± 2.27
	Nighttime	0.93 ± 0.46	0.11 ± 0.08	0.06 ± 0.05	0.03 ± 0.04	13.7 ± 8.21

Table 2. Average concentrations of carbonaceous components in FPs during the sampling periods.

FPs		OC ($\mu\text{g}/\text{m}^3$)	EC ($\mu\text{g}/\text{m}^3$)	Char-EC ($\mu\text{g}/\text{m}^3$)	Soot-EC ($\mu\text{g}/\text{m}^3$)	OC /EC	Char-EC /soot-EC
S1	Daytime	5.17 ± 1.96	2.43 ± 0.91	1.38 ± 0.62	1.17 ± 0.40	2.28 ± 0.98	1.22 ± 0.47
	Nighttime	4.61 ± 1.48	1.91 ± 0.60	1.05 ± 0.46	0.87 ± 0.28	2.43 ± 0.43	1.25 ± 0.58
S2	Daytime	5.59 ± 1.99	3.00 ± 1.30	1.85 ± 0.98	1.21 ± 0.43	2.07 ± 0.74	1.62 ± 0.79
	Nighttime	5.25 ± 2.08	2.15 ± 0.82	1.34 ± 0.72	0.82 ± 0.37	2.49 ± 0.56	1.86 ± 1.31
S3	Daytime	4.80 ± 1.62	2.21 ± 0.91	1.30 ± 0.64	1.07 ± 0.40	2.46 ± 1.07	1.32 ± 0.71
	Nighttime	4.15 ± 1.52	1.57 ± 0.65	0.89 ± 0.42	0.65 ± 0.31	2.87 ± 1.01	1.48 ± 0.64
S4	Daytime	3.55 ± 1.33	1.21 ± 0.59	0.70 ± 0.38	0.50 ± 0.27	3.61 ± 2.30	1.45 ± 0.66
	Nighttime	3.43 ± 1.81	0.95 ± 0.51	0.57 ± 0.34	0.39 ± 0.19	3.92 ± 1.22	1.52 ± 0.76

\pm indicates standard deviation of concentration or ratio for 13 days ($n = 13$)

Relative contribution of OC and EC for total carbon (TC) in daytime UFPs samples accounts for 83 – 86% and 14 – 17% respectively whereas those in nighttime UFPs samples accounts for 87 – 90% and 10 -13% respectively indicating high contribution of EC during daytime. The increased EC contribution during daytime is closely related to motor vehicle emissions while OC contribution during nighttime caused by relatively lower contribution of EC and condensed OC onto UFPs due to lower temperature. This tendency was also observed for FPs. The relative contribution of OC and EC for TC in daytime FPs samples accounts for 65 – 75% and 25 – 35% respectively whereas those in nighttime FPs samples accounts for 71 – 78% and 22 - 29% respectively. The contribution of OC in the two particle sizes tends to increase from S1 to S4 while that of EC in the two particle sizes showed the opposite tendency supporting strong influence of motor vehicle emissions. The OC/EC and char-EC/soot-EC ratios also clearly show this tendency reflecting higher contribution of motor vehicle emissions for the two particle sizes (Table 1).

Relationships between carbonaceous components at different sites

In order to find out the relationships between carbonaceous components in the two particle sizes, correlation coefficients (r^2) were calculated as shown in Table 3. These relationships were

calculated based on assumption that S1 is the main source of carbonaceous components. For the two particle sizes, higher relationships between the sampling sites were observed for nighttime samples than daytime samples. These high relationships may have caused by relatively stable atmospheric condition during the nighttime despite the lower concentrations of nighttime samples. Correlations of S1 with S2, S3, and S4 were observed for only OC and soot-EC in daytime UFPs samples while al components in daytime FPs samples showed high correlations. No correlations between sampling sites for daytime char-EC in UFPs was observed while nighttime char-EC in UFPs showed correlations between sampling sites ($r^2 = 0.93$ for S1 vs. S2, 0.38 for S1 vs. S3, and 0.47 for S1 vs. S4). The correlation between sampling sites for nighttime char-EC in FPs also shows stronger values than daytime samples. This relationship may reflect that char-EC in UFPs sizes has close relationship with the intersection at night (06:00 p.m. to 05:00 a.m. in this sampling).

Table 3. Relationships between sampling sites for daytime and nighttime samples in UFPs and FPs.

Species	S1 vs. S2				S1 vs. S3				S1 vs. S4			
	UFPs		FPs		UFPs		FPs		UFPs		FPs	
	Day	Night	Day	Night	Day	Night	Day	Night	Day	Night	Day	Night
OC	0.51	0.88	0.86	0.86	0.17	0.67	0.82	0.77	0.13	0.73	0.64	0.82
Char-EC	-	0.93	0.87	0.90	-	0.38	0.81	0.94	-	0.47	0.82	0.84
Soot-EC	0.69	0.81	0.61	0.69	0.49	0.80	0.39	0.87	0.39	0.47	0.71	0.39

p value < 0.05 except for those indicated in bold (*n* = 13), “-“ indicates no relationships.

Influence of intersection

Concentration of carbonaceous components in UFPs and FPs tends to decrease as a function of distance from the intersection (Fig.2).

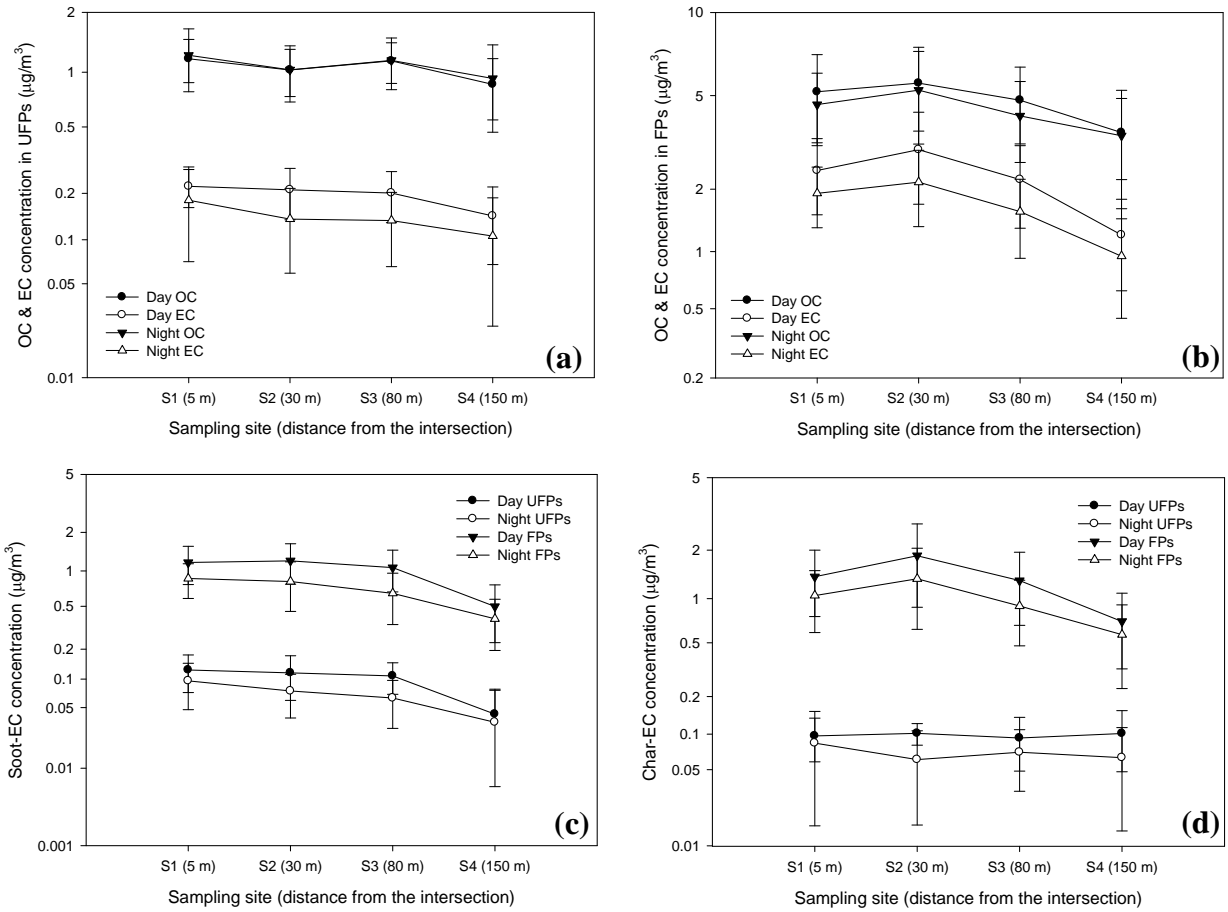


Fig. 2. Average concentration changes at the four sampling sites. (a) and (b) shows OC and EC concentration changes in UFPs and FPs; (c) and (d) shows soot-EC and char-EC changes in UFPs and FPs.

The decreasing tendency is significant for FPs than UFPs (Fig. 2. (a) and (b)). Especially, EC fractions clearly show this tendency as the distance from the intersection increases. Furthermore, the difference in concentrations for daytime and nighttime samples is significant for EC fractions in the two particle sizes while OC fractions show insignificant changes. This is strong evidence for high influence of motor vehicle emissions at an intersection. Fig. 2 (c) and (d) shows the concentration changes for char-EC and soot-EC. One objective of this study is to provide supportive data for possible emission of char particles from motor vehicles. If we assume that background levels (or transported carbonaceous components) of OC, char-EC, and soot-EC are equal for the four sampling sites, we can think that the influence of motor vehicles around the intersection is attributed to the increased concentration for the sampling sites (S1, S2, and S3). Lower concentrations at S4 indicate lower influence of motor vehicles. The decreasing tendency

of char-EC concentration is similar to soot-EC. Therefore, it can be thought that char-EC is emitted from motor vehicles. Some would insist that OC fractions can also be emitted from biomass burning and OC fractions also showed the same decreasing tendency with soot-EC. However, only insignificant concentration differences between daytime and nighttime samples were observed for OC fractions in UFPs (Fig. 2 (a)) and FPs (Fig. 2 (b)) whereas char-EC and soot-EC showed significant concentration differences showing higher concentrations for daytime samples and lower concentrations for nighttime samples with similar decreasing tendency as a function of distance from the intersection.

CONCLUSION

Atmospheric UFPs and FPs are simultaneously collected in January for 14 days at intersection. The relative contribution of OC in the two particle sizes tends to increase from S1 to S4 while that of EC in the two particle sizes showed the opposite tendency supporting strong influence of motor vehicle emissions reflecting higher contribution of motor vehicle emissions at intersection for the two particle sizes. Char-EC and soot-EC showed significant concentration differences showing higher concentrations for daytime samples and lower concentrations for nighttime samples with decreasing tendency as the distance from the intersection increases. This study is demonstrated strong influence of motor vehicles emissions around intersection and decreasing tendency of carbonaceous components as the distance from intersection increases. Furthermore, this study provides supportive data for possible char-EC emissions from motor vehicles around intersection.

ACKNOWLEDGMENTS

This study was supported in part by a Grant-in-Aid for Scientific Research (Kakenhi, No. 21120502) from the Ministry of Education, Culture, Sports, Science and Technology (MEXT) of Japan.

REFERENCES

- [1] Kim, K.H.; Sekiguchi, K.; Kudo, S.; Sakamoto, K. *Aerosol Air Qual. Res.* 2011, 11, 1-12.
- [2] Kim, K.H.; Sekiguchi, K.; Furuuchi, M.; Sakamoto, K. *Atmos. Environ.* 2011, 45, 1581-1590.
- [3] Chow, J.C.; Watson, J.G.; Pritchett, L.C.; Pierson, W.R.; Frazier, C.A.; Purcell, R.G. *Atmos. Environ.* 1993, 27A, 1185-1201.
- [4] Han, Y.M.; Cao, J.J.; Lee, S.C.; Ho, K.F.; An, Z.S. *Atmos. Chem. Phys.* 2010, 10, 595e607.

Characteristics on Air Quality during the 2010 Shanghai Expo

Qingyan Fu¹, Haiping Wei, Yanmin Huang, Song Gao, Yusen Duan and Yihua Zhang

1 Shanghai Environmental Monitoring Center, No.1 Nandan Road, Shanghai, 200030

Principal Contact: Fu Qingyan, Deputy Chief Engineer, Shanghai Environmental Monitoring Center, No.1 Nandan Road, Shanghai, 200030, China.

Tel: 13816108477 Fax: 021-64393639 E-mail: qingyanf@semc.gov.cn

Abstract

Since 2001, this air quality has been continuously improved and ranked the best in Shanghai during the period of 2010 Expo (May 1st to October 31, 2010) contributed by the comprehensive air pollution reduction measures in the Yangtze Delta. The attainment ratio of API (Air Pollution Index) and the number of good days (API less than 50) reached 98.4% and 94 in Shanghai during the 2010 Expo, which was 2.7% and 31 days higher than that in 2009 respectively. The daily average concentrations of PM₁₀, SO₂ and NO₂ were 0.021mg/m³, 0.041mg/m³ and 0.059mg/m³, which were decreased by 25.0%, 10.9% and 18.1% comparing with the same period in 2009. Illustrated by the concentration of PM_{2.5} at the demonstration station of Jing'an in the urban area, the pollution level of aerosol was mitigated, that the average concentration of PM_{2.5} was 0.036 mg/m³ during the 6 months of 2010 Expo, which also was the lowest value since 2006 when on-line monitoring of PM_{2.5} was initiated in Shanghai. At the same time, haze was reduced significantly. The ratio of hourly visibility higher than 20km was increased from 16% in 2009 to 23% in 2010. The successful achievement of air quality management for the 2010 EXPO proved the significance of integrated pollution control strategies, including the FGD of coal-fired boilers, motor vehicles exhaust reduction, fugitive dust and VOCs control, forecasting & action under pollution episode, the regional cooperation of reduction action as well as air quality information sharing. The above experiences could be summarized and applied in the future to realize the sustainable improvement of air quality in the Yangtze River delta.

Keywords: air quality, aerosol, API, 2010 EXPO, Shanghai.

Chemical characterization of aerosol collected at Mt. Yulong in winter time, Southeastern Tibetan Plateau

Ningning Zhang^{1,2}, Junji Cao¹ and Yuanqing He²

1 SKLLQG, Institute of Earth Environment, Chinese Academy of Sciences, Xi'an, China, 710075

2 State key Laboratory of Cryospheric science, Cold and Arid Regions Environmental and Engineering Research Institute, Chinese Academy of Sciences, Lanzhou, China, 730000

Principal Contact: Ningning Zhang, Doctor, Institute of Earth Environment, Xi'an, China, 710075.

Tel: +86-29-8832-6488 Fax: +86-29-8832-0456 E-mail: 236923zh@163.com

Abstract

In order to evaluate the chemical composition of aerosol at southeast of Tibetan Plateau, TSP samples were carried out at Mt. Yulong during Jan to Feb, 2010. Elements (Al, P, S, K, V, Cr, Mn, Ti, Fe, Ni, Zn, As, Br, Rb, Sr, Mo, Sn, Ba, Pb, and Cu.) and soluble ions (SO_4^{2-} , NO_3^- , Cl^- , Na^+ , NH_4^+ , K^+ , Mg^{2+} , and Ca^{2+}) were detected. The results show that Ca, Fe, Al, Si, S, K, Mg, Ti and Na are major element which mainly relate to crustal material. SO_4^{2-} and Ca^{2+} are dominant anion and cation in the samples. Result of ion balance indicate that our samples is alkaline and the compound of SO_4^{2-} is mainly $(\text{NH}_4)_2\text{SO}_4$ and CaSO_4 . EFs of As, Br, Ca, Cu, S, Pb and Zn are bigger than 10, especially As and Br are even bigger than 100. However, the high EF of As maybe caused by crustal sources because of the high enrichment of As in top soil and soil commonly over Tibetan Plateau. SEM observation, EFs, backward trajectories and correlation coefficients reveal that Al, Fe, Ca, Mg, Ti, Mn, Fe, K and Rb mainly originate from crustal source; Pb, Br, Cu, Ni, Zn, Sb and NO_3^- come from traffic-related emissions; and biomass burning have an influence on S, P, Cl, Br and NO_3^- . Moreover, concentrations of S, P, SO_4^{2-} and NH_4^+ have increased obviously during spring festival to lantern festival.

Keywords: Chemical characterization; Sources; Mt. Yulong; Tibetan Plateau; winter time

Determination of direct aerosol radiative forcing at Pune

G. R. Aher¹, G. V. Pawar¹ and P. C. S Devara²

1 Physics Dept., Nowrosjee Wadia College, Pune (India), 411 001

2 Indian Institute of Tropical Meteorology, Pashan, Pune (India), 411 008

Principal Contact: G. R. Aher, Dr., Physics Dept., Nowrosjee Wadia College, Pune, 411 001, India.

Tel: +91(020) 26162944 Fax: +91(020) 26163108 Email: aher.g.r@gmail.com

Abstract

Atmospheric aerosols are significant source of direct and indirect climate forcing hence are of primary concern due to their role in perturbing the Earth-atmospheric radiation balance. Direct radiative forcing is estimated by modeling and experimental techniques. In the experimental technique, sunphotometers and radiation sensors play major role in the measurement of aerosol optical properties and the global solar flux respectively. These data are employed to estimate aerosol direct radiative forcing (ARDF). MICROTOPS-II sunphotometer at 440, 500, 675, 870 and 1020 nm wavelengths and Eppley make Precision Spectral Pyranometer (PSP) in the spectral band 280-2800 nm are being simultaneously operated on clear sky days from Nowrosjee Wadia College, Pune to measure aerosol optical depth (AOD) and global solar flux respectively. Instantaneous AOD values normalized for air mass factor ($m = \sec Z$, $Z \leq 70^{\circ}$, Z being solar zenith angle) at $\lambda = 440, 500, 675$ nm are correlated with global solar flux by using linear regression technique. Slope of the linear regression fit yields a change in ground reaching global solar flux (ΔF) in W/m^2 per unit 0.1 increase in AOD at each wavelength. The zero AOD intercept gives surface reaching global solar flux for no aerosol. Analysis of the data indicates that there is a significant day- to- day variation in ARDF values. This may be correlated with meteorological conditions at the observing site. In the present paper, seasonal variation of ARDF will be discussed. ARDF data obtained will be validated using model calculations.

Keywords: Climate forcing, Aerosol direct radiative forcing, Aerosol optical depth.

Aerosol Optical and Radiative Properties Observed by Lidar and Sky-radiometer during a Haze Episode over Hefei

Zhenzhu Wang, Dong Liu, Decheng Wu and Chenbo Xie

Principal Contact: Zhenzhu Wang, Doctor, Key Laboratory of Atmospheric Composition & Optical Radiation, Anhui Institute of Optics & Fine Mechanics, Chinese Academy of Science, Hefei 230031, China.

Tel: +86-551-5591007 Fax: +86-551-5591579 E-mail: zzwang@aiofm.ac.cn

Abstract

Haze is an atmospheric phenomenon that leads to low visibility, and is mostly due to elevated levels of fine particulate matter. It can have effects on cloud formation, public health, agriculture, and even the global climate. Although urban haze has been increasing in occurrences over the past several years over Hefei, China, studies of the optical and radiative properties of ambient aerosol particles during haze episodes have rarely been conducted. Herein, the Raman lidar and POM-02 sky-radiometer are used to observe the aerosol loading during a typical haze episode on 1-7 October 2009 over Hefei of China. The result shows that the vertical structure of aerosol layer can be up to 4 km height and the lidar ratio varies from 45 to 55 Sr at 532 nm when haze aerosol loading. The average values of AOD and SSA at 500 nm are about 0.75 ± 0.22 and 0.92 ± 0.01 respectively with the Angstrom Index appearing 1.37 ± 0.06 . The volume size distribution of aerosol during this haze episode indicates that the fine particle in accumulation mode takes up a major position. Using the aerosol parameters and a RT model, aerosol radiative forcing at the surface, the top of the atmosphere and the atmosphere are estimated and the 24-hour average values are found to be -26.2 ± 2.8 , -46.6 ± 2.9 , and 20.5 ± 3.2 Wm⁻², respectively.

Keywords: Aerosol; Haze; Optical properties; Radiative forcing

Visual Range Trends in the Yangtze River Delta Region of China during 1981-2005

Lina Gao¹, Gensuo Jia², Renjian Zhang³, Huizheng Che⁴, Congbin Fu⁵, Tijian Wang⁶, Meigen Zhang⁷, Hong Jiang⁸ and Peng Yan⁹

1 Key Laboratory of Regional Climate-Environment Research for Temperate East Asia, Chinese Academy of Sciences, Beijing, Graduate school of the Chinese Academy of Sciences, Beijing, 100029, P. R. China

2 Key Laboratory of Regional Climate-Environment Research for Temperate East Asia Chinese Academy of Sciences, Beijing, 100029, P. R. China

3Key Laboratory of Regional Climate-Environment Research for Temperate East Asia, Chinese Academy of Sciences, Beijing, 100029, P. R. China

4 Key Laboratory of Atmospheric Chemistry (LAC), Centre for Atmosphere Watch and Services (CAWAS), Chinese Academy of Meteorological Sciences (CAMS), CMA, Beijing, P. R. China

5 Key Laboratory of Regional Climate-Environment Research for Temperate East Asia, Chinese Academy of Sciences, Beijing, Department of Climate and Global Change, Nanjing University, Nanjing, Jiangsu Province, P. R. China, 210093

6 Department of Atmospheric Science, Nanjing University, 22 Hankou Road , Nanjing, Jiangsu Province, P. R.China, 210093

7 State Key Laboratory of Atmospheric Boundary Layer Physics and Atmospheric Chemistry, Chinese Academy of Sciences, Beijing, P. R. China, 100029

8 Department of Atmospheric Science, Nanjing University, Nanjing, Jiangsu Province, P. R. China, 210093

9 Chinese Academy of Meteorological Sciences (CAMS), CMA, Beijing, P. R. China,100081

ABSTRACT

Visual range (VR) data from 1981 to 2005 are examined for 20 meteorological monitoring sites in the Yangtze River Delta Region (YRDR) of China. Cumulative percentile analysis was used to construct VR trend. The 25-year average domain average 50% VR was about 21.9 ± 1.9 km. Domain average 50% VR decreased from 1981 to 2005 with a trend of -2.41 km /decade. The worst 20%, 50% and best 20% VR and variation rates for the 20 sites are analyzed. The 50% VR of the town, county-level city and prefecture-level city sites are 24.1 km, 21.5 km and 19.4 km, respectively. The best 20% VR decreased fastest with the rate -3.5 km/decade. Regional median VR decreased from the coastal sites to the inland sites. Ridit analysis and cumulative percentile have been adopted to study the VR variation properties between economically developed areas (e.g., Nanjing and Hangzhou) and remote areas (e.g., Lvsj). The two analyses both show that VR decreased in Nanjing and Hangzhou while remained constant in Lvsj from 1981 to 2005.

KEYWORDS

Variation, Yangtze River Delta, China , Visual range

Introduction

Visual range (VR) refers to the maximum distance, usually horizontal, at which a given object or light is visible under particular conditions of atmospheric light transmission and background luminance^[1]. VR impairment is caused by scattering and absorption of light by fine particles and gases in the atmosphere^[2] which are aggravated under some weather conditions^[1]. In an uncontaminated atmosphere, VR normally ranges from 145 km to 225 km^[3] and is limited by scattering from O₂ and N₂ molecules. VR can be < 1 km at polluted sites^[4].

Long-term VR trends^[5] and the influence of major pollutants on local VR^[6] have been examined. Husar et al.^[4] summarized spatial and temporal patterns of haziness in the eastern United States using four historical data bases. Mahowald et al.^[7] studied global VR trends related to dust sources and man-made factors. Park et al.^[8] compared the contribution of natural and transboundary pollution influences to regional VR in the United States. Watson^[9] discussed some of the limitations of VR as related to more objective measure of light extinction at a point and along a select path. At the same time, VR analysis methods such as ridit analyses^[10] and cumulative percentiles which are based on statistical technique were developed. Sloane^[11-12] examined U.S. VR trends while Doyle and Dorling^[5] showed VR trends for the UK.

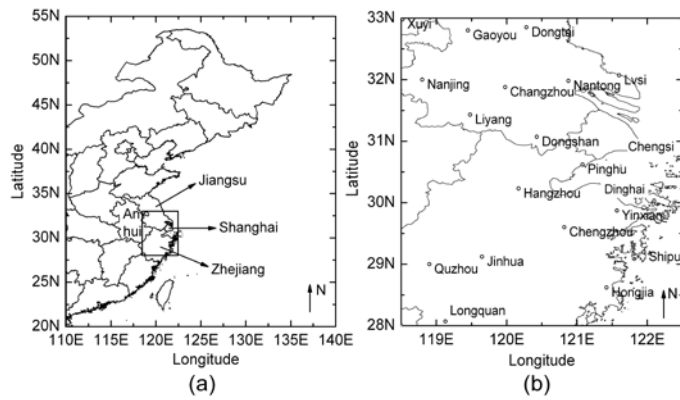
In China, Che et al.^[13] compared VR trends in China from 1981 to 2005 finding a significant decrease in VR (-2.1 km per decade from 1990 to 2005). Fan et al.^[14] analyzed VR trends around Beijing, Tianjin and Tangshan and showed that VR decreased from 1980 to 2003 with the steepest decline during summer. Song et al.^[15] related VR degradation to particle pollution in Beijing. Hong et al.^[16] found that VR decreased in Hangzhou, part of the Yangtze River Delta Region (YRDR), from average values of 10 km in the 1980s to 7 km in the first decade of the 21st century. Chang et al.^[1] found the impact of industrialization on VR from 1973 to 2007 in Shanghai. This study adds to these studies of VR in China by composing track among major cities in the YRDR.

Data and Methodology

The YRDR study area locates in the east of China(Figure1(a)), and it includes Shanghai, the eastern part of the Anhui Province (west of 118.5°E), the southern part of the Jiangsu Province (north of 33°N), and the northern part of the Zhejiang Province (south of 28°N). VR data as well as several meteorological variables, including relative humidity (RH) and

precipitation were obtained from China Meteorological Administration(CMA)/National Meteorological Center (<http://cdc.cma.gov.cn>) for each sites(Figure 1(b)) in this region for the 25-year of 1981 to 2005. Well trained observers measure the visual range using reference objects, such as buildings and mountains, in different directions at known distance from the observer. The data uncertainty is 0.1 km according to visibility observation guideline of China Meteorological Administration which was promulgated in 1980 ^[13].The industrial output data for Jiangsu, Shanghai and Zhejiang and Energy consumption in Jiangsu were obtained from www.stats.gov.cn. and www.Jssb.gov.cn, respectively.

Figure1. Locations of the YRDR (a) and its 20 sites (b). Area in the small box of (a) is the YRDR.



VR was recorded by our site observers 4 times (0200, 0800, 1400 and 2000, local standard time) per day at each station. The afternoon (1400, LST) readings are used in these analysis to minimize effects of morning radiation fogs and air pollutants trapped in shallow radiation inversions.

If the purpose of trend analysis is to detect any alterations of air quality because of man's activities then natural influence on air quality needs to be unfolded from the data ^[11]. In this study, VR measurements corresponding to precipitation were eliminated from the dataset¹⁰. As particle growth is affected by high RH which decreases VR ^[17], the data set was further limited to RH <90% ^[5]. The frequency of sand and dust storms was less than 1 time per year from 1954 to 1998 in the YRDR ^[18]. Asian dust^[19] is not detected in large quantities in the YRDR as it is at position further north, so sand or dust storms are retained in the data set. There are about 50.3% samples left out of the total possible in the analyzed data set. The fewest and most samples occurred in Quzhou (~42.9%) and Xuyi (~60.0%), respectively. As the ridit theory is adequately documented ^[10, 20-21], Ridit analysis is used. For example, VR observations for Nanjing site during 1981 to 2005 play the role of reference distribution V , and VR observation in 1981 is a comparison group X . Five VR categories (i.e., $K=5$) were selected according to Fan et al. ^[14]: 0-1.9 km, 2-9 km, 10-19 km, 20-39 km, and > 40 km.

Referring formulas in the appendix, the mean ridit of the VR observations in 1981 $\bar{r} = 0.66$ is obtained. This implies that VR in 1981 tends to be better than it was during the period 1981 to 2005 in Nanjing site. With sample size of 199 and 5226 respectively for X and V, the variance of \bar{r} is estimated by the equation in the appendix and this gives the test statistic $U = 9.24$. If we set confidence level $\alpha = 0.01$, we get $U_\alpha = 2.32$, i.e., at level $\alpha = 0.01$, VR in 1981 is better than it was during 1981 and 2005.

In this study we divided a year into the four seasons (i.e. March-April for Spring, June-August for Summer, September- November for Autumn, and December-February for Winter) and did separate Ridit analysis over time to examine the annual and seasonal VR trends of Nanjing, Hangzhou and Lvsj [5]. Different sites have different locations, populations and emission sources, so their VR distributions are different from each other. At each site, a reference distribution was obtained for 25-year or each season by pooling all the observations for the 25-year or that season. Ridit values are not comparable between different sites and seasons as they have different reference distributions. U has been calculate for each mean ridit, it is found that except for 2 to 3 mean ridits around the value 0.5, all the values pass the U -test at the confidence level $\alpha = 0.01$. Ridit analysis can be not only used to detect the general trend over a whole time period, but also can be used to determine whether or not a pollution strategy instituted at a particular time had been effective in improving visibility by examining the slope representing the periods before and after the policy changed [10].

Cumulative percentiles are also examined to compose visibility among the different measurement sites. The i - th cumulative percentile is the VR that is equal to or exceeds i percent of the time [22]. VR cumulative frequency distribution function is given by:

$$\frac{n_i}{n} = \int_{v_i}^{\infty} f(v)dv \quad (\text{Eq.1})$$

where $f(v)$ is the VR frequency distribution function. There are n_i observations that are equal or greater than v_i in n observations. Thus, the i - th cumulative percentile is given by

$$\frac{n_i}{n} \times 100\% .$$

5 categories just the same categories used in ridit analysis were provided here. The U.S. regional haze rule [23] uses the upper 20-th percentile of chemical extinction to represent “poor” VR and the lower 20-th percentile of chemical extinction to represent “good” VR, and this study uses the same convention. The worst 20%, 50%, and best 20% VR for the 20 sites from 1981 to 2005 have been calculated.

Linear regression analysis has been adopted to characterize long-term trends of VR. In this study VR rate denotes the slope of linear regression of VR against year. All VR rates pass the

t- test with confidence level 99% unless it is expressly stated. The worst 20%, 50% and best 20% 25-year average VR and rate for 20 sites in the YRDR are shown in Table 2. Domain average VR is the average value of the 20 sites' VR. The worst 20%, 50% and best 20% domain average VR values and variation trends are shown in Table 2 and Figure 2. Median visibility is frequently used to summarize visibility observations. In this study 50% VR (i.e. median VR) was used to represent level of VR of each site as it is a commonly used statistic and is readily understood^[24], and the result are shown in Figure 3.

Results and Discussion

VR properties of the YRDR

Variation trends of the worst 20%, 50% and best 20% VR are summarized in Figure 2 and Table 1. These can then be examined in order to identify either increasing, decreasing or combination of trends over time. The worst 20%, 50% and best 20% VR have similar fluctuations from 1981 to 2005. The worst 10% domain average VR degraded at a rate of 1.6 km per decade with a decline of 4 km over 25 years. The highest VR was 16.1 km in 1984 and the lowest value was 11.9 km in 2002. 50% VR decreased 6.0 km over the 25 years at a rate of 2.4 km per decade attaining the highest value 24.6 km in 1981 and the minimum of 18.1km in 2002. Best 20% VR declined at a rate of 3.5 km per decade with a decline of 8.8 km from 1981 to 2005. 50% VR rates of decline are on the order of the -2.1 per decade found by Che et al^[13].

Figure 2 . The worst 20%, 50% and best 20% domain average VR trends of the YRDR. Dashed lines are the linear regression curves of corresponding trend lines.

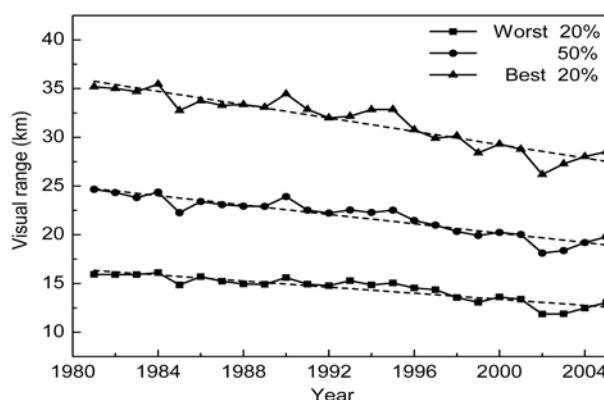


Table 1. The worst 20%, 50% and best 20% 25-year average VR and their rates in the YRDR.

Population	Site	Worst 20% VR		50% VR		Best 20% VR	
		VR (km)	Rate(km/ decade)	VR (km)	Rate(km/ decade)	VR (km)	Rate(km/ decade)
<500,000 (town)	Chengsi	13.7±1.4	-1.6	25.7±2.9	-3.1	40.5±3.6	-2.5
	Lvsi	22.4±0.8	0.1*	29.8±1.5	-0.2*	37.2±2.5	-0.6*
	Shipu	13.7±1.3	-1.5	21.8±2.7	-3.0	35.5±1.8	-1.6
	Longquan	20.9±1.8	-0.6	28.6±1.1	-1.0	36.1±1.1	-1.4
	Pinghu	14.4±1.1	0.1*	23.8±1.6	1.0	33.6±0.7	0.5*
	Quzhou	8.5±2.3	-0.1*	15.2±2.0	-1.5	25.6±4.5	-5.1
Average		15.6±5.1	-0.6	24.2±5.0	-1.3	34.8±5.3	-1.8
<1,500,000 (county-level city)	Dinghai	12.8±1.3	-1.6	20.4±2.0	-2.0	34.1±1.5	0.4*
	Chengzhou	13.0±0.9	-0.4*	19.5±2.2	-0.9*	32.8±3.2	-0.9*
	Xuyi	15.3±3.0	-2.7	22.9±5.0	-5.3	31.1±6.1	-7.0
	Yinxian	13.4±1.1	-0.7*	19.2±2.7	-2.0	30.3±5.1	-5.8
	Dongshan	11.0±1.6	-1.9	16.5±2.0	-2.4	25.3±5.2	-6.2
	Liyang	11.1±1.4	-0.1*	16.7±1.9	-1.8	25.7±5.7	-6.0
	Gaoyou	19.2±2.1	-0.7*	27.6±1.0	-0.6*	35.5±1.0	-0.9
	Dongtai	22.1±1.8	-1.8	28.9±1.0	-1.0	35.5±0.4	-0.4
	Jinhua	12.1±0.3	0.1*	16.1±0.6	-0.2*	21.9±3.0	-2.1
	Nantong	18.5±3.4	-2.7	26.6±2.6	-2.3	34.8±1.2	-1.2
Average		14.9±3.8	-1.3	21.4±4.8	-1.9	30.7±4.8	-3.0
>1,500,000 (prefecture-level city)	Hongjia	14.6±2.9	-3.7	22.8±4.3	-5.7	34.1±3.0	-3.7
	Changzhou	16.5±5.0	-6.1	23.3±6.2	-7.5	30.3±7.5	-8.7
	Nanjing	8.5±2.6	-3.2	16.5±4.3	-5.6	26.6±7.0	-9.2
	Hangzhou	7.8±2.1	-2.5	15.1±3.0	-3.5	26.4±5.7	-6.8
Average		11.9±4.4	-3.9	19.4±4.2	-5.6	29.4±3.2	-7.1
Domain	average	14.5±4.3	-1.6	21.9±4.9	-2.4	31.6±4.9	-3.5

Note: VR denotes the 25-year average VR value. VR rate with * represents the station reject the *t*-test at the confidence level of 0.01.

The 20 sites are categorized by town, county-level city and prefecture-level city according to population in Table 1. From Table 1, we can find that town sites have the highest worst 20%,

50% and best 20% VR and the prefecture-level city sites have the lowest. Smaller communities appear to have better visibility than larger cities. Quzhou is located in the Jinqu Basin with Qu River passing through it. Poor ventilation may lead to its low 50% VR just like Chengdu in the western Sichuan Basin as they have similar terrain features^[1, 25]. Only Pinghu site who is in the category of town sites shows upward trend for the worst 20%, 50% and best 20% VR. Many of the town sites have smaller worst decrease rates or even increase rates. Almost all the prefecture-level city sites have higher VR decrease rate than the other two category sites have. The best 20% decrease rate is greater than worst 20% or 50% VR decrease rate for most sites.

Figure 3. Spatial distribution of the 5-year average median (i.e. 50%) VR (km): (a) the first 5 years (i.e. from 1981 to 1985) and (b) the last 5 years (i.e. from 2001 to 2005). The interpolation error created by sparse sites in the south-west of Liyang, the coastal and south-east of Longquan should be considered in analysis.4. Ridit plot for Nanjing, Hangzhou, and Lysi.

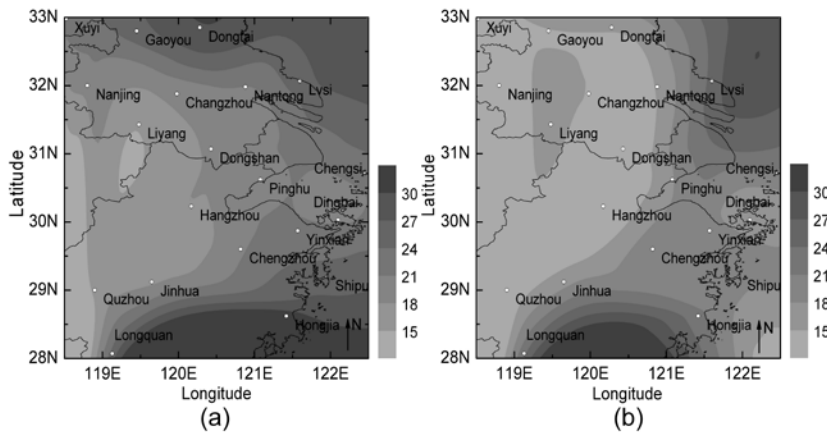


Figure 3 is five-year mean median VR of the first 5 years (i.e. 1981-1985) and the last 5 years (i.e. 2001-2005). Regional VR decreased from the coast to the inland. Kim et al.^[26] found that VR improved at two inland urban sites when cleaner air mass originated over the Pacific Ocean. The coastal sites rather than the inland sites will be the first to be affected by the clean air from the ocean, so clean air from the ocean may be one of the reasons why VR decreased from the coastal to the inland. Figure 3 contrasts the pre-development and post-development periods in the region. VR decreased at every site over the YRDR except for a few undeveloped sites along the coast. Median VR in Nanjing, Changzhou, Hangzhou and Dongshan (at Suzhou city) which has been developing fast since 1980 decreased from the grade 18-21 km to the grade less than 15 km.

Inter-comparision of VR of Nanjing, Hangzhou and Lysi

Urban sites Nanjing and Hangzhou and non-urban site Lysi are examined in more detail in Figure 4 and 5. Nanjing and Hangzhou are provincial capitals of Jiangsu and Zhejiang. Lysi town is located in the north-east of the YRDR, and it is a small town revolving around the fishing industry.

Figure4. Ridit plot for Nanjing, Hangzhou, and Lysi. A mean ridit value 0.5 means there is no difference with respect to the reference distribution, while less than 0.5 means lower VR and greater than 0.5 means better VR.

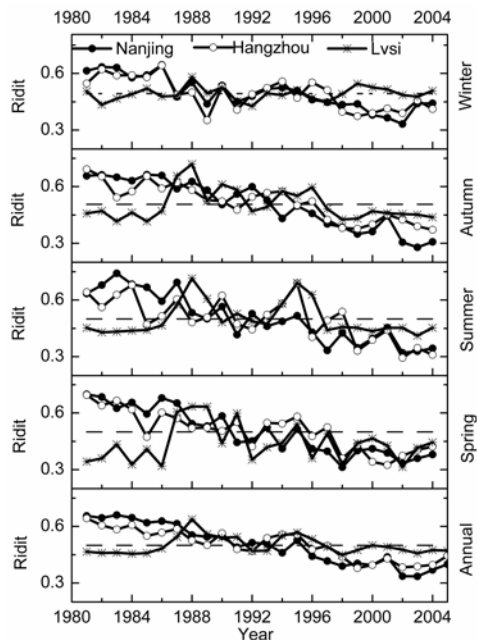
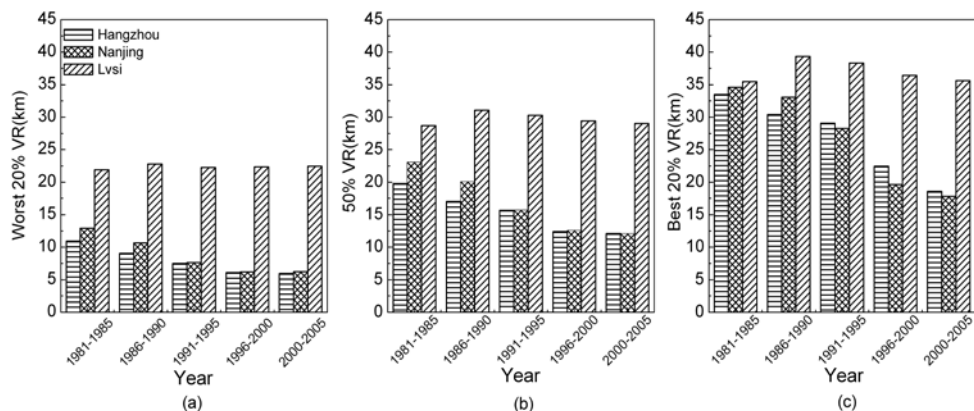


Figure 5.Five-year averaged VR of the worst 20% (a), 50% (median) (b), and best 20% (c) at Nanjing, Hangzhou and Lysi.



Results from the Ridit analysis are shown in Figure 4. The annual Ridit curves of Nanjing decreases from 1981 to 2005. The Ridit has a value above 0.5 before 1991, suggesting that the VR was better before 1991 in comparison to the entire period. The Ridit values were

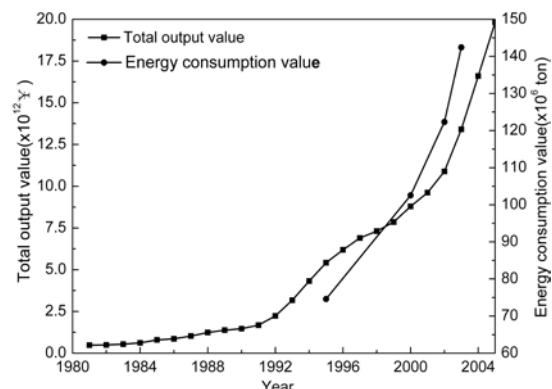
around 0.5 from 1992 to 1995, which could be regarded as the transition period. After 1996, the Ridit values were lower than 0.5, indicating that the annual average VR was worse than the entire record. The transition period for winter was within the period 1987 to 1996, and for spring it was 1987 to 1996. The transition period for summer occurred from 1991 to 1999. Even without a transition period, autumn VR became worse when compared to the post-1993 record length. Except for different transition periods, the seasonal Ridit value curves have trends that are similar to the annual one. The annual and seasonal Ridit trends at Hangzhou are similar to those at Nanjing, but Lvsi is different. Instead of degradation during the entire observation period, the annual and seasonal Ridit values remained almost constant. There was a steep change where the annual and seasonal Ridit values in 1988 went above 0.5, showing that the VR was better in 1988 compared to the entire period.

Figure 5(a) shows VR distances during the worst 20% days. VR at Lvsi are exceeding those in Nanjing and Hangzhou. VR during the worst 20% days is around 22 km at Lvsi, but only 4-12 km at Nanjing and Hangzhou. VR improved at Lvsi while decreasing at Nanjing and Hangzhou. 50% VR at Lvsi was 30 km in Figure 5(b). At Nanjing, VR decreased from 28 km to 12 km between 1981 and 2005. At Hangzhou, 50% VR decreased from 20 to 12 km. Lvsi had the highest best 20% VR in the value of 38 km from 1986 to 1995, and downward trends have been observed from 1981 to 2005 in Nanjing and Hangzhou.

The relationship between VR and development

Figure 6 shows industrial output for Jiangsu, Shanghai and Zhejiang increasing by a factor of 40 from 1981 to 2005. Energy consumption also increased since 1995 in Jiangsu along with economic development. Pollution controls were not a high priority during this growth, and primary particles and precursor were emitted into the atmosphere. The correlation coefficient between 50% VR over the YRDR and the total industrial output is -0.87, consistent with increasing uncontrolled pollutant emissions that follow economic growth.

Figure 6. Total industrial output values of Jiangsu, Shanghai and Zhejiang and energy consumption values in industrial enterprises of Jiangsu.



SUMMARY OR CONCLUSION

Cumulative percentile analysis was used to construct VR trend. The 25-year average domain average 50% VR was about 21.9 ± 1.9 km. Domain average 50% VR decreased from 1981 to 2005 with a trend of -2.41 km /decade. The domain average worst 20% and best 20% VR have a decrease rate of -1.6 and -3.5 km/decade respectively. The worst 20%, 50% and best 20% VR and variation rates for the 20 sites are analyzed. The 50% VR of the town, county-level city and prefecture-level city sites are 24.1 km, 21.5 km and 19.4 km, respectively. The best 20% decrease rate is greater than worst 20% or 50%VR decrease rate for most sites. Regional median VR decreased from the coastal sites to the inland sites.

Ridit analysis and cumulative percentile analysis have been adopted to study the VR variation properties between economically developed areas (e.g., Nanjing and Hangzhou) and remote areas (e.g., Lvs). The two analyses both show that VR decreased in Nanjing and Hangzhou while remained constant in Lvs from 1981 to 2005. Economic grow rapidly in the YADR. Pollution controls were not a high priority during this growth, and primary particles and precursor were emitted into the atmosphere. This may be the main reason why VR experienced a decrease trend in the YRDR.

ACKNOWLEDGMENTS

This research is supported by National Basic Research Program of China (No. 2010CB428503, 2009CB723904), Research and Development Special Fund for Public Welfare Industry of China Meteorological Administration (GYHY201006047) and the CAMS Basis Research Project (2009Z01).

REFERENCES

- [1] Chang, D.; Song, Y.; Liu, B. Visibility Trends in Six Megalopolis in China 1973–2007; *Atmos. Res.* **2009**, *94*(2), 161-167.
- [2] Leung, Y.K.; Wu, M.C.; Yeung, K.K. A Study on the Relationship among Visibility, Atmospheric Suspended Particulate Concentraten, and Meteorological Conditions in Hong Kong; *Acta Meteorologica Sinica*, **2009**, *23*(2), 250-260.
- [3] U.S. Environmental Protection Agency, Visibility in Mandatory Federal Class I Areas (1994–1998); EPA-452/R-01-008; Office of Air Quality Planning and Standards, Research Triangle Park, NC, **2001**.
- [4] Husar, R. B.; Holloway, J.M.; Patterson, D.E.; Wilson, W.E. Spatial and Temporal Pattern of Eastern U.S. Haziness: A Summary; *Atmos. Environ.* **1981**, *15*, 1919-1928.
- [5] Doyle, M.; Dorling, S. Visibility Trends in the UK 1950– 1997; *Atmos. Environ.* **2002**, *36*(19), 3136-3172.
- [6] Schichtel, A.S.; Husar, R.B.; Falke, S.R.; Wilson, W.E. Haze Trends over the United

- States, 1980–1995; *Atmos. Environ.* **2001**, *35*(30), 5205–5210.
- [7] Mahowald, N. M.; Ballantine, J.A.; Feddema, J.; Ramankutty, N. Global Trends in Visibility: Implications for Dust Sources; *Atmos. Chem. Phys.* **2007**, *7*, 3309–3339.
- [8] Park, R.J.; Jacob, D.J.; Kumar, N.; Yantosca, R.M. Regional Visibility Statistics in the United States: Natural and Transboundary Pollution Influences, and Implications for the Regional Haze Rule; *Atmos. Environ.* **2006**, *40*(28), 5405–5423.
- [9] Watson, J. G. Visibility: Science and Regulation - 2002 Critical Review; *J. Air Waste Manage. Assoc.* **2002**, *52*(6), 628–713.
- [10] Craig, C. D.; Faulkenberry, G. D. The application of ridit analysis to detect trends in visibility. *Atmos. Environ.* **1979**, *13*(12), 1617–1622.
- [11] Sloane, C.S. Visibility trends- I. Methods of analysis. *Atmos. Environ.* **1982**, *16*(1), 41–51.
- [12] Sloane, C.S. Visibility trends-II. Mideastern United States 1948–1978. *Atmos. Environ.* **1982**, *16*(10), 2309–2321.
- [13] Che, H.Z.; Zhang, X.Y. Horizontal Visibility Trends in China 1981–2005; *Geophys. Res. Lett.* **2007**, *34*, doi:10.1029/2007GL031450.
- [14] Fan, Y.Q.; Li, C.Q. Visibility trends in Beijing, Tianjin and Hebei Province during 1980–2003; *Plateau Meteorology* **2008**, *27*(6), 1392–1400 (in Chinese with English abstract).
- [15] Song, Y.; Tang, X.Y.; Fang, C.; Zhang, Y. H.; Hu, M.; Zeng, L.M.; Li, C.C.; Mao, J. T.; Bergin, M. Relationship between the Visibility Degradation and Particle Pollution in Beijing; *Acta scientiae Circumstantiae* **2003**, *23*(4), 468–471 (in Chinese with English abstract).
- [16] Hong, S.M.; Jiao, L.; He, X.; Bao, Z.; Sun, H.L.; Xu, H.; Ma, W. L.; Yang, L.; He, J.P. Variation of Visibility in Hangzhou Urban and Their Relation with Major Factors; *China Powder Science and Technology* **2009**, *15*(2), 56–61 (in Chinese with English abstract).
- [17] Tang, I.N.; Wong, W.T.; Munkelwitz, H.R. The relative importance of atmospheric sulfates and nitrates in visibility reduction; *Atmos. Environ.* **1981**, *15*, 2463–2471.
- [18] Zhou, Z.J. Blowing-sand and Sandstorm in China in Recent 45 Years; *Auaternary Sceince*. **2001**, *21*(1), 10–17.
- [19] Cai, C.X.; Jiang, W.M.; Huang, S.H. Chemical Characteristic of Two Dust storms in The South-east Coastal Area of China and Its Possible Origin; *Plateau Meteorology* **2000**, *19*(2), 179–186.
- [20] Faulkenberry, D.; Craig, C. D. The Application of Ridit Analysis to Detect Trends in Visibility - Reply. *Atmos. Environ.* **1980**, *14*(10), 1205–1206.
- [21] Beder, J. H.; Heim, R. C. On the use of RIDIT analysis; *Psychometrika* **1990**, *55*(4), 603–616.
- [22] Holzworth, G.E.; Maga, J.A. A Method for Analyzing the Trend in Visibility; *J. Air*

Pollut. Control. Ass. **1960**, 10(6), 430-435.

[23] U.S. Environmental Protection Agency. Regional Haze Regulations: Final Rule. 40 CFR Part 51; *Fed. Regist.* **1999**, 64 (126), 35714-35774.

[24] Lee, D. O. The Choice of Visibility Statistics in the Analysis of Long Term Visibility Trends in Southern England. *Weather.* **1988**, 43, 332–338.

[25] Li, Z.; Fu, G.; Hao, L. Climatologic Characteristics of Fog and Visibility in the Sichuan Basin Region. *Periodical of Ocean University of China.* **2007**, 37, 191–196 (In Chinese with English abstract).

[26] Kim, Y.J.; Kim, K.W.; Kim, S.D.; Lee B.K.; Hane, J.S. Fine Particulate Matter Characteristics and Its Impact on Visibility Impairment at Two Urban Sites in Korea: Seoul and Incheon; *Atmos. Environ.* **2006**, 40(Supplement 2): 593-605.

APPENDIX

Let V and X be the role of reference group and comparison group. K VR categories were selected. Referring Beder and Heim^[21], we let

$$q_k = P(V = k), \quad p_k = P(X = k), \quad k = 1, \dots, K \quad (\text{Eq.1})$$

and we denote the column vectors $(q_1, \dots, q_K)'$ and $(p_1, \dots, p_K)'$ by $\hat{\mathbf{q}}$ and $\hat{\mathbf{p}}$, respectively,

which are probability distributions on $\{1, \dots, K\}$. Such vectors are probability distributions on $\{1, \dots, K\}$.

The k -th ridit for the reference sample is

$$\hat{r}_k = \begin{cases} \frac{q_1}{2} & \text{for } k = 1, \\ q_1 + \dots + q_{k-1} + \frac{1}{2}q_k & \text{for } k > 1, \end{cases} \quad (\text{Eq.2})$$

and for the comparison sample is

$$\hat{t}_k = \begin{cases} \frac{p_1}{2} & \text{for } k = 1, \\ p_1 + \dots + p_{k-1} + \frac{1}{2}p_k & \text{for } k > 1. \end{cases} \quad (\text{Eq.3})$$

The mean ridit of the comparison with respect to the reference group is given by

$$\bar{r} = R(\hat{\mathbf{p}} | \hat{\mathbf{q}}) = \sum_{k=1}^K \hat{r}_k \hat{p}_k. \quad (\text{Eq.4})$$

And the variance of $r(X)$ is

$$\sigma^2 = \sum_{k=1}^K r_k \hat{p}_k^2 - (\sum_{k=1}^K \hat{r}_k \hat{p}_k)^2. \quad (\text{Eq.5})$$

If the roles of the two groups interchanged, we have the variance of $t(V)$

$$\tau^2 = \sum_{k=1}^K t_k \hat{q}_k^2 - (\sum_{k=1}^K \hat{t}_k \hat{q}_k)^2. \quad (\text{Eq.6})$$

The test statistic is U given by

$$U = \frac{\bar{\bar{r}} - R(\mathbf{p} | \mathbf{q})}{(Var(\bar{\bar{r}}))^{1/2}}. \quad (\text{Eq.7})$$

It is considered likely that VR in X would be higher than VR in V. And it was desired to test this hypothesis. In the terms of our introduction, the conjecture was that $P(V < X)$ would exceed 1/2. Then $R(\mathbf{p} | \mathbf{q})$ is a proxy for $P(V < X)$, and the problem becomes the testing the hypotheses

$$H_0 : R(\mathbf{p} | \mathbf{q}) \leq \frac{1}{2}.$$

The test statistic U is given by eq (7) with $R(\mathbf{p} | \mathbf{q}) = 0.5$ and H_0 is rejected if U is large.

The sample sizes for X and V were m and n, respectively. From eq (4), (5), (6), The variance of $\bar{\bar{r}}$ is estimated by

$$Var(\bar{\bar{r}}) = \frac{\sigma^2}{m} + \frac{\tau^2}{n} \quad (\text{Eq.8})$$

This gives the value U. If we set confidence level $\alpha = 0.01$, we get $U_\alpha = 2.32$, i.e., if $U > U_\alpha$, then we rejected H_0 at level $\alpha = 0.01$ and VR X is better than average VR level in V (equations 1-8 all from Beder and Heim [21]).

Simulation of Aerosol Optical Properties and Direct Radiative Forcing with RAMS-CMAQ in East Asia

Xiao Han¹, Meigen Zhang¹ and Cui Ge¹

1 State Key Laboratory of Atmospheric Boundary Layer Physics and Atmospheric Chemistry, Institute of Atmospheric Physics, Chinese Academy of Sciences, Beijing, China, 100029.

ABSTRACT

The air quality modeling system RAMS-CMAQ is developed to assess aerosol direct radiative forcing by linking simulated meteorological parameters and aerosol mass concentration with the aerosol optical properties/radiative transfer module in this study. The module is capable of accounting for important factors that affect aerosol optical properties and radiative effect, such as incident wave length, aerosol size distribution, water uptake, and internal mixture. Subsequently, the modeling system is applied to simulate the temporal and spatial variations in mass burden, optical properties, and direct radiative forcing of diverse aerosols over East Asia throughout 2005. Model performance is fully evaluated using various observational data, including satellite monitoring of MODIS and surface measurements. It is determined that the modeled aerosol optical depth (AOD) is in congruence with the observed results from the AERONET, the CSHNET, and the MODIS. The model results suggest that the strongest forcing effect ranging from -12 to -8 W/m² was mainly distributed over the Sichuan Basin and the eastern China's coastal regions in the all-sky case at TOA, and the forcing effect ranging from -8 to -4 W/m² could be found over entire eastern China, Korea, Japan, East China Sea, and the sea areas of Japan. Additionally, the model domain is divided into seven regions based on different administrative divisions or countries for investigating the detail information about ADRF spatial and temporal variations over East Asia in this paper. The model results indicate that the ADRF of sulfate, ammonium, BC, and OC were stronger in summer and weaker in winter over most regions of East Asia, except the South East Asia. However, the seasonal variation for ADRF of nitrate exhibited opposite trend. The strong ADRF of dust mainly appeared in spring over Northwest China and Mongolia.

KEYWORDS

CMAQ, AOD, aerosol direct forcing

Introduction

Atmospheric aerosols are an important component of the climate system that can affect the planetary energy balance and climate directly (by scattering and absorbing radiation) and indirectly (by modifying the amounts, life-times, and microphysical and radiative properties of clouds)^[1]. Since anthropogenic aerosols are very difficult to distinguish from natural ones using observation techniques (e.g., in situ measurements or satellite remote sensing) alone^[2], aerosol modeling is an indispensable primary way to estimate the aerosol effects on climate. Since the 1990s, numerous studies have attempted to simulate global aerosol-climate interactions using diverse types of global models coupled with different aerosol dynamic schemes^[3-7]. However, due to uncertainties in emissions and the complexity of the aerosol life cycle as well as the processes connecting the physical properties of aerosols to radiative forcing, global values of anthropogenic aerosol radiative forcing vary widely across models, ranging from -0.9 to -0.1 W/m² for direct forcing and from -1.8 to -0.3 W/m² for indirect forcing^[1].

In order to reduce uncertainties in aerosol radiative forcing estimates, detailed knowledge of the regional aerosol distribution, chemical composition, and mixing state are required. Thus, the impact of aerosols on climate must be understood and quantified on a regional scale rather than just as a global mean. For East Asia, the most populated and rapidly developing region in the world during the last few decades, aerosol and aerosol precursor emissions have been perturbed dramatically by the significant population growth and human activities. There are a number of estimates for the aerosol radiative forcing over East Asia (or China)^[8-16], but most of them focused on anthropogenic sulfate, mainly because its anthropogenic source is large and well known, and its microphysical properties are also known. However, as Ghan et al.^[2] note, all radiatively important aerosols must be treated in order to gain a precise estimate of the aerosol radiative forcing.

An aerosol optical properties/radiative transfer module is developed and incorporated into the RAMS-CMAQ modeling system. The module includes a parameterization for obtaining the aerosol optical properties under an internally mixed state, and a radiative transfer scheme for simulating the aerosol radiative effect in clear-sky and all-sky case. The major aerosol species, namely sulfate, nitrate, ammonium, black carbon, organic mass, dust, and sea salt, are considered in this modeling system. The detailed aerosol microphysical and dynamical properties are implemented for obtaining more realistic model results. The geographic distributions of aerosol optical depth (AOD) and direct radiative forcing over East Asia in

2005 were simulated and analyzed.

Experimental Methods

In this study, the air quality modeling system RAMS-CMAQ is used to simulate the meteorological data fields and spatial and temporal distribution of mass concentrations and size distributions of major aerosol species. The numerical prediction model RAMS^[17] has good capacity on simulating the boundary layer and underlying surface simulation. CMAQ is an Eulerian-type model developed by the U. S. Environmental Protection Agency. It simulates concurrently the atmospheric and land processes affecting the transport, transformation, and deposition of air pollutants and their precursors, on both regional and urban scales. The updated and expanded version of the Carbon Bond mechanism (CB05)^[18] was applied to simulate the gas-phase chemistry mechanisms and address the vapor phase precursors. The ISORROPIA model^[19] and the Regional Particulate Model (RPM)^[20] were used to calculate the thermodynamic equilibrium between inorganic aerosol species and gas-phase concentrations, and simulate the processes of aerosol dynamics in CMAQ, such as new particle production, coagulation, and condensation. The aerosol size distributions of Aitken mode, accumulation mode, and coarse mode in output results are assumed follow lognormal distributions.

A parameterization developed by Ghan et al.^{[7], [21]} is applied to calculate the aerosol optical properties (AOP), including extinction coefficients, single scatter albedo, and the asymmetry factor over the model domain. This method is suitable for any aerosol model that uses lognormal size distributions composed of internal mixtures of multiple aerosol components. It uses the Chebyshev polynomials to fit specific optical properties precalculated by the Mie theory under all possible ambient conditions, and creates a set of fitting coefficient tables which are applied to determinate the real aerosol optical properties in modeling system. Compared to other methods (e. g. lookup table or semiempirical method), this parameterization can provide more complete information of aerosol physical without expensive computation through the fitting step. The radiative transfer scheme CAMRT which was originally used in CAM3 for calculating the aerosol radiative effects in the climate system is modified and utilized in this study. The scheme covers the entire shortwave band, and considers cloud influence and gaseous molecule absorptions. CAM4 (released in April, 2010) still applied CAMRT because of its rationality and practicability.

Results and Discussion

1. Comparison with Measurement Data

To evaluate the model results, we compare the modeled AOD (550 nm) with the ground-based in situ measurements of AERONET (Aerosol Robotic Network) and CSHNET (Chinese Sun Hazemeter Network)^[22-24]. Here, comparisons at eight sites with relatively longer-term representative observations in East Asia are presented. There are two AERONET sites (Beijing and Shirahama) and six CSHNET sites (others). These sites are located in different environments, including urban (dominated by anthropogenic aerosol sources), agricultural (influenced by both natural aerosols and anthropogenic aerosols), and remote areas (dominated by natural aerosol sources). These comparisons can serve as a reference to determine, in part, whether the simulations of aerosol optical properties are realistic.

Figure 1 shows the time series comparison between observed and modeled daily average AOD, and the monthly mean scatter plots of modeled and observed AOD at eight surface sites, which are Beijing, Shirahama, Shanghai, Fengqiu, Sanjiang, Haibei, Changbai Mountain, Beijing Forest. The solid line is 1:1, and the dot-dashed lines are 1:2 and 2:1, respectively. Table 1 presents the site information and statistical parameters of the comparison between observed and modeled daily mean data.

Figure 1. Time series plot of regional daily mean modeled and observed AOD during 2005, and scatter plot of the monthly average modeled and observed AOD. The solid line is 1:1, and the dot-dashed lines are 1:2 and 2:1, respectively.

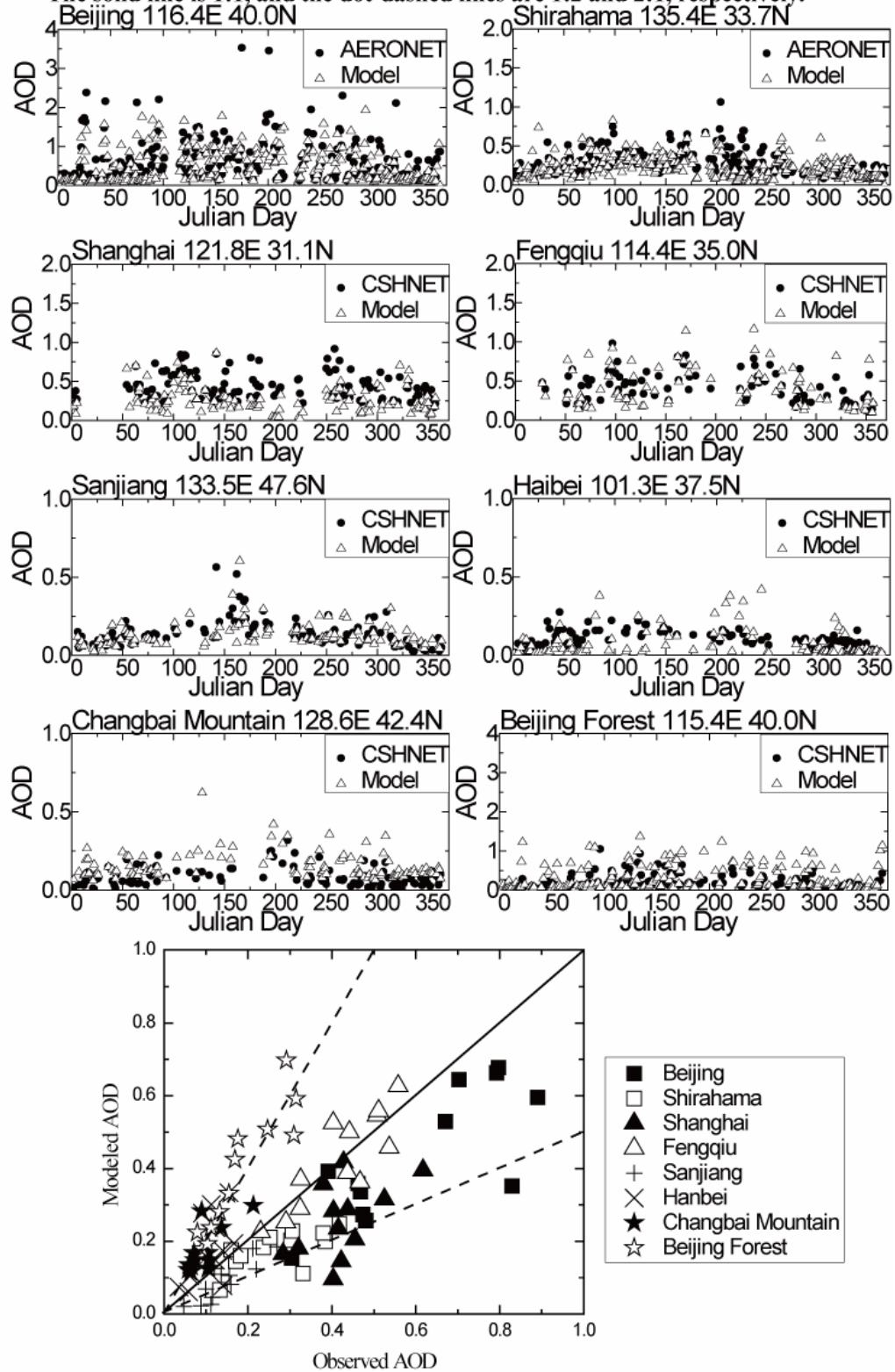


Table 1 Statistical summary of the comparisons of the daily average aerosol mass concentrations between simulations and surface observations

	Site	N^a	C_{obs}^b	C_{mod}^c	σ_{obs}^d	σ_{moe}^e	R^f
1	Beijing	285	0.58	0.50	0.57	0.44	0.60
2	Shirahama	287	0.27	0.23	0.15	0.14	0.58
3	Shanghai	122	0.44	0.34	0.17	0.21	0.56
4	Fengqiu	88	0.41	0.51	0.19	0.27	0.74
5	Sanjiang	121	0.14	0.13	0.09	0.08	0.53
6	Haibei	118	0.09	0.14	0.06	0.15	0.44
7	Changbai Mountain	115	0.08	0.15	0.06	0.08	0.49
8	Beijing Forest	205	0.17	0.36	0.16	0.35	0.80

^a Number of samples.

^b Total mean of observations.

^c Total mean of simulations.

^d Standard deviation of observations.

^e Standard deviation of simulations.

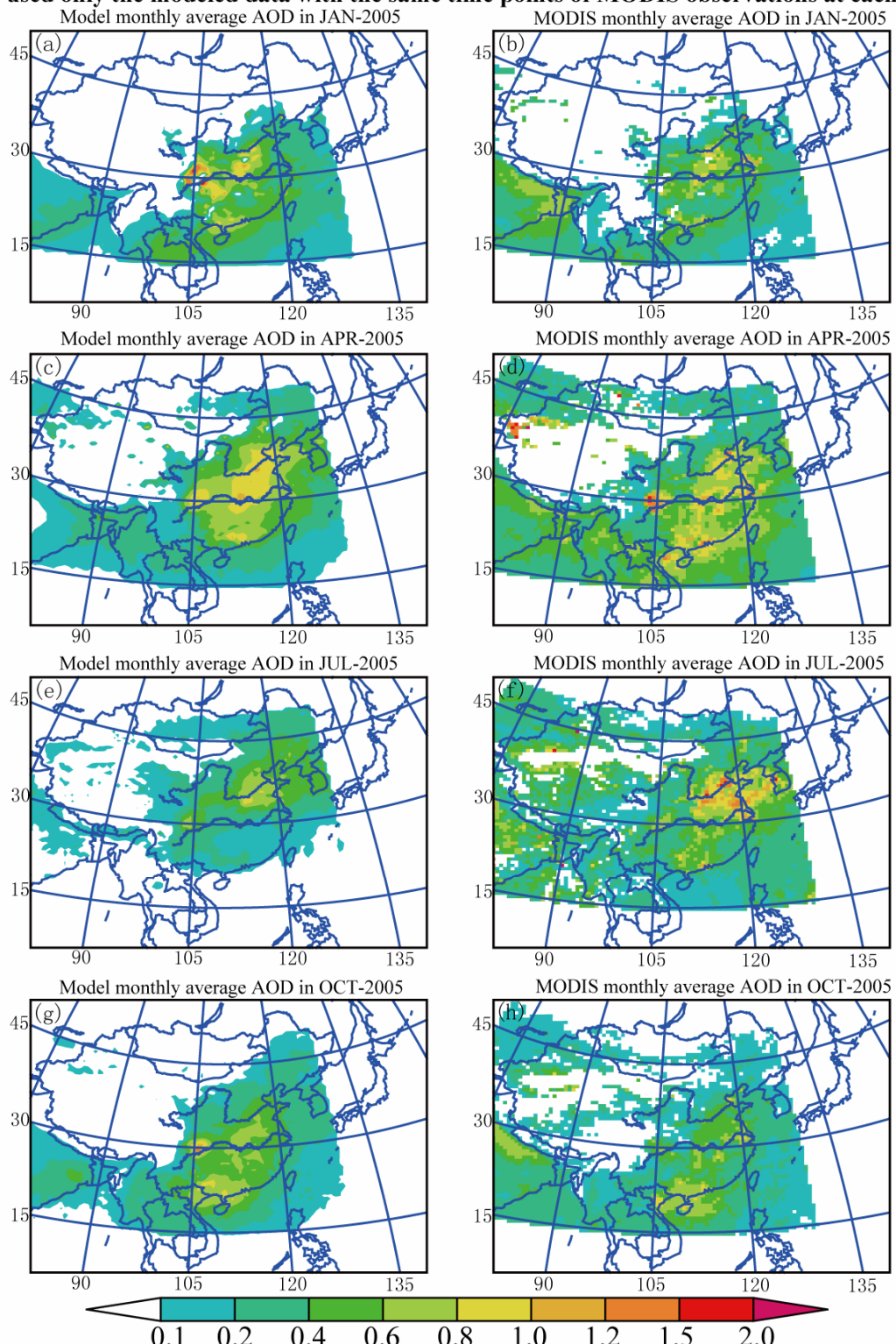
^f Correlation coefficient between daily observation and simulation.

The comparison results show that the modeling system performs well on simulating the aerosol optical properties. The total means and Standard deviations between simulations and measurements are quite close to each other, and the correlation coefficients are larger than 0.5 at most of the surface sites. However, from the scatter plot it can be found that the modeled AOD is relatively higher than observed AOD at Beijing Forest site. The possible reason is this site is close to Beijing urban area, and the low resolution of the model is difficult to capture the large differences between Beijing center and the surrounding areas. It also can be found that the modeled AOD is relatively lower than observed AOD at Shanghai site. This is mainly because of the local influence from anthropogenic emissions, and because the model results are interpreted as the average of each grid cell, which does not reflect local perturbations.

Figure 2 presents the monthly average AOD distributions of simulation and MODIS monitoring in January, April, July, and October. We can see that the modeled AOD broadly

captured the distribution patterns of MODIS observations in these four months, especially over high value regions such as the Sichuan Basin and the southeastern part of China. However, differences between the simulations and the observations over Tibet and South China for the month of July still existed. For differences over Tibet, a probable reason may be that the monitoring AOD was overestimated due to the inverse method over the relatively larger surface reflection^[25]. For differences over South China, it is probably because of the underestimate of less aerosol burden due to modeled higher wet deposition over this area.

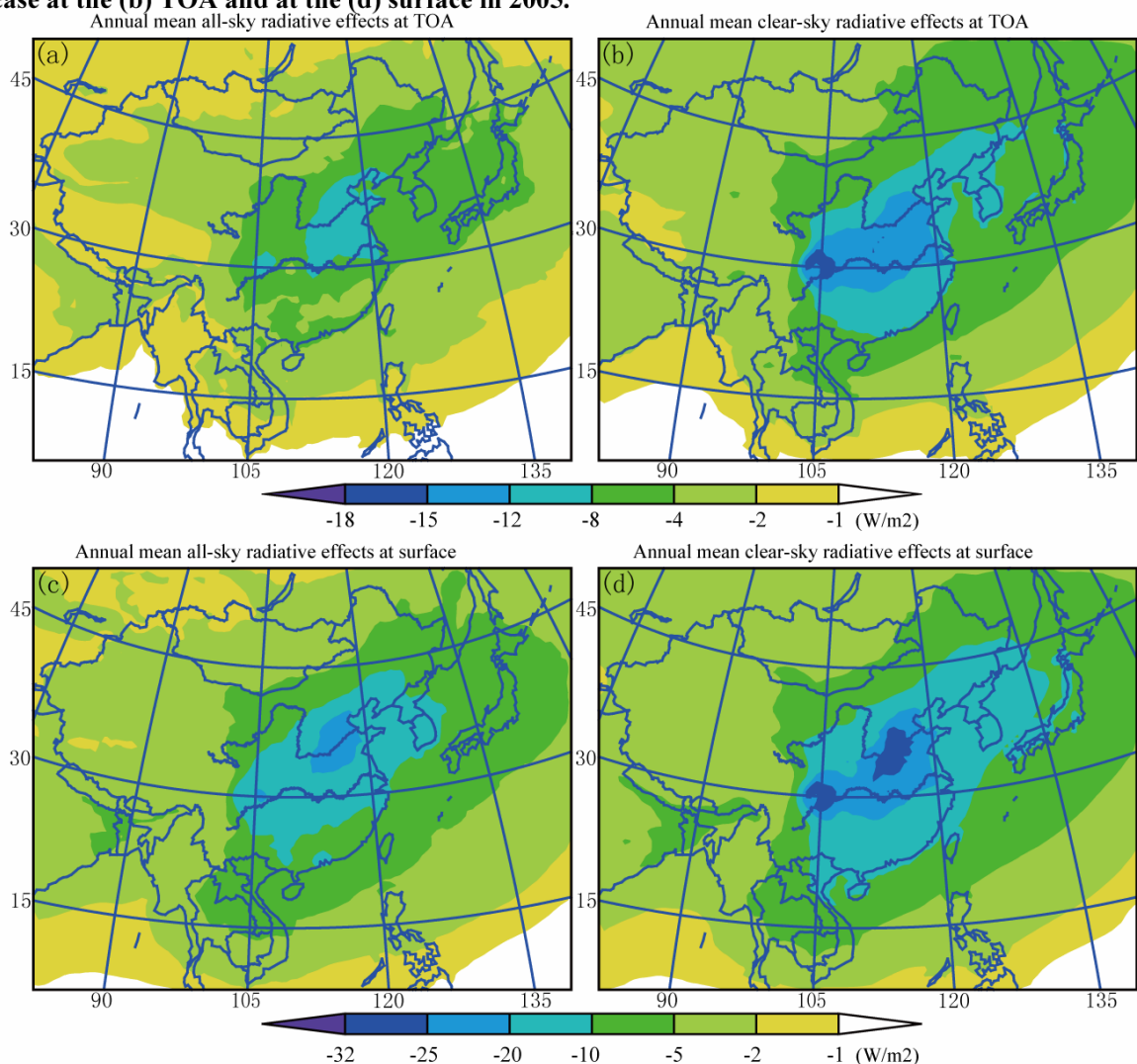
Figure 2. Spatial plots for the monthly average AOD at 550 nm from simulation (left) and MODIS monitoring data (right) in January (a-b), April (c-d), July (e-f), October (g-h) in 2005. The simulation results used only the modeled data with the same time points of MODIS observations at each grid.



2. Model results

Figure 3 shows the annual mean of modeled aerosol direct radiative forcing (ADRF) in clear-sky and all-sky cases at the top-of-the-atmosphere (TOA) and at the surface over East Asia in 2005. We can see that the ADRF was mostly negative because the incident solar radiation was largely reflected by the aerosol particles of sulfate, nitrate, and ammonium, which were the major aerosol species in this region. The negative effects in the all-sky case were obviously smaller than those in the clear-sky case due to the extinction effect of the clouds. In the all-sky case at the TOA, the strongest negative effects ranging from -12 to -8 W/m^2 mainly appeared over the Sichuan Basin, Central China, and the eastern China coastal regions. The relatively low values of ADRF ranging from -8 to -4 W/m^2 could be found over entire eastern China, Korea, Japan, East China Sea, and the coastal areas of Japan.

Figure 3. Spatial plots for the annual mean of modeled aerosol direct radiative forcing (W m^{-2}) in the all-sky case at (a) TOA and at (c) surface; and modeled aerosol direct radiative forcing in the clear-sky case at the (b) TOA and at the (d) surface in 2005.



For investigating the detail information about ADRF spatial and temporal variations over East Asia, the model domain is divided into seven regions broadly based on different administrative regions or countries. Figure 4 illustrates the geographical scopes of these regions.

Figure 4. Model domain and the sub-regions divided for investigating the detail information about for comparing different aerosol contributions to the aerosol direct radiative forcing.

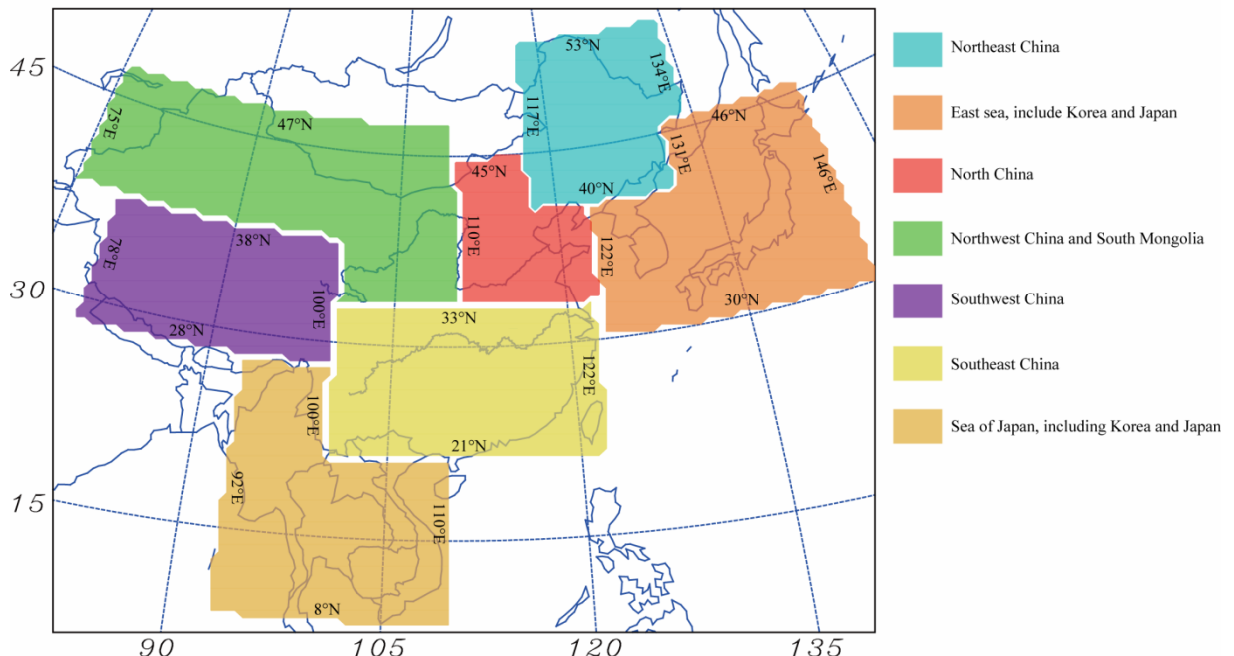
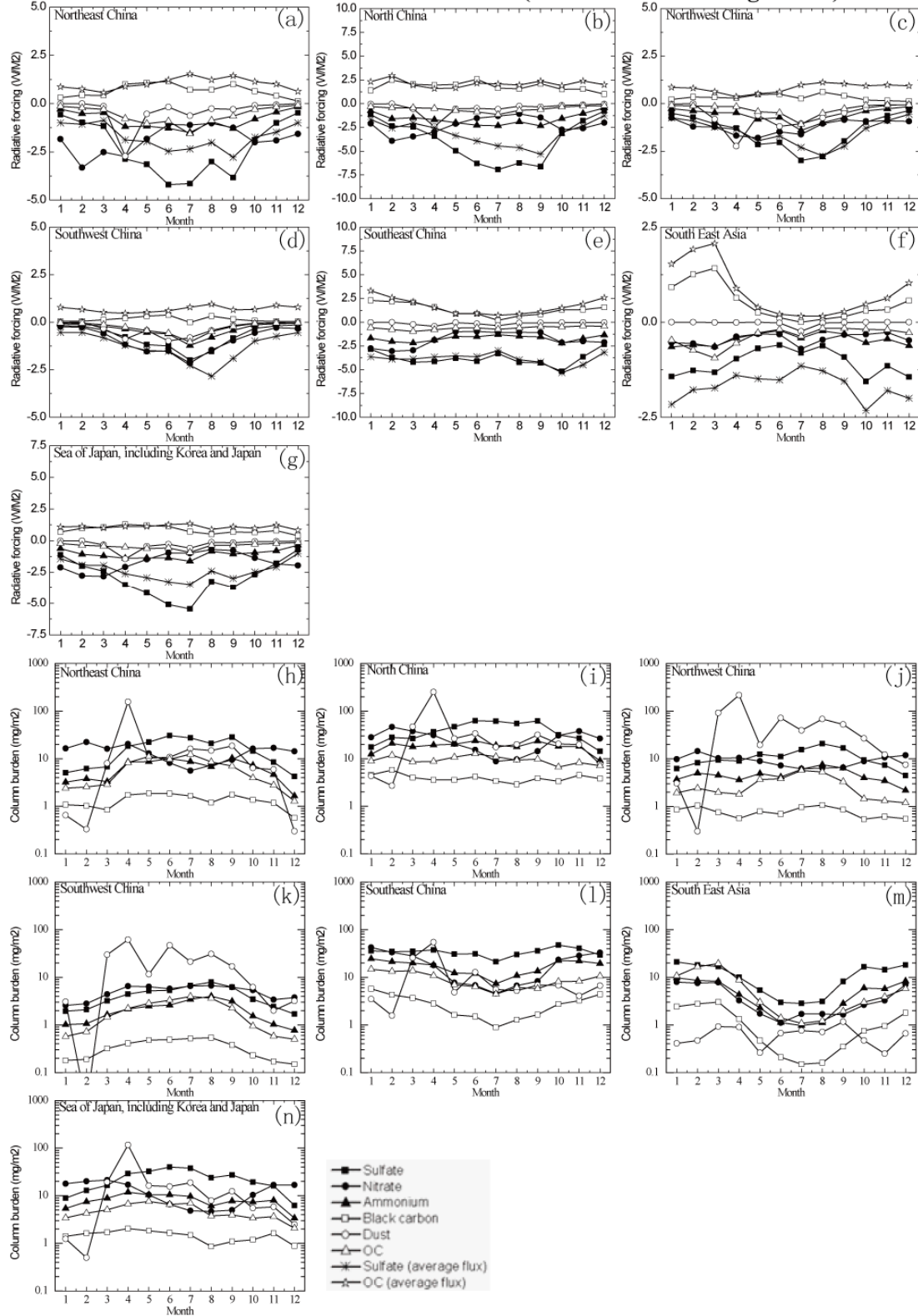


Figure 5 presents the time series changes of monthly average ADRF and column burden of aerosol mass concentrations in each region. From Figure 5 it can be found that the radiative forcing of sulfate, nitrate, and ammonium were stronger than other aerosol species due to their high mass concentrations and the water uptake properties over most regions. For seasonal variations, the radiative forcing of sulfate and ammonium were stronger in summer and weaker in winter over most regions except South East Asia. However, the nitrate presented opposite variation trend over all seven regions because the weak photochemical activity of its precursor brought about more nitrate mass concentration during winter time. The radiative forcing of dust was stronger than (or broadly equal to) those of sulfate and nitrate during spring time over Northeast China, North China, Northwest China, and South Mongolia. However, it was hardly to find strong radiative forcing derived from dust during other seasons.

Figure 5. Monthly means for the direct radiative forcing (a-g) and column burden of mass concentrations (h-n) of six major aerosol species over Northeast China, North China, Northwest China, Southwest China, Southwest China, Southeast China, South East Asia, and Sea of Japan, including Korea and Japan. The direct radiative forcing of sulfate and BC under fixed solar radiant flux is also shown (marked with "average flux").



CONCLUSION

In this study, an aerosol optical properties/radiative transfer module was developed and incorporated into the air quality modeling system RAMS-CMAQ to simulate aerosol mass concentrations, optical properties, and ADRF over East Asia in 2005. In the module, the parameterization method for obtaining aerosol optical properties considers all major impact factors, including particle size distribution, water uptake, incident wave length, and internal mixture of different aerosol components without expensive computation. The radiative transfer scheme CAMRT was used to calculate the radiation net field and obtain the ADRF in clear-sky and all-sky cases at the surface and the TOA. The major aerosol species, including sulfate, nitrate, ammonium, black carbon, organic carbon, dust, and sea salt were all included in this modeling system. The modeled results were compared to the multiple observation data of ground-based in situ measurements and satellite monitoring for evaluating accuracy and reliability. The distribution features of monthly and annual means of ADRF over East Asia were also analyzed in this study.

The strongest negative effect, which ranged from -12 to -8 w/m² in the all-sky case at the TOA was evident over the Sichuan Basin, central China, and eastern China's coastal regions, and was much stronger than the global average value [26]. Upon analyzing the distribution features of cloud fraction and modeled ADRF in clear-sky and all-sky cases, it was found that the ADRF was evidently weakened by the cloud extinction. Monthly average ADRF over seven different regions of East Asia were also summarized in this paper. The results show that sulfate, nitrate, and ammonium provided major contributions to ADRF over East Asia, and their negative radiative effects were concentrated over North China and Southeast China.

REFERENCES

- [1] Intergovernmental Panel on Climate Change (IPCC), Changes in Atmospheric Constituents and in Radiative forcing, in Climate Change 2007. Cambridge Univ. Press, New York, 2007.
- [2] Ghan, S., Easter, R. C., Chapman, E. G., et al., A physically based estimate of radiative forcing by anthropogenic sulfate aerosol, *J. Geophys. Res.*, 2001a, *106(D6)*, 5279–5293.
- [3] Liu, X., Pernner, J. E., Das, B., et al., Uncertainty in global aerosol simulation: Assessment using three meteorological data sets, *J. Geophys. Res.*, 2007, *D11212*, doi:10.1029/2006JD008216.
- [4] Liao, H., and Seinfeld, J. H., Global impacts of gas-phase chemistry-aerosol interactions on direct radiative forcing by anthropogenic aerosols and ozone, *J. Geophys. Res.*, 2005, *D18208*,

doi:10.1029/2005JD005907.

- [5] Wang, M., Penner, J. E., Liu, X., Coupled IMPACT aerosol and NCAR CAM3 model: Evaluation of predicted aerosol number and size distribution, *J. Geophys. Res.*, 2009, *D06302*, doi:10.1029/2008JD010459.
- [6] Zhang, K., Wan, H., Zhang, M., et al., Tropospheric aerosol size distributions simulated by three online global aerosol models using the M7 microphysics module, *Geophys. Res. Abs.*, 2008, *10*, EGU2008-A-06153.
- [7] Ghan, S., Laulainen, N., Easter, R., et al., Evaluation of aerosol direct radiative forcing in MIRAGE, *J. Geophys. Res.*, 2001b, *106 (D6)*, 5295–5316.
- [8] Zhang, L., and Shi, G., The simulation and estimation of radiative properties and radiative forcing due to sulfate and soot aerosols, *Chinese J. Atmos. Sci. (in Chinese)*, 2001, *25(2)*, 231–242.
- [9] Wang, X., and Shi, G., Estimation of the direct radiative forcing due to anthropogenic sulfate over Eastern Asia, *Plateau Meteor. (in Chinese)*, 2001, *20(3)*, 258–263.
- [10] Qian, Y., Leung, L. R., Ghan, S. J., et al., Regional climate effects of aerosol over China: Modeling and observation, *Tellus B*, 2003, *55*, 914–934.
- [11] Ma, X., Shi, G., Guo, Y., et al., Simulation of radiative forcing by sulfate aerosols, *Climatic Environ. Res. (in Chinese)*, 2004, *9(3)*, 454–464.
- [12] Gao, L., Wang, T., Fu, Y., et al., Modeling sulfate aerosol and its radiative forcing over China, *Plateau Meteor. (in Chinese)*, 2004, *23(5)*, 612–619.
- [13] Li, S., Wang, T., Zhuang, B., et al., Indirect radiative forcing and climatic effect of the anthropogenic nitrate aerosol on regional climate of China, *Adv. Atmos. Sci.*, 2009, *26(3)*, 543–552.
- [14] Wu, J., Jiang, W., Fu, C., et al., Simulation of the radiative effect of black carbon aerosols and the regional climate responses over China, *Adv. Atmos. Sci.*, 2004, *21(4)*, 637–649.
- [15] Wu, J., Fu, C., Jiang, W., et al., A preliminary simulation study of direct radiative forcing of mineral dust aerosol over the East Asia region, *Chinese J. Geophys. (in Chinese)*, 2005a, *48(6)*, 1250–1260.
- [16] Wu, J., Liu, H., Wang, W., et al., Simulation research of distribution transportation and radiative effect of black carbon aerosol in recent five spring seasons over East Asia region, *Chinese J. Atmos. Sci. (in Chinese)*, 2005b, *29(1)*, 111–119.
- [17] Cotton, W. R., Pielke, R. A., Walko, G. E., et al., RAMS 2001: Current status and futures directions, *Meteor. Atmos. Phys.*, 2003, *82*, DOI: 10.1007/s00703-001-0584-9.
- [18] Sarwar, G., Luecken, D., Yarwood, G., Whitten, G. Z., Carter, W. P. L., Impact of an updated carbon bond mechanism on predictions from the CMAQ modeling system: preliminary assessment. *J. Appl. Meteor. Climatol.*, 2008, *47*, 3-14.

- [19] Nenes, A., Pilinis, C., Pandis, S. N, Continued development and testing of a new thermodynamic aerosol module for urban and regional air quality models. *Atmos. Environ.*, 1999, 33, 1553-1560.
- [20] Binkowski, F. S. and Shankar, U., The regional particulate model, 1, Model description and preliminary results. *J. Geophys. Res.*, 1995, 100, 26191-26209.
- [21] Ghan, S. and Rahul, A. Z., Parameterization of optical properties for hydrated internally mixed aerosol. *J. Geophys. Res.*, 2007, 112, D10201, doi: 10.1029/2006JD007927.
- [22] Hollben, B. N., Eck, T. F., Slutsker, I., et al., AERONET—a federated instrument network and data archive for aerosol characterization. *Remote Sens. Environ.*, 1998, 16, 1-16.
- [23] Xin, J., Wang, Y., Li, Z., Wang, P., et al., AOD and Angstrom exponent of aerosols observed by the Chinese Sun Hazemeter Network from August 2004 to September 2005. *J. Geophys. Res.*, 2007, 112, D05203, 1-13.
- [24] Wang, L., Xin, J., Wang, Y., et al., Evaluation of the MODIS aerosol optical depth retrieval over different ecosystems in China during EAST-AIRE. *Atmos. Environ.*, 2007, 41, 7138-7149.
- [25] Xia, X., Chen, H., Wang, P., Validation of MODIS aerosol retrievals and evaluation of potential cloud contamination in East Asia. *J. Environ. Sci.*, 2004, 16, 832-837.
- [26] Bellouin, N., Boucher, O., Haywood, J., et al., Global estimate of aerosol direct radiative forcing from satellite measurements. *Nature*, 2005, 438, 1138-1141.

Reconstructed light extinction coefficient by chemical compositions of PM_{2.5} in winter in Urban Guangzhou, China

Jun TAO ^{1,2}, Ren-jian ZHANG ³, Jun-ji CAO ⁴, Lihua ZHU ^{1,2}, Tao ZHANG ¹, and Si SHI ²

1 South China Institute of Environmental Sciences, Guangzhou 510655, China

2 School of Environmental Science and Engineering of Sun Yat-Sen University, Guangzhou 510275, China

3 Institute of Atmospheric Physics, Chinese Academy of Sciences, Beijing 100029, China

4 Institute of Earth Environment, Chinese Academy of Sciences, Xi'an 710075, China

Principal Contact: Jun TAO, Associate professor, South China Institute of Environmental Sciences, 7 West Street, Tianhe District, Guangzhou, 510655.

Tel: +862085529552 Email: taojun@scies.org

Abstract

The objective of this study was to reconstruct light extinction coefficients by chemical compositions of PM_{2.5}. The online absorbing and scattering coefficients by nephelometer and aethalometer and PM_{2.5} samples were collected at the monitoring station of the South China of Institute of Environmental Science (SCIES) during January 2010. The measured b_{ap} and b_{sp} had significant correlation ($R^2 > 0.95$) with reconstructed b_{ap} and b_{sp} by modified IMPROVE formula, respectively. The result of source apportionment of b_{ext} showed that (NH₄)₂SO₄ was the largest contribution to the b_{ext} accounting for 33.6%, followed by ammonium nitrate (NH₄NO₃) (21.9%), POM (15.4%), elemental carbon (EC) (11.3%), sea salt (4.5%), NO₂ (9.2%) and other fractions (4.2%).

Keywords: Light extinction coefficients, PM_{2.5} aerosol, Chemical species

Characteristics of Carbon Aerosol Spectrum and Water Soluble Components Spectral in South China during 1988-2010 Period

Dui Wu¹ and Biting Liao²

1 Guangzhou Institute of Tropical Marine and Meteorology

2 Guangzhou Institute of Tropical Marine and Meteorology

ABSTRACT

By using the graded aerosol samples, which were determined in South China during 2006–2008 period, based on current analyzing methods of Elemental Carbon (EC), through comparative experiments, the proper experimental program of analyzing EC in historical samples are preliminarily established; The result shows, among the historical samples, only 4 group samples would melt over 700°C, and they are domestic glass fiber filter samples; while the others can bear the temperature as high as 870°C, they are domestic quartz fiber filter samples. It's reasonable and credible of using current heating program, “quartz parameter”, to analyze the historical domestic quartz samples, but not domestic quartz samples. Hereby, the EC spectrum and spectrum of water-soluble components over the past 23 years in South China will be studied and discussed according to different regions and different stages. Accordingly, provide valuable observational input parameters for the climate model assessing the regional climate and environmental change; thus, reduce the estimate value's uncertainty of aerosol radiative forcing.

KEYWORDS

South China , domestic quartz fiber filter samples, EC spectrum, spectrum of water-soluble components, aerosol radiative forcing

1.Introduction

Atmospheric aerosols are suspended in the atmosphere as solid or liquid particulates with the diameter ranging from 10^{-3} to 10 μm , they take up only one

billionth of the entire atmospheric mass but have great impacts on global climate, which has become an important research field on global change^[1-5]. In 1999 ,a 3-km thickness of “Asian Brown Cloud” was observed over South Asia .The brownish haze consists of a mixture of anthropogenic sulphate, nitrate, organics, black carbon, dust and fly ash particles and natural aerosols such as sea salt and mineral dust^[6]. Aerosols have important effects on human health, cloud formation, visibility, environmental quality, and the cycle of atmospheric trace constituents. Thus, there is a great interest in understanding the concentrations and distributions of carbonaceous aerosol in Asia atmosphere.

Carbonaceous aerosols include elemental carbon (EC), organic carbon (OC), and carbonate carbon (CC). Carbonate contributes less than 5% of total concentration of carbon. Carbonate contributes less than 5% of total concentration of carbon^[7]. As a result, only OC and EC are generally considered in carbonaceous aerosols^[8]. Due to its intense light absorptiveness, EC is also known as black carbon (BC), which has an important contribution to the radiative forcing of aerosols. It is a conventional viewpoint that aerosols cool the atmosphere. However, BC particles can directly absorb solar radiation at the lower troposphere, leading to heat the atmosphere. As a result, BC aerosols’ heating effect could offset the cooling effect of scattering aerosols^[9,10]. Recent studies suggest that in magnitude the direct radiative forcing of BC is between CO₂ and methane, making it the second most important factor in global warming^[11]. BC heat the air, alter regional atmospheric stability and vertical motions, and affect the large-scale circulation and hydrologic cycle with significant regional climate effects in China and India^[3]. Up to now, carbonaceous aerosols’ effect on the climatic change is also most un-certain, although many of the important atmospheric chemical reactions take place on the surface of the carbonaceous aerosols or are subjected to them. Aerosol particles are introduced into the atmosphere by a variety of natural and anthropogenic activities. Because of the diversity in the sources, their concentrations and compositions show significant spatial and temporal variations. This variability makes it difficult to assess the radiative forcing by aerosols on global scale^[12]. A clear understanding of the chemical composition of aerosols is also important in identifying their sources and sinks.

Knowledge of EC size distribution and the aerosols composition are essential in studying aerosol light extinction^[13,14]. EC size distribution measurements in the South China are limited. Gnauk et al.^[15] measured EC, OC, and a few selected organic compound classes in size-segregated aerosols in Xinken. Yu et al. reported EC size

distributions in Shenzhen and Guangzhou, two metropolitan cities in the PRD region^[16] and report the measurements of EC size distributions at five urban locations in Guangzhou from December 2006 to December 2007 in selected summer and winter months^[17]. Cao et al presented the concentrations and distributions of PM_{2.5}, PM₁₀, OC and EC from four cities (Hong Kong, Guangzhou, Shenzhen and Zhuhai) in the PRD Region^[18]. Wu et al analyzed the spectrum of mass and water soluble ion components and OC/EC of aerosol samples collected in Guangzhou from Sept. 2006 to Jan. 2007^[19]. In our study ,about 119 sets of samples were collected in South China during dry season and rainy season from 1988 to 2010 .The objective of this study was to present the nature of the spatial and temporal variation of the EC spectrum and spectrum of water-soluble over South China.

2. Carbonaceous Aerosol Analysis

Among our historical samples, only 4 group samples would melt over 700°C, and they are domestic glass fiber filter samples; while the others can bear the temperature as high as 870°C, they are domestic quartz fiber filter samples. Through comparative experiments, the proper experimental program of analyzing EC in historical samples are preliminarily established .It's reasonable and credible of using current heating program “quartz par” as Yu et al^[20,21], to analyze the historical domestic quartz fiber samples, while the domestic glass fiber filter ,samples using the “itmm_glass.par” .The “quartz par” and the “itmm_glass.par” are shown in table2. The terms OC1-OC4 and EC1-EC6 inside the parentheses refer to the amount of C released from the filter substrate corresponding to each temperature step.The location the locations of the measurement of cities are shown in the figure 1.

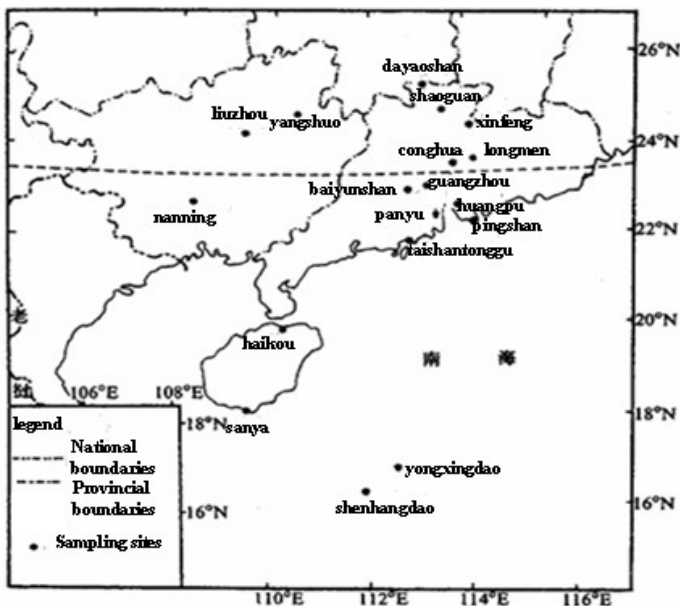


Figure 1 the locations of the measurement of cities and surrounding region

Table 1 Compotition Analysis Method

Method Type	Quartz-par		Itmm_glass.par	
Stage	Temp (°C)	Duration time	Temp (°C)	Duration time
Helium1	1	10	1	10
Helium2	310(OC1)	80	310(OC1)	80
Helium3	475(OC2)	60	475(OC2)	60
Helium4	615(OC3)	60	650(OC3)	120
Helium5	870(OC4)	90		
Cool_Helium1	0	45	0	45
<hr/>				
Oxygen1	550(EC1)	45	550(EC1)	45
Oxygen2	625(EC2)	45	625(EC2)	45
Oxygen3	700(EC3)	45	675(EC3)	120
Oxygen4	775(EC4)	45	700(EC4)	60
Oxygen5	850(EC5)	45		
Oxygen6	870(EC6)	-1	720(EC5)	-1
Oxygen7	870	45	720	45
Calibration Ox	1	110	1	110

3. Results and Discussion

3.1 The Averaged Concentration Of TC And EC

Table 2 The Averaged Concentration Of EC Over All Sampling Sites

Urban sites	TC(ug/m ³)		EC(ug/m ³)		rural sites	TC(ug/m ³)		EC(ug/m ³)	
	PM _{2.1}	PM ₁₀	PM _{2.1}	PM ₁₀		PM _{2.1}	PM ₁₀	PM _{2.1}	PM ₁₀
Huangpu	35. 4	46. 5	23.6	30.4	Fangcun	12.2	18.2	7.2	9.7
Shaoguan	13.0	18.9	8.2	10.2	Xinfeng	11.4	18	3.1	11.7
Nanning	20.9	26.7	6.5	8.1	Conghua	7.7	11.0	5.9	8.7
Liuzhou	12.3	17.3	12.4	14.2	Longmen	11.8	15.5	6.2	7.0
Guangzhou	13.5	22.4	8.6	12.6	Yangshuo	12.1	13.6	6.9	7.0
Baiyunshan	12. 5	15. 3	9.4	12.0	Dayaoshan	9.0	11.1	6.0	7.4
Yuexiu	13.6	23.3	7.6	11.9	Panyu	21.1	21.3	8.2	9.4
Redaisuo	24.5	38.7	11.1	12.4					
Tianhe	12.5	18.1	5.8	7.5					
averaged	17.6	25.2	10.4	13.2		12.2	15.5	6.2	8.7
	(69.6)	(78.1)				(78.5)		(71.4)	
Coastal sites	TC(ug/m ³)		EC(ug/m ³)		Islands	TC(ug/m ³)		EC(ug/m ³)	
	PM _{2.1}	PM ₁₀	PM _{2.1}	PM ₁₀		PM _{2.1}	PM ₁₀	PM _{2.1}	PM ₁₀
Sanya	7.1	11.3	3.7	4.5	Yongxing	3.5	5.2	1.2	1.7
Haikou	6.7	9.3	3.2	4.0					
Pingshan	14.2	23.0	4.1	4.8					
Tonggu	5.5	12.2	2.0	3.6					
averaged	8.4	14.0	3.7	4.4		3.5	5.2	1.2	1.7
	(60.0)	(82.7)				(67.3)		(70.6)	
South China.	10.4	15.0	5.4	7.0					
Ave	(69.4)	(76.3)							

A summary of the measurement results for average concentration of TC and EC 1988-2006 in the northern South China Sea and South China continent are given in Table 2. The highest loading of TC and EC were in HP, as high as 46.5 and 30.4 ug/m³, respectively, which may be due to a number of industrial emission located in the sampling point. The lowest loading of TC and EC were 5.2 and 1.7 ug/m³ in Yongxing, which may be related to its location being less affected by human activities.

The average TC concentration in PM_{2.1} and PM₁₀ were 10.4 and 15.0 ug/m³ and the average EC concentration in PM_{2.1} and PM₁₀ were 5.4 and 7.0 ug/m³, slightly higher than 6.1 ug/m³ of PRD obtained by Cao et al^[18], less than 25.3 ug/m³ in Beijing given by He et al^[22]. The average concentration of TC and EC in PM_{2.1} and PM₁₀ for the four regions were in the order of urban sites> rural sites>coastal sites>islands. The EC concentrations in all urban sites were almost higher than 8 ug/m³ , exceeding the haze reference standard ,which were about 3 times of the coastal sites and 7 times of the island , indicating that the high concentration of EC related highly to the process of urbanization.

On the average, 69.4% of TC and 76.3% of EC were associated with fine particle(PM_{2.1}) over the northern South China Sea and South China continent. The concentration of TC in PM_{2.1} in all sites were almost higher than 60 %, while the EC were above 70%, which was in agreement with prior studies that almost 75% of the total EC is mainly fine particles (PM₁)^[23].

SUMMARY

- 1、 The highest loading of TC and EC were in HP, as high as 46.5 and 30.4 ug/m³, respectively, while the lowest loading of TC and EC were 5.2 and 1.7 ug/m³ in Yongxingdao.
- 2、 The average concentration of TC and EC in PM_{2.1} and PM₁₀ for the four regions were in the order of urban sites> rural sites>coastal sites>islands.

REFERENCES

- [1] Penner J E, Dong X Q, Chen Y. Observational evidence of a change in radiative forcing due to the indirect aerosol effect. *Nature*, 2004, 427(6971): 231—234.
- [2] Lohmann U, Lesins G. Stronger constraints on the anthropogenic indirect aerosol effect. *Science*, 2002, 298(5595): 1012—1015.
- [3] Menon S, Hansen J, Nazarenko L, et al. Climate effects of black carbon aerosols in China and India. *Science*, 2002, 297(5590): 2250—2253.
- [4] Reddy M S, Venkataraman C. Atmospheric optical and radiative effects of anthropogenic aerosol constituents from India. *Atmos Environ*, 2000, 34: 4511—4523.
- [5] Babu S S, Moorthy K K. Anthropogenic impact on aerosol black carbon mass concentration at a tropical coastal station: A case study. *Curr Sci*, 2001. 81(9): 1208—1214.

- [6]Ramanathan.V., P. J. Crutzen, A. P. Mitra and D. Sikka, The Indian Ocean Experiment and the Asian Brown Cloud ,Current, Science, 2002,83(8): 947-955.
- [7] Japar S M, Brachaczek W W, Grose R A. The contribution of ele-ment carbon to the optical properties of rural atmospheric aerosols. Atmos Environ, 1986, 20: 1281—1289.
- [8] Clarke A G, Karani G N. Characterisation of the carbonate content of atmospheric aerosols. J Atmos Chem, 1992, 14: 119—128.
- [9] Meinrat O A. The dark side of aerosols. Nature, 2001, 409: 671—672.
- [10] Houghton J T, Ding Y, Griggs D J, et al. IPCC Climate Change 2001: The Scientific Basis, Radiative Forcing of Climate Change. Cam-bridge: Cambridge University Press, 2001.
- [11]Jacobson M Z. Strong radiative heating due to the mixing state of black carbon in atmospheric aerosols. Nature, 2001, 409: 695—697.
- [12]Charlson, R., Schwartz, J. S. E., Hales, J. M., Cess, R. D., Coakley, J. A., Hansen, J. E. and Hoffmann, D. J., *Science*, 1992, **255**, 423—430.
- [13]Van de Hulst, H. C.: Light Scattering by Small Particles, New York,Dover, 470pp., 1981.
- [14]Bohren, C. F. and Huffman D. R.: Absorption and scattering of light by small particles, John Wiley, Hoboken, N. J., 1983.
- [15]Gnauk, T., Müller, K., van Pinxteren, D., He, L. Y., Niu, Y., Hu, M.,and Herrmann, H.: Size-segregated particulate chemical composition in Xinken, Pearl River Delta, China: OC/EC and organic compounds, Atmos. Environ., 2008,42, 6296—6309.
- [16] Huang, X. F., Yu, J. Z., He, L.Y., and Hu, M.: Size distribution characteristics of elemental carbon emitted from Chinese vehicles:Results of a tunnel study and atmospheric implications, Environ. Sci. Technol., 2006, 40, 5355—5360.
- [17] H.Yu,C.Wu,D.Wu, and J.Z.Yu,Size distributions of elemental carbon and its contribution to light extinction in urban and rural locations in the pearl river delta region,China, Atmospheric Chemistry and Physics, 2010,10,5107-5119.
- [18]Cao J.J., Lee S .C., Ho K. F. Zhang X. Y., Zou S.C., Chow J.C., Watson J.G., Characteristics of carbonaceous aerosol in Pearl River Delta Region ,China during 2001 winter period. Atmospheric Environment,2003. 37, 1451~1460.
- [19]Wu Dui,Chen Weichao. A primary study of the size-distribution and water soluble composition distribution of atmospheric aerosols over south China. JOURNAL OF TROPICAL METEOROLOGY,1994, 10(1): 85-96.
- [20] Yang, H. and Yu, J. Z. Uncertainties in charring correction in the analysis of elemental and organic carbon in atmospheric particles by thermal/optical methods [J].

- Environ. Sci. Technol. 2002, 36(23): 5199-5204.
- [21] Yu, J. Z., Xu, J. H. and Yang, H. Charring characteristics of atmospheric organic particulate matter in thermal analysis [J]. Environ. Sci. Technol. 2002, 36(4): 754-761.
- [22] He, K.B., Yang, F.M., Ma, Y.L., Zhang, Q., Yao, X.H., Chan,C.K., Cadle, S., Chan, T., Mulawa, P., 2001. The characteristics of PM_{2.5} in Beijing, China. Atmospheric Environment 35, 4959–4970.
- [23] Nunes, T.V., Pio, C.A., 1993. Carbonaceous aerosols in industrial and coastal atmospheres. Atmospheric Environment 27, 1339–1346.

Mixing and water-soluble characteristics of particulate organic compounds in individual urban aerosol particles

Weijun Li¹, Longyi Shao²

1 Environment Research Institute, Shandong University, Jinan, Shandong 250100, China.

2 State Key Laboratory of Coal Resources and Safe Mining & College of Geoscience and Surveying Engineering, China University of Mining and Technology, Beijing 100083, P.R. China

Principal Contact: Weijun Li, Ph.D, Shandong University, Shanda Nanlu 27, Jinan, Shandong Province 250100.

Phone: 86-531-88364416 Email: liweijun@sdu.edu.cn

*Corresponding author Email: ShaoL@cumtb.edu.cn Tel/Fax: 86-10-62331248 ext. 8523

Abstract

Particulate Organic Compounds (POCs) in the atmosphere can alter the morphology and hygroscopicity of inorganic particles by coagulation and mixing. Direct observations can illustrate the mixing of organic and inorganic particles. Compositions, mixing states, and morphologies of 360 aerosol particles from urban Beijing collected on TEM grids with Si-O substrate were obtained using transmission electron microscopy coupled with energy-dispersive X-ray spectrometry (TEM/EDX). The Si-O substrate used in this study allows TEM/EDX to detect carbonaceous particles internally mixed with inorganic particles. POCs were present in approximately 90% of the nitrate-coated mineral particles on both hazy and clear days. Approximately 73% of K- and S-rich particles contained organic coatings and organic inclusions/aggregations on hazy days, while 53% of S-rich particles on clear days during the Beijing Olympics contained only organic coatings. Water dialysis of individual particles indicated that the organic inclusions/aggregations in the K- and S-rich particles were insoluble in water but that POCs from the coatings of individual particles were soluble. The organic coatings on individual inorganic particles may influence their surface hygroscopicity and optical properties.

Source:

Li, W.J., and Shao, L.Y.: Mixing and water-soluble characteristics of particulate organic compounds in individual urban aerosol particles, J. Geophys. Res., 115 (D02301), doi:10.1029/2009JD012575, 2010.

Experimental Set-up to Measure Particle Deposition from Turbulent Flow in Large Ventilation Ducts: Application to Food Industries

Guillaume Da¹, Evelyne Géhin¹, Mourad Ben-Othmane², Michel Hivet² and Camille Solliec³

1 CERTES, Université Paris Est, 61 avenue du Général de Gaulle, 94010 Créteil, France

2 UMR GEPEA, ONIRIS, rue de la géraudière, 44322 Nantes, France

3 UMR GEPEA, Ecole des Mines de Nantes, 4 rue A. Kastler, 44300 Nantes, France

ABSTRACT

This study is a part of the French project CleanAirNet, which proposes to characterize particle deposition (bioaerosols) in large ventilation ducts, in order to develop appropriated cleaning recommendations for food industries. A small body of experimental literature has been reported on large ventilation ducts^[1]. The purpose of this paper was to investigate particle deposition experiments in large circular ducts at high Reynolds number flow. An experimental bench was designed in a laboratory to validate a theoretically based model predicting particle deposition velocities for fully developed turbulent flow^[2]. The experimental bench included a ventilation system, a monodisperse fluorescent aerosol generation system (VOAG), and direct-reading instruments to monitor the following parameters in real time: air-velocity, temperature, relative humidity, particle aerodynamic diameter (APS). The deposition of particles mass to different surface orientations (with respect to gravity) was calculated after removing the material deposited on the inside surface of the duct, and subsequently measuring the concentration of fluorescein by spectrofluorometry (FluoroMax, HORIBA). The particle mass deposited on filter was also determined by fluorescent techniques. Experiments conducted at 5 m/s (Reynolds number of 5×10^4) in the circular duct system (160 cm in diameter), showed great stability for the generation of particles with nominal size of 1, 4 and 6 μm ; with trials lasted for 5, 3 and 1 hour respectively. The fluorescent technique allowed measuring deposited mass particle down to $4 \times 10^{-11} \text{ kg}$. The experimental approach proposed in this study can be used to validate models on particle deposition in ventilation ducts from food factories, by considering large circular sections, turbulent flows, and thermal gradients for thermophoresis. The CleanAirNet project “Hygienic design of ventilation duct networks in food factories” is supported by the ANR (Agence Nationale de la Recherche).

KEYWORDS

Bio-aerosol, Particle deposition, Ventilation ducts, Turbulent flow, Food-industries, Particle size distribution, Indoor air quality

Introduction

In the food industry a better understanding of particle behavior in ventilation ducts is needed to maintain acceptable quality of air in factories. However, a small body of experimental literature has been reported on large ventilation ducts^[1]. Sippola and Nazaroff have addressed the specific case of liquid particle deposition in HVAC systems and ventilation ducts^[3]. The authors showed that for particle larger than about 0.1 μm , deposition velocities to distinct internal surfaces of ventilation duct (floor, wall, and ceiling) differ owing to the influence of gravity. Recently, Ben Othmane *et al.* examined deposition velocity to the ventilation-duct surfaces within food factories^[4]. The study is based on in-situ measurements in three factories, and showed that food factory ventilation systems were characterized by the following physical parameters: high Reynolds number Re ($1.7 - 6.0 \times 10^5$), fluid friction viscosity u^* (0.2-0.5) and roughness height k ($5-60 \mu\text{m}$)^[4]. The authors also noted that the concentration of particulate matter of aerodynamic diameters in the size range $0.3-20 \mu\text{m}$ varied from 0.2 to $1.7 \mu\text{g.m}^{-3}$.

Our objective was to develop a lab-scale experimental method to investigate solid particle deposition in large circular ventilation ducts encountered in the food industry. An experimental bench was designed at a laboratory scale, not only to recreate similar conditions than in the three different food factories, but also to validate a theoretically based model predicting particle deposition velocities in hydraulically smooth turbulent regime.

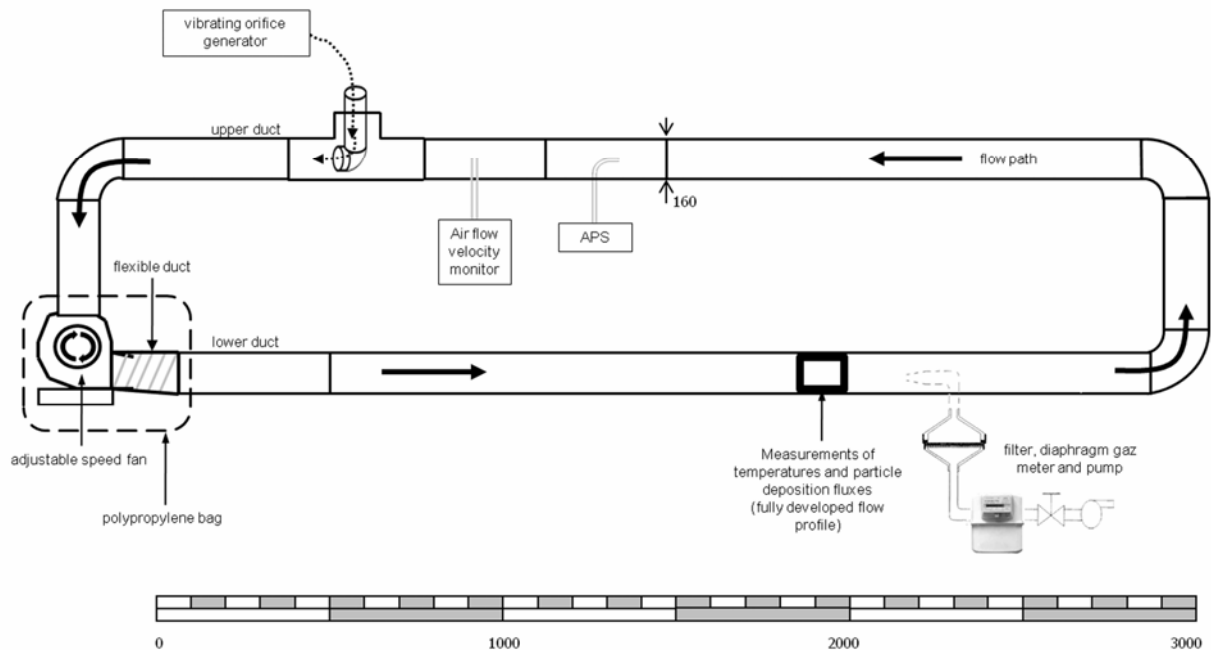
Experimental Methods

The experimental bench-duct system is presented on Figure 1. The apparatus included galvanized steel ducts with a ventilation device, a monodisperse fluorescent aerosol generator (VOAG model 3450, TSI), and direct-reading instruments to monitor the following parameters in real time: air-velocity, temperature, relative humidity, particle aerodynamic diameter (measured with an APS). The deposition of particles mass to different surface orientations, with respect to gravity, was calculated by wiping the fluorescent particles and subsequently by measuring their concentrations by spectrofluorometry^[5-6]. The deposition velocity, V_d (m.s^{-1}), was determined with:

$$v_d = \frac{m_{dep}}{S \cdot \Delta t \cdot C_{dep}} \quad (\text{Eq. 1})$$

where, m_{dep} (kg) is the deposited aerosol particle mass, S (m^2) is the surface, Δt (s) is the time period of the fluorescent aerosol in the bench, and C_{dep} ($\text{kg} \cdot \text{m}^{-3}$) is the mean mass aerosol concentration in the duct measured during the generation.

Figure 1. The experimental bench-duct system.



The VOAG used a liquid solution of ultra-pure water and sodium fluorescein (Figure 1). In our study, it is assumed that the generated residues are spherical and not porous^[7], and the sodium fluorescein density is $1530 \text{ kg} \cdot \text{m}^{-3}$. With these assumptions, the aerodynamic equivalent diameter (d_{ae}) can be solved with an iteration method.

Particle sampling on filter consisted of different equipments connected in series (Figure 1): a sampling inlet, transport lines, a stainless-steel filter-holder, a diaphragm gas-meter, a thermal mass flowmeter with pressure and temperature sensors, and a vacuum pump. The fluorescent solid particles were collected on a paper filter. The filter was immersed in a 20 cm^3 solution of water, and stored for fluorometric analysis.

Particle deposition fluxes to inside duct surfaces were measured where the turbulent flow had a fully developed flow profile. Surfaces to be analyzed for particle deposition were identified by a means of a stencil. The stencil was a thin sheet of leather with five surfaces. Each underlying surface window corresponded to different orientations from which the deposited particles were removed. The windows were associated with horizontal floor surface (0° upward facing), vertical wall surfaces (-90° and $+90^\circ$ vertically oriented), and intermediary surfaces (-40° and $+40^\circ$ upward facing). For each surface orientation, a lingette was used to wipe off the deposited material, and the lingette was immediately immersed in the remaining water for further analysis.

Fluorescent techniques, used to quantify airborne particle concentrations and particulate fluxes, were performed with a spectrofluorometer (FluoroMax-4, HORIBA-JOBIN YVON). The calibration on the sodium fluorescein mass concentration was obtained with standard solutions containing sodium fluorescein in the range 10^{-11} to 10^{-7} g.cm $^{-3}$. Uncertainties in concentration measurements which may arise from anisokinetic sampling, deposition losses in transport lines, cleaning procedures for collecting fluorescein, and dilution, were calculated and compared to experimental uncertainties.

Results and Discussion

Preliminary measurements were conducted to validate the operating conditions of the aerosol generator. Results showed that it was possible to generate highly monodispersed aerosol with aerodynamic diameter from 0.7 to 7.6 μm . For a given particle size, the validation of monodispersion was associated with low geometric standard deviation ($\sigma_g < 1.2$). The generated concentration varied from 4 to 36 cm $^{-3}$, and the total aerosol flow rate was 858 cm $^3\cdot\text{s}^{-1}$. These first experiments provided data for defining the operating conditions associated with the ventilation-duct bench. Up to 4 trials were performed for each nominal particle size to evaluate the repeatability of the experiments. A summary of measured particle and data from each experiment is presented in Table 1.

Table 1. Measured experimental parameters for different airborne solid particle nominal sizes during trials conducted in ventilation duct.

Parameters	1 μm	4 μm	6 μm
d_{ae} [μm]	1.2 ± 0.0	4.3 ± 0.2	7.3 ± 0.1
d_p [μm]	1.0 ± 0.0	3.5 ± 0.2	6.0 ± 0.1
u^* [m.s $^{-1}$]	0.25	0.25	0.25

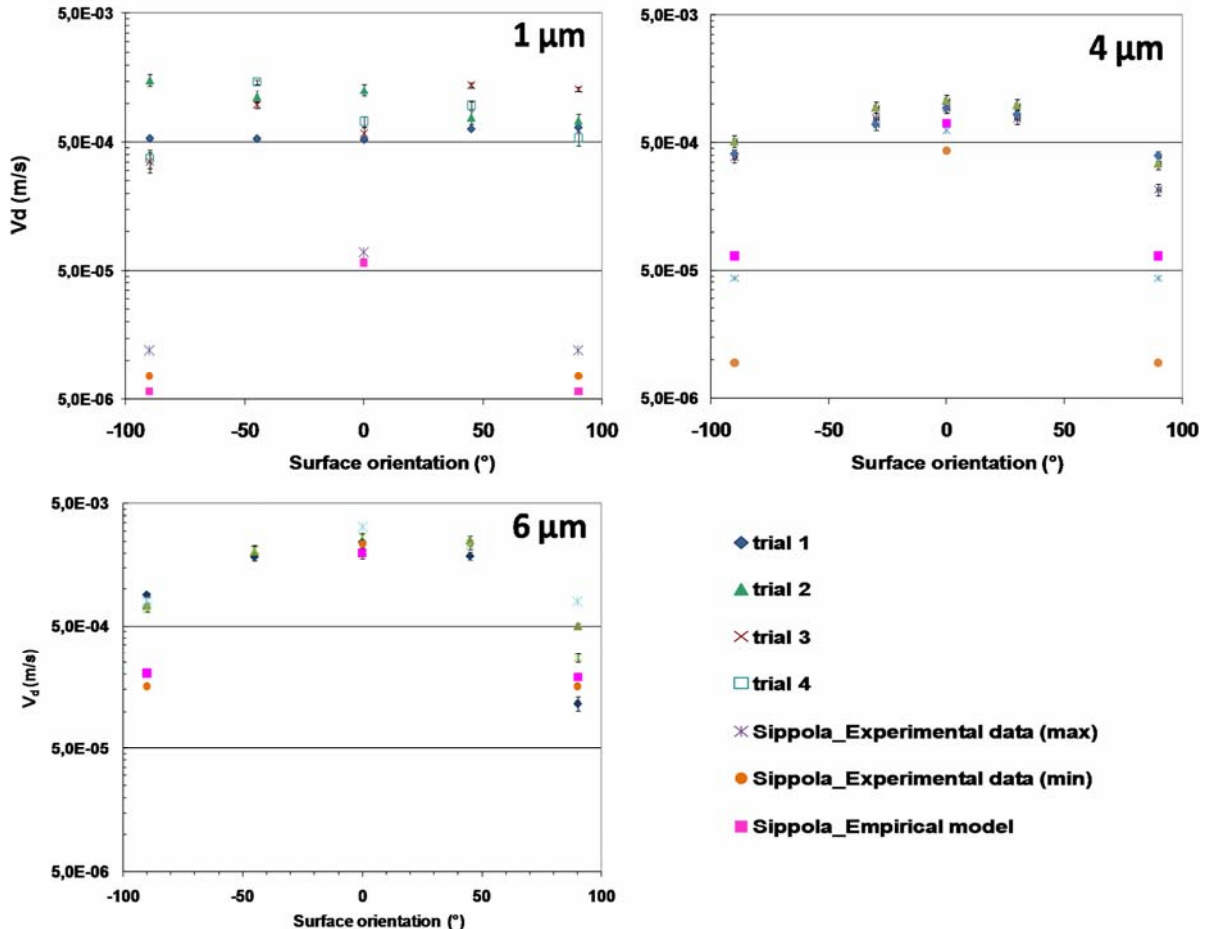
k [μm]	0.6	0.6	0.6
U_a [m.s⁻¹]	4.9 ± 0.1	5.0 ± 0.0	4.9 ± 0.0
C_{dep} [kg.m⁻³]	1.0 x 10 ⁻⁹ +/- 2.7 x 10 ⁻¹¹	3.6 x 10 ⁻⁸ +/- 1.7 x 10 ⁻⁹	1.9 x 10 ⁻⁷ +/- 2.7 x 10 ⁻⁹
Δt [s]	17,880 ± 240	10,525 ± 476	3,580 ± 35
m_{dep} [kg]	1.5 x 10 ⁻⁹ +/- 6.3 x 10 ⁻¹¹	4.5 x 10 ⁻⁸ +/- 7.2 x 10 ⁻¹⁰	9.1 x 10 ⁻⁹ +/- 1.2 x 10 ⁻¹⁰
Temperature [°C]	21.0 ± 1.3	21.9 ± 1.1	19.9 ± 0.9
ΔT [°C]	0.6 ± 0.3	0.1 ± 0.1	0.0 ± 0.2

d_{ac}, aerodynamic diameter; d_p, mean physical diameter; u*, fluid friction velocity; k, roughness; U_a, mean air speed through duct; C_{dep}, mean mass aerosol concentration in the duct; Δt, experimental time; m_{dep}, deposited aerosol particle mass; ΔT, differential temperature between the centerline of the duct and the duct wall. The data provides the average of experimental trials conducted with different particle sizes. The standard deviations are indicated with a “±” sign. The uncertainties are indicated with a “+/-” sign.

Experiments conducted at 5 m/s (Reynolds number of 5 x 10⁴) in the circular duct system, showed great stability for the detection of particles of 1, 4 and 6 μm nominal sizes. The physical diameter of particles varied from 2% to 5% during the experimental runs which lasted for 5, 3 and 1 hour respectively. Airborne particle concentrations in the duct differed between experiments, and concentrations were lower for smaller particles. Fluorescent technique allowed measuring deposited mass particle down to 4 x 10⁻¹¹ kg. No significant differential temperatures between the centerline of the duct and the inside duct wall were observed.

The experiments used commercial materials and deposition to duct surfaces with different orientations. The steady operating conditions in particle sizing presented above were translated into small errors in measured deposition rates. Figure 2 presented deposition velocity, measured in duct with fully developed turbulent flow.

Figure 2. Comparison of measured deposition velocity (V_d) to different surface orientations for all experiments in test ducts.



In these figures, measurements are shown as data points with vertical error bars indicating experimental uncertainties (10% maximum). For all particle sizes, measured deposition velocities to the inside surface of the duct (trials 1-4) showed great repeatability. For larger particle size (4 and $6\text{ }\mu\text{m}$), deposition rates to the floor were greater than to the wall surfaces. These results could be attributed to the influence of gravity; however, surface orientations had no influence on deposition velocity for smaller particle size ($1\text{ }\mu\text{m}$). Despite Sippola and Nazaroff reported that increases in particle diameter from 1 to $16\text{ }\mu\text{m}$ increase deposition rates to duct wall and floor^[3], but their experimental data remained up to 1-2 orders of magnitude lower than our experimental data. The same observation was obtained with the empirical model shown on Figure 2. A complementary study on the influence of roughness on deposition velocity would help to better understand these differences.

SUMMARY OR CONCLUSION

A lab-scale experimental method was developed to investigate solid particle deposition in large circular ventilation ducts encountered in the food industry. A non destructive technique was developed so that a ventilation duct apparatus could be used simply to investigate deposition of particles mass to different surface orientations with an accuracy of 10%. These data should help to illustrate the expected magnitudes of particle deposition rates under the diversity of systems encountered in the agro-food industries^[3-5, 8]. However, complementary research is needed to investigate discrepancies with other data and models developed for large ventilation ducts.

ACKNOWLEDGMENTS

This work was conducted within the framework of the CleanAirNet project (supported by the ANR), a joint project of research groups from CEMAGREF (METFRI-Rennes), GEPEA (Process Engineering laboratory), CSTB (Laboratory of Indoor Environment Microbiology), CERTES-Université Paris-Est (thermal and environmental research), ADRIA NORMANDIE (Center of technological resources devoted to food industry), and LAVAL MAYENNE TECHNOPOLE (Territorial agency for economical development and innovation promotion). Our thanks also go to Jean-Louis Goaziou for his collaboration at the beginning of this study.

REFERENCES

- [1] Sippola, M.R. Ph.D. Thesis, University of California, Berkeley, 2002.
- [2] Ben Othmane, M.; Havet, M.; Géhin, E.; Sollicec, C. *Aerosol science and technology*. 2010, 44, 9, 775-784.
- [3] Sippola, M.R.; Nazaroff, W.W. *Aerosol science and technology*. 2004, 38, 9, 12.
- [4] Ben Othmane, M.; Havet, M.; Gehin, E.; Sollicec, C.; Arroyo, G. *Journal of Food Engineering*. *In Press, Corrected Proof*.
- [5] Liu, B.Y.H.; Agarwal, J.K. *Aerosol Science and Technology*. 1974, 5, 145-155.
- [6] Sippola, M.R.; Nazaroff, W.W. *Aerosol Science and Technology*. 2005, 39, 2, 139-150.
- [7] Brockmann, J.E.; Rader, D.J. *Aerosol Science and Technology*. 1990, 13, 2, 162-172.
- [8] Zhao, B.; Wu, J. *Journal of Hazardous Materials*. 2007, 147, 1-2, 439-448.

Numerical Study on Seasalt Depositions in Niigata Prefecture, Japan

Naoto Kihara¹, Hiromaru Hirakuchi¹, Akira Takahashi¹, Shin Ohara¹ and Shin-ichi Fujita¹

1 Central Research Institute of Electric Power Industry, 1646 Abiko, Abiko-shi, Chiba, 270-1194, Japan

ABSTRACT

Large scale blackout was happened in Niigata Kaetsu area of Japan on December 22, 2005, and about 650,000 households suffered. The blackout was mainly caused by electrical flashovers due to accretion of seasalt-riched wet-snow on the porcelain long-rod insulators, which were occurred approximately 20-30km away from coastal lines. In this study, a regional-scale modeling of seasalt is carried out to investigate seasalt transport processes and depositions around Niigata Kaetsu area. In the model, spatial and temporal distributions of seasalt mass concentrations are estimated by considering seasalt-related physical processes, i.e. the emission, the transport, the dry deposition, the in-cloud scavenging and the below-cloud scavenging. Meteorological values, such as wind velocity, kinetic viscosity, precipitation and so on, are obtained by carrying out meteorology simulations using the WRF model. Numerical simulations focusing on Niigata Prefecture in January 2010 are carried out. In order to assess the accuracy, the numerical results are compared with observation data. The numerical results show agreement with the observation data, and high seasalt concentrations in the atmosphere and snows are observed in Niigata Kaetsu area under west wind conditions at the south side of a rain band.

KEYWORDS

Seasalt, Numerical simulations, Dry and Wet depositions

Introduction

Large scale blackout was happened in Niigata Kaetsu area of Japan on December 22, 2005 (cf. Fig. 1), and about 650,000 households suffered. The blackout was mainly caused by electrical flashovers that were occurred approximately 20-30km away from coastal lines. The electric flashover is due to accretion of wet-snow and a large amount of seasalt on porcelain long-rod insulators, leading to reductions of insulation strength.^{[1], [2]}

Seasalt aerosols in the atmosphere are produced from the ocean surface by breaking waves. They are transported in the atmosphere by advection and turbulent diffusion. Since they become cloud condensation nuclei^{[3], [4]}, they are captured into cloud waters and eventually fall onto the

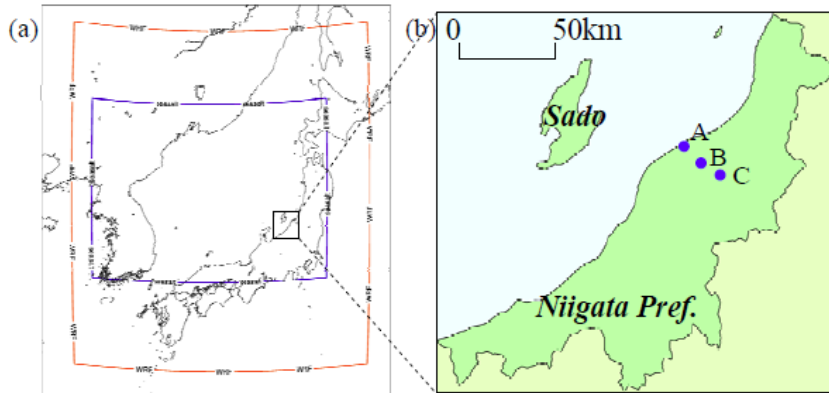


Figure 1. Computational domains of the seasalt and meteorology simulations (a), and location of field sites (b).

ground with water substances^{[5], [6]}. While water substances fall in the atmosphere, they collide with interstitial seasalt aerosols and the seasalt aerosols are captured into the water substances.^{[7], [8]} Both Interstitial and water substances-containing seasalt accrete on insulators during snowfall events, and would contribute to the electric flushover at the Niigata Kaetsu area. But it is not clear which seasalt is dominant.

In two decades, there have been many studies modeling seasalt aerosols in the atmosphere, and concentration and budget of the seasalt have been investigated both in the global and the regional scales.^{[9]-[13]} In the present study, a regional-scale model for seasalt is constructed to investigate transport processes of seasalt to Niigata Kaetsu area under strong snowfall events.

Numerical Set Up

Regional-Scale Seasalt Physical Process Analysis Model (Re-SPrAy) constructed in the present study is a 3D model taking into accounts following physical-processes: the emission of seasalt aerosols from the ocean, the transport in the atmosphere by wind and turbulence, the wet-deposition by water substances in the atmosphere and the dry-deposition on the ground and structures. The spatial and temporal distributions of seasalt mass concentrations are estimated with 8 bins of dry radii 0.1 μm -10.0 μm . The emission function of Gong^[14], the dry deposition scheme of Zhang^[15] and the wet deposition scheme of Slinn^[7] are adopted.

Meteorological fields, such as wind velocity, kinetic viscosity, precipitation and so on, are obtained by carrying out meteorology simulations using version 3.1 of the WRF (Weather Research and Forecasting) model. The analysis data of meso-scale model (MSM) of the Japan Meteorological Agency (JMA) is used for the initial and boundary conditions in the meteorology simulations.

Numerical simulations focusing on Niigata Prefecture are carried out. The computational domains of the simulations are shown in Figure 1. Niigata Kaetsu area is located near the Sea of

Japan (the East Sea) but about 150km away from the Pacific Ocean, and thus seasalt source transported to Niigata Kaetsu area is the Sea of Japan, and the computational domain include the Sea of Japan, but partially include the Pacific Ocean. The computational period is from 10 Jan. 2010 to 16 Jan. 2010, when a heavy snowfall event occurred at Niigata Kaetsu area.

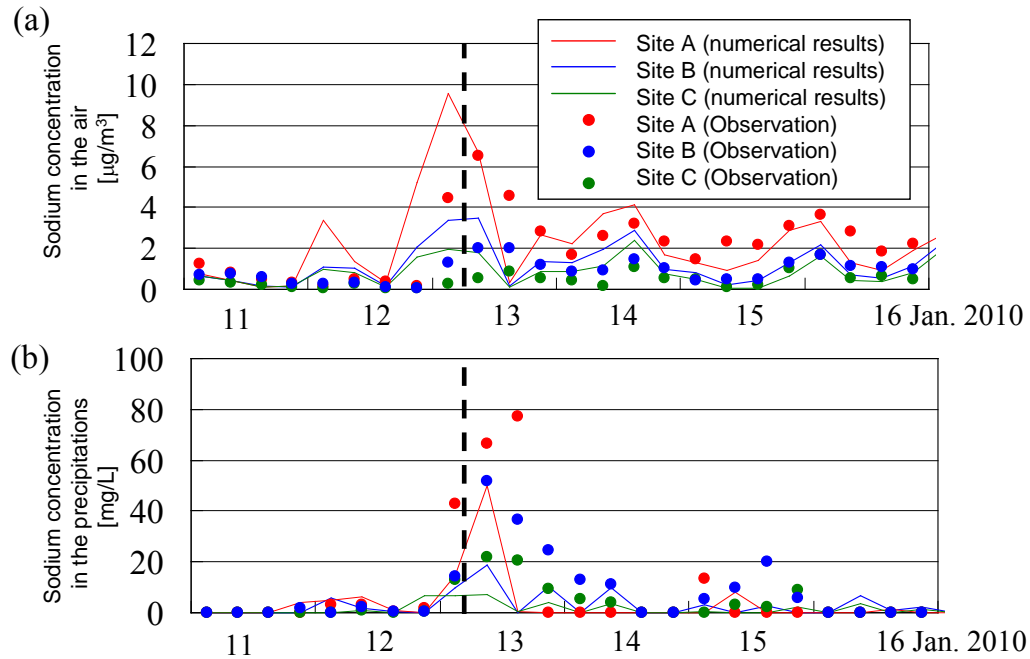


Figure 2. Time series of sodium concentrations in the air and the precipitations at Site A, B and C.

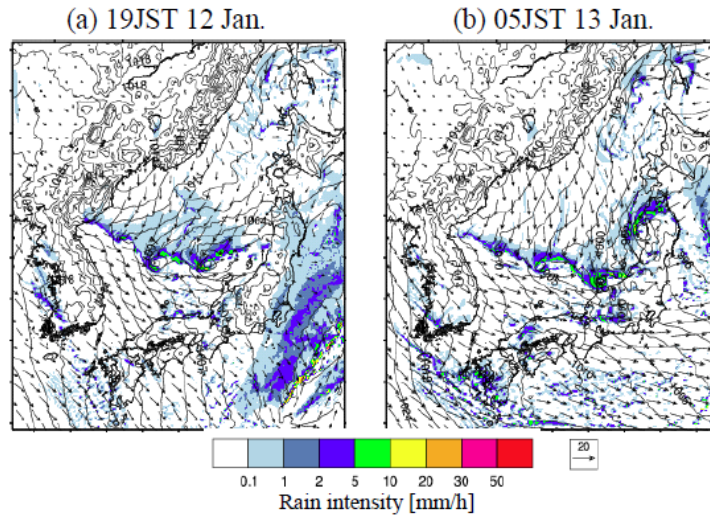


Figure 3. Distributions of wind vectors near the grounds, precipitations, and sea surface pressures at 19JST 12 Jan. and at 05JST 13 Jan, 2010.

Results and Discussion

In order to assess the model accuracy, numerical results are compared with observation data. The field measurement was carried out at three sites in Niigata Kaetsu area, 1km, 15km, 30km away from coastal lines (cf. Figure 1)^[16]. Atmospheric aerosol samples and snow samples were sequentially collected every 6 hours using a low-volume sampler and a wet-only sampler installed on the ground. The sodium concentrations, which are often used as representative values of seasalt concentration, were estimated by ion chromatography.

Time series of sodium concentrations in the air and the precipitations are shown in Figure 2. The sodium concentrations in the air are shown as mass of sodium aerosol per unit volume of the air, but that in the precipitations are shown as the mass of sodium ion per unit volume of the precipitation. From the observation data, high sodium concentrations both in the air and the precipitations are observed on 13 Jan., and the numerical results show roughly agreement with the observation data.

Distributions of wind vectors near the grounds, precipitations, and sea surface pressures at 19JST 12 Jan. and at 05JST 13 Jan. are shown in Figure 3. Rain bands are observed over the Sea of Japan. The wind directions are north or north-east at the north side of the rain band, but those are west or north-west at the south side of the rain band, and low pressure eddies develop along the rain band. Distributions of sodium concentration in the air and the precipitations near the ground at 19JST 12 Jan. and at 05JST 13 Jan. are shown in Figure 4. The figures show that the interstitial seasalt aerosols are transported southward in the north side of the rain band and eastward in the south side of the rain band over the Sea of Japan. In the rain band over the Sea of Japan, the seasalt concentrations in the precipitation are higher at north and south regions than those at center of the rain band. This shows that the seasalt in the rain band is provided from the north and south sides, and the seasalt is deposited near the center of the rain band.

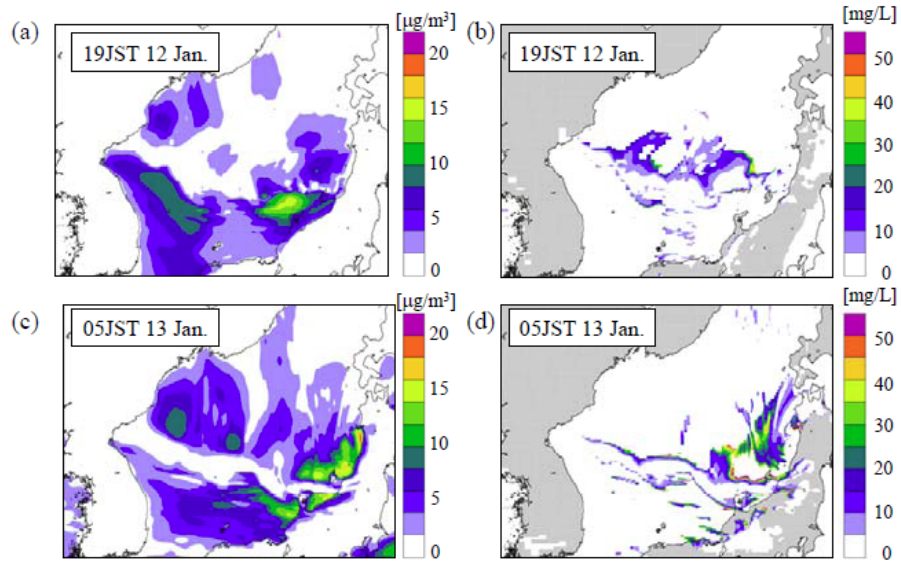


Figure 4. Distributions of sodium concentration in the air ((a), (c)) and the precipitations ((b), (d)) near the ground at 19JST 12 Jan. and at 05JST 13 Jan.

SUMMARY

We constructed a regional-scale model for seasalt, Re-SPRAY, and investigated the transport process of seasalt to Niigata Kaetsu area under a strong snowfall event of Jan. 2010. The numerical estimates of the seasalt concentrations in the air and the precipitations roughly agree with those obtained by the field measurements. The interstitial seasalt aerosols are transported eastward in the south region of the rain band over the Sea of Japan. In the rain band, the seasalt in the rain band is provided from the north and south sides, and the seasalt is deposited near the center of the rain band.

REFERENCES

- [1] Onodera, T.; Inukai, H.; Odashima, T. In *Proc. 13th International Workshop on Atmospheric Icing of Structures*, 2007.
- [2] Sakata, G.; Homma, H., In *Proc. 2009 World Congress on Insulators, Arresters and Bushings*, 2009.
- [3] O'Dowd, C.; Smith, M. H.; Consterdine, I. E.; Lowe, J. A. *Atmos. Env.* 1997, **31**, 73-80.
- [4] Yoon, Y. J.; Brimblecombe, *Atmos. Chem. Phys.* 2002 **2**, 17-30.
- [5] Svenningsson, B.; Hansson, H.-C.; Martinsson, B.; Wiedensohler, A; Swietlicki, E; Cederfelt, S. I.; Wendisch, M. *Atmos. Environ.* 1997, **31**, 2563-2475.
- [6] Ghan, S. J.; Guzman, G.; Abdul-Razzak, H. *J. Atmos. Sci.* 1998, **55**, 3340–3347.

- [7] Slinn, W. G. N. In *Atmospheric Science and Power Production*, edited by Randerson, D., U.S. Dept of Energy, Technical Information Center, Oak Ridge, Tenn., 1984, 466–532.
- [8] Dana, M. T.; Hales, J. M. *Atmos. Environ.* 1976, *10*, 45-50.
- [9] Gong, S. L.; Barrie, L. A.; Prospero, J. M.; Savoie, D. L.; Ayers, G. P.; Blanchet, J. –P.; Spacek, L. *J. Geophys. Res.* 1997, *102*, 3819-3830.
- [10] Grini, A.; Myhre, G.; Sundet, J.; Isaksen, S. A. *J. Clim.* 2002, *15*, 1717-1730.
- [11] Witek, M. L.; Flatau, P. J.; Quinn, P. K.; Westphal, D. L. (2007), *J. Geophys. Res.* 2007, *112*, D08215, doi:10.1029/2006JD007779.
- [12] Foltescu, V. L.; Pryor, S. C.; Bennet, C. *Atmos. Environ.* 2005, *39*, 2123-2133.
- [13] Manders, A. M. M.; Schaap, M.; Querol, X.; Albert, M. F. M. A.; Vercauteren, J.; Kuhlbusch, T. A. J.; Hoogerbrugge R. *Atmos. Environ.* 2010, *44*, 2434-2442.
- [14] Gong, S. L. *Global Biogeochem. Cycles* 2003, *17*, doi:10.1029/2003GB002079.
- [15] Zhang, L.; Gong, S.; Padro, J.; Barrie, L. *Atmos. Environ.* 2001, *35*, 549–560.
- [16] Takahashi, A.; Fujita, S.; Sakata, G. In *Proc. 14th International Workshop on Atmospheric Icing of Structures*, 2009.

Spatial and Seasonal Variability of Aerosol Organic Mass-to-Organic Carbon Ratios in Chinese Cities

Li Xing^{1,2}, Tzung-May Fu¹, Junji Cao³, Gehui Wang³, Kin Fai Ho⁴, Shun-cheng Lee⁴ and Tijian Wang²

1Department of Atmospheric and Oceanic Sciences and Laboratory for Climate and Ocean-Atmosphere Studies, School of Physics, Peking University, Beijing, China, 100871

2 School of Atmospheric Sciences, Nanjing University, No.22 Hankou Road, Gulou District, Nanjing, China. 210093

3 State Key Laboratory of Loess and Quaternary Geology, Institute of Earth Environment, Chinese Academy of Sciences, Xi'an, China. 710075

4 Research Center of Urban Environmental Technology and Management, Department of Civil and Structural Engineering, Hong Kong Polytechnic University, Hung Hom, Kowloon, Hong Kong.

ABSTRACT

Organic aerosols constitute a key component of atmospheric fine particles, impacting air quality, public health, and climate. The aerosol organic mass-to-organic carbon (OM/OC) value is an important parameter often used to estimate total aerosol organic mass (OM) from organic carbon (OC) measurements. It contains critical information about the chemical composition of organic aerosol, which in turn affects its hygroscopic properties. We calculate the OM/OC values for Chinese urban aerosols from PM_{2.5} filter samples collected in winter and summer of 2003 in 14 Chinese cities. Two methods are used for the analysis. The first is a mass balance method, in which the organic mass is calculated as the difference between total aerosol mass and the mass sum of the other major species, including sulfate, nitrate, ammonium, elemental carbon and trace elements. OC measurement follows the IMPROVE thermal/Optical reflectance protocol. With this method we find averaged OM/OC values of 1.83 in winter and 1.90 in summer. The second method is based on the chemical structures of recognized organic compounds extracted with dichloromethane/methanol and water from the PM_{2.5} samples. Based on this method, we calculate averaged OM/OC values of 1.59 in winter and 1.75 in summer, indicating stronger photochemical oxidation in summer. Further studies show that oxalic acid has the greatest impact on OM/OC in summer and winter, since excluding it will decrease the local OM/OC significantly. Subsequently levoglucosan in winter and fatty acid, bis(2-ethylhexyl) phthalate(C₂₄H₃₈O₄) in summer affect OM/OC significantly. Oxalic acid and Zn has the greatest correlation in summer, indicating that the source of oxalic acid is mostly anthropogenic.

KEYWORDS

OM/OC, organic aerosols, oxalic acid

Introduction

Organic aerosols (OA) constitute an important component of atmospheric particulate matter, impacting air quality, chemistry, and climate. OA are either emitted directly or formed secondarily in the atmosphere from oxidation of volatile organic precursors. The ratio of organic matter (OM) mass versus organic carbon (OC) mass in OA (hereafter refer to as OM/OC) is an important bulk indicator of OA chemical composition, which not only provide clues to the source of OA, but also determine their physical and chemical properties and subsequent impact. Higher OM/OC indicates that the OA are more oxidized, which may indicates secondary origin or significant aging. Organics influence the surface tension of aerosols, which could change the hygroscopicity and ability to act as CCN of aerosols.

Previous studies on OM/OC have assumed it to be in the range of 1.2 to 1.4.^[1] Due to the limited theoretical and analysis technique at that time, Turpin and Lim^[2] calculated the OM/OC value again and suggested the value to be 1.6 and 2.1 for urban and rural sites. Recently more studies have focused on this issue mostly in US region with the improving accuracy of analysis technique. The studies found higher OM/OC in rural and remote sites compared to urban area. For example, Bae et al^[3] showed OM/OC to be 1.5-1.9 in rural upstate New York and 1.3-1.6 in urban New York. Chan et al^[4] get the value to be 2.5 ± 0.2 and 1.9 ± 0.2 in a rural site in central Ontario during an intensive study in 2007 for the air masses from the south and north, because of different chemical composition and meteorological conditions. Sun et al^[5] calculated the value to be 1.62 ± 0.11 for PM1 in summer at Queens College in New York, an urban site. The result indicates that aerosols in rural areas contain more secondary organic aerosols or significant aging while more primary aerosols contained in urban area. In urban area, Bae et al^[6] calculated OM/OC to be 1.95 in summer and 1.77 in winter at the St. Louis - Midwest Super site, an urban site while Bae et al^[3] did not get obvious seasonal variability in urban New York.

Chen and Yu^[7] measured OM/OC in PM_{2.5} samples in a sub-urban site, Hong Kong, and classified the dominant air masses into continent-originated and marine-originated. They calculated the values to be 2.2 and 1.9 for the two air masses separately. The values are higher than 1.6 for urban aerosols suggested by Turpin and Lim^[2], which are mostly calculated in US regions. To the best of our knowledge, so far there has not been a systematic analysis of the seasonal and spatial variability of OM/OC values in Chinese urban air. So we analyze OM/OC values both in winter and summer in 14 Chinese cities and compare the results with previous studies.

Experimental and Analysis Methods

We use PM_{2.5} samples collected by Cao et al and the chemical compounds concentrations analyzed by Wang et al and Ho et al.^[8-10]

Two methods are used to analyze OM/OC value.

(1) Mass balance method. Organic mass is estimated as the difference between the total aerosol mass and the mass sum of other species, namely sulfate, ammonium, nitrate, chlorine, elemental carbon and trace elements, including Na, K, Ca, Mg, Al, Si, Fe, Ti, Mn, Ni, Zn, As, Br, Mo, Cd, Pb. Because these trace elements are usually not existed with ion forms in the aerosols, the conversion factors need to be applied to convert these elements to their oxides before used in this method. Details are shown in Table 1. What's more, for the unmeasured particle-bound water (PBW), we simplistically assumed it to be 5.8% of the particle mass according to previous studies.^[3, 11] For the quartz-fiber filters collecting during 24h, OC concentrations may be overestimated by absorption of gas carbon species and underestimated by volatilization already collected on the filters. In this experiment without a denuder removing the gas, we estimated 3.7% of organic carbon positive artifact.^[3] The final formula is Eq.1

$$\text{OM/OC} = \frac{[\text{PM}_{2.5}] - [\text{EC}] - [\text{NH}_4^+] - [\text{SO}_4^{2-}] - [\text{NO}_3^-] - [\text{Cl}^-] - [\text{PBW}] - [\text{metal oxides}]}{[\text{OC}] - 3.7\% * [\text{OC}]}$$

(Eq.1)

Table 1. Mass conversion factors used in this study for converting trace element mass to trace-element-containing oxide compound mass^[3, 12]

Al	2.2	Ti	1.94	Mn	2.02	Br	1.0
Si	2.49	Na	1.5	Ni	1.0	Mo	1.0
Ca	1.63	K	1.2	Zn	1.24	Cd	1.14
Fe	2.42	Mg	1.5	As	1.0	Pb	1.0

(2) Examining the detailed structure of organic compounds to calculate OM/OC value. Wang et al^[9] and Ho et al^[10] used different solvents and analyzed the extracts with GC-MS to get concentrations of different organic compounds of PM2.5 data for 14 Chinese cities, including n-alkanes(C₁₆₋₃₅), fatty acids(C₉₋₃₄), sugars, phthalates, fatty alcohols(C₁₂₋₃₂), polyols & polyacids, lignin & resin products, sterols, PAHs, hopanes, WSOC(dicarboxylic acids, ketocarboxylic acids, α-dicarbonyls). Much more classes of organics are recognized than that of White et al^[11]. OM/OC value could be calculated using Eq.2

$$OM/OC = \frac{\sum_{i=1}^n C_i}{\sum_{i=1}^n C_i * \frac{M_{ci}}{M_{mi}}} \quad (Eq.2)$$

C_i : the individual species concentration for i

M_{ci} : carbon weight in a molecular of i

M_{mi} : molecular weight for i

Results and Discussion

The OM/OC value results for two methods in 14 Chinese cities are shown in Table2. As shown in Table 2, using mass balance method, OM/OC values range from 1.11 to 3.08 in summer and 1.59 to 2.43 in winter, the average value is 1.90 in summer and 1.83 in winter. In comparison, these values are higher than urban New York State, which ranges from 1.27 to 1.59 using mass balance method,^[3] but lower than a mixed light industrial-residential area in Atlanta, which is 2.16 ± 0.43 averaged annually using mass balance method.^[13] There is no obvious seasonal variability in this method (95% confidence t-test). Since not all trace elements are detected in this study, the results provide upper limits for OM/OC values.

The OM/OC values calculated based on detailed organic species analysis are also shown in Table 2. The values range from 1.56 to 1.98 in summer and 1.38 to 1.96 in winter. We could see most cities (excluding HK, CQ, WH) have higher OM/OC values in summer than in winter, averaging 1.75 in summer and 1.59 in winter, which are significantly different, possibly indicating stronger secondary contribution to organic aerosols. This value is comparable with the recommendation value 1.6 for urban aerosols.^[2] OM/OC value is higher in south China than north in winter while there is no obvious difference in summer. Possibly because strong photo chemistry occurs in summer both in south and north China while heating equipment is widely used in winter in north China and more primary aerosols are emitted which has lower OM/OC value.

Table 2 winter and summer OM/OC in 14 Chinese cities determined by mass balance method and organic species analysis

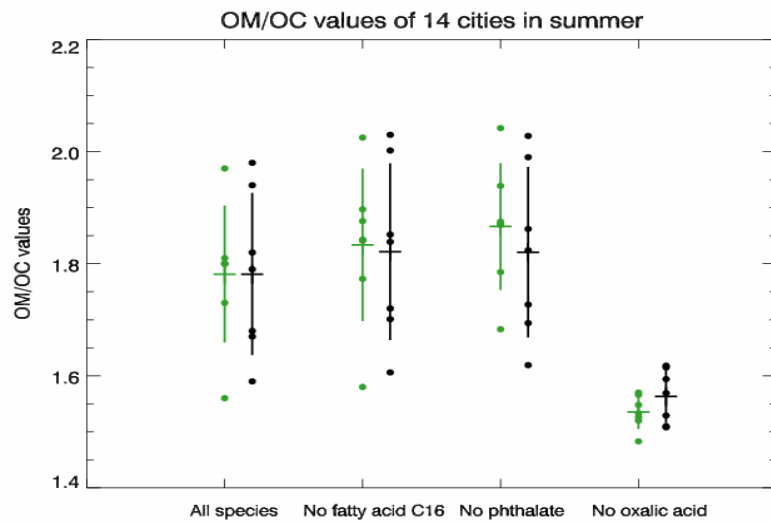
	XA	QD	YL	JC	TJ	BJ	CC	nort h aver age	HK	GZ	XM	CQ	HZ	WH	SH	south averag e	all averag e
summ	1.	1.	1.	1.	1.	3.	2.		1.	1.		2.	2.	2.	1.		
ss er	75	57	48	93	58	08	22	1.60	11	73	*	14	26	62	64	2.19	1.90
lance wint	1.	1.	2.	2.	1.	2.	1.		2.	1.	1.	1.	1.	1.	1.		
thod er	75	59	28	43	68	11	78	1.87	11	64	71	91	93	88	82	1.81	1.83
ganic summ	1.	1.	1.	1.	1.	1.	1.		1.	1.	1.	1.	1.	1.	1.		
ecies er	82	94	67	59	68	98	79	1.78	80	81	97	56	80	73	80	1.72	1.75
alysi wint	1.	1.	1.	1.	1.	1.	1.		1.	1.	1.	1.	1.	1.	1.		
er	52	59	38	46	61	50	49	1.51	96	54	90	56	76	82	76	1.65	1.59

To know better about OM/OC values and which kind of organic compounds influences the values significantly, we calculated OM/OC values excluding one species at a time in chemical analysis method, as shown in Fig 1 and Fig 2. The results show that oxalic acid has the most significant impact on OM/OC value. Excluding it decreases 0.16 and 0.23 of the whole OM/OC value in winter and summer. Subsequently, fatty acid ($\text{CH}_3(\text{CH}_2)_{14}\text{COOH}$) and bis(2-ethylhexyl) phthalate($\text{C}_{24}\text{H}_{38}\text{O}_4$) effect OM/OC value in summer while levoglucosan also influences OM/OC value in winter.

Levoglucosan is a tracer of biomass burning^[14], it has high concentrations in winter and Molecular weight/Carbon weight=2.25, so excluding it would decrease the whole OM/OC value, and indicating that biomass burning affect urban air quality in winter to some extent. Fatty acid $\text{CH}_3(\text{CH}_2)_{14}\text{COOH}$ has relatively low Molecular weight/Carbon weight 1.33 and high concentrations in summer, so excluding it would increase OM/OC value significantly. In urban area, cooking is the main source for fatty acids, especially meat cooking. Zhao et al^[15] reported that fatty acids account for 78% total quantified particulate organic matter with samples collected in a commercial restaurant. They exist in the form of phospholipids and triglycerides and are liberated, hydrolyzed or oxidized during the cooking process. Bis(2-ethylhexyl)phthalate contains the highest concentrations of phthalates, averagely 128.79 ng m^{-3} in winter and 300.00 ng m^{-3} in summer, extremely high 1748 ng m^{-3} in Chong Qing, summer. It has Molecular weight/carbon weight 1.35 and would increase OM/OC value if eliminating it. Bis(2-ethylhexyl) phthalate is widely used in plastic industry as softeners.^[16] Its high concentrations and effects for OM/OC ratios are due to the enhanced evaporation from the plastics in the hot season and subsequent

deposition on particles.^[17]

Fig.1 OM/OC values excluding fatty acid (C16), phthalate and oxalic acid in 14 Chinese cities in summer

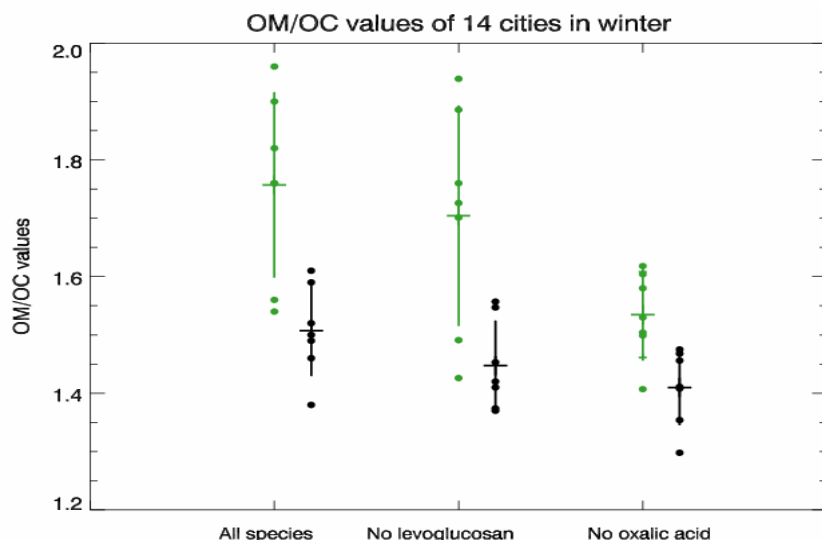


Black scatter dots: Northern China

Green scatter dots: Southern China

Vertical line: Average value and standard deviation

Fig.2 OM/OC values excluding levoglucosan and oxalic acid in 14 Chinese cities in winter



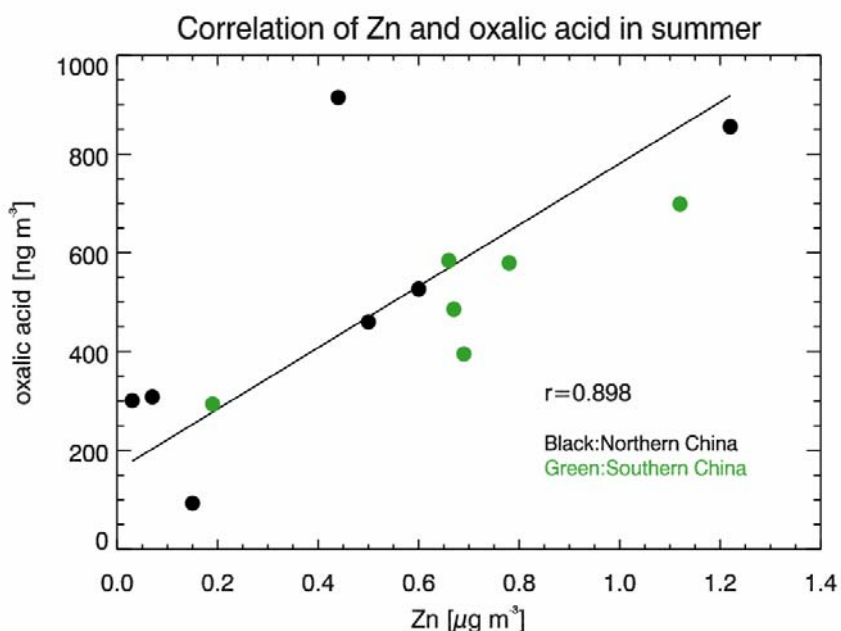
Black scatter dots: Northern China

Green scatter dots: Southern China

Vertical line: Average value and standard deviation

Oxalic acid is the most abundant dicarboxylic acid in the aerosols, accounting for 40% to 67% in winter and 40% to 66% in summer, and has very high Molecular weight/Carbon weight=3.75, so excluding oxalic acid would significantly decrease the local OM/OC value. To possibly identify the sources of oxalic acid, correlation of oxalic acid and other species are calculated. The result shows that oxalic acid and Zn has the greatest correlation in summer, with the correlation coefficient 0.898. Zn has been considered as the indicator of anthropogenic sources.^{[18-20] [21]} calculated that Zn emitted from anthropogenic sources accounted for 66% of the total emission on a global basis, this percentage may be higher in cities due to the industry. So the sources of oxalic acid are likely anthropogenic in urban area in summer.

Fig 3 Correlation of oxalic acid and Zn in summer in Chinese cities



SUMMARY OR CONCLUSION

OM/OC values for Chinese urban cities are estimated in two methods. The result shows that averagely 1.83 in winter and 1.90 in summer in mass balance method. Averagely 1.59 in winter and 1.75 in summer for chemical species analysis are consistent with the recommendation data 1.6 for urban aerosols of Turpin and Lim^[2]. Considering the higher ratio of unrecognized organic

compounds, the result provides the lower limit of OM/OCvalue. Regarding every species, Levoglucosan and oxalic acid in winter and fatty acid $\text{CH}_3(\text{CH}_2)_{14}\text{COOH}$, Bis(2-ethylhexyl) phthalate and oxalic acid in summer affect the values significantly. Oxalic acid has the most impact on OM/OC in winter and summer, while it has the greatest correlation with Zn in summer. Since Zn is an indicator of anthropogenic sources, the sources of oxalic acid are likely anthropogenic in urban area in summer.

ACKNOWLEDGMENTS

The author thanks for the guidance of Tzung-May Fu for the proceeding of the work. We are grateful for Li Nan's help for contacting with Cao, J.J. The author also thanks Junji Cao, Gehui Wang, Kin Fai Ho for providing the PM_{2.5} samples' data and chemical analysis data.

REFERENCES

- [1]White, W.H. and P.T. Roberts,*Atmospheric Environment*, 1977. **11**. 803-812.
- [2]Turpin, B.J. and H.J. Lim,*Aerosol Science and Technology*, 2001. **35**. 602-610.
- [3]Bae, M., K. Demerjian, and J. Schwab,*Atmospheric Environment*, 2006. **40**. 7467-7479.
- [4]Chan, T.W., L. Huang, W.R. Leaitch, S. Sharma, J.R. Brook, J.G. Slowik, J.P.D. Abbatt, P.C. Brickell, J. Liggio, S.M. Li, and H. Moosmuller,*Atmospheric Chemistry and Physics*, 2010. **10**. 2393-2411.
- [5]Sun, Y.L., Q. Zhang, J.J. Schwab, K.L. Demerjian, W.N. Chen, M.S. Bae, H.M. Hung, O. Hogrefe, B. Frank, O.V. Rattigan, and Y.C. Lin,*Atmospheric Chemistry and Physics*, 2011. **11**. 1581-1602.
- [6]Bae, M.S., J.J. Schauer, and J.R. Turner,*Aerosol Science and Technology*, 2006. **40**. 1123-1139.
- [7]Chen, X. and J.Z. Yu,*Atmospheric Environment*, 2007. **41**. 8857-8864.
- [8]Cao, J.J., S.C. Lee, J.C. Chow, J.G. Watson, K.F. Ho, R.J. Zhang, Z.D. Jin, Z.X. Shen, G.C. Chen, Y.M. Kang, S.C. Zou, L.Z. Zhang, S.H. Qi, M.H. Dai, Y. Cheng, and K. Hu,*Journal of Geophysical Research*, 2007. **112**.
- [9]Wang, G.H., K. Kawamura, S. Lee, K.F. Ho, and J.J. Cao,*Environmental Science & Technology*, 2006. **40**. 4619-4625.
- [10]Ho, K.F., J.J. Cao, S.C. Lee, K. Kawamura, R.J. Zhang, J.C. Chow, and J.G. Watson,*Journal of Geophysical Research-Atmospheres*, 2007. **112**.
- [11]Drewnick, F., J.J. Schwab, J.T. Jayne, M. Canagaratna, D.R. Worsnop, and K.L. Demerjian,*Aerosol Science and Technology*, 2004. **38**. 92-103.
- [12]Kleeman, M.J., J.J. Schauer, and G.R. Cass,*Environmental Science & Technology*, 2000. **34**. 1132-1142.

- [13]El-Zanan, H.S., B. Zielinska, L.R. Mazzoleni, and D.A. Hansen,*Journal of the Air & Waste Management Association*, 2009. **59**. 58-69.
- [14]Mochida, M., K. Kawamura, P.Q. Fu, and T. Takemura,*Atmospheric Environment*, 2010. **44**. 3511-3518.
- [15]Zhao, Y.L., M. Hu, S. Slanina, and Y.H. Zhang,*Environmental Science & Technology*, 2007. **41**. 99-105.
- [16]Bi, X.H., B.R.T. Simoneit, G.Y. Sheng, S.X. Ma, and J.M. Fu,*Atmospheric Research*, 2008. **88**. 256-265.
- [17]Wang, G.H., K. Kawamura, X. Zhao, Q.G. Li, Z.X. Dai, and H.Y. Niu,*Atmospheric Environment*, 2007. **41**. 407-416.
- [18]Schleicher, N., S. Norra, F.H. Chai, Y.Z. Chen, S.L. Wang, and D. Stuben,*Journal of Environmental Monitoring*, 2010. **12**. 434-441.
- [19]Heimburger, L.E., C. Migon, A. Dufour, J.F. Chiffolleau, and D. Cossa,*Science of the Total Environment*, 2010. **408**. 2629-2638.
- [20]Wang, X.L., T. Sato, B.S. Xing, S. Tamamura, and S. Tao,*Journal of Aerosol Science*, 2005. **36**. 197-210.
- [21]Nriagu, J.O.,*Nature*, 1989. **338**. 47-49.

Effects of Gel Network on the Formation of Mesoporous Titania Assisted by Resorcinol/Formaldehyde Gel

Mananya Thovicha and Varong Pavarajarn*

Center of Excellence in Particle Technology, Faculty of Engineering,
Chulalongkorn University, Bangkok, 10330, Thailand

* Principal Contact: E-mail: Varong.P@chula.ac.th.

ABSTRACT

Mesoporous structures of materials have attracted considerable attention because of their potential in a variety of applications. In this work, resorcinol/formaldehyde (RF) gel was used as a template for the synthesis of mesoporous titania, which is in great interest in catalysis, photocatalysis, gas sensor and photovoltaic applications. The RF-gel was prepared by the sol-gel polycondensation of resorcinol (R) and formaldehyde (F) using acetic acid (C) as catalyst, while titanium tetraisopropoxide (TTIP) was used as a precursor for titania. Titania sol was firstly prepared from TTIP via sol-gel process to avoid spontaneous reaction between TTIP and RF-gel that resulted in rapid solidification of the gel. After predetermined period of aging time, the titania sol was added into RF-gel that had also been aged for predetermined period. The mixture was further aged for another 36 hours before being dried at 80°C and subsequently calcined at 500°C for 4 hours. It was confirmed that the presence of RF-gel could introduce mesoporosity to the product, yet the interaction between titania sol and RF-gel was rather complicated. The titania/RF-gel interaction was confirmed by Fourier Self-Deconvolution (FSD) analysis of the Fourier-transform infrared spectra of the titania/RF-gel composite. The signal from Ti-O-C bonding increased as both methyl- and methylene ether bridges of the RF-gel were formed, which suggested that the porosity of the titania was controlled by the growth of RF-network. Effects of resorcinol-to-catalyst (R/C) molar ratio as well as that of resorcinol-to-formaldehyde (R/F) ratio on properties of the obtained products were also investigated. It was found that surface area of the product was increased as either the R/F ratio was decreased or the R/C ratio was increased.

KEYWORDS

Mesoporous, Titania, Resorcinol/formaldehyde gel

Introduction

Porous ceramics are essential for many industries where high permeability, high surface area, and insulating characteristics are required^[1]. Nanocrystalline titanium dioxide (TiO_2 or titania), as one of the most important oxide semiconductor materials, has been extensively researched during recent years for its superior physical and chemical properties (e.g., catalytic and photocatalytic activity, good stability toward adverse environment, sensitivity to humidity, dielectric character, photo-electrochemical conversion, nonlinear optics, and photoluminescence)^[2, 3].

Resorcinol-formaldehyde (RF) gel is formed from polymerization of resorcinol (R) with formaldehyde (F). RF-gel can be further processed into carbon aerogel with many common characteristics such as a tortuous open-cell structure, ultrafine pore size (< 50 nm) and high surface area ($400\text{-}1000 \text{ m}^2\text{g}^{-1}$)^[4]. The synthesis of RF aerogels consists of a polycondensation reaction between resorcinol and formaldehyde which is analogous to the sol-gel process for the synthesis of inorganic compound like silica- or titanium- based systems^[5].

In this study, porosity of RF-gel will be employed as template for the fabrication of porous titanium dioxide. Effects of many parameters in resorcinol/formaldehyde gel synthesis and titania-sol preparation were investigated in detail to understand the correlation between condition for resorcinol/formaldehyde and properties of the synthesized titania nanoparticles. This work focuses on the fabrication of porous titanium dioxide assisted by resorcinol/formaldehyde gel and its mechanism.

Experimental Methods

RF solution was firstly prepared by dissolving resorcinol (99%, Fluka) in ethanol under magnetic stirring, with the addition acetic acid. After dissolution, formaldehyde solution (37% in water, stabilized by 10-15% wt. methanol, Ajax Finechem) that was previously mixed with titanium tetraisopropoxide (TTIP 99%, Aldrich) in ethanol was added to the solution. The molar ratio of TTIP-to-ethanol-to-acetic acid was 1:9:0.1. The mixture was stirred for another 15 min at room temperature. Then, it was poured into a cup and aged at room temperature for 36 hours in a closed system to obtain RF/ TiO_2 hydrogels. After that, the obtained gel was dried for 3 hours at 80°C. The dried sample was calcined at 500°C for 4 hours in a box furnace to remove residual organic compound as well as RF gel from titania. The obtained products were characterized by various techniques. The specific surface area was determined from BET analysis. Fourier transform infrared spectroscopy (FTIR) was used for identification of functional group in the products.

Results and Discussion

Synthesis of Porous Titania using TTIP as Source: Effects of RF Composition

In the first part of the research, porous titania powders were prepared using TTIP as the precursor for titania with the aid by RF-gel. Effects of RF composition toward the formation of titania porous structure were investigated by varying R/F ratio (from 0.25, 0.5, 1.0, 1.5 and 2.0) and R/C ratio (from 0.18, 0.3, 1.3, 2 and 5), respectively. All products were calcined at 500°C in a box furnace.

Effects of R/F ratio on surface area of the product are shown in Figure 1. It can be seen that the surface area of the product is slightly decreased when the R/F ratio is increased from 0.25 to 0.5 beyond which the surface area is not significantly affected by the increased content of resorcinol. The effect of the R/C ratio is not significant toward the surface area of the final product either. This might be the result from the rapid interaction between TTIP and RF-gel. However, the average pore diameter of the sample increases with the increase in R/F ratio especially at high R/F ratio of 2.0 where pore diameter of about 6 nm can be achieved.

Figure 1. Surface area of titania product prepared from TTIP and RF-gel, using the R/C ratio of 0.18 (●), 0.3 (□), 1.3 (△), 2 (▲) and 5 (■), as a function of the R/F ratio of the RF-gel.

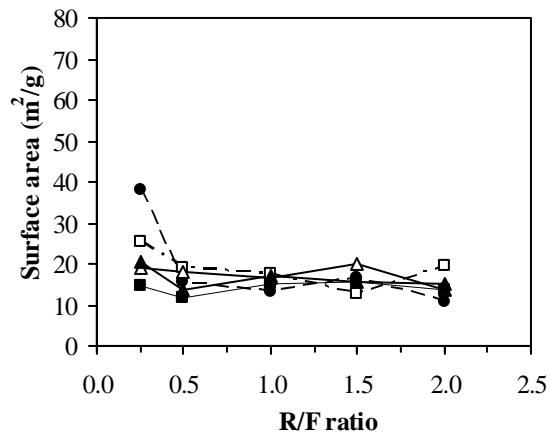
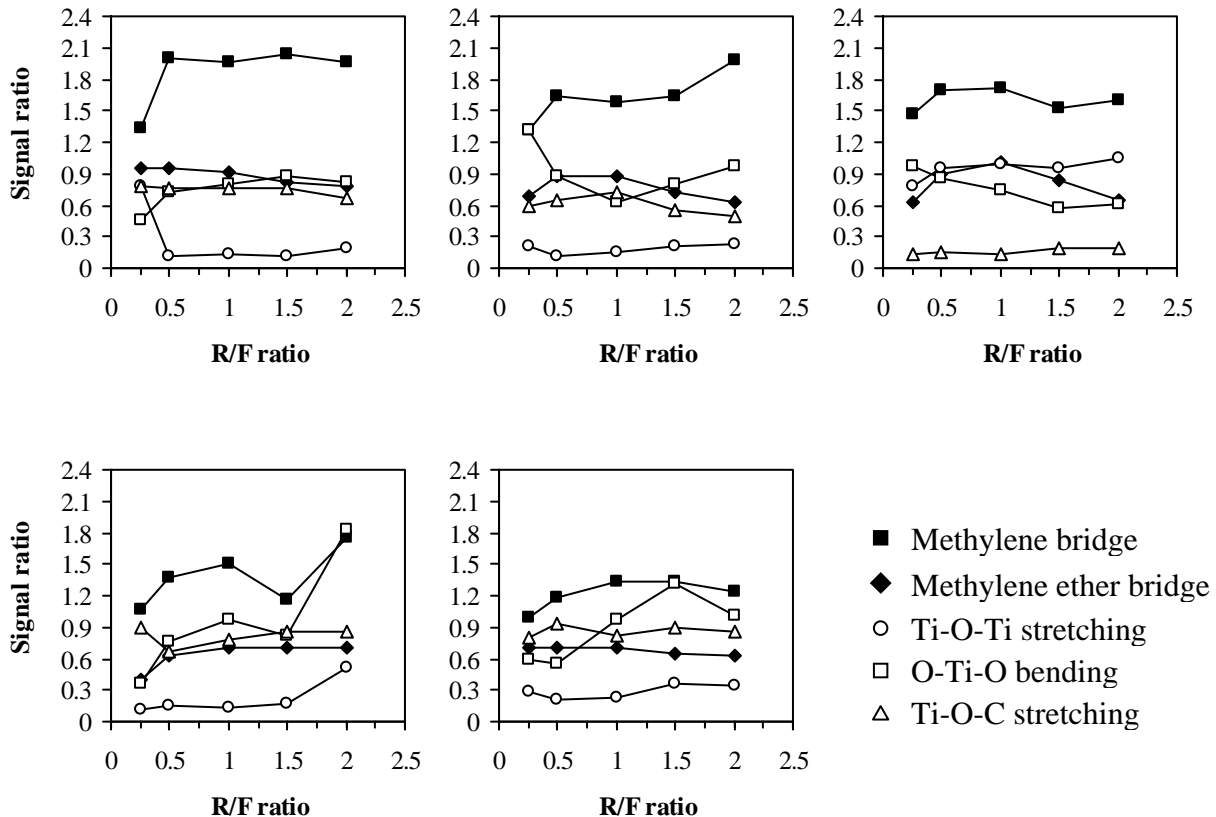


Figure 2. FTIR signal ratio for various functional groups within the RF/titania composite prepared from TTIP and RF-gel using the R/C ratio of 0.18 (a), 0.3 (b), 1.3(c), 2(d) and 5(e) as a function of the R/F ratio of the RF-gel.



The interaction between TTIP and RF-gel can be observed visually. The RF mixture changes its color right after it is mixed with TTIP solution. In some cases, the reaction takes place so rapidly that it causes instantaneous solidification of the gel. This TTIP-RF interaction was investigated further by examining intensities of signal in FTIR spectra. In order to eliminate the effect of sample amount that also affects the intensity of the signals, the signal ratio, which is intensity of the interested FTIR band divided by that of the reference signal within the same sample was employed. In this study, the signal from aromatic rings was used as the reference, since the polycondensation process of RF-gel does not involve breaking of aromatic rings. Furthermore, the Fourier Self-Deconvolution (FSD) algorithm was performed on the obtained FTIR spectra to get more defined band.

Figure 2 shows signal ratios of RF/titania composite prepared using the R/C ratio of 0.18 to 5. The R/F ratio is also varied in the range of 0.25 to 2.0. When the R/F ratio is increased, the signal

for methylene bridge increases indicating that RF solution forms more cross-linking network. At high R/F ratios (e.g., 1.5 and 2.0), it is found that signal of methylene ether bridge is decreased since there is not enough of formaldehyde in the solution for the formation of such bridge. It can be seen from the signals of Ti-O-Ti stretching and O-Ti-O bending vibrations that TTIP is converted to titania after being added into RF-gel. The interaction between TTIP and RF gel is also evident by the presence of Ti-O-C bonding. However, the signals of both Ti-O-Ti and Ti-O-C remain roughly unaffected by the R/F ratio.

Synthesis of Porous Titania using Titania Sol as Source

As mentioned earlier, TTIP often interacts with RF-gel instantaneously, resulting in rapid solidification of the gel, which also prevents addition of titania precursor in large quantity into the RF-gel. Therefore, in this section, the reactivity of the titania precursor was lowered by converting the precursor into preformed titania sol. Unless mentioned otherwise, titania sol was formed by aging TTIP solution at room temperature for 6 h prior to the addition into RF-gel. Effects of various parameters on porous structure of titania are presented.

Effects of RF Composition

In this section, RF solution was prepared using various values of R/F ratio (i.e., 0.25, 0.5, 1.0, 1.5 and 2.0) and R/C ratio (i.e., 0.18, 0.3, 1.3, 2 and 5). Then, the titania sol was added to the mixture in the amount corresponding to the R/TiO₂ ratio of 0.07. The mixture was stirred for 15 min and aged at room temperature for 36 hours.

The experimental results from Figure 3 indicate that the use of preformed sol can generally increase the surface area of titania product, comparing to that when TTIP is used as the precursor. The surface area of the product is in range of 30-40 m²/g, while the average pore diameter is 3-4 nm corresponding mesoporous structure. However, when the R/F ratio is increased, the surface area of the product generally decreases, except for the case when R/C ratio is 5.0. Brandt et al. reported that acetic acid at low content (i.e., at R/C ratio of 5.0) behaved in the same manner as the base catalyst such as sodium carbonate^[6], but the use of acetic acid for resorcinol-formaldehyde gel formation usually causes the surface area of the RF product to be lower than when sodium carbonate is used as the catalyst. In this study, high surface area of 70 m²/g was obtained when the highest value of the R/C ratio (i.e., 5.0) was used with the highest value of R/F ratio (i.e., 2.0). It has been reported that the gel can easily collapse when excessive amount of acetic acid (i.e., low R/C ratio) is used, thereby causing the decrease in the surface area of the product^[7].

Figure 3. Surface area of titania product prepared from titania sol and RF-gel, using the R/C ratio of 0.18 (●), 0.3 (□), 1.3 (△), 2 (▲) and 5 (■) as a function of the R/F ratio of the RF-gel.

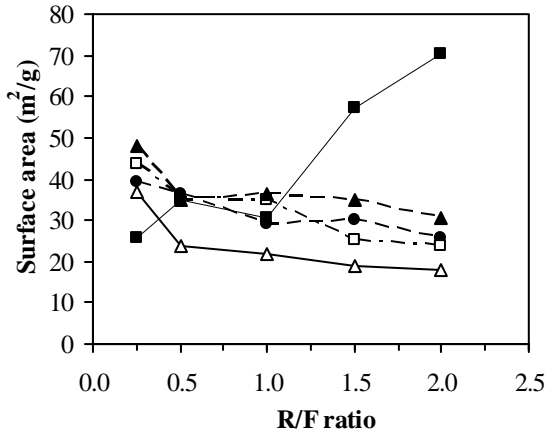


Figure 4. FTIR signal ratio for various functional groups within the RF/titania composite prepared from titania sol and RF-gel using the R/C ratio of 0.18 (a), 0.3 (b), 1.3(c), 2(d) and 5(e) as a function of the R/F ratio of the RF-gel.

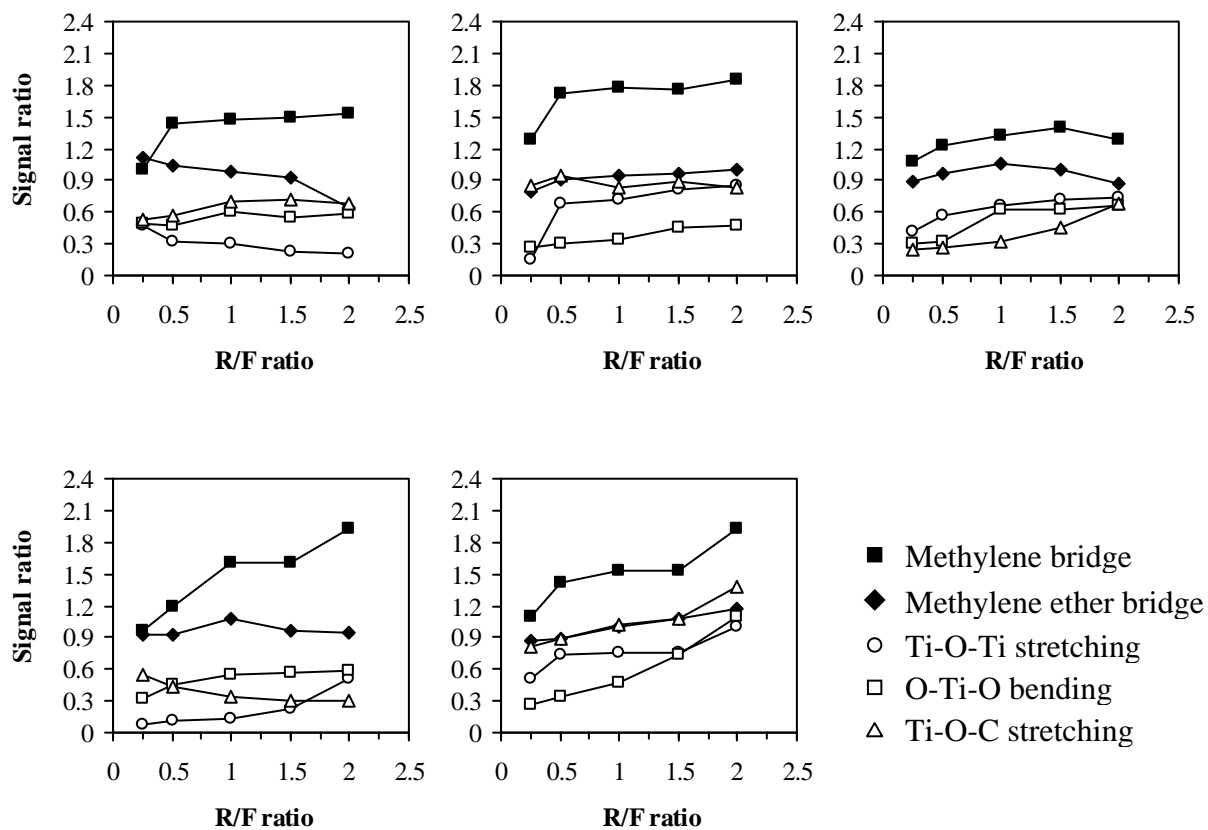
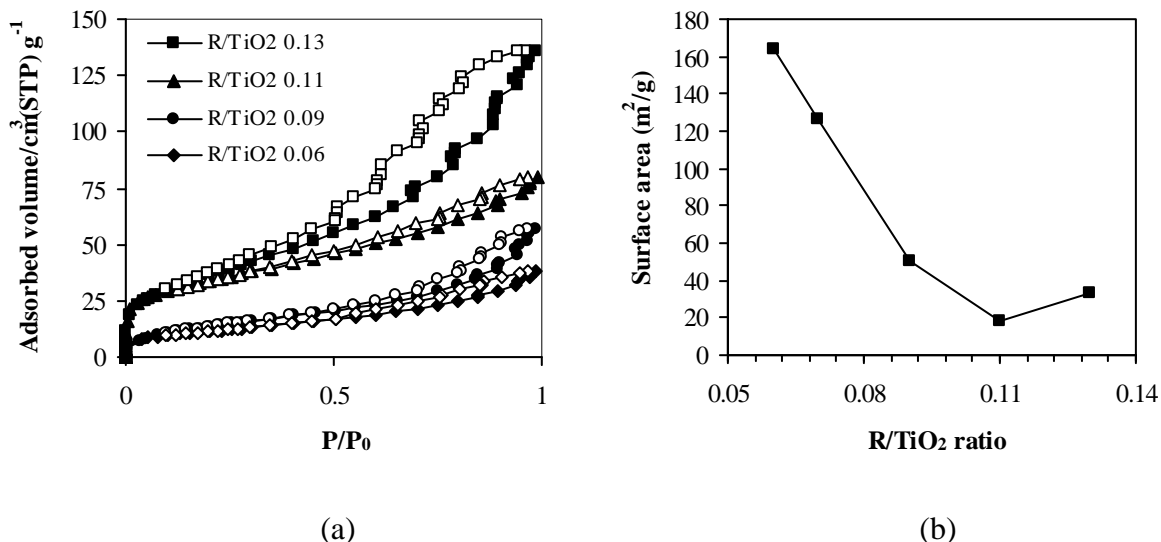


Figure 4 shows effects of R/C ratio and R/F ratio on the FTIR signal ratios obtained from RF/titania composite synthesized by using TiO_2 sol in similar manner to those presented in Figure 2. As the R/F ratio is increased, the signal from Ti-O-C bonding increases as those from both methylene and methylene ether bridges of the RF-gel, which suggests that the titania sol interacts with RF-gel in the manner that allows further networking of the RF-gel. Therefore, the porosity of the titania can still be controlled by the growth of RF-network. This is quite different than when TTIP is used as the precursor. This effect is less eminent at low R/C ratio (e.g., 0.18-3) because acetic acid used as the catalyst also reacts with resorcinol so that formaldehyde can not react with resorcinol to form bridges or RF-network.

Effect of R/ TiO_2 Ratio

In this section, the porous titania product was prepared using titania sol and RF-gel at the R/ TiO_2 molar ratio of 0.06, 0.07, 0.09, 0.11 and 0.13, respectively. The R/C ratio was fixed at 5.0. Figure 5a illustrates the nitrogen adsorption-desorption isotherms and pore size distributions of the calcined products prepared using the R/F ratio of 2.0. All products show Type IV isotherm with hysteresis loop, which is typical for mesoporous material. At the R/ TiO_2 ratio of 0.06, the sample shows the largest specific surface area among all samples ($164.3 \text{ m}^2/\text{g}$) with the average pore diameter of 3 nm. At high value of R/ TiO_2 ratio, the adsorption-desorption isotherm shows higher fraction of mesopore than that of micropores and the surface area decreases (see Figure 5b). The average pore diameter of product is about 2-5 nm. The pore size distribution becomes broaden as a result of greater amount of TiO_2 sol, which can react with RF solution and form greater extent of cross-linking in the network. It is also suggested that the interactions involving titania sols can be divided into two processes, i.e., the reaction between titania sol and RF-clusters and the interaction among titania sols to form large titania particles. According to the results, it is suggested that high content of RF-gel makes the titania clusters dispersed causing the porous structure to be easily collapsed during the calcination. Nevertheless, without the RF-gel, mesoporosity of titania porous structure could not be achieved.

Figure 5. Adsorption-desorption isotherm (a) and surface area (b) of titania product prepared from titania sol and RF-gel, using R/F ratio of 2.0, R/C ratio of 5.0 and various values of R/TiO₂ ratio.



CONCLUSION

RF gel can be used as a template for the mesoporous titania product. Reaction between TTIP and RF solution is so strong that rapid solidification takes place, resulting in a product with low surface area. The preformed titania sol can be used in place of TTIP to reduce the interaction with RF-gel. Yet, titania sol can still react with RF-gel and form into network. The mesoporosity of the product is achieved from the cross-linking network between titania sol and RF-gel.

ACKNOWLEDGMENTS

This study is partly supported by the Centennial Fund of Chulalongkorn University to the Center of Excellence in Particle Technology.

REFERENCES

1. Zhang, W., H. Wang, and Z. Jin, Gel casting and properties of porous silicon carbide/silicon nitride composite ceramics. *Materials Letters*, 2005. 59(2-3): p. 250-256.
2. Wang, C., Z.-X. Deng, and Y. Li, The Synthesis of Nanocrystalline Anatase and Rutile Titania in Mixed Organic Media. *Inorganic Chemistry*, 2001. 40(20): p. 5210-5214.
3. Mahshid, S., M. Askari, and M.S. Ghamsari, Synthesis of TiO₂ nanoparticles by hydrolysis and peptization of titanium isopropoxide solution. *Journal of Materials Processing Technology*, 2007. 189(1-3): p. 296-300.

4. Babic, B., Kalu·erovic B., Vracar Lj., Krstajic N., Characterization of carbon cryogel synthesized by sol-gel polycondensation and freeze-drying. *Carbon*, 2004. 42(12-13): p. 2617-2624.
5. Mirzaeian, M. and P. Hall, The control of porosity at nano scale in resorcinol formaldehyde carbon aerogels. *Journal of Materials Science*, 2009. 44(10): p. 2705-2713.
6. Brandt R., Petricevic R., Pröbstle H., Fricke J., Acetic Acid Catalyzed Carbon Aerogels. *Journal of Porous Materials*, 2003. 10(3): p. 171-178.
7. Wu, D., Fu R., Zhang S., Dresselhaus M.S., Dresselhaus G., The preparation of carbon aerogels based upon the gelation of resorcinol-furfural in isopropanol with organic base catalyst. *Journal of Non-Crystalline Solids*, 2004. 336(1): p. 26-31.

Polluted dust optics: Case of semi-external mixing

S. K. Mishra¹, S. N. Tripathi², S. G. Aggarwal¹, and A. Arola³

1 National Physical Laboratory, New Delhi, India, 110012

2 Indian Institute of Technology, Kanpur, India, 208016

3 Finnish Meteorological Institute, Kuopio, Finland, 70211

Principal Contact: S. K. Mishra, Mr., National Physical Laboratory, New Delhi, India, 110012.

Tel: +91-11-45608621 Fax: +91-11-45609310 E-mail: mishrask@mail.nplindia.ernet.in

Abstract

The radiative signature of polluted dust is completely different to that of pure dust when interacting with the solar radiation, hence the modeling/observation of polluted dust optics is imperative (Forster et al., 2007) for many sensitivity studies. During long-range transport, the pure mineral dust mixes with the carbonaceous pollutants in the atmosphere semi-externally (Li et al., 2010; Alexander et al., 2008) besides internal, external and core-shell mixing but the effect of semi-external mixing on the dust optics has not been studied in detail.

In present study, we consider the pure mineral dust composed of non-metallic components and metallic component such as hematite, Fe_2O_3 (Mishra and Tripathi, 2008). The hematite percentage in the pure mineral dust governs its absorbance considerably. Based on this hematite variation, the hematite fraction in pure mineral dust was constrained between 0–8%. The morphological and mineralogical characterization of the polluted dust led to consider the three sphere, two sphere and two spheroid model shapes for polluted dust particle system. These model shapes were considered for the mineral dust getting polluted with (1) organic carbon, OC (comprising of HUMic-Like Substances, HULIS) (2) brown carbon, BrC and (3) black carbon, BC by making a semi-external mixture.

The optical properties (e.g. Single Scattering Albedo, SSA; Asymmetry parameter, g and Extinction efficiency, Qext) of above model shapes for the polluted dust were computed using Discrete Dipole Approximation, DDA code. The SSA was found to vary depending on hematite content (0–8%) and model shape composition. For three-sphere model shapes with 0% hematite composed of black carbon-dust-dust (BCDD-0), brown carbon-dust-dust (BrCDD-0) and organic carbon-dust-dust (OCDD-0), the deviation of SSA and g relative to conjugate BC, BrC and OC spheres are ~68% and ~31%, ~83% and ~31% and ~70% and ~33%, respectively. The complete optical properties will be discussed in detail.

Keywords: Semi-external, mixing, mineral dust, optical properties

Modeling of the Influence of Aerosol Processes for the Dispersion of Traffic Exhaust in a Street Canyon

Xinling Li, Wei Liu, and Zhen Huang

Key Laboratory of power Machinery and Engineering Education Ministry Shanghai Jiao Tong University

Principal Contact: Xinling Li, Doctor, Shanghai Jiao Tong University, 800 Dongchuan Road, Shanghai 200240, China.

Tel: 021-34206728 Fax: 021-34205949 Email: lxl@sjtu.edu.cn

Abstract

As shown in the literature [Vertical variations of particle number concentration and size distribution in a street canyon in Shanghai, China, Science of the Total Environment, 2007, 378 (3): 306-316], the decay rate of the total particle number concentration (10-487 nm) was larger than those of PM_{2.5} and CO concentrations during the transportation and dispersion in the street canyon. The data indicates that aerosol dynamic processes, besides dilution process, affected particle number concentration. In order to study the influence of the aerosol dynamic process on the particle transformation from the street to the urban background, we have compared measured particle number size distribution data with the predictions of the operational street pollution model (OSPM) used in combination with an aerosol process model including dilution, coagulation, condensation and deposition. The result shows that the particle number concentration in the nucleation and Aitken modes decrease with increase the height under the effect of dilution, deposition, coagulation processes. The inter- and intramode coagulation of ultrafine particles and atmospheric suspended particles (for example PM_{2.5}) and particle depositional losses to the ground and walls is shown to be important process as the traffic pollutant disperse from the street to the urban background. The condensation of semi-volatile component on ultrafine particles also show to be an important process during traffic peak hours, while the effect of semi-volatile component on ultrafine particles transformation is negligible as the semi-volatile component concentration is below a threshold value. The effect of meteorology parameters, such as humidity, temperature, wind speed and solar radiation, on the particle nucleation and growth is also discussed in the paper.

Keywords: Particulate mass, Aerosol dynamics, Street canyon, Traffic exhaust

The Method to Control the Size of Generated Particles from a Spark Discharger by the Ion Bombardment with the Multi-ionizing

Kyu-Tae Park¹ and Jungho Hwang¹

1 Department of Mechanical Engineering, Yonsei University, Seoul, Republic of Korea, 120-749

ABSTRACT

This paper reports the effects of tremendous ions interrupting agglomeration of Nickel (Ni) aerosol from homogeneous spark generation. We made particles from spark discharger get charged with ions and take repulsive forces to interrupt the particle agglomeration. We set our experiment with clean air supply system, spark dischargers, ionizers with carbon fibers, and chambers for multi-ionizing. We designed our experimental system that we could shift the position of the ion chamber to control gaps between a spark discharger and an ion chamber. In addition, we took control the amount of ions in the ion-chamber. We used an electrometer and ion trap to evaluate the average charging number of particles. The size distribution, rate of generation, morphology, and structure of the particles were characterized by SMPS, scanning electron microscopy (SEM), transmission electron microscopy (TEM) methods. Finally, we got the information regarding the change of the size of particles as we controlled the position of the ion-chamber and the amount of ions.

KEYWORDS

Spark discharge, Particle size control, Particle agglomeration, Ionizer

Introduction

The generation of metallic nanoparticles has mainly been carried out in liquid solutions containing metal ions, reductants, and some polymers (protecting agents) (Devarajan, Bera,&Sampath, 2005). Recently, considerable attention has been focused on the characteristics of “naked” metal nanoparticles (Harada, Toshima, Yoshida, & Isoda, 2005), which are believed to be appropriate for examining the effect of surface structure and geometry. However, the addition of both reducing and protecting agents highlights the complexity of their generation (Yang, Wan, & Wang, 2004). Other methods for generating naked metallic nanoparticles include pyrolysis, chemical vapor deposition, and sputtering. However, these processes demand either high temperatures or a high vacuum environment, which are expensive to operate (Lu & Lin, 2000). Spark generation has been used to generate monometallic particles of a wide range of

conducting materials with particles sizes ranging from several nanometers up to $\sim 100\text{m}$ in an aerosol state because spark generation is simple, easily deliverable, and environmental friendly (Borra, 2006). While most of these studies introduced specific metal particles by spark generation for particular applications, few studies have discussed the aerosol behavior of these particles with the exception of Evans et al. (2003), Horvath and Gangl (2003), Kim and Chang (2005), and Schwyn et al. (1988), who measured the particle size distribution using a scanning mobility particle sizer (SMPS). Recently, needs for smaller particles are increasing in specific fields. Because using smaller particle is more economical and efficient. In case of anti-biotic coating, there are germs as spot, but it is very usual to cover all of domain with coating material. It could cause wasting of materials what we use on coating. On the other hand, we can save our material as taking spot selective coating with smaller particles. It means that we can take a coating at specific spot where germs exist. In addition, in case of catalyst, using smaller particles can boost reaction efficiency because it makes increase specific surfacearea. Moreover, Chin Li Cheung et al. report that CNT which has more smaller diameter, takes more higher value as material for application on broad field. As a sort of methods to get particles having smaller peak diameter, we generate particles with spark discharger and then use ionizers to interrupt agglomeration of particles. We even made pirex ionizing chamber for multi-ionizing which consist of several ionizers. The collision among ions and particles makes particles have charging number. Then, charged particles affect each other with repulsive force. This phenomenon disturbs agglomeration of particles. So, we can get particles having narrow distribution with smaller peak diameters.

Experimental Methods

Fig.1 shows a schematic of the spark generation process. A spark was generated between two either identical (homogeneous spark) or different (heterogeneous spark) metal rods (diameter: 3 mm, length: 100 mm, Nilaco, Japan) inside a reactor (volume: 42.8 cm³) under a pure nitrogen environment (less than 10–4 impurities) at STP (Byeon et al., 2006). The flow rate of nitrogen gas, which was controlled using a mass flow controller (MKS, USA), was set to 3 L/min. The electrical circuit specifications are as follows: a resistance of 0.5M Ω , a capacitance of 10 nF, a loading current of 2 mA, an applied voltage of 3.0 kV, and a frequency of 667 Hz. The gas temperature inside the spark channel was increased beyond a critical value (Berkowitz & Walter, 1987; Borra, 2006), which was sufficient to sublime parts of the electrodes. The duration of each spark was very short (~ 1.5 ms) and the vapors cooled rapidly downstream of the spark. This formed a supersaturation resulting particle formation through nucleation/condensation. As shown in figure 2, Ionizing chamber (ne²fs lab) was set up at specific point. The position of this chamber could be freely shifted if we wanted to change distance between ionizing chamber and spark discharging system. In this case, we observed that effects of disturbance of agglomeration of

particles by ions make different results as changing distance of ionizing. In addition, this ionizing chamber was designed to equip a number of ionizers(1-6). This design allowed us to control intensity of ionizing. Ions generated from the ion chamber affect both generation of spark discharge and agglomeration of aerosol particles from spark discharging system.

Results and Discussion

Ion concentration in ion chamber

Ion generation

Fig.3 shows the results of ion generation. We measured it as we controlled a number of ionizers(1-6) and distance between the ion chamber and the ion counter. We found that ion concentration increases with increasing number of ionizer and ion concentration decreases as the measurement point gets far from the ion chamber.

Particle size control

Distribution of particles

Fig.4-7 shows the results of the particle size control. In all the cases, as a number of ionizer increases, the mode diameter of particle shifts to left side. It means that we can make the generated particle get smaller with increasing number of ionizers. It is because more ions have possibilities to make particles get charged. Finally, particles get stronger repulsive forces and their agglomeration is interrupted.

Figures

Figure 1. Process of particle generation by spark discharger

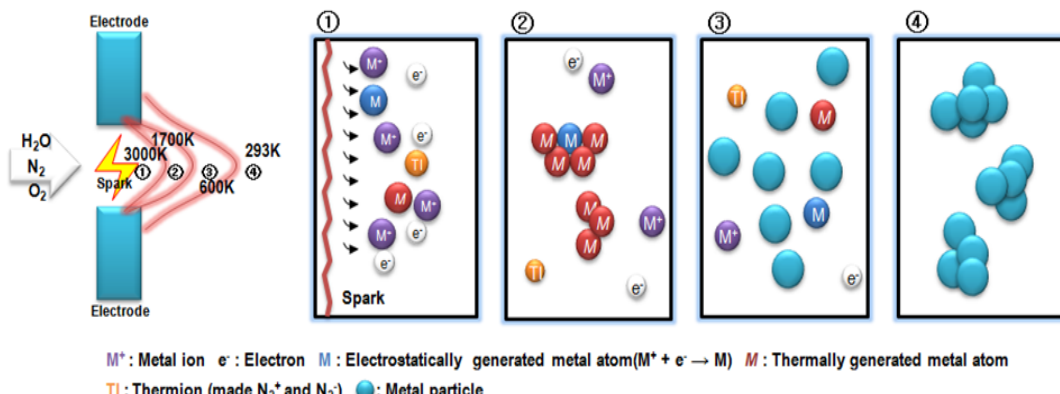


Figure 2. Schematic of experimental setup

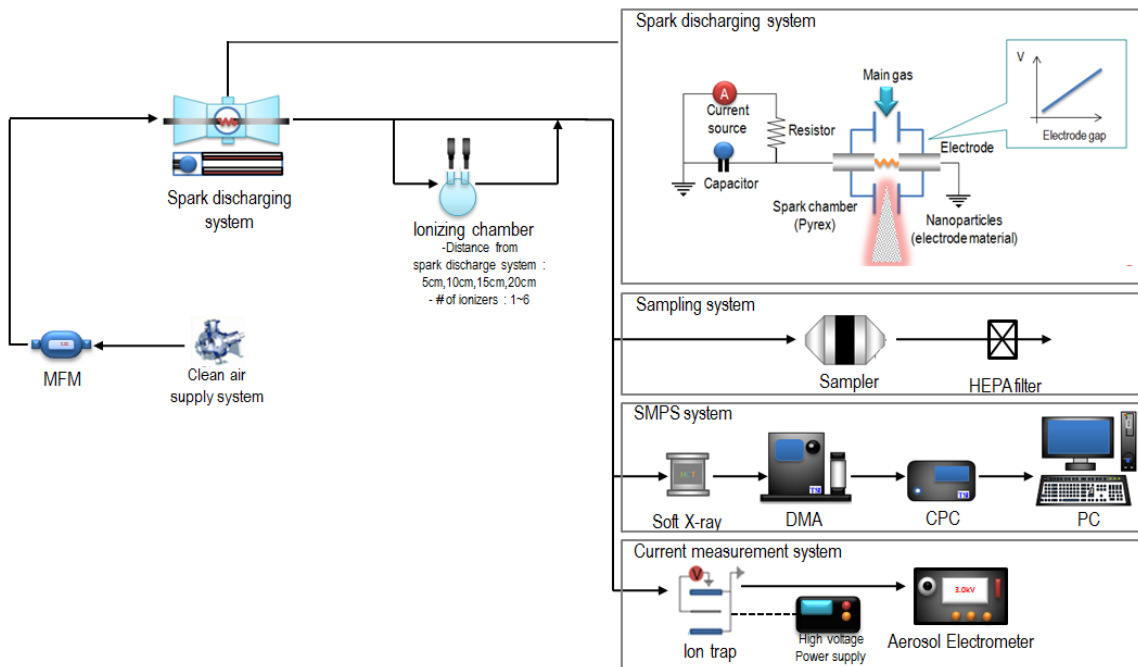


Figure 3. Result of ion generation

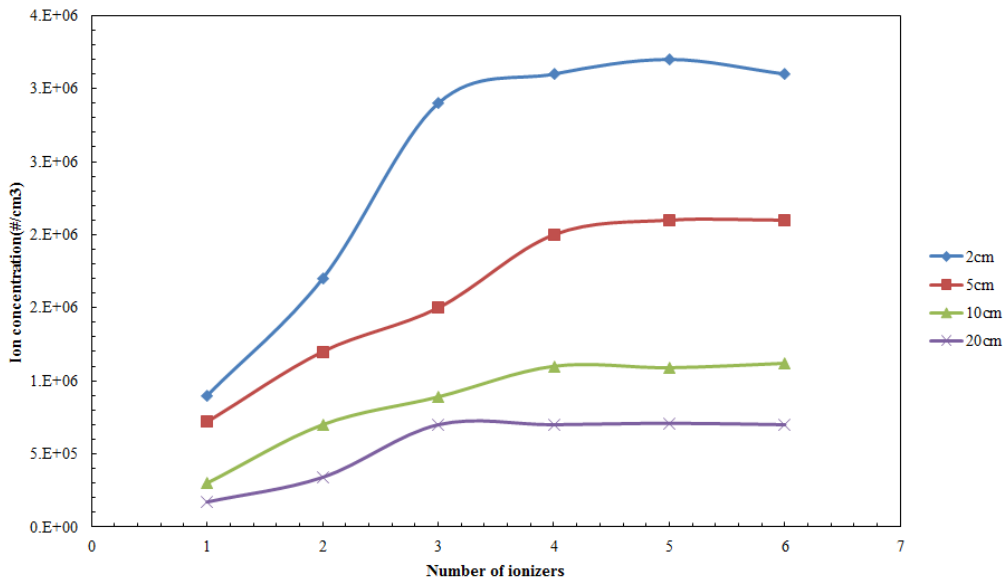


Figure 4. The change of size distribution of Ni particle (distance between spark discharer and ionchamber is 5cm)

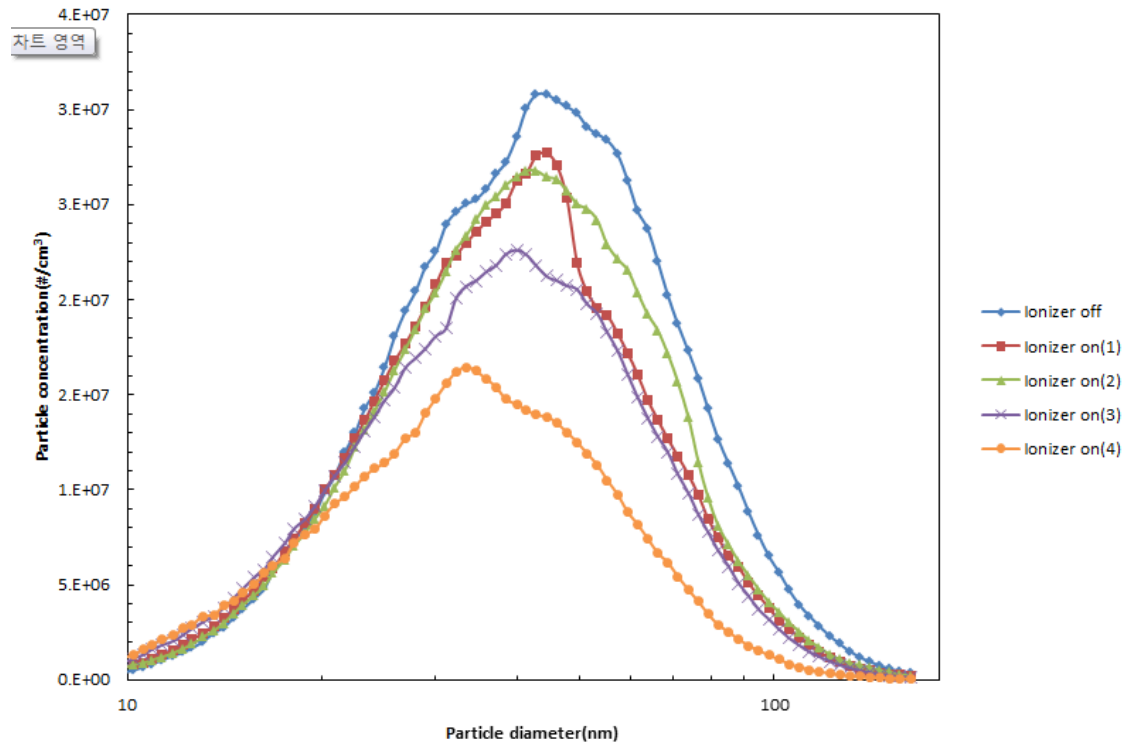


Figure 5. The change of size distribution of Ni particle (distance between spark discharer and ionchamber is 10cm)

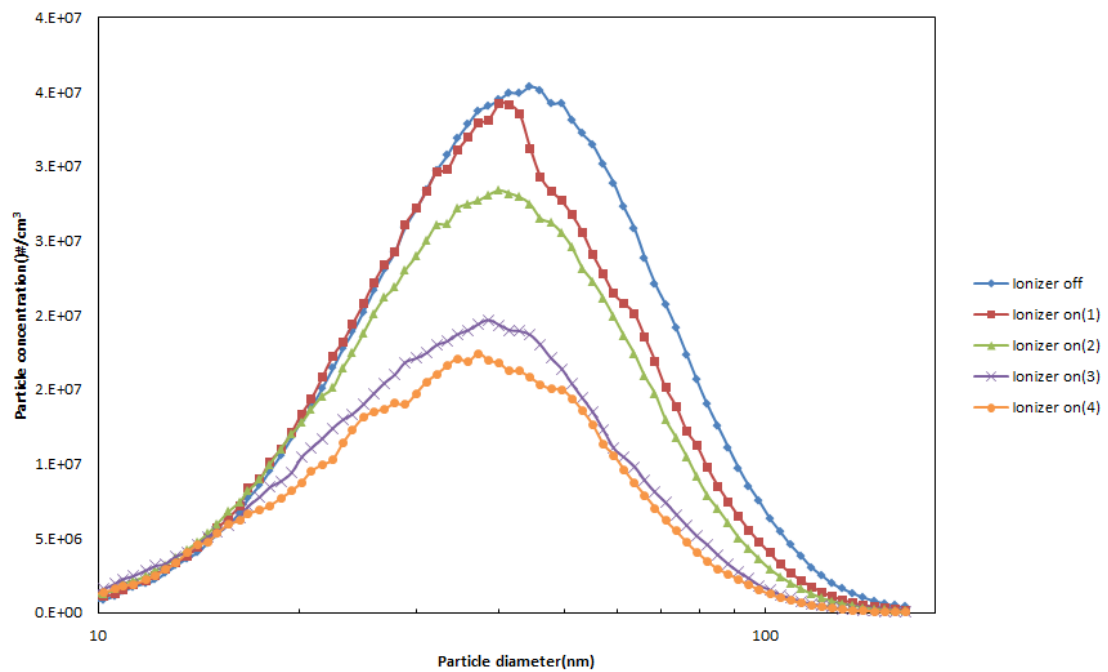


Figure 6. The change of size distribution of Ni particle (distance between spark discharer and ionchamber is 15cm)

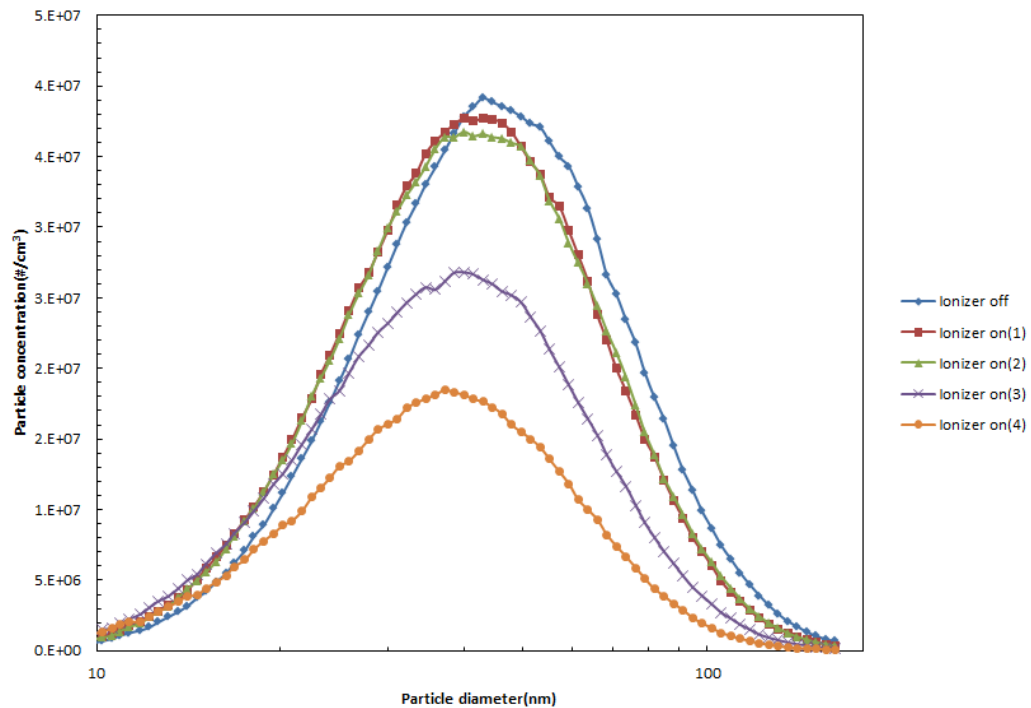
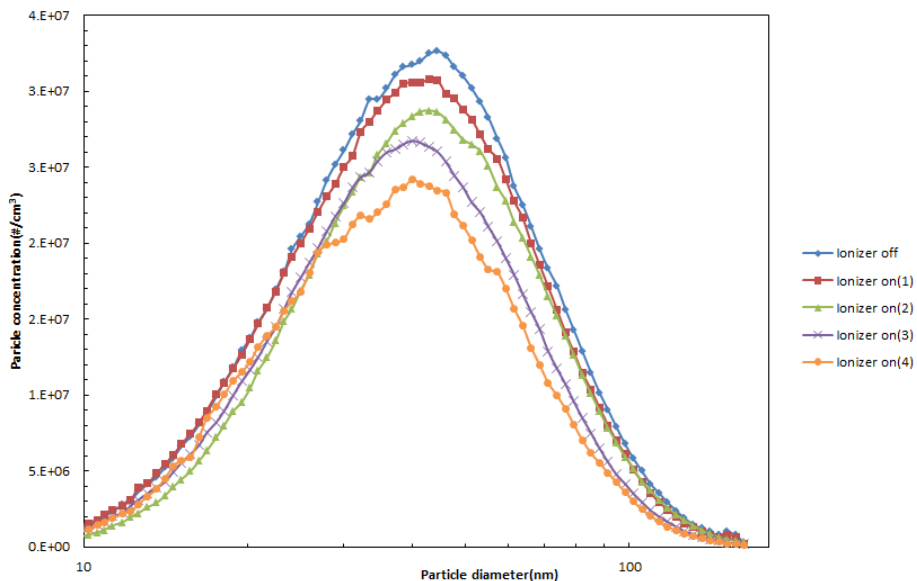


Figure 7. The change of size distribution of Ni particle (distance between spark discharer and ionchamber is 20cm)



SUMMARY OR CONCLUSION

We checked the effects of tremendous ions interrupting agglomeration of Nickel (Ni) aerosol from homogeneous spark generation. We made particles from spark discharger get charged with ions and take repulsive forces to interrupt the particle agglomeration. We set our experiment with clean air supply system, spark dischargers, ionizers with carbon fibers, and chambers for multi-ionizing. We found that increasing number of ionizers generates more ions and makes particles get stronger repulsive forces to interrupt their agglomeration.

ACKNOWLEDGMENTS

REFERENCES

Example References

- [1] Devarajan, S., Bera, P., & Sampath, S. (2005). Bimetallic nanoparticles: A single step synthesis, stabilization, and characterization of Au–Ag, Au–Pd, and Au–Pt in sol–gel derived silicates. *Journal of Colloid and Interface Science*, 290, 117–129.
- [2] Harada, M., Toshima, N., Yoshida, K., & Isoda, S. (2005). Aggregated structure analysis of polymer-protected platinum/ruthenium colloidal dispersions using EXAFS, HRTEM, and electron diffraction measurements. *Journal of Colloid and Interface Science*, 283, 64–78.
- [3] Yang, C.-C., Wan, C.-C., & Wang, Y.-Y. (2004). Synthesis of Ag/Pd nanoparticles via reactive micelles as templates and its application to electroless copper deposition. *Journal of Colloid and Interface Science*, 433–439.

Utilization of Three Plutonium Aerosol Monitoring Techniques for Continuous Monitoring of the Filtered Exhaust Gas in a Plutonium Reprocessing Facility

Yongyang Su*, Zhiming Li, Jiang Xu, Xiangjun Ren, Guoqing Zhou, Lihua Zhai, Longbo Liu, Mei Li and Xiaowei Yi

Northwest Institute of Nuclear Technology, PO 69-14, Xi'an, Shaanxi 710024, China

ABSTRACT

Continuous monitoring of the exhaust gas after filtration in nuclear facilities is vital for process control and environmental protection. In this work, three plutonium aerosol monitoring techniques have been utilized in a plutonium reprocessing facility. Through on-line monitoring of particle number concentration above 10 nm by a commercial Condensation Particle Counter and off-line monitoring of ^{239}Pu activity concentration by ^{242}Pu isotope dilution Inductively Coupled Plasma MS (ICP-MS), it's confirmed that the HEPA filter works properly during the operation process. Direct introduction and rapid determination of plutonium particle by ELEMENT ICP-MS has also been conducted. The results show that the detection limit for plutonium concentration is $5.0 \times 10^{-3} \text{ Bq/m}^3$. Concentrations in the filtered gas are on the order of 10^{-2} Bq/m^3 . It's discovered that some plutonium nanoparticles have penetrated the six-stage HEPA filter, which cannot be observed by CPC and traditional off-line monitoring method. This novel technique based on direct introduction and rapid determination of plutonium particle by ICP-MS is a powerful tool for continuous monitoring of ultratrace radioactive aerosol.

KEYWORDS

Plutonium aerosol, Continuous monitoring, filtered exhaust gas, ICP-MS, CPC

Introduction

High Efficiency Particulate Air (HEPA) filtration is the most widely used technique to remove radioactive and hazardous aerosols generated from nuclear facilities. It's vital to evaluate the performance of multiple-stage HEPA filters against plutonium aerosol because of its high toxicity and inhalation harm. Continuous monitoring of the exhaust gas after filtration is necessary for process control and environmental protection. The filtration of plutonium aerosol by HEPA filter has been disputed for decades. Theoretical and experimental studies on filtration efficiency of nanoparticle have been conducted by numerous groups ^[1-4]. However, clear conclusion for filtration efficiency of particles below 10nm has still not been achieved because of the experimental limit, especially the detection instrument. Thus, special attention must be paid to the

filtration efficiency of plutonium particles. Recently, a real-time monitoring technique for plutonium aerosol by ICP-MS has been established and validated preliminarily in our group^[5-7]. A field application of the novel technique for continuous monitoring of the filtered gas in a plutonium reprocessing facility is presented in this work. The gas samples were collected by cylinder samplers and sent to laboratory for plutonium analysis. A magnetic ICP-MS has been utilized for direct introduction and rapid determination of ultratrace plutonium concentration in the gas. Meanwhile, a commercial Condensation Particle Counter (CPC) and traditional off-line plutonium monitoring method based on ²⁴²Pu isotope dilution ICP-MS (ID-ICP-MS) have also been employed to determine the particle number concentration and plutonium activity concentration respectively. Performance of these three plutonium aerosol monitoring techniques is evaluated.

Experimental Methods

Instruments and reagents

ELEMENT ICP-MS (Finnigan MAT, now Thermo Fisher Inc.), Aridus membrane desolvation introduction system (CETAC Inc.), and CPC Model 3010 (TSI Inc.). Natural uranium standard solution (²³⁸U: 1004 μ g/g, RSD=0.3%, SPEX Inc.), ²⁴²Pu standard solution, six-stage HEPA filter (filtration efficiency >99.97% for single stage, NIOSH 7580P100). New Al-alloy seamless gas containers (ShenYang ZhongFu KeJin Pressure Vessels Inc.) are vacuumized to be below 0.1kPa, and then used as passive aerosol samplers.

Plutonium aerosol filtration, sampling and monitoring

In a plutonium reprocessing facility, plutonium aerosol is compressed into a sealed container for temporal storage. As shown in Figure 1, the gas driven by the high pressure flow through the HEPA filter, so the radioactive and toxic particles are removed. Three methods have been utilized to continuous monitor the plutonium concentration downstream of the HEPA filter.

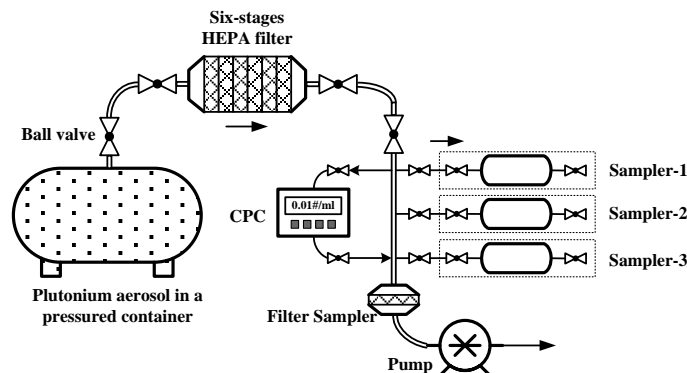


Figure 1 Schematic of plutonium aerosol filtration, monitoring and sampling system

During the whole process, the gas in the main tube flow through a filter sampler (>99.9%) and the gas volume is recorded. ^{242}Pu ID-ICP-MS method is employed to accurately determine the ^{239}Pu amount collected in the filter [8]. Thus, the ^{239}Pu concentration is obtained off-line by dividing the ^{239}Pu amount by the gas volume. The aerosol concentration after the HEPA filter was monitored on-line by CPC.

Three cylinder samplers (numbered S1 to S3) are connected to the main tube in parallel to sample the filtered gas at different times. When the ball valve at the inlet of the sampler is slowly opened, the gas of about 18 degree Celsius injects into the sampler. Representative samples could be obtained because nanoparticles below 100nm follow the carrier gas quite well. After achieving pressure equilibrium, the valves are closed quickly and the samplers are disconnected from the tube. The environmental aerosol is collected by the fourth sampler (numbered S0) and treated as the blank sample. Argon is pressured into these samplers to achieve about 200 kPa. These four samplers are sent to laboratory for direct determination of plutonium concentration by ICP-MS. It's desirable to inject ^{242}Pu aerosol as internal standard into the system to correct the efficiencies and losses in the whole process. However, normal nebulizer couldn't fulfill the leakage requirement of the system and work properly under high pressure. So the internal standard method has not been employed and loss correction couldn't be made in this work.

Direct determination of plutonium concentration by ELEMENT ICP-MS

The principle of the method is introduced in detail in Su et al [9]. The gas sample flow rate is introduced directly into ICP torch. Continuous ^{242}Pu aerosol, nebulized and desolvated by Aridus, is introduced simultaneously to calibrate the instrument sensitivity for ^{239}Pu . So the ^{239}Pu activity concentration in the gas sample is determined by

$$C_s = \frac{239AC_2Q_{\text{up}}}{242Q_s} \left(\frac{\sum ^{239}\text{Pu}}{\sum ^{242}\text{Pu}} \right) \left(\frac{R_{9/2,0}}{k} - \frac{R_{9/2,0}}{k_0} \right) \quad (\text{Eq.1})$$

It's usually observed that the ion signal at $m/z=239$ is weak, continuous and nearly stable while the ion signal at $m/z=242$ is stable under the same condition. So a simplified form is obtained

$$C_s = \frac{239AC_2Q_{\text{up}}}{242Q_s} \left(\frac{\overline{R_{9/2}}}{k} - \frac{R_{9/2,0}}{k_0} \right) \quad (\text{Eq.2})$$

where ^{239}Pu specific activity (A) equals 2.3×10^9 Bq/g, and the mass concentration of ^{242}Pu working solution (C_2) equals 2.67×10^{-12} g/g. Liquid uptake rate of Aridus (Q_{up}) is determined by dividing the decrease of ^{242}Pu solution mass by the uptake time. Aerosol generation efficiency of Aridus (η_a) is defined as the fraction of ^{242}Pu in aerosol particles at the outlet to that in the solution uptaked by the nebulizer [6]. The real volume flow rate of gas sample (Q_s) is determined from the fitted curve of pressure vs. time. $R_{9/2,0}$ and k_0 are the measured $^{239}\text{Pu}/^{242}\text{Pu}$ isotope ratio and the correction factor respectively when only ^{242}Pu solution is nebulized then introduced into

the torch. $\overline{R_{9/2}}$ is the average value of $^{239}\text{Pu}/^{242}\text{Pu}$ isotope ratios for six measurements during gas sample introduction. At last, uranium solution is nebulized instead of ^{242}Pu solution to obtain the k value while other introduction parameters remain the same. In order to eliminate the interferences between different samples, the $R_{9/2,0}$ value is measured at the beginning of each sequence to exclude the effect of the increasing background.

Results and Discussion

Plutonium concentration monitored by CPC and the filter sampler

No increase in the particle number is observed by CPC during the filtration process. However, particles below 10nm couldn't be detected because of the instrument response limit. Plutonium activity concentration monitored by the filter sampler shows that the average concentration is comparable to the background value.

Plutonium concentration determined directly by ICP-MS

The gas flow rate is limited to 15ml/min to avoid acute decrease of instrument sensitivity due to matrix effect. The liquid uptake rate of Aridus (Q_{up}) determined experimentally is 0.119g/min (RSD=3.8%). After optimization, the sweep gas flow rate is 2.8L/min corresponding to the aerosol generation efficiency (η_a) of 30%. When ELEMENT is used for analysis, k_0 and k are 0.994 (RSD=0.32%) and 1.025 (RSD=0.94%) respectively. The $^{239}\text{Pu}/^{242}\text{Pu}$ isotope ratio in the ^{242}Pu solution determined by ELEMENT is 1.20×10^{-3} ($\sigma=6.8 \times 10^{-5}$). Value of 3σ is used instead of $(\overline{R_{9/2}}/k - R_{9/2,0}/k_0)$ in equation (2) to calculate the detection limit (DL) for plutonium concentration. Assuming Q_s is 7.6ml/min, the result shows that DL for ELEMENT is 5.0×10^{-3} Bq/m³.

As shown in Table 1, plutonium concentration in sample S0 could not be detected due to the background. ^{239}Pu concentrations in samples S1~S3 are in the range of 2.0×10^{-2} Bq/m³~ 3.4×10^{-2} Bq/m³. Some plutonium particles may have penetrated the six-stage HEPA filter, although monitoring results using CPC and filter sample indicate that the HEPA filter operates normally. The concentration uncertainty indicates that a systematic error may exist. As nanoparticles below 100nm can follow the carrier gas quite well because of its small inertia, the sampling bias might not be serious. In the measurement, the transport losses due to gravitational deposition and diffusion loss in tubes could be ignored. Limited by the ultratrace concentration and the measurement uncertainty, the effect of ultrasonic vibration for the possible deposited and adhered particles couldn't be distinguished in this work.

In further study, the measurement uncertainty should be evaluated. Investigation of the penetrated plutonium particle including its size, morphology and inhalation harm is also interesting.

Table 1. ^{239}Pu concentration in four aerosol samples determined by ELEMENT

Sample no.	$Q_s/\text{ml min}^{-1}$	$C_s/\text{Bq m}^{-3}$
S0	7.6	Not detected
S1	5.3	1.7×10^{-2}
	7.6	2.4×10^{-2}
	mean	2.0×10^{-2}
	5.6	2.4×10^{-2}
S2	7.6	4.4×10^{-2}
	mean	3.4×10^{-2}
	5.3	2.1×10^{-2}
S3	7.4	2.9×10^{-2}
	mean	2.5×10^{-2}

SUMMARY

Three plutonium aerosol monitoring techniques have been utilized for continuous monitoring of the filtered exhaust gas in a plutonium reprocessing facility. Through on-line monitoring of particle number concentration by CPC model 3010 and off-line monitoring of ^{239}Pu activity concentration by ^{242}Pu ID-ICP-MS, it's confirmed that the HEPA filter works properly during the operation process. Direct introduction and rapid determination of plutonium particle by ELEMENT ICP-MS has been conducted. The results show that the detection limits for plutonium concentration is $5.0 \times 10^{-3} \text{ Bq/m}^3$. Concentrations in the filtered gas are on the order of 10^{-2} Bq/m^3 . It's discovered that some plutonium nanoparticles have penetrated the six-stage HEPA filter, which cannot be observed by CPC and traditional off-line monitoring method.

ACKNOWLEDGMENTS

The authors would like to express their gratitude to Prof. Fengrong Zhu for valuable comments on the paper and also appreciate Guanyi Li and Zhihong Zhang for their helps during the experiment.

REFERENCES

- [1] Cheng Y S and Yeh H C. *Journal of Aerosol Science*, 1980, 11: 313-320.
- [2] Wang H C and Kasper G. *Journal of Aerosol Science*, 1991, 22: 31-41.

- [3] Van Gulijk C, Bal E, Ott A S. *Aerosol Science and Technology*, 2009, 40: 362-369.
- [4] Heim M, Attoui M, Kasper G. *Journal of Aerosol Science*, 2010, 41: 207-222.
- [5] Su Yongyang, Li Zhi-ming, Zhou Guoqing, et al. *Journal of Instrumental Analysis (Fen Xi Ce Shi Xue Bao)*, 2009a, 28: 436-439. (in Chinese)
- [6] Su Yongyang, Li Zhiming, Dong Hongbo, et al. *Int J Environ Anal Chem*, 2011, 91: 473-483.
- [7] Su Yongyang, Li Zhiming, Zhou Guoqing, et al. *Atomic Energy Science and Technology (Yuan Zi Neng Ke Xue Ji Shu)*, 2010a, 44: 272-277. (in Chinese)
- [8] Zhou Guoqing, Zhu Fengrong, Zhang Zibin, et al. *Journal of Chinese Mass Spectrometry (Zhi Pu Xue Bao)*, 2002, 23: 151-155. (in Chinese)
- [9] Su Yongyang, Li Zhiming, Dong Hongbo, et al. *Chinese Journal of Analytical Chemistry (Fen Xi Hua Xue)*, 2010b, 8: 1139-1143b. (in Chinese)

Overlooking aerosol metrology: A big hole in atmospheric aerosol measurement studies

Shankar G. Aggarwal and Prabhat K. Gupta

Analytical Chemistry, National Physical Laboratory – CSIR, New Delhi 110012, India

Principal Contact: Shankar G. Aggarwal, Dr., National Physical Laboratory – CSIR, New Delhi 110012, India.

Tel: +91 11 4560 8376 Fax: +91 114560 9310 Email: aggarwalsg@nplindia.org

Abstract

Aerosols are short-lived as compared to greenhouse gases, their impact is more regional, and the extent of their cooling and heating effects on earth's system is still quite uncertain. The uncertainty in total anthropogenic radiative forcing (greenhouse gases + aerosols) is dominated by the uncertainty in aerosol radiative forcing. In the climate model, aerosol composition, optical and physical data are required as the inputs, therefore a small error in the aerosol measurements can further enhance the complexity in understanding its impact on climate. For example, black carbon (BC) intends warming effect, whereas other major components of aerosol particles, such as sulfates exhibit cooling effect to the earth's system. Therefore, accurate (traceable) measurements have a key role in our better understanding towards aerosol effects and its climate consequences. However, more than 30% variations in BC measurement data have been reported depending on (i) instrumental technique used (ii) measurement protocol used (iii) definitions of BC, which overlaps with elemental carbon, brown carbon, organic carbon, etc. Beside this, most importantly, traceability link is generally found missing in the measurement data. As far as these issues are concerned, the standard measurement protocols are required. Secondly, checking of the instrument performance using an aerosol certified reference materials (CRMs) is also a key for improving the quality of the measurement data (i.e., traceability issue) and reliability of the comparison results. So far, very few aerosol CRMs (with very limited types) are available at international level. Therefore the aerosol research community needs to give more emphasis on development of aerosol standards, standardization of measurement protocols for traceable aerosol measurements, inter-comparison studies at national as well as international level. The metrology institutes should encourage for this job. Recently in Europe, several studies and projects are undertaken to address this issue, and are also programmed for future. Now it is a high time to take initiatives collectively to plan such studies for Asian region.

Keywords: Aerosols, measurement, traceability, CRMs, inter-comparison studies

Nanoparticle characteristics at Lulin site, Taiwan

Sheng-Chieh Chen, Yi-Hong Hong and Chuen-Jinn Tsai*

Institute of Environmental Engineering, Nation Chiaotung University, No. 1001, University Road, Hsinchu 300, Taiwan

Principal Contact: Author Three, Prof., Institute of Environmental Engineering, Nation Chiaotung University, No.1001, University Road, Hsinchu 300, Taiwan,
Tel:+886-3-5731880 Fax:+886-3-5727835 E-mail: cjtsai@mail.nctu.edu.tw

Abstract

The characteristics of atmospheric ultrafine particles (<100 nm, nanoparticles or PM_{0.1}) were studied at the Lulin Atmospheric Background Station (LABS, with an altitude of 2862 m) in Taiwan from June to December in 2010. The real-time size distributions of particles in the size range of 8.5-350 nm or 5.5-210 nm were measured by the SMPS (TSI 3936). Meteorological and gaseous pollutants data monitored at the station such as temperature, relative humidity, solar radiation, O₃ and CO were compared with the SMPS data to study particle nucleation, condensation and SOA (secondary organic aerosol) formation at Lulin site. PM_{0.1}, PM_{2.5} and PM₁₀ were sampled by using two MOUDIs (MSP 110) and a Dichotomous PM₁₀ sampler (Andersen SA-241), and the filter samples were analyzed for both gravimetric mass and compositions, including organic carbon (OC), element carbon (EC), water-soluble ions and trace elements. SMPS data showed that the peak number concentration was associated with the smallest NMD (number median diameter) of 20-50 nm (particles with a lifetime of few minutes) indicated a local particle source (emission from the vegetation and undergo gas-to-particle conversion) dominated at the site. This postulation was confirmed by the high OC content (> 40 %) in PM_{0.1} after taking into account the OC artifact. The concentrations of trace elements K and Mn, which are good biomass burning makers, were normally low in both PM_{0.1} and PM_{2.5}. However, the concentrations were found to be elevated in PM_{0.1} (K: 1.7 ng/m³, Mn: 0.05 ng/m³) and PM_{2.5} (K: 48.6 ng/m³, Mn: 1.73 ng/m³) during November 9th-12th when air masses passed the South-eastern Asia continent prior reaching LABS. Therefore, K and M in both fine particles and nanoparticles at LABS could be good markers for biomass burning from South-eastern Asia.

Keywords: Ultrafine particle, Nanoparticle, Biogenetic aerosol, Biomass burning; Long-range transport.

Diurnal Variation of Chemical Composition in Ultrafine and Fine Particles in Urban Area

Kyung Hwan Kim¹, Takayoshi Okamoto¹, Shimpei Sato¹, Ortiz Ricardo¹, Kazuhiko Sekiguchi^{1,2}, Satoru Chatani³, Tazuko Morikawa³, Hiroaki Minoura³ and Kazuhiko Sakamoto^{1,2, 4*}

1 Graduate School of Science and Engineering, Saitama University, 255 Shimo-Okubo, Sakura, Saitama, 338-8570, Japan

2 Institute for Environmental Science and Technology, Saitama University, 255 Shimo-Okubo, Sakura, Saitama, 338-8570, Japan

3 Japan Petroleum Energy Center, 4-3-9, Toranomon, Minato-ku, Tokyo, 105-0001, Japan

4 Center for Environmental Science in Saitama, 914 Kami-tanadare, Kazo, Saitama 347-0115, Japan

ABSTRACT

Atmospheric ultrafine particles (UFPs; $D_p < 0.1 \mu\text{m}$) and fine particles (FPs; $D_p < 2.5 \mu\text{m}$) are simultaneously collected for 23 h (1 day) and 11.5 h (daytime and nighttime) respectively in November when the contribution of biomass burning increases to observe characteristics of chemical composition in FPs in comparison with those collected for 23 h in UFPs. Contribution of biomass burning in FPs was found to be significant during the sampling periods especially in nighttime. Levoglucosan in UFPs was measured for the first time with that in FPs. The observed concentrations of levoglucosan in UFPs and FPs are highly correlated ($r^2 = 0.92$, $n = 10$, $p < 0.001$) indicating that the observed levoglucosan in the two particle sizes had been originated from local biomass burnings close to the sampling sites. The simultaneous measurement of UFPs and FPs enabled us to find the emission sources (local or regional) in the study area. Negative correlation between organic carbon (OC) and soot-elemental carbon (EC) was observed for FPs collected at roadside while positive correlation between OC and soot-EC was observed for FPs collected at background site indicating different characteristics of carbonaceous components for different environment.

KEYWORDS

Ultrafine particles, Fine particles, Chemical composition, Levoglucosan, Biomass burning

Introduction

Ultrafine particles (UFPs) are important in terms of adverse health effect on human as well as particle growth into fine particles (FPs). Since the leading removal process of UFPs is coagulation to accumulation range, it is crucial to measure particles in UFPs size range ($D_p < 0.1 \mu\text{m}$) as well as fine size range ($D_p < 2.5 \mu\text{m}$) to provide information about their chemical composition and relationships since the two particle size ranges represent the highest particle number and mass concentrations in urban environment. Furthermore, finding the relationship in chemical composition between UFPs and FPs can provide insight into the fundamental particle emission sources¹⁾.

Our previous study revealed seasonal variation of chemical composition in UFPs and FPs and indicated higher (two or three times) concentrations in fall and winter season compared to summer²⁾. Moreover, positive and negative correlations between organic carbon (OC) and soot-elemental carbon (EC), which defined as EC2 plus EC3 analyzed by an Interagency Monitoring of Protected Visual Environment (IMPROVE) protocol with the thermal optical reflectance (TOR) method³⁾, were observed for UFPs and FPs, respectively indicating different characteristics of carbonaceous compounds in the two particle sizes possibly due to the influence of diesel vehicles operated near the sampling site¹⁾. However, these studies carried out only at a roadside environment thus it was necessary to carry out simultaneous sampling at a background site as well as at a roadside environment to support the findings of these studies.

In the present study, atmospheric UFPs and FPs are simultaneously collected for 23 h (1 day) and 11.5 h (daytime and nighttime) respectively in November. Field sampling was carried out for 10 days at a roadside and a background site. Carbonaceous and water soluble ionic components, water soluble organic compounds (WSOC), and levoglucosan, which has been well known as a tracer for biomass burning were analyzed. The objectives of present study are 1) to provide information about the sources (regional or local) of biomass burning in the two particle sizes, 2) to observe the relationships between OC and soot-EC at a roadside and background site in the two particle sizes.

Experimental Methods

Sampling site and sample collection

Saitama City is located on the Kanto Plain at 35. 867° N, 139.65° E to the northwest of the Tokyo Metropolis (Fig. 1). Field sampling was carried out in November for 10 days.

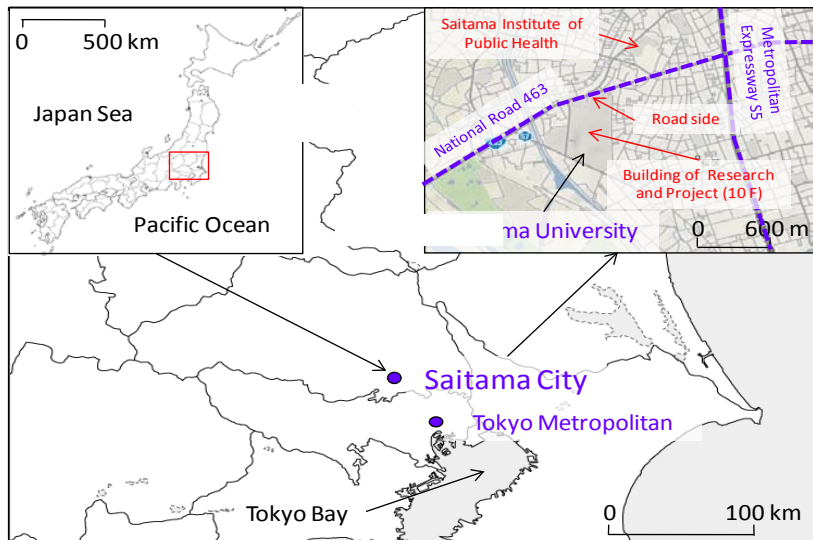


Fig. 1. Sampling locations.

The sampling sites were located on a roadside at the front gate of the Saitama University campus, located near the intersection of two roads and 10th floor (10F) of building in Saitama University (approximately 300 m away from the roadside sampling site). An EPA federal reference method (FRM) using a Partisol ambient particulate sampler (Model 2000-FRM, Thermo, USA) operated at 16.7 L/min and an INF sampler (Kanomax Japan, Inc., Osaka, Japan) operated at 40 L/min were used for the collection of FPs and UFPs, respectively. The sampling duration was 23.5 h and 11.5 h, which corresponds to a total sampling volume of 56.5 and 11.5 m³ for the collection of UFPs and FPs, respectively. Quartz fiber (2500 QAT-UP, Pallflex, CT, USA) filters were used to determine carbonaceous and water soluble ionic components. Teflon filters (PTFE, PP ring supported, Whatman, NJ, USA) were used for the measurement of FPs mass weight. The Teflon filters were measured after placing them in a clean room (temperature: 21.5 ± 1.5 °C, relative humidity: 35 ± 5%) for 24 h before and after each sampling.

Chemical analyses

Carbon analyses were carried out on a Desert Research Institute (DRI) Model 2001 Carbon Analyzer (Atmoslytic Inc., Calabasas, CA) following the IMPROVE_TOR method. In this study, the EC fractions were divided into char-EC and soot-EC⁴. Char-EC is defined as EC1 minus pyrolyzed organic carbon (POC), and the soot-EC is defined as the sum of EC2 and EC3. The total OC is defined as the sum of the four OC fractions plus POC, and the total EC is define as the sum of the three EC fractions minus POC. A quarter of the filter was used for extraction then ionic species were analyzed by ion chromatograph (DX-100, Dionex, CA, USA) and WSOC was analyzed on a total organic compounds analyzer (TOC-V, Shimadzu, Japan). A quarter of the

filter for FPs, and 47-mm whole quartz filter for UFPs samples with blanks were extracted, silylated, and analyzed for levoglucosan by gas chromatography–mass spectrometry (GCMS-QP2010, Shimadzu, Kyoto, Japan) with a DB-5 column (30 m length, 0.32 mm I.D., 0.32 μm film thickness, J&W Scientific)⁵⁾.

Results and Discussion

Concentrations of chemical composition

Overall, roadside samples showed higher mass concentration than those observed at a background site in FPs as expected (Table 1). For the diurnal variations of FPs, nighttime samples (06:00 p.m. to 05:30 a.m.) showed higher concentrations than daytime samples (06:00 a.m. to 05:30 p.m.). This may indicate relatively high contribution of biomass burning during the nighttime than daytime because concentrations of WSOC and levoglucosan for the nighttime samples also increased. The observed concentrations of levoglucosan in UFPs and FPs are highly correlated ($y = 0.048x - 2.6$, $r^2 = 0.92$, $n = 10$, $p < 0.001$) indicating that the observed levoglucosan in the two particle sizes had been originated from local emissions (biomass burnings) because the influence of regional air mass transport in UFPs size is difficult to consider⁶⁾. Unlike the high WSOC concentration in summer by photochemical reaction, it is likely that the contribution of biomass burning in winter would be the main source of the increased WSOC concentration.

When we consider relative contribution of each chemical components in FPs, carbonaceous components account for 50.0% (OC: 35.7%, EC: 14.2%) and 48.7% (OC: 39.5%, EC: 9.1%) at roadside and background site respectively for the daytime samples while those for the nighttime samples account for 51.5% (OC: 38.8%, EC: 12.7%) and 45.8% (OC: 37.5%, EC: 8.3%) at roadside and background site respectively. On the other hand, ionic components did not show significant differences (39.1 - 39.9% at roadside, 38.4 - 39.2% at background site).

Table 1. Average concentrations of chemical composition during the sampling periods.

Species	PM _{2.5} (R) ^c	PM _{2.5} (B) ^d	PM _{2.5} (R)	PM _{2.5} (B)	PM _{2.5} (R)	PM _{2.5} (B)	PM _{0.1} (R)	PM _{0.1} (B)
	Day	Day	Night	Night	23h	23h	23h	23h
PM2.5 mass ($\mu\text{g}/\text{m}^3$)	23.2 ± 14.1	18.84 ± 13.3	28.21 ± 16.8	26.59 ± 16.1	25.87 ± 14.49	22.72 ± 14.46	- ^e	- ^e
OC ($\mu\text{gC}/\text{m}^3$)	8.29 ± 4.06	7.45 ± 4.08	10.73 ± 6.22	9.52 ± 6.12	9.77 ± 4.99	8.75 ± 5.01	1.35 ± 0.42	1.39 ± 0.49
EC ($\mu\text{gC}/\text{m}^3$)	2.77 ± 0.37	1.39 ± 0.71	2.97 ± 1.06	1.78 ± 0.96	2.87 ± 0.59	1.58 ± 0.79	0.20 ± 0.08	0.11 ± 0.07
TC ($\mu\text{gC}/\text{m}^3$)	11.59 ± 4.35	9.17 ± 4.87	14.24 ± 7.41	11.73 ± 7.23	13.18 ± 5.67	10.71 ± 5.93	1.62 ± 0.52	1.56 ± 0.58
Char-EC ^a ($\mu\text{gC}/\text{m}^3$)	1.80 ± 0.78	1.13 ± 0.80	2.57 ± 1.37	1.63 ± 1.10	2.18 ± 1.00	1.38 ± 0.92	0.09 ± 0.05	0.08 ± 0.04
Soot-EC ^b ($\mu\text{gC}/\text{m}^3$)	1.50 ± 0.46	0.59 ± 0.10	0.94 ± 0.20	0.57 ± 0.12	1.22 ± 0.30	0.58 ± 0.05	0.18 ± 0.05	0.10 ± 0.04
Levoglucosan (ng/m^3)	251.5 ± 243.9	239.9 ± 195.4	453.2 ± 408.7	380.8 ± 310.8	360.2 ± 320.6	310.4 ± 244.6	14.12 ± 15.37	- ^e
WSOC ($\mu\text{gC}/\text{m}^3$)	4.49 ± 2.29	4.18 ± 2.14	6.09 ± 3.39	4.46 ± 2.85	5.29 ± 2.62	4.38 ± 2.28	0.61 ± 0.22	0.73 ± 0.28
Cl ⁻ ($\mu\text{g}/\text{m}^3$)	0.83 ± 1.04	0.63 ± 0.75	1.63 ± 0.37	1.78 ± 1.33	1.23 ± 0.44	1.15 ± 0.90	n.d.	n.d.
NO ³⁻ ($\mu\text{g}/\text{m}^3$)	3.33 ± 2.23	2.21 ± 1.68	3.90 ± 2.13	3.52 ± 2.32	3.61 ± 2.10	2.79 ± 1.86	0.09 ± 0.05	0.13 ± 0.09
SO ₄ ²⁻ ($\mu\text{g}/\text{m}^3$)	3.02 ± 2.09	2.23 ± 1.48	2.43 ± 1.39	2.12 ± 1.19	2.72 ± 1.55	2.30 ± 1.39	0.04 ± 0.02	0.08 ± 0.06
Na ⁺ ($\mu\text{g}/\text{m}^3$)	0.23 ± 0.25	0.43 ± 0.30	0.17 ± 0.08	0.46 ± 0.30	0.20 ± 0.13	0.49 ± 0.30	0.02 ± 0.01	0.03 ± 0.02
NH ₄ ⁺ ($\mu\text{g}/\text{m}^3$)	1.28 ± 0.68	1.24 ± 0.72	2.19 ± 1.01	1.73 ± 0.93	1.74 ± 0.80	1.47 ± 0.76	0.02 ± 0.01	0.03 ± 0.01
K ⁺ ($\mu\text{g}/\text{m}^3$)	0.26 ± 0.17	0.34 ± 0.22	0.31 ± 0.20	0.34 ± 0.14	0.29 ± 0.17	0.33 ± 0.16	n.d.	n.d.
Mg ⁺ ($\mu\text{g}/\text{m}^3$)	0.05 ± 0.05	0.04 ± 0.04	0.03 ± 0.03	0.01 ± 0.01	0.03 ± 0.03	0.03 ± 0.03	n.d.	n.d.
Ca ⁺ ($\mu\text{g}/\text{m}^3$)	0.26 ± 0.28	0.26 ± 0.25	0.18 ± 0.14	0.24 ± 0.12	0.21 ± 0.17	0.28 ± 0.22	n.d.	n.d.

\pm indicates standard deviation of concentrations ($n = 10$). n.d. indicates below method detection limit (MDL)

^aChar EC = EC1 – POC, ^bSoot-EC = EC2+ EC3, ^c(R) indicates roadside, ^d(B) indicates background (10F) ^e Not measured.

EC component showed clear difference on the sampling sites indicating EC fractions are mainly emitted by motor vehicles. When char-EC and soot-EC are compared, char-EC in FPs tends to increased during nighttime (9.3%) than daytime (7.3%) for roadside samples while those for background site hardly changed (daytime: 6.0%, nighttime: 6.1%). Soot-EC at roadside accounts

for 6.5 and 3.4% for the daytime and nighttime samples respectively, while soot-EC at background site accounts for 3.1 and 2.2% for the daytime and nighttime samples respectively. For UFPs, carbonaceous components account for 88% (OC: 73%, EC: 15%) and 82% (OC: 73%, EC: 9%) for roadside and background site respectively. Although OC in UFPs similarly accounts for the two sampling sites the contribution of WSOC was lower (33%) and WIOC (40%) was higher at roadside samples than background samples (WSOC: 38%, WIOC: 35%).

Table 2 shows the average OC/EC and char-EC/soot-EC ratios during the sampling periods. The ratios were low at the roadside and high at the background site indicating that the contribution of motor vehicles is high at roadside. Note that OC/EC and char-EC/soot-EC ratios become larger by biomass burning and smaller by motor vehicle emissions. Interestingly, OC/EC and char-EC/soot-EC ratios at roadside for the UFPs samples showed twice higher values than the ratios observed at the background site indicating the contribution of emission sources (e.g., motor vehicles and biomass burnings) can be clearly found by simultaneous collection of UFPs and FPs.

Table 2. Average OC/EC, and char-EC/soot-EC ratios during the sampling periods.

Ratios	PM _{2.5} (R)	PM _{2.5} (B)	PM _{2.5} (R)	PM _{2.5} (B)	PM _{2.5} (R)	PM _{2.5} (B)	PM _{0.1} (R)	PM _{0.1} (B)
	Day	Day	Night	Night	23h	23h	23h	23h
OC/EC	2.95 ± 1.32	5.42 ±1.05	3.39 ±0.84	5.30 ±0.94	3.25 ±0.95	5.45 ±0.73	7.08 ±1.08	14.59 ±4.79
Char-EC	1.62	1.92	3.04	2.76	2.15	2.34	0.48	0.84
/Soot-EC	± 1.61	±1.44	±1.96	±1.73	±1.76	±1.54	±0.15	±0.27

± indicates standard deviation of concentrations ($n = 10$).

Relationships between chemical species

Relationships between char-EC, levoglucosan, and K⁺

The well known indicators for biomass burning, levoglucosan and potassium (K⁺), and the biomass burning indicator, char-EC, which has been recently reported are plotted together to find the relationships between them. Good correlations were observed between the three chemical species for our FPs samples. Levoglucosan and char-EC showed the highest correlation ($r^2 = 0.79$, $n = 40$, $p < 0.001$) indicating char-EC is also derived from biomass burning.

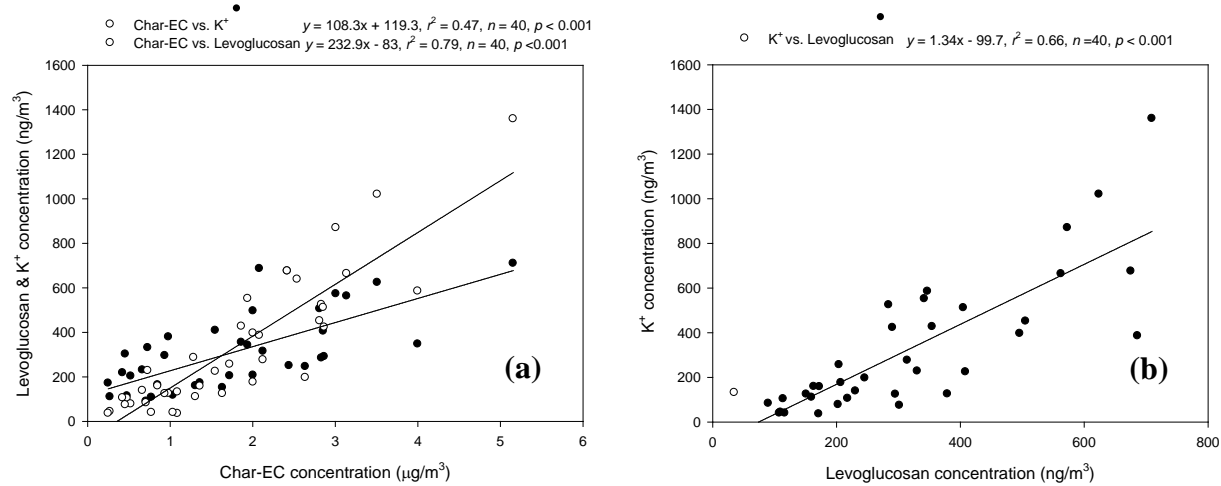


Fig. 2. Relationships between char-EC, levoglucosan, and K^+ (a), and between K^+ and levoglucosan (b) in FPs.

Relationships between OC, char-EC, and soot-EC

Positive and negative correlations between OC and soot-EC were observed for UFPs and FPs at roadside, respectively indicating different characteristics of carbonaceous compounds in the two particle sizes possibly due to the influence of diesel vehicles operated near the sampling site¹⁾. Similar relationships with our previous study were observed for roadside samples as shown in Fig. 3 (a) whereas the negative relationship between OC and soot-EC was not found for background samples (Fig. 3 (b)). This result strongly indicates that the negative relationship between OC and soot-EC is caused by motor vehicle emissions. All positive relationships between OC and soot-EC were obtained for UFPs samples for the two sampling sites (roadside: $r = 0.84, n = 10, p < 0.05$; background: $r = 0.94, n = 10, p < 0.001$).

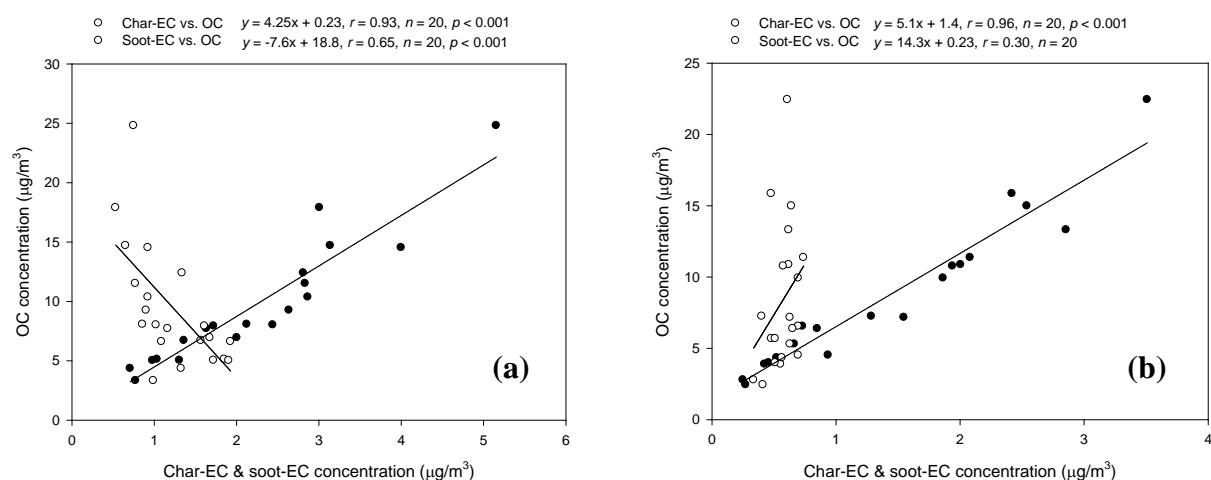


Fig. 3. Relationships between OC, char-EC, soot-EC in FPs; (a) at roadside, (b) background site.

CONCLUSION

Atmospheric UFPs and FPs are simultaneously collected in November for 10 days at a roadside and a background site. For the diurnal variations of FPs, nighttime samples showed higher concentrations than daytime samples indicating relatively high contribution of biomass burning during the nighttime in the study area when considering observed levoglucosan. The average OC/EC and char-EC/soot-EC ratios were low at the roadside and high at the background site indicating that the contribution of motor vehicles is significant at roadside. Interestingly, these ratios at roadside for the UFPs samples showed twice higher values than background site indicating the contribution of emission sources can be clearly found by simultaneous collection of UFPs and FPs. Positive and negative correlations between OC and soot-EC were observed for UFPs and FPs at roadside, respectively while only positive correlations between OC and soot-EC were observed for UFPs and FPs at background site supporting the findings of our previous study.

ACKNOWLEDGMENTS

This study was supported in part by Japan Auto-Oil Program (JATOP).

REFERENCES

- [1] Kim, K.H.; Sekiguchi, K.; Kudo, S.; Sakamoto, K. *Aerosol Air Qual. Res.* 2011, 11, 1-12.
- [2] Kim, K.H.; Sekiguchi, K.; Furuuchi, M.; Sakamoto, K. *Atmos. Environ.* 2011, 45, 1581-1590.
- [3] Chow, J.C.; Watson, J.G.; Pritchett, L.C.; Pierson, W.R.; Frazier, C.A.; Purcell, R.G. *Atmos. Environ.* 1993, 27A, 1185-1201.
- [4] Han, Y.M.; Cao, J.J.; Lee, S.C.; Ho, K.F.; An, Z.S. *Atmos. Chem. Phys.* 2010, 10, 595e607.
- [5] Kumagai, K., Iijima, A., Shimoda, M., Saitoh, Y., Kozawa, K., Hagino, H., Sakamoto, K., *Aerosol Air Qual. Res.* 2010, 10, 282-291.
- [6] Hagler, G.S.W., Baldauf, R.W., Thoma, E.D., Long, T.R., Snow, R.F., Kinsey, J.S., Oudejans, L., Gullett, B.K., *Atmos. Environ.* 2009, 43, 1229-1234.

Particulate Matters and Associated Polycyclic Aromatic Hydrocarbons in Atmospheric Environment of Songkhla, Thailand in Relation to Rubber-wood Combustion

P. Chaichana¹, S. Tekasakul¹, P. Tekasakul^{2,4}, M. Furuuchi³ and M. Hata³

¹Department of Chemistry and Center of Excellence for Innovation in Chemistry (PERCH-CIC), Faculty of Science, Prince of Songkla University, Hat Yai, Songkhla 90112, THAILAND

²Department of Mechanical Engineering, Faculty of Engineering, Prince of Songkla University, Hat Yai, Songkhla 90112, THAILAND

³Graduate School of Natural Science and Technology, Kanazawa University, Kakuma-machi, Kanazawa 920-1162, JAPAN

⁴National Center of Excellence for Environmental and Hazardous Waste Management (EHWMM)-Southern Consortium Universities at Prince of Songkla University, Hat Yai, Songkhla 90112, THAILAND

ABSTRACT

Each year, a lot of rubber-wood is used as fuel in several industries around Songkhla province, Thailand. Smoke from rubber-wood burning contains fine particles including nanoparticles and associated polycyclic aromatic hydrocarbons (PAHs) generated from incomplete combustion. In this work, characteristics of nanoparticles in atmospheric environment of Songkhla province during May-December, 2010 were investigated in order to find relation to rubber-wood combustion. Four sampling locations (Hat Yai, Muang, Bangkhlam and Sadao) surrounded by several factories using rubber-wood as fuel in burning process were chosen in this study.

Particles size distributions sampled from all locations show bi-modal behavior. They could be originated from biomass burning especially rubber-wood which is the most common fuel used in industries around the sampling sites, and re-suspension of ground dust or other atmospheric aerosol particles. Total suspended particulates (TSP) average 30.61, 27.67, 19.13 and 28.64 $\mu\text{g}/\text{m}^3$ for Hat Yai, Muang, Bangkhlam and Sadao, respectively. TSP was generally low, particularly when precipitation was high. PAHs size distributions of ambient air particles of all location show single-modal behavior. It can be concluded that most of the PAHs are associated with small particles. Total PAH concentration was low. PAHs in Hat Yai, Bangkhlam and Sadao was related to amount of rubber-wood used in the area. At Muang, the concentration was very low which could result from influence of wind and precipitation.

KEYWORDS

Nanoparticles, Size distributions, PAHs, Rubber-wood combustion

Introduction

Rubber-wood is used as fuel in several industries around Songkhla province, Thailand, especially in the ribbed smoked sheets (RSS) smoking process to supply heat to the rubber sheet^[1]. Smoke from the wood burning contains particulate matters including nanoparticles. Incomplete combustion of wood results in a formation of polycyclic aromatic hydrocarbons (PAHs) and other chemical components^[2]. PAHs are a group of hydrocarbon compounds that are carcinogenic and mutagenic, especially those containing 4-6 aromatic rings. PAHs generated from the wood burning causes a major indoor pollution problem because of the leakage of smoke particles into the working area, which then causes atmospheric pollution to nearby surroundings^[3,5]. In this work, characteristics of nanoparticles and PAHs in atmospheric environment of Songkhla province were investigated and relation to rubber-wood combustion was determined. Sampling sites surrounded by several rubber sheet smoking cooperatives and factories using rubber wood as fuel in burning process were chosen.

Experimental Methods

Air sampling

Size fractionated particles at every location were investigated using a nanoparticle air sampler (Kanomax, Japan). The cut-off aerodynamic diameters are 10.0, 2.5, 1.0, 0.5 μm and the last stage collects all particles smaller than 70 nm on a back-up filter. The particles were collected on a quartz fiber filter (Pallflex Products Corp., Type 2500QAT-UP). Donut-shape filters with 65x30 mm outer and inner diameters were used in impaction stages, and a 47 mm diameter circular filter was used in the backup stage, while 8-mm-thick stainless steel fiber mat with fiber diameter of 8 μm and packing density of 0.0065 was used as inertial filter in a stage prior to the backup filter^[4]. Sampling flow rate was 40 L min⁻¹ and sampling time was 3 day for each sampling to ensure sufficient amount of particles collected for PAH analysis. Total suspended particulates (TSP) were measured by the commercial portable high-volume sampler (Shibata, HV500F) where the sampling flow rate was set at a constant 500 L/min and sampling time was 24 hours. The filters used were identical-type quartz fiber filters (Advantec, QR-100) with 110-mm-diameters. All filters were pre-treated filters in a controlled environment (25°C, 50% RH) for 72 hours. Both the nanoparticle air sampler and high-volume samplers were placed at the open-roof top floors of each building every location once a month during May-December, 2010.

PAHs extraction method

All collected filter samples were then treated in the identical environment as the pre-treatment for 72 hours. A piece of each filter sample containing 4-5 mg of articulates was cut into small pieces.

PAHs were extracted ultrasonically twice using 40 mL of dichloromethane for 30 min^[6]. The solution was cleaned up by filtration using a filtration syringe filter unit (0.45 µm PTFE) for removal of insoluble particles and then 50 µL of dimethylsulphoxide (DMSO) was added for preservation of PAHs. The extracts were combined and concentrated using on a rotary evaporator to remove dichloromethane. The residues were then re-dissolved in with 450 µL of acetonitrile. Interfering compounds once again were removed with a 0.45 µm PTFE syringe filter. The filtrate was kept in a 1.5-mL amber glass vial, in a refrigerator and stored at 4°C prior to analysis.

PAHs Analysis

The 16 PAHs include Naphthalene (Nap), Acenaphthylene (Act), Acenaphthene (Ace), Phenanthrene (Phe), Anthracene (Ant), Fluorene (Fle), Fluoranthene (Flu), Pyrene (Pyr), Benzo[a]anthracene (BaA), Chrysene (Chr), Benzo[a]pyrene (BaP), Benzo[b]fluoranthene (BbF), Benzo[k]fluoranthene (BkF), Dibenz[a,h]anthracene (DBA), Indeno[1,2,3-cd]pyrene (IDP), and Benzo[g,h,i]perylene (BghiPe) were analyzed by high performance liquid chromatography (HPLC);(Agilent, 1100) with diode array detector (DAD). The mobile phase was a mixture of acetonitrile and de-ionized water with gradient elution from 35% acetonitrile to 100% acetonitrile at 25°C and flow rate of 1-1.2 mL/min^[5,6].

Results and Discussion

The total suspended particulates from ambient air at each sampling are shown in **Fig.1**. The results indicate that TSP depends on the precipitation^[1,5]. During October to December TSP decreases when the precipitation increases. However, during July to September TSP increases slightly as the precipitation increases when the RSS production is high.

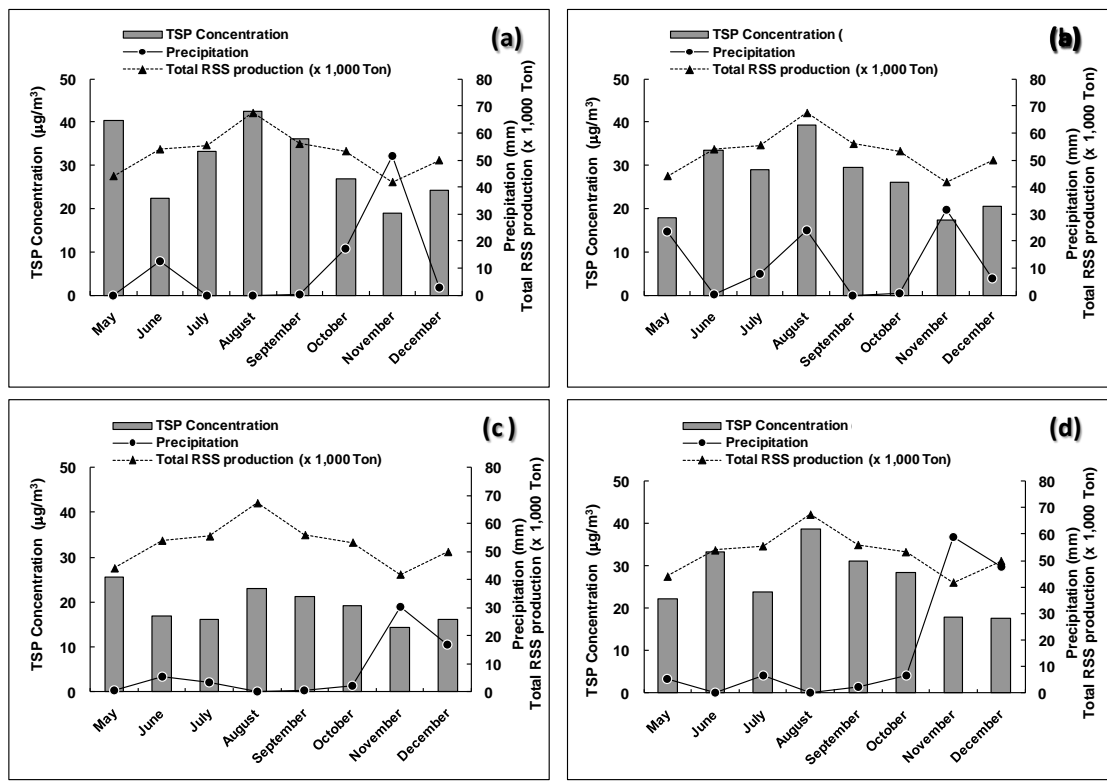


Figure 1. Relationship between the TSP, precipitation and RSS production at (a) Hat Yai, (b) Bangkhla, (c) Muang and (d) Sadao during May to December 2010

PM concentrations at each sampling site in May to December 2010 are shown in **Fig.2**. The highest concentration was observed in PM_{2.5-10} for every sampling site.

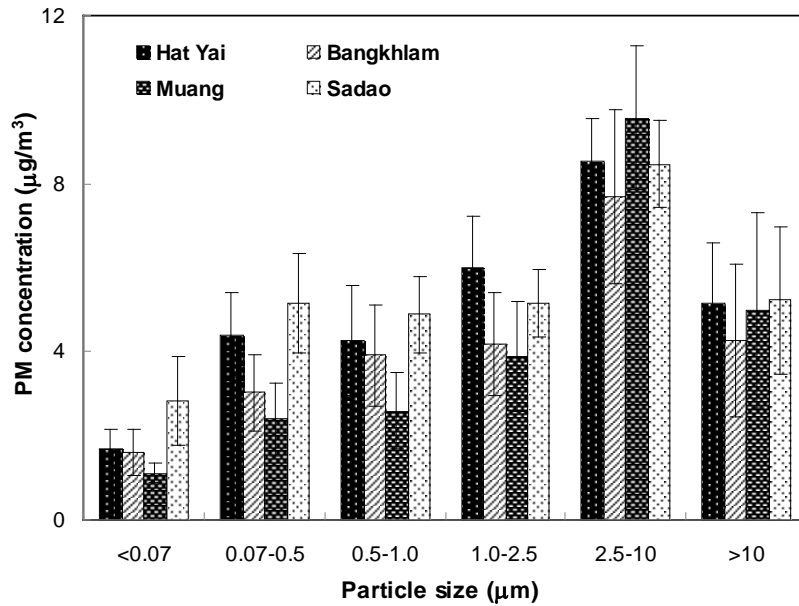


Figure 2. Particle mass concentration of each size range at different sampling sites
Total PAH concentrations are shown in **Fig.3** indicated that most of the PAHs are associated with small particles^[7] (smaller than PM_{1.0}).

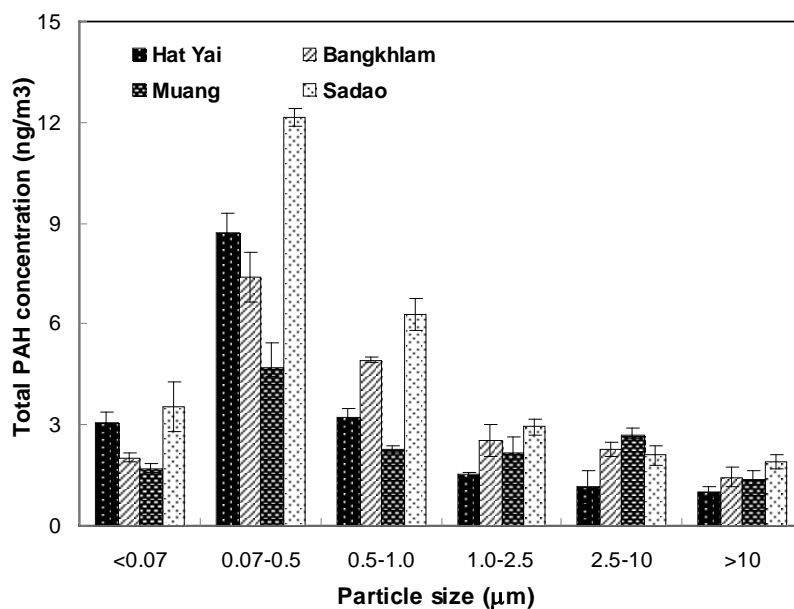


Figure 3. Total PAH concentration associated with particles size at different sampling sites.

CONCLUSION

Total suspended particulates of air sampled from each sampling site are generally low, averaging 30.61, 27.67, 19.13 and 28.64 $\mu\text{g}/\text{m}^3$ for Hat Yai, Muang, Bangkhlam and Sadao, respectively. The TSP depends on precipitation, RSS production and wind direction. TSP decreased almost linearly when the precipitation increased. The highest PM concentration was observed in $\text{PM}_{2.5-10}$ in every sampling site, while $\text{PM}_{0.07}$ fraction is rather low especially at Muang. This may be related to differences in contribution of possible emission sources. The average concentrations of total PAHs in ambient air are 18.64, 20.61, 13.27 and 28.86 ng/m^3 for Hat Yai, Muang, Bangkhlam and Sadao, respectively. The most of the PAHs are associated with small particles (smaller than $\text{PM}_{1.0}$). This behaviors of the PAH concentration is influenced by the precipitation, RSS production, and wind direction in a similar trend like those of TSP.

ACKNOWLEDGMENTS

This research has been financially supported from the Center of Excellence for Innovation in Chemistry (PERCH-CIC), Commission on Higher Education, Ministry of Education and Graduate school, Prince of Songkla University are gratefully acknowledged.

REFERENCES

- [1] Tekasakul, P.; Furuuchi, M.; Tekasakul, S. *Aerosol Air Qual Res.* 2008, 8, 265-278.
- [2] Furuuchi, M.; Tekasakul, P.; Murase, T.; Otani, Y.; Tekasakul, S; Bai, Y. *Ecotechnology Res.* 2006, 12, 135-139.
- [3] Chomanee, J.; Tekasakul S.; Tekasakul, P. *Aerosol Air Qual Res.* 2009, 9, 2071-1409
- [4] Otani, Y.; Eryu, K.; Furuuchi, M.; Tajima, N.; Tekasakul, P. *Aerosol Air Qual Res.* 2007, 7(3), 343-352.
- [5] Chomanee, J. M.Sc. Thesis, Prince of Songkla University, 2008.
- [6] Phoungthong, K. M.Sc. Thesis, Prince of Songkla University, 2010.
- [7] Furuuchi, M.; Otani, Y.; Tsukawaki, S.; Nakao, Y.; Hata, M.; Sieng, S. and Hang, P. *Asian Aerosol Conference (AAC) 2007*, vol.I, pp.41-42.

Characteristics of Ultrafine Particles Emitted from Compression Ignition Engines

Xinling Li, Wei Liu, and Zhen Huang

Key Laboratory of power Machinery and Engineering Education Ministry Shanghai Jiao Tong University

Principal Contact: Xinling Li, Doctor, Shanghai Jiao Tong University, 800 Dongchuan Road, Shanghai 200240, China.

Tel: 021-34206728 Fax: 021-34205949 Email: lxl@sjtu.edu.cn

Abstract

The measurements of effect of fuel properties and combustion mode on the ultrafine particle emission characteristics of compression ignition combustion engine were conducted. Three kinds of fuels: diesel (a baseline fuel), gas to liquid (GTL, with low sulfur and aromatic hydrocarbon) and dimethyl ether (DME, with oxygen content) were selected to test. Measurements of the ultrafine particle emission characteristics from a diesel engine fueled with diesel, GTL and DME under different engine loads and speeds were conducted respectively. The fuel sulfur and aromatic hydrocarbon and oxygen content show significant effect on the ultrafine particle number concentration and size distribution, in the meantime, the trade-off relationship between nucleation mode and accumulation mode particles in the exhaust was also observed. The effect of combustion modes (including compression ignition direct injection (CIDI), homogeneous charge compression ignition (HCCI) and compound charge compression ignition combustion (CCCI)) on ultrafine particles emitted from engines fuelled with n-heptane was studied. The results indicate that combustion modes significantly affect the ultrafine particle number concentration and size distribution. The number concentrations of nucleation mode particles and total particles have a significantly positive correlation with HC concentrations. The effect mechanism of fuel properties and combustion mode on the ultrafine particle emission characteristics was discussed in the paper.

Keywords: Compression Ignition Engines, ultrafine particle emission, fuel property, combustion mode

A Different Model for Estimating Monoterpene Emissions over Boreal Pine Forest

Qingyang He¹, Michael Boy¹, Jaana Bäck², Janne Rinne¹, Hannele Hakola³, Alex Guenther⁴, Sampo Smolander¹ and Markku Kulmala¹

¹Department of Physics, PO Box 64, FI-00014 University of Helsinki, Finland

²Department of Forest Sciences, PO Box 27, FI-00014 University of Helsinki, Finland

³Finnish Meteorological Institute, Sahaajankatu 20 E, FI-00880 Helsinki, Finland

⁴National Center for Atmospheric Research, Boulder, CO 80303, USA

Correspondence to: Qingyang He (qingyang.he@helsinki.fi)

ABSTRACT

As one of the important biogenic volatile organic compounds (BVOCs) groups, monoterpene has been drawing more and more scientific attention in atmospheric research because of their chemical reactions to produce and destroy tropospheric ozone, their effects on aerosol growth and formation and their potential influence on global warming. Regional measurements and estimates are urgently needed to study carbon budgets and global climate. However, since various factors such as vegetation type, temperature light and humidity have complicated impacts on monoterpene emissions, comprehensive inventories are not so often reliably defined. To further track monoterpene concentrations and their chemical transformations, the model SOSA (model to Simulate the concentrations of Organic vapours and Sulphuric Acid) is applied to investigate Scots pine (*Pinus sylvestris*) tree emissions in a boreal coniferous forest at SMEAR II (Station for Measuring forest Ecosystem-Atmosphere Relations) in Hyytiälä, Finland.

KEYWORDS

SOSA, monoterpenes

Introduction

Finland, as a densely-forested country, the emission pattern of VOCs is always dominated by biogenic emissions. Therefore, BVOC study in Finland is particularly critical. Since previous research shows that many of the tree species in the European

boreal zone are known to be monoterpene emitters (Janson, 1993; Hakola *et al.*, 1998; Hauff *et al.*, 1999), this study will focus on monoterpene emissions at Hyytiälä. Monoterpenes are emitted by plants because of their allelopathic function. They are of great importance in defence against insects and attraction of pollinators and enemies of other herbivores (Kesselmeier and Staudt, 1999). Temperature is the most significant factor of monoterpene emissions. Many other interlinked environmental and physiological parameters, such as light, humidity, CO₂ concentration, vegetation type and metabolic activity also affect monoterpene emissions (Guenther *et al.*, 1995).

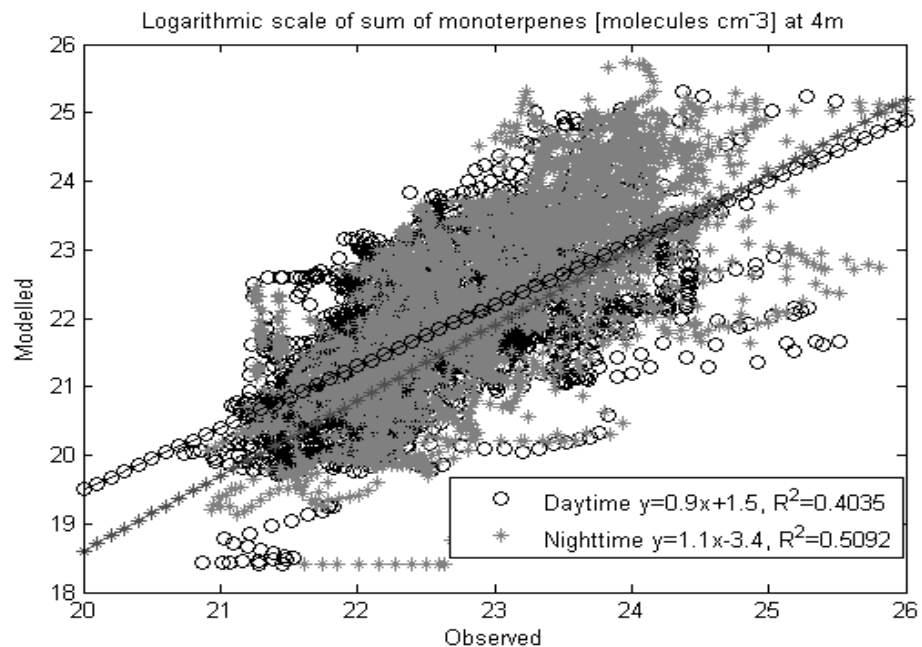
Experimental Methods

SOSA is a model which combines meteorological transport, BVOC emissions and chemistry (Boy *et al.* 2011). To test the reliability of SOSA, simulation outputs are compared with measurement data collected from on-line chambers analysed by Proton-transfer-reaction mass spectrometry (PTR-MS) and Gas chromatography-mass spectrometry (GC-MS) analyzer.

Results and Discussion

Result (Figure.1) indicates that modelling and observations of monoterpene concentrations reasonably agreed both day and night. However, the correlation coefficients still reveal some additional parameters like environmental stress, plant development and leaf maturation, nutrient and injury status also influencing monoterpene emissions, but were not taken into account in the model. In this case, the mechanisms of monoterpene emissions need to be understood better in order to improve the parameters used in model. May till September of the year was selected to make correlation test because emissions are productive and the simulation are representative during that period.

Fig 1. Correlation analysis between measured monoterpene concentration data with modelled from May to September 2007



The dominant monoterpene species emitted from these coniferous trees are α -pinene and Δ^3 -carene with the proportion of 48% and 23% respectively. Monoterpene emissions did continue with low rates during the night. Diurnal and seasonal variations are demonstrated both quantity and quality. Summer is the most active season and emission rate increases to the peak around 3pm during daytime. According to vertical profile, monoterpene concentrations are highest at lower high level during night and well mixed during day. All the results are generally supported by measurement.

Another significant phenomenon for monoterpene emitters is the discrepancy between branch scale emissions and above-canopy concentrations. In order to reduce uncertainty in measuring and modeling, a more detailed chemotypic characterization blends needs to be constructed. SOSA is also used to estimate the contribution of different monoterpene distributions to the total OH reactivity. Results show that by selecting α -pinene and sabinene as the chemotype-species, the OH reactivity differs by a factor of almost 3.

ACKNOWLEDGMENTS

Financial support was from Finnish Center of Excellence in Physics, Chemistry, Biology and Meteorology of Atmospheric Composition and Climate Change. All the

staff of the SMEAR II station is gratefully acknowledged.

REFERENCES

- [1] Boy, M., Sogachev, A., Lauros, J., Zhou, L., Guenther, A., and Smolander, S.: SOSA – a new model to simulate the concentrations of organic vapours and sulphuric acid inside the ABL – Part1: Model description and initial evaluation; *J. Atmos. Chem. Phys.*, 2011,11, 43-51.
- [2] Guenther, A., Hewitt, C. N., Erickson, D., Fall, R., Geron, C., Graedel, T., Harley, P., Klinger, L., Lerdau, M., Mckay, W. A., Pierce, T., Scholes, B., Steinbrecher, R., Tallamraju, R., Taylor, J., and Zimmerman, P. A.: Global-Model of Natural Volatile Organic-Compound Emissions; *J. Geophys. Res.*, 1995, 100(D5), 8873-8892.
- [3] Hakola, H., Rinne, J., and Laurila, T.: The hydrocarbon emission rates of tea-leaved willow (*Salix phylicifolia*), silver birch (*Betula pendula*) and European aspen (*Populus tremula*); *J. Atmos. Env.*, 1998,32, 1825-1833.
- [4] Hauff, K., Rössler, J., Hakola, H., and Steinbrecher, R.: Isoprenoid emission in the European boreal forests, in Proceedings of EUROTRAC symposium 98; WIT press, 1999.
- [5] Janson, R.: Monoterpene emission of scots pine and morwegian spruce; *J. Geophys. Res.*, 1993,98, 2839-2850.
- [6] Kesselmeier, J., Staudt, M.,: Biogenic volatile organic compounds (VOS): an overview on emission, physiology and ecology. *J. Atmos. Chem.*, 1999,33, 23-88.

Effects of Microwave Irradiation on Culturability and Diversity of Biological Aerosols of Different Sizes in Different Environments

Yan Wu and Maosheng Yao

State Key Joint Laboratory for Environmental Simulation and Pollution Control, College of Environmental Sciences and Engineering, Peking University, Beijing 100871, China

Principal Contact: Maosheng Yao, Professor, State Key Joint Laboratory for Environmental Simulation and Pollution Control, College of Environmental Sciences and Engineering, Peking University, Beijing 100871, China.

Tel: +86 010 6276 7282 Email: yao@pku.edu.cn

Abstract

Increasing evidences show that exposure to airborne biological aerosols has resulted in numerous adverse health effects and diseases. Thus, it is important to develop practical control technology. Previously, we have investigated the inactivation of total bioaerosols using microwave irradiation. Here, the effects of microwave irradiation (2450MHz) on the culturability and diversity of bioaerosols of different sizes were investigated. Air samples were taken using a six-stage Andersen impactor operated at a standard flow rate of 28.3 L/min without and with microwave irradiation for 45 seconds at three different power levels(119, 385, 700 W) in different environments (lab office, hotel and outdoor). For each experimental condition, three independent repeats were conducted. Air samples collected onto different stages of the Andersen sampler were incubated directly at room temperature, and colony forming units (CFU) were manually counted and statistically corrected. The CFUs were further washed off from agar plates using deionized water and subjected to polymerase chain reaction (PCR)-denaturing gradient gel electrophoresis (DGGE) for diversity analysis.

Results revealed that for outdoor environment, larger size bacterial aerosol dominated, while for the indoor environment smaller size bacterial aerosol dominated. Use of higher power level resulted in lower culturable bacterial counts regardless of the sampler stage and sampling environment. PCR-DGGE analysis indicated that in general use of higher power microwave irradiation resulted in less culturable bacterial diversity, while for medium and low power their culturable diversity appeared to be similar to that of control experiment. In contrast, smaller culturable fungal aerosols were found to dominate regardless of sampling environment. Application of microwave irradiation for 45 s was shown to result in complex effects on the culturability of fungal aerosols of different sizes. The results obtained might be negatively impacted by the environmental variations of biological aerosol concentration and composition. Overall, this study has demonstrated a practical control technology for environmental bioaerosols.

Keywords: six-stage Andersen sampler, Bioaerosols of different sizes, Microwave Irradiation

Differences in Positively and Negatively Charged Bacterial Aerosol Diversity in Indoor and Outdoor Environments

Fangxia Shen and Maosheng Yao

State Key Joint Laboratory for Environmental Simulation and Pollution Control, College of Environmental Sciences and Engineering, Peking University, Beijing 100871, China

Principal Contact: Maosheng Yao, Professor, State Key Joint Laboratory for Environmental Simulation and Pollution Control, College of Environmental Sciences and Engineering, Peking University, Beijing 100871, China.

Tel: +86 010 6276 7282 Email: yao@pku.edu.cn

Abstract

In this study, the positively and negatively charged culturable bacterial aerosol concentration and diversity were investigated both in indoor and outdoor environments. For both positively and negatively charged bioaerosols, the air samples were collected into different regions of two agar square plates using an electrostatic sampler (1.1 kv/cm) at a flow rate of 3 L/min for 40 min. The collected bacterial aerosols were cultured directly on agar plates, and the colony forming units (CFU) were manually counted. In addition, the CFUs were washed off from the agar plates, and further subjected to polymerase chain reaction (PCR) and denaturing gradient gel electrophoresis (DGGE) for culturable diversity analysis.

The results revealed that the positively and negatively charged culturable bacterial aerosol concentration and diversity strongly depended on the sampling environments. In indoor environment, negatively charged culturable bacterial aerosols dominated ($p\text{-value}=0.0489$), while in outdoor environment both polarities appeared to have similar concentration levels ($p\text{-value}=0.078$). PCR-DGGE analysis showed that positively charged culturable bacterial aerosol DGGE patterns were very different from those of negatively charged regardless of the sampling environments. In addition, positively charged culturable bacterial aerosols were found to have more phylogenetical similarity with those positively charged collected into different regions of agar plates from different environments, and the same was observed for negatively charged. Outdoor culturable bacterial aerosols were shown to have more bacterial species richness than those indoors. The information provided and the technique developed here could have great implications in electrostatic sampling and control of bioaerosols, and open a new arena for studying airborne microbes with different charge polarity

Keywords: Positive charge, negative charge, Bacterial aerosol, culturable diversity, PCR, DGGE, phylogenetic similarity

How Combustion of Energetic Materials Affects Viability of Aerosolized Bio-agents

Sergey A. Grinshpun¹, Michael Yermakov¹, Reshma Indugula¹, Atin Adhikari¹, Tiina Reponen¹, Shasha Zhang², Vern Hoffmann², Mirko Schoenitz² and Edward Dreizin²

1 Dept. of Environmental Health, University of Cincinnati, Cincinnati, OH 45267-0056, USA

2 Dept. of Chemical, Biological and Pharmaceutical Engineering, NJIT, Newark, NJ 07102, USA

Principal Contact: Sergey A. Grinshpun, Professor, University of Cincinnati, Cincinnati, OH 45267-0056, USA.

Tel: (513)558-0504 Fax: (513)558-2263 E-mail: sergey.grinshpun@uc.edu

Abstract

Inactivation of aerosolized microorganisms, including destruction of microbial bio-threat agents, is an important topic in biodefense and air quality control research. Energetic materials are currently being developed with the added capability to effectively inactivate stress-resistant aerosolized microorganisms under short-term exposure conditions. To evaluate how the combustion of energetic materials affects the viability of aerosolized bio-agents, it is imperative to distinguish between the heat-induced inactivation and the one caused by chemical products released during combustion. In this study, conventional and novel reactive materials, including aluminum-iodine based filled nanocomposite materials, were evaluated with respect to their biocidal capability against aerosolized *Bacillus* endospores and MS2 viruses, which are used as model organisms in bio-agent defeat studies. Two experimental setups were developed to determine the viability losses associated with the bioaerosol exposure to (i) high air temperatures and (ii) combustion products. Under the experimental conditions established in this study, the thermal exposure was shown to inactivate ~99.9–99.99% of airborne *Bacillus* spores at characteristic exposure temperatures of 300–400°C. The heat-induced inactivation was even greater for MS2 viruses. Halogenated products that were added to energetic formulations produced additional inactivation. For example, release of iodine from the tested Al-I₂ composites enhanced inactivation of aerosolized bacterial spores by almost two orders of magnitude compared to other advanced composite materials, some of which (e.g., B-Ti) actually generated higher flame temperatures. The two experimental setups and protocols developed in this study can be used to quantify the thermal and chemical biocidal effects provided by combustion of various reactive materials. This study was supported by the Defense Threat Reduction Agency and the Office of Naval Research (US Department of Defense).

Keywords: Bioaerosol, viability, inactivation, combustion.

Modifications in physicochemical properties of wood combustion aerosols due to chemical aging

Zhijun Wu¹, L. Poulaïn¹, O. Böge¹, R. Gräfe¹, H. Herrmann¹, A. Wiedensohler¹, K. Helbig², T. Schröder², J. von Sonntag², I. Hartmann², Min Hu³

1 Leibniz Institute for Tropospheric Research, Permoserstr. 15, 04318 Leipzig, Germany

2 German Biomass Research Centre, Torgauer Str. 116, D - 04347

3 College of Environmental Sciences and Engineering, Peking University, Beijing 100871, China

Principal Contact: Zhijun Wu, Dr., Leibniz Institute for Tropospheric Research (IfT), Leipzig, Permoserstraße 15, 04318, Leipzig.

Tel: +49-431-235-2152 Fax: ++49 (341) 235-2325 Email: wuzhijun@tropos.de

Abstract

Combustion of biomass is known to be a major source of gas- and particle- phase air pollution in the atmosphere and to be mainly made of a complex mixture of organics. To date, however, the atmospheric behaviours of these mixtures and their health effects are still largely unknown. In order to determine the modifications in physico-chemical properties of the wood burning aerosols and their toxicity due to chemical aging, we investigated the aging processes of different types of wood burning aerosols (Spruce log, Beech log, and WoodPellet). The wood burning aerosols are introduced into the IfT smog chamber (19 m^3) with and without ozone and /or UV lights simulating day- and night- times. The changes of their physical and chemical properties were measured by online instruments including a Hygroscopic Tandem Differential Mobility Analyzer (H-TDMA), a Volatility Tandem Differential Mobility Analyzer (V-TDMA), a Multi-Angle Absorption Photometer (MAAP), a Scanning Mobility Particle Sizer (SMPS), and an Aerosol Mass Spectrometer (AMS).

Keywords: Wood burning aerosols, AMS, hygroscopicity, volatility

Polybrominated diphenyl esters in the ambient air of southern Taiwan during the biomass burning periods

Shun-Shiang Chang^{1*}, Wen-Jhy Lee¹, Lin-Chi Wang², Kuo-Ping and Chang-Chien²

1 Department of environmental engineering, National Cheng Kung University, Tainan 70101, Taiwan

2 Department of Chemical and Materials Engineering, Cheng Shiu University, Kaohsiung 833, Taiwan

Principal Contact: Shun-Shiang Chang, MS graduated student, National Cheng Kung University, Tainan 70101, Taiwan.

Tel: +886-6-2093155 Fax: +886-6-275-2790 E-mail: changss0718@gmail.com

Abstract

Atmospheric concentrations of 30 PBDE congeners were measured at two areas (A and B, respectively). The first area (A) with four sampling sites was around a rice field and the second area (B) with three sampling sites were at approximately 3 km downwind side away from the area A. The effects of biomass burning on the atmospheric PBDE concentrations were investigated on the rice straw burning and non-burning periods, respectively. During the rice straw burning period, the mean concentrations of total-PBDEs were 249 and 70.8 pg m⁻³ at area A and B, respectively. However, during non-burning period, the mean concentrations of total-PBDEs were 87.5 and 49.8 pg m⁻³ at area A and B, respectively. The above results revealed that, during the biomass burning period, the atmospheric PBDE concentrations were 2.8 and 1.4 times higher than those of non-burning period, respectively. The BDE-209(Deca-BDE), was the most three dominant congeners (61.0% of total-PBDE mass) in the atmosphere. By using the gas/particle partition modeling, during the rice straw burning period, the total-PBDE were 87.0% and 83.6% in the particle phase, at area A and B, respectively. However, during the non-burning period, the total-PBDE were 86.2% and 77.7% in the particle phase, at area A and B, respectively. Higher brominated PBDEs were primarily in the particle phase, while lower brominated congeners were associated with the gas phase. Such as BDE-209(Deca-BDE), BDE-207(Nona-BDE) and BDE-208(Octa-BDE) were approximately 94.7%, 95.3% and 95.1% in the particle phase, while the BDE-7(Di-BDE),

BDE-17(Tri-BDE) and BDE-49(Buta-BDE) were approximately 1.45%, 2.68% and 7.42% in the particle phase. PBDE emissions from the rice straw burning were probably due to the survival of PBDEs during the biomass combustion and/or resulted from the reaction of brominated compounds. In order to prevent the damage of PBDEs, the control strategies for them were of great importance.

Keywords: PBDEs, atmosphere, partition, biomass, burning.

Injection Heights of Springtime Biomass Burning Plumes in Southeast Asia

Yue Jian¹ and Tzung-May Fu¹

¹Department of Atmospheric and Oceanic Sciences, School of Physics, Peking University, Beijing, 100871, China

ABSTRACT

Large-scale biomass burning events recur every spring over the Indochina Peninsula due to land-clearing practices before the local growing season. The pollutants from these biomass burning plumes are sometimes injected directly into the free troposphere, thus efficiently transported over long distances and impacting downwind regions such as southern China. We use the Multi-angle Imaging SpectroRadiometer (MISR) satellite data and the MISR INteractive eXplorer (MINX) software to analyze the biomass burning plume injection heights over the Indochina Peninsula during February to April, 2010. A total of 38 plumes were analyzed, evenly distributed across the burning areas. The plume injection heights range from a few hundred meters up to about 4000 meters. We find that around 40% of the analyzed plumes were injected above the local mean boundary layer height (1000 m). We use the GEOS-Chem model to simulate the injection and transport of biomass burning plumes to see whether the change in injection height has great impact on tracer concentrations in the Southeast Asia and the downwind regions including southern China. With 40% of plumes injected in 1-4 km, the concentration of CO changes little compared to the standard emission that all plumes emitted within the boundary layer. However, the change of reactive nitrogen and ozone cannot be ignored.

KEYWORDS

Biomass burning, Southeast Asia, Injection height, GEOS-Chem

Introduction

Biomass burning, as an important source of aerosols and trace gases, contributes a lot to the atmosphere composition and its chemistry like ozone formation. On the global scale, Southeast Asia is one of the major contributors of global biomass burning^[1].

Based on the TRACE-P and ACE-Asia aircraft measurements, there have been many researches about the influence of Southeast Asia biomass burning on downwind East Asia and western Pacific region^[2-6]. Biomass burning from Southeast Asia was thought to be transported in the warm conveyor belt of cold front at altitudes above 2 km and at latitudes below 30N^[2]. One study showed that Southeast Asia air constituted 45 and 60% of the sampled air masses in the lower troposphere (2-4km) and middle troposphere (4-8km), and was the predominant source of reactive nitrogen (NOx, PAN, HNO3, and nitrate) in the study region (17–30N, 110–150E). And about 70% of O3 produced in Southeast Asia was transported to the western Pacific^[5]. A study in the Pearl River Delta region also indicated that air pollutants in Guangzhou were higher when under the impact of the Southeast Asia biomass burning^[4].

In Southeast Asia, most fires occur in spring. Although it is the local dry season, anthropogenic activities are the main origins. The traditional slash and burn cultivation is still popular there. People clear land for agricultural use before a new year's farming, resulting in large biomass burning events. El Niño, as an important factor in interannual variability, intensifies the amount of fires due to droughts. And the height of smoke plumes is another crucial parameter. If the plumes rise above the boundary layer, the aerosols and trace gases emitted will be able to transport farther, stay in the atmosphere longer and then have a stronger impact on the environment.

The distribution of smoke plume heights has been studied in many regions^[7-13]. In recent years, the Cloud-Aerosol Lidar with Orthogonal Polarization (CALIOP) on board the CALIPSO satellite and the Multi-angle Imaging SpectroRadiometer (MISR) instrument on board the Terra satellite have made observation of plume heights much easier. The height is under the impact of fire energy and local meteorology condition. Each individual case could have very different vertical distribution. However, what we pay attention to is whether it is able to reach the free troposphere. By far, there is evidence that a significant part of plumes in most regions can rise above the boundary layer. In North America, the observed plume heights during the fire seasons of 2002 and 2004-2007 ranged from a few hundred meters up to 5000m, and 5-12% of them were injected above the boundary layer^[7]. Observations in Australia in 2000 and 2002 showed that grassland fires also had enough power to lift a plume into the free troposphere^[10]. The aerosol top heights in Europe during 2006-2008 fire seasons ranged between 1.6 and 5.9 km^[13]. On the contrary, a study of fires in the peat forests of Indonesia during 2001-2009 found that 96% of all plumes confined to within 500m of the boundary layer, which meant that they hardly reached the free troposphere. The relatively low fire intensities of the smoldering peat land might be the reason^[9].

Models have also been used to study the impact of injection heights^[14-17]. A GEOS-Chem simulation in the boreal forests in 1998 showed that a 40:60 split of biomass burning emissions between the boundary layer and 3–5 km matched the observed CO better than emissions distributed uniformly throughout the boundary layer or throughout the whole troposphere^[14]. One study of large fires in Alaska and the Yukon in 2004 indicated that results were not sensitive to a 40:60 versus a 60:40 split, but releasing a significant fraction of the emissions into the upper troposphere gave the best simulation^[15]. However, the simulation of North American boreal fire emissions during the 2004 fire season had a different conclusion that the influence of injection heights on CO concentration was very limited^[16].

Here we use the MISR instrument to analyze the injection heights of springtime biomass burning plumes over Southeast Asia. Based on the results, we then use a chemical transport model to study the impact of smoke plume injection heights on regional chemistry and pollutant transport out of Southeast Asia.

Experimental Methods

MODIS Fire Product

We use MODIS active fire product (MOD14 product) to find the possible biomass burning locations^[18-20]. The MODIS instrument we used is onboard Terra, which was launched in December 1999 and crosses the equator at approximately 10:30 a.m. and 10:30 p.m. local time. It is a multi-spectral sensor with 36 spectral bands, ranging in wavelength from 0.4 to 14.2 μm , and fires are detected at 1-km spatial resolution (at nadir) using radiance measurements in the 4 μm and 11 μm channels. The Fire Radiative Power (FRP) is calculated at the same time.

MISR Stereo Height Retrievals

The Multi-angle Imaging SpectroRadiometer (MISR) instrument, also on board Terra, has a unique design of multi-angle cameras. Nine push-broom cameras are placed at viewing angles from -70.5° to 70.5° in line with the ground track, with four cameras placed in front of and four cameras placed behind the nadir camera. Data are acquired in four spectral bands in each camera: 446, 558, 672, and 866 nm. The width of the MISR swath common to all 9 cameras is about 360 km, enabling it to obtain global coverage every 9 days at the equator and about every 2 days near the poles. Ground sample spacing is 275 meters in the red band of all 9 cameras and in all 4 bands of the nadir camera. The remaining 24 channels acquire data at 1100 meters resolution. The image shifts at different view angles, combined with stereoscopic techniques, enables

estimation of stereo heights, with a typical vertical resolution of 500 m or better.

The MISR INteractive eXplorer (MINX) software is a tool developed by Jet Propulsion Laboratory in 2008 specifically for retrieving heights and winds from aerosol plumes of wildfire smoke, dust or volcanic ash^[21, 22]. The algorithm is different from the height-retrieving algorithm of the standard MISR product and uses wind direction given by users and data from more cameras to retrieve more accurate winds and heights with higher resolution simultaneously.

To use MINX, the user needs to download MODIS fire product and MISR L1B2 Terrain Data, MISR Level 2 Aerosol parameters, MISR Level 2 TOA/Cloud Classifier parameters, MISR Geometric Parameters and MISR Ancillary Geographic Product data for the target region and time. MINX combines images from all nine cameras to form high-resolution real color images, which can be animated to provide a 3D-like effect. Each pixel in the images has a resolution of 275 meter. MODIS fire pixels are superposed to show the possible locations of smoke origin. Based on these imageries, the user subjectively determines and manually specifies the source and boundary of each plume, as well as the local wind direction. MINX can read the MISR Level 2 TOA/Cloud Classifier parameters to show the cloud mask or smoke mask, but it is not very accurate and may have no data in many regions. MINX then computes the winds, and albedos for each pixel of the plume, as well as zero-wind and wind-corrected pixel heights. Though using MINX will bring some man-made error, it is the most accurate way now to calculate the heights and has been used in several researches.

The wind-corrected height takes the wind speed's influence on the height retrieval into account, but it is inaccessible in pixels which near the surface or have along-track winds, so here we use the zero-wind heights.

GEOS-Chem Model

We use the GEOS-Chem global 3-D chemical transport model to simulate the chemistry and transport of biomass burning plumes injected at different heights. GEOS-Chem is driven by assimilated meteorological field, GEOS-5, from the Goddard Earth Observing System (GEOS) of the NASA Global Modeling Assimilation Office (GMAO)^[23]. To drive our simulation, the horizontal resolution of meteorological data is reduced to 2.0° latitude x 2.5° longitude. Vertical levels are reduced to 47 levels, including 8 levels in the lowest 1 km, and 12 levels between 1 and 4 km.

GEOS-Chem includes detailed O₃-NO_x-VOC-aerosol chemistry, and has been widely applied to

analyze the outflow of Southeast Asia biomass burning emissions compared with aircraft observation during TRACE-P [24].

Results and Discussion

Smoke Pixel Heights

We begin by searching for smoke plumes over Southeast Asia during February – April of 2010. Though there are thousands of fires detected by MODIS, many are not in the MISR swath or we could not see smoke plumes near the fires. In the end thirty-eight smoke plumes are found, where the origin of smoke is marked by MODIS hot spots and the plumes are clearly identified from the MINX animation. Figure 1 shows the spatial distribution of identified plumes, which covers the Indochina Peninsula. Out of the 38 smoke plumes, 23 took place over forest (including both evergreen and deciduous broadleaf forest), 14 took place over woody savanna, and one took place over a cropland/natural vegetation mosaic, according to the MODIS Land Cover Type product (MOD12Q1).

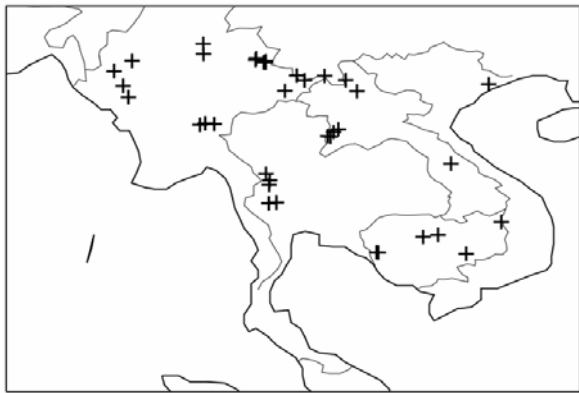


Figure 1: the location of smoke plumes analyzed in spring, 2010.

For each smoke plume, tens to hundreds of pixels are included. In all, more than three thousand smoke pixels are retrieved by MINX.

Figure 2 shows the probability distribution of all observed smoke pixel heights. The height of each smoke pixel is defined relative to the topography directly underneath that smoke pixel and ranges from a few hundred meters to around 4 km. About 60% of the smoke pixel heights are less than 1 km, which is the mean local boundary layer height at the satellite overpass time (10:30 a.m. local time). Approximately 29% of the smoke plumes are lifted to between 1 km and 2 km, and 11% of the smoke plumes are lifted to above 2 km. Overall, 40% of the smoke plumes are quickly lifted to heights above the boundary layer near the emission source. Though the vertical

resolution of MISR is a few hundred meters and there's bias in the MINX digitizing process, which makes the percentage somewhat uncertain, it is certain that some parts of the plumes are able to reach the free troposphere.

Vegetation types do not have a large impact here. Forest fires are often more intense than savanna fires [1], thus it is likely that smoke plumes from forest fires are quickly lifted to higher altitudes by local convection. Actually we find that a larger fraction of smoke pixels associated with forest fires were lifted to above 2000 m. However, the difference is small. This may be due to the similarity in biomass density in local forest and savanna. Alternative, large scale stability may be the major factor determining extent of vertical lifting.

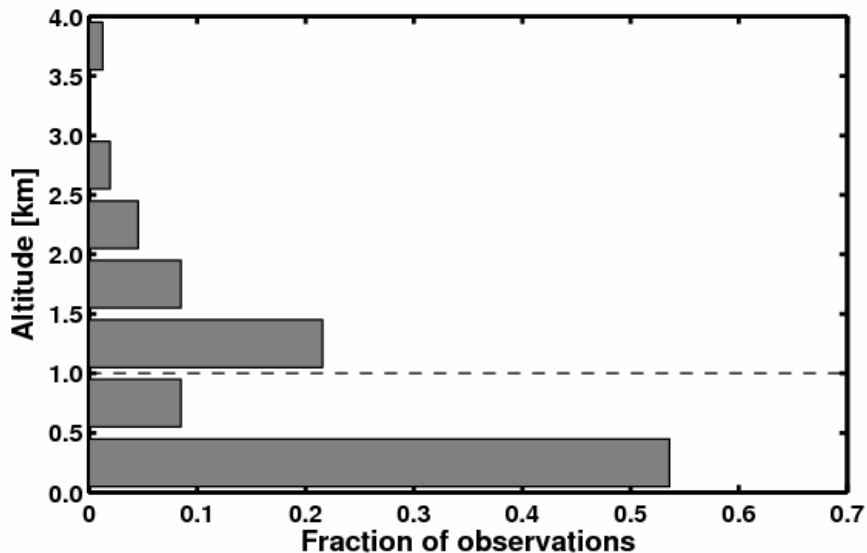


Figure 2: Frequency distribution of the pixel heights of observed smoke plumes from terrain in 500m height intervals. The local mean boundary layer is about 1 km high at 10:30 a.m. when they are observed.

Simulating the impacts of smoke injection heights on regional chemistry and transport of pollutants

Based on our results from the smoke pixel height analysis, we conduct a GEOS-Chem experiment simulation where 40% of biomass burning emissions are injected directly at height between 1 and 4 km, while the remaining 60% of biomass burning emissions are injected in the planetary boundary layer (PBL). The results are compared to a control experiment, where all biomass burning emissions are evenly distributed throughout the PBL. Biomass burning emissions are taken from Duncan et al. 2003, compounded with seasonal variation based on estimated from 4 years of fire-count data from the Along Track Scanning Radiometer (ATSR) and 1–2 years of similar data from the Advanced Very High Resolution Radiometer (AVHRR) World Fire Atlases^[25]. Mixing within the PBL is assumed to be instantaneous and full. We conduct test with a non-local PBL mixing scheme and found the results to be similar. Simulations are conducted from July 2005 to April 2006. The first seven months spin up the model; only results between February and April 2006 are analyzed, and we mainly discuss results in March, when the biomass burning is most heavy.

Figure 3 shows the monthly mean concentrations of CO over Southeast Asia and downwind regions in the surface and 3 km in control simulation. CO is highest in Southeast Asia surface due to biomass burning, but in 3km CO has been transported to southern China. So it is clear that emission from Southeast Asia biomass burning will influence our country.

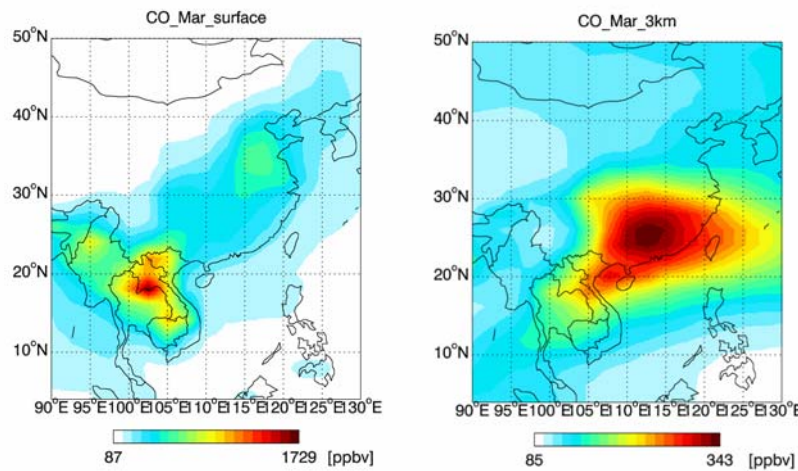


Figure 3: Monthly mean CO concentration in the surface and 3 km in March in the control simulation.

Figure 4-7 indicate the vertical distribution of monthly and regional mean tracer concentrations in

the two simulations above Southeast Asia (95° - 107.5° E, 12° - 22° N) and the downwind southern China (110° - 122.5° E, 20° - 30° N). The most obvious difference is around 3 km above Southeast Asia and 4 km above the downwind region, which is obviously caused by the change of injection height. And we can see that the traditional tracers CO and BC change only 10% and 7% in 3 km above Southeast Asia and less than 3% in the downwind region. At the same time, NO_x increases by a factor of 8 above Southeast Asia, leading to increase of PAN and ozone, and they also increase much in the downwind region.

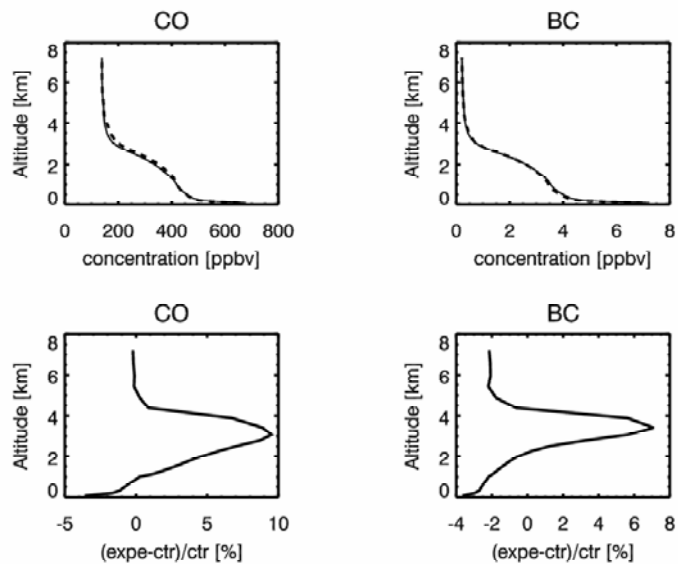


Figure 4: The first line shows CO and BC mean concentration in March above Southeast Asia (95° - 107.5° E, 12° - 22° N). The solid line stands for control simulation and the dotted line for experiment simulation. The second line shows the relative difference of the two simulations in percentage.

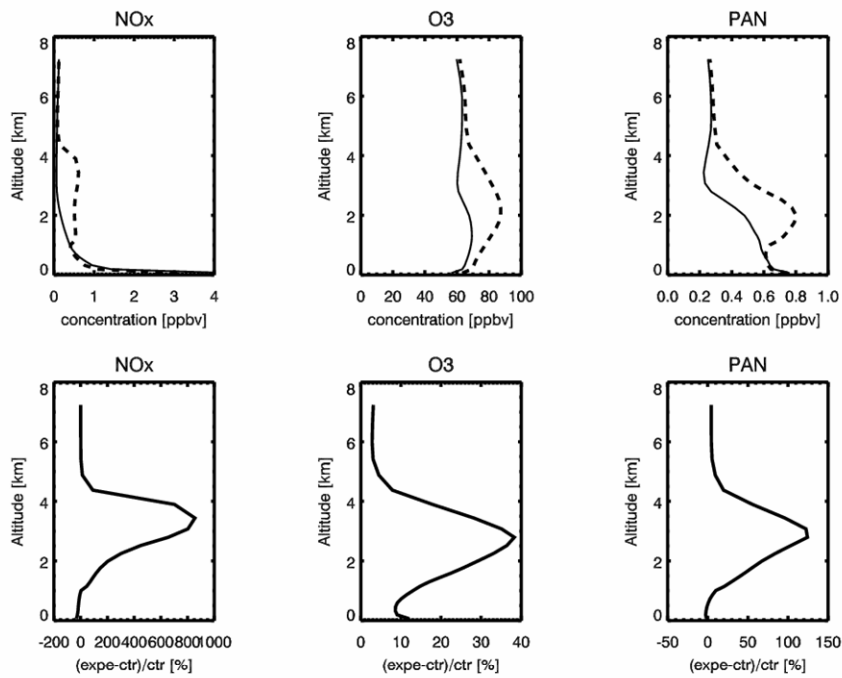


Figure 5: Same as figure 4, but for NO_x, PAN and ozone.

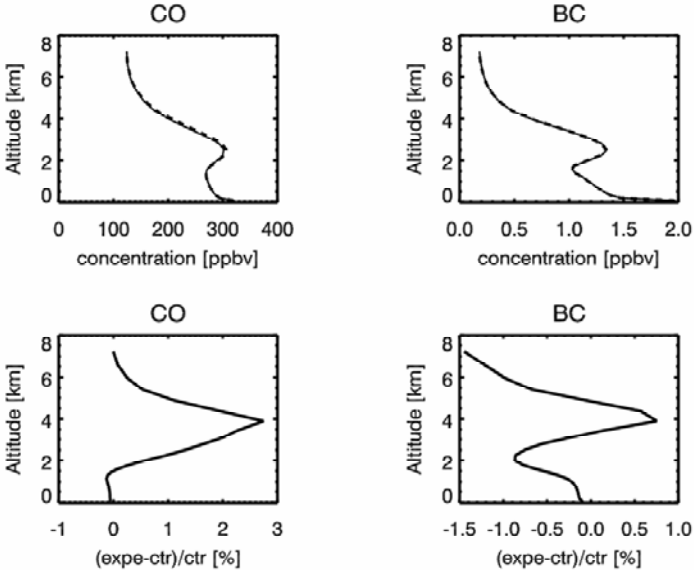


Figure 6: The first line shows CO and BC mean concentration in March above southern China (110° - 122.5° E, 20° - 30° N). The solid line stands for control simulation and the dotted line for experiment simulation. The second line shows the relative difference of the two simulations in percentage.

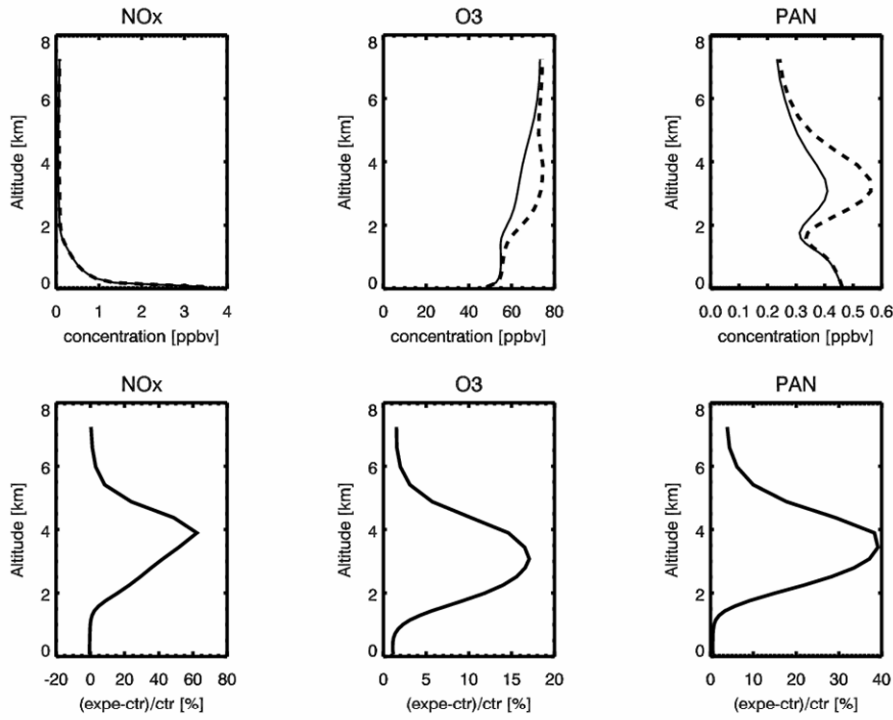


Figure 7: Same as figure 6, but for NO_x, PAN and ozone.

There are several reasons why the changes of CO and BC are small. CO concentration is decided by emissions, transport, convection, chemical produce and loss. Though CO is also emitted through anthropogenic and biofuel emission and chemical produce from monoterpenes and methanol, biomass burning is the major emission here. The advection changes little between two simulations. Convection changes some due to the decrease near surface and increase in high altitude of tracer concentration, but not enough to explain the phenomenon. Chemical produce reduces near the surface and increases above because the change of vertical distribution of other emitted organic matters.

The biggest change is in CO chemical loss due to reaction with OH. Because of the enhanced NO_x, OH doubles above Southeast Asia, which also doubles the chemical loss of CO. Figure 8 indicates that the increase of chemical loss can balance about a half of the emission put to 1-4 km in the experiment simulation.

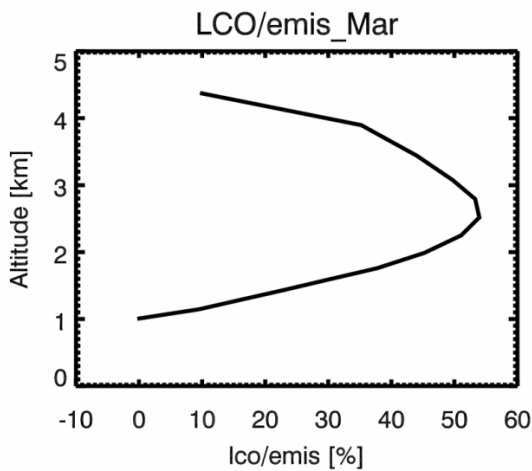


Figure 8: The increase of chemical loss of CO compared with the biomass burning emission of CO put in each layer between 1-4 km in the experiment simulation.

Background CO concentration may be another reason, as the mean CO mixing ratio at the surface of Southeast Asia ($95^{\circ} - 107.5^{\circ}$ E, $12^{\circ} - 22^{\circ}$ N) is over 400 ppbv in February, and in March the number is just above 600 ppbv. So biomass burning emission only contributes less than a half of the total CO concentration. The change of emission therefore has less influence on the total concentration.

Another factor is that we use mean CO concentration of the whole Southeast Asia, but biomass burning emission is unevenly distributed. If we only focus on one grid where the emission is largest, its CO concentration can increase 20% in 3 km. But there are also some grids with low emission, where emission's contribution to total CO concentration is not large and transport may also be important. Overall, we find the average change of CO limited.

BC acts like CO, but it does not have chemical produce or loss. Instead, BC has dry deposition. As there are less BC emitted near the surface, the dry deposition reduces. However, the main reasons may still be the background BC concentration and the mean concentration of the whole Southeast Asia we used.

However, changes in reactive nitrogen and ozone are clear. NO_x near the surface does not decrease that much, just like CO. But in the free troposphere they increase a lot. If we focus on one grid with biggest emission, the change is even larger. The altered dry deposition and convection of NO_x have some contribution, but the main reason is the short lifetime of NO_x . CO can live for more than two months while NO_x will disappear after around one day. So NO_x in the low layer hardly rise to higher layers and its concentration is quite low in high layers. Once we

put 40% emission directly to the free troposphere, NO_x concentration increase heavily.

The raise of NO_x concentration enhances the mixing ratio of subsequent products like PAN and ozone. Transport of enhanced PAN to the downwind region, in turn, increases NO_x in southern China. Mean concentrations of NO_x, PAN and ozone respectively increase 60%, 40% and 17% in 3-4 km above southern China (110° - 122.5° E, 20° - 30° N), which have important influence on atmospheric chemistry and pollution there.

CONCLUSION

We use images from the MISR satellite instrument to derive biomass burning smoke plume heights over Southeast Asia during spring 2010. We found that 40% of smoke pixels are lifted quickly to heights above the boundary layer (mean height 1 km in MISR overpass time) close to the point of emission. We use GEOS-Chem model to simulate the impact of injection heights on the regional chemistry and transport of biomass burning emissions. We found that putting 40% of Southeast Asia biomass burning emission to 1-4 km do not change much of CO and BC concentration. But NO_x, PAN and ozone increase much both above Southeast Asia and southern China, which have more important role in atmospheric chemistry. So the change in biomass burning injection height really impact the chemical environment of the source and the downwind region.

REFERENCES

- [1] van der Werf, G.R., J.T. Randerson, L. Giglio, G.J. Collatz, P.S. Kasibhatla, and A.F. Arellano, *Atmospheric Chemistry and Physics*, 2006, 6, 3423-3441.
- [2] Carmichael, G., Y. Tang, G. Kurata, I. Uno, D. Streets, J. Woo, H. Huang, J. Yienger, B. Lefer, R. Shetter, D. Blake, E. Atlas, A. Fried, E. Apel, F. Eisele, C. Cantrell, M. Avery, J. Barrick, G. Sachse, W. Brune, S. Sandholm, Y. Kondo, H. Singh, R. Talbot, A. Bandy, D. Thorton, A. Clarke, and B. Heikes, *Journal of Geophysical Research-Atmospheres*, 2003, -.
- [3] Chan, L., C. Chan, H. Liu, S. Christopher, S. Oltmans, and J. Harris, *Geophysical Research Letters*, 2000, 1479-1482.
- [4] Deng, X., X. Tie, X. Zhou, D. Wo, L. Zhong, H. Tan, F. Li, X. Huang, X. Bi, and T. Deng, *Atmospheric Environment*, 2008, 8493-8501.
- [5] Kondo, Y., Y. Morino, N. Takegawa, M. Koike, K. Kita, Y. Miyazaki, G. Sachse, S. Vay, M. Avery, F. Flocke, A. Weinheimer, F. Eisele, M. Zondlo, R. Weber, H. Singh, G. Chen, J. Crawford, D. Blake, H. Fuelberg, A. Clarke, R. Talbot, S. Sandholm, E. Browell, D. Streets, and B. Liley, *Journal of Geophysical Research-Atmospheres*, 2004, -.

- [6] Zhang, G., J. Li, X. Li, Y. Xu, L. Guo, J. Tang, C. Lee, X. Liu, and Y. Chen, *Environmental Pollution*, 2010, 3392-3400.
- [7] Martin, M., J. Logan, R. Kahn, F. Leung, D. Nelson, and D. Diner, *Atmospheric Chemistry and Physics*, 2010, 1491-1510.
- [8] Mazzoni, D., J. Logan, D. Diner, R. Kahn, L. Tong, and Q. Li, *Remote Sensing of Environment*, 2007, 138-148.
- [9] Tosca, M., J. Randerson, C. Zender, D. Nelson, D. Diner, and J. Logan, *Dynamics of fire plumes and smoke clouds associated with peat and deforestation fires in Indonesia*, in *Journal of Geophysical Research-Atmospheres*. 2011.
- [10] Mims, S., R. Kahn, C. Moroney, B. Gaitley, D. Nelson, and M. Garay, *Ieee Transactions on Geoscience and Remote Sensing*, 2010, 25-35.
- [11] Kahn, R., Y. Chen, D. Nelson, F. Leung, Q. Li, D. Diner, and J. Logan, *Geophysical Research Letters*, 2008, -.
- [12] Labonne, M., F. Breon, and F. Chevallier, *Geophysical Research Letters*, 2007, -.
- [13] Amiridis, V., E. Giannakaki, D. Balis, E. Gerasopoulos, I. Pytharoulis, P. Zanis, S. Kazadzis, D. Melas, and C. Zerefos, *Atmospheric Chemistry and Physics*, 2010, 11567-11576.
- [14] Leung, F., J. Logan, R. Park, E. Hyer, E. Kasischke, D. Streets, and L. Yurganov, *Journal of Geophysical Research-Atmospheres*, 2007, -.
- [15] Turquety, S., J. Logan, D. Jacob, R. Hudman, F. Leung, C. Heald, R. Yantosca, S. Wu, L. Emmons, D. Edwards, and G. Sachse, *Journal of Geophysical Research-Atmospheres*, 2007, -.
- [16] Chen, Y., Q. Li, J. Randerson, E. Lyons, R. Kahn, D. Nelson, and D. Diner, *Atmospheric Chemistry and Physics*, 2009, 6559-6580.
- [17] Pozzer, A., P. Jockel, and J. Van Aardenne, *Atmospheric Chemistry and Physics*, 2009, 9417-9432.
- [18] Kaufman, Y., C. Justice, L. Flynn, J. Kendall, E. Prins, L. Giglio, D. Ward, W. Menzel, and A. Setzer, *Journal of Geophysical Research-Atmospheres*, 1998, 32215-32238.
- [19] Giglio, L., J. Descloitres, C. Justice, and Y. Kaufman, *Remote Sensing of Environment*, 2003, 273-282.
- [20] Kaufman, Y., C. Ichoku, L. Giglio, S. Korontzi, D. Chu, W. Hao, R. Li, and C. Justice, *International Journal of Remote Sensing*, 2003, 1765-1781.
- [21] Nelson, D., C. Averill, S. Boland, and R. Morford, <https://www.openchannelsoftware.com/projects/MINX>, 2008.
- [22] Nelson, D., Y. Chen, R. Kahn, D. Diner, and D. Mazzoni, *Remote Sensing of Fire: Science and Application*, 2008, 8909-8909.
- [23] Bey, I., D.J. Jacob, R.M. Yantosca, J.A. Logan, B.D. Field, A.M. Fiore, Q.B. Li, H.G.Y. Liu, L.J. Mickley, and M.G. Schultz, *Journal of Geophysical Research-Atmospheres*, 2001, 106, 23073-23095.

- [24] Heald, C.L., D.J. Jacob, and A.M. Fiore, *Journal of Geophysical Research*, 2003, 108.
- [25] Duncan, B., R. Martin, A. Staudt, R. Yevich, and J. Logan, *Journal of Geophysical Research-Atmospheres*, 2003, -.

Emission Inventory of air pollutants from Biomass Burning in the Pearl River Delta Region, China

Yisheng Zhang¹ and Min Shao²

1 The Key Laboratory for Environmental and Urban Sciences, Shenzhen Graduate School, Peking University, Shenzhen, Guangdong 518055, China

2 State Joint Key Laboratory of Environmental Simulation and Pollution Control, College of Environmental Sciences, Peking University, Beijing 100871, China

Principal Contact: Min Shao, Professor, College of Environmental Sciences and Engineering, Peking University, Beijing, 100871.

Tel: 13301357920 Email: mshao@pku.edu.cn

Abstract

Biomass burning has been of increasing concerns for regional air quality issues. Emissions from burning of major agricultural residues were measured by a custom-made laboratory simulation system. Emission factors of CO₂, CO, PM₁₀, PM_{2.5}, and OC and EC in PM_{2.5} were measured to be 1105.2±189.3, 53.2±17.9, 14.0±5.1, 12.1±4.4, 10.53±4.87 and 0.49±0.22 g kg⁻¹ for rice straw burning in flaming condition, 1024.0±207.9, 110.6±37.9, 20.6±14.2, 18.3±13.5, 8.77±4.81 and 0.37±0.11 g kg⁻¹ for rice straw combustion in smoldering condition, and 1152.5±258, 40.1±15.7, 5.65±1.3, 4.12±1.1, 1.25±0.67 and 1.22±0.66 g kg⁻¹ for sugarcane leaves burning, respectively. The activity data of biomass burning were obtained in Pearl River Delta regional by in-house survey as well as questionnaires. The annual emissions of CO, NMHCs, NOx, PM_{2.5}, OC and EC in the PRD from biomass burning for the year 2008 were estimated to be 193.70, 18.34, 5.08, 15.31, 7.76, 2.71 kt, respectively. Field burning of straws made a major contribution to NMHCs, PM_{2.5} and OC emissions. Residential sector, including firewood and crop straw consumption, was the dominant source of EC, CO and NOx.

Keywords: Biomass burning, emission factor, chamber, emission inventory, regional distribution

Source Apportionment of Primary and Secondary Organic Aerosols at Urban and Rural Locations of Beijing

Song Guo, Min Hu^{*}, Qingfeng Guo and Xin Zhang

State Key Joint Laboratory of Environmental Simulation and Pollution Control, College of Environmental Sciences and Engineering, Peking University, Beijing, China 100871

ABSTRACT

Ambient sampling was conducted at an urban and a rural site of Beijing during CAREBEIJING-2008 field campaign. Secondary organic tracers derived from isoprene, α -pinene, β -caryophyllene, and toluene were measured using gas chromatography-mass spectrometry. Measured biogenic and anthropogenic secondary organic sources contributed $32.5 \pm 15.9\%$ at urban site and $35.4 \pm 14.1\%$ at rural site to the total organics, respectively. Toluene, isoprene, α -pinene, and β -caryophyllene SOC accounted for $16.6 \pm 8.4\%$, $8.9 \pm 5.8\%$, $4.8 \pm 2.2\%$ and $2.2 \pm 1.9\%$ of total OC at PKU. At Yufa, isoprene and toluene SOC were the major secondary contributors to OC with the contributions of $14.1 \pm 8.5\%$ and $13.9 \pm 8.9\%$. SOA formation mechanism was discussed. Producers VOCs, O₃ and ambient temperature had great effects on SOA formation, suggesting the importance of gas phase ozonation to SOA formation. The different correlations of SOA with O₃ and temperature suggested the mechanisms may be different from day to night. Relative humidity had no correlation with SOA concentration, but particle water uptake and acidity did, and the responses of SOA increase to water content and acidity were linear, indicating aqueous reaction may be also important for SOA formation. Primary source from CMB model and secondary source from tracer method can explain $72.2\% \pm 9.6\%$ and $80.2 \pm 10.5\%$ of the measured OC at PKU and Yufa, respectively. About 1/5-1/4 of the OC was not clear about their sources up to current knowledge.

KEYWORDS

Biogenic, Anthropogenic, Secondary organic aerosol, Source apportionment

1. Introduction

Secondary organic aerosols (SOA) are aerosols formed from the oxidation of volatile organic compounds (VOCs), which could contribute 50% to 90% of the organic carbon in particles. Thus a full understanding of their health, climate, and visibility effects requires the detailed

* Principal Contact: MIN HU, +86-01-62759880, minhu@pku.edu.cn

characterization of SOA composition and formation mechanism, so that their loading in the atmosphere can be accurately modeled. The conversion of inorganic gases into particulate phase sulfate, nitrate and ammonium is now fairly well understood. However, our understanding of SOA formation is very limited. There is considerable uncertainty over SOA. One important reason for this is the complexity of SOA composition. It is estimated that 10,000 to 100,000 different organic compounds have been measured in the atmosphere, and each VOC can undergo a number of atmospheric degradation processes to produce a range of oxidized products, which may or may not contribute to SOA formation and growth. Although clear progress has been made in recent years in identifying key biogenic and anthropogenic SOA precursors, significant gaps still remain in our scientific knowledge on the formation mechanisms, composition and properties of SOA.

These years, many efforts have been made to identify the tracers of SOA. A series of SOA tracers derived from isoprene, α -pinene, β -caryophyllene and toluene were affirmed in smog chamber experiments ^[1-3]. Based on the identified tracer compounds and their certain precursors, Kleindienst et al. recently developed a tracer based approach to estimate the contributions of individual biogenic and anthropogenic VOCs to ambient organic carbon (OC) ^[4]. In this approach, smog chamber studies provided the mass fractions of tracer compounds to SOA. Using these mass fraction results, the SOA tracer concentrations measured in ambient particles were used to derive the estimates of contributions of individual VOCs to SOA. This method has been used in some studies. However, no measurement of SOA tracers was carried out in Beijing.

In this study, aerosol samples were collected in an urban and a rural site of Beijing during CAREBEIJING-2008 field campaign. SOA tracers of isoprene, α -pinene, β -caryophyllene and toluene were quantified and used to estimate SOC and SOA. SOA formation mechanism was discussed, including concentrations of precursors and oxidants, ambient temperature and relative humidity. Thermodynamic model ISORROPIA was used to calculate aerosol water uptake and acidity, and their effects on SOA formation were also investigated. Primary source from CMB model and secondary source from tracer method were used to make a closure to total OC.

2. Experimental Methods

2.1 Sample collection

Two four-channel samplers (TH-16A, Tianhong, China) were used to collect 12h aerosol samples at PKU and Yufa simultaneously during CAREBEIJING-2008 summer intensive field campaign. The sampling flow rate was 16.7 L/min. Each set of the sample consisted of one Teflon filter and three quartz filters. PKU, the urban site ($39^{\circ}59'21''N$, $116^{\circ}18'25''E$), was on the roof of an academic building (about 15 m above the ground level) on the campus of Peking University in the northwestern of Beijing. There were no obvious emission sources nearby except two major roads, 150 m to the east and 200 m to the south. Yufa, the rural site ($39^{\circ}30'49''N$, $116^{\circ}18'15''E$), was about 53 km to the south of PKU, on top of a building (about 20 m above the

ground level) at the campus of Huangpu College. Around the site was nothing but farm land and residential area. Totally 75 and 74 sets of samples were collected at PKU and Yufa, respectively.

Before and after sampling, the Teflon filters were weighed in Peking University's clean room after 24h conditioning under constant temperature (20 ± 1 °C) and RH ($40\pm3\%$).

2.2 Chemical analysis

One punch (1.45 cm^2) was taken from the second channel quartz filter for EC and OC analysis via a thermal-optical method using a Sunset Laboratory-based instrument (NIOSH, 1996). The rest of the second channel and the third and forth channel quartz fibers were then extracted and analyzed using an Agilent GC-MS system (6890 plus GC-5973N MSD) to determine the chemical composition of particulate organic matters. The organic species were identified and quantified using authentic standards and internal standards. The details of the analytical procedures have been described previously [5]. Briefly, the samples were first spiked with a mixture of ketopinic acid (KPA), 26 deuterated compounds and 2 carbon isotope (^{13}C)-substituted compounds, and then ultrasonically extracted with dichloromethane/ methanol (3:1, v/v) at room temperature. The extracts were filtered and concentrated using a rotary vacuum evaporator and further condensed to about 0.5-1 ml under a flow of high purity nitrogen. Each extract was split into two fractions, one of which was derivatized with BSTFA (BSTFA/TMCS, 99:1; Supelco) to convert polar organic compounds to trimethylsilylized derivatives. Both the derivatized and underivatized fractions were analyzed using an Agilent GC-MS equipped with an Agilent DB-5MS GC column (length, 30 m; diameter, 0.25 mm; film thickness, 0.25 μm).

3. Results and Discussion

3.1 Concentrations of Secondary Organic Tracers

Totally 14 kinds of SOA tracers derived from isoprene, α -pinene, β -caryophyllene and toluene were quantified by using GC-MS (Table 1). Three isoprene SOA tracers identified by previous study were measured in this work [1], 2-methylglyceric acid and two 2-methyltetrosols, among which 2-methylglyceric acid had the highest concentration of $77.2\pm60.2\text{ ng/m}^3$ and $121.5\pm101.4\text{ ng/m}^3$ at PKU and Yufa, respectively. All these three tracers showed wide range of concentrations. The sum concentrations of three tracers were higher at Yufa than those at PKU. 9 α -pinene tracers were measured in this study, which also showed higher concentrations at Yufa indicating their biogenic source. The 2,3-dihydroxy-4-oxopentanoic acid was proposed to be a tracer compound for toluene SOA, whose concentrations were $13.3\pm7.7\text{ ng/m}^3$ at PKU and $11.7\pm6.9\text{ ng/m}^3$ at Yufa. The similar toluene SOA tracer concentration indicated the effect of anthropogenic source on regional SOA formation.

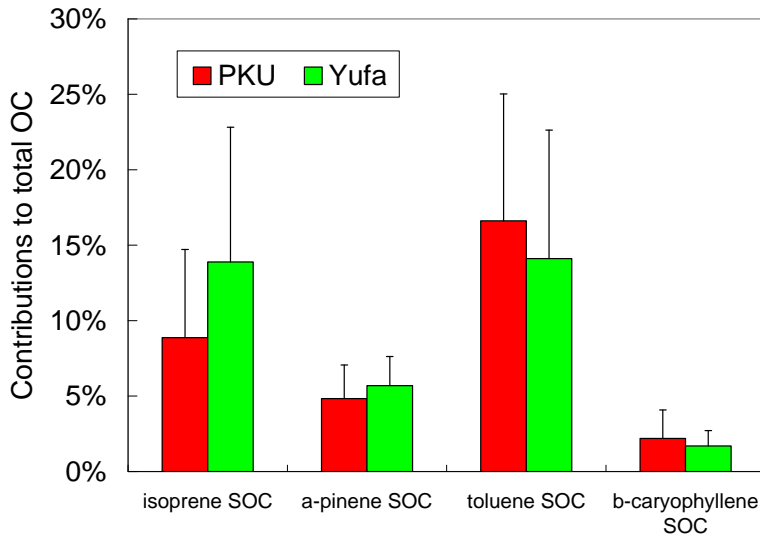
Table 1 Concentrations of SOA tracers as KPA (ng/m³)

compounds	PKU				Yufa			
	average	std	max	min	average	std	max	min
2-Methylglyceric acid	21.0	19.5	103.5	1.5	29.9	19.9	130.6	4.8
2-Methylthreitol	42.2	28.2	115.7	0.5	63.6	46.8	262.7	7.2
2-Methylerythritol	77.2	60.2	260.1	1.7	121.5	101.4	592.5	8.2
isoprene	140.4	100.9	470.4	10.3	215.0	160.3	913.4	25.5
3-Isopropylpentanedioic acid	8.7	7.1	34.3	0.6	9.6	7.2	31.6	1.3
3-Acetylpentanedioic acid	6.8	7.1	28.3	2.1	5.3	2.8	14.1	1.0
2-Hydroxy-4-isopropyladipic acid	4.6	4.0	15.7	n.d.	4.3	6.9	41.6	0.0
3-Acetylhexanedioic acid	8.3	5.8	28.3	2.1	7.7	5.5	42.2	0.4
3-Hydroxyglutaric acid	51.7	31.3	121.7	6.5	57.5	27.4	124.5	5.5
2-Hydroxy-4,4-dimethylglutaric acid	9.9	9.1	34.4	0.6	8.3	6.7	30.6	0.5
3-(2-Hydroxy-ethyl)-2,2-dimethylCyclobutane-carboxylic acid	8.5	10.1	74.1	0.6	6.1	5.5	44.7	0.9
Pinic acid	3.2	6.4	28.2	n.d.	3.4	5.7	28.8	0.0
Pinonic acid	11.9	6.3	27.3	n.d.	21.9	9.2	41.1	0.5
α-pinene	113.5	63.3	305.7	19.6	124.1	47.8	229.8	27.8
2,3-Dihydroxy-4-oxopentanoic acid	13.3	7.7	39.2	0.4	11.7	6.9	41.5	3.6
β-Caryophyllinic acid	5.1	4.5	17.8	n.d.	3.6	2.3	10.3	0.6

3.2 Estimation of biogenic and anthropogenic SOA

A tracer-based method first proposed by Kleindienst et al.^[4] was used to assess the SOC and SOA contributions of isoprene, α-pinene, β-caryophyllene and toluene to ambient OC and OM. Figure 1 showed the contributions of biogenic and anthropogenic SOC to OC. Four kinds of SOC accounted for 32.2%±15.2% and 39.2%±14.8% of the total OC at PKU and Yufa, respectively. At PKU toluene SOC contributed the largest fraction to OC with the percentage of 16.6±8.4%, followed by isoprene SOC and α-pinene SOC contributing 8.9±5.8% and 4.8±2.2%. β-caryophyllene SOC consisted of 2.2±1.9% of OC. At Yufa site, isoprene SOC and toluene SOC were the major contributors to OC with the contribution of 14.1±8.5% and 13.9±8.9%.

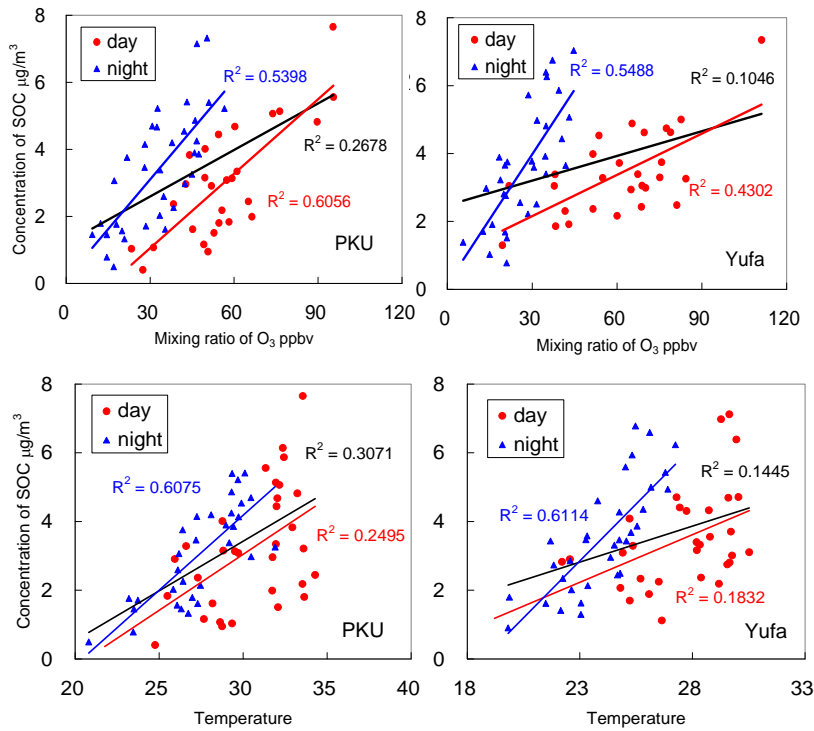
Figure 1. Contributions of biogenic and anthropogenic SOC to total OC



3.3 Formation of biogenic and anthropogenic SOA

The factors which could effect SOA formation were discussed in this study, including concentrations of precursors and oxidants, ambient temperature and relative humidity. As mentioned above, biogenic SOA appeared higher concentration at rural site; correspondingly, anthropogenic SOA at urban site, indicating the concentration of precursors had effect on SOA concentration. Figure 2 showed the correlations of SOC concentration with O₃ and temperature. SOC concentration had good correlation with both O₃ and temperature, suggesting the gas phase ozonization may be important to SOA formation. Moreover, it seemed that the formation mechanisms may be different from day to night due to the different correlations of SOC with O₃ and temperature. Both O₃ and temperature had better correlation with SOC at night, maybe due to the complexity of daytime oxidizing condition. The correlation between SOC concentration with RH was bad with $r=0.11$. However, it cannot conclude that water had no effect on SOA formation, since the aerosol water uptake is the direct factor to SOA formation.

Figure 2. Correlation of SOC concentration with O₃ and temperature



To investigate the effects of water uptake and acidity on SOA formation, Thermodynamic aerosol model ISORROPIA was used to calculate aerosol water uptake and acidity. The model was run in the reverse mode assuming the ambient particles were in thermodynamic stable state. Inputs to the model include concentrations of Na⁺, K⁺, Mg²⁺, Ca²⁺, NH₄⁺, NO₃⁻, SO₄²⁻ and Cl⁻ in PM_{2.5}, ambient temperature and relative humidity (RH). The results showed that SOC concentration had good correlation with water uptake and acidity, suggesting aqueous phase reaction may be important for SOA formation. At PKU, the correlation coefficients of SOC with water and H⁺ were both 0.81. The correlations at Yufa were not as good as those at PKU with the correlation coefficients of 0.53 to water and 0.60 to H⁺, maybe because the RH was too high at Yufa. The effects of water uptake and acidity were both linear on SOC formation, and this result was consistent with the chamber study [6].

3.4 Closure of primary and secondary

A closure of OC sources was made using trace based method for secondary OC sources and CMB model for primary OC sources. A chemical mass balance (CMB8.2) receptor model was used to apportion the primary sources of OC. The indicators for acceptable fitting results were R² (target >0.85), Chi-square value χ^2 (target <4), degrees of freedom DF (target >5), percentage of aerosol mass explained by the sources (target 80–120%), C/M ratio (ratio of calculated to measured concentration, target 0.5–2.0), and absolute value of the R/U ratio (ratio of residual to uncertainty, target <2). 5 primary sources were chosen in the model, including vegetative detritus,

wood burning, coal burning, non-catalyzed engines and diesel engines.

The result showed that At PKU, $40.0\% \pm 13.2\%$ of the OC was primary and $32.2\% \pm 15.2\%$ was secondary. Totally explained $72.2\% \pm 9.6\%$, and this fraction was $80.2 \pm 10.5\%$ at Yufa, including $41.0\% \pm 11.0\%$ of primary source and $39.2\% \pm 14.8\%$ of secondary sources. About 1/5-1/4 of the OC sources was not clear at Beijing according to our current knowledge.

SUMMARY

Totally 14 kinds of secondary tracers derived from isoprene, α -pinene, β -caryophyllene and toluene were quantified using gas chromatography-mass spectrometry. Biogenic SOA tracers showed higher concentrations at rural sites, by contraries, anthropogenic SOA tracer at urban sites. Tracer-yield method was used to estimate biogenic and anthropogenic SOA/SOC in the atmosphere at PKU and Yufa. Isoprene, α -pinene, β -caryophyllene and toluene SOC accounted for $16.6 \pm 8.4\%$, $8.9 \pm 5.8\%$, $4.8 \pm 2.2\%$ and $2.2 \pm 1.9\%$ of total OC at PKU. At Yufa, isoprene and toluene SOC were the major secondary contributors to OC with the contributions of $14.1 \pm 8.5\%$ and $13.9 \pm 8.9\%$. Producers VOCs, O₃ and ambient temperature had great effects on SOA formation, and the mechanisms may be different from day to night. Relative humidity had no correlation with SOA concentration, but particle water uptake and acidity did and the responses of SOA to water content and acidity were linear. Both gas phase and aqueous phase reaction may be important for SOA formation. Primary source from CMB model and secondary source from tracer method can explain $72.2\% \pm 9.6\%$ and $80.2 \pm 10.5\%$ of the measured OC at PKU and Yufa, respectively. About 1/5-1/4 of the OC was not clear about their sources up to current knowledge.

ACKNOWLEDGMENTS

This work is supported by Beijing Council of Science and Technology. It is also supported by the National Natural Science Foundation of China (20977001, 21025728).

REFERENCES

1. Claeys, M., et al., *Formation of secondary organic aerosols through photooxidation of isoprene*. Science, 2004. **303**(5661): p. 1173-1176.
2. Claeys, M., et al., *Hydroxydicarboxylic acids: Markers for secondary organic aerosol from the photooxidation of alpha-pinene*. Environmental Science & Technology, 2007. **41**(5): p. 1628-1634.
3. Jaoui, M., et al., *Identification and quantification of aerosol polar oxygenated compounds bearing carboxylic or hydroxyl groups. 2. Organic tracer compounds from monoterpenes*. Environmental Science & Technology, 2005. **39**(15): p. 5661-5673.

4. Kleindienst, T.E., et al., *Estimates of the contributions of biogenic and anthropogenic hydrocarbons to secondary organic aerosol at a southeastern US location*. Atmospheric Environment, 2007. **41**(37): p. 8288-8300.
5. Zhang, Y.X., et al., *Source profiles of particulate organic matters emitted from cereal straw burnings*. Journal of Environmental Sciences-China, 2007. **19**(2): p. 167-175.
6. Surratt, J.D., et al., *Effect of acidity on secondary organic aerosol formation from isoprene*. Environmental Science & Technology, 2007. **41**(15): p. 5363-5369.

Sources of Carbonaceous Aerosol in the Pearl River Delta region and Hong Kong

Mei Zheng^{1,2}, James Schauer³, Peter K.K. Louie⁴, Limin Zeng¹, and Yuanhang Zhang¹

1 College of Environmental Sciences and Engineering, Peking University, Beijing 100871, China

2 School of Earth and Atmospheric Sciences, Georgia Institute of Technology, Atlanta, GA 30332, USA

3 University of Wisconsin-Madison, Madison, WI 53706, USA

4 Hong Kong Environmental Protection Department

Principal Contact: Mei Zheng, Professor, College of Environmental Sciences and Engineering, Peking University, Beijing 100871, China.

Tel: 010-62752436 Email: mzheng@pku.edu.cn

Abstract

Carbonaceous aerosol plays an important role in fine particulate matter in the southern China. Molecular markers in fine particles can provide source information of carbonaceous aerosol. In this study, individual organic species were analyzed in PM2.5 samples from seven sites during four months using gas chromatography-mass spectrometry (GC-MS). These samples were collected simultaneously from four sites in the Pearl River Delta (PRD) and three sites in Hong Kong in order to investigate important sources of carbonaceous aerosol in this region. The application of molecular markers in a chemical mass balance model (CMB-MM) revealed that excess primary OC in the PRD was primarily composed of gasoline engine exhaust, diesel engine exhaust, biomass burning, and coal combustion. Mobile source emissions alone can contribute about 30% excess OC. This study identified important contributors to primary carbonaceous aerosol and pointed out the need to reduce its emissions in order to improve air quality in this region.

Keywords: Carbonaceous Aerosol, molecular marker, CMB, PRD, Hong Kong

Application of PMF to AMS Data Obtained at Fukue Island, Japan

Satoshi Irei¹, Akinori Takami¹, Toshihide Hikida² and Akio Shimono²

1 National Institute for Environmental Studies, 16-2 Onogawa, Tsukuba, Ibaraki, 305-8506, Japan

2 Shoreline Science Co., 3-12-7 Oowada machi, Hachioji, Tokyo, 192-0045, Japan

ABSTRACT

In the spring of 2009 we conducted a field study at Fukue island, Nagasaki, Japan, for analysis of chemical composition of ambient aerosols using Aerodyne's quadrupole aerosol mass spectrometer. The obtained data were analyzed by positive matrix factorization (PMF) analysis for better quantitative understanding of types of organic aerosols. Evaluation of the PMF results suggested that three to five factorial solutions seemed to give reasonable explanations for the observed data. The major factors extracted were highly oxygenated organic aerosols, hydrocarbon-like organic aerosols, and an unknown that has unique mass spectra.

KEYWORDS

(SOA, oxygenated organic aerosol, aerosol mass spectrometer, positive matrix factorization)

Introduction

Studies for fine ambient aerosols are very important due to potential link to the issues of the climate change and adverse health effect. Even though significant effort of the atmospheric scientists in the last two decades has given better understanding about sources, sinks, formation mechanisms for inorganic aerosols, current understanding for organic aerosols, particularly for secondary organic aerosols (SOA), is still insufficient. The objective of this project was to gain quantitative information of SOA and other types of organic aerosols observed during a field study carried out in the spring of 2009 at Fukue island, Nagasaki, Japan. It has been known that application of factor analysis to aerosol mass spectra can retrieve information of oxygenated organic aerosols associate with SOA^[1]. Here, we applied positive matrix factorization (PMF) analysis, a type of factor analysis, to retrieve such information.

Method

In the spring of 2009 (April 5 to May 10), field measurements were carried out at Fukue island in Nagasaki, Japan (32.8 N, 128.7 E). Chemical composition of fine aerosols was analyzed by a quadrupole aerosol mass spectrometer (Aerodyne Research Inc.). The

instrument basically measures mass spectra of aerosol components: molecules and atoms in particulate phase are flash-vaporized at a vaporizer heated to 600°C when particles in an aerosol beam formed by Aerodynamic lens collide the vaporizer, ionized by 70eV electron impact, and then analyzed by a quadrupole mass analyzer for their mass to charge ratios, m/z. It should be noted that due to the vaporizer, the instrument can analyze only non-refractory species that are vaporized at 600 °C under the vacuumed environment. Using fingerprinting fragment ions associate with parent molecules, quantitative information for sulfate, nitrate, chloride, water, and ammonium is obtained. The residual of mass spectra is treated as “organics”. 10 minute averaged mass spectra scanned from m/z 1 to m/z 300 were obtained during the field measurements.

The obtained mass spectra were analyzed by Positive Matrix Factorization (PMF)^[2] for better understanding of types of organic aerosols. An Igor macro developed by Ulbrich et al.^[3] was used to evaluate the output of the PMF program.

Results and Discussion

It was found that sulfate and organic were predominant species in the fine aerosols at Fukue island (Fig. 1). To date, it has been known that these two species are major components of fine aerosols at Fukue island^[4], thus, the observation in this study is consistent with the previous finding.

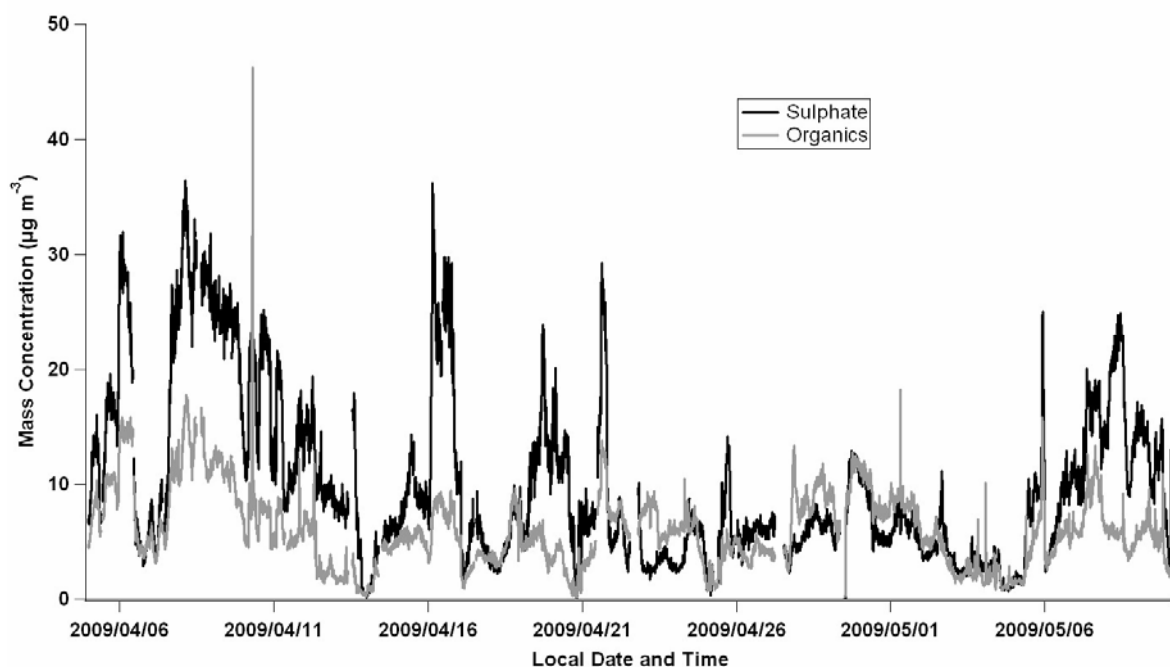


Fig. 1. Time Series Plot of Sulfate and Organic Concentrations Observed during the Field Study at Fukue Island in Spring of 2009.

The results of the PMF analysis suggest that two to five factorial solutions seem to explain the observation reasonably. The two major factors identified by comparing with literature mass spectra^[1] are highly oxygenated organic aerosols (OOA) and hydrocarbon-like organic aerosols (HOA). There is an unknown, but a major factor that has mass spectra with remarkable signals at m/z 85, 87, and 131. The identification of this requires further study.

The PMF results also give idea of proportion of these organic aerosols in the observed data. For example, the three factorial solution indicates that the proportions of the OOA, the HOA, and the unknown during the study are 32%, 20%, 46%, respectively (Fig. 2).

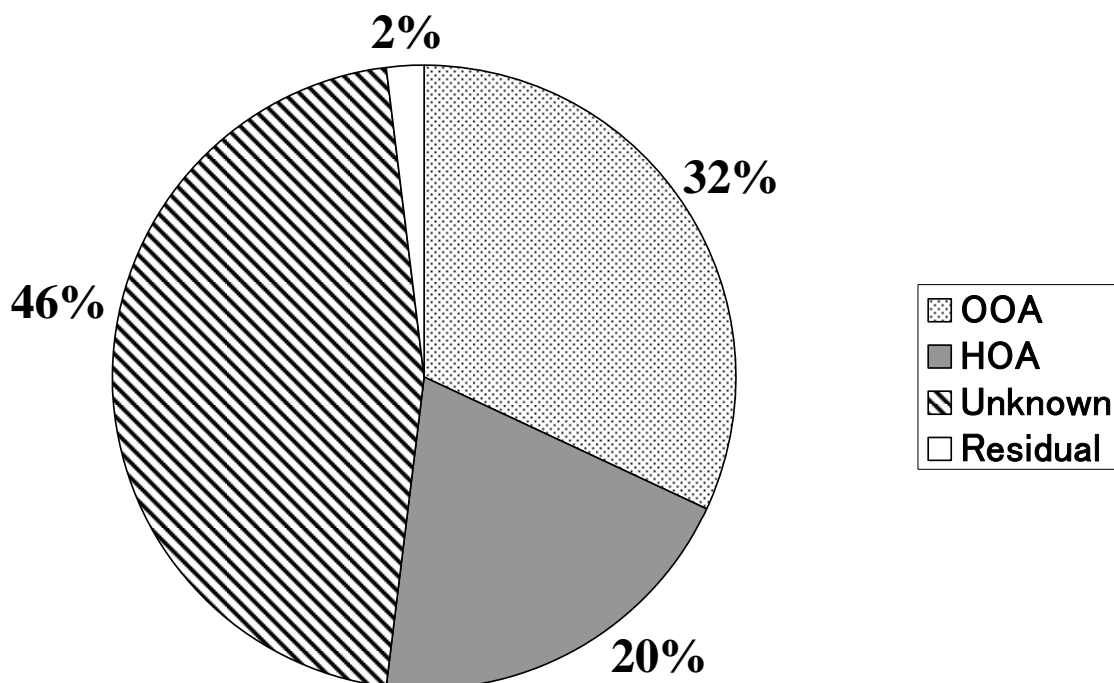


Fig. 2. Fraction of Type of Organic Aerosol Observed during the Field Study at Fukue Island in the Spring of 2009. OOA, oxygenated organic aerosol, HOA, hydrocarbon-like organic aerosol, and unknown. The fraction shown was estimated according to the PMF analysis with a three factorial solution.

CONCLUSION

We applied PMF analysis to the AMS data obtained during the field measurements at Fukue island in the spring of 2009. The results suggest that the organic aerosols observed seem to be explained by three to five factorial solutions. The major factors extracted are OOA, HOA, and unknown. The further evaluation of the PMF results as well as studies for identification of the unknown factor are needed for better understanding of organic aerosols there.

REFERENCES

- [1] Zhang, Q., Alfarra, M.R., Worsnop, D.R., Allan, J.D., Coe, H., Canagaratna, M.R., and Jimenez, J.L., *Env.Sci.Tech.*, 2005, 39, 4938-4952.
- [2] Paatero, P. and Tapper, U., *Environmetrics*, 1994, 5, 111-126.
- [3] Ulbrich, I.M., Canagaratna, M.R., Zhang, Q., Worsnop, D.R., and Jimenez, J.L., *Atm.Chem.Phys.*, 2009, 9, 2891-2918.
- [4] Takami, A., Miyoshi, T., Shimono, A., and Hatakeyama, S., 2005. *Atm. Env.*, 2005, 39, 4913-4924.

Multivariate Analysis of Particulate Polycyclic Aromatic Hydrocarbons in Bangkok Atmosphere

Siwatt Pongpiachan^{1,2}, Mattanawadee Hattayanone³, Charnwit Kositanone⁴, Kin Fai Ho², and Junji Cao²

1 School of Social and Environmental Development, National Institute of Development Administration (NIDA), 118 Moo 3, Sereethai Road, Klong-Chan, Bangkapi, Bangkok 10240, Thailand

2 SKLLQG, Institute of Earth Environment, Chinese Academy of Sciences (IEECAS), Xi'an 710075, China

3 Faculty of Environmental Management, Prince of Songkla University, Hat-Yai, Songkla 90120, Thailand

4 Inter-Department of Environmental Science, Faculty of Graduate Studies, Chulalongkorn University, Bangkok 10330, Thailand

Principal Contact: Dr. Siwatt Pongpiachan, Assist. Prof., School of Social and Environmental Development, National Institute of Development Administration (NIDA), 118 Moo3, Sereethai Road, Klong-Chan, Bangkapi, Bangkok 10240, Thailand.

Tel: +66-89637-2211, +66-27273113 E-mail: pongpiajun@gmail.com

Abstract

Atmospheric concentrations of low molecular weight PAHs (i.e. Phenanthrene, Anthracene, Pyrene and Fluoranthene) were measured in PM₁₀ at seven observatory sites operated by pollution control department of Thailand. Sampling was carried out at the Community Housing Klongchan, Nonsi Witthaya School, Singharat Pittayakhom School, Thon Buri Electricity Sub, Chok Chai 4 Police Station, Dindang Community Housing and Bodindecha (Sing Singhaseni). For all monitoring sites, each sample covered a period of 24 hours taken at a normal weekday every month from January-December 2006 forming a database of 84 individual air samples (i.e. 12 x 7 = 84). Ambient air samples were collected by using a Graseby-Anderson high volume air sampler with PM10 TE-6001. All quartz fiber filters (QFFs) were pre-cleaned with DCM in a Soxhlet extractor for 8 h prior to use. Extracting efficiency was evaluated by adding an aliquot of a known amount of internal standard (deuterated Fluorene) prior to extracting, to calculate any losses during the extracting process. In this research, analyses of all samples were carried out on a Varian Saturn 2000 gas chromatograph-mass spectrometry (GC/MS-MS) using a DB-5 (30 m x 0.25 mm, i.d. x 0.25 μm film thickness). Multivariate analysis such as multiple linear regression analysis (MLRA), hierarchical cluster analysis (HCA) and principal component analysis (PCA) were employed to investigate the potential emission sources of PAHs in Bangkok atmosphere.

Keywords: PAHs, Bangkok, PM₁₀, Cluster Analysis, Principal Component Analysis, Multiple Linear Regression Analysis

Lung Generated Aerosols

Wan-Ting Lin¹, Sheng-Hsiu Huang¹, Yu-Mei Kuo², Chun-Wan Chen³, Shih-Wei Tsai¹ and Chih-Chieh Chen¹

1 National Taiwan University, College of Public Health, 17 Xu-Zhou Road, Taipei, Taiwan.

2 Chung Hwa University of Medical Technology, 89 Wen-Hwa 1st Street, Jen-Te District, Tainan, Taiwan.

3 Institute of Occupational Safety and Health, Council of Labor Affairs, No. 99, Lane 407, Hengke Rd., Shijr District, New Taipei City, Taiwan

Principal Contact: Chih-Chieh Chen, Professor, National Taiwan University, College of Public Health, 17 Xu-Zhou Road, Taipei, Taiwan.

Tel: +886233668086 Fax: +886223938631 E-mail: ccchen@ntu.edu.tw

Abstract

In order to characterize the aerosol emission from exhaled breath, an Exhaled Breath Aerosol Monitoring System, comprised of a pneumotachograph, a condensation particle counter, an optical counter, and an aerosol-free chamber with flow rate over 200 L/min, was constructed and used as the principal apparatus in the present study. The subject(s) were asked to respire through a mouth piece and a pneumotachograph connected to an aerosol-free chamber. In order to monitor the aerosol concentration during exhalation period and to determine the location of aerosol generation, only high sampling rate (at least 10 Hz) aerosol instruments were employed. A nose clip was used to force the respiration through mouth only. Subjects were asked to perform a variety of breathing patterns generated by a cylinder-piston type breathing simulator, in order to study the breathing-pattern dependency.

Among the aerosol instruments tested, the Welas-2000H and the TSI CPC 3025 had the shortest response time. The Aerodynamic Particle Sizer and the TSI CPC 3010 had the highest aerosol count. The human lung needs to be cleaned with aerosol-free air before test to avoid the interference from indoor aerosols. Therefore, the subject's head was placed in a hood, supplied with humidified (RH 70%) aerosol-free air flow higher than the breathing flow rate, to speed up the test process. The aerosol generation rate increased with increasing tidal volume. For the same tidal volume, exhaled breath aerosol concentration of 1- μ m aerosol decreased with increasing breathing frequency, indicating that portion of the exhaled breath aerosols were deposited due to inertial impaction. The aerosol generation is likely due to the film burst in the expanding bronchiole during inhalation. The aerosols were drawn into alveoli first, and then expelled during exhalation. The aerosol concentration of exhaled breath is ranging from tens of particles to several hundred particles per breath.

Keywords: Exhaled breath, Aerosol generation, Tidal volume.

Control of Indoor Fungal Bioaerosols by Using Ozone

Hsiao-Lin Huang¹ and Jen-Hsuan Tai¹

1 Institute of Industrial Safety and Disaster Prevention, Chia Nan University of Pharmacy and Science, Tainan 71710, Taiwan

ABSTRACT

Most of people spend eighty to ninety percent of their time indoors due to lifestyle changes in Taiwan. The probabilities to expose to bioaerosols threat through indoor air are increasing. The objectives of this study were to disinfect indoor fungal bioaerosols by using high concentration ozone and assess the feasibility of purified indoor bioaerosols by ozone. Two kinds of fungal bioaerosols (*C. famata* and *P. citrinum*) with concentrations of 10^6 CFU/m³ were generated by Collison three-jet nebulizer. The germicidal effects to bioaerosols of ozone were measured at ozone concentration of 0~175ppm, relative humidity of 30~70%, and exposed time of 1~10sec. The results indicated that the needed concentrations of ozone to reach disinfection efficacy of 90% (at relative humidity of 70% and expose time of 10sec) for *Candida famata var. flareri* and *Penicillium citrinum* spore bioaerosols were 100 and 150ppm respectively. The orders of germicidal efficacy of ozone to bioaersols were *Candida famata var. flareri* > *Penicillium citrinum spore*. Increasing of relative humidity and exposure time could enhance the germicidal efficacy of ozone to the two fungal bioaerosols. Summary, the germicidal efficacies of ozone to two types of bioaerosols (one vegetative cells and one spore) were above 90%. Therefore, the ozone disinfection system had high germicidal efficacy showed that ozone was a feasible method to control indoor fungal bioaerosols and improve indoor air quality.

KEYWORDS

Ozone, Bioaerosol, Fungi, Indoor air quality

Introduction

The proportions of time to staying in indoor environments are generally greater than 80% for most of people in Taiwan. It is very important to control indoor bioaerosols because the probabilities to contact biohazards through the exposure pathway of indoor air are increasing. Many technical methods have been used to improve indoor quality of bioaerosols, such as ventilation, filtration, ultraviolet germicidal irradiation, and plasma^[1]. Many studies have been indicated that high surface disinfection efficacy can be reached by ozone^[2-4]. Although ozone has high germicidal ability, however, it is also harmful to humans. Therefore, practical applications to indoor air sterilization by using ozone are still limited now. In order to prevent from exposing

to ozone directly for indoor humans, the hybrid system of high concentration ozone and ozone decomposition by catalyst were used in accessing to the feasibility of sterilizing bioaerosols under different of ozone concentration, relative humidity, and exposed time.

Experimental Methods

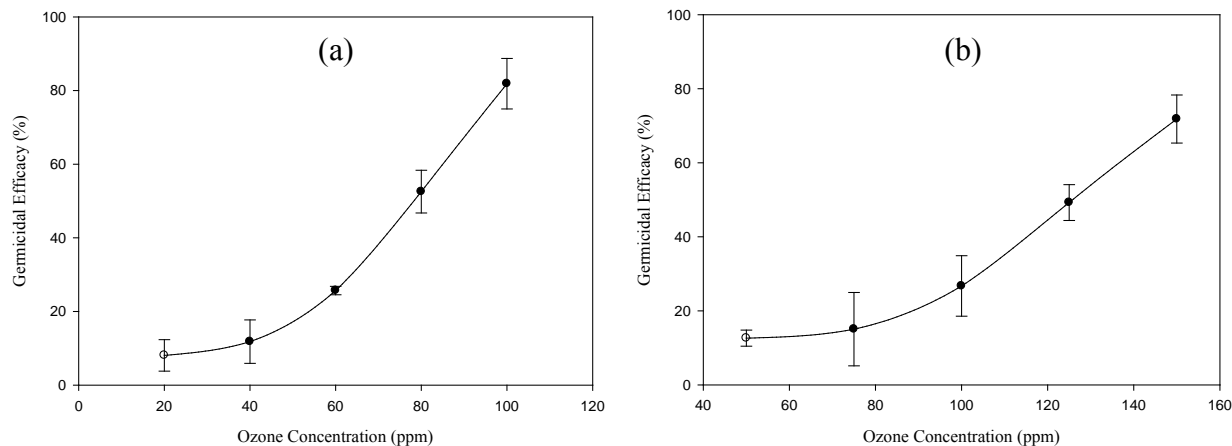
Ozone with concentrations of 0~175 ppm were generated by a non-thermal dielectric barrier discharge (DBD) system. Two kinds of bioaerosols (*C. famata* and *P. citrinum*) with concentrations of 10^6 CFU/m³ were generated by a Collison three-jet nebulizer (BGI Inc.) and a dilution system. The generated bioaerosols were passed through a Kr85 unit (Model 3077A, TSI, USA) to neutralize charges, and then mixed with ozone system in a chamber under the relative humidity of 30~70%, and exposed time of 1~10sec. Ozone in tail gas after disinfection was decomposed by MnO₂/AuO and MnO₂/AC catalysts. Ozone was detected by an ozone monitor (Models 106, 2B Technologies, Inc.). Bioaerosols were sampled by a one-stage Anderson bioaerosol sampler and then cultured to calculate germicidal efficacy.

Results and Discussion

Effects of Ozone Concentration

Figure 1 shows that the germicidal efficacies of ozone for *Candida famata* var. *flarerri* and *Penicillium citrinum* spore bioaerosols were increased with ozone concentrations at relative humidity of 50% and exposed time of 10 seconds. The germicidal efficacy of ozone for *Candida famata* bioaerosols can be reached to 81% at the ozone concentration of 100 ppm (Figure 1(a)). Ozone elevated disinfection efficacy significantly for *Candida famata* if ozone concentration was greater than 100 ppm. Compared to *Candida famata* bioaerosols, the germicidal efficacy of ozone for *Penicillium citrinum* spore was only 71% even at the ozone concentration of 150 ppm (Figure 1(b)). The lower germicidal efficacy of ozone for *Penicillium citrinum* spore than *Candida famata* bioaerosols was due to the structure of *Penicillium citrinum* spore has better tolerance to ozone. Therefore, *Penicillium citrinum* spores needed higher ozone concentration to be sterilized. The orders of germicidal efficacy for the two kinds of bioaerosols by using ozone were consistent with previous study about surface disinfection^[5].

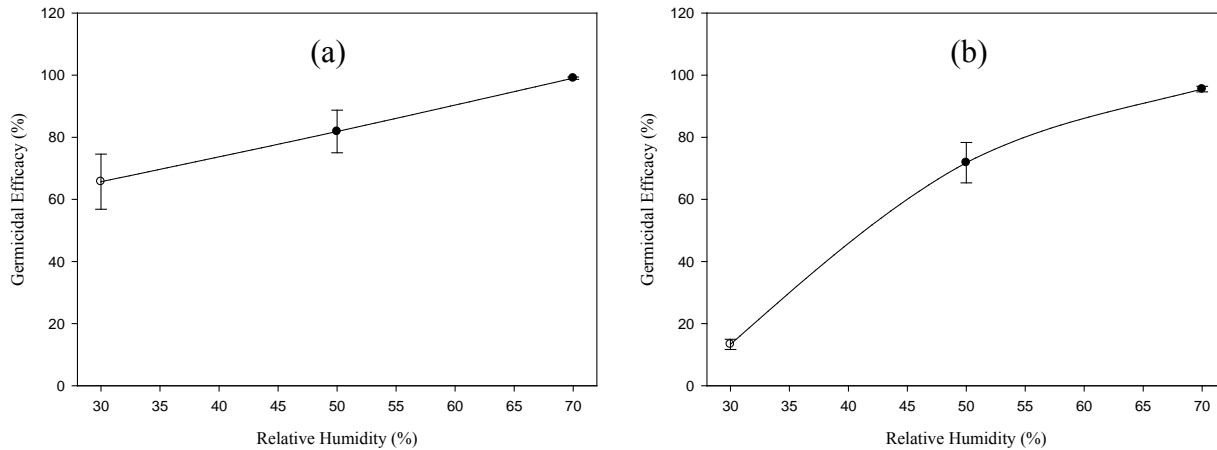
Figure 1. The Germicidal Efficacy of Ozone at Different Ozone Concentration for (a) *Candida famata* var. *flarerri* and (b) *Penicillium citrinum* Spore Bioaerosols (Relative Humidity: 50%; Exposed Time: 10 sec).



Effects of Relative Humidity

The germicidal efficacies of ozone for *Candida famata* var. *flarerri* and *Penicillium citrinum* spore bioaerosols at different relative humidity presents in Figure 2. The ozone germicidal efficacies for both bioaerosols were increased with relative humidity at ozone concentration of 100 ppm and 150ppm and exposing time of 10 seconds. The germicidal efficacies of ozone for *Candida famata* have been reached to 99% when relative humidity at 70% (Figure 2(a)). For *Penicillium citrinum* spore bioaerosols, the germicidal efficacy of ozone increased from 13% to 71% when relative humidity increased from 30% to 50%. Further elevating relative humidity to 70%, the germicidal efficacy even reached to 95% (Figure 2(b)). It was helpful to elevate disinfection efficacy significantly by increasing relative humidity for both bioaerosols. The germicidal effects on bioaerosols by elevating relative humidity could be due to large amount of OH radicals generated by reaction of ozone and H₂O^[1,5]. The high reactive species of OH radicals could interact with bioaerosols and then lead the survival rates of bioaerosols to decrease^[5].

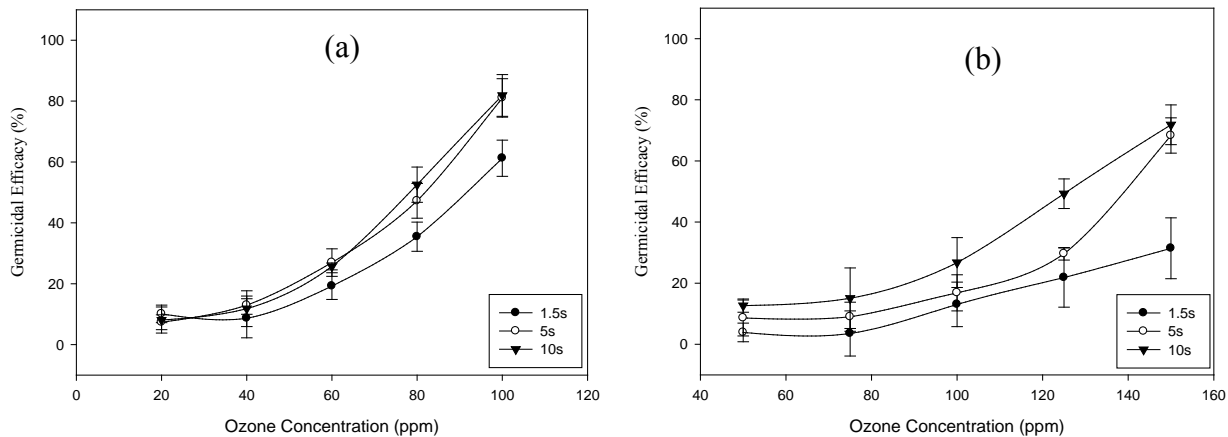
Figure 2. The Germicidal Efficacy of Ozone at Different Relative Humidity and Exposed Time of 10 sec for (a) *Candida famata* var. *flarerri* (Ozone: 100 ppm) and (b) *Penicillium citrinum* Spore Bioaerosols (Ozone: 150 ppm).



Effects of exposed Time

The germicidal efficacies of ozone for *Candida famata* var. *flarerri* and *Penicillium citrinum* spore bioaerosols at different exposed time are illustrated in Figure 3. The results indicated that the germicidal efficacy of ozone increased with exposed time at each specific ozone concentration. The orders of sterilizing *Candida famata* var. *flarerri* and *Penicillium citrinum* spore bioaerosols by ozone were $10\text{sec} \doteq 5\text{sec} > 1\text{sec}$ and $10\text{sec} > 5\text{sec} > 1\text{sec}$, respectively. The reason of enhancing disinfection effect by increasing exposed time was due to increasing exposed time that could elevate the collision probability between bioaerosols and ozone, and provide enough time for ozone to enter the cells of bioaerosols to oxidize. The results of elevating germicidal efficacy of ozone for both fungal bioaerosols when exposed time increased from 1 sec to 5 sec, they were similar to previous study about surface disinfection of ozone [5].

Figure 3. The Germicidal Efficacy of Ozone at Different Exposed Time and Relative Humidity of 50% for (a) *Candida famata* var. *flarerri* and (b) *Penicillium citrinum* Spore Bioaerosols.



Ozone Decomposition

The tail gas, ozone with the highest concentration of 175 ppm used in this study, was decomposed by MnO₂/AuO and MnO₂/AC catalysts in this study. The ozone concentrations were below to the detection limit of ozone monitor under the treatment of catalysts at the gas hourly space velocity of $3.287 \times 10^3 \text{ h}^{-1}$. This result demonstrated that catalysts have good ability to decompose residual ozone and protect people from exposing ozone directly during the period of disinfection.

CONCLUSION

Summary, the germicidal efficacies of ozone to two types of fungal bioaerosols (one vegetative cells and one spore) were above 90% at relative humidity of 70% and expose time of 10sec. Ozone with high concentration of 100~150 ppm have been proved to have good disinfection efficiency after few seconds treatment applied in small chamber. In addition, catalyst could completely decompose residual ozone in tail gas. Therefore, the hybrid system of ozone disinfection and catalyst not only had high germicidal efficacy and low cost but also can protect people indoor from exposing to ozone directly. In preliminary assessment of this study had showed that ozone combined with catalyst was a feasible method to control indoor biohazards and improve indoor air quality.

ACKNOWLEDGMENTS

The authors would like to thank the National Science Council of Republic of China for

financially supporting this research under Contract No. NSC 98-2622-E-041-008-CC3.

REFERENCES

- [1] *Aerobiological Engineering Handbook: A Guide to Airborne Disease Control Technologies*; Kowalski, W.J.; New York, McGraw-Hill, 2006.
- [2] Masaoka, T.; Kubota, Y.; Namiuchi, S.; Takubo, T.; Ueda, T.; Shibata, H.; Nakamura, H.; Yoshitake, J.; Yamayoshi, T.; Doi, H.; Kamiki, T. *Applied and Environmental Microbiology* 1982, 43(3), 509-513.
- [3] Kowalski, W.J.; Bahnfleth, W.P.; Striebig, B.A.; Whittamc, T.S. *AIHA Journal* 2003, 64(2), 222-227.
- [4] Klánová, K.; Lajciková, A. *Indoor Built Environ.* 2005, 15(1), 81-84.
- [5] Li, C.S.; Wang, Y.C. *American Industrial Hygiene Association Journal*, 2003, 64(4), 533-537.

A Case Study of the Impacts of Dust Aerosols on Surface Atmospheric Variables and Energy Budgets in a Semi-Arid Region of China

Xiaolu Ling^{1,2}, Weidong Guo^{3,2}, Lei Zhang¹ and Renjian Zhang²

1 Key Laboratory for Semi-Arid Climate Change of the Ministry of Education, College of Atmospheric Sciences, Lanzhou University, Lanzhou, 730000, China

2 Key Laboratory of Regional Climate-Environment for East Asia,, Institute of Atmospheric Physics, Chinese Academy of Sciences, Beijing, 100029, China

3 Insititute for Climate and Global Change Research, School of Atmospheric Sciences, Nanjing University, Nanjing, 210093, China

ABSTRACT

The authors present a case study investigating the impacts of dust aerosols on surface atmospheric variables and energy budgets in a semi-arid region of China. Enhanced observational meteorological data, radiative fluxes, near-surface heat fluxes, and concentrations of dust aerosols were collected from Tongyu station, one of the reference sites of the International Coordinated Energy and Water Cycle Observations Project (CEOP), during a typical dust storm event in June 2006. A comprehensive analysis of these data show that in this semi-arid area, higher wind velocities and a continuously reduced air pressure were identified during the dust storm period. Dust storm events are usually associated with low relative humidity weather conditions, which result in low latent heat flux values. Dust aerosols suspended in the air decrease the net radiation, mainly by reducing the direct solar radiation reaching the land surface. This reduction in net radiation results in a decrease in soil temperatures at a depth of 2 cm. The combination of increased air temperature and decreased soil temperature strengthens the energy exchange of the atmosphere-earth system, increasing the surface sensible heat flux. After the dust storm event, the atmosphere was dominated by higher pressures and was relatively wet and cold. Net radiation and latent heat flux show an evident increase, while the surface sensible heat flux shows a clear decrease.

KEYWORDS

Case Study, Dust Aerosol, Energy Budget, Semi-Arid Region

Introduction

Many studies have been conducted on the impact of dust aerosols on climate, while there is still great uncertainty in assessing the climatic impacts of dust aerosols^[1-3]. Meanwhile, most studies are focused on the global scale or on arid regions, and there is little information available describing the corresponding meteorological response caused by dust aerosols in semi-arid areas.

With respect to the relationship between arid and humid regions, semi-arid regions are characterized by their high vulnerability and sensitivity, particularly in the context of global warming^[4-5].

In this paper, we use a combination of meteorological elements, land surface radiative and heat fluxes, and dust aerosol data to analyze the impacts of dust aerosols on surface atmospheric variables and energy budgets in semi-arid regions of China.

Experimental Methods

Data were collected from Tongyu station (44°25' N, 122°52' E, 184 m above sea level), which is one of the reference sites of CEOP and in a semi-arid region of China.

The 30-minute resolution meteorological observation data including wind speed, pressure, temperature and humidity was collected at the degraded grassland site. The radiation instruments are installed at 3.0 m height.

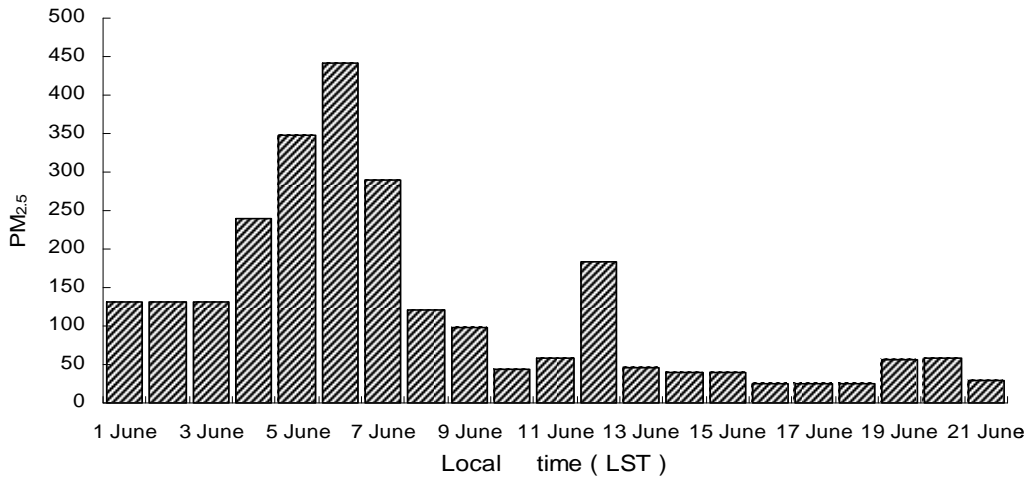
Particles with an aerodynamic diameter $\leqslant 2.5 \mu\text{m}$ ($\text{PM}_{2.5}$) were collected daily at the grassland site 3 m above ground level from 14 April to 23 June 2006^[6].

Results and Discussion

1 Weather Background

There was a dust storm event from 5 June to 7 June, followed by the dust particles subsided gradually. The rapid decline in dust concentration on 10 June was due to a precipitation event.

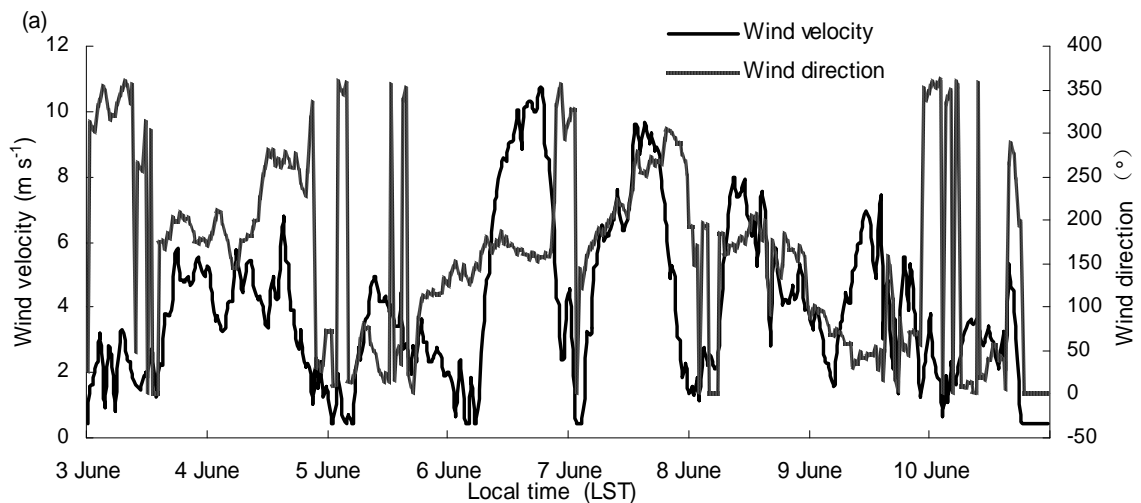
Figure 1 Temporal variations of PM_{2.5} at Tongyu station during June of 2006 (Units: $\mu\text{g m}^{-3}$).



2 Atmospheric Variables

2.1 Wind Velocity and Wind Direction

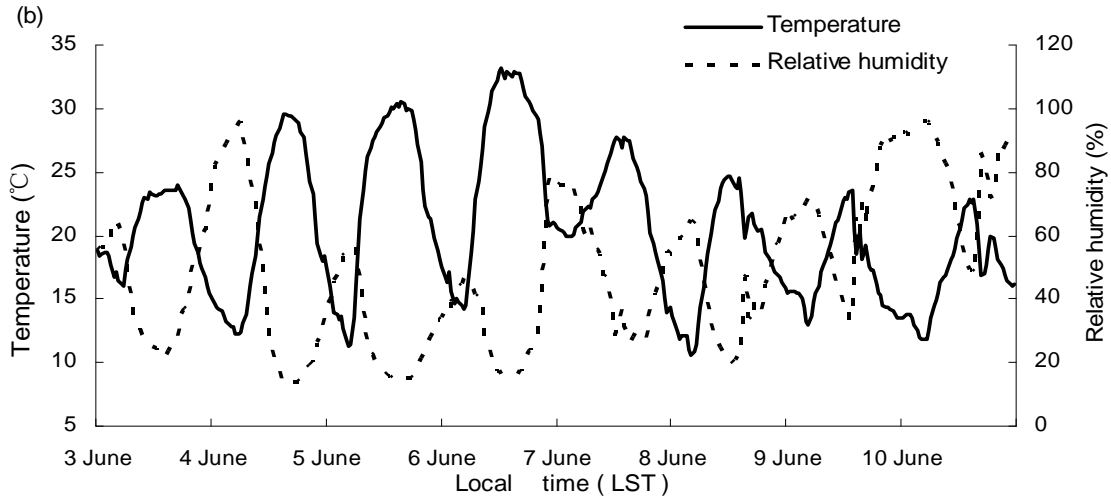
Figure 2 Variations of surface atmospheric variables at Tongyu station from 3 to 10 June
(a). wind velocity and wind direction



Before the dust storm events, wind velocity had two adjustments. The first adjustment suggested that the dust aerosols were blown in from the north and accumulated in the air, while the second wind direction changed gradually to the southeast. During the dust storm event, wind velocity increased rapidly and suddenly, while after which wind velocity weakened gradually.

2.2 Air Temperature, Soil Temperature at 2cm and Relative Humidity

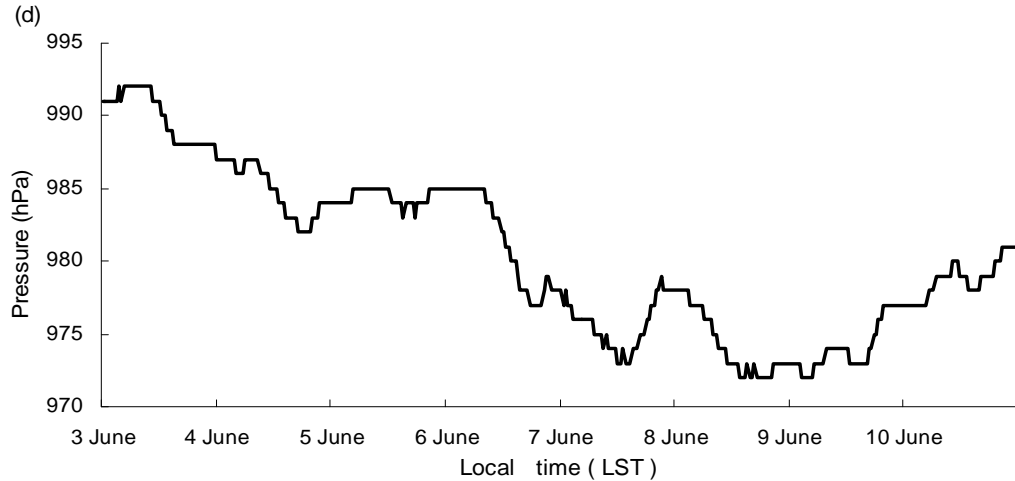
Figure 2 Variations of surface atmospheric variables at Tongyu station from 3 to 10 June
(b). air temperature and relative humidity



Air temperature and 2 cm soil temperature showed a close correlation (Fig. 2c (omitted)), while relative humidity and temperature showed generally opposing behaviors (Fig. 2b).

2.3 Air Pressure

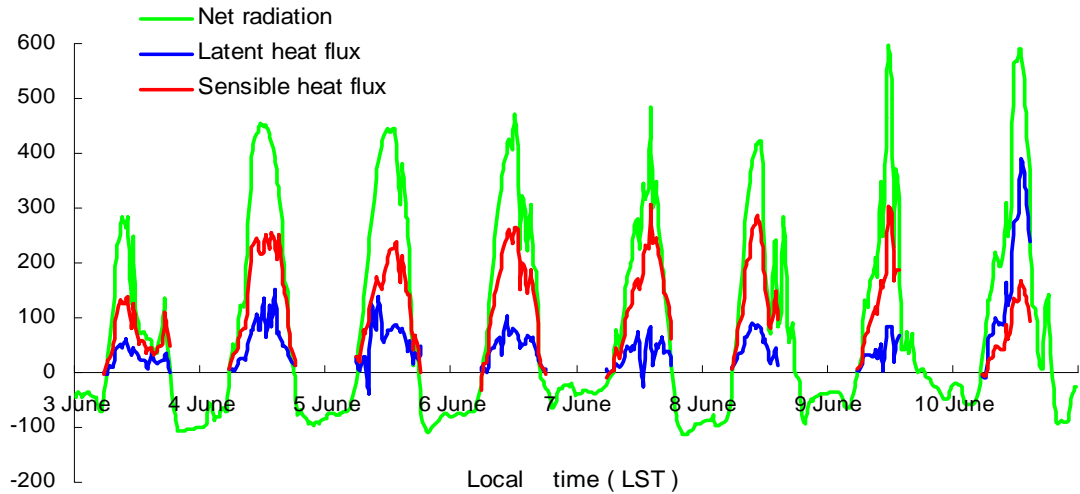
Figure 2 Variations of surface atmospheric variables at Tongyu station from 3 to 10 June
(d). air pressure



The whole dust storm event occurred under a state of continuously decreasing air pressure, indicating that low air pressure was one of the leading causes of this dust storm event.

3 Energy Budget

Figure 3 Variations of net radiation, latent heat flux, and sensible heat flux during the daytime at Tongyu station from 3 to 10 June (Units: W m^{-2}).



Net radiation displayed an increasing trend at Tongyu station. After 9 June, land surface net radiation increased gradually and reached a maximum of 497.9 W m^{-2} . The change in latent heat flux was much more intense than sensible heat flux. The lower the dust concentration, the smaller the sensible heat flux, while opposite the latent heat flux.

Sensible heat flux plays a dominant role in energy distribution in semi-arid regions on dust storm days, but that latent heat flux plays a dominant role on clear days.

CONCLUSION

Before the dust storm event, wind velocity underwent two adjustments, the atmosphere was dry and hot, and the air pressure was low. During the dust storm event, the wind velocity increased sharply, the air temperature increased, the air pressure continued to fall, as did the relative humidity. During this time, net radiation and latent heat flux maintained a low value, while sensible heat flux was relatively high. After the dust storm event, the relative humidity and air pressure began to increase, and the air temperature began to fall. The air was relatively wet and cold under the control of high pressure. Net radiation and latent heat flux showed a strong increase while sensible heat flux showed an apparent decrease.

This kind work requires further verification of long term observational data. It is necessary to test the inferences proposed in this paper in combination with physical models in a future study.

ACKNOWLEDGMENTS

This work was jointly supported by funds from the Knowledge Innovation Program of the Chinese Academy of Sciences (Grant No.KZCX2-YW-Q11-03) and the National Basic Research Program of China (Grant No.2006CB400501).

REFERENCES

- [1] Tegen, I., and I. Fung, 1994: Modeling of mineral dust in the atmosphere: Sources, transport, and optical thickness, *J. Geophys. Res.*, **99**(D11), 22897-22914.
- [2] Sokolik, I. N., and O. B. Toon, 1996: Direct radiative forcing by anthropogenic airborne mineral aerosols, *Nature*, **381**(20), 681-683.
- [3]IPCC, 2007: *Climate Change 2007: The Physical Science Basis, Contribution of Working Group I to the Fourth Assessment Report of the Intergovernmental Panel on Climate Change*, S. Solomon, D. H. Qin, M. Manning, et al., (Eds.), Cambridge University Press, Cambridge and New York, 996pp.
- [4]Fu, C. B., and D. Z. Ye, 1995: Global change and the future trend of ecological environment evolution in China, *Scientia Atmos. Sinica*, **19**(1), 116-126.
- [5] Fu, C. B., and G. Wen, 2002: Several issues on aridification in the northern China, *Climatic Environ. Res.* (in Chinese), **7**(1), 22-29.
- [6] Zhang, R. J., C. B. Fu, Z. W. Han, et al., 2008: Characteristics of elemental composition of PM_{2.5} in the spring period at Tongyu in semi-arid region of Northeast China, *Adv. Atmos. Sci.*, **25**(6), 922-931.

Contamination Assessment of Copper, Lead, Zinc and Chromium in Dust Fall of Jinan, NE China

Suping Feng*, Nannan Zhang, Hanchao Liu, Xiaolin Du and Yongli Liu

School of Environmental Science and Engineering, Shandong University, Jinan
250100, China

ABSTRACT

To assess the pollution of heavy metal in dust fall, nine dust fall samples were collected during the heating period and non-heating period from Jinan, a city in northeastern China. The samples were analyzed for Cu, Pb, Zn and Cr and the contamination level of heavy metals was assessed on the basis of the geo-accumulation index (I_{geo}). The results indicated that all of the four investigated metals accumulated significantly in the dust fall of Jinan, and the metal concentrations were much higher than background values. The mean values for Cu, Pb, Zn and Cr in the dust fall were 377.8, 736.3, 2867 and 841 mg kg^{-1} , respectively. The I_{geo} values calculated based on background values revealed that the contamination level of heavy metal in the dust fall ranges from moderately contaminated to heavily contaminated, and it mainly originates from traffic and industry. In this work, we also used the dust fall residue compared to the standard reference as the background value to calculate the I_{geo} value. This method is useful for situations in which the background value is difficult to obtain.

KEYWORDS

Contamination Assessment, Dust Fall, Heavy Metal, Geo-accumulation Index

1. Introduction

Soil, sediment and dust are the three materials which originate primarily from the earth's crust. Among them, dust fall is the most pervasive and important factor affecting human health and well-being. Non-exhaust particulate emissions resuspended by traffic often represent an important source of atmospheric particulate matter in urban environments^{[1][2]}. Consequently, resuspension of dust fall can lead to high human exposures to heavy metals, metalloids and mineral matter.

Dust fall is one of the most complex and hazardous pollutants in the atmospheric environment^[3]; its trace heavy metals are one of the largest pollution sources^[4]. In general, heavy metals are found in the atmospheric environment at low natural

concentrations. However, human activities like transportation, industrial discharges, domestic heating and waste incineration make a significant contribution to the high contents of toxic metals in dust fall^{[5][6]}. These elements get distributed among soils, air, surface dust and water. As a result, metals are accumulated, for they are not easily degraded or decomposed in the environment^{[7][8]}. Vehicle emission is another main source of the trace metals in dust fall, especially the traffic-related metals, such as Pb, Cu and Zn^{[9][10]}. Although the use of leaded gasoline has been prohibited for decades, Pb and the associated metals continue to accumulate in dust fall because of their non-biodegradability and long residence time^[11]. In addition, a variety of other sources, including coal combustion, metal smelting, etc, are important contributors of metals as well^{[12][13][14]}. Thereby, dust fall plays the role of a metal-sink in cities.

In recent years, methods of analyzing and determining the concentration of heavy metal in the sediment samples to assess the degree of heavy metal pollution and potential ecological risk have become quite accurate and dependable. Whereas dust fall and soil have similar constituents, the content of trace heavy metals of Cu、Pb、Zn、Cr in different forms in dust fall are determined by Tessier's^[15] method of conformation taxonomy and graphite furnace atomic absorption spectrometry^[16], but the degree of pollution was not quantitatively researched.

The vast majority of studies on the contents of heavy metals in dust fall have been carried out in developed countries but very few in China, and systematic studies of large regions in China have only been done in important cities such as Beijing or Dalian^{[17][18][19]}. Organic and inorganic constituents of dust fall in some areas have also been reported^{[3][20][21]}.

Based on the aforementioned facts, in this study we aimed to (1) determine the concentrations of selected metals from sampled dust fall collected from urban areas of Jinan; (2) map the metal distribution through geo-statistical analysis to identify their spatial patterns in the region; and (3) identify the main sources of individual metals in the dust fall using geo-statistical analyses. The results of this research may be useful for the city government in alleviating metal contamination in the course of Jinan's development.

2. Experimental Methods

2.1 Sample collection

Six dust fall sampling sites were selected in Jinan, including the campus of Shandong University, the provincial seed station, a fertilizer plant, a plastic factory, the Jinan steel industrial complex and the biotechnology park in the Jinan high-tech development zone. Sampling stations (1 m^2) 1.5 m above the ground were placed at

each site and dustfall samples were collected after about 1 day. Samples S1 to S9 represent the 6 samples taken during the non-heating period and 3 samples taken during the heating period. In order to collect comparable samples, all the dust fall samples were collected under similar weather conditions. All the collected samples were kept in sealed polyethylene (PE) packages to avoid contamination; subsequently the samples were transported to the laboratory and preserved in a refrigerator.

2.2 Sample processing

All of the samples were dried in an oven at 353 K for 24 h, and then the dried samples were milled and sieved to retain the 20-40 mesh fractions for analysis. To determine the total metal contents of the dust fall, 0.5 g samples were placed in polytetrafluoroethylene vessels and digested with HNO₃, HF and HClO₄ in a microwave oven (MDS-2002AT), according to the method described by Sandroni et al. [22]. Then the solutions were dissolved with distilled water to a final volume of 50 ml. The contents of elements Cu, Pb, Zn and Cr were analyzed by an atomic absorption spectrophotometer (AAS) (180-80, Polarized Zeeman, HITACHI).

To obtain the different speciation of heavy metals in the dust fall, the samples were treated with different solvent-extractions; for more details refer to Tessier et al. [15]. Sequential extraction was used for solid phase fractionation. All the extractions except the residual fraction were carried out in 50 ml polypropylene centrifugation tubes with tight lids. When continuous agitation was required, samples were shaken lengthwise on an end-to-end mechanical shaker. After each successive extraction, separation was done by centrifugation (800-Electric centrifugal precipitators) at 5000 rpm for 30 min at 298 K. The concentrations of heavy metals in the residual material were obtained by the same method described by Sandroni et al. [22] as the background values compared to the standard background values.

2.3 Choice of the elemental types of heavy metals

In this paper, Cu, Pb, Zn and Cr were the main research objects. The levels of the toxic metals Hg and As are very low in the atmosphere and particulate matter of Jinan, and the content of Cd was far below the limit of pollution emission required by state, so these metals were not considered. The four tested metals have standard methods to determine their contents, and their distributions in particulate matter have been widely reported, so Cu, Pb, Zn and Cr were chosen for evaluation.

2.4 Contamination assessment methods

Numerous calculation methods have been put forward to quantify the degree of metal enrichment or pollution in soil, sediments and dusts^{[23][24]}. In this study, the geo-accumulation index (I_{geo}) put forward by Muller^[25] was calculated to assess the heavy metal contamination level in the dust fall.

I_{geo} was originally used with bottom sediments^[25]. It is computed by the following equation:

$$I_{geo} = \log_2 \frac{C_n}{1.5 B_n} \quad (\text{Eq.1})$$

where C_n - represents the measured concentration of the element n and B_n -is the geochemical background value of the element in fossil argillaceous sediment (average shale). In this study, B_n is the standard reference value from data before worldwide industrialization as the background content of element n. The constant factor 1.5 was introduced to analyze natural fluctuations in the contents of a given substance in the environment and very small anthropogenic influence^[26]. Muller^[27] proposed seven classes of the geo-accumulation index, as shown in Table 1.

Table 1 Six classes of the geo-accumulation index

Class	I_{geo} value	Dust fall quality
0	$I_{geo} \leq 0$	Practically uncontaminated
1	$0 \leq I_{geo} \leq 1$	Uncontaminated to moderately contaminated
2	$1 \leq I_{geo} \leq 2$	Moderately contaminated
3	$2 \leq I_{geo} \leq 3$	Moderately to heavily contaminated
4	$3 \leq I_{geo} \leq 4$	Heavily contaminated
5	$4 \leq I_{geo} \leq 5$	Heavily to extremely contaminated
6	$5 \leq I_{geo}$	extremely contaminated

2.5 The choice of background reference value in geo-accumulation index (I_{geo})

The assessment results rely on the concentrations of the samples and the choice of geochemical background value. Different geochemical background values would distinctly affect the geological accumulation index (I_{geo}), so the choice of geochemical background value to calculate the geo-accumulation index should be the background value of sediment in the researched region. If the geochemical background value of researched region could not be ascertained, the sedimentary features, granularity and substance constitution of the sediment should be considered sufficiently, and the background value should be chosen from the geochemical background value approaching the sediment geochemical features and environmental features of the region. In this paper, the background values for the calculation of the geo-accumulation index were chosen from the residue of dust fall samples and standard reference values from data before worldwide industrialization, separately. The different reference values were listed in Table 2.

Table 2 standard reference values of metal element units: mg kg⁻¹

Source	Cu	Pb	Zn	Cr
Standard reference value	50	70	175	90
Dust fall residue	47.2	50.2	154	61.8

3. Results and Discussion

3.1 Metal levels of dust fall and source analysis

The concentration of metals (mean, maximum, minimum) and the sampling period are shown in Table 3. The average levels of the four observed metals in dust fall samples during the heating period were higher than the samples during the non-heating period. However, both period's metal levels were much higher than the background values before worldwide industrialization and the dust fall residue.

During the heating period, the arithmetic mean of Cu, Pb, Zn and Cr in the dust fall is 377.83, 736.25, 2867.00 and 841.00 mg kg⁻¹, respectively. During the Non-heating period, the arithmetic mean of Cu, Pb, Zn and Cr in the dust fall is 258.67, 603.67, 2149.67 and 27.2 mg kg⁻¹, respectively. So we can conclude that coal burning for heating increases the levels of metals in dust fall to a certain extent. The maximum values of Cu and Zn were found in the sample from a site 100 m from a heavily trafficked road, while their minimum values were detected in a dust sample from a residential site with less traffic density. The source of Cu and Zn in street dust has been shown to be tire abrasion, the corrosion of metallic parts of cars, lubricants and industrial and incinerator emissions^{[28][29]}. The maximum amounts of Pb and Cr were found in the dust sample collected from an industry area with an iron and steel mill, coke-oven plant, cement manufacturing plants, and a coal-fired power plant, while the lowest concentration was detected in the sample from a residential site with less traffic density. It may be concluded the sources of Pb and Cr in street dusts of Jinan mainly originated from industrial activities and automotive emissions. The dust fall has similar compositions to the road dusts and sediments. It is a common practice to compare mean concentrations of heavy metals in road dusts in different urban environments^{[30][31]}, although there are no universally accepted sampling and analytical procedures for geochemical studies of dust fall.

Table3 Heavy metal concentrations ($\text{mg}\cdot\text{kg}^{-1}$) in dust fall collected from Jinan city

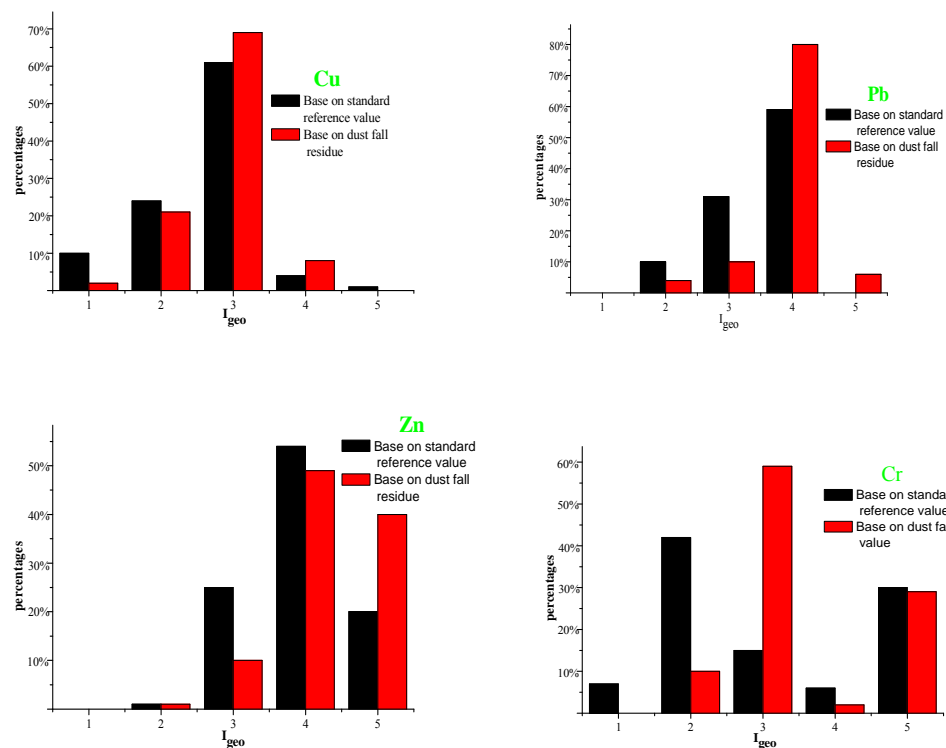
	parameter	Cu	Pb	Zn	Cr
Heating period	Average	377.83	736.25	2867.00	841.00
	Minimum	218	328.5	1095	335
	Maximum	568	1037.5	4492	2704
Non-heating period	Average	258.67	603.67	2149.67	138.73
	Minimum	107	264.5	985	27.2
	Maximum	364	1041.5	3080	265
Reference values	standard	50	70	175	90
	reference value				
	Dust fall residue	47.2	50.2	154	61.8

From the above results, we conclude that there are different main sources of metals in various areas of a city. Higher population density did not always result in heavier pollution. Both the levels of environmental management and the living habits of residents could influence the environmental quality.

3.2 Metal pollution assessment based on I_{geo}

Standard background value and dust fall residue were separately selected as the reference in the assessment of toxic metal pollution. The geo-accumulation method I_{geo} was used to calculate the degree of metal contamination in dust fall. The I_{geo} results are summarized in Fig. 1. The I_{geo} ranges from 1.54 to 3.00 with a mean value of 2.24 for Cu, 1.66 to 3.31 with a mean value of 2.71 for Pb, 2.06 to 4.10 with a mean value of 3.30 for Zn, 1.31 to 4.32 with a mean value of 2.20 for Cr. The mean values of I_{geo} decreased in the order of Zn > Pb > Cu > Cr. The mean I_{geo} value and 69% I_{geo} of Cu fall into class 3, indicating moderately to heavily contaminated, while 21% I_{geo} falls into class 2, indicating moderately polluted. The mean I_{geo} and percentage I_{geo} of Cr showed the samples were moderately to heavily contaminated. The mean I_{geo} obtained for Pb and Zn pointed to heavy pollution. In Fig. 1, the results calculated with standard reference value as background were close to those found using dust fall residue.

Fig. 1 Percentages of samples in varied I_{geo} classes



CONCLUSIONS

All four investigated metals were accumulated significantly in the dust fall of Jinan, and the metal concentrations were much higher than background values. Moreover the contents of the metal in the dust fall during the heating period were a little higher than during the non-heating period. The concentration of Cu, Pb, Zn and Cr in the dust fall ranges from 218 to 501, 328.5 to 1037.5, 1095 to 4492 and 335 to 2704 mg kg⁻¹, with an arithmetic mean of 377.8, 736.3, 2867 and 841 mg kg⁻¹, respectively. The choice of background reference value is important. If samples of some areas were special and the standard background reference value was inappropriate, we suggest that the residue value of the area be chosen as the background reference value.

The calculated I_{geo} of the analyzed heavy metals were in the order Zn > Pb > Cu > Cr. The high I_{geo} values for Zn, Pb, Cu and Cr in dust fall indicate that there was considerable Zn, Pb, Cu and Cr pollution, which mainly originated from traffic and industrial activities. With the increasing control of point-source pollution (e.g., industry), non-point source contaminants have become an international concern. However, the non-point pollution is difficult to characterize and monitor. More attention should be paid by both governments and scientists to the reckless and unconscious pollution of the environment in dust fall.

ACKNOWLEDGMENTS

One of the authors (Nannan Zhang) sincerely acknowledge the support and contributions of environmental monitoring station of Jinan for samples collection. Thanks are also due to Dr. Holt for her helpful English corrections.

REFERENCES

- [1] Thorpe, A., Harrison, R.M., 2008. Sources and properties of non-exhaust particulate matter from road traffic: a review. *Sci. Total Environ.* 400, 270-282.
- [2] Norman, M., Johansson, C., 2006. Studies of some measures to reduce road dust emissions from paved roads in Scandinavia. *Atmos. Environ.* 40, 6154-6164.
- [3] Joshi, U.M., Vijayaraghavan, K., Balasubramanian, R., 2009. Elemental composition of urban street dusts and their dissolution characteristics in various aqueous media. *Chemosphere* 77, 526-533.
- [4] Var, F., Nartia, Y., Tanaka, S., 2000. The concentration, trend and seasonal variation of metals in the atmosphere in 16 Japanese cities shown by the results of National Air Surveillance Network (NASN) from 1974 to 1996. *Atmos. Environ.* 34: 2755-2770.
- [5] Gibson, M.G., Farmer, J.G., 1986. Multi-step chemical extraction of heavy metals from urban soils. *Environ. Pollut. B* 11, 117-135.
- [6] Harrison, R.M., Laxen, D.P.H., Wilson, S.J., 1981. Chemical association of lead, cadmium, copper and zinc in street dust and roadside soil. *Environ. Sci. Technol.* 15, 1378-1383.
- [7] Banerjee, A., 2003. Heavy metal levels and solid phase speciation in street dusts of Delhi, India. *Environ. Pollut.* 123, 95-105.
- [8] Imperato, M., Adamo, P., Naimo, D., Arienzio, M., Stanzione, D., Violance, P., 2003. Spatial distribution of heavy metals in urban soils of Naples city (Italy). *Environ. Pollut.* 124, 247-256.
- [9] Salim Akhter, M., Madany, I., 1993. Heavy metals in street and house dust in Bahrain. *Water Air Soil Pollut.* 66, 111-119.
- [10] Omar, N., Abas, M., Rahman, N., Tahir, N., Rushdi, A., Simoneit, B., 2007. Levels and distributions of organic source tracers in air and roadside dust particles of Kuala Lumpur, Malaysia. *Environ. Geol.* 52, 1485-1500.
- [11] Wei, B., Jiang, F., Li, X., Mu, S., 2009. Spatial distribution and contamination assessment of heavy metals in urban road dusts from Urumqi, NW China. *Microchem. J.* 93, 147-152.
- [12] Kim, KW, Myung, JH, Ahn, JS, Chon, HT, 1998. Heavy metal contamination in dusts and stream sediments in the Taejon area, Korea. *Journal of Geochemical Exploration* 64, 409-419.
- [13] Zhang, H, He, P, Shao, L, 2008. Fate of heavy metals during municipal solid

- waste incineration in Shanghai. *Journal of Hazardous Materials* 156, 365-373.
- [14] Christoforidis, A., Stamatis, N., 2009. Heavy metal contamination in street dust and roadside soil along the major national road in Kavala's region, Greece. *Geo-derma* 151, 257-263.
- [15] Tessier, A., Campbell, P.G.C., Bisson, M., 1979. Sequential extraction procedure for the speciation of particulate trace metals. *Anal. Chem.* 51 (7), 844-850.
- [16] Saygi, K.O., Melek, E., Tuzen, M., Soylak, M., 2007. Speciation of selenium (IV) and selenium (VI) in environmental samples by the combination of graphite furnace atomic absorption spectrometric determination and solid phase extraction on Diaion HP-2MG. *Talanta* 71, 1375-1381.
- [17] Wei, B.G., Yang, L.H., 2009. A review of heavy metal contaminations in urban soils, urban road dusts and agricultural soils from China. *Microchem. J.* 94, 99-107.
- [18] Shi, G., Chen, Z., Bi, C., Li, Y., Teng, J., Wang, L., Xu, S., 2010. Comprehensive assessment of toxic metals in urban and suburban street deposited sediments (SDSs) in the biggest metropolitan area of China. *Environ. Pollut.* 158, 694-703.
- [19] Lu, X.W., Wang, L.J., Lei, K., Huang, J., Zhai, Y.X., 2009. Contamination assessment of copper, lead, zinc, manganese and nickel in street dust of Baoji, NW China. *J. Hazard. Mater.* 161, 1058-1062.
- [20] Boonyatumanond, R., Murakami, M., Wattayakorn, G., Togo, A., Takada, H., 2007. Sources of polycyclic aromatic hydrocarbons (PAHs) in street dust in a tropical Asian mega-city, Bangkok, Thailand. *Sci. Total Environ.* 384, 420-432.
- [21] Li, X.P., Feng, L.N., 2010. Spatial distribution of hazardous elements in urban topsoils surrounding Xi'an industrial areas, (NW, China): Controlling factors and contamination assessments. *J. Hazard. Mater.* 174, 662-669.
- [22] Sandroni, V., Smith, C.M.M., Donovan, A., 2003. Microwave digestion of sediment, soils and urban particulate matter for trace metal analysis. *Talanta* 60, 715-723.
- [23] Upadhyay, A.K., Gupta, K.K., Sircar, J.K., Deb, M.K., Mundhara, G.L., 2007. Dominance of lithogenic effect for nickel, cobalt, chromium and mercury as found in freshly deposited sediments of the river Subernarekha, India. *Environ. Geol.* 51, 1447-1453.
- [24] Upadhyay, A.K., Gupta, K.K., Sircar, J.K., Deb, M.K., Mundhara, G.L., 2006. Heavy metals in freshly deposited sediments of the river Subernarekha, India: an example of lithogenic and anthropogenic effects. *Environ. Geol.* 50, 397-403.
- [25] Muller, G., 1969. Index of geo-accumulation in sediments of the Rhine River. *Geo-journal* 2, 108-118.
- [26] Loska, K., Wiechula, D., Korus, I., 2004. Metal contamination of farming soils affected by industry. *Environ. Int.* 30, 159-165.
- [27] Muller, G., 1981. Die Schwermetallbelastung der sedimente des Neckars und

- seiner Nebenflusse: eine Bestandsaufnahme. Chem. Ztg. 105, 157-164.
- [28] Al-Khashman, O.A., 2004. Heavy metal distribution in dust, street dust and soils from the work place in Karak Industrial Estate, Jordan. Atmos. Environ. 38 6803-6812.
- [29] Jiries, A., Hussein, H.H., Halaseh, Z., 2001. The quality of water and sediments of street runoff in Amman, Jordan. Hydrol. Processes 15, 815-824.
- [30] De Miguel, E., Llamas, J.F., Chacon, E., Berg, T., Larssen, S., Rqyset, O., Vadset, M., 1997. Origin and patterns of distribution of trace elements in street dust: unleaded petrol and urban lead, Atmos. Environ. 31 (17), 2733-2740.
- [31] Duzgoren-Aydin, N.S., Wong,C.S.C., Aydin, A., Song, Z., You, M., Li, X.D., 2006. Heavy metal contamination and distribution in the urban environment of Guangzhou, SE China. Environ. Geochem. Health 28, 375-391.

Chemical Characteristics of Inhalable Atmospheric Aerosols in Urumqi During Winter

DILNUR Talip^{1,2}, YALKUNJAN Tursun², IGAWA Manabu³, and Abulizi Yimit²

1 Institute of Desert and Meteorology, CMA, Urumqi, Xinjiang China 830002

2 College of Chemistry and Chemical Engineering Xinjiang University, Urumqi, Xinjiang, China 830046

3 Faculty of Engineering, Kanagawa University, Yokohama, Japan 221-8686

Principal Contact: DILNUR Talip, Professor, College of Chemistry and Chemical Engineering Xinjiang University, Shengli road No.14, Urumqi, Xinjiang, 830046, China.

Tel: 13095031158 E-mail: dilnurt2000@yahoo.com.cn

Abstract

PM_{10-2.5} and PM_{2.5} samples were collected from December 2007 to January 2008 at six sampling sites in Urumqi Xinjiang, China. The concentrations of seven kinds of water-soluble ions—SO₄²⁻, NO₃⁻, Cl⁻, NH₄⁺, K⁺, Na⁺, and Ca²⁺—were analyzed using ion chromatography. The concentrations of heavy metal elements, Cr, Co, Cd, Pb, and Hg were measured using inductively coupled plasma mass spectrometry (ICP-MS). The results indicated that, in PM_{2.5} and PM_{10-2.5}, the average mass concentration of seven kinds of water-soluble ions were from 1.00 µg m⁻³ to 59.9 µg m⁻³ and 0.45 µg m⁻³ to 44.7 µg m⁻³, of which SO₄²⁻ was the most abundant water-soluble ion, accounting for 30.2% and 26.5% of the total ion concentration in PM_{2.5} and PM_{10-2.5} respectively. The water-soluble ions are the main components in the ambient particulate matter. The water-soluble elements should also be related with the research of health effects of the particulate matter. High enrichment factor values (EF>50) were obtained for Cd, Pb, and Hg reflecting the importance of anthropogenic inputs. According to the evaluation results of mull indexes, the indexes of Cd, Pb, and Hg were high, which also indicated severe pollution.

Keywords: Air pollution, Inhalable particulate matter, Water-soluble ions, Mull index

Analysis of the Diurnal Variation of Oxalic Acid in Aerosols by Desorption Electrospray Ionization Mass Spectrometry

Xiu Wu, Juntao Huo, Hong Chen and Xin Yang*

Principal Contact: Xin Yang, Professor, Department of Environmental Science & Engineering, Fudan University, 220 Handan Road, Shanghai 200433, China.

E-mail: 09210740012@fudan.edu.cn

Abstract

Dicarboxylic acids are an important group of water-soluble organic compounds (WSOC) in the atmospheric aerosols. They have received much attention because of their important roles in atmospheric chemistry. The most abundant diacid in the aerosol was oxalic acid (C₂) throughout the seasons. DESI-MS (Desorption Electrospray Ionization Mass Spectrometry) was applied for the first time to analysis the diurnal variation of oxalic acid (oxalate) in the ambient aerosols by using self-designed Time Resolved Aerosol Sampler (TRAS). TRAS can sample TSP or PM_{2.5} automatically with adjustable time resolution from 1 - 6 hours depending on the concentration of target compounds. Our 2-hr resolved data showed that the concentration of oxalate has a strong diurnal pattern with higher value during daytime. Peak concentration appeared in the morning from 6:30 am to 8:30 am and the lowest value occurred from 10:30 pm to 0:30 am. This daily variation may be attributed to the daytime photochemical reactions and/or direct emission from fossil fuel combustion. Standard samples of mixed dicarboxylic acids including oxalic acid, malonic acid and succinic acid were analyzed by DESI-MS under the common optimization parameters to confirm the validation of the above measurement. The limit of detection for each of the dicarboxylic acids is about 10 pg mm⁻². Calibrations for all the dicarboxylic acids showed linearity over a concentration range of 5 orders of magnitude with correlation coefficients R²>0.90.

Keywords: Desorption Electrospray Ionization Mass Spectrometry; oxalic acid; diurnal variation; Time Resolved Aerosol Sampler;

Characterization of Optical Properties and Chemical Compositions of Ambient Aerosols in Shanghai

Yong Tang, Hong Chen, and Xin Yang

Department of Environmental Science & Engineering, Fudan University, 220 Handan Road, Shanghai 200433, China

Principal Contact: Yong Tang, Hong Chen and Xin Yang, Department of Environmental Science & Engineering, Fudan University, 220 Handan Road, Shanghai 200433, China.

Tel: 86-21-55665272 Fax: 86-21-65642080 E-mail: 09210740008@fudan.edu.cn(Y.T), chong@fudan.edu.cn (H.C.), yangxin@fudan.edu.cn (X.Y.)

Abstracts

Characters of physical and chemical properties of ambient aerosols at single particle level were studied in Shanghai from 21 to 28 December, 2009. Cavity ring down spectrometer and nephelometer were deployed for measuring aerosol light extinction and scattering respectively. Particle size distributions was conducted by a Scanning Mobility Particle Sizer (SMPS) simultaneously with chemical analysis of each individual particle by Aerosol Time-of-Flight Mass Spectrometry (ATOFMS). The ATOFMS data were analyzed with ART-2a clustering algorithm to indentify the primary particle type/source, such as biomass burning, organic carbon, or soot and examine the extent of mixing with secondary species, such as ammonium, nitrate, and sulfate. For the primary particle cores, biomass burning represented the largest source of submicron particles: 33% by number. Organic carbon particles were the second most abundant type (24% by number) with elemental carbon (soot) particles comprising 14% by number. The elative intensity of elemental carbon had a much better correlation ($R^2=0.7$) with the aerosol light absorption coefficient (at 532nm) than any other particle types. The relative intensity of nitrate ion in all particle types had a better correlation with aerosol light scattering coefficients (532nm) than sulfate and ammonium. In general, biomass burning, organic carbon, and soot particles were frequently internally mixed with ammonium, nitrate, and sulfate. The mixing state switched to less sulfate and more nitrate mixtures when aerosol light extinction coefficients went higher. There was also a good correlation between size distributions of submicron aerosols with their light extinction coefficients. The variance of particle mixing state significantly changes the optical properties which must be taken into account in future models when calculating aerosol direct radioactive forcing.

Keywords: Optical property, chemical composition, ATOFMS

The Impact of the Pollution Control Measures for the 2008 Beijing Olympic Games on the Chemical Composition of Aerosols

Tomoaki Okuda¹, Shinichiro Matsuura¹, Daisuke Yamaguchi¹, Tomoaki Umemura¹, Eriko Hanada¹, Hiroki Orihara¹, Shigeru Tanaka¹, Kebin He², Yongliang Ma¹, Yuan Cheng² and Linlin Liang²

1 Dept. Applied Chemistry, Faculty of Science and Technology, Keio University, 3-14-1 Hiyoshi, Kohoku-ku, Yokohama 223-8522, Japan

2 Dept. Environmental Science and Engineering, Tsinghua University, Beijing 100084, China

ABSTRACT

We investigated the difference in the concentrations of air pollutants between the period of the Beijing 2008 Olympic Games and the same periods in the prior three years (2005-2007, the reference period), in particular, the chemical composition of the particulate matter. PM₁₀, Black carbon (BC), SO₂ and NO₂ were reduced by 33%, 31%, 32% and 51%, respectively, whereas PM_{2.5} was not reduced during the Olympic period when compared to the reference period. Many pollution control measures that had been applied to prevent air pollution from contaminating the air quality in Beijing during the Olympic Games significantly reduced the larger particles (PM₁₀), SO₂ and NO₂ but it did not as effectively reduce the much smaller particles (PM_{2.5}). The sum of the measured water-soluble ions in total suspended particles (TSP) during the Olympic period was reduced by 35% when compared to the reference period. We found a trend in the concentration of high-molecular weight polycyclic aromatic hydrocarbons (HMW-PAHs), which had 5-7 rings decreased during the Olympic period. We considered that the reduction of HMW-PAHs that could be associated with the reduction of BC was due to the reduction of traffic flow resulting from traffic control measures implemented during that time period.

KEYWORDS

Aerosol, Beijing, Black carbon, Olympic Games, PM₁₀, PM_{2.5}, Polycyclic aromatic hydrocarbons (PAHs), TSP, Water-soluble ions

Introduction

Strict pollution control measures were enforced during the Olympic (August 8-22, 2008) and Paralympic Games (September 6-17, 2008) by the Chinese government in order to reduce the air pollution^[1-2]. The details of the measures have been presented elsewhere^[2-6], but in brief, the

measures were effective for almost every activity that was a potential pollution source, including vehicle emissions, industry, construction, and so forth. Several field studies have investigated the effect of the pollution control measures for the Olympics on the surrounding environment. Traffic flow was reduced by 22%-43% during the Olympic Games when compared to the non-traffic control periods^[7-8]. Black carbon concentration was reduced by 28%-50% mainly due to the traffic control measures^[9]. Road dust-falls were more drastically reduced by 55%-88% due to the combined effect of the traffic and construction controls, in addition to street sweeping and washing^[10]. Satellite measurement over Beijing and neighboring provinces between July and September 2008 showed 43%, 13%, and 12% reductions of NO₂, SO₂, and CO, respectively, when compared to the prior three years (2005-2007)^[2]. Some researchers have pointed out that meteorological conditions had a great impact on the air quality of Beijing during the Olympic Games and therefore it was very difficult to resolve the complex effects between the changing emissions due to pollution control and meteorological conditions^{[5][11]}. However, no previous study has been published regarding detailed chemical compositions of aerosols before and during the Olympic Games.

This study presents the first results of the long-term measurements of chemical compositions of total suspended particles (TSP) and PM_{2.5} in Beijing before and during the Olympic Games. In particular, we focused on the difference between the Olympic Games period (2008) and the prior three years (2005-2007), so that we could get a much clearer understanding of how great an impact pollution control had on the air quality of Beijing, especially on the chemical composition of the particulate matter.

Experimental Methods

The details of the experimental procedure used in the present study have been described elsewhere^[12-16]. In brief, PM₁₀, SO₂ and NO₂ concentrations were obtained by converting the official Air Pollution Index (API) value that was provided by Beijing Municipal Environmental Protection Bureau^[17]. PM_{2.5} and black carbon (BC) concentrations were measured by a tapered element oscillating microbalance (TEOM) and an aethalometer, respectively, at Tsinghua University (THU). The sampling site was located 20 km in a northwesterly direction from the center of Beijing (Tiananmen Square). TSP and PM_{2.5} were collected on cellulose nitrate filters using a low-volume air sampler at Institute of Geographic Sciences and Natural Resources Research, Chinese Academy of Sciences (CAS), which is located 15 km north of the center of Beijing and also just 1 block away from Beijing National Stadium (bird's nest). The distance between THU and CAS is 5 km. A multinozzle cascade impactor was used as the PM_{2.5} impactor^[18]. TSP and PM_{2.5} samples were collected weekly from October 2004, 168 hours a week, at an air flow rate of 5 L min⁻¹. Approximately 150 samples each of TSP and PM_{2.5} were collected. We also collected blank samples, i.e., samples exposed to the air but no air had passed

through the filter, in order to evaluate the background contamination produced by gravitational deposition of the aerosols. Water-soluble inorganic ions were extracted by mechanical shaking with deionized water and analyzed by ion chromatography equipped with a suppressor system^[12-14]. Polycyclic aromatic hydrocarbons (PAHs) were also analyzed using the modified Soxhlet apparatus, followed by further purification and HPLC-fluorescence detection^[15].

Results and Discussion

During the Olympic period, PM₁₀, SO₂ and NO₂ were reduced by 33%, 32%, and 51%, respectively, when compared to the reference period. BC was also reduced by 31%. These results are well supported by previous studies^{[2][5][9]}. These pollutants have been simply reduced as a result of the pollution control measures. On the other hand, PM_{2.5} was not reduced during the Olympic period. The application of many pollution control measures to prevent the air quality in Beijing from the air pollution during the Olympic Games resulted in significant reductions in the larger particles (PM₁₀), SO₂ and NO₂ however smaller particles (PM_{2.5}) were not significantly reduced by these measures.

Total ions in TSP during the Olympic period were reduced by 35% when compared to the reference period. Each ion was reduced significantly by 43%-79% except for nitrogen-containing species. This reduction is consistent with the reduction in dust-fall due to the pollution control measures such as shutting down all construction sites, reduction in vehicles on the road, and due also to road sweeping and washing^[10]. Many ions in PM_{2.5} showed similar decreasing trends as those in TSP, but again, the trend in nitrogen-containing species concentrations was quite tricky. Generally, nitrate concentration is strongly dependent on temperature and relative humidity due to its high volatility and deliquescency^[19]. However, according to data for the temperature and relative humidity from July to September in 2005-2008^[20], the temperature and relative humidity in 2008 summer was not different from those measured in 2005-2007. Therefore, volatilization or deliquescence would be a minor reason for explaining the nitrate behavior mentioned above.

During the Olympic period, the atmospheric nitrogen cycle seemed to have been very complicated. It is possible that the increase of ozone and/or oxidants around the center of Beijing may have accelerated the oxidation of nitrogen oxides to form nitrate.

^a 2008/7/1-9/20 ^b 2005, 2006, 2007/7/1-9/20
^c Data from BMEPB ^d Measured by Aethalometer

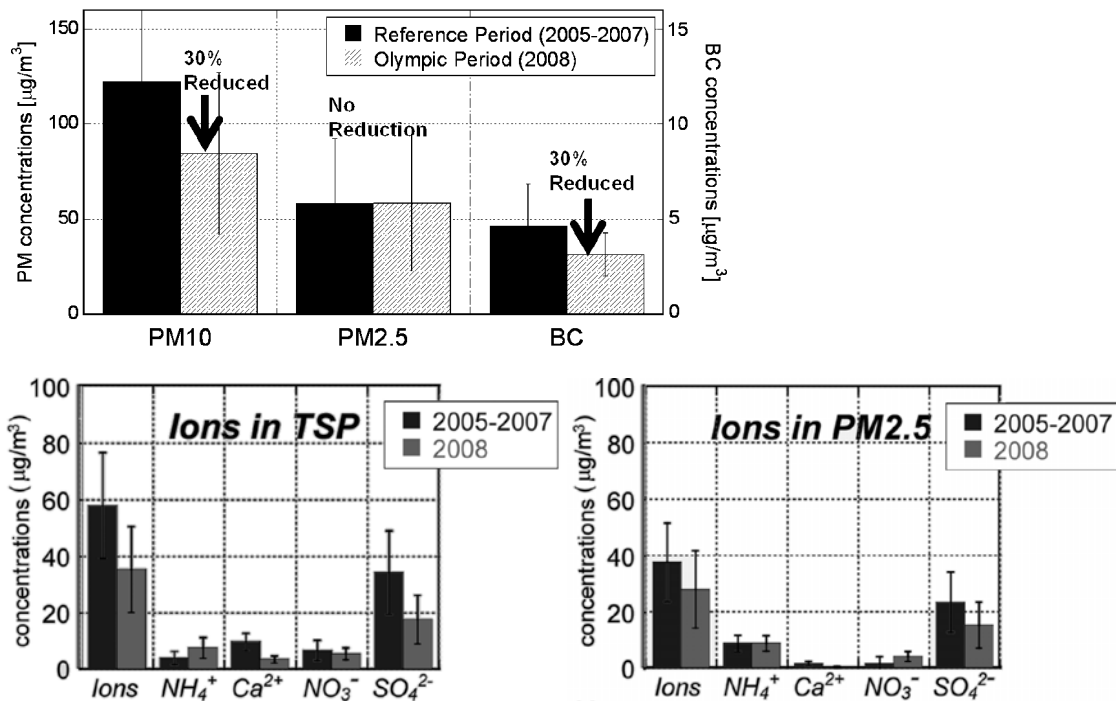


Figure 1. The PM₁₀, PM_{2.5}, SO₂, NO₂, black carbon, and ionic constituent concentrations in TSP and PM2.5 in Beijing, China, during the Olympic period (July 1st to September 20th, 2008) and the reference period (2005-2007)

ΣPAHs, i.e., the sum of the concentrations of all detected PAHs, in the Olympic period was not different from that in the reference period. However, we found a trend in individual PAH concentration that 3 and 4-ring PAHs increased while 5, 6, and 7-ring PAHs decreased during the Olympic period when compared to the reference period. We considered that the reduction of PAHs with relatively high molecular weight (HMW-PAHs, 5-7 rings) was due to the reduction of traffic flow related to the traffic control measures for the following reasons: (1) gasoline powered vehicles are considered a major source of HMW-PAHs in summer in China^{[15][21]}, and (2) BC, which is a unique tracer for vehicle emission and is also strongly associated with PAHs^[22], has been reduced as well as PAHs also have been reduced. We considered that HMW-PAHs were reduced due to the reduction in the number of gasoline vehicles, whereas BC was reduced due to the reduction in the number of both gasoline and diesel vehicles, according to a rough estimation as follows. We assumed that (1) gasoline vehicles emit HMW-PAHs 5-times as much as diesel vehicles^[23-24], (2) diesel vehicles emit BC 40-times as much as gasoline vehicles^[25-26], and (3) the ratio of the number of gasoline to diesel vehicles is 95:5 in Beijing, in other words, the number of gasoline vehicles is 19-times higher than that of diesel vehicles^[27]. Consequently, in Beijing city,

gasoline vehicle would be responsible for 99% of the vehicular HMW-PAHs emissions, whereas gasoline and diesel vehicle contributed one third and two third of the vehicular BC emissions.

Table 1. PAH concentrations in TSP in Beijing, China, during the Olympic period (July 1st to September 20th, 2008) and the reference period (2005-2007)

PAHs in TSP (ng/m ³)	Ring number	(R) Reference Period (2005-2007)		(O) Olympic Period (2008)		%Difference (O)-(R) (R)
		Mean ± SD	n	Mean ± SD	n	
Total (Σ PAHs)		39.3 ± 9.6	27	40.1 ± 7.3	10	2
Σ 3-ring PAHs	3	6.8 ± 3.1	27	10.4 ± 2.59	10	52
Σ 4-ring PAHs	4	14.9 ± 5.0	27	17.9 ± 4.26	10	20
Σ 5-ring PAHs	5	10.0 ± 3.0	27	7.15 ± 2.34	10	-29
Σ 6-ring PAHs	6	6.8 ± 2.0	27	4.31 ± 1.42	10	-36
Σ 7-ring PAHs	7	0.72 ± 0.45	27	0.36 ± 0.15	10	-50

SUMMARY

We investigated the difference in the concentrations of air pollutants between the period of the Beijing 2008 Olympic Games and the same periods in the prior three years (2005-2007, the reference period), in particular, the chemical composition of the particulate matter. PM₁₀ and Black carbon (BC) were reduced by 33% and 31%, respectively. PM_{2.5} was not reduced during the Olympic period when compared to reference period. Each water-soluble ion was reduced significantly by 43%-79% except for N-species. The reduction of HMW-PAHs was due to the traffic control measures during the Olympic. Detailed discussion about this study can be seen in our publication^[16].

ACKNOWLEDGMENTS

This research was supported partly by funds from the Grant-in-Aid for Scientific Research (18710014, 19404002, 22710016, 23120707) of Ministry of Education, Culture, Sports, Science and Technology (MEXT), Japan, the Environment Research and Technology Development Fund (B-0904) of Ministry of the Environment, Japan, Steel Industry Foundation for the Advancement of Environmental Protection Technology, and Mizuho Foundation for the Promotion of Sciences.

REFERENCES

- [1] Wang, S., Zhao, M., Yewu, J., Yulei, Y., He, K., Fu., L., Hao, J., 2010. Quantifying the air pollutants emission reduction during the 2008 Olympic Games in Beijing. Environmental Science & Technology 44, 2490-2496.

- [2] Witte, J.C., Schoeberl, M.R., Douglass, A.R., Gleason, J.F., Krotkov, N.A., Gille, J.C., Pickering, K.E., Livesey, N., 2009. Satellite observations of changes in air quality during the 2008 Beijing Olympics and Paralympics. *Geophysical Research Letters* 36, L17803, doi:10.1029/2009GL039236.
- [3] Beijing Municipal People's Government, 2008. Public Notice April 4th, 2008 and June 6, 2008.
- [4] United Nations Environmental Programme (UNEP), 2009. Independent Environmental Assessment: Beijing 2008 Olympic Games. UNEP division of Communication and Public Information, Nairobi, Kenya.
- [5] Wang, W., Primbs, T., Tao, S., Simonich, S. L. M., 2009. Atmospheric particulate matter pollution during the 2008 Beijing Olympics, *Environmental Science & Technology* 43, 5314–5320.
- [6] Wang, Y., Hao, J., McElroy, M.B., Munger, J.W., Ma, H., Chen, D., Nielsen, C.P., 2010. Ozone air quality during the 2008 Beijing Olympics: effectiveness of emission restrictions. *Atmospheric Chemistry & Physics* 9, 5237–5251.
- [7] Wang, T., Xie, S., 2009. Assessment of traffic-related air pollution in the urban streets before and during the 2008 Beijing Olympic Games traffic control period. *Atmospheric Environment* 43, 5682–5690.
- [8] Zhou, Y., Wu, Y., Yang, L., Fu, L., He, K., Wang, S., Hao, J., Chen, J., Li, C., 2010. The impact of transportation control measures on emission reductions during the 2008 Olympic Games in Beijing, China. *Atmospheric Environment* 44, 285-293.
- [9] Wang, X., Westerdahl, D., Chen, L.C., Wu, Y., Hao, J., Pan, X., Guo, X., Zhang, K.M., 2009. Evaluating the air quality impacts of the 2008 Beijing Olympic Games: On-road emission factors and black carbon profiles. *Atmospheric Environment* 43, 4535-4543.
- [10] Fan, S.-B., Tian, G., Li, G., Huang, Y.-H., Qin, J.-P., Cheng, S.-Y., 2009. Road fugitive dust emission characteristics in Beijing during Olympics Game 2008 in Beijing, China. *Atmospheric Environment* 43, 6003-6010.
- [11] Wang, T., Nie, W., Gao, J., Xue, L.K., Gao, X.M., Wang, X.F., Qiu, J., Poon, C.N., Meinardi, S., Blake, D., Wang, S.L., Ding, A.J., Chai, F.H., Zhang, Q.Z., Wang, W.X., 2010. Air quality during the 2008 Beijing Olympics: secondary pollutants and regional impact. *Atmospheric Chemistry & Physics* 10, 7603-7615.
- [12] Okuda, T., Kato, J., Mori, J., Tenmoku, M., Suda, Y., Tanaka, S., He, K., Ma, Y., Yang, F., Yu, X., Duan, F., Lei, Y., 2004a. Daily concentrations of trace metals in aerosols in Beijing, China, determined by using inductively coupled plasma mass spectrometry equipped with laser ablation analysis, and source identification of aerosols. *Science of the Total Environment* 330, 145-158.
- [13] Okuda, T., Tenmoku, M., Kato, J., Mori, J., Sato, T., Yokochi, R., Tanaka, S., 2006. Long-

- term observation of trace metal concentration in aerosols at a remote island, Rishiri, Japan by using inductively coupled plasma mass spectrometry equipped with laser ablation. Water, Air and Soil Pollution 174, 3-17.
- [14] Okuda, T., Katsuno, M., Naoi, D., Nakao, S., Tanaka, S., He, K., Ma, Y., Lei, Y., Jia, Y., 2008. Trends in hazardous trace metal concentrations in aerosols collected in Beijing, China from 2001 to 2006. Chemosphere 72, 917-924.
- [15] Okuda, T., Okamoto, K., Tanaka, S., Shen, Z.X., Han, Y.M., Huo, Z.Q., 2010. Measurement and source identification of polycyclic aromatic hydrocarbons (PAHs) in the aerosol in Xi'an, China, by using automated column chromatography and applying positive matrix factorization (PMF). Science of the Total Environment 408, 1909-1914.
- [16] Okuda, T., Matsuura, S., Yamaguchi, D., Umemura, T., Hanada, E., Orihara, H., Tanaka, S., He, K., Ma, Y., Cheng, Y., Liang, L., 2011. The impact of the pollution control measures for the 2008 Beijing Olympic Games on the chemical composition of aerosols. Atmospheric Environment, 45, 2789-2794.
- [17] Beijing Municipal Environmental Protection Bureau (BJEPPB), 2010.
<http://www.bjepb.gov.cn/>
- [18] Okuda, T., Katsuno, M., Tanaka, S., Kondo, Y., Takegawa, N., Komazaki, Y., 2007. Measurement and source identification of trace metals in PM_{2.5} and PM₁ collected by multi-nozzle cascade impactor in Tokyo metropolitan area, Japan. Earozoru Kenkyu (Journal of Aerosol Research, Japan), 21, 287-296 (in Japanese with English abstract).
- [19] Morino, Y., Kondo, Y., Takegawa, N., Miyazaki, Y., Kita, K., Komazaki, Y., Fukuda, M., Miyakawa, T., Moteki, N., Worsnop, D.R., 2006. Partitioning of HNO₃ and particulate nitrate over Tokyo: Effect of vertical mixing. Journal of Geophysical Research 111, D15215, doi:10.1029/2005JD006887.
- [20] National Bureau of Statistics of China, 2006-2009. China Statistical Yearbook 2005-2008. China Statistics Press, Beijing, China.
- [21] Zhou, J.B., Wang, T.G., Huang, Y.B., Mao, T., Zhong, N.N., 2006. Size distribution of polycyclic aromatic hydrocarbons in urban and suburban sites of Beijing, China. Chemosphere 61, 792-799.
- [22] Park, S.S., Kim, Y.J., Kang, C.H., 2007. Polycyclic aromatic hydrocarbons in bulk PM_{2.5} and size-segregated aerosol particle samples measured in an urban environment. Environmental Monitoring & Assessment 128, 231–240.
- [23] Ho, K.F., Ho, S.S.H., Lee, S.C., Cheng, Y., Chow, J.C., Watson, J.G., Louie, P.K.K., Tian, L., 2009. Emissions of gas- and particle-phase polycyclic aromatic hydrocarbons (PAHs) in the Shing Mun Tunnel, Hong Kong. Atmospheric Environment 43, 6343-6351.
- [24] Riddle, S.G., Jakober, C.A., Robert, M.A., Cahill, T.M., Charles, M.J., Kleeman, M.J., 2007. Large PAHs detected in fine particulate matter emitted from light-duty gasoline vehicles.

- Atmospheric Environment 41, 8658-8668.
- [25] Ban-Weiss, G.A., McLaughlin, J.P., Harley, R.A., Lunden, M.M., Kirchstetter, T.W., Kean, A.J., Strawa, A.W., Stevenson, E.D., Kendall, G.R., 2008. Long-term changes in emissions of nitrogen oxides and particulate matter from on-road gasoline and diesel vehicles. Atmospheric Environment 42, 220-232.
- [26] Cheng, Y., Lee, S.C., Ho, K.F., Chow, J.C., Watson, J.G., Louie, P.K.K., Cao, J.J., Hai, X., 2010. Chemically-speciated on-road PM_{2.5} motor vehicle emission factors in Hong Kong. Science of the Total Environment 408, 1621-1627.
- [27] Wu, Y., Wang, R., Zhou, Y., Lin, B., Fu, L., He, K., Hao, J., 2011. On-road vehicle emission control in Beijing: past, present, and future. Environmental Science & Technology 45, 147-153.

The Measurement of the Size Distribution of Cigarette Mainstream Smoke by ELPI

Yong Jin, Shitai Wang, Jinyun Liu, Ke Li, Hongmei Fan, Haifeng Tan, Xinliang Tan and Xiaochun Qian

China Tobacco Hunan Industrial Co.,Ltd., Technonlgy Center NO.426 Laodong Road, Changsha, Hunan, 410007, P.R. China

ABSTRACT

Cigarette smoke is a type of aerosol, there are the links between deposition in the respiratory tract of smokers and the physical properties of the aerosol, most notably the particle size distribution of the smoke aerosol. In order to study the number size distribution of fresh mainstream smoke, the modified smoke machine was connected with Electrical Low Pressure Impactor (ELPI). The different impactor collection substrates material (polycarbonate , Al foil, sintered plate) and the dilution system were selected for measurement of the number size distribution of mainstream according to standard smoke condition. The results showed that the impactor collection substrates in ELPI had effect on the measurement of the number size distribution of mainstream. The count mean diameter of particle for the three different impactor collection substrates was: PC<Al foil< sintered plate. The main effect of the impactor collection substrates on the size distribution of mainstream was in the 0.01-0.1 μ m. The impactor collection plate with grease reduced the loss of 0.01-0.1 μ m particles. The surface property of sintered plate could reduce the loss of particle bounce and diffusion on the surface of impactor collection substrate. The dilution method and dilution ratio also has effect on the number size distribution of mainstream. The increase of dilution ration led to the decrease of count mean diameter. Profile of size distribution was changed by the dilution ration.

KEYWORDS : aerosol, ELPI, dilution, number size distribution

Introduction

Smoke produced by a burning cigarette is one of the most common aerosols. To develop research protocols for investigation of the potential health effects of exposure to mainstream cigarette smoke, early studies were focused on selecting a standard smoking procedure and

characterizing the physical properties of cigarette smoke aerosol from different types of cigarettes and smoking devices^[1-4]. Cigarette smoke, however, is difficult to study because it has a high particle concentration (up to 10^9 /cm³), and contains highly volatile materials, which are susceptible to the influence of dilution air^[5-6]. Different sizing methods measure different size-related properties of the particles using various types cigarettes, puffing machines and sampling devices, no one has measured and compared size distributions under the same operating conditions and sampling techniques, because the condition of measurement was different. The objectives of this study were: 1) to evaluate effect of instrument and dilution condition on the measurement of aerosol from the smoking machine; 2) to estimate aerodynamic size distributions of cigarette smoke aerosols; 3) to determine the size distribution.

Experimental Methods

The particle size distribution of mainstream smoke was measured with an ELPI, the ELPI is a cascade impactor and provides a real time measurement of the particle size distribution by measuring the current produced by the charged particles depositing the impactor stages.

Due to the limitations of ELPI detection, the dilution system containing ejector diluter and axial diluter was needed for sampling.

The packs of cigarettes were opened, and the cigarettes were conditioned at $55\pm5\%$ relative humidity and $22\pm2^\circ\text{C}$ for 48 hours prior to use. A standard puff (2-s, one puff per minute), was controlled by programmable smoke machine, and the volume of each puff was maintained at 35 cm^3 .

A schematic drawing of the aerosols sampling system is shown in Figure 1. Smoke machine was used to generate the smoke. A smoking machine (celorean SM450) with fully programmable control of the puff profile, puff duration, puff volume and puff interval.

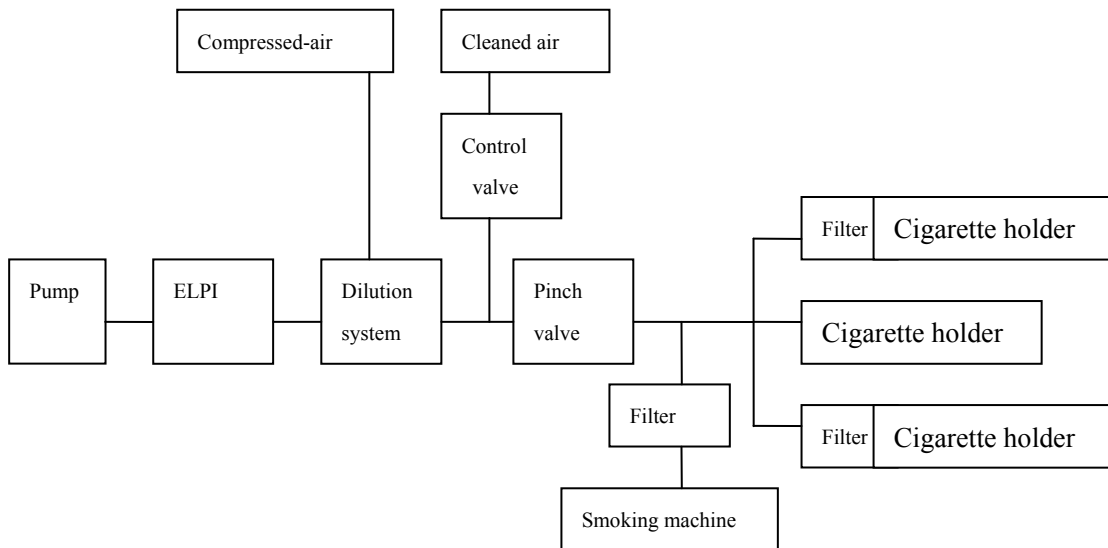


Figure 1 a schematic diagram of the smoking and dilution system for the ELPI measurements

Results and Discussion

1 Effect of impactor collected substrate material on size distribution of cigarette smoke aerosol

The different collection substrates (polycarbonate (PC), Al-foil, sintered plate) were used in the measurements of the size distribution under the same dilution condition. Figure 2 shows the relationship between the impactor collected substrates and the number size distribution of smoke aerosol.

From the figure 2, the measured number size distribution of the three impactor collection substrate materials are different. The size distribution of smoke particles is mainly affected in the range of 10-100nm. The results show in the size range of 0.1-1um the highest value of concentration peak is: sintered plate > Al-foil > PC. However the order in the size of range of 0.01-0.1um is reverse.

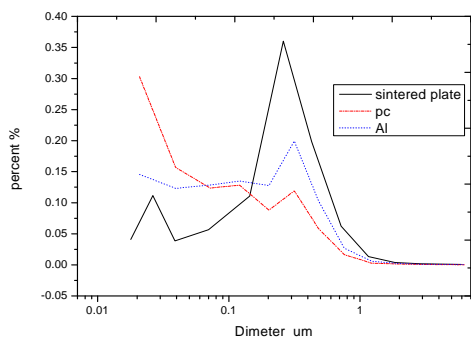


Figure 2 the relationship between the impactor collected substrate material and the number size distribution

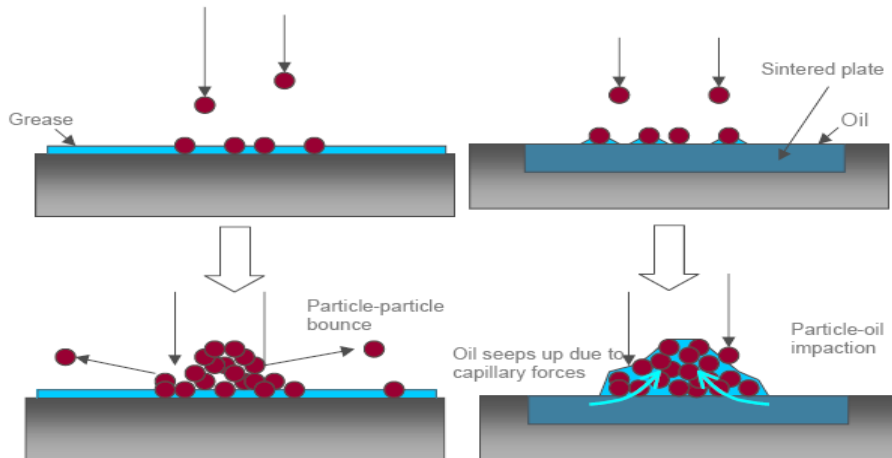


Figure 3 the schematic diagram of the impaction of particle^[7-10]

For ELPI, the size distribution was affected by the particles bouncing at the impactor collection surface. If particles impact and do not bounce from the collection surface, the charge transfer is annulled because the total charge number is preserved. From the figure 3, the impaction of particles may cause a charge transfer from the impactor surface to the particle with a unwanted result in the case of the particle bouncing to the lower stage^[7-9]. There was a strong signal when PC and Al-foil substrate was used, because of charge transfer. The use of an oil soaked sintered metal plate substrate reduces signal intensity on the lowest stage, the charge transfer was significantly reduced. For PC collection material, the signal of the lower stage is the strongest one. The size distribution results measured are related to the properties of the impactor collection plate surface.

2 Effect of dilution condition and treatment of impactor collected plate on size distribution of cigarette smoke aerosol

The different treatments of collected substrates (PC, Al-foil, sintered plate) were used in the measurement of the size distribution under the different dilution conditions.

Table1 the effect of three collected plate on the size distribution of cigarette smoke (μm)

Dilution ratio	PC collected	Al-foil collected plate	Sintered plate collected plate
799	0.168	0.252	0.307
2230	0.155	0.211	0.285
18494	0.127	0.200	0.089

As showed in table 1, there is different diameter of aerosol size for different dilution ratio. The dilution ratio is main effect for the measurement of average diameter.

The percent of particles versus particle size is illustrated by the bottom (dotted) line in figure 4. With the dilution ratio increase, the value of the peak in the range 100-300nm shows the significant reduction, but the value of the peak in the range 10-100nm show the significant increase.

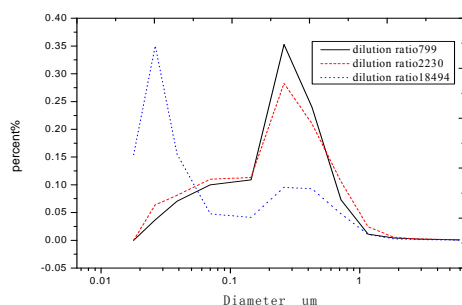


Figure 4 the size distribution under different dilution with sintered plate collected plate (without oil)

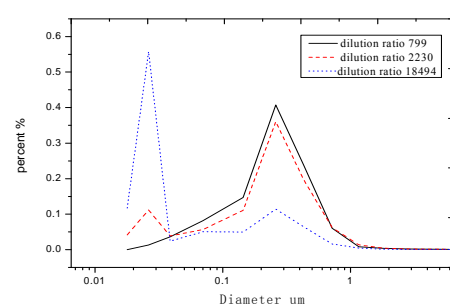


Figure5 the size distribution under different dilution with sintered plate collected plate (with oil)

From figure4 and 5, there was discrepancy in measurement results of collected impactor suface between with oil and without oil. With dilution ratio of 2230, there is peak in the range of 20-30nm because of impactor collection plate with oil.

3 Effect of dilution gas on the size distribution

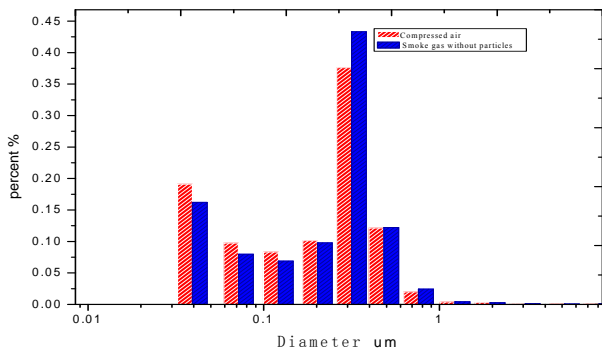


Figure 6 the effect of dilution gas on the size distribution under the same dilution ratio

As showed in figure 6, there is the different size distribution because of the type of dilution gas. The average diameter of aerosol diluted by smoke gas without particles are the bigger than by compressed air. These were caused by the volatilizable vapor components in dilution smoke gas. The vapor components inhibit the decreasing of particles diameter. The dilution ratio is important for the measurement of size distribution of smoke aerosol.

4 The size distribution of smoke aerosol

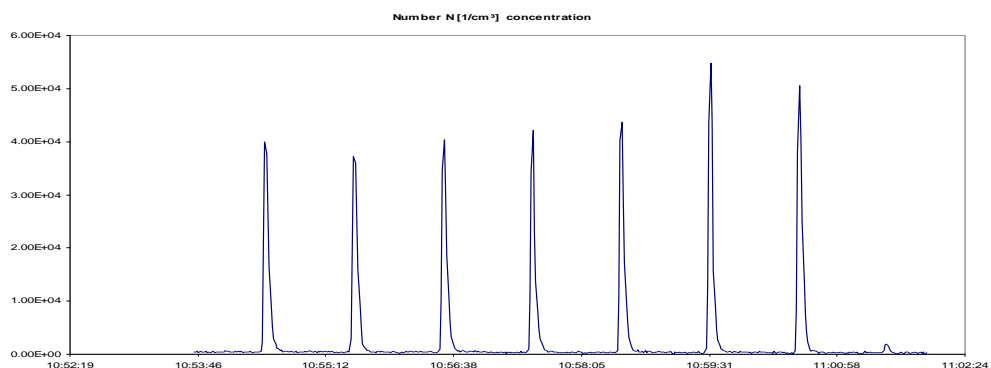


Figure 7 the time –dependent total particle measured over the seven puffs on a cigarette (dilution ratio 2230, puff volume 35ml, puff interval 58s, sinusoidal puff)

The ELPI runs continuously during the combustion of cigarette. The dilution system and ELPI response provided puff-by puff particle size number distribution. The figure showed the time –dependent total particle measured over the seven puffs on a cigarette. It is obviously that the particle concentration returns to baseline within 10s. These sharp peaks represent the time of the puffs (2s) of cigarette. In general,

fresh cigarette smoke has been found to have a count median diameter in the range of 0.18-0.34um. In our test, the count median diameter was in the range of 0.18-0.34um.

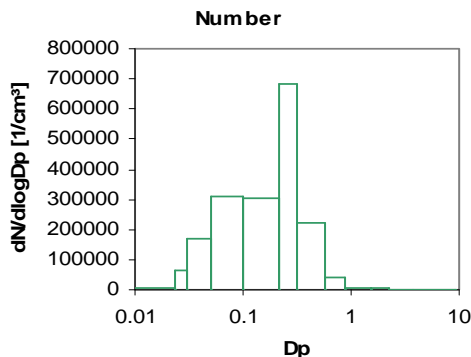


Figure 8 the size distribution of cigarette smoke for 2s

5 Limitation of this study

There are several limitations to this study .there are the losses of particles during dilution and the aerosol flowing. It is possible that these losses may affect the particle size distribution results. With <10% of the total particle matter lost within the dilution system and transfer line, the size distribution results were little affected.

Evaporation and coagulation occurring during the sampling and measurement of smoke will affect the measured results. The rapid dilution of fresh smoke was demanded to minimize the error of the size distribution.

Despite the limitations of the experiments instruments and measurement method, it is reasonable to draw some conclusion from the data. To improve upon the measurement, the exploitation of better method will be need.

CONCLUSION

The impactor collected substrate material in ELPI had effect on the measurement of the number size distribution of mainstream. The count mean diameter of particle for the three different impactor collected substrate material was: PC<Al foil< sintered plate.

The main effect of the impactor collected substrate material on the size distribution of mainstream was in the 0.01-0.1μm. The impactor collected plate with grease reduced the loss of 0.01-0.1μm particles. The surface property of sintered plate could reduce the loss of particle bounce and diffusion on the surface of impactor substrate. The dilution method and dilution ratio also have effect on the number size distribution

of mainstream.

ACKNOWLEDGMENTS

We would like to acknowledge support from DEKATI and RENPRO for their help and assistance in experimental phase of this study. Special thanks to Dr. LIU Cheng from BAT and Dr. David.B.Kane from ALTRIA for the help on the measurement of aerosol.

REFERENCES

- [1] Shen,Guanglin,Kong Haohui,Li Feng. CORESTA,Shanghai: 2008,103.
- [2] Chung I.P. and D.Dun-Rankin. Aerosol Sci Technol.,1996 ,24:85-101.
- [3] Ingebrethsen, B.J. and Lyman C.S. Aerosol Science and Technology, 2002,36: 267-276.
- [4] Shimada, Manabu , Okuyama, Kikuo, Okazaki. Aerosol Science and Technology, 1996,25: 242 – 255.
- [5] Shen,Guanglin, Kong Haohui, Li Feng. Acta Tabacaria Sinica,, 2009, 15:14-19.
- [6] David B. Kane, Bahman Asgharian, Owen T. Price, Ali Rostami1, and Michael J. Oldham.Inhalation Toxicology, 2010,22:199-209.
- [7] Hu Wangyun,Cai Rong,Ren Wei. Smoking aerosols and filtration of cigarette filter. Kunming: Yunnan sci.& tech. press,2000:20-100.
- [8] Mikko Moisio, Ph. D. Thesis. Tampere University of Technology,1999.
- [9] Moisio, M., Hautanen, J.,Marjamäki,M., Keskinen, J., Valmari, T. and Kauppinen E. (1995a) EPRI/DOE International Conference on Managing Hazardous and Particulate Air Pollutants, book 2: Toronto, August 15-17, 1995.
- [10] DEKATI homepage. See <http://www.deksti.com/cms/>

From the Risk/Benefit Aspect to Determine the Optimal Operation Condition for Simultaneously Controlling the Emissions of PCDD/Fs and PAHs from the Iron Ore Sintering Process

Perng-Jy Tsai¹, Yu-Cheng Chen¹, Jin-Luh Mou², Yu-Chieh Kuo¹ and Shih-Min Wang¹

¹Department of Environmental and Occupational Health, Medical College, National Cheng Kung University, 138, Sheng-Li Road, Tainan 70428, Taiwan

²Department of Occupational Safety and Health, Chung Hwa University of Medical Technology, 89 Wenhwa 1st St., Rende Shiang, Tainan 71703, Taiwan

ABSTRACT

In this study, the risk-benefit analysis technique was developed and incorporated into the Taguchi experimental design to determine the optimal operation combination for the purpose of reducing both emissions of PCDD/Fs and PAHs, and increasing both the sinter productivity (SP) and sinter strength (SS) simultaneously. Four operating parameters, including the water content, suction pressure, bed height, and type of hearth layer, were selected and conducted on a pilot-scale sinter pot to simulate various sintering operating conditions of a real-scale sinter plant. The resultant optimal combination could reduce the total carcinogenic potency arising from both emissions of PCDD/Fs and PAHs (i.e., the risk) by 49.8%, and increase the sinter benefit associated with the increase in both SP and SS (i.e., the benefit) by 10.1%, as in comparison with the operation condition currently used in the real plant. The ANOVA results indicate that the suction pressure was the most dominant parameter in determining the optimal operation combination. The above result was theoretically plausible since the higher suction pressure provided more oxygen contents leading to the decrease in both PCDD/F and PAH emissions. The proposed technique can also be used in other manufacturing processes for determining the optimal operation condition for the process emission control purpose.

KEYWORDS

Iron ore sintering, PCDD/Fs, PAHs, Risk-benefit analysis, Emission control

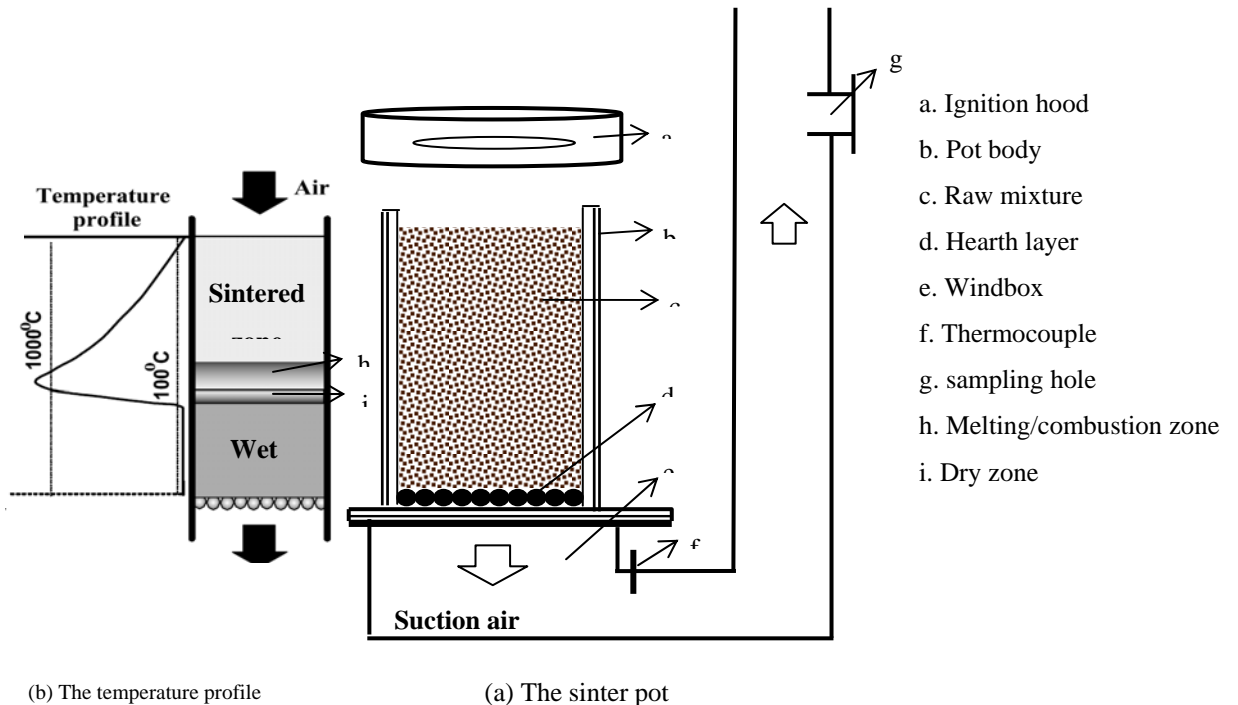


Figure 1 The schematic of the pilot-scale sinter pot and the temperature profile its zone combustion process

Table 1 The magnitudes of the RBR, risk (including EF_{PCDD/F_s} and EF_{BaPeq}) and benefit (including SP and SS), and their resultant decrease(-)/increase(+) rate by conducting confirmation tests in the sinter pot under the conditions of the reference and optimal operation combination, respectively

Testing results	Confirmation		Decrease(-)/ increase(+) rate
	reference operation combination	optimal operation combination	
RBR	2.96×10^{-2}	9.30×10^{-3}	- 68.6%
Risk	8.18×10^{-1}	4.11×10^{-1}	- 49.8%
EF _{PCDD/F_s} (ng I-TEQ/kg-feedstock)	1.18	0.523	- 55.8%
EF _{BaPeq} ($\mu\text{g}/\text{kg}$ -feedstock)	23.2	9.58	- 58.6%
Benefit	16.3	18.0	+ 10.1%
SP (t/m ² /day)	25.9	28.6	+ 10.2%
SS (%)	62.8	63.7	+ 1.50%

Single-particle characterization of wintertime atmospheric particles collected at Taiyuan city, China on haze and non-haze days

Hong Geng^{1*}, Shila Maskey² and Chul-Un Ro²

1 Research Center of Environmental Science and Engineering, Shanxi University, Taiyuan, 030006, China

2 Department of Chemistry, Inha University, YonghyunDong, NamGu, 402-751, Incheon, Korea

Principal Contact: Hong Geng, associated professor, Research Center of Environmental Science and Engineering, Shanxi University, Taiyuan, 030006, China.

Phone /Fax: +86 0351 7011011 E-mail: genghong2004@126.com

Abstract

A quantitative energy-dispersive electron probe X-ray microanalysis (ED-EPMA), namely low-Z particle EPMA, was used to characterize the chemical compositions of individual aerosol particles collected at Taiyuan city (a typical coal-burning city), Shanxi Province, China on haze and non-haze days. Two sets of haze aerosol samples (8 and 9 January, 2010) and two sets of non-haze aerosol samples (29 and 30 December, 2009) were obtained by a seven-stage May cascade impactor with cut-off diameters of 16, 8, 4, 2, 1, 0.5, and 0.25 μm for stages 1-7, respectively. The morphologies, mixing state, and chemical compositions of overall 1200 particles on stages 3, 4, and 5 were examined using a JEOL JSM-6390 SEM equipped with an Oxford Link SATW ultra-thin window EDX detector, and classified based on their secondary electron images and X-ray spectra. In general, on non-haze days mineral dust particles (including alminosilicate, SiO_2 , $\text{CaCO}_3/\text{CaMg}(\text{CO}_3)_2$, and TiO_x) were the most frequently encountered, followed by elemental carbon (EC), organic carbon (OC), and Fe-rich particles while on haze days OC particles on stage 6 were significantly increased in relative abundance and many reacted $\text{CaCO}_3/\text{CaMg}(\text{CO}_3)_2$ and alminosilicate particles with airborne $\text{SO}_2/\text{H}_2\text{SO}_4$ were encountered. It indicated that the haze episode can elevate OC and sulfate-containing particles in number.

Keywords: Single-particle characterization, haze, Taiyuan, ED-EPMA

Comparison of source contributions to urban ultrafine particles and other pollutants

Yungang Wang¹, Philip K. Hopke¹, David C. Chalupa², Mark J. Utell²

1 Center for Air Resource Engineering and Science, Clarkson University, Potsdam, NY 13699-5708, USA

2 Department of Environmental Medicine, University of Rochester Medical Center, Rochester, NY 14642, USA

Principal Contact: Yungang Wang, PhD, Center for Air Resources Engineering & Science, Clarkson University, 8 Clarkson Avenue, Box 5708, Potsdam, NY 13699-5708, USA.

Phone: 1-315-268-4489 Fax: 1-315-268-4410 Email: yuwang@clarkson.edu

Abstract

In this study, sources contributing to the ultrafine particles (10-500 nm) and other pollutants ($\text{PM}_{2.5}$, CO, black carbon (BC), Delta-C ($\text{UVBC}_{370\text{nm}} - \text{BC}_{880\text{nm}}$), SO_2 , O_3) measured during 2005-2010 at the New York State Department of Environmental Conservation (NYSDEC) site in Rochester, New York are identified and apportioned using a bilinear receptor model, positive matrix factorization (PMF2). Each calendar year is divided into three seasons, i.e. winter (December, January and February), summer (June, July and August) and the transitional periods (March, April, May, September, October and November) so as to avoid experimental uncertainty resulting from too large season-to-season variability in ambient temperature and solar photon intensity that would lead to unstable particle size distributions. Ten sources were previously identified at the monitoring site including traffic, nucleation, residential/commercial heating, industrial emissions, secondary nitrate, ozone-rich secondary aerosol, secondary sulfate, regionally transported aerosol, and a mixed source of nucleation and traffic. The highway diesel fuel sulfur program (U.S. EPA 2007 Heavy-Duty Highway Rule) resulted in the national transition in 2006 of on-road diesel fuel from low-sulfur diesel (LSD, 500 ppm) to ultra-low-sulfur diesel (ULSD, 15 ppm). In addition, a large coal-fired power plant with a capacity of 260 MWe was shut down for conversion to natural gas in May 2008. The other major SO_2 emitter, the Eastman Kodak complex, is located 6 km northwest of the site. Its production and SO_2 emissions substantially decreased in recent years because of the decline in film use. The impacts of the source changes on the ambient ultrafine particle number concentrations and other pollutants will be quantified using PMF results.

Keywords: Ultrafine particles, Urban, Coal-fires power plant, Diesel, Source apportionment, Positive matrix factorization

Characterization of Particles from Residential Coal Combustion

Kun Wang¹, Junhua Li¹, Jiming Hao¹, Chunmei Geng² and Hongjie Liu²

1 School of Environment, Tsinghua University, Beijing 100084, P.R. China

2 Chinese Research Academy of Environmental Science, Beijing 100012, P.R. China

ABSTRACT

As one of the most widely used energy source in rural areas in China, residential coal is mainly burned in small stoves under poor combustion conditions and without any emission control. This results in high particulate matter and other air pollutant emissions which may leads to serious air pollution and healthy danger. Combustion smoke emitted from a residential coal-stove burning five different kinds of residential coal was determined using a dilution tunnel system. The particulate matters and the gas-phase products including NO、NO₂、SO₂、O₃ and TCH (total hydrocarbons) were determined simultaneously and the results shows that TCH in the flue gas from the combustion play an important role in the size distribution and concentrations of the emitted particles. Characterization of the particles with size range of 6~523 nm were performed using an engine exhaust particle sizer. The particles are mainly emitted at the beginning stage of the combustion and a bimodal size distribution of the particles can be found for all five kinds of coal. The size distributions for different coals are dissimilar at the beginning stage of combustion and alike for particles emitted at the ending stage. The in situ photo-oxidation of the smokes was performed in a dynamic chamber and the results shows that secondary ultrafine particle formation is dominated by SO₂ and reactive organic compounds. The results suggest that the coal combustion pollutants may serve as an important source of ultrafine particles, especially in rural areas where large amount of residential coal are burned and large amount of reactive plant emissions are released.

KEYWORDS

Particle, Combustion, Residential coal, TCH, Size distribution

Introduction

China has the largest coal production and consumption in the word. It is now estimated that coal contribute 70% of China total energy consumption and this tendency will keep quite a long time in the future due to the limited storage of other alternatives ^[1]. Unfortunately, coal combustion produces a wide variety of air pollutants including carbon monoxide (CO), carbon

dioxide (CO_2), sulfur dioxide (SO_2), nitrogen oxides (NO_x), particulate matter (PM) and a large suite of organic toxics^[2-6]. The environmental and public health concerns over the coal emissions from the coal combustion have motivated the popularization of coal briquette and honeycomb to reduce toxic emissions. However, direct combustion of raw coal in domestic stove for cooking and heating in winter is still very common, especially in northern rural areas^[7]. In the present work, to expand our knowledge of emissions from raw coal combustion, the in situ characterization of the gaseous and particulate pollutants from the combustion of five common raw coals in a domestic stove was performed. The concentrations of CO, NO, NO_2 , SO_2 and TCH emitted from raw coal combustion were monitored continuously during the combustion. The size distribution and concentrations of the emitted fine particles are detected. In situ photo-oxidation simulation of the flue gases was performed in a dynamic chamber under short time UV light illumination conditions to investigate the potential formation of secondary ultrafine particle.

Experimental Methods

The details of the dilution tunnel system used in this work can be found elsewhere^[8]. The dynamic chamber used is actually a Teflon-film bag housed in a light tight box made of wood. The box is equipped with 24 lamp-holders on the interior wall for fixing black light lamps. The black light lamps (Model F40T8BL, Beijing Light Research Institute, China) provide ultraviolet light with an emission wavelength range of 290~430 nm. Five raw coals (marked as YC, DT, DS, JX, and ZJ) which are all produced from state-own coal mines and cover a wide range of quality were selected. Raw coal samples were ignited from the bottom in the stove using pre-weighed charcoal (0.5 kg). To avoid the interference from the charcoal, the raw coal samples (1.0 kg for each sample) were put into the stove until smoking from charcoal combustion stopped. The weights of raw coal samples before and after combustion were recorded to obtain the actual weight of the coal that is consumed.

Sampling periods, which started when the raw coal samples were put into the stove and ended until the combustion finished, lasted for about one hour. All measurements of the gaseous and particulate components were performed at the end of the dynamic smoke chamber. The NO_x concentration was monitored by a Model 42 i- NO_x Analyzer (Thermo Electron Corporation, USA). SO_2 and TCH were monitored by a Model 43 i- SO_2 Analyzer (Thermo Electron Corporation, USA) and a TCH-600A Analyzer (Xin Branch Analytical Instruments Ltd., China) respectively. A Model 3090 EEPSTTM spectrometer (TSI, USA) was used to monitor the particulate component in the chamber continuously.

Results and Discussion

Gaseous emissions

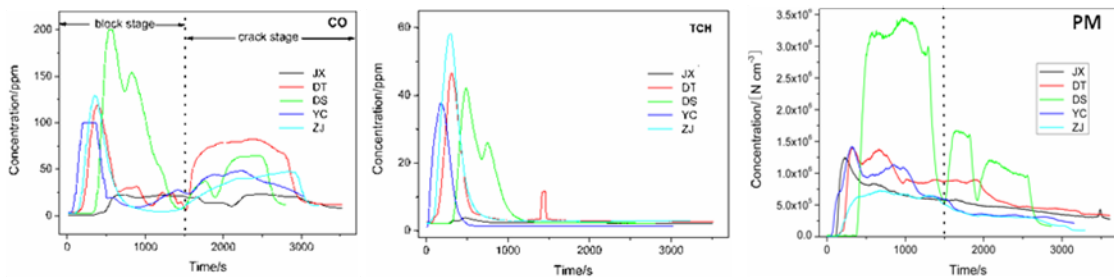
The real time concentration of CO, NO, NO₂, SO₂ and TCH are monitored continuously. The total emissions of NO, NO₂, SO₂ and TCH calculated from the real time data and the actual combustion amount of coal samples are listed in Table 1.

Table 1. Total emission of gaseous products during combustion of raw coals (1.0 kg).

	JX	DT	DS	YC	ZJ
NO/g	8.31×10^{-3}	2.68×10^{-2}	3.16×10^{-2}	1.98×10^{-2}	5.87×10^{-2}
NO ₂ /g	3.49×10^{-2}	2.83×10^{-1}	2.27×10^{-1}	1.57×10^{-1}	4.36×10^{-1}
SO ₂ /g	1.93×10^{-3}	4.0×10^{-2}	7.84×10^{-2}	2.54×10^{-2}	9.02×10^{-1}
TCH/gC	2.13×10^{-1}	5.63×10^{-1}	6.08×10^{-1}	3.64×10^{-1}	6.47×10^{-1}

In our experiments, coal chunks which are 5-8 cm in diameter were burned. The combustion of such large coal chunks in a domestic stove made it very difficult to characterize the three-stage process mentioned by other literatures for pulverized coal samples [9-10]. CO, which is formed by the incomplete combustion, is chose here as an indicator of combustion conditions.

Figure 1 Real-time monitoring of gaseous emissions of CO and TCH and total number concentration of particles for five different raw coal samples.



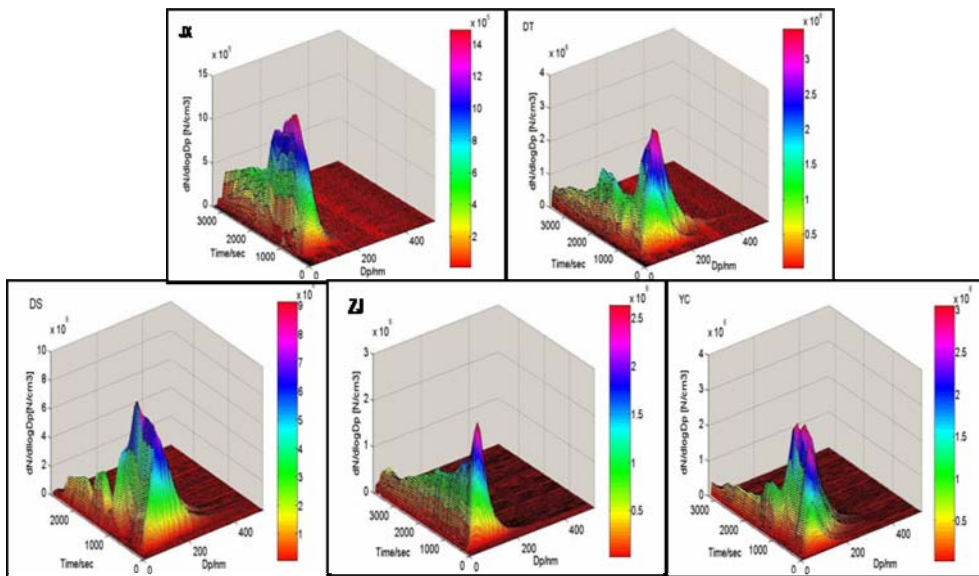
As displayed in Figure 1 that for all the coals the total CO emission process can be divided into two stages here defined as “block stage” and “crack stage” with 1500 s as the cut point. And there are some similarities between the emission curves in the two stages. For example, two peaks can be found at both the “block stage” and “crack stage” for DS sample and the peaks at the “block stage” are always higher than those at the “crack stage” for all coal samples. At the “block stage”, the coal chunks are ignited and burned initially at the surface. During this stage, coal is burned under oxygen shortage conditions. Thus more and more gaseous products including CO are produced until the combustible materials at surface are burned out. Then the emissions begin to decrease rapidly. During “block stage”, the coal chunks are heated and begin to break slowly. At the “crack stage”, where the coal chunk is broken into smaller chunks because of thermal stresses induced by internal fissures and cracks, new gaseous products are emitted from combustion of the combustible in the smaller chunks and these emissions correspond to the peaks at the “crack stage” for CO in Figure 1.

The two stages and the cut point, which are obtained by monitoring the real time concentration of CO, are applicable for NO, NO₂ and SO₂ emissions. However the two stages and the cut point, which are obtained by monitoring the real time concentration of CO, are not applicable for TCH emissions. Unlike CO (and SO₂ and NO_x), TCH are mainly emitted at the beginning stage of the combustion and correspondingly the TCH curves contain a sharp peak at the beginning stage. The reason of such difference is that the emission of TCH depends strongly on temperature and oxygen conditions while CO, SO₂ and NO_x are easy to be formed under a wide range of temperature under our experimental conditions. During the combustion, the stove was heated and the temperature in the stove rose quickly. At the beginning, the volatile compounds in the coal and the volatile products of coal pyrolysis begin to volatilize from the coal. The released TCH are mainly composed of the homologous series of the alkylated benzenes and phenol derivatives as well as alkenes [11]. But when the temperature in the stove reaches the burning point of these organic compounds, these organic compounds are burned to form CO, CO₂, H₂O and other inorganic compounds and TCH are no longer detectable. Thus TCH are mainly emitted at the beginning stage of the combustion and correspondingly the TCH curves contain a sharp peak at the beginning stage.

Particulate emissions

Comparison of the particle concentration profiles and CO emission profiles reveals that peaks in particle concentration profiles correspond well with the peaks in CO emission profiles and the two stages and the cut point are applicable for particle concentration profiles. A comprehensive view of the particle-size distribution for the fine particles ($D_p \leq 500\text{nm}$) during combustion of five coal samples measured with EEPS was shown in Figure 2.

Figure 2. Particle-size distribution for the fine particles from different coals



In this study, particles emitted from raw coal burning are largely in the range of 6-250nm (the EEPS is limited to 6-523 nm). The size distributions for coals are related to the different burning period. And it is found that the particle size distributions for different coals are dissimilar at the beginning stage of combustion and alike for particles emitted at the ending stage. Upon the addition of coal chunks into the stove, particles of 60-150 nm diameters are emitted, and the concentration and size of the emitted particles increase slowly. During this period, particles from different coal samples differs greatly both in concentration and size distribution. After 15-20 mins, the concentration and size of the emitted particles began to decrease rapidly. And it is noted that the particle size distributions during this period are typically bimodal which is also found in other studies^[2, 12]. Among these particles of bimodal size distributions, those particles of 6-30 nm size distributions are thought to be formed directly in the flame while the others appear to result from vaporization-condensation processes^[2]. When attention is focused on the total emissions, the concentrations of the particles with size distribution of 6-30 nm, which dominate the emissions of the ending period, vary very little during the total combustion. Whereas the concentrations of the 120-250 nm diameter particles change greatly during combustion and these particles are mainly emitted at the beginning period.

Significant correlations between the emission of TCH and particles are observed for all samples. As displayed in Figure 1 that the peaks of TCH emissions always correspond to high concentrations of particles, and during the ending period when very little TCH are emitted the concentrations of particles are also very small. This is in good agreement with the results obtained by Tian et al. who reported that the emission factors of gaseous TCH and PM agree very well with each other^[13]. At the beginning, the concentrations of TCH are very high. Correspondingly, the particles increase quickly and the detected particles are always of large size. During the ending period when little TCH was emitted, the increase of the freshly emitted particles becomes very small and fine particles are detected correspondingly.

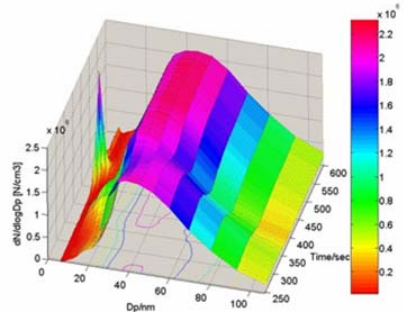
Obviously, the residence time of particles emitted before being detected and the dilution ratios of air to the emissions can significantly affect the total particle number concentration and size distribution and longer residence time will shift the particles to larger size while a greater dilution ratio will increase the concentration of ultrafine particles^[14-15]. Although in our experiment the most detected particle fractions, which are around 120-250 nm, are somewhat different with those reported by Bond et al. of 20-100 nm^[16] and Chen et al. of less than 290 nm^[17], these results are still agrees well with each other if experimental details including combustion conditions, the residence time and dilution ratio in these experiments are considered. As mentioned in the experimental section, the residence time and dilution ratio in the present experiments are about 10s and 60:1, respectively, which are much too small as compared to the actual in domestic living. This means that the actual fine particles emitted from the domestic

combustion of raw coals can penetrate deeper into the alveolar regions of the lung and pose greater threat to human health^[18].

In situ photooxidation of the combustion flue gases

The in situ photooxidation of the flue gases from the residential combustion of different raw coals are performed in the dynamic chamber before the pollutants are detected. For most of the experiments, no evident change in gas-phase and particulate reactant is observed during UV light illumination lasted for 2 minutes. However, the introduction of isoprene into the combustion smoke results in evident new particle formation during the 2 minutes UV light illumination. A typical example of new particle formation under UV light illumination conditions are given in Figure 3. At time 450s, ultrafine particles of 6-10nm diameter were observed. The concentrations of these new particles are comparable to the original particles.

Figure 3. Typical example of new particle formation under UV light illumination



Special experiments were performed to investigate the formation of new particles. During these experiments, 1.0 ppmV of isoprene and/or 0.5 ppmV SO_2 was introduced into the flue gas before UV light illumination. No new particles are detected when the light are turned off. For coals of low sulfur, no change resulting from the introduction of either isoprene or SO_2 was found. But when both isoprene and SO_2 were introduced, substantial new small particles were observed. For ZJ coal which is of high sulfur content, the introduction of isoprene would also result in new particle formation. Obviously, new particle formation was dominated by SO_2 and reactive organic compounds and the TCH from the combustion of coal seems to be of little importance for ultrafine particle formation.

Conclusion

CONCLUSION

We have provided an in situ characterization of the freshly emitted gaseous and particulate pollutants from the residential combustion of raw coals. Under equal dilution ratio conditions, the gas-phase product including CO , NO , NO_2 , SO_2 and TCH detected. The results show that these gaseous pollutants are mainly emitted at the beginning stage of the combustion. For particulate product, the size distribution and concentrations are characterized during total combustion

process. It is found that TCH in the flue gas from the combustion play an important role in the size distribution and concentrations of the emitted particles. And it is estimated that most of the particles emitted from the domestic combustion of raw coals are ultrafine particles and could directly threat human health. UV light illumination of the flue gases suggests that coal combustion pollutants may serve as an important source of secondary ultrafine particles, especially in rural areas where large amount of raw coal are burned and large amount of reactive plant emissions are released.

ACKNOWLEDGMENTS

This project was supported by The Central Level, Non-profit, Scientific Research Institutes' Basic R & D Operations Special Fund (Grant No.2009KYYW01) of Chinese Research Academy of Environmental Science and the National Natural Science Foundation of China (Contract No. 20937004)

REFERENCES

- [1]Lin W. *World Science-Technology R & D* 2000, 22, 50-53
- [2]McElroy M.W.; Carr R.C.; Ensor D.S. et al., *Science* 1982, 215, 13-19.
- [3]Gammage R.B.; Wachter E.A.; Wade J. et al., *Environ. Int.* 1993, 19, 133-145,
- [4]Lan, Q.; Chen W.; Chen H. et al., *Biomed. Environ. Sci.* 1993, 6, 112-118.
- [5]Zhang J.F. and Smith K.R., *Environ. Sci. Technol.* 1999, 33, 2311-2320.
- [6]Su G.; Xu X.; Judith C. et al., *Environ. Sci. Technol.* 2004, 38, 4612-4618
- [7]*China Statistical Yearbook, 2003*, China Statistics Press: Beijing, 2004.
- [8]Zhou N.; Zeng L.M.; Yu X. et al. *Acta Sci. Circumstan.* 2006, 26, 764-772
- [9]Smith S.E.; Neavel R.C.; Hippo E.J. et al., *Fuel* 1981, 60, 458-462
- [10]Milligan J.B.; Thomas K.M. and Crelling J.C. *Fuel* 1997, 76, 1249-1255
- [11]Streibel T.; Geißler R.; Saraji-Bozorgzad M. el al., *J. Therm. Anal. Calorim.* 2009, 96, 795-804
- [12]Markowski G.R.; Ensor D.S. and Hooper R.G. *Environ. Sci. Technol.* 1980, 14, 1400-1402.
- [13]Tian L.; Lucas D. Fischer S.L. et al. *Environ. Sci. Technol.* 2008, 42, 2503–2508
- [14]Robinson A.L.; Pandis S.N.; Lipsky E., et al. *Annual Technical Progress Report*, August, 2001.
- [15]Chow J.C. and Watson J.G. May 15-17, Hong Kong and Guangzhou, People's Republic of China, 2002.
- [16]Bond T.C.; Covert D.S.; Kramlich J.C., et al. *J. Geophys. Res.* 2002, 107, 8347
- [17]Chen Y.; Sheng G.; Bi X. et al. *Environ. Sci. Technol.* 2005, 39, 1861-1867
- [18]Dockey D.W., Pope C.A., Xu, X. et al. *N. Engl. J. Med.* 1993, 329, 1753-1759.

Impact of Air Pollution from North Korea to Seoul

In Sun Kim, Ji Yi Lee, and Yong Pyo Kim

Departent of Environmental Science and Engineering, Ewha Womans University, 11-1 Daehyun-Dong, Seodaemun-Gu, Seoul, 120-750, Korea

Principal Contact: In Sun Kim, Student, Department of Environmental Science and Engineering, Ewha Womans University, 11-1 Daehyun-Dong, Seodaemun-Gu, Seoul, 120-750, Korea.

Tel: 822-3277-2902 Fax: 822-3277-3275 E-mail: supidang@gmail.com

Abstract

Since Seoul is only 40km from North Korea, it is expected that air pollution from North Korea affect the air quality in Seoul. However, due to a lack of information for the energy consumption and air quality in North Korea, the impact of air pollution from North Korea to Seoul is not well understood. In this study, to understand the impact of air pollutants from North Korea to Seoul, the data on the energy usage including biomass, emissions of air pollutants, and resultant air quality in North Korea were collected, analyzed, and discussed. In addition, using the ambient polycyclic aromatic hydrocarbons (PAHs) concentration measured at Seoul, South Korea between 2002 and 2003, chemical mass balance (CMB) model and the backward trajectory analysis were applied to quantify the contribution from North Korea. Since Seoul is only 40km from North Korea, it is expected that air pollution from North Korea affect the air quality in Seoul.

Keywords: North Korea, PAHs, backward trajectory analysis

Elemental Composition of Atmospheric Particles during Periods with and without Traffic Restriction in Beijing: The Effectiveness of Traffic Restriction Measure

Renjian Zhang¹, Zhenxing Shen², Leiming Zhang^{1,3} and Meigen Zhang⁴

1 Key Laboratory of Regional Climate-Environment Research for Temperate East Asia, Institute of Atmospheric Physics, Chinese Academy of Sciences, Beijing, 100029, China

2 Department of Environmental Science and Engineering, Xi'an Jiaotong University, Xi'an 710049, China

3 Air Quality Research Division, Science and Technology Branch, Environment Canada, Toronto, Ontario, M3H 5T4, Canada

4 LAPC, Institute of Atmospheric Physics, Chinese Academy of Sciences, Beijing 100029, China

ABSTRACT

In order to evaluate the effectiveness of air pollution control through traffic restriction measure, continuous atmospheric particle samples were collected using step sampler at an urban site in Beijing in August 2007 during traffic restriction and non-restriction periods. Elements concentrations of aerosol samples were analyzed using Particle Induced X-Ray Emission (PIXE). As expected, the concentrations of most elements during the restriction period were considerably lower than those during the non-restriction period. The concentration ratios of most dust elements such as Al, Si, Ca, Ti, and Fe between the restriction and non-restriction periods were less than 0.3, indicating that the traffic restriction measure is an effective way in reducing soil dust trace elements in Beijing. The Enrichment factor (EF) values of elements Al, Si, K, Ca, Ti, Cr, Mn, and Fe were lower than 10 during both the restriction and non-restriction periods while EF values of other elements were in the range of 20-2000 during both periods. The EF values of Cl and Ni were lower during the restriction period compared to the non-restriction periods while the EF of S, Zn, As, and Br were higher during the restriction period. Soil dust concentrations during the traffic restriction period were only about 1/5 of those during the non-restriction period. These results suggested that traffic restriction is more effective on reducing dust elements concentrations, but less effective on reducing anthropogenic elements concentrations.

KEYWORDS

Atmospheric particles; traffic restriction; element concentration; enrichment factor

BODY

Introduction

Atmospheric particles are multi-phase mixture, consisting of solid particles and liquid droplets in the atmosphere, and are important compositions in the atmospheric environment. They play important roles on atmospheric chemistry in both troposphere and stratosphere and thus have strong impacts on air quality and climate related issues such as acid deposition, atmospheric radiation,

cloud and precipitation, visibility^[1-7], etc. The mass concentration of atmospheric particles is one important measure in assessing the atmospheric quality since breathable particles (PM_{2.5}) have important effects on human health^[8]. With the rapid economic development in Beijing, the size of city area, its population, and the total number of vehicles have all increased substantially. All of these have caused the already-polluted air even more polluted. For example, the PM₁₀ mass concentrations in Beijing were much higher than those in Helsinki and Los Angles, the two previous Olympic-host cities^[9-11]. It was once reported that the hourly average PM₁₀ mass levels were as high as 400 µg/m³ in urban area of Beijing^[12]. The air quality in Beijing needed to be improved for the promised “Green Olympic Game” in 2008. The ‘traffic restriction’ measure, which allowed vehicles on road in alternative business days according to their even and odd plate numbers, was proposed to reduce the air pollution. For this purpose, the project, “Lucky Beijing Environment Observation”, was first conducted during Aug 17-20, 2007 to accumulate experience and scientific evidence for the preparation of the 2008 Olympic game. In the present study, the chemical compositions and elements concentrations in aerosol particles collected during Aug. 17-23, 2007 in Beijing are analyzed to evaluate the effectiveness of the ‘traffic restriction’ measure.

Experimental Methods

Sampling instruments in the experiment were mounted at the top of a two-floor building, about 8 m above ground surface, 50 m east of the 325 m-height meteorological tower of the Institute of Atmospheric Physics (39°58' N, 116°22'E), which locates between the North-Third-Ring road and the North-Fourth-Ring road in Beijing. The aerosol samples were collected using the linear step sampler KE-101 made by Green and Blue Corporation, Japan. The sample stepped interval was 6h. The sample diaphragm is the Teflon of nuclepore (Green and Blue Corporation, Japan) with a pore diameter of 1 µm. A sample strip is 34 mm wide and 256 mm long and can usually collects as many as 40 samples. Each sample was a circular orifice with a diameter of 4.7 mm; the distance between two conjunctive sample centers was 5 mm^[13]. The sampler flow was one liter per minute. A total of 29 samples were collected in this experiment. The collected aerosol samples were analyzed using proton induced x-ray emission (PIXE) in a 2×1.7MV tandem electrostatic accelerator, which belonged to the Institute of Low-Energy Physics, Beijing Normal University^[14]. The PIXE analyses were carried out by 2.5 MeV proton bombardments with a beam of 30–40 nA; the beam spot size was about 5 mm; the resolution of Si (Li) sounding system was 175eV; and the X-ray spectrum recorded by S-35 multi-channel pulse height analyzer was transferred to IBM-PC. The element concentrations of Mg, Al, Si, P, S, Cl, K, Ca, Ti, Cr, Mn, Fe, Ni, Cu, Zn, Pb, Br, and As were obtained by energy spectrum analysis using AXIL program. The quality control and accuracy tests showed that both the precision (10%) and accuracy (15%) were satisfactory^[15-16].

Results and discussion

Variation of elements concentrations in the atmospheric particles between restriction and non-restriction periods

Table 1 lists the mean and standard deviation (SD) of element concentration values in the atmospheric particles for two time periods: restriction (Aug. 17-20), and non-restriction (Aug. 21-23) the traffic restriction. In the following discussions, only data collected during and after

traffic restriction periods are analyzed in details to evaluate the effectiveness of traffic restriction measure on air pollution reduction. For easy discussion, the after traffic restriction period is also referred to as the non-traffic restriction period. The concentrations during traffic restriction period were much lower than those during the traffic non-restriction period, suggesting that traffic restriction removed a large portion of particles. The mean element concentrations during the traffic restriction period followed the decreasing order: Si > S > Ca > Fe > Al > K > Mg > Zn > P > Br > As > Ti > Pb > Mn > Cl > Cu > Ni > Cr, with the sum of their mean concentrations being $14.13 \mu\text{g}/\text{m}^3$. A somewhat different order was found during the traffic non-restriction period: Si > Ca > Fe > S > Al > K > Mg > Zn > Cl > Ti > P > As > Mn > Pb > Br > Ni > Cu > Cr, with the sum of their mean concentrations being $55.29 \mu\text{g}/\text{m}^3$. During the whole observation period (Aug.17~23), the sum of the mean concentrations of all the elements from all atmospheric particle samples was $33.28 \mu\text{g}/\text{m}^3$. Dust trace elements such as Si, Ca, Fe, and Al during the non-restriction period were much higher than those during the restriction period. The total concentrations of all the detected elements after traffic restriction was nearly four times of those in restriction period, suggesting that the aerosol loading increased substantially once the traffic restriction was over. Table 1 also shows that the elements Si, Ca, S, Fe, Al, K, and Mg had much higher concentrations than the rest of the elements and accounted for more than 90% of the total concentrations, indicating that these elements were the major composition in the atmospheric particles in Beijing area. The element concentration ratios between the restriction and the non-restriction periods are also shown in Table 1. A value of close to 1 means small variations of element concentrations during and after restriction periods, as was the case for the elements of Br and S. However, the concentration ratios for all other elements were smaller than 0.4, suggesting much lower concentrations of these elements during the traffic restriction period compared to the non-restriction period. These results indicate that the ‘traffic restriction’ measure is an effective way in reducing particle air pollution in Beijing. A study by Wang et al.^[17] also indicated the reduction of NO_x emissions in Beijing during the traffic restriction period of November 4-5, 2006.

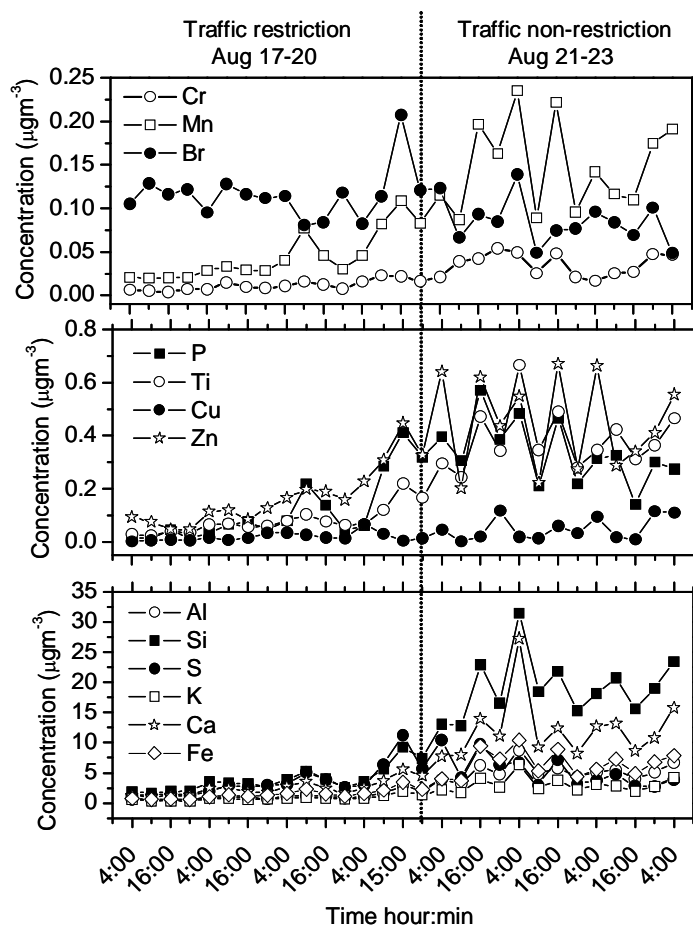
Table 1. Element concentrations of the atmospheric particles in Beijing during the observation period ($\mu\text{g}/\text{m}^3$)

element	Traffic restriction (Aug. 17~20)		non-restriction (Aug. 21~23)		Ctr/ Cutr
	mean	SD	Mean	SD	
Mg	0.1	0.07	1.33	0.76	0.08
Al	1.12	0.64	5.28	1.43	0.21
Si	3.88	2.12	19.2	5.06	0.2
P	0.12	0.12	0.34	0.12	0.35
S	3.57	2.58	5.31	2.6	0.67
Cl	0.01	0.02	0.37	0.37	0.03
K	0.81	0.41	3.12	1.26	0.26
Ca	2.52	1.3	12.26	5.18	0.21
Ti	0.08	0.05	0.39	0.11	0.21
Cr	0.01	0.01	0.03	0.01	0.33
Mn	0.04	0.03	0.15	0.05	0.27
Fe	1.48	0.76	6.61	2.15	0.22
Ni	0.01	0.004	0.06	0.05	0.17
Cu	0.02	0.02	0.05	0.04	0.4
Zn	0.17	0.11	0.45	0.17	0.38
Pb	0.04	0.04	0.12	0.09	0.36
Br	0.11	0.03	0.08	0.03	1.38
As	0.02	0.02	0.1	0.07	0.2
Sum	14.13		55.29		

C_{rf} and C_{urf} stand for the any element concentration sampled during the restriction and non-restriction period, respectively.

Figure 1 is the time-series of the element concentrations in the atmospheric particle samples covering the whole measurement period. All elements, except Br, had a similar time trend. The diurnal variations and the day-to-day variations of the Br concentration were different from the rest of the elements during both the traffic restriction and the non-restriction periods. Traffic restriction had no apparent effect on the element Br concentration, suggesting that other local sources played more important roles than the transportation on the Br concentrations. During the traffic restriction period, the concentrations for all the elements, except Br, were evidently lower than those after the restriction period. The diurnal variations of the element concentrations during the restriction period were also evidently smaller than those after the restriction. During the period of non-traffic restriction, higher concentrations were observed during 04:00-10:00 and 16:00-22:00 local standard time (LST), which apparently caused by traffic rush hours. In contrast, such high concentrations were not detected during the traffic restriction period, suggesting that the emissions from transportation played important roles in the level of atmospheric particles in Beijing.

Figure 1. The temporal variation of the elemental concentrations of the atmospheric particle over Beijing



Enrichment factor analysis

Enrichment factor (EF) can be used to characterize the distribution, transportation and enrichment degree of the chemical elements in atmospheric aerosols, and to determine the source and pollution characterization of the correlative composition in the aerosols. EF for an element in the atmospheric particle is defined as:

$$EF = (C_x/C_r)_a / (C_x/C_r)_b \quad (\text{Eq.1})$$

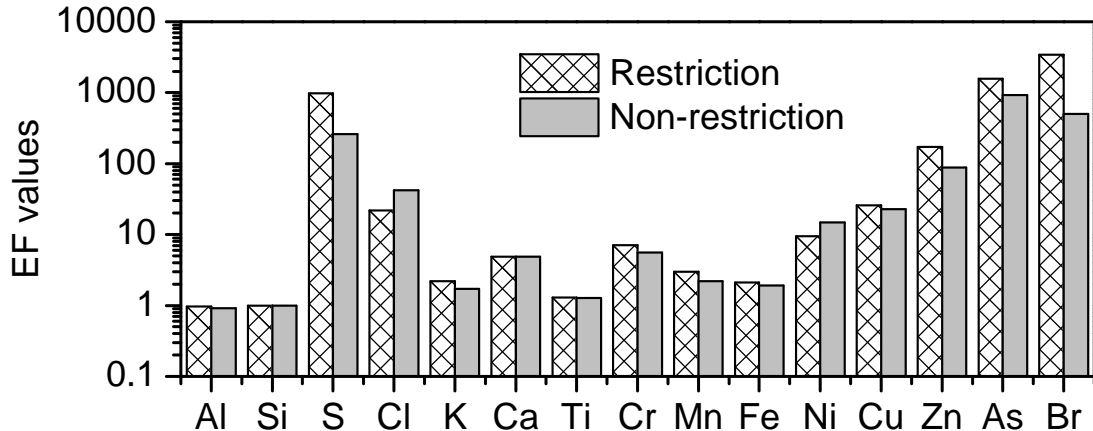
where C_x stands for the element concentration to be analyzed and C_r stands for the concentration of reference element. Subscripts a and b stand for the atmospheric aerosol and background aerosol, respectively. Elements coming from crustal or ocean with less polluted were generally chosen as the reference elements, such as Al, Si, Fe, etc. In the current study, Si was chosen as the reference element, whose reference concentration can be found in Winchester et al.^[18]. The calculated element EF in the aerosols is shown in Figure 2.

Larger EF value corresponds to higher enrichment degree, which implies more important contribution from human sources. For instance, for a given element, $EF > 10$ indicates an evident enrichment for this element; its sources should be from anthropogenic pollution. Under the condition of $EF < 10$, the element can be considered as not enriched; thus, the element would mainly come from crustal soil and natural dust^[19]. During both the restriction and the non-restriction periods, the EF values of elements Al, K, Ca, Ti, Cr, Mn and Fe were smaller than 10, indicating

that these elements were not enriched yet and mainly contributed from soil (such as natural dust).

The EF values of elements S, Zn, As, and Br were very high, and these elements were closely

Fig. 2 Element EF values of the atmospheric particle over Beijing during the restriction and non-restriction periods



related to human activities. The variations of the EF values for elements Al, Ca, Ti, Fe, and Cu between the restriction and the non-restriction periods were not large. The EF value of Cl increased from 22 during the restriction period to 42 after the restriction periods. The EF values of several other elements, S, Zn, As, and Br, were higher during the restriction period than those after the restriction period; e.g., EF value of S were 973 and 262 during the restriction and non-restriction periods, respectively. This is mainly because S was related with emission source of coal combustion^[20]. The differences among the elements in the change of their EF values during and after restriction periods were, to a large extent, caused by their relative percentage changes of concentrations (as measured by the concentration ratios listed in the last column of Table 1) in comparison with that of the reference element (Si). This was explained by the definition of EF (see the equation in Section 3.2). For example, the concentration ratio of Cl between restriction and non-restriction periods is 0.03, much smaller than that of Si (0.20), while the concentration ratios of S, Zn, and Br were all higher than 0.20. One major conclusion that can be drawn from the above discussion is that traffic restriction is more effective on the reduction of dust elements than on the anthropogenic elements.

Effectiveness of traffic restriction on roadside soil dust mass concentration

$$C_{\text{soil}} = 2.2C_{\text{Al}} + 2.49C_{\text{Si}} + 1.63C_{\text{Ca}} + 2.42C_{\text{Fe}} + 1.94C_{\text{Ti}} \quad (\text{Eq.2})$$

where C_{soil} is the estimated soil dust mass concentration, and C_{Al} , C_{Si} , C_{Ca} , C_{Fe} , and C_{Ti} are the concentrations of Al, Si, Ca, Fe, and Ti, respectively, in the samples. The estimated average soil dust mass concentrations in PM_{2.5} were 54.12 µg/m³ with a range of 8.56 to 168.83 µg/m³ from all samples, 19.96 µg/m³ with a range of 8.56 to 47.53 µg/m³ from samples collected during restriction period, and 96.16 µg/m³ with a range of 61.73 to 168.83 µg/m³ from samples collected during non-restriction period. The average soil dust concentration during traffic restriction period was only one fifth of that during the non-restriction period. These results support the above conclusion that

the traffic restriction is an effective way in reducing soil dust emission in Beijing. It was thus recommended to use the measure during the ‘Olympic Game’ period.

CONCLUSIONS

A detailed analysis of the element concentrations in the atmospheric aerosol samples continuously collected at an urban site in Beijing in August 2007 during the traffic restriction and non-restriction periods reveals the following major findings:(1) The concentrations of elements of Mg, Cl, Al, Ti, Cr, Mn, Cu, and Pb during the restriction period were considerably lower as compared to those during the non-restriction period. The concentration ratios between the restriction and non-restriction periods were less than 0.4, indicating that the traffic restriction is an effective way in decreasing dust trace elements in Beijing. Such a conclusion was also supported by the elements EF analysis. (2) The much smaller diurnal variations of the element concentrations during the restriction period, as compared to those during the non-restriction period, implied that the traffic emissions played important roles affecting the atmospheric particle concentration levels.(3) Soil dust concentrations, estimated from five crustal elements, during the traffic restriction period were only one fifth of those during the non-restriction period, indicating that the traffic restriction is an effective measure on reducing roadside dust in Beijing.

ACKNOWLEDGEMENTS

This research is supported by National Basic Research Program of China (No.2010CB428503, 2009CB723904).

REFERENCES

- [1] Sokolik, I.N., and O.B. Toon, 1996: Direct radiative forcing by anthropogenic airborne mineral aerosols. *Nature*, **381**(20), 681-683.
- [2] Wang, M.X., R.J. Zhang, Y.F. Pu, 2001: Recent research on aerosol in China. *Adv. Atmos.Sci.*, **18**(4), 576-586.
- [3] Watson, J.G., 2002: Visibility: Science and regulation. *Journal of the Air & Waste Management Association*, **52**(6), 628-713.
- [4] Menon, S., J. Hansen, L. Nazarenko, and Y.F. Luo, 2002: Climate effects of black carbon aerosols in China and India. *Science*, **297**, 2250-2253.
- [5] Cao, J.J., S.C. Lee, K.F. Ho, X.Y. Zhang, S.C. Zou, K.K. Fung, J.C. Chow, J.G. Watson, 2003: Characteristics of carbonaceous aerosol in Pearl River Delta Region, China during 2001 winter period. *Atmos. Environ.*, **37**, 1451–1460.
- [6] Zhang, M.G., I. Uno, Y. Yoshida, Y. Xu, Z. Wang, H. Akimoto, T. Bates, T. Quinn, A. Bandy, and B. Blomquist, 2004: Transport and Transformation of Sulfur compounds over East Asia during the TRACE-P and ACE-Asia Campaigns. *Atmos. Environ.*, **38**(40), 6947-6959.
- [7] Shen, Z. X., J.J. Cao, R. Arimoto, Y. M. Han, C. S. Zhu, J. Tian, S. X. Liu, 2010: Chemical characteristics of fine particles (PM_{1}) over Xi'an, China. *Aerosol Science and Technology*, **44**, 461-472.
- [8] He, K.B., F.M. Yang, Y.L. Ma, Q. Zhang, X.H. Yao, C.K. Chan, S. Cadle, T. Chan, and P. Mulawa, 2001: The characteristics of $PM_{2.5}$ in Beijing, China. *Atmos. Environ.*, **35**, 4959-4970.
- [9] Viidanoja, J., M. Sillanpaa, J. Laakia, V. Kerminen, R. Hillamo, P. Aarnio, T. Koskentalo, 2002:

- Organic and black carbon in PM_{2.5} and PM₁₀: 1 year of data from an urban site in Helsinki, Finland. *Atmospheric Environment*, **36**, 3183–3193.
- [10] Wang, W., D.G. Tang, H. Liu, X. Yue, Z. Pan, Y. Ding, 2000: Research on current pollution status and pollution characteristics of PM_{2.5} in China. *Research of Environmental Sciences*, **13**(1), 1-5. (in Chinese with English abstract)
 - [11] Li, W.J., L.Y. Shao, J.J. Li, S.S. Yang, 2006: The pollution characteristics level of PM₁₀ and PM_{2.5} at Beijing. *Environment and Sustainable Development*, **19**(2), 18-20.(in Chinese)
 - [12] Shi, Z.B., L.Y. Shao, T.P. Jones, A.G. Whittaker, S.L. Lu, K.A. Bérubé, T.E. He, R.J. Richard, 2003:Characterization of airborne individual particles collected in an urban area, a satellite city and a clean air area in Beijing, 2001. *Atmos. Environ.* **37**, 4097–4108.
 - [13] Zhang, R.J., Z.W. Han, Z.X. Shen, J.J. Cao, 2008: Continuous measurement of number concentrations and elemental composition of aerosol particles for a dust storm event in Beijing. *Adv. Atmos.Sci.*, **25**(1), 89-95.
 - [14] Zhang, R.J., Z.W. Han, T.T. Cheng, J. Tao, 2009: Chemical properties and origin of dust aerosols in Beijing during springtime. *Particuology*, **7**(1), 61-67.
 - [15] Zhang, X.Y., J.J. Cao, L.M. Li, R. Arimoto, Y. Cheng, B. Huebert, and D. Wang, 2002: Characterization of atmospheric aerosol over XiAn in the south margin of the Loess Plateau, China. *Atmos. Environ.*, **36**, 4189–4199.
 - [16] Zhang, R.J., R. Arimoto, J.L. An, S. Yabuki, J.H. Sun, 2005: Ground observations of a strong dust storm in Beijing in March 2002. *J. Geophys. Res.*, **110**(D18S06), doi: 10.1029/2004JD004589.
 - [17] Wang, Y. X., M.B. McElroy, K.F. Boersma, H.J. Eskes, and J.P. Veefkind, 2007: Traffic restrictions associated with the Sino-African summit: Reductions of NO_x detected from space. *Geophys. Res. Lett.*, **34**, L08814, doi: 10.1029/2007GL029326
 - [18] Winchester, J.W., M.X. Wang, W.X. Lu, L.X. Ren, and W. Maenhaut, 1981: Fine and coarse aerosol composition from a rural area in northern China. *Atmos.Environ.*, **15**,933-937.
 - [19] Taylor, S.R., and S.M. McLennan, 1985: *The Continental Crust: Its Composition and Evolution*. Blackwell, New York: Oxford, 315pp.
 - [20] Shen, Z. X., J. J. Cao, R. Arimoto, R. J. Zhang, D. M. Jie, S. X. Liu, and C. S. Zhu, 2007: Chemical composition and source characterization of spring aerosol over Horqin sand land in northeastern China. *J. Geophys. Res.*, **112**, D14315, doi:10.1029/2006JD007991.

Characteristics of Volatile Organic Compounds in Seoul, Korea

H.J. Shin^{1,2}, J.C. Kim², and Y.P. Kim¹

1 Department of Environmental Science and Engineering, Ewha Womans University, 11-1 Daehyun-dong, Seodaemun-gu, Seoul, 120-750, Korea

2 Air Quality Research Division, National Institute of Environmental Research, Kyungseodong, Seo-gu, Incheon, 404-708, Korea

Principal Contact: Y.P. Kim, Professor, Ewha Womans University, 11-1 Daehyun-dong, Seodaemun-gu, Seoul, 120-750, Korea.

Tel: +82 2 3277 2832 Fax: +82 2 3277 3275 Email: yong@ewha.ac.kr

Abstract

Characteristics of volatile organic compounds (VOCs) in Seoul, Korea are investigated. The hourly based VOCs concentrations were measured from 2004 to 2008 at Bulgwang site, one of the Photochemical Assessment Monitoring Station, representing the VOCs concentration of Seoul. The 15 highest concentration VOCs composed over 85% of the total VOCs concentration. The most abundant component in Seoul was toluene accounting for 23.5 % of the total VOCs, followed by propane, n-butane, and ethane. Time series analysis such as a diurnal, weekly, and monthly variations of VOCs are investigated. The diurnal variations of toluene, m/p-xylene, o-xylene, and ethylbenzene, mainly emitted from solvent usage, showed high in daytime and low in nighttime due to high temperature in daytime, preferable condition for evaporation of VOC species from solvent. Otherwise, the diurnal variation of propane, butanes, ethane, and pentanes, the main components of vehicle exhaust and gasoline solvent, showed bimodal peaks; high in the morning and evening around the commuting hours. For toluene, xylenes, and ethylbenzene, dramatic decrease of concentration was shown in Sunday due to less industrial activities in weekend. The species mainly emitted from solvent usage and gasoline vapor showed high in summer due to preferable condition for evaporation. Propane and ethane, main component of liquefied petroleum gas (LPG) for residential usage and one of components of natural gas, respectively, showed high in winter and low in summer due to residential heating in winter. Benzene to toluene ratio in Seoul is 0.16 which is much lower than the typical value for traffic related area implying that the main emission source of VOCs in Seoul is not a vehicular emission. From the result for correlation between total VOCs and NOx, it is inferred that the condition of Seoul atmosphere is VOCs-limited condition.

Keywords: VOCs, Time series analysis

Size Distributions of Polycyclic Aromatic Hydrocarbons in Diesel Exhaust Particles Collected by Newly Developed Ultrafine Particles Sampler

Keiko Shibata¹, Nobuhiro Yanagisawa¹, Kenji Enya¹, Kaoru Satou¹ and Kazuhiko Sakamoto^{2,3}

1 Isuzu Advanced Engineering Center, LTD., 8 Tsuchidana, Fujisawa-city, Kanagawa 252-0881, Japan

2 Institute for Environmental Science and Technology / Graduate School of Science and Engineering, Saitama University, 255 Shimo-Okubo, Sakura-ku, Saitama 338-8570, Japan

3 Center for Environmental Science in Saitama, 914 Kamitanadare, Kazo-city, Saitama 347-0115, Japan

ABSTRACT

A new type ultrafine particles ($< 0.1 \mu\text{m}$) sampler called Nanosampler was developed for size-classified sampling of atmospheric particles. The sampler can operate at atmospheric pressure under low pressure drop and high sampling flow rate. Six stages can classify particles from less than $0.1 \mu\text{m}$ to more than $10 \mu\text{m}$. In this study, the size distributions of diesel exhaust particles (DEP) were compared with two types of sampler, Nanosampler and Electrical Low Pressure Impactor (ELPI). In addition, total DEP masses were compared with three types of sampler, Nanosampler, conventional filter sampler for DEP and ELPI. DEP was collected from 3-L diesel engine equipped with and without diesel particulate filter (DPF). The results showed the size distributions of DEP without DPF were unimodal with peak at less than $0.1 \mu\text{m}$ and at $0.11\text{-}0.17 \mu\text{m}$ by Nanosampler and ELPI, respectively. DEP mass of ultrafine particles fraction by Nanosampler was higher than ELPI. Total DEP masses by ELPI were higher than Nanosampler and conventional filter sampler because the density used in the calculating the mass might be difference from a true value. Polycyclic aromatic hydrocarbons (PAHs) in collected DEP using Nanosampler were analyzed by thermal desorption gas chromatography-mass spectrometer (TD-GC-MS). PAHs had clearly unimodal with peak at $0.1\text{-}0.5 \mu\text{m}$ under low load (75 Nm) without DPF. When middle load condition, PAHs emission was so small that peak was not clearly. Consequently, Nanosampler was useful to investigate chemical composition of ultrafine particles fraction in DEP.

KEYWORDS

Ultrafine particles sampler, Electrical low pressure impactor, Size distribution, PAHs, DEP, DPF

Introduction

In order to assess the adverse health effect of diesel exhaust particles (DEP) smaller than $0.1\mu\text{m}$, it is necessary to measure their chemical composition. However, little is known about size-segregated chemical composition of DEP. Because DEP masses less than $0.1\mu\text{m}$ are very small, it is difficult to analyze that composition. Thermal desorption GC-MS (TD-GC-MS) method required no sample preparation, small sample mass, rapid and sensitive analysis^[1]. Fushimi et al (2007)^[2] also reported that TD-GC-MS could be applied to extremely small amount (e.g., $5\mu\text{g}$) of DEP. Low pressure impactor (LPI) can classify nanoparticles at a fairly high airflow rate, but the evaporation of unstable chemical species is inevitable because small size stages are operated at low pressures. Recently developed Nanosampler for ultrafine particles sampling controls its diffusion collection increasing filtration velocity and has a low pressure drop ($< 20\text{-}30\text{ kPa}$) compared to current methods applicable to the nano-size range, such as LPI (70-80 kPa) and nano-MOUDI ($\sim 60\text{ kPa}$)^[3]. 3-L diesel engine was operated steady state conditions equipped with and without diesel particulate filter (DPF) to collect various size fractions of DEP, Nanosampler and Electrical Low Pressure Impactor (ELPI) were used. Polycyclic aromatic hydrocarbons (PAHs) are one of important chemical compositions to evaluate the adverse health effects because of their potential carcinogenicity. International Agency for Research on Cancer (IARC) classified strength of the carcinogenesis of PAHs^[4]. We selected eight PAHs from four to six aromatic rings including high carcinogenesis for analysis by TD-GC-MS. ELPI has 12 stages in the size range from $0.07\mu\text{m}$ to $6.8\mu\text{m}$, Nanosampler has 6 stages in the size range from $0.1\mu\text{m}$ to $10\mu\text{m}$, they differs in that the number of stages and range of each stage. We compared Nanosampler and conventional filter sampler for DEP with ELPI as instrument of low pressure impactor for total masses of DEP.

Experimental Methods

The specifications of the test engine, fuel and oil are shown in Table 1. To suit Japan New Long Term Regulations, DOC and DPF as aftertreatment devices were needed. The DOC catalyzed the oxidation of CO and hydrocarbons. The DPF is a filter to collect diesel particulate matter coated with a precious metal catalyst. A Diesel engine with and without the aftertreatment devices (it wrote as DPF after this) was operated for 1 hour, the loads are 75 Nm (low) and 225 Nm (middle), and speed is 1600 rpm fixation at all experiment condition. We used HORIBA micro tunnel as a partial flow dilution system^{[5],[6]} to dilute and cool the exhaust during sampling. Nanosampler Model 3180 (KANOMAX Japan Inc; Osaka, Japan) was set behind the partial flow dilution tunnel. The upper inlet of Nanosampler was processed to suit the general filter holder for DEP sampling, and operated at 40 L/min.

For quantification of the PAHs, standard reference material (SRM) 1647e (NIST; Gaithersburg,

MD, USA) solution was used. Eight PAHs as target compounds were benz(*a*)anthracene (BaA), chrysene(CHR), benzo(*b*)fluoranthene(BbF), benzo(*k*)fluoranthene(BkF), benzo(*a*)pyrene (BaP), indeno(1,2,3-*cd*)pyrene(IcdP), dibenz(*a,h*)anthracene(DahA), and benzo(*ghi*)perylene (BghiP). They are molecular weights > 220 and have four, five, or six aromatic rings and are difficult to volatize. Chrysene-*d*₁₂ (CHR-*d*₁₂) solution (Supelco; Bellefonte, PA, USA) was used as an internal standard because its analytical behavior is similar to that of the target compounds [7]. To prepare a calibration curve, we spiked diluted SRM 1647e and 0.4 ng of CHR-*d*₁₂ solution on quartz-fiber filter. The calibration curve was obtained from the area ratio PAH/CHR-*d*₁₂ and the concentration ratio PAH/CHR-*d*₁₂. Collecting material for DEP is a 55 φ mm diameter Teflon-impregnated glass fiber filter, T60A20 (PALL Life Science; Ann Arbor, MI, USA) except 0.1-0.5 μm fraction of Nanosampler. That fraction used stainless steel fiber filter. The filters were weighed before and after collection of DEP by means of a microbalance M3P-F (readability 1 μg, Sartorius AG; Goettingen, Germany) in a chamber in which the temperature and relative humidity were controlled at 23 ± 5°C and 50 ± 5%, respectively. Before analysis, 6 fractions of DEP were individually extracted by organic solvent for 16 hours and concentrated to 0.5 ml. We injected 0.4 ng of this solution on the quartz filter and an internal standard solution was added. The filters were dried with helium gas for about 1.5 min prior to TD-GC-MS analysis. Each filter sample was set into the middle of a TD tube. To remove interference matter, the TD tubes were baked for 1 h at 400 °C with helium gas before analysis. The PAHs were analyzed with a T-Dex II TD system (GL Sciences Inc; Tokyo, Japan) installed on a Varian GC-3800 GC with a Varian 300-MS (Varian Inc; Lake Forest, CA, USA). The TD tube (Pyrex, 89 mm length, 4 mm I.D., 6 mm O.D.) was automatically placed in the TD area under the injection port of the GC by a TD auto sampler system. The cryogenic-focus trap system was located below the TD area in the GC oven and was cooled initially at – 100°C with liquid nitrogen. We selected 350°C as the TD temperature because this temperature does not favor pyrolysis and is effective for desorption of PAHs. TD tube was heated from 45°C (held for 1 min) to 350°C (held for 10 min) at a rate of 5°C/s by means of a split (1:1) mode injection. Desorbed compounds were collected in the cryogenic-focus trap at – 100°C with liquid nitrogen in a cryotube (0.53 mm i.d., inert fused silica capillary column) and reheated from – 100°C (held for 1 min) to 300°C (held for 10 min) at a rate of 50°C/s and then were sent to capillary column (VF-5ms; 30 m×0.25 mm i.d., 0.25 μm film thickness, Varian Inc.) The GC was heated from 60°C (held for 3 min) to 200°C at a rate of 15°C/min and then to 325°C (held for 10 min) at a rate of 5°C/min. The helium carrier gas was supplied at 1.3 mL/min. SIM mode was used for quantitative analysis in this study. The GC injector, ion-source, and transfer-line temperatures were 280, 230, and 280°C, respectively.

Results and Discussion

Size distributions of DEP

The size distributions of DEP were compared with two types of sampler, Nanosampler and ELPI. The results by ELPI were shown Figure 1 and 2. DEP had unimodal with peak in the size range of 0.11 - 0.17 μm without DPF under both load condition. When equipped with DPF under both load conditions, their values were very small. This seems to be influenced by DEP collection efficiency of DPF. Mass concentration of DEP at the middle load was higher than at the low load. This result was same trend as previous report [8].

The result by Nanosampler was shown Figure 3. DEP of $< 0.1 \mu\text{m}$ diameter (backup filter stage) was the highest at without DPF, and decreased gradually as diameter grows.

DEP mass of ultrafine particles fraction by Nanosampler was higher than ELPI. Nanosampler is also suitable for ultrafine particles collection in DEP.

Comparison with three type samplers for total DEP masses

To compare the collection masses of total DEP, three type samplers were used. They were Nanosampler, conventional filter sampler for DEP, and ELPI. Total masses of 6 stages of Namosampler, conventional filter, and 12 stages of ELPI were compared. Figure 4 showed Nanosampler and conventional filter sampler were almost same, but value of ELPI was more remarkably higher than the others. This reason was the density used in the calculating the mass might be difference from a true value. The density was used as 1.0 g/cm^3 for all size range of DEP. Effective density of agglomerated diesel particles decreases as a function of particle size [9]. Though the density of primary particles (diameter of 50 nm) varies from 1.1 g/cm^3 to 1.2 g/cm^3 , but agglomerated particle (diameter of $1 \mu\text{m}$) is about 0.5 g/cm^3 [9]. Thus, it is necessary to change the density of each size used with ELPI. If the density matched to the particle size, DEP mass will become almost same value among three type samplers.

Size distributions of PAHs

Size distributions of BaA emission in DEP was shown Figure 5 and 6. The result showed that emitted had clearly unimodal with peak in the size range of $0.1 - 0.5 \mu\text{m}$ under low load condition equipped without DPF. When middle load condition, emission was so small that peak was not clearly. Other PAHs were almost same tendency as BaA. When low load condition, emission of PAHs were higher than middle load condition. This tendency was converse to that of DEP mass. It shows organic compound emission is small at middle load condition.

Table 1. Specifications of the test engine, fuel and oil.

Engine	Type	ISUZU DI Diesel
	Cylinder number	4
	Displacement	2.999 (L)
	Max power	110 kW @ 2800 rpm
	Max torque	375 Nm @ 1600 rpm
	Injection system	Common rail
	Air charging system	Inter-cooled turbocharger
Fuel	Type	JIS 2
	Cetane index	57.8
	Sulfur content	5 (ppm)
	Density	0.8202 (g/cm ³) @ 15°C
	Viscosity	2.946 (mm ² /s) @ 30°C
Oil	SAE grade	10W-30

Figure 1. Size distribution of DEP equipped without DPF by ELPI.

Figure 2. Size distribution of DEP equipped with DPF by ELPI.

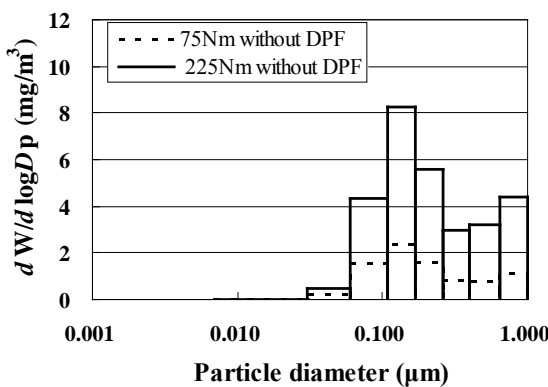


Figure 1.

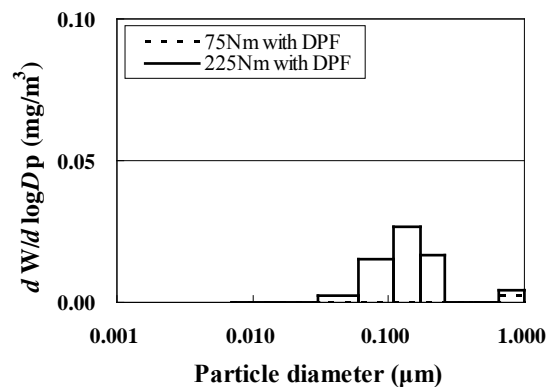


Figure 2.

Figure 3. Size distribution of DEP equipped without and with DPF by Nanosampler.

Figure 4. Comparison with Nanosampler, conventional filter sampler and ELPI for total DEP masses.

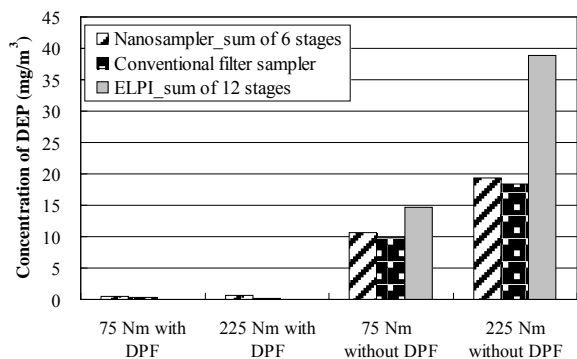
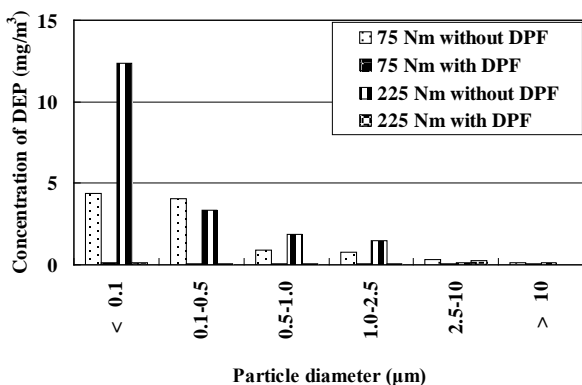


Figure 5. Size distribution of BaA emission in DEP under 75 Nm load condition.

Figure 6. Size distribution of BaA emission in DEP under 225 Nm load condition.

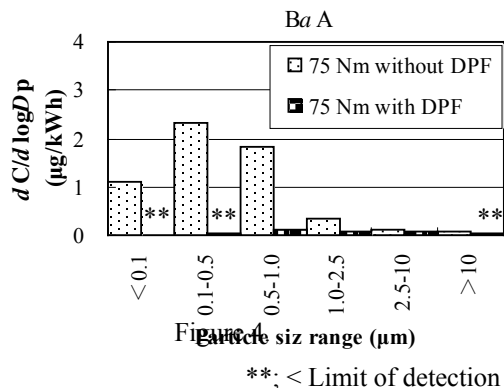


Figure 5.

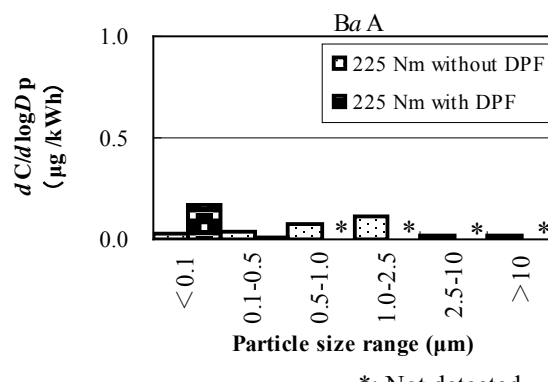


Figure 6.

CONCLUSION

Size distributions of diesel exhaust particles (DEP) were compared with two types of sampler, Nanosampler and ELPI. Size distributions of DEP under both load conditions without DPF were unimodal with peak at $< 0.1\mu\text{m}$ and $0.11\text{-}0.17\mu\text{m}$ by Nanosampler and ELPI, respectively. DEP mass of ultrafine particles fraction by Nanosampler was higher than ELPI.

Total DEP masses were compared with three types of sampler, Nanosampler, conventional filter sampler, and ELPI. The results showed Nanosampler and DEP mass sampler were almost same, but value of ELPI was more remarkably higher than the others. Because the density used in the calculating the mass might be difference from a true value. If the density matched to the particle size, DEP mass will become almost same value among three type samplers.

Size distribution of emitted PAHs had clearly unimodal with peak in the size range of $0.1\text{-}0.5\mu\text{m}$ under low load condition equipped without DPF. When middle load condition, PAHs emission was so small that peak was not clearly. Emission of PAHs under low load condition was higher than middle load condition. This tendency was converse to that of DEP mass.

Consequently, Nanosampler is useful to investigate chemical composition of ultrafine particles fraction in DEP.

ACKNOWLEDGMENTS

The authors acknowledge Mr. Kanno, Isuzu Advanced Engineering Center, LTD., for his engine operating support.

REFERENCES

- [1] Falkovich, A.H.; Rudich, Y. *Environmental Science and Technology*. 2001, 35, 2326-2333.

- [2] Fushimi , A.; Tanabe, K.; Hasegawa, S.; Kobayashi, S. *Science of the Total Environment*. 2007, 386, 83-92.
- [3] Otani, Y.; Eryu K.; Furuuchi, M.; Tajima, N.; Takasakul, P. *Aerosol and Air Quality Research*, 2007, 7(3), 343-352.
- [4] *IARC Monographs on the Evaluation of Carcinogenic Risks to Humans*; Some Non-heterocyclic Polycyclic Aromatic Hydrocarbons and Some Related Exposures, volume 92, 2010.
- [5] Khalek, I.A.; Ullman, T.L.; Shimpi, S.A.; Jackson, C.C.; Dharmawardhana,B.; Silvis, W.M.; Kreft, N.; Harvey, R.N.; Munday, D.; Yamaguchi, Y.; Graze, R.; Smitherman, J.; Adkins, J. *SAE Paper*, 2002, 2002-01-1718.
- [6] Ayala, A.; Chernich, D.J.; Huai, T.; Johnson, K. C.; Miller, W. *SAE Paper*, 2005, 2005-01-3798.
- [7] *Compendium of methods for determination of toxic organic compounds in ambient air second edition; Compendium methods TO-13A*; U.S. Environmental Protection Agency; EPA's office of Research and Development (ORD): Washington, DC, 1999; EPA/625/R-96/010b.
- [8] Shibata, K.; Yanagisawa, N.; Tashiro, Y.; Mukunashi, T.; Onodera, T.; Sakamoto, K. *Journal of Health Science*, 2010, 56(1), 31-40.
- [9] Virtanen, A.; Ristimäki, J.; Marjamäki, M.; Vaaraslahti, K.; Keskinen,J.; Lappi, M. *SAE Paper*, 2002, 2002-01-0056.

Characterization and Source Apportionment of Submicron Aerosols at a Regional Site in Pearl River Delta of China Using an Aerodyne High-Resolution Aerosol Mass Spectrometer

Z.-H. Gong¹, L.-Y. He¹, X.-F. Huang¹, Z.-J. Lan¹, L. Xue¹ and L.-W. Zeng¹

1 Key Laboratory for Urban Habitat Environmental Science and Technology, School of Environment and Energy, Peking University Shenzhen Graduate School, Shenzhen 518055, China

ABSTRACT

Submicron aerosol particles (PM_1) were sampled and measured in Heshan, a regional site downwind of Guangzhou megacity in Pearl River Delta (PRD) of South China, using an Aerodyne High-Resolution Time-of-Flight Aerosol Mass Spectrometer (HR-ToF-AMS) in November 2010, during the time of 2010 Guangzhou Asian Games. The mean measured PM_1 mass concentration was $68.7 \pm 23.6 \mu g m^{-3}$ during the campaign, with organic aerosol (OA) and sulfate being the two dominant species, accounting for 41.9% and 28.8%, respectively. The diurnal cycles of OA, sulfate, nitrate and ammonium all rise to high peaks at morning and dusk due to transport of traffic emissions from upwind Guangzhou city. The average size distributions of the species were mainly dominated by an accumulation mode peaking at 500~600 nm. Calculations based on high-resolution organic mass spectra show that on average, C, H, O and N contributed 58.1, 7.3, 30.7, and 3.9% to the total organic mass, respectively. The average OM/OC ratio was 1.73 ± 0.08 . The Van Krevelen diagram of OA yielded a significant anti-correlation ($R^2=0.70$) between H/C and O/C, with a slope of -0.96.

KEYWORDS

Chemical composition, Diurnal variation, Organic aerosols, Regional transport, HR-ToF-AMS

Introduction

The Pearl River Delta (PRD) region is one of the three areas in China that have experienced extremely fast development during the last two decades. With the rapid progress of urbanization in the area, industrial emissions and traffic exhausts together contribute to high level of air pollutants, including ozone and particulate matter, both of which result in a combined air

pollution condition characterized by high level of oxidation. Recent years many field campaigns have been carried out in the PRD region to get better understanding of the characterization of the emission sources of air pollutants in the local as well as their transportation mechanisms in regional scale. Xiao et al used a Q-AMS in PRD in 2006, finding out that most oxygenated organic aerosol were water soluble^[1]. Huang et al analyzed the data obtained by an HR-ToF-AMS in STAR2008 PRD campaign using Positive Matrix Factorization (PMF) analysis and differentiated the organic aerosol into three components: biomass burning (BBOA) and two oxygenated (LV-OOA and SV-OOA) organic aerosols^[2].

With researches going deeper, the need for a high resolution in both time and species to characterize in depth the pollution mechanisms and atmospheric chemical and radiative processes in the PRD region, and to give support for the atmospheric air condition assurance of the 2010 Guangzhou Asian Games, a campaign was carried out in November 2011 in Heshan, a regional site downwind of Guangzhou city. An Aerodyne HR-ToF-AMS was used in the campaign to measure the chemical composition and size distribution of non-refractory submicron particulate matter (NR-PM₁).

Experimental Methods

Sampling site description

Heshan supersite is located on the top of a small rural hill (22.711°N, 112.927°E, 40 m a.s.l.) in Guangdong province, China, in a flat plain between the NanLing Mountains in the North and the South China Sea in the south. 7 km away from downtown Heshan City, the site is far from industrial sources. Farmlands and forests are in dominance within 100 meters around the site, and villages scattering from west to north within 1 km circumference. The major anthropogenic source was biomass burning observed occasionally in the fields around. The site is to the southwest of central PRD megacities Guangzhou and Foshan, with distances of 40 and 57 km, respectively. In the observation period of November and early December, the prevailing wind direction in PRD is northeast, making the site downwind of Guangzhou and Foshan.

HR-ToF-AMS operation

An Aerodyne High-Resolution Time-of-Flight Aerosol Mass Spectrometer (HR-ToF-AMS) was deployed in Heshan supersite from 13 November to 1 December. A detailed description of the instrument can be found in DeCarlo et al^[3]. The sampling inlet was positioned ~1.5 m above the roof of a one-storage air-conditioned room, consisting of a PM2.5 cyclone followed by a copper tube. The instrument operated under "V" and "W" mode alternately every 4 min, with the 2 min V-mode cycling through the mass spectrum (MS) mode and the particle time-of-flight (PToF)

mode every 25 s, spending 5 s and 20 s each, to obtain mass concentrations of non-refractory species as well as their size distributions, and the 2 min W-mode to obtain high resolution mass spectral data. The PToF mode was not run under the W-mode due to the limited signal-to-noise ratio. The HR-ToF-MS was calibrated for inlet flow, ionizatione efficiency (IE), and particle sizing at the beginning and the end of the campaign following the standard protocols^[4-6].

HR-ToF-AMS data processing

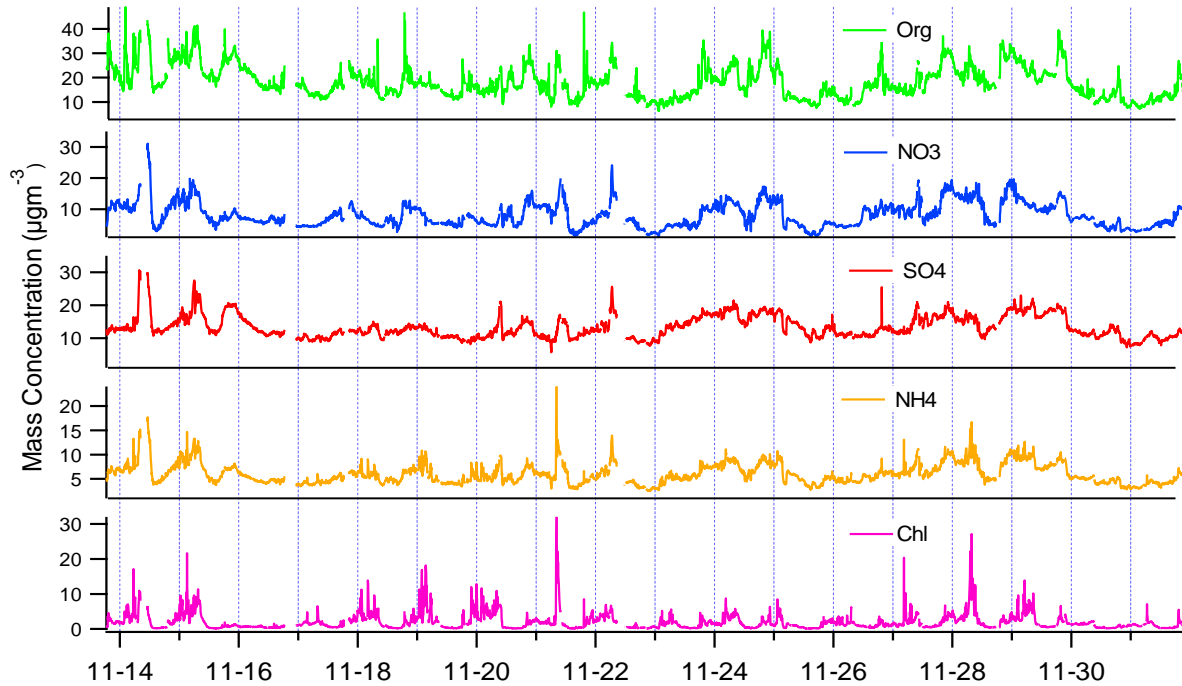
The mass concentrations and size distributions of the species measured with the HR-ToF-AMS were calculated using the standard AMS data analysis software packages (SQUIRREL version 1.51B and PIKA version 1.10B, Sueper^[7]) compiled and executed on Igor Pro 6.21 were used to generate unit and high-resolution mass spectra from the V-mode and W-mode data, respectively. For mass concentration calculations an empirical particle collectione efficiency (CE) factor of 0.5 was used to account for the incomplete detection of species due to particle bouncing at the vaporizer and partial transmission through the aerodynamic lens^[8].

Results and Discussion

Variations of submicron aerosol particles

Figure 1 present the time series of the PM₁ mass concentrations of different components during the campaign. The series showed 3 episodes of air pollution accumulation and removal processes, happening on 14-16, 23-26 and 28-30 November, respectively. The secondary components, namely sulfate, nitrate and ammonium, showed quite similar trends through the whole campaign, indicating a regional transportation of pollutants, in that their major sources are all secondary formation process. Sharp peaks of organic appeared occasionally during the observation period, mainly because of the rice straw burning after the harvest, smoke of which could even be seen rising from around the site.

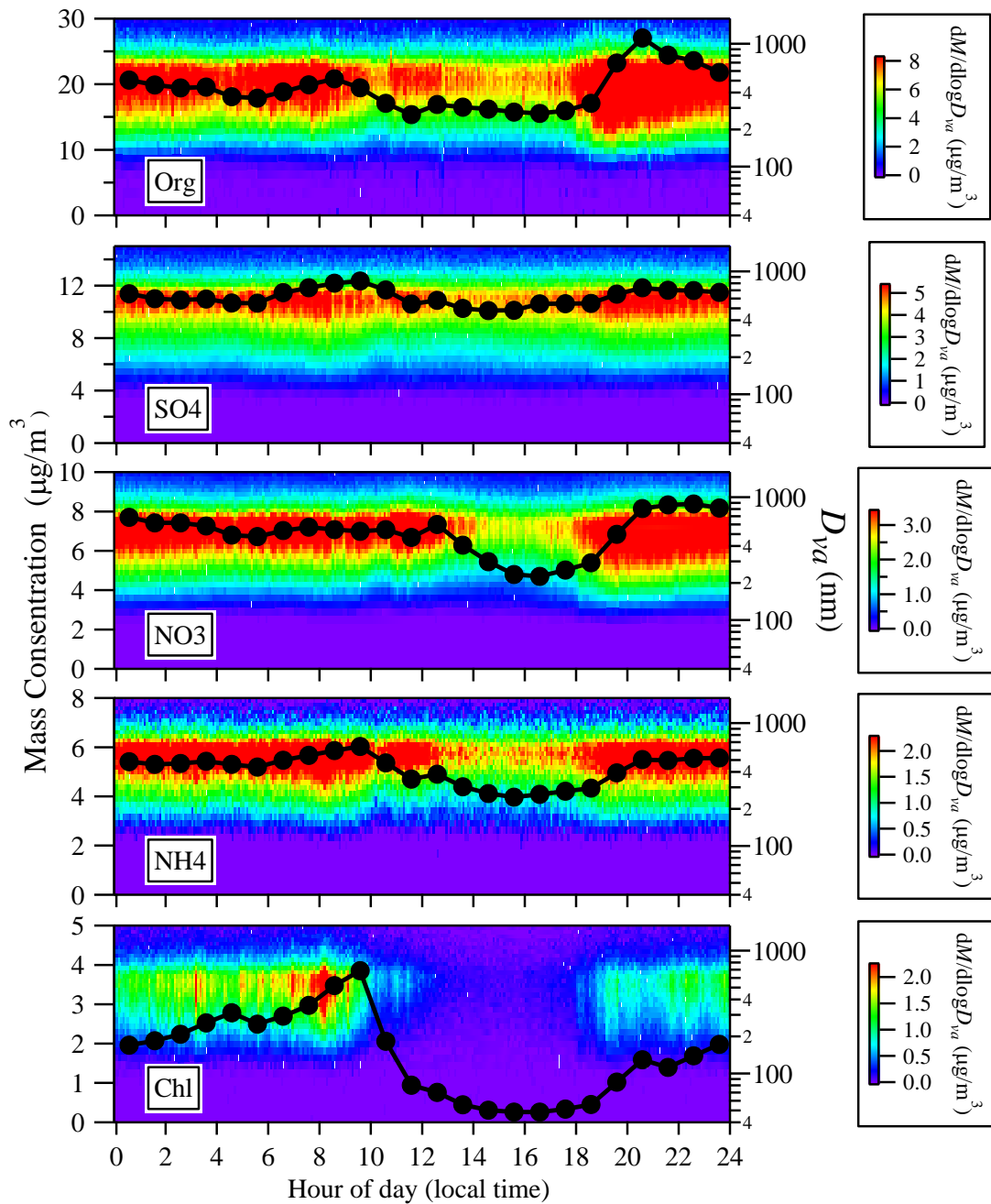
Figure 1. Time series of mass concentrations of NR-PM₁ major components



Diurnal patterns of PM₁ components

The mean diurnal variations of major PM₁ components are given out in Figure 2. The diurnal cycles of different species all showed a double-peak pattern, with the two peaks appearing at around 8:00 a.m. local time and 7:00-8:00 p.m., correlating to the heavy traffic peaks in upwind Guangzhou City. Compared with the sharp slopes in the afternoon, the patterns all showed gradual declines after the evening peaks, owing to the more intense secondary formation and transportation processes of traffic emission pollutants from upwind Guangzhou City, as well as the lower planetary boundary layer (PBL) during the nighttime. In the afternoon the components were all in a low level, owing to the higher planetary boundary layer, and the transformation from particle phase to gas for nitrate, ammonium and chloride due to stronger sunlight and higher temperature. During the high mass concentration periods (deep red zones in Figure 2) of the day, the size distributions of the species were mainly dominated by an accumulation mode peaking at 500~600 nm.

Figure 2. Diurnal trends of the mass concentrations (solid black circles) and the size distributions of NR-PM₁ major components

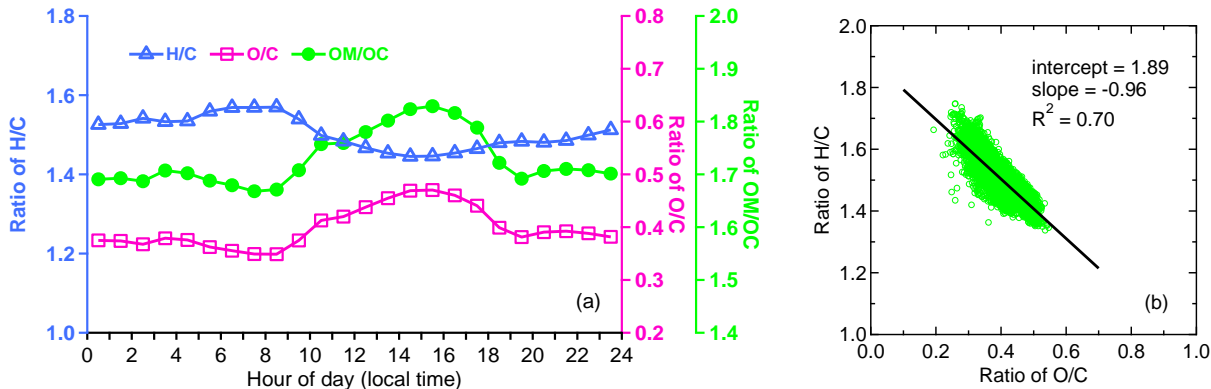


Elemental composition of organic aerosol

The high-resolution organic mass spectral dataset obtained are used to calculate the elemental composition and OM/OC (the ratio of organic mass/organic carbon mass) of organic aerosols

following the methods described previously^[9, 10]. On average, C, H, O, and N contributed 58.1, 7.3, 30.7, and 3.9% to the total organic mass, respectively. The OM/OC ratio (1.73 ± 0.08) and O/C ratio (0.40 ± 0.06) both increased gradually from morning to late afternoon, owing to enhanced photochemical SOA formation, while the H/C ratio (1.50 ± 0.06) showed an opposite diurnal pattern (Figure 3a), with a significant morning peak possibly owing to local biomass burning. The Van Krevelen diagram (Figure 3b) of OA showed a significant anti-correlation ($R^2=0.70$) between H/C and O/C, with a slope of -0.96. This slope is similar to those (about -1.0) observed in Riverside, the Central Amazon Basin, and Mexico City^[11], suggesting that the chemical evolution of OA in the atmosphere may be simply represented by the movement along this line in models^[11].

Figure 3. (a) Diurnal trends of the H/C, O/C and OM/OC ratios; (b) The Van Krevelen diagram.



SUMMARY

An Aerodyne HR-ToF-AMS was deployed to measure NR-PM₁ in Heshan, a regional site downwind of Guangzhou in PRD in November 2010, during the time of 2010 Guangzhou Asian Games. The mean measured PM₁ mass concentration was $68.7 \pm 23.6 \mu\text{g m}^{-3}$ during the campaign, including organic aerosol (41.9%), sulfate (28.8%), nitrate (11.0%), ammonium (14.5%) and chloride (3.7%). The diurnal cycles of OA, sulfate, nitrate and ammonium all rise to high peaks at morning and dusk due to transport of traffic emissions from upwind Guangzhou City. The average size distributions of the species were mainly dominated by an accumulation mode peaking at 500~600 nm. Calculations based on high-resolution organic mass spectra show that on average, C, H, O and N contributed 58.1, 7.3, 30.7, and 3.9% to the total organic mass, respectively. The average OM/OC ratio was 1.73 ± 0.08 . The Van Krevelen diagram of OA yielded a significant anti-correlation ($R^2=0.70$) between H/C and O/C, with a slope of -0.96.

REFERENCES

- [1] Xiao, R., N. Takegawa, M. Zheng, et al., Characterization and source apportionment of submicron aerosol with aerosol mass spectrometer during the PRIDE-PRD 2006 campaign. *Atmospheric Chemistry and Physics*, 11, 1891–1937, 2011. doi: 10.5194/acpd-11-1891-2011
- [2] Huang, X., L.-Y. He, M. Hu, et al., Highly time-resolved chemical characterization of atmospheric submicron particles during 2008 Beijing Olympic Games using an Aerodyne High-Resolution Aerosol Mass Spectrometer. *Atmospheric Chemistry and Physics*, 10, 25841 – 25869, 2010. doi: 10.5194/acpd-10-25841-2010
- [3] DeCarlo, P.F., J.R. Kimmel, A. Trimborn, M.J. Northway, J.T. Jayne, A.C. Aiken, M. Gonin, K. Fuhrer, T. Horvath, K. Docherty, D.R. Worsnop, and J.L. Jiménez, A Field-Deployable High-Resolution Time-of-Flight Aerosol Mass Spectrometer, *Analytical Chemistry*, 78, 8281-8289, 2006.
- [4] Jayne, J.T., D.C. Leard, X. Zhang, P. Davidovits, K.A. Smith, C.E. Kolb, and D.R. Worsnop, Development of an aerosol mass spectrometer for size and composition analysis of submicron particles, *Aerosol Sci. Technol.*, 33, 49-70, 2000.
- [5] Jimenez, J.L., J.T. Jayne, Q. Shi, C.E. Kolb, D.R. Worsnop, I. Yourshaw, J.H. Seinfeld, R.C. Flagan, X. Zhang, K.A. Smith, J. Morris, and P. Davidovits, Ambient Aerosol Sampling with an Aerosol Mass Spectrometer. *J. Geophys. Res. - Atmospheres*, 108(D7), 8425, doi:10.1029/2001JD001213, 2003.
- [6] Drewnick, F., S.S. Hings, P.F. DeCarlo, J.T. Jayne, M. Gonin, K. Fuhrer, S. Weimer, J.L. Jimenez, K.L. Demerjian, S. Borrmann, D.R. Worsnop. A new Time-of-Flight Aerosol Mass Spectrometer (ToF-AMS) – Instrument Description and First Field Deployment. *Aer. Sci. Technol.*, 39:637–658, 2005.
- [7] Jimenez Group Wiki. See <http://cires.colorado.edu/jimenez-group/ToFAMSResources/ToFSoftware/index.html> (accessed April 2011).
- [8] Canagaratna, M.R., J.T. Jayne, J.L. Jiménez, J.D. Allan, M.R. Alfarra, Q. Zhang, T.B. Onasch, F. Drewnick, H. Coe, A. Middlebrook, A. Delia, L.R. Williams, A.M. Trimborn, M.J. Northway, P.F. DeCarlo, C.E. Kolb, P. Davidovits, and D.R. Worsnop, Chemical and Microphysical Characterization of Ambient Aerosols with the Aerodyne Aerosol Mass Spectrometer, *Mass Spectrometry Reviews*, 26, 185-222, 2007.
- [9] Aiken, A.C., P.F. DeCarlo, and J.L. Jimenez. Elemental Analysis of Organic Species with Electron Ionization High-Resolution Mass Spectrometry. *Analytical Chemistry*, 79, 8350-8358, doi:10.1021/ac071150w, 2007.
- [10] Aiken, A.C., P.F. DeCarlo, J.H. Kroll, D.R. Worsnop, J.A. Huffman, K. Docherty, I.M. Ulbrich, C. Mohr, J.R. Kimmel, D. Sueper, Q. Zhang, Y. Sun, A. Trimborn, M. Northway, P.J. Ziemann, M.R. Canagaratna, T.B. Onasch, R. Alfarra, A.S.H. Prevot, J. Dommen, J. Duplissy, A. Metzger, U. Baltensperger, and J.L. Jimenez. O/C and OM/OC Ratios of

Primary, Secondary, and Ambient Organic Aerosols with High Resolution Time-of-Flight Aerosol Mass Spectrometry Environmental Science and Technology, 42, 4478–4485, doi: 10.1021/es703009q, 2008.

- [11] Heald, C.L. J.H. Kroll, J.L. Jimenez, K.S. Docherty, P.F. DeCarlo, A.C. Aiken, Q. Chen, S.T. Martin, D.K. Farmer, P. Artaxo, A.J. Weinheimer. A simplified description of organic aerosol composition and implications for atmospheric aging. Geophysical Research Letters, 37, L08803, doi:10.1029/2010GL042737, 2010.

Modification of dust particles through heterogeneous reactions uptake of SO₂ over Chinese continent during dust storm episodes

Weijun Li¹ and Longyi Shao²

1 Environment Research Institute, Shandong University, Jinan, Shandong, 250100, China

2 State Key Laboratory of Coal Resources and Safe Mining & College of Geoscience and Surveying Engineering, China University of Mining and Technology, Beijing 100083, P.R. China

Principal Contact: Weijun Li, Ph.D, Shandong University, Shanda Nanlu 27, Jinan, Shandong Province 250100, China.

Phone: 86-531-88364416, Email: liweijun@sdu.edu.cn

*Corresponding author Email: ShaoL@cumtb.edu.cn Tel/Fax: 86-10-62331248 ext. 8523

Abstract

Two dust episodes (D1: 13 February and D2: 28-29 March) of long-range transport from desert and loess sources and one dust episodes (D3: 30 March) mainly from local area were monitored in spring 2004 in Beijing, China. Scanning electron microscope with X-ray energy dispersive detector was applied to study morphologies, elemental compositions and the degree of modification of dust particles with radius from 0.1 to 6.4 μm . The morphological features of particles reveal that the three dust plumes carried both dust particles(90-98 % by number) and anthropogenic pollutants (e.g., fly ash and soot, 2-10 %) Compositions of individual mineral particles show that number percentages of the S-bearing dust particles in the D1 and D2 dust storms were higher than those in the D3 dust storm. Sulfur in mineral dust particles was through heterogeneous uptake of SO₂ during their transport. In all three dust episodes, fine dust particles (radius less than 1 μm) show a high degree of modification by SO₂. Dust particles of long-range transport also show a high degree of modification by SO₂. During the three dust storm periods, heterogeneous uptake of SO₂ on mineral particles would decrease SO₂ concentrations in air, and increase mass of the sulfates internally mixed with mineral dust.

Keywords: Asian dust storm, individual dust particle, aerosol particle, heterogeneous chemical reaction, mixing state

On-line Analysis and Mass Concentration Characters of Nitrate in Aerosol PM₁₀ in Beijing

Kai Zhang^{1,2}, Yuesi Wang², Tianxue Wen², Fahe Chai¹ and Guangren Liu²

1 Chinese Research Academy of Environmental Sciences, Beijing, 100012, China;

2 LAPC, Institute of Atmospheric Physics, Chinese Academy of Science, Beijing, 100029, China

ABSTRACT

Nitrate is one of the most important components in water-soluble aerosols. The nitrate in PM₁₀ measured from January 2004 to December 2005 in Beijing was determined using a system of combining rapid collection of fine particles and Ion Chromatography (RCFP-IC). The scientific research showed that the annual average concentration of water-soluble nitrate in PM₁₀ in the urban area in Beijing was about 9.2 (10.5 ± 5.3) $\mu\text{g}\cdot\text{m}^{-3}$ in 2004 and 8.9 (7.7 ± 3.0) $\mu\text{g}\cdot\text{m}^{-3}$ in 2005 respectively. The concentration of nitrate in summer and autumn was higher than that in spring and winter. Trends of the statistics diurnal variation of nitrate showed different in different seasons. In summer, the higher concentration appeared at forenoon and the lower appeared in the afternoon. While in winter, the higher concentration appeared in the afternoon and the lower appeared at forenoon. In summer and autumn, the diurnal variation of nitrate was different in 2004 and 2005. The typical diurnal variations of nitrate was analyzed in this paper, such as heating period and non-heating period, sunny day and rainy day, less polluted period and more polluted period. The relationship of nitrate and meteorological factors can be investigated using correlation analysis.

KEYWORDS

Beijing, PM₁₀, nitrate, water-soluble, diurnal variation

1. Introduction

Nitrate was one of the most dominant components in the water-soluble ions, which is also one of the most important components of the acid depositions^[1] (Baez et al., 1997). Nitrate plays an important role in physical and chemical processes in the atmosphere such as climate forcing, heterogeneous chemistry and cloud formation^[2] (Lee et al., 2002). Sun (2004)^[3] analyzed the concentration of nitrate in PM₁₀ in Beijing from 2002 to 2003, and the result of experiment showed the concentration of nitrate was $3.6\text{-}65.6\mu\text{g}\cdot\text{m}^{-3}$. Usually, the aerosol samples were collected in filter in sampling site and be analyzed in laboratory. As we all know, nitrate is a volatile substance. So this method would underestimate the concentration and the percent of

nitrate in aerosol^[4] (Wang and John, 1988). In this paper, the method of online automatic analysis of water-soluble was used to analyze the nitrate. The nitrate in PM₁₀ measured from January 2004 to December 2005 in Beijing was determined using a system of combining rapid collection of fine particles and Ion Chromatography (RCFP-IC). The annual average concentration, seasonal character, diurnal variation and typical daily variation of nitrate were analyzed.

2. Experimental Methodology

RCFP-IC system was used in the experiment, and the detail experimental theory of this system was in Wen et al.^[5] and Weber et al.^[6]. The concentration of NO-NO₂ was measured using the chemiluminescence reaction (ThermoModel 42C Trace Level) made by Thermo Environmental Instrument, USA.

The sampling instruments were installed on the roof of a building of State Key Laboratory of Atmospheric Boundary Layer Physics and Atmospheric Chemistry (LAPC), the Institute of Atmospheric Physics (IAP). The building is about 15 meters above the ground and located, near a residential area, in the northwest part of Beijing (39°58'N, 116°22'E) between the third and 4th ring roads of the city. There were no direct industrial sources of atmospheric pollutants. The experimental period ran continuously from January 2004 to 16 December 2005.

3. Results and Discussion

The scientific research showed that the annual average concentration of water-soluble nitrate in PM₁₀ in the urban area in Beijing was about 9.2 (10.2 ± 5.3) $\mu\text{g} \cdot \text{m}^{-3}$ in 2004 and 8.9 (7.7 ± 3.0) $\mu\text{g} \cdot \text{m}^{-3}$ in 2005 respectively. The concentration of nitrate in summer and autumn was higher than that in spring and winter. The concentration variation of nitrate in summer was related to solar radiation, precipitation, relative humidity, the concentration of NO_x and NOR (Nitrogen Oxidation Ratio), and in winter, which was related to wind speed and relative humidity.

Trends of the statistics diurnal variation of nitrate depended on seasons. In summer, the higher concentration appeared at forenoon (11:00-12:00) and the lower appeared in the afternoon (17:00-20:00). In spring, autumn and winter, the diurnal variation of nitrate was different in 2004 and 2005 (Fig.1, Fig.2). The diurnal variation of nitrate was different between heating period (15th November to 15th March, next year) and non-heating period (15th March to 15th November). During the heating period, the lowest concentration appeared in the forenoon. During the non-heating period, the lowest concentration appeared in the afternoon, and the concentration

increased after 8:00, and the highest concentration appeared at noon (11:00-12:00). After 12:00 the concentration decreased. The concentration of nitrate in heating period was 60%~70% compared with that in non-heating period. The nitrate took on different diurnal variation pattern in sunny day and in rainy day, and the daily average concentration of nitrate in rainy day decreased with the rainfall intensity increasing.

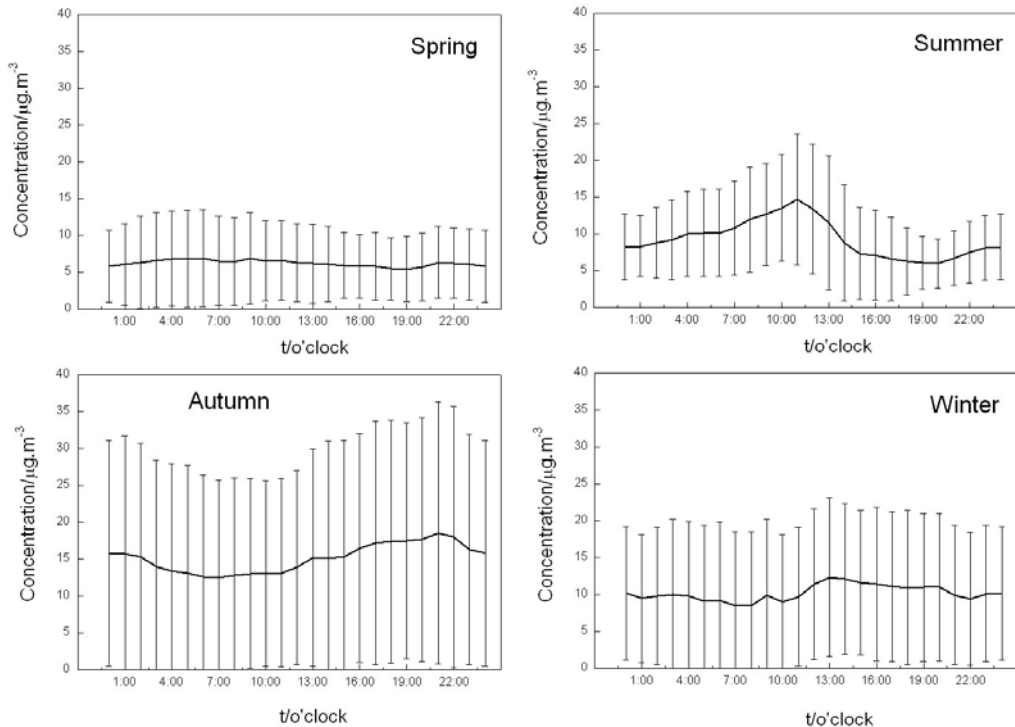


Fig. 1 Diurnal variation of nitrate in PM₁₀, 2004, in Beijing

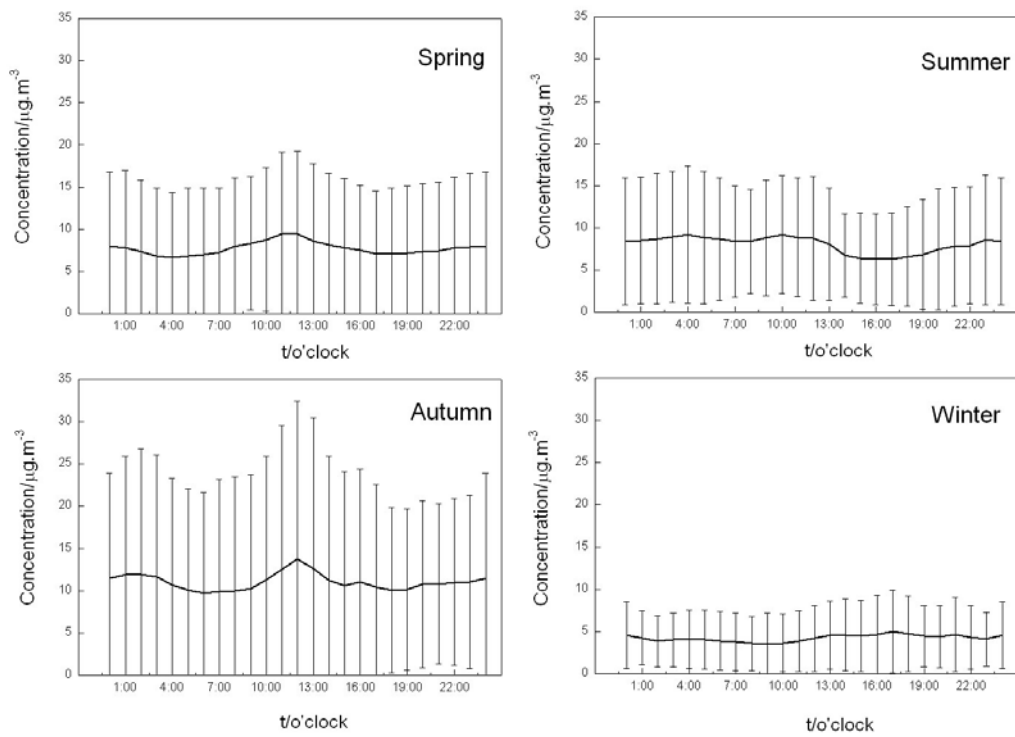


Fig. 2 Diurnal variation of nitrate in PM_{10} , 2005, in Beijing

The relationship of nitrate and meteorological factors can be investigated using correlation analysis. The result showed that in summer, the correlation between concentration of nitrate and wind speed was not obvious ($r=-0.35$), and the correlation coefficients between nitrate and relative humidity was 0.15. While in winter, the correlation between nitrate and wind speed showed negative value ($r=-0.44$), and the correlation between nitrate and relative humidity showed high positive value ($r=0.75$).

CONCLUSION

- (1) The annual average concentration of nitrate in PM_{10} was about $9\sim10 \mu\text{g}\cdot\text{m}^{-3}$.
- (2) The statistics diurnal variation of nitrate was different in different seasons.
- (3) The relationship of nitrate and meteorological factors (wind speed and relative humidity) was higher in winter than that in summer.

ACKNOWLEDGMENTS

This research was financially supported by Special Welfare Foundation for Environment Protection (201009001).

REFERENCES

- [1] Baez A.P., Belmont R.D., Padilia H.G., Chemical composition of precipitation at two sampling sites in Mexico: A 7-year study, *Atmospheric environment*, 1997, 31(6), 915-925.
- [2] Lee L. Y., Sequeira R., Water-soluble aerosol and visibility degradation in Hong Kong during autumn and early winter, 1998, *Environmental Pollution*, 2002, 116, 225-233.
- [3] Sun Y., Zhuang G. S., Wang Y., et al., The air-borne particulate pollution in Beijing – concentration, composition, distribution and sources. *Atmospheric Environment*, 2004, 38, 5990-6004.
- [4] Wang H. C., and John W., Characteristics of the Berner impactor of sampling inorganic ions, *Aerosol Science and Technology*, 1988, 8: 157-172.
- [5] Wen T.X., Wang Y.S., Chang S.Y., et al. On-line measurement of water-soluble ions in ambient particles, *Advances in atmospheric sciences*, 2006, 23(4): 586-592.
- [6] Weber, R.J., Orsini, D., Daun, Y., et al. A particle-into-liquid collector for rapid measurement of aerosol bulk chemical composition. *Aerosol Sci. Technol*, 2001, 35 (3), 718–727.

An Improved Thermal Oxidation Method for the Quantification of Organic and Black Carbon in Soot Based on the Difference of Pyrolytic Behavior

Mingyu Jiang, Zhuling Chen, Xinmei Wang and Fengfu Fu

Key Lab of Analysis and Detection Technology for Food Safety of Ministry of Education,
Department of Chemistry, Fuzhou University, Fuzhou, Fujian 350108, China

ABSTRACT

Pyrolysis combustion methods (also called as thermal oxidation methods) are widely used for the quantification of organic carbon (OC) and black carbon (BC) in aerosols. However, a part of OC aerosols undergoes charring to form pyrolytically generated elemental carbon (PEC) during OC evaporated in the inert atmosphere, and PEC seriously affects the accuracy of thermal oxidation method. In this study, the pyrolytic behaviors of OC, PEC and BC particles in both inert and air atmosphere have been studied in detail in order to develop a new correction method of PEC for the thermal oxidation method. Our results indicate that weight-loss rate of PEC is 5.6 times faster than that of BC particles at 500 °C in air atmosphere, although they begin to lose weight at approximately the same temperature. Based on the difference of the weight-loss rate between PEC and BC, a new method of PEC correction was advanced for the thermal oxidation method. With the help of the new PEC correction method and thermal analyzer, we successfully determined OC and BC concentrations in actual soot sample, atmospheric aerosol samples and artificial soot samples. The results obtained with our PEC correction method are consistent well with the real value or those analyzed with thermal-optical method, suggesting that the novel PEC correction method have a high accuracy.

KEYWORDS

Black carbon aerosols, Organic carbon aerosols, Thermal oxidation method, Soot.

Introduction

At present, a variety of techniques have been used to determine particulate OC and BC, these include thermal oxidation method and thermal-optical method. Thermal analysis is probably the most widely used technique for the determination of total OC and BC in the aerosols^[1]. In most of thermal techniques, the split between OC and BC is based on the temperature and/or the type of purge gas used for analysis^[2]. However, the results of BC concentration determined with thermal method are always higher than real concentration since a

fraction of OC undergoes charring to form PEC during the initial heating stage^[3]. In fact, the results of BC determined with thermal method included BC, PEC and refractory OC^[4]. In order to get more accurate BC concentration, an optical correction, which based either on optical transmittance or optical reflectance, has been applied in thermal-optical techniques to correct for this PEC. Although it is not currently possible to evaluate the accuracy of thermal-optical method since no BC standard exists that properly represents BC in the atmospheric sample, thermal-optical methods are considered to give the most reliable distinction between OC and BC at present^[5]. However the uncertainty in transmittance or reflectance measurement leads to uncertainty in the OC and BC concentrations, and another disadvantage of thermal-optical methods is that the analyzer is relatively expensive.

In order to obtain the difference of pyrolytic characteristics among OC, BC and PEC, which used to develop a new method of correcting PEC when the thermal oxidation method was used for the quantification of organic and black carbon in aerosols. The pyrolytic characteristics of OC aerosols, BC aerosols and PEC have been studied in detail in both inert and air atmosphere in this study.

Experimental Methods

Soot samples were collected from the exhaust of a diesel-fuelled bus by a high volume air sampler (10-810, ThermoFisher Scientific, USA). All-sized particles were collected on a piece of aluminum plate. The BC particles were separated from other carbonaceous aerosols with a method reported in our previous paper^[6].

A thermal analyzer of SDT Q600 (TA Company, American), which has a balance with sensitivity of 0.1 µg and a temperature precision of 0.01 °C, was used to study the pyrolytic characteristics of BC particles, OC and PEC. The pyrolytic characteristics of BC particles, OC and PEC were studied in both inert atmosphere and air atmosphere, respectively. In the case of inert atmosphere, sample was determined at a flow rate of 100 ml/min pure N₂ gas, and in the case of air atmosphere, sample was analyzed at a flow rate of 100 ml/min pure air. About 2.00 mg of sample was used for each thermal analysis.

Results and Discussion

1. The pyrolytic behaviors of OC and BC particles in inert atmosphere

The pyrolytic behaviors of OC and BC were studied in the range of 30-1000 °C by using thermal analyzer at a 100 ml/min flow of N₂ and a 10 °C/min rate of rising temperature. The thermal results were observed: 1) OC began to lose its weight when the temperature reached 400 °C and OC can not be evaporated completely even if the temperature rises to 1000 °C, indicating that some OC was charred to form PEC and a part of refractory OC or inorganic salt existed. 2) the weight of BC particles almost remained unchanged under 400 °C, BC particles began to lose

its weight when the temperature reached 550 °C.

2. The pyrolytic behaviors of PEC and BC particles in air atmosphere

The pyrolytic behaviors of PEC and BC particles in air atmosphere were studied in the range of 30-1000 °C by using the thermal analyzer in pure air at a flow rate of 100 ml/min and a 10 °C/min of the rate of rising temperature. The results indicated that PEC and BC began to lose their weight at a similar temperature, but the temperatures of the fastest weight-loss rate are quite different. The PEC derived from the charring of OC will increase the thermal analytical results of BC, and the effect of PEC could not be eliminated completely by controlling the temperature and time of combustion since the pyrolytic behaviors of PEC and BC in air atmosphere are similar.

3. The difference of weight-loss rate between BC and PEC in air atmosphere

In order to eliminate the disturbance of PEC, the decomposition rate of BC and PEC derived from the charring of humic acid was measured at 400 °C, 500 °C and 600 °C in air atmosphere (see Figure 1). The TG and DTG curves shown in Figure 1 reveal that the weight-loss rate (decomposition rate) of PEC and BC are quite different in air atmosphere, the weight-loss rate of PEC is much faster than that of BC and the difference of weight-loss rate between PEC and BC varied as a function of temperature. According to the TG and DTG curves in Figure 1, we calculated that the average ratio ($n=5$) of weight-loss rate between PEC and BC (R_{PEC}/R_{BC}) is 3.4 ± 0.2 at 400 °C, 5.6 ± 0.2 at 500 °C and 1.1 ± 0.1 at 600 °C.

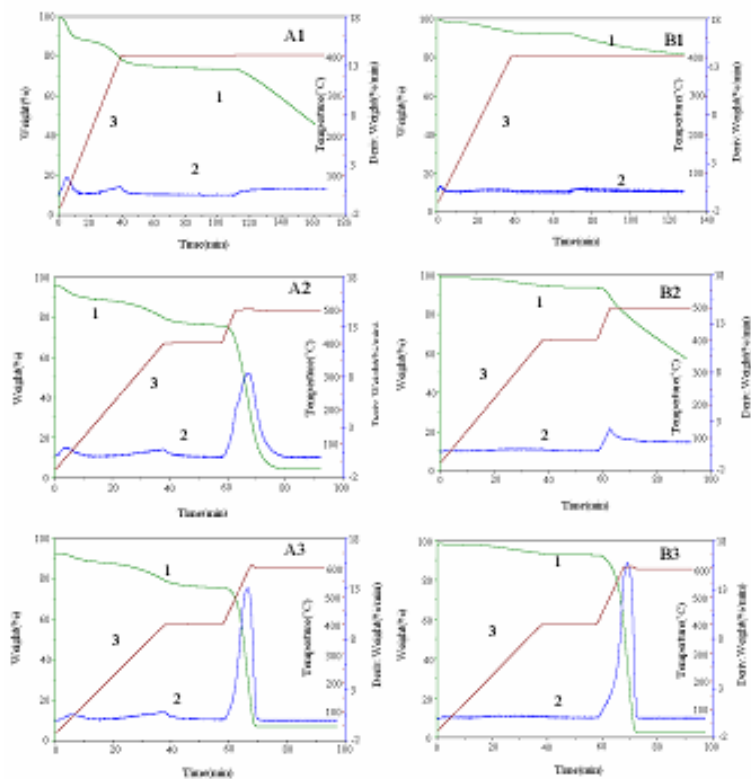


Figure 1: The difference of weight-loss rate between PEC and BC particles in air atmosphere at different temperature. 1 is TG curve, 2 is DTG curve and 3 is temperature curve. A1: OC (humic acid) was pyrolyzed and charred to form PEC at 400 °C in inert atmosphere and then was combusted at 400 °C in air atmosphere, B1: BC particles were heated at 400 °C in inert atmosphere and then were combusted at 400 °C in air atmosphere. A2: OC (humic acid) was pyrolyzed and charred to form PEC at 400 °C in inert atmosphere and then was combusted at 500 °C in air atmosphere, B2: BC particles were heated at 400 °C in inert atmosphere and then were combusted at 500 °C in air atmosphere. A3: OC (humic acid) was pyrolyzed and charred to form PEC at 400 °C in inert atmosphere and then was combusted at 600 °C in air atmosphere, B3: BC particles were heated at 400 °C in inert atmosphere and then were combusted at 600 °C in air atmosphere. About 2 mg of sample was used for each experiment.

4. A novel PEC correction method based on the difference of pyrolytic behaviors between BC and PEC

The experimental results shown in Figure 1 reveal that the PEC combusts much faster than BC particles at 500 °C in air atmosphere, therefore, the interference caused by PEC can be corrected with a proper mathematics treatment. Based on above deduction, we developed a novel correction method of PEC for the thermal oxidation method. The detailed process is: carbonaceous aerosols sample was firstly heated at 400 °C for 20 min in an inert atmosphere to evaporate a part of OC (first heating step), then sample was combusted at 500 °C for 10 min in air atmosphere to combust all PEC (second heating step). And, finally the samples were combusted at 600 °C for 20 min in air atmosphere to completely combust BC particles (third heating step).

The weight-loss in the first heating step (at 400 °C in inert atmosphere) is volatile OC (VOC), the weight-loss in second heating step (at 500 °C in air atmosphere) is PEC and part of BC (BC_1), in third heating step (at 600 °C in air ambience) is another part of BC (BC_2) and residues is inorganic salt. If the weight-loss of a real sample in the first heating step is $P_1\%$, in the second heating step is $P_2\%$ and in the third heating step is $P_3\%$, then we obtained: the concentration of BC is:

$$C_{BC} = P_3 \% + \frac{P_2 \%}{6.6} \quad (I)$$

and the concentration of OC is:

$$C_{OC} = P_1 \% + \frac{5.6 \times P_2 \%}{6.6} \quad (II)$$

CONCLUSION

Our results indicated that a part of OC is evaporated by heating at 400 °C in inert atmosphere and a part of OC was charred to form PEC during this step. The combusting

temperature of PEC is quite similar to that of BC in air atmosphere. Therefore, the presence of PEC seriously disturbs the quantification of BC when thermal oxidation method was used to detect it. The weight-loss rate of PEC is quite different from that of BC in air atmosphere. The weight-loss rate of PEC was calculated to be 5.6 times faster than that of BC particles at 500 °C in air atmosphere. Based on the difference of weight-loss rate between PEC and BC, a new method of PEC correction was developed for the thermal oxidation method in the quantification of BC and OC in carbonaceous aerosols. Using the novel PEC correction method and thermal analyzer, we have successfully determined the BC and OC concentrations in artificial and actual soot samples with a RSD (n=5) smaller than 10%.

ACKNOWLEDGMENTS

This work was financially support by the National Natural Science Foundation of China (40875087).

REFERENCES

- [1] Turpin, B. J.; Cary, R. A.; Huntzicker, J. J. *Aerosol Sci. Technol.* 1990, 12, 161-171.
- [2] Fung, K. *Aerosol Sci. and Technol.* 1990, 12, 122-127.
- [3] Yu, J. Z.; Xu, J. H.; Yang, H. *Environ. Sci. and Technol.* 2002, 36, 754-761.
- [4] Novakov, T.; Corrigan, C. E. *Mikrochimica Acta* 1995, 119, 157-166.
- [5] Viidanoja, J.; Kerminen, V. M.; Hillamo, R. *Aerosol Sci. and Technol.* 2002, 36, 607-616.
- [6] Fu, F-F; Watanabe, K.; Shinohara, N.; Xu, X. Q.; Xu, L. J.; Akagi, T. *Sci. Total Environ.* 2008, 393, 273-282.

The Emission Factor and Chemical Characteristics of Particulate N-alkanes Originated from the Combustion of Different Fossil Fuel and Biomass

Yiqing Wu, Gongshi Lin and Fengfu Fu

Key Lab of Analysis and Detection Technology for Food Safety of Ministry of Education,
Department of Chemistry, Fuzhou University, Fuzhou, Fujian 350108, China

ABSTRACT

In order to obtain the emission factor and the chemical signatures of n-alkanes to help we identify the sources of particulate n-alkanes in the atmosphere, different carbonaceous aerosols were generated by burning different fossil fuels and biomass under different conditions in lab and their chemical characteristics of 26 n-alkanes was studied in detail by using gas chromatography-mass spectrometry. The experimental results showed that: (a) In the case of domestic burning, the emission factor of particulate n-alkanes with an order of diesel fuel > leaf of woody plant \approx herbaceous plant > bituminous coal > stem of woody plant \approx gasoline > heavy oil. (b) the domestic burning of biomass and coal mainly emitted the particulate n-alkanes with a carbon chain longer than 25, whereas, the burning of fossil oils mainly emitted the particulate n-alkanes with a carbon chain shorter than 25. (c) the particulate n-alkanes derived from the domestic burning of biomass have a high CPI, whereas, that derived from the domestic burning of fossil fuels have a lower CPI, indicating that the CPI are suitable for the use as signatures of particulate n-alkanes in the atmosphere.

KEYWORDS

Particulate n-alkanes, Aerosols, Emission factor, Carbonaceous aerosols

Introduction

In general, particulate n-alkanes are mainly from two types of sources: anthropogenic source and biogenic source. The anthropogenic source includes the combustion of different fossil fuels and biomass, and the biogenic source includes particles emitted from the plants waxes, pollen and bacteria etc^[1]. Many studies have revealed that particulate n-alkanes originated from anthropogenic source and biogenic source have quite different chemical characteristics. For example, particulate n-alkanes originated from anthropogenic source has a lower CPI (concentration ratio of the odd/even terms in the series) and shorter carbon-chain, whereas, those originated from biogenic source has a much higher CPI and relative long carbon-chain^[2, 3]. These

features make n-alkanes become a useful marker for the sources identification of fine aerosols and have been used in the chemical mass balance model for the source apportionment of fine aerosols^[4]. Today, the anthropogenic source is becoming a major source of particulate n-alkanes in megacities, so, the study on the emission factor and chemical signatures of particulate n-alkanes from the burning of different fossil fuels and biomass is of great significance. In this study, we generated different carbonaceous aerosols by burning different fossil fuels and biomass under different conditions in lab and determined 26 n-alkanes in each carbonaceous aerosols sample, in order to obtain the emission factor and the chemical signatures or characteristic factors of particulate n-alkanes originated from different anthropogenic sources. We also hope to provide our data as a database, to help we study the source identification of particulate n-alkanes in the atmosphere and further understand the impact of anthropogenic n-alkanes on global climate system.

Experimental Methods

A Model series 10-810 air sampler (Thermo Instrument, GA, USA) was employed for the collection of different carbonaceous aerosols. Carbonaceous aerosols derived from the domestic burning of bituminous coal, diesel fuel, gasoline, heavy oil, herbaceous plant and woody plant were generated by burning above fossil fuels or biomass on a furnace as closely as household one used in China. Suitable amount of each above fossil fuel or biomass was burnt on an open fire in a completely uncontrolled manner, and then all-sized aerosols were collected on a quartz filter during all burning process with a flow rate of 28.3 L/min. The quartz filters (Pall flex 2500 QAT-UP) used in the experiments has a collection efficiency of 99.99% for 0.3μm sized particles.

Results and Discussion

1. The emission factor of n-alkanes from the combustion of different fossil fuels and biomass

Our results showed that the carbonaceous aerosols derived from the combustion of biomass and coals contained 26 n-alkanes from n-C11 to n-C36, whereas, the carbonaceous aerosols derived from the combustion of fossil oil contained only 22 n-alkanes from n-C11 to n-C32. The emission factors revealed that: 1) the domestic burning of diesel oil has much more strong ability of emitting particulate n-alkanes in comparison with biomass and coal, although the aerosols originated from the domestic burning of diesel oil has a much lower concentration of total n-alkanes than the aerosols originated from the domestic burning of biomass and coals. 2) for woody plant, the burning of leafs has a much more strong ability of emitting particulate n-alkanes than stem, this may be attributed to the reason that the leaves contain more of the plant wax. 3) the high-temperature combustion of fossil oil seem emitted much fewer particulate n-alkanes in comparison with the domestic burning, although the n-alkanes emission factor of the high-temperature combustion of diesel oil was not calculated since we did not accurately measure the

consumption of oil during the sampling of aerosols.

2. Chemical Characteristics of particulate n-alkanes derived from the domestic burning of different biomass and fossil fuels.

Figure 1 showed the percentage of each n-alkane in total n-alkanes (the concentration ratio of each n-alkane to the total n-alkanes) in the carbonaceous aerosols derived from the burning of different biomass and fossil fuels. As showed in Figure 1, the carbonaceous aerosols derived from the combustion of biomass and coals contained 26 n-alkanes from n-C11 to n-C36, whereas, the carbonaceous aerosols derived from the combustion of fossil oil contained only 22 n-alkanes from n-C11 to n-C32. In addition, we found that carbonaceous aerosols derived from the domestic burning of biomass have a high contribution of the max concentration of n-alkanes in the total n-alkanes and a CPI much bigger than 1. Whereas, carbonaceous aerosols derived from the domestic burning of fossil fuels have not a high contribution of the max concentration of n-alkanes in the total n-alkanes and a CPI closed to 1. All above facts indicated that the C_{max} and CPI are suitable for use as signatures of particulate n-alkanes in the atmosphere.

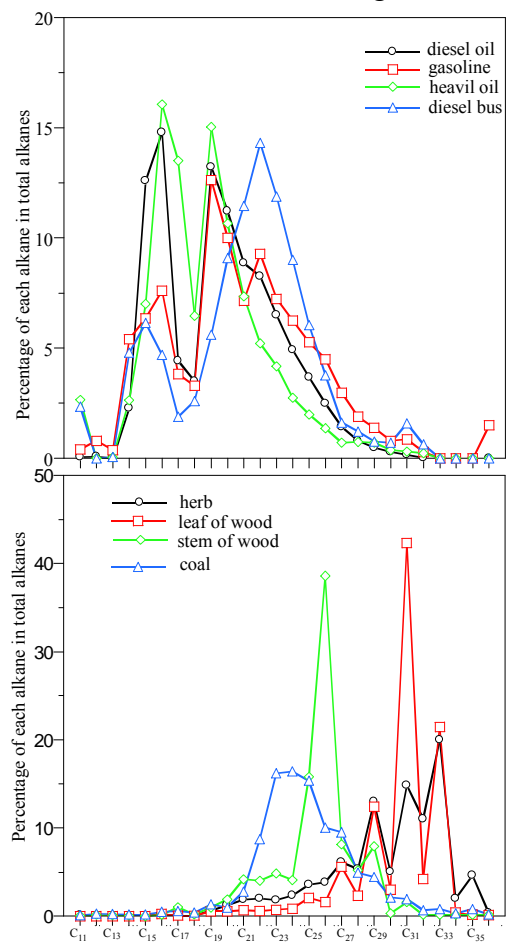


Figure 1: The percentage of each n-alkane in total n-alkanes (the concentration ratio of each n-alkane to the total n-alkanes) in carbonaceous aerosols derived from the burning of

different biomass and fossil fuels.

ACKNOWLEDGMENTS

This work was financially support by the National Natural Science Foundation of China (40875087).

REFERENCES

- [1] Brown, S. G.; Herckes, P.; Ashbaugh, L.; Hannigan, M. P.; Kreidenweis, S. M.; Collett, J. L. *Atmospheric Environment* 2002, 36, 5807-5818.
- [2] Pietrogrande, M. C.; Mercurialt, M.; Perrone, M. G.; Ferrero, L.; Sangiorgi, G.; Bolzacchini, E. *Environ. Sci. Technol.* 2010, 44, 4232-4240.
- [3] Lin, J. J.; Lee, L. C. *Atmospheric Environment* 2004, 38, 2983-2991.
- [4] Zheng, M.; Cass G. R.; Schauer, J. J.; Edgerton, E. S. *Environ. Sci. Technol.* 2002, 36, 2361-2371.

Investigation about the Association of Children's Lung Function and Air Pollution in Kaohsiung City

Yu-Ju Ke², Chih-Sean Ou², and Pei-Shih Chen¹

1 Department of Public Health, Kaohsiung Medical University 100, Shih-Chuan 1st Road, Kaohsiung, 80708, Taiwan

2 Graduate Institute of Occupational Safety and Health, Kaohsiung medical university 100, Shih-Chuan 1st Road, Kaohsiung, 80708, Taiwan

Principal Contact: Pei-Shih Chen, Department of Public Health, Kaohsiung Medical University 100, Shih-Chuan 1st Road, Kaohsiung, 80708, Taiwan.

Tel: +886-7-312-1101-2141-34 Fax: +886-7-321-2062 E-mail: pschen@kmu.edu.tw

Abstract

Recently, the association between the air pollution and human health has been widely mentioned. Children are more sensitivity to air pollution than adult. In present studies, they measured children's lung function and air pollutants (CO, CO₂, NO₂, O₃, PM₁, PM_{2.5}, PM₁₀, ultrafine, fungal and bacterial) in classrooms to evaluate the association.

Three elementary schools, were selected in Kaohsiung City (Background, Industry and Traffic). Twenty classrooms were randomly selected in each school. Temperature, relative humidity, CO, CO₂, NO₂, O₃, PM₁, PM_{2.5}, PM₁₀, ultrafine were monitored in real-time from 8 am to 4 pm between April 2009 and November 2009. We also sampled fungal and bacterial in indoor and outdoor of classroom at 8 am and 4 pm. TSZ and MEA were used for cultivated of bacteria and fungus, respectively. Lung function was measured for 1026 schoolchildren. To investigate the explainability of air pollution for children's lung function, we analyze the concentration and the abnormal rate of lung function in the same classroom by using multiple regression.

Analyzing the abnormal rate of lung function's parameter, if combine these schools, the indoor fungus ($R^2=10\%$); ultrafine ($R^2=12\%$); PM_{2.5} ($R^2=8\%$) can significant affect the VC abnormal rate's change. In each school, Traffic is PM_{2.5} and ultrafine (each $R^2=20\%$), Industry is the indoor fungus and CO ($R^2=12\%$ and 39%), Background is only temperature ($R^2=12\%$). In the part of FVC, there are only combination of three schools have the significant variable

can affect the product variable's change for PM_{2.5} ($R^2=6\%$), ultrafine ($R^2=6\%$) and indoor fungus ($R^2=15\%$)

In this study we observed the difference schools have different air pollutions to affect the lung function's abnormal rate. The true measurement of school children's lung function data and the abnormal rate can help us to understand the acute effect of the air pollution on the lung function.

Keywords: Lung function, air pollution, children

Indoor Air Monitoring in Day-care Centers

Yu-Ju Ke², Yi-Lien Lee¹, and Pei-Shih Chen¹

1 Department of Public Health, Kaohsiung Medical University 100, Shih-Chuan 1st Road, Kaohsiung, 80708, Taiwan

2 Graduate Institute of Occupational Safety and Health, Kaohsiung medical university 100, Shih-Chuan 1st Road, Kaohsiung, 80708, Taiwan

Principal Contact: Pei-Shih Chen, Department of Public Health, Kaohsiung Medical University 100, Shih-Chuan 1st Road, Kaohsiung, 80708, Taiwan.

Tel: +886-7-312-1101-2141-34 Fax: +886-7-321-2062 E-mail: pschen@kmu.edu.tw

Abstract

Nowadays, most children stay in day-care centers for a long time. Recent studies indicated, the incidence of many infectious diseases in day-care center children particularly respiratory symptoms were greater than those in home care children. A possible pandemic caused by influenza virus in the near future. There is need to monitor indoor air quality, especially airborne influenza virus concentration in day-care center. Therefore, the aim of this study is to monitor the airborne influenza A and B virus in two day-care centers with different ventilation form.

Environmental monitoring was from August 2006 to January 2007. Day-care center A was near a busy traffic street and with both natural ventilation and air conditioning while center B was only with air-conditioning system and located in a small lane. The sampling parameter are as follow: the concentration of bacteria and fungus, influenza virus in the air , indoor meteorological factors, particle numbers, CO and CO₂ were also measured simultaneously. The seasonal variation is also investigated (Summer, Fall and Winter) to investigating the relation between the concentration of airborne pathogen and occurrence of respiratory infections.

Airborne influenza A and B virus were both successfully quantified from two centers by filter and real-time qPCR. The mean concentration of 179 samples of influenza A and B virus is 8.03×10^4 copy/m³ and 1.59×10^5 copy/m³. The average of influenza A virus is significantly higher in summer ($p = 0.019$). The positive rate of influenza A and B virus is 29% and 53%.

Comparing different ventilation system from two centers, the air contaminant : total cultivable

bacteria, CO and CO₂ concentration : center A > center B ($p <0.01$). The positive rate of influenza A and B virus: B>A ($p <0.05$). The mechanical exhaust system with less fresh air of center B might be the reason.

Keywords: Indoor air, influenza virus

Real-time monitoring of PM_{2.5} in primary school

Yi-Chieh Chen¹ and Pei-Shih Chen¹

1 Department of Public Health, Kaohsiung Medical University 100,Shih-Chuan 1st Road,Kaohsiung,80708,Taiwan.

Principal Contact: Pei-Shih Chen, Department of Public Health, Kaohsiung Medical University, 100,Shih-Chuan 1st Road, Kaohsiung, 80708, Taiwan,
Tel:[+886-7-312-1101~2141-34](#) Fax: +886-7-321-2062 E-mail: pschen@kmu.edu.tw

Abstract

Introduction:

PM_{2.5} may increase the risk of heart disease, stroke and some cardiovascular diseases. In this study, we monitored PM_{2.5} in the classrooms of the primary schools in Kaohsiung.

Methods:

Three primary schools, industrial, traffic, and background school, were selected to assess PM10, PM2.5, and PM1 concentration. The distance between EPA's Monitoring Station and industrial, traffic, and background school, is about 300 m, 0 m, and 537 m, respectively. Real-time monitoring of PM2.5 from 08:00 to 16:00 was held simultaneously indoor and outdoor of the classroom to a total of 26 and 35 classrooms during April 13th, 2009 to Jun 13th, 2009 and September 7th, 2009 to November 6th, 2009, respectively (DUSTTRAK™ Aerosol Monitor ; Model 8520, TSI USA).

Results:

We found that the trends of indoor and outdoor PM_{2.5} were the same, and the concentration of indoor PM_{2.5} is higher than outdoor PM_{2.5} in the classrooms of the schools. The concentrations of indoor and outdoor PM_{2.5} in fall were significantly higher than in spring. For I/O ratio, the indoor concentrations of PM_{2.5} were significantly higher than outdoor PM_{2.5} concentrations in both spring and fall in traffic, and background school. The relationship between the indoor concentrations of PM_{2.5} in classrooms and the data from monitoring stations was not significant. The typical trend of hour-average PM_{2.5} in the classrooms was shown in Figure 1. The hour-average trend of indoor and outdoor concentration was similar and the indoor concentration was higher than outdoor. But the data from the monitoring station was lower than the indoor and outdoor hour-average concentrations in classrooms. It was indicated that the data from the monitoring stations could not represent of the actually exposure of school children.

Keywords: PM_{2.5}, primary school, indoor, outdoor.

The distribution of PM₁₀, PM_{2.5}, and PM₁ concentrations in primary school in Kaohsiung City

Yi-Chieh Chen¹ and Pei-Shih Chen^{1*}

¹* Department of Public Health, Kaohsiung Medical University 100, Shih-Chuan 1st Road,Kaohsiung,80708,Taiwan.

Principal Contact: Pei-Shih Chen, Department of Public Health, Kaohsiung Medical University, 100,Shih-Chuan 1st Road, Kaohsiung, 80708, Taiwan,

Tel:[+886-7-312-1101](tel:+886-7-312-1101)~[2141-34](tel:+886-7-2141-34) Fax: +886-7-321-2062 E-mail: pschen@kmu.edu.tw

Abstract

Introduction:

PM₁₀, PM_{2.5} and PM₁ may increase the risk of heart attack, stroke and some cardiovascular diseases. Lung function of school children, the susceptible groups, could be decreased by particulate matter. Although Kaohsiung is an industrial city, there's no any study aiming the particular matter exposure of the school children in Kaohsiung. Therefore, the purpose of this study is to evaluating PM₁₀, PM_{2.5}, and PM₁ concentration in school children's classrooms in Kaohsiung.

Methods:

Three primary schools, industrial, traffic, and background school, were selected to assess PM₁₀, PM_{2.5}, and PM₁ concentration. Real-time monitoring of PM₁₀, PM_{2.5}, PM₁ from 08:00 to 16:00 was held in the classroom to a total of 26 and 35 classrooms during April 13th, 2009 to Jun 13th, 2009 and September 7th, 2009 to November 6th, 2009, respectively (DUSTTRAK™ Aerosol Monitor ; Model 8520, TSI USA). In addition, PM₁₀, PM_{2.5}, and PM₁ concentration were simultaneously monitoring indoor and outdoor in the morning and afternoon.

Results:

The concentrations of PM₁₀, PM_{2.5}, and PM₁ in fall were significantly higher than that in spring. In spring, three schools' means of PM₁/PM₁₀ was 0.84, 0.81, and 0.86 in industrial, traffic, and background school, respectively, whereas the means of PM_{2.5}/PM₁₀ was 0.87, 0.84, and 0.88 respectively. In fall, the means of PM₁/PM₁₀ was 0.91, 0.90, and 0.88; the means of PM_{2.5}/PM₁₀ are 0.93, 0.91, and 0.88 in industrial, traffic, and background school, respectively. The means of the ratio in fall were significantly higher than in spring. Furthermore in fall, there was significantly medium positive correlation between the PM₁₀ concentration of monitoring stations and classroom in traffic and industrial school.

Conclusion:

The concentration of PM₁₀ in the classrooms and data from air monitoring station indicated that the data from the air monitoring station could not represent the exposure of the personal school children.

Keywords: PM₁₀, PM_{2.5}, PM₁, primary school.

Airborne Mycobacterium tuberculosis Profiles in a Hospital with a Nosocomial TB outbreak

Wei-Che Houng¹ and Pei-shih Chen^{1*}

1 Department of Public Health, Kaohsiung Medical University

Principal Contact: Pei-shih Chen, 100, Shih-Chuan 1st Road,Kaohsiung,80708,Taiwan.

Tel: 886-7-312-1101~2141-34 E-mail: cool996862@gmail.com

Abstract

The main purpose of this study was assessing the airborne Mycobacterium tuberculosis profiles in this hospital to identify the high risk area. In addition, the difference of airborne Mycobacterium tuberculosis concentration before and after ventilation improvement was also evaluated.

The airborne samples were collected by a Nuclepore filter with sampling time of 8 hr at sampling flow rate of 20 L/min. A total of 192 air samples were taken from negative pressure isolation wards, medical wards, waiting rooms and consulting rooms of medical department and pediatric department in the period of December 2005 to July 2006. The concentration of airborne M. tuberculosis was quantitatively determined by the ABI 7700 real-time quantitative polymerase chain reaction (real time qPCR) system.

It was found that the positive rate of airborne M. tuberculosis is 6.25%. In addition, all positive samples were in the wards of chest and infectious disease division in internal medicine department. The airborne M. tuberculosis concentration was in the range of 54 copies/m³ to 1109 copies/m³. The highest concentration was found in the nursing station of chest division. After improvement of ventilation system, no M. tuberculosis was detected in the air. In addition, the airborne bacteria concentrations were also declining after the improvement. Our results showed that the improvement of air conditioning may reduce the risk of M. tuberculosis exposure. In addition, it was found a good correlation between M. tuberculosis and airborne bacteria.

In regard to the culturable bacteria and fungi concentration in the air, 122 samples were analyzed in the hospital. According to the IAQ Recommended Values of Taiwan EPA, the failure rate was 64% and 8% for bacteria and fungi, respectively. In addition, the airborne bacteria concentrations in the nursing station of chest division were all higher than the recommended values, even after the improvement of ventilation.

Keywords: M. tuberculosis, outbreak ,real time qPCR.

Exposure Assessment of Ozone in elementary school in Kaohsiung,Taiwan

Wei-Che Houng¹, Pei-shih Chen^{1*}

1.Department of Public Health, Kaohsiung Medical University

Principal Contact: Pei-shih Chen , 100, Shih-Chuan 1st Road,Kaohsiung,80708,Taiwan.

Tel: 886-7-312-1101~2141-34 E-mail: cool996862@gmail.com

Abstract

In the previous studies, children's health effect was related to ozone. Kaohsiung daily average ozone concentration is much higher than the average of Taiwan. The objective of this study is to evaluate the ozone concentration in elementary schools in Kaohsiung.

From April to June (spring) and September to November (autumn) in 2009, 62 classrooms were selected from three elementary schools in Kaohsiung to monitor indoor and outdoor ozone by Ozone Monitor Model 202 (2B Technologies, Inc) in real-time for continuous eight hours.

In spring, the indoor and outdoor ozone concentration were from 6.06 to 93.52 ppb and 11.78 to 53.33 ppb, respectively, with failure rate of 58% and 0%, respectively, when comparing to the recommendation of Taiwan Environment Protection Administration (30ppb). In fall, the indoor and outdoor ozone concentration was from 7.6 to 86.1 ppb and 7.14 to 94.57 ppb, respectively, with failure rate was 77% and 46%, respectively.

The concentration of ozone rose in the morning and the maximum value appeared between 11:00 to 12:00. In autumn, the outdoor ozone concentrations were slightly higher than indoor in three schools. Indoor/Outdoor ratios (I/O ratios) of ozone varied in a range from 0.9 to 1.1. I/O ratios observed in our studies were higher than that in other previous studies. From our studies, high failure rate and high I/O ratio observed in spring and autumn in Kaohsiung implied that indoor ozone exposure of children in classroom should be an important issue and need further studies of its health effect.

Keywords: ozone I/O ratios.

Characterization of the bacterial and fungal bioaerosols in three elementary school in Kaohsiung

Pei-Chun Yen², Pei-Shih Chen^{1*}, and Chih-Sean Ou²

1 Department of Public Health, Kaohsiung Medical University 100, Shih-Chuan 1st Road, Kaohsiung, 80708, Taiwan

2 Graduate Institute of Occupational Safety and Health, Kaohsiung medical university 100, Shih-Chuan 1st Road, Kaohsiung, 80708, Taiwan

Principal Contact: Pei-Shih Chen, Department of Public Health, Kaohsiung Medical University 100, Shih-Chuan 1st Road, Kaohsiung, 80708, Taiwan.

Tel: +886-7-312-1101-2141-34 Fax: +886-7-321-2062 E-mail: pschen@kmu.edu.tw

Abstract

Recently, indoor air quality (IAQ) including bioaeorosls at school had drawn much attention by people. In South Taiwan, the average temperature and total cumulative rainfall in 2009 is 23.7°C and 1756.3 mm. It's a great environment for fungi and bacteria. Therefore, we tried to characterize the distribution of the fungal and bacterial bioaeorosols in classrooms in three elementary schools in Kaohsiung.

Three primary schools, industrial, traffic, and background school, were selected to assess PM₁₀, PM_{2.5}, and PM₁ concentration. The distance between EPA's Monitoring Station and industrial, traffic, and background school, is about 300 m, 0 m, and 537 m, respectively. Total number of 27 classrooms was evaluated both indoor and outdoor during April 13th to Jun 13th, 2009. Bacterial and fungal bioaerosols were sampled at 8 am and 3 pm(MAS-100 ; MERCK, USA)and cultivated in Tryptic soy agar(TSA)and Malt extract agar(MEA), respectively. Colony-Forming Unit (CFU) after 24hr and 48hr were counted for bacteria and fungi, respectively.

The average concentration of bacterial bioaerosols inside classrooms in traffic, industry, and background school was 785.3 \pm 538.4 CFU/m³(means \pm SD), 383.1 \pm 138.5 CFU/m³, 904.1 \pm 610.8 CFU/m³, respectively, whereas the average concentration of bacterial bioaerosols outside classrooms was 444.2 \pm 201 CFU/m³,231.5 \pm 68.6 CFU/m³,623.6 \pm 510.7 CFU/m³, respectively. For fungal bioaerosols, the average indoor concentration at traffic, industry, and background school was 471.9 \pm 295.8 CFU/m³(means \pm SD),354.2 \pm 194.8 CFU/m³ and 998.8 \pm 536 CFU/m³, respectively. Whereas the average concentration of fungal bioaerosols outside classrooms was 491.1 \pm 379.2, 239.6 \pm 166.7, 1448.2 \pm 649.3, respectively.

The result both bacteria and fungal was shown that indoor concentration was higher than the outdoor concentration in most cases.

There are not only the environment but the micro-environment can affect the concentration of bacteria and fungus in classroom in school, instead of the industry school, many classroom's concentration of fungus and bacteria bioaerosols have show to above the guideline value of the IAQ in Taiwan, it's require to pay more attention about this topic

Keywords: airborn; bacteria, bacteria, elementary school

Characterization of organic particles from incense burning using a high-resolution time-of-flight aerosol mass spectrometer

Yong Jie Li¹ and Chak Keung Chan^{1,2}

1 Division of Environment

2 Department of Chemical and Biomolecular Engineering, Hong Kong University of Science and Technology, Clear Water Bay, Kowloon, Hong Kong, China

Principal Contact: Chak Keung Chan, Prof., Division of Environment, Department of Chemical and Biomolecular Engineering, Hong Kong University of Science and Technology, Clear Water Bay, Kowloon, Hong Kong, China.

Tel: 852-23587124 Email: keckchan@ust.hk

Abstract

Incense burning serves a number of purposes in various settings, including in temples/churches, in residential homes, and even as a way of spiritual therapy. This practice generates a large amount of particulate matters (PM) in indoor, and sometimes outdoor (e.g., busy temples) environments. A better understanding of the impacts of incense burning to human health requires more chemical information of the particles emitted from incense burning. Organic particles from incense burning were characterized by the Aerodyne high-resolution time-of-flight aerosol mass spectrometer (HR-ToF-AMS). Results from both unit mass resolution (UMR) and high resolution (HR) mass spectra showed that particles from incense burning highly resemble those from other biomass burning processes. In UMR mass spectral data, three groups of ions including the homologous series, the sugar- and aromatic-related ions, and the lignin-related ions, were found to be of relatively high intensity in particles from burning all three types of incense, including incense sticks, incense coils, and mosquito coils. Ion peaks with m/z values higher than 100 accounted for 16-26% of the organic signals in the UMR mass spectra, indicating that this high mass region should not be ignored when analyzing AMS data of biomass-derived particles. The HR mass spectral data further confirmed that ion peaks at m/z 60 and 73 are related to the sugar anhydrides as in particles from other biomass burning processes. In addition, the ion peaks at m/z 107, 121, 137, 151, 167, and 181, some of which have been commonly observed in particles from biomass burning, were assigned to lignin-related components by investigating their HR peaks. Elemental analysis using the HR data reveals that organic particles from incense burning are oxygenated and unsaturated in nature.

Keywords: Incense, biomass, aerosol, AMS, organics, marker

Physicochemical Fingerprints of Particulate Matter Emitted from Various Sources in Kin-Xia Region

Chung-Yi Wu¹, Tsung-Chang Li¹, Chung-Shin Yuan¹, Shuei-Ping Wu², Xin-Hong Wang²

1 Institute of Environmental Engineering, National Sun Yat-sen University, Taiwan, R.O.C.

2 State Key Laboratory of Marine Environmental Science, Xiamen University, Xiamen, P.R.C.

Principal Contact: Chung-Shin Yuan, Prof., Institute of Environmental Engineering, National Sun Yat-sen University, No. 70, Lienhai Rd., Kaohsiung 80424, Taiwan, R.O.C.

Tel: 886-7-5252000 ext 4409 Fax: 886-7-5254409 E-mail:ycsngi@mail.nsysu.edu.tw

Abstract

In recent years, air pollution of Kin-Xia region (including Kinmen and Xiamen Islands) has become one of the most serious environmental problems accompanying with rapid urbanization and economic development. In order to understand the physicochemical fingerprints of particulate matter emitted from various sources in Kin-Xia region, this study selected seven major air pollution sources (ex: tile kiln stoves, power plants, soil dusts, biomass burning, and etc.) in Kin-Xia region to collect their emitted particulate samples which were initially sieved with Tyler 400 mesh ($d_p < 38\mu\text{m}$) to obtain approximately 5 g dusts. The dusts were then resuspended in a self-designed resuspension chamber to sample PM_{2.5} and PM_{2.5-10} with two separate dichotomous samplers for chemical analysis. Major ionic species (F⁻, Cl⁻, NO₃⁻, SO₄²⁻, K⁺, Na⁺, NH⁴⁺, Ca²⁺ and Mg²⁺), metallic elements (Cr, Mn, Fe, Ni, Zn, Cd, Pb, Mg, K, Ca, Ti, Al, As, Cu and V) and carbonaceous contents (OC, EC, and TC) of particulate samples were analyzed with an ion chromatography (IC), an inductively coupled plasma-atomic emission spectrometry (ICP-AES), and elemental analyzer (EA), respectively. The physicochemical fingerprints of particulate matter emitted from various air pollution sources were then established as the source profile for further receptor modeling.

Keywords: particulate matter, resuspension chamber, chemical composition, physicochemical Fingerprints.

Field test for fine dust collection in an MVAC of Metro subway

Dong Ki Lee, Yun-Hui Lim, and Young Min Jo

Department of Environmental Engineering, Kyung Hee University, South Korea, 446-701

Principal Contact: Young Min Jo, Prof., Department of Environmental Engineering, Kyung Hee University, South Korea, 446-701.

Email: ymjo@khu.ac.kr

Abstract

An air handling unit of subway in Seoul metro area provides a large volume of cleaned air to the ticket waiting rooms, platforms and tunnel in part. Because of energy consumption and air supplying rate, a low grade pre-filter has been installed after the wire – nets preventing large street impurities from inflowing. According to the current tendency of stringent regulation and passengers' needs for comfortable environment, the management level of IAQ becomes higher and detailed. Thus, in this work, two stage filtration was attempted in a local subway MVAC room which treats 900 CCM. An objective of the present experiment was to improve fine dust collection while maintaining the air control volume. In order to meet the experimental requirement, two types of electrostatically charged filters: electret pleated filter (EPF) and electret fiber bundle (EFB) filter, were compared in terms of pressure drop and dust collection efficiency. As a result of a long term test for EPF, PM_{2.5} could be collected up to 55% with an additional increase of pressure drop; 5 mmAq. Despite of lower pressure drop across the filter medium, dust collection efficiency of EFB filter has gradually decreased in the practical field condition. The serial lay-out followed by a pre-filter enabled to extend the replacement period of the filters.

Keywords: Air ventilation, Subway MVAC, Dust filtration, Electret filter, IAQ

Method for Combining Electrical Mobility and Optical Size Distributions for Wide Range Particle Size Distribution Measurement

Hee-Siew Han, Avula Sreenath, Nathan T. Birkeland and George J. Chancellor

TSI Incorporated, Shoreview, MN 55126, USA

ABSTRACT

A method is proposed for combining distributions measured with the scanning mobility particle sizer (SMPS) and optical particle counter (OPC). Since SMPS measures mobility diameters and OPC measures optical diameters, to combine these two distributions, the optical diameters need to be converted to mobility diameters first. For aerosols with known refractive indices, the conversion can be done with Mie scattering calculation. If refractive indices are unknown, additional calibration step is needed before performing the Mie scattering calculation. The SMPS and OPC used in this study were a TSI Model 3936 SMPS and a TSI Model 3330 OPS, respectively. Various test aerosols such as emery oil, dioctyl sebacate (DOS or DEHS) with known refractive indices, and ambient aerosols with unknown optical properties were used to evaluate the method. It was found that agreement between the SMPS and OPS distributions in the overlap region was good.

KEYWORDS

SMPS, OPC, Mie scattering, refractive index

Introduction

Size distributions of airborne particles often span a wide size range from a few nanometers to several micrometers, which typically exceeds the measurement size range of any single instrument. Therefore, researchers often combined data from multiple instruments. One such combination is that of electrical mobility-based instrument such as the scanning mobility particle sizer (SMPS) and light scattering-based instrument such as the optical particle counter (OPC). The SMPS is regarded as the gold standard for submicron aerosol size distribution measurement. Depending on the configuration, it can cover the size range from 2.5 nm to 1 um. The OPC is one of the most widely used instruments for coarse particles especially in areas such as filter testing, indoor air quality, cleanroom monitoring, etc. Typical OPC size range is 0.3 to 10 um.

The SMPS and OPC have different measurement principles. The SMPS classifies particles according to their electrical mobility, and for spherical particles, the electrical mobility size is same as the geometric sizes. The OPC, on the other hand, measures sizes according to the amount of light scattered by the particles. The light scattering phenomenon can be described by the Mie scattering theory. The sizes measured by the OPC are typically referred to as optical diameters. Because of the different measurement principles, in order to combine SMPS and OPC distributions into a single size spectrum, particle shape factors and refractive indices are needed. Unfortunately, except for laboratory generated aerosols, shape factors and refractive indices of aerosols of interest are typically unknown. In this study we attempted to fit the optical particle size distributions to the SMPS distributions for aerosols with known and unknown refractive indices. For aerosols with known refractive indices, the optical size distributions are adjusted with Mie scattering calculation. If refractive indices are unknown, an additional calibration step is performed. Several laboratory generated aerosols with known refractive indices were used to evaluate the method. The method was then further evaluated with various ambient aerosols with unknown refractive indices.

Experimental Methods

The electrical mobility instrument used in this study was a TSI Model 3936 SMPS. The differential mobility analyzer (DMA) and condensation particle counter (CPC) were LDMA Model 3081 and CPC Model 3010, respectively. The size range was 10 nm to about 500 nm. The OPC used in this work was a recently developed high resolution optical particle spectrometer TSI 3330 Optical Particle Sizer (OPS). The OPS is a light, portable, battery-powered unit that is capable of detecting particles from 0.3 to 10 μm in diameter in up to 16 channels^[1]. The OPS also features real-time Mie scattering calculation capability. Test aerosols emery oil and DOS were generated with a Collison atomizer, and then dried with a diffusion dryer.

Results and Discussion

One of the ambient aerosol distributions measured in this work is shown in Figure 1. Agreement between the SMPS and OPS distributions in the overlap region is good.

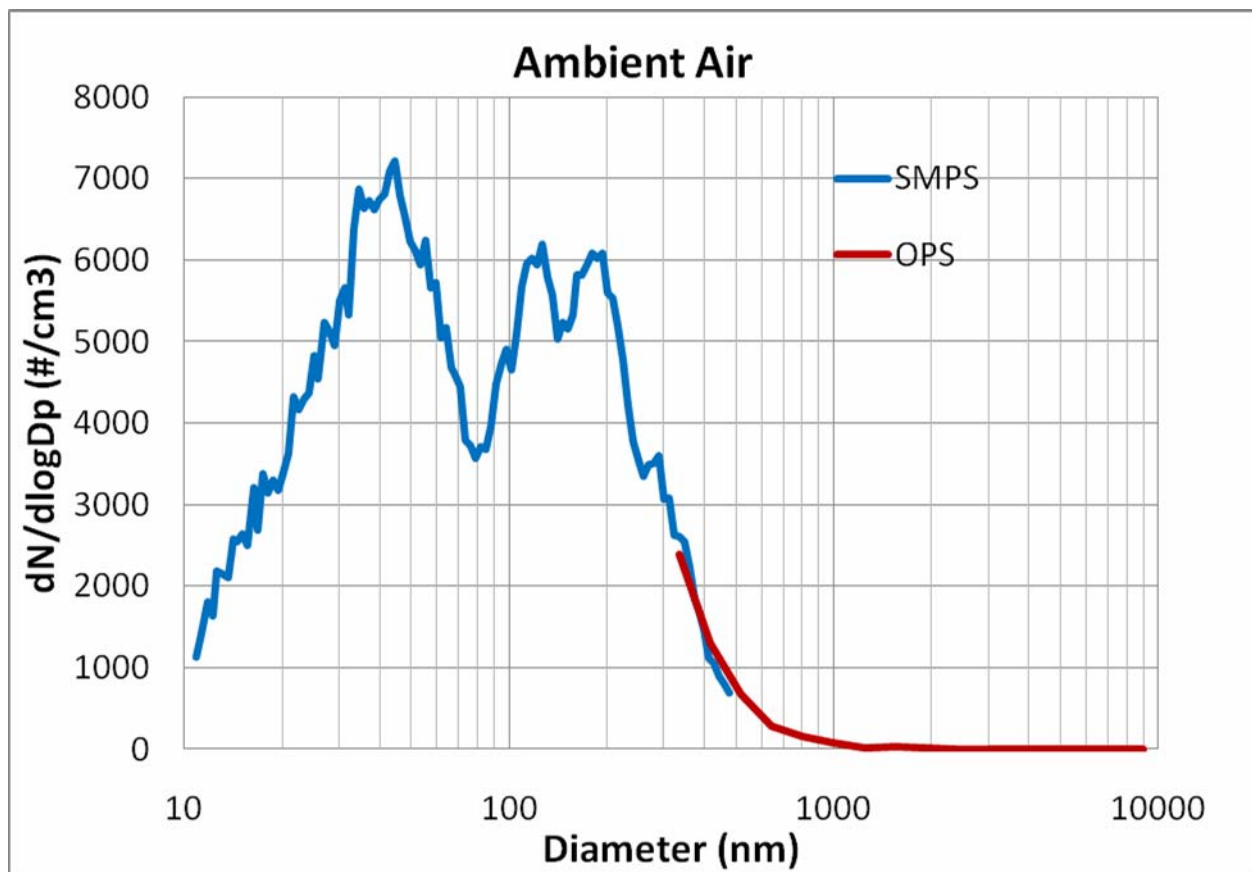


Figure 1 Ambient aerosol distribution.

REFERENCES

- [1] Han, H. S., Sreenath, A., Birkeland, N. T. and Chancellor, G. J. (2010). Evaluation of a High Resolution Optical Particle Spectrometer. *AAAR 29th Annual Conference*, Paper Number 8.E.17, Portland, Oregon.

The properties of water-soluble ions in the Asian Brown Cloud: observation over the Mountain Lulin site in Taiwan

Ming-Tung Chuang¹, Chuang-Te Lee¹ and Neng-Huei Lin²

1 Department of Environmental Engineering, Air Quality Research Lab, National Central University, Jhung-Li, Taoyuan 32001, Taiwan

2 Department of Atmospheric Sciences, National Central University, Jhung-Li, Taoyuan 32001, Taiwan

Principal Contact: Ming-Tung Chuang, Postdoctoral Researcher, Department of Environmental Engineering, No. 300. ChuangDa Road, Jhung-Li, Taoyuan, 32001, Taiwan.

Tel: +886-983932906 Fax: (886)-3-4226551 E-mail: mtchuang100@gmail.com

Abstract

Biomass burning (BB) in Southeast Asia (Indochina Peninsula and southern China) occurs frequently in March and April every year. The burning plume is ordinarily transported eastward by the prevailing westerly, further affecting downstream air quality in East Asia. In this study, atmospheric aerosols were collected at the downstream Lulin Atmospheric Background Station (LABS, 2,862 m a.s.l., central Taiwan) from April 2003 to April 2009. Results show that monthly means of PM_{2.5} were highest during the BB period, especially in March. The background PM_{2.5} level in free troposphere of the West Pacific was at $3.7 \pm 1.8 \mu\text{g m}^{-3}$. This mean is roughly the same regardless of the air masses moving from China, Pacific Ocean, and South China Sea toward LABS. In addition, the highest PM_{2.5} level occurred in 2004, making it the most active year of BB for the whole observation period. Greater amounts of nitrate and potassium ions were observed in the PM_{2.5} collected during the BB period compared to the non-BB (NBB) period. For all trajectory source origins, ammonium ion had the best correlation ($R^2=0.84$) with non-sea-salt sulfate when the air masses were influenced by anthropogenic sources during the NBB period. The enhancement ratios of nitrate ion during the BB period could reach 6.7 and 9.7 relative to air masses from the BB source region and from the pristine area during the NBB period, respectively. During the study period, ammonia gas was found to be insufficient to neutralize sulfuric and nitric gases. Therefore, most aerosols were more acidic than basic. Our long-term observation of atmospheric aerosols with inter-annual variability is valuable in providing data for verifying BB source inventory and model performance in East Asia.

Keywords: PM_{2.5}, biomass burning, water-soluble ions.

Quantifying the Black Carbon Reduction during the 2008 Olympic Games in Beijing, China

Yang Yu¹, Kuang Cen¹, Stefan Norra^{2,3}, Nina Schleicher² and Mathieu Fricker⁴

1 China University of Geosciences (CUG), Beijing, Xueyuan Road No.29, Haidian District, Beijing, China, 100083

2 Institute of Mineralogy and Geochemistry, Karlsruhe Institute of Technology (KIT), Adenauerring 20b, Building 50.40 (FZU), Karlsruhe, Germany, 76131

3 Institute of Geography and Geoeontology, Karlsruhe Institute of Technology (KIT), Kaiserstr. 12, Karlsruhe, Germany, 76128

4 German Meteorological Service, Research Center Human Biometeorology, Stefan-Meier-Str. 4, Freiburg, Germany, 79104

Principal Contact: Yang Yu, Ph.D.(Cand.), China University of Geosciences (CUG), Beijing, Xueyuan Road No.29, Haidian District, Beijing, China, 100083.

Tel: +86 010 82321836 Fax: +86 010 82321836 E-mail: yuyang_cugb@126.com or bj_yuyang@126.com

Abstract

To ensure good air quality for the 29th Olympics Games, Beijing municipal government performed an “Air Quality Guarantee Plan” for the Games. The compelling traffic interventions and emission control measures created a valuable case study to investigate the effectiveness of traffic control regulations. In this paper, suspended particulate matter smaller than 2.5 μm in diameter ($\text{PM}_{2.5}$) were collected in the urban area of Beijing during the Olympic Games (2008), peer-period before Olympic year (2007) and after Olympic year (2009). Concentrations of black carbon (BC) in $\text{PM}_{2.5}$ were determined by an optical oil-immersion technique and the considerable reduction during the Olympic Games (2008) was qualitatively discussed. The daily BC concentration ranged from $0.24 \mu\text{g m}^{-3}$ to $4.30 \mu\text{g m}^{-3}$, with the average of $1.92 \mu\text{g m}^{-3}$ for the Olympic sampling period from August 1st to September 30th, which was dramatically lower than the average value on non-traffic-control days $4.08 \mu\text{g m}^{-3}$ and $3.66 \mu\text{g m}^{-3}$ for the peer-period in 2007 and 2009, respectively. This indicates the effectiveness of traffic control regulations and emission control measures in BC reduction, probably dominated by traffic. This is supported by scanning electron microscopy analysis which showed a clear imprint of component of BC in $\text{PM}_{2.5}$. A major part of BC in $\text{PM}_{2.5}$ can be classified as soot, including soot chain and soot agglomerate. These patterns strongly suggest that traffic is a major source of BC in Beijing. This study is only a small contribution to the understanding of the variations of BC concentration which accurate and quantitatively reflect the emission changes attributable to air pollution control measures taken during the 29th Olympic Games in 2008. More effort is required for reducing BC pollution in Beijing, which is still a big and complex challenge for the sustainable development of the city.

Keywords: Olympics, Air pollution, Black carbon, Traffic control, Beijing

The Research on the CCN Activation of Aerosols in Shanghai

Chunpeng Leng¹ and Tiantao Cheng²

1 Postgraduate, Fudan University, No.220 Handan Road, Shanghai, China.200433

2 Professor, Fudan University, No.220 Handan Road, Shanghai, China.200433

Principal Contact: Chunpeng Leng, Postgraduate, Fudan University, No.220 Handan Road, Shanghai, China, 13761338176, 09210740018@fudan.edu.cn

ABSTRACT

The cloud condensation nuclear (CCN) is the suspended particle that the atmospheric water could condense on it to form the cloud droplet and it is an important component of atmospheric aerosols. The CCN can affect the atmospheric condition largely by reflecting and absorbing the radiation of the sunlight. It plays a vital role in the global water recycle as well. The research on the CCN activation of aerosols in Shanghai was carried in September to December, 2010 and we found that it was the aerosols with a diameter between 100nm and 150nm that contributed mostly to the CCN number concentration in Shanghai. Chemistry component contained in those aerosols played an important role in the CCN activation. We found that the SO₄ and NH₄ ions were the main inorganic component which had high relevance and high contribution weight to the CCN activation, followed by NO₃. We also found that some other factors such as the meteorology、O₃、NO_X、humidity and temperature were important indicators for CCN variation.

KEYWORDS

CCN、aerosols、Shanghai

1. Introduction

Some of the aerosols in the atmosphere known as cloud condensation (CCN) are one of the most important aspects in climate study because they are typically effective at scattering/absorbing light and hygroscopic, and also affect the cloud droplet formation and precipitation. Their ability of scattering and absorbing light is determined by the ambient humidity and thus has an important implication for radiative forcing of climate, known as the “aerosol direct effect”. Moreover, that can also affect the cloud formation and alter the cloud radiative properties, known as the “aerosol indirect effect”. The ability of aerosol to act as CCN depends on the efficiency it takes up water vapor and which in turn depends on many

factors, among which size and chemical composition is the most important^[1].

As the development of the instruments in recent years, it makes it more possible to extend the study of the relationship between CCN and particle size distribution, chemical composition and meteorological factors and some other aspects. Much work has been done on the CCN all around the world. U. Dusek etc. measured the size-resolved cloud condensation nuclei spectra for various aerosol types at a non-urban site in Germany showed that CCN concentrations are mainly determined by the aerosol number size distribution. Distinct variations of CCN activation with particle chemical composition were observed but played a secondary role and when the temporal variation of chemical effects on the CCN activation is neglected, variation in the size distribution alone explains 84to 96% of the variation in CCN concentrations^[2]. Daniel Rosenfeld pointed out that the power of the gases to warm the planet may have been underestimated, because much of it has been masked by the cooling effects of aerosols from combustion and other pollution sources, and, because pollution aerosols act as cloud condensation nuclei, cloud forming in a more polluter atmosphere contain a larger number of smaller drops that are slower to merge and fall as precipitation. As a result, the clouds are brighter, thicker, long-lived, and more extensive, thus reflecting more sunlight back into space and partially mitigating global warming^[3].

2. Measurement program

The measurements of CCN in Shanghai were made in September, 2010-June,2011 on the campus of Fudan University which is located in the northeast of Shanghai. The instrumentation consisted of sensors for meteorological conditions, solar radiation, inorganic ions, particle size distribution, laser radar and BC.

The continuous-flow design, the Droplet Measurement Technologies (DMT) Cloud Condensation Nuclei Counter (CCN) is based on the design of Dr. Greg Roberts of Scripps Institute of Oceanography and Dr. Athanasios Nenes of Georgia Institute of Technology. The CCN measures aerosol particles called cloud condensation nuclei that can form into cloud droplet. The instrument takes an air sample and operates by supersaturating air to the point where the CCN become detectable particles, which are then sized using an optical particle counter and distributed into 20 bins. It makes an measurement approximately every second and particles with critical supersaturations less than the controlled value activate and grow in the instrument chamber to size of cloud droplets within about 20s. A laser illuminates these droplets and the scattered light intensity is collected and focused on a photodetector. The output of this detector is recorded and converted to a particle number concentration based on

calibrations.

Figures

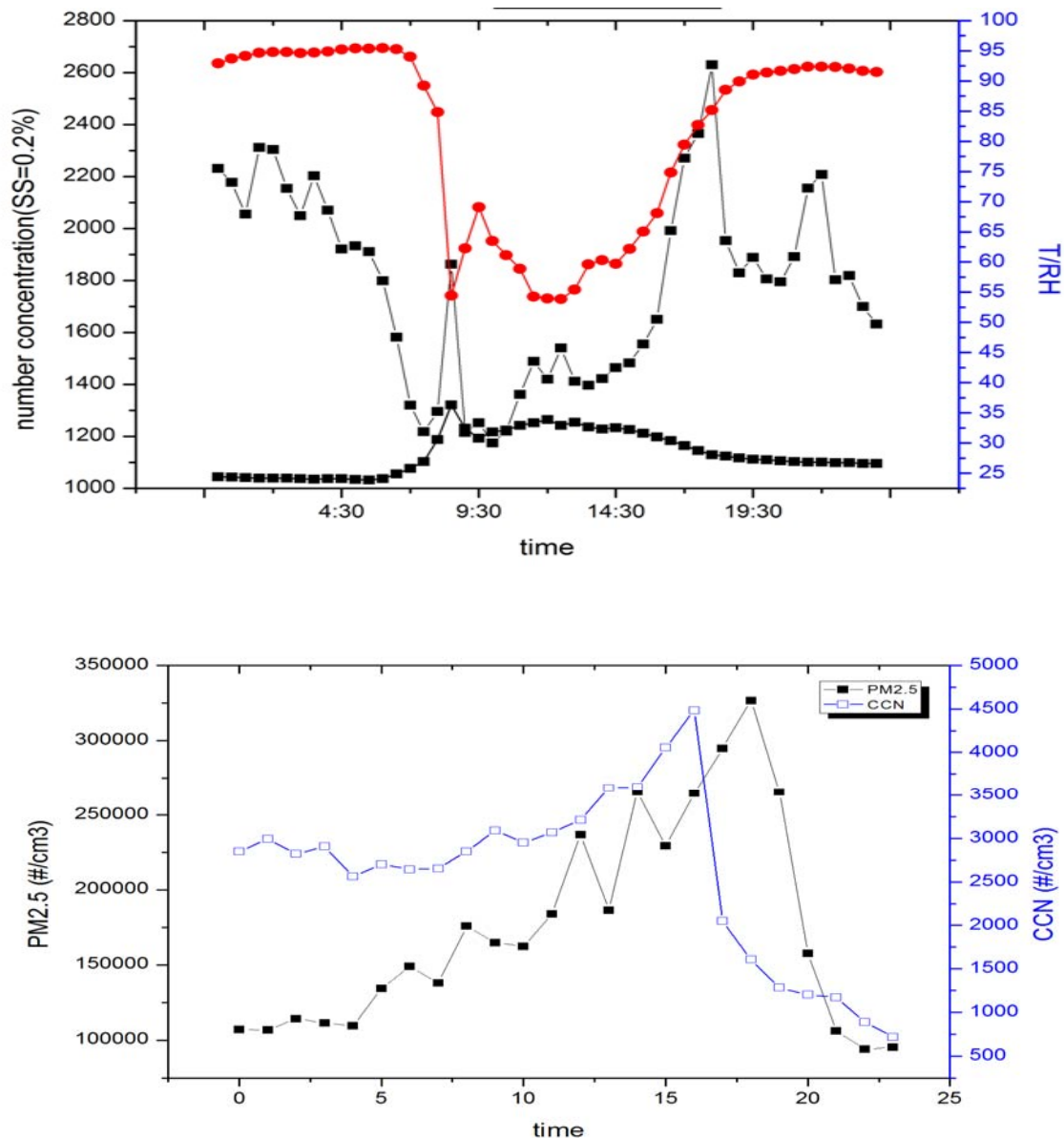


Fig. 1. Time series of CCN data during the measurement program is shown. Panel (a) is the daily trend of CCN (black solid line) with humidity ((%), red solid line) and temperature (black cube). Panel (b) shows the daily relationship between CCN (blue) and PM_{2.5} (black).

REFERENCES

- [1] Evidence for the formation of CCN by photochemical processes in Mexico City. D. Baumgardner, G. B. Raga, A. Muhlia. Atmospheric environment. 2003
- [2] U. Dusek, G. P. Frank, L. Hildebrandt, size matters more than chemistry for cloud-nucleating ability of aerosol particles. Science.2006.
- [3] Daniel Rosenfeld. Aerosols, clouds, and climate. Science. 2006

Strong Absorption Associated with Coarse Mode Particles over CTCZ Region: Results from Aircraft Experiment 2009

J. Jai Devi, Priya Choudhry, Marykutty Michael, S.N. Tripathi, Tarun Gupta

Department of Civil Engineering, Indian Institute of Technology Kanpur, Kanpur, India

Principal Contact: S.N. Tripathi, Associate Professor, Department of Civil Engineering, Indian Institute of Technology Kanpur, Kanpur, India.

Tel: +91-512-259 7845 Email: snt@iitk.ac.in

Abstract

Recent studies suggest that desert dust from west transported through the Indo-Gangetic (IG) plains gets mixed with locally generated anthropogenic aerosols and is further carried over to the Himalayan foothills. The mixing of dust and absorbing aerosols increases the dust absorption. Studies show strong dependence of radiative forcing on aerosol size distribution and presence of coarse mode absorption (Tripathi et al., 2011). Aircraft measurements were carried out over the Continental Tropical Convergence Zone (CTCZ) region up to 4 km during early monsoon season (Jun-Jul), 2009 to study the vertical and spatial variation of aerosol optical, microphysical, chemical, hygroscopic and morphological properties. Based on simultaneous measurements using four instruments onboard (Photoacoustic Soot Spectrometer, Scanning Mobility Particle Sizer, Aerodynamic Particle Sizer and PM_{2.5} sampler) and the subsequent SEM/EDAX analysis, strong association between absorption and coarse mode aerosols is found. A shift in absorption is seen from accumulation mode in central (78°-81°E) to coarse mode in east (81°-84°E) CTCZ indicating the possibility of ageing of aerosols during long range transport. Aerosols below 2 km show absorption in coarse modes over central and east. The SEM/EDX analysis of particles collected on ground filter over the central CTCZ showed angular and flaky particles with high amount of silicon (Si) and aluminum (Al). The SEM images also showed chain like structures of carbon spherules. Aircraft filters for the same day and zone showed particles formed by agglomeration of particles with significant amount of iron in addition to Si and Al. The chain like structure of carbon collapsed and internally mixed with other elements. Column-integrated in situ size distributions were also compared with the ground based AERONET columnar size distributions.

Reference:

Tripathi, S. N., S. Dey, J. J. Devi, B. N. Singh, M. Michael, and T. Gupta (2011), Thick absorbing aerosol layer observed in the monsoon season over India, *Atmos. Chem. Phys. Discuss.*, under preparation.

Keywords: CTCZ, aircraft, size distribution, SSA, SEM/EDX

Particulate Mercury and Gas-solid Partition of Gaseous Elemental Mercury in Kaohsiung Area

Yi-Shiu Jen¹, Chung-Shin Yuan¹, and Chang-Gai Lee²

1 Institute of Environmental Engineering, National Sun Yat-Sen University, No.70, Lian-Hai Road, Kaohsiung City 804, Taiwan

2 Graduate Institute of Environmental Management, Tajen University, No.20, Weisin Road, Yanpu Township, Pingtung County 907, Taiwan

Principal Contact: Chang-Gai Lee, Associate professor, Graduate Institute of Environmental Management, Tajen University, No.20, Weisin Road, Yanpu Township, Pingtung County 907, Taiwan.

Fax: 886-7-3591160 E-mail: maxlee@mail.tajen.edu.tw

Abstract

Atmospheric mercury has been claimed as the second global environmental issue following the greenhouse gases. Mercury is released into the atmosphere from a variety of natural and anthropogenic sources. The emission from natural sources is about 2,000 tons per year; while the emission of manmade sources, mainly from coal-fired plants and waste incinerators, accounts for around 4,000 tons per year. Mercury is considered as a global pollutant by USEPA and European Union because of its characteristics of being poison-persistence and concentrated up the food chain by bioaccumulation. However, up to now, very few literatures have quantitatively addressed this issue of mercury pollution in Taiwan. Such data are, however, essential to be investigated, specially for such a highly polluted region as the Kaohsiung area with several industrial parks located in it. In this study. Atmospheric mercury will be captured upon the surface of gold-coated sands through the amalgamation. Then, both the gaseous and particulate mercury will be measured via the cold vapor atomic fluorescence spectrometry (CVAFS). Accordingly, both the ambient and background sampling sites located in Kaohsiung will be chosen to investigate the temporal and spatial variations of atmospheric mercury. These obtained ambient data will further be compared with data measured at a background site to elucidate the difference between urban and rural areas. Furthermore, this study will correlate the relationship between the GEM, HgP, air pollutants (such as CO, SO₂, NO_X and O₃) and meteorological parameters via principle component analysis (PCA) method. Since the atmospheric mercury can be transported to a long distance in the atmosphere, a backward trajectory model will also be used to address the possibility of mercury contributed from Mainland into this study area.

Keywords: Kaohsiung area, Atmospheric mercury, GEM and HgP, Partition of Hg

Numerical Investigation of Electrostatic Effect on Indoor Particle Resuspension Due to Human Activity

Xinyu Zhang,¹ Goodarz Ahmadi,¹ Jing Qian², Andrea Ferro² and Lin Tian³

1 Department of Mechanical and Aeronautical Engineering, Clarkson University, Potsdam, NY, 13699, U.S.A.

2 Department of Civil and Environmental Engineering, Clarkson University, 13699, Potsdam, NY, 13699 U.S.A.

3 Department of Science and Engineering Technology, SUNY Canton, Canton NY 13617 U.S.A.

ABSTRACT

A numerical study was carried out for indoor particle resuspension due to human walking. The electrostatic effect on particle detachment and resuspension is included in the analysis using a capacitor theory. The shoe-floor system is treated as a plate capacitor. The electrostatic charges and the electric field strength generated by the tribocharging at shoe-floor contact are estimated by the capacitor theory. The Coulomb force, image force, dielectrophoretic force and polarization force are evaluated in the study. The foot stepping down and up processes are treated as the motion of an effective circular disk toward or away from a stationary surface. The surface roughness, the adhesion, lift and drag forces as well as hydrodynamic moment exerted on the particles are also included in the study. The critical radii and particle resuspension rate under various conditions are estimated.

KEYWORDS

Capacitor Theory, Electrostatic Forces, Particle Resuspension, Human Walking

Introduction

Yakovleva et al.^[1] reported that 30% of personal PM₁₀ exposure is due to resuspended particles. Zhang et al.^[2] modeled particle resuspension due to human walking by including the effects of the particle-wall (surface) adhesion force and the hydrodynamic drag and lift forces in the particle detachment model. Human walking on untreated vinyl floor may generate charges forming an electrostatic voltage of 250 to 12000 volts (READE.^[3]) which can have effects on indoor particle resuspension. Therefore, a thorough understanding of the electrostatic forces and its effect on indoor particle resuspension is very important for indoor human exposure assessment.

In this work, a numerical simulation on the rolling detachment and resuspension of Arizona Road Dust particles in the presence of electrostatic forces due to indoor human walking on vinyl tile floor are performed. The foot stepping down and up processes are treated as the motion of an effective circular disk with the radius of 0.05 m toward or away from a stationary surface. The squeezing flow or suction flow generated from these motions are assumed to be laminar and the flow outside the foot is evaluated based on the radial wall jet theory. The surface roughness and the adhesion, lift and drag forces were taken into account. The shoe-floor system is treated as a plate capacitor. The total electrostatic charges and the electric field strength generated by the friction in the shoe-floor system are evaluated using a capacitor theory. The simulation results are compared with the experimental data.

Numerical Methods

The models used in this study are similar to those in the previous work by Zhang et al.^[2].

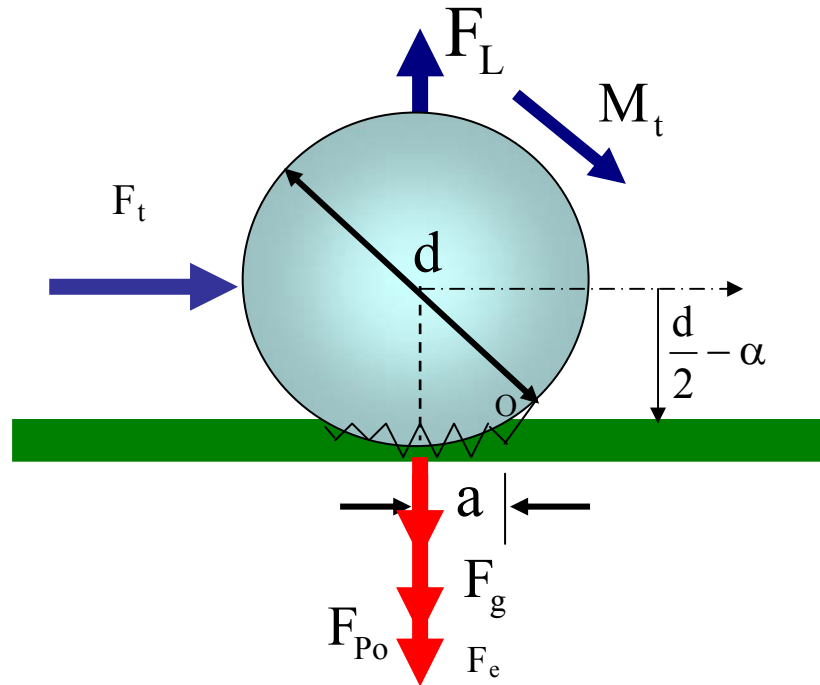


Figure 1. Geometric features of a spherical particle attached to a flat floor surface.

Rolling Detachment Model

Figure 1 shows a spherical particle which is attached to a plane surface. Here a is the contact radius, F_g is gravity force, F_{po} is pull-off force, F_e is electrostatic force given as:

$$F_e = -qE + \frac{q^2}{4\pi\epsilon_0 d^2} - \frac{qE}{2} + \frac{3\pi\epsilon_0 d^2 E^2}{8} \quad (\text{Eq.1})$$

Where q is the total electrical charge on the particle, E is the electric field strength, d is the particle diameter, $\epsilon_0 = 8.859 \times 10^{-12}$ amp \cdot s /V \cdot m is the permittivity of space (dielectric constant of free space). The first term on the right-hand side of equation (1) is the Coulomb force. The second term is the image force. The third and forth terms are the dielectrophoretic force and polarization force respectively. The image and polarization forces are always toward the substrate, but the Coulomb and dielectrophoretic forces can be either toward or away from the substrate. The electric field strength E can be evaluated using capacitor theory by treating the shoe-floor system as a plate capacitor. The electrostatic charge q was obtained by assuming that the electrostatic charges are concentrated on the particles under the shoes.

According to Tsai et al.^[4] and Soltani and Ahmadi^[5], a particle will be detached when the external force moment about point “O”, the rear point at the perimeter of the contact circle, overcomes the resisting moment due to the adhesion force F_{po} and the electrostatic forces F_e , which is,

$$M_t + F_t \left(\frac{d}{2} - a \right) + F_L a \geq (F_{po} + F_e) a \quad (\text{Eq.2})$$

where F_L is the lift force given by Mei^[6], α is the relative approach between the particle and surface (at equilibrium condition), which is negligibly small in most cases and can be neglected. F_t is the fluid drag force and M_t is the external moment of the surface stresses about the center of the particle.

Particle Resuspension Model

The present model assumes that only 10% of the detached particles originally located under the shoes can be finally resuspended to the environment. Other particles will stick to the foot or fall to the floor. After being detached, a particle can be suspended only if the combination of the lift force and electrostatic force are larger than the gravity force.

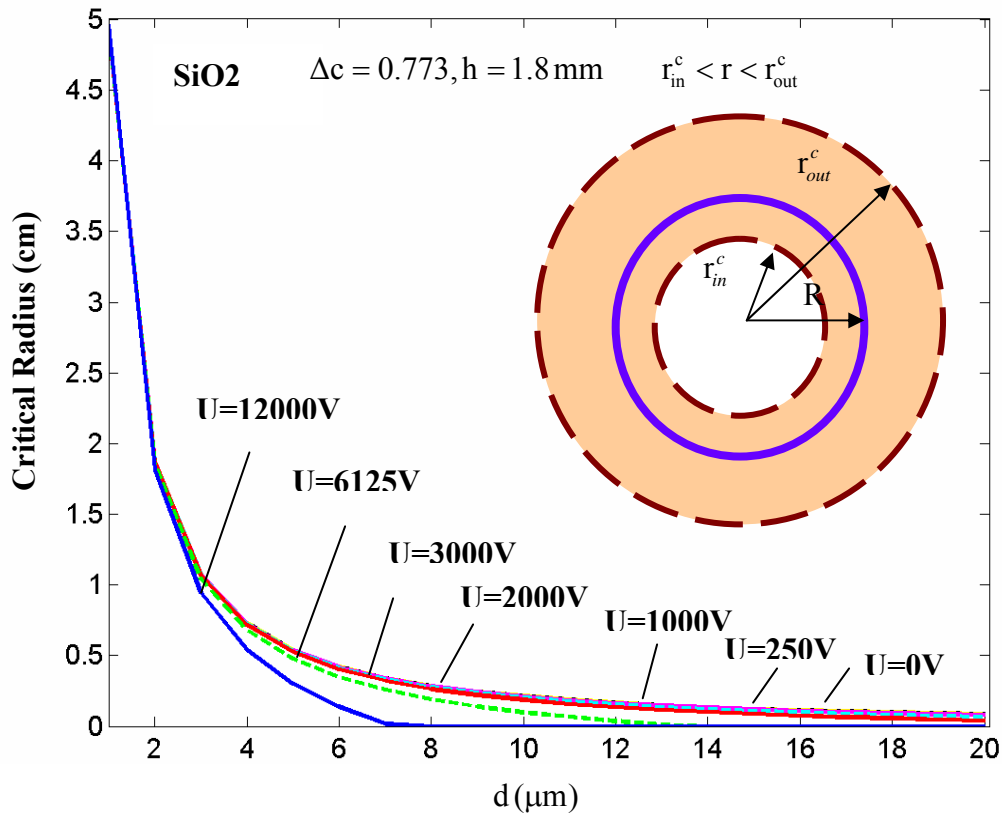


Figure 2. Critical radii for rolling detachment of particles during stepping down process under various voltage with upward Coulomb and dielectrophoretic forces.

Particle Deposition Model

Resuspended particles could be re-deposited because of Brownian motion, turbulent eddy impaction, and gravitational sedimentation. Here the particle deposition velocity was estimated according to Wood^[7].

Results and Discussion

Figure 2 shows the critical radii for rolling detachment of particles inside the shoe during the stepping down process under various voltage. Here Coulomb and dielectrophoretic forces are upward. The shoe-floor gap size is 1.8mm and the roughness ratio is $\Delta_c = 0.773$. It is seen that the critical radius decreases with the increasing particle size, which implies that larger particles can be more easily detached compared to smaller particles. It is also found that the critical radius decreases with the increasing voltage, which means that particles can be more easily detached under higher voltage due to the help of increasing upward Coulomb and dielectrophoretic forces. The polarization force, which always holds the particles to the floor like the image force, also increases with the increasing voltage. However, the sum of image and polarization forces is

smaller than the sum of Coulomb and dielectrophoretic forces as shown by Zhang and Ahmadi^[8]. Thus, the resulting effect of the upward Coulomb and dielectrophoretic forces shows advantage for particle detachment. This effect is not observable under a voltage smaller than 1000 V.

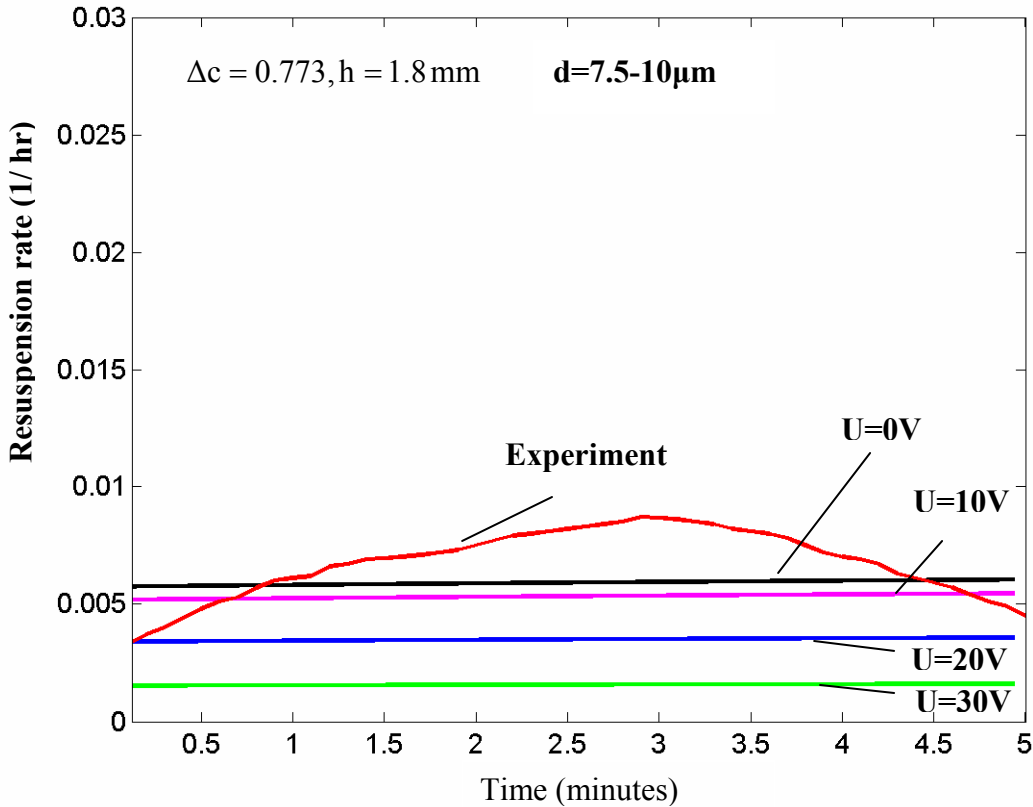


Figure 3. Variation of the particle resuspension rate with time under effects of downward Coulomb and dielectrophoretic forces.

Figure 3 shows the variation of 7.5-10 μm particle resuspension rate with time at different voltages. The simulations are performed with downward Coulomb and dielectrophoretic forces except for the case of no voltage, where there is only image force due to lack of electric field strength. The shoe-floor gap size is assumed to be 1.8mm and the roughness ratio is $\Delta_c = 0.773$. It can be seen that the particle resuspension rates decrease with the increasing voltage, and this effect is more sensitive compared to that in the case with upward Coulomb and dielectrophoretic forces. A voltage of 30 V can make an obvious difference. As mentioned above, image and polarization forces are always downward and hold the particles to the floor. An increase in voltage will increase polarization force as well as Coulomb and dielectrophoretic forces. If Coulomb and dielectrophoretic forces are upward, their upward effect will be impaired by the downward effect of image and polarization forces; If Coulomb and dielectrophoretic forces are

downward, their downward effect will be strengthened by the downward effect of image and polarization forces, therefore hold the particles more strongly to the floor and thus decrease particle resuspension more effectively.

SUMMARY

The electrostatic effect on particle detachment and resuspension is numerically studied using a capacitor theory. The shoe-floor system is treated as a plate capacitor. The Coulomb force, image force, dielectrophoretic force and polarization force are included in the analysis. The simulation results are in good agreement with the experimental data. It is shown that when Coulomb and dielectrophoretic forces are upward, particles can be more easily detached. But this effect is not observable under a voltage smaller than 1000 V. If Coulomb and dielectrophoretic forces are downward, particle resuspension rates decrease with increasing voltage, and this effect is more sensitive to voltage as compared to the case with upward Coulomb and dielectrophoretic forces. A voltage of 30 V can result in an obvious difference.

ACKNOWLEDGMENTS

This material is based in part upon work supported by the National Science Foundation under Grant Number CBET 0846704 and the Syracuse Center of Excellence in Environmental and Energy Systems. Their financial supports are gratefully acknowledged.

REFERENCES

- [1] Yakovleva, E.; Hopke, P. K.; Wallace, L. *Environ. Sci. Technol.* 1999, 33, pp. 3645-3652.
- [2] Zhang, X.; Qian, J.; Ferro, A.; Ahmadi, G. *J. Adhesion Sci. Technol.* 2008. 22 (5-6), pp. 591-621.
- [3] READE. Electrostatic discharge (ESD) briefing at READE, 2009. Publicly available information at <http://www.reade.com/Safety/esd.html>
- [4] Tsai, C. J.; Pui, D. Y. H.; Liu, B. Y. H. *J. Aerosol Sci.* 1991. 22, pp. 737-764.
- [5] Soltani, M.; Ahmadi, G. *J. Adhesion Sci. Technol.* 1994. 7, pp. 763-785.
- [6] Mei, R. *Int. J. Multiphase Flow*, 1992. 18, pp. 145-147,
- [7] Wood, N. B. *J. Aerosol Sci.* 1981. 12, pp. 275-290.
- [8] Zhang, X.; Ahmadi, G. *J. Adhesion Sci. Technol.* 2011. 25 (11), pp. 1175-1210.

Aircraft measurements of aerosol composition over eastern coastal, Yangtze River areas and Pearl River delta of China

Lihong Ren^{1,2}, Wei Wang¹, Jianhua Chen¹, Hongjie Liu¹, and Renjian Zhang²

1 Chinese Research Academy of Environmental Sciences, Beijing Chaoyang district Dayangfang NO.8, Beijing, 100012

2 Institute of Atmospheric Physics, Beijing Chaoyang district Qijiahuozi, Beijing, 100029

Principal Contact: Lihong Ren, Associate researcher, Chinese Research Academy of Environmental Sciences, Beijing Chaoyang district Dayangfang NO.8, Beijing, 100012.

Tel: 010-84934330 Fax: 010-84934330 E-mail: renlh@craes.org.cn

Abstract

Aircraft measurements were carried out over eastern coastal areas of China in spring and winter of 2002, Yangtze River areas in summer of 2003 and spring of 2004 and Pearl River delta region in autumn of 2004, respectively. Eight ionic components of particulate matters were sampled by filters. In these experiments, nitrate, sulfate and ammonium were the main water-soluble components in particulate matters. The total fraction of SO_4^{2-} and NH_4^+ accounted for over 60% in PM_{10} and $\text{PM}_{2.5}$. Crustal species (K^+ , Ca^{2+} and Mg^{2+}) had lower fractions (less than 5%). These indicate that coal combustion pollution is the main pollution type in most regions of China. For latitudinal distribution, the concentrations of ionic species observed in northern regions were higher than those obtained in southern regions. It is due to the effects of coal burning for warming in winter and dust storm in spring in northern areas. For longitudinal distribution, the concentrations in south-western region were obviously lower than those in eastern region. Vertical distribution of ionic species showed a general decreasing trend with increasing flight altitude. For seasonal variation, the ionic species has lower concentration in summer due to wet deposit. Analysis of correlations between ionic species suggests that these components had the same source, i.e., they are mainly influenced by anthropogenic source. NH_4^+ and SO_4^{2-} were strongly correlated, indicating that combustion was the dominant source, and they existed as $(\text{NH}_4)_2\text{SO}_4$ and NH_4HSO_4 . The depletion of Cl^- was existed in air-suspended particles. The ratio of SO_4^{2-} to NO_3^- is between 1.0 and 4.0, indicating particulate matters mainly come from emission of coal burning in China.

Keywords: Aircraft measurements, Ionic components, Particulate matters, China

Investigation of Indoor Air Quality in Children's Day Care Centers in Korea

Hyeun Jun Moon¹ and Soo Hyeun Yang¹

¹ Dankook University, Yongin, Korea

ABSTRACT

Indoor Air Quality is one of dangerous threats to occupants in built environment due to harmful health effects. Particularly, indoor environment where children stay most of time should be carefully monitored and maintained since children is more susceptible to indoor contaminants, such as particulate matters, VOCs, microbial contaminants and so on.

In this study we investigated the level of indoor pollutants in children's day care centers in Korea. Measurements were performed for volatile organic compounds, formaldehyde, PM10, CO₂, CO, airborne mold spores and bacteria. Based on this, we analyzed current status of main contaminants and seasonal differences in the concentrations of indoor air pollutants in children's day care centers.

KEYWORDS

Indoor contaminants, Day care center, IAQ

Introduction

In these days, the number of infants and children who are exposed to asthma, atopic, dermatitis and allergies which is considered environmental illness have increased. Carrer, et al, a study have suggested that the increase in morbidity and mortality for asthma and allergies may also be due to an increase in exposure to allergens in the modern indoor environment. ^[1]

In Korea, recently a few studies on IAQ in children's day care centers have been conducted, there should be maintained under the standard of IAQ in child care facilities including air pollutants such as PM10, CO₂, HCHO and VOCs.

Korea IAQ maintenance standard in child care facilities is shown in Table 1. ^[2]

Table 1. Maintenance standard of IAQ in child facilities in Korea

PM10 ($\mu\text{g}/\text{m}^3$)	CO₂ (ppm)	CO (ppm)	HCHO ($\mu\text{g}/\text{m}^3$)	VOC ($\mu\text{g}/\text{m}^3$)	Bacteria (CFU/m^3)
below 100	below 1,000	below 10	below 100	below 400	below 800

This study aims to investigate the current status of indoor contaminants in children's day care centers and analyze the seasonal differences in the concentrations of indoor air pollutants.

Experimental Methods

In this study, 75 children's day care centers are selected located in the center and suburban of Seoul, Korea. The research team has conducted measurement including VOCs, HCHO, PM10, CO₂, CO, mold and bacteria in each selected facilities. Within the 75 buildings, 10 children's day care centers are chosen to investigate the seasonal differences in indoor contaminants in winter, spring and summer days.

Measurement items and equipments are shown in Table 2.

Table 2. Measurement items and equipments

Measurement items	Measurement equipment
VOCs	MP-Σ30 (SIBATA-Japan)
HCHO	MP-Σ100 (SIBATA-Japan)
PM10	MINI VOLUME SAMPLER
CO ₂	TSI-Model 7545
CO	TSI-Model 7545
Mold	Anderson sampler
Bacteria	Anderson sampler

Results and Discussion

Concentration of indoor pollutants in children's day care centers

From the measurement results, VOCs, PM10, CO₂ and bacteria have exceeded the limit value of indoor air contaminants by Korean guideline. The results of VOCs, PM10, CO₂, mold and bacteria level from the investigation in 75 facilities are shown in Fig. 1~Fig. 5. The blue line represents a guideline of maintenance standard of IAQ in child facilities. The standard of VOCs levels in children's day care centers is 400μg/m³ and about 30% of the measurement results are exceeded. This result is shown in Figure 1. Figure 2 is the result of PM10. The guideline value of PM10 levels in children's day care centers is 100μg/m³ and 20% of the measurements are exceeded the guideline. As for CO₂ in Figure 3, more than 50% of CO₂ results are exceeded in child care facilities. Thus, special management is needed for CO₂ concentrations. For bacteria, more than 45% of measurement results are exceeded as shown in Figure 4. And it is shown in Figure 5 that Mold results are distributed in the range of 10~735CFU/m³.

Figure 1. Percentile of VOC concentrations

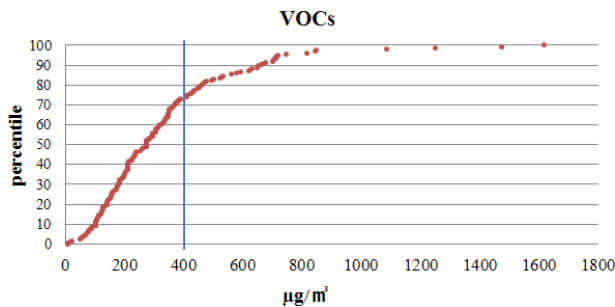


Figure 3. Percentile of CO₂ concentrations
concentrations

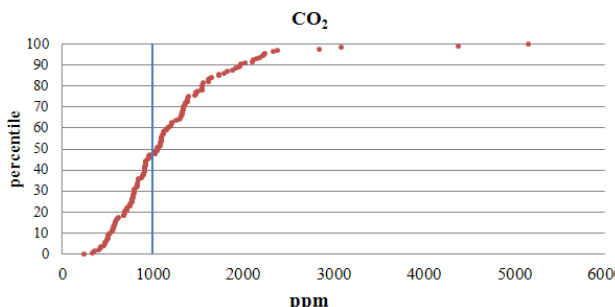


Figure 2. Percentile of PM10 concentrations

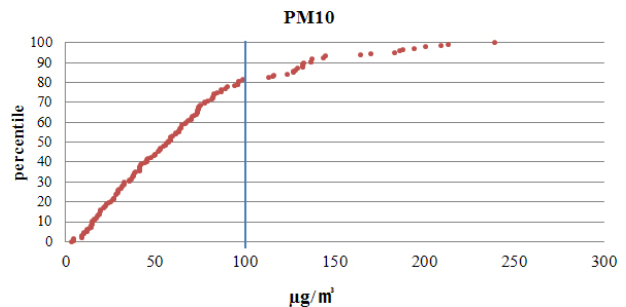


Figure 4. Percentile of Bacteria

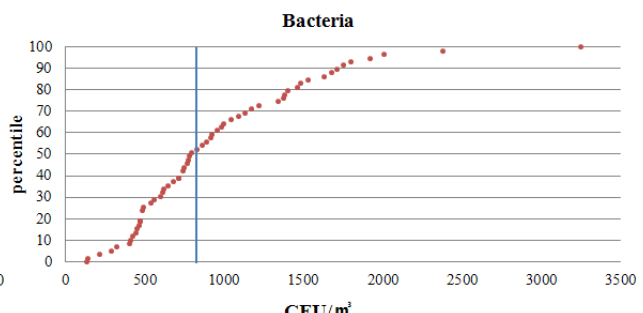
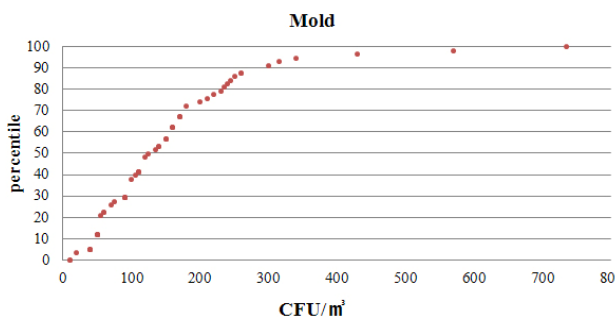


Figure 5. Percentile of Mold concentrations



Seasonal differences of indoor contaminants in children's day care centers.

The research team has conducted measurement including VOCs, HCHO, PM10, CO₂, CO, mold and bacteria in 10 children's day care centers to investigate the seasonal differences of indoor contaminants in winter, spring and summer days.

Upon investigation VOCs, HCHO, PM10, CO₂ and bacteria has exceeded the limit value of indoor air contaminants. The blue line represents a guideline of maintenance standard of IAQ in

children's facilities.

Figure 6 shows the result of VOCs. About 10% of the measurement results are exceeded the guideline value in winter and spring seasons. However, more than 30% of the measurement results are exceeded in summer season. Concentration of HCHO is likewise higher in summer season than other seasons, which are shown in Figure 7. HCHO distributions show does not over the guideline value in winter season, but about 30% of the measurements are exceeded in spring season and 60% of results are exceeded in summer season. It is thought that VOCs and HCHO are higher in summer season due to high temperature and relative humidity. Thus, management of VOCs and HCHO is important especially in summer season than other seasons.

The result of PM10 is shown in Figure 8. The concentration of PM10 is higher in winter season than summer season. There are not many children's day care centers that exceed the guideline value and show no big differences between seasons. The concentration of PM10 is considered depending on residents activities rather than seasons.

Figure 6. The seasonal variation of VOCs

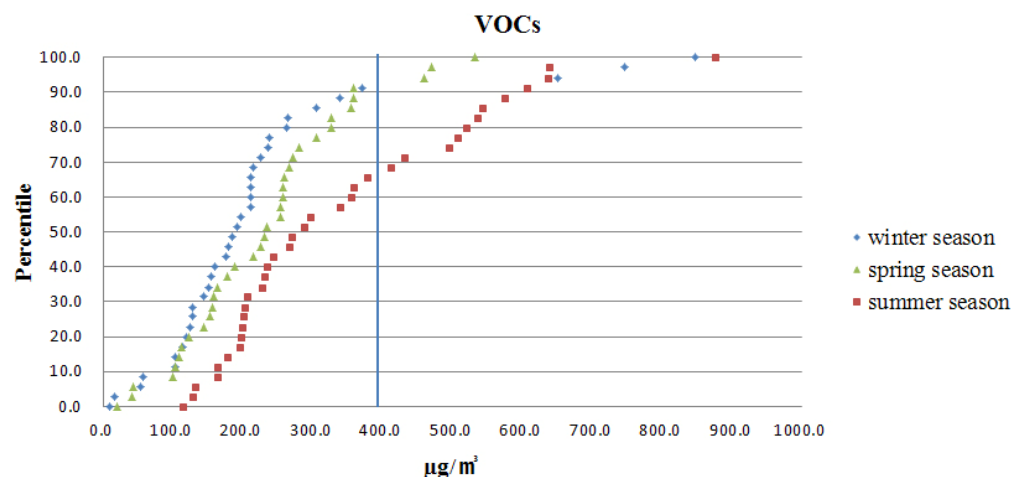


Figure 7. The seasonal variation of HCHO

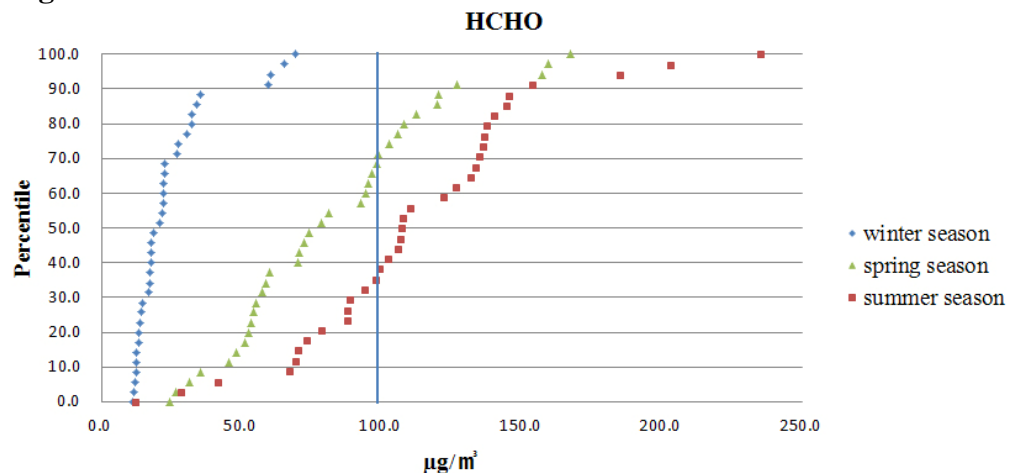


Figure 8. The seasonal variation of PM10

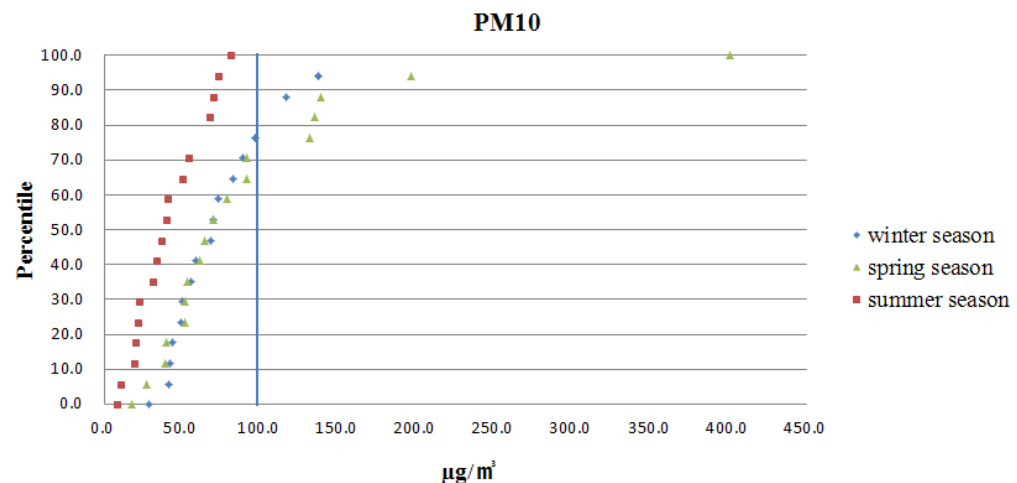
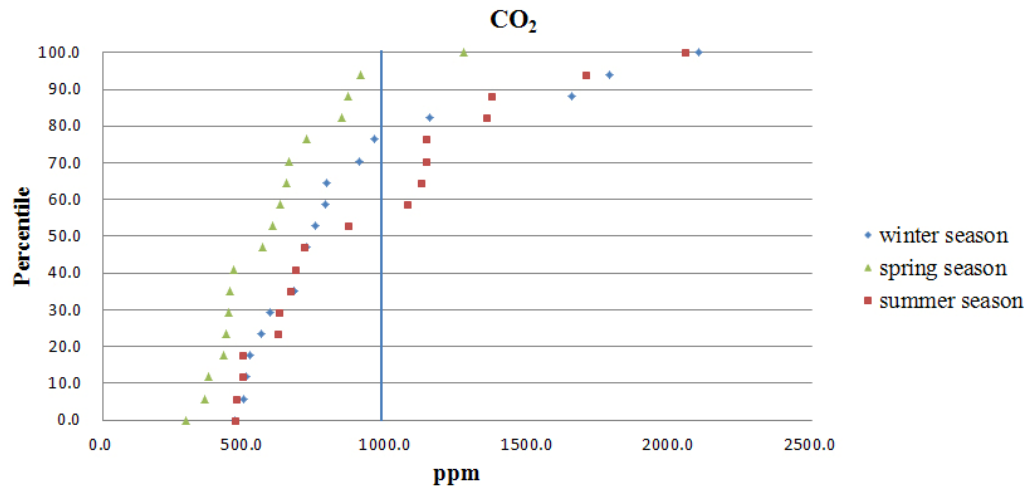


Figure 9 shows the result of CO₂. About 20% of the measurement results are exceeded in winter and more than 40% of the measurement results are exceeded in summer season. The concentration of CO₂ is higher in summer and winter season than spring season. It is considered reduction of air ventilation rate using air conditioning and heating instrument.

Figure 9. The seasonal variation of CO₂



Concentration of bacteria and mold is shown in Figure 10 and Figure 11. Mold and bacteria show higher concentration in summer season than winter and spring seasons. Because mold growth requires favourable temperature condition(a range of 22 °C to 35 °C)^[3], it is thought that the increase of mold concentration is influenced by high temperature in summer season.

Figure 10. The seasonal variation of Bacteria

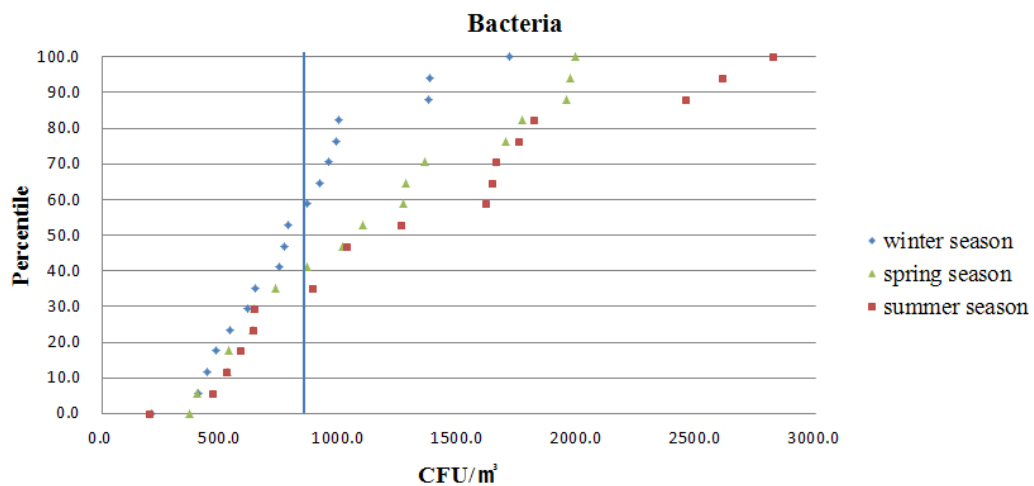
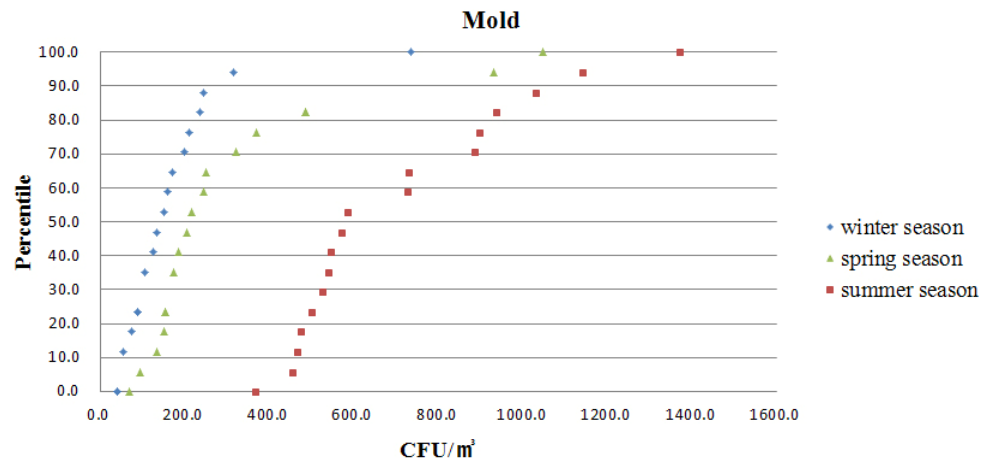


Figure 11. The seasonal variation of Mold



CONCLUSION

This paper investigated the current indoor air quality conditions of children's day care centers in Korea in the selected 75 facilities. 10 children's day care centers of these are chosen to investigate the seasonal differences of indoor contaminants in winter, spring and summer days. The research team has conducted measurement including VOCs, HCHO, PM10, CO₂, CO, mold and bacteria. From this study, VOCs, PM10, CO₂ and bacteria has exceeded the limit value of indoor air contaminants. Thus, careful management of these contaminants is required in children's day care centers. Also, VOCs, HCHO, PM10, CO₂ and bacteria have exceeded the limit value of indoor air contaminants in seasonal measurements. Especially, the concentration of VOCs, HCHO, mold and bacteria is higher in summer season than winter and spring seasons. Thus, appropriate methods considering the characteristics of indoor pollutants are required for the management of good indoor air quality in children's day care centers.

ACKNOWLEDGMENTS

This work was supported by the Korea Research Foundation Grant funded by the Korean Government (MOEHRD, Basic Research Promotion Fund) (KRF-2008-331-D00655).

REFERENCES

- [1] Carrer, P.; Maroni, M.; Alcini, D.; Cavallo, D. *Allergens in indoor air environmental assessment and health effects*, Science of the Total Environment 2001, 270, 1-3, 33-42
- [2] Ministry of Environment, Standard of Indoor Air Quality in Crowd Facilities, 2007
- [3] Hyeun Jun Moon; Young Ran Yoon, *Investigation of Physical Characteristics of Houses and Occupants' Behavioural Factors for Mould Infestation in Residential Buildings*, Indoor and Built Environment 2010, 19, 1, 57-64

Characteristics and Sources of Elements in Atmospheric Particles before and in Heating Period of Beijing

Lingda Yu¹, Guangfu Wang^{1,2,*}, Guanghua Zhu^{1,2} and Renjiang Zhang³

1. Key Laboratory of Beam technology and Materials Modification of Ministry of Education, College of Nuclear Science and Technology, Beijing Normal University, Beijing 100875
2. Beijing Radiation Center, Beijing 100875
3. Key Laboratory of Regional Climate-Environment Research for Temperate East Asia(RCE-TEA),Institute of Atmospheric Phisics, Chinese Academy of Science, Beijing 100029

ABSTRACT

In order to investigate the characteristics of atmospheric particles before and in heating period in Beijing, aerosol samples were collected during October ~ December 2008. Mass concentrations of 16 elements were determined using Proton Induced X-ray Emission (PIXE) technique. The results showed that total concentration of 16 elements in heating period increased by 3 percent than that before heating period. However, several elements concentrations increased evidently. For example, concentrations of As and Cu increased by more than 30 percent, and Pb concentration in fine particles increased by 27 percent. The enrichment factors of Cu, As, and Pb decrease largely compared with those in 1999, which indicated that the controlling methods for particle pollution in Beijing were very effective.

KEYWORDS

atmospheric particles; size distribution; heating period; Enrichment factor

1. Introduction

In most cities of China, atmospheric particles are one of the major air pollutants, especially in Beijing, atmospheric particles have already become the most important air pollutants^[1]. Since 2001, Beijing has implemented more than 160 air pollution control measures on coal-burning, motor vehicle emission, industrial pollution and the dust. The <2008 Beijing environmental aspect bulletin> published by Beijing municipal environmental protection bureau indicates that the concentrations of SO₂, CO and NO₂ in the air of Beijing in 2008 reach level 2 national standards(GB3095-1996),but the concentration of inhalable particles(PM₁₀)exceeds the standard by 22%. In order to investigate the properties of atmospheric particles pollution, there is a need for studies concerning concentrations and composition of atmospheric particles,

and for studies where aerosol size distributions and the origin of the various particles are addressed.

2. Experimental Methods

2.1 Sample collection

The experiment site was located on the top of a 5-m height building above the ground. This site was located in Beijing Normal University (BNU) about 8km north from the centre of Beijing.

Atmospheric particles samples were collected during October 21 to December 12, and were collected 7 times before heating period (from October 21 to November 5) and 9 times during heating period (from Nov 11 to Dec 12). An eight-stage cascade impactor (PIXE international Corp.) was employed to collect aerosol samples, with eight fraction level of <0.25, 0.25-0.5, 0.5-1, 1-2, 2-4, 4-8, 8-16 and >16 μm respectively. The flow rate at the beginning and the end of each sampling interval were recorded and averaged for mean flow rate to calculate the volume of sample air.

2.2 Analysis of the samples

The collected samples were analyzed by PIXE in the BNU by using 2.5 MeV proton bombardments with a beam of 30-40 nA. This method has been compared internationally many times in terms of standard samples to assure the reliability of the method. The concentrations of 16 elements were determined including Mg, Al, Si, S, P, Cl, K, Ca, Ti, Mn, Fe, Ni, Cu, Zn, As and Pb.

3. Results and discussion

3.1 Element concentrations of particles

Total concentration of 16 elements in atmospheric particles before and in heating period in Beijing was plotted in Fig.1. The data of 1999 were quoted from the research results of Renjian Zhang *et al.*^[2]. Total concentrations of 16 elements before heating period increased by 17 percents than that in the same time in 1999. While during the heating period, the total concentrations of 16 elements were almost the same as that in 1999. What should be take note of is that the averaged air pollution index over the sampling days of this study is 25 percents higher than that over the 3 months (October-December), so we can not conclude that the situation of air pollution aggravates in 2008 than in 1999 is based on the growth of 16 elements concentrations as shown in Fig.1. Fig.1 also shows that total concentrations of 16 elements in heating period in 2008 increased by 3 percents than that before heating period, far below the 22 percents growth rate during the same period in 1999. Therefore we can conclude that due to the air pollution control measures implemented in Beijing in recent years, the

impact of heating period on the air quality of Beijing was weakened obviously.

Fig.1 Total concentration of 16 elements of atmospheric particles in Beijing (HP is the abbreviation for heating period)

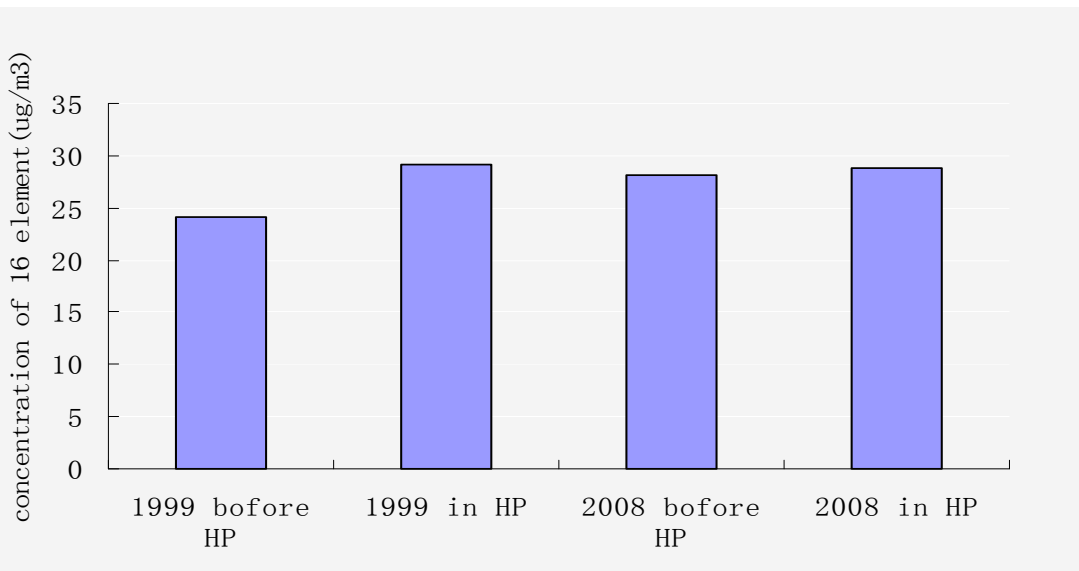


Table 1 shows the ratios of atmospheric particles elemental concentrations in and before heating period in 2008 and 1999. All of the ratios in 2008 are smaller than 1.4. The ratios of K(1.2), Cu(1.32), Fe(1.33) and As(1.39) have relatively large growth rate, the other elements have little change in their concentrations before and in heating period in 2008, while in 1999, the ratios of Al (1.41), Si(1.81), Ti(2.47), Cu(2.01) have rather large growth rate.

Table 1 Ratios of particles elemental concentrations in and before heating period in 2008and 1999

year	Mg	Al	Si	S	P	Cl	K	Ca
2008	1.05	1.13	0.88	1.08	1.02	0.93	1.20	0.99
1999	0.91	1.41	1.81	0.75	1.03	0.57	0.73	0.9
Year	Ti	Mn	Fe	Ni	Cu	Zn	As	Pb
2008	0.88	1.06	1.33	0.92	1.32	1.19	1.39	0.98
1999	2.47	0.87	1.26	1.02	2.01	0.63	0.74	0.38

Table 2 shows the elemental concentrations of fine ($<2\mu\text{m}$) and coarse ($>2\mu\text{m}$) atmospheric particles in Beijing before and in heating period. As shown in Fig.2, the concentrations of 16

elements in fine particles during heating period increased by 17 percents than that before heating period. The fine particles mainly come from human activities and industrial emissions, so the concentration growth in fine particles indicated a contribution of increase of anthropogenic emissions during the heating period. The concentrations of 16 elements in coarse particles decreased by 6 percents in heating period. Coarse particles mainly come from soil and construction dust. The concentration decrease of coarse particles may be due to the temperature in heating period was lower and the ground surface was frozen and hard to generate dust outflow.

Table2 Elemental concentrations of atmospheric particles in Beijing before and in heating period

元素	Before heating period				In heating period				总浓度 /(ng·m ⁻³)		
	Fine particle(<2μm)		coarse particle(>2μm)		总浓度 (ng·m ⁻³)	细粒子(<2μm)		粗粒子(>2μm)			
	浓度	百分比	浓度	百分比		浓度	百分比	浓度			
	/ (ng·m ⁻³)		/ (ng·m ⁻³)			(ng·m ⁻³)		/ (ng·m ⁻³)			
Mg	1679	44%	2119	56%	3798	1708	43%	2291	57%	3999	
Al	1441	39%	2275	61%	3716	1746	41%	2467	59%	4213	
Si	1859	28%	4674	72%	6533	2147	37%	3617	63%	5764	
S	1672	59%	1167	41%	2839	1933	63%	1129	37%	3062	
P	518	50%	522	50%	1040	501	47%	564	53%	1065	
Cl	1087	57%	830	43%	1917	1252	70%	539	30%	1791	
K	631	53%	549	47%	1180	853	60%	567	40%	1420	
Ca	1420	30%	3302	70%	4722	1645	35%	3034	65%	4679	
Ti	32	23%	109	77%	141	37	30%	88	70%	125	
Mn	26	40%	39	60%	65	37	54%	32	46%	69	
Fe	506	33%	1038	67%	1544	761	37%	1291	63%	2052	
Ni	11	18%	49	82%	60	13	24%	42	76%	55	
Cu	51	62%	31	38%	82	75	69%	33	31%	108	
Zn	164	55%	135	45%	299	295	83%	62	17%	357	
As	15	65%	8	35%	23	23	72%	9	28%	32	
Pb	45	44%	58	56%	103	57	56%	44	44%	101	
总量	11157	40%	16905	60%	28062	13083	45%	15809	55%	28892	

3.2 Spectral distribution of element concentrations

In order to better understand the chemical element composition of atmospheric particles before and in heating period in Beijing, the mass particle-size distributions (MSDs) were determined for major elements Si, Mg, Al, Ca, Ti, Fe, As, S, K, Pb and Cu.

3.3 enrichment factor analysis

Table 3 compares the EF values of atmospheric particles in Beijing before and in heating period in 1999 and 2008. As shown in table 3, the EF values of Al, K, Ti, Mn, Fe are generally below 5, indicating these elements are mainly from natural source. The EF values of S, Cl, Zn, As, Pb are much larger than 10, and the degree of enrichment in fine particles are much higher than that in coarse particles, indicating that these elements are mainly from anthropogenic source. The EF values of Cu, Zn, As and Pb in fine particles have a significantly increase during heating period in 2008, reflecting the pollution characteristics of coal and heavy oil burning in Beijing City.

Table 3 Enrichment factors of atmospheric particles in Beijing Before and in heating period

Time	Particles	Mg	Al	S	Cl	K	Ca	Ti	Mn	Fe	Ni	Cu	Zn	As	Pb
1999 before HP	Fine		4	1205	1596	6	3	1	12	2	19	128	566	4036	1644
	Coarse		2	129	145	1	6	1	4	2	40	55	72	1399	157
1999 in HP	Fine		3	649	790	2	2	1	7	2	31	395	319	3697	523
	Coarse		2	77	50	1	3	2	2	1	19	30	25	510	41
2008 before HP	Fine	12	3	951	1237	4	6	1	4	2	22	137	345	1241	515
	Coarse	6	2	264	376	1	5	2	2	1	38	33	114	263	264
2008 in HP	Fine	10	3	952	1234	4	6	1	5	2	34	175	542	1648	565
	Coarse	8	2	330	315	2	6	2	3	2	59	46	67	383	259

CONCLUSIONS

- 1, Total concentrations of 16 elements in heating period in 2008 increased by 3 percents than that before heating period in Beijing, far below the 22 percents growth rate during the same period in 1999. The impact of heating period on the air quality of Beijing was weakened obviously.
- 2, The concentrations of S, As, Cu and Pb in fine particles increased by 8, 39, 32 and 27 percents during heating period than that before heating period, this was mainly due to the combustion of coal and heavy oil during heating period.
- 3, Total concentrations of 16 elements in coarse particles during heating period in 2008 decreased by 25 percents than that in 1999, indicated that the dust pollution in Beijing winter

had been controlled effectively,

4, The analysis of enrichment factors showed that the EF values of typical pollution elements Cu, As and Pb in fine particles before and during heating period decreased obviously than that in the same time in 1999.

REFERENCES

- [1]Yu S Q,Lin X C,Xu X D. Temporal and spatial characteristics of air pollution in Beijing[J].Journal of Applied Meteorological Science, 2002.13(suppl.):92-99
- [2] Zhang R J,Wang M X,Hu F,*et al.* Elemental concentrations and distributions of atmospheric particles before and in heating period in Beijing[J]. Journal of the Graduate School of the Chinese Academy of Sciences, 2002. 19(1): 75-81

Emission of Particulate Polycyclic Aromatic Hydrocarbons from Various Combustion Sources in China

Xinghua Li¹, Shuxiao Wang², Duan Lei², and Jiming Hao²

1 Beihang University, 37 Xuyuan Road, Haidian District, Beijing, China 100191

2 Tsinghua University, Tsinghua Park, Haidian District, Beijing, China 100084

Principal Contact: Xinghua Li, Ph.D, Associate Professor, Beihang University, 37 Xuyuan Road, Haidian District, Beijing, China 100191.

Tel: 86-10-82316160 Fax: 86-10-82314215 Email: lixinghua@buaa.edu.cn

Abstract

Field measurements were conducted to investigate particulate polycyclic aromatic hydrocarbons (PAHs) from various combustion sources in China. The combustion sources include biomass open burning, coal and biofuel combustion. Tests were carried out to determine air pollutants from open burning of two major agricultural residues, wheat straw and maize stover. The headfire ignition technique was adopted and sampling was performed downwind from the agricultural fire. Coal was burned in a household stove, two grate boilers (equipped with a cyclone and a wet limestone scrubber, respectively), a pulverized coal fired boiler (equipped with an electrical precipitator and a wet flue gas desulfurization system), respectively. Three types of biofuels (wheat straw, maize stover, and wood) were burned in a household stove. A dilution sampler was applied to measure stack gas emissions from coal and biofuel combustion. The collected PM_{2.5} samples were analyzed by GC-MS to determine 16 priority US EPA PAHs. Emission factors of PAHs from various combustion sources were determined. The results indicate that the coal burned in the household stove produces the highest PAH emissions among the measured sources, i.e. 24.5 mg/kg of 16 PAHs. The next is biofuel burning and their emission factors range from 10.4 to 13.9 mg/kg. Biomass open burning emitted a little less PAHs than biofuel combustion. While coal fired boilers yielded much less PAHs than the above three types of sources. The pulverized coal fired boiler produces 3 orders of magnitude lower than coal fired stove, only 0.03 mg/kg.

Keywords: Biomass open burning, biofuel combustion, coal combustion, PAHs, emission factors

Components of PM_{2.5} and its source apportionment by PFA from 2000 to 2001 in Shanghai

Guangli Xiu^{1,3,4}, Qi Ying², Donald Lucas^{3,4}, Koshland³ and Danian Zhang¹

1 East China University of Science & Technology, 130 Meilong Road, Shanghai 200237, China

2 Department of Civil Engineering, Texas A&M University, College Station, TX 77845, USA

3 School of Public health, University of California at Berkeley, Berkeley, CA 94702, USA

4 Environmental Energy Technologies Division, Lawrence Berkeley National Laboratory, Berkeley, CA 94702

Principal Contact: Guangli Xiu, Professor, East China University of Science & Technology, 130 Meilong Road, Shanghai 200237.

Tel: 86-21-64251927 Fax: 86-21-64253113 Email: xiugl@ecust.edu.cn

Abstract

The PM_{2.5} samples were collected in typical seasons in five sampling sites from 2000 to 2001. The constituents including elements, ionic compositions, and carbonaceous species were analyzed. Except ammonium, the size distribution of most other ions such as sulfate, nitrate, chloride took bimodal type with coarse particle mode (4μm) and accumulation mode (0.5~0.7μm). The seasonal characteristics of size distribution of ions varied with different sampling location. Sulfate had the largest fraction followed by nitrate, chloride and ammonium sequentially. Based on the molar ratio between ammonium, sulfate, nitrate and chloride, (NH₄)₂SO₄ was predicted to be the major existing state in fine particle while NH₄HSO₄ and (NH₄)₂SO₄ might be the main species in coarse particle mode. The organic carbon (OC) and elemental carbon (EC) were also measured and compared.

The correlation to characteristics component, principal component analysis- and single particle micro-analysis were combined to identify the sources of particles. The results indicated that re-suspended dust might be a significant contributor to PM_{2.5} in Shanghai. SEM/EDX was used to study the elemental compositions and surface morphology of single particle. The lead isotope and its ²⁰⁷Pb/²⁰⁶Pb ratio were measured to separate contribution of coal combustion and traffic exhaust. Through comparing the characteristics components, the sources of PM_{2.5} were proposed.

Keywords: PM_{2.5} Shanghai, source apportionment

Different Characteristics of Carbonaceous Components in Size-Segregated Particles between a Roadside and a Suburban site

Linfa Bao^{1,2}, Masami Furuuchi¹, Mitsuhiro Hata¹ and Kazuhiko Sakamoto²

1 College of Science and Engineering, Kanazawa University, Kakuma-machi, Kanazawa 920-1192, Japan

2 Graduate School of Science and Engineering, Saitama University, 255 Shimo-Okubo, Sakura, Saitama 338-8570, Japan

Principal Contact: Linfa Bao, College of Science and Engineering, Kanazawa University, Kakuma-machi, Kanazawa 920-1192, Japan.

Tel: +81-76-2344647 E-mail: linfabao@gmail.com

Abstract

Carbonaceous aerosol has been receiving increased attentions due to its link with regional climate, water resources, visibility reduction, air quality, and public health. Aerosol carbon is commonly classified as organic carbon (OC) and elemental carbon (EC). EC is emitted directly from combustion sources and undergoes little chemical transformation after emission. It is thus a good indicator of primary anthropogenic air pollutants. However, OC and WSOC are emitted from primary emission sources and can also be derived from chemical reactions of gaseous organic precursors in the atmosphere. Water-soluble organic compounds potentially play an important role in aerosol–cloud interaction, and are contributors to cloud condensation nuclei (CCN). The ability of water-soluble organic particles to act as CCN has been explained on the basis of both the hygroscopic and surface-active properties of water-soluble organic compounds, which in turn depend on their chemical composition. It is commonly believed that the water-soluble organic carbon (WSOC) fraction is “low” for primary organic carbon (OC) and that it increases with aging of the aerosol, together with the general oxidation state of organic matter. This study focused on carbonaceous components of size-segregated particles collected by aerosol samplers at a roadside site and a suburban site in Saitama, Japan. Detailed chemical characterizations of carbonaceous components (including OC, EC, char-EC, soot-EC, Py-OC, WSOC) as well as water-soluble organic acids and levoglucosan in size-segregated samples were measured to clarify the sources and formation pathways of carbonaceous particles.

Keywords: organic carbon, elemental carbon, water-soluble organic carbon, organic acids, levoglucosan, secondary formation.

Size Distribution and Chemical Composition of PM_{1.0}, PM_{2.5} and PM₁₀ in the Industrial City in Korea

Minkyun Kim

RIST (Research Institute Industrial Science and Technology), #32 Hyoja-Dong Nam-Gu, Pohang City, 790-330 Gyeongbuk Korea

Principal Contact: Minkyun Kim, Senior Researcher, RIST, #32 Hyoja-Dong Nam-Gu, Pohang City, 790-330 Gyeongbuk Korea.

Tel: +82 54 279 6541 Fax: +82 54 279 6239 Email: kimmk@rist.re.kr

Abstract

The twenty two inorganic elements such as iron, manganese, nickel, lead, carbon, nitrate, sulfate and 16 PAHs were determined from selected PM_{1.0}, PM_{2.5} and PM₁₀ samples collected at six monitoring sites near iron and steel complex of Pohang during different seasons from March 2009 to February 2010. Pohang is the largest industrial city producing iron and steel in Korea and has distinguishing chemical composition in the airborne particular matter. Particulate matter was collected at 10 repetitions for each season. The average mass concentrations of PM_{1.0}, PM_{2.5} and PM₁₀ were 17.6 ug/m³, 31.3 ug/m³ and 48.2 ug/m³, respectively. PM_{1.0}/PM₁₀ of six monitoring sites ranged from 0.29 to 0.45 (average 0.37). The toxic elements such as arsenic, lead, cadmium, nickel, chromium, carbon were founded about 80% of PM₁₀ in PM_{1.0}. In contrast, nitrate, sulfate and ammonium ions were higher in PM₁₀ than PM_{1.0}. The contents of poly aromatic hydrocarbons showed many difference in variation of PM size for each compounds.

Keywords: PM₁₀, PM_{2.5}, PM_{1.0}, size distribution, PAHs, Korea

Carbonaceous, inorganic, some molecular markers and stable isotopic compositions in the Mumbai aerosols for the implications of their sources and atmospheric processing

Shankar G. Aggarwal^{1,2}, Kimitaka Kawamura², Govindraj S. Umarji³, Eri Tachibana², Rashmi S. Patil³, and Prabhat K. Gupta¹

1 National Physical Laboratory-CSIR, New Delhi 110012, India

2 Institute of Low Temperature Science, Hokkaido University, Sapporo 060-0819, Japan

3 Centre for Environmental Science and Engineering, Indian Institute of Technology Bombay, Mumbai - 400076, India

Principal Contact: Shankar G. Aggarwal, Dr., National Physical Laboratory – CSIR, New Delhi 110012, India.

Tel: +91 11 4560 8376 Fax: +91 114560 9310 E-mail: aggarwalsg@nplindia.org

Abstract

Aerosol chemical compositions, i.e., total carbon (TC), organic carbon (OC), elemental carbon (EC), water-soluble organic carbon (WSOC), inorganic ions together with some marker species, e.g., nssSO₄²⁻, nssCa²⁺, nssK⁺, methanesulfonate (MSA), oxalic acid (C₂), azelaic acid (C₉), levoglucosan determined in PM₁₀ samples revealed that biofuel/biomass and fossil fuel burning are the major sources of the Mumbai aerosols. Nitrogen-isotopic ($\delta^{15}\text{N}$) composition of aerosol total nitrogen ranged from 18.1 to 25.4‰, suggesting that biofuel/biomass burning is the dominant source in both summer and winter seasons. Chemical composition and aerosol mass loading were observed to be sensitive to transport patterns as well as seasons. Aerosol mass loading and concentration of bulk species increased 3-4 times in wintertime. Photochemical production tracers, oxalic acid and nssSO₄²⁻ do not show diurnal changes. Concentrations of C₂ and WSOC show an excellent correlation ($r^2 = 0.95$). In addition, WSOC to OC (or to TC) ratios remain almost unchanged for day- (0.37 (0.28)) and nighttime (0.38 (0.27)), suggesting that the influence of local sources, i.e., mixing of fresh aerosols was not significant rather aerosols were photochemically well processed. Concentrations of MSA and C₉ showed a good correlation ($r^2 = 0.75$), indicating a marine influence in aerosol. Stable C-isotopic ratios ($\delta^{13}\text{C}$) of TC ranged from -27.0 to -25.4‰ with lower average (-26.5 ± 0.3‰) in summer and slightly higher in winter (-25.9 ± 0.3‰). Correlations between $\delta^{13}\text{C}$ values and ratios of some specific markers with TC, e.g., nssSO₄²⁻/TC, levoglucosan-C/TC and EC/TC also supported the major sources identified for the Mumbai aerosols. While the correlation between $\delta^{13}\text{C}$ values and WSOC/TC ratios suggested that the increment in ¹³C of aerosol C in wintertime can be regarded as prolonged photochemical processing of organic aerosols and/or enhanced biofuel/biomass burning emissions in this season.

Keywords: Tropical urban aerosols, composition, sources, atmospheric processing

Metals in aerosol as potential tracers for waste, fossil fuel, biomass/biofuel burning and dust sources

Shankar G. Aggarwal, Sudhanshu Kumar, Rajeev K. Saxena, Khem Singh, and Prabhat K. Gupta

Analytical Chemistry, National Physical Laboratory, New Delhi 110012, India

Principal Contact: Shankar G. Aggarwal, Dr., National Physical Laboratory, New Delhi 110012, India.

Tel: +91-11-45608376 Fax: +91-11-45609310 Email: aggarwalsg@mail.nplindia.ernet.in

Abstract

The source apportionment studies are important to control the sources of anthropogenic aerosols, and to better understand the impact of a particular source on aerosol loading. Several chemical tracers and/or compound classes have been reported for particular source identification. Compound specific stable carbon isotope composition has also been used to trace the sources. Similarly, stable -carbon and -nitrogen of total carbon and nitrogen of aerosol, respectively have also been reported for the tracing of aerosol source contributions. Radio-carbon isotope composition in aerosol is also one of the potential tools to identify fossil fuel and biomass burning source contributions in organic aerosols. However, the reports on such chemical tracers are very limited, and more extensive research is needed in this area. We collected aerosol types using low-volume handy samplers, very close to the vicinity of a particular source, such as open-waste burning at a land fill site, beside a road at jam-packed traffic site, smokestack at thermal power plant, and biomass/biofuel burning at domestic cooking stove in New Delhi. We also collected some dust aerosol samples from the desert site in India. Using ICP-HRMS technique, we found a prominent existence of Sn in waste burning; Pb, Pt, and Pd in traffic sites, Hg in power plant site, K in biomass/biofuel burning, and Fe in dust aerosols. We also collected particulate material in New Delhi using high-volume samplers and found these metals in urban aerosols, suggesting these metals may be the potential tracers for identifying the major sources of aerosols. A case study for source apportionment based on these metal tracers with their specific isotope ratios will be presented.

Keywords: Aerosol types, metal tracers, isotope ratio, sources

Fine and coarse particle mass distributions in New Delhi

Khem Singh¹, Arvind K. Jha¹, Shankar G. Aggarwal¹, Z. H. Khan², and Prabhat K. Gupta¹

1 National Physical Laboratory -CSIR, New Delhi 110012, India

2 Department of Physics, Jamia Millia Islamia University, New Delhi 110025, India

Principal Contact: Khem Singh, Mr., National Physical Laboratory, New Delhi 10012, India.

Tel: +91 11 4560 8392 Fax: +91 11 4560 9310 Email: khem008@nplindia.org

Abstract

Mass distributions of fine and coarse aerosol particles in New Delhi were studied for ~2 years, i.e. from December 2005 – January 2008. Particles were collected on pre-treated quartz filter using mid-volume 8-stage Andersen cascade impactor sampler. The mass of fine ($PM_{2.5}$) and coarse (PM_{10}) particles was integrated from particle mass determined in different stages. New Delhi experiences three distinct seasons: summer (March to June), monsoon (July to October) and winter (November to February). The highest concentrations of PM_{10} (874 g m^{-3}) and $PM_{2.5}$ (368 g m^{-3}) were observed in the month of June 2006, whereas the lowest concentrations of PM_{10} (64 g m^{-3}) and $PM_{2.5}$ (29 g m^{-3}) were determined in the month of September 2007. An increased trend of aerosol loading was observed during summer and winter, whereas aerosol mass was found to decrease during monsoon season. In summer, because of the frequent dust storms, coarse particles are dominant than that of fine particles, and during winter, $PM_{2.5}$ contribution became more pronounced as compared to summer. This is probably due to the enhanced emissions from local/surrounding sources, such as biofuel/biomass burning in winter season. A high ratio (0.58) of $PM_{2.5}/PM_{10}$ was obtained during winter 2005-2006, which was found to decrease with the onset of summer and reaches to a low ratio (0.36) during May 2006. A strong relation between PM_{10} and $PM_{2.5}$ is observed, which indicates that variation in PM_{10} mass is governed by the variation in $PM_{2.5}$ mass. The present concentration of PM_{10} in New Delhi is found to exceed the permissible limits of national ambient air quality standards of India.

Keywords: Aerosol mass, $PM_{2.5}$ and PM_{10} , seasonality

Characteristics and source regions of the biomass burning tracer levoglucosan in spring at four background sites in South China

Zhisheng Zhang¹, Chuen-Yu Chan¹, Guenter Engling², Xuefang Sang¹ and Ting Zhang¹

1 School of Environmental Science and Engineering, Sun Yat-sen University, Guangzhou, 510275, China

2 National Tsing Hua University, Department of Biomedical Engineering and Environmental Science, Hsinchu 300, Taiwan

Principal Contact: Chuen-Yu Chan, Professor, School of Environmental Science and Engineering, Sun Yat-sen University, Guangzhou, 510275.

Tel: +86-020-84112400 Email: chzy@mail.sysu.edu.cn

Abstract:

An intensive field study was carried out to identify the influence of biomass burning and the associated source regions during spring in South China. Ambient concentrations of the biomass burning tracer levoglucosan were determined at four background stations: Jianfengling (JFL) on Hainan Island, Hok Tsui (HT) in Hong Kong, Lin'an (LA) in Zhejiang province and Tengchong (TC) in Yunnan province. Exceptionally high levels of levoglucosan were found in TC, with an average concentration of $1070 \text{ ng} \cdot \text{m}^{-3}$, while those at the other sites were lower by two orders of magnitude. Elevated levoglucosan levels were further investigated with the help of fire hot spot counts and aerosol index derived from satellite data, as well as backward trajectories. Southwest Asia, the Philippines and the Southeast China coast area were identified as source regions of biomass burning aerosol transported to South China. Using a simplified receptor-based model, the contribution of biomass burning to OC was estimated to be as high as 73% at the TC site due to strong influence by biomass burning activities in Southwest Asia. Moreover, the widespread biomass burning smoke plumes derived from the Philippines were reported for the first time in this study, accounting for 21% and 4.5% of OC in $\text{PM}_{2.5}$ at JFL and HT, respectively.

Keywords: Biomass combustion; Levoglucosan; Source apportionment; Long-range transport

Characterization of water-soluble organic carbon in ash samples from a coal combustion boiler

Seung Shik Park, Ja-Hyun Kim, and Jae-Uk Jeong

Department of Environmental Engineering, Chonnam National University, 300 Yongbong dong, Buk-ku, Gwangju 500-757, Korea

Principal Contact: Seung Shik Park, Professor, Department of Environmental Engineering, Chonnam National University, 300 Yongbong dong, Buk-ku, Gwangju 500-757, Korea.

Tel: +82-62-530-1863 Fax: +82-62-530-1859 E-mail: park8162@chonnam.ac.kr

Abstract

Chemical characterization of organic carbon soluble in water in dust emitted from a coal combustion boiler has not been reported yet. A total of 5 ash samples were collected from the outlet of an electrostatic precipitator in a commercial 500 MW coal-fired power plant for their chemical characterization. XAD7HP resin was used to quantify hydrophilic and hydrophobic water-soluble organic carbons (WSOC), which are termed the fractions of WSOC that penetrate and retained on the resin column, respectively. Calibration results performed using a variety of organic standards indicated that hydrophilic fraction included aliphatic dicarboxylic acids and carbonyls (<4 carbons), amines, and saccharides, while the hydrophobic fraction included aliphatic dicarboxylic acids (>4-5 carbons), phenols, aromatic acids, cyclic acid, and humic acid. Average mass of the WSOC in the ash samples depended on the coal type burned, ranging from 179 to 300 µg C/L, which accounts for 0.02-0.03 wt% of the used ash mass. Results indicated that the hydrophilic WSOC fraction in the ash samples accounted for 64-82% of the total WSOC, which are 2-4 times greater than the masses of hydrophobic WSOC fraction.

Keywords: Coal combustion, ash, WSOC, XAD7HP resin

Characterization of hydrophilic and hydrophobic fractions of water-soluble organic carbon in PM_{2.5} at an urban site

Seung Shik Park, Jae-Uk Jeong, and Ja-Hyun Kim

Department of Environmental Engineering, Chonnam National University, 300 Yongbong dong, Buk-ku, Gwangju 500-757, Korea

Principal Contact: Seung Shik Park, Professor, Department of Environmental Engineering, Chonnam National University, 300 Yongbong dong, Buk-ku, Gwangju 500-757, Korea.

Tel: +82-62-530-1863 Fax: +82-62-530-1859 E-mail: park8162@chonnam.ac.kr

Abstract

The current understanding of the atmospheric carbonaceous particles describes their water-soluble organic carbon (WSOC). In order to better understand the characteristics of the WSOC fraction, daily PM_{2.5} aerosol samples were collected during the winter (November 26, 2008 – February 27, 2009) and summer (July 28 – August 22, 2009) intensive observation periods at an urban site of Gwangju, Korea. The extracted filter samples were filtered with 0.45 μm syringe filter and separated into two WSOC fractions, i.e., hydrophobic and hydrophilic fractions, using a solid phase extraction technique. A commercial glass column filled with XAD7HP resin was used to separate total WSOC into hydrophilic and hydrophobic fractions. Hydrophobic had been adsorbed onto column when the pH of the samples is adjusted to 2, and hydrophilic then had passed through the column. Group-separated fractions were quantified with Total Organic Carbon (TOC) analyzer. Higher WSOC/OC was found in summer (mean: 0.53, range: 0.40-0.68) than in winter (mean: 0.43, range: 0.19-0.68). Considering that the average WSOC/OC in summer is greater than that in winter, these results suggest that the aerosols collected in summer were more aged or photo-chemically processed than those in winter.

Keywords: Organic aerosol, water-soluble organic carbon, XAD resin, hydrophilic fraction, and hydrophobic fraction

The study for inorganic compounds in ambient aerosols by FTIR in Hefei

Xiuli Wei, Minguang Gao, Jianguo Liu, Yihuai Lu, Wenqing Liu, Bei Wang, Liang Xu and Tianshu Zhang

Anhui institute of optic and fine mechanics, Chinese Academy of Science, Hefei P. O. box 1125 Anhui, China

Principal Contact: Xiuli Wei, Anhui institute of optic and fine mechanics, Chinese Academy of Science, Hefei P. O. box 1125 Anhui, China.

Tel: 0551-5593693 Email: xlwei@aiofm.ac.cn

Abstract

The study for inorganic compounds in ambient aerosols by FTIR indicate that what is the source of ambient aerosols in Hefei. In winter, when the diameters are smaller than $2.5 \mu m$, the human activities is the main sources, such as waste dumping, landfills and the exhaust gas from the vehicle. When the diameters are larger than $2.5 \mu m$, the ore is the main sources .

Keywords: ambient aerosols, FTIR, inorganic compound

Observational Study of Black Carbon in Urumqi in Winter of 2009

Xin-chun Liu^{1,2}, Yu-ting Zhong^{1,2}, Qing He^{1,2}, Mamtimin Ali^{1,2}, Zhi-zhong Guo³

1 Institute of Desert Meteorology, CMA, Urumqi 830002, China

2 Key Laboratory of Tree-ring Physical and Chemical Research of China Meteorological Administration/Xinjiang Laboratory of Tree Ring Ecology, Urumqi 830002, China

3 Urumqi meteorologicsatellite ground station, xinjiang, Urumqi 830011, China

Principal Contact: Xin-chun Liu, Vice researcher, Institute of Desert Meteorology, CMA, No.46 Jianguo Road Urumqi Xinjiang 830002 China.

Tel:0086 991 2651450 Fax:0086 991 2621387 E-mail: liuxinchun2001@163.com

Abstract

Based on Black Carbon aerosol (BC) observations in Urumqi atmospheric composition observatory station from December of 2009 to February of 2010, as well as the PM observations and the BC result of other areas, the Black Carbon aerosol (BC) variation characters and effect factor were studied. The result shows that the daily average concentration of BC was $12.442 \pm 5.407 \mu\text{g} \cdot \text{m}^{-3}$ with the range $2.685 \sim 26.691 \mu\text{g} \cdot \text{m}^{-3}$ in winter in Urumqi. The variational trend of BC was close to API with the correlation coefficient 0.660. In addition, the daily variation of BC concentration was characterized by obvious two peaks character during in winter with the highest concentration at forenoon and nighttime and the lowest at wee hours and afternoon. There were sharp increase of 2~3 days to several days in the daily distribution, and there was coincident with the process activities of the weather. The weekly variation of BC concentration decreases from Monday to Thursday and increases from Friday with a little tendency, while the difference between working day and weekend is unobvious. The third, the frequency of BC hourly average concentration was consistent with lognormal distribution in winter, and the background concentration was $6.146 \mu\text{g} \cdot \text{m}^{-3}$. The variational trend of BC was close to the daily average concentration of PM₁₀, PM_{2.5} and PM_{1.0} at the level of 0.001 with the correlation coefficient 0.526, 0.538 and 0.548; and BC in PM₁₀, PM_{2.5} and PM_{1.0}, respectively were about 6.8 %, 8.2% and 9.2%, which indicated that BC was an important component of PM. The last, BC concentration of Urumqi was higher compared with some cities at home and abroad, significantly higher than the relatively clean remote areas, and larger than the value at Waliguan Global Atmospheric Baseline Observatory and South Pole.

Keywords: Black Carbon aerosol, variation character, winter, Urumqi

The Features of Ionic Components of TSP and Factors Analysis in Urumqi

Qing He^{1,2}, Hao Yang^{1,2}, Xinchun Liu^{1,2} and Yuting Zhong^{1,2}

1 Institute of Desert Meteorology, CMA, Urumqi 830002, China;

2 Key Laboratory of Tree-ring Physical and Chemical Research of China Meteorological Administration/ Xinjiang Laboratory of Tree Ring Ecology, Urumqi 830002, China

Principal Contact: Qing He, Professor, Institute of Desert Meteorology, CMA, No.46 Jianguo Road Urumqi Xinjiang 830002 China.

Tel: +086 991 2642256 Fax: +086 991 2621387 E-mail: qinghe@idm.cn

Abstract

According the data of 4 atmospheric total suspended particles (TSP) observation sites in Urumqi from 2007 to 2011, The article analyses the space-time distribution characteristics of TSP. Meanwhile, the paper emphatically analyzes the water-soluble ionic components of 2009 TSP through the ion chromatography. The results show that: (1) Mass concentration of TSP in Urumqi main city zone has significant seasonal variation, winter>spring> autumn> summer. As space distribution concerned, Weixing station>Annual rings laboratory>Leida station>Baiyang station. The mass concentration of TSP of every stations has been increasing trend.(2) SO_4^{2-} , Ca^{2+} , NO_3^- and NH_4^+ levels higher than the other ions of TSP in 2009. Every ion concentration has significant seasonal variation characteristics. All the concentration of the ions increased obviously in heating period. SO_4^{2-} 、 NO_3^- gained the most growth. (3) The total ion concentration in Urumqi main city zone is $151.28\mu\text{g}/\text{m}^3$, and in Baiyang station is $40.83\mu\text{g}/\text{m}^3$. The ratio of $\text{NO}_3^-/\text{SO}_4^{2-}$ in every station is low. It shows that the atmospheric pollution is mainly from fixed pollution sources in Urumqi. (4) Through the analysis of each major ions relevant, it shows that the correlation coefficient of NH_4^+ and SO_4^{2-} is 0.828, and the correlation coefficient of NH_4^+ and NO_3^- is 0.659, this suggests that ammonium compounds mainly exists in the form of ammonium sulfate and ammonium nitrate. The correlation coefficient of NO_3^- and SO_4^{2-} is 0.973, this suggests that they come from sulfur dioxide and nitrogen oxides. The crust elements have close correlation between Ca^{2+} and Mg^{2+} , the correlation coefficient is 0.914. It shows that they come from the common place. They may come from sand dust , soil dust, road dust and building dust.

Keywords: TSP, Chemical composition, Influence factors, Urumqi.

Characteristics of Chemical Compositions and Sources of PM₁₀ in Resuspended Dust in Taiyuan, Changzhi and Jincheng City

Pengjiu Zhang¹, Lin Peng^{*1}, Ling Mu¹, Ying Wang¹ and Haodong Ji¹

1 Institute of Environment Science and Engineering, Taiyuan University of Technology,
Taiyuan 030024, China

ABSTRACT

Samples of urban resuspended dust were collected in Taiyuan, Changzhi and Jincheng city, and the chemical composition characteristics of PM₁₀ from resuspended dust were researched respectively. Crustal elements and TC were in abundance in resuspended dust. Some trace elements enriched in suspended dust indicated that it correlated closely with human activities such as producing and consuming. The profiles of resuspended dust were different in these cities. According to the results of CMB receptor mold, soil, coal combustion and cement were the main source types of resuspended dust in these cities, and the contributions in Taiyuan were 48%、24%、15%, in Changzhi were 45%、31%、18%, and in Jincheng were 51%、27%, 14% respectively.

KEYWORDS

Resuspended Dust, PM₁₀, Chemical Composition, Sources

BODY

1. Introduction

Resuspended dust is a very complex mixture dust source category, and wind caused soil dust, construction dust, vehicle exhaust dust, steel dust, and etc. are single dust source category. The study conducted by Feng yinchang from Nankai university in China suggests

*Corresponding author: Peng Lin.penglin6611@163.com

This research project was financially supported by the Natural Science Foundation of China (NSFC)(No.40873004).

that after particulate matter from the single dust source emitted into atmosphere, the matter would settle to the ground, roads, buildings, roof, bay windows and any other places where can accommodate particulate matter due to the effect of gravity, and then, these particulate matter would re-emit into atmosphere again and again, which caused by the forces of nature power or human activities, this kind of particulate matters are called resuspended dust^[1].

In recent years, many cities in China are using chemical mass balance (CMB) receptor model to analyze the source of TSP and PM₁₀ in air^[2,3], and some research results show that the dust is the main contributors of TSP and PM₁₀^[4]. But the rate of dust emission is difficult to determine, therefore, there were few reports about the source of emissions, especially the chemical composition of fine particulate matter PM₁₀^[4].

The analysis was made about the comparison of the characteristics of respirable particulate matter in the dust, especially the source of PM₁₀ dust and chemical compositions in Taiyuan, Changzhi and Jincheng. The objective is intended to establish component spectrum to investigate the source of dust, in order to assist a scientific and rational decision-making associated with source emissions reduction.

2.Experimental Methods

2.1 Sampling and Processing

The resuspended dust sample was collected in Changzhi, Jincheng and Taiyuan , sampling time and sample number in Table 1. The collection point of urban dust is generally located in the window sill or platform on the building which did not clean for such long period of time, the sampling height was 5 ~ 15m, sampling method was to use a clean brush to collect the sill or the plains of dust,which was stored in a polyethylene bag. Sample points were set in different functional zones within three cities. The surrounding environments of sampling sites stay away from interference caused by smoke, industrial smoke, automobile, construction sites and other man-made sources.

Table 1. Time of sampling and numbers of samples for resuspended dust

City	Time of sampling	Sampling spots
Taiyuan	2007.1.20 -24, 4.9.-13, 9.25 -29	40
Changzhi	2007.1.20 -24, 4.10 -14	30
Jincheng	2006.9.12 -16, 12.21 -25	40

2.2 Chemical Analysis

The elemental analysis, carbon analysis and ion analysis were conducted for the collected samples of dust particles. The dust samples were baked in the oven with the condition of 50 °C for 24 hours, then over 150 mesh nylon sieve, the sifted sample were graded by using Bake Grade Instrument, and finally acquired the dust samples with particle size less than or equal 10μm . Samples of soluble fractions SO_4^{2-} , NO_3^- , Cl^- were analyzed using ion chromatography, total carbon (TC) and organic carbon (OC) were analyzed using the carbon analyzer, inorganic elements were analyzed by ICP analysis. Analysis and testing technologies as follows:

1. ICP analysis of 19 elements: Na, Mg, Al, Si, K, Ca, Ti, V, Cr, Mn, Fe, Co, Ni, Cu, Zn, As, Hg, Cd, Pb;
2. China's Ministry of SMT-2 type of pyrolytic carbon analyzer, analysis of TC, OC + EC;
3. British Diane's DX-100 IC Ion chromatography analysis of Cl^- , NO_3^- , SO_4^{2-} .

3. Results and Discussion

3.1 The Resuspended Dust Ingredients Spectrum

The results of chemical analysis of samples for three different cities were averaged together to calculate the annual mean value. Table 2 shows the chemical composition of fine dust particles for Taiyuan, Changzhi, Jincheng three cities.

Table 2. Profiles of resuspended dust for PM₁₀ in the three different cities %

Chemical components	Taiyuan		Changzhi		Jincheng	
	Content	deviation	Content	deviation	Content	deviation
Na	1.4062	0.1064	1.241	0.226	1.599	0.170
Mg	1.3771	0.0299	1.333	0.430	1.430	0.121
Al	6.2185	0.3825	6.489	0.837	9.168	1.008
Si	19.4124	2.7613	16.316	3.397	21.712	1.360
K	1.7110	0.6456	1.383	0.216	2.084	0.280
Ca	8.4552	1.3520	9.775	2.512	12.465	1.469
Ti	0.3968	0.0266	0.448	0.126	0.640	0.075
V	0.0032	0.0003	0.003	0.000	0.003	0.001
Cr	0.0136	0.0010	0.019	0.014	0.023	0.005
Mn	0.0431	0.0026	0.099	0.083	0.085	0.008
Fe	2.1172	0.3408	2.333	0.468	3.020	0.466
Co	0.0046	0.0043	0.007	0.006	0.003	0.001

Ni	0.0214	0.0184	0.009	0.005	0.011	0.001
Cu	0.0028	0.0017	0.014	0.009	0.010	0.001
Zn	0.0256	0.0073	0.092	0.038	0.089	0.019
As	0.0013	0.0000	0.002	0.001	0.010	0.001
Hg	0.0000	0.0000	0.000	0.000	0.000	0.000
Cd	0.0001	0.0000	0.000	0.000	0.000	0.000
Pb	0.0053	0.0014	0.008	0.015	0.010	0.002
TC	10.2590	1.1937	11.511	14.084	9.893	1.350
OC	4.9662	0.8955	6.156	7.848	5.711	0.928
Cl⁻	0.0342	0.0133	0.926	1.298	0.457	0.419
NO₃⁻	0.0277	0.0172	1.983	3.788	0.035	0.018
SO₄²⁻	0.2389	0.2160	2.379	3.868	3.409	1.607
Total	62.526		71.867		56.7414	

SPSS software was used to conduct the correlation analysis for chemical compositions of three cities, we generated which revealed chemical components in three cities have very high correlation coefficient which was all over 0.95. This fact illustrates that the chemical composition of fine dust particles in three cities have very high similarity. It also reflects the PM₁₀ dust sources have a certain similarity in the three cities.

According to Table 2, the crustal elements Si, Ca, Al, Fe, Mg, K and etc, all have a relatively high percentage within all the components in the spectrum, while they have a relatively smaller deviation. The element Si accounts the most percentage of the three highest concentrations of dust in the chemical composition. In addition, Si is the most abundant elements within the spectral composition of wind caused soil dust (see Table 3), and is the representative element for the wind caused soil dust in three cities. Therefore, the wind caused dust is the most significant contributor to fine particle dust.

Table 3. Mass percent of Si in soil profiles in the three different cities %

City	Taiyuan	Changzhi	Jincheng
The percentage of Si in wind soil dust	25.694±0.710	27.079±0.531	26.865±0.560

Table 4. Mass percent of TC in coal combustion profiles in the three different cities %

City	Taiyuan	Changzhi	Jincheng
The percentage of TC in soot	31.390±6.418	25.428±7.167	23.960±5.571

Beyond the crustal elements, also found a higher content of TC in resuspended dust in the three cities ,Taiyuan had percentage of $10.259\pm1.194\%$, Changzhi had $11.511\pm14.084\%$, Jincheng had $9.893 \pm 1.350\%$. The percentage of TC component were also relatively high in the spectrum of coal combustion (Table 4), Table 4's data shows the percentage of coal combustion in Taiyuan were significantly higher than that of Changzhi and Jincheng city, indicating that fine particles of dust in Taiyuan were more severely impacted by coal combustion than the other cities. For the percentage OC content in TC: Taiyuan 48%, Changzhi 53%, Jincheng 57%, indicating that the main form of total carbon in the presence is OC.

The existence of Zn, Cu, Cr and other trace elements are related to human activities such as mechanical processing, construction materials used and so on. Table 5 compared the percentage of Zn, Cu and Cr content of wind caused soil dust and dust in the cities, the results show that except the wind dust in Taiyuan which has higher Cu content than resuspended dust, the rest two cities have the dust which were more enriched by Zn, Cu and Cr contents than wind caused soil dust. It illustrates that the dust composition was not only impacted by crust, but also closely related with human production, consumption and other activities.

Table 5. Mass percent of Zn, Cu and SO_4^{2-} in soil and resuspended dust profiles %

City	Zn		Cu		Cr		SO_4^{2-}	
	Wind soil	Urban dust	Wind soil	Urban dust	Wind soil	Urban dust	Wind soil	Urban dust
	dust	dust						
Taiyu an	0.009±0 .001	0.026±0 .007	0.007±0 .006	0.003±0 .002	0.005±0 .002	0.014±0 .001	0.180±0 .041	0.239±0 .216
Chan gzhi	0.010±0 .003	0.092±0 .038	0.003±0 .001	0.014±0 .009	0.005±0 .001	0.019±0 .014	0.406±0 .089	2.379±3 .868
Jinche ng	0.013±0 .003	0.089±0 .019	0.004±0 .002	0.010±0 .001	0.016±0 .003	0.023±0 .005	0.103±0 .113	3.409±1 .607

Sulfate secondary ion were mainly dependent on the emission of SO₂ by burning coal, because coal is a major fuel, SO₄²⁻ content in dust were high in three cities (Table 5). The percentage of NO³⁻ and Cl⁻ in dust were relatively low, 0.035% ~ 1.983%.

3.2 The Contribution Rate of The Flying Dust to PM₁₀.

The wind caused dust in urban area is a kind of very complex mixture of dust source type, and acts as a source of air particulate matter. Therefore, the calculation of the contribution of dust on particulate pollution control is very important. This study established an environmental airborne particles spectrum from different sources in Taiyuan, Changzhi, Jincheng. The contribution rates of PM₁₀ with each source category are calculated by using CMB receptor model(Table 6). The different characteristics of the particulate pollution sources in three cities resulted the division are also different for source categories. For Taiyuan, the source category of dust contains Iron and Steel, while is neglectable in Changzhi and Jincheng city. As can be see from Table 6, the PM₁₀ in ambient air dust were the biggest sources of pollution in three cities, the contribution rate were much higher than other dust sources.

Table 6. Contributions of different source types to ambient PM₁₀ in the three cities %

Kind of source	Taiyuan	Changzhi	Jincheng
Urban dust	27	31	25
Coal combustion	22	24	18
Building cement dust	16	12	8
Soil dust	6	10	11
Motor vehicle exhaust dust	16	8	10
Steel dust	2	-	-
Sulfate	6	3	13
Nitrate	5	9	11
Other	2	2	4

3.3 The Source of Resuspended Dust

We treated the urban dust as receptor, and calculated the share rate of single dust source of the fine particles of dust (particle size $\leq 10\mu\text{m}$) by using CMB model, the results in Table 7. Based on Table 7, the soil dust were still main source of resuspended dust in three cities, followed by coal combustion and construction of cement dust. It should be noted that the wind caused soil dust in Changzhi has less contribution rate to the urban

resuspended dust than that in Taiyuan and Jincheng, however, the contribution rate of construction cement dust and coal combustion in Changzhi were higher than the other two cities.

Table 7. Each single source of urban resuspended dust of the contribution of fine particulates %

Kind of source	Taiyuan	Changzhi	Jincheng
Coal combustion	24	31	27
Building cement dust	15	18	14
Soil dust	48	45	51
Motor vehicle exhaust dust	2	1	4
Sulfate	1	0	0
Other	10	5	3

SUMMARY OR CONCLUSION

1. The urban resuspended dust component spectrum in the three cities all contains higher percentage of crustal elements including Si, Ca, Al, Fe, Mg, K and TC and etc, indicating that the crustal elements and TC are the main component of dust within the three cities.
2. The resuspended dust is the main source of PM₁₀ in the air in Taiyuan, Changzhi, and Jincheng. The contribution rate are 27%, 31% and 25%. Controlling the emissions of the resuspended dust has a crucial significance on improving the pollution caused by PM₁₀.
3. The main sources of the resuspended dust in the three cities are soil, coal combustion and cement. The contribution to the dust in Taiyuan were 48%, 24%, 15%; in Changzhi were 45%, 31% and 18%, and in Jincheng were 51%, 27% and 14% .

ACKNOWLEDGMENTS

Thanks for the help that the environmental testing stations offered us when we were sampling. This research project was financially supported by the Natural Science Foundation of China (NSFC)(No.40873004).

REFERENCES

- [1] Feng, Y.C; Wu, J.H; Zhu, T. *Chemical Composition of Urban Fugitive Dust of Jinan and Shijiazhuang* [J]. *Urban Environment & Urban Ecology*, 2003, 16: 57-59
- [2] Bing, D.M; Chen, J.J; Feng, Y.C. *Study on Source Apportionment for Ambient Air PM10 in*

Nanjing [J]. Environmental Science And Management,2008,33 (4): 56-61

[3]Liu,X.D;Feng.Y.P;Jia,H. *Source Apportionment of Qingdao Atmospheric Aerosol with Chemical Mass Balance Method* [J].Research of Environmental Sciences,1998,11 (5) :51-54

[4]Pu,S.Z;Feng,Y.C;Zhu,T. *Characterizations of resuspended dust in six cities of north China* [J].Atmospheric environment,2006,40:5807-5814

Chemical characterization of water-soluble organic carbon aerosol by group separation method of a XAD resin

Jae-Uk Jeong¹, Ja-Hyun Kim¹, Seung Shik Park¹, K.-J. Moon², and Seok Jo Lee²

1 Department of Environmental Engineering, Chonnam National University, 300 Yongbong dong, Buk-ku, Gwangju 500-757, Korea

2 Division of Climate & Air Quality, Research, National Institute of Environmental Research

Principal Contact: Seung Shik Park, Professor, Department of Environmental Engineering, Chonnam National University, 300 Yongbong dong, Buk-ku, Gwangju 500-757, Korea.

Tel: +82-62-530-1863 Fax: 82-62-530-1859 E-mail: park8162@chonnam.ac.kr

Abstract

24-hr integrated measurements of water-soluble organic carbon (WSOC) in PM_{2.5} were made between May 5 and September 25, 2010, on a six-day interval basis, at the Metropolitan Area Air Pollution Monitoring Supersite. A macro-porous XAD7HP resin was used to separate hydrophilic and hydrophobic WSOC. Compounds that penetrate the XAD7HP column are referred to hydrophilic WSOC, while those retained by the column are defined as hydrophobic WSOC. Laboratory calibrations using organic standards suggest that hydrophilic WSOC includes low-molecular aliphatic dicarboxylic acids and carbonyls with less than 4 or 5 carbons, amines, and saccharides. While the hydrophobic WSOC is composed of compounds of aliphatic dicarboxylic acids with carbon numbers larger than 4-5, phenols, aromatic acids, cyclic acid, and humic-like Suwannee River fulvic acid. Over the entire study period, total WSOC accounted for on average 48% of OC, ranging from 32 to 65%, and hydrophilic WSOC accounted for on average 30.5% (9.3-66.7%) of the total WSOC. Based on the previous results, our measurement result suggests that significant amounts of hydrophobic WSOC during the study period were probably from anthropogenic combustion emissions.

Keywords: PM_{2.5}, water-soluble organic carbon, XAD7HP resin, hydrophilic fraction, and hydrophobic fraction

Acknowledgement

This work was partially supported by the Metropolitan Area Air Pollution Monitoring Supersite Project funded by National Institute of Environmental Research and a Mid-career Researcher Program through a NRF grant funded by the Korea government (MEST) (No. R01-2008-000-20255-0).

Insights into summer haze pollutions over shanghai based on aerosol water-soluble ionic composition

Huanhuan Du, Lingdong Kong, Tiantao Cheng, Jianmin Chen, Ling Li and Jianfei Du

Department of Environmental Science & Engineering, Fudan University, Shanghai 200433, China

Principal Contact: Tiantao Cheng, Dr., Fudan University, Shanghai, 200433,China.

Tel: +86-21-65642521 Fax: +86-21-65642080 E-mail: ttcheng@fudan.edu.cn

Abstract

An online analyzer of Monitoring for AeRosols and Gases (MARGA) was employed to measure major water-soluble (WS) inorganic ions in aerosols below 10 μm (PM10) at 1-h time resolution in Shanghai from May 27 to June 16, 2009. During the field campaign, hazy days were encountered over which atmospheric visibility was commonly less than 10 km, and the hourly concentration of PM10 reached peak values of more than 150 $\mu\text{g m}^{-3}$. Based on WS ions and pollution gases, the haze events were classified as biosmoke, complicated and secondary pollutions depending on their distinct formation schemes. During the biosmoke pollution aroused from biomass burning plume, the concentration of water-soluble K^+ was increasing up to a maximum about 15 times higher than the average of clear days, and K^+ behaved a strong positive linear correlation with Cl^- . Because of sulfate and nitrate significantly enhanced by secondary production, in which precursor gases of SO_2 and NO_2 were converted into SO_4^{2-} and NO_3^- on the surface of pre-existing KCl particles, the complicated pollution was responsible for a combining contribution of biosmoke aerosols directly transported from biomass burning emission and known secondary aerosols linked to local emission. Under high atmospheric oxidation ability and steady atmosphere condition, the secondary pollution resulted from a significant increase of sulfate and nitrate aerosols which were oxidized from large amounts of anthropogenic pollution gases of SO_2 and NO_2 in the urban atmosphere.

Keywords: aerosol, haze pollution, water-soluble ion, biosmoke.

Particulate Matter Source Apportionment Based on a Back Trajectory Model during the Episodes in Central Taiwan

Chien-Lung Chen¹, San-Fu Lee², Feng-Chao Chung³, Su-Ching Kuo⁴, Jeng-Lin Tsai⁵, Pei-Hsuan Kuo⁵, Li-Ying Hsieh⁶, and Ying I. Tsai⁷

1 Dept. of Industrial Engineering & Management, Fortune Institute of Technology, Kaohsiung, Taiwan

2 Dept. of Finance, Fortune Institute of Technology, Kaohsiung, Taiwan

3 Dept. of General Education Center, Fortune Institute of Technology, Kaohsiung, Taiwan

4 Dept. of Medicinal Chemistry, Chia Nan University of Pharmacy & Science, Tainan, Taiwan

5 Dept. of Environmental Engineering, National Chung Hsing University, Taichung, Taiwan

6 Dept. of Chemistry, National Cheng Kung University, Tainan, Taiwan

7 Dept. of Environmental Eng. & Science, Chia Nan University of Pharmacy & Science, Tainan, Taiwan

Principal Contact: Ying I. Tsai, Professor, Department of Environmental Engineering & Science, Chia Nan University of Pharmacy & Science, Tainan 717, Taiwan.

Tel: +886-6-2660208 Fax: +886-6-2669090 E-mail: mtsaiyi@mail.chna.edu.tw

Abstract

It is important to realize the contribution of emission sources of air pollutants to establish proper and effective strategies of air resource management. We applied the Gaussian trajectory transfer-coefficient model to simulate the particulate matter (PM) concentrations and the source apportionments at Chungming Station in central Taiwan during the PM episodes in 2008. Two kinds of PM episodes are selected. One PM episode is during the Asian dust storm period (2-4 March 2008) and the other PM episode is affected by ill-dispersion synoptic pattern (29 March 2008). The correlation coefficient (*r*) between the observed and calculated daily PM₁₀ concentrations from 28 February to 5 March 2008 is 0.72. The source apportionments indicated that the primary sources for PM₁₀ were subsidence (31%) during the Asian dust storm period and upwind boundary concentration (26%) during the non-dust storm period. The subsidence played an important role during the Asian dust storm. The subsidence increased 12% of PM₁₀ apportionment during the dust storm period than that during the non-dust storm period. On the other hand, the *r* value between the observed and calculated daily PM₁₀ concentrations from 26 March to 1 April 2008 is 0.97. The primary sources for PM₁₀ were the upwind boundary concentration (24%) and point sources (23%) in this PM episode. The high pressure circulation affected Taiwan which often causes the ambient in relatively stable condition. Not like the PM₁₀ source apportionment during the Asian dust storm period, the subsidence was less important and the long range secondary aerosol transport and local emissions seemed to have much influence on the PM₁₀ contribution to a receptor.

Keywords: Source apportionment, trajectory model, PM episode

Relationship between Aerosol and Visibility at an Urban Area in Southern Taiwan

Chien-Lung Chen¹, Feng-Chao Chung², San-Fu Lee³, Li-Ying Hsieh⁴, and Ying I. Tsai⁵

1 Dept. of Industrial Engineering & Management, Fortune Institute of Technology, Kaohsiung, Taiwan

2 Dept. of General Education Center, Fortune Institute of Technology, Kaohsiung, Taiwan

3 Dept. of Finance, Fortune Institute of Technology, Kaohsiung, Taiwan

4 Dept. of Chemistry, National Cheng Kung University, Tainan, Taiwan

5 Dept. of Environmental Engineering & Science, Chia Nan University of Pharmacy & Science, Tainan, Taiwan

Principal Contact: Chien-Lung Chen, Assistant professor, Department of Industrial Engineering & Management, Fortune Institute of Technology, Kaohsiung 831, Taiwan.

Tel: +886-955343966 Fax: +886-77889777 E-mail: clchen@center.fotech.edu.tw

Abstract

Aerosol can cause a decrease in the atmospheric visibility. Visibility could be shown as $L_v = k / M_c$, where L_v is the prevailing visibility (km), M_c is the airborne particulate matter (PM) concentrations (mg m^{-3}) and k is the concentration-visibility ratio (g m^{-2}). This study tries to establish the regression equation between particulate concentrations and atmospheric visibility in Kaohsiung, Taiwan. We used the average daily PM₁₀ and PM_{2.5} concentrations including nine air quality monitoring stations around Kaohsiung and average daily visibility data at Kaohsiung weather station from 2005 to 2009. However, visibility can be reduced by precipitation effects. The concentrations and visibility data were screened for precipitation events. PM₁₀ and PM_{2.5} concentrations show negative correlation with visibility (regression coefficient, $r = -0.72$ and -0.75 , respectively), revealing elevated PM concentrations impaired the atmospheric visibility. Then the data from 2005 to 2008 were applied as the regression period and the k values for PM₁₀ and PM_{2.5} are obtained as 0.358 and 0.196 g m^{-2} ($r = 0.74$ and 0.75, respectively). Finally the regressed k values are used to calculate the daily PM concentrations in 2009 as the verification period. The correlation coefficient and absolute bias between observed and calculated PM concentrations for PM₁₀ are 0.73 and 22.4%, similarly for PM_{2.5} are 0.80 and 24.4%. The calculated PM₁₀ and PM_{2.5} concentrations match well with the observed data at Kaohsiung weather station in 2009.

Keywords: Visibility, particulate matter, regression equation

Seasonal characteristics of dust aerosol in three cities of northern China

Youbin Sun¹, Yan Yan^{1,2}, Lianji Liang^{1,2}, Hongyun Chen^{1,2}, Jianbo Zhao^{1,2}

1 Institute of Earth Environment, Chinese Academy of Sciences, 10 Fenghui South Road, Hi-tech Zone, Xi'an, 710075, China

2 Graduate University of Chinese Academy of Sciences, Beijing 100049, China

Principal Contact: Youbin Sun, Professor, Institute of Earth Environment, Chinese Academy of Science, 10 Fenghui South Road, Hi-tech Zone, Xi'an, 710075, China.

Tel: +86-29-8832-1862 Email: sunyb@ieecas.cn

Abstract

Asian dust not only affects the climatic and environmental changes in the northern hemisphere through physical and biochemical processes, but also casts significant influences on air quality and human health in East Asia. Characteristics of the dust aerosol over northern China have been studied intensively. Yet debates still go on around the seasonal variations of its physical and chemical properties. In this study, we collected dust aerosol samples in Beijing, Xi'an and Qingyang for over a year, for dust flux estimation, and grain size and magnetic susceptibility analyses. The results show that dust flux and magnetic susceptibility exhibit distinct seasonal fluctuations, but grain size does not. In spring season, dust flux peaks in all three cities, however in other seasons the variation pattern differs in different regions. Magnetic susceptibility peaks in both autumn and winter, suggesting great influences of human activities. With a short distance in between, and similar geographical and climatic settings, Xi'an and Qingyang display similar variation patterns in all three parameters. But compared with Qingyang, Xi'an is characterized by a relatively lower dust flux as well as a systematic higher magnetic susceptibility. Seasonal patterns of the dust flux, grain size and magnetic susceptibility in Beijing are quite different from those of Xi'an and Qingyang due to its different geographical and meteorological settings. Moreover, we picked out some representative dust events to conduct back trajectory analysis, and found that most of them were originated from the Gobi-sandy deserts in southern Mongolia and northern China and transported by the cold fronts controlled by Siberian-Mongolian high.

Keywords: Dust aerosol; flux; magnetic susceptibility; seasonal characteristics

Sources, Solubility, and Deposition Fluxes of Trace Elements in Atmospheric Aerosols over the Yellow Sea

Tianran Zhang¹, Jinhui Shi¹, Xiaohong Yao¹ and Huiwang Gao¹

1 Key Laboratory of Marine Environmental Science and Ecology (Ocean University of China),
Qingdao, 266100, China;

ABSTRACT

Atmospheric dry deposition is reported as one of important sources of trace elements in the Yellow sea. Besides particle loadings, solubility of trace elements in sea-water is an important parameter determined the bioavailability of these deposited elements. In this study, 36 total suspended particulate samples were collected over the Yellow Sea during four cruises during the period from February to August, 2009 and were used to investigate solubility of trace elements in sea-water. The solubility of these metals was Fe($4.2\% \pm 3.3\%$), Al($7.8\% \pm 12\%$), Ba($23\% \pm 26\%$), Cd($48\% \pm 36\%$), Mn($50\% \pm 29\%$), P($56\% \pm 26\%$), Zn($53\% \pm 31\%$), Cu($58\% \pm 34\%$), Pb($75\% \pm 28\%$), respectively. The solubility of these elements was apparently affected by their corresponding sources and aging processes, e.g., the solubility of Fe in the aerosol from the continental source was 5-6% higher than that from oceanic source. Bio-available dry deposition fluxes are thereby estimated considering element's solubility in sea water

KEYWORDS

Trace elements; Solubility; Atmospheric aerosol; Dry deposition flux; the Yellow Sea.

Introduction

Iron, which plays an important role in photosynthesis and nitrogen fixation, is recognized as an essential nutrient to marine primary productivity in oligotrophic seas (Boyd et al., 2007). Some other trace elements, like Mn, Co, Zn, and Cu, may also influence the growth and community structure of marine phyto-planktons by involving in many enzyme processes (Paytan et al., 2009). Though the riverine inputs of trace elements are large, they are rapidly removed (Jickells et al., 2005); atmospheric deposition of aerosols thus becomes the primary source to sustain the concentrations of these trace elements in surface water of open oceans (GEOTRACES, <http://www.geotraces.org>).

Although evidence shows that particulate iron can be assimilated by some organisms (Kraemer et al., 2005), the amount of Bio-available trace metals are constrained by their solubility. In the case of iron, the reported solubility widely from 0.01% to 80% (Mahowald et al., 2005). Hence

solubility remains a key uncertainty affecting our understanding of the relationship between atmospheric deposition and primary production. Leaching solutions and aerosol history, for instance the sources, pathways and mixing mechanisms with anthropogenic air mass during long distance transport, was proposed to exert a significant influence on the solubility (Mackie et al., 2005; Hsu et al., 2010).

Pure-water or acid buffer solution has been used in leaching in recent studies(e.g., Bonnet et al., 2004; Desboeufs et al., 2005; Hsu et al., 2010). However, it should be noticed that the amount trace elements leached in sea-water, which is much lower than that in pure water, can better represent dry deposition input in real situation (Chen et al., 2006; Buck et al., 2010). Early studies have mainly focused on the Atlantic Ocean and Mediterranean Sea and little information is provided about the Pacific Ocean(e.g., Bonnet et al., 2004 ; Buck et al., 2006 ; Chen et al., 2006), and the China Seas, which is strongly influenced by the Asian dust(Hsu et al., 2005, 2008). In this study, sea-water is used to test the solubility of trace elements in aerosols collected over the Yellow Sea. Source of aerosols and its relationship with solubility are discussed in terms of meteorological data and air mass back trajectories. Bio-available dry deposition fluxes are thereby estimated considering element's solubility in sea water.

Experimental Methods

2.1 Sampling and Experiment Methods

A total of 36 samples are collected at $1.05 \text{ M}^3\text{min}^{-1}$ and the duration was 15h for each samples. in all cases. Whatman®41 cellulose filters, low-value blank of trace metal, are employed for filtration. The filters are cut by plastic scissors for subsequent use.

Filtered seawater is irradiated by ultraviolet light to break down dissolved organics and then purified through ion-exchange resin columns (Chelex-100,Na-form) to minimize the content of dissolved metal impurities(Hsu et al., 2005). In dissolution experiment, extractions are performed using ultrasonic wave at 0°C for 60min. The extracts are then filtered through $0.2 \mu\text{m}$ PTFE syringe filters, and refrigerated in polyethylene jars at 4°C . All samples are digested using a mixture of strong acids ($\text{HNO}_3 + \text{HClO}_4 + \text{HF}$) following the procedure provided by Zhuang (2001). The concentrations of trace elements are determined using an inductively coupled plasma atomic emission spectrometer (ICP-AES).

2.2 Statistics Methods

The sea-water solubility of a given trace element can be calculated by the following equation:

$$\text{Solubility} = \frac{\text{seawater soluble concentration}}{\text{total concentration}} \times 100\% \quad (\text{Eq.1})$$

To identify the source of the Yellow Sea aerosol, an enrichment factor is defined and the following equation is used for calculation. Al is used as reference element:

$$EF_{crust} = \frac{(X/Al)_{aerosol}}{(X/Al)_{crust}} \quad (\text{Eq.2})$$

In addition, 72-h isentropic air mass back trajectories were calculated at 500m height level for each sample using a tool from the National Oceanic and Atmospheric Administration (NOAA). The result showed that there were four transport pathway for the aerosol particle arriving at the Yellow sea, i.e., the northern continent source (NCS), the southern continent source (SCS), the marine source (MS), and the Korea and Japan source(KJS).

The dry deposition fluxes of sea-water soluble elements were estimated, assuming a dry deposition velocity (V_t) for each element and the concentration of the element in aerosol (C_x). To obtain the Bio-available fluxes (F_d), solubility (S) of the element should be considered.

$$F_d = S \times C_x \times V_t \quad (\text{Eq.3})$$

Results and Discussion

3.1 Solubility of Aerosol Trace Element

The results showed that, solubility of Al and Fe for the Yellow Sea aerosols was low with the values of 7.8%($\pm 12\%$) and 4.2%($\pm 3.3\%$). Cr was even lower with an average value of 2.7%. Compared with the values reported by Hsu et al.,(2005),Buck et al., (2006) and Chen et al.,(2006), the solubility of Fe in this study was higher than those in the Gulf of Aquaba (0.7%) and Taiwan Strait (1.1%), but close to that in the North Pacific Ocean ($6 \pm 5\%$). The solubility of particulate Mn ($50\% \pm 29\%$) and Zn ($53\% \pm 31\%$) in this study were comparable to those in Taiwan Strait, Helgoland and the Atlantic Ocean. Comparison may also suggest that dissolution medium has little influence on Mn and Zn, while Fe solubility in sea-water is about a factor of 1-2 lower than that in acid water (pH4-5, Theodos et al., 2010). In addition , the solubility of anthropogenic elements Cu, Cd and Pb reached ~50-75%.

3.2 Enrichment Factor Analysis

Enrichment factor (EF) can be used to identify whether a given element is mainly from soil source or anthropogenic source. When the solubility was investigated according to the EF of the respective element, the elements can be grouped into three regimes: (1) low polluted and low solubility (LPLS) elements, including Al, Fe and Cr; (2) low polluted and high solubility (LPHS) elements, including Mn, P and Cu ; (3) high polluted and high solubility (PHPS) elements, including Cd, Zn and Pb.

3.3 Back Trajectories Analysis

Most cruises samples collected in winter and spring were impacted by NTS. Trace elements in these samples exhibited a high concentration, but not a low solubility. This may be related to winter heating in northern China, where large emissions of sulfur dioxide will be enriched in the aerosol surface, providing acidic environment for heterogeneous reactions and enhancing solubility of some elements.

3.4 Bio-available Dry Deposition Fluxes

Bio-available dry deposition fluxes of Al and Fe were estimated as $6\text{-}23\mu\text{g m}^{-2}\text{d}^{-1}$, and $6\text{-}28\mu\text{g m}^{-2}\text{d}^{-1}$, respectively. Polluted elements Cu, Pb and Zn are $0.08\text{-}0.24\mu\text{g m}^{-2}\text{d}^{-1}$, $0.27\text{-}0.40\mu\text{g m}^{-2}\text{d}^{-1}$, and $0.8\text{-}1.4\mu\text{g m}^{-2}\text{d}^{-1}$, respectively. With distinguished seasonal differences, the maximum value of polluted element occurred in the spring, which was 2-4 times more than the deposition flux in winter. This also reflects that marine ecosystem may be mostly affected by anthropogenic pollution in spring. Overall, the averaged bio-available deposition flux of polluted elements was, in general, less than $1\mu\text{g m}^{-2}\text{d}^{-1}$, with exceptions of Pb and Zn at $1.4\mu\text{g m}^{-2}\text{d}^{-1}$ and $3.3\mu\text{g m}^{-2}\text{d}^{-1}$ in spring.

CONCLUSION

The solubility of particulate trace elements in this study were apparently determined by multiple factors such as EF, source, concentration, etc. Compared with those values measured in the Atlantic Ocean, Mediterranean Sea and the Pacific Ocean, bio-available dry deposition fluxes of the Yellow Sea were evidently larger because of high loadings of mineral aerosols originated from the long-distance transport.

REFERENCES

- [1] Boyd, P.W.; Mackie, D.S.; Hunter, K.A. *Marine Chemistry*. 2010, 120(1-4), 128-143.
- [2] Paytan, A. et al., *Proceedings of the National Academy of Sciences*, 2009, 106 (12), 4601-4605.
- [3] Jickells, T.d. *Ocean Biogeochemistry and Climate*. 2005, 308: 67-71.
- [4] Kraemer, S.M., Butler, A., et al., *J. Molecular Geomicrobiology. Rev. Mineral. Geochem.* 2005. 53-84.
- [5] Mahowald, N.M., et al., *Glob. Biogeochem. Cycles* 2005. 19, GB4025. doi:10.1029/2004GB002402.
- [6] Mackie, D.S.; Boyd, P.W.; Hunter, K.A. *Geophys. Res. Lett.* 2005. 32, L06809. doi: 10.1029/2004GL022122.
- [7] Hsu, S. et al., *Marine Chemistry*. 2010. 120(1-4): 116-127.
- [8] Bonnet, S., Guieu, C., *Geophys. Res. Lett.* 2004. 31. doi:10.1029/2003GL018423.

- [9] Desboeufs, K.V.; Sofikitis, A.; Losno, R.; et al., *Chemosphere*, 2005. 58(2), 195-203.
- [10] Hsu, S., Lin, F. and Jeng, W., *Atmospheric Environment*, 2005. 39(22), 3989-4001.
- [11] Zhuang, G.S., Guo, J.H., Yuan, H., et al., *China Science Bulletin*. 2001. 46 (11), 895–901.
- [12] Buck, C.S., Landing, W.M., Resing, J.A. and Lebon, G.T., *Geochem. Geophys. Geosyst.* 2006, 7(4): Q04M07.
- [13] Chen, Y., Street, J. and Paytan, A., *Marine Chemistry*, 2006. 101(1-2): 141-152.
- [14] Theodosi, C., Markaki, Z., Tselepidis, A. and Mihalopoulos, N., *Marine Chemistry*, 2010. 120(1-4): 154-163.

ESR signal intensity and crystallinity of quartz in desert surface samples from three major Asian dust sources

Hongyun Chen^{1,2}, Youbin Sun¹, Ryuji Tada³, Dominik Weiss⁴, Min Lin⁵, Shin Toyoda⁶ and Yuko Isozaki³

1 State Key Laboratory of Loess and Quaternary Geology, Institute of Earth Environment, Chinese Academy of Science, Xi'an 710075, China

2 Graduate University of Chinese Academy of Sciences, Beijing 100049, China

3 Department of Earth and Planetary Science, University of Tokyo, Tokyo 113-0033, Japan

4 Department of Earth Science and Engineering, Imperial College London, London SW7 2AZ, England

5 China Institute of Atomic Energy, Beijing 102413, China

6 Department of Applied Physics, Okayama University of Science, Okayama 700-0005, Japan

Principal Contact: Youbin Sun, Professor, Institute of Earth Environment, CAS, Xi'an 710075, China.

Tel: +86 29 88321862 E-mail: sunyb@ieecas.cn

Abstract

We systematically characterized the Electron Spin Resonance (ESR) signal intensity and Crystallinity Index (CI) of quartz in desert surface samples from western China, northern China and southern Mongolia, and assessed the variability of these parameters in the fine-($<16 \mu m$) and coarse-grained ($>16 \mu m$) quartz fractions within each desert and among different deserts. The ESR and CI data suggest that for the coarse-grained quartz fraction, we are able to separate the different deserts of the western China and southern Mongolian, but not for the northern Chinese deserts including Badain Juran, Tengger and Mu Us deserts. For the fine-grained quartz, the ESR and CI results are slightly different within three deserts (the southern Mongolia Gobi, Badain Juran deserts and Taklimakan Desert), but almost identical within two deserts in northern China (the Tengger and Mu Us deserts). Spatially, the fine-grained quartz discriminate each desert especially better than the coarse-grained quartz, and allowed us to trace the dust derived from three major Asian dust sources, i.e., the Gobi-sandy deserts in western China, northern China and southern Mongolia . Our results suggest that combination of ESR and CI should enable us to improve the source tracing of Asian dust in the Chinese Loess Plateau and North Pacific.

Keywords: Asian dust sources, Quartz, ESR signal intensity; Crystallinity Index.

Numerical Simulation of Nanoparticle Pattern Fabricated by Electrostatic Spray Deposition

Wei Wei¹, Sheng Wang², Zhaolin Gu¹, Takeshi Fukuda³, Kiwamu Kase², Jungmyoung Ju², Yutaka Yamagata² and Yusuke Tajima²

1 Xi'an Jiaotong University, No.28, Xianning West Road, Xi'an, Shaanxi, 710049, P.R. China

2 RIKEN Institute, 2-1 Hirosawa, Wako City, Saitama 351-0198, Japan

3 Saitama University, 255 Shimo-Okubo, Sakura-ku, Saitama 338-8570, Japan

ABSTRACT

Patterning of nanoparticle over large areas is a prerequisite for realizing nanodevices. Electrospray deposition (ESD) as a patterning method of nanoparticle deposited on a substrate has attracted great attentions recently due to several advantages over the other deposition methods. However, obtaining an optimum ESD processing condition for nanoparticle pattern relies heavily on many trial experiments because of the lack of a reliable numerical simulation technique. In this study, the deposition characteristics of nanoparticle generated by electrospray were investigated with numerical method by using a three-dimensional Lagrangian model. Three important process parameters including solution dielectric constant, applied voltage and surface charge density on mask were considered by fixing the geometrical parameters of ESD device. The simulation result shows that with the increase of solvent dielectric constant, the spray diameter also increases. The higher applied voltage will make spray area wider. The focusing controllability by changing surface charge density on mask was confirmed, and the higher surface charge density would result in more focused deposition. The validity of the numerical simulation technique developed in this study was verified by comparing with experimental data.

KEYWORDS

Nanoparticle pattern, Electrospray deposition, Deposition characteristics, Lagrangian model

Introduction

Patterning of nanoparticles over large areas is a prerequisite for realizing nanodevices employing the unique properties of nanoparticles. Several spray deposition approaches have been proposed for patterning surfaces with nanoparticles. Compared with other deposition techniques, electrostatic spray deposition (ESD) bears several advantages, such as high deposition efficiency, no ring stain effect during deposition process, high resolution and uniform patterning, the controllability of the size of dried nanoparticle and so on^[1]. It has been used in various processes including sample preparation in mass spectrometry, polymer coatings, DNA and protein films for scanning tunneling microscopy, functionally and biologically active protein deposition, organic film formation in solar cells, fuel cells and ink-jet printing, and *et al.*

Electrospray is an aerosolization method that involves both surface tension force and electrical force to feed a liquid through a capillary and to create an electric field gradient between the capillary tip and an electrode. When the surface tension force and electrical force in the liquid meniscus at the capillary outlet are in balance, the liquid takes a conical shape, called Taylor cone, and emits a liquid jet^[2-3]. Viscous instabilities in the liquid cause the jet to break into highly charged droplets that undergo a series of fissions and generate smaller droplets, until the droplets completely evaporates and finally becomes nanoparticle deposited on a substrate. The fine drops has a nearly monodisperse size distribution^[4], and the average droplet diameter can be precisely controlled by adjusting process parameters^[5-6].

To obtain an optimum deposition condition using electrospray device, many parameters have to be considered carefully, and a lot of efforts have to be made if it entirely relies on experiments. Numerical simulation techniques have been developed greatly and become an indispensable tool in both academic field and industrial field. However, up to now only few numerical works have been published on the modeling of nanoparticle generated by ESD.

Gañán-Calvo *et al.*^[7] developed a numerical model to describe the transport of electrosprayed droplets. Wilhelm *et al.*^[8] studied the electrospray transport, evaporation and deposition on a heated substrate with Lagrangian tracking of single droplet, and further predicted the size of primary and satellite electrospray droplets. Jung *et al.*^[9] investigated the characteristics of spray evolution and deposition patterns as a result of multiple EHD spraying with a capillary-extractor-substrate configuration by changing the applied extractor-substrate voltages, the moving speed of nozzles, and the distance between nozzles. Kim *et al.*^[10] reported a concept of parallel focusing of nanoparticles via ion injection together with charged aerosols to create nanoarrays of nanoparticles on a surface. A self-assembly process of charged nanoparticles on a silicon substrate was demonstrated by Tang *et al.*^[11]. They also discussed the dynamics of the focusing process and the spray time which affects the focusing effect both experimentally and by Monte Carlo simulation.

However, the above studies didn't consider the material property itself. To provide more detailed and reliable analysis for investigating the feasibility of using electrospray to aerosolize the organic solution to fabricate the photovoltaic devices, this paper focuses on the investigation of the deposition characteristics through numerical methods using a three-dimensional Lagrangian model. The effects of three important parameters including solution dielectric constant, applied voltage and surface charge density on the mask to the deposition characteristics are studied by fixing the geometrical parameters of ESD device.

Numerical Method

A numerical simulation method to track the trajectory of charged nanoparticles generated by electrostatic spray was developed in order to examine the spatial distribution of the spray and deposition patterns. A three-dimensional Lagrangian model based on the works of Gañán-Calvo *et al.*^[7] was used in this study under the assumption of spherical particles. Brownian motion of particles can be negligible, because the particle kinetic energy caused by the electric field is much greater than random thermal energy^[10]. The equation for the motion of the particle *i* based on Newton's second law can be written as follows:

$$\frac{\pi}{6} d_i^3 \rho_d \frac{d^v}{dt} = C_D \frac{\pi}{8} \rho_g d_i^2 |v_i|^2 + q_i E_{ext} + \frac{1}{4\pi\epsilon_0} \sum_{i,j,i \neq j} \frac{q_i q_j v}{|r_{ij}|^3} + \frac{\pi}{6} d_i^3 \rho_d g \quad (\text{Eq. 1})$$

where C_D is the drag coefficient, E_{ext} indicates the external electric field intensity, ρ_g is the density, q_i is the droplet charge, r_{ij} is the distance from the i th droplet to the j th droplet, d_i is the droplet diameter, v_i is the droplet velocity, ϵ_0 is the permittivity of a vacuum, g is the gravitational acceleration, the indices i and j refer to the droplet numbers, and the indices d and g refer to the liquid and the gas.

The left-hand side of Eq. 1 accounts for the inertia of the particle i . The terms on the right-hand side account for the drag force by the surrounding gas, the electrical forces exerted by the external electric field, the mutual electrical repulsion forces between the charged particles, and the gravitational force, respectively.

The drag coefficient of Newton's resistance law can be expressed as follows.

$$C_D = \frac{24}{Re} (1 + 0.15 Re^{0.678}) \quad \text{for } Re < 800 \quad (\text{Eq. 2})$$

where Re is the Reynolds number.

In electrohydrodynamics, the dynamic currents are small, and hence the magnetic induction effects can be ignored, so the electric field is given as

$$\vec{E} = -\nabla \varphi \quad (\text{Eq. 3})$$

where φ is the applied voltage. The electrical potential distribution can be written as

$$\nabla^2 \varphi = 0 \quad (\text{Eq. 4})$$

With a proper boundary condition, the external electric field can be calculated by Eq. 3 and Eq. 4.

In the present investigation, the particles with the diameters of Gaussian distribution are assumed to be electrically charged even before entering the electric field.

As a highly charged droplet evaporates, its mass decreases while the number of charges on the droplet remains constant; thus the surface charge density increases. Simultaneously, the electrostatic repulsion between charges with a same polarity increases at the droplet surface. Above a critical point, known as the Rayleigh limit^[12], the droplet will become unstable and will release charge through a series of fissions. The total number of charges on a single particle is calculated according to its diameter, and the value of charge will be smaller than the Rayleigh limit.

All the particles are generated near the tip of capillary and randomly distributed in X and Y directions with the initial speed of $(0, 0, w)$. Because of the same charge polarity, there is no interaction like collision or coagulation/agglomeration between particles.

Results and Discussion

Verify the Validity by Comparing with Experiment

A typical electrospray system is sketched in Fig. 1. It consists of a capillary needle through which a liquid that may be a pure solvent, a solution, or a suspension is fed, a high voltage

source connected to the capillary, and a grounded electrode placed perpendicularly to the capillary to create a strong electric field gradient.

In the experiment, the initial flow rate is determined by the liquid's gravity, and for a given liquid the ESD device parameters such as needle radius, capillary-to-substrate distance are fixed. The value of the controlling parameter, i.e., potential difference between capillary and substrate, will be adjusted until a steady cone-jet configuration is obtained. The image of the spatial distribution of nanoparticles as shown in Fig. 2 was took by CCD camera, then the spray diameters at different positions could be measured.

Figure 1. Electrospray deposition experiment configuration

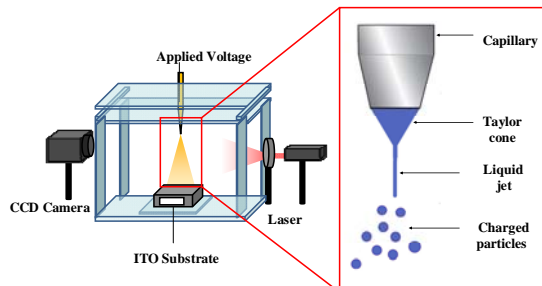


Figure 2. Typical spatial distribution of charged particles



Figure 3 shows the comparison between experimental data and calculation result of spray diameter at the position of 3 mm far away from the capillary tip. In general the calculation results match the experimental data well, except that the spray diameter from experiment is slightly higher than the one from our calculation in most case. This may be caused by the difference in particle number density. The particle number density in the calculation is smaller than the one in the experiment, which results in a lower repulsion force in the calculation, and thus a smaller spray diameter. The good agreement between our calculation and the experimental data validates that the proposed numerical method can provide a reliable analysis for nanoparticle deposition pattern fabricated by ESD method. From Fig. 3 we also can find that with the increases of applied voltage, the spray diameter increases greatly thanks to the enhancement of electrostatic force.

Figure 3. Spray diameter comparison between experimental results and calculation result

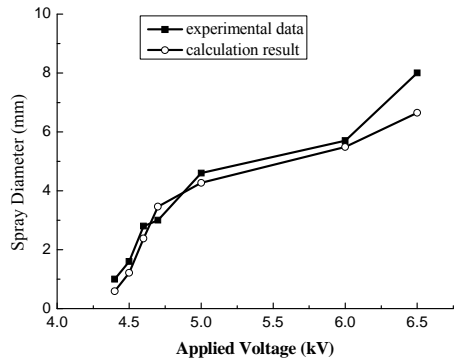
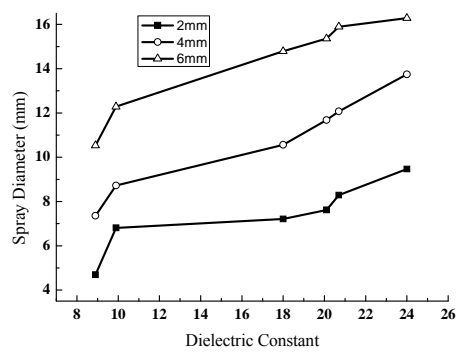


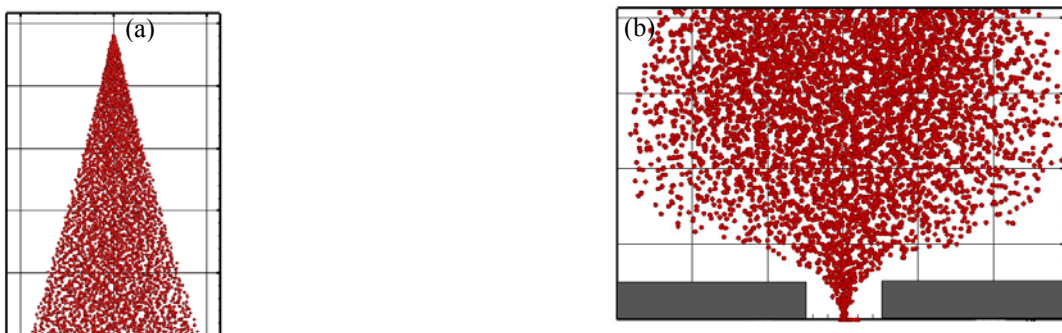
Figure 4. Effect of solution dielectric constant to spray diameter



Simulation Results on Deposition Pattern

Figure 4 shows that the spray diameters at three positions under a given applied voltage have an increasing tendency with the increase of liquid's dielectric constant. It arises from the fact that in the case of high dielectric constant, the initial volume charge density of nanoparticles is large, which makes high initial nanoparticle charge, and thus large electrostatic repulsion force.

Figure 5. Nanoparticle trajectory (a) without mask, (b) with mask

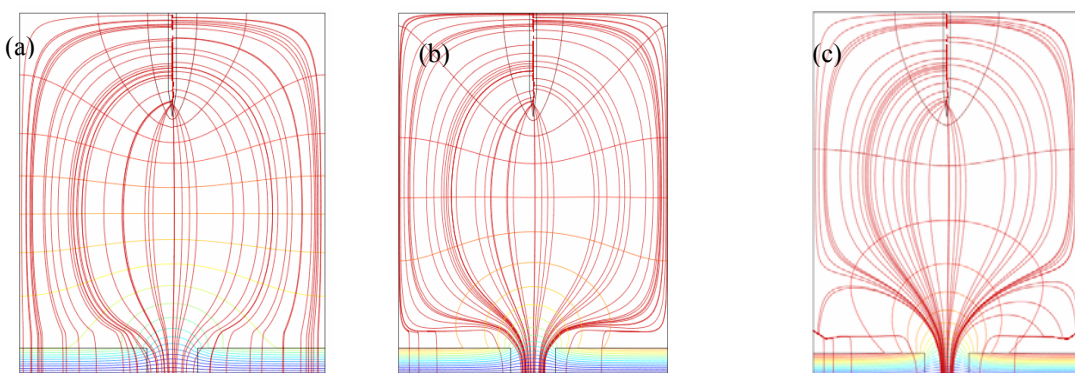


By using a non-conductive mask, the nanoparticles can be efficiently deposited on a desired location of conductive substrate. Due to the insulating property the charges of the nanoparticles will be preserved after deposition on the mask, while all the charges on the substrate will be lost. The gradually formed difference on charge density between the substrate and the mask will create an electric field that drives the arriving nanoparticles towards the substrate surface.

For square patterns, three-dimensional nanoparticle trajectory calculations have been carried out. Figure 5 shows the particle deposition patterns with and without mask. In the case of no mask, the particles will be deposited on all substrate surfaces, whereas the focused deposition will occur when there are masks.

As shown in Fig. 6(a)–(c), depending on the accumulated charges on the mask the curvature of convex potential lines can be changed, which means that the extent of focusing could be controlled. The figure reports the calculation results of equipotential and electric field lines under the conditions of surface charge density of $3 \times 10^{-5} \text{ C/m}^2$, $4 \times 10^{-5} \text{ C/m}^2$ and $5 \times 10^{-5} \text{ C/m}^2$, respectively. In the case of low surface charge density the equipotential lines are nearly flat and the field lines are only slightly convergent (see Fig. 6(a)), which indicates that nanoparticle deposition is possible on all areas, including mask. However, when the surface charge density increases, the field lines become strongly convergent and only focus into the spot on the substrate surface (see Fig. 6(c)). This study indicates that the adjustment of the surface charge density on mask is a very efficient way to achieve the desired focusing effect. Furthermore, the three-dimensional nanoparticle trajectory in Fig. 5 (b) was modeled based on the electric field in Fig. 6(c). By comparing the two figures, you may find that the inertial motion of charged nanoparticle almost follows the electric field.

Figure 6. Control of focusing effect with the increase of surface charge density on the mask. Red line: electric field streamline, color line: equipotential lines (a) surface charge density $3 \times 10^{-5} \text{ C/m}^2$; (b) surface charge density $4 \times 10^{-5} \text{ C/m}^2$; (c) surface charge density $5 \times 10^{-5} \text{ C/m}^2$.



CONCLUSION

A simulation tool that could describe the particle trajectory and deposition during electrospray deposition process has been developed. The modeling of electrostatic focusing of charged nanoparticles was successfully carried out. The numerical simulation results were compared with experimental data, and showed a good agreement. Our study indicated that the higher solution dielectric constant may result in wider spray area, and the electric force is the decisive factor to the particle deposition pattern. The controllability of focusing through the surface charge density on mask was confirmed by our simulations. Higher surface charge density would result in more focused deposition.

ACKNOWLEDGMENTS

This work was funded by Grant-in-Aid for Young Scientists (No. 23760070) sponsored by Japan Society for the Promotion of Science.

REFERENCES

- [1] Ju J. Ph.D. thesis, the University of Tokyo, Tokyo, 2009.
- [2] Fernández de la Mora J. *J. Colloid Interface Sci.* 1996,178, 209-218
- [3] Taylor G. *Proceedings of the Royal Society of London. Series A, Mathematical and Physical Sciences* 1964,280, 383-397
- [4] Nemes P, Marginean I, Vertes A. *Analytical Chemistry* 2007,79, 3105-3116
- [5] Gañán-Calvo AM, Dávila J, Barrero A. *J. Aerosol. Sci.* 1997,28, 249-275
- [6] Tang K, Gomez A. *Physics of Fluids* 1994,6, 2317-2332
- [7] Ganancalvo AM, Lasheras JC, Davila J, Barrero A. *J. Aerosol. Sci.* 1994,25, 1121-&
- [8] Wilhelm O, Madler L, Pratsinis SE. *J. Aerosol. Sci.* 2003,34, 815-836
- [9] Jung JH, Oh H, Kim SS. *Powder Technology* 2010,198, 439-444
- [10] Kim H, Kim J, Yang H, Suh J, Kim T, et al. *Nat Nano* 2006,1, 117-121
- [11] Tang J, Verrelli E, Tsoukalas D. *Nanotechnology* 2009,20
- [12] Doyle A, Moffett DR, Vonnegut B. *Journal of Colloid Science* 1964,19, 136-143

Size Distributions of Ambient Aerosol in the Vicinity of Semiconductor Plants

Chih-Chung Lin¹, Shui-Jen Chen^{1,*}, Jen-Hsiung Tsai¹, Kuo-Lin Huang¹ and Chun-Li Chou²

1 Department of Environmental Science and Engineering, National Pingtung University of Science and Technology, Pingtung County, Nei Pu, 91201, Taiwan

2 Content Engineering Consulting Services, Ltd., New Taipei City, Zhonghe Dist., 23553, Taiwan

Principal Contact: Shui-Jen Chen, Professor, Department of Environmental Science and Engineering, National Pingtung University of Science and Technology, Pingtung County, Nei Pu, 91201, Taiwan, Phone: +886-8-7740263, Fax: +886-8-7740256, E-mail: chensj@mail.npu.edu.tw

ABSTRACT

This study was conducted from November, 2009 to July, 2010 at a semiconductor plant in a science park in southern Taiwan to understand the characteristics of ambient atmospheric aerosol using a micro-orifice uniform deposition impactor (MOUDI) and a nano-MOUDI equipped with Teflon filters (with diameters of 37 and 47 mm, respectively) in the vicinity of semiconductor plants. The sampling periods covered three types of days: episode days (PM concentration > 100 $\mu\text{g m}^{-3}$), sunny days, and sunny days after rain. The particle mean concentrations of PM₁, PM_{2.5}, PM_{2.5-10}, and PM₁₀ followed the order episode days > sunny days > sunny days after rain; however, the mean concentration of PM_{0.1} was in order sunny days after rain > sunny days > episode days. Episode day and sunny day samples exhibited a similar bi-modal particle size distribution within the size range 0.01–100 μm , with a major and a secondary peak in the coarse and fine size ranges, respectively. The particles collected on sunny days after rain displayed a tri-modal distribution, with a major, a secondary, and a minor peak in the coarse (3.2–5.6 μm), fine (0.56–1.0 μm), and nano (0.01–0.032 μm) size ranges, respectively. With an additional minor peak in the nano size range (0.018–0.032 μm), the particles collected following rain had a tri-modal size distribution.

KEYWORDS

Size Distribution, Ultrafine, Semiconductor Plant, Washout.

Introduction

The adverse effects of ambient particles on human health have been an environmental concern for decades. Epidemiological studies have successfully related ambient particulate matter (PM) exposures with adverse respiratory effects, including chronic obstructive pulmonary disease (COPD) and asthma, and PM may cause increases in pneumonia and cardiopulmonary diseases^[1, 2]. This study was conducted from November, 2009 to July, 2010 at a semiconductor plant in a science park in southern Taiwan to understand the characteristics of ambient atmospheric aerosol using a micro-orifice uniform deposition impactor (MOUDI) and a nano-MOUDI equipped with Teflon filters (with diameters of 37 and 47 mm, respectively) in the vicinity of semiconductor plants. The sampling periods covered three types of days: episode days (PM concentration > 100 $\mu\text{g m}^{-3}$), sunny days, and sunny days after rain.

Results and Discussion

The mean concentrations (with standard deviations) of the PM_{0.1}, PM₁, PM_{2.5}, PM_{2.5-10}, and PM₁₀ particles were 4.31 ± 1.35 , 38.8 ± 9.24 , 66.3 ± 17.1 , 50.0 ± 9.23 , and $116 \pm 25.9 \mu\text{g m}^{-3}$ on the episode days, respectively (Fig. 1). On the sunny days, the mean concentrations (with standard deviations) of the PM_{0.1}, PM₁, PM_{2.5}, PM_{2.5-10}, and PM₁₀ particles were 7.14 ± 4.64 , 33.8 ± 17.2 , 48.4 ± 22.6 , 27.8 ± 4.39 , and $76.1 \pm 24.8 \mu\text{g m}^{-3}$, respectively; however, on the sunny days after rain, these PM data were 7.71 ± 5.71 , 22.8 ± 6.38 , 28.7 ± 7.49 , 13.1 ± 1.69 , and $41.8 \pm 7.23 \mu\text{g m}^{-3}$, respectively. The particle mean concentrations of PM₁, PM_{2.5}, PM_{2.5-10}, and PM₁₀ followed the order episode days > sunny days > sunny days after rain; however, the mean concentration of PM_{0.1} was in order sunny days after rain > sunny days > episode days.

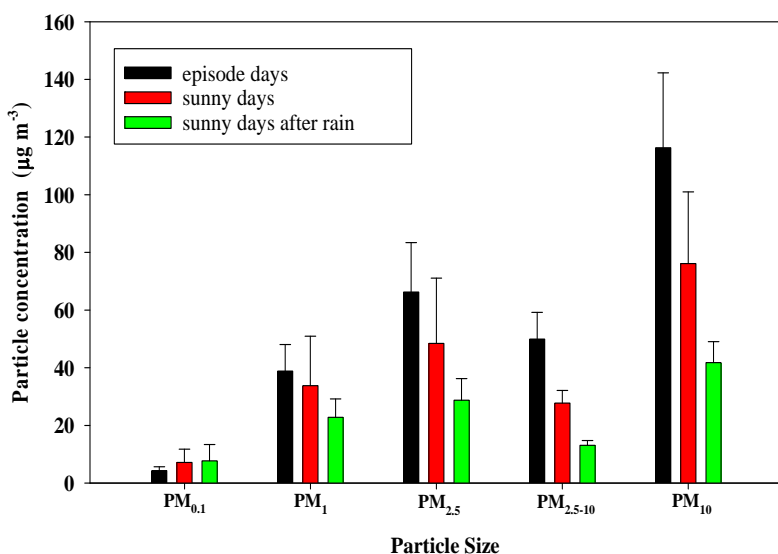


Figure 1. Mean concentrations of the PM_{0.1}, PM₁, PM_{2.5}, PM_{2.5–10}, and PM₁₀ collected on episode days, sunny days, and sunny days after rain.

Episode day and sunny day samples exhibited a similar bi-modal particle size distribution within the size range 0.01–100 µm, with a major and a secondary peak in the coarse and fine size ranges, respectively (Fig. 2). The particles collected on sunny days after rain displayed a tri-modal distribution, with a major, a secondary, and a minor peak in the coarse (3.2–5.6 µm), fine (0.56–1.0 µm), and nano (0.01–0.032 µm) size ranges, respectively. With an additional minor peak in the nano size range (0.018–0.032 µm), the particles collected following rain had a tri-modal size distribution. The former result follows from the fact that the washout coefficients for PM sizes of 3–10 µm may increase significantly during heavy rain events^[3]. The latter result may be associated with the fact that the sampling site was close to the emission sources (semiconductor plants) and most of the collected ultrafine particles were freshly emitted in the stack flue gases from the sources. Therefore, the effect of rain on the ultrafine particle size distribution was not significant.

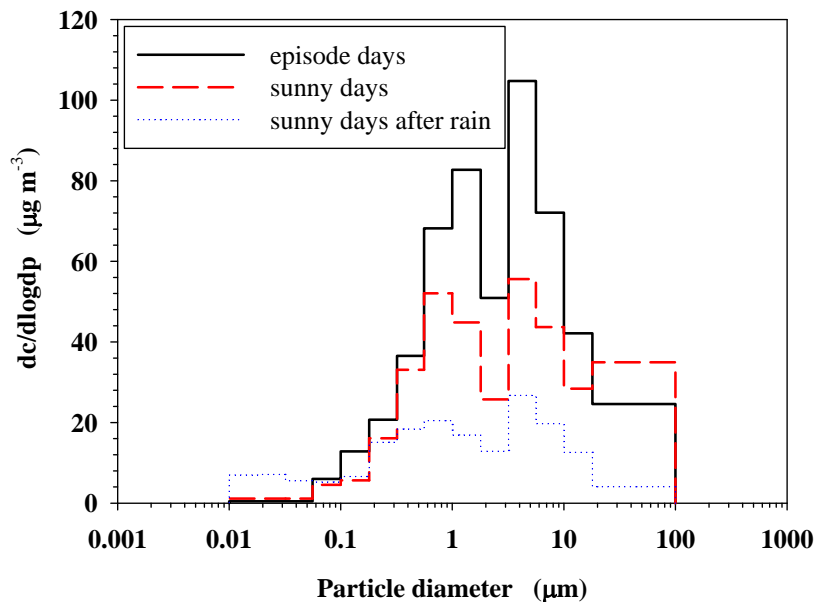


Figure 2. Size distributions of the mean PM collected on episode days, sunny days, and sunny days after rain.

REFERENCES

- [1] Pope III, C.A., Bates, D.V. and Raizenne, M.E., *Environ. Health Persp.* 1995, **103**, 472–480.
- [2] Tao, F. and Kobzik, L., *Am. J. Respir. Cell Mol. Biol.* 2002, **26**, 499–505.

[3] Chate, D.M. and Pranesha, T.S., *J. Aerosol Sci.* 2004, *35*, 695–706.

Rare Earth Composite Materials for the Reduction of Ammonia in Biomass Gasification. Part 1. Synthesis and Structure Properties of the Catalyst

Chang-Mao Hung

Department of Vehicle Engineering, Yung-Ta Institute of Technology and Commerce, 316 Chung-Shan Road, Linlo, Pingtung 909, Taiwan.

Principal Contact: Chang-Mao Hung, Association Professor, Department of Vehicle Engineering, Yung-Ta Institute of Technology and Commerce, 316 Chung-Shan Road, Linlo, Pingtung 909, Taiwan, Phone: +886-8-7233733, Fax: +886-8-7232559, E-mail: hungcm1031@gmail.com

ABSTRACT

This study addresses the synthesis and structure properties of the copper-based, rare earth composite metal material that was prepared by coprecipitating copper nitrate, lanthanum nitrate and cerium nitrate at various molar ratios. The catalysts were characterized using BET, XRD, and UV-Vis techniques. Results from the BET tests revealed that the optimal catalyst for catalytic performance had the highest specific surface area ($43\text{ m}^2/\text{g}$). The XRD and UV-Vis patterns for the various CuLaCe ternary catalysts, which verify the presence of the CuO , La_2O_3 , and CeO_2 phases on the catalyst.

KEYWORDS

Rare Earth Composite Materials, BET, XRD, UV-Vis.

Introduction

NH_3 is an important chemical product of diverse industrial processes, including ammonium nitrate production, livestock feedlots, urea manufacturing, nitrogen fertilizer production, fossil fuel or biomass combustion, petroleum refining and the refrigeration industry. This work addresses the synthesis and structure properties of the copper-based, rare earth composite metal materials with various relevant parameters. Moreover, catalytic oxidation methods have been developed to enhance the effectiveness of advanced oxidation process technologies (AOPs). Dedicated catalysts potentially shorten the reaction time for oxidation and allow it to proceed under milder operating conditions. One scheme for mitigating NH_3 pollution is the selective

catalytic oxidation (SCO) of ammonia to produce N₂ and H₂O from biomass gasification. To facilitate the application of the catalytic oxidation technique, the synthesis and structure properties of CuLaCe ternary catalysts for NH₃ oxidation and decomposition via SCO was investigated under various molar ratios and reaction parameters. Finally, the obtained catalysts were characterized using BET, XRD, and UV-Vis.

Experimental Methods

Copper-based, rare earth composite metal materials (CuLaCe ternary catalysts) were prepared by coprecipitation with copper (II) nitrate (GR grade, Merck, Darmstadt, Germany), lanthanum (II) nitrate (GR grade, Merck, Darmstadt, Germany), and cerium (III) nitrate (GR grade, Merck, Darmstadt, Germany) in four molar ratios: 6:1:3, 6:2:2, 7:1:2, and 7:2:1. These compounds were then calcined in an airstream at 773 K for four hours and the resulting powder was made into tablets using acetic acid as a binder. The tablets were reheated to 573 K to burn off the binder from the CuLaCe composite. The tablets were then crushed and sieved into various particle sizes ranging from 0.15 to 0.25 mm for later use. The specific surface areas of the composite catalysts were determined by the physical adsorption of nitrogen at 77 K using a BET surface area analyzer (ASAP 2000, Micromeritics, Norcross, Georgia). The reflectance was measured in relation to a BaSO₄ standard. X-ray diffractograms (XRD) were generated using a Diano-8536 diffractometer with a CuK α radiation source. UV-Vis absorption spectra of the solid sample were obtained using a spectrophotometer (MCPD-3000, OTSUKA Electronics, Osaka, Japan).

Results and Discussion

The adsorptive and catalytic behavior of a catalyst is strongly influenced by the extent and texture of its exterior surface. Figure 1 summarizes the properties of the test catalysts as determined by BET (Brunauer-Emmett-Teller method) analysis, including specific surface area. For a molar ratio of 6:1:3, the specific surface area was 43 m²/g. This surface area decreased slightly for a molar ratio of 7:2:1 to 27 m²/g. This test showed that the catalysts associated with higher loads caused metal sintering, which may have reduced catalytic activity. Clearly, the molar ratios of metals play an important role in activating the generated surface, and an increase in surface area may be the main factor that promotes catalytic activity.

Figure 1. BET specific surface area as a function of catalyst metal molar ratio.

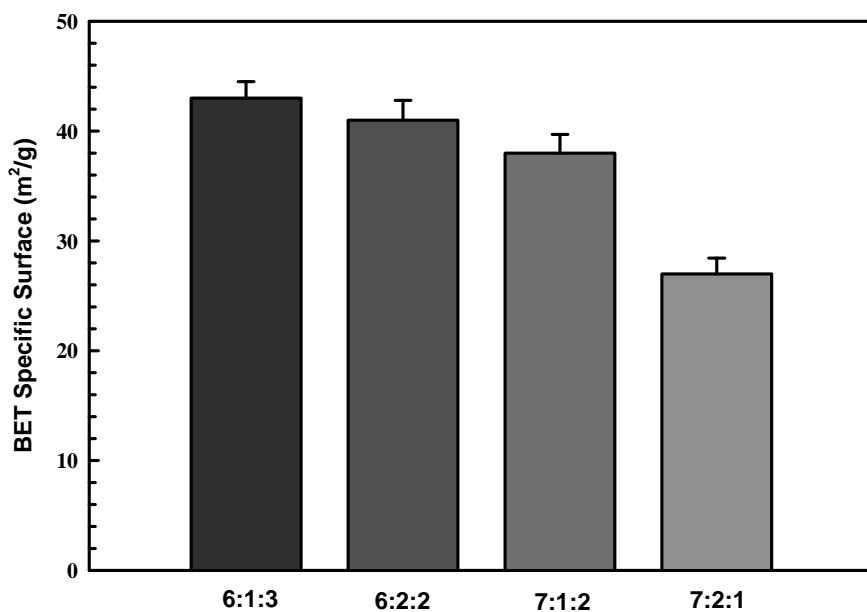
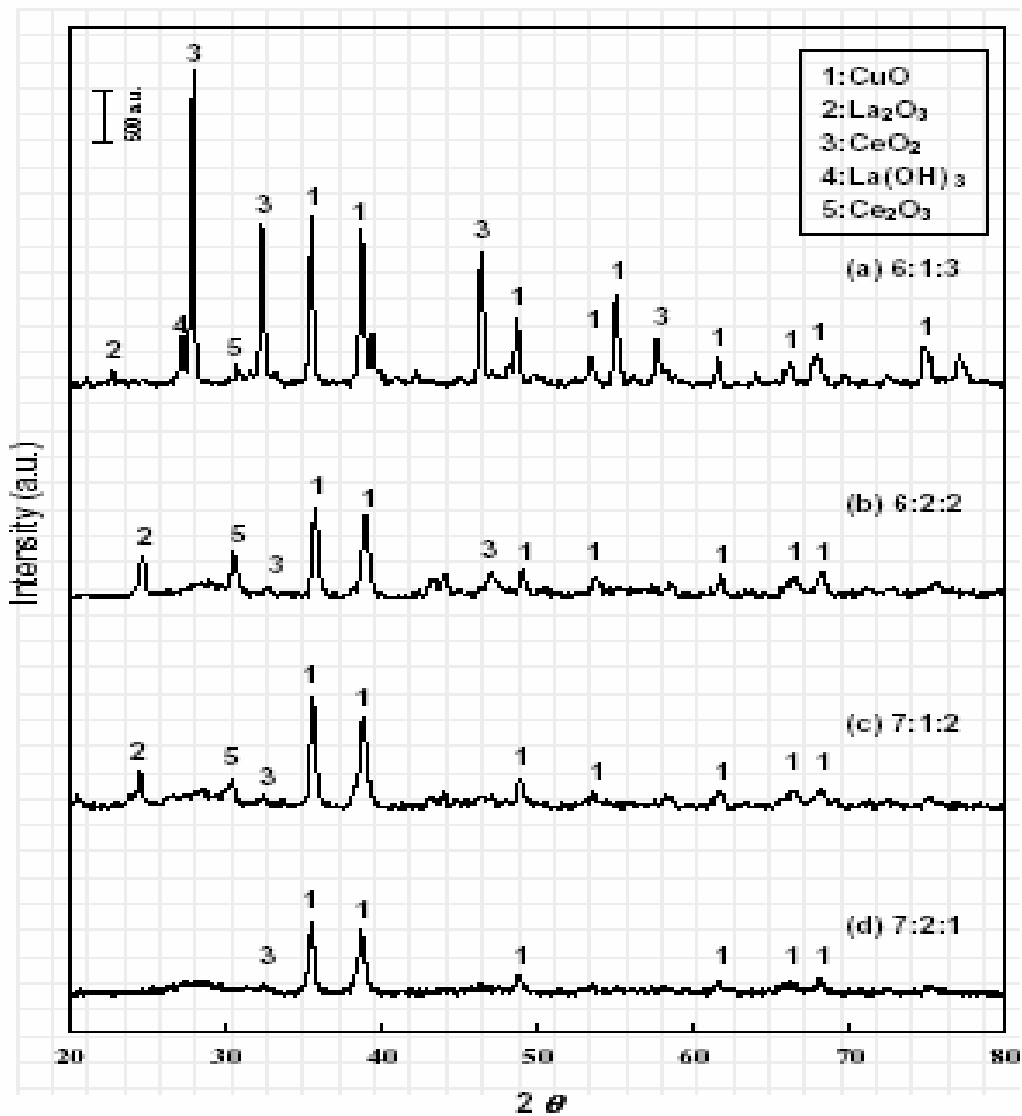


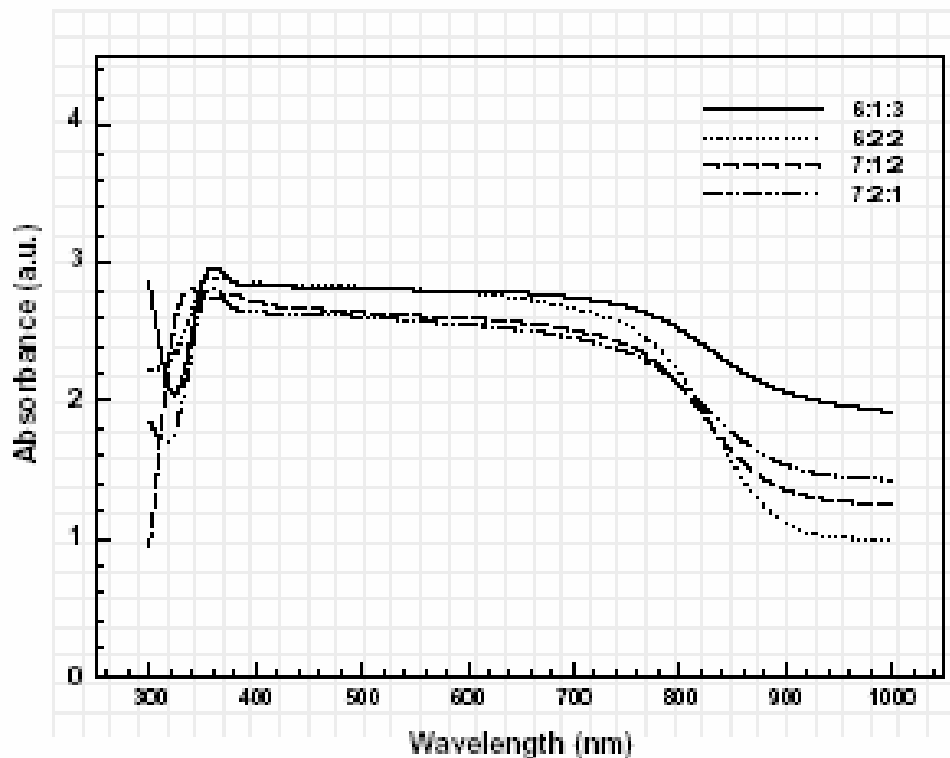
Figure 2 shows the XRD patterns for the various fresh CuLaCe ternary catalysts, which verify the presence of the CuO, La₂O₃, and CeO₂ phases. The dominant CuO diffraction peaks appear near $2\theta=35.4926$ and 38.7593° . This result established that CuO is the most active phase. As reported previously La₂O₃ can be converted to La(OH)₃. However, under the oxidation conditions present over the CuLaCe catalyst, the oxidation state of cerium can vary between Ce³⁺ and Ce⁴⁺. The CeO₂ is the most active phase in the catalytic reaction because it is a good promoter of O₂ storage capacity, and some noble metals have been used as major catalysts in this process. The CeO₂ in a copper catalyst may be assumed to promote the formation of the active phase of CuO during NH₃ oxidation. Consistent with these results, X-ray powder diffraction confirmed the presence of copper (II), lanthanum (III) and cerium (IV) oxide active sites on the CuLaCe ternary catalyst. These XRD peak intensities were strongest for the 6:1:3 CuLaCe ternary catalyst.

Figure 2. XRD patterns for the various catalysts tested.



UV-Vis spectroscopic studies were conducted to gain further information on the state of Cu, La, and Ce species in the fresh catalysts; spectra are shown in Fig. 3. Generally, bands were observed in the ranges of 300-350 nm and 700-900 nm and were attributed to the Cu²⁺-O²⁻ electronic transition species and the d-d transitions of Cu²⁺ in an octahedral environment with O_h symmetry, respectively. As in the XRD spectra, the 6:1:3 CuLaCe ternary catalyst in the UV-Vis spectrum produced the strongest peaks of the tested catalysts.

Figure 3. UV-Vis absorption spectra for the various catalysts tested.



CONCLUSION

This study demonstrates synthesis and structure properties for copper-based rare earth composite metal materials for SCO of NH₃. CuLaCe ternary catalysts were prepared by coprecipitation in various molar ratios and were found to promote the oxidation of NH₃ from biomass gasification. The synthesized 6:1:3 CuLaCe catalyst exhibited the highest specific surface area (43 m²/g), which is may associated with higher catalytic performances. The XRD and UV-Vis spectroscopic for the various CuLaCe ternary catalysts, which verify the presence of the CuO, La₂O₃, and CeO₂ phases on the catalyst.

ACKNOWLEDGMENTS

The author would like to thank the National Science Council of Taiwan, for partial financial support of this research under Contract No. NSC 98-2221-E-132-003-MY3.

Emission Source of Atmospheric Ultrafine Particles Clarified by Simultaneous Sampling and Data Comparison with PM_{2.5}

Kazuhiko Sekiguchi ^{1,2*}, Masatoshi Kinoshita ¹, Shinji Kudo ¹, Kyung Hwan Kim ¹, Seiyo O ^{1,2} and Kazuhiko Sakamoto ^{1,2,3}

1 Graduate School of Science and Engineering, Saitama University, 255 Shimo-Okubo, Sakura, Saitama 338-8570, Japan

2 Institute for Environmental Science and Technology, Saitama University, 255 Shimo-Okubo, Sakura, Saitama 338-8570, Japan

3 Center for Environmental Science in Saitama, 914 Kami-tanadare, Kazo, Saitama 347-0115, Japan

*Corresponding author; Tel./Fax: + 81-48-85-9542; E-mail: kseki@mail.saitama-u.ac.jp

ABSTRACT

Atmospheric samplings of PM_{0.1} ($D_p < 0.1 \mu\text{m}$; PM_{0.1}) and PM_{2.5} ($D_p < 2.5 \mu\text{m}$; PM_{2.5}) were conducted from August 7 to 19 and the sampling duration time was 11.5 h to observe the variation of chemical components between daytime and nighttime. An inertial filter sampler operated at 40 L/min and a PM_{2.5} cyclone operated at 16.7 L/min were used for collection of PM_{0.1} and PM_{2.5}, respectively. The collected samples were analyzed for carbonaceous (organic carbon and elemental carbon) and ionic compounds using a thermal/optical carbon analyzer based on IMPROVE method and ion chromatograph, respectively. The relative contribution of carbonaceous compounds accounted for 80 ~ 90 % in PM_{0.1} and accounted for 40 % in PM_{2.5} at two sites, respectively. Generally, the carbonaceous and ionic components in PM_{0.1} and PM_{2.5} tended to increase in the daytime during summer, whereas some samples tended to increase in the nighttime due to stable atmospheric condition. In this study, we found that PM_{0.1} at the roadside was affected by the source of not only primary vehicle but also secondary particle formation. In contrast, at the background site, secondary particle formation and transportation by wind were more strongly affected to PM_{0.1} than the vehicle emission.

KEYWORDS

Fine particles (PM_{2.5}) , Ultrafine particles (PM_{0.1}), vehicle, Secondary particle formation

Introduction

The ambient carbonaceous aerosol is composed of primary emissions, including both elemental

and organic aerosols, and secondary organic compounds formed in the atmosphere. Organic carbon (OC) is the major constituents of fine particulate matter, and is either directly emitted from sources or formed in the atmosphere via secondary gas-to-particle conversion processes¹⁾. Atmospheric aerosols, and especially fine particles, are important because of their effects on climate, health, and visibility. Moreover, in relation to air pollution, the airborne particulate matter has received considerable attention because it is proved to be associated with an increase in the morbidity and mortality. Because of these adverse effects, regulation of PM_{2.5} has been undertaken in Japan since 2010 to control mass concentrations of PM_{2.5}. However, the core of PM_{2.5} consists of imperceptible smaller particles PM_{0.1} that have a high number concentration in the atmosphere whereas their mass concentration is low. Therefore, this study focused on chemical composition of PM_{0.1} and PM_{2.5} in roadside and background site in order to estimate the possible pollution source. Moreover, sampling duration time was 11.5 h to observe the variation of chemical components between daytime and nighttime. The higher time resolution sampling and comparison between PM_{0.1} and PM_{2.5} bring more valuable data in this research field.

Experimental Methods

Sampling

PM_{0.1} and PM_{2.5} were measured at suburban roadside and background sites (**Fig. 1**) during summer for 12 days to estimate the possible emission sources from chemical components.

Atmospheric samplings of PM_{0.1} and PM_{2.5} were conducted from August 7 to 19, 2010. The sampling duration was 11.5 h (daytime: 08:00 ~ 19:30, nighttime: 20:00 ~ 07:30) to observe the variation of chemical components between daytime and nighttime.

An inertial filter sampler (Nihon Kanomax, Osaka, Japan) operated at 40 L/min and a PM_{2.5} cyclone (University Research Glassware, Co. Inc., NC, USA) operated at 16.7 L/min were used for the collection of PM_{0.1} and PM_{2.5}, respectively. The inertial filter sampler consists of four impaction stage that classify particle diameter of PM₁₀, PM_{2.5}, PM_{1.0}, and PM_{0.5} and an inertial filter with an aerodynamic cutoff diameter of PM_{0.1}²⁾. Quartz fiber filters (2500 QAT-UP, Pallflex, CT, USA) to collect PM_{0.1} at the downstream of the PM_{0.5} impaction stage were per-baked at 900 °C for 2 h to remove contamination.

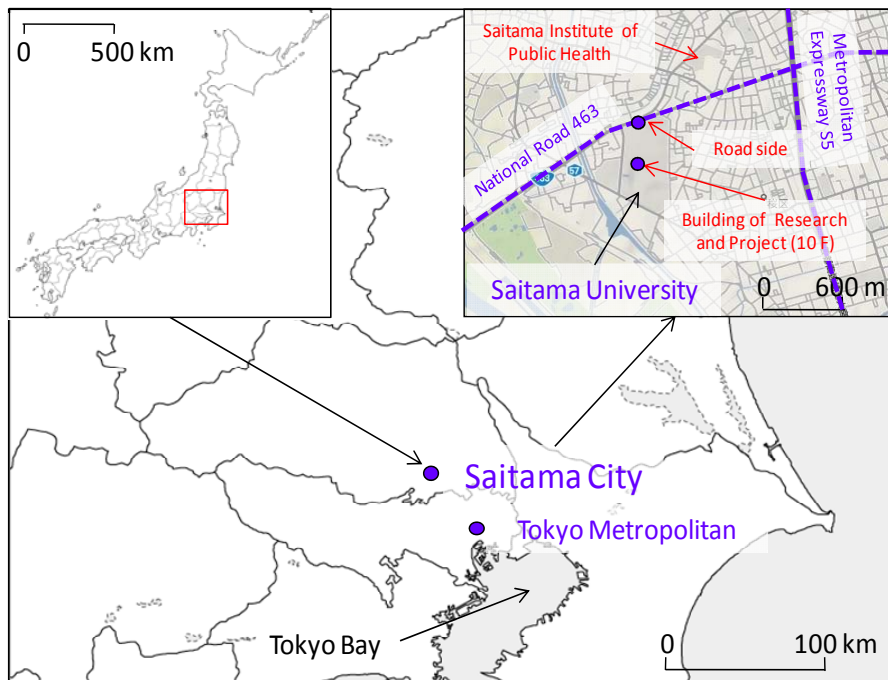


Fig. 1. Sampling locations.

Meteorological parameters

One hour averaged meteorological parameters and pollutants monitoring data (wind speed, wind direction, temperature, relative humidity, O₃ and NO_x) were measured in an ambient air quality monitoring station nearby at a 20 m height above ground, or provided by the Saitama Institute of Public Health.

Analysis

The collected samples were analyzed for carbonaceous (OC and elemental carbon (EC) classified into char-EC and soot-EC as shown in **Table 1**) components using a thermal/optical carbon analyzer (DRI Model 2001, Atmoslytic, Inc., CA, USA) based on IMPROVE method (**Table 1**). The collected samples punched (0.503 cm²) then placed onto the sample load position of the analyzer.

A quarter of the PM_{2.5} filter with 10 mL and a half of the PM_{0.1} filter with 5 mL of distilled water in a glass vial was extracted in an ultrasonic bath for 60 min. After extraction, ionic species were analyzed by ion chromatograph (DX-100, Dionex, CA, USA). Water-soluble organic carbon was analyzed on a total organic compounds analyzer (TOC-V, shimadzu, Japan).

Table 1. Temperature program of IMPROVE method.

Carbon fraction	Temperture (°C)	Atmosphere
OC1	120	He
OC2	250	
OC3	450	
OC4	550	
EC1	550	He:O ₂ (98:2)
EC2	700	
EC3	800	

$$\text{OC} = \text{OC1} + \text{OC2} + \text{OC3} + \text{OC4} + \text{POC}$$

$$\text{EC} = \text{EC1} + \text{EC2} + \text{EC3} - \text{POC}$$

$$\text{char-EC} = \text{EC1} - \text{POC}, \text{soot-EC} = \text{EC2} + \text{EC3}$$

Results and Discussion

Concentration of carbonaceous and ionic species during sampling periods

The mean concentrations of carbonaceous components (OC, char-EC and soot-EC) and ionic species (NH_4^+ , Cl^- , NO_3^- and SO_4^{2-}) in the two particles are summarized in **Fig. 2**. The carbonaceous components accounted for 80 ~ 90% and 40% in $\text{PM}_{0.1}$ and $\text{PM}_{2.5}$ at two sites, respectively. Generally, the carbonaceous and ionic components in $\text{PM}_{0.1}$ and $\text{PM}_{2.5}$ tended to increase in the daytime during summer. OC fractions can be generated from not only primary emission (motor vehicles) but also secondary particle formation (photo-chemical reaction). However, EC fractions can be emitted from primary emission (motor vehicle emissions and biomass burning) thus, we tried to find relationships between OC and EC. At roadside, the correlation coefficient (*r*) tended to increase from daytime to nighttime in $\text{PM}_{2.5}$ and $\text{PM}_{0.1}$, indicating that nighttime samples had more influences from primary emission than daytime samples ($\text{PM}_{2.5}$: daytime: *r* = 0.68, *p* < 0.5 nighttime: *r* = 0.94, *p* < 0.01, $\text{PM}_{0.1}$: daytime: *r* = 0.89, *p* < 0.05 nighttime: *r* = 0.93, *p* < 0.01). However, the good positive correlations were also observed at background site in the two particles, although the background site is more than 300 m away from the roadside ($\text{PM}_{2.5}$: daytime: *r* = 0.95, *p* < 0.05 nighttime: *r* = 0.99, *p* < 0.05 $\text{PM}_{0.1}$: daytime: *r* = 0.85, *p* < 0.05, nighttime: *r* = 0.88 *p* < 0.05). This may be explained by wind direction during the sampling periods. The main wind direction during the sampling period blew from south to north and there is the Saitama industrial area where more than ten of big and small factories at southern part to the sampling site. Because of these wind direction for the sampling periods, the background samples may have been influenced by the Saitama industrial area. In this study, we found that $\text{PM}_{0.1}$ at the roadside was affected by the source of not only primary vehicle

emission but also secondary particle formation. In contrast, at the background site, secondary particle formation and transportation by wind were more strongly affected to PM_{0.1} than the vehicle emission. But, in order to clarify the typical emission source in two sampling sites, we need to more discussion and analysis in detail. Hereafter, we will apply to GC/MS to analyze in detailed OC such as hopane. Moreover, although good positive correlations between OC and EC at PM_{0.1} were observed at two sampling sites, generally PM_{0.1} is general distributed to the atmosphere widely and uniformly by the diffusion³⁾. Therefore, we tried to show variation of WSOC in the next section to do additional discussion.

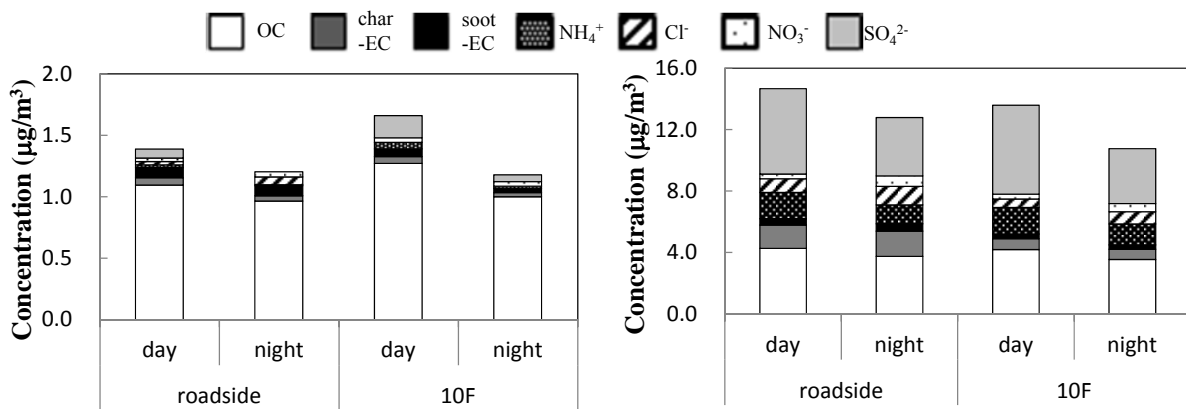


Fig.2 Carbonaceous and ionic components in PM_{0.1} and PM_{2.5} during measuring period at background (10F) and roadside (top: concentration, bottom: fraction).

Variation of WSOC and gas pollutant concentrations during summer

The variation of WSOC and gas pollutant concentrations is shown in Fig.3 in order to find out the secondary particle formation in the two size particles. In general, secondary organic aerosol (SOA) is water soluble because they contain polar functional groups which can be formed via atmospheric oxidation. Thus, WSOC is able to be used as an indicator of SOA, because most SOA is WSOC except for some high molecular compounds such as levoglucosan. WSOC concentrations were elevated with oxidants (Ox) from August 14 to 17. Because Ox has a capability to oxidize organic compounds, we may consider that the secondary particles formation was more occurred than during other periods. Furthermore, wind direction changed from the southern part to northern part and wind speed was lower than 3.0 m/s during these periods. It also indicates that the transport of polluted aerosols was different from other sampling periods. Because PM_{0.1} are not only small contribution to mass concentration but also small influence of advection, the concentration changes for PM_{0.1} was not remarkable compared to PM_{2.5} during these periods. Therefore, PM_{0.1} had small influence of advection, so PM_{0.1} may be able to used as a clearer indicator of the local emission source while PM_{2.5} was strongly influenced by meteorological parameter (wind speed, wind direction, etc) that the both local and regional

emission sources could be responsible for PM_{2.5}.

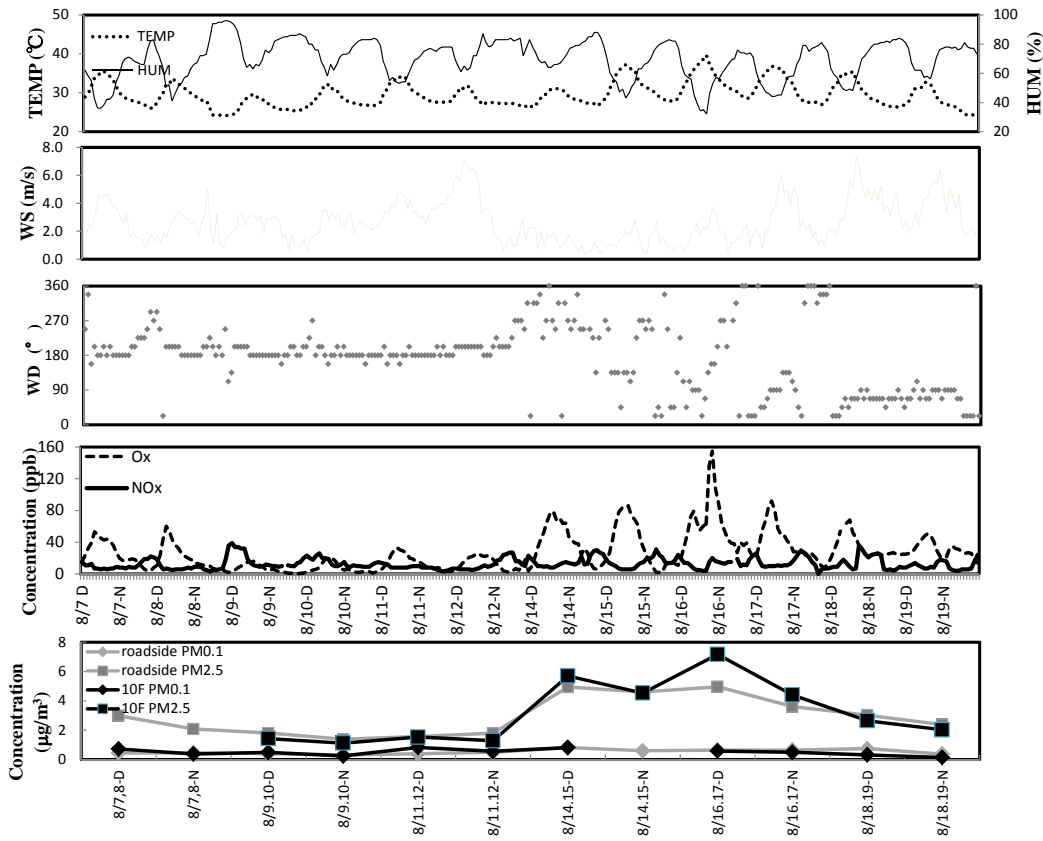


Fig. 3 Variation of WSOC and gas pollutant concentrations during sampling period at roadside and 10F.

CONCLUSION

PM_{0.1} and PM_{2.5} were measured at suburban roadside and background sites during summer for 12 days to estimate the possible emission sources from chemical components. In addition, sampling duration time was 11.5 h to observe the variation of chemical components between daytime and nighttime. The carbonaceous components accounted for 80 ~ 90% and 40% in PM_{0.1} and PM_{2.5} at the two sampling sites, respectively. The carbonaceous and ionic components in PM_{0.1} and PM_{2.5} tended to increase in the daytime during summer. The correlation between OC and EC tended to increase from daytime to nighttime in the two particles indicating that daytime samples may have been influenced by primary emission and secondary particles formation. But, PM_{0.1} was distributed to the atmosphere widely and uniformly by the diffusion as compared to PM_{2.5}. The WSOC concentrations in PM_{2.5} were more elevated with Ox concentrations from August 14 to 17 than other periods. Therefore, it is possible to think that meteorological parameter hardly influenced to the chemical composition in PM_{0.1} while PM_{2.5} was reflecting strongly influenced

by meteorological parameter that the local emission sources could be responsible for PM_{0.1} while both local and regional emission sources could be responsible for PM_{2.5}.

ACKNOWLEDGMENTS

This study was supported in part by a Grant-in-Aid for Scientific Research (Kakenhi, No. 21120502) from the Ministry of Education, Culture, Sports, Science and Technology (MEXT) of Japan.

REFERENCES

- [1] Biswas, S.; Philip, M. F.; Michael, D. G.; Susanne, V. H.; and Constantinos, S. *Aerosol Sci. Technol.* 2005, 39, 419–427.
- [2] Furuuchi, M.; Eryu, K.; Nagura, M.; Mitsuhiro, H.; Kato, T.; Tajima,N.; Sekiguchi,K.; Ehara,K.; Seto, T.; Otani, Y. *Aerosol Air Qual. Res.* 2010, 5, 10: 185–192
- [3] Zhu, Y.; Hinds, W.; Kim, S.; Shen, S.; Sioutas, C. *Atmospheric Environment*. 2002, 36 4323–4335.

Chemical and physical characterization of marine aerosols on board RV Polarstern

Zhijun Wu¹, Katrin Mildenberger¹, Shan Huang¹, Friederike Höpne¹, Julia Wenzel¹, Susanne Fuchs¹, Laurent Poulain¹, Hartmut Herrmann¹, Alfred Wiedensohler¹, Min Hu²

1 Leibniz Institute for Tropospheric Research (IfT), Permoserstraße 15, Leipzig, 04318

2 College of Environmental Sciences and Engineering, Peking University, Beijing 100871, China

Principal Contact: Zhijun Wu, Dr., Leibniz Institute for Tropospheric Research (IfT), Leipzig, Permoserstraße 15, 04318, Leipzig.

Tel: +49-431-235-2152 Fax: +49 (341) 235-2325 Email: wuzhijun@tropos.de

Abstract

Exchange of gases and aerosol particles between ocean and atmosphere is not well understood currently, although it has received considerably and intensively attention. In order to 1) better understand the formation mechanism of secondary fraction in marine aerosols particles, 2) characterize the optical properties of marine aerosols, 3) investigate the interaction between sub-micron marine aerosols and water vapor, and 4) identify the particle-based exchange of organic compound between ocean and atmosphere, we operated the physical laboratory container of IfT equipped with a number of scientific instruments during Polarstern ANT- XXVII/4 leg from Cape Town to Bremerhaven. The chemical compositions and physical and optical properties of marine aerosols were detected by on-line measurements of a High-Resolution Time-of-Flight Aerosol Mass Spectrometer (HR-ToF-AMS), a Scanning Mobility Particle Sizer (SMPS) combining an Aerodynamic Particle Sizer (APS), a Hygroscopicity Tandem Differential Mobility Analyzer (HTDMA), a Cloud Condensation Nuclei Counter (CCNC), an Integrating Nephelometer, and the Multi Angle Absorption Photometer (MAAP) and off-line analysis of filter samples from DIGITEL aerosol sampler.

Keywords: Marine aerosol, AMS, hygroscopicity, optical properties

Rare Earth Composite Materials for the Reduction of Ammonia in Biomass Gasification. Part 2. Reactivity and Characterization in Selective Catalytic Oxidation Processes

Chang-Mao Hung

Department of Vehicle Engineering, Yung-Ta Institute of Technology and Commerce, 316 Chung-Shan Road, Linlo, Pingtung 909, Taiwan.

Principal Contact: Chang-Mao Hung, Association Professor, Department of Vehicle Engineering, Yung-Ta Institute of Technology and Commerce, 316 Chung-Shan Road, Linlo, Pingtung 909, Taiwan, Phone: +886-8-7233733, Fax: +886-8-7232559, E-mail: hungcm1031@gmail.com

ABSTRACT

This study addresses the oxidation of ammonia (NH_3) at temperatures between 423 and 673 K by selective catalytic oxidation (SCO) over a copper-based, rare earth composite metal material that was prepared by coprecipitating copper nitrate, lanthanum nitrate and cerium nitrate at various molar ratios. The catalysts were characterized using FTIR and SEM. At a temperature of 673 K and an oxygen content of 4%, around 99% of the NH_3 was reduced by catalytic oxidation over the 6:1:3 CuLaCe (molar ratio) catalyst from biomass gasification. N_2 was the main product of this NH_3 -SCO process. Results from the activity and selectivity tests revealed that the optimal catalyst for catalytic performance had the highest possible cerium content. The FTIR spectra confirms the presence of a CuO -like phase and a CeO_2 phase on the surface of the CuLaCe ternary catalyst.

KEYWORDS

Selective Catalytic Oxidation, Ammonia, Biomass Gasification.

Introduction

Ammonia (NH_3) is a toxic, highly reactive inorganic gas with a pungent odor under ambient conditions that has been reported to be potentially harmful to public health and the environment. Typical biological and physicochemical treatments, which use biofilters, stripping, scrubbing with water, post-combustion controls and electrochemical oxidation methods, all induce a phase transformation and may yield contaminated sludge or adsorbent that requires further treatment.

The maintenance and operating costs associated with these physical and chemical methods are high. Accordingly, it is important to improve methods for the removal and control of NH₃ from air and waste streams especially as the laws and regulations regarding environmentally safe discharges are becoming increasingly strict. The copper, lanthanum, and cerium metals exhibited remarkable activities and capacities to elucidate the reduction characteristics of NH₃ conversion in an oxidation system. In addition, as has been previously reported, the interactions between copper, lanthanum oxide and the cerium are complex because synergistic effects may enhance catalytic characteristics. However, few studies have investigated the use of the copper-based rare earth composite metal materials (CuLaCe ternary catalysts) for the catalytic gaseous-phase oxidation of NH₃ from biomass gasification. To facilitate the application of the catalytic oxidation technique, the activity of CuLaCe ternary catalysts for NH₃ oxidation and decomposition via SCO was investigated under various molar ratios and reaction parameters. Finally, the obtained catalysts were characterized using FTIR and SEM.

Experimental Methods

Copper-based, rare earth composite metal materials (Cu-La-Ce ternary catalysts) were prepared by coprecipitation with copper (II) nitrate (GR grade, Merck, Darmstadt, Germany), lanthanum (II) nitrate (GR grade, Merck, Darmstadt, Germany), and cerium (III) nitrate (GR grade, Merck, Darmstadt, Germany) in four molar ratios: 6:1:3, 6:2:2, 7:1:2, and 7:2:1. These compounds were then calcined in an airstream at 773 K for four hours and the resulting powder was made into tablets using acetic acid as a binder. The tablets were reheated to 573 K to burn off the binder from the Cu-La-Ce composite. The tablets were then crushed and sieved into various particle sizes ranging from 0.15 to 0.25 mm for later use. Diffuse reflectance FTIR spectra of the phase species on the catalyst were measured at room temperature using a Bruker Vector 22 FTIR spectrometer equipped with a diffuse reflectance attachment with a resolution of 4 cm⁻¹ (Bruker, Germany). Scanning electron microscopy (SEM, JEOL, JSM-6400, Kevex, DeltaII) was used to elucidate the morphology of the catalysts and to collect information on the catalyst surfaces.

Results and Discussion

Catalysts with various copper, lanthanum and cerium contents were prepared, characterized and tested for their effectiveness for SCO. Figure 1 plots the catalytic activities measured for the CuLaCe samples of interest as a function of temperature. NH₃ was converted even at 423 K. The extent of NH₃ conversion over all of the composite catalysts increased with temperature; at 673 K, conversion reached 99.0%, 97.7%, 95.6%, and 94.3% over 6:1:3, 6:2:2, 7:1:2 and 7:2:1 (CuLaCe) ternary catalysts, respectively. Notably, the optimal catalyst exhibited the highest possible molar ratio of cerium. However, Figure 1 shows that the 6:1:3 catalyst performed less well than the 6:2:2 and 7:2:1 catalysts in the temperature range 573-623 K.

Figure 2 shows a comparison of the FTIR spectra at various molar ratios of fresh catalyst and also confirms the presence of a CuO-like phase and a CeO₂ phase on the surface of the CuLaCe ternary catalyst. The CuO-like phase on the catalyst surface is associated with a peak at around 1384 cm⁻¹; peaks associated with the CeO₂ phase and La³⁺ cations that are adsorbed onto copper oxide clusters are seen at 1524 cm⁻¹ and 1635 cm⁻¹, respectively. The CuO and CeO₂ were thought to exhibit strong synergistic effects when prepared as a composite CuO/CeO₂ binary catalyst. Therefore, the catalytic activity of the CuO-La₂O₃-CeO₂ ternary oxide catalyst system for oxidizing ammonia could be explained by the reversible redox behavior of CuO-La₂O₃-CeO₂ couples, which promote the functional reaction mechanism.

Figure 1. Dependence of NH₃ content on the temperature of the CuLaCe ternary catalyst.

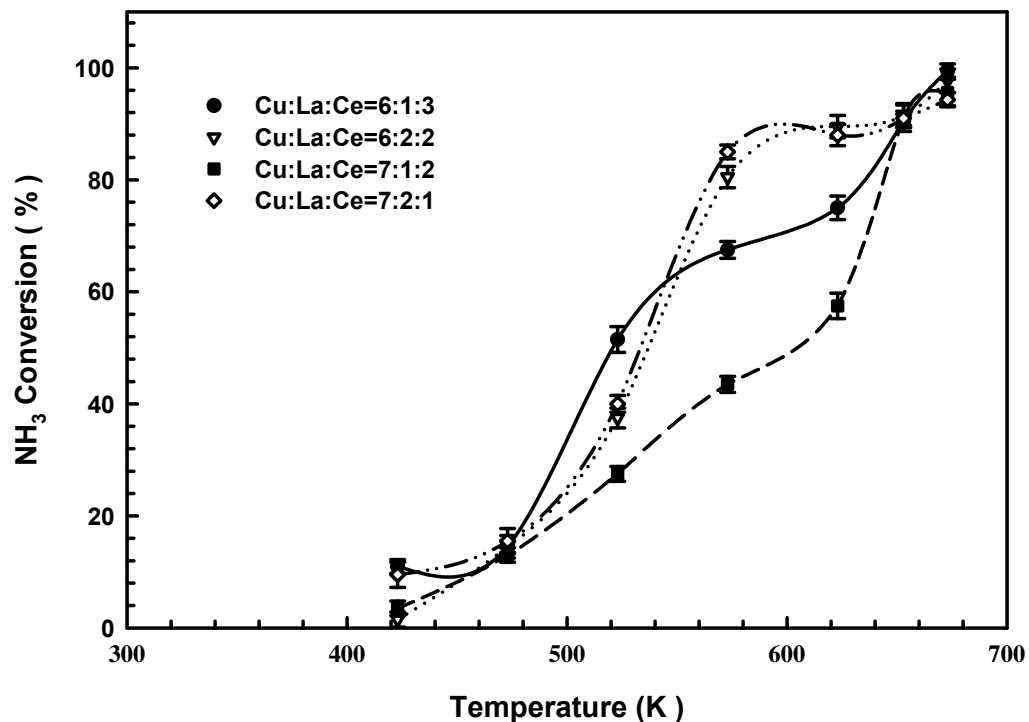
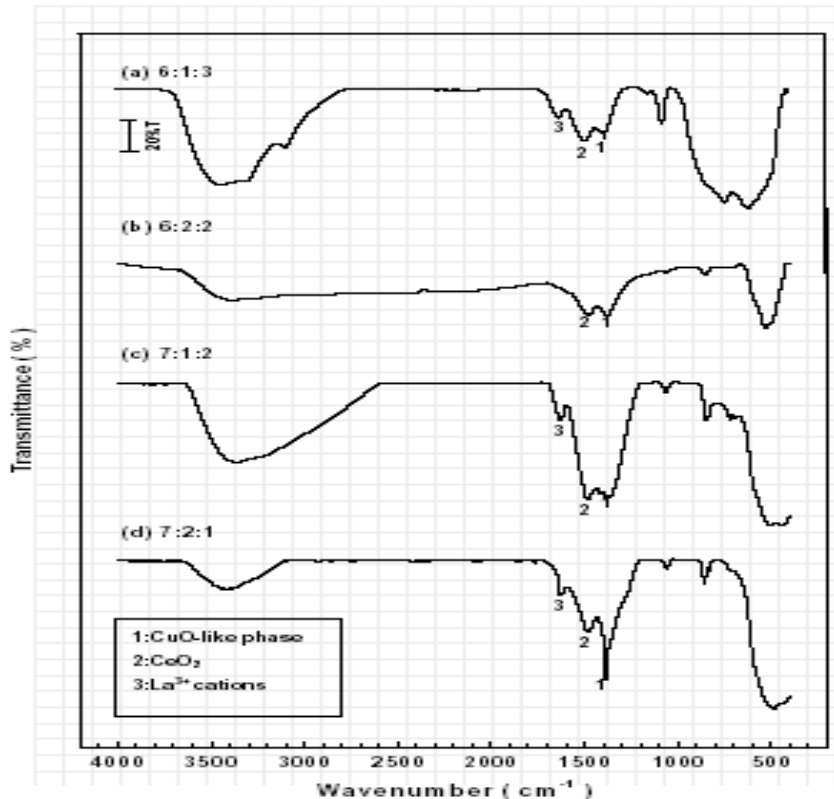
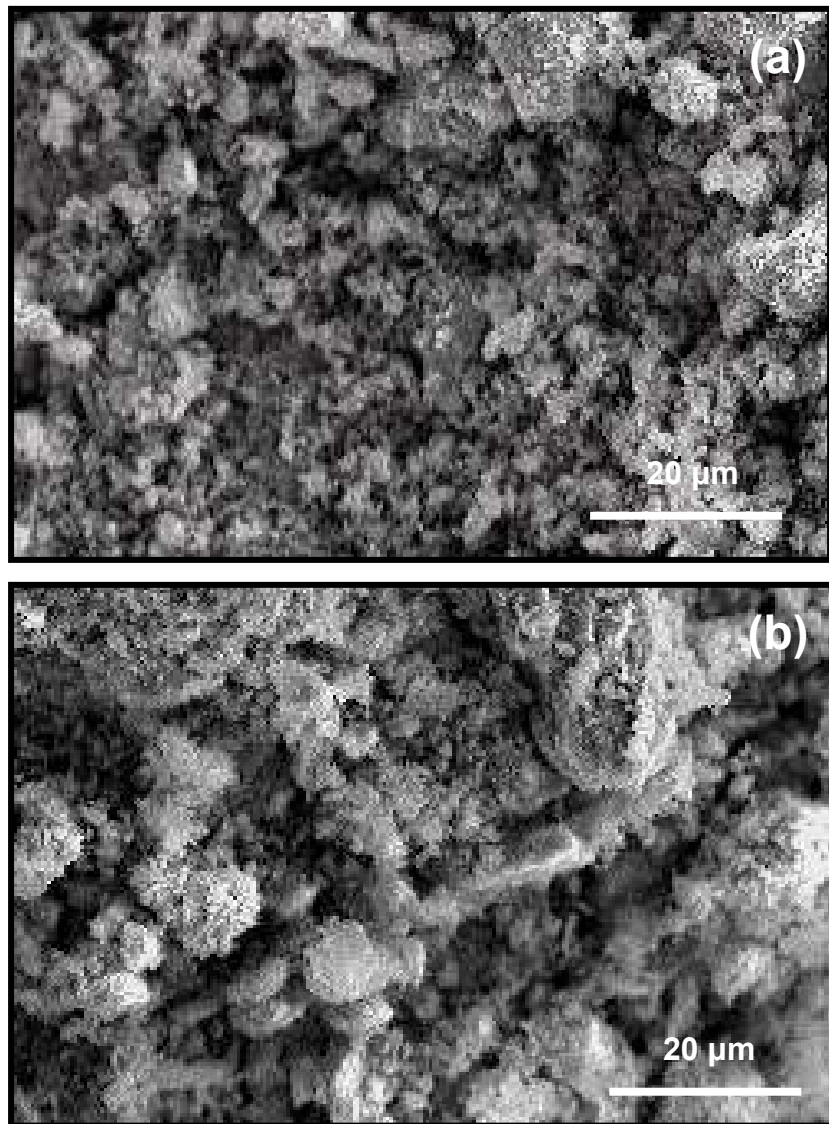


Figure 2. FTIR patterns for the various catalysts tested.



SEM was used to elucidate the surface morphological changes of the 6:1:3 CuLaCe ternary catalyst; the surface structures of the fresh and aged catalysts are shown in Fig. 3. The surface of the catalyst was more aggregated and crystalline in Fig. 3 (a) than in Fig. 3 (b), indicating that the disaggregated and dispersed phases in Fig. 3 (b) were formed when the surface of the catalyst was aged or when poisoning occurred due to plugging, which implies a porosity changed. These crystal phases may be responsible for the high activity of the catalysts. These results also confirm that catalyst dispersion phenomena increase the efficiency of NH₃ removal.

Figure 3. SEM photographs showing (a) fresh and (b) used CuLaCe catalyst.



CONCLUSION

This study demonstrates an environmentally friendly technology for SCO of NH₃ by copper-based rare earth composite metal materials. CuLaCe ternary catalysts were prepared by coprecipitation in various molar ratios and were found to promote the oxidation of NH₃. N₂ was the main product of NH₃-SCO over the 6:1:3 CuLaCe catalyst. The overall by-product selectivity of NO production varied from 0% to 20%, N₂ production ranged from 10% to 70%, and NH₃ conversion ranged from 11% to 99%. The synthesized 6:1:3 CuLaCe catalyst exhibited the

highest specific surface area ($43\text{ m}^2/\text{g}$), which is associated with higher catalytic performances. The FTIR spectra confirm the presence of a CuO-like phase and a CeO₂ phase on the surface of the CuLaCe ternary catalyst. Further studies on the reaction kinetics will be conducted in the future. This work shows that the NH₃-SCO process has the potential to treat streams highly contaminated with NH₃ and could improve the ability of industrial plants to achieve regulatory discharge standards.

ACKNOWLEDGMENTS

The author would like to thank the National Science Council of Taiwan, for partial financial support of this research under Contract No. NSC 98-2221-E-132-003-MY3.

Structural Design Optimum of the Compound Electrostatic-bag Filter

Wenge Hao¹, Mengcheng Li¹ and Yan Li¹

(1 College of Resources and Civil Engineering, Northeastern University, Shenyang, Liaoning 110819, China)

ABSTRACT

The compound electrostatic-bag filter has been used more and more widely as a new dust collector with its high collection efficiency and low operating energy consumption. The mathematical model of the manufacturing cost and the operating cost was established by studying its structure and system mechanism. The filtration airspeed and other parameters were optimized with the aim of achieving the lowest total cost of the bag filter (BF). And in order to minimize the total cost of the compound electrostatic-bag filter, their respective efficiency of dust collection, the cleaning share rate of the electrostatic precipitator (ESP), the length of the electric-field of the electrostatic precipitator and other parameters were optimized. This provides some valuable reference for the structure-designing and the operating parameters in the compound electrostatic-bag filter.

KEYWORDS

Electrostatic-bag filter, Energy consumption, Filtration airspeed; Cost analysis, Structure optimum

1 Introduction

Electrostatic-bag filter, a new dust collection device with high efficiency and low energy consumption, is more and more widely applied. In recent years, there are many studies on the application and the economic and technology^[1-5]. The professor Manyin Hu studied the corresponding simulative mathematical-model about the body structure of electrostatic-bag filter, the operating performance parameters and the total collection efficiency^[6-7]. Jian'e Chang etc. carried out the optimized combination studies of the cleaning system of the electrostatic-bag filter^[8]. However, the research on the optimization about the structure of the electrostatic-bag filter and the operating parameters has not been reported until now. To the electrostatic-bag filter, the structural design and the determine of the operating parameters are still largely based on the experience, we used to superimpose the electrostatic precipitator

with the bag filter simply, and never take into account the electrostatic-bag filter as a system. The result will lack of scientific when designing the structure and determining the operating parameters, and affected the electrostatic-bag filter exerting its superiorities.

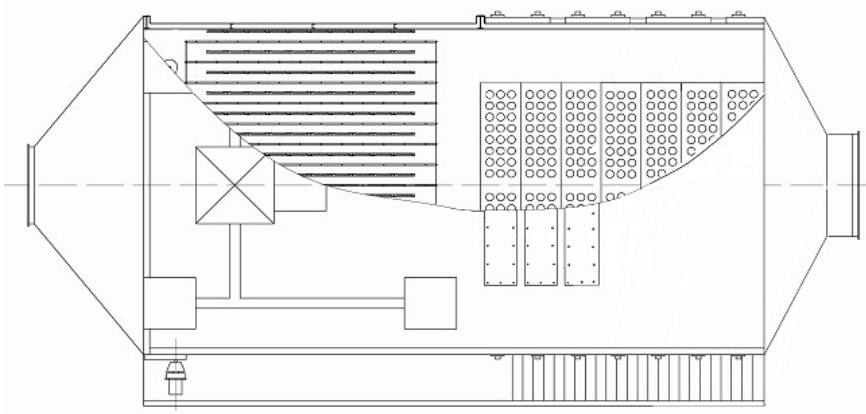
The important structure and operating parameters had been optimized, basing on the mathematical model to calculate the manufacturing costs and the running costs of the electrostatic-bag complex collecting system and making the minimum total cost of the complex filter as the target, which included the share rate of dust cleaning in electrostatic and bag dust removal unit, the length of electric-field and the filtration airspeed of bag filter in the new working conditions. This has provided scientific basis for designing the structure and determining the operating parameters of the electrostatic-bag filter.

2 Structural Designing and Parameter Selection of the Electrostatic-bag

Filter

In view of a single filter whose the volume of handled gas was $13 \times 10^4 \text{ m}^3/\text{h}$ and the dust concentration was 20 g/m^3 , serially combined the electrostatic precipitator with the bag filter, the former class adopted the horizontal line-plate electrostatic precipitator, the second part was chambered and pulse entrained bag filter . ESP was designed into a single room and adopted the Z385-type collecting plate and 6000mm high, the plate spacing was 400mm and the outermost plate was 100mm away from the inner wall of the dust collector. The corona electrode was RS-type corona wire, 5600mm long and line spacing was 400mm. Both the vertical distance from the upper of the corona-electrode's framework to the underside of the beam and the vertical distance from the bottom of the framework to the centerline of the impact bar of the collecting pole were 300mm. The distance from the underside of top beam to the upper surface of the hopper was 6300mm, and from the upper of the hopper to the fundamentals of the Pillar was 1000mm.

Figure.1 Top Viewport of the Electrostatic-bag Filter



The number of the channel of the electric-field was 15, and the wind velocity of electric-field selected 1.0m/s. The effective migration velocity (ω) of the charged particles selected 0.08m/s based on the experience. Chambered and pulse entrained bag filter was designed into two-rows compartments, the length was 770mm and the width was 2000mm of every compartment, and each compartment was equipped with round bags(3×8), whose diameter was 150mm and the length was 5200mm. Both sides were set air inlet channel, 850mm high and 1100mm wide. The handled gas entered into the bag room from the air-duct of front and sides, and the purified gas from each compartment of the upper box entered into the gas-collecting box through the partition window. Started the electromagnetic pulse valve when cleaned dust, and the pressed air sprayed out with high-speed from the nozzle which ejected the air of the gas-collecting box, the formed jet entered into the compartment of the upper box through the partition window, and relied on the static pressure formed by injected air in the compartment to clean the filter bags of this compartment^[9]. Figure 1 is the structure of the electrostatic-bag filter. The structural components of the dust removal unit were selected based on analyzing the loading and force of the steel structure of the shell of the dust removal system and meeting the stiffness, strength of the body structure.

3 Economic and Technical Analysis of the Dust Collector

3.1 The Economic and Technical Analysis of the ESP Unit

3.1.1 Manufacturing Costs

Set the length of the electric-field of the electrostatic precipitator unit as L_m , the thickness of plate as 2mm, and the market-price calculated as 12000yuan/t. The upper and lower ends of each row of plates were fixed two scalene angle-irons ($L110\times70\times8$). Each distance of two plates was fixed I-beam (25b) as girder to support the collecting pole. The average market-price of RS corona wire was 15yuan/m. The columns of the shell' four sides and the

auxiliary columns were selected I-beam (Q34532C) and groove steel (No.16) respectively. The I-beam (40a) was used for four sides' girders. The thicknesses of the top cover steel and the shell's sidewall board were 8mm and 4mm respectively. Each interval of 800mm was fixed unequal angle-steel ($L110\times70\times6$) as reinforcing-rib of side sheet vertically, the middle was fixed a trabecula. The thickness of the troughed hopper wall was 6mm, each interval of 800mm was fixed unequal angle-steel($L80\times50\times5$) as reinforcing-rib, the weight per unit area was 30.030kg/m^2 . the angles between hopper wall with the bottom were 70° and 60° respectively along airflow direction and the vertical airflow direction。The specification of steel of the hopper edge beam was HM390 $\times300\times10\times16$. All steel price (including installation cost) was calculated as 10000 yuan/t. At the same time, taking into account the following costs: insulation box, heater, rapping hammer, deflector plate, air distribution plate, high-voltage silicon rectifier, unloading and conveying system, porcelain, geared motor and so on, insulation materials of ESP, and insulation construction(accounted 15% of the total price of the equipment), we could get the total investment cost of ESP. Considering the depreciation, because of the ESP has its useful life, the manufacturing cost per year of ESP(yuan) : $E_{\text{manufacture}}=3174.6L+23348.6$.

3.1.2 Operating Cost

(1) Power consumption of high silicon rectifier

Select the technology of three-phase silicon rectifying power supply unit, so the electricity consumption (KW):

$$P_1 = \frac{U \times S_1 \times I}{1000\eta_1} \quad (\text{Eq1})$$

P_1 is the daily power consumption of the ESP, KW; U is the average operating voltage ,50KV; S_1 is the total area of collecting plate, m^2 ; I is the surface current density , $0.4\text{mA}/\text{m}^2$; η_1 is the efficiency of power supply, selected 94.99%. 300 working days per year was calculated, the price of the industry used electricity is 0.6 yuan/KWh, so the total cost of electricity consumption (yuan): $E_1 = 16372.4L$.

(2) The energy consumption of the airflow resistance of the electric-field

The resistance along the direction of electric field was 10Pa/m, the local resistance of the import is larger, selected 50Pa, so the energy consumption of this part (KW):

$$p_2 = \frac{Q_0 \times (50 + 10 \times L)}{3600 \times 1000 \times \eta_2} \quad (\text{Eq2})$$

Q_0 is the air amount of entrance, m^3/h ; η_2 is the efficiency of the fan, selected 0.92, so the

electricity consumption of overcoming the airflow resistance of the electric field to the ESP per year(yuan): $E_2=1728L+8640$.

(3) Other electricity consumption

The corona electrode adopted electromagnetic hammer vibration to clean dust on the top, and the collecting plate adopted the bilateral radial-arm hammer vibration to clean dust. The cleaning began when the thickness of one side of the collecting plate was 10mm, the amount of the accumulated dust was $5\text{kg}/\text{m}^2$. The type of the rapping gear motor was XWED0.37-63-1/1505. The total power of tubular heater was very small, counted as 1KW. The rapping energy consumption of the flexible-arm hammer:

$$E_3 = P \times t_1 \times n_1 \quad (\text{Eq3})$$

P is the rated power of rapping motor, KW; t_1 is the needed time when the axis of flexible-arm hammer turns one circle; n_1 is the times of rapping per year. So the rapping energy consumption (yuan): $E_3 = 9206.8(0.02 - \rho)$.

The quantity of accumulated dust in hopper when cleaning the dust:

$$n_2 \times 5 \times 2S_2 \times 16 = \rho_1 \times V \quad (\text{Eq4})$$

n_2 is the dust-discharging times of the collecting plate when the hopper discharges dust; S_2 is the one side area of each row collecting plate, m^2 ; ρ_1 is the packing density of dust, kg/m^3 ; V is the volume of dust in the hopper, m^3 ; the needed cleaning time $t_2 = V / 20$ (h). So the electricity cost of screw conveyor per year (yuan): $E_{4.1} = 34712L(0.02 - \rho)$, and the electricity cost of star-shaped cinder-valve per year(yuan): $E_{4.2} = 12317.2L(0.02 - \rho)$.

In addition, the cost of maintenance of every year was lower because the ESP was steel basically, and the cost of maintenance was 5000 yuan according to the actual situation.

3.2 Economic and Technical Analysis and Optimization of the Bag Filter

3.2.1 Manufacturing Costs

Selected domestic coated filter media, the average market-price $a_1=200\text{yuan}/\text{m}^2$. The total area of bag $S_3 = n_3\pi DL$ (m^2), D and L is the diameter and length of the bag respectively(m), n_3 is the number of bag, the total cost of bag $B_1=58810.6\text{Nyuan}$. Each one cage rack $a_2=100\text{yuan}$ according to the average market-price, the total cost $B_2=4800\text{Nyuan}$. Each sub-set was set up a pulse valve, the average market-price $a_3=300\text{yuan}$ of each pulse valve, and the total cost $B_3=600\text{Nyuan}$. The total area of flower board at the top of bag filter $S_4=0.77\times 2\times 2N$, the total

cost $B_4=1452.5$ Yuan. Sidewall board, hopper wallboard, the stiffener of hopper plate, hopper edge-beam, the column, ash disposal system, insulation materials, insulation construction and other parts, all the above were calculated the same as ESP. So the manufacturing cost per year (yuan): $B_{\text{manufacture}}=3070N+7008.7$.

3.2.2 Operating Cost

(1) Filtration energy consumption

The structural resistance of filter (Δp_c), the resistance of the clean filter (Δp_f) and the resistance of the dust layer (Δp_d) attached to the filter make up the pressure loss of the bag filter (Δp):

$$\Delta p = \Delta p_c + \Delta p_f + \Delta p_d \quad (\text{Eq5})$$

$$\Delta p_d = cmv \quad (\text{Eq6})$$

c is the resistance coefficient of the dust layer, $56003/60\text{min}^{-1}$; m is the dust load, kg/m^2 ; v is the filtration velocity, m/min .

Usually, $\Delta p_c = 200 \sim 500\text{Pa}$, Δp_f can be ignored. ρ is dust concentration of the bag filter's entrance, kg/m^3 ; t_2 is the filter time, min; the average collection efficiency is about 100%. So the dust load on the filter $m = \rho v t_2$ after t_2 minutes, and after t_2 minutes the pressure loss of the dust layer:

$$\Delta p_d = c\rho v^2 t_2 \quad (\text{Eq7})$$

The dust cleaning began when the pressure of the bag filter was 1500Pa and the pressure loss of the bag filter's structure (Δp_c) was 500Pa, so the filtration energy consumption of the filtration bags per cleaning cycle:

$$N_0 = \int_{\frac{500}{c\rho v^2}}^{1500} Q_0 \Delta p_t dt \quad (\text{Eq8})$$

And then the filtration energy consumption of the bag filter was calculated (yuan): $B_5=87346$.

(2) Dust-cleaning energy consumption

The air pulse-blew out from the compartment pulse ejector bag filter and the air ejected from around forms the anti-blown air, the amount of this air should satisfy the needs of cleaning of the filter bag^[10]. And the air amount injected from the nozzle is determined by the injection pressure and the diameter of the nozzle. 3-inch pulse valve was selected by calculation, and

the injection pressure was 0.6Mpa. The cleaning energy consumption of each compartment once a time was theoretical calculated (KWh):

$$N_1 = \frac{H_a \times Q}{1000 \times 3600 \times \eta_3} \quad (\text{Eq9})$$

H_a is the injection pressure, KPa; Q is the injected gas volume, m^3/s ; η_3 is the efficiency coefficient.

Therefore, the cleaning energy consumption of BF per year (KWh): $N_1 = 543772.3N\rho v^2$.

The formula about the the number of compartment and the filtration velocity (v) was obtained from the relationship between the total area of bags and the total amount of inlet air of the ESP:

$$N \times v = 18.976 \quad (\text{Eq10})$$

The electricity consumption of dust cleaning of the ESP per year was calculated (yuan):

$$B_6 = 195806491.7\rho / N .$$

(3) The electricity consumption of the ash disposal system

The calculation of this part is the same as ESP's. The electricity consumption of the screw conveyor (yuan): $B_7 = 5987.1\rho v N$. The electricity consumption of the star-shaped cinder

valve per year (yuan): $B_8 = 2124.5\rho v N$

(4) Maintenance cost

The dust concentration of the gas which was purified by the ESP and then entered the BF was very low, the filtration resistance grew slowly which extended the dust-cleaning cycle, extended the replacement cycle of bags and reduced the cost of the replacement of bags, so the operating cost lowered. The service life of the bags was counted by the times of dust cleaning, and the maintenance cost = the total price of the bags/ the service life of the bags + the total price of the pulse valves/ the service life of the pulse valves. Generally, the use of bags are related with the times of dust cleaning, and the annual cost of replacement of bags (yuan): $B_9 = 158128645.7\rho / N + 120N .$

3.2.3 Optimization of Filtration Velocity of the BF Unit

Summarized the above analysis about the annual manufacturing costs and operating costs of BF, the mathematical model to calculate the total cost of BF was obtained:

$$B_{total} = \frac{3539351374\rho}{N} + 1539257\rho + 3190N + 943547 \quad (\text{Eq11})$$

In order to get the optimal value of the total cost of the compound electrostatic-bag filter, the total cost of the bag filter had been analysis firstly, and the minimum value of the cost was optimized.

See from the formula (11), the number of compartment is inversely proportional to the filtration velocity, the smaller the filtration velocity, the lower the operating cost; but the increase of the number of compartment increases the manufacturing cost of BF; otherwise, the bigger the filtration velocity, the higher the operating cost, while the number of compartment reduces and lowers the manufacturing cost.

With the aim of achieving the lowest total cost of BF, the derivation of N was set zero, we can get:

$$N = 333\sqrt{\rho} \quad (\text{Eq12})$$

The optimal filtration velocity of BF:

$$v = \frac{18.976}{333\sqrt{\rho}} \quad (\text{Eq13})$$

The optimized total cost of BF was obtained taking the formula (13) into the formula (11):

$$B_{total} = 2125737\sqrt{\rho} + 153925.7\rho + 94354.7 \quad (\text{Eq14})$$

4 Overall Optimization of the Compound Electrostatic-bag Filter

Integrated the mathematical model of the manufacturing cost and operating cost of the electrostatic precipitator unit and bag filter unit, and substituted into the formula of Deutsch which expressed the relationship between the length of the electric-field and collection efficiency of the ESP, we obtained the total cost of the compound electrostatic-bag filter:

$$F = 55539 \ln\left(\frac{\rho_0}{\rho}\right) - 117573\rho \ln\left(\frac{\rho_0}{\rho}\right) + 144718.9\rho + 2125737\sqrt{\rho} + 135663.3 \quad (\text{Eq15})$$

Analyze the formula (15), the entered gas concentration (ρ) of the BF is a series of discrete values because that the number of the compartment (N) is a integer. Substituted ρ into the formula (15), the figure describing the relationship between the total cost of the compound electrostatic-bag filter and the number of the compartment (N) was got (Fig.2).

The analysis shows that:

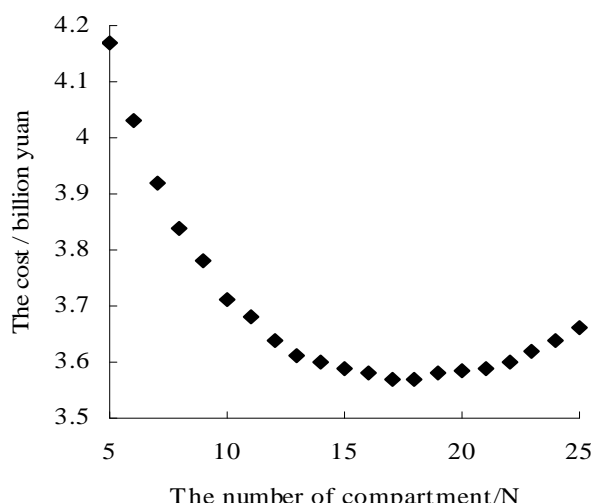
(1) The total cost of the compound electrostatic-bag filter declines rapidly with the increase of

the number of compartment (N) each row of the BF. The reason is that with the increase of the number of compartment (N), the cleaning share rate of ESP reduces, and the length of the ESP decreases, so the total cost of the ESP declines rapidly. Although the manufacturing cost of bag filter increase correspond, the manufacturing cost of bag filter is lower than ESP's, the filtration velocity of bag filter decreases and the operating cost declines with the increase of the number of compartment, so the decrease of the cost of ESP is a bigger effect to the compound electrostatic-bag filter. Therefore the total cost decreases rapidly

(2) The total cost of the compound electrostatic-bag filter begins increasing when N has increased certain degree. It is because that, the manufacturing costs of bag filter increases with the increase of the number of the compartment, and the increasing-speed of the cost of bag filter is bigger than the decreasing-speed of the ESP's. However, the increased degree of the total cost of the compound electrostatic-bag filter is small because that the manufacturing costs of bag filter is smaller than the ESP's, and the operating cost of bag filter decreases with the increase of the number of the compartment which leads the total cost of the compound electrostatic-bag filter increase slowly.

(3) The total cost of the compound electrostatic-bag filter has an optimal value when the number of the compartment near 16. In this condition, the density(ρ) of the exit is 2.3086 g/m³, the length of the electric-filed is 5.4m, the filtration airspeed(v)of bag filter is 1.186m/min, and the cleaning share rate of the ESP is 88.457%.

Figure.2 The Cost Graph of the Compound Electrostatic-bag Filter



CONCLUSIONS

- (1) The structure of the ESP and the BF was selected and designed based on the systematically analysis of their structure and the operating mechanism, and their manufacturing cost was calculated.
- (2) The mathematical model of the electricity consumption and the energy consumption of the airflow resistance of the electric-field of the ESP, and the filtration energy consumption and the dust-cleaning energy consumption were proposed in view of the operating energy consumption of ESP.
- (3) With the aim of achieving the lowest total cost of the compound electrostatic-bag filter, the share rate of dust cleaning in electrostatic and bag dust removal unit, the length of electric-field and the filtration airspeed of BF in the new working conditions had been optimized. The optimized results indicated that the efficiency of dust collection of the former ESP was 88.457% and the optimum filtration airspeed of the latter bag filter was about 1.2 m/min to the gas whose entrance density was 20g/m³ and the amount of air was 13×10^4 m³/h.

REFERENCES

- [1].*Development Report on Electrical Dust Precipitation Industry of China in 2004.* Committee of Electrical Dust Precipitation, China Association of Environmental Protection Industry, 2005.
- [2] Miller, S., Schelkoph, G, Dunham, G; Walker, K; Krigmont, H. *Advanced Hybrid Particulate Collector, a New Concept for Air Toxics and Fine-Particle Control.* EPRI-DOR-EPA Combined Utility Air Pollution Control (MEGA) Symposium. Washington, D.C. 1997, pp25-29.
- [3]Xianghong Zhang. Application Practice of Electro-bag Compound Dust Removing Technology. *Meishan Technology*, 2006, 1, 23-24.
- [4] P.V.Bush, T.R.Snyder. Implications of Particulate Properties on Electrostatic Precipitator and Fabric Filter Performance. *Powder Technology*, 1992, 72(3):207-213.
- [5] Bergeles.G.C. Numerical Simulation of the Flow and the Collection Mechanisms inside a Laboratory Scale Electrostatic Precipitator. *Journal of Electrostatics*, 2005,63(5):423-443.
- [6]Manyin Hu, Ruiying Zhang,Yong Yang. Economic Technical Analysis on Electro-bag Filte. *Electric Power Science and Engineering*, 2008, 24(1):58-60.
- [7] Manyin Hu, Ruiying Zhang. The Study on Simulation Mathematical Model of Electrostatic Precipitator-bag Dust Remover in Power Plant. *Chinese Journal of Environmental Engineering*, 2008, 26 (5):54-57.

- [8] Jian'e Chang, Beichuan Han. Cleaning System of Electrostatic Fabric Filter: Optimization Portfolio. *China Cement*, 2006, 10:26-25.
- [9] Yan Wu. Study on Cleaning Mechanism of Chamber Type Jet Injection Bag Filter. Northeastern University at Shenyang, 2008.
- [10] Yan Wu, Wenge Hao, Yingying Pei et al. Establishment of Technical Parameters for the Dust-cleaning System of the Air Chamber Type Pulse-jet Bag Filter. *Acta Scientiae Circumstantiae*, 2008, 28(8): 1593-1598.

A Facile One-Step Route to BiOBr-Graphene Composites and Their Enhanced Visible Light Photocatalytic Removal of Gaseous NO

Zhihui Ai¹, Lizhi Zhang¹ and Shuncheng Lee²

1 Key Laboratory of Pesticide & Chemical Biology of Ministry of Education of College of Chemistry, Central China Normal University, Wuhan 430079

2 Department of Civil and Structural Engineering, Research Center for Environmental Technology and Management, The Hong Kong Polytechnic University, Hong Kong

Principal Contact: Zhihui Ai, Dr., Associate Prof., Central China Normal University, Wuhan, 430079.

Tel/Fax: 0086-27-67867535 Email: jennifer.ai@mail.ccnu.edu.cn

Abstract

In view of increasingly serious energy and environmental problems, applications of environmentally harmonious photocatalysts are urgently desired for the purification of polluted water/air, the decomposition of offensive atmospheric odors as well as toxins on a huge global scale. As a new visible light responding photocatalyst, BiOBr has been recently developed and utilized for environment cleaning under visible light irradiation in order to utilize solar light. In addition, graphene is an attractive material for fabricating graphene containing inorganic composites, for instance, graphene hybrids with metal oxides, metals and polymers have been developed recently for various applications. In this study, we developed a facile route to bismuth oxybromide (BiOBr) and graphene nanocomposites (BGCs) using graphene oxide, bismuth nitrite, and cetyltrimethyl ammonium bromide (CTAB) as the precursors. During the one-step hydrothermal synthesis, both of the reduction of graphene oxide and the formation of BiOBr nanocrystals were achieved simultaneously. The as-prepared BGCs were found to display a superior performance on degradation of gaseous nitrogen monoxide (NO) to the pure BiOBr photocatalysts under visible light irradiation ($\lambda > 420$ nm). The enhanced photocatalytic activity of the BGCs composites could be attributed to the presence of graphene, which was favorable for the extension in light absorption in the visible region, higher surface area, as well as effectively increasing charge separations. The study provides a facile method to synthesize BGCs with enhanced efficiency in the visible-light spectral range, as well as significantly facilitates the application of graphene in environment pollutants remediation.

Keywords: BiOBr; Graphene; Photocatalysis; Nanocomposite; Visible Light

The Effect of Atmospheric Parameters on Fine Particulate Concentration in the Suburbs of Shanghai

Jian Yao¹, Wei Liu¹, Wangkun Chen^{2*}, Guanghua Wang¹, Xuebo Fan¹, Yanhong Geng¹, Nannan Wei¹, Youshi Zeng¹, Yu Huang¹ and Jun Lin¹

1 Key Laboratory of Nuclear Analysis Techniques, Shanghai Institute of Applied Physics, Chinese Academy of Sciences, Shanghai 201800, China

2 Department of Environment and Property Management, Jin Wen University of Science & Technology, Taipei 23154, Taiwan

ABSTRACT

This paper presents a study on the effect of atmospheric parameters on fine particulate mass concentrations in the suburbs of Shanghai. Temperature, wind speed, relatively humidity and particulate mass concentration were measured discontinuously from January 2009 to January 2010 in the Jiading district of Shanghai, China. A sensitivity analysis was conducted between atmospheric parameters and particulate mass concentration. For difference particle sizes, the atmospheric parameters have a different effect on the particulate mass concentration. A significant boundary for these effects is the diameter of $1\mu\text{m}$. The ventilation index and dilution index were calculated using the data of December 2009. A correlation analysis was conducted between the two indexes and particulate mass concentration. The results indicated that there was a tight correlation between the two indexes and the particulate concentration of three particle sizes ($<0.1\mu\text{m}$, $0.1\text{-}1.0\mu\text{m}$, $1.0\text{-}2.5\mu\text{m}$). The Spearman correlation coefficient values were -0.45, -0.56 and -0.47, while the coefficient values of the dilution index were -0.36, -0.42 and -0.45, respectively. It was also found that the effects of temperature and relative humidity on the particulate concentration differed for various particle sizes.

KEYWORDS

Atmospheric parameters, Particulate concentration, Sensitivity analysis, Correlation analysis, Size distribution

Introduction

Fine particulate (particle size less than $2.5\mu\text{m}$) plays an important role in air pollution because of its impact on health and visibility degradation. Particulate concentration is greatly influenced by atmospheric conditions that can determine the transport, diffusion, transformation, and removal of fine particulates. However, there is little research focused on the relationship between

atmospheric parameters (AP) and particulate mass concentration (PMC) because of its uncertainty and regional differences.

Jeroen J. de Hartog^[1] describes the relationship between different size classes of PMC and AP in three European cities. Christopher A. Noble^[2] claims that the Pearson correlation coefficients (in urban El Paso, Texas) between PM₁₀ mass concentration and temperature, relative humidity, and wind speed were 0.2, -0.18, and 0.19, respectively. Bhaskar and Mehta^[3] found a negative correlation between PM₁₀ and rainfall, humidity and wind speed during a study period in Ahmedabad.

Their disadvantages are that the particulates they cared about are larger than 2.5μm and the sampling sites are all in foreign countries. Therefore, it is necessary for us to consider the dependence of fine particulate mass concentration (FPMC) on the AP in China, especially in Shanghai. In this article, the relationship between AP and FPMC of different particle sizes were investigated. Also, it is suggested to study more samples to better understand the exact relationship between AP and the FPMC over the course of the entire year and throughout the different seasons.

Experimental Methods

Sampling

Measurements for FPMC were made over a period of one year from January 2009 to January 2010 at Jiading district in Shanghai. The site was located in the Shanghai Institute of Applied Physics of Chinese Academy of Sciences (31°24'N, 121°17'E, 15 meters above ground level). An Electrical Low Pressure Impactor (ELPI , DEKATI Company) at a nominal flow rate of 10 L/min was employed to collect the FPMC once every minute in real-time. The particles ranged in size from 30 nanometers to 2.5 micrometers^[4]. The Aerodynamic D_{50%} values of each stage are listed in Table 1.

Table 1. The ELPI aerodynamic D_{50%} values of each stage.

Stage	1	2	3	4	5	6	7	8	9	10
D _{50%} (μm)	0.03	0.06	0.108	0.17	0.26	0.4	0.65	1	1.6	2.5

Temperature, wind speed, and relative humidity were simultaneously measured every 30 minutes using a Davis Pro weather station (Davis Instruments Corp., USA), which was located 18 m above ground level. The mixing layer height and atmospheric stability were downloaded every three hours from the website of the Air Resources Laboratory^[5].

Sensitivity analysis

Temperature, relative humidity and wind speed were selected because of their importance in determining the concentration level of the pollutants. The sensitivity study was carried out using a series of measured data after the appropriate parameters were determined. Taking the temperature analysis as an example, the procedure consisted of the following steps:

1. Calculate the mean values of the PMC every 30 minutes.
2. Calculate the cumulative frequency of the temperature, and list each temperature value for the cumulative frequencies of 0, 10%, 20%, 30%, 40%, 50%, 60%, 70%, 80%, 90% and 100%, respectively.
3. Find the PMC values that corresponds to the temperature values obtained in the previous step. Because the particulate mass concentration values that correspond to a temperature value may not be singular, we must average these values.
4. Draw the figures taking the temperature accumulative frequency as the X axis and the average PMC as the Y axis.

From the previous steps we can get a rough idea of the relationship between FPMC and the temperature. Then a new index is defined to characterize the sensitivity of the particulate concentration to the outside temperature.

$$Mv = \frac{VC}{W} \quad (\text{Eq.1})$$

Where, Mv is the marginal variable, VC is the variation in the particulate mass concentration, and W is the variation in temperature.

The procedures for data analysis of the other parameters are as mentioned above.

Correlation analysis

In order to have a better idea of the relationship between AP and FPMC, two new indexes were defined as follows. One is the ventilation index and the other one is the dilution index. The ventilation index is calculated as follows.

$$\Omega = H \bullet V \quad (\text{Eq.2})$$

Where, Ω is the ventilation index, H is the mixing layer height, and V is the average wind speed at 10m below the mixing layer.

$$\Psi = \sigma_y \bullet \sigma_z \bullet V \quad (\text{Eq.3})$$

Where, Ψ is the dilution index, σ_z is the vertical diffusion coefficient, σ_y is the horizontal diffusion coefficient, and V is the average wind speed at 10m below the mixing layer.

According to the literature, σ_z , σ_y are defined as Eq. (3):

$$\sigma_y(x) = R_y x^{r_y}, \sigma_z(x) = R_z x^{r_z}. \quad (4)$$

$R_y, R_z, x^{r_y}, x^{r_z}$ are given by the Klug experiment, and the values are listed in Table 2.

Table 2. The $R_y, R_z, x^{r_y}, x^{r_z}$ values given by the Klug experiment.

Stability	A	B	C	D	E	F
R_y	0.469	0.306	0.23	0.219	0.237	0.273
r_y	0.903	0.885	0.855	0.764	0.691	0.594
R_z	0.017	0.072	0.076	0.140	0.217	0.262
r_z	1.380	1.021	0.879	0.727	0.610	0.500

Taking the data for December as an example and taking into consideration their complexity, the data analysis procedures can be shown as follows:

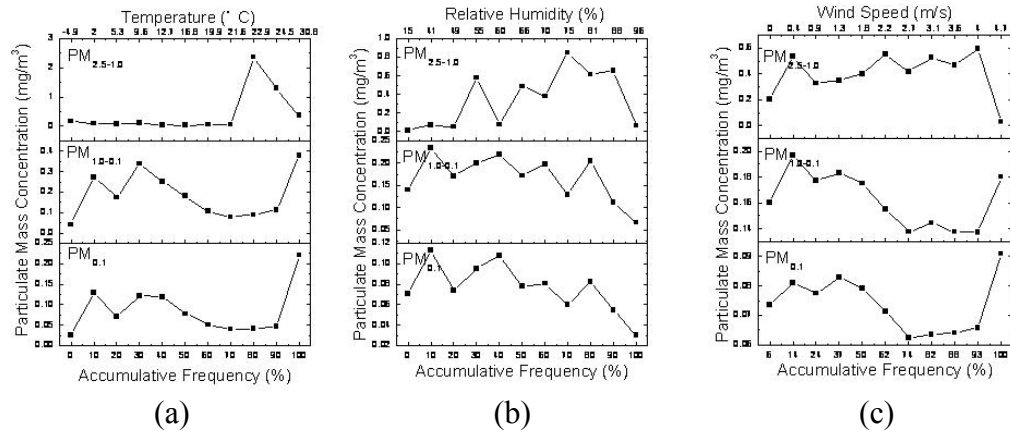
1. Calculate the average value of the temperature, wind speed, relative humidity and PMC every 3 hours.
2. Calculate the ventilation index and the dilution index as per Eqs. (2-3).
3. Finally, conduct the correlation analysis^[6] to determine Spearman's coefficients between temperature, wind speed, relative humidity, mixing layer height and the PMC.

Results and Discussion

Effects of atmospheric parameters

Fig. 1 shows the relationship between average PMC of different size ranges and AP. No matter which AP, its influence on PMC for the first two particle size ranges ($<0.1\mu\text{m}$, $0.1\mu\text{m} \sim 1\mu\text{m}$) is consistent. However, the influence of the 3rd size range ($1\mu\text{m} \sim 2.5\mu\text{m}$), is different from the previous two.

Figure 1. The relationship between average particulate mass concentrations of different size ranges and atmospheric parameters. Different sub-graphs with different atmospheric parameters: (a): temperature, (b): humidity, (c): wind speed.



The effect of the wind speed to PMC should be particularly noticed. It is found that at a lower wind speed, the PMC are generally higher for the three particle size ranges. Depending on the wind speed, the PMC maintain a higher level for the third particle size range, while the concentrations decrease gradually for the other two ranges. When the wind speed is equal to 4.7 m/s, the PMC decrease rapidly for the third particle size range, while increasing rapidly for the first two particle size ranges.

The marginal analysis result shows the marginal variables of the AP in the different size ranges. It also indicates that the fluctuation of the marginal variables increases with the increase in particle size.

Influence of the ventilation index and the dilution index

In the previous section, we discussed the effect of the AP on the FPMC on a qualitative basis, and exact figures are required to describe this relationship.

Table 3 shows the Spearman coefficient between AP and the PMC of different size ranges in December, 2009. From the point of view of AP, the Spearman coefficients of the temperature are -0.434, 0.04, and 0.084 respectively in the three particle size ranges. The last two values should be ignored because they did not reach a significant level. This finding is consistent with the results from Hamdy K. Elminir^[7], whose coefficient between temperature and PM_{10} in December was -0.53.

Table 3. The Spearman coefficient between atmospheric parameters and the particulate mass concentration of different size ranges using SPSS.

	Atmospheric parameters					
	Temperature	Relative Humidity	Mixing Layer Height	Wind Speed	Ventilation Index	Dilution Index
	PM_{0.1}	-0.434 ^a	-0.110	-0.44 ^a	-0.262 ^a	-0.454 ^a
PM_{1.0-0.1}	0.040	0.115	-0.511 ^a	-0.354 ^a	-0.558 ^a	-0.426 ^a
PM_{2.5-1.0}	0.084	-0.200 ^b	-0.383 ^a	-0.360 ^a	-0.473 ^a	-0.446 ^a

Confidence level: a:0.01, b:0.05.

The Spearman coefficients of relative humidity are -0.11, 0.115, and -0.2 respectively (the first two values are unusable), when compared to the research result of 0.15 by Hamdy K. Elminir. This may be due to the fact that the weather conditions of the two sampling sites are different. The sampling background of Hamdy K. Elminir was a desert, while our sampling background was a flat area during the rainy period in winter.

Both the ventilation index and the dilution index characterize the diffusion rate of the particulate including the influences of wind speed and mixing layer height.

From a size distribution point of view, the coefficients of dilution index and ventilation index are very close for the three particle size ranges. In contrast, temperature and relative humidity show a strong difference in particle size. This infers that although both the dilution index and ventilation index have a better correlation with the FPMC, temperature and relative humidity still requires our full attention in Jiading district when it comes to fine particulate control, because of their different effect in winter based on particle size .

CONCLUSION

The aim of the present study was to determine which AP influences the FPMC most, to characterize the transport of airborne particles and to standardize the concentrations with respect to the AP.

From the results of this research we can conclude the following.

1. The effect of AP on the FPMC are obviously particle size difference and a boundary of 1μm.
2. The dilution index and ventilation index show a high correlation to FPMC during the winter in Jiading district.
3. Our findings indicate that we should concentrate on both temperature and relative humidity if we want to find a way to control fine particulates during the winter months in the Jiading district .

In further work, it is suggested to study the effect of size distribution and provide more evidence.

REFERENCES

- [1] De Hartog, J.J.; Hoek, G.; Mirme, A.; Tuch,T.; Kos, G.P.A.; Brink, H.M.; Brunekreef, B.; Cyrys, J.; Heinrich, J.; Pitz, M.; Lanki, T.; Vallius, M.; Pakkanen, J.; Kreyling, W.G. *Journal of Environmental Monitoring*. 2005, 7, 302-310.
- [2] Noble, C.A.; Mukerjee, S.; Gonzales, M. *Atmos. Environ.* 2003, 37, 827–840.
- [3] Bhaskar, B.V.; Mehta, V.M. *Aerosol Air Qual. Res.* 2010, 10, 301-305.
- [4] Ojanperä, J.Y.; Kannisto, J.; Marjamäki, M.; Keskinen, J. *Aerosol Air Qual. Res.* 2010, 10, 360-366.
- [5] National Oceanic and Atmospheric Administration (NOAA). See <http://www.ready.arl.noaa.gov> (accessed October 2010).
- [6] Myers, J.L; Well, A.D. *Research Design and Statistical Analysis*. Lawrence Erlbaum Associates, USA, 2003.
- [7] Elminir, H.K. *Science of the Total Environment*. 2005, 350, 225-237.

The Variation of PM_{2.5} Concentration under Different Weather Systems in Hangzhou Urban

Hong Shengmao and Jiao Li

Hangzhou Environmental Monitoring Center Station, Hangzhou, China 310007

Principal Contact: Hong Shengmao, professor, environment science, No.4, Hangda road, Handzhou, Zhejiang Prov., China.

Tel: 0571-87998260/13858179159 Fax: 0571-87998310 E-mail: honglaomao@hotmail.com

Abstract

The paper analyze the data of air quality and meteorology from 2006-2009 , these datas used to study the variation of PM_{2.5} annual average concentration and change of different weather systems, the paper also research the relationship between PM_{2.5} and meteorological factors. The results show that the annual PM_{2.5} concentrations from 2006 to 2009 have a greater range, which are 0.078 mg • m⁻³, 0.061 mg • m⁻³, 0.083 mg • m⁻³, 0.061 mg • m⁻³, respectively. The max amplitude of PM_{2.5} annual concentration is 0.022 mg • m⁻³, and about 1/3 in annual average value. The PM_{2.5} concentrations from big to small in eight weather systems are Following Cold-front, High-pressure Control, Back of High-pressure, Bottom of High-pressure, Front of High-pressure, Inverted Trough, Anterior Cold-front, Cyclone system, and Easterlies system, respectively. The max PM_{2.5} concentration among several weather systems is 0.091 mg • m⁻³, and the min's is 0.038 mg • m⁻³, their rate of PM_{2.5}/PM₁₀ are 0.64, 0.58, respectively. The weather systems of Following cold-front and Easterlies system are two typical different systems, which appear in autumn and winter, summer, respectively. The higher PM_{2.5} concentration in the Following cold-front system, which caused to frequency inversion-layer phenomenon, the lower PM_{2.5} concentration appeared in the Easterlies system, which lead to multiple rain cases and larger wind speed. The correlation of PM_{2.5} concentration between with PM₁₀ in autumn and winter is better relationship than that of summer. The differentias of PM_{2.5} concentration are larger among the three types of PM₁₀ pollution, which include Large-scale Continual-pollution, Tocal continual-pollution, and Individual-pollution. The highest PM_{2.5} concentration is 0.117 mg • m⁻³ in the Large-scale Continual-pollution, even if the PM₁₀ pollution is non, the PM_{2.5} average concentration is 0.063 mg • m⁻³, which is also double of the U.S. standard.

Key words: weather system, the Following Cold-front, the Large-scale continual pollution.

Energy saving and CO₂ emission reduction in the refinery furnace

Chien-li Lee¹, Yu-Shan Wang² and Chih-Ju G. Jou^{2*}

1 Research and Development Center for Water Resource and Conservation, National Kaohsiung First University of Science and Technology, Taiwan

2 Department of Safety, Health and Environmental Engineering, National Kaohsiung First University of Science and Technology, Taiwan

Principal Contact: Chih-Ju G Jou, Department of Safety, Health and Environmental Engineering, National Kaohsiung First University of Science and Technology, Taiwan.

Tel: 886-7-601-1000 Ext. 2316 Fax: 866-7-601-1061 E-mail: george@ccms.nkfust.edu.tw

Abstract

Through the tip of the burner, the fuel is injected into a heating furnace where it is burnt to produce heat. The resulting heat gas flow moves upward in the furnace under the influence of the draft produced in the smoke stack; a pressure difference is thus generated in the furnace. Excessive furnace pressure difference will cause a short residence time of the hot flow in the furnace that adversely affects the overall heat efficiency of the furnace to waste precious fuels. On the other hand, a pressure difference too small will cause the flame in the furnace to back fire that may damage the furnace structure and jeopardize the operational safety. In this study, the furnace internal pressure is altered by adjusting the opening of the furnace flue baffle. Laboratory studies show that if the opening is reduced from 45% to 38%, 1.7×10^6 m³ of natural gas consumption can be saved to reduce the CO₂ emission by 3.7×10^3 tons annually. The observations demonstrate that the optimum control of the furnace internal pressure will be the key for an existing furnace to achieving energy savings and reducing CO₂ emission without major physical changes of an existing furnace.

Keywords: Furnace pressure; Damper; Carbon dioxide

The Influence of Aerosol Particles Emitted from Smoking and Candle Burning on the indoor Radon and Thoron Progeny Concentration

Jin Wang¹, Juan Liu¹ and Yongheng Chen¹

1 Guangzhou University, School of Environmental Science & Engineering, Wai Huan Xi Road 230, Guangzhou 510006, China

Principal Contact: Jin Wang, PhD, Guangzhou University, School of Environmental Science & Engineering, Wai Huan Xi Road 230, Guangzhou 510006, China.

Phone: +86-20-39366013 Fax: +86-20-39366236 E-mail: wangjin200726@hotmail.com

Abstract

The influence of typical aerosol particles emitted from cigarette smoking and candle burning on indoor radon (^{222}Rn) and thoron (^{220}Rn) progeny concentration was examined in an experimental model room with 7.1 m^3 . The model room was mainly built with powdered granite and clay material, represented certain indoor activity concentration of radon and thoron for study under controlled conditions. The affect of aerosol from cigarette smoking and candle burning was tested separately. A mixing fan was operated to ensure that aerosol particles did not build up near the aerosol source. Aerosol particles number concentration and size distribution were measured using SMPS (Scanning Mobility Particle Sizer). Potential alpha energy concentrations of radon and thoron progeny were determined by WLM (Working Level Monitor). Furthermore, the attached and unattached fraction of radon and thoron progeny was simultaneously distinguished, to precisely assess the influence and contribution of those typical anthropogenic indoor aerosol particles.

Keywords: smoking; candle; size distribution; radon and thoron

Mixing State Variations of Fine Dust Particles in Atmospheric Boundary Layer of Yellow Sea in Spring

Chengming Pang¹ and Zifa Wang²

1 Beijing Institute of Aviation Meteorology, Beijing 100085

2 LAPC, Institute of Atmospheric Physics, Chinese Academy of Sciences, Beijing 100029

Principal Contact: Pang Chengming, Ph. D., Beijing Institute of Aviation Meteorology, An Ning Zhuang Road, Beijing, 100085, China.

Tel: 13671346321 Email: chengmingpang@126.com

Abstract

The mixing state of aerosols plays important role in their effect on the climate force and cloud physics. In order to understand the mixing state of dust aerosol in its transport in East Asia, the Asia outflow aerosol observed in spring of 2001 in atmospheric boundary layer (ABL) of Yellow Sea is analyzed. The analysis of ionic imbalance and ions correlation are carried out with the ionic concentration of fine particles observed in research flights over ABL of Yellow Sea in ACE-Asia experiment. The mixing state of fine dust particles can judge by the composition change of CaCO_3 (and MgCO_3) and the ratio of internal mixture can be estimated using the fraction of reacted carbonate to total carbonate. According to the change of carbonate in dust fine particles, partial fine dust particles changed to internal mixture in the research flight legs influenced by dust storm in Yellow Sea ABL. The ratio of internal mixture varied temporally and spatially. In different dust episodes the average ratio of internal mixture for fine dust particles in Yellow Sea ABL legs (RF06, RF07, RF10, and RF13) is 11%, 27%, 33%, and 5%, respectively. Comparison with some single particle observations indicates it is reasonable. In different dust episodes the ratio of internal mixture of fine dust particles is opposite to the dust intensities. The intenser the dust is, the bigger the wind speed being, the speedier the dust's moving is, so the shorter the reacting time of dust with other substance is, and the smaller the ratio of internally mixed dust fine particles is.

Keywords: ABL of Yellow Sea, dust, fine particles, mixing state, ratio of internal mixture

Simultaneous Measurement of Particle Optical Extinction and Scattering Using the CAPS PM_{SSA} (Single Scattering Albedo) Monitor

Timothy B. Onasch, Paola Massoli, Paul L. Kebabian and Andrew Freedman

Center for Sensor Systems and Technology, Aerodyne Research, Inc., Billerica, MA 01821, U.S.A.

ABSTRACT

We present preliminary results of studies detailing the efficacy of a compact, robust instrument that determines the single scattering albedo of ambient particles by simultaneously measuring both total extinction and scattering of a common ambient air parcel; measurement wavelengths of 450, 530 and 630 nm are available. Particle extinction is measured using the cavity attenuated phase shift approach. Particle scattering is determined using an inverse nephelometer facilitated by the incorporation of an integrating sphere within the extinction measurement volume. This approach, as compared to using a cosine-corrected detector, results in minimal truncation errors - <10% for particles of diameter 1 micron or less and ≤ 20% for particle diameters of 2.5 microns as measured using polystyrene latex spheres. Both extinction and scattering can be measured with a time response (10-90%) of ~ 1 second. The short term noise in both extinction and scattering channels is less than 0.5 Mm⁻¹ with 1 second sampling time.

KEY WORDS

Single Scattering Albedo, Particle Extinction, Particle Scattering, Cavity Attenuated Phase Shift

Introduction

At present, the uncertainties in the magnitude of aerosol-induced radiation forcing present a critical limitation in our understanding of climate change.^[1-3] The aerosol single scattering albedo (SSA) is a critical parameter in global climate change models because it represents the partitioning of optical extinction between scattering and absorption. Currently, this measurement requires the use of two separate instruments; filter-based instruments are

typically used to measure absorption while a nephelometer is used to measure particle scattering. Each type of instrument has its own set of limitations with respect to accuracy.

To meet this need for accurate and robust instrumentation for the measurement of particle optical extinction, we have developed the CAPS PM_{SSA} Particle Single Scattering Albedo Monitor. The monitor, which samples ambient air, employs the cavity attenuated phase shift (**CAPS**) technique to produce measurement pathlengths on the order of 2 km, allowing it to accurately measure particle optical extinction for PM_{2.5} from 0 to 4000 Mm⁻¹ with 1 second time resolution.^[4-6] In addition, the monitor incorporates an integrating sphere within the measurement volume which provides a light scattering measurement based on inverse nephelometry. We present below preliminary results for this instrument.

Experimental Methods

The CAPS PM_{SSA} monitor is expressly designed to integrate two functions: measurement of both the extinction of the optical beam by a particle-laden air sample and light scattered from the particles without introducing a bias with respect to particle diameter. We first discuss the former measurement. The CAPS-based extinction measurement involves an optical absorption spectrometer, utilizing in this case a green light-emitting diode ($\lambda = 530$ nm) as a light source, a sample cell incorporating two high reflectivity mirrors ($R \sim 0.9999$) (which provides a long effective pathlength) and PMT-based single photon counting module. The square-wave modulated light (17 kHz) from the LED passes through the extinction cell and is detected as a distorted waveform which is characterized by a phase shift ($\sim 35^\circ$) at the fundamental frequency of the initial modulation. The amount of that phase shift is a function of fixed instrument properties - cell length, mirror reflectivity, and modulation frequency – and of the presence of scattering/absorbing species. Complete details of this measurement are provided elsewhere.⁴⁻⁶

As shown in Figure 1, the extinction cell, constructed from aluminum, is divided into three sections. (Note: the cell is actually constructed in two parts, each containing one arm of the extinction monitor and a hemisphere and then joined in the middle.) The middle section, defined by two small orifices (7 mm diameter), contains a spherical volume ~ 7.5 cm in diameter which acts as the scattering measurement volume for the particle-laden air sample. Within the scattering cell, the sample flows through a quartz tube which both constrains the sample and allows free passage of the scattered photons. The air sample flows into and out of this volume at near atmospheric pressure and then through a limiting orifice under choked flow conditions into a diaphragm pump. The two end sections contain inlets for a gas purge which prevents particulate matter from contaminating the mirrors. The gas purge flow is effective at this task when comprising $\sim 3\%$ of the total gas flow of 0.85 slpm. Under these conditions, the measured time response of the monitor is between 1 and 2 seconds (10-90%

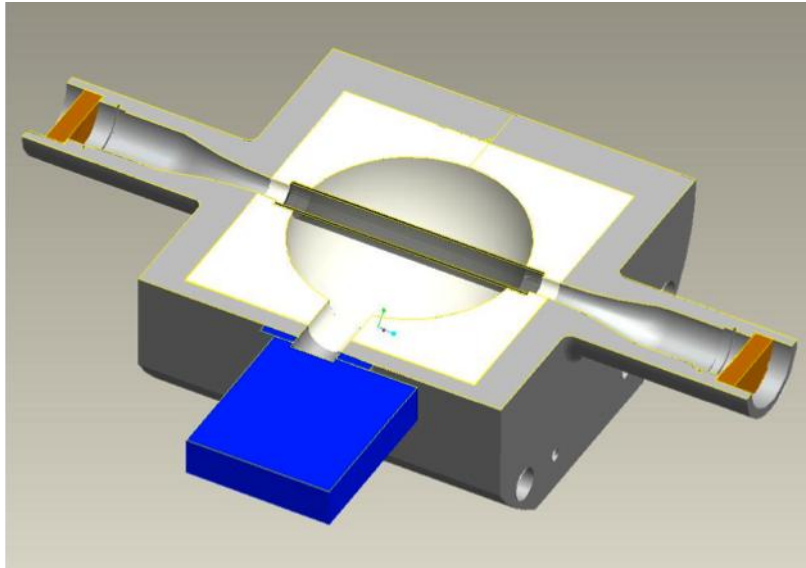


Fig. 1 Schematic of CAPS PMSSA monitor

to maximize the collection of scattered light at the photomultiplier tube which views scattered light from the optical cell at right angles to the optical beam. The second is to minimize the light collection bias with respect to angle. At short wavelengths, Mie scattering calculations of scattering by non-absorbing particles indicate a pronounced forward bias in the scattering distribution of particles with diameters above 600 nm compared to particles with smaller diameters.⁷ The presence of an integrating sphere serves to provide efficient collection of that forward scattered light. Of course, the integrating volume is not perfect in this respect given that its reflectance is not 100% and there are finite openings in the volume to allow the optical beam to enter and exit. The choice of 7 mm apertures on the entrance and exit orifices was based on minimizing the loss of forward scattered light ($\pm 5\%$) while allowing sufficient light through the volume to provide useful measurement precision.

The scattered light is detected by the PMT using single photon counting techniques with a suitable amplifier and discriminator, the output of which is sent to a separate digital counter. The reader should note that there is no shield or baffle which prevents the PMT from viewing light which emanates from the light source and is scattered by the mirrors, optical apertures and various surfaces within the system back into the integrating volume. We are able to dispense with this requirement by electrically gating the signal accumulation counter so that it is operating only when the LED is off. This mode of operation is made possible by the fact that the use of a low-loss cavity provides substantial optical circulating power within the cavity for ~8 microseconds after the LED is turned off, a function of the 35 °phase shift in the signal. The only light within the cavity when the LED is off is highly collimated – i.e.,

response). Both temperature and pressure within the cell are recorded using a thermistor and silicon pressure sensor respectively.

In order to perform the scattering measurement, an integrating sphere is constructed within the middle section of the optical cell. This integrating volume serves two purposes. The first is

reflecting back and forth between the mirrors – and thus minimizes unwanted scattering from the monitor surfaces.

Results and Discussion

In order to measure truncation effects in the scattering measurement, flows of polystyrene latex (PSL) particles of a variety of diameters and particle concentrations entrained in air were sent into the SSA monitor, which employed a green (530 nm) light source. PSLs are assumed to have an albedo of 1.0 – i.e., they are pure scatterers. The left panel shows the measured scattering signals as a function of the measured extinction for three particle sizes. Note that there is a small downward shift in the slope of the line as the particle diameter increases, an indication that there is some truncation of the scattering signal. These measurements were repeated for a wide range of particle diameters (70-2000 nm) and the results are shown in the panel at right where the result obtained at 70 nm is used to normalize the data. Note that there is minimal truncation (<10%) for particle diameters smaller than 1000 nm with somewhat larger effects at diameters above this. The exact shape of this truncation curve is currently being modeled in an attempt to allow a generalization of these results to particles with a wide range of real and imaginary indices of refraction. Massoli, et al. have presented evidence that truncation effects in nephelometers are far greater for absorbing particles (i.e., $\text{SSA} < 1$) than for PSLs.^[7]

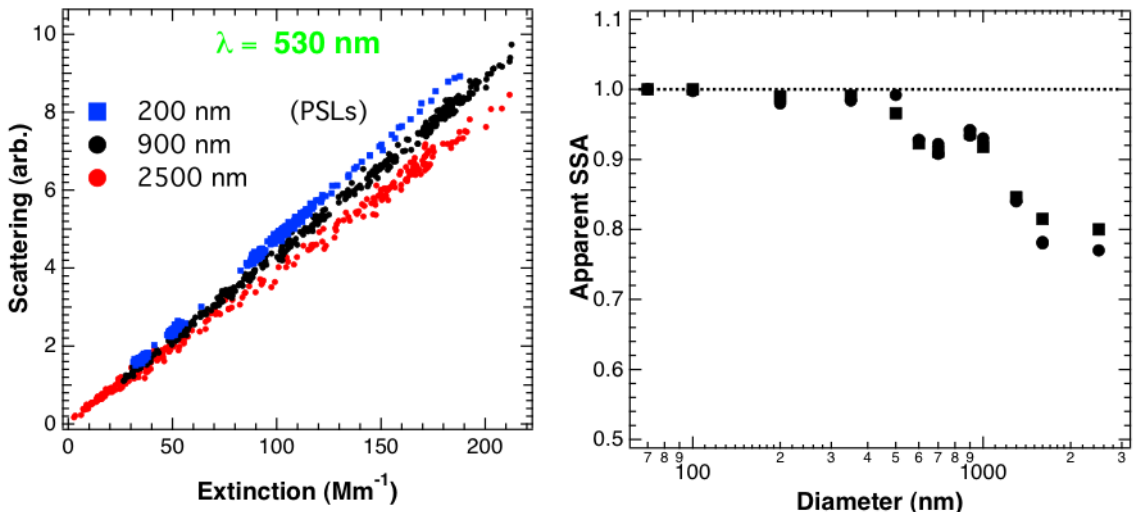


Fig. 2 Left: Measured scattering signal as a function of measured particle extinction for three different size PSls. Right: The apparent SSA calculated from the ratio of the scattering to extinction measurements (normalized to 1.0 for 70 nm particles).

The noise characteristics of both scattering and extinction channels were measured by allowing the monitor to operate for a period of approximately 24 hours without user interaction in order to determine the short term noise characteristics and a sense of the baseline drift. The results are presented in Figure 3 as an Allan plot where the logarithm of the standard deviation (i.e., r.m.s. noise) of the data is plotted versus the integration time. The short term noise at 1 second integration time is below $0.5 Mm^{-1}$ in both channels. The SNR in the extinction channel reaches a minimum of $<0.04 Mm^{-1}$ at ~ 300 s before baseline drift causes the noise levels to increase. The scattering channel reaches a minimum at 2000 s without any noticeable baseline drift. At these levels of noise, instrument performance is typically limited by fluctuations in the number densities of the particles within the effective

$\sim 2 \text{ cm}^3$ measurement volume subtended by the light beam.

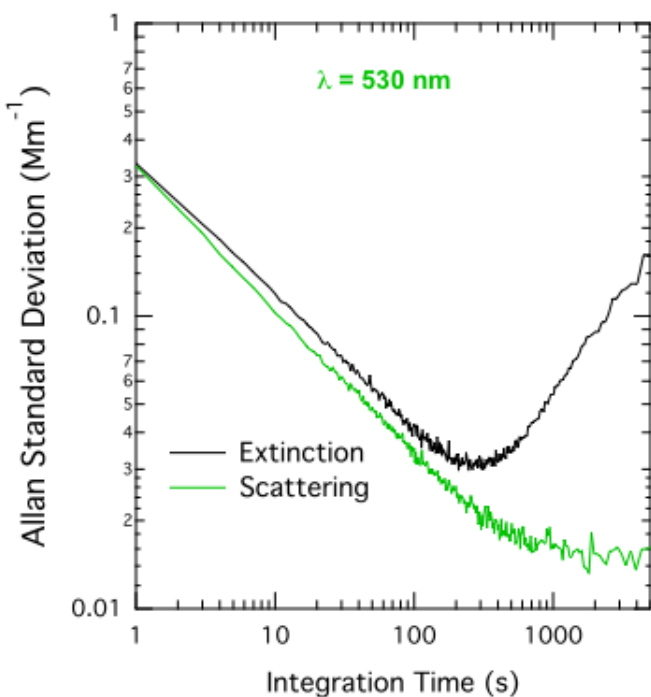


Fig. 3 Allan standard deviation plotted as a function of integration time for both the extinction and scattering channels of the CAPS PM_{SSA} monitor.

SUMMARY

In summary, we have presented preliminary data demonstrating the performance of a newly developed particle single scattering albedo monitor capable of providing accurate and precise measurements of the partitioning of particle single scattering albedo. The individual measurements comprising the SSA determination, extinction and scattering, demonstrate excellent precision and reasonable baseline drift. In particular, the scattering measurement demonstrates minimal truncation effects as a function of particle size. The rack mounted instrument, which can be outfitted to operate at 450, 530 or 630 nm (blue, green or red) weighs 11 kg and utilizes less than 50W of electrical power. The monitor operates in a completely autonomous fashion, requiring no user interaction or expendables such as zero gas, and can be remotely controlled. Only periodic calibration with a gas with a Rayleigh scattering coefficient greater than air is required.

ACKNOWLEDGMENTS

We acknowledge financial support for our participation in the studies presented here from NASA and the National Institutes of Health through the Small Business Innovation Research program.

REFERENCES

- [1] IPCC (2007) Climate Change 2007: the physical science basis- contributions of working group I to the fourth assessment report of the intergovernmental panel on climate change, available at <http://www.ipcc.ch/SPM2feb07.pdf>
- [2] Seinfeld, J.H.; S.N. Pandis, *Atmospheric chemistry and physics: from air pollution to climate change*, 1998, New York, Wiley
- [3] Chen, W.T.; H. Liao; J.H. Seinfeld, Future climate impacts of direct radiative forcing of anthropogenic aerosols, tropospheric ozone and long-lived greenhouse gases, *J. Geophys. Res.* **2007** 112, D14209, doi:10.1029/2006JD008051
- [4] Kebabian, P.L.; Freedman, A., System and method for trace species detection using cavity attenuated phase shift spectroscopy with an incoherent light source, U.S. Patent 7301639, 2007
- [5] Kebabian, P.L., W.A. Robinson and A. Freedman, Optical Extinction Monitor Using CW Cavity Enhanced Detection. *Rev. Scien. Instrum.* **2007** 78, 063102
- [6] Massoli, P.; Kebabian, P.L.; Onasch, T.B.; Hills, F; Freedman, A., Aerosol light extinction measurements by Cavity Attenuated Phase Shift Spectroscopy (CAPS):

laboratory validation and field deployment of a compact aerosol extinction monitor,"
Aerosol Sci. Technol. **2010** 44:428–435

- [7] Massoli, P.; Murphy, D. M.; Lack, D. A.; Baynard, T.; Brock, C. A.; Lovejoy, E. R., Uncertainty in Light Scattering Measurements by TSI Nephelometer: Results from Laboratory Studies and Implications for Ambient Measurements, *Aerosol Sci. Technol.*, **2009** 43:1064-1074

Study on Collection Characteristic of Impactor with Single Nozzle for Different Particle Collecting Directions

C.H. Huang and S.W. Shen

Department of Environmental Engineering and Health, Yuanpei University, 300, Hsinchu, Taiwan

Principal Contact: C.H. Huang; Department of Environmental Engineering and Health, Yuanpei University; No. 306, Yuanpei St., 300, Hsinchu, Taiwan.

Tel: +886-3-6102335 Fax: +886-3-6102337 E-mail: chhuang@mail.ypu.edu.tw

Abstract

In this study, the particle collection efficiencies of impactor with single nozzle for the porous substrate and flat plate in the upright and inverted directions were tested for various particle diameters and Reynolds numbers. Tested particles with various aerodynamic diameters were generated in the chamber by mixing with filtered air to measure the particle collection efficiency of the impactor with single nozzle. The experimental results show that the particle collection efficiencies of impactor with single nozzle for the porous substrate within the collection trap are higher and the curves are less sharp than those of the flat plate. The particle collection efficiencies of impactor with single nozzle for the inverted direction were found to be near to those for the upright direction for both of the porous substrate and the flat plate. Results show that the differences between the particle collection curves of impactor with single nozzle for the upright and inverted directions are not obvious at the ratio of jet to plate diameter of 0.48 for the Reynolds numbers of 1,954 and 2,931. Presently, we are going to simulate the flow field and particle trajectory in the classification trap of the impactor to obtain the numerical collection efficiency. The numerical results of the particle collection efficiencies of impactor with single nozzle for the porous substrate within the collection trap will be compared to the experimental data.

Keywords: Impactor, collection efficiency, single nozzle.

Estimate of Air Exchange Rate Based on Aerosol Concentration Curve

Jin Wang^{1,2}, Oliver Meisenberg², Jochen Tschiersch², Juan Liu¹ and Yongheng Chen^{1,*}

1 Guangzhou University, School of Environmental Science & Engineering, Wai Huan Xi Road 230, Guangzhou 510006, China

2 Helmholtz Zentrum München, German Research Center for Environmental Health, Institute of Radiation Protection, 85764 Neuherberg, Germany

Principal Contact: Yongheng Chen, PhD, Prof., Guangzhou University, School of Environmental Science & Engineering, Wai Huan Xi Road 230, Guangzhou 510006, China. Phone: +86-20-39366013 Fax: +86-20-39366236 E-mail: chenyong_heng@163.com

Abstract

Indoor air quality was concerned with a variety of mixed pollutants, whose concentrations and toxic effects could be largely influenced by the air exchange rate. Therefore, the air exchange rate measurement is of significance. In mechanically ventilated buildings, the air exchange rate can be estimated using either fan-wheel anemometers or tracer techniques; for naturally ventilated buildings, it is far more difficult to estimate air exchange rate. A novel method of estimating air exchange rate based on aerosol concentration curve has been illustrated and suggested. By applying aerosol generating source like mosquito coil, candle or cigarette in indoor environment, the exponential decay of aerosol concentration in a function of time would be obtained and fitted in a model to get the equivalent value of air exchange rate. The method was tested and compared with classical methodology of carbon dioxide tracer, providing excellent agreement and feasibility. The visualized idea of the air exchange rate estimate by aerosol concentration curve was much simpler and more suitable for general indoor environment.

Keywords: air exchange rate; aerosol; exponential decay; fitting

Influence of Turbulent Diffusion in an Electrical Mobility Spectrometer

Jaan Salm¹, Panich Intra², Artit Yawootti³ and Nakorn Tippayawong³

¹ Institute of Physics, University of Tartu, Tartu 50090, Estonia

² College of Integrated Science and Technology, Rajamangala University of Technology Lanna, Chiang Mai 50300, Thailand

³ Department of Mechanical Engineering, Faculty of Engineering, Chiang Mai University, Chiang Mai 50300, Thailand

ABSTRACT

Electrical mobility spectrometer (EMS) is one of most commonly used instruments for measuring the distribution of nanometer-sized aerosol particles. Typically, the EMS has a particle charger, an electrical mobility classifier, and an electrometer. Its principle of operation of is the following: The aerosol to be tested is charged by a unipolar diffusion charger and then classified by electrical mobility in the classifier, which consists of coaxial cylindrical electrodes. The inner electrode is at a high voltage and deflects the charged particles in the flow field toward the outer electrodes. These then collect the particles only within narrow bands of the overall mobility spectrum of the aerosol. In an ideal case, as the charged particles in the classifier move along precisely determined trajectories, they produce the true mobility spectrum. Practically however, molecular and turbulent diffusion randomly scatters the trajectories of the particles, giving a smoothed mobility spectrum. The degree of smoothing can be characterized by the resolution. Fortunately, molecular diffusion submits itself relatively well to a theoretical description and the analytical equation expresses the resolution of the EMS. Because of the complexity of turbulent diffusion, simplifying assumptions were made for this work. The EMS resolution values were calculated based on expected turbulence parameter data.

KEYWORDS

Aerosol, Diffusion, Mobility Spectrometer, Nanoparticles, Turbulence

Introduction

The electrical mobility spectrometer (EMS) is one of the most commonly used instruments for classifying and measuring aerosol particles between 1 nm and 1,000 nm in diameter [1 – 6]. An overview of contemporary electrical mobility spectrometers was given in [6]. The multi-channel

design of an EMS is especially efficient for rapid measurement of aerosol particles with an unstable size spectrum.

According to the idealized theory of EMS, the charged aerosol particles move along precisely determined trajectories in the analyzer, and as a result of measurement one obtains a mobility distribution, or mobility spectrum, that exactly characterizes the concentration of the particles in the vicinity of a mobility Z . In practice, due to molecular and turbulent diffusion, the trajectories of the particles are scattered randomly. Thus the particles of many different mobilities hit the collector calculated for a definite mobility Z , and for that reason, the mobility spectrum gets smoothed. The degree of smoothing can be characterized by the resolution.

In our previous work, a simplified method for the estimation of the influence of particle Brownian diffusion on mobility resolution and performance of the long EMS was analytically investigated. We reported an increase in the inner electrode voltage resulting in an increase in the resolution of the mobility spectrometer. The resolution of the long EMS decreased with electrometer rings of lower numbers. Influence of Brownian diffusion on the resolution of the long EMS was significant for particles smaller than 100 nm, corresponding to the electrometer ring numbers lower than 10.

However, the effect of turbulent diffusion commonly is much greater and because of its complexity, its theoretical study is more intricate. In this presentation, we calculate EMS resolution values based on expected turbulence parameter data.

Methods

Description of the EMS

The long EMS had one long column of coaxial, cylindrical electrodes. The outer chassis consisted of a 481 mm long aluminum tube with an internal diameter of 55 mm. The inner electrode was made of a 25 mm in diameter stainless steel rod. The width of the aerosol inlet channel was 2 mm. There were two streams: charged particle and sheath air flow. The inner electrode of the spectrometer was maintained at a high DC voltage while the outer chassis of the spectrometer was grounded. The charged particles were collected on a series of electrically isolated electrometer rings positioned at the inner surface of the outer chassis of the spectrometer column. The inputs of highly sensitive electrometers were connected to these electrometer rings. These measured the currents corresponding to the number concentration of elementary charges in a given mobility fraction, which in turn was related to the particle size distribution. In this spectrometer, the 22 electrometer rings used resulted in the classification of aerosols into 22 mobility ranges. The electrometer rings had a width of 19 mm. The entire size range of particles collected on the electrometer rings could be varied by adjusting the aerosol and sheath airflow rates, the voltage applied to the inner electrode, and the operating pressure.

Modeling

For approximate estimations, consider a model of mobility classifier with parallel plain electrodes and a uniform gas flow. Such a simplified classifier model has a characteristic (limiting) mobility [7, 8]:

$$Z_c = \frac{ud^2}{VL}, \quad (\text{Eq.1})$$

where u is the gas flow velocity, d is the gap width between the electrodes, V is the central rod voltage, and L is the distance from aerosol inflow section to the corresponding electrometer ring (collector). Charged aerosol particles with a mobility of Z reach the electrometer ring with a characteristic or central mobility of Z_c , if $Z = Z_c$. The distance L determines a particular electrometer ring.

According to the theory proposed by Salm [8], the mobility resolution can be expressed as

$$R_d = \frac{Z_c}{\Delta Z_{\min}} = \frac{\sqrt{ud/D}}{2\sqrt{2}\sqrt{L/d + d/L}}, \quad (\text{Eq.2})$$

where ΔZ_{\min} is the least distinguishable interval of the mobility spectrum and D is the diffusion coefficient of charged particles.

If only molecular diffusion is considered, then the diffusion coefficient is expressed as:

$$D = \frac{kTZ}{n_p e}, \quad (\text{Eq.3})$$

where k is Boltzmann's constant, T is the absolute temperature n_p is the number of elementary charges per particle, and e is the elementary charge.

Taking into account Eq.1 and Eq.2, the mobility resolution can be expressed as

$$R_d = \frac{1}{2} \sqrt{\frac{n_p e V}{2kT(1+d^2/L^2)}}. \quad (\text{Eq.4})$$

On the average, the larger aerosol particle produces the larger charge number n_p . In general, the larger the aerosol particles, the higher voltage V is needed for their classification,. Thus Eq.4 shows that the larger the aerosol particles the higher the mobility resolution.

Molecular diffusion and turbulent diffusion share attributes. However, turbulent diffusion has two essential peculiarities. First, the coefficient of turbulent diffusion does not depend on the mobility of a particle. Therefore, Eq.3 and Eq.4 are not valid for turbulent diffusion. Second, in general the correlation between successive random displacements of a particle cannot be neglected.

In the case of small-scale turbulence ($\lambda \ll d$, where λ is the Eulerian length scale of turbulence), the coefficient of turbulent diffusion may be defined in its first approximation as:

$$D_T = u' \lambda, \quad (\text{Eq.5})$$

where u' is the root-mean-square pulsation velocity of gas flow.

Neglecting the evolution and the decay of turbulence in the classifier, the resolution R_d may be approximately estimated from Eq.2 when substituting D_T for D . The root-mean-square pulsation velocity u' inside the classifier depends on the intensity of turbulence of the inflowing gas and on the flow conditions in the classifier. Usually the pulsation velocity is roughly proportional to the average velocity u and considerably less than u . The turbulence intensity is calculated as u'/u . A turbulence intensity of 1% or less is generally considered low and turbulence intensities greater than 10% are considered high. If the EMS is operated in a still environment, a low turbulence intensity is expected. The turbulence length scale, λ , is a physical quantity related to the size of the large eddies that contain the energy in turbulent flow. In ducts or channels, λ is restricted by the size of the duct, since the turbulent eddies cannot be larger than the duct. In the classifier, it is rational to assume that usually $\lambda \ll d$. Homogeneity and isotropy of the flow field are also simplifying conditions.

Results and Discussion

The following are the numerical values of the model parameters that are in accordance with the real EMS described above: $d = 1.5$ cm, $V = 3000$ V, $u = 0.25$ ms $^{-1}$, $k = 1.38 \times 10^{-23}$ JK $^{-1}$, $e = 1.6 \times 10^{-19}$ C, $T = 294$ K.

For the electrometer ring No. 22, $L_{22} = 0.45$ m; Eq.1 yielded $Z_c = 4.17 \times 10^{-8}$ m 2 V $^{-1}$ s $^{-1}$, and Eq.2 yielded $R_{d,22} = \frac{0.0039}{\sqrt{D}}$. The resolution essentially depended on the diffusion coefficient of the particles. Supposing $n_p = 1$, Eq.3 gave $D = 1.05 \times 10^{-9}$ m 2 s $^{-1}$ for molecular diffusion. The resolution was $R_{d,22} = 120$.

For an example with low and small-scale turbulence in the classifier: e.g. the turbulence intensity was 1% and length scale $\lambda = d/15$, i.e. $u' = 0.0025$ ms $^{-1}$ and $\lambda = 0.001$ m. These numbers when substituted into Eq.5 yielded $D_T = 2.5 \times 10^{-6}$ m 2 s $^{-1}$ for turbulent diffusion, and the resolution for the electrometer ring No. 22 was $R_{d,22} = 2.5$. As Eq.2 showed, a relatively short, $L \approx d$, classifier is advisable for increasing the resolution.

CONCLUSION

The detailed description of the operating principle of the EMS for aerosol size distribution measurements was presented in this work. A simplified method for the estimation of the influence of turbulent diffusion on mobility resolution and performance of the EMS was analytically studied and discussed. The study demonstrated that the mobility resolution decreased considerably even with a low turbulence in the classifier. This information will be used in future experimental research to estimate the influence of turbulent diffusion on the mobility resolution of the EMS.

ACKNOWLEDGMENTS

The authors wish to express their gratitude to the National Electronic and Computer Technology Center, Thailand for their support (contract no. NT-B-22-SS-11-50-18). The Estonian Science Foundation through grants 8342 and 8779, and the Estonian Research Council Project SF0180043s08 also supported this research.

REFERENCES

- [1] Tammet, H.F.; Jakobson, A.F.; Salm, J. *Acta Comm. Univ. Tartu* 1973, **320**, 48-75.
- [2] Mirme A.; Noppel, M.; Peil, I.; Salm, J.; Tamm, E.; Tammet, H. In *11th Int. Conf. on Atmospheric Aerosols, Condensation and Ice Nuclei*, 2, Budapest, 1984, pp. 155-159.
- [3] Tammet, H.; Mirme, A.; Tamm, E. *Atmos. Res.* 2002, **62**, 315-324.
- [4] Intra, P.; Tippayawong, N. *Korean J. Chem. Eng.* 2009, **26**, 269-276.
- [5] Intra, P.; Tippayawong, N. *Korean J. Chem. Eng.* 2011, **28**, 279-286.
- [6] Intra, P.; Tippayawong, N. *Songklanakarin J. Sci. Technol.* 2008, **30**, 243-256.
- [7] Tammet, H. *The Aspiration Method for the Determination of Atmospheric Ion Spectra*, Israel Program for Scientific Translations, Jerusalem, 1970.
- [8] Salm, J. *Aerosol Sci. Technol.* 2000, **32**, 602-612.

Effects of Biodiesel and Engine Load on Nanoparticle Emissions from a Heavy-Duty Diesel Engine

Yi-Jyun Liou¹, Li-Hao Young¹, Man-Ting Cheng², Hsi-Hsien Yang³, Ying I. Tsai⁴ and Lin-Chi Wang⁵

1 Dept. of Occupational Safety and Health, China Medical University, Taichung, Taiwan

2 Dept. of Environmental Engineering, National Chung Hsing University, Taichung, Taiwan

3 Dept. of Environmental Engineering and Management, Chaoyang University of Technology, Taichung, Taiwan

4 Dept. of Environmental Engineering and Science, Chia Nan University of Pharmacy and Science, Tainan, Taiwan

5 Dept. of Chemical and Materials Engineering, Cheng Shiu University, Kaohsiung, Taiwan

ABSTRACT

Diesel engine exhaust contains large numbers of fine particles that degrade air quality and contribute to adverse human health effects. This study aims to characterize the changes of nanoparticle number emission characteristics from a heavy-duty diesel engine, operating with selected blends of low-sulfur biodiesel (B2_S50, B10, and B20) and engine loads (0%, 25%, 50%, 75%) under steady cycle. Raw exhaust were sampled with a rotating disc thermo-dilution system, followed by measurements of number size distributions of 10 – 1000 nm non-volatile particles using a scanning mobility particle sizer and condensation particle counter (SMPS) system. The results show that the particle number emission concentrations decrease with increasing blends of biodiesel from 2% to 20%, resulting in a particle number reduction of 35%. Increasing the engine load from 25% to 75%, on the other hand, resulted in a particle number increase of 64%. Among various loads, the highest particle number emission concentrations were observed when running on B2_S50 fuel under idle condition, with the presence of non-volatile nucleation mode particles. The number size distributions of non-volatile particles showed an increase of mode diameters when increasing engine load, whereas increasing blends of biodiesel resulted in a relatively small increase of mode diameters. Overall, the present results suggest the increase of biodiesel content in fuels resulted in a minor reduction of nanoparticle number concentration and small increases of particle mode diameters. The increase of engine load resulted in moderate increases of particle number concentration and moderate increases of particle mode diameters.

KEYWORDS

Diesel engine exhaust, Control technology, Number concentration, Size distribution

Introduction

Diesel engine has found widespread use in on-road vehicles and off-road equipments. However, its exhaust contains large numbers of fine particles that have been linked to a variety of adverse health effects^[1] and environmental impact^[2]. Heavy-duty diesel engines are of special interest because these vehicles contribute significantly to the on-road PM_{2.5} emission despite comprising only a small fraction of total vehicles. Most of the diesel particle mass is contributed by the accumulation particles (> 50 nm), whereas the vast majority of particle number is contributed by nanoparticles (< 50 nm). As mass-based particle emission standards have become increasingly stringent, growing attention is directed towards measurements of nanoparticle number concentration. Number-based method has shown of improved detection limit, accuracy, discrimination power, variability and reduced volatile artifacts over the conventional gravimetric method^[3].

The number size distribution of diesel engine particles is typically bimodal; a nucleation mode (< 30 nm) and an accumulation mode. The former arises from nucleation of H₂SO₄/H₂O or low-volatile organic compounds, whereas the latter comprises of soot formed in the engine. The occurrence, sizes and concentrations of the modes depend on engine type, speed, load, fuel type, aftertreatment devices and sampling conditions^[4]. As nucleation is nonlinear by nature, the variability of nucleation particle concentrations is considerably larger than that of accumulation particles. This gives rise to the measurements of non-volatile particles larger than 23 nm, i.e., soot particles, developed by the Particulate Measurement Programme (PMP) and currently adopted in the UNECE Regulation.

As part of a larger project that aims to develop low-cost and high-efficiency diesel exhaust aftertreatment devices, this study set out to characterize the dependency of non-volatile submicrometer particle number size distributions in raw exhaust on engine load and low-sulfur biodiesel. Laboratory experiments were conducted on a heavy-duty diesel engine with an engine dynamometer. The results serve as the baseline data needed to evaluate the reduction efficiencies of the aftertreatment devices under study.

Experimental Methods

The experiments were conducted on a 6-cylinder, 6 L, naturally aspirated, water-cooled, direct-injection diesel engine (Hino W06E). The engine was tested using three out of the 13 European Steady Cycle modes: mode 1 (Idle, 0% load), mode 3 (1800 rpm, 25% load) and mode 9 (1800 rpm, 50% load). The biodiesel fuels were prepared using low-sulfur (< 50 ppmw) biodiesel (B2) that is further blended with waste cooking oil to 10% (B10) and 20% (B20) biodiesel fuels.

Raw exhaust were directly sampled with a rotating disc thermo-dilution system (TDS), followed by measurements of number size distributions of 10-1000 nm non-volatile particles

using a scanning mobility particle sizer and condensation particle counter (SMPS) system^[5]. In the TDS, the raw exhaust was first diluted and then heated to 300 °C to remove volatile compounds. The SMPS was operated with a sample and sheath flow of 0.3 and 3 lpm, producing one average particle number size distribution every 3.5 min.

Results and Discussion

Effects of Engine Load

The average particle number emission concentrations under different engine loads are presented in Figure 1. Also included is the concentration difference with respect to 25 % load (baseline); idle condition was not used as the baseline because its particle emission characteristics are substantially different from other test conditions, discussed below. As shown, the measured number emission concentrations ranged from $3.0 \times 10^7 - 5.0 \times 10^7 \text{ cm}^{-3}$, which is 10^3 times higher than typical ambient particle number concentration. Under idle condition, the number emission concentrations were higher than that under 25% load but lower than 50% and 75% load. Beginning from 25% load, the number emission concentrations increase with increasing engine load; the concentration differences are in the range of 50-70%. This observed trend is consistent with earlier studies^[6,7].

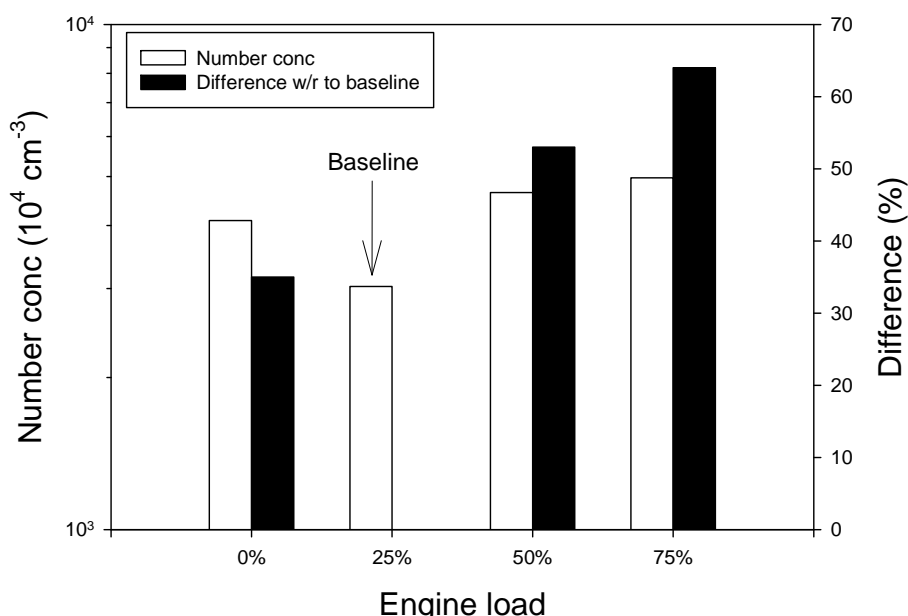


Figure 1. Average particle number emission concentrations under different engine loads.

The measured average particle number size distributions under different engine loads are shown in Figure 2. The size distributions under idle condition are bimodal and very different from other test conditions, showing a predominant nucleation mode of 14.5 nm and a substantially minor accumulation mode of ~70 nm. This shows the persistence of non-volatile nucleation mode particles after thermal treatment of 300 °C, contradicting to the notion that nucleation particles are completely volatile^[8]. Kittelson et al.^[6] suggested ash nuclei may form if the metal-to-carbon is sufficiently high, of which the metals come from metallic additives in the lubricant oil. Under higher engine loads, the size distributions were unimodal with a accumulation mode of diameter greater than 50 nm. In addition, the mode diameter increases with increasing engine load. As fuel injection increases with increasing engine load, it is suggested that more soot particles are produced as a result of diffusion combustion.

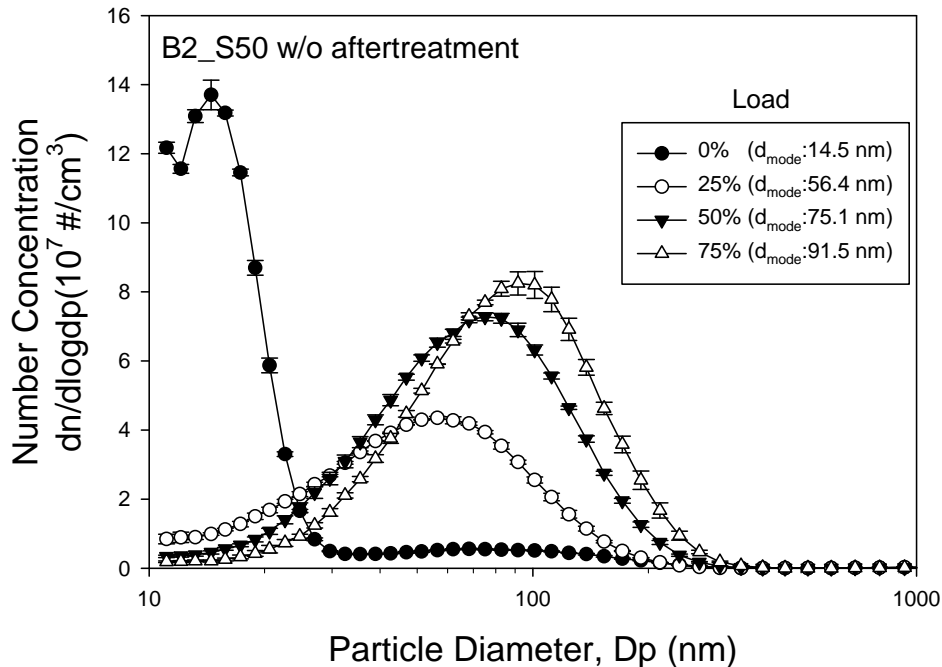


Figure 2. Average particle number size distributions under different engine loads.

Effects of Biodiesel

Figure 3 shows the weighted number size distributions with the engine running on different blends of biodiesel fuel. To focus on the effects of biodiesel fuels, data weighting was carried out with respect to the engine load (0%:25%:50% = 1.5:1:1), based on the weighting factors given in European Steady Cycle. As a result, the presented size distributions are all bimodal. As shown, the number emission concentrations decrease with increasing biodiesel content in the fuel. Using B2_S50 as the baseline, the reduction ranged from 21-40%. Meanwhile, the particle mode diameters increase with increasing biodiesel content in the fuel. This is in line with results reported in Kittelson^[4] but contradicts with a number of other studies^[9]. The observed disparities

between the presented results and earlier studies are likely due to the differences in sampling protocol. The major difference is the thermo-conditioning of diesel particles prior to measurements in the present study whereas most of the earlier studies did not. The removal of low-volatile compounds in the sample exhaust evidently would change the number size distributions; most likely a shift towards smaller particle sizes. More work is needed to examine these issues and their associated implications in human and environmental health.

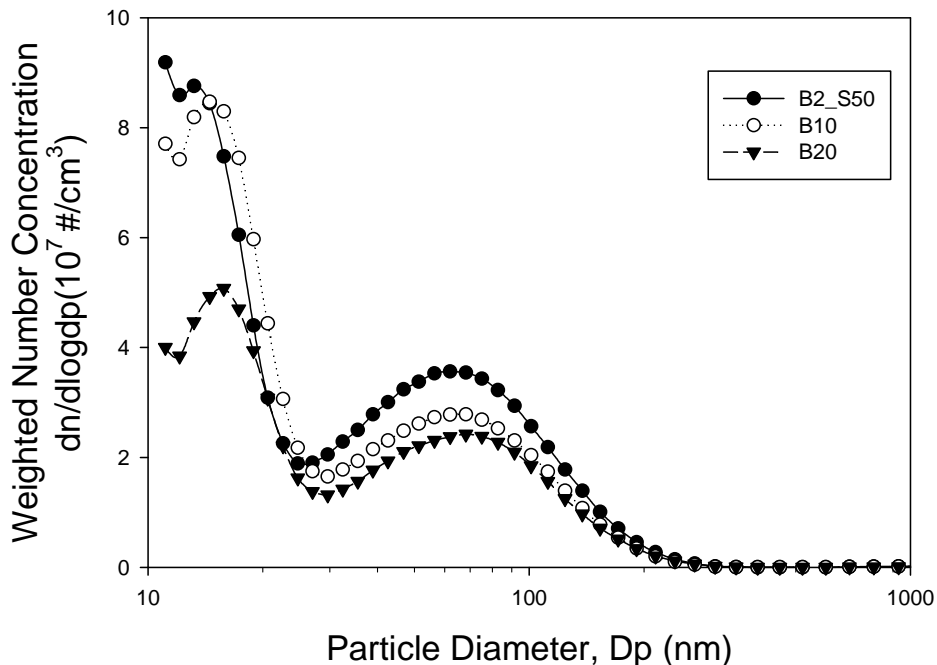


Figure 3. Weighted particle number size distributions with the engine running on different blends of biodiesel fuel.

SUMMARY

The present results show that the increase of biodiesel content in fuels resulted in a minor reduction of nanoparticle number concentration and small increases of particle mode diameters. The increase of engine load resulted in moderate increases of particle number concentration and moderate increases of particle mode diameters. High number concentrations of non-volatile nucleation mode particles were observed only under idle condition. More work is needed to elucidate the effects of condensable vapors on the number size distributions and their associated implications in human and environmental health.

ACKNOWLEDGMENTS

The financial and administrative support from the Taiwan EPA and NSC under the Contract# of NSC 98-EPA-M003-002 and NSC-99-EPA-M-002-002 are gratefully acknowledged.

REFERENCES

- [1] US EPA *Health assessment document for diesel engine exhaust*; National Center for Environmental Assessment, Office of Transportation and Air Quality: Washington, DC, 2002; EPA/600/R-90/057F.
- [2] Eldering, A., Cass, G.R. *J. Geophys. Res.* 1996, **101**, 19343-19369.
- [3] Andersson, J.; Giechaskiel, B.; Munoz-Bueno, R.; Dilara, P. *Particle Measurement Programme (PMP) Light-Duty Inter-Laboratory Correlation Exercise (ILCE LD)*; PMP Working Meeting; Final Report No. GRPE-PMP-18-2.
- [4] Kittelson, D.B. *J. Aerosol Sci.* 1998, **29**, 575-588.
- [5] Heim, M.; Kasper, G.; Reischl, G. P.; Gerhart, C. *Aerosol Sci. Technol.* 2004, **38**, 3-14.
- [6] Kittelson, D.B.; Watts, W.F.; Johnson, J.P. *J. Aerosol Sci.* 2006, **37**, 913-930.
- [7] Zhu, L.; Cheung, C.S.; Zhang, W.G.; Huang, Z. *Aerosol Sci. Technol.* 2010, **44**, 362-369.
- [8] Schneider, J.; Hock, N.; Weimer, S.; Borrmann, S. *Environ. Sci. Technol.* 2005, **39**, 6153-6161.
- [9] Di, Y.; Cheung, C.S.; Huang, Z. *Aerosol Sci. Technol.* 2009, **43**, 455-465.

Sand Emission Rate Study in Wind Tunnel by Particle Image Velocimetry

Xiaohui Lv¹, Lei Guo¹ and Ning Huang¹

1 Key Laboratory of Mechanics on Disaster and Environment in Western China, The Ministry of Education of China, Lanzhou, 730000

ABSTRACT

Sand emission rate is important parameter in study aeolian sand movement, wind erosion and dust prediction model. Wind tunnel experiments were carried out to measure the sand emission rate along the windstream by Particle Image Velocimetry. The results suggest that the sand emission rate exponential increase rapidly with increasing wind speed. We divide sand particle into two parts: one is upward movement sand grains; the other is downward movement sand grains. The numbers of these two kinds' particles exponential decrease with increasing height. Sand emission rate and sand fall rate increases with the fetch length.

KEYWORDS

Wind tunnel, Sand flow, Sand emission rate, Fetch length

Introduction

Sand flow is typical of gas-solid two-phase flow, is one of the important research contents of the physic of wind blow sand. Aeolian researchers have long realized the importance of understanding the movement process of blown particle, especially the sand (dust) emission rate. Sand emission rate means the number of sand grains that take off from bed per unit area and unit time. It consists of 3 portions: one part sand grains are entrained by wind flow directly; other parts sand grains are rebounded and splashed respectively after the saltation sands drop down to the surface by the act of gravity and impact the bed. The research of sand emission rate is limited by laboratory facilities. At present, the research of this problem is confined to numerical simulation in windblown sand flow. Anderson^[1] considering that sand grains is affected by gravity and fluid drag force in steady wind field. It is found that Sand emission rate is $8.75 \times 10^6 / (\text{m}^2/\text{s})$, while friction wind velocity is 0.5m/s. Schmidt et al.^[10] Found that saltation sand gravity and electrostatic force are in the same order of magnitude in windblown sand field. Hence, Huang et al.^[9]considering that sand grains is affected by gravity, fluid drag force and electrostatic force in unsteady wind field. It is found that Sand emission rate is $9.52 \times 10^6 / (\text{m}^2/\text{s})$, while friction wind velocity is 0.5m/s. Compared with linear relationship, the nonlinear relationship between sand emission rate and friction

wind velocity is more appropriate, brought up by He.^[8] and sand emission rate increase rapidly along with friction wind velocity. Sand emission models are even based on some simplifications in the simulation process of windblown sand which is not conform to actual situation. In addition, these results are not validated by experiment.

The fetch effect is an increase of the aeolian sediment transport rate with distance downwind over an erodible surface. The significance of the fetch effect has been explored in relation to desert dunes, the initial formation of dunes formation^[2], wind erosion^{[6][7][13]}, snowdrift^[14] and Aeolian transport of sand from beaches to coastal dunes^[4]. Under ideal state the number of grains within the saltating cloud increases exponentially to a maximum condition. This maximum condition reflects saturation of the system where sand movement carries all the vertical momentum flux of the wind and when the transport rate becomes independent of distance. Bagnold^[3] noted that the sand flux needs 9m to attain equilibrium. Shao and Raupach^[11] found that their 17m long wind tunnel did not observe the final equilibrium state of transport with high wind velocities. Dong et al^[5] found that as wind speed increases more grains travel at a greater height and further downwind with the distance required to achieve equilibrium also increasing. Andreotti et al.^[2] found that direct and indirect measurements agree that the saturation length is almost independent of the wind strength.

The development of Particle Image Velocimetry (PIV) helps to improve the measurement of particle velocity. This technique is non-intrusive experiment method and widespread used in other field and wind blow sand^[15]. This paper used this technique to measure the velocity field of the sand particles in saltating cloud. Based on sand particle location and velocity, we could be obtained the sand emission rate.

Experimental Methods

We performed our experiments in wind tunnel at the Key Laboratory of Mechanics on Disaster and Environment in Western China, the Ministry of Education of China. The blow-type non-circulating wind tunnel has a total length of 55m, with a 20m long test section. The cross-sectional area of the test section is 1.3m×1.45m. The free-stream wind velocity in the wind tunnel can be adjusted from 4 to 40m/s.

The sand used for the test was typical dune sand from the Minqin, southeast of the Badain Jaran Desert of China. The mean diameter was 332.65μm. Prepared sand samples were put in a 15m long, 1.3m wide and 0.15m deep sand bed. The length of sand bed chosen ensured a significant development of the saltating cloud.

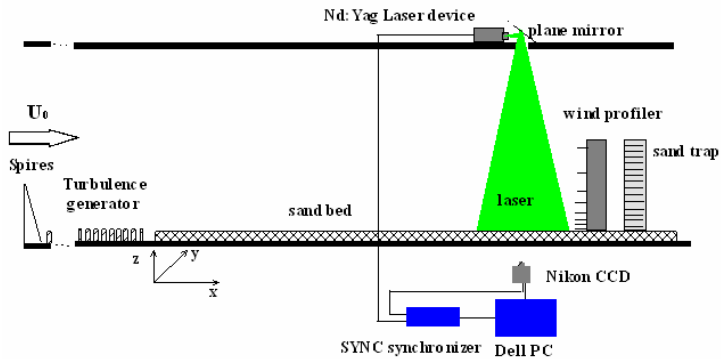


Figure 1. Layout of the test

The main purpose of the experiments was to measure the mean number of sand particle through the 4mm height from the sand bed by statistics the location and velocity of sand. Those velocities were measured by PIV. In PIV, the velocity vectors are derived from sub-sections of the target area of the particle-seeded flow by measuring the movement of particles between two light pulses. For more details of the measurement principle, refer to Stanislas et al.^[12]. In the experiment, the CCD camera was set 0.65m from the light sheet, resulting in a target area of about 213mm wide \times 160mm high (The image size was 1600 pixels wide \times 1200 pixels high with an amplification factor of 0.133). The image acquisition rate was set at 15 frames per second. The final particle number represented the average over 20s, so the final particle number was the average over 150 samples. Wind speeds were measured by a windprofiler at the different height behind the light sheet. Sand mass flux was measured by sand trap to compare the results of PIV (Fig 1.).

Results and Discussion

In experiment, we measured the wind speed profile without sand at 5 wind speed(8, 9, 10, 11, 12m/s). Figure 2 show the measured wind speed profile of the clean wind. The wind profile defined as:

$$u(z) = \frac{u_*}{\kappa} \ln\left(\frac{z}{z_0}\right) \quad (\text{Eq.1})$$

where $u(z)$ is the wind speed at the height z ; κ is von Karman's constant, equal to 0.4; z_0 is aerodynamic roughness length, u_* is shear velocity, defined as:

$$u_* = \sqrt{\tau / \rho} \quad (\text{Eq.2})$$

where τ is surface shear stress, ρ is air density.

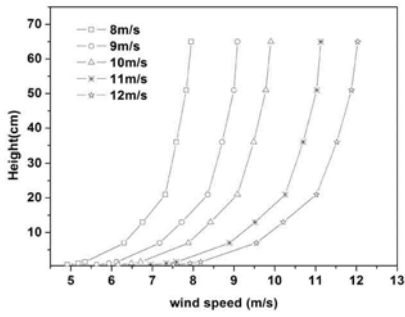


Figure 2. Wind speed profiles over beds without sand grains.

Confirmation method

At present, most of experiments used sand trap measured sand flow profiles that reflect the grains trajectory relation to grains velocity and angles. When we know the grains location and velocity, determined the sand profiles by statistics to sand particle numbers thorough cross section at unit time. According to this method, we compared PIV result to sand trap's experimental result in Figure 6. Fig. 6 shows a good correlation between the PIV and sand trap. This demonstrated that our statistics method to sand grains is viable.

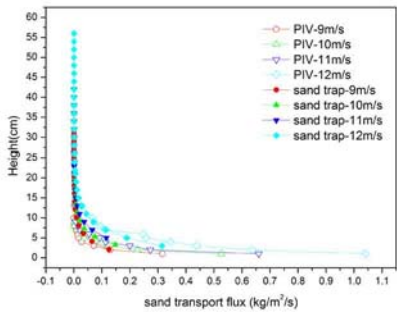


Figure 3. Comparison of PIV and sand trap result at different wind speed

Sand emission rate

Based on the analysis of the sand flow vertical profiles is viable, we used similar statistics method to analysis the sand emission rate. We selected 4mm height from the sand surface as statistics on the height of sand emission rate. Fig 5 shows that the sand emission rate increase with wind speed. He^[14] note that sand emission rate and shear velocity is nonlinear relationship. We used Origin 7.5 to fit the wind speed and sand emission rate in quadratic polynomial (eq.3), $R^2=0.9988$. When we took the parameters into the equation 3, found that sand emission rate exist minimal value between 8m/s and 9m/s, wind speed equals to 8.8m/s. This phenomenon is not according with nature discipline. So, we used exponential function to fit the data (eq. 4), $R^2=0.9987$.

$$N_e = A + BU + CU^2 \quad (\text{Eq.3})$$

$$N_e = D \exp(E + FU) \quad (\text{Eq.4})$$

where N_e is sand emission rate, in m^2/s ; U is axis wind speed, in m/s ; A, B,C,D,E,F are fitting parameters.

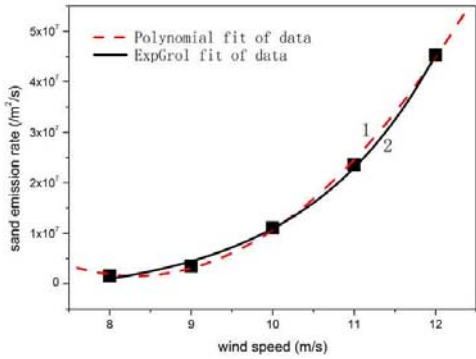


Figure 4. Sand emission rate increase with wind speed

We statistics the downward sand grains number (sand fall rate) at the same height of upward sand grains number (sand emission rate) (Fig. 4). Fig. 4 shows the sand emission rate more than sand fall rate at different wind speed. This meaning that upward sand grain lager than the impacting sand grain, the sand flow was also in developing, did not reach the saturation state. The sand fall rate also increase with wind speed.

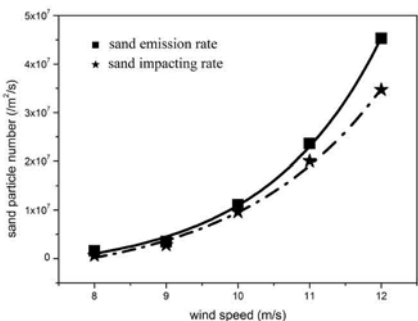


Figure 5. Sand fall rate and sand emission rate increase with wind speed

Fetch length on the sand emission rate

Dong et al.^[5] propose sand mass flux increase with wind velocity based on wind experiment, the expression is:

$$Q = C(I - U_t/U)U^3(\rho/g) \quad (\text{Eq.5})$$

where Q is the sand mass flux, in $\text{g cm}^{-1}\text{s}^{-1}$, U is the wind speed, in cm s^{-1} , U_t is the threshold speed measured at the same height as U , 620 cm s^{-1} , ρ is the density of air, 0.00125 g/cm^3 , g is the acceleration due to gravity, 981 cm/s^2 , and C is a proportionality coefficient that varies with the fetch length. C can be expressed by:

$$C = 0.000306L^{2/3} \quad (\text{Eq.6})$$

where L is fetch length. If took the eq.7 into the eq.6, we can change the eq.6 to:

$$Q=0.000306L^{2/3}(1-U_t/U)U^3(\rho/g) \quad (\text{Eq.7})$$

Eq.(8) implies that the mass flux increases with the fetch as a power function, but the rate of increase becomes less as the fetch length increase.

Wind blowing sand, wind erosion and dust prediction model often limited the sand (dust) emission rate and wind speed relationship, less result involved sand (dust) emission rate variation along the fetch length or used the mass flux refutations the dust emission rate. Less field results touchon dust emission rate and its variation with fetch length. So, we

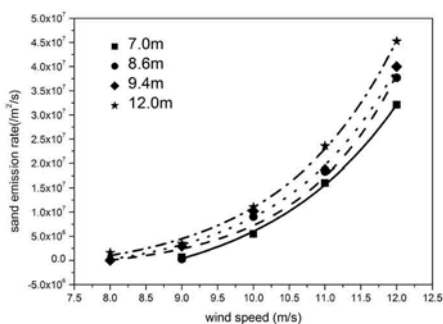


Figure 6. Variation of sand emission rate with fetch length at different wind speed

took experiments to measure the sand emission rate variation along the fetch length, behind the roughness element 7.0, 8.6, 9.4 and 12.0m (Fig 12, 13). Fig. 12 shows sand emission rate vary with fetch length at different wind speed. From Fig.12, we can know that sand emission rate fit the exponential function with wind speed at different; at the same wind speed, sand emission rate increase with fetch length. From the Fig. 13, the impacting sand as sand fall rate similar to sand emission rate and fetch length relationship. Sand fall rate increase with fetch length at different wind speed.

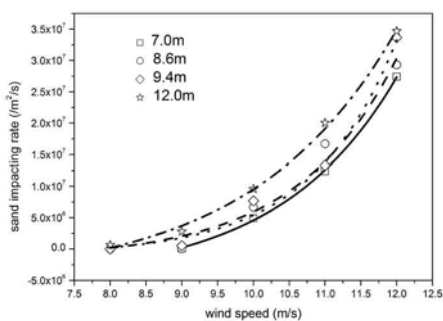


Figure 7. Variation of sand fall rate with fetch length at different wind speed

CONCLUSION

We measured the sand emission rate and its variation with fetch length in a wind tunnel by

Particle Image Velocimetry. This paper gets the following aspects of conclusions:

1. Sand emission rate and sand fall rate increase with wind speed with exponential function
2. Sand emission rate which is not only related with wind speed, but also with fetch length, increase with fetch length. So does sand fall rate.

REFERENCES

- [1] Anderson, R.S; Haff, P.K. *Acta Mechanica*, 1991, (Suppl.) 1, 21-51.
- [2] Andreotti, B.; Claudin, P.; Pouliquen, O. *Geomorphology*, 2010, 123, 343-348
- [3] Bagnold, R. A. Methuen, London, 1941.
- [4] Delgado-Fernandez, I. *Aeolian Research*, 2010, 2, 61-70.
- [5] Dong, Z.B.; Wang, H. T.; Liu, X.P. *Geomorphology*, 2004, 57:117-127.
- [6] Fryrear, D.W.; Saleh, A. *Solid Science*, 1996, 161, 398-404.
- [7] Gillette, D. A.; Herbert, G. *Earth surface Procession and Landform*, 1996, 21:641-659.
- [8] He, L.H. Ph.D. Thesis, Lanzhou University, 73-75.
- [9] Huang, N.; Zheng, X.J. *Chinese Journal of Theoretical and Applied Mechanics*, 2006, 38, 146-152.
- [10] Schmidt, D.S.; Schmidt, A.S.; Dent, J.D. *Journal of Geophysical Research*, 1998, 103, 8997-9001.
- [11] Shao, Y. P.; Raupach, M.R. *Journal of Geophysical Research*, 1992, 97, 20559-20564.
- [12] Stanislas, M.; Kompenhas, J.; Westerweel, J. Kluwer Academic Publishers, Dordrecht. The Netherland. 2000.
- [13] Stout, J.E. *Trans. Am. Soc. Agric. Eng.*, 1990, 33, 1597- 1600
- [14] Takeuchi, T. *Journal of Glaciology*, 1980, 26, 481-492.
- [15] Yang, P.; Dong, Z.B.; Qian, G.Q. *Geomorphology*, 2007, 89, 320-334.

Wind Tunnel Study on Aeolian Farmland Soil Movement

Ning Huang¹ and Lei Guo²

¹Key Laboratory of Mechanics on Disaster and Environment in western China, Ministry of Education, Department of Mechanics, Lanzhou University, Lanzhou, China ,730000

²Key Laboratory of Mechanics on Disaster and Environment in western China, Ministry of Education, Department of Mechanics, Lanzhou University, Lanzhou, China ,730000

ABSTRACT

A new experimental method was used for studying the dust emission. In the wind tunnel of Lanzhou University, the experiment of aeolian farmland soil movement was made by using the particle image velocimetry system (PIV). The farmland soil particles contain discrete soil grain (dust) and aggregate of soil. The variation of dust emission, the grain size of dust emission, the vertical number flux of soil aggregates and the grain size of the soil aggregates vertical flux with wind friction velocity is obtained. Dust emission increases with wind friction velocity and is the same with field results in magnitude. The velocity of soil particles is obtained, which increases somewhat with friction velocity.

KEYWORDS

Wind tunnel, Dust emission, Farmland soil, PIV

Introduction

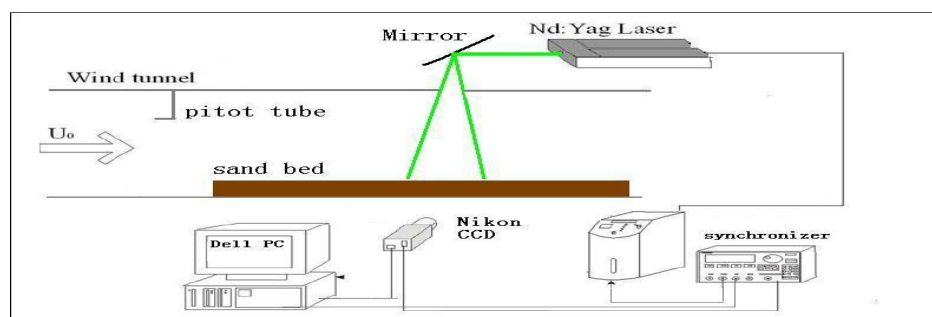
Dust storm is a global weather disaster that occurred and was launched in the desert and its surrounding areas [1]. Since 1920s many scholars had begun to research the spatial and temporal distribution, causes, structure, monitoring and countermeasures of dust storm [2-6]. The fallow cropping field near the desert is one of the major source of dust storm. Dust emission is the important input term for models of predicting dust storm [7]. Gillette assume the coefficient of exchange for dust equal to the eddy viscosity, dust emission rate was derived from the concentration of dust in the air [8]. Then with this indirect method, a lot of

field observations had been made and dust emission rate was obtained in the desert and its surrounding areas [9-11]. Unfortunately, so far there is no effective method to directly measure dust emission rate. In recent years, with the continuous development of optical technology PIV technology has been introduced into the study of windblown sand movements, and some progress has been made. Its advantage is that the instantaneous, contactless measurement of whole field can be achieved [12, 13]. In this study, we improved the resolution of the CCD camera by close-up lens, so dust grain can be captured. Dust emission rate and the velocity of soil grain are directly measured by wind tunnel experiments using PIV. We expanded the methods of studying dust emission, and the direct measurement of dust emission come true.

Experimental Conditions and Methods

This experiment is made in multi-functional environment wind tunnel where is affiliated with Key Laboratory of Mechanics on Disaster and Environment in western China, Ministry of Education in Lanzhou University. This wind tunnel can provide continuously adjustable DC blowing type wind, which is equipped with 20-meters-functional interval with 1.3m width and 1.45m height, wind speed ranged from 4 to 40m/s. We can simulate flow around atmosphere boundary layer in ground spires and roughness elements conditions. The soil of arable land abandoned around Badan Jaran Desert is chosen to do the laying of bed. New Wave Co. Mini-YAG laser with max 120mJ capacity, frequency 15Hz, being able to emit 532nm wavelength single light, TSI Co. 10-30 CCD camera with image grabbing card for capture pictures, all of these are required. We utilize the synchronizer as control between laser and CCD camera for making those equipment work. Experimental instrument arrangement is shown in Fig. 1:

Figure 1: Experimental instrument arrangement



The PIV system captures 14 and a half couples/pair of pictures consisted of Frame A and Frame B. In 5 different wind speed conditions, we would obtain 70 pairs of 2D instantaneous images showing wind-sand flow motion. By analyzing any one pair of images, we can obtain soil particles coordinates X_1, Y_1 in Frame A and X_2, Y_2 in Frame B. We assume a horizontal plane 5mm from bed surface, whose coordinate is Y_0 . If $Y_1 < Y_0, Y_2 > Y_0$, we can regard the soil particle as transiting the plane. We can note quantity of the soil particle, N . Dust emission rate, Q , is:

$$Q = q \times \frac{4}{3} \pi R^3 \times \rho \quad q = \frac{N}{L \times D \times \Delta T} \quad (\text{Eq.1})$$

where L is the width of computational field in photos, D is the thickness of laser, T is the time interval of one pair of photos, R is the sand particle radius, ρ is the density of soil grain=2650kg/m³, q is the rate of dust emission number. Otherwise we obtain the grain size of soil particle via analyzing photos. For the sake of reliability of experimental results, 200 pairs of photos are analyzed for taking the average number.

Results and Discussion

Dust emission rate of the farmland soil from the fallow cropping field near the desert was obtained, which increases and has a nonlinear relationship with wind friction velocity (Fig.2), and is the same with field results in magnitude[14, 15]. To further analyze the grain size of dust emission, we found that the average grain size of dust emission is almost unchanged with wind friction velocity(Fig.3).

Figure 2: Dust emission rate with wind friction velocity

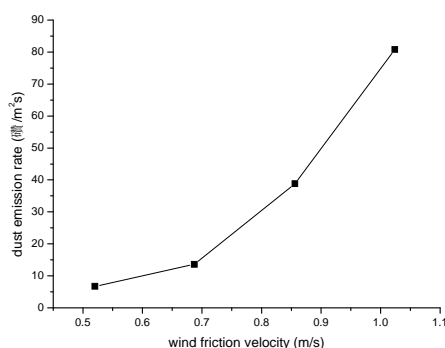
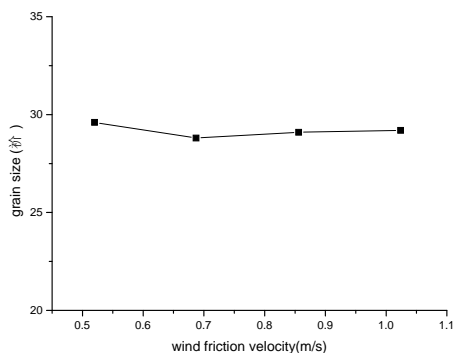
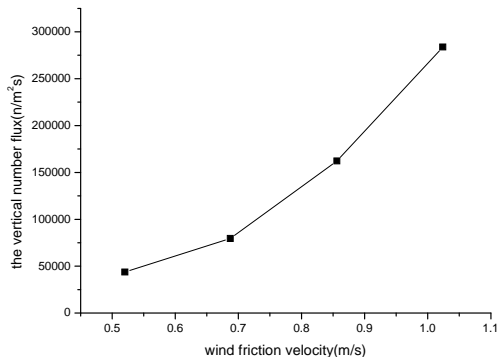


Figure 3: the average grain size of dust emission with wind friction velocity



Most of soil of the fallow cropping field exists in the form of aggregate of soil. After a small amount of dust at the surface was blown away, as the sandblasting theory stating[16], saltation of aggregate of soil dominate the process of dust emission. Dust emission rate is related with the strength of saltation of soil aggregates. And the grain size of dust emission is related with the kinetic energy of the saltating soil aggregates, showing that the larger the kinetic energy of the saltating soil aggregates, the larger the proportion of very fine particles in the flux of particles released by the sandblasting process[17]. Dust emission and saltation of soil aggregates exist simultaneously, which we captured with the camera together. The vertical number flux of soil aggregates increases and has a nonlinear relationship with wind friction velocity(Fig.4). After wind-blown particle movement has stabilized, the number of particle lifting off and falling down are approximative. It was derived that the shocks of the saltating soil aggregates and the strength of saltation are increasing. This directly reflects that the dust emission rate increase is closely related with the strength of saltation of soil aggregates.

Figure 4: The vertical number flux of soil aggregates with wind friction velocity



The grain size of the soil aggregates vertical flux increases a little (Fig.5), and the impact velocity of soil aggregates increases somewhat with friction velocity (Fig.6). This shows that the kinetic energy of the saltating soil aggregates also changes very small. Our findings suggest that the average grain size of dust emission will be almost unchanged with wind friction velocity if the kinetic energy of saltating soil aggregates has smaller change. This is similar to some field results. The size distribution of dust released by wind erosion will not change, with Little change in wind friction velocity of wind erosion events. For the greater wind friction velocity of wind erosion events, the proportion of very fine particles in the flux of particles released by the sandblasting process will increase [17].

Figure 5: The grain size of the soil aggregates vertical flux with wind friction velocity

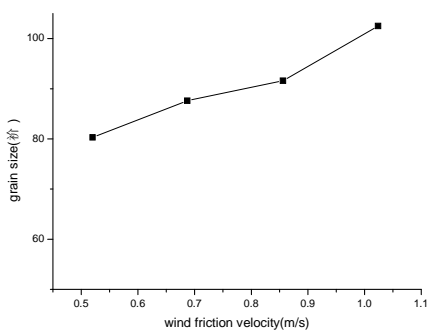
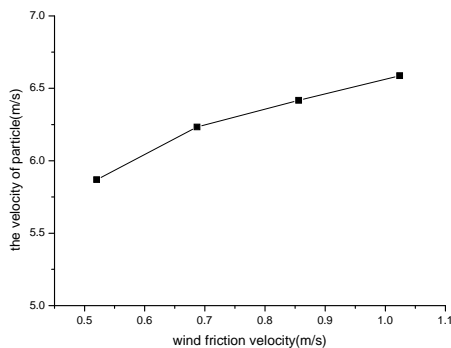


Figure 6: the impact velocity of soil aggregates with wind friction velocity



CONCLUSION

Dust emission are directly measured by wind tunnel experiments using PIV, which increases and has a nonlinear relationship with wind friction velocity and is the same with field results in magnitude[14, 15]. It is directly reflected that the dust emission rate increase is closely related with the strength of saltation of soil aggregates. The average grain size of dust emission will be almost unchanged with wind friction velocity if the kinetic energy of saltating soil aggregates has smaller change. This is in good qualitative agreement with the field results previously [17]. We expanded the methods of studying dust emission, and the direct measurement of dust emission come true. How to better apply this method will be the subject of our future work.

REFERENCES

- [1] Zheng, X.J. *Mechanics of Wind-Blown Sand Movements*; Springer, Berlin, Germany, 2009.
- [2] Hankin, E.H. *India Met Memoirs* 1921, 22:past VI.
- [3] Idso, S.B.; Ingram, S.; Pritchard, J.M. *Bull AMS* 1972, 53:930-935.
- [4] Joseph, P.V.; Raipal, D.K.; Deka, S.N. *Mausam* 1980, 31:431-442.
- [5] Ott, S.T.; Ott, A. *Mon. Wea. Rev.* 1991, 119(8):1832-1850.
- [6] Prospero, J.M.; Ginoux, P.; Torres, O.; Nicholson, S.E. and Gill, T.E. *Rev. Geophys.* 40(1), 1002, doi:10.1029/2000RG000,095, 2002.
- [7] Gillette, D.A.; Gill, T.E.; Ley, T.; etc. *J. Geophys. Res.* 1997, 102(D22): 26009-26015.
- [8] Gillette, D.A.; Blifford, I.H. and Fenster, C.R. *J. Appl. Meteorol.* 1972, 11: 977-987.

- [9] Gillette, D.A. *Spec. Pap. Geol. Soc. Am.* 1981, 86:11–26.
- [10]Nickling, W.G.; Houser, C.A. *Sedimentology* 2001, 48: 255-267.
- [11]Rojo, L.; Gill, T.E. and Gillette, D.A. *X-Ray Spectrom.* 2008, 37:111-115.
- [12]Qian, G.Q.; Dong, Z.B.; Luo, W.Y., etc. *JOURNAL OF DESERT RESEARCH* 2009, 29(1):10-17.
- [13]Lee, S.J.; Kim, H.B. *Wind Eng Ind. Aerodyn* 1999, 80:311-326.
- [14]Gillies, J.A.; Nickling, W.G. and Mctainsh, G.H. *Atmospheric Environment* 1996, 30(7):1081-1090.
- [15]Cheng, T.t.; Lv, D.r. and Xu, Y.f. *PLATEAU METEOROLOGY* 2006, 25(2):236-241.
- [16]Shao, Y.P.; Raupach, M.R.; Findlater, P.A. *J. Geophys. Res.* 1993, 98(D7): 12719-12726.
- [17]Sow, M.; Alfaro, S.C.; Rajot, J.L., etc. *Atmos. Chem. Phys. Discuss.* 2009, 9: 5549–5581.

Environmental Benefit to Enhance the Dust Filtration in a Subway Ventilation Chamber

Huang shan¹, Hyun Hee Lim¹, Ju Yeol Lee² and Young Min Jo¹

1 Department of Environmental Engineering, Kyung Hee University, South Korea, 446-701

2 Anytech Co.Ltd, South Korea

ABSTRACT

Air quality of underground railway is of critical interests in Seoul, Korea. National government has emphasized the stringent management of IAQ of metro-subway. In order to satisfy the legislative standard and public needs, air purification must be much more enhanced with the addition of high quality control facilities. Thus, this work focused on the review of cost effectiveness for replacing fine dust filters. The inflow amount of PM10 and PM2.5 into the test ventilation chamber in which deals with the air, 900 CMM, was 19.4 kg/yr and 8.9 kg/yr respectively. It corresponds to US \$ 5,857 for PM 10 and US \$ 6,608 for PM2.5 based on the environmental cost evaluation. The current filtration system collects approximately 55% of the inlet PM10 and 35% of PM2.5. Even if it obeys the National IAQ regulation for platforms and ticket rooms, civic groups strongly insist better quality of air inside. Thus, additional facilities to improve the air filtration up to 80% of PM10 and 55% of PM2.5 would cost US\$ 8,756 per year. However, the increase of environmental benefit on the atmospheric dust will in part compensate the cost.

KEYWORDS

Air ventilation, Subway IAQ, Filtration, Electret filter, Environmental benefit

Introduction

The air quality of public indoor space has been of great interest in Korea. In particular, metro-subway lines that millions people have used every day have to maintain a high standard IAQ. Recently installed modern screen doors for safety do not contribute to enhance the environmental condition. This study attempted to evaluate the cost effectiveness and environmental values, so that a model from EU was utilized in this work.

Experimental Methods

1 Field test

Real time analysis of fine dust was carried out with a particle counter procured from

Grimm(Germany, Portable Aerosol Spectrometer 1.108. The field test has been fulfilled for 85 days since 8th of september, 2010. As seen in Fig. 1, pressure drop across each filter was red on-line by three digital manometers. Average flow velocity was evaluated by measuring across the filter surface.

2. Evaluation of cost and benefit

Weight of inflow dust into the chamber was estimated by measurement of each concentration for PM2,5 and PM10 respectively. Social cost was evaluated by the following equation:

$$\text{Environmental cost} = \text{social cost of individual air pollutants} \times \text{emission amount} \quad (1)$$

Capital cost and running cost were received from the office of Metro-subway, and additional facility was also considered for final cost evaluation. Running cost includes fresh filters, labor charge for periodic replacement and disposal cost for used filters.

Results and Discussion

1. Inflow fine dust to ventilation chamber

Fig. 1 is concentration profiles for 85 days in a ventilation chamber. External air quality directly affects the inlet dust concentration for both PM10 and PM2.5. The average PM10 concentration during the test term was $43.7 \mu\text{g}/\text{m}^3$ slightly below than the average of Metro-area($47 \mu\text{g}/\text{m}^3$). The average of PM2.5 was, as for reference, $20 \mu\text{g}/\text{m}^3$. The air flow rate entering the chamber has maintained at approximately $900 \text{ m}^3/\text{min}$.

Except unexpected harsh episodes of yellow dust and extremely cold weather, it has operated for 342 days in 2010. It resulted in the annual inflow air volume of $44,323 \times 10^4 \text{ m}^3$. Thus the fed PM10 and PM2.5 were 19.4 kg and 8.9 kg last year respectively.

2. Renovation of ventilation chamber

The MVAC was designed for optimal treatment of inflow dust. The present filter is a flat panel type with a pre-filter grade. Such a low level filter indicates a critical decrease of collection efficiency at the initial time for first 3 to 5 days after replacement as shown in Fig. 3.

Collection efficiency reached at the maximum, about 80%, right before replacement. However, pressure resistance also rose subject to the dust collection. Thus, it is a main purpose to install a low resistance with high efficiency filter behind the conventional pre-filter. The additional filter is a type of electret filter and pleated to provide large filtration area (40 m^2) and low pressure drop. It could capture the penetrated dust particles through the front pre-filter.

Fig 4. shows a certain amount of increase in dust collection efficiency throughout the size. Although pressure drop was higher comparing to a single layer of pre-filter in early times, it did not increase as much as the pre-filter with accumulation of dust particles inside. Conversely the combined layer would be more effective as crossing the areal mass collection of $0.6 \text{ kg}/\text{m}^2$.

3. Assessment of cost and benefit

Table 1 is the estimated amount of dust collection for each filtration lay-out. At present, the pre-filter has been replaced twice a month, which costs US \$ 252 every time, so that the annual cost becomes US \$ 6,048. Meanwhile, the actual expense for a rear filter lay-out was US \$ 6,000 for the first test installation. This filter can be replaced every three month, and each costs US \$ 450. In the long run, the new combined filtration lay-out costs approximately US \$ 8,756 per year including filter disposal, labor charge and the equipment depreciation cost for 20 years. According to the human health effects and national environmental standard, the social cost was found to be US \$ 300 for PM10 and US \$ 742 for PM2.5. Table 2 shows that the social payment due to fine dust in indoor air of subway would be US \$ 5,857 for PM10 and US \$ 6,608 for PM2.5 unless filtration. The newly proposed filter lay-out greatly reduces its cost down to US \$ 1,171 for PM10 and US \$ 2,973 for PM2.5. Nevertheless, the effect of benefit achieved from the investment of the filtration facilities could be 54% for PM10, which is somewhat lower than the conventional system(58%).

Table 1. Estimation of dust amount collected by test filters (kg/yr)

Filter lay-out	PM10	PM2.5
Pre - filter	9.68	3.09
Combined filter	15.5	7.1

Table 2. Social cost and benefit rate due to fine dust (US \$)

Filter \ Dust	PM10	PM2.5
W/O filter	5857	6608
Pre - filter	2635 (58%)	4295 (41%)
Pre-filter + Electret filter	1171 (54%)	2973 (41%)

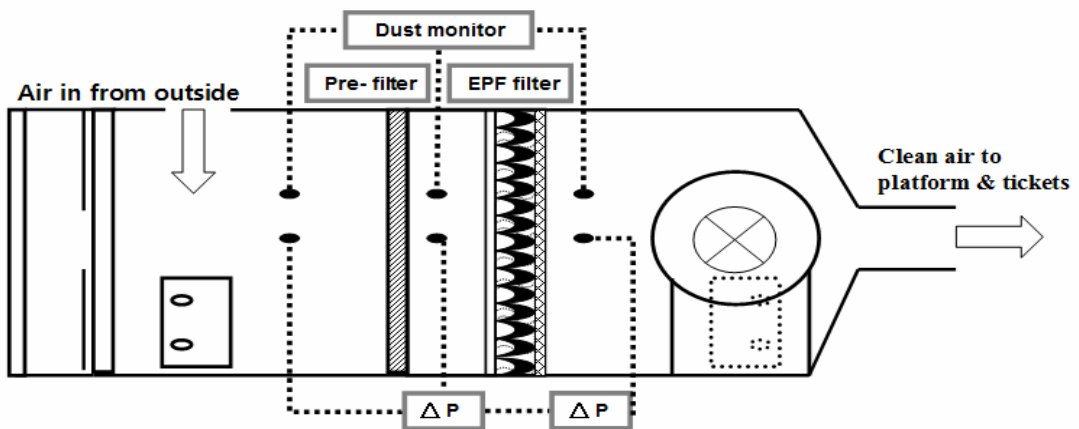


Fig. 1. Filter lay-out in a ventilation chamber.

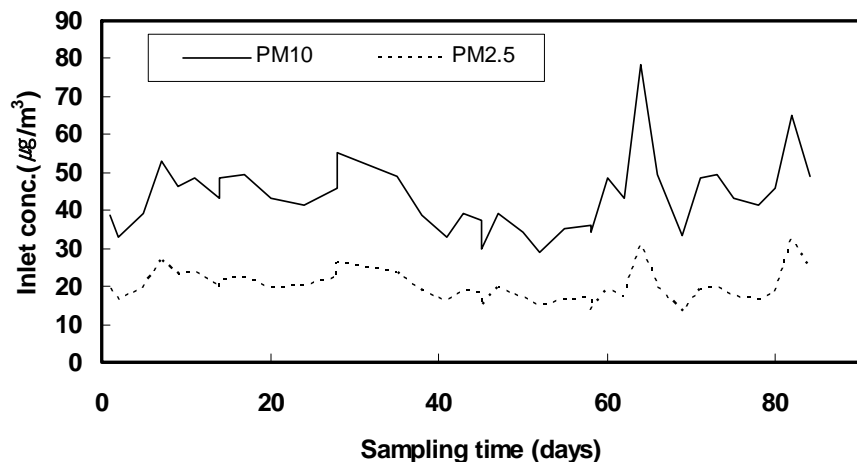


Fig. 2. Inlet concentration of fine dust to test MVAC.

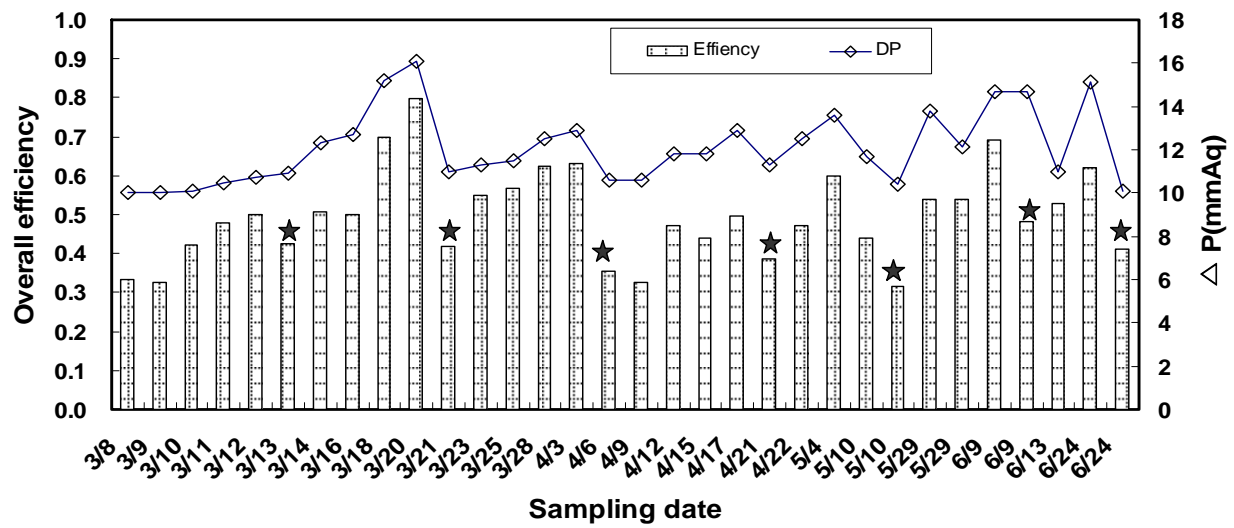


Fig 3. Long term filtration test in field MVAC.

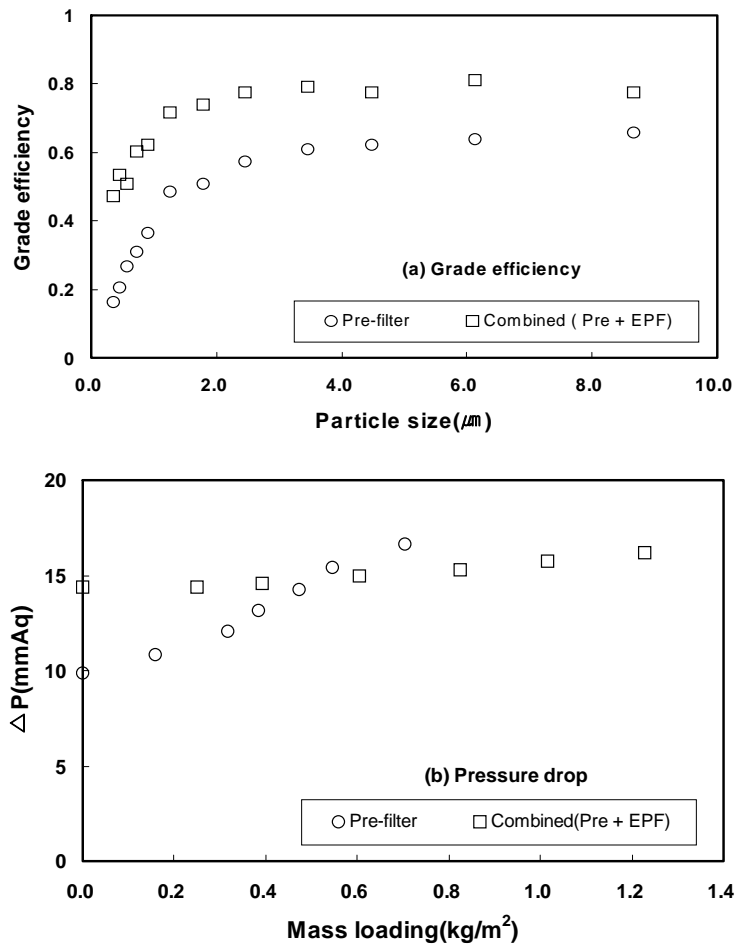


Fig. 4. Dust collection and pressure drop across the filtration unit.

ACKNOWLEDGMENT

This research was supported by Seoul R&BD Program (CS070160).

REFERENCES

- [1] Kang Gwang Gyu, The economical efficiency valuation about the capital area air quality improvement special counter plan, 2003
- [2] Kim Jin Kyoung, Paik Nam Won. A study on characteristics of Airborne Dust in Seoul Subway stations. Kor. J. Env. Hlth. Vol. 30. No. 2, 2004: 154~160
- [3] Eom Young Sook. Valuing Health Effects of Air Pollution ; An Application of the Averting Behavior Method. Kor. J. Env Vol 7. No 2, 1998: 1~23
- [4] Cho Yongsung, Sonn YangHoon. Estimation of the Health Benefits for Improving Air Quality. Kaae. Vol 6 No. 1, 2004
- [5] Ministry Environment, The cost-benefit analysis guide book of the environmental policy. Annual report of EPA, 2003

Field observation of the hygroscopic properties of the ambient aerosols in Beijing

Jian-hua Chen¹, Xuan Wang¹, Wenjie Zhang¹, Jianmin Chen², Xingnan Ye², Hongjie Liu¹, Wen Yang¹, Wei Wang¹ and Jianguo Deng¹

1 Chinese Research Academy of Environmental Sciences, Beijing 100012, China

2 Department of Environmental Science & Engineering, FUDAN University, Shanghai 200433, China

Principal Contact: Jian-hua Chen, Professor, Chinese Research Academy of Environmental Sciences, Beijing 100012.

Tel: 8610-84934330 Fax: 8610-84934330 E-mail: chenjh@craes.org.cn

Abstract

The hygroscopic properties of aerosols have significant effects on the climate change and human health. The hygroscopicity of ambient aerosols was conducted during December 8-20, 2009 in Beijing, and the influencing factors were also discussed. It was found that the aerosol hygroscopic growth factors were between 1.01 and 1.4 in winter in Beijing, with the property of weak hygroscopicity and nearly hydrophobic characteristics. The major influencing factors included aerosol size distribution, the air pollution situation, different sources such as vehicle exhausts, meteorological conditions and so on. The aerosol growth factors in accumulation mode were higher than those in atiken mode. With the API gradually falling down during monitoring, the environmental aerosol growth factors declined also. For those days with good atmospheric stability, the aerosol hygroscopic growth factors showed a bimodal variation, i.e. two peaks at noon and midnight and two valleys in the morning and evening. While, for those days with poor atmospheric stability, the aerosol growth factors showed a single-peak variation, i.e. a peak at midnight and a valley at noon. In addition, aerosol components with weak hygroscopicity were predominant for “peak” growth factors, and those with nearly hydrophobic characteristics were predominant for “valley” growth factors. The result in Beijing in this work supplied the necessary scientific basis for the atmospheric hygroscopic characteristics and related radiative forcing and climate changes.

Keywords: field observation, hygroscopic properties, aerosols, Beijing.

Unsteady SO₂ Absorption by a Moving Water Aerosol with Chemical Dissociation

Ke-Miao Lu¹, Wei-Hsin Chen², Yuan-Yi Chen³, Chen-I Hung³, Wen-Jhy Lee¹ and Ta-Chang Lin¹

1 Department of Environmental Engineering, National Cheng Kung University, Tainan, Taiwan, ROC, 701

2 Department of Greenergy, National University of Tainan, Tainan, Taiwan, ROC, 700

3 Department of Mechanical Engineering, National Cheng Kung University, Tainan, Taiwan, ROC, 701

ABSTRACT

Transient chemical absorption dynamics of sulfur dioxide by a water aerosol droplet at three Reynolds numbers of 0.643, 1.287 and 12.87 are predicted. In this study, a sinusoidal velocity distribution at the droplet surface is assumed to approach the flow field inside the droplet and a single-phase simulation method (SPSM) is developed to compare with the two-phase simulation method (TPSM). Considering the physical SO₂ absorption processes with internal circulation, the predictions based the SPSM are very close to those of the TPSM, revealing that the SPSM is a proper method to evaluate the mass transport phenomena for SO₂ uptake by an aerosol droplet. When chemical reactions in the course of absorption are taken into account using the SPSM, it is noteworthy that the transient absorption process is almost independent of the Reynolds number. This arises from that fact that the entire mass transfer process is controlled by mass diffusion and dominated by the dissociation of sulfurous acid (SO₂·H₂O). It is also found that the chemical absorption period is elongated markedly compared to the physical absorption process, approximately by the factors of 5.6-13.1. Eventually, an analysis on the characteristic times of various transport processes is performed to elucidate mass transport mechanisms and the reasonability of the SPSM developed in this study.

KEYWORDS

Droplet and aerosol; Sulfur dioxide (SO₂) uptake; Transient chemical absorption; Reynolds number; Mass diffusion number; Drop mass transport number.

Introduction

The mass transfer of SO₂ and other trace gases into droplets is a fundamental behavior in the atmosphere and environmental engineering, the modeling and simulation of the mass transfer

between the two phases have received a great deal of attention in recognizing and predicting the mass transport phenomena in the environment^{[1][2]}. For example, in the earlier study of LeClair et al.^[3], they theoretically developed a model to describe the flow patterns outside and inside a convecting droplet; but the mass transfer was not considered in their research. Chen^{[4][5]} developed a two-phase simulation method to predict physical SO₂ uptake by a single droplet and raindrops. By solving heat and mass transfer equations, Elperin et al.^[6] focused their attention on the conjugate problem of non-isothermal physical absorption of tracer gases by raindrops with internal circulation to aid in describing the scavenging behavior in the atmosphere.

Most of the research emphasized on the physical absorption processes and the effect of chemical dissociation in the aqueous phase was usually disregarded^{[4][5][6]}. In some studies^{[7][8][9][10]} the reactions of chemical dissociation have been taken into account. Unfortunately, detailed transport dynamics of SO₂ uptake in association with internal circulation were absent, that is, the information concerning the effect of chemical reactions on the absorption processes in a convecting water aerosol remains insufficient. For this reason, one of the purposes of the present study is to investigate SO₂ absorption by a moving water droplet with chemical dissociation reactions. Meanwhile, the model proposed by LeClair et al.^[3] will be utilized to predict the momentum and mass transport phenomena. With the aforementioned model, the conjugate problem (i.e. the two-phase phenomena) can be simplified through the use of a single-phase simulation method (SPSM). The predicted results based on the SPSM will be compared with the results of Chen^[4] where a two-phase simulation method (TPSM) has been developed. In particular, attention of this study will be paid to the effect of the ionization on the absorption processes so that one is able to recognize the discrepancy between the physical absorption and the chemical absorption.

Mathematical Formulation

Governing equations

In a previous study^[11] a mass diffusion number were conducted to elucidate the ratio of interfacial concentration gradient of a solute between the gas phase and the liquid phase. It was reported that the mass diffusion number of SO₂ is fairly small ($=4.011 \times 10^{-3}$), implying that the concentration of SO₂ is nearly uniform in the gas phase. It is thus reasonable to ignore the gaseous SO₂ concentration gradient. Accordingly, the governing equations of the investigated system consist of the aqueous continuity, momentum (Navier-Stokes) and species conservation equations. These equations are expressed as follows.

Continuity equation:

$$\frac{\partial \rho}{\partial t} + \nabla \cdot (\rho \vec{V}) = 0 \quad (\text{Eq.1})$$

Momentum equations:

$$\frac{\partial}{\partial t} (\rho \vec{V}) + \nabla \cdot (\rho \vec{V} \vec{V}) = -\nabla p + \nabla \cdot [\mu (\nabla \vec{V} + (\nabla \vec{V})^T)] \quad (\text{Eq.2})$$

Species equations:

$$\frac{\partial C_i}{\partial t} + \nabla \cdot (\vec{V} C_i) = \nabla \cdot (D_i \nabla C_i) + R_i \quad (\text{Eq.3})$$

In the species equations, the subscript i designates $\text{SO}_2 \cdot \text{H}_2\text{O}$, HSO_3^- , SO_3^{2-} or H^+ . The reaction source term (viz. R_i) is related to the aqueous ionization of $\text{SO}_2 \cdot \text{H}_2\text{O}_{(\text{aq})}$ and $\text{HSO}_3^-_{(\text{aq})}$ and these chemical reactions are reversible. i.e 1.

Initial and boundary conditions

The initial conditions corresponding to the sudden exposure of a water aerosol droplet into a uniform flow are

$$u = v = C_{\text{SO}_2 \cdot \text{H}_2\text{O}} = C_{\text{HSO}_3^-} = C_{\text{SO}_3^{2-}} = 0, \quad C_{\text{H}^+} = C_{\text{OH}^-} = 10^{-7} M \quad (\text{Eq.4})$$

As far as the boundary conditions, they are expressed as

Droplet surface:

$$C_{\text{SO}_2 \cdot \text{H}_2\text{O}} = H_{\text{SO}_2} P_{\text{SO}_2} \quad (\text{Eq.5})$$

$$V_\theta = \frac{1}{2} \frac{\mu_g}{\mu_l} U_\infty \sin \theta \quad (\text{Eq.6})$$

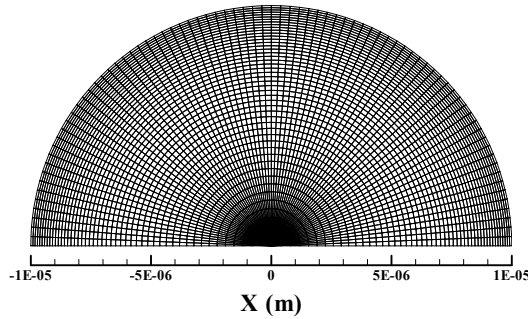
Axis of symmetry:

$$v = \frac{\partial u}{\partial r} = \frac{\partial p}{\partial r} = \frac{\partial C_i}{\partial r} = 0 \quad (\text{Eq.7})$$

Numerical method

To solve the governing equations in association with the initial and boundary conditions, the governing equations were discretized into the algebraic counterparts based on the finite-volume method^[12]. Then, the SIMPLE algorithm was employed to solve the flow field. In the course of calculation, the first order upwind scheme was used for evaluating the convective and diffusive fluxes over control volume surface. An orthogonal grid system was constructed to perform the simulations. On account of severe variations of velocity and concentration in the vicinity of droplet surface, the grid distribution was controlled to be finer nearby. Three different grid systems of 25×41 , 49×81 and 63×105 have been tested for grid independence. The grid system of 49×81 was adopted for simulations, as shown in Fig. 1.

Figures 1. The adopted orthogonal grid system (49×81).



Results and Discussion

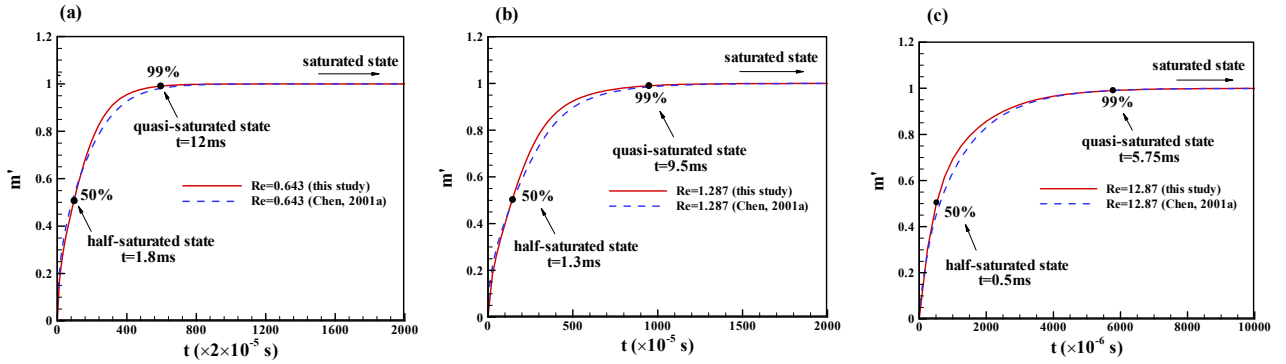
A water aerosol droplet with the radius of 10 μm in the atmosphere absorbing gaseous sulfur dioxide at 25°C (298K) serves as the basis of the present study. The concentration of sulfur dioxide in the atmosphere is 0.1ppm^[13]. In the meantime, three Reynolds numbers in terms of droplet diameter, gaseous density and viscosity are taken into account; they are 0.643, 1.287 and 12.87. Corresponding to the preceding values, the relative velocities between the droplet and its surrounding are 0.5, 1 and 10 m s⁻¹, respectively. Detailed values of fluid properties, aqueous mass diffusivity, Henry's law constant, mean droplet surface velocity and Reynolds number are listed in Table 1.

Table 1. Values of fluid properties, aqueous mass diffusivity, Henry's law constant, mean droplet surface velocity and Reynolds number in terms of gas properties^{[4][8][14]}.

Denotation	ρ_g (kg m ⁻³)	ρ_l (kg m ⁻³)	μ_g (Pa s)	μ_l (Pa s)	D_l (m ² s ⁻¹)	H (M atm ⁻¹)		
Value	1.184	997	1.84×10 ⁻⁵	8.91×10 ⁻⁴	1.8×10 ⁻⁹	1.26		
r_s (μm)		U_∞ (m s ⁻¹)		\bar{V}_θ (m s ⁻¹)		$\text{Re}_g = \frac{2\rho_g U_\infty r_s}{\mu_g}$		
10	0.5			0.00405		0.643		
	1			0.00806		1.287		
	10			0.0808		12.87		

The velocities at the droplet surface based on the model of LeClair^[3] are first compared with the numerical results of Chen^[4]. For the Reynolds numbers of 0.643 and 1.287, the velocity distributions from LeClair's model are relatively close to the numerical results of Chen^[4]. As a matter of fact, the model of LeClair was developed based on the situation of creeping flow. Because the flow fields with the Reynolds numbers of 0.643 and 1.287 behave as a creeping flow in nature, it is not surprising that the velocity distributions between the two different methods are close to each other. When the Reynolds number is 12.87, the difference in velocity distribution is somewhat amplified, especially at the front-half portion (i.e. $\theta < 90^\circ$) of the droplet surface. This arises from the fact that the gaseous streamlines near the droplet surface departs from symmetry to a certain extent, as a consequence of the difficulty in pressure recovery at the aft regions of the droplet.

Next, the interest of the study is on the physical SO₂ absorption processes by the droplet and to validate the accuracy of the SPSM. As a whole, as shown in Fig. 2, the predicted results based on the SPSM are consistent with those based on the TPSM, regardless of what the Reynolds number is. This indicates that the mass transport processes in the droplet can be predicted well by the SPSM, even though the gas phase transport processes are ignored. This is attributed to the solute SO₂ being characterized by a small mass diffusion number^[11]. When the Reynolds number is 0.643, the half-saturated time (HST) and the quasi-saturated time (QST) are 1.8 and 12 ms, respectively (Fig. 2a). HST is defined as the moment when SO₂ accumulated inside a droplet reaches 50% of the saturated amount, whereas QST is identified as the time for the droplet absorbing SO₂ reaches 99% of the saturated amount. When the Reynolds number is increased, the strength of the internal circulation is enhanced, that is, more SO₂ absorbed from the interface is transported into the interior of the droplet via internal circulation. This renders that SO₂·H₂O diffusion has a trend to move from the circular streamlines toward the vortex center. As a result, the HST and the QST at Re=1.287 are 1.3 and 9.5 ms, respectively. The higher the Reynolds number, the faster the internal vortex motion. This is the reason that, when the Reynolds number is 12.87, the HST and the QST are further reduced to 0.5 and 5.75 ms, respectively.



Figures 2. Comparisons of time variation of physical SO_2 uptake by the droplet at the Reynolds numbers of (a) 0.643, (b) 1.287 and (c) 12.87.

CONCLUSION

The coupling behavior of fluid dynamic, mass diffusion and chemical dissociation for SO_2 absorbed by a convecting droplet has been modeled successfully and investigated numerically. With the assumption of sinusoidal velocity distribution at the droplet surface, it enables us to predict the absorption process by developing a single-phase simulation method (SPSM). Considering the three Reynolds numbers of 0.643, 1.287 and 12.87, the results indicate that the physical absorption processes predicted based on the SPSM are close to those based on the two-phase simulation method (TPSM), resulting from the mass transfer of SO_2 characterized by a low mass diffusion number. When dissociation reactions inside the droplet are taken into account, it is found that the production of $\text{SO}_2 \cdot \text{H}_2\text{O}$ has a great trend to dissociate. It is thus realized that the formation of HSO_3^- is the dominant mechanism in determining the SO_2 uptake behavior.

Furthermore, in view of the pronounced impact of HSO_3^- formation on the absorption process, it is of interest to observe that the chemical absorption process is almost independent of the Reynolds number. Eventually, an analysis on the characteristic times of various transport processes is performed to evaluate the developed SPSM. As a whole, the characteristic time of mass diffusion is much larger than the others. Therefore, the assumptions adopted in this study are reasonable. In summary, on account of the controlling mechanism of mass diffusion and a large amount of HSO_3^- accumulated inside the droplet, this leads to the elongation of the entire absorption process. A comparison suggests that time required for the droplet reaching the quasi-steady state with ionization is larger than the physical absorption by the factors of 5.6-13.1.

ACKNOWLEDGMENTS

The authors gratefully acknowledge the financial support of the National Science Council, Taiwan, ROC, on this study.

REFERENCES

- [1] Saboni, A., Alexandrova, S., 2001. Sulfur dioxide absorption and desorption by water drops. *Chemical Engineering Journal* 84, 577-580.
- [2] Alexandrova, S., Marion, M., Lepinasse, E., Saboni, A., 2004. Mass Transfer Modeling of SO₂ into Large Water Drops. *Chemical Engineering Technology* 27, 676-680.
- [3] LeClair, B.P., Hamielec, A.E., 1972. A theoretical and experimental study of the internal circulation in water drops falling at terminal velocity in air. *Journal of the Atmospheric Sciences* 29, 728-740.
- [4] Chen, W.H., 2001a. Unsteady absorption of sulfur dioxide by an atmospheric water droplet with internal circulation. *Atmospheric Environment* 35, 2375-2393.
- [5] Chen, W.H., 2001b. Dynamics of sulfur dioxide absorption in a raindrop falling at terminal velocity. *Atmospheric Environment* 35, 4777-4790.
- [6] Elperin, T., Fominykh, A., Krasovitov, B., 2010. Scavenging of soluble gases by falling rain drops in inhomogeneous atmosphere. *Atmospheric Environment* 44, 2133-2139.
- [7] Baboolal, L.B., Pruppacher, H.R., Topalian, J.H., 1980. A sensitivity study of a theoretical model of SO₂ scavenging by water drops in air. *Journal of the Atmospheric Sciences* 38, 856-870.
- [8] Schwartz, S.E., Freiberg, J.E., 1981. Mass-transport limitation to the rate of reaction of gases in liquid droplets: application to oxidation of SO₂ in aqueous solutions. *Atmospheric Environment* 15 (7), 1129-1144.
- [9] Schwartz, S.E., Freiberg, J.E., 1981. Oxidation of SO₂ in aqueous droplets: mass-transport limitation in laboratory studies and the ambient atmosphere. *Atmospheric Environment* 15 (7), 1145-1154.
- [10] Elperin, T., Fominykh, A., Krasovitov, B., 2008. Scavenging of soluble gases by evaporating and growing cloud droplets in the presence of aqueous-phase dissociation reaction. *Atmospheric Environment* 42, 3076-3086.
- [11] Chen, W.H., 2002. An analysis of gas absorption by a liquid aerosol in a stationary environment. *Atmospheric Environment* 36, 3671-3683.
- [12] Patankar, S.V., 1980. Numerical Heat Transfer and Fluid Flow. Hemisphere, Washington, D.C.
- [13] Seinfeld, J.H., 1986. Atmospheric Chemistry and Physics of Air Pollution. Wiley, New York, pp. 202-204.
- [14] Mott, R.L., 1994. Applied Fluid Mechanics, 4th Edition. Prentice-Hall, NJ.

Long-range transport of aerosols to the central Tibet, China, a case study using ground and satellite remote sensing data

Xiangao Xia¹

1 Institute of Atmospheric Physics, Chinese Academy of Sciences, Beijing, China, 100029

Principal Contact: Xiangao Xia, Dr., Institute of Atmospheric Physics, Chinese Academy of Sciences, Beijing, 100029, China.

Tel: 010-82995071 Fax: 010-82995073 E-mail: xxa@mail.iap.ac.cn

Abstract

Using ground-based sunphotometer and satellite remote sensing of aerosol optical properties, a case of long-range transport of aerosols from India and South Asia to the central Tibetan during March 2009 is presented. Remarkable increase of aerosol optical depth at 500 nm during March 2009 from the background level to more than 0.4 is evidenced by sunphotometer observations at Nam Co, an AERONET station located in the central Tibetan Plateau. Angstrom exponent and single scattering albedo indicate that fine model particle dominates during this period. Satellite remote sensing observations including CAPLISO, MODIS, OMI suggest long-range transport of biomass burning aerosols in South Asia to the central Tibet, which is supported by back trajectory analysis. Long-range transport of aerosols to the Tibet and its potential climatic and environmental effects need further study.

Keywords: Aerosol, Tibet, Long range transport, Climate

An Experiment on Energy Reduction of an Exhaust Air Heat Recovery Type Outdoor Air Conditioning System for Semiconductor Manufacturing Clean Rooms

Kyung-Hoon Yoo¹, Gen-Soo Song¹, Hyung-Tae Kim¹, Seung-Woo Son² and Dug-Jun Park³

1 Nanoscale Contamination Control Laboratory, Korea Institute of Industrial Technology (KITECH), 1271-18, Sa-1-dong, Ansan-si, 426-171, Gyeonggi-do, South Korea

2 Sunglim PS Co., 1301, Namseong Plaza, 345-30, Gasan-dong, Geumcheon-gu, Seoul, 153-802

3 Shinsung ENG Co., 404-1, Baekhyeon-dong, Bundang-gu, Seongnam-si, 463-420

ABSTRACT

In recent semiconductor manufacturing clean rooms, the energy consumption of an outdoor air conditioning system represents about 45 % of the total air conditioning load required to maintain a clean room environment. Meanwhile, there is a large amount of exhaust air from a clean room. From an energy conservation point of view, heat recovery from the exhaust air is therefore useful for reducing the outdoor air conditioning load for a clean room. In the present work, an energy-efficient outdoor air conditioning system was proposed to reduce the outdoor air conditioning load by utilizing an air washer to recover heat from the exhaust air. The proposed outdoor air conditioning system consisted mainly of a pre-heater, an air washer, two stage cooling coils, a reheating coil, a humidifier and two heat recovery cooling coils inserted into the air washer and connected to a wet scrubber. It was shown from the lab-scale experiment with outdoor air flow of 1,000 m³/h that the proposed system was more energy-efficient for the summer and winter operations than an outdoor air conditioning system with a simple air washer.

KEYWORDS

Semiconductor Manufacturing Clean Room, Outdoor Air Conditioning System, Air Washer, Heat Recovery, Energy Reduction

Introduction

For recent semiconductor manufacturing clean rooms, the energy consumption of an outdoor air conditioning (hereafter OAC) system represents about 45 % of the total air conditioning load required to maintain a clean room environment^[1,2]. In addition, there is a large quantity of exhaust air from a clean room, leading to the consequent large amount of waste heat. From an energy saving point of view, heat recovery from the exhaust air is therefore helpful for reducing

the outdoor air conditioning load for a clean room. Recently, air washers have been sometimes used in OAC systems for semiconductor manufacturing clean rooms to control humidity and simultaneously remove suspended dusts and gaseous contaminants such as NH₃, SO_x, NO_x and organic gases in incoming outdoor air, as shown in Figure 1. Meanwhile, since the exhaust air carries chemically toxic gaseous matter, a wet scrubber has to be used to handle it before it is discharged to the atmosphere. In the wet scrubber the heat transfer between the exhaust air and the scrubbing water always takes place. The transferred heat deserves utilizing to heat or cool the incoming outdoor air, which needs to be contacted indirectly with the scrubbing water because of protection from contamination

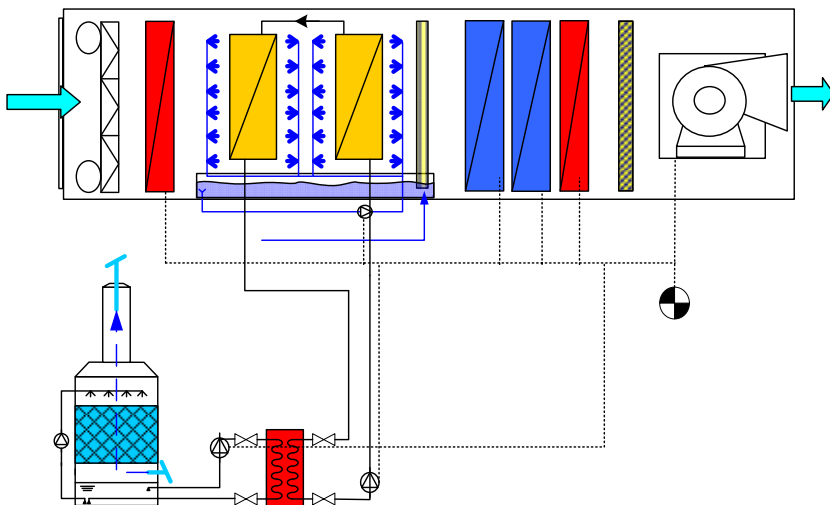


Figure 2. Schematic diagram of the proposed energy efficient outdoor air conditioning system with an air washer of heat recovery function.

Pre-heater

Air washer

Eliminator

Reheating coil

So far only a few studies regarding the air washer with the heat recovery function for semiconductor clean rooms have been conducted by Fujisawa et al.^[3,4], Shiroma et al.^[5] and Yamamoto et al.^[6]. None of the above mentioned publications seems to have been described sufficiently in detail to allow the understanding of the overall energy consumption and saving performance of the OAC system. They focused only on heat recovery equipment, not on the OAC system itself. Therefore the effect of air conditioning process constraints such as supply air condition and the combination with heating/cooling coils on the energy saving performance of an energy-efficient OAC system design needs to be taken into account. In the present work, an energy-efficient OAC system is proposed to reduce the outdoor air conditioning load by utilizing the air washer with heat recovery function based on the previous work by Fujisawa et al.^[3]

Wet Scrubber

al.^[3,4] and Yamamoto et al.^[6]. The proposed OAC system consisted mainly of air filters, a pre-heater, an air washer, two stage cooling coils, a reheating coil, a humidifier, and two heat recovery cooling coils inserted into the air washer and connected to a wet scrubber, as shown in Figure 2. An experiment was carried out on the lab-scale with an air flow of 1000 m³/h regarding energy consumption and saving of the proposed energy-efficient OAC system compared with the OAC system with a simple air washer shown in Figure 1.

Experimental Methods

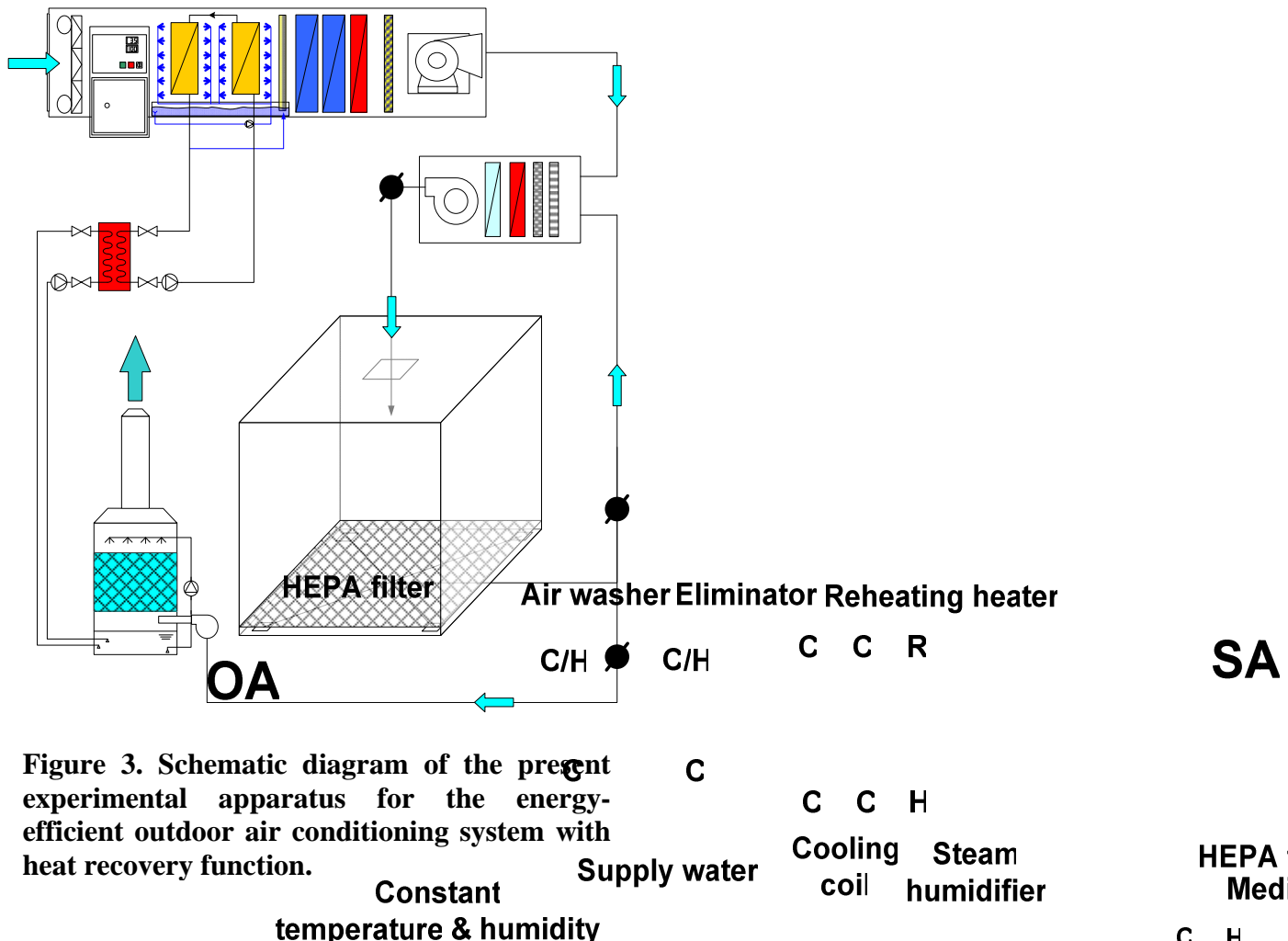


Figure 3. Schematic diagram of the present experimental apparatus for the energy-efficient outdoor air conditioning system with heat recovery function.

Figure 3 shows the schematic diagram of the overall experimental apparatus for the proposed energy-efficient OAC system to evaluate the energy consumption and saving performance. The experimental apparatus for the simple air washer OAC system with no heat recovery consisted of a clean wind tunnel, a HEPA filter, a constant temperature and humidity chamber, an air washer,

Primary pump Secondary pump

an eliminator, two stage cooling coils, a reheating electric heater, a humidifier and a fan. As for the experimental apparatus for the energy-efficient OAC system with heat recovery function a wet scrubber, an intermediate heat exchanger, primary and secondary water pumps, two cooling/heating coils in the air washer and a small clean room as shown in Figure 3 were added to that of the above mentioned simple air washer OAC system. Table 1 shows the experimental condition of the present energy-efficient OAC system with heat recovery function.

The air washer was installed in the clean wind tunnel with the cross section of $0.33 \times 0.33 \text{ m}^2$, and had 2 modules comprised of 4 banks of 48 nozzles. The present nozzles with outer diameter of 1/8 in sprayed city water with 0.7 MPa in both of the counter- and co-current directions simultaneously. For the energy-efficient OAC system a cooling coil was additively inserted in the middle of air washer module in order to recover waste heat through the intermediate heat exchanger from the exhaust air in the wet scrubber and use it to heat or cool the incoming outdoor air, as shown in Figure 3. As for the reheating coil and steam humidifier an electric heater and an electrode-type steam humidifier were used respectively instead of a fossil fuel boiler to unify the measurement into electric power. The electric power sensors were installed to measure the electric power consumption, as shown in Figure 1 and 2. ALMEMO MA5990-2 data logger and sensors were installed to measure temperature and relative humidity in the wind tunnel. The temperature and humidity sensor was installed at the each outlet of the constant temperature and humidity chamber, the air washer, the cooling coil, the reheating heater and the humidifier to investigate the air conditioning process and recovered heat of the OAC system on a psychrometric chart.

Table 1 Experimental condition of the present exhaust air heat recovery type OAC system.

Air flow rate and average velocity	1000 m^3/h , 2.5 m/s
Outdoor Air condition	Winter: -18°C , 70.4 %RH Summer: 38°C , 50 %RH Midterm: 22°C , 55 %RH
Supply air condition	12°C , 90 %RH
Exhaust air condition	23°C , 45 %RH
Class of spraying water for air washer	City water
Total flow of spraying water	8 ℓ/min
Number of nozzles in air washer	48
L/G, gravimetric ratio of water to air	0.4
Flow of water for heat recovery heat exchanger	40 ℓ/min

Results and Discussion

Figure 4 shows the experimental results of the psychrometric process for the simple air washer OAC system and the energy-efficient OAC system for the winter operation shown in Table 1. Because the two OAC systems have the same upstream conditions, the constant temperature and humidity chamber shown in Figure 3 created the inlet condition of air washer, 16.5°C , 9 %RH, as shown in Figure 4. It can be seen in Figure 4 that the energy-efficient OAC system recovered specific enthalpy 3 kJ/kg from the exhaust air. The corresponding recovered heat is 1.01 kW for

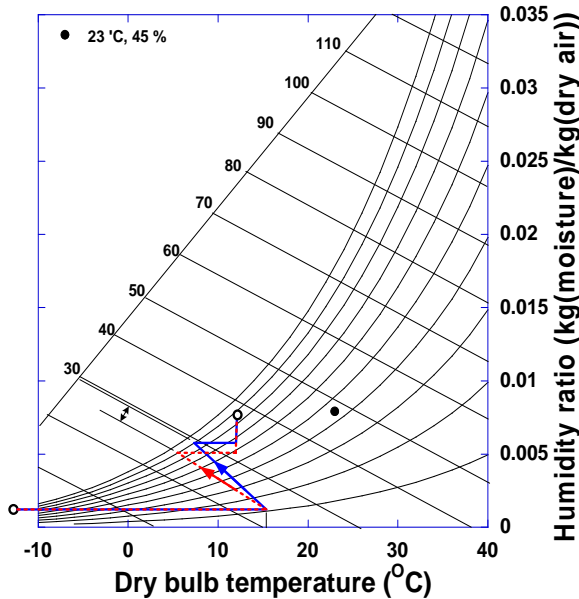


Figure 4. Variation of the air conditioning process on psychrometric chart by heat recovery for the winter operation.

$1000 \text{ m}^3/\text{h}$.

Figure 5 shows the experimental results of the psychrometric process for the simple air washer and the energy-efficient OAC systems for the summer operation shown in Table 1. It can be seen in Figure 5 that the energy-efficient OAC system recovered 15.5 kJ/kg from the exhaust air, corresponding to 5.18 kW for $1000 \text{ m}^3/\text{h}$. Table 2 summarizes the experimental results of recovered heat, electric power consumption and saving for the present OAC systems for semiconductor clean rooms with the operational condition of Table 1. It can be seen in the table that the recovered heat leads to the electric power reduction for the winter and summer operations. It is also observed for the winter and summer operations that although the recovered heat for the summer operation is much larger than that for the winter operation the reduced electric power for the summer case is smaller than that for the winter case. In addition the corresponding reduced power for the summer case is small compared to the recovered heat mainly because of the COP

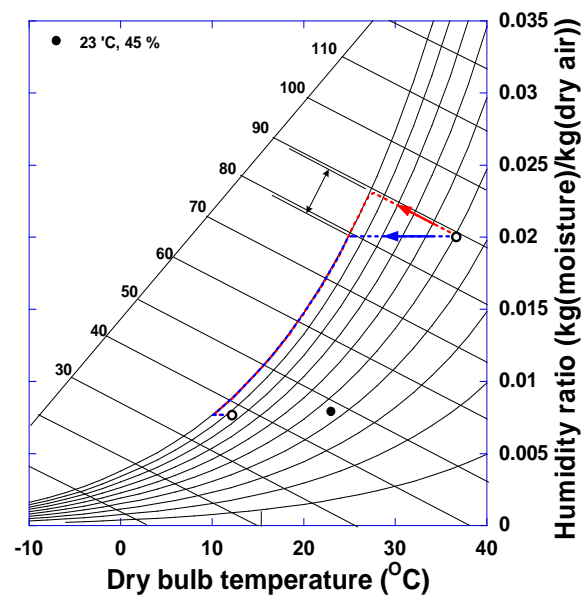


Figure 5. Variation of the air conditioning process on psychrometric chart by heat recovery for the summer operation.

Recovered heat :

3kJ/kg 11.5°C
1006 86%

0.0078

of chiller. On the other hand, as for the midterm operation the recovered heat does not make reduction of electric power because the amount of heat recovered is too small to surpass the additive power consumption due to primary/secondary pumps and increased pressure drop of inserted cooling coils in the air washer for heat recovery operation.

Table 2 Summary of energy consumption and heat recovery

Outdoor air condition	Item	Simple air washer [kW]	Exhaust air heat recovery [kW]
Winter -18°C, 70.4 %RH	Recovered heat	0	1.01
	Power consumption	13.8	10.98
	Reduced power	0	2.82
Summer 38°C, 55 %RH,	Recovered heat	0	-5.18
	Power consumption	12.68	11.28
	Reduced power	0	1.4
Midterm 22°C, 55 %RH	Recovered heat	0	-0.21
	Power consumption	5.68	6.5
	Reduced power	0	-0.82
All seasons	Fan	0.51	0.83
	Primary pump	0	0.3
	Secondary pump	0	0.3

CONCLUSION

Following observations are obtained from the present experimental results on the recovered heat and the energy consumption and saving for the simple and energy-efficient air washer type OAC systems for semiconductor manufacturing clean rooms.

- (1) The proposed energy-efficient OAC system recovered some of the waste heat of the exhaust air and saved the consequent electric power consumption for the winter and summer operations compared with the simple air washer OAC system.
- (2) Contrary to the winter operation the reduced power is smaller for the summer case than the recovered heat, mainly because of the COP of chiller.
- (3) For the midterm operation the recovered heat was not able to surpass the additive power consumption due to heat recovery operation and save the energy consumption.

ACKNOWLEDGMENT

The present work was supported partly by Gyeonggi Institute of Science and Technology Promotion and partly by Korean Small and Medium Business Administration.

REFERENCES

- [1] Hu, S.C.; Wu, J.S.; Chan, D.Y.L.; Hsu, R.T.C.; Lee, J.C.C. *Energy and Buildings* 2008, 40, 1765-1770.
- [2] Tsao, J.M.; Hu, S.C.; Chan, D.Y.L.; Hsu, R.T.C.; Lee, J.C.C. *Energy and Buildings* 2008, 40, 1387-1393.
- [3] Fujisawa, L.; Moriya, M.; Yosa, K.; Ikuta, M.; Yamamoto H.; Nabeshima. Y. In *Proc. of the 19th Annual Technical Meeting on Air Cleaning and Contamination Control*; Japan Air Cleaning Association: Tokyo, 2001; pp 166-168 (in Japanese).
- [4] Fujisawa, S.; Moriya, M.; Yosa, K.; Nishiwaki, S.; Yamamoto H.; Katsuki, T.; Nabeshima, Y.; Oda, H. In *Proc. of the 20th Annual Technical Meeting on Air Cleaning and Contamination Control*; Japan Air Cleaning Association: Tokyo, 2002; pp 162-165 (in Japanese).
- [5] Shiroma, S.; Tomita, H.; Yoshizaki, S.; Suzuki, K. In *Proc. of the 20th Annual Technical Meeting on Air Cleaning and Contamination Control*; Japan Air Cleaning Association: Tokyo, 2002; pp 260-262 (in Japanese).
- [6] Yamamoto H.; Katsuki, T.; Fujisawa, S.; Yosa, K.; Nishiwaki, S.; Nabeshima, Y.; Oda, H. In *Proc. of the 20th Annual Technical Meeting on Air Cleaning and Contamination Control*; Japan Air Cleaning Association: Tokyo, 2003; pp 151-154 (in Japanese).

Particle Deposition on a Semiconductor Wafer Larger than 300 mm

Kyung-Hoon Yoo¹, Gen-Soo Song¹, Hyung-Tae Kim¹ and Kun-Hyung Lee²

1 Nanoscale Contamination Control Lab, Korea Institute of Industrial Technology (KITECH), 1271-18, Sa-1-dong , Sangnok-gu, Ansan-si, 426-171, South Korea

2 Samsung Electronics, San #16, Banwol-ri, Taean-eup, Hwasung-si, 445-701, South Korea

ABSTRACT

Particle deposition on a semiconductor wafer larger than 300 mm was studied experimentally and numerically. In particular the electrostatic effect on particle deposition velocity was investigated. The experimental apparatus consisted of a particle generation system, a particle deposition chamber and a wafer surface scanner. Experimental data of particle deposition velocity were obtained for a semiconductor wafer of 200 mm diameter with the applied voltage of 5000 V and PSL particles of the sizes between 83 and 495 nm. The experimental data of particle deposition velocity were compared with the present numerical results and the existing experimental data for a 100 mm wafer by Ye et al.^[1] and Opiolka et al.^[2]. The present numerical method took into consideration the particle transport mechanisms of convection, Brownian diffusion, gravitational settling and electrostatic attraction in an Eulerian frame of reference. Based on the comparison of the present experimental and numerical results with the existing experimental results the present experimental method for a 200 mm semiconductor wafer was found to be able to present reasonable data.

KEYWORDS

Particle Deposition, Semiconductor Wafer, 300 mm Diameter Wafer, Electrostatic Effect

Introduction

Since the year of 2000, the semiconductor wafer diameter for mass production has been changed gradually from 200 mm to 300 mm in the integrated circuit manufacturing industry. According to ITRS, the wafer diameter of 450 mm with 32 nm design rule is anticipated for mass production in the year of 2012. Meanwhile, from the practical point of view the semiconductor wafer in process needs to be protected against all particles down to 10 nm in the case of 32 nm design rule technology because of the one third rule for the killing particle size^[3]. Consequently, in order to establish the particle contamination control strategy for the next generation semiconductor wafer technology it is first necessary to understand the flow field and particle dynamics on the surface

of a 300 mm sized semiconductor wafer, which is the main objective of the present study. Many researchers have investigated experimentally and/or numerically particle deposition on a horizontal semiconductor wafer 100 mm in diameter with various particle deposition mechanisms such as diffusion, gravitational settling, themophoresis and electrophoresis^[1,2,4-7]. However, so far there have not been sufficient studies to fully understand the particle deposition behavior on the surface of a semiconductor wafer larger than 300 mm in diameter.

In the present study, the characteristics of particle deposition velocity on the upper surface of 100, 300, 450 mm sized wafers were investigated both experimentally and numerically. As for the experimental part, particle deposition experiments were conducted for a 200 mm sized stationary horizontal unheated wafer with an applied voltage. The experimental results were then compared with the present corresponding numerical results. Sizes of PSL particles for the present deposition experiment were 83, 100, 150, 200, 300 and 495 nm. As for the numerical part, particle deposition simulations were performed to characterize the flow field and particle deposition on 100, 300, 450 mm sized horizontal wafers in a unidirectional air flow. Particle transport mechanisms considered were convection, Brownian diffusion, gravitational settling and electrophoresis. Averaged particle deposition velocities and their radial distributions on the upper surface of the wafer were calculated for various particle sizes between 10 nm and 10^4 nm(10 μm) from a particle concentration equation in the Eulerian frame of reference.

Experimental and Numerical Methods

Experiments were conducted in an ISO class 2 clean room of the line 10 fab of SAMSUNG Electronics Co., Hwasung-Si, Gyeonggi-Do, South Korea. The present experimental apparatus consisted of a atmospheric deposition chamber(MSP 2300) and a PSL particle generation system. The deposition chamber and wafer configuration is shown in Figure 1. The wafer diameter in the present experimental study was 200 mm(8 in). A wafer stage made of stainless steel was used to hold a 200 mm sized semiconductor wafer, to which high voltage of up to 5000 V can be applied. PSL particles(Duke Scientific Co.) with sizes of 83, 100, 150, 200, 300 and 495 nm were used respectively in the present study. The aerosol particles were then introduced into the chamber through a show-head type circular inlet, which has 126 holes of 0.3 mm diameter, as shown in Figure 1. The mean flow velocity in the chamber was 0.3 m/s. A wafer surface scanner (KLA-Tencor SP1) with a lower detection limit of 65 nm was used to scan the wafer surface before and after each particle deposition experiment.

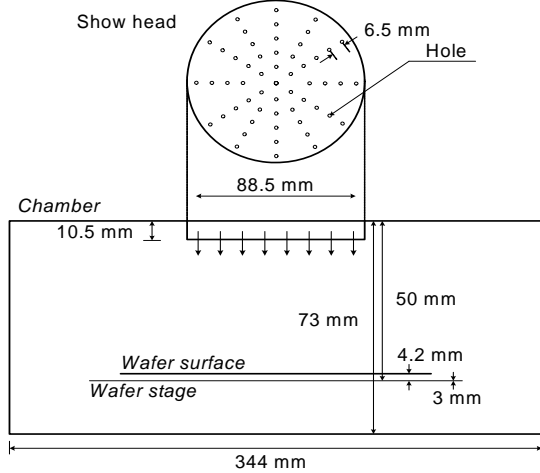


Figure 1. Schematic diagram of the present particle deposition chamber.

Figure 2 shows the calculation domain for the present numerical study. The wafer geometry shown in Figure 2 can be solved as a 2-dimensional problem because of axial symmetry. Free air stream with the velocity $U_0=0.3$ m/s on the upper surface of the wafer with applied voltage $V_d=5000$ V. The calculation domain covers 10 times the radius of wafer in the upward direction and 15 times in the downward direction from the upper surface of the wafer to guarantee the fully developed condition. The side boundary is located 10 times the radius of wafer in the radial direction from the center of the wafer to recover the free stream condition of $u_z=U_0$, $u_r=u_\theta=0$ sufficiently. The radius and thickness of the wafer are $R=225$ mm and $t=0.925$ mm, respectively.

The air flow can be assumed to be laminar because the rotational Reynolds number $Re = \frac{2U_0R}{\nu}$

is 8,951 for $R=225$ mm. As for the governing equations of flow fields, the Navier-Stokes equations for steady, incompressible and axisymmetric laminar flow were considered. Meanwhile,

The Stokes number for the flow $Stk = \frac{\tau_p U_0}{2R}$ can be obtained as 0.00022($\ll 1$) for the largest

particle size of 10^4 nm(10 μ m). Therefore, particle concentration equation in the Eulerian point of view can be obtained. The electrostatic force was considered, taking into account the Coulomb force and neglecting the image, dielectrophoretic and dipole-dipole forces^[2].

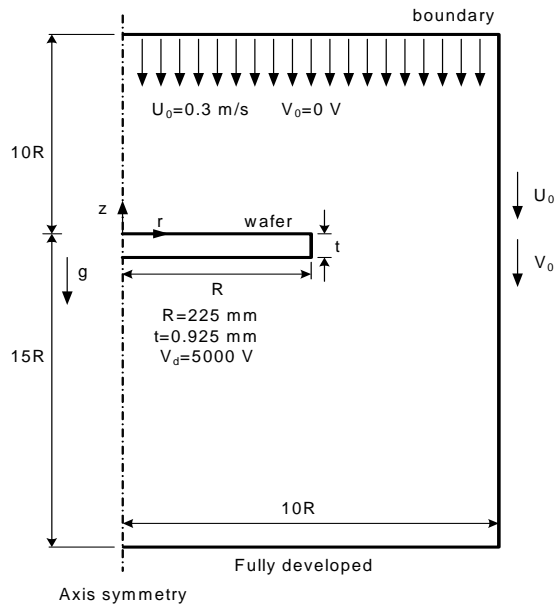


Figure 2. Schematic diagram of the present calculation domain.

The electric field components were calculated from the electric potential which is the solution of the Laplace equation. The SIMPLE algorithm by Patankar^[8] was modified to consider the particle transport including the migration due to the external force fields as pointed out by Stratmann and Whitby^[9]. The non-staggered grid system employed here consisted of 154(axial)×136 (radial). The first grids from the surface of the wafer were located at the distance of 5 μm from the wafer surface^[5] and the other grids were arranged to increase geometrically with geometric ratios of about 1.2. The grid dependencies were checked numerically with the increase of the grid number and the location of boundaries of the calculation domain, respectively. For details of the present numerical method, readers can refer to that of a 100 mm sized wafer by Oh et al.^[5] and Yoo and Oh^[7].

Results and Discussion

Figure 3 shows the variation of averaged particle deposition velocity with respect to particle size for various wafer diameters. It can be seen in the curves for the uncharged wafer with applied voltage of 0V that the deposition velocities are increased for the particle sizes below 0.3 μm as the wafer diameter increases. It is due to diffusion dominance. The increase of wafer diameter causes the air velocity boundary layer to become thinner and leads to the consequent increase of the particle concentration gradient and the consequent increase of the Brownian diffusion flux to the surface. While in the particle sizes larger than 1 μm no difference is found because of

gravitational settling dominance, which have little effect by the air velocity boundary layer. Also one can observe in Figure 3 that in the curves for the charged wafer with 5,000V and charged particles with one electron charge the particle deposition velocities are rapidly increased in the particle size range generally less than 3.0 μm as the wafer diameter increases. This significant increase of deposition velocity is basically due to electric field strength on the upper surface of the charged wafer. The increase of wafer diameter causes the electric field strength to become larger and leads to the consequent increase of the particle deposition velocity.

Meanwhile, the present numerical results show relatively good agreement with the present experimental results and those of Ye et al.^[1] and Opiolka et al.^[2].

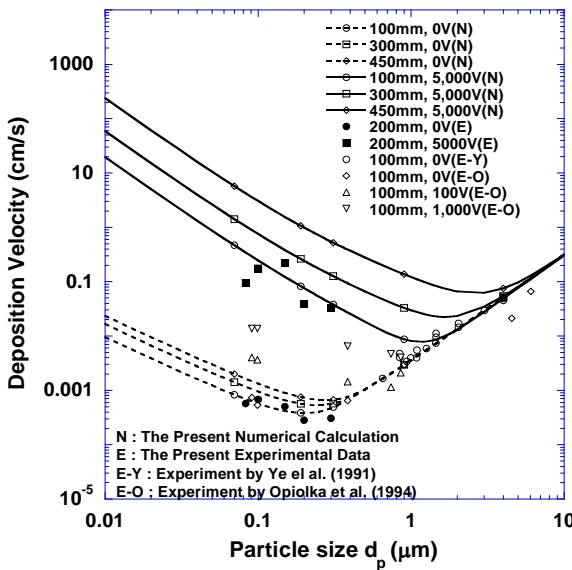


Figure 3. Variation of the averaged particle deposition velocity with respect to particle size for various wafer diameters.

CONCLUSION

Following conclusions are obtained from the experimental result and the numerical results on the particle deposition velocity on the uncharged and 5,000V charged wafers with diameters of 100, 300 and 450 mm.

- (1) The present experimental and numerical results showed relatively good agreement with the available experimental ones.
- (2) The increase of wafer diameter causes the velocity boundary layer to become thinner and leads to the increase of the particle concentration gradient and the consequent increase of the Brownian diffusion flux to the surface. While in the particle sizes larger than 1 μm no difference

is found because of gravitational settling dominance, which have little effect by the boundary layer.

(3) The charging of the wafer with 5,000V increases the averaged particle deposition velocities over a fairly broad range of particle sizes by the electrophoresis effect. The increase of wafer diameter causes the electric field strength on the upper surface of the wafer to become larger and leads to the increase of the particle deposition velocity in the particle size range generally less than 3.0 μm .

ACKNOWLEDGMENTS

The present work was supported by Gyeonggi Institute of Science and Technology Promotion in the province of Gyeonggi, South Korea.

REFERENCES

- [1] Ye, Y.; Pui, D.Y.H.; Liu, B.Y.H.; Opiolka, S.; Blumhorst, S.; Fissan, H. *J. Aerosol Science* 1991, 22, 63-72.
- [2] Opiolka, S.; Schmidt, F.; Fissan, H. *J. Aerosol Science* 1994, 25, 665-671.
- [3] Chae, S.K.; Sun, J.J.; Liu, B.Y.H.; Yoo, S.H. *Future Fab International* 1999, 6, 229-237.
- [4] Liu, B.Y.H.; Ahn, K.H. *Aerosol Science and Technology* 1987, 6, 215-224.
- [5] Oh, M.D.; Yoo, K.H.; Myong, H.K. *Aerosol Science and Technology* 1996, 25, 141-156.
- [6] Tsai, R.; Chang, Y.P.; Lin, T.Y. *J. Aerosol Science* 1998, 29, 811-825.
- [7] Yoo, K.H.; Oh, M.D. *J. Aerosol Science* 2005, 36, 235-246.
- [8] *Numerical Heat Transfer and Fluid Flow*; Patankar, S.V.; McGraw-Hill: New York, 1980.
- [9] Stratmann, F.; Whitby, E.R. *J. Aerosol Science* 1989, 20, 437-440.

Particle-Free Atomic Layer Deposition of Transparent Conductive Oxide on Flexible Substrate

Kyung-Hoon Yoo, Gen-Soo Song and Hyung-Tae Kim

Nanoscale Contamination Control Lab, Korea Institute of Industrial Technology (KITECH), 1271-18, Sa-1-dong , Sangnok-gu, Ansan-si, 426-171, South Korea

ABSTRACT

Aluminum-doped Zinc Oxide(AZO) is considered as an excellent candidate to replace Indium Tin Oxide(ITO) as transparent conductive oxide(TCO) for organic electronic devices produced onto both rigid and flexible substrates for applications in flat panel displays, organic light emitting diodes(OLEDs) and organic solar cells(OSCs). In the present study, AZO thin film was applied as the transparent conductive oxide of flexible organic solar cell by a low-temperature atomic layer deposition(ALD) process. This low-temperature ALD leads to a particle free process because gas-phase particle nucleation cannot take place at this lower process temperature. AZO thin films were deposited on a Poly-Ethylene Naphthalate(PEN) substrate using Di-Ethyl-Zinc(DEZ) and Tri-Methyl-Aluminum(TMA) as precursors and H₂O as an oxidant for the atomic layer deposition at the deposition temperature of 130 °C. The pulse and purge time of TMA, DEZ and H₂O were 0.1 second and 20 second, respectively. The electrical and optical properties of the AZO films were characterized as a function of film thickness. The 300 nm-thick AZO film grown on PEN substrate exhibited sheet resistance of 87 Ω/square and optical transmittance of 84.3 % at wavelength range between 400 and 800 nm. The present particle free atomic layer deposition technique for the production of TCO film is regarded to be promising for the fabrication of a flexible organic solar cell.

KEYWORDS

Atomic Layer Deposition(ALD), Transparent Conductive Oxide(TCO), Flexible Organic Solar Cell, Aluminum-doped Zinc Oxide(AZO), Poly-Ethylene Naphthalate(PEN)

Introduction

Transparent conductive oxide (TCO) films with good optical and electrical properties have been widely applied to optoelectronics such as liquid crystal display(LCD), plasma display panel(PDP), organic light-emitting diode(OLED) and flexible organic solar cell. ITO(Indium Tin Oxide, Sn-doped In₂O₃) thin films have been practically used as TCO for most of the various types of optoelectronics.^[1-5] In addition, the total amount of indium used for optoelectronics has been

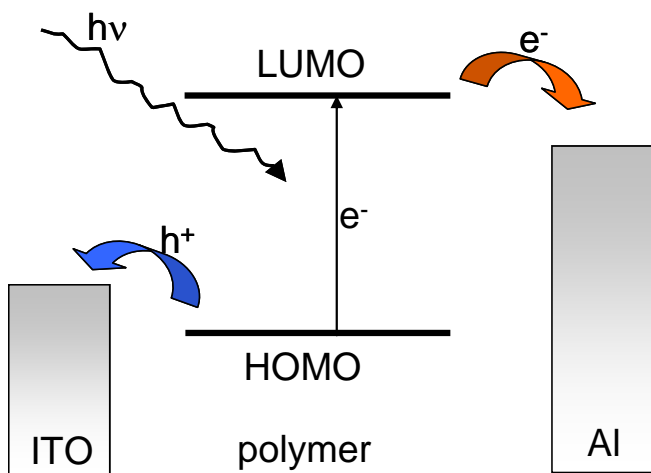


Figure 1. The structure and photovoltaic principle of a flexible organic solar cell.

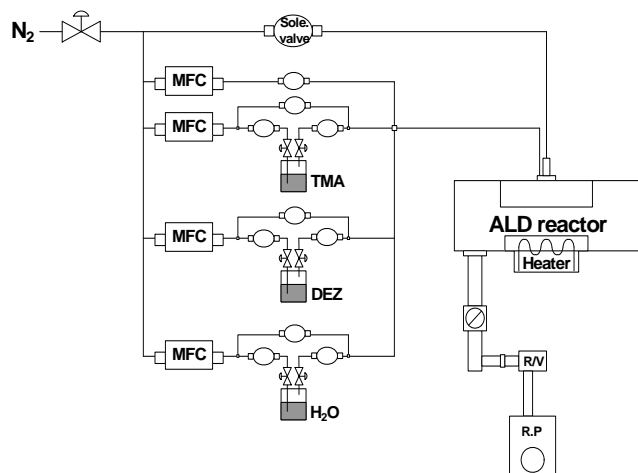


Figure 2. Schematic diagram of the present ALD experimental apparatus.

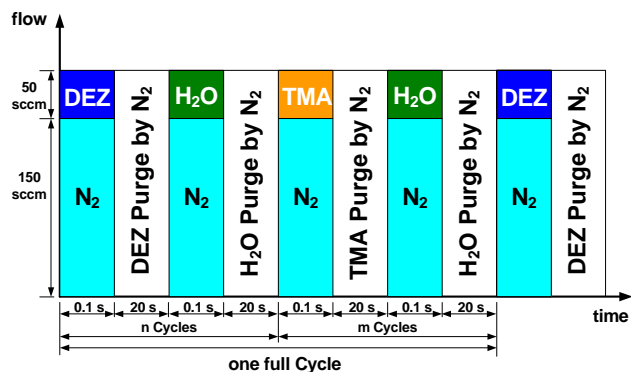


Figure 3. The present ALD cycle procedure.

remarkably expanding in recent years. It is widely believed that a shortage of indium may occur in the near future because of the limited nature of world indium reserves. As a result, the price of indium has been increased sharply. Therefore, it is important to develop alternatives to the ITO thin-film TCO.

Recently, aluminum-doped zinc oxide(AZO, ZnO:Al) films exhibited comparable optical and electrical properties with ITO films and have drawn increasing attention as a route to replace ITO films. As for the preparation of AZO films, radio-frequency(RF) magnetron sputtering, chemical vapor deposition(CVD), atomic layer deposition(ALD), reactive magnetron sputtering, thermal evaporation, pulsed laser deposition(PLD) and sol-gel methods have been studied.

In the present study, AZO transparent conductive oxide films have been prepared on PEN substrate by particle-free low-temperature atomic layer deposition. Moreover, electrical and optical properties of the films are investigated.

Experimental Methods

Al-doped ZnO(AZO) transparent conductive oxide thin films were deposited on PEN substrate by particle-free low-temperature atomic layer deposition(ALD) process.

Figure 2 and 3 show the schematic diagram of the present ALD system and ALD cycle procedure respectively. Di-ethyl-zinc(DEZ) and tri-methyl-aluminum(TMA) as precursors and H₂O as an oxidant are alternately supplied onto a PEN substrate mounted on the susceptor in the ALD reactor.

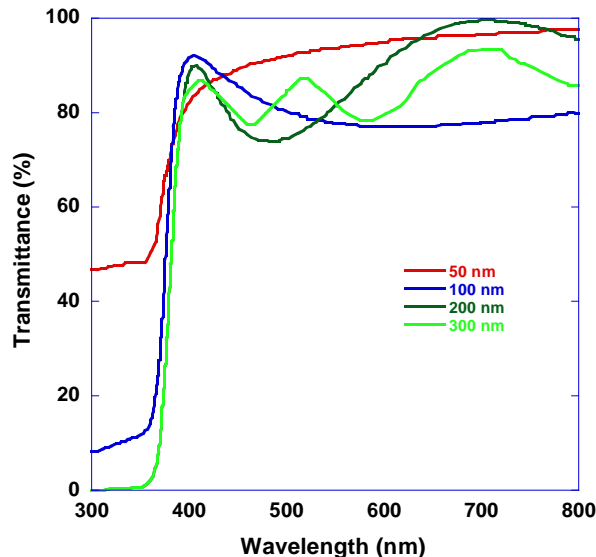


Figure 4. Variation of transmittance with respect to AZO film thickness.

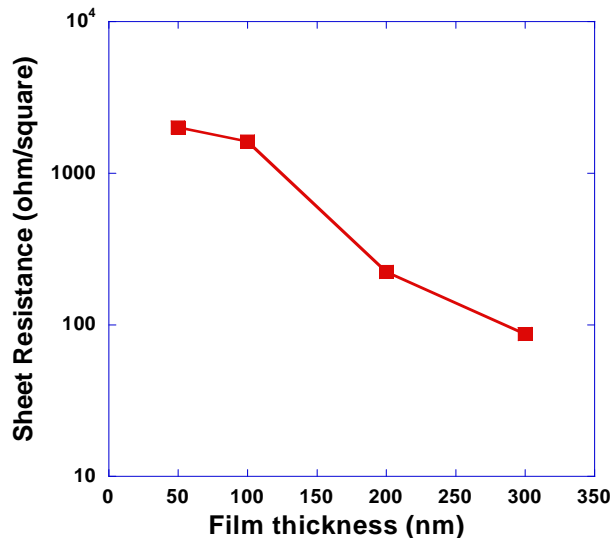


Figure 5. Variation of sheet resistance with respect to AZO film thickness.

is acceptable for TCO of organic solar cells. Therefore the present particle-free atomic layer deposition technique for the production of AZO film is regarded to be promising for the fabrication of a flexible organic solar cell.

The pulse and purge time of TMA, DEZ and H₂O were 0.1 second and 20 second, respectively. The deposition temperature and system pressure are 130 °C and 0.5 Torr, respectively. The weight percent (wt. %) of Al dopant in the AZO films was 1.5 %. The thickness of AZO films considered in the present work ranges from 50 to 300 nm. All experiments were conducted in class 100 super clean room. Meanwhile, the optical transmittance measurements were performed with the UV/visible spectrophotometer. The electrical resistance was measured by the four-point-probe method.

Results and Discussion

Figure 4 shows the variation of optical transmittance with respect to light wavelength for various thicknesses of AZO film. It can be seen in the figure that the transmittance of AZO film tends to decrease with AZO film thickness. 300 nm thickness of AZO film grown on PEN substrate exhibited optical transmittance of 84.3 % at wavelength range between 400 and 800 nm, which is acceptable for TCO of organic solar cells.

Figure 5 shows the variation of sheet resistance with respect to AZO film thickness. It is observed that the sheet resistance of AZO film decreases with AZO film thickness. 300 nm thickness of AZO film grown on PEN substrate exhibited sheet resistance of 87 Ω/square, which

CONCLUSION

Following conclusions are obtained from the experimental results on the optical transmittance and electrical resistance of AZO film on PEN substrate.

- (1) 300 nm thickness of AZO film grown on PEN substrate exhibited optical transmittance of 84.3 % at wavelength range between 400 and 800 nm.
- (2) 300 nm thickness of AZO film grown on PEN substrate exhibited sheet resistance of 87 Ω/square .
- (3) The present particle-free atomic layer deposition technique for the production of AZO film is regarded to be promising for the fabrication of a flexible organic solar cell.

ACKNOWLEDGMENTS

The present work was supported by Gyeonggi Institute of Science and Technology Promotion in the province of Gyeonggi, South Korea.

REFERENCES

- [1] Minami, T. *Thin Solid Films* 2008, 516, 5822-5828.
- [2] Berginski, M.; Hupkes, J.; Reetz, W.; Rech, B.; Wuttig, M. *Thin Solid Films* 2008, 516, 5836-5841.
- [3] Fragala, M.E.; Malandrino, G. *Microelectronics Journal* 2009, 40, 381-384.
- [4] Murdoch, G.B.; Hinds, S.; Sargent, E.H.; Tsang, S.W.; Mordoukhovski, L.; Lu, Z.H. *Applied Physics Letters* 2009, 94, 213301.
- [5] Saarenpaa, H.; Niemi, T.; Tukiainen, A.; Lemmetyinen, H.; Tkachenko, N. *Solar Energy Materials & Solar Cells* 2010, 94, 1379-1383.

Comparative Study on Steam Humidification Type and Water Spray Humidification Type Outdoor Air Conditioning Systems for Semiconductor Manufacturing Clean Rooms

Kyung-Hoon Yoo¹, Hyung-Tae Kim¹, Gen-Soo Song¹, Seung-Woo Son² and Dug-Jun Park³

1 Nanoscale Contamination Control Laboratory, Korea Institute of Industrial Technology (KITECH), 1271-18, Sa-1-dong, Ansan-si, 426-171, Gyeonggi-do, South Korea

2 Sunglim PS Co., 1301, Namseong Plaza, 345-30, Gasan-dong, Geumcheon-gu, Seoul, 153-802

3 Shinsung ENG Co., 404-1, Baekhyeon-dong, Bundang-gu, Seongnam-si, 463-420

ABSTRACT

In a recent large-scale semiconductor manufacturing clean room, in order to improve clean room air quality, air washers are used to remove suspended particles and airborne gaseous contaminants such as NH₃, SOx and organic gases from the outdoor air introduced into clean room. At the same time air washers can humidify the incoming outdoor air because of water spray evaporation, which can replace steam humidification in wintertime. From the energy saving point of view, compared with steam humidification by fossil fuel boiler water spray humidification technique can be regarded to be useful for the reduction of air conditioning energy consumption for the clean room. In the present study, an experiment with an outdoor air flow of 1000 m³/h was conducted to compare the air conditioning process and energy consumption of steam humidification type and water spray humidification type outdoor air conditioning systems. It was shown from the experimental results that the water spray humidification type outdoor air conditioning system exhibited lower electric power consumption and was more energy-efficient for the winter operation than the steam humidification type one.

KEYWORDS

Semiconductor Manufacturing Clean Room, Outdoor Air Conditioning System, Steam Humidification, Water Spray Humidification, Energy Reduction

Introduction

For recent semiconductor manufacturing clean rooms, the energy consumption of an outdoor air conditioning (hereafter OAC) system to heat, humidify, cool and dehumidify incoming outdoor air accounts for about 45 % of the total air conditioning load required to maintain a clean room

environment^[1,2]. In particular the energy requirement to humidify the incoming outdoor air in wintertime is enormous. Recently, air washers have been sometimes used in OAC systems for semiconductor manufacturing clean rooms to remove suspended dusts and gaseous contaminants such as NH₃, SO_x, NO_x and organic gases in incoming outdoor air. Simultaneously the air washers can humidify the incoming outdoor air with water spray evaporation^[3-6]. Therefore the evaluation and comparison of the energy consumption of basic humidifying means, steam and water spray, for the OAC system is useful for reducing the outdoor air conditioning load for a clean room.

In the present study, a water spray humidification type OAC system with an air washer was compared with a conventional steam humidification type OAC system concerning energy consumption.. An experiment was carried out on the lab-scale with an air flow 1000 m³/h regarding electric power consumption and saving for outdoor air conditioning load of the OAC systems.

Experimental Methods

Figures 1 and 2 show the schematic diagram of the present steam humidification type and water spray humidification type OAC systems, respectively. The present water spray humidification type OAC system consisted mainly of air filters, a pre-heater, an air washer, two stage cooling coils, a reheating heater and a humidifier, as shown in Figure 2, whereas the present steam humidification type OAC system is the case of Figure 1 without an air washer. An experiment with an air flow of 1000 m³/h was carried out on the laboratory scale regarding the energy consumption of the two OAC systems.

Table 1 shows the experimental condition of the present water spray humidification type OAC system with an air washer. The air washer was installed in the clean wind tunnel with the cross section of 0.33×0.33 m², and had 2 modules comprised of 4 banks of 48 nozzles.

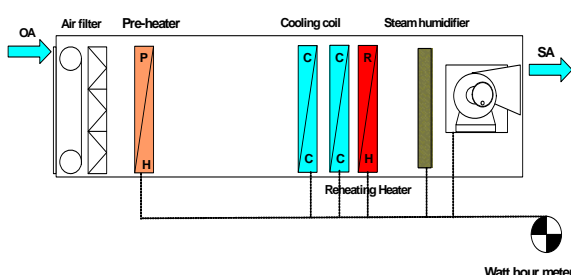


Figure 1. Schematic diagram of the present steam humidification type OAC system.

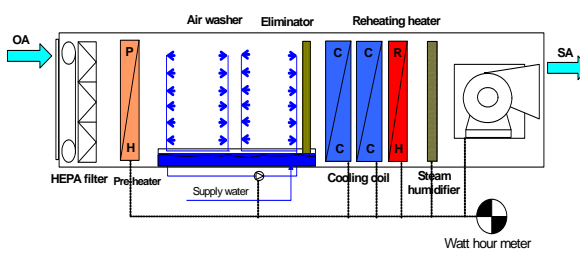


Figure 2. Schematic diagram of the present water spray humidification type OAC system with an air washer.

Table 1. Experimental condition of the present water spray OAC system.

Air flow rate and average velocity	1000 m ³ /h, 2.5 m/s
Outdoor Air condition	Winter: -18°C, 70.4 %RH Summer: 38°C, 50 %RH Midterm: 22°C, 55 %RH
Supply air condition	12 °C, 90 %RH
Class of spraying water for air washer	City water
Total flow of spraying water	8 ℓ/min
Number of nozzles in air washer	48
L/G, gravimetric ratio of water to air	0.4

The present nozzles with outer diameter of 1/8 in sprayed city water with 0.7 MPa in both of the counter- and co-current directions simultaneously. One thing to be noted here is that as for a reheating coil and a humidifier an electric heater and an electrode-boiler humidifier were used respectively instead of a fossil fuel boiler to unify the measurement into electric power. The electric power sensors were installed to measure the electric power consumption, as shown in Figures 1 and 2. ALMEMO MA5990-2 data logger and sensors were installed to measure temperature and relative humidity in the wind tunnel. The temperature and humidity sensors were installed at the each outlet of the constant temperature and humidity chamber, the air washer, the cooling coil, the reheating heater and the humidifier to investigate the air conditioning process of the OAC system on psychrometric chart.

Results and Discussion

Figure 3 shows respectively the experimental results of air conditioning process for the water spray humidification and steam humidification type OAC systems for the winter operation shown in Table 1. Because the two OAC systems the same upstream air conditioning process condition for the winter operation, experimental outdoor air condition(OA) the winter operation shown in Figure 1 5 °C, 10 %RH rather than -18 °C, 70.4 %RH for the convenience of experiment. Table 2 summarizes the

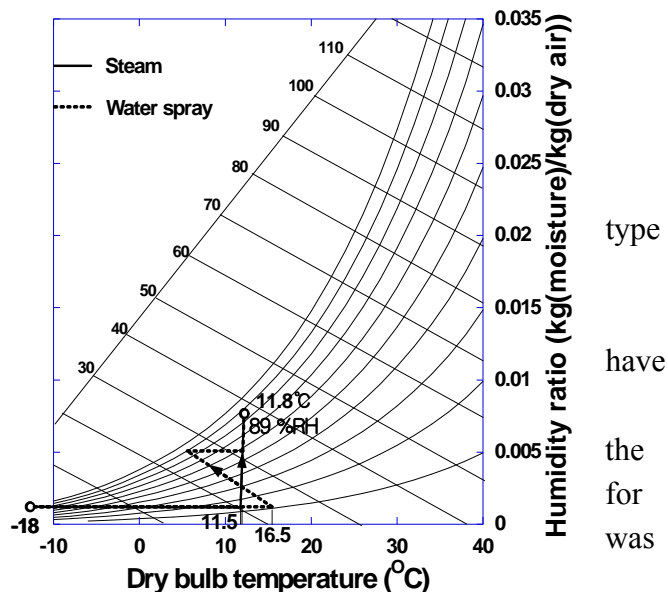


Figure 3. Comparison between the air conditioning processes on the psychrometric chart for the winter operation

experimental results of electric power consumption for the present OAC systems with an air flow of 1000 m³/h. It can be seen in the table that the electric power reductions with the water spray humidification type OAC system were 5.39 kW and -1.88 kW for the winter and summer operations respectively compared with the steam humidification type OAC system, which leads to the conclusion that the water spray humidification type OAC system is more energy-efficient throughout the year.

Table 2 Summary of energy consumption

Outdoor air condition	Steam humidification	Water spray humidification
Winter -18 °C, 70.4 %RH	23.67 kW	18.28 kW
Midterm 22 °C, 55 %RH	6.2 kW	5.68 kW
Summer 38 °C, 50 %RH	10.8 kW	12.68 kW

CONCLUSION

Following observations are obtained from the present experimental results on energy consumption and saving for the water spray humidification type and steam humidification type OAC systems for semiconductor manufacturing clean rooms.

- (1) Electric power reductions for the winter and summer operations were 5.39 kW and -1.88 kW respectively compared with the steam humidification type OAC system.
- (2) The water spray humidification type OAC system is more energy-efficient throughout the year than the steam humidification type one.

ACKNOWLEDGMENT

This work was supported partly by Korean Small and Medium Business Administration and partly by Gyeonggi Institute of Science and Technology Promotion.

REFERENCES

- [1] Hu, S.C.; Wu, J.S.; Chan, D.Y.L.; Hsu, R.T.C.; Lee, J.C.C. *Energy and Buildings* 2008, 40, 1765-1770.
- [2] Tsao, J.M.; Hu, S.C.; Chan, D.Y.L.; Hsu, R.T.C.; Lee, J.C.C. *Energy and Buildings* 2008, 40, 1387-1393.
- [3] Fujisawa, L.; Moriya, M.; Yosa, K.; Ikuta, M.; Yamamoto H.; Nabeshima. Y. In *Proc. of the 19th Annual Technical Meeting on Air Cleaning and Contamination Control*; Japan Air Cleaning

Association: Tokyo, 2001; pp 166-168 (in Japanese).

[4] Fujisawa, S.; Moriya, M.; Yosa, K.; Nishiwaki, S.; Yamamoto H.; Katsuki, T.; Nabeshima, Y.; Oda, H. In *Proc. of the 20th Annual Technical Meeting on Air Cleaning and Contamination Control*; Japan Air Cleaning Association: Tokyo, 2002; pp 162-165 (in Japanese).

[5] Shiroma, S.; Tomita, H.; Yoshizaki, S.; Suzuki, K. In *Proc. of the 20th Annual Technical Meeting on Air Cleaning and Contamination Control*; Japan Air Cleaning Association: Tokyo, 2002; pp 260-262 (in Japanese).

[6] Yamamoto H.; Katsuki, T.; Fujisawa, S.; Yosa, K.; Nishiwaki, S.; Nabeshima, Y.; Oda, H. In *Proc. of the 20th Annual Technical Meeting on Air Cleaning and Contamination Control*; Japan Air Cleaning Association: Tokyo, 2003; pp 151-154 (in Japanese).

Scavenging of Sea-salt Aerosol by Snow in Niigata Prefecture, Japan

Shin Ohara¹, Shin-ichi Fujita¹, Soichiro Sugimoto¹, Gaku Sakata² and Akira Takahashi¹

1 Central Research Institute of Electric Power Industry, 1646 Abiko, Abiko-shi, Chiba 270-1194, Japan

2 Tohoku Electric Power Company, 2-1-9 Honcho, Yamagata-shi, Yamagata 990-0043, Japan

ABSTRACT

By discriminating snow from rain, the scavenging ratio of Na^+ for snow was evaluated in order to examine the formation mechanism of sea-salt-rich snow in Niigata Prefecture, Japan. Winter-time field measurements of Na^+ concentration in precipitation and aerosol were conducted at three sites, located at different distances from the coast of the Sea of Japan. The geometric mean of the scavenging ratio of Na^+ for snow was 7.7×10^6 , being greater than that for rain (2.9×10^6). The scavenging ratio of Na^+ for snow appeared to remain constant with precipitation intensity, whereas there was an inverse dependence of that for rain on precipitation intensity. The scavenging ratios of Na^+ for snow and rain increased with the distance from the coast. These results suggest that snow can be a more efficient scavenger of sea-salt aerosol than rain in the area during the winter season, and the scavenging mechanism of sea-salt aerosol would be different between the inland area and the coastal area.

KEYWORDS

Sea-salt aerosol, Scavenging ratio, Snow

Introduction

In December 2005, because of a severe snowstorm, a large-scale power outage occurred in Niigata Prefecture, Japan, causing a blackout affecting more than 600,000 households^[1-2]. One of the main causes of the power outage was the accretion of wet and sea-salt-rich snow on the insulators of transmission lines. Many of the electrical flashovers on the insulators occurred in an area 20-30 km from the coast. Thus far, no accretion of sea-salt-rich snow on the insulators inland has ever been reported^[3].

Several field studies have quantified the scavenging ratio of sea-salt components at coastal sites of the Sea of Japan, reporting that the scavenging ratio of Na^+ was relatively high during the winter season^[4-5]. From the results, it is suggested that the scavenging ratio of sea-salt components differs between snow and rain. However, in the coast of the Sea of Japan, the

scavenging ratio of sea-salt components has not been well studied with distinction between snow and rain thus far.

In the study reported here, we evaluated the scavenging ratio of Na^+ for snow by discriminating snow from rain in order to examine the formation mechanism of sea-salt-rich snow in Niigata.

Experimental Methods

The field sampling of precipitation and sea-salt aerosol was conducted in Niigata (site A), Niitsu (site B) and Gosen (site C), located in the area where the power outage occurred in 2005, during the winter season from 2008 to 2010 (Fig. 1). The distances from the coast to these sites are 1 km, 17 km and 29 km, respectively. The method of the sampling and chemical analysis of precipitation and aerosol is described in the proceedings by Takahashi *et al.*^[6]. The precipitation type of the samples was classified by the method of Meteorological Research Institute^[7] and Matsuo and Sasyo^[8] based on the observational data for 35 years at a meteorological observational site, which is the closest one from the three sites. The scavenging ratio of Na^+ , K , is expressed as

$$K = \frac{C_p}{C_a},$$

where C_p and C_a are Na^+ concentration in precipitation (mg L^{-1}) and Na^+ concentration in ambient air ($\mu\text{g m}^{-3}$), respectively.

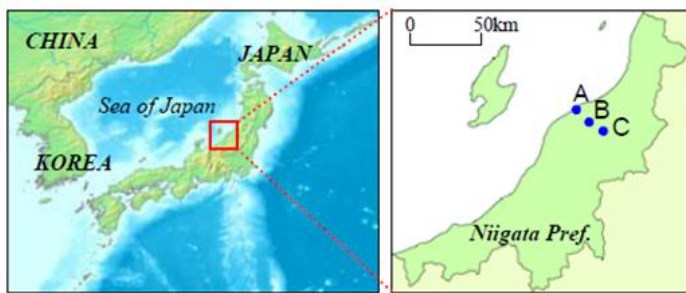


Fig. 1. Locations of field sites where precipitation and aerosol samples were collected.

Results and Discussion

1. Distribution of scavenging ratio of Na^+

The Na^+ concentrations in precipitation ranged from 0.01 mg L^{-1} to 77.2 mg L^{-1} , with a volume-weighted mean of 4.24 mg L^{-1} , while those in ambient air ranged from $0.02 \mu\text{g m}^{-3}$ to $8.2 \mu\text{g m}^{-3}$, with an average of $0.80 \mu\text{g m}^{-3}$ (Fig. 2). The Na^+ concentration in snow appeared to be higher than that in rain.

The scavenging ratios of Na^+ for snow and rain are distributed approximately log-normally, with geometric means of scavenging ratios for snow and rain, 7.7×10^6 and 2.9×10^6 , respectively (Fig. 3). These results agree with those in the previous studies about the scavenging ratio of sea-salt components^[4-5, 9-11] (Table 1). The fact that the scavenging ratio for snow is higher than that for rain indicates that snow is a more efficient scavenger of sea-salt aerosol than rain. Sparnacher *et al.* reported that the scavenging coefficient of polystyrene latex particles for snow was determined to be about five times larger than that for rain from the results of the chamber experiments^[12].

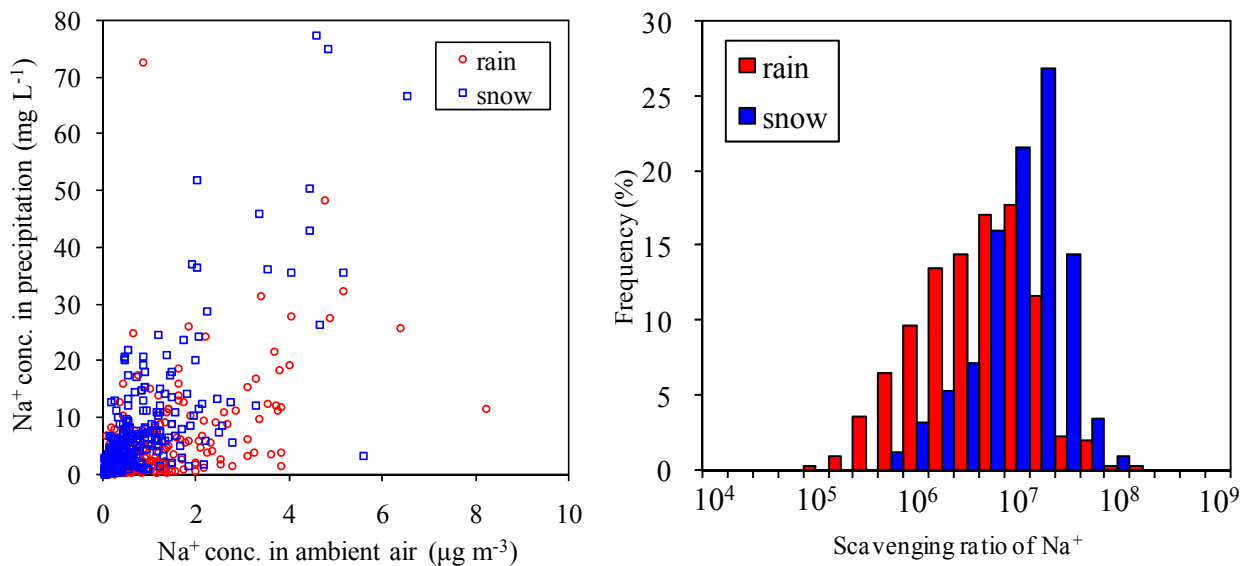


Fig. 2. Scatter plot for Na^+ concentrations in snow and rain against those in ambient air.

Fig. 3. Frequency distributions of scavenging ratios for two groupings—rain and snow.

Table 1. Comparative values of scavenging ratios of sea salt species reported from the literature.

Site	Species	$K \times 10^6$	Season	Reference
Miami, USA	Na^+	0.46	A	Savoie <i>et al.</i> (1987)
American Samoa	Na^+	0.43	A	Savoie <i>et al.</i> (1987)
Bermuda, Atlantic Ocean	Na^+	1.58	A	Savoie <i>et al.</i> (1987)
Northwestern Kyushu, Japan	ss-SO_4^{2-}	0.54	A	Fujita and Takahashi (1990)
Eastern England	Cl^-	0.58	A	Harrison and Allen (1991)
Yahiko, Niigata, Japan	Na^+	0.32-24	W	Fukuzaki <i>et al.</i> (2005)
	Na^+	1.24-29	C	Fukuzaki <i>et al.</i> (2005)
Coasts of the Sea of Japan, Japan	Na^+	0.49	W	Fujita <i>et al.</i> (2010)
	Na^+	1.82	C	Fujita <i>et al.</i> (2010)
Niigata, Japan	Na^+	2.9	C, rain	This work
	Na^+	7.7	C, snow	This work

*A: Annual, W: Warm season, C: Cold season

2. Dependence of scavenging ratio of Na^+ on precipitation intensity

For rain, the scavenging ratio is inversely proportional to approximately one-third power of the precipitation intensity, P (Fig. 4(1)). Several studies also reported that the scavenging ratios of SO_4^{2-} and Na^+ are inversely proportional to about one-third power of the precipitation amount in the event^[5,11,14]. On the other hand, for snow, there is no dependence of scavenging ratio on precipitation intensity (Fig. 4(2)). The scavenging ratio of snow appeared to remain constant with precipitation intensity. This relatively high scavenging ratio would lead to the high wet deposition of Na^+ in this area.

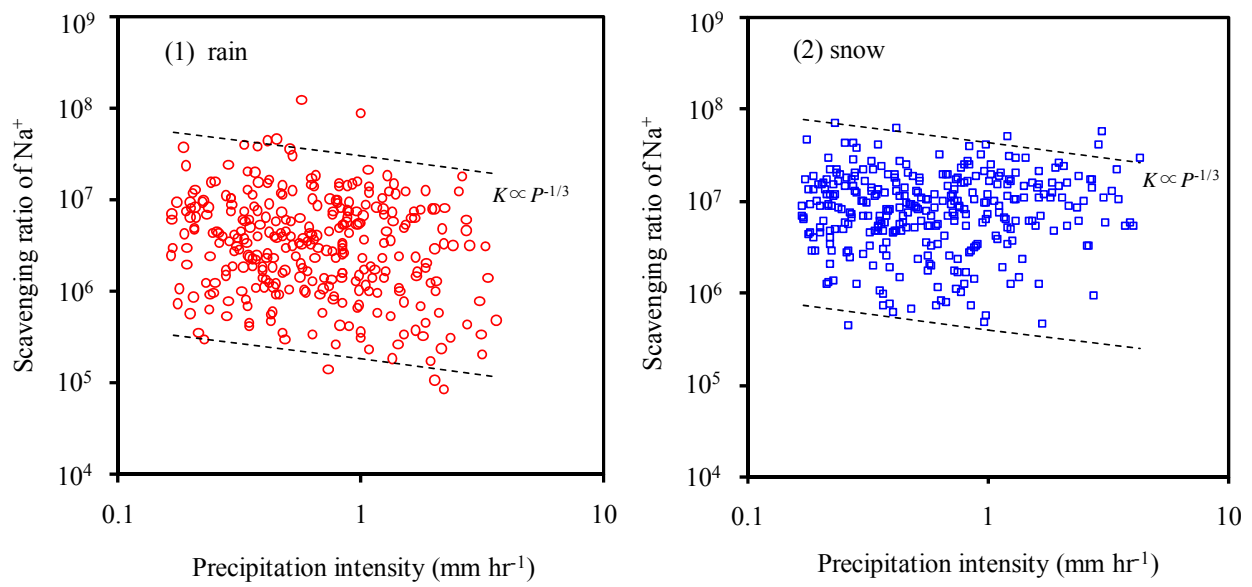


Fig. 4. Dependences of scavenging ratio of Na^+ on precipitation intensity for (1) rain and (2) snow.

3. Spatial distribution of scavenging ratio of Na^+

The scavenging ratio increased with the distance from the coast (Fig. 5). This tendency was observed for both snow and rain. In addition, the increase in scavenging ratio with the distance from the coast for snow might be smaller than that for rain. These results suggest that the scavenging mechanism of sea-salt aerosol would be different between the inland area and the coastal area.

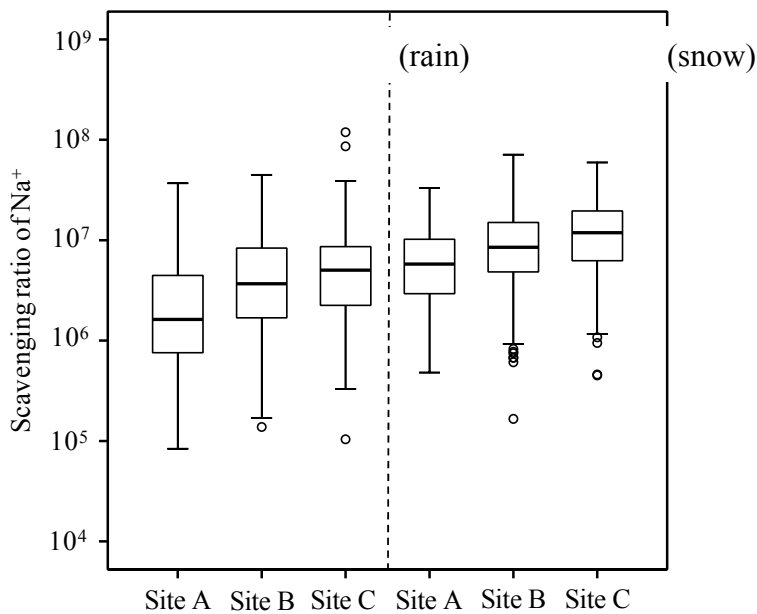


Fig. 5. Box-Whisker plots of scavenging ratio of Na^+ for rain and snow at the three sites.

CONCLUSION

By distinguishing between snow and rain, the scavenging ratio of Na^+ for snow is found to be higher than that for rain. The scavenging ratio of snow appeared to remain constant with precipitation intensity, whereas that of rain is inversely proportional to precipitation intensity. The scavenging ratios of snow and rain increased with the distance from the coast. It is concluded that snow can be a more efficient scavenger of sea-salt aerosol than rain in Niigata Prefecture during the winter season, and the scavenging mechanism of sea-salt aerosol would be different between the inland area and the coastal area.

ACKNOWLEDGMENTS

We wish to thank Tohoku Electric Power Company for helping us in the field measurements.

REFERENCES

- [1] Onodera, T.; Inukai, H.; Odashima, T. In *Proc. 13th International Workshop on Atmospheric Icing of Structures*, 1982
- [2] Sakata, G.; Homma, H., In *Proc. 2009 World Congress on Insulators, Arresters and Bushings*, 2009
- [3] Takahashi, A.; Fujita, S.; Sakata, G. In *Proc. 14th International Workshop on Atmospheric Icing of Structures*, 2009

- [4] Fukuzaki, N.; Kondo, S.; Maeda, M.; Totsuka, T. *J. Jpn. Soc. Atmos. Environ.* 2005, 40, 250-259
- [5] Fujita, S.; Okamura, K.; Miura, K.; Takahashi, A. *Earozoru Kenkyu* 2010, 25, 349-354
- [6] Takahashi, A.; Fujita, S.; Sakata, G. In *Proc. 2010 International Aerosol Conference*, 2010
- [7] Meteorological Research Institute, Japan *Technical Reports of the Meteorological Research Institute* 1984, 8
- [8] Matsuo, T.; Sasyo, Y. *J. Meteorol. Soc. Jpn.* 1981, 59, 10-25
- [9] Savoie, D. L.; Prospero, J. M.; Nees, R. T. *Atmos. Environ.* 1987, 21, 103-112
- [10] Harrison, R. M.; Allen, A. G. *Atmos. Environ.* 1991, 25A, 1719-1723
- [11] Fujita, S.; Takahashi, A. *J. Jpn. Soc. Air Pollut.* 1990, 25, 27-231
- [12] Sparmacher, H.; Fülber, K.; Bonka, H. *Atmos. Environ.* 1993, 27A, 605-618
- [13] Barrie, L. A. *J. Geophys. Res.* 1985, 90, 5789-5799

Heterogeneous Nucleation of Water Vapor onto Nanoparticles

Shusuke Nakajima, Yusuke Kuromiya, Yoshio Otani and Takafumi Seto

Department of Chemical and Material Engineering, Kanazawa University, Kakuma, Kanazawa, Ishikawa 920-1192, Japan

ABSTRACT

Laboratory-scale experiments of nucleation of water vapor onto aerosol particles were performed. In order to investigate the nucleation and growth process under precisely controlled supersaturation, we developed a laboratory-made particle growth tube (PGT). Being similar to the water CPC, the PGT was equipped with water-soaked tubular porous ceramics installed in the stainless steel tube with well-defined wall temperature profile. In the PGT, water vapor condenses onto the aerosol particles with different sizes depending on the supersaturation. Activation efficiencies of DMA-classified monodispersed aerosol particles were measured for the supersaturation from 1.4 to 3.1 by using an optical particle counter. As a result, the PGT was capable of activating 50% of 6-nm Ag particles at the supersaturation of $S = 1.8$. Computational fluid dynamics (CFD) simulation was introduced to calculate the profiles of temperature, gas velocity and vapor concentration in the PGT, and the activation efficiency was predicted by accounting for the local supersaturation distribution based on the classical nucleation theory (Kelvin-Thomson's theory). The predicted activation efficiency was in good agreement with the experimental data.

KEYWORDS

Nucleation, Condensation, Nanoparticles, Instrumentation

Introduction

Formation and long-range transport of atmospheric aerosol in the East Asia region has become of important issue. Heterogeneous nucleation of water vapor on hydrophilic/ hydrophobic secondary organic aerosol particles in nanometer size range is an initial step of atmospheric aerosol and cloud formations ^[1]. Laboratory-scale experiments are effective means to obtain detailed data of the atmospheric nucleation and growth rates depending on the nuclei size and chemical components. However the laboratory experiments are limited in application because high thermal diffusivity of water vapor causes significant wall losses. Therefore it is necessary to develop an instrument for the study of heterogeneous nucleation process of water vapor onto various kinds of

nanoparticles.

In this study, particle growth tube (PGT) is developed in order to analyze the nucleation process of nanoparticles. The PGT is equipped with water-soaked tubular porous ceramics installed in the stainless steel tube with a well-defined wall temperature profile. In the PGT, water vapor condenses onto the aerosol particles with different sizes depending on the supersaturation. Activation efficiencies of DMA-classified monodispersed aerosol particles are measured and they are compared with those predicted by the profiles of temperature, gas velocity and vapor concentration in the PGT calculated with a CFD simulation.

Experimental Methods

Figure 1 shows the schematic illustration of the PGT and the experimental setup used in this study. The test silver particles are generated by an evaporation-condensation method. The generated particles are charged to be in equilibrium state as they pass through the ^{241}Am bipolar charger. The size of test particles is controlled by classification with a differential mobility analyzer (DMA). The monodispersed particles are split into two flows. One of the flow is introduced to a CPC (TSI 3775, 50% detectable size of 4.0 nm) to measure the reference particle number concentration of test aerosol, and the other flow is introduced to the particle growth tube (PGT) of various supersaturations. Being similar to the water CPC [2], the PGT is equipped with water-soaked tubular porous ceramics (ID: 10 mm, L = 100 mm) installed in a stainless steel tube (ID: 20 mm, L = 100 mm). The wall temperatures of two parts (evaporator and condenser) are controlled with a temperature controller. In the PGT, water vapor condenses onto the aerosol particles with different sizes depending on the supersaturation. The saturation ratio is controlled by changing the temperature of heating unit from 40 to 74°C, while the cooling temperature is maintained at 5 °C. An optical particle counter (OPC; Rion KC-01C, detection range of larger than 0.3 μm) is used as a counter of the number concentration of grown droplets. The activation efficiency is defined by;

$$\eta = C_{\text{PGT}} / C_{\text{CPC}} \times 100 \quad (\text{Eq.1})$$

where C_{PGT} and C_{CPC} are the concentrations measured by PGT/OPC and the reference CPC.

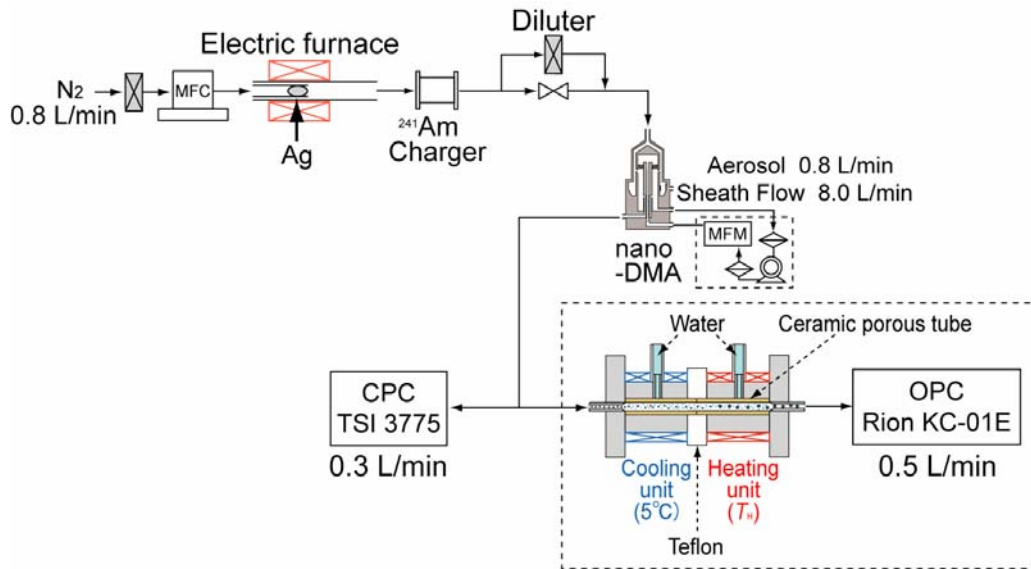


Fig. 1 Schematic illustration of the PGT and experimental setup.

Numerical Calculation of Activation Efficiency

In order to analyze nucleation and growth processes of nanoparticles theoretically, we employed a computation fluid dynamics (CFD) software, “Fluent (ver.6.3.26)”. The distributions of temperature, vapor concentration and velocity in PGT are calculated by solving the equations of momentum, energy and diffusion by a control volume method. Then, the local saturation ratio in PGT is calculated from the distributions of temperature and vapor concentration. Figure 2 shows the calculated profile of saturation ratio in PGT when the evaporator temperature is set at 74°C. As seen in the figure, the maximum saturation ratio ($S_{\max} = 3.1$) appears on the central axis at $x = 206$ mm. Similar profiles are obtained for a saturator temperature from 40 to 50°C. The critical diameter corresponding to the saturation ratio is calculated by the following Kelvin-Thomson’s equation^[3],

$$S^* = \exp \left[\frac{M}{\rho RT} \left\{ \frac{4\gamma}{D_p} - \frac{q^2 (1 - 1/\varepsilon)}{2\pi\varepsilon_0 (D_p)^4} \right\} \right] \quad (\text{Eq.2})$$

where S^* is the critical supersaturation ratio, M the molecular weight, ρ the density, R the universal gas constant, T the absolute temperature, γ the surface tension, D_p the particle diameter, ε the dielectric constant and ε_0 is the space permittivity. The flow region which gives the local saturation ratio larger than S^* is determined from the distribution of supersaturation in the PGT and the fraction of volumetric flow rate through the region, which is equal to the activation efficiency, is determined.

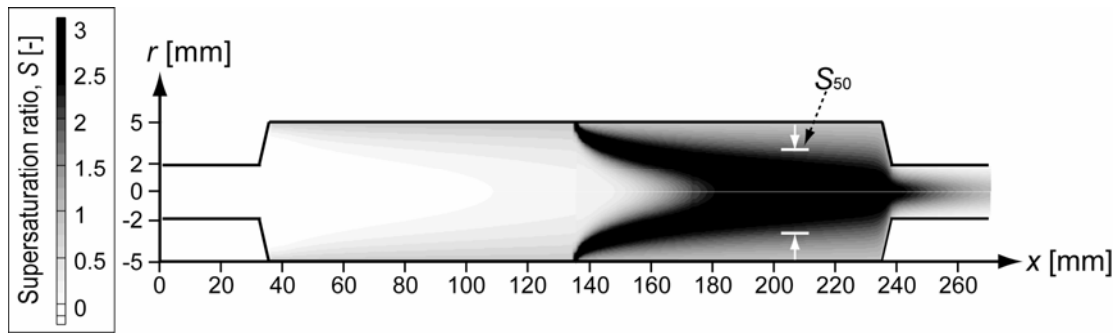


Fig. 2 Distribution of saturation ratio in PGT at $T_H = 74^\circ\text{C}$.

Results and Discussion

Figure 3 shows the comparison of experimental activation efficiencies (solid circles) with those calculated by CFD (solid line) at the saturator temperature of $T_H = 50^\circ\text{C}$. We cannot measure D_{p50} when the supersaturation is over 1.5 because the grown droplets are too large to be measured by the OPC (probably because of gravitational wall loss in the instrument). In Fig.3, the experimental activation efficiencies are in fairly good agreement with the predicted line, indicating that the PGT is capable of activating 50% of 6-nm Ag particles and 90% of 14-nm particles at $T_H = 50^\circ\text{C}$.

In Figure 4, the 50% activation diameters, D_{p50} , the particles with which are activated by 50% at $T_H = 40, 45$, and 50°C , are plotted as a function of supersaturation ratio. The solid line in Fig. 4 is the theoretical curve calculated by Eq. (2). The flow region which gives 50% of total volumetric flow rate is depicted by S_{50} in Fig.2 (all particles passing through this region are activated). As seen in Fig.4, the experimental data are in good agreement with the predicted line, suggesting that the 50% activation diameter is well predicted by accounting for the local distribution of supersaturation. However, we cannot measure the 50% activation diameter when S_{50} is higher than 3.1, which corresponds to the theoretical minimum detection limit of 1.9 nm. Therefore further improvement of PGT is necessary in order to activate smaller nanoparticles.

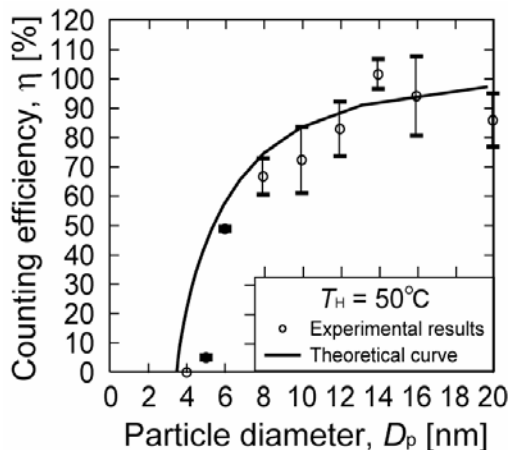


Fig. 3 Comparison of measured activation efficiency with those calculated by numerical calculation at $T_H = 50^\circ\text{C}$.

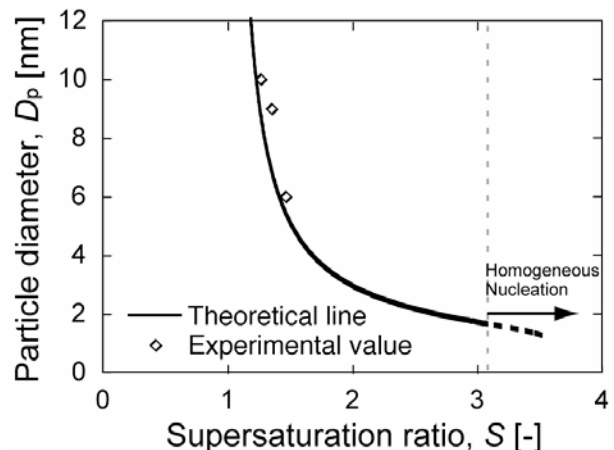


Fig. 4 Comparison of experimental and theoretical 50% activation particle diameter

SUMMARY

In order to investigate the process of nucleation and growth of water vapor onto nanoparticles, we developed a prototype PGT. The activation efficiency calculated by accounting for the local supersaturation obtained with a CFD simulation is in fairly good agreement with the experimental data. We also found that the PGT has potential to activate nanoparticles as small as 1.9 nm but further improvement is necessary to achieve this high activation efficiency.

REFERENCES

- [1] Sipilä, M.; Berndt, T.; Petäjä, T.; Brus, D.; Vanhanen, J.; Stratmann, F.; Patokoski, J.; Mauldin, R.L.; Hyvarinen, A.; Lihavainen, H.; Kulmala, M. *Science*. 2010, 327, 1243-1246.
- [2] Hering, S.V.; Stoltzenburg, M.R. *Aerosol Sci. Technol.* 2005, 39, 428-436.
- [3] Thomson, J.J. *Conduction of electricity Through Gases*, Cambridge University Press, London, 1906.

Durability Investigation of Carbon Supported Platinum Electrocatalysts Synthesized by Microwave Polyol Method

Yu-Chun Chiang^{1*}, Jinxiao Zhao^{1,2}, Jhao-Ruei Ciou¹, Zhaoping Zhong² and Shih-Yu Lin³

1 Department of Mechanical Engineering, Yuan Ze University, 135 Yuan-Tung Rd., Chung-Li, Taoyuan 320, Taiwan.

2 School of Energy and Environment, Southeast University, Nanjing 210096, China.

3 Department of Mechanical Engineering, Hwa Hsia Institute of Technology, Taipei, Taiwan.

ABSTRACT

Due to the simple and rapid processes, the microwave-assisted polyol method has received much attention as a promising technique for preparation of metal nanoparticles with small particle sizes and narrow size distributions. The platinum (Pt) nanoparticles supported on carbon black, currently the most widely used electrocatalysts in proton exchange membrane fuel cells, tend to degrade under extended operating conditions, probably due to the agglomeration/dissolution of Pt particles or the corrosion of the carbon support. Therefore, in the present study the microwave-assisted polyol technique was utilized to prepare the Pt nanoparticles supported on two nano-scale carbon supports, carbon nanotubes (CNTs) and Vulcan XC-72R (VXR), with a Pt loading of 20 wt. %. The ethylene glycol was acted as both solvent and reducing agent, and the pH value of the reaction solution was adjusted to 7 by KOH solution. The mixture was placed in a household microwave oven (Tatung, 800 W) and heated for 90 s. One commercial Pt/C catalyst (E-TEK) was used for comparison. The results show that Pt nanoparticles were dispersed uniformly on the surface of different carbon supports. The mean particle sizes of Pt were 3.1 ± 0.33 , 3.9 ± 0.26 and 2.9 ± 0.47 nm for Pt/CNTs, Pt/VXR and Pt/C catalysts. The microwave synthesized Pt nanoparticles supported on CNTs and VXR formed a face-centered cubic structure. The TGA profiles indicated that Pt/CNTs performed better oxidation resistance. The estimations of the electrochemical surface area (ESA) were 55, 58 and $64 \text{ m}^2/\text{g}$ for Pt/CNTs, Pt/VXR and Pt/C catalysts, but the degradation of the ESA after 600 cycles were 16, 21 and 28 %, respectively. The data suggested that the ESA of Pt/CNTs or Pt/VXR prepared by microwave method was comparable to the commercial Pt/C and the Pt/CNTs exhibited better durability than other samples.

KEYWORDS

Carbon nanotubes; Platinum nanoparticles; Catalyst support; Cyclic voltammetry; Durability

Introduction

Metal nanoparticles supported on carbon materials with high surface area have been used extensively as catalysts for a wide variety of applications, where carbon black supported platinum nanoparticles (Pt/C) are currently known as the most widely used electrocatalysts in proton exchange membrane fuel cells (PEMFCs). There are several methods for preparing Pt nanoparticles on carbon supports, such as microwave-assisted polyol method^[1-2], impregnation method^[3-4], micro-emulsion method^[5-6], colloidal method^[7-8], co-precipitation method^[9], alcohol reduction method^[10-11]. Among them, the microwave-assisted polyol method has received much attention as a promising technique for preparation of Pt nanoparticles with small particle sizes and narrow size distributions.

The catalytic activity of the metal particles is strongly dependent on their size and size distribution. The Pt particles prepared by a polyol process assisted with pulse microwave activation had a mean particle size of 2.5 nm and displayed higher active surface areas toward oxygen reduction reaction than the one prepared by conventional polyol method^[1]. Li et al.^[2] synthesized Pt nanoparticles supported on carbon nanotubes (Pt/CNTs) by microwave polyol process, finding the solution pH was an important factor that influenced the metal size. The Pt particles became smaller (from 5.8 to 2.7 nm) and were better dispersed on CNTs when the solution pH increased from 3.4 to 9.2. When the solution pH was 7.4, Pt/CNTs exhibited the better performance for methanol electrooxidization. Wang et al.^[12] and Radziuk et al.^[13] studied the effect of ultrasonic treatment on polyol method and found a longer treatment time was needed to form crystalline or amorphous Pt nanoparticles, where ethylene glycol acted as the solution preventing the destruction of Pt crystals. Moreover, it was reported that the activity of Pt/C catalysts was related to the microwave heating time and the optimal performance was observed when the heating time was 40 s^[14].

The durability of the Pt/C nanoparticles is one of the major concerns when they are used as the electrocatalysts for fuel cells^[15]. The degradation of cathode catalyst for oxygen electroreduction was one of the main factors affecting on the performance decay of PEMFC^[16]. Adding a dispersion of Nafion® ionomer to the ink containing the Pt precursor produced more durable Pt/C catalysts because the Pt particles were protected against dissolution and sintering by the surrounding Nafion layer^[17]. A durability study reported that the Pt structure changed during the single fuel cell test and sulfate from Nafion would react with the Pt forming PtS^[18]. It has been shown that the electrochemical surface area (ESA) decreased more rapidly under higher humidity and higher oxygen concentrations^[19].

Pt/C catalysts are though known as a promising electrocatalyst in PEMFCs, they tend to degrade under extended operating conditions, probably due to the agglomeration/dissolution of Pt

particles or the corrosion of the carbon support. Therefore, in the present study the microwave-assisted polyol technique was utilized to prepare the Pt nanoparticles supported on two nano-scale carbon supports, carbon nanotubes (CNTs) and Vulcan XC-72R, with a Pt loading of 20 wt %. One commercial Pt/C catalyst (E-TEK) was used for comparison.

Experimental Methods

The CNTs used in this study was the multi-walled CNTs, which was provided by Conyuan Biochemical Technology Co. of Taiwan. The Vulcan XC-72R was supplied by Cabot. The microwave-assisted polyol method was conducted to prepare the carbon supported Pt nanoparticles (20 wt % Pt), where ethylene glycol (EG) was acted as both solvent and reducing agent. First, 2 ml aqueous solution of H_2PtCl_6 (50 mM) and 80 mg carbon supports were added into 50 ml EG. The mixture was ultrasonically treated for 2 h to ensure the carbon supports uniformly dispersed in the solution. Next, the pH value of the mixture was adjusted to 7 by KOH. Then the mixture was mixed with the assistance of ultrasonic vibration for another 2 h. After that, the mixture was placed in a household microwave oven (Tatung, 800 W) and heated for 90 s. The solution was centrifuged, and the collected solids were washed with acetone and de-ionized water, and then dried in a vacuum oven at 373 K for 24 h. The CNTs and Vulcan XC-72R supported Pt nanoparticles were denoted as Pt/CNTs and Pt/VXR, respectively. One commercial Pt/C catalyst (E-TEK) was used for comparison.

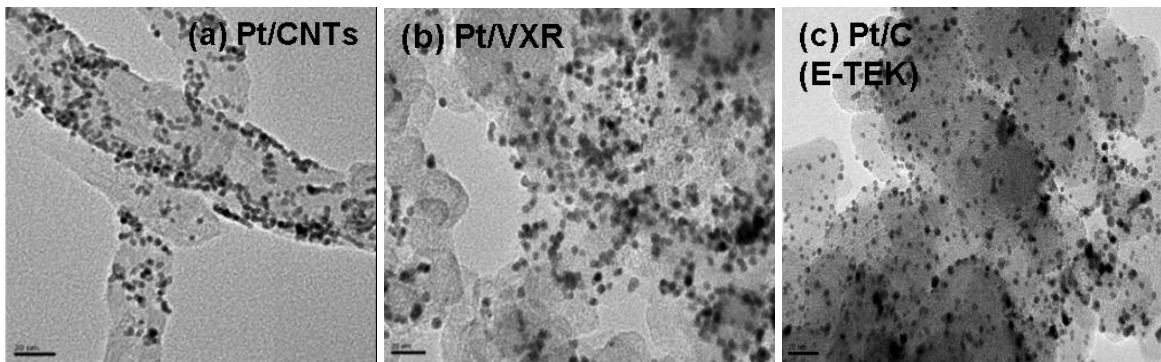
The size distribution and dispersion of the Pt particles on carbon supports were examined by High-Resolution Transmission Electron Microscopy (HRTEM, JEOL JEM2010F). The crystallinity of the Pt particles was determined by X-ray diffraction (XRD, Japan MAC Science, MXP18). The radiation used was $Cu K\alpha$ with a wavelength of 0.15418 nm. The 2-theta (2θ) ranged from 10° to 90° , where θ is the diffraction angle. Thermal analysis was carried out in a thermogravimetric analyzer (Dynamic TGA 2950 in TA Instrument 5100), measuring changes in the weight of a sample as a function of temperature (thermogravimetric analysis, TGA, plot) and the rate of weight loss versus temperature (differential thermogravimetry, DTG, plot). A CHI 614C electrochemical workstation was employed for the electrochemical study of carbon supported Pt samples. The working electrode was a thin layer of Nafion-impregnated catalyst sample cast on a vitreous carbon electrode. A Pt wire and a saturated calomel electrode (SCE) were used as the counter and reference electrodes, respectively. The measurements of cyclic voltammetry (CV) were conducted at room temperature using 0.5 M H_2SO_4 as the electrolyte solution at a scan rate of 20 mV/s from -0.4 – 0.8 V vs. SCE.

Results and Discussion

HRTEM Images

Figure 1 shows HRTEM images of Pt nanoparticles supported on CNTs and VXR, and for comparison, the micrograph of Pt/C (E-TEK) is also presented. These images indicated that the Pt particles were uniform and well distributed on all of the carbon surfaces. The mean sizes of Pt particles were 3.1 ± 0.3 , 3.9 ± 0.3 and 2.9 ± 0.5 nm for Pt/CNTs, Pt/VXR and Pt/C, respectively.

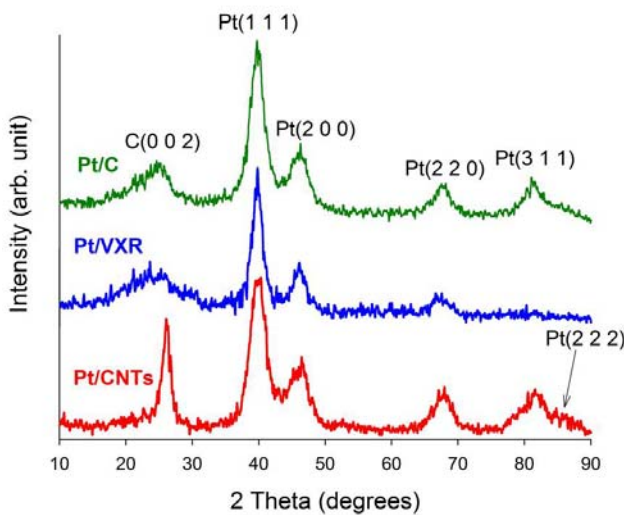
Figure 1. HRTEM images and Pt particle size distributions of all samples.



XRD Analysis

The XRD patterns for all samples were shown in Figure 2. The peak C(002) at about $2\theta = 26^\circ$ can be attributed to the graphite structure of CNT, while the characteristic peak of carbon black was shifted to about 25° . The XRD patterns all indicated five characteristic f.c.c. Pt peaks, indexed as Pt(111), Pt(200), Pt(220), Pt(311) and Pt(222). But both Pt (311) and Pt (222) were not significant on Pt/VXR catalysts.

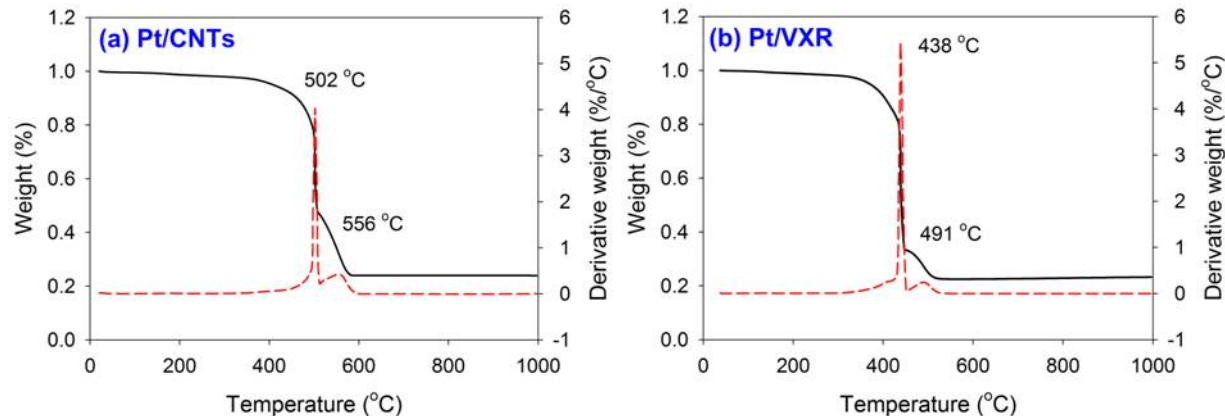
Figure 2. XRD patterns for all samples.



TGA

Oxidation resistance of the carbon support plays an important role on the electrochemical performance of the carbon-based Pt catalyst. Figure 3 gives the TGA and DTG profiles measured in flowing air for Pt/CNTs and Pt/VXR samples, where the samples were heated at a heating rate of 10 °C/min. The temperatures of the maximum rate of weight loss for Pt/CNTs and Pt/VXR were 502 and 438 °C, respectively, and both were higher than that of commercial Pt/C (401 °C, not shown here). As seen from the data, the CNTs-based Pt catalysts exhibited the higher resistant to oxidation than carbon black-based ones. It could be attributed to the graphite structure and tubular form of CNTs. In addition, the residue revealed that the Pt content was approximately 20 wt. %, close to the designed value.

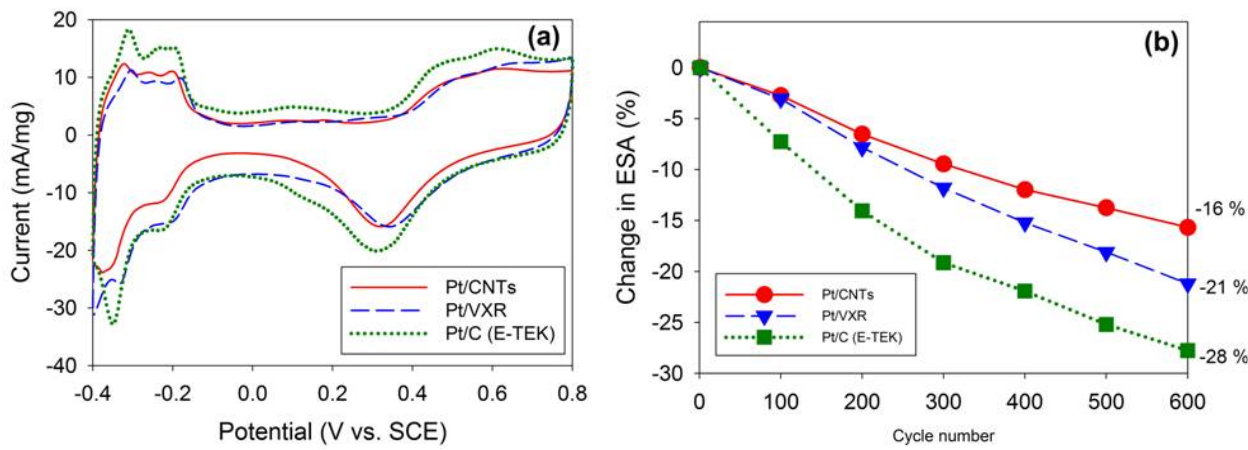
Figure 3. TGA and DTG profiles of Pt/CNT (a) and Pt/VXR (b).



CV Analysis

The cyclic voltammograms of Pt/CNTs and Pt/VXR are shown in Figure 4 and that of commercial Pt/C is also presented for comparison. All voltammograms display a well-defined hydrogen adsorption/desorption region (-0.4 to -0.1 V vs. SCE). It is clear that Pt/CNTs had a narrower width of the double layer region than Pt/VXR and Pt/C. The estimations of the ESA were 55, 58 and 64 m²/g for Pt/CNTs, Pt/VXR and Pt/C catalysts, but the degradation of the ESA after 600 cycles were 16, 21 and 28 %, respectively. The data suggested that the ESA of Pt/CNTs or Pt/VXR prepared by microwave method was comparable to the commercial Pt/C and the Pt/CNTs exhibited better durability than other samples.

Figure 4. Cyclic voltammograms (a) and degradation of ESAs for all samples.



CONCLUSIONS

Carbon supported Pt electrocatalysts were prepared successfully by microwave polyol method. Mean size of Pt particles were 3.1 ± 0.3 , 3.9 ± 0.3 and 2.9 ± 0.5 nm for Pt/CNTs, Pt/VXR and commercial Pt/C catalysts, separately. The XRD patterns indicated C(002) and five characteristic f.c.c. Pt peaks. The CNTs-based Pt particles performed a higher potential for oxidation resistance. The electrochemical activity for the samples prepared by microwave polyol method was comparable to the commercial Pt/C catalysts. It should be noted that the electrochemical stability of Pt/CNTs was superior to other samples. Specifically, the changes in ESA after 600 cycles were 16 % (Pt/CNTs), 21 % (Pt/VXR) and 28 % (Pt/C, E-TEK), respectively. This may be associated with the intrinsic structure of CNTs and the network structure formed by CNTs. As a result, the CNTs have been approved to be a candidate as a support for Pt particles and the microwave polyol method has also been verified as a promising technique for preparation of electrochemically active Pt nanoparticles.

REFERENCES

- [1] Lebègue, E.; Baranton, S.; Coutanceau, C. *J. Power Sources* 2011, 196 (3), 920-927.
- [2] Li, X.; Chen, W.X.; Zhao, J.; Xing, W.; Xu, Z.D. *Carbon* 2005, 43 (10), 2168-2174.
- [3] Kawaguchi, T.; Sugimoto, W.; Murakami, Y.; Takasu, Y. *J. Catal.* 2005, 229 (1), 176-184.
- [4] Takasu, Y.; Matsuyama, R.; Konishi, S.; Sugimoto, W.; Murakami, Y. *Electrochim. Solid State Lett.* 2005, 8 (9), B34-B37.
- [5] Solla-Gullón, J.; Gómez, E.; Vallés, E.; Aldaz, A.; Feliu, J. *J. Nanoparticle Res.* 2010, 12 (4), 1149-1159.
- [6] Rong, C.; Jiang, R.; Sarney, W.; Chu, D. *Electrochimica Acta* 2010, 55 (22), 6872-6878.

- [7] Escobar Morales, B.; Gamboa, S.A.; Pal, U.; Guardián, R.; Acosta, D.; Magaña, C.; Mathew, X. *Int. J. Hydrot. Energy* 2010, 35 (9), 4215-4221.
- [8] Wu, Y.; Liao, S.; Wang, K.; Chen, M.; Birss, V. *Sci. China Technol. Sci.* 2010, 53 (1), 264-271.
- [9] Guo, D.J.; Jing, Z.H. *J. Power Sources* 2010, 195 (12), 3802-3805.
- [10] Górzny, M.Ł.; Walton, A.S.; Evans, S.D. *Adv. Funct. Mater.* 2010, 20 (8), 1295-1300.
- [11] Ribeiro, V.A.; Correa, O.V.; Neto, A.O.; Linardi, M.; Spinacé, E.V. *Appl. Catal.* 2010, A372 (2), 162-166.
- [12] Wang, Z.C.; Zhao, D.D.; Zhao, G.Y.; Li, H.L. *J. Solid State Electrochem.* 2009, 13 (3), 371-376.
- [13] Radziuk, D.; Mohwald, H.; Shchukin, D. *J. Phys. Chem.* 2008, C112 (49), 19257-19262.
- [14] Chu, Y.Y.; Wang, Z.B.; Gu, D.M.; Yin, G.P. *J. Power Sources* 2010, 195 (7), 1799-1804.
- [15] Yu, X.; Ye, S. *J. Power Sources* 2007, 172 (1), 145-154.
- [16] Wang, Z.B.; Zuo, P.J.; Chu, Y.Y.; Shao, Y.Y.; Yin, G.P. *Int. J. Hydrot. Energy* 2009, 34 (10), 4387-4394.
- [17] Curnick, O.J.; Mendes, P.M.; Pollet, B.G. *Electrochem. Commun.* 2010, 12 (8), 1017-1020.
- [18] Mamat, M.S.; Grigoriev, S.A.; Dzhus, K.A.; Grant, D.M.; Walker, G.S. *Int. J. Hydrot. Energy* 2010, 35 (14), 7580-7587.
- [19] Ohyagi, S.; Matsuda, T.; Iseki, Y.; Sasaki, T.; Kaito, C. *J. Power Sources* 2011, 196 (8), 3743-3749.

A Dynamic Aerosol Generation System for Aerosol Sensor Calibration

Qiaoling Liu¹ and Da-Ren Chen¹

¹ Department of Energy, Environmental & Chemical Engineering, Washington University in St. Louis, Brauer Hall, Campus Box 1180, One Brookings Drive, St. Louis, MO, 63130

ABSTRACT

Airborne particles in the ambient are often time-varied in concentration and size. It is because of either the time-variation or moving of particle sources. Existed aerosol generators or techniques are however designed to produce stable aerosol in constant concentration. In our effort of developing personal aerosol sensors it becomes desired to evaluate the performance of aerosol sensors under the challenge of time-varying aerosol in the laboratory setting. A new dynamic polydisperse aerosol generation system, enabling the programmable variation of test aerosol concentration, is thus developed. The dynamic aerosol generation system consists of a custom-made Collison atomizer and dynamic aerosol dilution chamber. The atomizer generates polydisperse aerosols in fixed concentration and size distribution. Produced aerosol is then diluted in the mixing chamber by clean air while keeping the same particle size distribution as original. A mass flow controller is used to program the time-variation of dilution flow into the mixing chamber. A computer program is designed to control the system setting time, time-varying dilution flowrate ratio, and to establish the stepping/continuous mode of dilution process. In this study the performance of the above-described dynamic aerosol system is evaluated by a condensation particles counter (CPC) for total number concentration, quartz crystal microbalance (QCM) for total mass concentration and Fast Mobility Particle Sizer (FMPS) for size distribution measurement. We will present the detail of system setup and evaluation result in this talk.

KEYWORDS

Aerosol Generator, Dynamic Aerosol, Aerosol Sensor Calibration, Time-varied, Dilution

Introduction

Because of the dynamics of particle sources, ambient particles are often time-varied in the physical property, such as concentration and size. Existed laboratory aerosol generators are however developed to produce stable aerosol in concentration and fixed size distribution.

These aerosol generators are good for the calibration of aerosol instruments. The performance of aerosol instruments is typically evaluated under stable laboratory aerosol condition. We however have no means in the laboratory to investigate the response of aerosol instruments or monitors under the dynamic aerosol condition. The above information is of importance in the experimental evaluation of an instrument because it enables us to understand how the instruments will be behaved when used in the ambient environment. If an instrument was slow responding, the measured data would not be representative for actual particle dynamics. It is thus desired to develop a dynamic polydisperse aerosol generation system for evaluating the performance of aerosol sensors.

Our ultimate goal in this study is to develop a programmable aerosol system to generate time-varied polydisperse aerosol. Two specific challenges in this development are: (1) to produce well-defined size distribution of particles under a wide range of aerosol dilution ratio; (2) to precisely control various modes of dilution.

Experimental Methods

To develop this new dynamic polydisperse aerosol generation system, a custom-made collision atomizer, mass flow controller and dynamic aerosol dilution tube were used. Figure 1 shows the schematic diagram of experimental setup for the system. A custom-made Collison atomizer generated polydisperse aerosols in a stable concentration and size distribution from its aqueous solutions (e.g. 0.01% KCl). Generated aerosol was then delivered into a cylindrical aerosol dilution tube. Particle-free dilution air was injected into the tube in radial direction (see Figure 1). The flowrate of dilution air was controlled by a mass flow controller (MFC) to achieve the desired dilution ratios according to the computer program. A perforated screen or woven mesh was used in the upstream part of dilution tube to produce a well-controlled turbulent flow for mixing aerosol flow with clean dilution air. As an aerosol generator it is desired to have the same size distribution of particles as that originated after the mixing. At the tube exit excess aerosol flow after the dilution can be discharged via an excess flow outlet.

In this study, scanning mobility particle sizer (SMPS) was used to characterize the performance of the above-described dynamic aerosol system for its steady state total number concentration and particle size distribution. The transient behavior of dynamic aerosol was further characterized by a quartz crystal microbalance (QCM) for total mass concentration and Fast Mobility Particle Sizer (FMPS) for size distribution measurement.

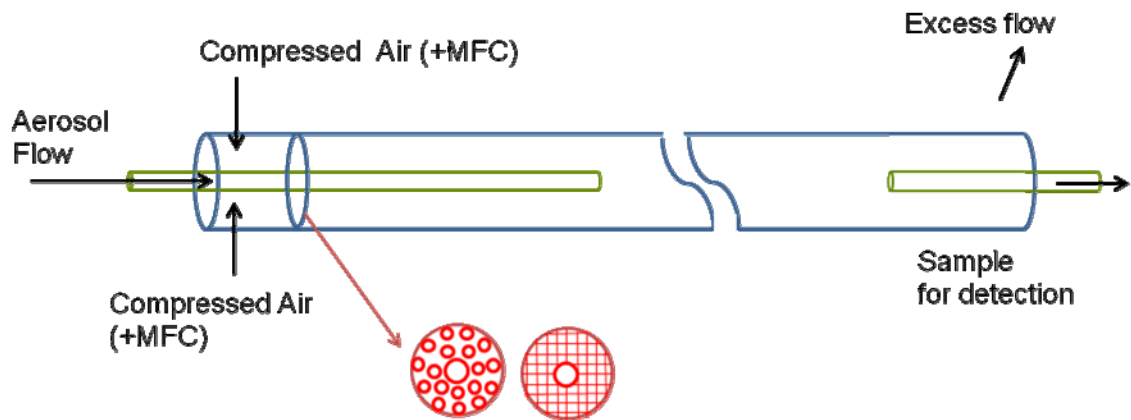


Figure 1 Experiment Setup for Dynamic Aerosol Generation System

Results and Discussion

The proposed new dynamic polydisperse aerosol generation system with programmable time-varied aerosol concentration is thus developed. A small software written in Visual Basic language is shown in Figure 2. This program is designed to control the system running time, time-varying dilution flowrate ratio and detector working time. It can be used to control analyzer's software to trigger measurement once or continuously within a certain measurement period. Four kinds of dilution modes are set in the program: continuously single dilution ratio mode, rectangular wave type of dilution process, stepping mode of dilution process and continuously uprising dilution mode. Users can select one dilution mode among four and set the run time, dilution ratio or dilution air flowrate desired. The program has been tested for a long period of system operation in order to demonstrate it's stable, reliable, flexible and user friendly.

To characterize the performance of dynamic polydisperse aerosol generation system, SMPS was firstly introduced as an instrument for evaluating the steady state performance of system. Particle number concentration and size distribution were obtained during this part of experiment. Tests on perforated screens all showed that particle number concentration decreased along with increasing dilution ratio. Actual aerosol dilution ratios (defined as diluted aerosol concentration/original aerosol concentration) were not exactly the same as dilution ratios derived from the flowrate. Particle size distribution after the dilution was kept in the same shape in any designed dilution mode, but particle mode diameter shifted to the small diameter range, for example from 52 nm in original distribution to 47.5 nm in diluted one under the high dilution case, such as, 2 lpm aerosol flow: 200 lpm dilution air flow. The observation indicates particle loss happened in the cases with very high dilution air flowrate.

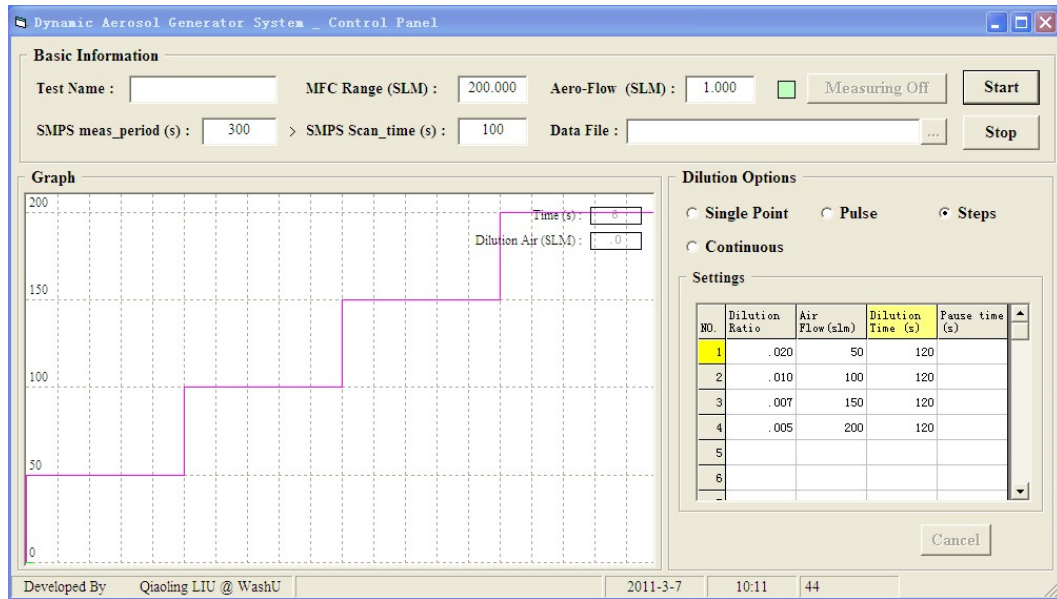


Figure 2 Visual Basic Program for Controlling Dynamic Aerosol Generation System

SUMMARY OR CONCLUSION

In our effort of developing dynamic polydisperse aerosol generation system for the evaluation of the dynamic performance of aerosol sensors or instruments, we have completed the design of programmable dilution ratio controller and the controller performance has been tested for its long time operation. We have achieved the dilution ratio of 50 without altering the shape of particle size distribution (as originated). Continuous efforts are ongoing to achieve the dilution ration of 100 by improving the configuration of dilution tube. Further experimental result will be given in this presentation.

The Advanced Aerosol Neutralizer

Markus Gaelli¹, Stan Kaufman¹, Philip Poeschl¹ and Rob Caldow¹

1 TSI Incorporated, 500 Cardigan Road, Shoreview, MN 55126, USA

Principal Contact: Markus Gaelli, TSI Inc., 500 Cardigan Rd, Shoreview, MN 55126, USA.

Tel: +1-651-490-3898 Fax: +1-651-490-4025 E-mail: markus.gaelli@tsi.com

Abstract

Aerosol neutralization is important for many measurement techniques used in the field of Aerosol science and technology, including DMAs, SMPS systems, and APMs. All these instruments depend on a known, stable charge distribution. Most neutralizers available rely on radioactive material to achieve this charge distribution. More and more stringent regulations can make the use of radioactive neutralizers very difficult, if not impossible. A number of different non-radioactive neutralization approaches have been investigated. However, most of them have problems such as inconsistent charge distributions, particle production, and the inability to neutralize highly charged aerosols.

We present a new Advanced Aerosol Neutralizer, based on the use of soft X-rays for charge neutralization in aerosols. It provides a number of advantages:

- It does not use any radioactive material, posing fewer regulatory challenges.
- It works on the same ionizing principle as the radioactive devices, so the final charge distribution is similar to the ones obtained with radioactive neutralizers.
- The x-rays can be turned on and off on demand, which enhances the lifetime of the neutralizer.
- The neutralizer has been designed to fit into existing instruments such as the 3080 Electrostatic Classifier and the 3034 SMPS.

The Advanced Aerosol Neutralizer has been extensively tested, covering a wide range in particle size, concentration, polarity, charge state, and composition. Very good agreement between the Advanced Aerosol Neutralizer and radioactive neutralizers was found in size distribution measurements.

Keywords: Aerosol neutralization, non-radioactive, soft X-ray.

Experimental Study of Axial-flow Cyclone in the Air Handing Unit

Seyoung Kim^{1,4}, Soon-Bark Kwon¹, Duck-Shin Park¹, Youngmin Cho¹, Joon-Goo Kang², Chang-Heon Shin³, Myungjoon Kim⁴ and Taesung Kim⁴

¹ Korea Railroad Research Institute, Woram,Uiwang, 437-757, Korea

² RITCO, Ywoksam, Seoul, 120-700, Korea

³ Seoul Metro, Dongjak, Seoul, 156-080, Korea

⁴ Sungkyunkwan University, Chonchon, Suwon, 440-746, Korea

ABSTRACT

Particulate matter (PM) is one of the major indoor air pollutants especially in the subway station in Korea. In order to remove PM in the subway station, several kinds of PM removal system such as medium filter, auto suction filter, auto washing filter and electrostatic precipitator are used in the air handling unit (AHU) of subway stations. However, those systems are prone to operation and maintenance problems since the filter-regeneration unit consisting of electrical or water jet parts might malfunction due to the high load of particulates unless the filter medium is periodically replaced.

In this study, we developed a novel particle removal system with minimized maintenance requirement comparing to above mentioned methods. The novel system consists of cyclone units and dust trap was developed based on previous numerical study. The mock-up system was evaluated by particle collection efficiency and pressure drop experimentally. The results obtained from particle number concentration showed that the collection efficiency of 41.2 ~ 85.9% for the particles of 1 ~ 6.5 μm with the pressure drop of less than 20 mmH₂O. The collection efficiency estimated by total mass collection also showed 65.7% which was higher than that of current filter system by 2 times. We believed that the novel axial-flow cyclone system is cost-effective and efficient way of removing particulate matters in the size range of 1~10 μm in the AHU of subway station or buildings.

KEYWORDS

Air handing unit, Axial-flow cyclone, Air filter, Subway station

Introduction

Since the first Korean subway line was opened in 1974, the subway network system has been expanded to cover Seoul metropolitan area and other cities, Busan, Daegu, Daejeon, and

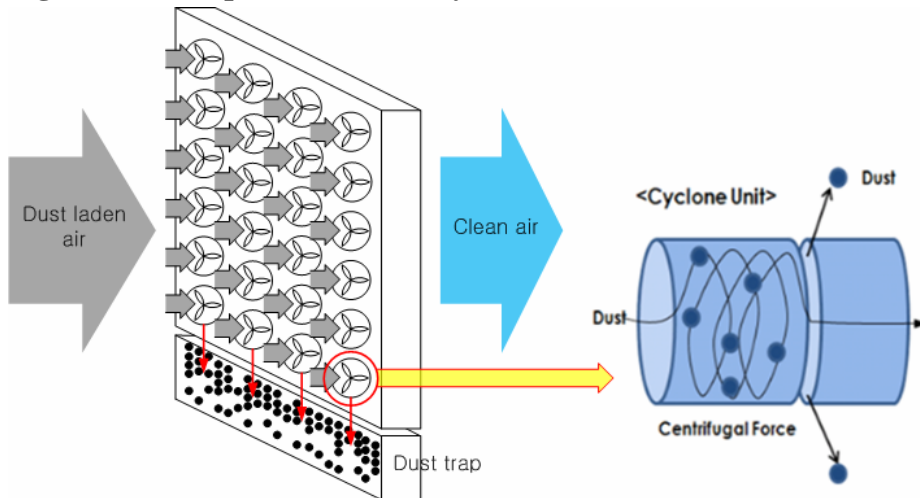
Gwangju and their traffic share among public transportation has been increased significantly. According to statistics compiled from Korean Ministry of Land, Transport and Maritime affairs (MLTM), a number of daily nationwide subway system users are about 7.2 million in 2009 and it is still increasing [1].

In Korea, particulate matter (PM) is one of the major indoor air pollutants especially in the subway. In order to remove PM in the subway station, several kinds of PM removal system such as medium filter, auto suction filter, auto washing filter and electrostatic precipitator are used in the air handling unit (AHU) of subway stations. However, those systems are prone to operation and maintenance problems since the filter-regeneration unit consisting of electrical or water jet parts might malfunction due to the high load of particulates unless the filter medium is periodically replaced.

Cyclones are particle collectors which utilize the centrifugal force created by flow vortexes in the devices to capture particles of high inertia. Because of the low cost of manufacturing, operating and maintaining cyclones, they are widely used in a variety of industrial sectors. This device has some advantages such as, constant pressure drop, high throughput with moderate efficiency and low maintenance cost [2].

There are only few researches which studied the axial-flow cyclones compared to those on the tangential-flow cyclone. *Nieuwstadt et al.* reported a fluid-mechanics model for the axial-flow cyclone [3], and *Maynard* studied axial-flow cyclone performance under laminar flow condition theoretically [4]. *Hsu et al.* argued that axial-flow cyclone can collect ultrafine particles [5], and *Tsai et al.* performed a research on the axial-flow cyclone operated in vacuum conditions [6]. In this study, we developed a novel concept of panel-type cyclone system, designed the axial-flow cyclone, and evaluated it using experimental method. The novel axial-flow cyclone system was analyzed in terms of particle collection efficiency and pressure drop.

Figure 1. Concept of axial-flow cyclone.

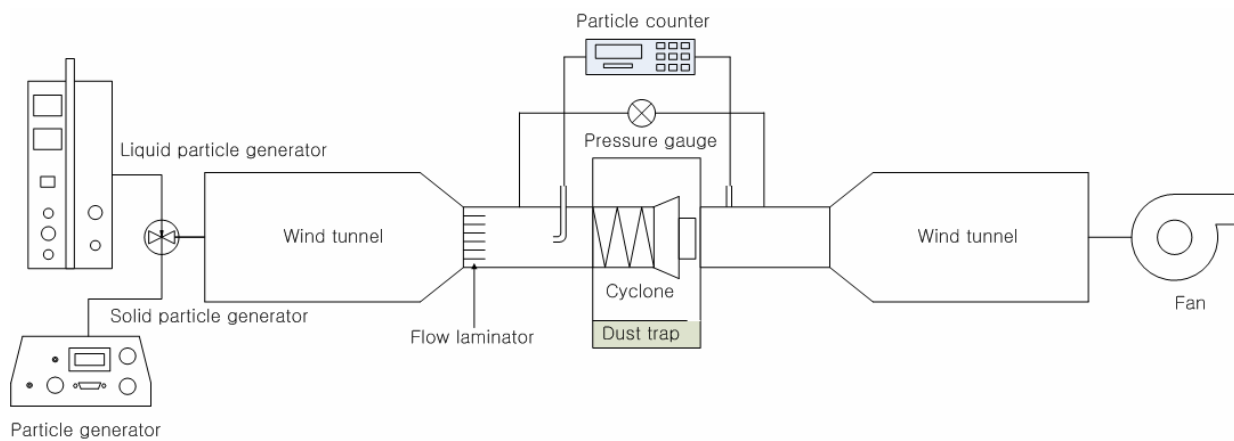


Experimental Methods

Mock-up model was designed using the previous study about the simulation data [7]. We selected model based on the simulation result which they have optimum condition such as, collection efficiency and pressure drop. Fig. 2 shows the experimental setup, which consist of mock-up model, particle generator, wind tunnel, sampling tube, pressure gauge, and fan. Upstream and downstream of axial-flow cyclone were installed additional acrylic duct, because area of wind tunnel (600 mm x 600 mm) and axial-flow cyclone (210 mm x 360 mm) were different. Inlet velocity of flow was set to 2.5 m/s and flow velocity in wind tunnel was measured in front of wind tunnel by flow meter (EBT 721, TSI). Because the typical face velocity of air filter in an AHU is 2.5 m/s in Korea. Test particles were used two types of liquid and solid particles by MAG3000 (PALAS) and SAG410 (TOPAS), respectively.

To calculate particle collection efficiency of axial-flow cyclone, a particle counter (Dust spectrometer, Grimm model 1.108) was used to measure the particle concentration in the upstream and downstream of the axial-flow cyclone. Pressure drop measurement was carried out by measuring pressure difference between the points upstream and downstream.

Figure 2. Experimental setup for particle collection efficiency and pressure drop measurement.



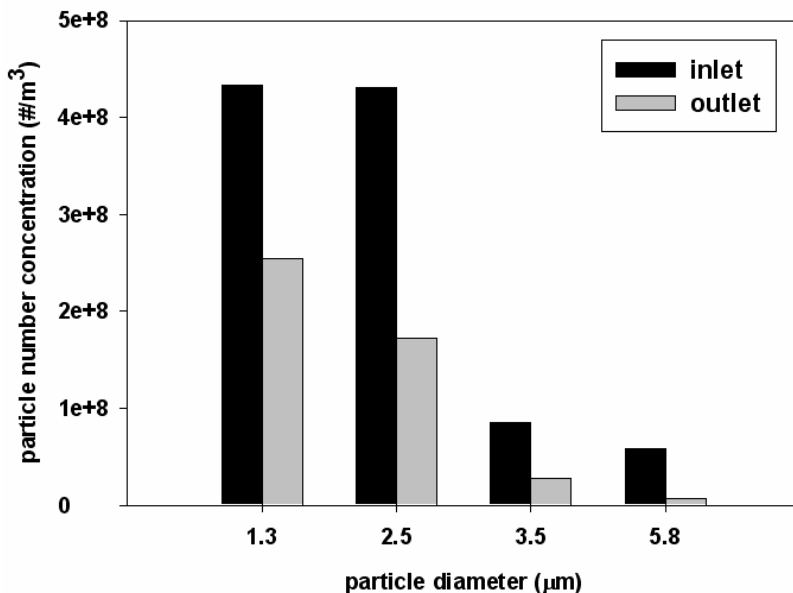
Results and Discussion

Table 1 shows performance evaluation results about the axial-flow cyclone. Pressure drop through the axial-flow cyclone while experiments was fixed with 200 Pa. Liquid particle was generated by MAG 3000 based on the principle of the heterogeneous condensation and generated particle was range of 1~6.5 μm . Generated particle concentration of cyclone inlet and outlet showed from figure 3. Collection efficiency was measured 41.2%, 60.8%, 68.4%, 85.9%, respectively.

Table 1. Collection efficiency of axial-flow cyclone for liquid and solid particles.

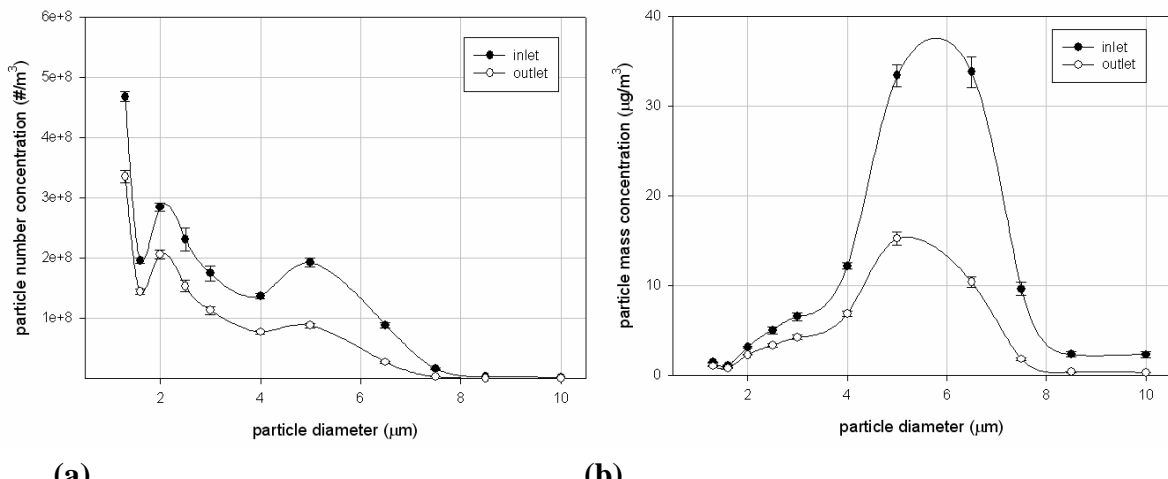
Number concentration based - liquid particle (DEHS)		Mass concentration based - solid particle (A1 dust)		Pressure drop (pa)
size range (μm)	collection efficiency (%)	size range (μm)	collection efficiency (%)	
1~1.6	41.2	1 ~ 10	65.7	200
2~3	60.8			
3~4	68.4			
5~6.5	85.9			

Figure 3. Particle number concentration at the inlet and outlet of axial-flow cyclone.



In case of solid particle, particle was generated by SAG 410 and particle size was generated range of 1~10 μm . Figure 4 shows particle distribution of A1 dust in the upstream and downstream of axial-flow cyclone. To calculate collection efficiency based on mass concentration, we converted from number concentration to mass concentration by particle density (A1 dust density = 2650 Kg/m^3). The collection efficiency estimated by total mass collection showed 65.7. According to the previous studied, particle collection efficiency of current filter system is 33.1% by weighing method [8].

Figure 4. Size distribution of A1 dust at the axial-flow cyclone inlet and outlet for (a) number distribution and (b) mass concentration (particle density = 2650 kg/m^3).



(a)

(b)

In this study, we evaluated the axial-flow cyclone using experimental analysis. Cutoff diameter of axial-flow cyclone was $1.9 \mu m$, approximately. Axial-flow cyclone was higher than that of current filter system by 2 times. In conclusion, axial-flow cyclone was found to have good performance with the potential for lower operating and maintenance cost. Therefore it can be a more suitable pre-filter than other pre-filters to be used in the subway station HVAC system.

ACKNOWLEDGMENTS

This work was partly supported by grant (Urban Transit Standardization A01) from “The 2nd phase of R&D on the urban transit standardization” funded by Ministry of Land, Transport and Maritime Affairs (MLTM) of Korean government.

REFERENCES

- [1] Korean Ministry of Land, Transport and Maritime Affairs (MLTM), *Statistical Yearbook of Construction & Transportation*. 2009.
- [2] Slack, M. D.; Prasad, R. O.; Bkker, A. Advances in cyclone modeling using unstructured grids, *Chem. Eng. Res. Des.* 2000, 78, 1098-1104
- [3] Nieuwstadt, F. T. M.; Dirkzwager, M. A fluid mechanics model for an axial cyclone separator, *Industrial and Engineering Chemistry Research*. 1995, 34, 3399-3404.
- [4] Maynard, A. D. Simple model of axial flow cyclone performance under laminar flow conditions, *J. Aerosol Science*. 2000, 31, 151-167.
- [5] Hsu, Y. D.; Chein, H. M.; Chen, T. M.; Tsai, C. J. Axial flow cyclone the segregation and collection of ultrafine particles: theoretical and experimental study, *Environmental Science and Technology*. 2008, 39, 1299-1308.
- [6] Tsai, C. J.; Chen, D. R.; Chein, H. M.; Chen, S. C.; Roth, J. L.; Hsu, Y. D.; Li, W.; Biswas, P. Theoretical and experimental study of an axial flow cyclone for fine particle removal in

- vacuum conditions, *J. Aerosol Science*. 2004, 35, 1105-1118.
- [7] Lim, M.; Kim, H.; Kwon, S. B.; Kim, S.; Kim, J. K.; Shin, C. H.; Bae, S. J.; Hwang, S. H.; Kim, T. Numerical analysis of axial-flpw cyclone separator for subway station HVAC system pre-filter, *J. Air-Conditioning and Refrigeration*. 2009, 17, 94-99.
- [8] Kim, S. M.C. Thesis, University of Sungkyunkwan at Korea, 2010.

Exhaust of Air Flow and Fine Particles from a Tunnel using an Air Curtain near a Ventilation Opening

Bangwoo Han¹, Hak-Joon Kim¹, Yong-Jin Kim¹, Sang-Hyeon Jeong¹, Yong-Min Kim² and Jong-Ryul Kim²

1 Korea Institute of Machinery and Materials, 171 Jang-dong, Yuseong, Daejeon, 305-343, Korea

2 FT-ENE, 475-31 Bangbae-dong, Seocho, Seoul, 137-060, Korea

Principal Contact: Bangwoo Han, Senior Researcher, Korea Institute of Machinery and Materials, 171 Jang-dong, Yuseong, Daejeon, 305-343, Korea.

Tel: +82-42-868-7068 Fax: +82-42-868-7284 E-mail: bhan@kimm.re.kr

Abstract

Recently, platform screen doors (PSDs) are being installed in every subway stations in Korea to prevent train-induced wind and dust. They will probably provide clean environment for passengers in platforms but on the contrary deteriorate the air quality in subway tunnels because PSDs prevent dust diffusion from tunnels to platforms. To improve the air quality of the tunnels, active air ventilation controls have been suggested these days. In this study, a high flow velocity air curtain near a ventilation opening was used to increase air ventilation rate from a tunnel. Air flow rate and particle concentration were measured at the ventilation open for the cases with and without using of air curtains and also for different air curtain locations and angles in a tunnel model of 500 mm width and 400 mm height. Main air velocity of a tunnel was 4 m/s and air velocity of air curtain was controlled in the range of 40-80 m/s. Air flow rate at the ventilation open increased by about 20% as air curtain of 80 m/s was used vertically and by about 40% as air curtain of 80 m/s was used at the angle of 30° from the vertical base line. The optimal angle of air curtain was found to be about 30° from the vertical base line. Particle concentration at the ventilation open increased by about 1.8 times and particle concentration at the main tunnel decreased by about 2 times as air curtain of 80 m/s was used at the angle of 30°. Therefore, it can be found that ventilation from a subway tunnel can be improved by applying air curtains near the ventilation openings with appropriate air flow rate, location and angle of air curtain.

Keywords: Ventilation rate, particle concentration, subway tunnel, platform screen door (PSD).

Reactions of CaCO₃ Sorbent Particles at an O₂/CO₂ Atmosphere

Seongha Jeong¹, Kang Soo Lee¹, Sang In Keel² and Sang Soo Kim¹

1 Department of Mechanical Engineering, KAIST, 335, Gwahangno, Yusong-gu, Daejeon, 305-701, Republic of Korea
2 Environmental Systems Research Division, KIMM, 104 Sinseongno, 305-343, Daejeon, Republic of Korea

ABSTRACT

As the regulation about the emission of the greenhouse gas has become more severe, the O₂/CO₂ combustion system, which enables the easy CO₂ recovery, was introduced as one of the promising combustion system in a power plant industry and the in-furnace desulfurization technique can be adapted to the system due to the high sulfation efficiency. In this study, reactions of CaCO₃ particle, which can be used as a sorbent for the in-furnace desulfurization, were investigated in an O₂/CO₂ atmospheric condition. To determine the size effect of the CaCO₃ sorbent particles, three different-sized particles (9, 23, and 40 μm by mean diameter, respectively) were used. In an air atmosphere, calcination was conducted actively in a short residence time as the particle size increased. In an O₂/CO₂ atmosphere, on the other hands, tendency of the calcination was reversed in comparison to the air atmosphere. On the evidence of experiments, the formulas for calcination were suggested for each atmospheric condition.

KEYWORDS

O₂/CO₂ Combustion, In-furnace Desulfurization, Calcination, Sintering, particle size

Introduction

CCS(Carbon Capture & Storage) is any technology or process that captures CO₂ emitted from a point location, such as power plants or steel mills, transports the processed CO₂, and then captures it for underground storage. Oxy-combustion, in particular, has high thermal efficiency and reduced emissions of thermal NOx. Thus, it has been noted as a useful technology for capturing CO₂. However, separating O₂ is very expensive, and the flame temperature is extremely high. Therefore, application of oxy-combustion in industrial processes has been challenging. Flue-gas recirculation has been used to overcome the problem of high flame temperature^[1].

For CO₂ capture, it is important to obtain pure CO₂, but flue gases include pollutants such as SO_x, NO_x, and particulate matter. In desulfurization process, a SO_x scrubber unit filled with wet

sorbent particles, such as CaCO_3 , is placed next to a boiler at existing facilities. In contrast, the SO_2 concentration in furnaces increases because flue gases are recirculated in oxy combustion. Therefore, in-furnace desulfurization that directly sprays pulverized sorbent particles, such as limestone, into a furnace can be applied in the oxy-combustion process. If SOx is desulfurized in a furnace, the expense of a SOx scrubber unit is spared. In oxy-combustion, flue-gas recirculation creates an atmosphere that is primarily CO_2 with a small amount of O_2 (O_2/CO_2 atmosphere). Therefore, the phenomena of sorbent particles in an O_2/CO_2 atmosphere are different compared with those in an air atmosphere^[2,3].

Although many studies have focused on desulfurization of CaCO_3 sorbent particles in an air atmosphere, few studies have considered an O_2/CO_2 atmosphere. The phenomena of CaCO_3 sorbent particles, particularly in high-temperature furnaces in an O_2/CO_2 atmosphere, are not well known. Thus, the aim of this study was to investigate the reactions of CaCO_3 sorbent particles in a high-temperature furnace in an O_2/CO_2 atmosphere. Under real-world conditions, power plant operators can only control the size of sorbent particles by controlling the degree of pulverization of limestone. Therefore, this study focused on understanding how the size of sorbent particles affects the sulfation mechanism in an O_2/CO_2 atmosphere compared with an air atmosphere.

Experimental Methods

Figure 1. shows the experimental setup. A high-temperature drop-tube furnace was operated electrically, and the temperature was maintained using a proportional-integral-derivative (PID) controller. Atmospheric composition was controlled using a mass flow controller (MFC). In an air atmosphere, only the air line was opened. In an O_2/CO_2 atmosphere, O_2 and CO_2 lines were opened and were independently controlled by MFCs to maintain an atmospheric composition of 80% CO_2 and 20% O_2 . To control residence time, flow rates were regulated by a pump at the upper chamber. A rotary feeder supplied uniform CaCO_3 sorbent particles to the drop-tube furnace, where the sorbent particles reacted with the gas phase. During the reactions, sorbent particles were sampled from the upper and lower sampling chambers. The aerodynamic GMDs of the particles were measured in real time using an aerodynamic particle sizer (APS, 3320 TSI).

Sorbent particles that reacted in the furnace were collected for various analyses. The specific surface area of particles was analyzed by the Brunauer–Emmett–Teller (BET) method using absorbed N_2 molecules. When CaCO_3 sorbent particles are fully calcined, their mass is reduced to 56% of the initial mass. If the mass of sorbent particles reacted in the furnace (m_s) and the mass of particles fully calcined during Thermogravimetric Analysis(TGA) (m_∞) are measured, the calcination rate of the sorbent particles reacted in the furnace can be calculated.

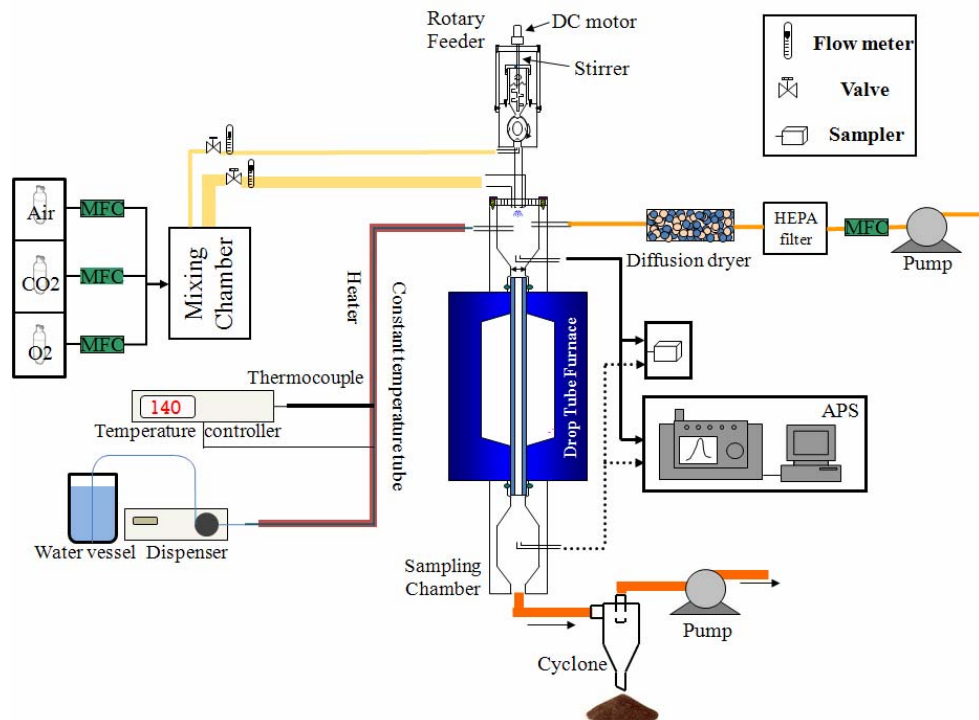
Experiments were conducted in an air atmosphere and an O_2/CO_2 atmosphere. A mixture of 80%

CO_2 and 20% O_2 was supplied to the drop-tube furnace for experiments conducted in an O_2/CO_2 atmosphere, and 100% air was supplied for experiments conducted in an air atmosphere. To study the effect of particle size, CaCO_3 sorbent particles were divided into three groups based on their mean diameters: 9 μm , 23 μm , and 40 μm . Residence time was adjusted from 0.5 s to 1.25 s by controlling the flow rate. The mean temperature in the furnace was maintained at 1027°C. A summary of the experimental conditions is presented in Table 1.

Table 1. Conditions of experiments

Variables	Conditions
Atmosphere gas	Air atmosphere : Air 100% O_2/CO_2 atmosphere : CO_2 80 % + O_2 20 %
Size of particles (mean diameter)	9 μm , 23 μm , 40 μm
Residence time	0.5sec~1.25sec
Mean temperature	1027 °C

Figure 1. Schematic diagram of the experimental setup



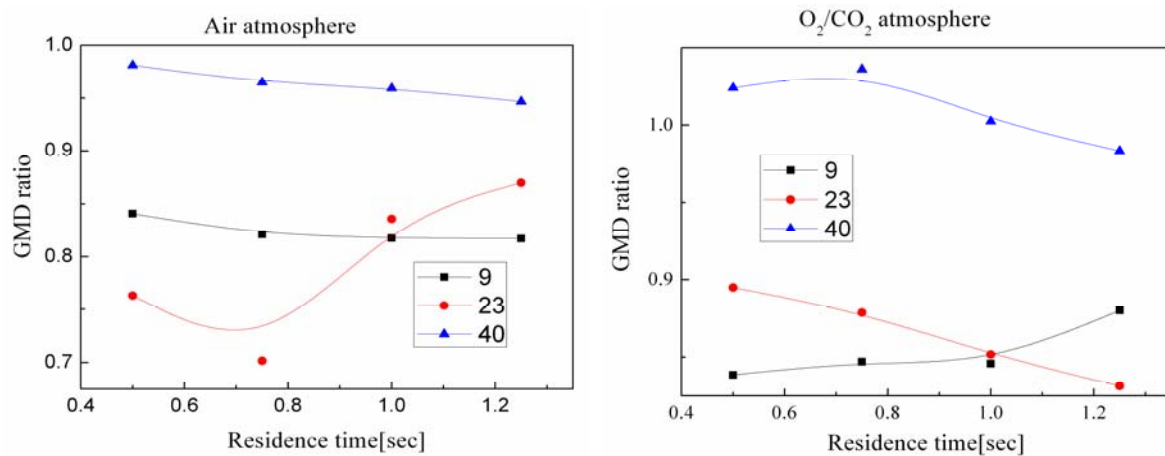
Results and Discussion

Measuring GMD ratio

Figure 2 shows that in an air atmosphere, the GMD ratio of sorbent particles with a mean diameter of 9 μm gradually decreased. Although the GMD ratio of sorbent particles with a mean

diameter of 23 μm decreased initially, it increased with increasing residence time. For 40- μm sorbent particles, the GMD ratio did not change significantly. The experimental residence time ranged from 0.5 s to 1.25 s. Sintering was the dominant process for 40- μm particles, whereas calcination was dominant for 9- μm and 23- μm particles. After calcination, sintering occurred as time progressed, indicating that the residence time at which the calcination-dominant process transitioned to the sintering-dominant process increased with increasing sorbent particle size. If small particles, which have high specific surface area, are exposed to high temperatures, a pre-sintering time, in which heat energy is consumed as sintering increases, delays calcination because sintering is proportional to specific surface area. Thus, calcination was increasingly delayed as particle size increased.

In an O_2/CO_2 atmosphere with an experimental residence time from 0.5 s to 1.25 s, the GMD ratio of 9- μm sorbent particles increased, indicating that sintering was more active than calcination, because calcination occurred prior to the residence start time (0.5 s). For 23- μm particles, the GMD ratio decreased, indicating that calcination was more active than sintering. For 40- μm particles, calcination progressed gradually after a residence time of 0.75 s. Thus, the residence time for which sorbent particles were actively calcined was delayed as the size of the sorbent particles increased. Due to the CO_2 partial pressure, calcination occurred at the surface of



the particles. Therefore, smaller particles with higher specific surface area were calcined within shorter residence times.

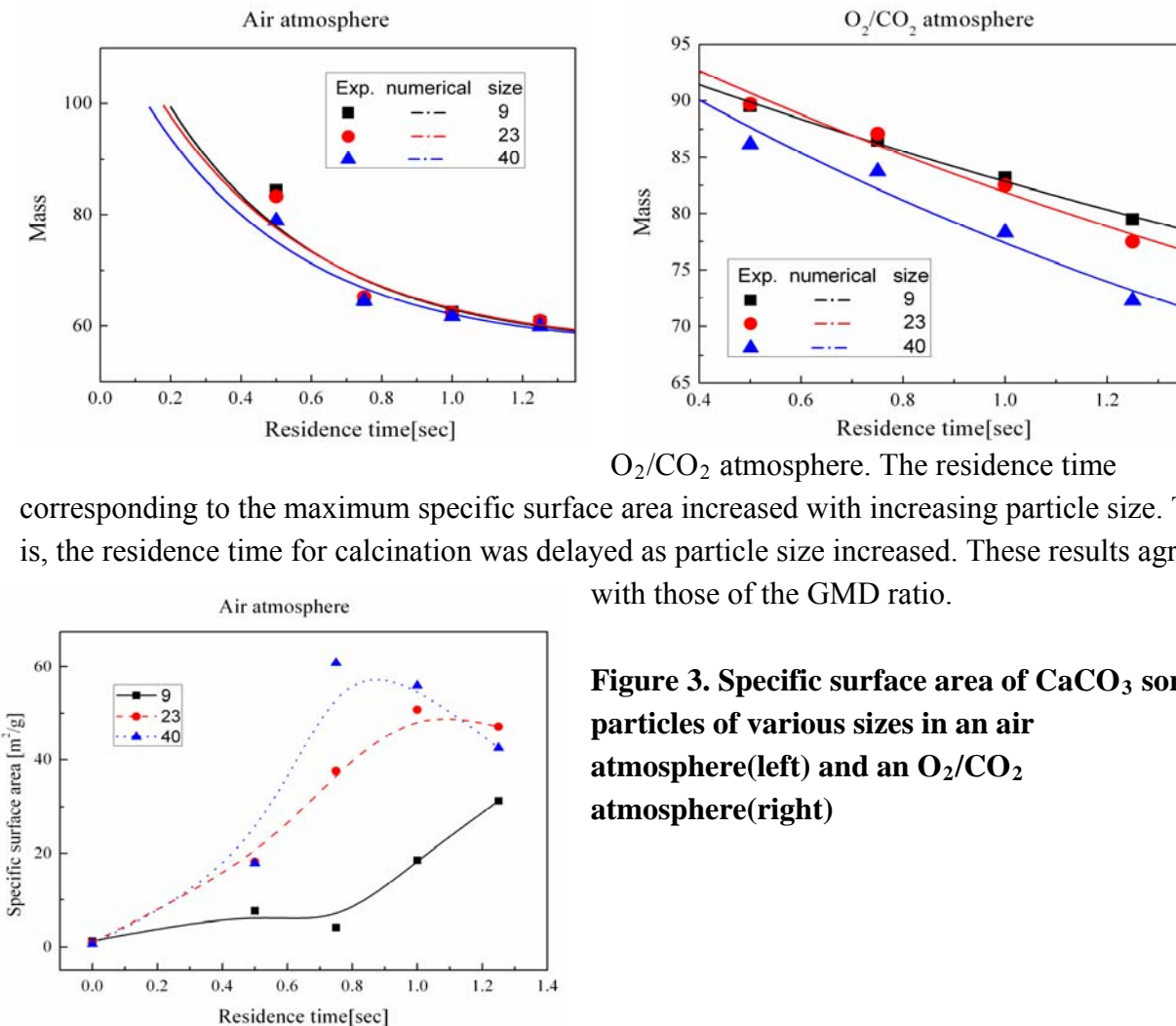
Figure 2. GMD ratio of CaCO_3 sorbent particles of various sizes in an air atmosphere(left) and an O_2/CO_2 atmosphere(right)

Measuring specific surface area

Specific surface area measurements are useful for interpreting the behavior of sorbent particles in a high-temperature furnace. Calcination increases specific surface area by forming pores on the surface of sorbent particles. In contrast, sintering decreases specific surface area.

Figure 3 shows the specific surface area of sorbent particles reacted in the furnace as a function of residence time for various particle sizes. In an air atmosphere, the specific surface area increased after ~ 0.8 s for the 9- μm particles. The residence time at which the specific surface area switched from increasing to decreasing was ~ 1.0 s for 23- μm particles and ~ 0.75 s for 40- μm particles. These results indicate that the residence time at which the calcination-dominant process switched to a sintering-dominant process increased with increasing particle size.

Figure 3 shows the residence time for active calcination as a function of particle size in an



O_2/CO_2 atmosphere. The residence time corresponding to the maximum specific surface area increased with increasing particle size. That is, the residence time for calcination was delayed as particle size increased. These results agreed with those of the GMD ratio.

Figure 3. Specific surface area of CaCO_3 sorbent particles of various sizes in an air atmosphere(left) and an O_2/CO_2 atmosphere(right)

Figure 4. Variation in mass of CaCO₃orbent particles of various sizes and the graph predicted by curve fitting in an air atmosphere(left) and an O₂/CO₂ atmosphere(right)

Measuring calcination rate and formulation of calcination

Initially, the calcinations rate rapidly increased in an air atmosphere, indicating that the mass reduction rate was proportional to the uncalcined mass, and the residence time at which calcination occurred for larger particles was earlier than that of smaller particles. Based on these results, the following formula was derived:

$$\frac{d(m - m_{\infty})}{dt} = -k_c(m - m_{\infty}) \quad (\text{Eq.1})$$

The calcination start time, t_s, is defined as the residence time at which calcination begins; it was assumed that the initial mass of unreacted sorbent particles was 100 prior to t_s. After calcination began, the mass of sorbent particles decreased in proportion to the amount of unreacted mass. The calcination rate constant, k_c, is a proportionality constant. The exact solution of Eq. 1 is given by Eq. 2.

$$m = m_{\infty} + (m_0 - m_{\infty}) \exp(-k_c(t - t_s)) \quad (\text{Eq.2})$$

The calcination rate constant, k_c, and the residence start time, t_s, were calculated by curve-fitting the experimental data. The results are presented in Table 2. The fitted curve is shown in Figure 5, and confirmed that the experimental data accurately corresponded to Eq. 3. Table 2 shows that t_s increased with increasing particle size, but the calcination rate constant remained fairly constant. Thus, calcination occurred within a shorter residence time as particle size increased.

The increase in the calcination rate was not proportional to unreacted mass, in contrast to the results in an air atmosphere. Therefore, the increase in the calcination rate was assumed to be proportional to the unreacted surface area of the particles (i.e., the core). This assumption led to a mass reduction rate that can be expressed by Eq. 3,

$$\frac{d(m - m_{\infty})}{dt} = -k_c(m - m_{\infty})^{2/3} \quad (\text{Eq.3})$$

In an O₂/CO₂ atmosphere, it was assumed that calcination began immediately. That is, the residence start time was 0, in contrast to that in an air atmosphere. The initial mass of CaCO₃ sorbent particles (m₀) was 100 g. The exact solution of Eq. 3 is given by Eq. 4,

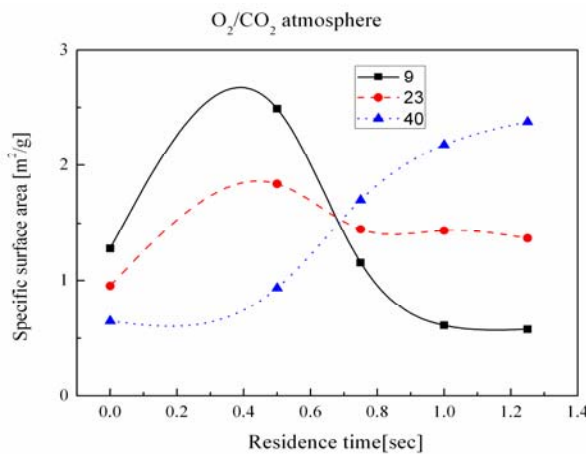


Table 2. Calcination rate constant and start residence time of CaCO₃ sorbent particles of various sizes in an air atmosphere and an O₂/CO₂ atmosphere

Atmosphere condition	GMD of sorbent particles[μm]	9	23	40
Air atmosphere	The calcination rate constant k _c [sec ⁻¹]	2.282	2.200	2.272
	The start residence time t _s [sec]	0.194	0.179	0.133
O ₂ /CO ₂ atmosphere	The Calcination rate constant k _c [g ^{1/3} sec ⁻¹]	1.448	1.816	2.333

$$(m - m_{\infty})^{1/3} = (m_0 - m_{\infty})^{1/3} - \frac{k_c}{3} t \quad (\text{Eq.4})$$

The calcination rate constant, k_c, in an O₂/CO₂ atmosphere was calculated by curve-fitting the experimental data. and the results are presented in Table 2. The fitted curve is shown in Figure.4 and confirmed that the experimental data adequately corresponded to Eq. 4. The data in Table 2 indicate that k_c increased with increasing particle size. That is, the larger sorbent particles were calcined faster.

CONCLUSION

The residence time of the calcination-dominant phase was delayed in an O₂/CO₂ atmosphere because of the CO₂ partial pressure above the sorbent particles. The residence time at which the calcination-dominant process switched to a sintering-dominant process increased with increasing particle size. However, the residence time at which calcination actively occurred was delayed as particle size increased in an O₂/CO₂ atmosphere.

The mass reduction rate due to calcination was proportional to the amount uncalcined mass in an air atmosphere, whereas the mass reduction rate was proportional to the unreacted surface area in an O₂/CO₂ atmosphere. Thus, calcination reactions were suggested and verified based on experimental data.

ACKNOWLEDGMENTS

This work was supported by the Energy Efficiency & Resources of the Korea Institute of Energy Technology Evaluation and Planning (KETEP) grant funded by the Korea government Ministry of Knowledge Economy(No. 2010201010108B).

REFERENCES

- [1] S. H. Tak et al., Journal of Mechanical Science and Technology, vol. 24, no. 9, 2010.
- [2] Y. Yan et al., “Study on kinetics of desulfurization reaction by CaO particles”, Heat Transfer –Asian Research, vol. 32, no. 5, 2003.

[3] S. K. Muhuli et al., “Combined calcination, sintering, and sulfation model for CaCO_3 – SO_2 reaction”, AIChE Journal, vol. 45, no. 2, 1999.

Surface Area and Size Distribution Measurements for Nanoparticles Generated from Nanopowders by a Small-Scale Powder Disperser

Chi-En He¹, Chun-Nan Liu¹, Sheng-Chieh Chen¹, Cheng-Yu Huang¹, Chun-Wan Chen², Cheng-Ping Chang², and Chuen-Jinn Tsai¹

1 Institute of Environmental Engineering, National Chiao Tung University, No. 1001, University Road, Hsin Chu, Taiwan 30010

2 Institute of Occupational Safety and Health, Council of Labor Affairs, Executive Yuan, 99, Lane 407, Hengke Road, Shijr, Taipei, Taiwan 22143

Principle Contact: Chuen-Jinn Tsai, Professor, National Chiao Tung University, HsinChu, Taiwan 30010.

Tel: +886-3-5731880 Fax: +886-3-5727835 Email: cjsai@mail.nctu.edu.tw

Abstract

A TSI Small-Scale Powder Disperser (SSPD, Model 3433) was used to disperse three nanopowders, nano-TiO₂, nano-ZnO and nano-SiO₂, and the distinctness was analysed based on number distributions, mass distributions and surface area (SA) concentration which were measured by a TSI Scanning Mobility Particle Sizer (SMPS) and a TSI Aerodynamic Particle Sizer (APS), a MSP Micro-Orifice Uniform Deposit Impactor (MOUDI) and a TSI Aerotrak™ 9000, respectively.

It was found that among three nanopowders, the total specific number concentration measured by the SMPS (electrical mobility diameter range: 15 to 661 nm) was the highest for nano-TiO₂, followed by nano-SiO₂ and nano-ZnO. Both nanoparticle (electrical mobility diameter <100 nm) number and mass concentrations were negligibly low with the number median diameters (NMDs) ranging from 164 to 305 nm and the mass median aerodynamic diameters (MMADs) ranging from 1.1 to 2.1 m. Both number and mass distributions were found to be lognormal and unimodal with almost the same geometric standard deviations (GSDs) for each of the three nanopowders in the 30-min test. The NMDs and GSDs were 225 nm and 2.13, 305 nm and 1.98, 164 nm and 2.22, while the MMADs and GSDs were 1.1 μm and 2.1, 1.3 μm and 1.9, and 2.1 μm and 2.7, for nano-TiO₂, nano-ZnO and nano-SiO₂,

respectively. The SA concentration distribution was converted from the number and mass distribution data and the lung deposited SA concentration was then calculated based on the ICRP lung deposition model.

The calculated lung deposited SA concentrations were compared with those measured by the TSI AerotrakTM 9000. It was found that the agreement was quite satisfactory with the difference in the alveolar and tracheobronchial deposited SA concentrations ranging from +10~+32 % and +7~-17 % for three nanopowders, respectively.

Keywords: Nanoparticle, Dustiness test, Surface area, Small-Scale Powder Disperser

The Influence of Various Sorbent Properties to Remove SO₂ in Fluidized Bed Reactor

Young-Ok Park¹, Jei-Pil Wang² and Yong-Ha Kim³

¹Clean Coal Research Center, Korea Institute of Energy Research, Daejeon, 305-343, Korea

²Department of Metallurgical Engineering, Pukyong National University, Busan, 608-739, Korea

³Department of Chemical Engineering, Pukyong National University, Busan, 608-739, Korea

ABSTRACT

The removal of SO₂ in flowing gas using the fluidized bed (F.B.) as a reactor with bed materials was conducted in dry and/or semi-dry flue gas desulfurization (F.G.D.) processes to achieve high desulfurization efficiency in this study. The effect of different properties of Ca(OH)₂ and NaHCO₃ as sorbents was investigated with operating variables such as molar concentration of sorbent types, water injection flow rate, different gas flow rate, and specific water volume using a bench scale plant of stainless steel column. Based on the results, the dry and/or semi-dry processes using proper types of Ca(OH)₂ and NaHCO₃ sorbents were newly proposed to remove SO₂ from flue gas.

KEYWORDS

Flue gas desulfurization (F.G.D.), Fluidized bed (F.B.), Sorbent, Bed materials

Introduction

The SO₂ emissions from coal-fired power plants have caused significant bad effect on environmental and human health. Currently, reducing SO₂ emission from power plants is a main issue for the environmental protection. Conceptually, flue gas desulfurization (FGD) can be grossly classified into three types: wet scrubbers, semi-dry and dry processes. Where, wet scrubbers have been shown to be reliable for a variety of fuels and have been widely commercialized in industry for achieving SO₂ removal in excess of 95%. However, it generates a large amount of wet solid waste and requires treatment of wastewater which leads to higher operation cost. Dry processes are attractive in principle as compared to wet scrubbers in terms of cost because they do not require water. Nonetheless, this type has not yet been widely used due to the low SO₂ removal and poor sorbent utilization. Therefore, semi-dry processes have been developed as an alternative to avoid the disadvantages of wet scrubbers and dry FGD techniques. Spray dry scrubber as a typical semi-dry FGD has been used commercially since the 1980s and has the second largest market share following wet scrubbers, but the relatively low SO₂ removal

efficiency (85%) restricts their wider application^[1-5]. Accordingly, fine powder based semi-dry FGD was proposed for higher SO₂ removal efficiency which was accomplished by interacting flue gas and powder sorbent to be adhered on to the surface of particle^[6-7]. The FGD was much advanced as it investigated the effects of operating parameters on SO₂ removal efficiency as stated.

The aim of the present research is to study dry and semi-dry FGD in fluidized bed reactor to be appropriate in the one-body cleaning process, evaluating the effects of water injection flow rate, Ca/S molar ratio, different gas flow rate, specific water volume on SO₂ removal efficiency. Experiments were carried out to obtain fundamental data for SO₂ removal efficiency of above 98% so as to aid in the optimum FGD design to be suitable for minimizing the deactivation of De-NOx catalyst by residual SO₂ in the flue gas.

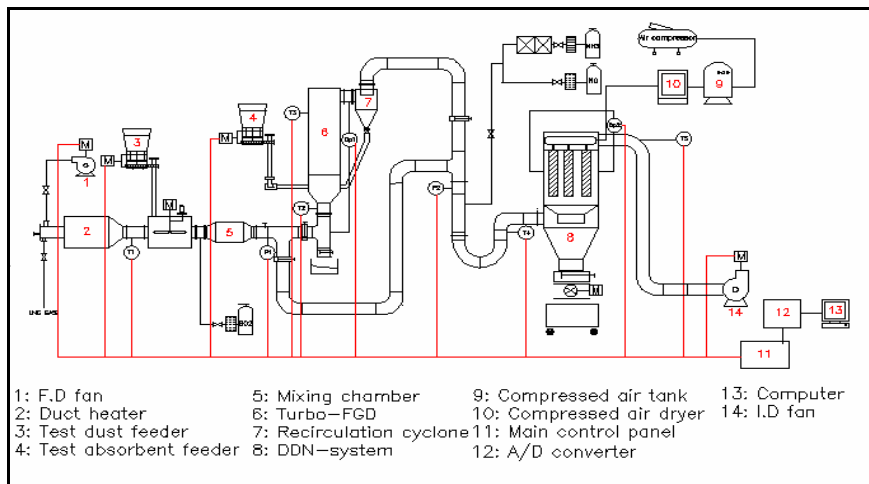
Experimental Methods

The bench-scale FB experimental facility is consisted of (i) the sorbent and water feeding system, (ii) the flue gas generation system and (iii) the FB reactor, as shown in Figure 1. Flue gas generated by the gas burner was mixed a small amount of cool air to produce about 350 °C simulated flue gas. SO₂ gas was added to the flue gas before the FB reactor. The FB reactor is made up of the upper cylindrical part (0.5 m - I.D. x 3.9 m - high), middle taper part (0.2 m - I.D. at the bottom x 0.246 m – high and taper angle of 31°) and lower cylindrical part (0.2 m – I.D. x 0.104 m – high). The perforated plate as a gas distributor has a square arrangement of 1 mm holes at a pitch of 9 mm with a fractional opening area of 1.5%. Glass beads of about 2 mm were used as bed materials

The flue gas flow rate was varied from 12 to 20 Nm³/min. The commercial grade calcium hydroxide (Ca(OH)₂) and sodium bicarbonate (NaHCO₃) powders with 99% purity (Tae Young EMC Co. Ltd., Korea) were used as sorbents. The sorbent and water were continuously fed separately to a lower zone in which bed materials were fluidized violently with flue gas in a tapered part just above the gas distributor. The flue gas passed the FB reactor and reacted with the sorbent and then went through a cyclone and bag filter before being emitted from the stack. The SO₂ concentration in the flue gas was measured online at the inlet and outlet of the FB reactor

The inlet SO₂ concentration was fixed at 500 ppm. SO₂ removal efficiency was calculated from the inlet and outlet SO₂ concentrations in the reactor at interval of five minutes. In order to confirm the reliability of the test results, the long operation of 6~8 hours was carried out at each operating condition

Figure 1. Bench-Scale experimental facility.



Results and Discussion

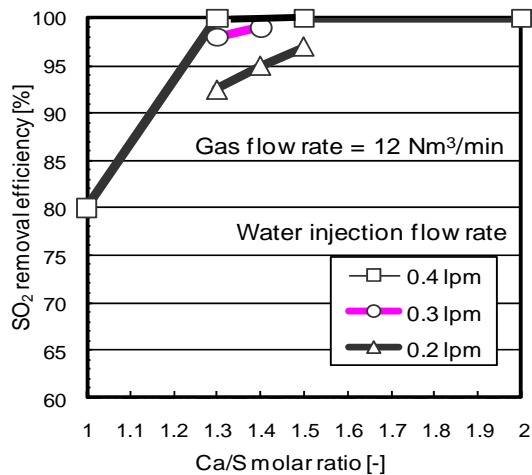
Effect of Ca/S and NSR molar ratio

The effect of Ca/S molar ratio on SO₂ removal efficiency as a function of water injection flow rate is shown in Figure 2. Under the optimum operating condition using stoichiometric Ca/S molar ratio of 1.0, sufficient water content and higher temperature, the following reaction might take place in semi-dry flue gas desulfurization process.



As expected from the previous reports^[1-7], SO₂ removal efficiency increases with an increase in the Ca/S molar ratio since a larger Ca/S molar ratio means that more sorbents are fed into the reactor for a given inlet SO₂ concentration in the flue gas. It is also seen that the sensitiveness of SO₂ removal efficiency to the Ca/S molar ratio is higher as water injection flow rate decreases. It can be concluded that the higher the Ca/S molar ratio and lower the utilization efficiency of SO₂ sorbents. It was 70.8% and 64.7% at Ca/S molar ratio of 1.3 and 1.5 respectively, using 0.2 liter/min water injection flow rate. SO₂ removal efficiency could not be influenced effectively by further increase in Ca/S molar ratio.

Figure 2. Effect of Ca/S molar ratio on SO₂ removal efficiency as a function of water injection flow rate.

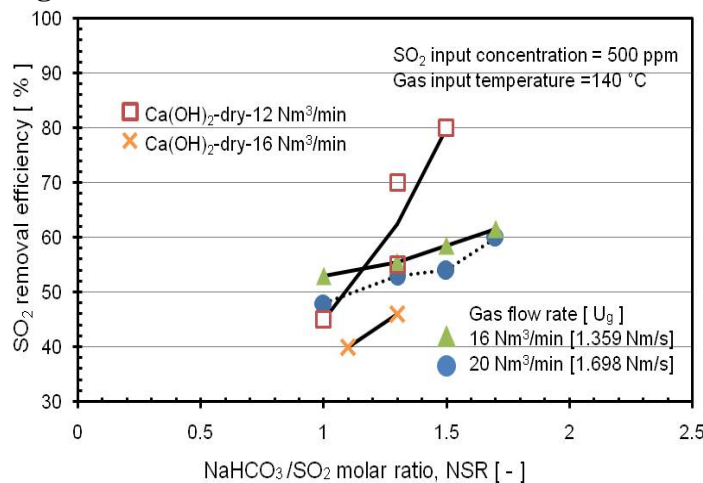


Different sorbent, sodium bicarbonate (NaHCO₃), was also used to remove SO₂ and the effect of NaHCO₃/SO₂ molar ratio on SO₂ removal efficiency in a dry-FGD test at KIER Lab-scale Turbo-FGD reactor is shown in Figure 3. The following reaction might take place in a dry-FGD test stated below.



It is clearly seen that SO₂ removal efficiency of about 50~60% was achieved using NaHCO₃ as sorbent in dry-FGD test that is higher than SO₂ removal efficiency using Ca(OH)₂.

Figure 3. Effect of NaHCO₃/SO₂ molar ratio on SO₂ removal efficiency in dry-FGD test.



Effect of specific water volume

Figure 4 shows the relation between SO_2 removal efficiency and specific water volume at different gas flow rates. Specific water volume, F_L , is defined as liter-water per $\text{Nm}^3\text{-gas}$, and numerical value in parenthesis is water injection flow rate in liter/min. It can be seen that SO_2 removal efficiency increases as the value of specific water volume increases. SO_2 removal efficiency of up to 98% at gas flow rate of 12 and 20 Nm^3/min can be obtained at specific water volume of 0.025 and 0.035 liter-water/ $\text{Nm}^3\text{-gas}$, respectively. It should be noted that the specific water volume for up to any required value of SO_2 removal efficiency becomes greater as the gas flow rate increases, as shown in Figure 4.

Figure 4. Effect of specific water volume on SO_2 removal efficiency at different gas flow rates.

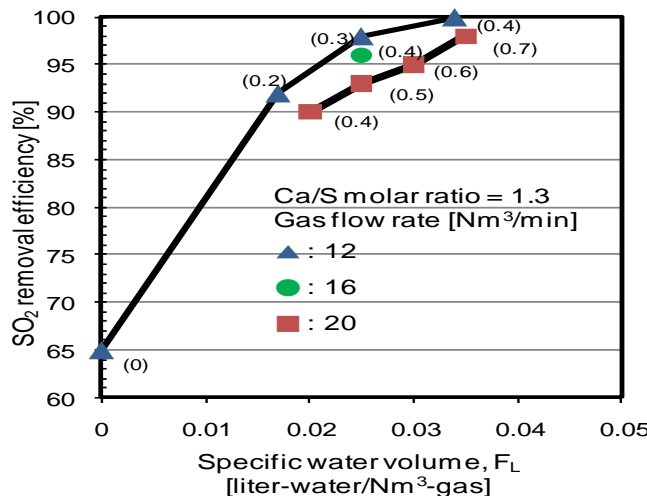
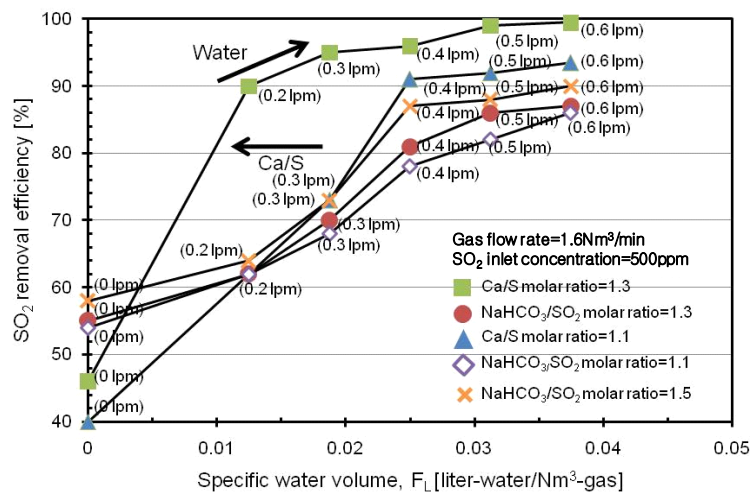


Fig. 5 illustrates SO_2 removal efficiency on specific water volume at different sorbents of NaHCO_3 and $\text{Ca}(\text{OH})_2$. It is seen that SO_2 removal efficiency used with $\text{Ca}(\text{OH})_2$ is higher than it used with NaHCO_3 in semi-dry flue gas desulfurization and increasing specific water volume would influence on increase of SO_2 removal efficiency. In addition, SO_2 removal efficiency used with NaHCO_3 was little affected by an increase of NSR ($\text{NaHCO}_3/\text{SO}_2$ molar ratio) in semi-dry flue gas desulfurization.

Figure 5. Effect of specific water volume on SO₂ removal efficiency at different sorbents. (NaHCO₃/Ca(OH)₂)



ACKNOWLEDGMENTS

This work was supported in part by the Power Generation & Electricity Delivery of the Korea Institute of the Energy Technology Evaluation and Planning (KETEP) grant funded by the Korea Government Ministry of Knowledge Economy.

CONCLUSION

The target efficiency (>98%) was achieved by specific water volume of 0.035 liter-water/Nm³-gas as optimum operating condition at Ca/S molar ratio of 1.3 and gas flow rate of 20 Nm³/min. SO₂ removal efficiency of about 50~60% was achieved using NaHCO₃ as sorbent in dry-FGD test and SO₂ removal efficiency used with Ca(OH)₂ was higher it used with NaHCO₃ in semi-dry flue gas desulfurization.

REFERENCES

- [1] Neathery, James K. *AICHE Journal*, 1996, 42, 259-268.
- [2] Zhou, Y.; Zhu, X., Peng, J.; Liu, Y.; Zhang, D.; Zhang, M. *J. Hazard. Mater.* 2009, 170, 436-442.
- [3] Bandyopadhyay, A.; Biswas, M. N. *Chem. Eng. Tech.* 2006, 29, 130-145.
- [4] Ollero, P.; Salvador, L.; Canadas, L. *Environmental Progress*, 1997, 16, 20-28.
- [5] Wang, J.; Keener, T.C. *Environmental Technology*, 1996, 17, 1047-1057.
- [6] Xu, G.; Guo, Q.; Kaneko, T.; Kato, K. *Advances in Environmental Research*, 2000, 4, 9-18.
- [7] Guo, Q.; Noriaki, I.; Kato, K. *Kagaku Kogaku Ronbunshu*, 1996, 22, 1400-1406.

Simultaneous Removal Characteristics of Fine Particulate and Elemental Mercury in Integrated Particulate Collector

Young-Ok Park[★] and Ju-Yeong Jeong

Clean Coal Research Center, Korea Institute of Energy Research, Korea

ABSTRACT

The pleated filter bags which were used during this study were made of pleated nonwoven fabric of heat and acid resistant polysulfonate glass fibers which can withstand the heat up to 300 °C and have a filtration area which is 3 to 5 times larger than the conventional round filter bags.

Cartridge module filled with HGR® Granular Activated Carbon was inserted in the inner of the pleated filter bag. This type of pleated filter bag was designed to remove not only the particulate matter but also the gaseous elemental mercury. The electrostatic precipitator part can enhance the particulate removal efficiency and reduce the pressure drop of the pleated filter bag by forcing particles to form a more porous dust layer on the surface of the pleated bag increasing thus the bag pulse cleaning interval. In addition, the gross particles are separated from the stream through the cyclone part which is installed at the bottom of the housing and replaces the conventional hopper. Thus enhanced filtration performance of the hybrid collector was applied in this study to analyze the removal characteristics of particulate matter and gaseous elemental mercury.

KEYWORDS

Integrated particulate collector, Particulate matter, Gaseous elemental mercury, Sulfur impregnated activated carbon, Pleated filter bag.

Introduction

Injecting a sorbent such as powdered activated carbon into the flue gas represents one of the simplest and most mature approaches to controlling mercury emissions from coal-fired boilers. The gas-phase mercury in the flue gas contacts the sorbent and attaches to its surface. The sorbent with the mercury attached is then collected by the existing particle control device, either an electrostatic precipitator or fabric filter. Over past several years, the results from numerous full-scale evaluations of activated carbon injection for mercury removal indicate that activated carbon is a viable technology for mercury control on coal-fired power plants^[1]. For some plants, one of the disadvantages of the injecting activated carbon is its impact on the salability or reuse of ash.

Integrated particulate collection technology, in which the fine particulate and elemental mercury

can be removed simultaneously. In this configuration, particulate is collected on surface of pleated filter bag and elemental mercury is removed in the sulfur impregnated activated carbon packed cartridge which is installed inside of the pleated filter bag. To enhance particulate collection efficiency, the electrostatic precipitation part is equipped with outside of pleated filter bag. The aim of the present research is to study the integrated particulate collector can be removed the fine particulate and gaseous elemental mercury, evaluating the effects of electrostatic precipitation, face velocity on elemental mercury removal efficiency.

Experimental Methods

The bench-scale integrated particulate collection test unit is consisted of mercury injection unit, test dust feeding and dispersion unit, integrated test chamber and activated carbon tower as shown in Figure 1. The test for removal of fine particulate and elemental mercury conducted with electrostatic precipitator power on and off conditions in the integrated test chamber. The inlet dust concentration and inlet mercury concentration were fixed at 20 g/m^3 and $30 \mu\text{g}/\text{m}^3$ respectively. The filtration velocity was varied from 0.5 to 1.0 m/min. The experimental conditions is shown in Table 1.

Figure 1. Schematic diagram of test unit.

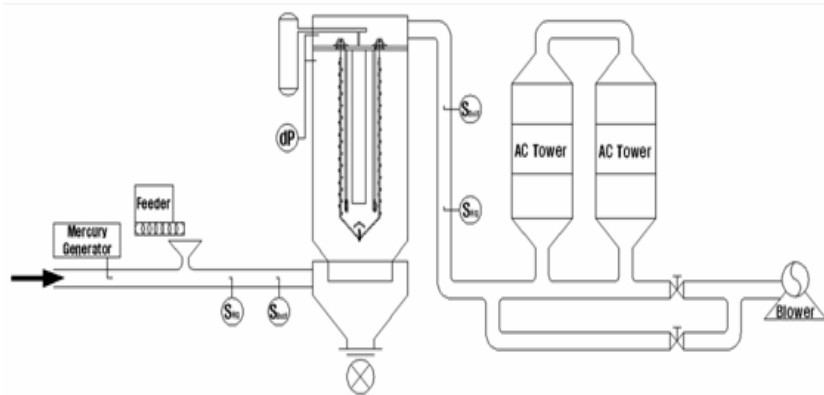


Table 1. Experimental condition of particulate collection

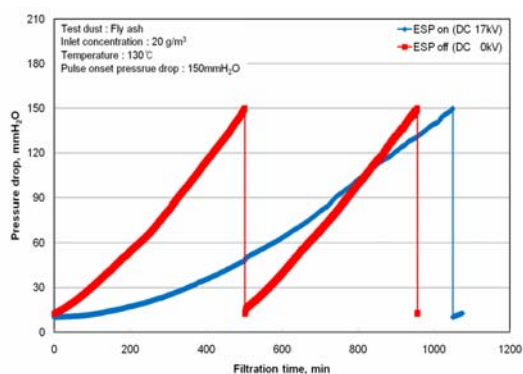
Conditions	Value
Test filter	High temp. pleated filter bags with activated carbon mounting cartridges
Test dust	Fly-ash, $D_{p,\text{mean}}: 19.0 \mu\text{m}$ (mass median diameter)
Test activated carbon	Sulfur impregnated activate carbon(BR4, RBHG3 ; N人, HGR,

Test dust density, g/cc	1.177
Applied Voltage, kV	ESP on : 17.0, ESP off : 0 (ESP off) : 0
Filtration area, m²	3.6
Filtration velocity(V), m/min	0.5, 0.8, 1.0
Inlet dust concentration(C_i), g/m³	20.0
Inlet Hg⁰ concentration, µg/m³	30
Operating temperature, °C	130
Cleaning start pressure drop, mmH₂O	150
Cleaning air pressure(P_p), kg/cm²	5.0

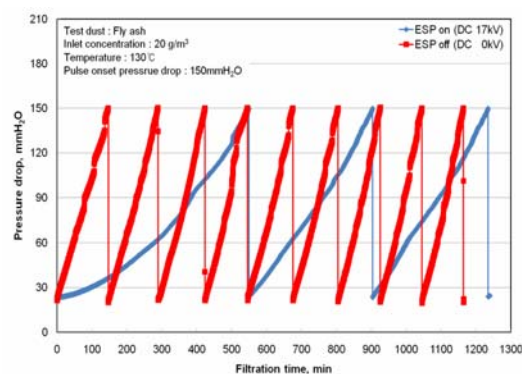
Results and Discussion

The effect of electrostatic precipitator on and off conditions on pressure drop of test unit is shown in Figure 2. As expected from the previous reports^[2-4], the pressure drop rapidly increases with an increase in filtration velocity. The filter cleaning interval means the time between 1st filter cleaning and next filter cleaning. The filter cleaning interval is approximately 2 times increased on electrostatic precipitator power on condition than that of electrostatic precipitator off condition at 1.0 m/min of filtration velocity.

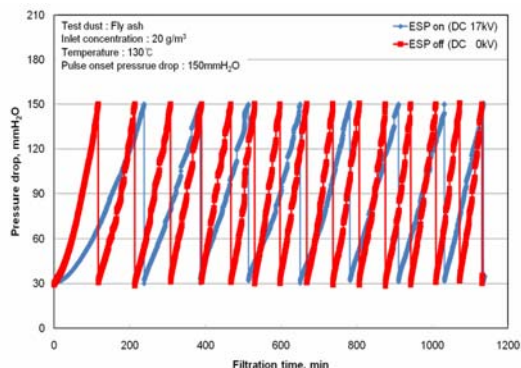
Figure 2. Variation of pressure drop with filtration time.



(a) Filtration velocity : 0.5 m/min



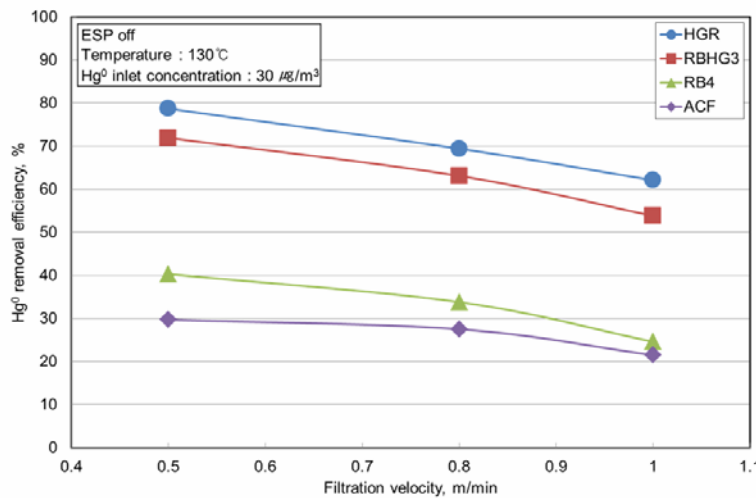
(b) Filtration velocity : 0.8 m/min



(b) Filtration velocity : 1.0 m/min

Figure 3 shows the filtration velocity characteristics of elemental mercury efficiency according to the various sulfur impregnated activated carbons. The sulfur impregnation rate for test activated carbon is 0.02wt.% of ACF, 1.0wt.% of RB4, 16.5wt.% of RBHG3 and 18.9 wt.% of HGR, respectively. The elemental mercury removal efficiency increases with the increase of sulfur impregnation rate and decrease with filtration velocity. Four sulfur impregnated activated carbons were evaluated at various filtration velocities from 0.5 m/min to 1.0 m/min to achieve target removals ranging from 50% to greater than 80%. Removals were calculated by comparing the test unit inlet mercury concentration to the test unit outlet mercury concentration.

Figure 3. Results of sulfur impregnated activated carbon tests.



CONCLUSION

The amount of dust entering the integrated dust collector is reduced by the cyclone part which is

installed at the lower part of the collector. The rest of the dust load is separated by the electrostatic (ESP) parts and on the surface of the pleated filter bags. The effect of the electrostatic charge of particles is observed to build a more porous dust cake on the surface of the pleated filter bags thus reducing the pressure drop across the filtration area of pleated filter bags. The elemental mercury removal efficiency of the integrated particulate collector decreases with increase filtration velocity and increases with increase sulfur impregnated rate.

ACKNOWLEDGMENTS

This work was supported in part by the Eco-technopia21 Project of the Korea Environmental Industry & Technology Institute(KEITI) grant funded by the Korea Government Ministry of Environment.

REFERENCES

- [1] Durham, M. D., J. Bustard, T. Starns, S. Sjostrom and R. Afonso, "Full-Scale Evaluation of Mercury Control by Injecting Activated Carbon Upstream of ESPs," presented at the International Conference on Air Quality IV, Arlington, VA, September 22 (2003).
- [2] Y. O. Park, Naim Hasolli and H. K. Choi, "Efficient and economic particulate collection from the flue gas by the advanced hybrid particulate collectors", 10th World Filtration Congress Proceedings, (2008) pp. III-367-III-3711.
- [3] Y. O. Park, J. Y. Jeong, Y. C. Seo, "Simultaneous removal characteristics of particulate and element mercury in the integrated particulate control device", Proceeding of the 51st Meeting of KOSAE (2010), pp. 372.
- [4] J. Y. Jeong, "Simultaneous removal characteristics of fine particulate and elemental mercury in integrated particulate collector", Master degree thesis, (2011)

Characteristics of Aerosol Droplets Generated by Cough Simulator

Soon-Bark Kwon^{1*}, Jae-Hyoung Park¹, Youngmin Cho¹, Wotae Jeong¹, Duck-Shin Park¹ and Gwi-Nam Bae²

1 Korea Railroad Research institute, Gyeonggi-do, 437-757, Korea

2 Korea Institute of Science and Technology, Seoul, 136-731, Korea

ABSTRACT

Airborne disease transmission has been a topic of interests in various fields over decade. The aerosol droplets emitted by a patient's cough with infectious disease such as Severe acute respiratory syndrome (SARS), influenza and Tuberculosis and so on. Coughing is found to be one of the primary sources of airborne disease. We constructed the characterization system and a cough simulator for repeating experiment which can simulate the aerosol droplets produced by human expiratory activities. The Particle Image Velocimetry system (PIV) and acrylic glass chamber were used to cough velocity measurement. Total volume of air was measured by the spirometer (CHEST corp., HI-801) as used by lung capacity factor, and forced vital capacity (FVC) was regarded as the emitted volume by human cough. More than 20 recruited persons were asked to generate coughs in the system and we measured the velocity distribution and FVC of them. Based on the physical measurement of human coughs, we developed a cough simulator to imitate a human cough. A volume of cough simulator's air tank was replicated to the lung capacity and automatic valve system can control the opening time of mouth during a cough. In this study, we analyzed the size distribution and flying distance of aerosol droplets exhaled by the cough simulator.

KEYWORDS

Airborne transmission, PIV, Cough simulator, Velocity vector

Introduction

The severe acute respiratory syndrome (SARS) and swine-novel influenza (H1N1a) have been a topic of interest in the whole world over decade. SARS is a recently described illness of human with a high case fatality rate that has spread widely since November 2002. By the end of April, 2003, over 4300 SARS cases and 250 SARS-related deaths from over 25 countries around the world were reported by the World Health Organization (WHO) [1]. Furthermore H1N1a has been occurred for 12 March 2010 - As of 7 March 2010, worldwide more than 213 countries and

overseas territories or communities have reported laboratory confirmed cases of pandemic influenza H1N1 2009, including at least 16713 deaths (WHO) [2]. Most of these cases occurred after exposure to SARS patients in household or healthcare settings.

Olsen et al (2003) has confirmed the transmission of SARS in the aircraft cabin [3]. And Cole and Cook (1998) had found that airborne transmission starts from infectious viruses exhaled to infected persons [4]. The bioaerosol droplets emitted by a patient's cough with infectious diseases.

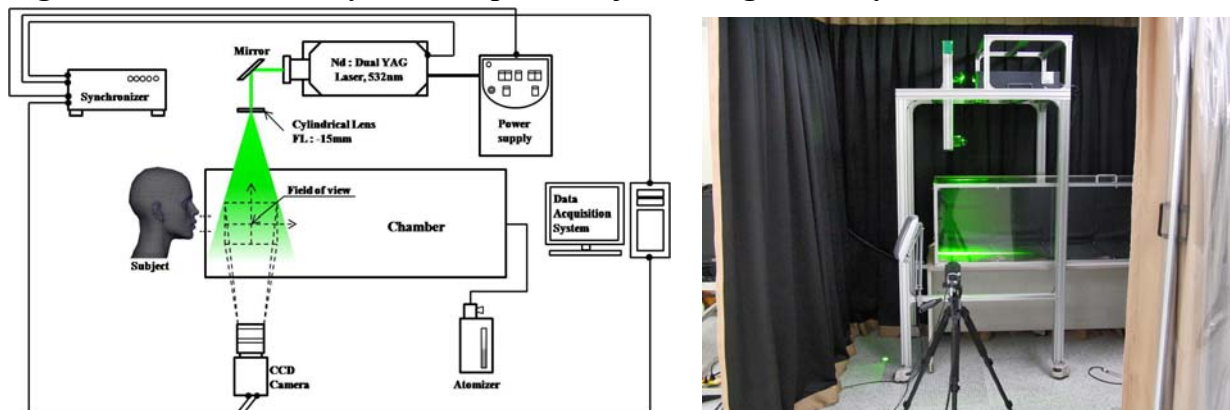
In this study, we have constructed the characterization system for saliva droplets produced by human expiratory activities and performed the preliminary experiments on the velocity of expelled droplet particles such as emitted cough velocity, angle and volume by subject. Based on cough physical results, cough simulator was developed.

Experimental Methods

Coughing velocity measurement system

For the measurement of velocity field, the PIV and chamber system were constructed. The Particle system (PIV) and acrylic glass acrylic glass chamber were used to cough velocity. The PIV system was consist of laser source(Nd: YAG, $\lambda=532\text{nm}$), CCD camera(1600x1200 pixel) with macro lens, atomizer(Oil Droplet, TSI Model 9307, generated $1\mu\text{m}$ -sized olive oil) and synchronizer. The chamber was setup in the air-conditioned room (clean room) where the temperature and humidity were under control and the background aerosol concentration (over 0.3 m-sized) was maintained less than 0.1 cm^{-3} achieved by vertical flow ventilation with HEPA filter. The air temperature and relative humidity inside the clean room is controllable between 15~30°C and 10~80% for different case simulation of indoor environment.

Figure 1. Measurement system setup for subject's cough velocity



The rectangular acrylic glass chamber of 500 mm x 500 mm with the length of 1500 mm was used. Both ends of the chamber were open and there was no mechanically induced background airflow in the chamber when the clean room ventilation stopped. A laser safety shield (1-mm thick galvanized steel base plate) with opening (diameter: 30 mm) was installed at one end of the chamber. The subjects coughed through the opening into the measurement area. The measurement area by the CCD camera was varied from 70mm x 70mm to 120mm x 120mm depending on the focus length of macro lens. Table 1 shows the operating parameters for PIV measurement. All the measurements were performed over 17 male and 9 female subjects to obtain realistic velocity distributions of cough with an approval from the institutional ethics committee. The subjects were first given an overview of the research and were told about the risk involved in the measurements. Asthma sufferers, people who were experiencing illness, who had recently experienced expiratory problems or were likely to experience discomfort in confined spaces were excluded.

Every volunteer was asked to cough following a standard protocol. When the volunteer was positioned comfortably in the correct position with his/her mouth placed at the opening of the safety shield, they were asked to cough 3 times with a break time of each cough (up to 1 min). During 3 times coughs, PIV measurements for each cough were made and 1 PIV measurement was made for counting numbers. Because the PIV system used was incapable of continuous measurement, the flow field around the mouth of the subject was measured repeatedly at intervals of 70 ms.

Table 1. Operating parameter and values for PIV measurement.

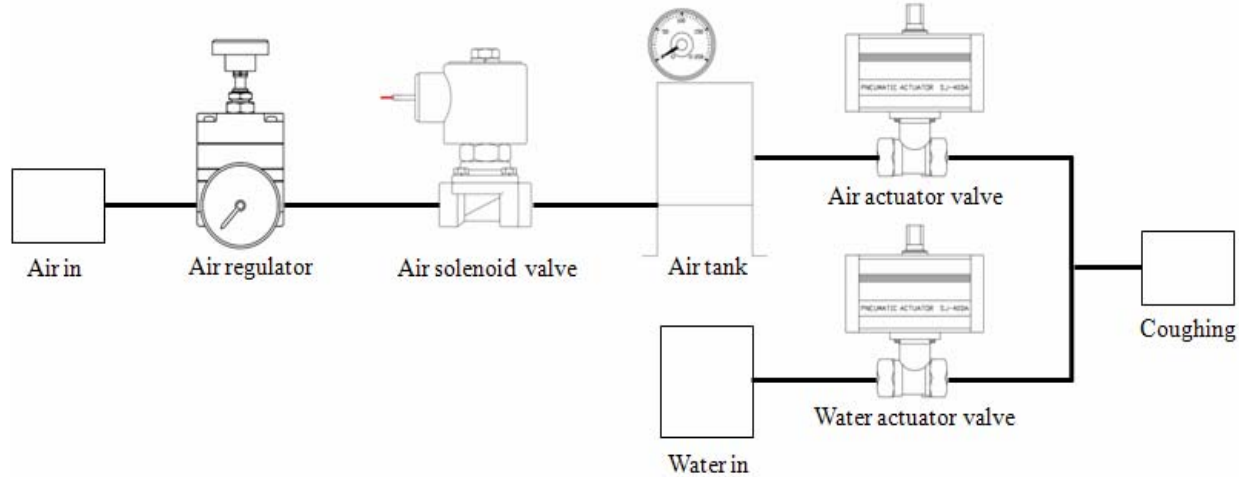
PIV Parameters	Values
Pulse Rep Rate(Hz)	14.50
Laser Pulse Delay(μs)	400.00
Delta T(μs)	100.00
PIV Exposure(μs)	490
Field of View	247mm × 184mm
Image Dimensions	1487 pixels × 1039 pixels
Cylindrical Lens	FL : -15mm

Cough simulator

A cough simulator was designed for producing a repetitive and controllable coughing flow including water droplets. It mainly consists of air tank for compression and water spray system for simulating saliva droplets as shown in Figure 2. By adjusting air regulator, pressure of air tank could be changed and the discharge time was varied by the air actuator valve up to 1 s. The amount of water was controlled by the water actuator valve. Both actuator valves were

synchronized for generating water droplets during a cough. The operating parameters, air pressure of tank and discharge time, will be determined from the comparison of experimental results obtained from subjects' cough experiment (26 volunteers) using the PIV system in this study.

Figure 2. Apparatus for a cough simulation



Results and Discussion

Distribution of Subject's Velocity Vectors

From the measurement of 26 recruited persons' cough, we found that the velocity profiles of cough. Figure 3 shows the one example of velocity distributions. Most frequent range of velocity was found to be 0.5~1 m/s, but the highest velocity was about 25~30 m/s.

Exhaled air jet dispersed to the horizontal direction with time. For the estimation of velocity magnitude, the components of horizontal (u) and vertical (v) velocities were analyzed separately. It was found that the maximum u -velocity was 14.4 m/s and the maximum v -velocities were 5.2 m/s (upward direction) and -4.7 m/s (downward direction) averaged from 9 male subjects. The maximum u -velocity was 10.1 m/s and v -velocities were 2.7 m/s (upward direction) and -3.1 m/s (downward direction) averaged from 8 female subjects. The velocity vectors were shown in Figure 3. The magnitude of cough velocity vector for males was higher than that of female by 45%, however, the spread directions (θ_{up} and θ_{down}) were found to be similar for male and female. These preliminary results of cough velocity obtained from our new PIV system showed good agreement with average velocity of cough obtained by Zhu et al. (2006) [5] and Chao et al. (2009) [6]. Cough volume was performed by the spirometer (CHEST corp., HI-801), one of the lung capacity factors, Forced Vital Capacity (FVC) was regarded as the emitted volume by human cough. The male and female average FVC were 4.44L and 3.40L.

Figure 3. Velocity distributions of one cough with time

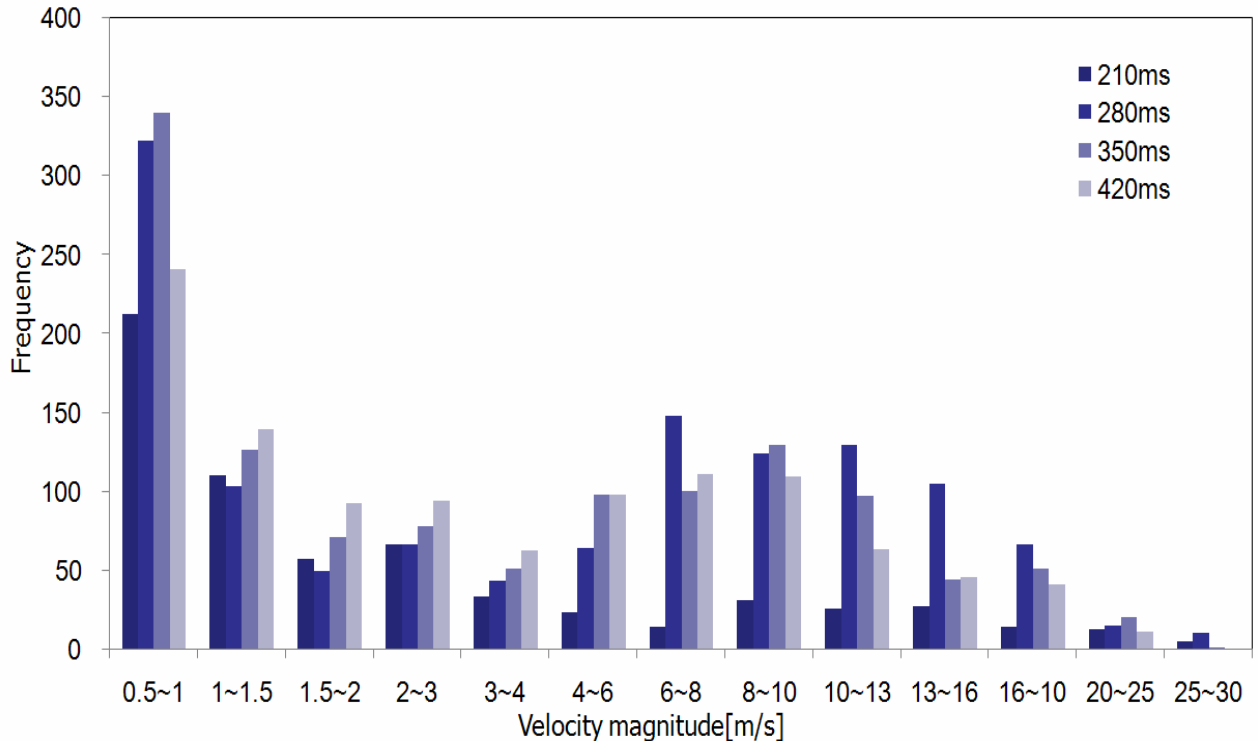
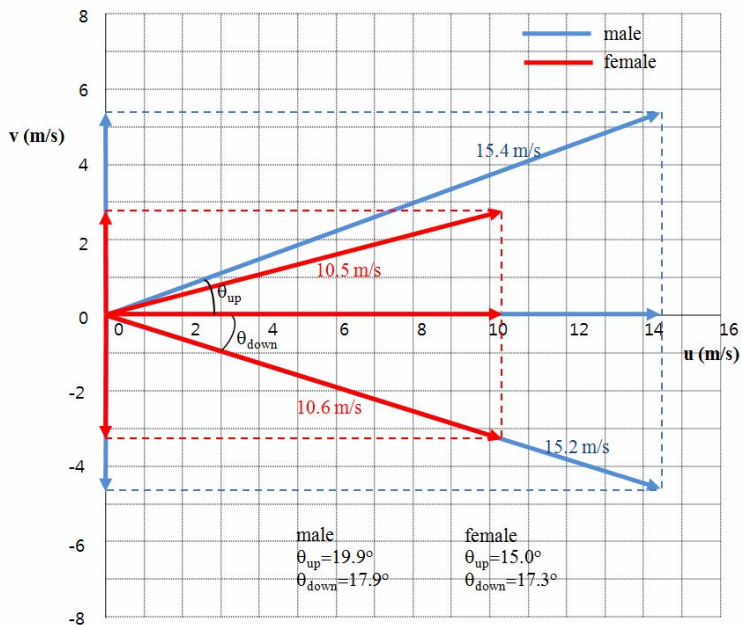


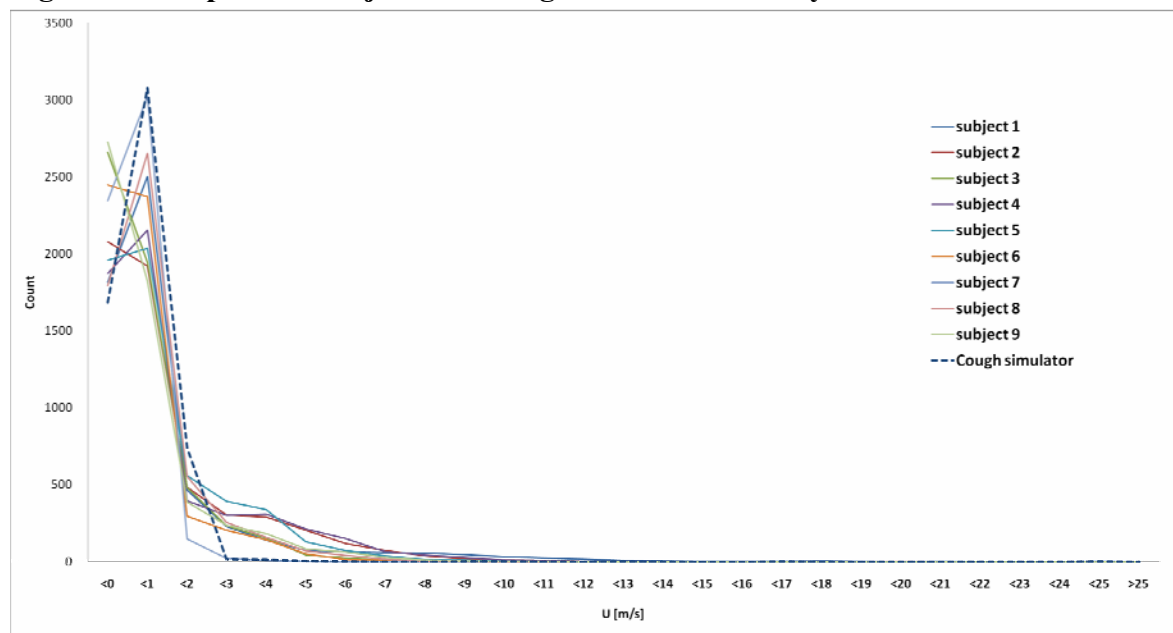
Figure 4. Maximum velocity vectors of coughing jet for male and female.



Comparison Subject vs. Cough simulator velocity distribution

The cough simulator was operated that subject physical data used such as mouth opening time and emitted volume. The valve open time was set 0.56 sec. Emitted volume was controlled 3.40L by female's FVC average. Figure 5 shows the velocity distribution which of the comparison female subject with cough simulator. The 9 female subjects and cough simulator show the results which have high similarity.

Figure 5. Comparison subject with cough simulator velocity distribution.



SUMMARY OR CONCLUSION

The Particle system (PIV) and acrylic glass chamber were used to cough velocity. The Average maximum u-velocity was 14.4m/s and v-velocities were 5.2m/s (upward direction) and -4.7m/s (downward direction) from male subjects. The female average maximum u-velocity and v-velocities were 10.1m/s, 2.7m/s and -3.1m/s. Cough volume was performed by the spirometer one of the lung capacity factors. The male and female average FVC were 4.44L and 3.40L.

A cough simulator's air tank was replicated to the lung. It is possible that air tank would be flexible volumes by regulator and cough velocity be control actuate-valve opening time by timer.

ACKNOWLEDGMENTS

This research was supported by the Converging Research Centre Program Through the National Research Foundation of Korea(NRF) funded by the Ministry of Education, Science and Technology (2009-0082056).

REFERENCES

- [1] Rota PA et el.; World Health Organization (accessed November 2003) .
- [2] *World Health Organization online*: WHO Pandemic (H1N1)-update 91 (accessed December 2009)
- [3] Olsen S. J. et el. *N Engl J Med* 349(25): Centers for Disease Control and Prevention, Nonthburi Thailand 2003; pp 2416-2422.
- [4] Eugene C. Cole DrPH : Carl E. Cook, MS : AJIC *Am J Infect Control* 26 : DynCorp Health Research Services Durham USA 1998; pp 453-464.
- [5] Zhu, S. Kato, S and Yang, J-H. *Building and Environment* 41: University of Tokyo, Institute of Industrial Science, Japan 2006: pp 1691-1702.
- [6] C.Y.H. Chao et el. *Aerosol Science* 40 : The Hong Kong University of Science and Technology, Clear Water Bay, Hong Kong 2009; pp 122-133.

Dry Adsorption of CO₂ by Granular Sorbents

Yun Hui Lim, Huang Shan, Hyun Hee Lim and Young Min Jo

Department of Environmental Engineering, Kyung Hee University, South Korea, 449-701

Corresponding author: Prof. Young Min Jo, + 82-31-201-2860,

+ 82-31-203-4589, ymjo@khu.ac.kr

ABSTRACT

In order to meet the domestic IAQ(Indoor Air Quality) standard, granular adsorbents including activated carbon particles(AC) and activated carbon fiber(ACF) were prepared, and attempted to capture the gaseous CO₂ molecules. In this work, a few commercial particulate AC and ACF were modified with Ca-base precursors such as Calcium hydroxide(Ca(OH)₂) and Calcium acetate monohydrate(Ca(CH₃COO)₂), then pelletized to the spherical granules. The CO₂ adsorption capacity of each sorbent was evaluated in a fixed-bed reactor. It was found that the selectivity of the sorbent in favor of CO₂ to a certain degree could be enhanced through the impregnation of calcium elements.

Characterization of the impregnated sorbents showed that the AC particles could have better surfacial distribution of calcium ions than ACF. The TPD(Temperature Programmed Desorption) test indicated strong interforces of CO₂ molecules with Ca elements originated from Ca(OH)₂ rather than Ca(CH₃COO)₂ on the AC particle surface.

KEYWORDS

Granular sorbents, Dry adsorption, AC, ACF, Cation impregnation

Introduction

Modern people spend more than 80~90 % of their daily time in indoor such as residential housings, buildings, schools, subway, etc(Lim et al., 2001). Well insulation of public space due to rising energy cost deteriorates the indoor air quality. Carbon dioxide is one of critical elements for the IAQ regulation in Korea. Most researches for carbon dioxide adsorption for both indoor and outdoor have been carried out focusing on new materials including dry sorbents. Adsorption process has paid much attention to the low energy consumption, low equipment cost, and easy application. In addition, the adsorption process consists of simple devices than other gas

capturing systems. Zeolites, molecular sieves and activated carbon particles are popular sorbents for CO₂ capture(Jadhav et al., 2007). Walton et al. (2006) have attempted to exchange cations of Li⁺, K⁺, Rb⁺, and Cs⁺ into the zeolites Na-Y and Na-X, which then could achieve the enhanced CO₂ adsorption capacity. Lee et al. (2008) studied the effect of modification by adding alkali metals(K⁺, Li⁺, Mg⁺, Ca⁺) on activated carbon. The present work evaluated the effect of impregnation of Ca elements on adsorption/desorption of CO₂ in AC and ACF.

Experimental Methods

This work used Calcium hydroxide(Ca(OH)₂) and Calcium acetate monohydrate(Ca(CH₃COO)₂) as calcium base precursors. Activated carbon(AC: WAC & BPL) and activated carbon fiber(ACF) were selected for porous supports. Figure 1 is a brief diagram of adsorbent preparation. AC particles or ACF were immersed in an aqueous solution of 1.0 M for calcium hydroxide or calcium acetate monohydrate for a sufficient time at 25 °C. Calcium impregnated sorbent particles were washed by distilled water to cleanse the impurities. Then, they were completely dried at 120 °C, and reserved in a dry desicator.

Schematic diagram of the experimental apparatus for the adsorption of CO₂ and TPD(Temperature programmed desorption) test are shown in Figure 2. It includes a gas supply unit, a stainless packed bed and a gas analyzer. The CO₂ flow was fed to the fixed bed of the sorbent at 3000 ppm. In a TPD test, the packing reactor was heated up to 600 °C for complete desorption with supply of helium gas. CO₂ adsorption amount of the test sorbent was evaluated by equation (1).

Results and Discussion

Breakthrough curves were depicted based on the experimental results. This work compared the intrinsic sorbent and calcium precursor in focusing on adsorption capacity.

1. Adsorption amount

Table 1 is an overall summary of experimental results including surface area of test sorbent particles and CO₂ adsorption amount. The specific surface area was 602.84 to 1469.61 m²/g for AC and 943.64 to 1072.49 m²/g for ACF respectively. The raw particulate AC and ACF indicated the larger surface area than the calcium ion impregnated sorbents. Modification with the treatment of calcium precursors reduced the surface area due to blocking of micropores by added elements. However, adsorption amount of modified sorbents could be increased based probably on acid-base interactions. Stronger attraction of CO₂ at the basic sites led to greater

capture of CO₂ molecules. The amount of adsorption on an adsorbent depends on the available surface and the affinity for the adsorbate.

The origin of activated carbon could influence the adsorption amount, WSC which is made of coconut shell showed better quality by –OH impregnation rather than –CH₃COO. Basic properties by –OH might induce acidic carbon dioxide. BPL based on coal contains more acidic functional groups, so that the basic –OH could be impregnated with simplicity. Figure 3 shows the breakthrough curves obtained from the experiment. While AC from WSC had higher affinity for Ca(CH₃COO)₂, AC-BPL was affinitive to Ca(OH)₂ than Ca(CH₃COO)₂.

2. Desorption characteristics

Figure 4 shows TPD profiles of the modified AC adsorbents. Desorption was found to be depending more on the precursor of calcium. Most of all the adsorbed CO₂ molecules on the AC sorbent with Ca(CH₃COO)₂ could be detached by heating before 400 °C. Whilst Ca(OH)₂ resulted in almost complete desorption under 500 °C. Desorption at low temperatures would be detachment of the molecules bound by weak physical forces. Some molecules which were dominated by chemical interactions were released at higher temperature as above 500 °C.

CONCLUSION

Comprehensive characterization of modified AC adsorbents revealed the possibility of CO₂ adsorption. Constituents of calcium could enhance the adsorption capacity, in particular coal based AC sorbent with calcium hydroxide did not only showed the highest potential of CO₂ capture, but also more consolidated binding forces

Equation

$$q = \frac{Q \times C_i}{W} \left[\int_0^{t_s} \left(1 - \frac{C_o}{C_i} \right) dt \right] \quad (\text{Eq.1})$$

where q: the adsorbed amount (mmol/g), Q: the inlet flow rate (l/min), W: the sorbent weight (g), C_i and C_{out}: inlet and out CO₂ concentrations (ppm) respectively, and t_s: the saturation time(s).

Table**Table 1. BET surface area and adsorption amount of test sorbents with Ca-base precursors.**

Precursor	AC				ACF	
	WSC-AC		BPL-AC		Surface area (m ² /g)	Adsorptio n amount (mmol/g)
	Surface area (m ² /g)	Adsorbed amount (mmol/g)	Surface area (m ² /g)	Adsorptio n amount (mmol/g)		
Raw	1469.61	0.035	1173.58	0.024	1072.49	0.030
Ca(OH)₂	1243.27	0.040	974.66	0.060	-	-
Ca(CH₃COO)₂	747.32	0.054	602.84	0.043	964.96	0.041

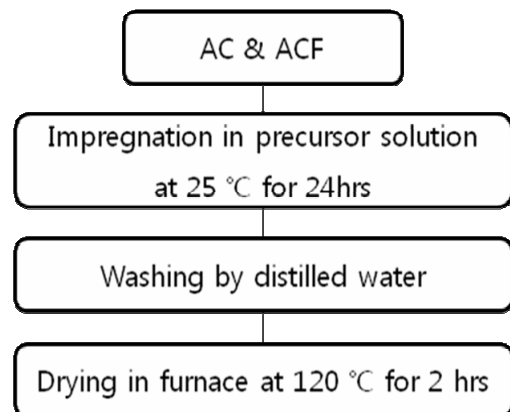
Figure**Figure 1. Procedure for preparation of test sorbents.**

Figure 2. Schematic diagram of experimental set-up.

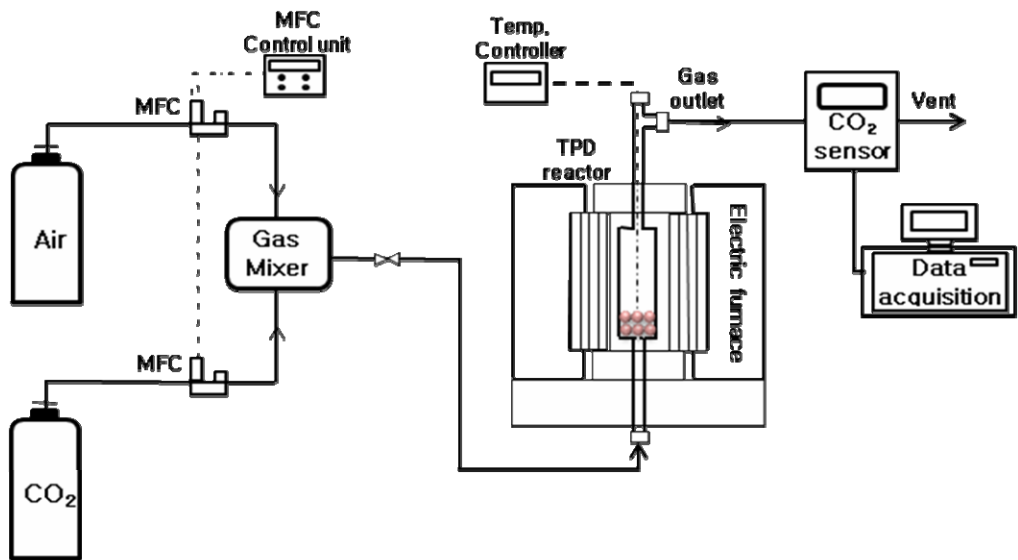


Figure 3. Breakthrough curves of CO₂ adsorption with adsorbent type(CO₂ Conc. 3000ppm, Reaction Temp. & pressure – RT & 1atm).

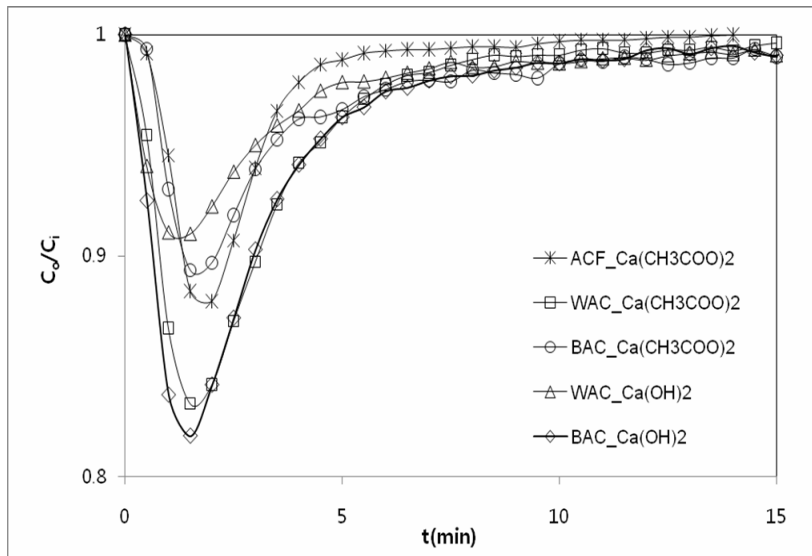
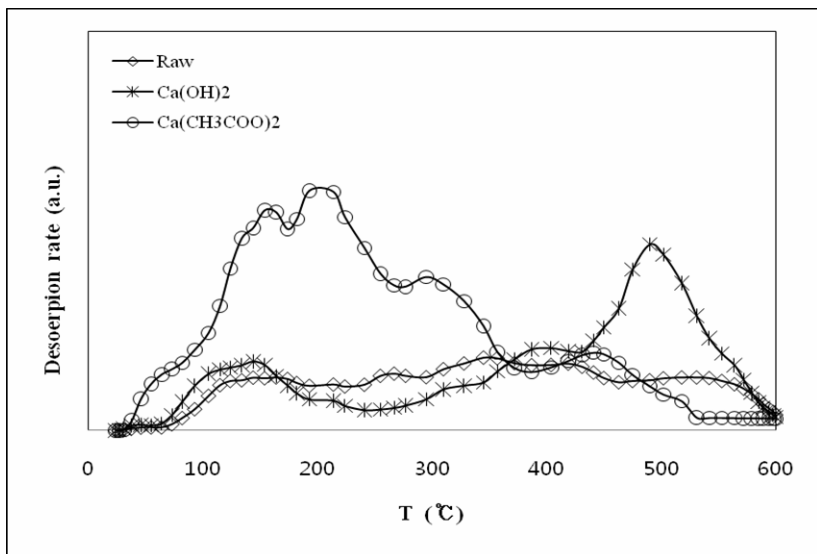
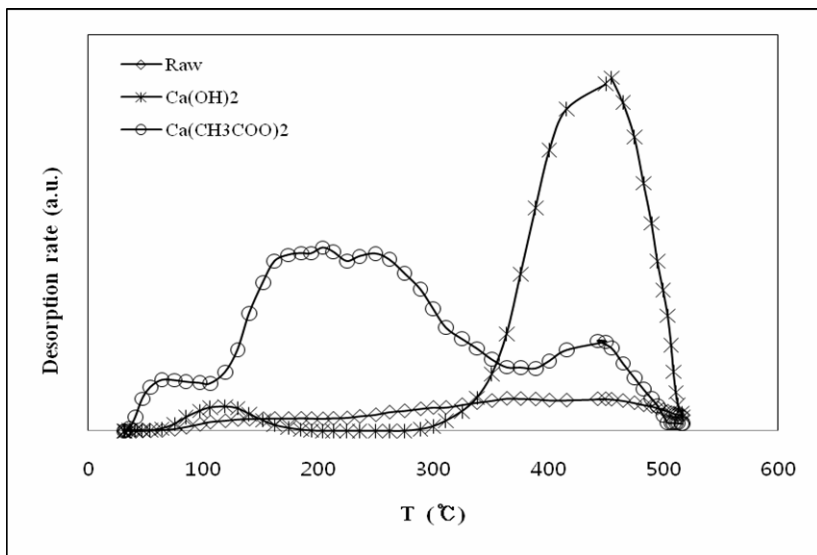


Figure 4. CO₂-TPD profiles for AC adsorbent.



(a) WSC-AC



(b) BPL-AC

ACKNOWLEDGMENTS

This research was supported by Basic Science Research Program through the National Research Foundation of Korea(NRF) funded by the Ministry of Education, Science and Technology(2011-0004968).

REFERENCES

- [1] Lim, Y.H.; Lee, K.M.; Lee, H.S.; Jo, Y.M.; Adsorption capacity of CO₂ adsorbent with the pretreatment temperature, Journal of Korean Society for Atmospheric Environment, 2010, 26(3), 286-297.
- [2] Lee, K.M.; Jo, Y.M.; Adsorption Characteristics of Chemically Modified Sorbents Carbon dioxide, Journal of the Korean Industrial and Engineering Chemistry, 2008, 19(5), 533-538.
- [3] Song, H.K.; Lee, K.H.; Adsorption of Carbon Dioxide on Chemically Modified carbon Adsorbents, Separation Science and Technology, 1998, 33(13), 2039-2057.
- [4] Jadhav, P.D.; Chatti, R.V.; Biniwale, R.B.; Labhsetwar, N.K.; Devotta, S.; Rayalu S.S.; Monoethanol Amine Modified Zeolite 13X for CO₂ Adsorption at Different Temperatures, Energy & Fuels, 2007, 21, 3555-3559.
- [5] Walton, K.S.; Abney, M.B.; LeVan, D.; CO₂ adsorption in Y and X zeolites modified by alkali metal cation exchange, Microporous and Mesoporous Materials, 2006, 91, 78-84.

Important note: Each abstract would be identified by the author(s) for their intention as presentation in oral or poster session and submission will be due on January 31, 2011.

Evaluation of Filtration Performance for Depth Filter Media using Different Standard Test Dusts

Young-Ok Park¹ and Naim Hasolli^{1,2}

1 Korea Institute of Energy Research Center, Clean Fossil Energy Research Center, Daejeon, Korea

2 Chungnam National University, Chemical Engineering Department, Daejeon, Korea

ABSTRACT

Initial filtration performance and loading characteristics are the main parameters of the depth filter media. These parameters give an overview of the filtration performance based on which the future specification of the depth filter media is made. Initial filtration performance as well as the characterization of the filter media structure is made using the flat sheet media. The dust loading characteristics of the depth filter media are evaluated using the assembly as a filter cartridge made of the same depth filter media as flat sheet media. During this study we have used the samples of the depth filter media TFM2 and the test apparatuses designed in our laboratory to meet some of the standard test procedures. Test particles used during these tests include the test with KCl particles and A2 fine as a standard test dust and NaCl in our previous tests. The results from the conducted tests indicate a low pressure drop due to multilayer structure and a high particle collection efficiency which is mainly attributed to the final layer consisting of meltblown fibers of small diameters and dense packing structure.

KEYWORDS

Depth filter media, filtration performance, monodisperse, polydisperse, collection efficiency, initial pressure drop, dust holding capacity, dust loading.

Introduction

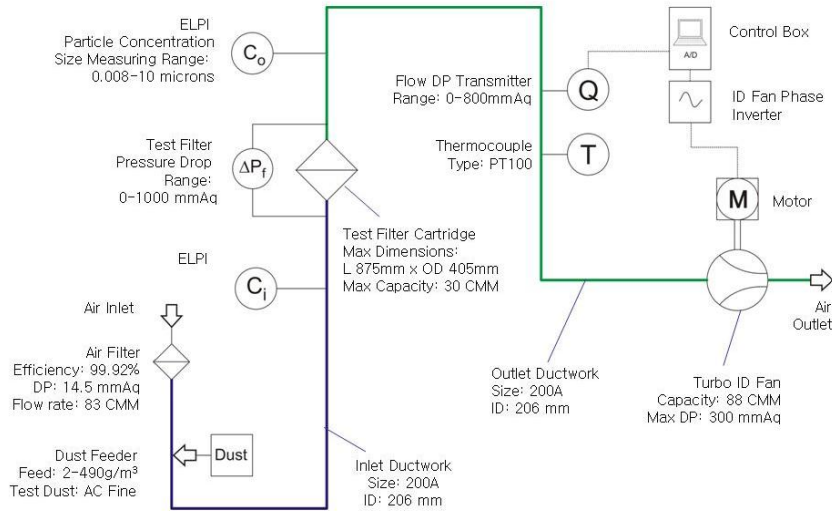
Initial filtration performance of the filter media is usually evaluated by measuring two of the most significant parameters: the initial pressure drop and fractional collection efficiency. In the literature [1,2,3] these parameters are described as indicators whether the filter media is suitable for their intended application. Each of these parameters can be used as an indicator for the filter media performance. Initial pressure drop of the depth filter media is an indicator for the flow resistance of the depth filter cartridge or assembly sample, to the air stream for upstream and downstream of the depth filter cartridge and is directly correlated with the layer structure of the depth filter media as well as the fiber structure and packing density. Dust loading characteristics

include the behavior of the pressure drop as function of the dust loading and the dust holding capacity which indicates the ability of the depth filter media to hold certain amount of dust within filter media. For the purpose of filter media particle collection efficiency, test particles injected in the upstream of the test filter media can be of poly- or monodisperse nature. The test with monodisperse particle has been conducted and results are reported in our previous work [4]. This study has been initiated to evaluate the filtration performance by using our laboratory test units for flat sheet media and the depth filter media test unit for cartridge assembly.

Experimental Methods

For the test with KCl particles we have used the test unit developed in our institute for the purpose of testing the flat sheet filter media. The tests were made using flat sheet depth filter media samples of the size 52 mm with the effective filtration area of 13.8 cm^2 . The particles are generated using small size atomizer to generate the KCl particles from the initial solution of 10 wt%. The entire range of particles measured by the unit SMPS (TSI) is between 20 and 600 nm. Test with filter cartridge was conducted under ambient air temperature and humidity conditions. Figure 1 shows the experimental setup with main functional units. The test filter cartridges have the following dimensions: inner diameter (ID) is 212 mm; outer diameter (OD) is 320 mm and the length (L) of the cartridge is 660 mm. Test dust was the standard ISO A2 Fine (ISO Standard 12103-1). Initial pressure drop (DP) characteristics of the filter cartridge were evaluated by varying the flow rate below and above the value of the nominal flow rate ($1000 \text{ m}^3/\text{min}$) without injecting the test dust. Dust holding capacity (DHC) test is made by loading the cartridge with dust of high inlet concentration C_i . DHC is expressed in amount of the dust collected during dust loading time which is determined by gravimetric measurements of the cartridge made before and after the test. During the DHC tests, collection efficiency is calculated from the measurements of particle concentration in feed air upstream and downstream of the filter cartridge. Some of these procedures are in compliance with the standard testing procedures of ASHRAE 52.2 [5].

Figure 1. Flow schematic of the test unit for testing the depth filter media cartridge

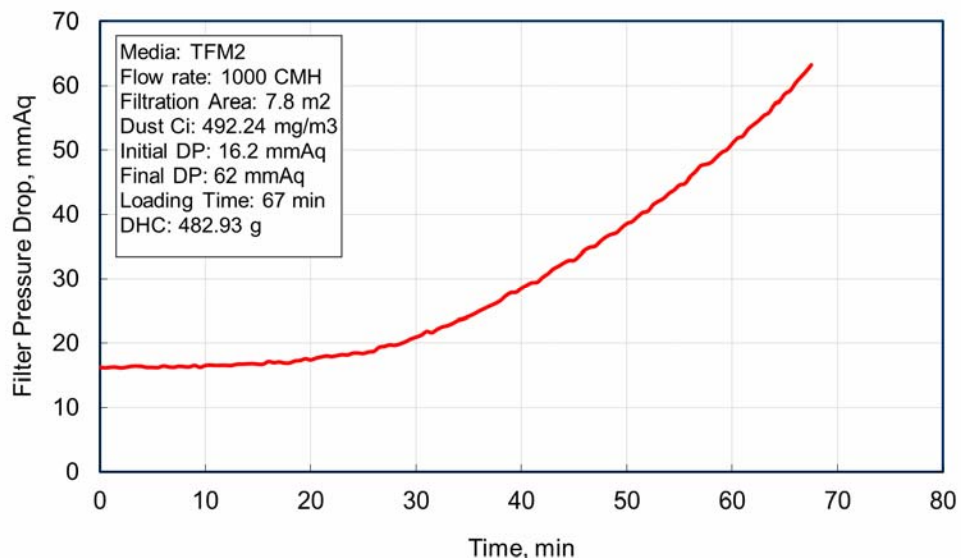


Results and Discussion

From the test from our previous work [4] with flat sheet media we can see that the test media TFM2 has the initial pressure drop of 10 mmH₂O for the face velocity 9.6 m/min and with the test with KCl particles this value is 11 mmH₂O which is similar to the result from the test with NaCl particles. Results from the test with KCl particles show high particle collection efficiency of the depth filter media TFM2 with the decreasing tendency as the filtration velocity is increased from 3.2 m/min to 9.6 m/min with values 95.89% and 90.51% respectively which is lower than that from the tests with NaCl with 99.8% and 98.3% respectively.

From the test with cartridge filter we could obtain data for the pressure drop variation with the dust loading as shown in Figure 2. The dust holding capacity at the final pressure drop 62 mmH₂O is 482 g. The overall collection efficiency at the initial stage of dust loading is over 99.99% and at the final pressure drop 62 mmH₂O. The overall estimation of the filtration performance is that the depth filter media exhibits high collection efficiency and relatively low pressure drop due to the optimal combination of the filter media layer structure. Especially the high collection efficiency even for submicron particles is due to the filter media final layer made of meltblown fibers. This layer also has the effect on increasing pressure drop so that future development and optimization of the layer structure would lead to better results.

Figure 2. Pressure drop characteristics as function of dust loading time



ACKNOWLEDGMENTS

This work was supported in part by the Eco-technopia21 Project of the Korea Environmental Industry & Technology Institute(KEITI) grant funded by the Korea Government Ministry of Environment.

REFERENCES

- [1] Huttun, I. M., *Handbook of Nonwoven Filter Media*, Elsevier, Oxford, 2007.
- [2] Brown, R. C., *Air Filtration, An integrated Approach to the Theory and Applications of Fibrous Filters*, Pergamon Press, Oxford, 1993.
- [3] Hinds, W. C., *Aerosol Technology, Properties, Behavior, and Measurement of Airborne Particles*, 2nd Edn. Wiley, New York, 1982.
- [4] Park, Y.O., Hasolli, N., Choi, H.K., Rhee, Y. W., Characterization of depth filter media for gas turbine intake air cleaning, PAAR, Volume 4, No. 5, December 2009.
- [5] ANSI/ASHRAE 52.2-1999, *Method of Testing General Ventilation Air Cleaning Devices for Removal Efficiency by Particle Size*, American Society of Heating, Refrigerating, and Air-Conditioning Engineers, Atlanta, G.A., USA (1999).

Removal Characteristics of SO₂ in Absorbents Internal Circulating Desulfurization Equipment

Young-ok Park¹ and Hyun-Jin Park¹

1 Korea Institute of Energy Research, Daejeon, 305-343, Korea

ABSTRACT

SO₂ gas present in the atmosphere is generated mainly through the industrial processes of fuel combustion, especially those of oil and coal combustion where the discharge rates of SO₂ gas are the highest. Herein, we consider that the introduction of new desulfurization technology for efficient removal of high content of SO₂ gas from industrial discharge sources is necessary. In our study we have conducted the tests using the absorbent internal circulating Turbo-FGD unit to identify the most efficient of three applied absorbents for the SO₂ removal at high flue gas temperatures 300 to 400°C and to evaluate their performance. By maintaining the flue gas high temperature and fluidizing the absorbents and bed materials, this unit has proven the ability of keeping the SO₂ removal rate high while preventing the absorbent to adhere on the internal wall of the desulfurization unit. The pressure drop and SO₂ removal efficiency characteristics were closely investigated by varying test parameters such as Ca/S mole ratio, water injection feed rate, flue gas flow rate, absorbent material, the amount of bed material, SO₂ inlet concentration and reaction temperature.

KEYWORDS

Desulfurization, Absorbent internal circulating desulfurization equipment, Glass bead, Fluidized bed reactor, Absorbent

Introduction

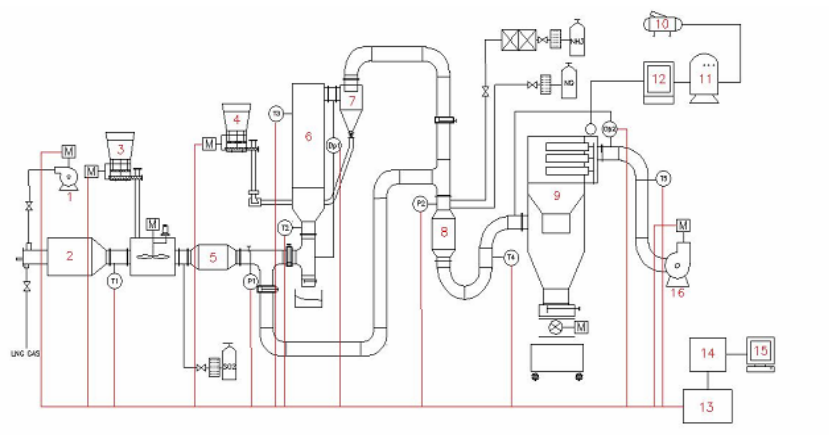
Subject of this study is investigation of the dry desulfurization process for removal of sulfur dioxide emissions from power plants. Desulfurization processes have been studied actively in the 1960s to the 1970s. At that time, SO₂ removal efficiency and technical reliability and economic efficiency of the dry process were lower than of that of the wet type desulfurization plant and therefore haven't been developed intensively. But recently, the interest of applying the dry desulfurization process is increasing due to the possible application for treatment of the flue gas from high-temperature combustion processes and the injection of sorbents into the duct combined with lower investment cost than the wet process to meet the emission standard. In this study, high

reactive Turbo-FGD and newly developed sorbent were used to evaluate the desulfurization efficiency.

Experimental Methods

The flow schematic of the Turbo-FGD is displayed in Figure 1. The experimental unit consists of following parts: hot gas generation part, the sorbent feeding part, sorbent recirculation cyclone part, part of clean gas emission, SO₂ injection part, water pump and spray nozzle part, operation control and data recording unit. The injected Ca(OH)₂ and glass bead are fluidized and the reaction of the sorbent with the flue gas is facilitated. The circulated sorbent particles which are collected at the lower part of the cyclone are re-injected and mixed with the fresh sorbent to reach high desulfurization rates.

Figure 1. Diagram of sorbent internal circulating Turbo-FGD unit.



- | | | | |
|--------------------------|--------------------------------|---------------------|----------------------|
| 1: F.D fan | 5: SO ₂ chamber | 9: DDN-system | 13: Main control box |
| 2: Duct heater | 6: Turbo FGD | 10 : Air compressor | 14: A/D converter |
| 3: Test absorbent feeder | 7: Recirculation cyclone | 11: Air tank | 15: Computer |
| 4: Test dust feeder | 8: NO, NH ₃ chamber | 12: Air dryer | 16: ID fan |

For simulation of the test conditions a SO₂ of 100% purity was used. The injection rate was controlled through the regulation of the concentration using MFC (mass flow controller. Brooks CO.). SO₂ concentration was measured by flue gas analyzer (MADUR, model PHOTON). Variation of gas velocity, Ca/S molar ratio and water supply speed were carried out. In Table 1 the experimental conditions of Turbo-FGD test unit are displayed.

Table 1. Experimental conditions.

No	Variables[unit]	Range
1	Ca/S mole ratio[-]	1.0 ~ 1.5
2	Water injection flow rate[liter/min]	0 ~ 1.2
3	Superficial gas velocity[Nm/sec]	1.0 ~ 1.7
4	SO₂ inlet concentration[ppm]	250 ~ 800
5	Operating temperature[°C]	110 ~ 350
6	Absorbent type[-]	Ca(OH) ₂ : A, B, C type
7	Weight of bed materials[kg]	0 ~ 10

Results and Discussion

Desulfurization efficiency was measured by using the Ca/S molar ratio increases beyond 1.3 for sorbent Ca(OH)₂ powder of A, B, C type. According to the results, the higher the Ca/S ratio the higher desulfurization efficiency increases. In terms of surface area the sorbent species have the following characteristics: C type (55 m²/g), A type (18m²/g) and B type (15 m²/g). Based on the surface area the desulfurization performance of these three types was compared and displayed in figure below. The highest desulfurization performance exhibited the type C of sorbent even at low Ca/S ratio.

Fig. 2. SO₂ removal efficiency of A, B, C type absorbent as function of Ca/S mole ratio.

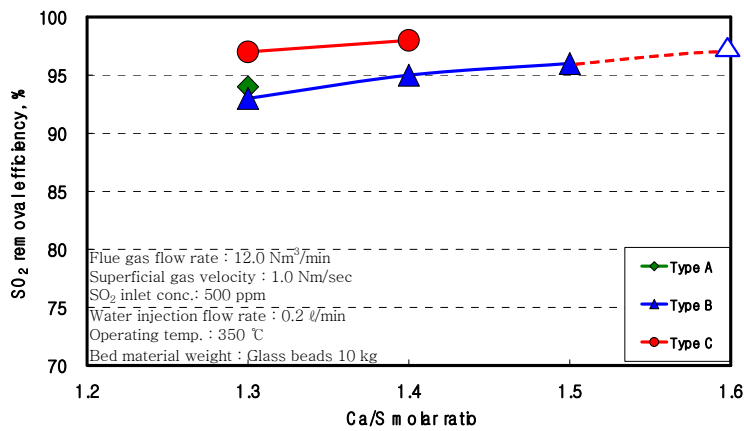
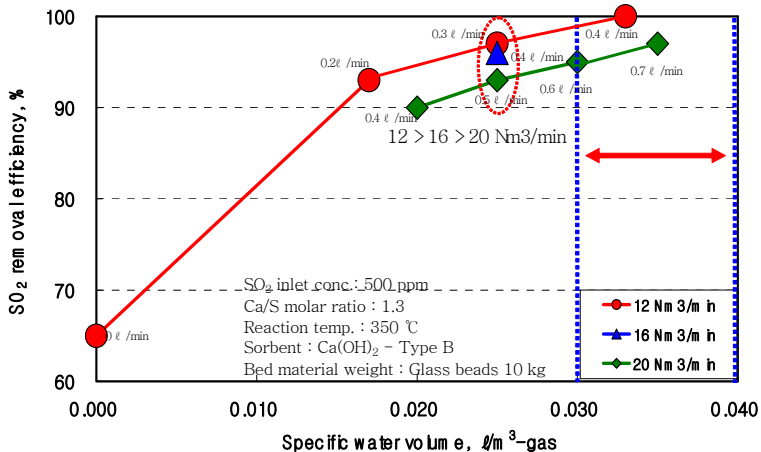


Figure 3 shows the SO₂ removal efficiency according to the water flow rate and as function of flue gas flow rate. Gas desulfurization efficiency increases with the increase of the amount of

water injected. The desulfurization performance degradation is visible for increasing rate of flue gas flow.

Fig. 3. The effect of water injection flow rate on SO₂ removal efficiency at various flue gas flow rate.



CONCLUSION

In this study, 3 species of high-temperature sorbent (Ca(OH)₂) was used and the performance of the Turbo-FGD was evaluated according the sorbent type. The total 7 experimental variables were changed in order to determine the performance characteristics of removal of SO₂ and the following conclusions can be made: depending on the variation of 0 ~ 10 kg glass bead amount of filling the SO₂ removal efficiency increased by 55-100%, respectively. By increasing of flue gas velocity the SO₂ removal efficiency decreases due to the reducing resident time of gas in the fluidized bed. With increasing gas flow rate the reaction time is also reduced and therefore the decreasing of the removal rate is expected. Desulfurization efficiency increasing tendency is observed when Ca/S molar ratio and water feed rate were increased and a decreasing tendency when the flue gas velocity and inlet gas temperature increased. By increasing the speed of the water supply certain desulfurization efficiency can be maintained. Round 98% desulfurization efficiency is observed for the optimal value between 0.03 and 0.04 liter-water/Nm³-gas for the specific water volume 1.7 Nm/sec in the gas flow.

ACKNOWLEDGMENTS

This work was supported in part by the Power Generation & Electricity Delivery of the Korea Institute of the Energy Technology Evaluation and Planning (KETEP) grant funded by the Korea Government Ministry of Knowledge Economy.

REFERENCES

- [1] Jan B.W. Frandsen, SØren Kiil, Jan Erik Johnsson, "Optimisation of FGD pilot plant using fine limestone and organic acids", *Chem. Eng. Sci.*, 56, 3275.(2001)
- [2] C. David Cooper, F. C. Alley, *Air Pollution Control : A Design Approach*, Chap. 15, pp. 463~496.(2003)
- [3] Halt, B.W., Sedman, C.B Current Status of the ADVA-CATE Process for Flue Gas Desulfurization, *J. Air Waste Management Association*, 42(1).(1992)
- [4] Martinez, J. G., Lopez, A. B., Garcia, A. G., and Solano, A. Linares, "SO₂ retention at low temperatures by Ca(OH)₂-derived CaO : a model for CaO regeneration," *Fuel*, 81, 305~313.(2002)
- [5] Yuan C. S. : Ph. D. Dissertation, Illinois Univ., Urbana-Champaign, U.S.A.(1990)
- [6] Gupta, R. P., Turk, B. S. and vierheiling, A. A. : "Desulfurization sorbents for transport-bed applications", *In proceedings of the advanced coal-based power and environmental system '97 conference, pittsburgh PA. July.*(1997)
- [7] Keener, T. C. and Khang, S. J, "Kinetics of the sodium bicarbonate-sulfur dioxide reaction," *Chem. Eng. Sci.*, 48(16), 2859~2865.(1993)
- [8] Erdos, E. et al, "Application of the active soda process for removing sulfur dioxide from flue gases," *JAPCA*, 39, 1206~1209.(1989)

Formation of Non-Agglomerated Titania Nanoparticles in a Flame Reactor

Akihiro Ishibashi, Hirofumi Ozaki and Yoshiki Okada

Department of Chemical Engineering, Kansai University, Osaka 564-8680, Japan

Principal Contact: Akihiro Ishibashi, Department of Chemical Engineering, Kansai University, Osaka 564-8680, Japan.

Tel: 06-6368-1121 Email: uc70008@edu.kansai-u.ac.jp

Abstract

Flame technology is attractive for manufacture of nanosized powders. The product of flame reactors, however, tends to be agglomerated particles which limit their application.

Generation method has been called one of those flame method nanoparticle formation. The flame method, it is possible to generate a large number of particles in low-cost and easy operation. However, particles produced by collisions, aggregation of particles away causing thermal fusion, particle size becomes larger.

In this study, the formation of non-agglomerated titania particles by oxidation of titanium-tetra-isopropoxide (TTIP) has been studied in a methane/oxygen coflow diffusion-flame reactor. A change in the proportion of virtually non-agglomerated particles in TEM images was observed using a rapid cooling of the entire flame aerosol with a blow of cold Ar quenching gas and supercooling in a Laval nozzle placed above the flame. The proportion of non-agglomerates was 25% for TiO₂ particles produced without any cooling steps. When the quenching gas of 25 L/min Ar cooled at -70 degrees blew on the tip of the flame, the proportion of non-agglomerates was 70%. When the flame aerosol was supercooling in the Laval nozzle after blowing -70 degrees Ar quenching gas, a decrease in the aerosol temperature was induced from approximately 1500 to 300 degrees in 0.9 ms and, as a result, the proportion of non-agglomerates was as large as 90%. It was found that the rapid cooling in the region of the flame tip is quite effective for preventing agglomeration.

Keywords: Flame Aerosol Reactor, Non-Agglomeration, Titania Nanoparticles

Numerical Analysis of Multi Axial-Flow Cyclone for AHU Pre-Filter in Subway Station

Myungjoon Kim¹, Hojoong Kim², Soon-Bark Kwon³, Seyoung Kim³, Jin-Kwan Kim⁴ and Taesung Kim^{1,2}

1 School of Mechanical Engineering, Sungkyunkwan University, Suwon, Korea

2 SKKU Advanced Institute of Nano Technology, Sungkyunkwan University, Suwon, Korea

3 Railroad Environment Research Department, Korea Railroad Institute, Uiwang, Korea

4 Institute of Engineering Technology, Dongmyeong Engineering, Seoul, Korea

ABSTRACT

In Korean subway station, auto suction roll filter, auto cleaning demister and electrostatic precipitator is used as pre-filter of subway station air handling unit (AHU). These kinds of filter require high maintenance and effort. To alternate these kinds of filters, we suggest cyclone type filter. A Cyclone is widely used device which remove dust or droplet by centrifugal force. It has many advantages such as constant performance, high throughput and low maintenance cost. If it is installed in subway station AHU, maintenance and effort can be reduced. The Cyclone separator is classified into tangential-flow cyclone and axial-flow cyclone according its main flow direction. Although tangential-flow cyclone is more widely used because of high particle removal rate, it cannot be installed in subway station AHU because it needs large space. However axial-flow cyclone does not require such spaces, so it can be used as a pre-filter of subway station AHU. However compare with tangential-flow cyclone, related studies are insufficient especially for axial-flow cyclone in parallel. In this study, we evaluated new kind of pre-filter which consist of multiple axial-flow cyclones connected in parallel by computational fluid dynamics (CFD).

KEYWORDS

axial-flow cyclone, pre-filter, subway station, CFD

BODY

Introduction

In Korean subway station, auto suction roll filter, auto cleaning demister and electrostatic precipitator (ESP) is commonly used as a pre-filter of subway station air handling unit (AHU). These kinds of filters show good performance in particle remove, however they have some problem in maintenance. In case of auto suction roll filter and auto cleaning demister, because

collected dust is blocked the filter, the pressure loss is deteriorates with the increase of their operating time. Because high pressure loss makes fan consumes more electric power, running cost of AHU is increased. Therefore these filters need regular cleaning and replace. ESP also consumes high running cost due to its dust remove mechanism, and ESP is not suitable for pre-filter, because it has lower efficiency at large particle removal. For these reasons, cyclone separator which is the one of low maintenance device is suggested to new kind of pre-filter.

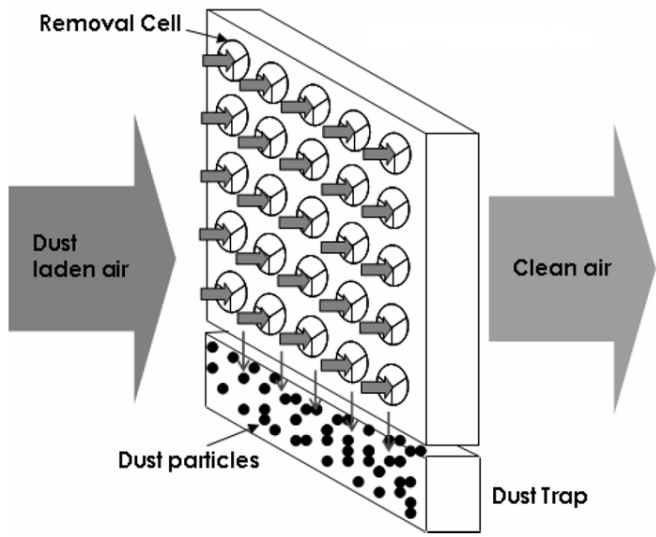
Cyclone separator is widely used for dust removing in industry. It has constant pressure loss, high throughput with moderate efficiency, and low maintenance cost. Cyclone separator is classified into two kinds by direction of inlet and outlet. One is tangential-flow cyclone which changes main flow direction by 90 degree angle and the other one is axial-flow cyclone which does not change main flow direction. Tangential-flow cyclone is extensively researched and widely used. Compared with tangential-flow cyclone, relatively few researches studied about axial-flow cyclone. For example, Weiss *et al.* developed respirable air generating axial-flow cyclone for Czechoslovakian miner^[1], and Weiss *et al.* developed pre-filter type axial-flow cyclone for 10 micron particle removal^[2]. These are one of the earliest applications of axial-flow studies. In recently Hsiao et al. developed five-stage axial-flow cyclones^[3], and measure nano size particle removal efficiency of axial-flow cyclone using SMPS(Scanning Mobility Particle Sizer)^[4].

Tangential-flow cyclone is more common and well designed. However in this case because there are no enough spaces in AHU unit, tangential-flow cyclone which requires large volume space is not suitable to install as a pre-filter.

The purpose of this study was to suggest and evaluate axial-flow cyclone as a new kind of pre-filter. Compared with total flow rate of AHU unit, one axial-flow cyclone has small throughput. Therefore as shown in figure 1, panel type axial-flow cyclone which is consisted of several axial-flow cyclones connected parallel was designed. Each axial-flow cyclone was designed to have pressure loss smaller than 40 mmH₂O and cut off diameter smaller than 5 micron.

In this study, we evaluated multi-unit axial-flow cyclone which is consist of 4 axial-flow cyclones according to outlet shape using numerical method.

Figure 1. Schematic of panel type axial-flow cyclone filter.



Numerical Methods

Transport equation

FLUENT (ANSYS, version 12.1.2) which is a one of commercial computational fluid dynamics (CFD) tool was used for this study. Grid of each 3D model was constructed with about 3 million tetrahedral mesh and prism mesh. With the inlet flow velocity of 5 m/s, the flow in the axial-flow cyclone is in the turbulent regime. In previous axial-flow cyclone study which is compare numerical result with experimental result showed SST (Shear-Stress Transport) $k-\omega$ model was well correlated with experimental result^[5]. Therefore SST $k-\omega$ model was used in this study also. SST $k-\omega$ model was developed by Menter^[6].

Continuity equation, momentum equation and transportation equation of k and ω is described by the following expression. We assumed steady state and incompressible flow.

$$\rho \frac{\partial}{\partial x_i} (u_i) = 0 \quad (\text{Eq. 1})$$

$$\rho \frac{\partial}{\partial x_j} (u_i u_j) = - \frac{\partial}{\partial x_i} p + \frac{\partial}{\partial x_j} \left[\mu \left(\frac{\partial u_i}{\partial x_j} + \frac{\partial u_j}{\partial x_i} \right) \right] \quad (\text{Eq. 2})$$

$$\rho \frac{\partial}{\partial x_i} (k u_i) = \frac{\partial}{\partial x_j} \left[\Gamma_k \frac{\partial k}{\partial x_j} \right] + G_k - Y_k \quad (\text{Eq. 3})$$

$$\rho \frac{\partial}{\partial x_i} (\omega u_i) = \frac{\partial}{\partial x_j} \left[\Gamma_\omega \frac{\partial \omega}{\partial x_j} \right] + G_\omega - Y_\omega \quad (\text{Eq. 4})$$

where G_k represents the generation of turbulence kinetic energy and G_ω represents the generation of ω . Γ_k and Γ_ω represent the effective diffusivity of k and ω . Y_k and Y_ω represent the dissipation of k and ω .

Equations of motion of particles

In this study, we used Euler-Lagrangian method for analysis of particle motion. It predicts the trajectory of a discrete phase particle by integrating the force balance on the particle inertia with the forces acting on the particle, and can be written as

$$\frac{du_p}{dt} = F_D(u - u_p) + \frac{g_x(\rho_p - \rho)}{\rho_p} \quad (\text{Eq. 5})$$

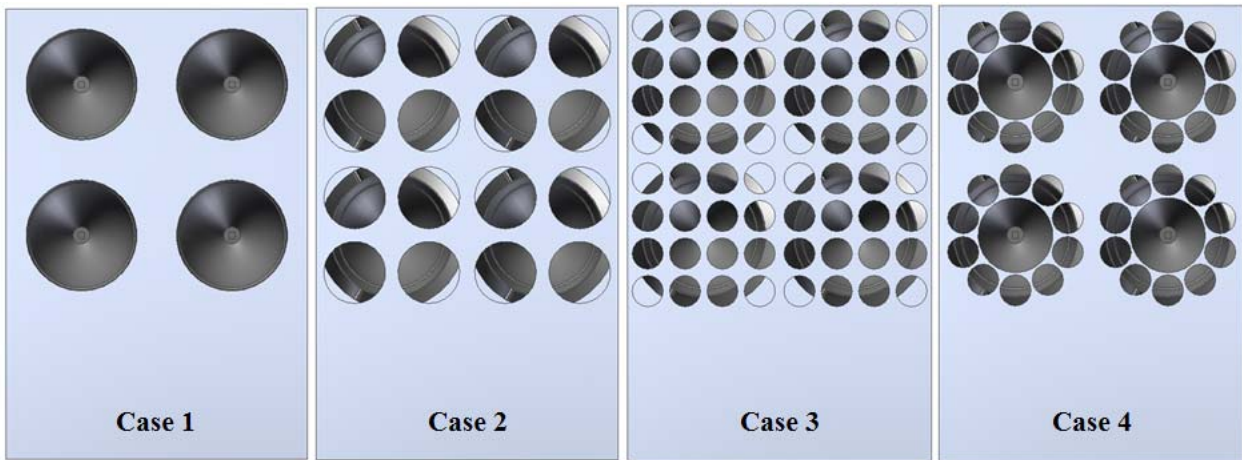
where first term of the right hand side is the drag force and second term is gravitation force term. 1 to 10 micron particle which have 3 g/cc density was tracked at inlet, and if it was deposit in the wall we assumed that particle is removed. Therefore particle removal efficiency was defined as ratio of tracked particle number and removed particle number.

Results and Discussion

Outlet shape

Based on our previous work, blade, casing and inlet part of axial-flow cyclone was designed^[5]. However outlet part was not considered in previous study. Therefore in this study, we studied about relationship between outlet and performance of the axial-flow cyclone. At first, we designed four kinds of multi axial-flow cyclone according to outlet shape like figure 2.

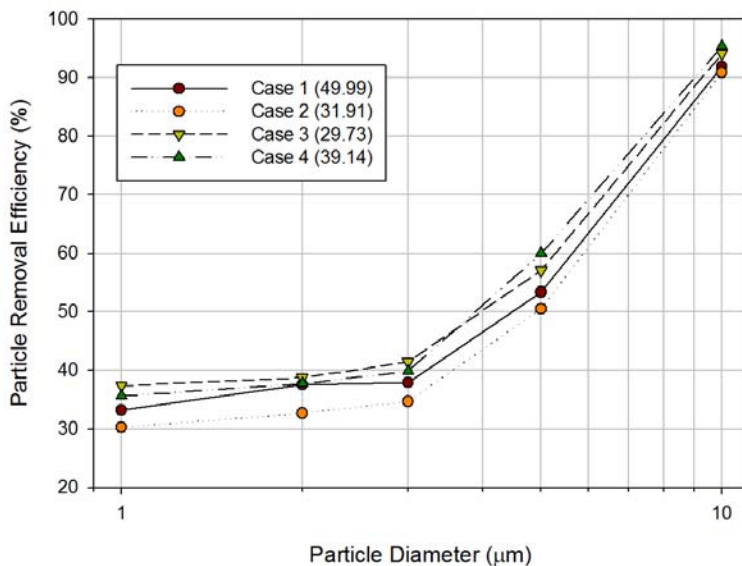
Figure 2. Four multi axial-flow cyclone model according to outlet shape.



Outlet shape of case 1 was designed as a single circle, and each of case 2 and case 3 was designed as 4 and 16 circles. Case 4 was designed as a flower shape. It has one large circle in the center and ten small circles around the large circle.

Figure 3 shows numerical results of these models. Number in bracket is the pressure loss (mmH₂O) of each model.

Figure 3. Numerical results of case 1 to 4.



From the particle removal efficiency view, case 3 and case 4 showed better performance and case 2 and case 3 showed relatively good pressure loss. It is caused by total area, outlet location, and number. In case of case 1 and 2, Case 2 showed lower particle removal efficiency and pressure loss than case 1. It caused by outlet area. Because total outlet area of case 2 was about 20% larger than case 1, particles after blade lost inertia due to slower flow velocity. However case 3 showed

better performance than case 2 although it had same outlet area with case 2. Because several outlets of the case 3 act as the mesh, particles were trapped in between of the outlets. Therefore particle removal efficiency was increased. In case of pressure loss, because outlet of case 3 was located in outside from the axis, flow pass through outlet more easily. It makes lower pressure loss.

CONCLUSION

In this study, we developed and evaluated the multi axial-flow cyclone pre-filter consists of four parallel axial-flow cyclones for replacing the pre-filter in AHU unit of subway station in Korea. Four cases which have different outlet shape were simulated with commercial CFD and the results showed the area, location and number of outlet affect the performance of multi axial-flow cyclone unit. Larger area outlet made lower particle removal efficiency and pressure loss, many numbers of outlet increased particle removal efficiency because they act as a mesh. Outlet which located in outside from the axis made flow could easily pass through the device. It makes pressure loss decrease.

Because numerical results showed multi axial-flow cyclone could have a 5 micron cut off diameter and pressure loss less than 40 mmH₂O, we believe that axial-flow cyclone pre-filter system can be economical and efficient device for removing dust after some modification and verification.

ACKNOWLEDGMENTS

This work was partly supported by grant (Urban Transit Standardization A01) from “The 4th phase of R&D on the urban transit standardization” funded by Ministry of Land, Transport and Maritime Affairs (MLTM) of Korean government

REFERENCES

- [1] Weiss, Z.; Martinec, P.; Vitek, J.; SNTL Praha, 1987.
- [2] Wedding, J. B.; Weigand, M. A.; Carney, T. C. *Environ. Sci. Tech.* 1982, 16, 602-606.
- [3] Hsiao, T. C.; Chen, D.; Greenberg, P. S.; Street, K. W. *J. Aerosol Sci.* 2011, 42, 78-86.
- [4] Hsiao, T. C.; Chen, D. R.; Li, L.; Greenberg, P. Street, K. W. *Aerosol Sci. Tech.* 2010, 44, 253-261.
- [5] Kim, M.; Kim, H.; Kwon, S. B.; Kim, S. Y.; Kim, J. K.; Shin, C. H.; Bae, S. J.; Hwang, S. H.; Kim, T. *International Journal of Air-Conditioning and Refrigeration* 2009, 17, 77-82.
- [6] Menter, F. R. *AIAA-Journal* 1994, 32, 1598-1605.

Submicron diesel PM removal performance of an electrostatic filtration device combined with a metallic foam filter

Hak-Joon Kim¹, Bang-Woo Han¹, Yong-Jin Kim¹, Gyu-Baek Cho¹, Sang-Hyen Jung¹, Sung-Hoon Sim¹, Won-Suk Hong¹, Wan-Ho Shin¹ and Tetsuji Oda²

1 Korea Institute of Machinery and Materials (KIMM), 104 Sinseongno, Yuseong-Gu, Daejeon 305-343, Republic of Korea

2 The University of Tokyo, 7-3-1, Hongo, Bunkyo-ku, Tokyo 113-8656, Japan

Principal Contact: Yong-Jin Kim, Dr., KIMM, 104 Sinseongno, Yuseong-Gu, Daejeon 305-343, Republic of Korea.

Tel: 82-42-868-7475 Fax: 82-42-868-7284 E-mail: yjkim@kimm.re.kr

Abstract

A newly developed electrostatic diesel particulate matter filtration device for heavy duty diesel engines has been tested using a 3400 cc diesel engine with an engine dynamo at steady-state (idle, 2000 rpm, 2000 rpm 25/50/75% load) engine operational conditions. The system consisted of an ionization section, electrostatic field additional section and a metallic foam filter, and the high voltage electrode inserted in the ionization section was electrically insulated using air insulation device in order to maintain stable corona discharge under high exhaust temperature over 300°C. The performance test of the device showed a high removal performance (over 95%) at all engine operation conditions, while the efficiency of the metallic foam filter was maintained at average 50% with gas temperatures less than 250 °C and at average 90% with gas temperatures over 250 °C. It is concluded that adding the electrostatic charging and field imposing device to a metallic foam filter could significantly enhance the removal performance of the metallic foam filter to remove ultrafine diesel PMs, especially at low gas temperature conditions less than 250°C with a negligible pressure drop.

Keywords: electrostatic, PM removal, metallic foam filter, submicron.

Particle size control using flame spray pyrolysis with emulsion

Shin Ae Song¹, Dae Soo Jung², and Seung Bin Park²

1 Fuel cell center, Korea Institute of Science and Technology, 39-1 Hawolgok-dong, Seongbuk-gu, Seoul, Republic of Korea, 136-791

2 Department of Chemical and Biomolecular Engineering, KAIST, 335 Gwahangno, Yuseong-gu, Daejeon, Republic of Korea, 305-701

Principal Contact: Seung Bin Park, PhD, Professor, Department of Chemical and Biomolecular Engineering, KAIST, 335 Gwahangno, Yuseong-gu, Daejeon, Republic of Korea, 305-701.

Tel: +82-42-350-3928 Fax: +82-42-350-3910 Email: sbpark7@kaist.ac.kr

Abstract

Control of particle size is very important technology in area of particle production because particle size is one of the most important factors affecting the material properties of ceramic particles. Many researchers have investigated the development of preparation methods that enable control of particle size and the effects of particle size on adsorption/desorption, magnetic, photoluminescence and mechanical properties. Of the many particle preparation methods, spray pyrolysis is a convenient technique for producing fine powders and materials. In spray pyrolysis, particles with spherical and non-agglomerated morphologies are prepared through the atomization of a precursor solution into discrete atomized droplets; the mean particle size and size distribution of the resulting particles are determined by the size and size distribution of the atomized droplets and the initial concentration of the solution. Thus, powder production rate is changed with particle size in spray pyrolysis. In this work, flame spray pyrolysis using water-in-oil emulsion precursor solution is proposed to overcome the limitation of control of droplet size and production rate. In flame spray pyrolysis with emulsion, one particle is made from one droplet of emulsion. So, particle size is determined by droplet size of emulsion. Droplet size of emulsion can easily control by types of surfactant, amount of surfactant. In this study, we found that by varying the emulsion droplet size, the particle size of the prepared particles can easily be varied from 30 to 700 nm. Particle size control was achieved successfully by varying the emulsion droplet size, which results in no decrease in the particle generation rate.

Keywords: Flame spray pyrolysis, particle size control, w/o emulsion, emulsion droplet size

Fracturing of Nanoparticle Agglomerates by Supersonic Flow Impaction with a Laval Nozzle

Masaki Yabuhana, Takeshi Kawabata and Yoshiki Okada

Department of Chemical Engineering, Kansai University, Osaka, 564-8680, Japan

ABSTRACT

We developed a technology for generation of non-agglomerated nanoparticles by impaction of agglomerates on a plate in a supersonic flow. For generating the supersonic flow, we utilized a Laval nozzle. The Laval nozzle made a supersonic flow, caused by large difference in pressures between the upstream and downstream of the nozzle. Agglomerated particles in the supersonic flow collided with the impaction plate which was set in the downstream of the nozzle and were fractured by this impaction. Particles before and after the impaction were caught on grids and analyzed with a transmission electron microscope. The probability of fracturing was investigated by counting the number of non-agglomerated particles and agglomerated particles in TEM images. From the results of experiment, it was found that the fracturing of nanoparticle agglomerates was dependent on the inertial force accelerated in the supersonic flow.

KEYWORDS

Non-agglomerated nanoparticles, Impaction, Supersonic flow, Inertial force

Introduction

Nanoparticles show unique characteristics of the quantum size effect and the catalyst effect, etc. However agglomeration induced by collisions of the particles takes place frequently after the generation of nanoparticles^[1]. Agglomerated nanoparticles can not show the peculiar characteristics efficiently compared with primary particles in uniform diameter. Then technology for fracturing of agglomerated nanoparticles is essential so that the fractured particles can make the best use of their unique characteristics. Agglomeration of nanoparticles is caused mainly by van der Waals

forces between the particles. In the present study, we aimed at developing a technology for generation of non-agglomerated nanoparticles by impaction of agglomerates on a plate in a supersonic flow.

Experimental Methods

Figure 1 shows a schematic diagram of the experimental setup. Figure 2 shows an impaction and deposition system. The distance D from the nozzle to the impaction plate was 14.5mm, 11.5mm, 8.5mm or 6.5mm. Silica particles 80nm in the average diameter dispersed in methanol were used as the test particles. The liquid sample was atomized by using a nebulizer with N₂ gas. The aerosol gas passed on a ²⁴¹Am plate for ionization, and was introduced into a differential mobility analyzer (DMA). The DMA classified the agglomerated silica particles. The classified agglomerated particles 102nm in diameter were introduced into the impaction and deposition system. In the system, the Laval nozzle makes a supersonic flow caused by large differences in pressures between the upstream and downstream of the nozzle. The agglomerated particles in the supersonic flow collide with a 45° impaction plate which is set up in the vicinity of the nozzle and are fragmented by the impaction. Particles fractured by impaction were caught on a grid and were observed by transmission electron microscope (TEM). The probability of fracturing was investigated by counting the number of non-agglomerated and agglomerated particles in TEM images.

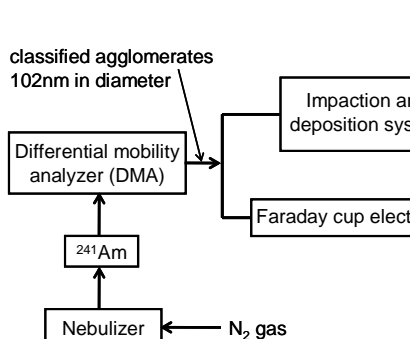


Fig.1 Experimental setup

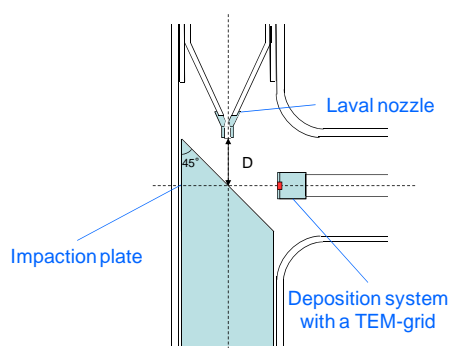


Fig.2 Impaction and deposition system

Results and Discussion

Table 1 Probabilities of fracturing of agglomerates under various conditions

pressure in the downstream region of the nozzle [Torr]	distance from nozzle to the impaction plate [mm]	probabilities of fracturing of agglomerates
5	14.5	73%
5	11.5	68%
5	8.5	72%
5	6.5	77%
10	14.5	91%
10	11.5	85%
10	8.5	86%
10	6.5	48%
15	14.5	94%
15	11.5	96%
15	8.5	96%
15	6.5	90%

We investigated the dependences of the probabilities of fracturing on the downstream pressure of the nozzle and the distance from the nozzle to the impaction plate. Table 1 shows the probabilities of fracturing of agglomerates under various conditions. When the pressure at downstream of the nozzle was 15 Torr, the probabilities of fracturing were higher than 90% at any distances from the nozzle to the impaction plate. This result indicates that an optimum expansion jet was attained in the downstream. At 10 Torr and 5 Torr of the pressure at downstream of the nozzle, the probabilities of fracturing were relatively low and strongly dependent on the distance from the nozzle to the impaction plate. This result indicates that the flows at the downstream of the nozzle were under-expansion jets in these conditions. We found that the optimum expansion jet gives us the highest efficiency for fracturing of agglomerates.

CONCLUSION

Our technology for generation of non-agglomerated nanoparticles, with a Laval nozzle can fracture agglomerated silica nanoparticles at high probabilities. We confirmed that the optimum expansion jet was the most suitable for efficient fracturing of nanoparticle agglomerates.

REFERENCE

- [1] T.Wu and A.P.Weber, European Aerosol Conference Abstract, T09A021, 2007

Study of Aerosol Optical Properties over Shanghai

Xuan Jia¹, Tiantao Cheng^{1*}, Jianmin Chen¹ and Yonghang Chen²

1 Department of Environmental Science and Engineering, Fudan University, Shanghai 200433

2 College of Environmental Science and Engineering, Donghua University, Shanghai 201620

ABSTRACT

Measurements of spectral Aerosol Optical Depth (AOD) have been carried out at Shanghai during November 2009 to October 2010 by using a hand-held multi-band sun photometer MICROTOPS II. Combining with the data from CALIPSO satellite and the NOAA-HYSPLIT model trajectory map, we studied both the seasonal and diurnal variation of AOD over Shanghai. The finding indicates that the AOD values are mainly low during Nov 2009 to Oct 2010, especially during the period of EXPO. And the seasonal variations of AOD and Angstrom exponent (α) are both remarkable. The highest and lowest of AOD appear in wintertime and summertime of 0.6861 ± 0.1541 and 0.2358 ± 0.1361 respectively, and the highest and lowest of α appear in springtime and summertime of 0.8701 ± 0.1889 and 1.5140 ± 0.2389 respectively. The study of three cases (2009.12.06, 12.22 and 12.31) in winter when the highest AOD value appears suggests a high loading of fine-mode particles which mainly caused by local pollution during wintertime in Shanghai. The heights of aerosol layer are generally less than 2 km, and highest AOD mainly appears at noon.

KEYWORDS

Atmospheric Aerosol optical depth, CALPSO, Sun photometer, HYSPLIT

Introduction

Aerosol play an important role in the global and regional climate change as their direct radiative forcing as well as indirect effects on clouds^[1]. Although many studies about the aerosol optical properties, their characters of spatial and temporal variations and influence on climate have been carried out, these aerosol effects still contain considerable uncertainties due to the poor understanding of aerosol properties and their spatial and temporal variation^[2]. With the unprecedented development of China, many studies about aerosol properties over Yangtze River Delta region(including Shanghai) shows heavy aerosol load and low visibility in this area^[3-5].

The objective of this study is (1) to analyze the seasonal variation of AOD and α over Shanghai during November 2009 to October 2010. (2) to study the diurnal variation of the aerosol optical

properties of three cases in wintertime by both the ground observation and satellites data.

Experimental Methods

A hand-held multi-band sun photometer MICROTOPS II developed by Solar Light Company is used to measure AOD at different wavelengths (340nm, 500nm, 675nm, 870nm and 1020nm). It has been settled at 31.17°E 121.30°N, and the data were collected 1:00-7:00 UTC at 40-60 minute intervals on the days of clear sky during November 2009 to October 2010. The data from CALIPSO satellite (CALIPSO Lidar Level 1B Profile Products) and the NOAA-HYSPLIT model trajectory map have also been used in this study.

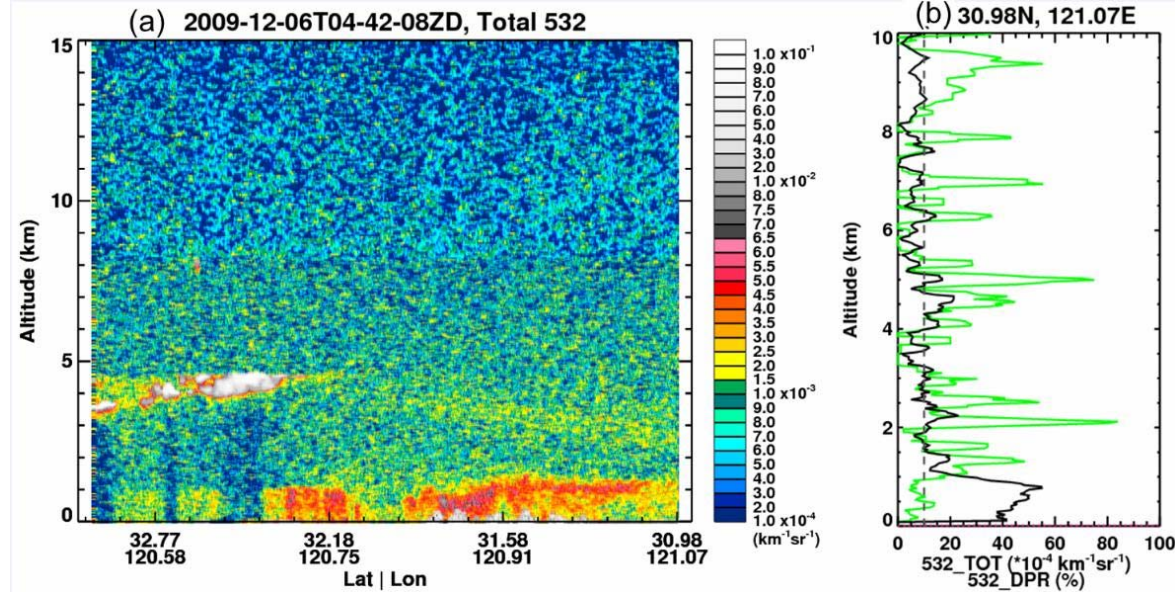
Results and Discussion

Table 1. Variation of Monthly Averaged AOD and Angstrom Exponent

	AOD(550nm)	α (550nm-675nm)	Day
Nov	0.6861±0.1541	1.3092±0.3078	12
Dec	0.5256±0.2310	1.2715±0.2121	11
Jan	0.5385±0.1080	1.3789±0.0956	8
Feb	0.4544±0.0729	1.2385±0.1956	6
Mar	0.6137±0.3096	0.8701±0.1889	11
Apr	0.6122±0.2171	0.9074±0.2752	10
May	0.4768±0.1918	0.9298±0.2090	6
Jun	0.4623±0.2304	1.5140±0.2389	6
Jul	0.2422±0.2459	1.3781±0.1858	6
Aug	0.2358±0.1361	1.4517±0.3644	12
Sep	0.3271±0.2173	1.4826±0.2674	15
Oct	0.5955±0.1729	1.4447±0.2664	13

The table1 indicates that the AOD values are mainly low during Nov 2009 to Oct 2010, especially during the period of EXPO. And the seasonal variations of AOD and α are both remarkable. The highest and lowest of AOD appear in wintertime and summertime of 0.6861±0.1541 and 0.2358±0.1361 respectively, and the highest and lowest of α appear in springtime and summertime of 0.8701±0.1889 and 1.5140±0.2389 respectively.

Figures 1. Aerosol Vertical Distributions from CALIPSO Lidar at Dec 12th 2009 over Shanghai : (a) Attenuated Backscatter Profiles 532nm (b) Depolarization Ratio(black) and Color Ratio(green) at 30.98 °E 121.07 °N



The figure 1 suggests a high loading of fine-mode particles which mainly caused by local pollution at Dec 12th, 2009 in Shanghai. And the height of aerosol layer is generally less than 2 km.

SUMMARY OR CONCLUSION

Measurements of AOD have been carried out at Shanghai during November 2009 to October 2010 by using a hand-held multi-band sun photometer MICROTOPS II. Combining with the data from CALIPSO satellite and the NOAA-HYSPLIT model trajectory map, we studied both the seasonal and diurnal variation of AOD over Shanghai.

The study indicates that the AOD values are mainly low during Nov 2009 to Oct 2010, especially during the period of EXPO. And the seasonal variations of AOD and α are both remarkable. The highest and lowest of AOD appear in wintertime and summertime of 0.6861 ± 0.1541 and 0.2358 ± 0.1361 respectively which is different from the previous study^[5]. It might due to the actions which have been taken by the Shanghai government and Meteorological conditions. The highest and lowest of α appear in springtime and summertime of 0.8701 ± 0.1889 and 1.5140 ± 0.2389 respectively. The study of three cases (2009.12.06, 12.22 and 12.31) in winter when the highest AOD value appears suggests a high loading of fine-mode particles which mainly caused by local pollution during wintertime in Shanghai. The heights of aerosol layer are

generally less than 2 km. However, more information such as the size distribution, chemical composition of the aerosol particles and so on is needed to get better understanding.

ACKNOWLEDGMENTS

The CALIPSO data were obtained from the NASA Langley Research Center Atmospheric Sciences Data Center.

REFERENCES

- [1] Charlson, R.J., Schwartz, S.E., Hales, J.M., Cess, D., Coakley, J.A., Hansen, J.E., *Climate forcing by anthropogenic aerosols*. Science. 1992,255, 423-430.
- [2] Climate change 2001 the scientific basis. In: Solomon, S., Qin, D., Manning, M., et al. (Eds.), Contribution of Working Group I to the Forth Assessment Report of the Intergovernmental Panel on Climate Change. *IPCC(2007)*; Cambridge University Press, Cambridge, United Kingdom and New York, NY, USA.2007.
- [3] Chen, R., Jiang, H., Xiao, Z., Yu, S., Jiao, L., Hong, S. *Monitoring aerosol optical properties using ground based remote sensing and the change of atmospheric environment in Hangzhou region. Research of Environmental Sciences*, 2008, 21, 22-26.
- [4] Cui, W., Guo, R., Zhang, H., *The long-range transport of dust from Mongolia Gobi to the Yangtze River basin and its mixing with pollutant aerosols*. Journal of Fudan University (Natural Science). 2009, 48 (5), 585-592.
- [5] Liang,p.,Huizheng,C.,Fuhai,G.,Xianggao,X.,Yaqiang,W.,Chize,Z.,Min,C.,Wei,G.,Jianping,G. *Aerosol optical properties based on ground measurements over the Chinese Yangtze Delta Region*. Atmospheric Environment, 2010, 44, 2587-2596.

Electrostatic Collection of Fine Particles at High Temperature and High Pressure for Wastes Gasification

Bangwoo Han¹, Hak-Joon Kim¹, Dong-Keun Song¹, Won-Seok Hong¹, Wan-Ho Shin¹, Han-Seok Kim¹ and Yong-Jin Kim¹

1 Korea Institute of Machinery and Materials, 171 Jang-dong, Yuseong, Daejeon, 305-343, Korea

Principal Contact: Yong-Jin Kim, Principal Researcher, Korea Institute of Machinery and Materials, 171 Jang-dong, Yuseong-gu, Daejeon, 305-343, Korea.

Tel: +82-42-868-7475 Fax: +82-42-868-7284 E-mail: yjkim@kimm.re.kr

Abstract

It has been focused on the collection of fine particles at high temperature and high pressure in the gasification processes such as integrated gasification combined cycle (IGCC). Ceramic candle filters have been widely used in the high temperature and high pressure. However, they are weak at heat stress and lead to high pressure losses during operations. Therefore, alternative filtration methods with high durability and low pressure loss have been necessary to be used for the high temperature and high pressure gasification processes. In this study, electrostatic collection of submicron particles at high temperature and high pressure has been investigated in the temperature range of 20-500°C and the pressure of 1-5 bars for use in the wastes gasification processes. As gas temperature increased, the corona onset voltage decreased and as gas pressure increased, the voltage increased. High temperature and high pressure led to the increase of the collision frequency between the ions and particles. Therefore, the charging and collection efficiency at a specific corona power increased as gas temperature and pressure increased. However, in experiments, it was difficult to apply high corona voltage due to the instability of corona discharge at high temperature and high pressure, and thus, the collection efficiency on the contrary decreased as gas temperature and pressure increased at the maximum power. Therefore, it was necessary to retard the instability of corona discharge to maintain high particle collection performances in high temperature and high pressure by introducing cooling gas near the discharging pin or completing the insulation parts using high electrical resistivity of materials.

Keywords: Collection efficiency, corona discharge, mobility of ions, electrostatic precipitator.

Efficiency of Dust Removal Device in Subway Cabin

Jong Bum Kim¹, Soon-Bark Kwon¹, Duck-Shin Park¹, Youngmin Cho¹, Seok Namgoong², Tae-Woo Han³, Kwanhyun Cho⁴ and Taesung Kim⁵

1 Railroad Environment Research Department, Korea Railroad Research Institute, Woram-dong, Uiwang-si, Gyeonggi-do, 437-757, Korea

2 R&D System Team, Seungchang Airtek, Naegachoen-ri Wongok-myeon, Anseong-si, Gyeonggi-do, 456-811, Korea

3 Environment Assessment Dept., SUNJIN Engineering & Architecture Co., Ltd, Yangpyeong-dong, Youndungpo-gu, Seoul, 150-102, Korea

4 R&D center, Seoulmetro, Dongjak-dong, Dongjak-gu, Seoul, 137-712, Korea

5 School of Mechanical Engineering, Sungkyunkwan University, Chonchon-dong, Suwon, Gyeonggi-do, 440-746, Korea

ABSTRACT

In the modern society various types of transportation mode are utilized, among them the subway system is the one of the main transportation mode which more than 7.21 million people ride a day. Because of interests on the indoor air quality (IAQ) of underground public facilities, concerns on IAQ of subway system by many people are increasing. There are several approach to improve IAQ of subway station, such as installing platform screen door (PSD), frequent tunnel washing-out, and etc, however there has not been any attempt to improve IAQ of subway cabin inside. Most technologies for removing airborne particulate matters are known to be difficult to adopt on the subway cabin since the problem of maintenance cost. Therefore, the ultimate object of this study is a practical development of cabin air cleaning system which can reduce the concentration of airborne particles and harmful gases at the same time. In this paper, we focused on the development of particle removing system utilizing a roll-filter for increasing operating time of air filter. The whole system was designed and the roll-filter device was manufactured based on numerical prediction results. For roll-filter device, 5 candidate filter materials were tested in point of particle collection efficiency and pressure drop. It was found that the electrically charged filter material showed highest performance among them.

KEYWORDS

Subway cabin, IAQ, PM10, Roll-filter

Introduction

The Seoul Metropolitan Subway (SMS) is an important transportation means as it transports an average of 7.4 million passengers on 5,697 subway trains journeying 736.6km a day as of 2009 [1]. Modern people spend most of their day indoors, and the air quality of the subway, the key transportation means, has gained much attention because it is related to quality of life issues. The indoor air quality of the subway becomes more important with the installation of PSDs (Platform Screen Doors). Although the installation of PSDs has helped to improve the air quality on the platform and waiting areas^[2], the pollution inside the tunnel is expected to have become relatively worse. As such, deterioration of the air quality inside the subway cabins of the urban subway operating in the tunnel zones has been a major issue. Air-tightening the cabin to prevent the inflow of polluted air from the outside can cause discomfort and cause drowsiness because of the increased carbon dioxide coming from the breathing of the passengers inside the cabin^[3]. The ultimate object of study develop independent cleaning device that reduce efficient fine particle so this study's purpose develope cleaning device that carry out reducing fine particles.

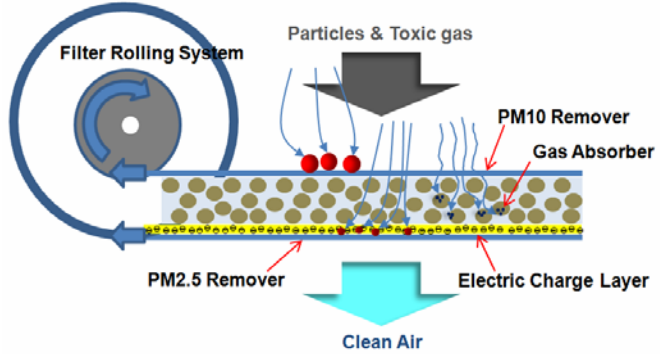
Experimental Methods

We designed the subway cabin air purifier (SCAP) for reducing aerosol particles and carbon dioxide based on field survey and numerical prediction. The system can be installed on the ceiling of cabin as shown in Figure 1. The main parts of SCAP are electrically charged roll-filter for removing particulate matters and gas absorbent for absorbing gaseous pollutants (Figure 2). Two layered electrically pre-charged filters were used for removing particulate matters and gas absorbers are packed between two layer filters for removing gases pollutants such carbon dioxide, volatile organic carbons and formaldehyde. From the field survey of operating subway cabin inside, we found the space for installing SCAP system on the ceiling as shown in Figure 1.

Figure 1. Installing place at subway cabin

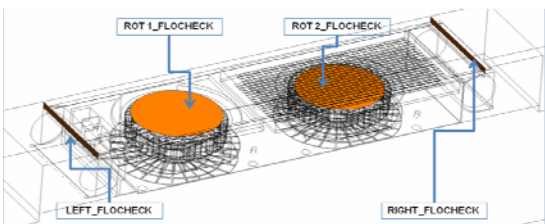


Figure 2. Installing place at subway cabin

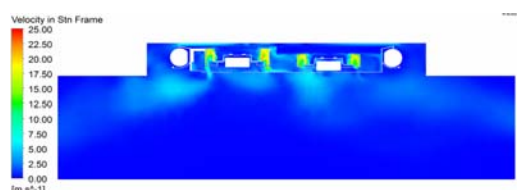


Using the concept of roll-filter system (Figure 2), we estimated generated flow pattern using computational fluid dynamics (CFD). Figure 3 shows the geometry of SCAP on the ceiling in subway cabin. Velocity distributions were analyzed and the maximum pressure drop of 10 mmH₂O was determined for achieving 300 m³/h air supply into the cabin.

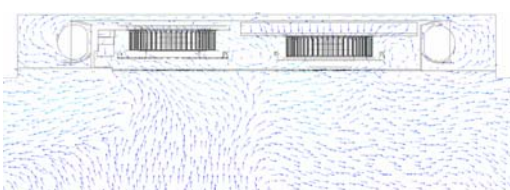
Figure 3. Numerical analysis of SCAP



(a) Inlet and outlet for flow check



(b) velocity distribution



(c) velocity vectors

In order to evaluate the filtration efficiency, we tested 5 different types of filter for roll-filter material. K1 and K2 are polyethylene (PE) filters and E1, E2, and E3 are polypropylene (PP) filters as shown in Table 2. E1~E3 filters were electrically pre-charged filters and their electrical potentials were measured as 0.84, 0.52, and 0.45kV, respectively, following the method of Park and Lim^[4]. The particle collection efficiency was estimated by counting inlet and outlet sample air using Dust Spectrometer (Grimm, 1.108). Test particles of AC Fine dust (PTI, A1) were generated by dust generator (Topas, SAG410).

Results and Discussion

The collection efficiency of electrical filters (E1, E2, E3) were higher than that of normal PE filters (K1, K2). The E3 filter showed the highest collection efficiency and E2 and E3 showed the similar collection efficiency for 0.5~7.8 μm . The pressure drop of each filter was also measured at the operating flowrate of 300 m^3/h . Table 1 shows the overall collection efficiency and pressure drop results for each filter.

Figure 4. Size dependent collection efficiency

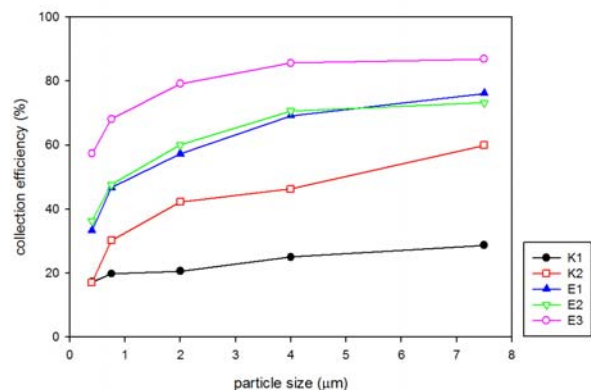


Table 1. Collection efficiency and pressure drop.

	Overall collection efficiency (%)	Pressure drop @300 m^3/h (mmH ₂ O)
K1	22.3	2.6
K2	39.2	6.1
E1	56.5	8.7
E2	57.6	8.5
E3	75.4	10.2

The overall collection efficiency was increased with increased pressure drop of filters. E2 filter showed the best performance based on the calculation of collection efficiency divided by pressure drop. We estimated that the filter replacement time is about 6 month when 20 m length filter material is rolled up.

SUMMARY OR CONCLUSION

The subway cabin air purifier (SCAP) was developed for removing particulate matters and gases pollutants inside a cabin. The whole system was designed and the roll-filter device was manufactured based on numerical prediction results. For roll-filter materials, E2 showed the best performance among 5 candidate filters. The gas absorber part will be tested for removing efficiency and pressure drop as our ongoing study. It is expected that SCAP could reduce indoor air pollutants in the subway cabin practically and it can be applied to other part of transportation vehicles.

ACKNOWLEDGMENTS

This work was supported by a grant (11 Urban Railroad A-01) from Urban Railroad Technology Development Program funded by Ministry of Land, Transport and Maritime Affairs of Korean government.

REFERENCES

- [1] Kwon S. B et al : *Up-to date Technology for Enhancing IAQ of Subway* : KOSAE autumn Conference Paper, Korea 2010; pp. 122
- [2] Lee T. J et al : *A Comparative Study on PM10 Source Contributions in a Seoul Metropolitan Subway Station Before/After Installing Platform Screen Doors* : J KOSAE, Korea 2010 ; Vol. 26(5) pp 543-553
- [3] Kwon, S.B et al : *Study on the indoor air quality of Seoul metropolitan subway during the rush hour* : Indoor and Built Environment, Denmark 2008 ; 17(4), 361-369.
- [4] Park H.S et al : *Aerosol filtration and electrostatic properties of electrospun nanofiber air filters*, PAAR, Korea 2009 ; Vol. 5, NO. 2, pp. 71~81.

Fabrication of polyurethane nano fibers by electrospinning

Hyun-Jin Choi^{1,2}, Sang Bum Kim¹, Sung Hyun Kim² and Myong-Hwa Lee¹

1 Green Manufacturing Process R&D group, Korea Institute of Industrial Technology, Cheonan, Chungnam 331-825, South Korea

2 Department of Chemical and Biological Engineering, Korea University, 1, 5-Ga, Anam-dong, Sungbukku, Seoul 136-701, South Korea

Principal Contact: Myong-Hwa Lee, Dr., Green Manufacturing Process R&D group, Korea, Institute of Industrial Technology, Cheonan, Chungnam 331-825, South Korea.

Tel: +82-41-589-8268 Fax: +82-41-589-8580 E-mail: myonghwa@kitech.re.kr

Abstract

Electrospinning is a very simple and versatile process to produce polymer nanofibers ranging from a few nanometers to submicrometers. These nanofibers have a large specific surface area and also provide high collection performance of nanoparticles. Polyurethane polymer has excellent mechanical properties such as elasticity, tensile strength and durability. Therefore, we have chosen polyurethane polymer as filter media in this study. Polyurethane polymer was dissolved in Dimethylformamide and Tetrahydrofuran chemicals, and electrospun by a electrospinning system. We investigated the influence of operating conditions such as concentration, viscosity, electric field and feed rate of the solution on fiber morphology. The morphology of the fiber was measured by scanning electron microscope and filtration performance was measured by a filtration system.

Keywords: Electrospinning, Polyurethane, Morphology, Filtration.

Filter cleaning of PTFE coated composite filter

Byung Hyun Park^{1,2}, Sang Bum Kim¹, Young Min Jo², and Myong-Hwa Lee¹

1 Green Manufacturing Process R&D Group, Korea Institute of Industrial Technology, 35-3 Hongchon-ri, Ipjang-myun, Chonan-si, Chungnam, 331-825, Republic of Korea

2 Department of Environmental Science & Engineering, KyungHee University, Youngin, Kyunggi, 331-825, Republic of Korea

Principal Contact: Myong-Hwa Lee, Dr., Green Manufacturing Process R&D Group, Korea Institute of Industrial Technology, 35-3 Hongchon-ri, Ipjang-myun, Chonan-si, Chungnam, 331-825, Republic of Korea.

Tel: +82-41-589-8286 Fax: +82-41-589-8580 E-mail: myonghwa@kitech.re.kr

Abstract

Bag house is usually used to control particulate matters and to recover valuable resources in industrial fields. Bag filter is the most important component in a bag house system. Therefore, we need to make best-quality filter media and also to determine optimum operation conditions of a bag house system. In this study, we focused on the operating conditions of bag house system. Dust cakes deposited on the filter surface are repeatedly formed and cleaned during filtration process. We investigated the relationship between dust clogging and dust penetration as a function of pressure drop across filter media and pulsing pressure. In conclusion, during filter cleaning process, collection efficiency of 2.5 μm particles was over 99.999 % at the pressure drop higher than 20 mmH₂O in newly developed porous filter (permeability= $5.78 \times 10^{-11} \text{ m}^2$). Moreover, collection efficiency of particulate matters are strongly dependent upon filter cleaning, i.e., high penetration of particles during dust-cake removal. As particle size decreases, penetration of particles increases. However, collection efficiencies of particulate matters are quickly recovered over time because recovery time during one filtration cycle is getting shorter.

Keywords: Filter cleaning, PTFE, Bag filter, Dust cake

Deposition of submicron aerosols on both sides of a substrate derived from charged droplets of aqueous suspension

Masao Gen, Shin-ichi Sagawa, Hidehiro Kamiya, and Wuled Lenggoro

Graduate School of Bio-Applications and Systems Engineering, Tokyo University of Agriculture and Technology, Koganei, Tokyo 184-8588, Japan

Principal Contact: W. Lenggoro, Tokyo University of Agriculture and Technology, Koganei, Tokyo, Japan.

E-mail: wuled @cc.tuat.ac.jp

Abstract

The deposition mechanism of the particles in the size range of submicro-meter (submicron), between 100 and 400 nm in particular, is not well characterized. Considering a study on the impact of aerosols on plants, the importance of issues on trans-boundary air pollution including submicron aerosols and their depositions on the surfaces of the plants has been pointed out. The objective of this study is to investigate a method to deposit sub-micron sized carbon particles on to substrates and to measure the size and distribution of the deposited particles on the substrates and its relationship with the starting materials. For the purpose, a single nozzle electrostatic-assisted spray-drying system was manufactured. Carbon suspensions were prepared as the starting materials. The size distributions of the samples in liquid- and gas-phase were measured by a dynamic light scattering and a differential mobility-based particle sizer, respectively. It was clear that aggregates of carbon (100-200 nm) in the liquid-phase (as suspension) and in the gas-phases (as aerosols) were suspended. A glass plate (insulator) and an aluminum plate (conductor) were used as model substrate. The non-grounded as well as the grounded substrates were used in the experiments. The nozzle tip of the particle generator was fixed perpendicularly to the substrate. Particles deposited on to the substrates were observed by a Field Emission-Scanning Electron Microscope. It was found that sub-micron carbon particles were simultaneously deposited on to not only front side of the substrates (glass and aluminum) but also on the back side. This system can be applied for studying the impact of aerosols on the plants.

Keywords: Carbon, submicro-meter, particles, electrostatic

Capture of particulate matters and odorous species by in-flight adsorbents

Myong-Hwa Lee¹, Byung Hyun Park¹, Seong-Kyu Park², and Sang-Jin Choi²

1 Green Manufacturing Process R&D group, Korea Institute of Industrial Technology, Cheonan, Chungnam 331-825, South Korea

2 KOFIRST R&D Center, KF E&E Co. Ltd., Gunpo-si, Gyunggi-do 435-833, South Korea

Principal Contact: Myong-Hwa Lee, Dr., Green Manufacturing Process R&D group, Korea, Institute of Industrial Technology, Cheonan, Chungnam 331-825, South Korea.

Tel: +82-41-589-8268 Fax: +82-41-589-8580 E-mail: myonghwa@kitech.re.kr

Abstract

Particulate matters including oil droplets as well as odorous species are emitted from meat cooking restaurants. Most of restaurants are installing a smoke discharging system to remove generated smoke quickly in order to reduce human exposure to hazardous contaminants. The flow velocity in the duct is higher than 10 meters per second, which indicates very short residence time in a smoke discharging system. Usually, we need enough residence time to remove gaseous species by adsorption and oxidation methods. To accomplish these, we have to make a big-sized control device to obtain desirable residence time. However, there is no enough space to install such kind of control device in urban area. Therefore, new approaching method to remove particulate matters and odorous species at the same time is required.

Newly developed treatment method which uses in-flight adsorbents was suggested in this study. This method can overcome the disadvantage of conventional control devices, which require long residence time. Adsorbents suspended in the duct flow along with gas molecules and particulate matters, and collide with each other. Eventually, they are adsorbing gaseous species and make agglomerates, resulting in easy capture by a particle collector.

Keywords: Particulate Matters, Odorous Species, In-flight adsorbent, Meat cooking

Reduction in Nanoparticle Formation by Ventilation for Ozonolysis of Volatile Organic Compounds Emitted from a Commercial Air Freshener

Thai Phuong Vu^{1,2}, Sun-Hwa Kim¹, Seung-Bok Lee¹ and Gwi-Nam Bae^{1,*}

1 Global Environment Center, Korea Institute of Science and Technology, 39-1 Hawolgok-dong, Seongbuk-gu, Seoul 136-791, Korea.

2 Construction Environment Engineering, University of Science and Technology, 113, Gwahangno, Yuseong-gu, Daejeon 305-333, Korea.

Principal Contact: Gwi-Nam Bae, Global Environment Center, Korea Institute of Science and Technology, Seoul 136-791, Korea.

Tel: +82-2-958-5676 Fax: +82-2-958-5805 E-mail: gnbbae@kist.re.kr

Abstract

Secondary pollution such as nanoparticle formation due to reaction of volatile organic compounds (VOCs) with ozone can be severe in closed indoor environment. Ventilation or exchanging air is a simple method to reduce an indoor concentration of the secondary pollutants. In this study, effect of air exchange rate (AER) on nanoparticle formation during the reaction of ozone and VOCs emitted from a commercial air freshener were investigated in a 1-m³ reaction chamber (1×1×1 m), which was installed in a wooden box to avoid light disturbance from outside. A 0.5-mL test specimen of a liquid-typed air freshener, containing various VOCs, particularly terpenes, was contained in a 50-mL petri dish placed on the bottom of the chamber. A 100-ppb ozone was continuously injected into the center of the chamber with a fixed flow rate of 4 L/min using a photometric O₃ calibrator. Three different levels of AER (0.24, 0.74, and 1.24 ACH) were controlled by making an additional flow of pure air and balancing a total exhaust flow rate using mass flow controllers. The temperature and relative humidity were controlled at 20±1°C and < 20%, respectively. The total number concentration and size distribution of nanoparticles were measured using an ultrafine condensation particle counter and a scanning mobility particle sizer, respectively. When AER increased 3 and 5 times greater than 0.24 ACH, the peak particle number concentration decreased by about 36% and 69%, and the peak were delayed by 5 and 11 min, respectively. The particle mass concentration decreased by about 60% and 90% compared with values at the same elapsed time for 0.24 ACH, respectively. The lower AER was applied, the larger particle mean diameter was observed because of rapid coagulation under the high particle number concentration.

Keywords: Air freshener, Volatile organic compounds, Ozone, Ventilation, Nanoparticle formation.

An aerosol generator system for long-duration exposures of plants to submicrometer-sized particles

W. Lenggoro^{1,2}, M. Gen², F.-Z. Lim², S. Ikawa², M. Yamaguchi³, and T. Izuta⁴

1 Institute of Engineering

2 Graduate School of Bio-Applications and Systems Engineering, Tokyo University of Agriculture and Technology (TUAT), Koganei, Tokyo 184-8588 Japan

3 Department of Environmental and Natural Resource Science

4 Institute of Agriculture, TUAT, Fuchu, Tokyo 184-8509 Japan

Principal Contact: W. Lenggoro, Tokyo University of Agriculture and Technology (TUAT), Koganei, Tokyo, 184-8588, Japan.

Tel: 81-42-388-7987 E-mail: wuled @cc.tuat.ac.jp

Abstract

One of the most important particle size suspended in the atmosphere is submicron ($0.1\sim1\mu\text{m}$). However there is no study considering long-term impact of submicron sized aerosol particles on the physiological functions of plants. The objectives of our study are to develop an exposure system for investigating the impact of submicron particles on plant growth, photosynthesis and other physiological functions. In order to achieve our purpose, carbon suspension was selected as a model material. The suspension was prepared by dispersing carbon nanopowders into water. Using a specially designed aerosol generator based on electrical- and ultrasonic-driven generators, submicron carbon aerosols were dispersed in the gas phase from the suspension. The electrical mobility-based diameter of the carbon aerosols were measured by a differential mobility analyzer system. The main peaks of the size distributions measured from the aerosols were between 100 and 200 nm, indicating that the carbon aerosols were suspended as agglomerates. Four types of plants were placed in six chambers, including three chambers without aerosol exposure system. For each plant, more than 15 seedlings were set into pots. Temperature and humidity in the chambers were controlled. Exposure time is 15 or 30 minutes per day. To clarify the deposited submicron particles, three types of substrates made from glass plate, glass filter, and metal plate were placed in the chamber for more than 30 days. From observation of the substrates by electron microscope, it was found that the carbon aerosols had sufficient charges to enable them to be deposited onto the substrates.

Keywords: Vegetation, carbon, deposition, phytotron

Diffuser Design for the Particulate Filter of Diesel Engine

Jau-Huai Lu, Wei-Hsin Chang, Jhih-Wei Liao, and Hong-Jin Lin

National Chung Hsing University, 250 Kuokwang Rd., Taichung, Taiwan

Principal Contact: Jau-Huai Lu, Associate Professor, Department of Mechanical Engineering, National Chung Hsing University, 250 Kuokwang Rd., Taichung, Taiwan.

Tel: 886-4-22850339 Fax: 886-4-22877170 E-mail: jhlu@dragon.nchu.edu.tw

Abstract

Diesel engine is considered to play a more and more important role in the application of automobiles as it has relatively high energy efficiency and emits less carbon dioxide. However, the fine particulates emitted in the engine exhaust has raised great concern because of their harmful effects on human health.

Diesel particulate filter (DPF) is an effective way to reduce the fine particles generated in the combustion process of diesel engine. It is made of partially permeable ceramic material. Solid particles will be trapped inside the filter as exhaust flow goes through it. The DPF is installed at the downstream of the engine exhaust pipe and a diffuser is adopted between the exhaust pipe and the DPF. It is noted that a well designed diffuser will uniformly distribute the particles on the front surface of the filter such that the regeneration cycle could be prolonged, and the durability of the filter could be improved.

Several different types of diffuser were designed and tested in this study. CFD calculations were conducted at first to find the velocity distribution inside the space between the diffuser and the filter. Hot wire anemometer was then used to measure the flow velocity in a real DPF model. Finally, a Cummins 5900c.c. diesel engine equipped with direct oxidation catalyst (DOC) and DPF was used to investigate the effectiveness of the diffuser.

It was found that the inverted disk type diffuser with holes on its surface has the best performance. The black carbon particles are uniformly distributed, and those particles are burned smoothly during the regeneration process.

Keywords: Diesel particulate filter (DPF), diffuser, particulate

An Efficient Wetted-wall Venturi Scrubber with a Two Stage Throat

Shin-You Chen¹, Hau-Chieh Lin¹, Fang-Tang Chang², Hung-Min Chein² and Chuen-Jinn Tsai¹

1 Institute of Environmental Engineering, National Chiao Tung University, No. 1001, University Road, Hsin Chu, 30010, Taiwan.

2 JG Environmental Technology Co., Ltd, No.70, Guangming 1st Rd., Jhu bei, Hsinchu county, 302, Taiwan.

Principle Contact: Chuen-Jinn Tsai, Professor, National Chiao Tung University, HsinChu, Taiwan 30010.

Tel: +886-3-5731880 Fax: +886-3-5727835 E-mail: cjtsai@mail.nctu.edu.tw

Abstract

In traditional venturi scrubbers, the gas pressure drop is too high when removing submicron particles. In addition, particles will be plugged in the venturi throat when particle concentration is high and particles are sticky, which results in high pressure drop and high running cost. In order to avoid the plugging of the venturi throat and improve the removal efficiency of fine particles, this research intends to develop a wetted wall 2-stage venturi scrubber. Heterogeneous growth of fine particles by using super-saturation of water vapor is employed to increase the removal efficiency of the venturi scrubber. The venturi tube of the present design is divided into inner and outer venturi tubes for ease of manufacturing and assembly. There are two connecting tubes that transport the cleaning fluid at the converging section into the liquid storage tank. The scrubbed clean gas will exit from the diverging section of the inner venturi, while the cleaning water for removing deposited particles on the outer venturi's wall is discharged into the diverging section of the outer venturi to avoid high pressure drop. The current 2-stage venturi scrubber is simple and easy to make. Its cost is lower than other air pollution control devices.

The experimental results showed that the cut-off diameter of wetted wall 2-stage venturi scrubber was 130 nm in aerodynamic diameter under a reasonable pressure drop of 10.7 in H₂O. The collection efficiency for particles larger than 300 nm in aerodynamic diameter was

higher than 80 % and 90 % for oil and salt particles, respectively. More than 80 % total mass removal efficiency was predicted for removing fine particles in the exhaust of an ABS plant ($\text{MMAD}=562 \text{ nm}$, $\sigma_g=1.81$). To remove fine particles from a high temperature gas exhaust with a flow rate of 500 CMM, the theoretical running cost of this high efficiency venturi scrubber is predicted to be NT 397 thousands per year.

Keywords: air pollution control, fine particles, venturi scrubber.

Hydrothermal Synthesis of TiO₂ Nanostructured Arrays and Their Photocatalytic Activity for Methylene Blue Degradation in Microreactor

N. Dech-rat¹, N. Viriya-empikul², K. Faungnawakij² and V. Pavarajarn^{1,*}

1 Center of Excellence in Particle Technology, Faculty of Engineering,
Chulalongkorn University, Bangkok, 10330, Thailand

2 National Nanotechnology Center, National Science and Technology Development Agency
Thailand Science Park, Pathumthani, Thailand

*** Principal Contact:** E-mail: Varong.P@chula.ac.th.

ABSTRACT

Oriented titanium dioxide (TiO₂) thin film arrays were directly synthesized on a titanium plate by hydrothermal method. A titanium plate was put into 50 ml solution of 10 M NaOH in a 50 ml teflon-lined stainless steel autoclave and heated to temperature of 180°C for 3-48 h in an oven. The sample was completely washed with distilled water and dried in the oven at 80°C. The resulting sample consisted of sodium titanate thin film on the plate. To transform sodium titanate into hydrogen titanate, the sample was washed with 100 ml of 0.1 M HCl. Thereafter, the distilled water was used to remove excess HCl on the sample. After dried, the sample was calcined at 600°C for 2 h to transform the hydrogen titanate into titanium dioxide. The samples were characterized by scanning electron microscope (SEM, Hitachi S-3400N TypeII), transmission electron microscope (TEM, Hitachi H-9000UHR III), and X-ray diffraction (XRD, Bruker D8 Advance) to observe morphology, crystal structure, and crystalline phase, respectively, of the TiO₂ thin film. The photocatalytic activity of the samples was tested by means of methylene blue (MB) degradation in a microreactor equipped with UV lamp (wavelength of 253.7 nm). As the result, the control of morphology, size and structure of TiO₂ thin film was achieved by varying the hydrothermal time and calcination temperature. After 3 h of hydrothermal reaction at 180°C, the TiO₂ thin film was observed on the surface of the titanium plate. As the hydrothermal time was increased from 3 to 48 h, the roughness of the film was increased by the sequential formation of titanate nanosheets, nanotubes and nanofibers, respectively. Upon the calcination at 600°C for 2 h, the TiO₂ nanotubes deformed into lump-shaped aggregates, while the form of nanofibers could withstand the thermal transformation.

KEYWORDS

TiO₂ thin film, Hydrothermal process, Degradation

Introduction

Titanium dioxide (TiO₂) is a semiconductor suitable for numerous applications, such as photocatalyst^[1], solar cells^[2], electrochromic devices^[3], and sensors^[4]. Increased attention has been paid on one-dimensional aligned nano-TiO₂ array. The synthesizing methods for one-dimensional TiO₂ nanostructures include high temperature oxidation^[5], anode oxidation^[6], templated sol-gel methods^[7] and metal organic chemical vapor deposition (MOCVD)^[8]. Nevertheless, most methods are costly and complicated. Hydrothermal method is another technique capable of producing one-dimensional TiO₂ that is simple and convenient. This technique has been used to synthesize well crystallized nanostructures with uniform morphology^[9]. It is well known that crystalline TiO₂ exists in three polymorphs, including rutile (tetragonal), anatase (tetragonal), and brookite (orthorhombic)^[10]. Rutile and anatase are more common forms of TiO₂, but anatase exhibits higher photocatalytic activity than rutile^[11]. Nevertheless, it has been reported that the mixed phase of anatase and rutile can increase the photocatalytic activity of TiO₂^[12].

In this work, the growth mechanism of TiO₂ arrays during the hydrothermal synthesis in NaOH solution is investigated. Size, morphology and crystallinity of the fibers as well as the thickness of the growth layer were found to depend upon temperature and duration of the hydrothermal treatment as well as the calcination temperature. The photocatalytic activity of the grown TiO₂ arrays was also tested using methylene blue degradation.

Experimental Methods

Preparation of TiO₂ Nanotube Array on Titanium Plate

Titanium plate (1 cm x 1.5 cm x 0.127 cm thick) was put into 50 ml solution of 10 M NaOH in a 50 ml Teflon-lined stainless steel autoclave and kept at temperature of 180°C for 3 to 48 h. After being held at the desired temperature for predetermined period of time, the sample was took out of the autoclave, completely washed with distilled water and dried in an oven at 80°C. At this point, the obtained product was consisted of sodium titanate. To transform sodium titanate into hydrogen titanate, 500 ml of 0.1 M HCl solution was used to wash the sample. Then, the product was washed with water to remove excess HCl and subsequently calcined at 600°C for 2 h to transform hydrogen titanate into titanium dioxide.

Photodegradation of Methylene Blue

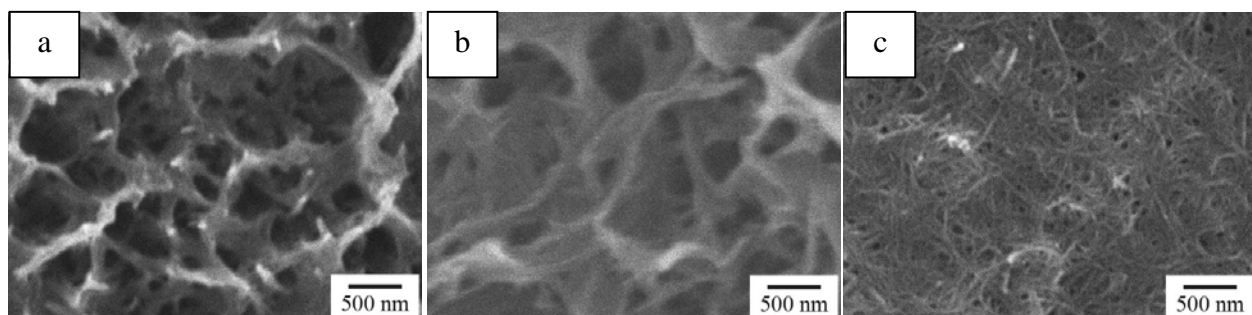
Photocatalytic degradation of methylene blue (MB) solution was employed to investigate the photocatalytic activity of the synthesized TiO₂. The reaction was conducted within a microreactor to minimize the effect of mass transfer from bulk solution to the surface of the catalyst. The initial concentration of methylene blue solution was fixed at 5 ppm. The solution was continuously pumped into microchannal of the microreactor via a syringe pump. Flow rate of the solution was fixed at 15.4 µL/min. At first, the solution was supplied to the reactor in the dark to monitor adsorption behavior of the synthesized TiO₂. After the TiO₂ sample was saturated with methylene blue, the photocatalytic reaction was initiated by exposing the microreactor to light from UV light (SEN UVL20PL-6 20W low pressure mercury lamp). The sample was periodically collected to be analyzed by UV/Visible spectroscopy for the concentration of methylene blue.

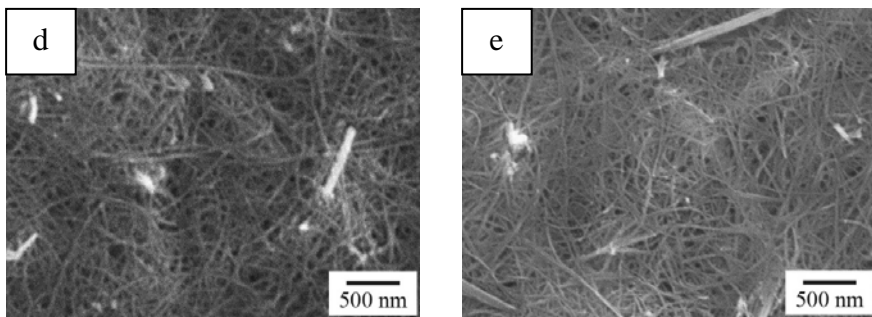
Results and Discussion

Growth of TiO₂ Array on Titanium Plate

Figure 1 shows SEM micrographs of the samples synthesized by hydrothermal at 180°C for various periods of time. It should be noted that surface of titanium plate before the treatment was relatively smooth. After 3 h of hydrothermal treatment, a sponge-like layer consisting of rod-shape particles is formed on the surface of titanium plate (Figure 1a). When the hydrothermal time is increased to 6 h (Figure 1b), the rods appeared longer than that observed in Figure 2a. For 9 h of the hydrothermal treatment, diameters of the rods are decreased, while the length increases dramatically (Figure 1c), becoming nanofibers. The nanofibers are clearly observed on the surface of the titanium plate after the 12 h treatment (Figure 1d). Finally, the morphology of the products remains unchanged during the period of hydrothermal treatment of 12-48 h (Figure 1d-e).

Figure 1. SEM micrographs of products from hydrothermal treatment at 180°C for 3 h (a), 6 h (b), 9 h (c), 12 h (d) and 48 h (e).





By subjecting to the calcination, morphology of the TiO_2 thin film formed on the titanium plate is changed. As shown by SEM images, deformation of the rods takes place after being calcined at 600°C (Figure 2). Nevertheless, it is found from TEM images that the as-synthesized products are nanotubes (Figure 3a) mixed with nanofibers (Figure 3b). After calcination at 600°C , the nanotubes aggregate and deform into collective of nanoparticles, while structure of the nanofibers remains unchanged (Figure 3d). During the calcination at such high temperature, dehydration of interlayered OH groups within the nanotubes results in the gradual decrease in the interlayer distance, which subsequently transforms them into lotus-root-like structure (Figure 2b). At the same time, previously formed defects also transform into amorphous nanoparticles attached to the nanorods^[13].

Figure 2. SEM micrographs of products from hydrothermal treatment at 180°C for 48 h before (a) and after calcination at 600°C (b).

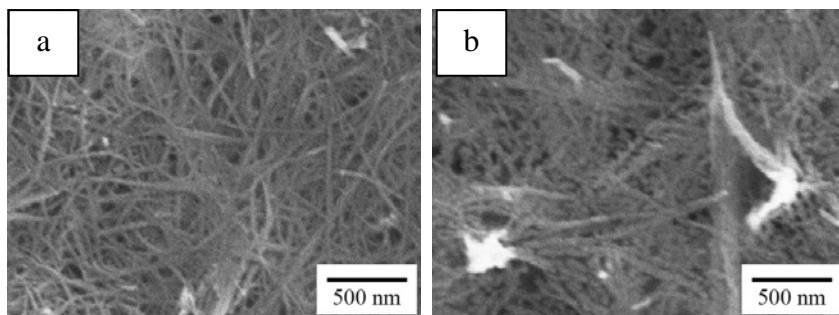


Figure 3. TEM images of products from hydrothermal treatment at 180°C for 48 h before (a,b) and after calcination at 600°C (c,d).

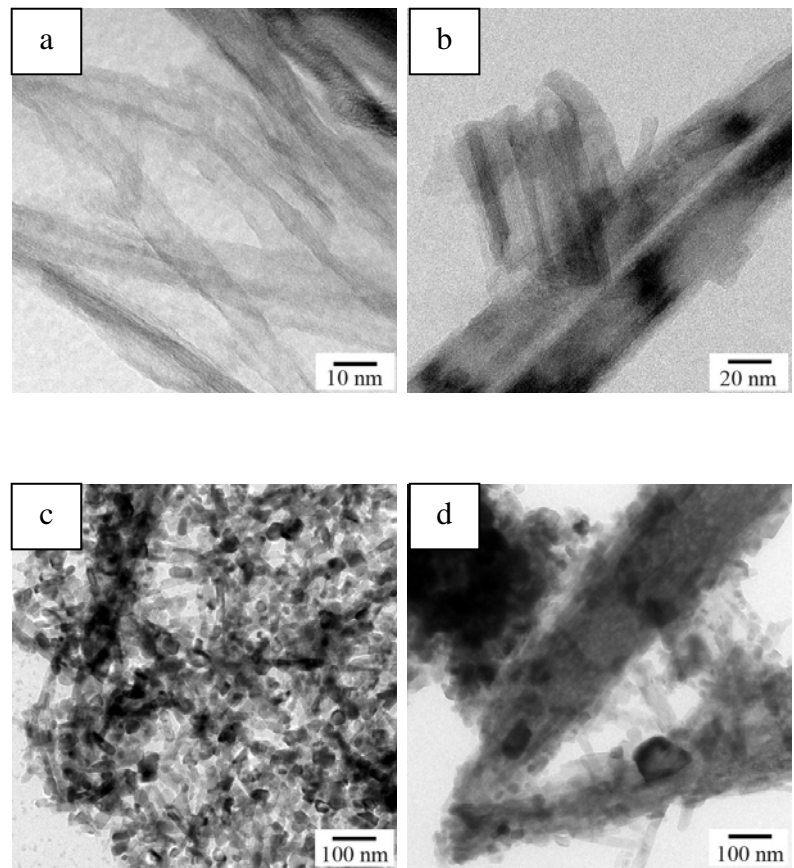


Figure 4 compares XRD patterns of samples prepared using different hydrothermal time. It is found that the increase in the hydrothermal time facilitates the formation of rutile phase during the calcination at 600°C (Table 1). In the other word, the thermal stability of anatase phase in the product is decreased when the hydrothermal time is prolonged.

Figure 4. XRD patterns of products synthesized by hydrothermal treatment in NaOH at 180°C for different period of time, and subsequently calcined at 600°C: (○) titanium, (▲) anatase, (□) rutile.

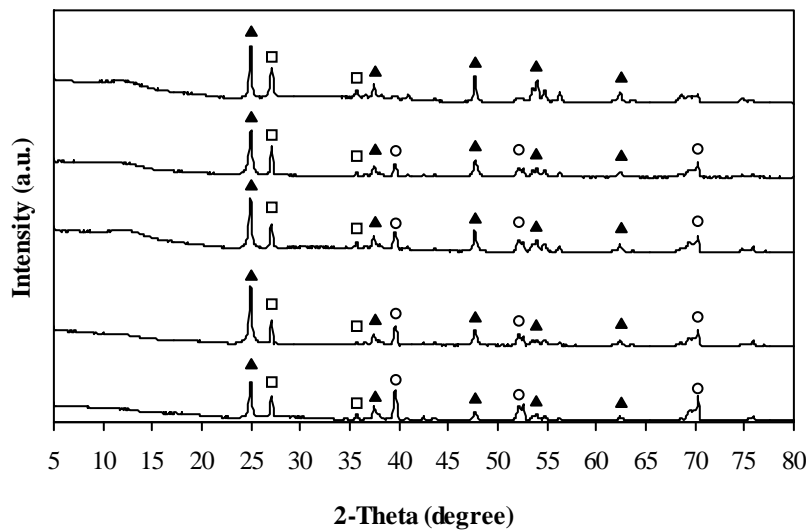


Table 1. Anatase content (%) of products synthesized by using different hydrothermal time

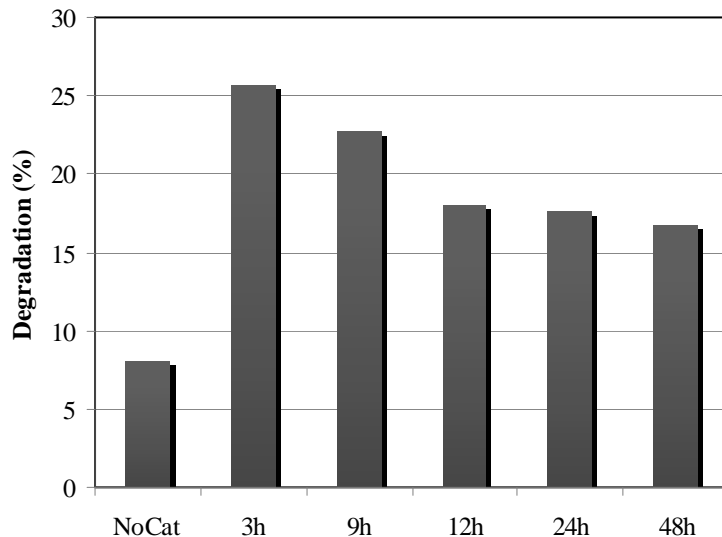
Hydrothermal time (h)	Anatase content (%)	Rutile content (%)
3	73.2	26.8
9	66.7	33.3
12	61.8	38.2
24	59.2	40.8
48	58.8	41.2

Degradation of Methylene Blue

Figure 5 shows the percentage of methylene blue degradation on TiO₂ array that was synthesized using of different hydrothermal time. The residence time in the reaction system, i.e., a microreactor, was kept at 5 min. All grown TiO₂ array was calcined at 600°C before being used as the photocatalyst because this calcination condition resulted in anatase mixed with rutile phases and it has been reported that the rutile/anatase mixed phase has higher photocatalytic activity than the pure anatase^[14]. When the hydrothermal time is increased, the percentage of methylene blue degradation is decreased because the content of anatase phase is decreased. The

hydrothermal time of 3 h yields the highest degradation percentage, since it yields the highest content of anatase phase in the product (Table 1).

Figure 5. Percentage of methylene blue degradation on TiO₂/Ti plate synthesized for different period of the hydrothermal time.



CONCLUSION

Titania could be grown from titanium plate via hydrothermal process. Size, morphology and crystallinity of the fibers depend upon duration of the hydrothermal treatment and calcination temperature. The hydrothermal treatment at 180°C for 3 h yields the highest degradation percentage, since it yields the highest content of anatase phase in the product.

ACKNOWLEDGMENTS

This study was partly supported by the Centennial Fund of Chulalongkorn University to the Center of Excellence in Particle Technology and a grant from Thailand Graduate Institute of Science and Technology (TGIST), Number TGIST 01-53-052. Characterizations of the samples were supported by National Nanotechnology Center, Thailand (NANOTEC).

REFERENCES

- [1] Negishi, N.; Iyoda, T.; Hashimoto, K.; Fujishima, A. *Chem. Lett.* 1995, 9, 841-842
- [2] Bach, U.; Lupo, D.; Comte, P.; Moser, J. E.; Weissertel, F.; Salbeck, J.; Spreitzer, H.; Gratzel, M. *Nature*. 1998, 395, 583-585.

- [3] Cinnsealach, R.; Boschloo, G.; Nagaraja Rao, S.; Fitzmaurice, D. *Sol. Energ. Mater. Sol. Cell.* 1998, 55, 215-223.
- [4] Chen, X.; Mao, S. S. *Chem. Rev.* 2007, 107, 2891-2959.
- [5] Peng, X.; A. Chen, *Appl. Phys. A Mater.* 2005, 80, 473-476.
- [6] Centi, G.; Passalacqua, R.; Perathoner, S.; Su, D. S.; Weinberg, G.; Schlägl, R. *Phys. Chem. Chem. Phys.* 2007, 9, 4930-4938.
- [7] Wei, Q.; Hirota, K.; Tajima, K.; Hashimoto, K. *Chem. Mater.* 2006, 18, 5080-5087.
- [8] Chen, C. A.; Chen, K. Y.; Huang, Y. S.; Tsai, D. S.; Tiong, K. K.; Chien, F. Z. *J. Cryst. Growth.* 2008, 310, 3663-3667.
- [9] Wang, C.-C.; Ying, J. Y. *Chem. Mater.* 1999, 11, 3113-3120.
- [10] Yamamoto, S.; Sumita, Sugiharto, T.; Miyashita, A.; Naramoto, H. *Thin Solid Film.* 2001, 401, 88-93.
- [11] Zhao, L.; Han, M.; Lian, J. *Thin Solid Film.* 2008, 516, 3394-3398.
- [12] Martra, G.. *Appl. Catal. Gen.* 2000, 200, 275-285.
- [13] Xiao, N.; Li, Z.; Liu, J.; Gao, Y. *Thin Solid Film.* 2010, 519, 541-548.
- [14] Jung, K.Y.; Park, S.B. *J. Photochem. Photobiol. Chem.* 1999, 127, 117-122.

Fabrication of Core-Sheath Fibers by Electrospinning for the Formation of Flexible Carbon Nanofibers

Chanwit Apibanborirak, Chinarat Tongtaow, Farkfun Duriyasart and Varong Pavarajarn*

Center of Excellence in Particle Technology, Faculty of Engineering,
Chulalongkorn University, Bangkok, 10330, Thailand

*** Principal Contact:** E-mail: Varong.P@chula.ac.th.

ABSTRACT

Carbon nanofiber is a promising material for several applications such as advanced catalyst support, adsorbent and filtration. In this work, carbon nanofibers were formed by the pyrolysis of polyacrylonitrile (PAN)/poly vinyl pyrrolidone (PVP) core-sheath nanofibers, which were fabricated by co-axial electrospinning technique. The presence of PAN, which degraded at higher temperature than PVP, could provide flexibility to the final carbon nanofibers. For the fabrication of the core-sheath nanofibers, solution of PAN and solution of PVP, both in dimethyl formamide (DMF), were supplied separately to a co-axial nozzle. The concentration of the polymer was varied in the range of 6-10% wt. Upon the application of high electrical potential in the range of 15-18 kV, the solutions were ejected from the nozzle and deposited on the grounded collector set the distance of 12-18 cm from the nozzle. The products were analyzed by scanning electron microscope (SEM) and transmission electron microscope (TEM). It was found that concentration of both PAN and PVP in the solutions, the applied potential and the distance from the nozzle to the collector affected morphology and size of the product. In general, the average diameter of the fibers increased with the increase in polymer concentration of the spinning solutions.

KEYWORDS

Core-sheath, Nanofibers, Electrospinning

Introduction

Carbon fibers having very large surface area-to-volume ratio, flexibility in surface modification and superior mechanical performance have been receiving increasing attention for various applications. Important characteristics of the carbon fibers include high strength and light weight which are useful in wide range of applications^[1]. In addition, it can be synthesized in porous form. This form is usually used as catalyst support, adsorbent and filtration because of its high surface

area^[2]. The fabrication of such carbon fiber can be achieved by many methods. Nevertheless, one of the suitable techniques for the fabrication of nanosized carbon fibers is carbonization of electrospun polymer nanofibers^[3].

Electrospinning has been recognized as a simple technique for producing fibers with size in the range of nanometer to micrometer. The conventional process is consisted of applying electrical potential between a grounded collector and a droplet of polymer solutions or melt held at the end of capillary tube by its surface tension. When the applied electric field overcomes the surface tension of the droplet, a charged jet of the solution or melt is ejected. The jet grows longer and thinner due to bending instability or splitting^[4]. While the jet travels toward to a collector, the solvent evaporates or the polymer solidifies. The products are randomly deposited as non-woven fibers on the collector^[5].

In this work, a co-axial electrospinning of polyacrylonitrile (PAN)/polyvinylpyrrolidone (PVP) core/sheath fibers is investigated. A polyacrylonitrile core will reside within the fiber after pyrolysis, causing the carbon fiber to become flexible. The present study is focused on the effects of electrospinning parameter on electrospun fibers and morphology of carbon fibers after pyrolysis.

Experimental Methods

Preparation of PAN solution and PVP solution

PAN solution was prepared by dissolving polyacrylonitrile (PAN, Sigma-Aldrich, Mw~30,000) in N,N'-dimethylformamide (DMF, Sigma-Aldrich) at 60°C, while PVP solution was prepared by dissolving polyvinylpyrrolidone (PVP, Sigma-Aldrich, Mw~1,300,000) in DMF at room temperature. There values of concentration of each solution were prepared, i.e., 6, 8, 10 %wt.

Co-axial electrospinning

A high voltage DC power supply (ES30PN, Gamma High Voltage Research Inc., USA), two syringe pumps, two plastic syringes furnished into a co-axial nozzle of which the core diameter was equal to that of the stainless needle No.22 (the inner diameter of 0.7 mm) and an aluminum foil were considered to be the tools for electrospinning. The nozzle was connected to the negative electrode of the power supply; while the aluminum collector was attached with the grounding electrode. The distance between the tip of the nozzle and the collector was in the range of 12 to 18 cm. During electrospinning, the PAN and PVP solution were fed into the nozzle via syringe pumps with constant volumetric flow rate at 0.8 ml/h.

Pyrolysis of fibers

Pyrolysis of the electrospun PAN/PVP core-sheath nanofibers was performed in a horizontal tubular furnace constantly supplied with nitrogen gas at 50 ml/min. The temperature of the furnace was raised from room temperature to 400°C with heating rate at 10°C/min and held at this temperature for 2 h.

Characterizations

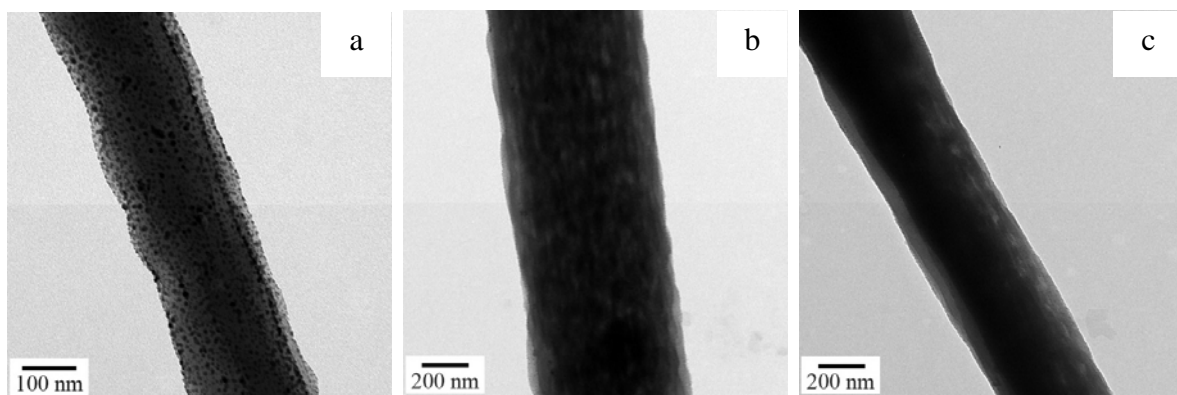
Morphology of the obtained products was observed by using a scanning electron microscope (SEM, JEOL JSM-6400). Size of the products was then measured from the micrographs, using image processing software (JEOL SemAfore 5.0). The surface area, pore volume and pore size were measured by a BELSORP-mini nitrogen adsorption analyzer.

Results and Discussion

Effects of Electrospinning Parameters

The examination of TEM images shown in Figure 1 reveals that the products of electrospinning are indeed co-axial fibers form which the size of fiber is mainly controlled by the core because polyacrylonitrile solution has viscosity higher than that of polyvinylpyrrolidone. It should be noted that dark spots observed on the fibers are the result from formation of nanoparticles of silver added into the fiber to enhance the contrast of the TEM micrographs.

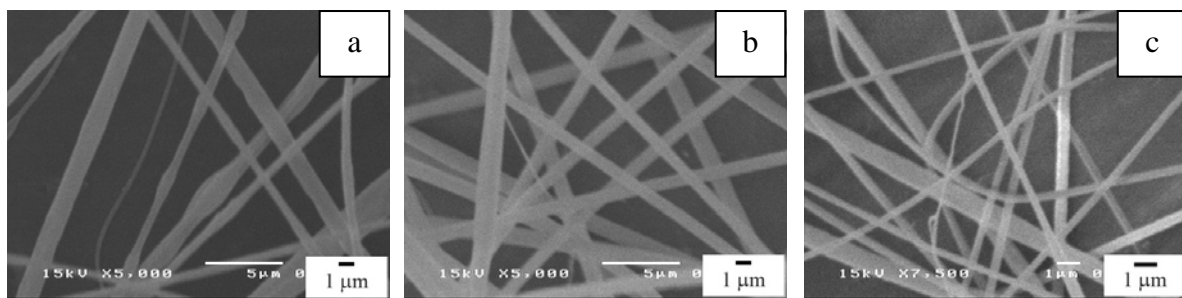
Figure 1. TEM micrographs of products obtained from co-axial electrospinning of PAN solution and PVP solution using applied potential of 16 kV and the distance from nozzle to collector of 18 cm, whereas the concentrations of PVP and PAN solutions are 8/6 (a), 8/8 (b), and 10/6 (%wt/%wt, respectively).



SEM micrographs in Figure 2 show that the smooth and uniform fibers could be fabricated only when the concentration of both solutions are in proper range. Beads are formed on the fibers

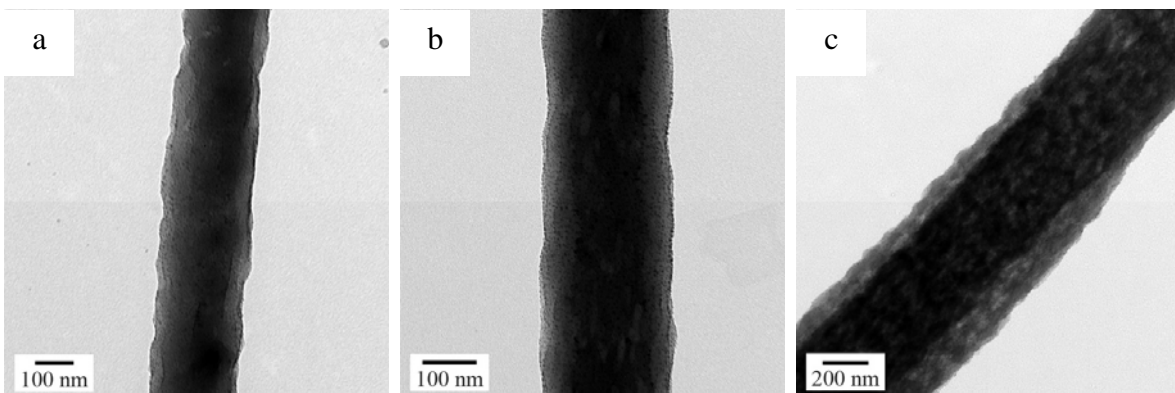
when the polyacrylonitrile (PAN) concentration is 6 %wt, which indicates non-uniform ejection of the jet of polymers from the nozzle. On the other hand, when the concentration of PAN is increased to 10 %wt, the fibers formed are less uniform in size. The proper concentration of PAN was found to be 8 %wt. However, for PVP, it is found that its concentration within the investigated range does not have significant effect toward the uniformity of the fibers.

Figure 2. SEM images of products obtained from co-axial electrospinning of PAN solution and PVP solution using applied potential of 15 kV and the nozzle-to-collector distance of 12 cm, whereas the concentrations of PVP and PAN solutions are 10/6 (a), 10/8 (b), and 10/10 (c) %wt/%wt, respectively.



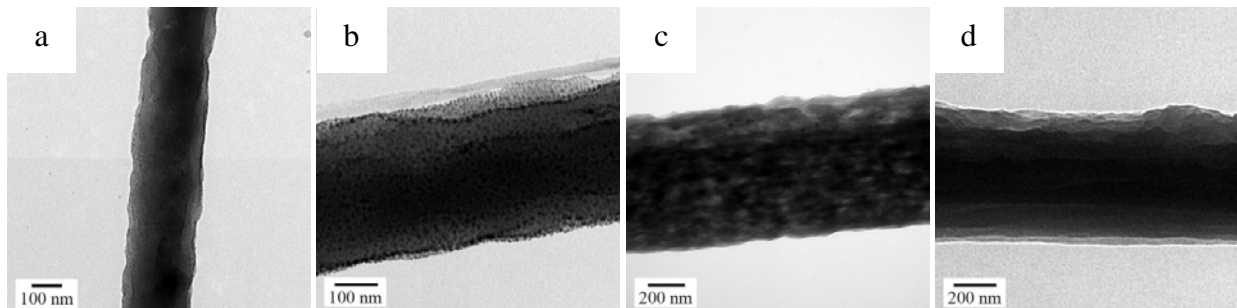
The effect of the distance between the tip of the co-axial nozzle and grounded collector is shown in Figure 3. When the distance is increased, the core-sheath structure is well defined since there is more time for evaporation of the solvent from the fibers before the fibers are deposited on the collector, hence less extent of inter-diffusion between PVP and PAN within the fiber.

Figure 3. TEM micrographs of products obtained from co-axial electrospinning of 6 %wt. PVP solution and 6 %wt. PAN solution using applied potential of 15 kV and the nozzle-to-collector distance of 12 cm (a), 15 cm (b) and 18 cm (c).



The electric potential is another important parameter in electrospinning. For the investigation of this parameter, the initial concentrations of PAN and PVP were fixed at 6% wt., while the nozzle-to-collector distance was fixed at 18 cm. It is found from TEM micrographs in Figure 4 that, when the electric potential is increased, surface of the obtained fibers are relatively rough. This was caused by the increased electric force pulling the jet of the solution.

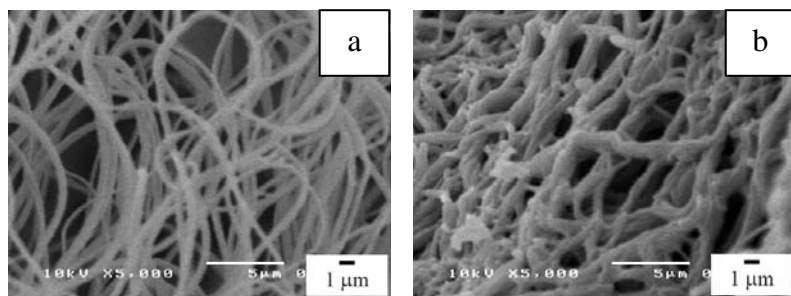
Figure 4. TEM micrographs of products obtained from co-axial electrospinning of 6 %wt. PVP solution and 6 %wt. PAN solution using the nozzle-to-collector distance of 18 cm and the applied potential of 15 kV (a), 16 kV (b), 17 kV (c) and 18 kV (d).



Pyrolysis of Core-Sheath PAN-PVP Fibers

The products obtained from the co-axial electrospinning of PAN and PVP were subjected to the pyrolysis at 400°C which is high enough for decomposition of PVP, but not enough for total decomposition of PAN. The results shown in Figure 5 reveal that the products remain in fiber form even after the pyrolysis. However, the fibers are no longer straight fibers, most probably due to the shrinkage by the partial removal of carbonaceous species during the pyrolysis. Nevertheless, by overall observation, the products still retain its flexibility, which is different than the pyrolyzed product of pure PVP nanofibers.

Figure 5. SEM micrographs of co-axial product before (a) and after (b) pyrolysis at 400°C.



CONCLUSION

PAN/PVP core-sheath electrospun fiber can be used as a precursor for the flexible carbon fibers synthesis. Initial concentration, electrical potential applied and distance between the nozzle and collector can be adjusted to control morphology of the product.

ACKNOWLEDGMENTS

This study is partly supported by the Centennial Fund of Chulalongkorn University to the Center of Excellence in Particle Technology.

REFERENCES

- [1] D. D. Edie, "The effect of processing on the structure and properties of carbon fibers." *Carbon*, vol. 36, pp. 345-362, 1998.
- [2] Fang Z. Jiaming G. Feng Z. Ruowen F. Dingcai W. Tiangang L. Yexiang T. Tongbu L. Gangfeng O. "Preparation and characterization of porous carbon material-coated solid-phase microextraction metal fibers " *Journal of Chromatography A*, vol. 1217, pp. 7848-7854, 2010.
- [3] S.Y. Gu. J.Ren. G.J.Vancso. "Process optimization and empirical modeling for electrospun polyacrylonitrile (PAN) nanofiber precursor of carbon nanofibers." *European Polymer Journal*, vol.41, pp. 2559-2568, 2005.
- [4] Darrell H. Reneker. Alexander L. Yarin. "Electrospinning jets and polymer nanofibers." *Polymer*, vol.49, pp. 2387-2425, 2008.
- [5] G. Srinivasan, Reneker, "Structure and morphology of small diameter electrospun aramid fibers," *Polymer International*, vol. 36, pp. 195-201, 1995.

The feasibility study for silicon determination in airborne particulate matter using an electrical low pressure impactor and laser ablation/inductively coupled plasma mass spectrometry

Chu-Fang Wang^{1,2}, Yi-Kong Hsieh¹, and Bing-Shen Yang¹

1 Department of Biomedical Engineer and Environmental Sciences, National Tsing Hua University, Hsinchu, 30013

2 Institute of Nuclear Engineering and Science, National Tsing Hua University, Hsinchu, 30013

Principal Contact: Chu-Fang Wang, Professor, Department of Biomedical Engineer and Environmental Sciences, National Tsing Hua University, Hsinchu, 30013.

Tel: +886-3-5715131 Ext. 34222 Fax: +886-3-572-7298 E-mail: cfwang@mx.nthu.edu.tw

Abstract

In this work we report a new procedure for elemental analysis of silicon in airborne particulate matter by laser ablation inductively coupled plasma mass spectrometry (LA-ICP-MS). Airborne particulate matter collection is conducted using an electrical low pressure impactor (ELPI) which is the typical twelve-stage cascade impactor. The samples collected on the Teflon filter medium by ELPI present clear and well-defined multiple spots. We prepared laboratory-made standard filter samples by placing drops of liquid standard solutions onto the filter to simulate the ELPI collection of samples. Otherwise, we also used standard addition method to acquire the results and compared with those acquired by external standard calibration method. The procedure was applied for the analysis of silicon in the nanometer ($<0.1 \mu\text{m}$), submicrometer ($0.1\text{--}1.0 \mu\text{m}$), and micrometer ($>1.0 \mu\text{m}$) size ranges airborne particulate matter collected at Central Taiwan science park. The absolute limits of detection is 1.06 ng, which translates to method detection limits of approximately 0.5 to 11.1 ng m^{-3} when considering the amounts of sample spots and the volumes of air collected per investigated sample. The obtained results reveal that the airborne silicon particles not only contribute from natural source, but also emit from traditional and semiconductor industry. The mass median diameter for Si is in $\text{PM}_{0.4\text{--}0.51}$, and particle-bound Si is more abundant in the accumulation mode than in the nucleation or coarse mode. The data obtained from sampling period represents the possible nanometer particle growth mechanism in the atmosphere and exhibits the nearby potential pollution source.

Keywords: Aerosol particle, semiconductor, LA-ICP-MS

Reactions of Calcium Carbonate Particles: Effect of Temperature, Residence Time, and Atmospheric Condition

Kang Soo Lee¹, Jae Hee Jung², Seongha Jeong¹, Sang In Keel³, Jin Han Yun³, and Sang Soo Kim¹

1 Department of Mechanical Engineering, KAIST, 373-1, Guseong-dong, Yuseong-gu, Daejeon, Republic of Korea 305-701

2 Global Environment Center, Korea Institute of Science and Technology (KIST), Seongbuk-gu, Seoul, Republic of Korea 136-130

3 Environmental Systems Research Division, Korea Institute of Machinery and Materials (KIMM), Daejeon, Republic of Korea 305-343

Principal Contact: Kang Soo Lee, Ph.D candidate, Department of Mechanical Engineering, KAIST, 373-1, Guseong-dong, Yuseong-gu, Daejeon, Republic of Korea 305-701.

Tel: +82-42-350-3061 Fax: +82-42-350-8207 Email: ks-lee@kaist.ac.kr

Abstract

The lab-scale experimental system which can simulate the O₂/CO₂ combustion system was developed. To examine the physical/chemical characteristics of the calcium carbonate (CaCO₃) which are used as a sorbent particle for in-furnace desulfurization at O₂/CO₂ combustion system, they were injected into the high temperature drop tube furnace. Experiments were conducted for the various temperatures, residence times, and atmospheres. To determine the characteristics of the CaCO₃ sorbent particles, they were sampled at inlet and outlet of the reactor and analyzed by using thermogravimetric analyzer (TGA), BET, and SEM. It was shown that the starting temperature of the calcination was higher in an O₂/CO₂ atmosphere in contrast to the air atmosphere. Sorbent particles were calcined rapidly and sintered subsequently in air atmosphere, whereas calcination was delayed in O₂/CO₂ atmosphere due to the higher partial pressure of the CO₂. From the SEM images, it was shown that the morphology changes of the sorbent particle were different between the air and O₂/CO₂ atmospheres. Finally, it was shown that the O₂ concentration in an atmosphere has less effect on the characteristics of the sorbent particles.

Keywords: In-furnace desulfurization, calcinations, sintering

Hygroscopicity of Benzoic acid Aerosol Particles at Room Temperature: Setup and First Applications of H-TDMA system

Yajun Shi, Maofa Ge, and Weigang Wang

State Key Laboratory for Structural Chemistry of Unstable and Stable Species, Beijing National Laboratory for Molecular Sciences (BNLMS), Institute of Chemistry, Chinese Academy of Science, Beijing, 100190, P. R. China

Principal Contact: Maofa Ge, Professor, State Key Laboratory for Structural Chemistry of Unstable and Stable Species, Beijing National Laboratory for Molecular Sciences (BNLMS), Institute of Chemistry, Chinese Academy of Science, Beijing, 100190, P. R. China.

Tel: +86-10-62554518 Fax: +86-10-62559373 Email: gemaofa@iccas.ac.cn

Abstract

Atmospheric aerosols contain various inorganic and organic species, which can change the hygroscopicity of aerosols. The hygroscopicity of aerosols is a vital factor affecting air quality, visibility, formation of clouds and precipitation. Benzoic acid (BA) is one of the main products from photochemical degradation of aromatic hydrocarbons in the urban atmosphere and has been identified in the particle phase. Recent studies have shown that the interaction between BA and atmospheric sulfuric acid promotes efficient formation of organic and sulfate aerosols that are associated largely with acid rain. Thus, it is important to study the hygroscopicity of BA to better understand critical atmospheric process associated with aerosols. However, little information exists on the hygroscopicity of BA.

A Hygroscopicity Tandem Differential Mobility Analyzer (H-TDMA) system was designed to investigate the hygroscopicity of atmospheric aerosol particles. This system has been applied to measure deliquescence relative humidities (DRHs) and hygroscopic growth factors (GFs) of atomizer-generated NaCl and $(\text{NH}_4)_2\text{SO}_4$ particles at room temperature. The obtained DRHs and GFs agree well with the literature values and the theoretical Köhler curve, respectively. These results indicate that the H-TDMA system can be used to accurately and reliably research the hygroscopicity of aerosol particles.

In this study, we applied the H-TDMA system to investigate the hygroscopicity of BA at room temperature. Data showed that BA particles deliquesced at RH $70 \pm 0.8\%$, and the GF of BA particles was 1.05 ± 0.015 at RH $= 85 \pm 0.8\%$. Furthermore, it was observed that particle size keeps constant before 30% RH, and apparently decreases and then increases with the increasing RH in the range of 30%~65%, which suggested that BA particles may experience a significant restructuring at RH close to DRH. To better understand the effects of BA and other aromatic acids on the hygroscopicity of inorganic aerosols, further research is clearly needed.

Keywords: Hygroscopicity, benzoic acid, H-TDMA, deliquescence relative humidity, growth factors

Wind Speed Enhancement of Marine Aerosol Optical Depth

S. Gerard Jennings¹, Jane P. Mulcahy², Claire Scannell³, Darius Ceburnis¹ and Colin O'Dowd¹

1 School of Physics & Centre for Climate and Air Pollution Studies, Ryan Institute, National University of Ireland Galway, University Road, Galway, Ireland

2 Global Model Evaluation and Development, Met Office, Exeter, Devon EX1 3PB, UK

3 Université Paris 6, LATMOS/IPSL, CNRS/INSU, 75005 Paris, France

ABSTRACT

The relationship between aerosol optical depth (AOD) and wind speed (U), obtained at the Mace Head atmospheric research station, is presented for clean marine (Northeast Atlantic) conditions under steady-state wind speed scenarios. AOD measurements were made under much higher wind speed conditions (up to 18 m s^{-1}) than hitherto measured. The AOD is found to be approximately dependent on U^2 , with a high correlation ($r^2 = 0.97$) determined at all measured wavelengths of 862 nm, 500 nm, 412 nm and 368 nm. The power-law parameterization^[19], derived at the coastal Atlantic station Mace Head, between clean marine aerosol optical depth (AOD) and wind speed is compared to open ocean MODIS-derived AOD versus wind speed. The open ocean MODIS-derived AOD at 550 nm and 860 nm wavelength, is in overall good agreement with the general magnitude of the parameterization based on Mace Head AOD measurements. The results also show that wind generated sea spray AOD values approaching 0.3 under moderately high winds, can rival or even exceed AOD values usually associated with polluted air.

KEYWORDS

Marine Aerosol, Aerosol Optical Depth (AOD), Wind Speed, MODIS derived AOD

Introduction

Naturally occurring marine aerosol plays an important role in the Earth's climate system and in the global radiative budget^[1,2,3], given that over 70% of the Earth's surface is covered by ocean. Marine aerosol comprises both primary-produced sea spray and secondary aerosol components and have both a direct and indirect effect on climate^[4,5,6,7]. Sea spray aerosol is also an important component in atmospheric light scattering processes^[8,9,10,11]. The aerosol optical depth (AOD),

which is the integral measurement of the combined aerosol scattering and absorption in the atmospheric column, is a key parameter in the measurement of the direct aerosol effect.

There is a relative lack of clean marine AOD reported data compared to anthropogenic AOD. Under more polluted regimes, AOD values are typically in the range of 0.2 to 0.5^[12]. A mean AOD (495.7nm) value of 0.23 for air masses of Central-Eastern Europe origin is reported^[13], while an average AOD (440nm) of 0.26 is reported^[14] for Paris, France. Median AOD values of 0.052 and 0.071 are reported^[15] for the Atlantic and Pacific oceans respectively. Over the North Atlantic region, the AOD is influenced by dust transport from the Sahara, pollution from continental Europe and biomass burning from South America and Africa. An in-depth comprehensive overview is given^[16] of aerosol optical measurements in marine and coastal areas, reporting AOD ($\lambda=500\text{nm}$) for the Atlantic Ocean region in the range of 0.04 to 0.2, and reaching 0.5 in the presence of dust particles. Based on these findings, aerosol models used in aerosol satellite remote sensing retrievals use only AOD values less than 0.15 and Ångstrom exponent values below 1.0 for marine aerosol^[17]. Over the Pacific Ocean, over 75% of the measured AOD ($\lambda=500\text{nm}$) is less than 0.15. An AOD range between 0.05 – 0.12 with between 50-75% being contributed by the coarse aerosol mode, has been determined^[18]. Measurements of AOD obtained at the Mace Head atmospheric research station under much higher wind speed conditions^[19] (up to 18m s^{-1}) than hitherto measured are presented. Results indicate that even moderate-to-high wind speed conditions, sea-spray AOD can rival or even exceed anthropogenic AOD.

Few open-ocean measurements have been made. MODIS-derived AOD versus wind speed^[20] for remote regions in the North Pacific and Southern Oceans are compared to clean marine AOD versus wind speed measurements taken at the Mace Head site. The Mace Head Global Atmosphere Watch (GAW) research station on the west coast of Ireland (53.3°N, 9.9°W) provides an ideal site to carry out studies in a pristine marine environment. Unique in its location on the western edge of Europe, the station lies directly in the path of the prevailing westerly-south westerly airflow approaching from the Atlantic Ocean. Over 52% of all air masses arriving at the site are clean marine in origin, with little or no anthropogenic influences^[21].

Experimental Methods

Continuous measurements of aerosol optical depth (AOD) have been made at Mace Head since March 2000, with a Precision Filter Radiometer (PFR). The PFR was developed at the World Radiation Centre in the Physikalisch Meteorologisches Observatorium Davos (PMOD-WRC), Switzerland, and is part of the international GAW-PFR (Global Atmosphere Watch-PFR) AOD

network^[22]. The AOD is derived from direct solar radiation measurements made every 2 minutes at four wavelengths centered at 368, 412, 500, and 862nm.

The precision of the PFR instrument is estimated to be approximately 0.01 optical depth, based on inter-comparison studies with other sunphotometer systems^[23], including the Aerosol Robotic Network (AERONET). The full period of operation of the PFR instrument (PFR-No.2) used in this study was January 2002 to December 2004. During this time the stability of the calibration constants for all four spectral channels was monitored by calibration against a standard instrument at PMOD-WRC before deployment and after removal of the instrument at Mace Head. During the period of operation at Mace Head, a number of Langley calibrations were performed *in situ* when favorable, stable airmass conditions were met. The stability of the calibration constants were determined to have remained within 1% for the duration of instrument operation. Cloud-screening of the AOD measurements is carried out by implementation of the AERONET cloud-screening algorithm^[24] along with an additional filter, which flags all measurements if the AOD in the infrared channel is greater than 2. Meteorological parameters such as wind speed and wind direction are measured on an ongoing long-term basis at the station.

The study was strictly limited to winter periods (November–March) and clean marine air masses, in order to maximize the impact of sea salt scattering. Sea salt dominates all aerosol size ranges during wintertime and the contributing fractions of biogenically produced inorganic and organic matter to the marine aerosol are relatively small compared with summer values.

The following criteria were applied in order to select time periods corresponding to clean marine conditions only:

- i) The wind direction measured at Mace Head was in the designated 180°–300° clean marine sector
- ii) The measured black carbon mass concentration was less than 50 ng m⁻³
- iii) The total particle number concentration was less than 700 cm⁻³
- iv) For each individual steady state wind speed event, hourly air mass back trajectories were calculated to further support the clean marine conditions for the duration of the AOD observations. These criteria are based on a number of previous studies, which investigated the cleanest marine air conditions at Mace Head and the accompanying microphysical and physico-chemical aerosol characteristics^{[25][26]}.

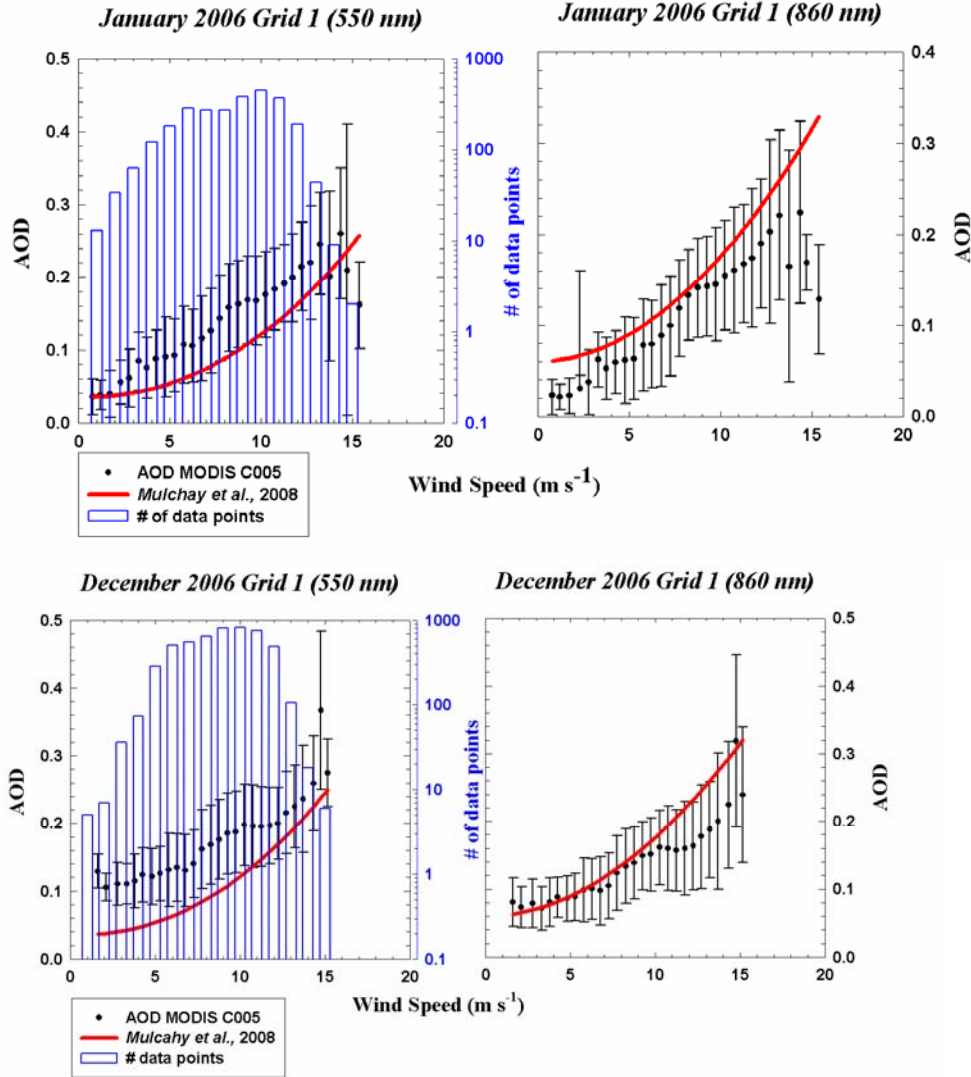
Results and Discussion

The AOD and wind speed data were sorted into bins based on wind speed. Each bin was 1 m s⁻¹ wide and spaced in 1 m s⁻¹ increments. The AOD is observed to increase by nearly an order of magnitude over a wind speed range of 4 – 18 m s⁻¹, shown for wavelengths 550 and 860nm in

Figure 1 (red curve). This significant increase in AOD is due to the enhanced contribution of the supermicron mode to the aerosol scattering at higher wind speeds, as a direct result of an increase in the concentration of larger sized sea salt particles. However, this behavior is also observed at the shorter wavelengths, down to 368 nm, illustrating the equally important influence of wind speed on the submicron sea salt aerosol particles. A power law curve of the form $\tau = \tau^0 + a.U^b$ was fitted to the data and a strong dependence ($r^2 \sim 0.97$) of AOD on the approximate square of wind speed (U) was observed^[19] at all 4 wavelengths ($b = 1.95, 2.195, 1.755$ and 2.4 for $\lambda = 862, 500, 412$ and 368nm respectively).

The AOD-wind speed relationship^[19] was compared to MODIS-derived AOD versus wind speed for a remote region over the North Pacific Ocean ($0^\circ \text{N} - 20^\circ \text{N}$ and $180^\circ \text{W} - 110^\circ \text{W}$) during the months of January and December 2006. For this analysis^[20], $1^\circ \times 1^\circ$ resolution *C005* MODIS daily AOD data were taken from the Ocean level-3 MODIS Atmosphere Daily Global Product for 2006 at 550 nm and 860 nm. Criteria used for data selection: only clean air masses were examined as determined by back-trajectory analysis; there must be no cloud contamination; and there must be variable wind speeds during the period. Wind Speed data was retrieved from the SeaWinds instrument on the QuickSCAT satellite. SeaWinds is a microwave radar that measures near-surface wind speed and direction with a swath resolution of $0.25^\circ \times 0.25^\circ$. For this analysis, wind speed was interpolated to a $1^\circ \times 1^\circ$ grid to compare to a $1^\circ \times 1^\circ$ AOD grid and each wind speed data point was matched to its corresponding AOD data point at each time and location. MODIS level 2 *C005* data has a stringent cloud screening procedure^[27]. There are a number of uncertainties associated with satellite measurements, for example: the presence of clouds which are not removed by the filtering process and whitecaps at high wind speeds lead to emissivity effects which can affect the quality of the retrieved MODIS AOD^[28].

Figure 1. A comparison of the AOD wind-speed relationship^[19] (red curve) based on measurements at Mace Head with MODIS C005 AOD inferred data (black circles) over the North Pacific (0° N - 20° N and 180° W - 110° W) at 550 nm and at 860nm during December and January 2006. Also shown is the number of data points per wind speed average bin.



The results (black circles) for December and January 2006 are shown in Figure 1 and cover a wind speed range of 2 m s^{-1} to 15 m s^{-1} . For December, the 550 nm MODIS AOD is higher than that based on Mace Head data^[19] for the lower wind speeds, increasing up to 10 m s^{-1} where it levels out between $10\text{-}13 \text{ m s}^{-1}$, after which AOD increases again. For the 860 nm wavelength, there is excellent agreement with Mace Head data^[19] up to 10 m s^{-1} , after which AOD levels out

until it starts to increase with wind speed above 13 m s^{-1} . For the January case, a similar trend is seen where in the 550 nm case, AOD is higher than that reported^[19], and for 860 nm, AOD is marginally lower. Between $9\text{--}13 \text{ m s}^{-1}$, there is a slight reduction in the slope of the AOD-wind speed relationship, although not as drastic as the December case where it more or less levels off. The fitted power-law relationship for the December 550 nm case possessed an exponent of 2.47, and for the 860 nm wavelength, the exponent was 2.36. These exponents are slightly higher than the exponents derived from Mace Head AOD-Wind Speed data^[19], (2.2 for 500 nm and 1.95 for the 832 nm wavelengths). For the January case, the exponents are significantly lower with a value of 0.72 for the 550 nm wavelength and 0.77 for the 860 nm wavelength. For these four MODIS derived relationships, the correlation coefficient (r^2) was between 0.88 and 0.91.

SUMMARY

It should be noted that AOD derived from the precision filter radiometer is a more direct measurement and many more assumptions are required in the MODIS retrieval algorithm than in the precision filter radiometer. Consequently, one would expect the radiometer data to reflect the more accurate AOD – wind speed relationship. So, the main conclusions arrived at^[19] still hold, namely, that sea-spray contributions to marine AOD can approach or even exceed values of 0.3, and that natural sea-spray, under moderately high wind speed regimes can rival or even exceed values normally associated with anthropogenic aerosols.

ACKNOWLEDGEMENTS

This work was supported by the European Commission through the MAP (Marine Aerosol Production) Project, the Network of ACCENT (Atmospheric Composition Change – Network of Excellence) Project and by the Irish Environmental Protection Agency ERDTI Programme 2000–2006. The authors also wish to acknowledge the World Optical Depth Research and Calibration Centre (WORCC) and Senior Scientist Christoph Wehrli and his team for facilitation of the quality controlled PFR AOD data at Mace Head.

REFERENCES

- [1] Solomon, S.; Qin, D.; Manning, M.; Chen, Z.; Marquis, M.; Averyt, K.B.; Tignor, M.; Miller, H.L. *Climate Change 2007: The Physical Science Basis. Contribution of Working Group I to the Fourth Assessment Report of the Intergovernmental Panel on Climate Change*, Cambridge University Press, Cambridge, UK and New York, USA, 2007.

- [2] O'Dowd, C. D.; de Leeuw, G. *Phil. Trans. R. Soc. A.* 2007, 365, 1753-1774.
- [3] Ayash, T., Gong, S.; Jia, C.Q. *J. Clim.* 2008, 21, 3207-3220, doi: 10.1175/2007JCLI2063.1.
- [4] Latham, J.; Smith, M. H. *Nature.* 1990, 347, 372-373.
- [5] O'Dowd, C. D.; Lowe, J.; Smith, M.H.; Kaye, A.D. *Quart J. Roy. Meteorol. Soc.* 1999, 125, 1295-1313, doi:10.1256/smsqj.55609.
- [6] Charlson, R. J.; Lovelock, J.E.; Andreae, M.O.; Warren, S.G. *Nature.* 1987, 326, 655-661.
- [7] Fitzgerald, J. M. *Atmos. Environ. Part A.* 25, 533-545.
- [8] Murphy, D. M.; Anderson, J.R.; Quinn, P.K.; McInnes, L.M.; Brechtel, F.J.; Kreidenweis, S.M.; Middlebrook, A.M.; Posfai, M.; Thomson, D.S.; Buseck, P.R. *Nature.* 1998, 392, 62-65.
- [9] Quinn, P. K.; Coffman, D.J.; Kapustin, V.N.; Bates, T.S.; Covert, D.S. *J. Geophys. Res.* 1998, 103, 16,547-16,563.
- [10] Kleefeld, C.; O'Dowd, C.D.; O'Reilly, S.; Jennings, S.G.; Aalto, P.; Becker, E.; Kunz, G.; de Leeuw, G. *J. Geophys. Res.* 2002, 107, 8103, doi:10.1029/2000JD000262.
- [11] Bates, T. S.; Anderson, T.L.; Baynard, T.; Bond, T.; Boucher, O.; Carmichael, G.; Clarke, Erlich, C.; Guo, H.; Horowitz, L.; Howell, S.; Kulkarni, S.; Maring, H.; McComiskey, A.; Middlebrook, A.; Noone, K.; O'Dowd, C.D.; Ogren, J.; Penner, J.; Quinn, P.K.; Ravishankara, A.R.; Savoie, D.L.; Schwartz, S.E.; Shinozuka, Y.; Tang, Y.; Weber, R.J.; Wu, Y. *Atmos. Chem. Phys.* 2006, 6, 1657-1732.
- [12] Ramanathan, V.; Crutzen, P.J.; Kiehl, J.T.; Rosenfeld, D. *Science.* 2001, 294, 2119-2124.
- [13] Pace, G.; di Sarra, A.; Meloni, D.; Piacentino, S.; Chamard, P. *Atmos. Chem. Phys.* 2006, 6, 697-713.
- [14] Dubovik, O.; Holben, B.; Eck, T.F.; Smirnov, A.; Kaufman, Y.J.; King, M.D.; Tanre, D.; Slutsker, I. *J. Atmos. Sci.* 2002, 59, 590-608.
- [15] Kaufman, Y. J.; Smirnov, A.; Holben, B.N.; Dubovik, O. *Geophys. Res. Lett.* 2001, 6, 3251-3254.
- [16] Smirnov, A.; Holben, B.N.; Kaufman, Y.J.; Dubovik, O.; Eck, T.F.; Slutsker, I.; Pietras, C.; Halthore, R.N. *J. Atmos. Sci.* 2002, 59, 501-523.
- [17] Smirnov, A.; Holben, B.N.; Dubovik, O.; Frouin, R.; Eck, T.F.; Slutsker, I. *J. Geophys. Res.* 2003, 108, 4033, doi:10.1029/2002JD002701.
- [18] Reid, J. S.; B. Brooks, B.; Crahan, K.K.; Hegg, D.A.; Eck, T.F.; O'Neill, N.; de Leeuw, G.; Reid, E.A.; Anderson, K.D. *J. Geophys. Res.* 2006, 111, D02202, doi:10.1029/2005JD006200.
- [19] Mulcahy J. P.; O'Dowd, C.D.; Jennings, S.G.; Ceburnis, D. *Geophys. Res. Lett.* 2008, 35, L16810, doi:10.1029/2008GL034303.
- [20] O'Dowd, C.; Scannell, C.; Mulcahy, J.; Jennings, S.G. *Adv. Meteorol.* 2010, doi: 10.1155/2010/830846.
- [21] Jennings, S. G.; Kleefeld, C.; O'Dowd, C.D.; Junker, C.; Spain, T.G.; O'Brien, P.; Roddy, A.F.; O'Connor, T.C. *Boreal Env. Res.* 2003, 8, 303-314.

- [22] Wehrli, C. GAWPFR: *A network of aerosol optical depth observations with precision filter radiometers*, in WMO/GAW Experts Workshop on a Global Surface-Based Network for Long Term Observations of Column Aerosol Optical Properties, *GAW Report No. 162*, WMO TD No. 1287, Baltensperger, U.; Barrie, L.; Wehrli, C. Eds.; 2004; pp. 36-38.
- [23] McArthur, B. L. J.; Halliwell, D.H.; Niebergall, O.J.; O'Neill, N.T.; Slusser, J.R.; Wehrli, C. *J. Geophys. Res.* 2003, 108, 4596, doi:10.1029/2002JD002964.
- [24] Smirnov, A.; Holben, B.N.; Eck, T.F.; Dubovik, O.; Slutsker, I. *Remote Sens. Environ.* 2000, 73, 337-349.
- [25] Jennings, S. G.; Geever, M.; McGovern, F.M.; Francis, J.; Spain, T.G.; Donaghy, T. *Atmos. Environ.* 1997, 31, 2795– 2808.
- [26] O'Dowd, C. D.; Smith, M.H.; Jennings, S.G. *J. Geophys. Res.* 1993, 98, 1123–1135.
- [27] Martins, V. J.; Tanre, D.; Remer, L.; Kaufman, Y.; Mattoo, S.; Levy, R. *Geophys. Res.Lett.* 2002, 29, doi:10.1029/2002JD002964.
- [28] Tanre, D.; Kaufman, Y.J.; Herman, M.; Mattoo, S. *J. Geophys. Res.* 1997, 102, 16,971 – 16,988.

Distribution Characteristics of nano-TiO₂ Aerosol at Work Place

Yi Yang, Ping Mao, Chun-lan Xu, Shou-wen Chen, Zheng-ping Wang, Jin-hua Zhang

Principal Contact: Yi Yang, Associate professor, School of Chemical Engineering, Nanjing University of Science and Technology, Nanjing 210094, China.

Email: yyi301@163.com

Abstract

To learn the suspension, congregation and sedimentation performances of nanoaerosols at work place, the distribution of nano-TiO₂ in workshop has been characterized in this paper. A wide-range particle spectrometer and cascade impactor samplers have been employed to test the number concentration and mass concentration of aerosols in the workplace atmosphere, respectively. Water or liquid based wet nanoaerosol samplers, as well as its corresponding analysis method based on ultraviolet spectrometer, have been developed to learn the mass concentration at workplace quickly. To get a comparison of the test results with each other, sampling point has been set at the height of 1.5m and at the distance of 1m to 5m from the aerosol source. The results show that all the number concentration curves display two peaks at 10nm to 200nm and 500nm to 900nm, respectively, and the aerosol particles at the distance of 3m exhibit the highest number concentration at all the diameter of particles except for diameter less than 20nm. However, aerosol at the distance of 5m presents a highest number concentration, up to 12000 unit per cm³, in the area of diameter less than 20nm. This has been attributed to the spray forces of the aerosol source and the floating of nanoaerosol particles. The mass concentration and particle weight percentage at different diameter tested by cascade impactor show highly in accordance with the results of number concentration. Data tested by wet method also provide an agreement with that by cascade impactor. Furthermore, wet aerosol sampler presents a quick sampling performance with the sampling time no more than 2h, while cascade impactors always need sampling for more than 6h.

Keywords: Nanoaerosol, Mass concentration, Number concentration, Dioxide titanium, Work place

Skyradiometer Measurements for Monitoring Columnar Aerosol Properties in the Antarctic Research Program of Japan

Masataka Shiobara¹, Hiroshi Kobayashi², Masanori Yabuki³, Maki Yamano⁴, and Yoshitaka Muraji⁴

1 National Institute of Polar Research, Tachikawa, Tokyo 190-8518, Japan

2 University of Yamanashi, Kofu, 400-8511, Japan

3 National Institute of Polar Research, now at Kyoto University, Uji, 611-0011, Japan

4 Energy Sharing Co. Tokyo, Nakano-Ku, Tokyo 165-0034, Japan

Principal Contact: Masataka Shiobara, Dr., National Institute of Polar Research, Midoricho 10-3, Tachikawa, Tokyo 190-8518, Japan.

Tel: +81 42-512-0678 Fax: +81 42-528-3497 Email: shio@nipr.ac.jp

Abstract

Atmospheric aerosol has a potential to change the global climate by the direct and indirect effects on the radiation balance in the planetary atmosphere. The direct effect is generally expected to be small in the polar regions, but the indirect effect may cause a large difference of cloud optical properties between the Arctic and Antarctic regions. National Institute of Polar Research promotes the atmospheric research in both polar regions, and employs remote-sensing instruments for aerosol and cloud studies. For investigating the columnar aerosol optical properties, sky-radiometry based on a radiation inversion algorithm is powerful to retrieve the aerosol volume size distribution, single scattering albedo and complex refractive index as well as aerosol optical thickness and Angstrom exponent. In order for long-term monitoring of the aerosol properties, we are operating a Prede POM-02 skyradiometer at Syowa Station (69.0N, 39.6E) in Antarctica. Also we recently developed a new skyradiometer POM-01 MK III for ship-based measurements. In this paper, we will show preliminary results from surface-based and ship-based skyradiometer measurements during winter-over research activities at Syowa Station and the Antarctic cruises by Icebreaking R/V Shirase of the Japanese Antarctic Research Expeditions.

Keywords: Columnar aerosol properties, skyradiometer, Icebreaking R/V Shirase, Syowa Station, Antarctica

The Preliminary Study of Aerosol Leakage at Low Gas Leakage Situation

Zhihong Zhang¹, Haijun Dang¹ and Longbo Liu¹

1 Northwest Institute of Nuclear Technology, Xi'an, Shaanxi 710024, China.

ABSTRACT

The radioactive aerosol leakage is one of the key issues of radiation protection for nuclear research and industry. The aerosol leaking behaviours of cracks with low gas leakage rate were investigated in this paper. The theory method of evaluating air and aerosol leakage rate was summarized. The effects of cross section shape of cracks, air velocity on the aerosol penetration were studied by theoretical analysis and experimental studies. It's shown that aerosol penetration of a capillary is usually more than that of a slot while both have the same gas leakage rate. The aerosol penetration decreased with the reduction of air flow velocity. For practical application the aerosol leakage rate could be expressed as a function involving the air leakage rate and the length of cracks when diffusion deposition is overwhelming, and key parameters were recommended to estimate the aerosol leakage rate through a crack.

KEYWORDS

Aerosol Leakage, Capillary, Low Air Leakage

Introduction

The study of aerosol leaking behaviours through cracks is one crucial issue of radiation protection, while the inhalation of radioactive aerosol is the main way of suffering from internal exposure of the staff in the nuclear industry and the public in the unclear leakage accidents. It's widely accepted to employ a conservative gas leakage requirement for nuclear facilities to decrease aerosol leakage risk. Technique difficulty and cost of those air-tight systems usually increase as a result. The discovery of aerosol leaking behaviours through cracks is the aerosol leakage rate would decline rapidly at low air leakage situation ($<10^{-4}$ Pa·m³·s⁻¹), which indicated that the risk of aerosol leakage could be avoided with an appropriate air leakage standard. In this paper, the theory method of evaluating gas and aerosol leakage rate was summarized, and the aerosol leaking behaviours through cracks was investigated by experiments. An estimation method of the aerosol leakage rate was constructed as a result.

Theory

There are two ideal cross section shapes of cracks for leaking studies, slot and capillary. Gas leakage rate is often used to evaluate the airtightness of devices, using $\text{Pa} \cdot \text{m}^3 \cdot \text{s}^{-1}$ as unit^[1]. Air flow is laminar and the gas leakage rate can be computed according to formula f from literatures^[2,3]. e.g.

for capillary,

$$La = \frac{\pi d^4}{128\eta l} \cdot \frac{p_u^2 - p_d^2}{2} \quad (\text{Eq.1})$$

where La is the gas leakage rate, $\text{Pa} \cdot \text{m}^3 \text{s}^{-1}$; d is the diameter of capillary, m; η is the air viscosity, $\text{Pa} \cdot \text{s}$; l is the length of the capillary, m; p_u and p_d is the pressure of upstream and downstream respectively, Pa.

The aerosol penetration which is the ratio of particle number concentration of downstream to that of upstream is defined to characterize loss of aerosol in cracks, and influenced by gravity sedimentation and diffusion deposition. The aerosol leakage rate can be obtained by the following formula^[3,4]:

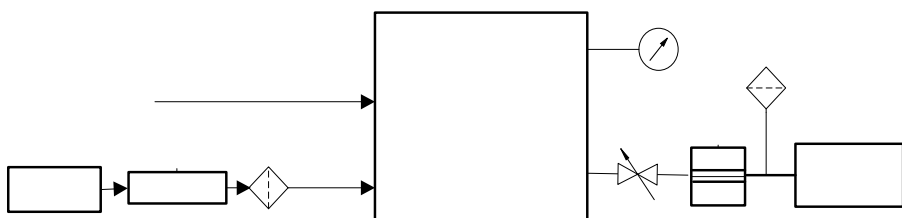
$$LA = \frac{C_{Au}}{p_u} La \cdot P_g \cdot P_D \quad (\text{Eq.2})$$

where LA is the aerosol leakage rate, s^{-1} ; C_{Au} is the upstream particle number concentration, m^{-3} ; P_g is the aerosol penetration due to gravity sedimentation alone; P_D is the aerosol penetration due to diffusion deposition alone.

Experimental Methods

Two types of cracks, capillaries and slots which were made of various flanges and swageloks were investigated by the experiments. Their gas leakage rates were measured by the pressure drop method. Their aerosol penetrations were obtained according to the aerosol concentration out of the cracks as well as that in the pressure vessel measured by Condensation Particle Counter (CPC) (see Figure 1).

Figure 1. Experimental Setup for Measuring the Aerosol Leakage Rate of Cracks.

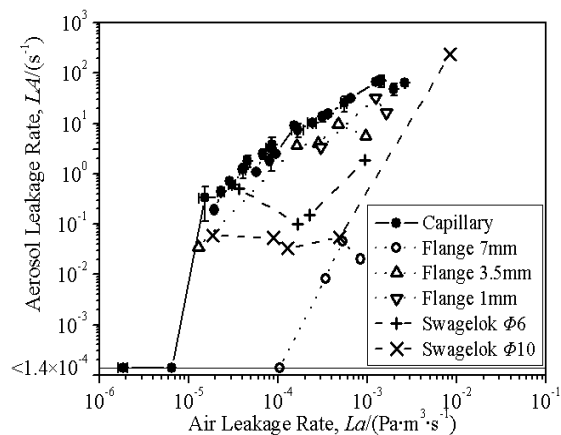


Results and Discussion

Cross Section Shape of Cracks

The aerosol leakage rate of the capillaries is higher than that of slots, while both have the same gas leakage rate, as shown in Figure 2. It indicates that capillaries are the more serious leak crack form than slots. Capillary should be paid more attention, and slot will be neglected in the following context.

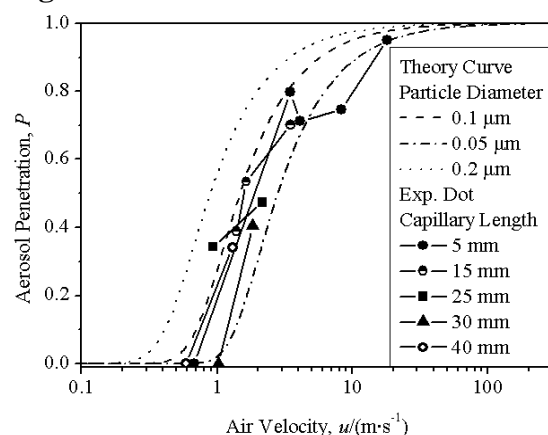
Figure 2. The Comparation of the Aerosol Leakage Rate of Capillary to Slot.



Air Flow Velocity

The aerosol penetration decreased with the reduction of air flow velocity, shown as Figure 3. When the air flow velocity is $0.5 \text{ m} \cdot \text{s}^{-1}$, the aerosol penetration decreased to 3% which is the detectability of the experimental method. The results are in accordance with the evaluation value. The effects of air flow velocity are of importance to prevent aerosol leaking.

Figure 3. Aerosol Penetration versus Air Flow Velocity. (The Upstream Pressure is 180 kPa).

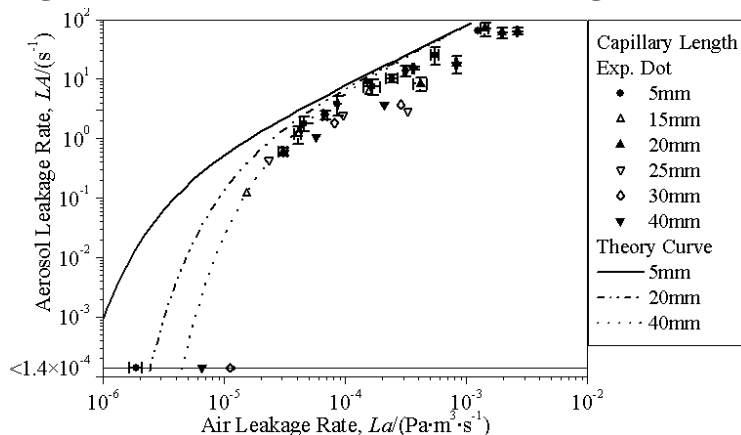


Correlation of the Aerosol Leakage Rate with the Gas leakage rate

The aerosol leakage rate which drops rapidly at low air leakage situation as shown in Figure 4, could be expressed as a function involving the air leakage rate and the length of capillary when diffusion deposition is overwhelming. The aerosol leakage rate could be estimated by the following equation:

$$LA = 8.19 \times 10^{-6} C_{Au} La e^{-8.87 \times 10^{-4} \cdot \frac{l}{La}} \quad (\text{Eq.3})$$

Figure 4. the Correlation of Aerosol Leakage Rate with Gas Leakage Rate



CONCLUSION

Aerosol penetration of a capillary is usually more than that of a slot while both have the same gas leakage. The aerosol penetration decreased with the deceleration of air flow. An equation involving the air leakage rate and the length of cracks was recommended to estimate the aerosol leakage rate through a crack.

REFERENCES

- [1] American National Standards Institute I. *American National Standard for Radioactive Materials-Leakage Tests on Packages for Shipment*. Management I O N M, 1997: February 5, 1998.
- [2] Clement C F. *J. Aerosol Sci.* 1995, 26(3): 369-385.
- [3] Liu D L, Nazaroff W W. *Atmospheric Environment*, 2001, 35(26): 4451-4462.
- [4] Fuchs A. *The Mechanics of Aerosols*. Pergamon, Oxford, 1964.

The Evaluation of Aerosol Monte Carlo Simulation undergoing Simultaneous Coagulation and Settling

Longbo Liu and Lixing Zhang

Northwest Institute of Nuclear Technology, Xi'an , Shaanxi 710024, China

ABSTRACT

Because of its advantage, such as less-complexity and high-efficiency, the Direct Simulation Monte Carlo method (DSMC) is one of the popular numerical simulation methods for solving the General Dynamic Equation (GDE). Coagulation and Settling are usually the most important mechanisms in the GDE and numerous codes have been developed to solve them in various systems. A modified DSMC is proposed to save the computation time of simulation and the evaluation of this method is also studied in the present paper. The evaluation methods of DSMC for simulation of coagulation and settling individually have been well investigated and but seldom applied to both simultaneously. An evaluation method was proposed in this paper as following: Firstly, for the coagulation scenario, the DSMC method and the sectional method are programmed respectively and validated by self-preserved distribution. Secondly, for the simultaneous coagulation and settling scenario, by adding the analytical solution for the settling mechanism into the sectional method, the results could be served as a benchmark for evaluation. Finally, the DSMC method for the simultaneous scenario is tested and validated by the previous results. The results of simulations show that the time consumption of the DSMC method could be reduced by a factor of 100 and 1000 while running 1000 and 10000 particles respectively. And the results of the DSMC method are consistent with those of the sectional method.

KEYWORDS

Numerical Simulation, Direct Simulation Monte Carlo method (DSMC), General Dynamic Equation (GDE), Validity

Introduction

Because of its advantage, such as less-complexity and high-efficiency, the Direct Simulation Monte Carlo method (DSMC) is one of the popular numerical simulation methods for solving the General Dynamic Equation (GDE). Coagulation and Settling are usually the most important mechanisms in the GDE and numerous codes have been developed to solve them in various systems. The evaluation methods of DSMC for simulation of coagulation and settling individually have been well investigated and but seldom applied to both simultaneously. A

modified DSMC is proposed to save the computation time of simulation and the evaluation of this method is also studied in the present paper.

Simulation Methods

GDE

The GDE for coagulation and settling simultaneously is as following:

$$\frac{\partial C(d_i)}{\partial t} = \frac{1}{2} \sum K(d_i, d_j) C(d_i) C(d_j) - C(d) \sum K(d, d_i) C(d_i) - \beta_i C(d_i) \quad (\text{Eq.1})$$

where $C(d_i)$ is the concentration of aerosol with the diameter d_i , m^{-3} ; K is the collision rates, $\text{m}^3 \text{s}^{-1}$; β_i is the decay rate of aerosol with the diameter d_i , s^{-1} .

Coagulation

Two methods, the sectional method and DSMC, are applied to solve the GDE. For the coagulation process, the classic four-stage Runge-Kutta is used in the sectional method. DSMC has been investigated thoroughly in literatures and the simulation here bases on the so-called fast DSMC by Kruis^[1]. The main idea is application of the possible sum of collision rates of each particle (Eq.2) instead of solely collision rates.

$$S_i = \sum_{k \neq i} K_{i,k} \quad (\text{Eq.2})$$

The most time-consuming step in the DSMC is renewal of S_i since the collision rates between any two of all particles need to be calculated once after one event. A new renewal method is proposed in this DSMC. After each event, S_i of the new formed particle is calculated as follows:

$$S_{i,\text{new}} = \sum_{k \neq i,j} K_{i,k} \quad (\text{Eq.3})$$

Then the collision rates relevant to the new formed particle and the disappeared particle instead of all particles, are re-calculated for other simulation particles. Their S_i are revised accordingly (Eq. 4).

$$S_{k,\text{new}} = S_{k,\text{old}} + K_{i(\text{new}),k} - K_{i(\text{old}),k} - K_{j,k} \quad k = 1 \dots N, k \neq i \quad (\text{Eq.4})$$

The computational times of one renewal process is $O(N)$ in this DSMC as a result, which is much less than $O(N^2)$ in the traditional DSMC.

The self-preserved distribution (SPD)^[2, 3] defined by the Eq.5, is applied to validate the above sectional method and the DSMC for the coagulation process.

$$\mu_k = \int_0^\infty v^{*k} \psi dv^* = 1 \quad k = 0, 1 \quad (\text{Eq.5})$$

where v^* is a dimensionless particle volume and ψ is a dimensionless number distribution function.

Simultaneous Coagulation and Settling

The analytical solution for the settling decay in the GDE is applied directly in the sectional

method. Because the computation error of the analytical solution can be ignored, the results of the sectional method can be used to evaluate those of other simulation. In the DSMC, an appropriate time step is selected and then the event numbers of coagulation and settling during this time increment are calculated individually. The simulation for both is implemented in turn. The initial aerosol diameter is 0.5 μm and the initial concentration is 10^{22} m^{-3} . Three settling heights 0.1, 1 and 10 m are involved in simulation. The characteristic time τ_0 is defined by Eq. 6.

$$\tau_0 = \frac{3\eta}{2k_B T C_0} \quad (\text{Eq.6})$$

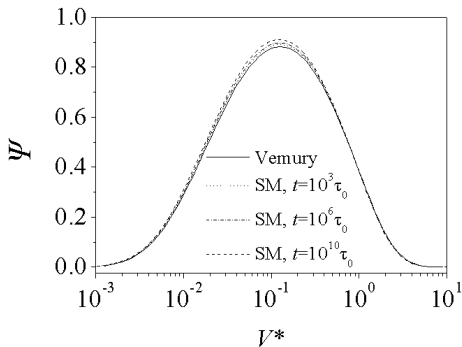
where η is the gas viscosity, Pa s; k_B is the Boltzmann's constant; T is the absolute temperature, K; C_0 is the initial aerosol concentration, m^{-3} .

Results and Discussion

Coagulation

The SPD by the sectional method is shown in Figure 1. The obtained distribution is obviously consistent with the results of Vemury^[2].

Figure 1. The SPD Function at Different Simulation Time by the Sectional Method (SM).



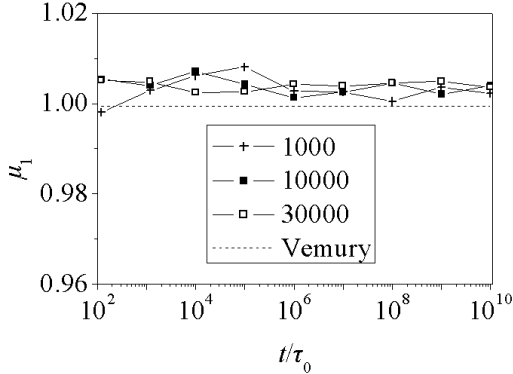
The CPU time of this DSMC is much less than the traditional method by a factor of 100 and 1000 for running 1000 and 10000 particles respectively (see Table 1). It also shows a tendency of more effective while the simulation number increases.

Table 1. The comparison of the CPU time of this DSMC method with the traditional method. The total simulation duration is $10^{10} \tau_0$.

Simulation Particle Number	CPU time /s	
	Traditional method	This method
1000	1.1×10^3	1.2×10^1
10000	7.3×10^5	6.3×10^2

The μ_1 in the Eq. 2 is calculated by the results of the DSMC (see Figure 2). The obtained μ_1 are close to the theoretic value 1. Those show that the simulation results are consistent with the SPD and both simulation methods are validated. The renewal method in the DSMC proposed in the paper is then proved to be effective and accurate.

Figure 2. Calculated μ_1 versus Simulation Duration by the DSMC.

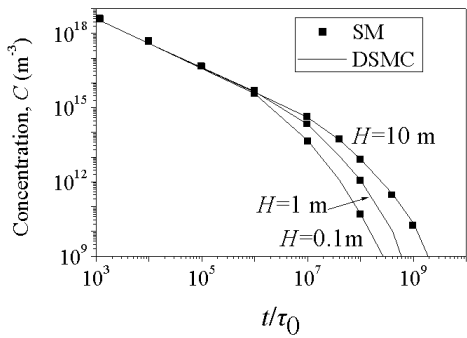


Simultaneous Coagulation and Settling

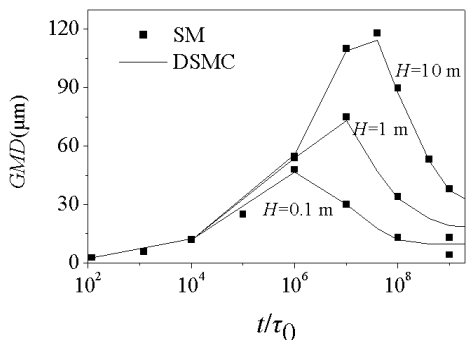
The concentration and the Geometric Mean Diameter (GMD) of simultaneous coagulation and settling are simulated by the two methods, as illustrated in Figure 3 (a) and (b). The results of the DSMC are consistent with those of the sectional method, which show that the present DSMC has been validated for simulating aerosols undergoing simultaneous coagulation and settling. The evolution of the concentration and GMD is also clear. The concentrations decrease and is not affected by the settling height while time is less than $10^6 \tau_0$. The GMDs increase during the same time. Those indicate that the coagulation is overwhelming at that time and then the settling mechanism shows its effect. The concentrations decrease more rapidly as settling height is higher, and the GMDs also decrease after reaching their maximum values.

Figure 3. The Concentration (a) and GMD (b) Evolution of Aerosol undergoing Simultaneous Coagulation and Settling by the Sectional Method (SM) and the DSMC Method.

(a)



(b)



SUMMARY

The sectional method and the DSMC for the GDE have been investigated in this paper. A novel renewal method of the crucial parameter, S_i is proposed in the DSMC to save the computation time and is proved to be effective and accurate. The DSMC for simultaneous coagulation and settling is also validated by the sectional method. The results show that this evaluation method is effective. The results of the DSMC are consistent with those of the sectional method.

REFERENCES

- [1] Kruis F. E. *AICHE J.* 2000, 46(9): 1735-1742.
- [2] Vemury S.; Kusters K. A.; Pratsinis S. E. *J. Colloid Interface Sci.* 1994, 165: 53-59.
- [3] Dekkers P. J.; Friedlander S. K. *J. Colloid Interface Sci.* 2002, 248(2): 295-305.

Uniform Coating of Multiple Layers on Particles by PCVD Process

Hung-Cuong Pham and Kyo-Seon Kim

Department of Chemical Engineering, Kangwon National University, Chuncheon, Kangwon-do, 200-701 Korea

Principal Contact: Kyo-Seon Kim, Professor, Department of Chemical Engineering, Kangwon National University, Chuncheon, Kangwon-do, 200-701 Korea.

Tel.: +82-33-250-6334 Fax: +82-33-251-3658 E-mail: kkyoseon@kangwon.ac.kr

Abstract

The plasma chemical vapor deposition (PCVD) process has been widely used for preparation of high quality thin films and can also be used to coat the uniform thin films on particles. To coat uniformly thin film on particles, we need to make the particles stay in gas phase for some time. In the rotating cylindrical PCVD reactor, the particles will rotate with the cylindrical PCVD reactor. The active radicals for particle coating are generated by the plasma. Some particles will be coated with the active chemicals while they stay on the cylindrical tube wall. The other particles will stay in the gas phase of bulk plasma to coat uniform films on the particles.

In our study, we coated double layers of $\text{SiO}_2/\text{TiO}_2$ thin films on particles using PCVD reactor and investigated the effects of process variables on growth of thin films onto the particles. We analyzed the film thickness coated on the particles from SEM measurements for various process conditions. The thin films grew more quickly on the particles with increasing mass flow rate of precursor, deposition time, or rotation speed of the reactor.

Keywords: Particle coating, PCVD, $\text{TiO}_2/\text{SiO}_x$ double-layer films, photocatalyst

Preparation of Nanostructured TiO₂ Thin Films with Controlled Morphology by Aerosol Flame Deposition Process

Jinrui Ding and Kyo-Seon Kim

Department of Chemical Engineering, Kangwon National University, Chuncheon, Kangwon-Do, 200-701 Korea

Principle Contact: Kyo-Seon Kim, Professor, Department of Chemical Engineering, Kangwon National University, Chuncheon, Kangwon-Do, 200-701 Korea.

Tel: +82-33-250-6334 Fax: +82-33-251-3658 E-mail: kkyoseon@kangwon.ac.kr

Abstract

Nanostructured TiO₂ thin films have been widely used in solar energy applications, such as photosplitting of water and dye sensitized solar cell. The aerosol flame deposition (AFD) process is capable of preparing nanostructured TiO₂ thin films from liquid precursors. Nanoparticles were generated in the aerosol phase and then deposited onto a substrate via thermophoresis. In this study, we prepared TiO₂ thin films with well controlled morphologies by the AFD process. Three important parameters that influenced film characteristics were titanium precursor feed rate, deposition height and substrate temperature. The relationship of these process parameters to the resultant morphology of the film was investigated.

Keywords: TiO₂ Thin Films, Particle Deposition, Morphology, AFD Process

Synthesis of Multifunctional Nanoparticles with Tunable Magnetic and Optical Properties

Kyo-Seon Kim and Dung T. Nguyen

Department of Chemical Engineering, Kangwon National University, Chuncheon, Kangwon-Do, 200-701 Korea

Principal Contact: Kyo-Seon Kim, Professor, Department of Chemical Engineering, Kangwon National University, Chuncheon, Kangwon-Do, 200-701 Korea.

Tel: +82 33 250 6334 Fax: +82 33 251 3658 Email: kkyoseon@kangwon.ac.kr

Abstract

Gold/iron oxide nanoparticles (NPs) represent a multifunctional system. They contain both Au and Fe_3O_4 nanoparticles, which are known to be biocompatible and have been used extensively for optical and magnetic applications in biomedicine. The structure of gold/iron oxide NPs is suitable for simultaneous optical and magnetic detection. The presence of Fe_3O_4 and Au facilitates the attachment of different chemical functionalities for target-specific imaging and delivery applications. Obtaining materials with controlled size, shape or component is an issue that has engaged many researchers. In this study, we prepared Au and iron oxide NPs and, then, used them as the seed particles for further growth process to control the particle size and to develop the composite NPs. Those NPs were characterized by TEM, XRD, UV-Vis and VSM in order to elucidate their morphologies and properties.

Keywords: Gold nanoparticles, iron oxide nanoparticles, composite, multifunctional nanoparticles, TEM.

Plasma Chemical Vapor Deposition Method to Prepare Nano TiO₂ Thin Films

Kyo-Seon Kim and Nguyen Hoang Hai

Department of Chemical Engineering, Kangwon National University, Chuncheon, Kangwon-Do, 200-701 Korea

Principal Contact: Kyo-Seon Kim, Professor, Department of Chemical Engineering, Kangwon National University, Chuncheon, Kangwon-Do, 200-701, Korea.

Tel: +82 33 250 6334 Fax +82 33 251 3658 Email: kkyoseon@kangwon.ac.kr

Abstract

Plasma Chemical Vapor Deposition (PCVD) is an important technique for surface modification by deposition of thin films on substrate. Nano TiO₂ thin films are grown on substrate using an rf PCVD process for different substrate temperatures. The powered electrode was designed to have many perforations so that the precursor gas can pass through the electrode and the gas flow pattern inside the PCVD reactor was controlled to be uniform. The substrate was placed on the ground electrode. Titanium tetra-isopropoxide was supplied as the precursor of TiO₂ and the pure N₂ or mixture of N₂ and O₂ was used as the plasma gas. In this study, we controlled the substrate temperature, residence time and reaction time and we analyzed the effects of those process variables on morphologies of TiO₂ thin film. The prepared samples were mainly characterized by X-ray diffraction, SEM, EDS and ultraviolet-visible spectroscopy.

Keywords: Plasma chemical vapor deposition, nano TiO₂ thin film, uniform flow inside plasma reactor, morphologies of TiO₂ thin film

Modeling Study of Aerosol Indirect Effects on Climate with an AGCM-aerosol Coupled System

Zhili Wang¹, Hua Zhang², Zaizhi Wang², Xiaoye Zhang¹ and Sunling Gong¹

1 Chinese Academy of Meteorological Sciences, No. 46 Zhongguancun Nandajie Haidian District, Beijing, China, 100081

2 National Climate Center, China Meteorological Administration, No. 46 Zhongguancun Nandajie Haidian District, Beijing, China, 100081

ABSTRACT

Aerosol indirect effects (AIEs) on global climate are quantitatively investigated by introducing aerosol–cloud interaction parameterizations for stratus clouds into an AGCM (BCC_AGCM2.0.1) developed by the National Climate Center of the China Meteorological Administration coupling with the Canadian Aerosol Module (CAM). The study yields a global annual mean of -1.57 W m^{-2} for the first indirect radiative forcing. The second indirect effect leads to global annual mean changes in net shortwave flux of -0.58 W m^{-2} at the top of the atmosphere (TOA). The total AIE reduces the global annual means of net shortwave flux at the TOA and of surface temperature by 2.27 W m^{-2} and 0.12 K , respectively. Change in surface temperature induced by the total AIE is clearly larger in the Northern Hemisphere (-0.21 K) than in the Southern Hemisphere, where changes are negligible. The interhemispheric asymmetry in surface cooling results in significant differences in changes of the interhemispheric annual mean precipitation rate, which could lead to a tendency for the ITCZ to weaken and broaden. In summer, the northeasterly or northerly flows in most areas of east and south China and over the nearby oceans are enhanced due to the total AIE, which weakens the transport of warm and moist air carried by the East Asian summer monsoon, and decreases the summer monsoon precipitation in east and south China.

KEYWORDS

aerosol, cloud, radiation, indirect effects

Introduction

Cloud, aerosol, and radiation interactions are among the greatest uncertainties in the study of climate change and climate simulation. Aerosol particles can change cloud microphysical properties by acting as cloud condensation nuclei or ice nuclei and thereby alter the radiation balance of the earth–atmosphere system and the cloud lifetime. These effects are called aerosol indirect effects (Forster et al., 2007). When liquid water content is stable in cloud, an increase in

aerosol particles can increase the cloud droplet number and decrease the cloud droplet effective radius, leading to an increase in cloud albedo. This is referred to as the first indirect effect (Twomey, 1977; Ramaswamy et al., 2001). On the other hand, reduction of the cloud droplet effective radius caused by an increase in aerosol particles can weaken the precipitation efficiency of the cloud and increase the cloud lifetime or liquid water content. This is referred to as the second indirect effect (Albrecht, 1989; Lohmann and Feichter, 2005).

Observational studies have enhanced understanding of aerosol indirect effects on regional and global climate. For example, L'Ecuyer et al. (2009) founded that aerosols could suppress the formation of precipitation in polluted regions. With the use of measurements from CALIPSO, MODIS and PARASOL, Costantino and Bréon (2010) showed that aerosols had a strong impact on the cloud microphysics and the Twomey effect was clearly detectable when cloud and aerosol were well mixed. AGCMs are also useful and important tools in the study of AIEs on global climate (e.g., Menon et al., 2002; Kristjansson et al., 2005; Ming and Ramaswamy, 2008). The IPCC (2007) summarized the results from different models and found that the first indirect effect of anthropogenic aerosols led to radiative forcing from -0.22 to -1.85 W m^{-2} at the top of the atmosphere (TOA), and the second indirect effect led to radiative flux changes from -0.3 to -1.4 W m^{-2} at the TOA (Forster et al., 2007). However, many uncertainties remain in the study of AIEs on climate, and further investigation of these effects is thus worthwhile.

The goal of the current study is to provide a more attentive assessment of AIEs on global climate by using a recent version of an AGCM (BCC_AGCM2.0.1) developed by the National Climate Center (NCC) of the China Meteorological Administration (CMA) coupling with the Canadian Aerosol Module (CAM). Five aerosol species were taken into account, including sulfate, BC, OC, soil dust, and sea salt. Please refer to Wang et al. (2010) and Zhang et al. (2010) about the description of the models in detail.

Experimental Methods

The parameterization of aerosol indirect effects is presented by Wang et al. (2010). To evaluate various AIEs on climate, four experiments are conducted. Experiment CONT is a control test that did not consider any AIEs. To study the first indirect effect, experiment FAIE only includes the effect of aerosol on the cloud droplet effective radius. To study the second indirect effect, experiment SAIE only includes the effect of aerosol on the precipitation efficiency. Finally, experiment TAIE includes both of the above effects to study the total AIE. In each experiment, we run the model for 11 years, with the first year as the spin-up time. The results for the last 10 years are averaged and analyzed for this study.

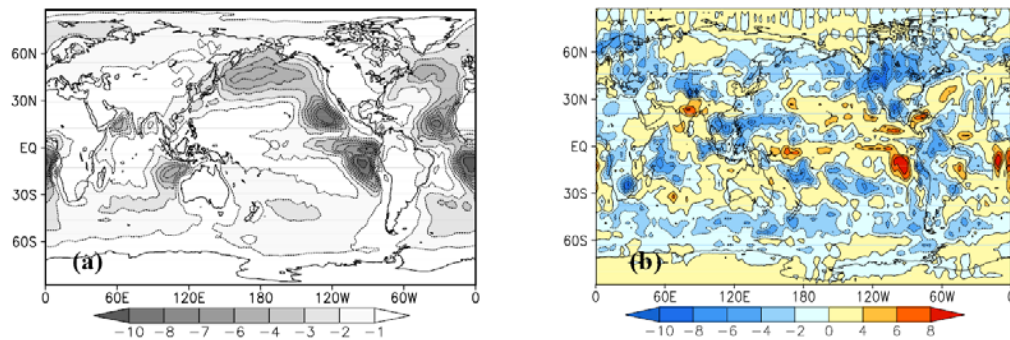
Results and Discussion

- *The first IRF and shortwave flux changes due to the second indirect effect*

Figure 1(a) shows the annual mean distribution of the first IRF at the TOA. The simulated results show significantly higher absolute values of the first IRF over ocean than over land, with the opposite pattern found for the aerosol concentration. The four negative radiative forcing centers are located over the North Pacific Ocean, North Atlantic Ocean, and west coasts of the Americas and Africa, with minimum values of -10 W m^{-2} . This result can be explained as follows.

Long-range transport of aerosols significantly increases cloud droplet numbers over oceans near aerosol sources; stratus easily forms over these oceans and is readily affected by the aerosols. Here, the global annual mean of the first IRF is estimated to be -1.57 W m^{-2} . Figure 1(b) presents the net shortwave flux changes due to the second indirect effect at the TOA. Although the net shortwave flux changes could be positive or negative, most are negative, with centers over the northern Indian Ocean, western Pacific Ocean, and the regions between 30° and 60° of both Hemispheres. There are two positive centers over the eastern Pacific Ocean and eastern Atlantic Ocean because of the obvious decreasing in total cloud cover after climate response to the second indirect effect. The global annual mean of these changes is -0.58 W m^{-2} .

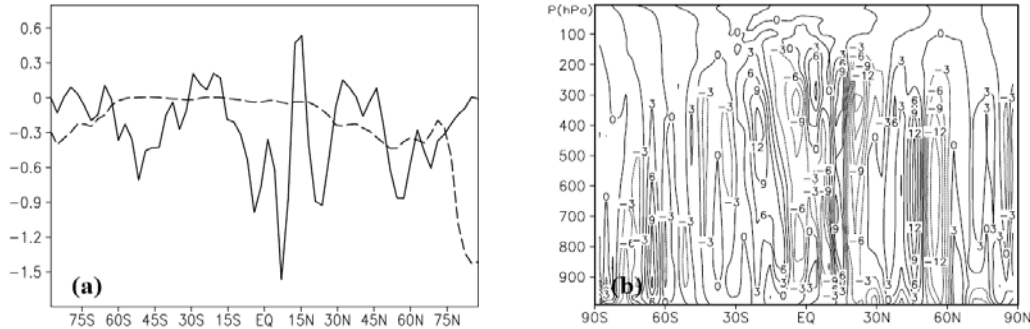
Figure 1. The annual mean distributions of (a) the first IRF and (b) the shortwave flux changes due to the second indirect effect at the TOA (unit: W m^{-2}).



● *Effect on global climate due to AIE*

The total AIE reduces the global annual means of net shortwave flux at the TOA and of surface temperature by 2.27 W m^{-2} and 0.12 K , respectively. Change in surface temperature induced by the total AIE is clearly larger in the Northern Hemisphere (-0.21 K) than in the Southern Hemisphere, where changes are negligible. Temperature decreases are mainly found in mid to high latitudes of the Northern Hemisphere, especially in the Arctic regions, where annual mean temperature drops by approximately 2 K (Fig. 2a). The interhemispheric asymmetry in surface cooling results in significant differences in changes of the interhemispheric annual mean precipitation rate, which could lead to a tendency for the ITCZ to weaken and broaden (Fig. 2).

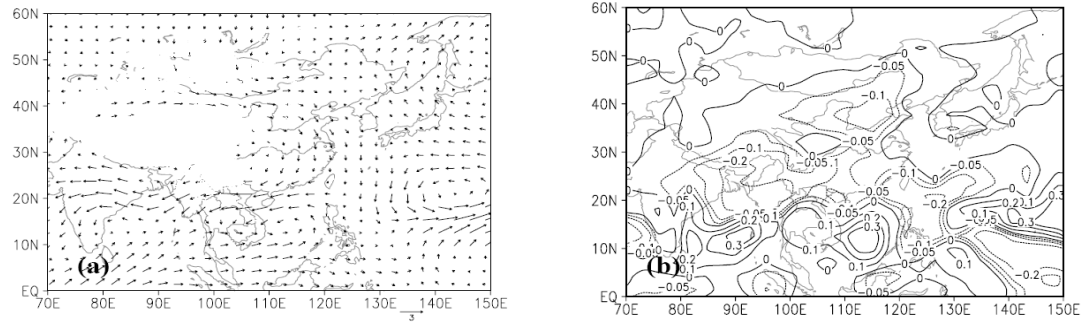
Figure 2. Annual zonal mean changes of (a) precipitation rate (unit: 10^{-1}mm d^{-1}) (solid line) and surface temperature (unit: K) (dashed line) and (b) vertical velocity (unit: $-10^{-2}\text{ hPa s}^{-1}$) due to total AIE.



- ***Effect on East Asian summer monsoon due to AIE***

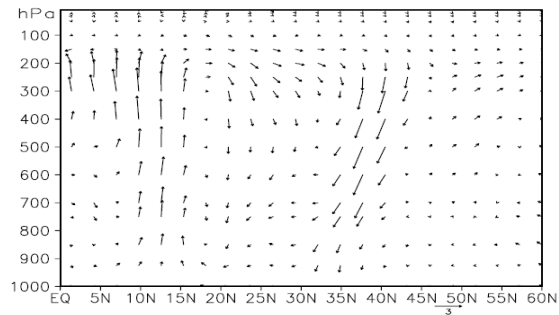
In summer, the northeasterly or northerly flows in most areas of east and south China and over the nearby oceans at 850 hPa are enhanced due to the total AIE (Fig. 3a), which weakens the transport of warm and moist air carried by the East Asian summer monsoon, and decreases the summer monsoon precipitation in east and south China (Fig. 3b).

Figure 3. Summer mean changes of (a) wind field at 850 hPa and (b) precipitation (unit: mm d^{-1}) due to total AIE.



The local meridional circulation is also affected due to AIE, and a clockwise rotation appears between 10°N and 40°N . The increased subsidence between 15°N and 40°N strengthens the southward motion in lower troposphere, which weakens the northward transport of warm and moist air carried by the East Asian summer monsoon, and moreover decreases the summer monsoon precipitation in south and east China (Fig. 4).

Figure 4. The changes of summer mean vertical meridional circulation zonally averaged between 105°E and 120°E due to total AIE.



CONCLUSION

Aerosol indirect effects on global climate are investigated by introducing aerosol–cloud interaction parameterizations for stratus clouds into the BCC_AGCM2.0.1 coupling with the CAM. The simulated global annual mean first indirect radiative forcing is -1.57 W m^{-2} at the TOA. The second indirect effect leads to global annual mean changes in net shortwave flux of -0.58 W m^{-2} at the TOA. The total AIE reduces the global annual means of net shortwave flux at the TOA and of surface temperature by 2.27 W m^{-2} and 0.12 K , respectively, which could lead to a tendency for the ITCZ to weaken and broaden. In summer, the northeasterly or northerly flows in most areas of east and south China and over the nearby oceans are enhanced due to the total AIE, which weakens the transport of warm and moist air carried by the East Asian summer monsoon, and decreases the summer monsoon precipitation in east and south China.

ACKNOWLEDGMENTS

This work is financially supported by National Basic Research Program of China (Grants No. 2011CB403405 and 2006CB403707), the Public Meteorology Special Foundation of MOST (Grant No. GYHY200906020), and the National Key Technology R & D Program (Grant No. 2007BAC03A01&2008BAC40B02).

REFERENCES

- [1] Albrecht, B. Aerosols, cloud microphysics, and fractional cloudiness, *Science*, 1989, 245, 1227-1230.
- [2] Costantino, L.; Bréon, F.M. Analysis of aerosol - cloud interaction from multisensor satellite observations, *Geophys. Res. Lett.*, 2010, 37, L11801, doi:10.1029/2009GL041828.
- [3] Forster, P.; Coauthors. Changes in Atmospheric Constituents and in Radiative Forcing. *Climate Change 2007: The Physical Science Basis. Contribution of Working Group I to the*

Fourth Assessment Report of the Intergovernmental Panel on Climate Change; Solomon et al., Ed.; Cambridge University Press, 2007, 131-217.

- [4] Kristjansson, J.E.; Iversen, T.; Kirkevag, A.; Seland, Ø.; Debernard, J. Response of the climate system to aerosol direct and indirect forcing: Role of cloud feedbacks, *J. Geophys. Res.*, 2005, 110, D24206, doi:10.1029/2005JD006299.
- [5] L'Ecuyer, T.S.; Berg, W.; Haynes, J.; Lebsack, M.; Takemura, T. Global observations of aerosol impacts on precipitation occurrence in warm maritime clouds, *J. Geophys. Res.*, 2009, 114, D09211, doi:10.1029/2008JD011273.
- [6] Lohmann, U.; Feichter, J. Global indirect aerosol effects: A review, *Atmospheric Chemistry and Physics Discussions*, 2005, 5, 715-737.
- [7] Menon, S.; Genio, A.D.D.; Koch, d.; Tselioudis, G. GCM Simulations of the Aerosol Indirect Effect: Sensitivity to Cloud Parameterization and Aerosol Burden, *Journal of Aerosol Science*, 2002, 33, 692-713.
- [8] Ming, Y.; Ramaswamy, V. Nonlinear climate and hydrological responses to aerosol effects, *J. climate*, 2008, 22, 1329-1339.
- [9] Ramaswamy, V.; Coauthors. Radiative forcing of climate change. In: *Climate Change 2001: The Scientific Basis. Contribution of Working Group I to the Third Assessment Report of the Intergovernmental Panel on Climate Change*, Houghton et al., Ed.; Cambridge University Press, 2001, 349-416.
- [10] Twomey, S.A. The influence of pollution on the shortwave albedo of clouds. *J. Atmos. Sci.*, 1977, 34, 1149-1152.
- [11] Wang, Z.L.; Zhang, H.; Shen, X.S.; Gong, S.L.; Zhang, X.Y. Modeling study of aerosol indirect effects on global climate with an AGCM. *Adv. Atmos. Sci.*, 2010, 27(5), 1064-1077.
- [12] Zhang, Hua; Zhili Wang; ZaiZhi Wang; Coauthors. Simulation of direct radiative forcing of typical aerosols and their effects on global climate using an online AGCM-aerosol coupled model system, Submitted to *Climate Dynamic*, 2010.

Numerical Studies of Slip Correction in Low-pressure Impactor

Junho Hyun¹, Yunhaeng Joe² and Jungho Hwang^{1,2}

1 Department of Clean Technology, Yonsei University, 134 Shinchon-dong, Seodaemun-gu, Seoul, 120-749, Korea

2 Department of Mechanical Engineering, Yonsei University, 134 Shinchon-dong, Seodaemun-gu, Seoul, 120-749, Korea

ABSTRACT

This study investigated the characteristics of low-pressure impactors by the numerical solution of the Navier-Stokes equations and of the equation of motion of particles. Designing impactor required many variables such as jet velocity, nozzle-to-plate distance and Stokes number. Cunningham slip correction factor was one of variables and affected other variables but it neglected in most cases. Initially we designed low-pressure impactors which having 100nm as cut-off diameter not considering slip correction factor and solved using FLUENT. The cut-off diameter was changed from 292nm to 92 nm when we put slip correction factor to calculation of particle motion. And the cut-off diameter changed gradually when pressure ratio (P/P_0) was changed from 0.1 to 0.9.

KEYWORDS

Low-pressure impactor, Numerical simulation, Particle tracking

BODY (INTRODUCTION, EXPERIMENTAL METHODS, RESULTS and DISCUSSION)

Introduction

Inertial impactors are common tools for the collection and classification of aerosol particles. Traditional impactors offer poor size resolution for submicron particles; typically their finest size cut is around $0.4\mu\text{m}$. To obtain smaller cutpoints, two types of impactors have been developed, namely microorifice impactors and low-pressure impactors. Low-pressure impactors are commonly used in sampling and determining the size distribution.

Designing the impactors was developed based on the numerical analysis of the Navier-Stokes

equations to obtain the flow field and the subsequent numerical integration of particle equations of motion to obtain the particle trajectories and collection efficiency curve. The cut-off diameter, which is the most important variable, is usually described by Stk , the Stokes number, which was defined by

$$Stk = \frac{\tau U}{W/2} = \frac{\rho_p d_p^2 U C_c}{9 \mu W} \quad (\text{Eq. 1})$$

In above equation, τ is the particle relaxation time, and U is the flow velocity, W is the nozzle diameter, μ is the dynamic viscosity of air, and C_c is the slip correction factor. Abouali et al.^[1] studied cut-off characteristics of supersonic/hypersonic impactors using numerical simulations. The result showed that in the range of $0.5 < L/W < 0.3\sqrt{P_0/P_b}$, with nozzle to plate distance L , the flow field properties at the impactor does not depend on the pressure ratio. Flagan^[2] showed that the critical Stokes number is still constant in terms of the flow properties corresponding to the stagnation conditions on the impactor plate, which need to be determined by theory or experiment. But Leduc et al.^[3] showed that the simulation result of submicron impactor stages were different to experimental result. The conclusion from Aboulali could not applied in Leduc's case.

We studied the design of the low-pressure impactors which having 100nm as cut-off diameter and solved its flow field and particle trajectories and we focused on the pressure ratio and other variables which depends on pressure ratio that expected to give the difference result.

Experimental Methods

The studied impactor was a one-stage impactor. The jet diameter of the nozzle was 0.5mm. Jet length was 2mm and jet to plate distance was 0.8mm then ratio of distance and jet diameter was 1.6. The flow entered with a pressure of 1 atm and temperature of 293K. We expected the cut-off diameter was 100nm.

A numerical evaluation was carried out to understand the flow field and behavior of particles. The flow field can be obtained by solving the following mass and momentum conservation equations.

$$\frac{\partial \rho}{\partial t} + \nabla \cdot (\rho \vec{u}) = 0 \quad (\text{Eq. 2})$$

$$\rho \frac{\partial \vec{u}}{\partial t} + \rho (\vec{u} \cdot \nabla) \vec{u} = -\nabla p + \mu \nabla^2 \vec{u} \quad (\text{Eq. 3})$$

where ρ is the density of air, μ is the viscosity of air.

For calculation of particle trajectories, the particle equations of the motion were solved after obtaining the flow field.

$$\frac{d\dot{u}_p}{dt} = \frac{18\mu}{\rho_p d_p^2} \frac{C_c Re}{24} (\dot{u} - \dot{u}_p) + \frac{g(\rho_p - \rho)}{\rho_p}. \quad (\text{Eq. 4})$$

In above equation, Re is the particle Reynolds number, subscript p means the particle properties, C_c is the slip correction factor defined by

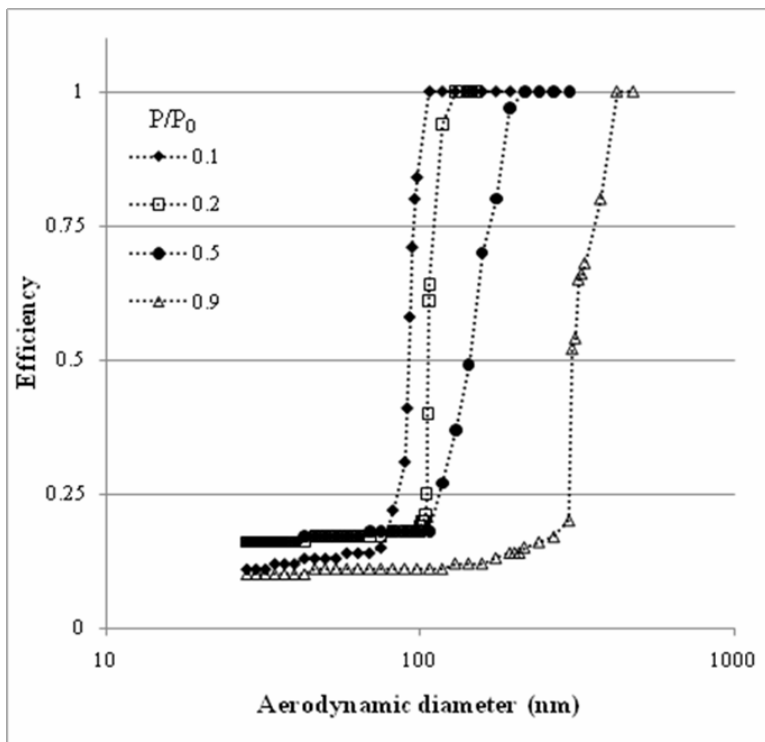
$$C_c = 1 + \left[\frac{15.6 + 7 \exp(-0.059 d_p p)}{d_p p} \right]. \quad [\text{Eq. 5}]$$

For turbulent flows, simulations were performed with $k-\varepsilon$ model and axi-symmetric flow was assumed.

Results and Discussion

We changed the output pressure from 0.1 to 0.9 atm. Ratio of nozzle-to-plate distances to nozzle diameter is 1.6 and this value exceeded the range from Abouali et al. The cut-off diameter when the output pressure was 0.9 atm was 292 nm, which was similar to the result of Leduc. And the cut-off diameters when the output pressure was 0.1 and 0.2 atm were 92nm and 106nm, respectively, which was very close to designed cut-off diameter.

Figure 1. Collection efficiencies from simulation



CONCLUSION

The result showed that the pressure ratio did affect on the particle trajectories and collection efficiencies. Most papers gave no attention to slip correction factor and considered as constant but it was deeply depended on the pressure ratio. The variables to determine the cut-off diameter are much more and this study had fixed other variables and one specific previous research. If the pressure range had applied to other studies, it would give more general result for relation between pressure ratio and cut-off diameter.

ACKNOWLEDGMENTS

This work is supported by Korea Environmental Industry and Technology Institute (KEITI) funded by the Ministry of Environment as "Next-Generation Eco Innovation project."

REFERENCES

- [1] Abouali, O.; Saadabadi, S.; Emdad, H. *J. Aero. Sci.*, 2011, **42**, 65-77.
- [2] Flagan, R.E. *J. Colloid Interface Science*, 1982, **87**, 291-299.
- [3] Leduc, S.; Fredriksson, C.; Hermansson, R. *Advanced Powder Technol.*, 2006, **17**, 99-111
- [4] Hinds, W. *Aerosol Technology: Properties, Behavior, and Measurement of Airborne Particles*, 2nd edition, Wiley-Interscience, 1999

Performance Test of a Two-staged Impactor for Morphology Analysis of Diesel Exhaust Particles

Sang-Gu Lee¹, Junho Hyun¹and Jungho Hwang^{1,2}

¹ Department of Clean Technology, Yonsei University, 134 Shinchon-dong, Seodaemun-gu, Seoul, 120-749, Korea

² Department of Mechanical Engineering, Yonsei University, 134 Shinchon-dong, Seodaemun-gu, Seoul, 120-749, Korea

Principal Contact: Sang-Gu Lee, Ph.D candidate, Department of Clean Technology, Yonsei University, 134 Shinchon-dong, Seodaemun-gu, Seoul, 120-749, Korea, 82-2-2123-2821, 82-2-312-2821, oh239@yonsei.ac.kr

ABSTRACT

This study describes a serial method to estimate the effective density and fractal dimension of particles, especially diesel exhaust particles. Physical and morphological parameters such as fractal dimension, effective density, bulk density and dynamic shape factor were derived or at least approximated from simultaneous measurements of electrical mobility diameter and aerodynamic diameter. For this purpose, we designed an impactor and evaluated its performance using an aerosol electrometer. Then, diesel exhaust particles from a Common-rail DI engine were measured with the impactor and a differential mobility analyzer (DMA). We determined the effective density and also estimated the fractal dimension of diesel exhaust particles from these data.

KEYWORDS

Low-pressure impactor, Effective density, Fractal dimension

Introduction

Density is an important property of aerosol particles. For example, density is required to determine the relationship between Stokes and aerodynamic diameters and to convert measured number distributions to mass distributions. The particle effective density is a lump parameter which describes the combined effects of particle density and shape on aerosol motion.

Experimental Methods

Our impactor was designed based on the procedure described by Hillamo and Kauppinen (1991). Table 1 summarizes the design specification of the stages.

Table 1. Specification of each stage of impactor

Stage	Cut-off diameter(nm)	Nozzle diameter(mm)	Inlet pressure(atm)	Stk ^{1/2}
1	96	0.5	1	0.49
2	96	0.5	0.43	0.49

To calculate the effective density, the following equation is needed (Maricq et al., 2000),

$$\rho_{eff} = \rho_0 \frac{d_a^2 C_a}{d_m^2 C_m}, \quad (\text{Eq.1})$$

where d_a and d_m are the aerodynamic diameter and mobility diameter, respectively, C_a and C_m the slip correction factors for the aerodynamic diameter and mobility diameter, respectively. ρ_0 is the unit density ($=1 \text{ g/cm}^3$). ρ_{eff} is the effective density which is also expressed by Eq. (2) (Kelly and McMurry, 1992),

$$\rho_{eff} = \rho_p \left[\frac{d_{ve}}{d_m} \right]^3, \quad (\text{Eq.2})$$

where ρ_p is the bulk density of a particle, d_{ve} is the volume equivalent diameter.

In this study, the mobility diameter and the aerodynamic diameter were obtained from measurements with a DMA and an impactor, respectively. Then the effective density was calculated from Eq. (1). With this calculated effective density, we estimated the volume equivalent diameter from Eq. (2), and then the shape factor was calculated from Eq. (3),

$$\chi = \left[\frac{C_{ve}}{C_m} \right] \left[\frac{\rho_p}{\rho_{eff}} \right]^{1/3}, \quad (\text{Eq.3})$$

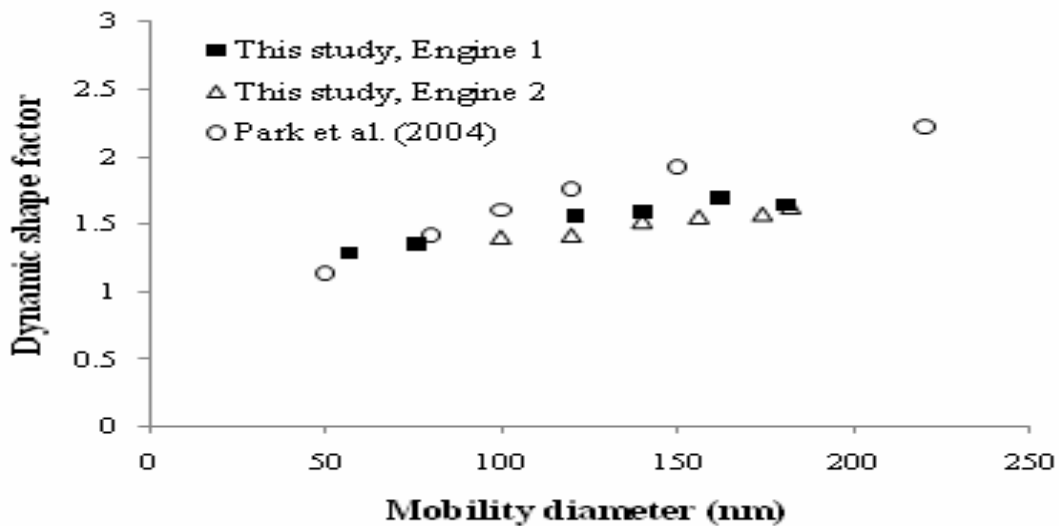
where χ is the dynamic shape factor and C_{ve} is the slip correction factor for the volume equivalent diameter of particle. For non-spherical particles, the drag and hence the measured dynamic equivalent diameters depend on particle orientation. In general, the orientation-averaged χ is larger than unity ($\chi = 1$ for spheres).

Two diesel engines were tested in this study. Engine 1 was a 1-cylinder common-rail direct injection (CRDI) diesel engine and was run at idling mode of 1500RPM with load of 6 bar. Engine 2 was a 4-cylinder single overhead camshaft (SOHC) diesel engine on Sportage (Kia Moters, Korea). The engine 2 was at idling mode of 1500RPM with no load.

Results and Discussion

We calculated Eq. (2) with effective density which was obtained from Eq. (1) then we need to assume a bulk density of diesel exhaust particles. We assumed that a bulk density of diesel exhaust particles was very close to a carbon density. The bulk density of carbon refers to several studies. Fig. 7 shows the dynamic shape factor for engine 1 and 2. The dynamic shape factors increased from 1.28 to 1.64 for engine 1 and from 1.40 to 1.62 for engine 2, as the mobility diameter was increased from 50 to 180 nm. Park et al. (2004) studied the structural properties of diesel particles in the size range of 50 to 220nm with transmission electron microscopy (TEM) and obtained the dynamic shape factors from 1.11 to 2.21.

Fig. 1. Dynamic shape factor of diesel exhaust particles



SUMMARY OR CONCLUSION

We found that the effective density is a function of mobility diameter, and it relates to a fractal dimension. Dynamic shape factor can be estimated. The effective density decreases as the mobility diameter increases and dynamic shape factor increases as the mobility diameter increase

ACKNOWLEDGMENTS

This work is supported by Korea Environmental Industry and Technology Institute (KEITI) funded by the Ministry of Environment as "Next-Generation Eco Innovation project."

REFERENCES.

- [1] Hillamo, R. E. and Kauppinen, E. I. (1991), On the performance of the Berner low pressure impactor, *Aerosol Sci. Technol.*, 14, 33-47.
- [2] Maricq, M. M., Podsiadlik, D. H., and Chase, R. E. (2000), Size distribution of motor vehicle exhaust PM: A comparison between ELPI and SMPS measurement, *Aerosol Sci. Technol.*, 33, 239-260
- [2] Kelly, W. P. and McMurry, P. H. (1992), Measurement of particle density by inertial classification of Differential Mobility Analyzer-generated monodisperse aerosols, *Aerosol Sci. Technol.*, 17, 199 - 212
- [2] Park, K., Kittelson, D., and McMurry, P., (2004), Structural properties of diesel exhaust particles measured by Transmission Electron Microscopy (TEM): Relationships to particle mass and mobility, *Aerosol Sci. Technol.*, 38, 881-889.

Preparation of PCBM Micro- and Nanoparticles via Electrohydodynamic Spray Route for Organic Photovoltaic Applications

Sung-Eun Park, Ji-woon Park, Sang-Yoon Kim and Jungho Hwang

Department of Mechanical Engineering, Yonsei University, Seoul, 120-749, Korea

ABSTRACT

Recently, organic electronic devices have been focused for its characteristic advantages, such as low process cost, flexibility, large process area and mass productivity. In this paper, we propose fabrication method of micro- and nanoaprticles which consists thin film via electrohydrodynamic spray route. 1-(3-methoxycarbonyl)-propyl-1-phenyl-(6,6)C₆₁ (PCBM), often used as an electron acceptor, was dissolved in organic solvent, dichloromethane, and sprayed. The monodisperse particles were collected when the stable cone-jet mode was realized; however, the size of PCBM particles was coarse and ranged in several micro meters. The efforts to decrease the size of generated particles were conducted with controlling the experimental conditions, such as liquid flow rate, sampling distance, and solid fraction of solution. The final particle size was ranged in order of 100 nano meters.

KEYWORDS

Electrohydrodynamic atomization, Organic photovoltaics, PCBM nanoparticles and microparticle

Introduction

Organic electronic devices based on solution process of polymer materials are of increasing interest as one of the most promising applications in printed electronics area [1-3]. Organic electronic devices are expected to be lighter, more flexible, low process temperature, and less expensive than traditional silicon-based devices whereas traditional devices are fabricated with the use of several steps of fabrication process, masks and liquids for etching. The most well-known solution process is spin coating. Although the spin coating process was considered to be reliable and applied to the many cases of lab-scale organic electronic devices, it is discontinuous batch process and not scalable to roll-to-roll(R2R) production. Moreover, the processing areas of spin coating process at once is limited to small areas and considerable mass of material is consumed as waste. Therefore, alternative solution processes, containing spray deposition, inkjet

and screen printing, and doctor blading, has been focused for large area and low cost fabrication. Recently, the spray deposition technology used in various applications such as surface coating, painting, humidification, combustion, is focused for its advantages of simplicity, large process area availability, low cost and energy consumption^[4-6].

Electrohydrodynamic (EHD) spray process can substitute the airbrush spray process to fabricate the layer of organic polymer. EHD spray, also referred to as electrospray, is the most novel approach to generate fine particles of which size ranges from micro to nanoscales. Relatively monodisperse solute particles with a narrow size distribution can be produced from polymer solutions. Hogan et al.^[7] demonstrated that water soluble and water insoluble, low dispersity polymer particles could be readily prepared by EHD with geometric mean diameters in the 0.35–2.71 μm size range. Yao et al.^[8] introduced fabrication of 1 μm sized polymeric particles in a modified EHD system. They used organic liquid polylactide co-glycolicacid(PLGA) and suggested an empirical equation for the droplet size.

In this paper, we produced mono-dispersed 1-(3-methoxycarbonyl)-propyl-1-phenyl-(6,6)C₆₁ (PCBM) micro- and nanoparticles from PCBM solution dissolved in dichloromethane(DCM) using EHD spray deposition techniques. The size and morphology of PCBM particles in this study was observed with SEM image. The solution concentration, flow rate, and collecting distance between nozzle and substrate were varied. The major findings from this study, support that the nanoparticles fabrication from the liquid solution with low conducting DCM solvent is quite difficult as described by Smith^[9]

Experimental Methods

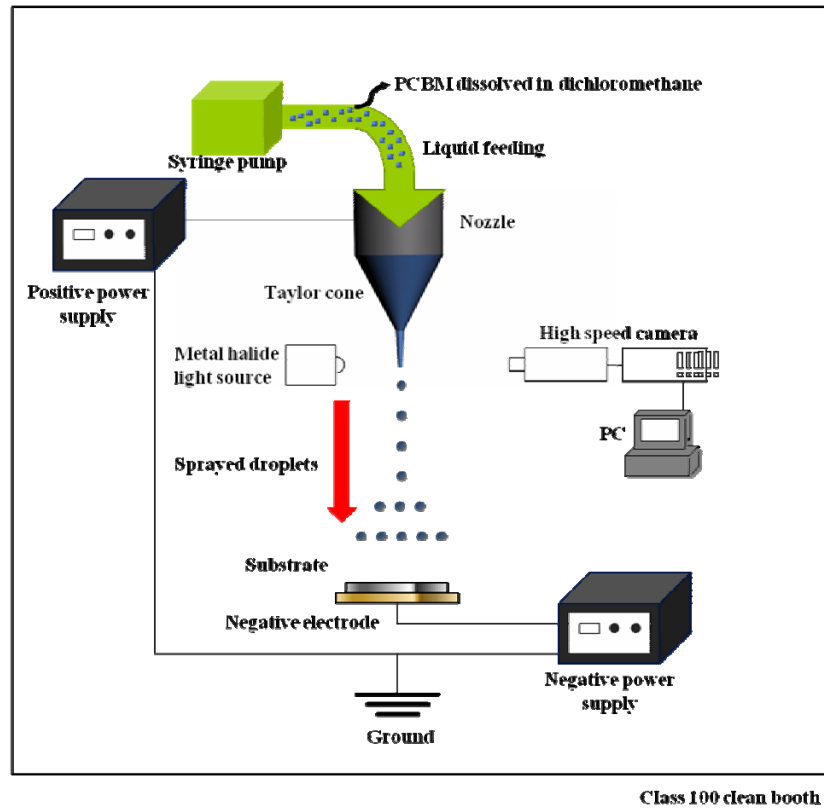
In the present experiments, a fine spray of droplets in the approximate diameter range of 20-50 μm were generated electrohydrodynamically by supplying PCBM solution at a fixed mass flow rate (1-10 $\mu\text{L}/\text{min}$) from a capillary nozzle. For the fabrication of PCBM micro- and nanoparticles, PCBM with various contents (0.012-1.2 g) (purchased from Nano C) was dissolved in 100 ml of dichloromethane. The dichloromethane was purchased from Sigma-Aldrich Co. was used for the EHD carrier liquid. The particle generation and the size distribution of generated particles via electrohydrodynamic route are dominated by some physical properties, such as viscosity, surface tension, electrical conductivity, and dielectric constant. The viscosity was measured using a viscometer (SV-10, A&D Co., Ltd.) and the surface tension was measured using a surface tensiometer (Manual model 20, Fischer Scientific.). The dielectric constant measurement was conducted using Rufuto dielectric constant meter (Model 871, Nihon Rufuto Co., Ltd.). Also, the electric conductivity measurement was tried using a benchtop conductivity meter with Pyrex electrode (YSI-3200, YSI Inc.) whose minimum resolution was down to 0.1 nS/m. However, although this instrument was the most precisely measurable conductivity meter, could be tested, the electric conductivity of the PCBM-DCM solution was lower than the

minimum measurable limit. The electric conductivity of solution was assumed to be similar with that of bulk DCM solvent from handbook^[10]. The physical properties of PCBM solution are shown in Table 1.

Physical properties	
Density	1270 kg/m ³
Viscosity	0.85 mPa·s
Surface tension	28.1 mN/m
Dielectric constant	9.1
Electric conductivity	4.3 * 10 ⁻⁹ S/m ^[10]

The experimental setup shown in Fig. 1 consisted of a liquid supply system, an electrical system, a visualization system, and a collecting substrate. The liquid supply system included a syringe pump (Model 200, KD Scientific Inc.) and a stainless steel syringe nozzle (inner diameter: 150 µm, outer diameter: 320 µm). The electrical system consisted of two high voltage power supply units (DC +15 kV and -15 kV) with two electrodes. One electrode from the power supply units is high voltage electrode and another is just a ground earth. In this system, the syringe nozzle used for the liquid supply system was also used as the anode and substrate copper plate, below the nozzle, was used as the ground electrode. However, there were considerable losses in collecting the PCBM particles when the collecting distance was far away. This is caused by the electric field disturbance with substantial experimental instruments such as a syringe pump. The detailed appearance of jetting mode was captured using a high speed camera (Motion Pro HS-4, Redlake Inc.), which is capable of capturing 5130 frames per second when the image size was fixed at a 512 pixel resolution. The exposure time for each image was fixed to less than 10 µs to minimize the illusionary problems. To minimize the penetration of impurity aerosol particles in ambient air into the experimental setup, all experiments were conducted in a class 100 (above 0.5 µm) clean room, repeated three times and the results of measurements were averaged.

Figure 1. Experimental set-up



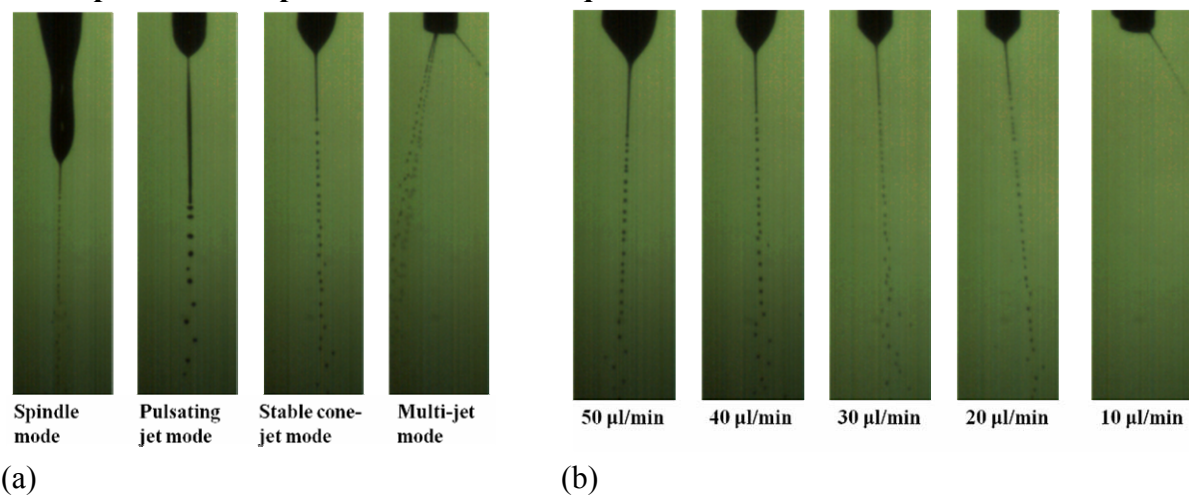
Results and Discussion

The high speed camera still image with various EHD jetting mode was shown in Fig. 2 (a). With changing the applied potential and liquid flow rate, detailed appearance of development of jetting mode can be observed at a frame rate of 20000 fps and exposure time of 5 μ s. The solution droplet was emitted by the syringe pump with simple dripping mode below 4.7 kV of applied voltage. The typical developing was observed: spindle mode, pulsating jet mode, stable cone-jet mode, and multi-jet mode. It is well known that the size and charge of electrohydrodynamic spray process depend on liquid flow rate and physical properties of solution such as electrical conductivity, dielectric constant, surface tension, and viscosity. Fernandez de la Mora and Loscertales [11] suggested scaling law which describes the correlation of the size of primary droplet and physical properties based on their experimental data, which agrees well with subsequent experimental results [12, 13].

$$d_d = G(\varepsilon) \left(\frac{\varepsilon \varepsilon_0 Q}{K} \right)^{1/3} \quad G(\varepsilon) = -10.9 \varepsilon^{-6/5} + 4.08 \varepsilon^{-1/3} \quad (\text{Eq.1})$$

where d_d is droplet diameter, ε is dielectric constant, ε_0 is the permittivity of vacuum, Q is the liquid flow rate, and K is the liquid electric conductivity. However, their scaling law was derived from the experimental data with relatively highly conducting liquids than the DCM. As shown in Fig. 2 (b), all the cone-jet disintegrated into the droplets with varicose break-up mode, which is known to be occurred with low conducting liquids^[14]. In 1955, Drozin^[15] concluded that it was impossible to electrohydrodynamically spray the low conducting liquids, such as xylol, toluene, benzene, without the use of an additive. However, the PCBM-DCM solution could be sprayed without

Figure 2. Shapes of (a) jetting mode developed with increased electric potential and (b) jet break-up into the droplets with increased liquid flow rate.



Scanning electron microscope image of EHD generated microparticles collected on substrate is shown in Fig. 3. Evaporation time was varied with three different collection distances. When the collection distance was as closed as 35 mm, 3-5 µm sized microparticles were collected and shown to be coalesced upon impaction onto the substrate plate, which resulted from insufficient evaporation of the dichloromethane solvent in the solution droplet as shown in Fig 3(c). However, dichloromethane is one of the most volatile organic solvent, with a boiling temperature of just 40°C. Therefore, when the pin-plate distance was increased by 65 mm, some particles were coalesced with each other and others were shown to be evaporated sufficiently as shown in Fig. 3(b). Figure 3(a) shows corresponding trends of the full evaporated microparticles collected at a distance of 100 mm.

However, the generated PCBM particles have average diameter of several micrometers, which is not significantly advanced results compared with traditional spray techniques. The electric conductivity of solution was increased when highly conducting ethanol (purchased from Dae-Jung Co.) was added to the precursor solution. As shown in Fig. 4, the size of generated PCBM

particles was observed to be dramatically decreased by about 100 nm.

Figure 3. EHD generated microparticles collected at a distance of (a) 100 mm, (b) 65 mm, and (c) 35 mm (PCBM concentration: 1.2 w/v%, flow rate: 10 μ l/min)

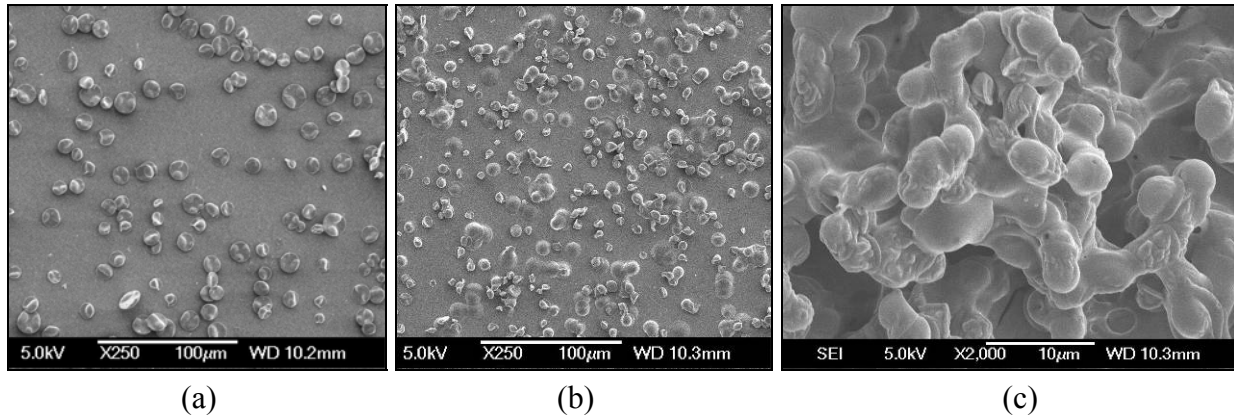
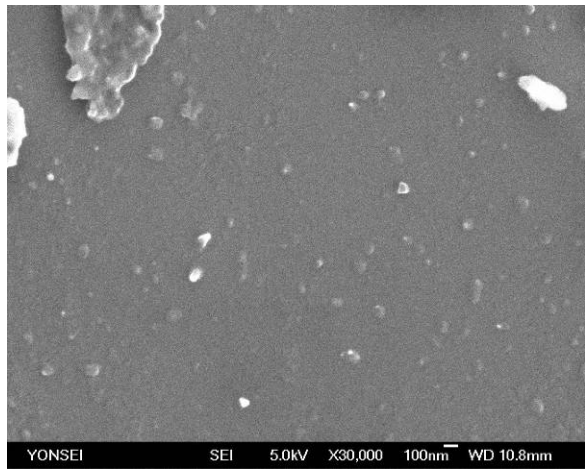


Figure 4. EHD generated nanoparticles (collecting distance: 65mm, PCBM concentration: 0.006 w/v%, flow rate: 1 μ l/min)



SUMMARY

It was demonstrated that electron acceptor material PCBM dissolved in organic solvent can be prepared via electrohydrodynamic route and expands the concept of spray deposition in organic electronics for its characteristic advantages. We generated micro- and nanoaprticles which consists thin film via electrohydrodynamic spray route. The monodisperse particles were collected when the stable cone-jet mode was realized; however, the collected 3-5 μ m sized microparticles were coalesced with short collection distance. size of PCBM particles was coarse and ranged in several micro meters. The efforts to decrease the size of generated particles were conducted with controlling the experimental conditions, such as liquid flow rate, sampling

distance, and solid fraction of solution. The final particle size was ranged in order of 100 nano meters.

ACKNOWLEDGMENTS

This study was supported by a R&D project from the Korea Energy Management Corp. (KEMCO; Grant 2008-N-PV08-P-06-0-000).

REFERENCES

- [1] Koo, H.S.; Chen, M.; Pan, P.C.; Chou, L.T.; Wu, F.M.; Chang, S.H.; Kawai, T. *Displays*, 2006, 27, 124-129.
- [2] Shimoda, T.; Morii, K.; Seki, S.; Kiguchi, H. *MRS Bulletin*, 2003, 28, 821-827.
- [3] Yoshioka, Y.; Jabbour, G.E. *Synthetic Met.* 2006, 156, 779-783.
- [4] Vak, D.; Kim, S. Jo, J.; Oh, S.; Na, S.; Kim, J.; Kim, D. *Appl. Phys. Lett.* 2007, 91, 081102.
- [5] Girotto, C.; Rand, B.P.; Genoe, J.; Heremans, P. *Sol. Energy Mat. Sol. C.* 2009, 93, 454-458.
- [6] Abdellah, A.; Fabel, B.; Lugli, P.; Scarpa, G. *Org. Electron.*, 2010, 11, 1031-1038.
- [7] Hogan, C.J.; Yun, K.M.; Chen, D.-R.; Lenggoro, I.W.; Biswas, P.; Okuyama, K. *Colloid. Surface. A*. 2007, 311, 67-76.
- [8] Yao, J.; Lim, L.K.; Xie, J.; Hua, J.; Wang, C.-H. *J. Aerosol Sci.*, 2008, 39, 987-1002.
- [9] Smith, D.P.H. *IEEE T. Ind. Appl.*, 1986, IA-22, 527-535.
- [10] *Handbook of Organic Solvent*; Smallwood, I.M.; John Wiley and Sons Inc., 1996.
- [11] Fernandez de la Mora, J.; Loscertales, I.G. *J. Fluid Mech.*, 1994, 260, 155-184.
- [12] Chen, D.R.; Pui, D.Y.H. *Aerosol Sci. Tech.*, 1997, 27, 367-380.
- [13] Rossel-Llompart, J.; Fernandez de la Mora, J. *J. Aerosol Sci.*, 1994, 25, 1093-1119.
- [14] Cloupeau, M.; Prunet-Foch, B. *J. Aerosol Sci.*, 1994, 25, 1021-1036.
- [15] Drozin, V.G. *J. Colloid Interf. Sci.*, 1955, 10, 158-164.
- .

Characteristic of Charged Particle at Ansan Atmosphere

Kang Ho Ahn¹ and Hong Ku Lee²

1 Department of Mechanical Engineering, Hanyang University, 1271 Sa-3dong, Ansan, Gyunggi- do 425-791, Republic of Korea

2 Department of Mechanical Engineering Graduate School, Hanyang University, 17Haengdang -dong, Seongdong-gu, Seoul133-791, Republic of Korea

Principal Contact: Kang Ho Ahn, Prof., Department of Mechanical Engineering, Hanyang University, 1271 Sa-3dong, Ansan, Gyunggi- do 425-791, Republic of Korea.

Tel: +82-31-417-0601 Fax: +82-31-436-8184 Email: khahn@hanyang.ac.kr.

Abstract

Several particle nucleation mechanisms including ion-induced, ternary, binary and kinetic nucleation had been proposed by many researchers, but the exact particle nucleation mechanism still remains unknown. These days, the probability particles are mostly neutral and its formation is activated by ion-cluster (Hoppel et al., 1994; Kulmala et al., 2000, 2006) are proposed. Actually many research have been carried to verify the relation between ion and particle nucleation using electrical characteristic. Usually, particles at atmosphere are charged by radioactive substance irradiated from GCR(Galactic Cosmic Ray) and generated by human activities. Seasonal air mass variation and change of Earth's axis of rotation also affect on the charging characteristic. In this study, we performed the atmosphere sampling for analyzing particle charging characteristic according on atmospheric conditions using already calibrated Aerosol Electrical Mobility Spectrum Analyzer(AEMSA).

From the result, we found that at Ansan atmosphere the number of each charged particle (Negativley or Positively) is generally equal, but the imbalance occurs at atmospheric events such as raining and lightening.

Acknowledgement

This project was supported by Korea Environmental Industry & Technology Institute as “The Eco-Innovation Project”

Keywords: Nano-particle, Nucleation, Charged particle, Atmosphere Sampling

Development and performance evaluation of Single Fiber MWCNT Generator

Kang-ho Ahn¹, Sun-man Kim¹, Gun-ho Lee¹, Ji-hyun Lee² and Il-je Yu²

1 Department of Mechanical Engineering, Hanyang University, Ansan, Republic of Korea

2 Toxicological Research Center, Hoseo University, Ansan, Republic of Korea

Principal Contact: Kang-ho Ahn, Prof., Dept. of Mechanical engineering, Hanyang University, 1271 Sa-3dong, Ansan, Gyunggi-do 426-761, Republic of Korea.

Tel: +82-31-417-0601 Email: khahn@hanyang.ac.kr

Abstract

In recent years, engineered nano-particles have been synthesized and mass produced because of their exceptional physical, chemical, optical, magnetic, and electrical properties compared to bulk material. The application areas of nano-materials are expanding widely from consumer goods to medical applications. Multi-walled carbon nano-tube(MWCNTs), which is one type of nano-material, is now in mass production because of its excellent mechanical and electrical properties. Some nano-tubes have already been used in medicine for cancer treatment

During the research, production and handling of MWCNTs, researchers and workers may be directly exposed to this material. Health effect of carbon nano-tubes (CNTs) have been studied by many researchers. One paper reported on the adverse effects on human pulmonary cells by MWCNTs. To verify the health effects of MWCNTs when inhaled, a good MWCNT generation technique or instrument is needed.

In this study, a MWCNT aerosolization method with MWCNTs dispersed in water without any surfactant is introduced. MWCNTs dispersed in water were aerosolized Collision type atomizer and the aerosolized MWCNT shape were monitored with scanning electron microscopy(SEM)

Acknowledgement

This research was supported by the Nano R&D program through the National Research Foundation of Korea funded by the Korean Ministry of Education, Science and Technology(2010-0019156).

Keywords: Multi-walled carbon nano-tube, Aerosol generation, Surfactant

The Measurement of Atmospheric Aerosol at Ansan, Korea

Ha-Gue Chung¹, Kang-Ho Ahn¹ and Young-Jun Yoon²

1 Department of Mechanical Engineering, Hanyang University, 1271, Sa 3-dong, Sangrok-gu, Ansan, Kyunggi-do, 426-791, KOREA, Rep. of

2 Korea Polar Research Institute, Get-pearl Tower, 12 Gaebeol-ro, Yeonsuu-gu, Incheon, 406-840, KOREA, Rep. of

Principal Contact: Kang Ho Ahn, Prof., Department of Mechanical Engineering, Hanyang University, 1271, Sa 3-dong, Sangrok-gu, Ansan, Kyunggi-do, 426-791, Korea, Rep. of

Tel: +82-31-417-0601 Fax: +82-31-436-8184 Email: khahn@hanyang.ac.kr

Abstract

These days, due to the increasing seriousness of environmental problem, there has been a tremendous interest in air pollution and atmospheric aerosols. To upper atmospheric aerosol, majority of research has been performed using aircraft. However, the measurement using aircraft is unable to measure vertical distribution of aerosol and has many restrictions as well.

In this study, we performed atmospheric aerosols measurement using already developed Mini-Condensation Particle Counter suitable to upper atmosphere. Developed Mini-CPC is smaller and lighter than commercial devices and able to maintain constant temperature on condensation and saturation section even below 15°C.

The measurements were performed from ground level to 1km in Hanyang University ERICA Campus at 2011.03.31 and 2011.05.03 twice. The package of measurement system consisted of Mini CPC, OPC, GPS, temperature/humidity sensor and was suspended from Helium Balloon with parachute. The altitude of Balloon was controlled by electrical winch.

At first measurement, we found that the number concentration of atmospheric aerosol generally decreases with altitude. And drastic decrease of number concentration is observed at about altitude 400m which is inversion layer. However, at second measurement, the drastic drop was not observed. It is shown that the high concentration of yellow sand transferred from China affected the absence of inversion layer.

Acknowledgement

This project was supported by Korea Polar Research Institute as “pe11010”

Keywords: Atmospheric aerosols, Balloon, CPC

The study of Number Concentration Measurement method of Particles Generated by Laser Printer

Ha-Gue Chung, Sun-Man Kim and Kang-Ho Ahn

Departoment of Mechanical Engineering, Hanyang University, 1271, Sa 3-dong, Sangrok-gu, Ansan, Kyunggi-do, 426-791, KOREA, Rep. of

Principal Contact: Kang Ho Ahn, Prof., Department of Mechanical Engineering, Hanyang University, 1271, Sa 3-dong, Sangrok-gu, Ansan, Kyunggi-do, 426-791, KOREA, Rep. of

Tel: +82-31-417-0601 Fax: +82-31-436-8184 Email: khahn@hanyang.ac.kr

Abstract

Nowadays, Indoor air pollution has been gaining more attention due to more indoor activities. On the account of the gradual increase of indoor contaminants, people who spend lots of time indoors have suffered from headache, dizziness, eye irritation, laryngitis and so on. Because of indoor air pollution, there are many indoor devices. Especially Laser printers and copiers generate many pollutants such as nano-particles or chemical substance. Particle concentration generated by printers and copiers depend on device model, printing speed, toner, paper, humidity and so on. Particle concentration generated by printers and copiers are usually in the range of nano sizes. Those nano-particles are able to affect human body. To evaluate the emission rate of nano-particles from laser printers, the mass concentration measurement method has been used (BAM, 2004). However, mass concentration measurement method sample fine particle by filter (Glass fiber or Membrane filter). So pores of the filter determine sampled particle size, usually large particles are sampled. Therefore, we developed a new method to evaluate the nano-particle emission rate from laser printers and copiers.

The experiments were performed in a chamber with interior volumes of $1m^3$ which meets the requirement of DINEN ISO 16000-9(2006). The printer is prepared inside the chamber. The nano-particles from the printer were measured through an outlet of the chamber. The outlet diameter is 5cm. Before the experiment with the printers, we have to prove that the sampled air from the outlet represents the mean aerosol concentration from the printer.

We injected NaCl particles with NMD of 80nm at the centre of the chamber. Artificially generated NaCl particles are the most similar with the particles generated from the printers. Since we measure the test NaCl particle concentration we can predict the particle concentration at the outlet of the chamber if the test particles are well mixed before sampling at the outlet. At the exit of the test chamber, several different types of mixers are located for well mixing.

At the high air exchange rate, the mixing of particles was not satisfactory. We can get near perfect sampling efficiency at 3 air exchanges with 3 perforated plates installed at the outlet.

Acknowledgement

This project was supported by Korea Environmental Industry & Technology Institute as "The

Eco-Technopia 21 projects”

Keywords: Nano-particle, Sampling, Laser printer

Behavior of Inorganic Secondary Aerosols and Precursors during a Typical Haze Episode in Shanghai

Yihua Zhang¹, Yusen Duan¹, Song Gao¹, Qingyan Fu¹, Haiping Wei¹, Fei Sha², Yan Cai²

1 Shanghai Environmental Monitoring Center, No.1 Nandan Road, Shanghai, China, 200030

2 Pudong New Area Environmental Monitoring Station, No.51 Lingshan Road, Shanghai, China, 200135

Principal Contact: Yihua Zhang, assistant engineer, Shanghai Environmental Monitoring Center, No.1 Nandan Road, Shanghai, China, 200030.

Tel: +8621-24011578 Fax: +8621-64393639 Email: zyh911@gmail.com

Abstract

A continuous haze episode with high concentration of fine particulate matter occurred in Shanghai from May 19th to May 21st, 2010. Average hourly concentration of PM_{2.5} reached (0.096 ± 0.041) mg/m³ during these three days. Results of semi-continuous monitor of water-soluble ions in aerosols indicated that three secondary ions, sulfate, nitrate and ammonium, were the main contributors to this haze episode, accounting for about 70% of PM_{2.5} mass concentration. At the first day's night, nitrate formation rate was fast due to high temperature, low relative humidity and sufficient gaseous precursors, which caused high nitrate concentration. In the second day's morning, another nitrate peak occurred due to favorable reaction conditions and enough atmospheric oxidation capacity. On the third day, concentration of sulfate instead of nitrate was high because the sulfate aerosols were transported back from sea after secondary transformation from SO₂, which was emitted from human activities on land. Because of different transformation mechanism and different reaction factors, nitrate and sulfate peaks occurred alternatively, forming continuous haze event. Therefore, nitrogen oxides and sulfur dioxide should be controlled synergistically to effectively control haze in Shanghai. For nitrogen oxides, local emission sources should be controlled strictly due to the fast transformation rate and complex effects. For sulfur dioxide, attention should be paid to regional joint control due to its long-range transportation.

Keywords: fine particulate matter; PM_{2.5}; haze; inorganic secondary aerosol; water-soluble ions; Shanghai

Daytime Variation of PM_{2.5} Concentration in Street Canyons on Weak-Wind Summer Days

**Yun-Wei Zhang¹, Zhao-Lin Gu², Yan Cheng², Zhen-Xing Shen¹, Jun-Gang Dong³ and
Shun-Cheng Lee⁴**

¹ School of Energy and Power Engineering, Xi'an Jiaotong University, Xi'an, 710049

² Department of Environmental Science and Technology, School of Human Settlements and Civil Engineering, Xi'an Jiaotong University, Xi'an, 710049

³ Architecture and Technology Department, Xi'an University of Architecture and Technology, Xi'an, 710055

⁴ Department of Civil and Structural Engineering, The Hong Kong Polytechnic University, Hung Hom, Kowloon, Hong Kong, China

Principal Contact: Dr., Zhao-Lin Gu

Department of Environmental Science and Technology, School of Human Settlements and Civil Engineering, Xi'an Jiaotong University, Xi'an, 710049,
+86-29-8339-5100, guzhaoln@mail.xjtu.edu.cn.

ABSTRACT

Daytime variations of PM_{2.5} concentration in three street canyons in Xi'an were measured during June 11-15, 2010. Weather conditions, including ambient wind condition and street canyon air temperature were recorded as well. These measurement were conducted under weak-wind summer days, when the mean ambient wind velocity was 1.26 m/s. The measurement results showed that, under weak-wind conditions, PM_{2.5} concentrations and vehicle flux inside the street canyons did not have good correlation. PM_{2.5} concentrations accumulated inside the street canyons in daytime with near uniform horizontal distribution at the pedestrian level. These results indicated the absence of the typical primary air flow re-circulation inside the street canyons under the weak-wind conditions, and the dispersion and transportation of the vehicle exhausts inside and out of the street canyons were influenced by vehicle induced air flow and thermal induced buoyancy.

KEYWORDS

PM_{2.5} concentration, Weak-wind condition, Street canyon, Xi'an

Introduction

The link between certain respiratory health issues, such as the increase in asthma cases and mortality, and suspended particulate matter^[1] in the atmosphere, especially in urban environments have been established by epidemiological and toxicological studies^[2, 3]. The dominant sources of PM_{2.5} are from the traffic emissions in urban street canyons^[4].

High pollutants concentrations inside street canyons could also have an impact on indoor air quality^[5-7]. It is therefore important to understand the dispersion characteristics of pollutants in the street canyons under various urban meteorological conditions, to formulate effective strategies such as positioning of ventilation air intake, for emission control; and for urban planning. Several methods, such as laboratory-scale experiments^[5, 8], in-situ measurements^[9-11], computation fluid dynamics (CFD) simulations^[12-14], have been used to investigate airflow and pollutant dispersion in street canyon.

However, in-situ measurements are still lack and can not fit the requirements for model validation^[15]. Especially measurements and simulations of air flow and pollutant distributions and dispersions on weak-wind conditions are relatively rare.

When the mean ambient wind velocity is lower than 1.5 ms⁻¹, there is no primary air flow vortex inside street canyons. Traffic induced air flow and turbulence and the thermal conditions are the main factors affecting on air flow and pollutant distribution and dispersions in street canyons under weak-wind conditions^[16, 17]. Xie et al.'s^[18] numerical simulation exhibited the strong effects of thermal condition of solid wall in street canyon on air flow. Solazzo et al.^[19] introduced a vehicle induced turbulence model to WinOSPM and achieved well simulation of CO concentration in street canyons under weak-wind conditions.

Tree plantings in street canyons can decrease the dispersion of pollutant from canyons to the air aloft^[20, 21]. However, tree plantings would also change the thermal conditions inside the street canyons^[21]. Thus, the difference of pollutant distributions and dispersion in street canyons with and without tree plantings under weak-wind conditions is interesting, which has not been studied before.

In this work, day time variation PM_{2.5} concentrations and temperature are measured in street canyons with and without tree plantings in hot summer days in Xi'an, China. Traffic flux and ambient wind velocity are recorded as well. Main factors affecting on PM_{2.5} concentration variation and dispersion are analyzed.

Methodology

Measurement Sites

The measurement sites were selected in three South-North street canyons inside the City-Wall of Xi'an, China, which are Tian Shui Jing Road (TSJR), Zhu Que Road (ZQR) and He Ping Road (HPR), respectively. The TSJR and ZQR with little plantings on both sides of the road, which can

be described as exposed canyons. The HPR was covered by tree planting canopy. The experiment sites were about 150 m from the City-Wall. The three urban area sites located in three street canyons of similar geometry, with the road widths are about 30 m and the building heights are about 30 m. Buildings heights of the HPR site are a little lower, about 24 m, with obviously building height undulations along the street canyon. The TSJR and ZQR are nearly uniform street canyons. Background concentration was measured on a building top in the suburban area about 5 km from the city centre. The background measurement point was 300m away from the nearest road, thus the vehicle emission effect is hoped can be neglected.

Equipments and Measurements

In the current measurements, the daytime variation of fine particle ($PM_{2.5}$) mass concentration on the road side and air and wall temperatures were measured. Fine particle mass concentrations were measured by Dust Trak (TSI). The solid wall temperatures (road surface and building surfaces) were measured with Infrared Thermometer (Nicetyl) and the air temperatures were measured with the Air Thermometer (Apuhua). Traffic fluxes were recorded manually. The measurements were carried out from June 11, 2010 to June 15, 2010 for 5 days. As limited equipments were used, measurements were carried out site by site, i.e. on June 11, measurements were carried out on site ② (ZQR); on June 12 and 14, measurements were carried out on site ③ (HPR); on June 13, measurements were carried out on site ① (TSJR); and the background fine particle mass concentration were carried out on day June 15 on site ④. Measurements were start at 7:00 and end at 19:00, except on the day June 11, which ended at 14:00 as the equipments were power out. It should be pointed out that, the local area were undergoing similar weather conditions in those fine days, with hot sunshine, high air temperature and weak-winds.

Results

The wind velocity and wind direction data are provided by the Meteorological Agency of Shaanxi Province, China. The average wind velocity is about 1.26 m/s, which shows the weak-wind conditions^[16]. The wind direction changed frequently without obvious prevailing wind direction. Figure 1 shows the temporal variation of fine particle mass concentrations and vehicle fluxes. In urban area sites (Figure 1(a-c)), it shows the variation of pollutant concentrations have no clearly consistency with the traffic fluxes as reported by Longley et al.^[22] Fine particle mass concentrations in the urban area sites decay from about 12:00, with the minimum values occur on about 16:00, which is similar to that of the background fine particle mass concentration measured on June 15 (Figure 1(d)). It follows that the pollutant concentration variations in urban street canyons in these hot summer days are significantly impacted by background concentrations. The variation of fine particle mass concentration also shows no correlation with the wind velocities. In the hours when the particle mass concentration decaying, the air temperatures are keeping

increasing and the road surface temperatures are much higher than the air temperatures in site ZQR, as shown in Figure 2, indicating the instability of street canyon air. It follows that the temperature and the instability of air dominate the variation of pollutants in these weak-wind hot summer days.

Figure 1. Measured day time variation of fine particle mass concentrations and traffic fluxes.

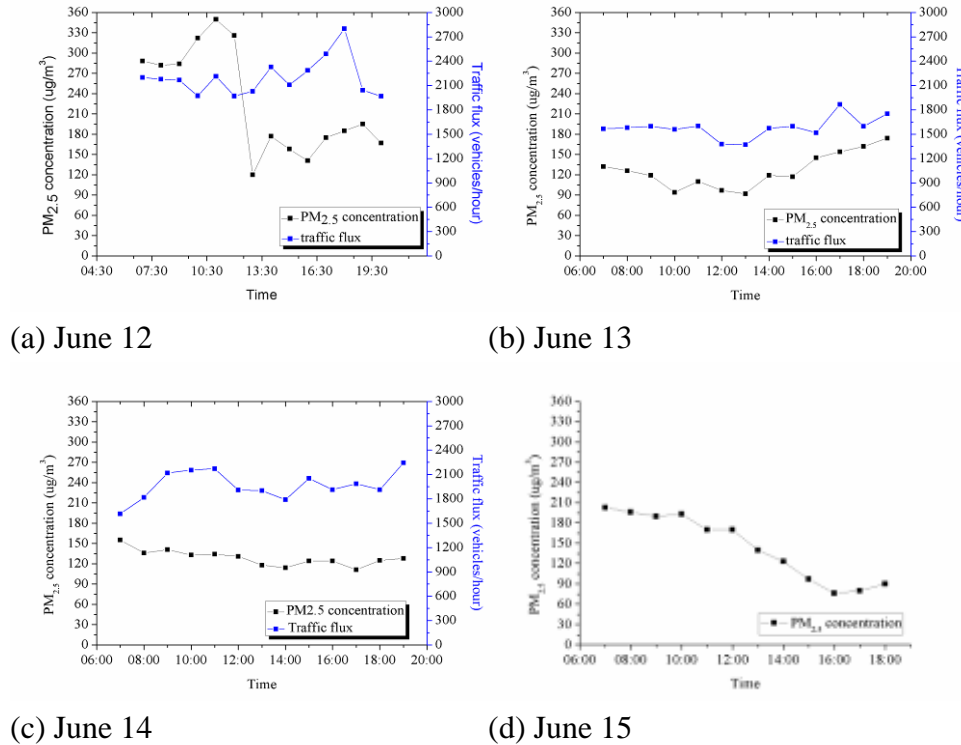
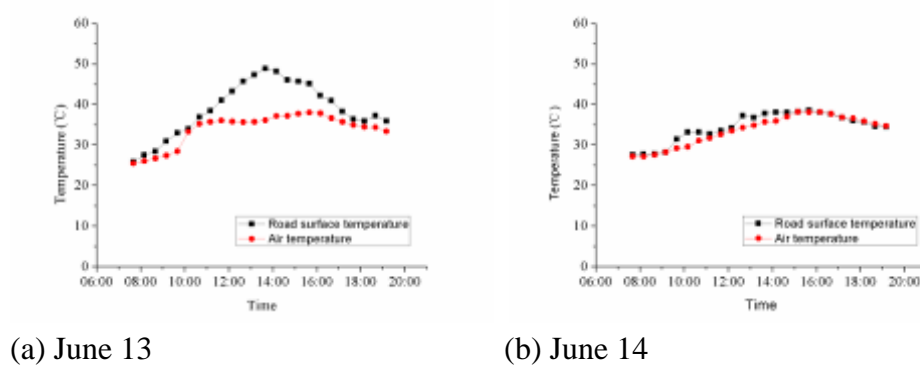


Figure 2. Measured day time variation of temperature.



Discussions

The dispersion of pollutant from urban street canyons to upper air is usually related to wind conditions, especially the wind velocity aloft [23, 24]. However, in such weak-wind hot summer days, the main factors affecting on the pollutant dispersion in urban street canyons have been rarely discussed. On the other hand, it is commonly known that the weak-wind condition would cause the poor air quality in urban street canyons. Dose the pollutants accumulated in these measurement days? These two points will be discussed in the following.

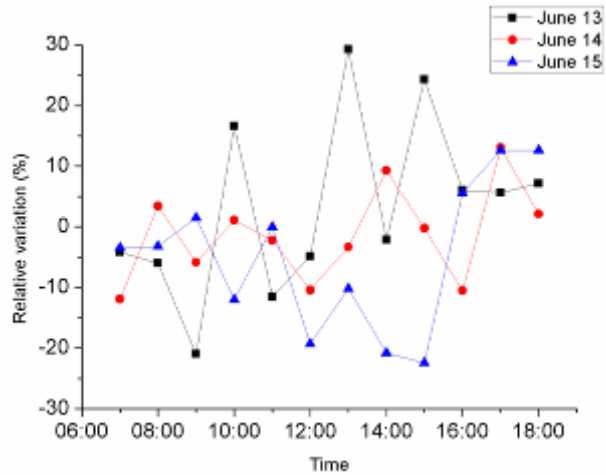
Pollutant Accumulation

The worst air qualities in urban street canyons have been frequently observed under weak-wind condition^[25]. Pollutant concentrations inside urban street canyons are influenced by both vehicle emissions and background concentrations. The directly measured pollutant concentrations can not reflect the accumulations of vehicle emissions. The background concentrations are usually taken away from the total concentrations in order to show the contributions of vehicle emissions. However, in the current work, background concentrations are not measured simultaneously with the street canyon measurements. Thus we proposed the relative variations of concentrations (RVC), which is calculated by

$$RVC = (C_{i+1} - C_i) / C_i \quad (\text{Eq. 1}),$$

where C_i is the measured average pollutant concentration in hour i . The variations of pollutant concentration on days June 13, 14 and 15 are shown in Figure 3, indicating the result measured in site TSJR, HPR and background, respectively. The negative value means the concentrations are decreasing in the current hour, and the positive value means the concentrations are increasing in the current hour. Figure 3 obviously shows that from 12:00 to 16:00, the values of RVC inside the street canyons are significantly larger than that of the background. It follows that the vehicle emissions are accumulated inside the urban street canyons in such period of time. In the morning, the RVC show small values. The RVC values of the background concentrations are positive after 16:00, indicating the atmosphere boundary layer start to contract. In order to get the clean air through traffic control, the current work suggests restricting the traffic flow in hours from 12:00 to 16:00 in weak-wind hot summer days.

Figure 3. Variations of relative variations of concentrations (RVC).



Main Affecting Factors

We have shown that the temperature and the instability of street canyon air are ones of the main factors affecting the pollutant dispersions inside urban street canyons. If the ambient wind is strong enough to drive the air circulation inside urban street canyon, the pollutants from vehicles will be transported to the leeward side, and then transport to the upper layer with the air circulations [13, 14, 26, 27], which results in the higher pollutant concentration near the leeward side than those near the windward side [13, 14]. The vehicle movement induced air flow and turbulence also have significant effect of pollutant distributions in urban street canyons [28, 29]. The current measurements show that the pollutant concentrations on the horizontal level near the road have no obviously variations. It follows that under such weak-wind conditions, the ambient wind can not drive the air circulations inside street canyons, and the vehicle movements have effect on the pollutant distributions in the urban street canyons.

When the ambient wind is strong enough and the air circulation is driven inside the urban street canyons, tree panting on road sides would increase the pollutant concentration inside the street canyons [20, 21]. On the other hand, tree plantings will also change the instability of air inside street canyons. Figure 1 (b) and (c) show no obviously concentration difference in the two street canyons without tree planting (TSJR) and with tree planting (HPR) respectively. The reason should be the total effects of tree planting under such weak-wind hot summer days are not evident.

CONCLUSIONS

The measurements show that, under weak-wind hot summer conditions, the PM_{2.5} concentrations inside urban street canyons have unsatisfactory correlation with the vehicle fluxes

and the ambient wind velocities. The PM_{2.5} concentrations are significantly impacted by background concentrations. The measured PM_{2.5} concentrations in urban street canyons are decaying from 12:00 to 16:00, while the PM_{2.5} from the vehicle exhausts accumulated inside the street canyons in these hours. In order to get the clean air through traffic control, the current work suggests restricting the traffic flow in hours from 12:00 to 16:00 in weak-wind hot summer days.

The weak-wind velocities can not drive the primary air circulation inside street canyons. The main factors influencing the pollutant dispersion inside street canyons are the air temperature and vehicle induced air flows. The total effects of tree planting under such weak-wind hot summer days are not evident.

ACKNOWLEDGMENTS

The authors would thanks peoples for their participation in the experiments, such as Fan Min, Wang Ning, et al. This work was supported by the National Natural Science Foundation of China (No. 40675011 & 10872159).

REFERENCES

- [1] Ali-Toudert, F.; Mayer, H. Building and Environment. 2006, *41*, 94-108.
- [2] Cooke, R.M.; Wilson, A.M.; Tuomisto, J.T.; Morales, O.; Tainio, M.; Evans, J. Environment Science and Technology. 2007, *41*, 6598-6605.
- [3] Nag, S.; Gupta, A.K.; Mukhopadhyay, U.K. Indoor and Built Environment. 2005, *14*, 381-389.
- [4] Charron, A.; Harrison, R.M. Environment Science and Technology. 2005, *39*, 7768-7776.
- [5] Ahmad, K.; Khare, M.; Chaudhry, K.K. Journal of Wind Engineering and Industrial Aerodynamics. 2005, *93*, 697-717.
- [6] Vardoulakis, S.; Fisher, B.E.A.; Pericleous, K.; Gonzalez-Flesca, N. Atmospheric Environment. 2003, *37*, 155-182.
- [7] Chan, A.T.; So, E.S.P.; Samad, S.C. Atmospheric Environment. 2001, *35*, 4089-4098.
- [8] Pavageau, M.; Schatzmann, M. Atmospheric Environment. 1999, *33*, 3961-3971.
- [9] Murena, F.; Favale, G.; Vardoulakis, S.; Solazzo, E. Atmospheric Environment. 2009, *43*, 2303-2311.
- [10] Li, X.L.; Wang, J.S.; Tu, X.D.; Liu, W.; Huang, Z. Science of The Total Environment. 2007, *378*, 306-316.
- [11] Zhang, Y.W.; Gu, Z.L.; Lee, S.C.; Fu, T.M.; Ho, K.F. Indoor and Built Environment. 2011, Inpress.
- [12] Xie, X.M.; Wang, J.S.; Huang, Z. Journal of Hydrodynamics, Ser. B. 2009, *21*, 108-117.
- [13] Li, X.X.; Liu, C.H.; Leung, D.Y.C. Atmospheric Environment. 2009, *43*, 2410-2418.
- [14] Walton, A.; Cheng, A.Y.S. Atmospheric Environment. 2002, *36*, 3615-3627.

- [15] Kumar, P.; Fennell, P.; Langley, D.; Britter, R. *Atmospheric Environment*. 2008, *42*, 4304-4319.
- [16] Coppalle, A. *International Journal of Environment and Pollution*. 2001, *16*, 417-424.
- [17] Okamoto, S.; Ohnishi, H.; Yamada, T.; Mikami, T.; Momose, S.; Shinji, H.; Itohiya, T. *International Journal of Environment and Pollution*. 2001, *16*, 69-79.
- [18] Xie, X.M.; Liu, C.H.; Leung, D.Y.C.; Leung, M.K.H. *Atmospheric Environment*. 2006, *40*, 6396-6409.
- [19] Solazzo, E.; Vardoulakis, S.; Cai, X. *Atmospheric Environment*. 2007, *41*, 5357-5370.
- [20] Ries, K.; Eichhorn, J. *Meteorologische Zeitschrift*. 2001, *10*, 229-233.
- [21] Gu, Z.L.; Zhang, Y.W.; Lei, K.B. *SCIENCE CHINA Technological Sciences*. 2010, *53*, 1928-1937.
- [22] Longley, I.D.; Gallagher, M.W.; Dorsey, J.R.; Flynn, M. *Atmospheric Environment*. 2004, *38*, 3595-3603.
- [23] Depaul, F.T.; Sheih, C.M.; Noll, K.E. *Aerosol Science and Technology*. 1983, *2*, 167-167.
- [24] Depaul, F.T.; Sheih, C.M. *Atmospheric Environment*. 1985, *19*, 555-559.
- [25] Kukkonen, J.; Valkonen, E.; Walden, J.; Koskentalo, T.; Aarnio, P.; Karppinen, A.; Berkowicz, R.; Kartastenpaa, R. *Atmospheric Environment*. 2001, *35*, 231-243.
- [26] Hoydysh, W.G.; Dabberdt, W.E. *Atmospheric Environment*. 1988, *22*, 2677-2689.
- [27] Chan, A.T.; Au, W.T.W.; So, E.S.P. *Atmospheric Environment*. 2003, *37*, 2761-2772.
- [28] Depaul, F.T.; Sheih, C.M. *Atmospheric Environment*. 1986, *20*, 455-459.
- [29] Qin, Y.; Kot, S.C. *Atmospheric Environment. Part B. Urban Atmosphere*. 1993, *27*, 283-291.

Analysis of the PM₁₀ concentration difference by different sampling methods at Gosan, Korea

So Eun Shin¹, Jung Chang Hoon², and Yong Pyo Kim¹

1 Department of Environmental Science and Engineering, Ewha Womans University, 11-1 Daehyun-dong, Seodaemun-gu, Seoul, 120-750, Korea

2 Department of Health Care Management, Kyung In Women's College, 101 Gyesangil, Kyeyanggu, Inchon, 407-740, Korea

Principal Contact: So Eun Shin, Student, Department of Environmental Science and Engineering, Ewha Womans University, 11-1 Daehyun-dong, Seodaemun-gu, Seoul, 120-750, Korea.

Tel: +822-3277-2902 Fax: +822-3277-3275 E-mail: witwm11@gmail.com

Abstract

Reliability of the measurement of ambient trace species is an important issue, especially, in a background area such as Gosan in Jeju Island, Korea. However, the measured particulate matter less than 10 μm in diameter (PM₁₀) mass concentrations by the β -ray absorption method (BAM) and gravimetric method (GMM) at Gosan have shown consistent difference. Based on the previous studies, two probable reasons for the discrepancy were identified; (1) negative measurement error by the volatilization of volatile ambient species at the filter in GMM such as nitrate, chloride, and ammonium and (2) positive error by the absorption of water vapor during measurement in BAM. There was no heater at the inlet of BAM in Gosan during the sampling period. We have analyzed negative and positive error quantitatively by using a gas/particle equilibrium model SCAPE 2 (Simulating Composition of Atmospheric Particles at Equilibrium) for the data between May 2001 and June 2008 with the aerosol and gaseous composition data. After considering negative and positive error above, discrepancy between GMM and BAM is reduced from 69% to 25%. However, there remains discrepancy and the correlation between them is still not good. Result of multiple linear regression analysis shows that the two third of the PM₁₀ concentration by GMM can be explained by that of BAM, water content, volatilization, temperature, and wind direction. Also, it is found that the measurement error is mostly influenced by water content.

Keywords: β -ray absorption method, gravimetric method, water content, volatile ionic species, multiple regression analysis

Variability of blowing dust weather frequency over semi-arid areas of China (Baicheng, Jilin Province) and relationships with climatic factors during 1951-2006

Yun-Fei Wu^{1,2}, Ren-Jian Zhang¹, Cong-Bin Fu¹, Zong-Ting Gao³

1 Key Laboratory of Regional Climate-Environment Research for Temperate East Asia, Chinese Academy of Sciences, Beijing 100029, China

2 Graduate University, Chinese Academy of Sciences, Beijing 100049, China

3 Jilin Meteorological Science Institute, Changchun 130062, China

Principal Contact: Ren-Jian Zhang, Professor, Institute of Atmospheric Physics, Chinese Academy of Sciences, Beijing, 100029, China.

Tel: +86-10-62064089 Email: zrj@mail.iap.ac.cn

Abstract

We analyzed the variability of blowing dust weather frequency (BDWF) and patterns in climatic factors over Baicheng for the period 1951-2006 in this study. The data showed that blowing dust over Baicheng occurs intensively during the spring and shows significant inter-decadal variability. One of the main findings is that the occurrence of blowing dust has significantly decreased after the mid-1980s. The mean wind speed (WS), diurnal temperature range (DTR), relative humidity (RH) and precipitation at Baicheng during the spring show decreasing trends. The decreasing trends of the mean WS and DTR are significant at 99 % confidence levels according to the t-test; the dataset also indicated a sharp decrease in WS occurred after the mid-1980s. The mean surface air temperature (SAT) escalated in a fluctuating manner during 1951-2006. BDWF at Baicheng was significantly related to local WS, SAT and DTR during the spring (correlation coefficients (CCs) are 0.41, -0.47 and 0.36, respectively). The correlation between BDWF at Baicheng and selected climatic factors over the sand-dust source regions and transmission paths were also calculated. We found that BDWF is well correlated to the mean WS and SAT during the spring, with CCs of 0.45 and -0.48, respectively. The most likely causes for the dramatic decrease observed in BDWF after the mid-1980s were related to the adjustment of large-scale circulation patterns in response to a decrease of meridional temperature differences, the weakening of steering westerlies and the strengthening of downward motions that has occurred at the middle latitudes of eastern Eurasia in recent decades.

Keywords: blowing dust weather frequency, climatic factors, variability, relationship

Single Particle Analysis of Ambient Aerosols in Shanghai during World EXPO, 2010: Two Case Studies

Shikang Tao, Hong Chen, and Xin Yang

Department of Environmental Science and Engineering, Fudan University, 220 Handan Rd., Shanghai 200433

Principal Contact: Shikang Tao, Department of Environmental Science and Engineering, Fudan University, 220 Handan Rd., Shanghai 200433, China.

Tel: 13761907061 Email: scappy_527@yahoo.com.cn

Abstract

A TSI Model 3800 aerosol time-of-flight mass spectrometer (ATOFMS) was deployed for single-particle analysis in Shanghai during World EXPO, 2010. Measurements on two extreme cases: heavily polluted day (1st May) and clean day (25th September) were compared to show how meteorological conditions affect the concentration and composition of aerosols. Mass spectra of 90,496 and 50,407 particles were recorded respectively during the two sampling periods. The ART-2a neural network algorithm was applied to sort the collected particles. Seven major classes of particles were obtained: dust, sea salt, heavy metal containing particles, biomass burning particles, OC, EC and NH₄-rich particles. Analysis of mass spectrum in the two studies showed that biomass burning particles were the most populated group in both May and September, accounting for 43.3% and 21.6%, respectively. All the sea salt particles were deeply aged when reaching the sampling site. Heavy metal containing particles in May and September had a close connection with nearby waste incineration. Dust number concentration was elevated and particle size increased in heavy polluted day, which were mostly due to the long-range transport of dust particles from north China. But in September clean day, dust particles were relatively smaller and fresh, mostly coming from local emissions. Because of different wind direction and speed, the abundance of sea salt in clean day was much higher (13.3%) than in heavy polluted day (2.1%). The presence of ammonium salt in May often accompanied with EC particles while in September, they often accumulated on OC particle surface and were relatively fresh.

Keywords: Shanghai, EXPO, ambient aerosol, ATOFMS

Simulation of the Brownian Coagulation of Smoke Agglomerates in the Entire Size Regime using a Nodal Method

Jae-Hark Goo

Department of Fire and Safety, Woosuk University, Jeonbuk, 565-701, South Korea

Principal Contact: Jaehark Goo, Ph.D., Professor, Department of Fire and Safety, Woosuk University, 443 Samnye-ro Wanju-gun Jeonbuk, 565-701, South Korea.

Tel: +82-63-290-1428 E-mail: jaygoo@woosuk.ac.kr

Abstract

The size distributions of smoke particles from fire are prerequisites for the studies on fire detection and adverse health effects. Above the flame of the fire, coagulation dominates and the smoke particles grow from 1 to 50 nm up to 100 to 3000 nm, sizes ranging from the free-molecular regime to the continuum regime. The characteristics of the agglomeration of the smoke particles are well known, independently for each of the free-molecular and continuum regimes. However, there are not many systematic studies in the entire regime by the complexity of the mechanisms. The purpose of this work is to find the characteristics of the development of the size distribution of smoke particles by agglomeration in the entire size range covering the free-molecular regime, via transition regime, to the continuum regime. In this work, the dynamic equation for the discrete-size spectrum of the particles was solved using a nodal method based on the modification of a sectional method. In the calculation, the collision frequency function for the entire regime, which is derived by using the concept of collision volume and general enhancement function, was applied. The self-preserving size distribution is applicable in the free-molecular and continuum regimes. However, it changes with time in the entire regime. The characteristics of the size distribution, obtained by using the collision frequency functions for the entire regime, was compared with ones for the other regimes for each variation of parameters such as fractal dimension, initial particle size distribution, and coagulation time.

Keywords: Smoke, Soot, Particle, Agglomerates, Coagulation, Size distribution, Number concentration, Fractal dimension, Entire regime, Nodal method, Collision volume.

Fuel based emission factors for carbonaceous particles from commercial ship emissions

Shao-Meng Li¹, Katherine Hayden¹, Ibraheem Nuamann^{1,2}, Eric Williams³, and Robert McLaren²

1 Air Quality Research Division, Environment Canada, 4905 Dufferin Street, Toronto, Ontario M3H 5T4, Canada

2 Department of Chemistry, York University, Toronto, Ontario, M3J 1P3, Canada

3 NOAA CSD, 325 Broadway, Boulder, Colorado, 80305, USA

Principal Contact: Shao-Meng Li, Research Scientist, Air Quality Research Division, 4905 Dufferin Street, Toronto, Ontario M3H 5T4, Canada.

Tel: 1-416-739-5731 Fax: 1-416-739-4281 Email: shao-meng.li@ec.gc.ca

Abstract

Aerosol black carbon, organic carbon, and sulfate have strong radiative forcing potentials in the global atmosphere but the magnitudes of such potential remain uncertain due to incomplete knowledge of their sources, including emissions from global commercial shipping. During the California Nexus (CALNEX) 2010 experiments, ship emissions were studied from the R/V Atlantis from near the coast of southern California including the ports of Los Angeles and Long Beach. Plumes from over 120 ships were sampled, including those from container ships, ferries, fishing boats, among others. Extensive high time resolution (1-second) measurements of particulate black carbon (BC), organic carbon (OC), and sulfate were made along with gas phase measurements of NOx, SO2, volatile organic carbon, CO, and CO2. Individual ship plumes were identified by elevated concentrations of these pollutants above background levels which typically lasted from less than 1 minute to several minutes. By integrating these elevated concentration over the time of these plumes, and using a fuel carbon content of 0.87, the fuel based emission factors for BC, OC, and SO₄⁻ for ships are estimated for each individual plume from all ship emissions that were encountered during the study. For example, during an encounter with the Margrethe Maesk, a container ship, the emission factors for BC, OC, and SO₄⁻ are determined to be 0.197 ± 0.015, 0.230 ± 0.020, and 0.129 ± 0.056 g kg⁻¹, respectively. For the gases, emission factors for CO, NOx, and SO₂ are observed as 3.00 ± 0.21, 131.1 ± 9.9, and 6.0 ± 1.5 g kg⁻¹, respectively. More details will be presented at the conference.

Keywords: Ship emissions, black carbon, organic carbon, sulfate

The Long-term variation of haze weather in Zhejiang urban areas

Yu-wen Niu¹, Jun-qiang Gu¹, Jing-jiao Pu¹, Wen-juan Li², and Jin-sheng Wu³

1 Zhejiang Meteorological Institute, Hangzhou 310017, China

2 Zhejiang Meteorological Observatory, Hangzhou 310017, China

3 Zhejiang Meteorological Information Center, Hangzhou 310017, China

Principal Contact: Yu-wen Niu, Engineer, Zhejiang Meteorological Institute, No.73, Genshan West Road, Hangzhou, Zhejiang, China, 310017.

Tel: 0571-86042592, 13777836065 Email: niuyuwen@yahoo.com.cn

Abstract

Haze weather caused by particulate pollution has become an important environmental problem in many cities in China. The good understanding of temporal and spatial variation of the haze weather is of great significance for reducing haze weather. In order to investigate the temporal and spatial variation of haze weather in urban areas in Zhejiang Province since the 1950's, the haze historical data from 11 urban meteorological watching stations were analyzed in this study. The results showed that haze pollution was very serious during periods of 1951~1953 and 30 years since the establishment of the Reform and Opening up policy in China, furthermore the occurrence frequency of haze weather after 2000 was highest. The haze days during period of 1957 to the late 1970's were the least since the 1950's. In the early 1950's, haze pollution was serious in Hangzhou, Wenzhou and Quzhou areas. With rapid development of the market economy and private economy during the period of 1978 to 1999, there was more haze weather in Huzhou, Hangzhou, Zhoushan, Jinhua, Wenzhou and Quzhou; From the beginning of 2000, haze days were sharply increasing in Zhejiang urban areas and was particularly obvious in Huzhou, Shaoxing, Hangzhou, Jiaxing of northern Zhejiang where the haze days were more than total haze days during period of the decades before 2000, which implies the worrying atmospheric pollution in Zhejiang Province, especially in northern Zhejiang, in recent years. So, controlling atmospheric particulate matter pollution, improving air quality and improving the atmospheric visibility has become very urgent in Zhejiang Province.

Keywords: haze weather, temporal and spatial variation, Zhejiang province

Characterization of Individual Atmospheric Fine and Coarse Particles during Winter in Xi'an, China

Tafeng Hu¹, Junji Cao^{1,3} and Zhenxing Shen²

1 SKLLQG, Institute of Earth Environment, Chinese Academy of Sciences, Xi'an, China, 710075

2 Department of Environmental Science and Engineering, Xi'an Jiaotong University, Xi'an, China, 710049

3 Institute of Global Environmental Change, Xi'an Jiaotong University, Xi'an, China, 710049

Principal Contact: Tafeng Hu, Doctor, Institute of Earth Environment, Xi'an, China, 710075, Tel.: +86-29-8832-6488 Fax: +86-29-8832-0456 E-mail: hutf@ieecas.cn

Abstract

Atmospheric fine and coarse particles, including PM_{1.0}, PM_{2.5}, PM₁₀, and TSP were collected in Xi'an city during haze period, cloudy, and sunny days in winter 2010. Individual particles were analyzed using scanning electron microscopy and energy dispersive X-ray spectrometer. The morphologies, elemental compositions, and relative abundance of each type of aerosol particles collected at an urban and a roadside site were compared. The monomodal particle size distribution was found in all the samples under different weather conditions, with the peaks located between 0.5~1.0 μm at the urban site, and <0.5 μm at the roadside site. The majority of particles were composed of soot, mineral dust, and tar ball, with minor flyash particles. Soot aggregates were the predominant species (in numbers) in all the fine and coarse mode samples, ranging from 62.1% in TSP at a haze day to 86.3% in PM_{1.0} at a sunny day, with an average of 76.5%. In each size mode, the abundances of soot aggregates at the highway roadside were higher than those on the roof of an urban office building, implying vehicle emission was the major source of atmospheric particulate matters during the winter season in Xi'an. In addition to their physical and chemical activities, the abundant carbonaceous particles, including soot aggregates and tar balls, may lead to potential health hazards.

Keywords: Aerosol particles, SEM-EDX, Fine and coarse mode, Xi'an city.

The chemical composition of PM_{2.5} in rural areas of Shannxi, China

Chongshu Zhu^{1*}, Junji Cao^{1,2} and Ting, Zhang¹

1 SKLLQG, Institute of Earth Environment, Chinese Academy of Sciences, Xi'an, China

2 Institute of Global Environmental Change, Xi'an Jiaotong University, Xi'an, China

Principal Contact: Chongshu Zhu, Ph.D., Institute of Earth Environment, Chinese Academy of Sciences (CAS), No. 10 Fenghui South Road, High-Tech Zone, Xi'an 710075, China.

Tel: 86-29-8832-6128 Fax: 86-29-8832-0456 E-mail:chongshu@ieecas.cn

Abstract

The chemical composition of PM_{2.5} was studied during summer and winter sampling campaigns conducted at three different rural sites in Shannxi. PM_{2.5} samples were chemically analysed for minerals (Ca, Mg, Fe, Ti, K, Na), trace elements (Cd, Cr, Mn, Pb, Zn, Br, Mo, S, Cl), water-soluble ions (F⁻, Cl⁻, NO₃⁻, SO₄²⁻, Na⁺, K⁺, NH₄⁺, Ca²⁺, Mg²⁺) and carbonaceous compounds (OC, EC). Results showed that the most important fractions were organic matter (24.4%- 41.2%), SO₄²⁻ (16.7%-24.0%), NO₃⁻ (5.9%-10.6%), NH₄⁺ (5.6%-7.7%) and elements (7.6%-11.1%). Seasonal variations of atmospheric concentrations showed significantly higher levels of OM, NO₃⁻ and NH₄⁺, especially for K⁺ and Pb were observed in winter. During the period examined, the mean values of the element concentrations decreased in the following order: S>K>Cl>Si>Ca>Fe>Zn>Na>Pb>Al>Mg>Mn≈Ti≈Mo≈Br≈Cd≈Cr for winter and S>K>Si>Ca>Fe>Zn>Na>Al>Mg>Pb>Cl>Ti≈Mo≈Mn≈Cd≈Br≈Cr for summer, respectively. In addition, wintertime concentrations of OM, K⁺, Mg²⁺, Pb, NO₃⁻ and Cl⁻ are increasing at about 3 times of summertime. This was probably due to the strong impact of the local emission sources. The fraction unaccounted for by chemical analysis comprised on average 7% during winter and 17% during summer.

Keywords: Chemical composition; Rural area; Northwest China

Optical, microphysical and chemical properties of aerosols: a comparison between foggy and non-foggy days over a typical location in Indo-Gangetic plains

D. S. Kaul, S. N. Tripathi and Tarun Gupta

Department of Civil Engineering, Indian Institute of Technology, Kanpur, India

Principal Contact: S.N.Tripathi, Associate Professor, Department of Civil Engineering, Indian Institute of Technology, Kanpur, India.

Tel: +91-5122597274 Fax: +91- 512-2597395 Email: snt@iitk.ac.in

Abstract

Frequent occurrences of radiation fog over Indo-Gangetic plains render it as an ideal region to study the changes in optical, microphysical and chemical properties of aerosols during fog events. Total 180 PM₁ samples (six every 24 hours) were collected from January 16, 2010 to February 20, 2010, of which 54 represented foggy days. Carbonaceous component and ionic species of aerosol were analyzed using TOC analyzer, EC-OC analyzer and ion chromatograph, respectively. Precise duration of fog was obtained by Micro-Pulse Lidar. Optical properties and Black Carbon were measured using Photo-Acoustic Absorption Spectrometer and Aethalometer, respectively. Scanning Mobility Particle Sizer and Optical Particle Counter were used for measuring aerosol size distributions. Preliminary analysis shows that number concentration of particles during fog events was significantly higher in size range of 14.6 nm to 1 μm whereas it was lower in the size range of 1 to 15 μm , suggesting enhanced concentration of fine particles and reduced concentration of coarse particles during fog episodes. Absorption and scattering coefficients were higher during foggy events whereas single scattering albedo and black carbon concentration was higher throughout the day. Such higher values can be attributed to the coating of water soluble organic and inorganic salts over interstitial black carbon particles. For most of daytime, absorption exponent during foggy days was relatively lower suggesting limited mixing and presence of relatively freshly emitted particles. Detailed analysis and interdependence of optical, microphysical and chemical properties of aerosol will be presented.

Keywords: optical, chemical, microphysical, properties, aerosol

Correlation of black carbon aerosol and carbon monoxide concentrations measured in the high-altitude environment of Mt. Huangshan, eastern China

X.L.Pan^{1,2}, Y.Kanaya¹, Z.F.Wang², Y.Liu², P.Pochanart¹, H.Akimoto¹, H.B.Dong², and J.Li²

1 Research Institute for Global Change, Japan Agency for Marine-Earth Science and Technology, Japan

2 Institute of Atmospheric Physics, Chinese Academy of Sciences, Beijing, China

Principal Contact: X.L.Pan, Doctor, Affiliation: Research Institute for Global Change, Japan Agency for Marine-Earth Science and Technology, Yokohama Institute for Earth Science, 3173-25 Showa-machi, Kanazawa-ku Yokohama Kanagawa 236-0001 Japan.

Tel: +81-45-778-5944 Fax: +81-45-778-5496 Email: xlpanelf@jamstec.go.jp

Abstract

Understanding the relationship between black carbon (BC) and carbon monoxide (CO) will help improve BC emission inventories and the evaluation of global/regional climate forcing effects. In the present work, the BC (PM_{1}) and CO mixing ratio was continuously measured at a high-altitude background station on the summit of Mt Huangshan between 2006 and 2009. Annual mean BC concentration was $654.6 \pm 633.4 \text{ ng/m}^3$ with maxima in spring and autumn, when biomass was burned over a large area in eastern China. The yearly averaged CO concentration was $446.4 \pm 167.6 \text{ ppbv}$, and the increase in the CO concentration was greatest in the cold season, implying that the large-scale domestic coal/biofuel combustion for heating has an effect. The BC–CO relationship was found to have different seasonal features but strong positive correlation ($R > 0.8$). Back trajectory cluster analysis showed that the $\Delta BC/\Delta CO$ ratio of plumes from the Yangtze River Delta region was $6.58 \pm 0.96 \text{ ng/m}^3/\text{ppbv}$, which is consistent with result from INTEX-B emission inventory. The $\Delta BC/\Delta CO$ ratios for air masses from northern, central eastern and southern China were 5.2 ± 0.63 , 5.65 ± 0.58 and $5.21 \pm 0.93 \text{ ng/m}^3/\text{ppbv}$ respectively. Over the whole observation period, the $\Delta BC/\Delta CO$ ratio had unimodal diurnal variations and had a maximum during the day (0900–1700 LST) and minimum at night (2100–0400 LST) in spring, summer, autumn and winter, indicating the effects of the intrusion of clean air mass from the high troposphere. The case study combined with measurements of urban PM_{10} concentrations and satellite observations demonstrated that the $\Delta BC/\Delta CO$ ratio for a plume of burning biomass was $12.4 \text{ ng/m}^3/\text{ppbv}$ and that for urban plumes in eastern China was $5.3 \pm 0.53 \text{ ng/m}^3/\text{ppbv}$. Transportation and industry were deemed as controlling factors of the BC–CO relationship and major contributions to atmospheric BC and CO loadings in urban areas. The loss of BC during transportation was also investigated on the basis of the $\Delta BC/\Delta CO$ –RH relationship along air mass pathways, and the results showed that 30–50% BC was lost when air mass traveled under higher RH conditions ($> 60\%$) for 2 days.

Keywords: Black carbon, Carbon monoxide, $\Delta BC/\Delta CO$ ratio, Emission inventory, BC loss rate

Graphite Particle Generation in Steel Piles

Zhipeng Chen and Suyuan Yu*

Institute of Nuclear Energy Technology, Tsinghua University, Beijing, 100084, China

Principal Contact: Institute of Nuclear Energy Technology, Tsinghua University
Beijing, 100084, China.

Tel: +86-10-62794613 Fax: +86-10-6279 4678 Email: suyuan@tsinghua.edu.cn

Abstract

Graphite Particle is one of the key safety issue in high temperature gas-cooled reactors. It can transport the irradiated elements from the reactor core to the primary circuit. Moreover, it can also bring the irradiated material into air in case some leaking happens. It is very important to get clear the generation source of the graphite particles. A set of tests have been done to measure the graphite generation rate inside the graphite fuel ball loading piles with different atmosphere, different velocity and different temperatures. The results show that the graphite particles are mostly generated in the uploading pile lines.

Particulate Matters and Associated Polycyclic Aromatic Hydrocarbons in Atmospheric Environment of Songkhla, Thailand in Relation to Rubber-wood Combustion

P. Chaichana¹, S. Tekasakul¹, P. Tekasakul^{2,4}, M. Furuuchi³ and M. Hata³

¹Department of Chemistry and Center of Excellence for Innovation in Chemistry (PERCH-CIC), Faculty of Science, Prince of Songkla University, Hat Yai, Songkhla 90112, THAILAND

²Department of Mechanical Engineering, Faculty of Engineering, Prince of Songkla University, Hat Yai, Songkhla 90112, THAILAND

³Graduate School of Natural Science and Technology, Kanazawa University, Kakuma-machi, Kanazawa 920-1162, JAPAN

⁴National Center of Excellence for Environmental and Hazardous Waste Management (EHW-M) Southern Consortium Universities at Prince of Songkla University, Hat Yai, Songkhla 90112, THAILAND

ABSTRACT

Each year, a lot of rubber-wood is used as fuel in several industries around Songkhla province, Thailand. Smoke from rubber-wood burning contains fine particles including nanoparticles and associated polycyclic aromatic hydrocarbons (PAHs) generated from incomplete combustion. In this work, characteristics of nanoparticles in atmospheric environment of Songkhla province during May-December, 2010 were investigated in order to find relation to rubber-wood combustion. Four sampling locations (Hat Yai, Muang, Bangkhlam and Sadao) surrounded by several factories using rubber-wood as fuel in burning process were chosen in this study.

Particles size distributions sampled from all locations show bi-modal behavior. They could be originated from biomass burning especially rubber-wood which is the most common fuel used in industries around the sampling sites, and re-suspension of ground dust or other atmospheric aerosol particles. Total suspended particulates (TSP) average 30.61, 27.67, 19.13 and 28.64 $\mu\text{g}/\text{m}^3$ for Hat Yai, Muang, Bangkhlam and Sadao, respectively. TSP was generally low, particularly when precipitation was high. PAHs size distributions of ambient air particles of all location show single-modal behavior. It can be concluded that most of the PAHs are associated with small particles. Total PAH concentration was low. PAHs in Hat Yai, Bangkhlam and Sadao was related to amount of rubber-wood used in the area. At Muang, the concentration was very low which could result from influence of wind and precipitation.

KEYWORDS

Nanoparticles, Size distributions, PAHs, Rubber-wood combustion

Introduction

Rubber-wood is used as fuel in several industries around Songkhla province, Thailand, especially in the ribbed smoked sheets (RSS) smoking process to supply heat to the rubber sheet^[1]. Smoke from the wood burning contains particulate matters including nanoparticles. Incomplete combustion of wood results in a formation of polycyclic aromatic hydrocarbons (PAHs) and other chemical components^[2]. PAHs are a group of hydrocarbon compounds that are carcinogenic and mutagenic, especially those containing 4-6 aromatic rings. PAHs generated from the wood burning causes a major indoor pollution problem because of the leakage of smoke particles into the working area, which then causes atmospheric pollution to nearby surroundings^[3,5]. In this work, characteristics of nanoparticles and PAHs in atmospheric environment of Songkhla province were investigated and relation to rubber-wood combustion was determined. Sampling sites surrounded by several rubber sheet smoking cooperatives and factories using rubber wood as fuel in burning process were chosen.

Experimental Methods

Air sampling

Size fractionated particles at every location were investigated using a nanoparticle air sampler (Kanomax, Japan). The cut-off aerodynamic diameters are 10.0, 2.5, 1.0, 0.5 μm and the last stage collects all particles smaller than 70 nm on a back-up filter. The particles were collected on a quartz fiber filter (Pallflex Products Corp., Type 2500QAT-UP). Donut-shape filters with 65x30 mm outer and inner diameters were used in impaction stages, and a 47 mm diameter circular filter was used in the backup stage, while 8-mm-thick stainless steel fiber mat with fiber diameter of 8 μm and packing density of 0.0065 was used as inertial filter in a stage prior to the backup filter^[4]. Sampling flow rate was 40 L min⁻¹ and sampling time was 3 day for each sampling to ensure sufficient amount of particles collected for PAH analysis. Total suspended particulates (TSP) were measured by the commercial portable high-volume sampler (Shibata, HV500F) where the sampling flow rate was set at a constant 500 L/min and sampling time was 24 hours. The filters used were identical-type quartz fiber filters (Advantec, QR-100) with 110-mm-diameters. All filters were pre-treated filters in a controlled environment (25°C, 50% RH) for 72 hours. Both the nanoparticle air sampler and high-volume samplers were placed at the open-roof top floors of each building every location once a month during May-December, 2010.

PAHs extraction method

All collected filter samples were then treated in the identical environment as the pre-treatment for 72 hours. A piece of each filter sample containing 4-5 mg of articulates was cut into small pieces. PAHs were extracted ultrasonically twice using 40 mL of dichloromethane for 30 min^[6]. The solution was cleaned up by filtration using a filtration syringe filter unit (0.45 μm PTFE) for

removal of insoluble particles and then 50 µL of dimethylsulphoxide (DMSO) was added for preservation of PAHs. The extracts were combined and concentrated using on a rotary evaporator to remove dichloromethane. The residues were then re-dissolved in with 450 µL of acetonitrile. Interfering compounds once again were removed with a 0.45 µm PTFE syringe filter. The filtrate was kept in a 1.5-mL amber glass vial, in a refrigerator and stored at 4°C prior to analysis.

PAHs Analysis

The 16 PAHs include Naphthalene (Nap), Acenaphthylene (Act), Acenaphthene (Ace), Phenanthrene (Phe), Anthracene (Ant), Fluorene (Fle), Fluoranthene (Flu), Pyrene (Pyr), Benzo[a]anthracene (BaA), Chrysene (Chr), Benzo[a]pyrene (BaP), Benzo[b]fluoranthene (BbF), Benzo[k]fluoranthene (BkF), Dibenz[a,h]anthracene (DBA), Indeno[1,2,3-cd]pyrene (IDP), and Benzo[g,h,i]perylene (BghiPe) were analyzed by high performance liquid chromatography (HPLC);(Agilent, 1100) with diode array detector (DAD). The mobile phase was a mixture of acetonitrile and de-ionized water with gradient elution from 35% acetonitrile to 100% acetonitrile at 25°C and flow rate of 1-1.2 mL/min^[5,6].

Results and Discussion

The total suspended particulates from ambient air at each sampling are shown in **Fig.1**. The results indicate that TSP depends on the precipitation^[1,5]. During October to December TSP decreases when the precipitation increases. However, during July to September TSP increases slightly as the precipitation increases when the RSS production is high.

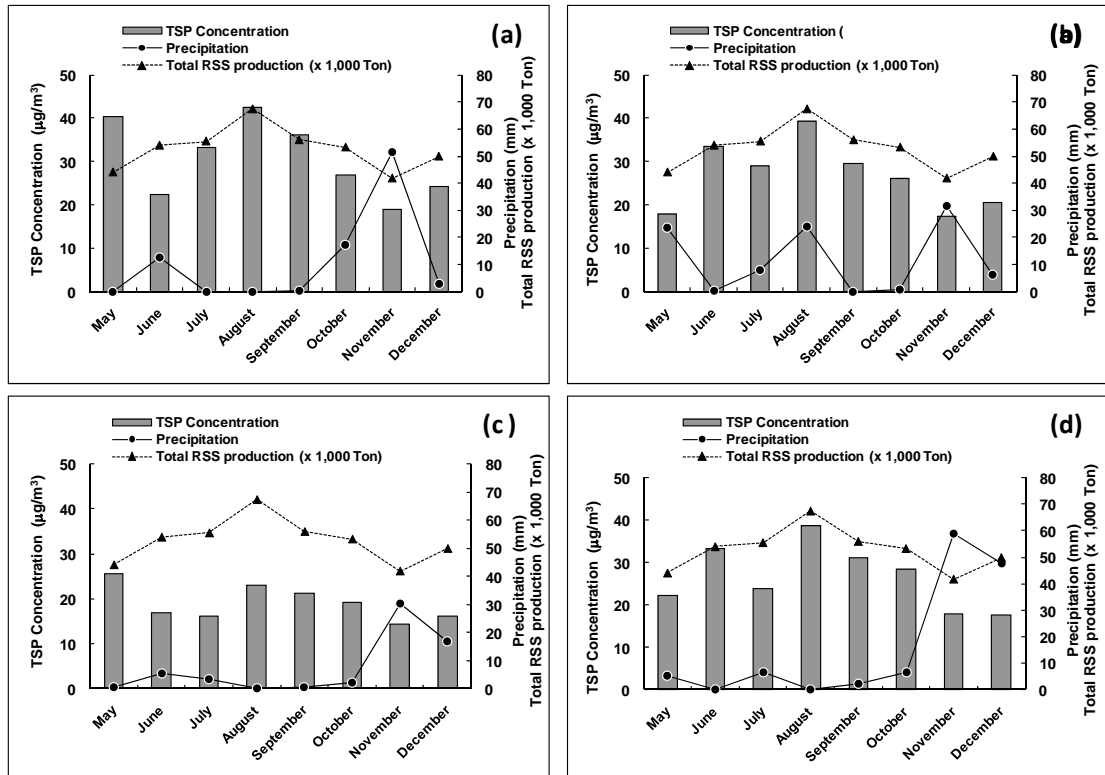


Figure 1. Relationship between the TSP, precipitation and RSS production at (a) Hat Yai, (b) Bangkhla, (c) Muang and (d) Sadao during May to December 2010

PM concentrations at each sampling site in May to December 2010 are shown in Fig.2. The highest concentration was observed in PM_{2.5-10} for every sampling site.

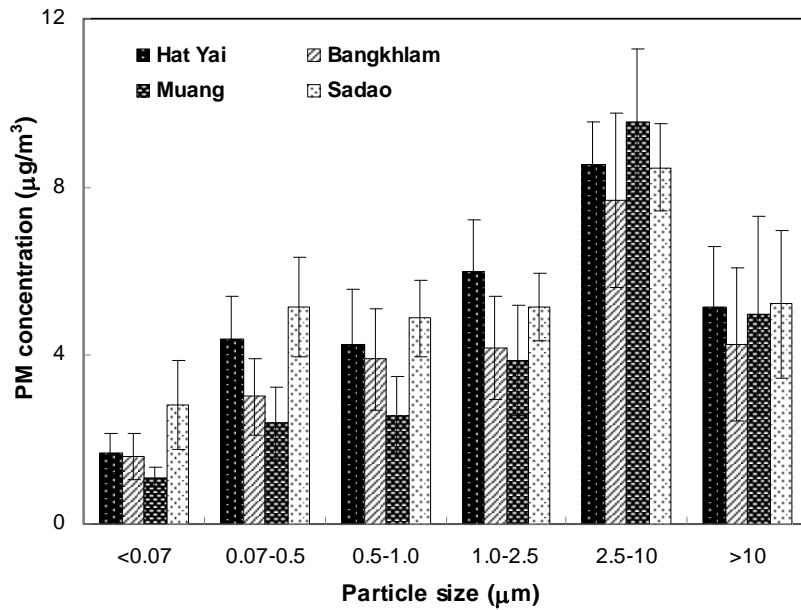


Figure 2. Particle mass concentration of each size range at different sampling sites

Total PAH concentrations are shown in **Fig.3** indicated that most of the PAHs are associated with small particles^[7] (smaller than PM_{1.0}).

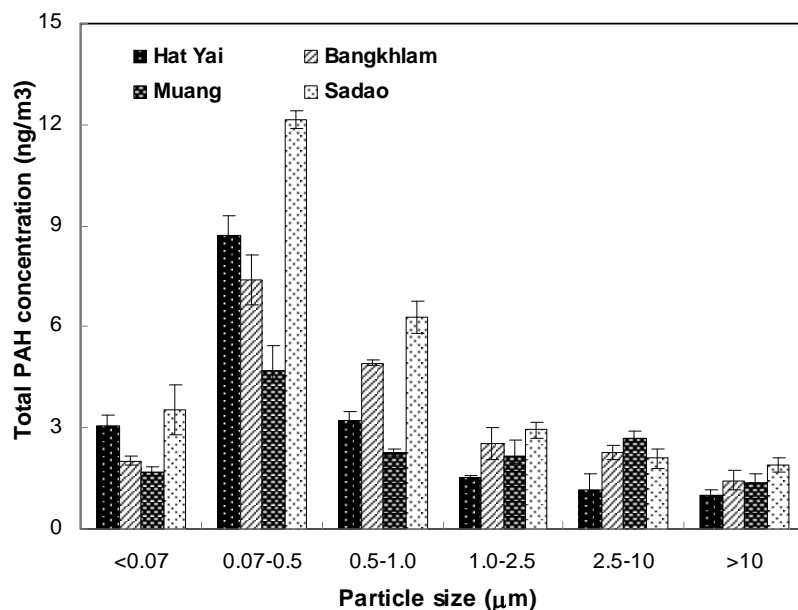


Figure 3. Total PAH concentration associated with particles size at different sampling sites.

CONCLUSION

Total suspended particulates of air sampled from each sampling site are generally low, averaging 30.61, 27.67, 19.13 and 28.64 $\mu\text{g}/\text{m}^3$ for Hat Yai, Muang, Bangkhlam and Sadao, respectively. The TSP depends on precipitation, RSS production and wind direction. TSP decreased almost linearly when the precipitation increased. The highest PM concentration was observed in $\text{PM}_{2.5-10}$ in every sampling site, while $\text{PM}_{0.07}$ fraction is rather low especially at Muang. This may be related to differences in contribution of possible emission sources. The average concentrations of total PAHs in ambient air are 18.64, 20.61, 13.27 and 28.86 ng/m^3 for Hat Yai, Muang, Bangkhlam and Sadao, respectively. The most of the PAHs are associated with small particles (smaller than $\text{PM}_{1.0}$). This behaviors of the PAH concentration is influenced by the precipitation, RSS production, and wind direction in a similar trend like those of TSP.

ACKNOWLEDGMENTS

This research has been financially supported from the Center of Excellence for Innovation in Chemistry (PERCH-CIC), Commission on Higher Education, Ministry of Education and Graduate school, Prince of Songkla University are gratefully acknowledged.

REFERENCES

- [1] Tekasakul, P.; Furuuchi, M.; Tekasakul, S. *Aerosol Air Qual Res.* 2008, 8, 265-278.
- [2] Furuuchi, M.; Tekasakul, P.; Murase, T.; Otani, Y.; Tekasakul, S; Bai, Y. *Ecotechnology Res.* 2006, 12, 135-139.
- [3] Chomanee, J.; Tekasakul S.; Tekasakul, P. *Aerosol Air Qual Res.* 2009, 9, 2071-1409
- [4] Otani, Y.; Eryu, K.; Furuuchi, M.; Tajima, N.; Tekasakul, P. *Aerosol Air Qual Res.* 2007, 7(3), 343-352.
- [5] Chomanee, J. M.Sc. Thesis, Prince of Songkla University, 2008.
- [6] Phoungthong, K. M.Sc. Thesis, Prince of Songkla University, 2010.
- [7] Furuuchi, M.; Otani, Y.; Tsukawaki, S.; Nakao, Y.; Hata, M.; Sieng, S. and Hang, P. *Asian Aerosol Conference (AAC) 2007*, vol.I, pp.41-42.

Estimation of selected heavy metals in respirable size range particulates at New Delhi (India)

Monika J Kulshrestha, Subhash Chandra, and Nahar Singh

National Physical Laboratory, New Delhi 110012

Principal Contact: Monika J Kulshrestha, Dr., Research Scientist, Radio & Atmospheric Sciences Division, National Physical Laboratory, New Delhi 110012, India.

Tel: +91-9958538995 Fax: +91-11-45609310 E-mail: monikajk@yahoo.com

Abstract

Metal aerosols are hazardous and toxic air pollutants. Continuous exposure to high concentrations of metals may cause severe health effects such as cancer. The present study reports estimation of selected metals in PM₁₀ aerosols in the urban atmosphere of one of the ten most polluted cities of the world. Aerosol samples were collected at the terrace of our institute building using PM₁₀ aerosol sampler. Selected heavy metals (Zn, Fe, Cu, Mn, Cd) were determined in these samples. Analysis results showed the highest concentration of Zn followed by Fe >Cu>Mn>Cd. The ranges of concentration of these metals were found to be 214 to 3184 ng/m³ for Zn, 411 to 1544 ng/m³ for Fe, 38 to 204 ng/m³ for Cu, 36 to 204 ng/m³ for Mn and 28 to 70 ng/m³ for Cd. The main sources of Zn are casting of different metals, rubber and chemical industries. The vehicles running on roads also contribute zinc metal. Zn is also emitted from scrape of tires. Fe comes from natural as well as anthropogenic sources. The natural source of Fe is of crustal origin while anthropogenic sources include iron and steel manufacturing units, weathering of iron in contact with moisture and air. Fe is also used as a base for construction of buildings and flyovers. Lethal exposure to Fe may affect the enzymatic activities in human beings. Cu is emitted by copper alloy industries in Delhi. There are several units installed. Mn is also used as an additive in unleaded gasoline. The sources of Cd are of anthropogenic nature. Cd is mainly used in making alloys, stabilizers in polyvinyl plastics, batteries, electroplating industries and pigments. Cd is also contributed to the atmosphere by coal combustion and mining, oil combustion, production of pyrometallurgical metals. Cd exposure may result in many respiratory and heart related diseases.

Keywords: PM₁₀ aerosols, heavy metals, anthropogenic sources, health effects

Suzhou: air quality real-time monitoring system

Francesco Petracchini¹, Catia Atturo¹, Marco Panunzi² and Andrea Ceolin²

1 CNR-IIA, Via Salaria Km 29.300, Monterotondo (Rome), Italy, 00040

2 Unitec srl Via F.L. Ferrari 31/D, Ferrara Italy, 44122

Principal Contact: Catia Atturo, dr, CNR - Institute of Atmospheric Pollution Research, Area della Ricerca di Roma 1, Via Salaria Km 29,300, Monterotondo (RM) 00016, Italy.

Tel: +390690672395 Fax: +390690672660 E-mail atturo@iaa.cnr.it

Abstract

Since much of the atmospheric pollution comes from China exhausts, there has been lately a lot of research to better understand the relation between traffic patterns and the actual spread of emissions in this context.

The objective of this project has been to develop a mobile system capable of monitoring in real time most conventional pollutants. The mobile system has been assembled in a car outfitted with a complete package of instrumentation to collect, elaborate and transfer all data in real time. The system has been developed in Italy by CNR IIA with the technological support of Unitec srl, while the actual assembly has been performed in Suzhou in order to carry out the campaign in January-February 2010. The car has been equipped with both innovative and commercial environmental probes to acquire gaseous organic compounds such as CO, NO₂, NO_x, O₃, C₆H₆, particulate PM10, PM2.5 and Volatile Organic Compounds (VOC). The package also included a weather station, a video camera, a GPS, along with a GPRS modem and a data processing unit.

All data has been processed by the on-board computer and then sent by modem each 5 sec to the base station for permanent archiving. The base station lab further processes the data; however a real-time rendering and a first analysis performed by GIS is possible directly on board as soon as the data is acquired.

At the beginning to calibrate the sensors installed in the mobile units data collected from the have been compared with those collected in the reference station. Data collected demonstrated the capability of this system to perform assessment directly on the streets and in real time. The system represents a new approach useful for researcher and policy makers to get information on air quality of Chinese cities.

Keywords: urban air quality, monitoring, GIS, traffic emissions.

Gas-Particle Distribution of Polycyclic Aromatic Hydrocarbons (PAHs) from Rubber-wood Combustion

J. Chomanee¹, M. Furuuchi², M. Hata², S. Tekasakul¹ and P. Tekasakul³

1 Department of Chemistry and Center of Excellence for Innovation in Chemistry (PERCH-CIC), Faculty of Science, Prince of Songkla University, Hat Yai, Songkhla 90112, THAILAND

2 Graduate School of Natural Science and Technology, Kanazawa University, Kakuma-machi, Kanazawa 920-1162, JAPAN

3 Department of Mechanical Engineering, Faculty of Engineering, Prince of Songkla University, Hat Yai, Songkhla 90112, THAILAND

Principal Contact: Jiraporn Chomanee, Department of Chemistry and Center of Excellence for Innovation in Chemistry (PERCH-CIC), Faculty of Science, Prince of Songkla University, Hat Yai, Songkhla 90112, THAILAND.

Tel: 66-84-313-0128 Fax: 66-74-558-841 Email address: chomanee_j@yahoo.co.th

Abstract

Gas and particle distribution of polycyclic aromatic hydrocarbons (PAHs) emission from biomass (Rubber-wood) combustion were studied in a laboratory-scale combustion tube furnace. The size distribution of PAHs in particle were collected by a 10-stage Andersen sampler equipped with an inertial-filter stage (ANIF) simultaneously, attached between 0.43 μm stage and the backup filter on binder-less quartz fiber filters. The inertial filter has a cutoff size of ~70 nm. PAHs in Gas phase were collected by using XAD-2. The sixteen PAHs compounds emitted in particle and gas phase were analyzed using a high performance liquid chromatography (HPLC) with a fluorescence detector. The BaP-TEQ was discussed in relation to gas and particle emission. Results showed that the gas-particle distribution of PAHs are varid. Nap is dominant PAH in gas phase and a larger amount of 4-6 ring PAHs are emitted in particulate phase than gas phase, especially particle in nano-size range. The 4-6 ring PAHs in particulate phase is dominated by Flu and Pyr. Moreover, the results of BaP-TEQ indicate an important of toxicity nanoparticles as PAHs carrier to the ambient.

Keywords: Gas-particle emission, PAHs, Rubber-wood, Combustion.

Formation of Non-Agglomerated Titania Nanoparticles in a Flame Reactor

Akihiro Ishibashi, Hirofumi Ozaki and Yoshiki Okada

Department of Chemical Engineering, Kansai University, 3-3-35, Yamate-cho, Suita-shi,
Osaka 564-8680, Japan

ABSTRACT

The formation of non-agglomerated titania particles by oxidation of titanium-tetra-isopropoxide (TTIP) has been studied in a methane/oxygen coflow diffusion-flame reactor. A change in the proportion of virtually non-agglomerated particles in TEM images was observed using a rapid cooling of the entire flame aerosol with a blow of cold Ar quenching gas and supercooling in a Laval nozzle placed above the flame. The proportion of non-agglomerates was 25% for TiO_2 particles produced without any cooling steps. When the quenching gas of 25 L/min Ar cooled at -70°C blew on the tip of the flame, the proportion of non-agglomerates was 70%. When the flame aerosol was supercooled in the Laval nozzle after blowing -70°C Ar quenching gas, a decrease in the aerosol temperature was induced from approximately 1500 to 300°C in 0.9 ms and, as a result, the proportion of non-agglomerates was as large as 90%. It was found that the rapid cooling in the region of the flame tip is quite effective for preventing agglomeration.

KEYWORDS

Flame aerosol reactor, Non-agglomeration, Titania nanoparticles

Introduction

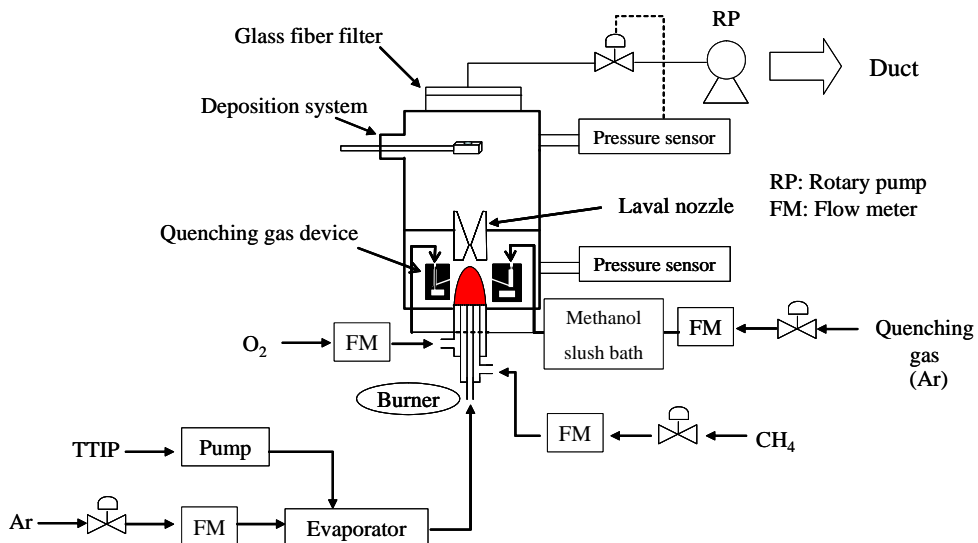
Flame aerosol synthesis has been used to produce a variety of nanoparticles with a high specific surface area^[1]. For example, fine particles such as titania, carbon black, and silica are industrially produced in cost-effective and versatile flame aerosol processes^[2].

The collisions between particles with high surface temperatures cause a coalescence of particles after their formation in flames. For the production of nanoparticles smaller than 100 nm

with a low degree of agglomeration, several studies have investigated techniques such as the introduction of a quenching gas^{[3][4]} and adiabatic expansion in a supersonic nozzle^{[5][6]}, for rapid cooling of hot nanoparticles. The blow of cold quenching gas from the outside of flames can decrease the surface temperature of the particles after production. The adiabatic expansion in a supersonic nozzle, caused by large differences in pressures between the upstream and downstream of the nozzle, can rapidly lower the internal energy of the gas and the surface temperature of the particles. Several studies have examined the production of non-agglomerated titania nanoparticles using supersonic nozzles.

However, in past studies, no quantitative data have been discussed regarding the dependence of rapid cooling conditions for quenching gases or supersonic nozzles on the degree of non-agglomeration. In this work, we quantitatively investigate the degree of non-agglomeration of titania nanoparticles produced in a coflow diffusion flame reactor under various cooling conditions by distinguishing non-agglomerates from agglomerates through virtual inspection on microscopy images of particles.

Experimental Method



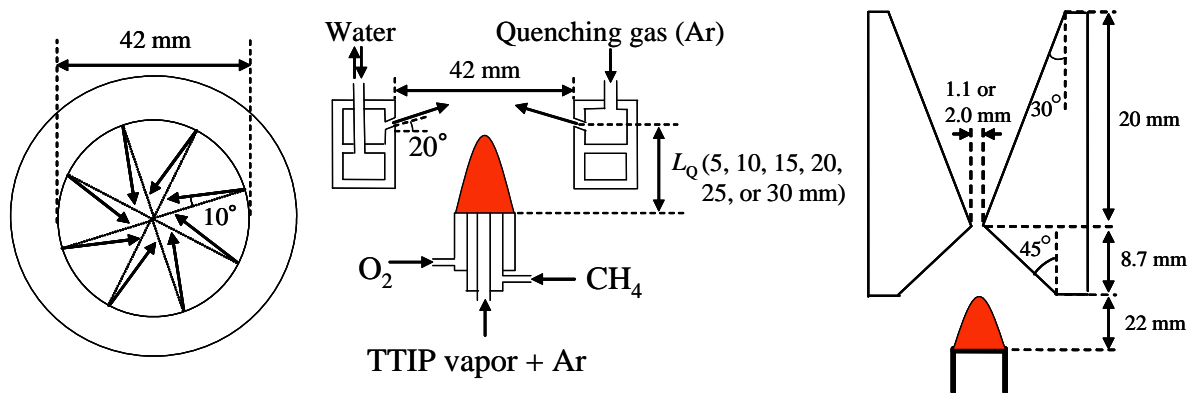


Fig.1 Experimental setup

Figure 1 shows our experimental setup. A coflow diffusion burner consisting of three concentric stainless steel tubes was used. The inner diameters of the tubes were 4.35, 7.0, and 10.0 mm. The tube wall thickness was 1.0 mm. A titanium-tetra-isopropoxide (TTIP) precursor was carried into an evaporator at 0.126 g/min using a peristaltic pump. An argon stream of 0.5 L/min carrying TTIP vapor from the evaporator flowed through the center tube, and 0.5 L/min of methane and 4.0 L/min of oxygen flowed through the second and third tubes of the burner, respectively. The height of the flame was approximately 20 mm. The evaporator, the delivery tube, and the burner were kept at 180°C to prevent the condensation of TTIP vapor. A portion of the product titania particles were collected on a transmission electron microscopy (TEM) grid set in the tip of the deposition system for analysis and the others on a glass-fiber filter. The deposition system was positioned approximately 0.2 m downstream from the Laval nozzle. Since the deposition system was far enough from the Laval nozzle, there was no influence of the Laval nozzle on the speed of the gas and the gas flowed around the deposition system at a similar velocity to the case without the Laval nozzle. Throughout the experiments, a pressure of 750 Torr was maintained in the reaction chamber.

Figure 1 also shows the details of the quenching gas device. The quenching gas ring had eight nozzles for the exit of Ar quenching gas. The nozzles were pointing upward at an angle of 20°. Each nozzle had an angular offset of 10° relative to the center axis. The quenching gas ring

was positioned above the burner mouth. The distance L_Q between the exit of the Ar quenching gas and the burner mouth was changed in the range of 5 to 30 mm. The cold Ar quenching gas at approximately -70°C was prepared by allowing it to flow through a methanol slush bath cooled at -97.8°C.

The Laval nozzle shown in Figure 1 was set at 22 mm downstream from the burner mouth. We used two types of Laval nozzles with throat diameters of 1.1 and 2.0 mm, respectively. The pressure in the downstream region of the Laval nozzle was maintained at 50 Torr.

The diameters and degrees of non-agglomeration of approximately 300 and over titania particles obtained under each condition were analyzed by TEM (JEM-2010-K, Jeol Ltd., 100 kV). In the TEM images, the isolated particles were distinguished from the overlapping particles. The former were defined as non-agglomerates, while the latter as agglomerates. The Feret diameters of agglomerates and non-agglomerates in the TEM images were obtained as the distances between their edges.

Result and Discussion

Table 1 Median diameter of agglomerates and proportion of non-agglomerates under the several conditions

Flow rate of quenching gas [L/min]	Laval nozzle	Median diameter of agglomerates [nm]	Proportion of non-agglomerates [%]
0	without	85	25
25	without	21.7	70
12.5	with	19.2	90

Table 1 shows the median diameters of agglomerates and proportion of non-agglomerates at the different flow rates of the quenching gas without/with the Laval nozzle. First, without any cooling step (Ar quenching gas blow or Laval nozzle), the proportions of non-agglomerates was 25%. Second, using only quenching gas for cooling, the proportion of non-agglomerates was 70%. It was found that Ar quenching gas flow from the gas ring positioned outside of the flame was effective for preventing agglomeration. Finally, using quenching gas and Laval nozzle, the

proportion of non-agglomerates was 90%. We obtained the largest value of the proportion of non-agglomerates in this work. We found that the supercooling of the aerosol accompanied by cold quenching gas in the Laval nozzle was quite efficient for the generation of non-agglomerated TiO₂ particles.

CONCLUSION

We have investigated the proportions of virtually non-agglomerated TiO₂ nanoparticles produced in a diffusion-flame reactor equipped with a rapid cooling system of the flame aerosol based on the blow of cold quenching gas and supercooling in a Laval nozzle. When the Laval nozzle supercooled the flame aerosol after -70°C Ar quenching gas blew on the tip of the flame, the proportion of non-agglomerates was as large as 90%. We believe that this increase in the proportion of non-agglomerates is caused by the rapid cooling of the flame aerosol from approximately 1500 to 300°C in an instant as short as 0.9ms.

REFERENCES

- [1] Ulrich, G. D.; "Flame Synthesis of Fine Particles," *Chem. Eng. News.*, **62**, 22-29 (1984)
- [2] Pratsinis, S. E.; "Flame Aerosol Synthesis of Ceramic Powders," *Prog. Energy Combust. Sci.*, **24**, 197-219 (1998)
- [3] Hansen, J. P., J. R. Jensen, H. Livbjerg and T. Johannessen; "Synthesis of ZnO Particles in a Quench-Cooled Flame Reactor," *AICHE J.*, **47**, 2413-2418 (2001)
- [4] Rulison, A. J., P. E. Miquel and J. L. Katz; "Titania and Silica Powders Produced in a Counterflow Diffusion Flame," *J. Mater. Res.*, **11**, 3083-3089 (1996)
- [5] Wegner, K., W. J. Stark and S. E. Pratsinis; "Flame-Nozzle Synthesis of Nanoparticles with Closely Controlled Size, Morphology and Crystallinity," *Mater. Lett.*, **55**, 318-321 (2002)
- [6] Wegner, K. and S. E. Pratsinis; "Nozzle-Quenching Process for Controlled Flame Synthesis of Titania Nanoparticles," *AICHE J.*, **49**, 1667-1675 (2003)

Particulate pollutants generated from co-combustion of biomass and coal fuels

P. Saetiew¹, A. Suriyawong¹, M. Hata², and M. Furuuchi²

1 Department of Environmental Engineering, Faculty of Engineering, Chulalongkorn University, Bangkok, 10330, Thailand

2 Graduate School of Natural Science and Technology, Kanazawa University, Kakuma-machi, Kanazawa, 920-1162, Japan

Principal Contact: Achariya Suriyawong, Dr., Department of Environmental Engineering, Faculty of Engineering, Chulalongkorn University, Bangkok, 10330, Thailand.

Tel: +662-218-6667 Fax: +662-218-6666 Email: Achariya.S@eng.chula.ac.th

Abstract

In the past decade, energy has been an issue of great concern worldwide. Like other countries, Thailand has been facing this energy issue, especially on energy security and its impact on environment. To mitigate the problem, one of the Thai government's energy policies is to promote energy recovered from agricultural by-products. Combustion or Co-combustion of these products with coal seems to be the most cost-effective approach. The combustion process typically results in emissions of pollutants, especially fine particles and trace elements. This paper presents the results of an experimental study of particulate emission and the fate of trace elements (As, Cr, Cu, Pb, Mn and Ni) during combustion tests of agricultural by-products and coal. Three different types of coal, including bituminous, sub-bituminous and lignite and five different types of agricultural by-products, e.g., bagasse, palm oil fiber, palm oil empty fruit bunch and rice husk were used as test fuels. The emissions from combustions of coal or agricultural by-products alone were compared with those of co-combustion of agricultural by-products with coal. The distribution/partitioning of these toxic elements between a coarse mode ash ($d_p > 0.5$ m), a submicrometer mode ash ($d_p < 0.5$ m), and flue gases was also evaluated.

Keywords: Combustion, Biomass, Coal, Heavy Metals, Pollutants

Temperature Response of the Submicron Organic Aerosol from Temperate Forests

Richard Leaitch¹, Anne Marie Macdonald¹, Peter C. Brickell¹, John Liggio¹, Steve J. Sjostedt¹, Alexander Vlasenko¹, Jan W. Bottenheim¹, Lin Huang¹, Shao-Meng Li¹, Peter S.K. Liu¹, Desiree Toom-Sauntry¹, Katherine A. Hayden¹, Sangeeta Sharma¹, Nicole C. Shantz¹, H. Allan Wiebe¹, Wendy Zhang¹, Jonathan P.D. Abbatt², Jay G. Slowik², Rachel Y.-W. Chang², Lynn M. Russell³, Rachel E. Schwartz³, Satoshi Takahama³, John T. Jayne⁴, and Nga Lee Ng⁴

1 Environment Canada, Toronto, Ontario, Canada M3H 5T4

2 University of Toronto, 80 St. George St., Toronto, Ontario, M5S 3H6, Canada

3 Scripps Institution of Oceanography, La Jolla, California, USA

4 Aerodyne Research Inc., 45 Manninng Road, Billerica, Massachusetts, USA, 01821

Principal Contact: Richard Leaitch, Dr., Environment Canada, Toronto, Ontario, Canada M3H 5T4.

Tel: 1-416-739-4616 Email: Richard.Leaitch@ec.gc.ca

Abstract

Observations from four periods (three late springs and one early summer) at two temperate forest sites in western and eastern Canada offer the first estimation of how the concentrations of submicron forest organic aerosol mass (SFOM) from the oxidation of biogenic volatile organic compounds (BVOC) vary over the ambient temperature range of 7°C to 30°C. For the measurement conditions of clear skies, low oxides of nitrogen and within approximately one day of emissions, 49 estimates of SFOM concentrations show the SFOM to increase progressively with increasing temperature, more than would be predicted from the standard terpene emissions function; at a temperature of 30°C the best fit to the SFOM observations is about 25-50% higher than would be predicted from the commonly used terpene emissions function. The difference may be made up by increased yield of SFOM from terpene oxidation as the SFOM concentrations increased, which implies a degree of self-amplification of the atmospheric SFOM. Based on the changes in ozone, there is no evidence that an increase in the oxidizing capacity of the atmosphere is responsible for the difference, but an effect from the OH radical can not be ruled out. The contribution to the SFOM from isoprene oxidation is estimated to be <5%.

Keywords: Biogenic aerosol, secondary organic aerosol, temperature

On-road Emission Factor Distributions of Individual Diesel Vehicles in Beijing and Chongqing, China

Xing Wang¹, Dane Westerdahl¹, Ye Wu², and K Max Zhang¹

1 Sibley School of Mechanical and Aerospace Engineering, Cornell University, Ithaca, New York, 14853, USA

2 Department of Environmental Science and Engineering, Tsinghua University, Beijing 100084, China

Principal Contact: Xing Wang, Ph.D candidate, Upson 127, Cornell University, Ithaca NY, 14853, USA.

Tel: 001-607-379-1378 Fax: 001-607-255-1222 Email: xw66@cornell.edu.

Abstract

We conducted field studies to characterize on-road emissions of individual diesel vehicles in multiple cities in China. In the winter 2009 campaign, we sampled over 240 individual trucks on 4 major expressways in and around Beijing as well as 60 individual buses on city streets using refined chasing techniques. During winter of 2010, we extended the work to Chongqing and sampled over 400 individual trucks on expressways in Beijing and Chongqing. In addition, a comparison study between our chasing method and a Portable Emissions Measurement System (PEMS) was carried out. The 2009 data showed that the black carbon (BC) and PM_{0.5} number emission factors (EF) for non-Beijing trucks were significantly higher than those of Beijing trucks. We identified “heavy emitters”, finding that 5% of diesel trucks were responsible for 50% of total BC emissions, and that 20% trucks were responsible for 50% of CO and PM_{0.5} number emissions and over 70% of BC emissions. This suggests that control programs might be most effective if focused on removing the heavy emitters from the road, or improving their emissions. In addition, we reported size-resolved PM_{0.5} number EF and estimated PM mass EF distributions of the heavy emitters and other individual vehicles. The BC mass emissions were shown to be highly correlated with the mass emission of particles with 100~250nm diameters, consistent with the results from laboratory dynamometer tests. The data collected from 2010 winter study are been processing and will include NOx emission factors and comparison results between the on-road chasing method and PEMS. These studies demonstrate a cost effective approach to obtain the emission characteristics of large numbers of individual on-road vehicles.

Keywords: Climate Change, Air quality, Diesel, Emission factor, Chasing study

The evaluation of PM_{2.5} by filter based and continuous measurements in Cincinnati, Ohio

Carlos Pacas¹, Xianlie Wan¹, Mingming Lu¹, and Anna Kelley²

1 Department of Civil & Environmental Engineering, University of Cincinnati, Cincinnati, OH 45221-0071

2 Hamilton County Environmental Services, Cincinnati, OH 45221

Principal Contact: Mingming Lu, Dept. of Civil and Environ. Eng. Univ. of Cincinnati, Cincinnati, OH 45221, USA.

Tel: 513-556-0996 Fax: 513-556-2599 Email: Mingming.lu@uc.edu

Abstract

The filter based methods have been “the gold standard” of PM measurement in spite of its cost and labor intensiveness. Meanwhile many continuous instruments have been employed side by side at many US sites, and the results from the continuous instruments have been used in forecasting air quality index and applications other than compliance. This goal of this study is to evaluate the data agreement of fine particulate matter (PM_{2.5}) concentrations from filter based Federal Reference Method (FRM) and continuous instruments, such as tapered element oscillating microbalance (TEOM), and β-gauge-nephelometers. The study was performed on three sites (Lebanon, Sycamore, and Taft) managed by the Hamilton County Department of Environmental Service (HCDOES), Ohio. The monitoring period ranges from April 2007 to May 2008. The concentrations from continuous monitoring were averaged in 24 hours as a diurnal level in order to compare with FRM. The linear regression was performed between continuous and FRM monthly data. According to EPA PM2.5 is considered as Class II (some details on what is Class II). Thus, the intercept and the slope of the linear regression were put into an EPA template to evaluate the equivalence of the candidate method vs. the standard (FRM). The same approach was performed with all the instruments of HCDOES. Some continuous instrument exhibited higher correlation with the FRM than others. However, Seasonal changes such as winter to spring and summer to fall might result in larger statistical differences, especially in March and October. Future analysis will be made with a non-linear regression, where the temperature and relative humidity will be included in the data analysis. Also the evaporating of volatiles organic compounds (VOC's) should be analyzed as it may also affect PM_{2.5} concentrations.

Keywords: Federal Reference Method (FRM), PM_{2.5}, continuous measurement, filter based

Dry Deposition of Sulfate on Actual Foliar of *Quercus serrata*

Hiroshi Hara, Shogo Ota, Yuki Kimura, Kyo Kitayama, and Sonoko Drothea Kimura

College of Agriculture, Tokyo University of Agriculture and Technology, Saiwaicho 3-5-8, Fuchu, Tokyo 183-8509 Japan

Principal Contact: Hiroshi Hara, Prof., College of Agriculture, Tokyo University of Agriculture and Technology, Saiwaicho 3-5-8, Fuchu, Tokyo 183-8509 Japan.

Tel: +81-42-367-5818 Email: harahrs@cc.tuat.ac.jp

Abstract

Sulfate deposited on actual foliar of a broad-leaf tree was evaluated to discuss dry deposition processes by the amount rinsed out from the sampled leaves in an experimental forest in the suburbs of Tokyo. Five samples of a 20 m high-*Quercus serrata* tree were manually collected at four heights (6m, 10 m, 14 m, and 20 m) from a 30 m-high observation tower which routinely measures meteorological parameters at six heights, and subjected to distilled-water rinsing for ion chromatographic analysis of sulfate. The deposited amount of sulfate was normalized with leaf surface.

The vertical profile of the normalized deposition showed no systematic patterns so far. The deposition of sulfate, however, was found to increase with relative humidity, which strongly suggested the wetted surface plays a key role in the deposition processes.

In order to evaluate the representativeness of the sample, 153 sample leaves were collected from a single branch of the sample stand in May 2010. The distribution showed a monomodal pattern with the following percentiles: 10%; 12.2, 25%; 15.0, 50%; 20.2, 75%; 28.3, and 90%; 44.9 micromole per square meter. The actual deposition on each sample leaf was also discussed in terms of the normalized deposition and sample position in the branch.

The results support the view that the foliar rinsing method will offer a powerful tool for studies of aerosol dry deposition to forests.

Keywords: dry deposition, sulfate, forest.

Contribution of New Particle Formation to Cloud Condensation Nuclei in the Beijing Megacity

D.L. Yue^{1,2}, M. Hu^{1,*}, R.Y. Zhang^{1,3}, Z.J. Wu⁴, H. Su⁵, Z.B. Wang¹, J.F. Peng¹, L.Y. He⁶, X.F. Huang⁶, Y. G. Gong⁷ and A. Wiedensohler⁴

¹ State Key Joint Laboratory of Environmental Simulation and Pollution Control, College of Environmental Sciences and Engineering, Peking University, Beijing 100871, China

² Guangdong Provincial Environmental Monitoring Center, Guangdong, 510045, China

³ Department of Atmospheric Science, Texas A&M University, College Station, Texas 77843, USA

⁴ Leibniz Institute for Tropospheric Research, Permoserstrasse 15, Leipzig 04318, Germany

⁵ Biogeochemistry Department, Max Planck Institute for Chemistry, Becherweg 27, Mainz 55128, Germany

⁶ Key Laboratory for Urban Habitat Environmental Science and Technology, Shenzhen Graduate School of Peking University, Shenzhen 518055, China

⁷ Research Institute of Chemical Defence, Beijing 102205, China

ABSTRACT

New particle formation (NPF) events have been recognized as an important process contributing to the cloud condensation nuclei (CCN) formation. In this study, measurement of NPF and predicted number concentrations of CCN using κ -Köhler theory were analyzed to assess the contribution of NPF to CCN. The enhancement ratios (the ratio of CCN concentrations after to before NPF) were higher under high supersaturation (S). For example, it is about 30-50% higher under $S=0.86\%$ than under $S=0.07\%$. The enhancement ratios were higher during the sulfur-poor NPF events with larger growth rates and exhibited similar seasonal variation as the growth rates with a larger value in summer than other seasons. Our results suggest that NPF events increase the CCN number concentrations by 0.4-6 times in the Megacity area of Beijing, growth rate is the key factor in the conversion of NPF to possible CCN, and organic species are implicated as the dominant contributor in facilitating the conversion of newly formed particles to possible CCN.

KEYWORDS

New particle formation; Particle growth; CCN

1 Introduction

New particle formation (NPF) events, one of the important sources of ambient aerosols, are frequently observed worldwide [1-2]. Several species, including sulfuric acid,

ammonia, organic compounds, are supposed to participate in the nucleation process and the subsequent growth of nanoparticles [3]. In addition to their potential effects on human health, NPF events lead to increased number and mass of aerosol, which modify aerosol optical properties and provide cloud condensation nuclei (CCN) to influence cloud formation. The contribution of NPF events to formation of CCN has been suggested to differ under different conditions depending on geographic locations [4] or the chemical species contributing to new particle formation [5]. Previous work on the conversion of newly formed particles to possible CCN has performed primarily on the basis of laboratory experiments [6] or simulations using a global model [7] but little on the basis of field measurements.

In this investigation, we performed an analysis of the measurement of NPF events and predicted number concentrations of CCN to assess the contribution of NPF events to the number concentration of possible CCN. Measured particle number size distributions (3-900 nm) and particle chemical composition (in PM_{2.5}) were employed to determine the possible CCN number concentrations under different water supersaturations (S) from March, 2004 to October, 2008. The dominating factor contributing to the conversion to CCN was identified through an analysis of the parameters about NPF events and the predicted CCN number concentrations.

2 Methodology

NPF events were observed by a twin differential mobility particle sizer (TDMPS)^[2] from March, 2004 to October, 2008 on the rooftop of a building (about 15 m above the ground level) on the campus of Peking University. Simultaneous measurement of particle chemical composition size distributions from 60-600 nm (vacuum dynamic diameter, corresponding to approximately 40-400 nm in Stokes diameter assuming an average particle density of 1.5 g/cm³) was performed by an Aerodyne aerosol mass spectrometer (AMS, Model HR-ToF) from August 31 to September 18, 2008. Mass concentrations and chemical compositions in fine particles (PM_{2.5}) were measured by four channel PM_{2.5} samplers and subsequent chemical analysis from 2006 to 2008.

All CCN number concentrations were calculated based on the methods introduced by Rose et al., 2008. In short, the CCN number concentration at S ($N_{\text{CCN}}(S)$) was calculated by integrating the measured aerosol size distribution above the critical dry particle diameter for CCN activation that corresponds to the values of the “effective” hygroscopicity parameter (κ) and S ^[9, 10].

3 Results and discussion

Figure 1 shows the enhancement ratios with different formation and growth rates during NPF events and in different seasons. The enhancement ratios during different types of NPF events from July 12 to September 25, 2008 are summarized in Table 1.

High particle formation rates lead to high particle number concentrations, which

may be correlated to the subsequent CCN number concentrations. Under S of 0.07-0.86%, the CCN enhancement ratios after NPF events were insensitive to the new particle formation rates. There are two plausible explanations: (1) The formation and growth of particles are two separate and self-governed processes. Larger formation rates do not necessarily correspond to larger growth rates, if freshly formed new particles do not have sufficient time to grow to the CCN size. (2) Coagulation between particles decreases the particle number concentration, leading to a reduced CCN enhancement. For the case on August 31, 2008 the ratio of coagulation loss to the formation rate ($F_{\text{coag}}/\text{FR}$) is 45%, indicating a large decrease in the particle number concentration, and hence, a reduced enhancement of possible CCN.

Large growth rates of newly formed particles facilitate the growth of freshly formed particles to the CCN size. For all NPF events between 2004 and 2008, the enhancement ratios of CCN were larger with larger particle growth rates, and the values were 1-2 times larger for NPF events with a growth rate over 6 nm h^{-1} than those with a growth rate below 3 nm h^{-1} .

The CCN enhancement ratios after NPF events were between 1.4 and 7, highest in the summer (Fig. 1), when the measured growth rates were larger. The difference in the CCN enhancement ratios among different seasons was larger with higher S . Since the effective diameter of CCN is smaller when S is higher (e.g., the activation diameter of particles to act as CCN is 237 nm at $S=0.07\%$ and 43 nm at $S=0.86\%$, respectively), it takes less time to grow to the CCN size range. Hence, our results clearly indicate that the growth rates of NPF events represent the decisive factor in the conversion of newly formed particle to possible CCN. The higher enhancement ratios after the sulfur-poor NPF events further support this result, because the measured growth rate of the sulfur-poor NPF events was nearly twice of that of the sulfur-rich type.

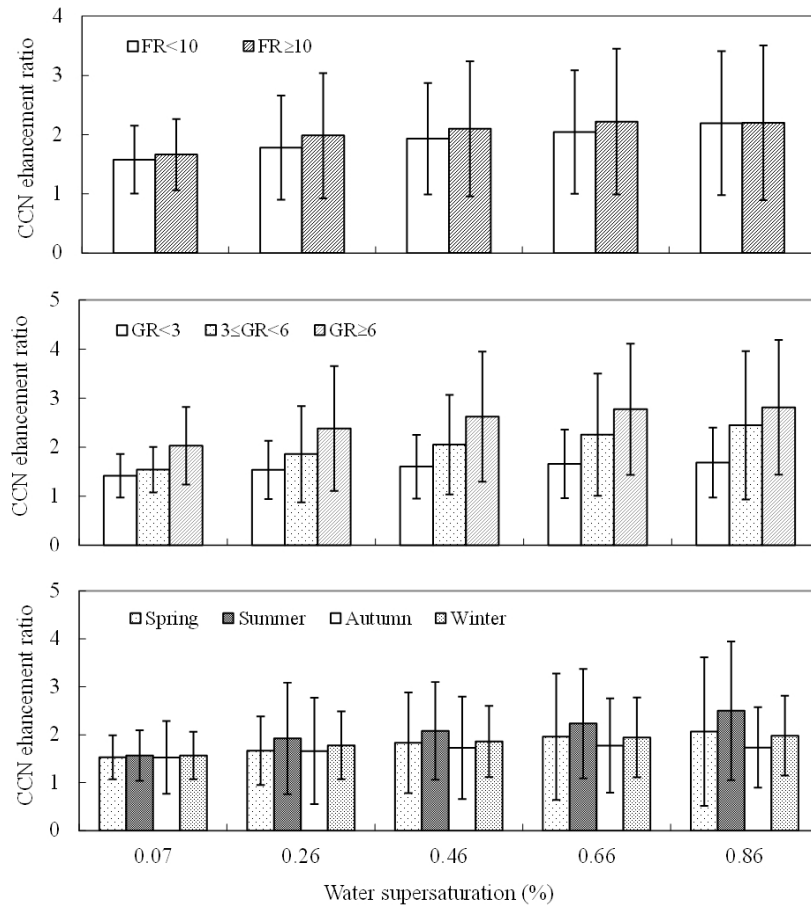


Fig. 1. Comparison of CCN enhancement ratios from NPF events with different formation rates (FR), growth rates (GR), and seasons.

Table 1 CCN enhancement ratios from the two types of NPF events

NPF event	CCN enhancement ratios under different S (mean $\pm \sigma$)				
	$S=0.07\%$	$S=0.26\%$	$S=0.46\%$	$S=0.66\%$	$S=0.86\%$
Sulfur-rich	1.4 ± 0.3	1.7 ± 0.6	2.0 ± 1.0	2.4 ± 1.3	2.8 ± 1.7
Sulfur-poor	2.0 ± 0.8	2.3 ± 1.5	2.6 ± 1.3	2.7 ± 1.4	2.9 ± 1.2
Average in All	1.7 ± 0.6	2.2 ± 1.4	2.4 ± 1.2	2.5 ± 1.2	2.8 ± 1.4

SUMMARY AND CONCLUSION

NPF events increased the number concentrations of possible CCN by 0.4-6 times and the enhancement ratios were larger for higher S . It is approximately 30-50% higher for S of 0.86% compared to 0.07%. The measured growth rate was identified as the key factor for the conversion of newly formed particles to possible CCN. The enhancement ratios were larger during the sulfur-poor NPF events and exhibited an increased larger value in summer compared to other seasons, which can be explained by the variation of the measured growth rates. OM was implicated as an important contributor in facilitating the conversion of newly formed particles to possible CCN, because the larger growth rates were mainly contributed by OM.

ACKNOWLEDGEMENTS

This work is supported by the National Natural Science Foundation of China (20977001, 21025728).

REFERENCES

- [1] Kulmala, M., Vehkamaki, H., Petajda, T., Dal Maso, M., Lauri, A., Kerminen, V.M. Birmili, W., McMurry, P.H., *Aerosol Sci.*, 2004, 35, 143-176.
- [2] Yue, D., Hu, M., Zhang, R., et al., *Atmos. Chem. Phys.*, 2010, 10, 4953-4960.
- [3] Zhang, R., Suh, I., Zhao, J., Zhang, D., Fortner, E.C., Tie, X.X., Molina, L.T., Molina, M.J., *Science*, 2004, 304(5676), 1487-1490.
- [4] Spracklen, D. V., Carslaw, K. S., Kulmala, M., et al., *Geophys. Res. Lett.*, 2008, 35(L06808), doi:10.1029/2007GL033038.
- [5] Pierce, J.R., and Adams, P.J., *Atmos. Chem. Phys.*, 2009, 9, 1339-1356.
- [6] Merikanto, J., Spracklen, D. V., Mann, G. W., Pickering, S. J., and Carslaw, K. S., *Atmos. Chem. Phys.*, 2009, 9, 8601-8616.
- [7] Yu, F., and Luo, G., *Atmos. Chem. Phys.*, 2009, 9, 7691-7710.
- [8] Wiedensohler, A., Cheng, Y. F., Nowak, A., et al., *J. Geophys. Res.*, 2009, 114(D00G08), doi: 10.1029/2008JD010884.
- [9] Petters, M. D., and Kreidenweis, S. M., *Atmos. Chem. Phys.*, 2007, 7, 1961-1971.
- [10] Rose, D., Nowak, A., Achtert, P., et al., *Atmos. Chem. Phys.*, 2010, 10, 3365-3383.

Experimental Investigation of Transient CaCO₃ Scale Formation in Commercial 90/10 Cu/Ni Tubes

M. IZADI¹, D.K. AIDUN¹, P. MARZOCCA¹ and L. TIAN²

1 Mechanical & Aeronautical Eng. Dept., Clarkson University, PO Box 5725, Potsdam, NY 13699 USA

2 Engineering Technology - Air Conditioning Eng Tech, SUNY Canton, Canton, NY 13617 USA

Principal Contact: M. IZADI, Ph.D. Candidate, Mechanical & Aeronautical Eng. Dept., Clarkson University, PO Box 5725, Potsdam, NY 13699 USA.

Tel: +13152619448 Fax: +13152686695 E-mail: izadim@clarkson.edu

Abstract

Calcium carbonate is predominantly present in cooling tower's water and is usually the principal cause of hard water. The effect of surface roughness on the transient calcium carbonate scale formation process was experimentally investigated. The real operating conditions of a tubular heat exchanger were simulated by performing prolonged experiments with durations of 48 to 300 hours. The solution used was a mixture of sodium bicarbonate and calcium chloride in de-ionized water. An on-line fouling evaluation system was developed such that the fouling resistance and pressure drop between inlet and outlet could be measured in real time. The experiments were repeated with the same procedure for 90/10 Cu/Ni tubes with different internal surface roughness. The surface was analyzed by analytical microscopy to investigate the morphology of the deposit layer. Comparison of the experimental results of smooth and rough surfaces showed a higher fouling resistance for the rough surface. A matured deposit layer was found after several hours on the smooth surface while the deposit layer on the rough surface was not matured after several days. The fouling resistance of the smooth surface with the average roughness of 34 µm was around 20% lower than that of the rough surface with the average roughness of 65 µm. Accordingly, great amount of saving can be achieved by decreasing the surface roughness of the tube in practical situations. Experimental data is important for the design, and formulating operating, and cleaning schedules of equipment.

Keywords: fouling, heat exchanger, crystallization, calcium carbonate

Are Volatile Organic Components Responsible for Driving the Oxidative Capacity of Combustion Generated Particles

Zoran Ristovski¹, Branka Miljevic¹, Nicholas Surawski¹, Svetlana Stevanovic¹, Steve Bottle², and Richard Brown³

1 International Laboratory for Air Quality and Health, Queensland University of Technology, Brisbane, Australia

2 ARC Centre of Excellence for Free Radical Chemistry and Biotechnology, Brisbane, Australia

3 School of Engineering Systems, QUT, Brisbane, Australia

Principal Contact: Zoran Ristovski, ILAQH, Queensland University of Technology, 2 George street, Brisbane, QLD 4000, Australia.

Email: z.ristovski@qut.edu.au

Abstract

There is strong evidence that organic compounds, which comprise only a small fraction of particle mass, are most responsible for the toxicity of airborne particles. The mechanisms by which these compounds cause adverse health effects still remain to be fully understood. Some recent toxicological studies indicate that particulate matter related reactive oxygen species and the resulting oxidative stress might be responsible for instigating the adverse health effects. In this study we have assessed the potential toxicological impact of combustion related particles using a novel profluorescent nitroxide probe BPEnit. The probe is weakly fluorescent, but yields strong fluorescent emission upon radical trapping or redox activity. This makes it a powerful optical sensor for radicals and redox active compounds. Measurements of the semi volatile organic fraction of combustion particles were conducted using the Aerodyne aerosol mass spectrometer (AMS) and the Volatility-DMA. A number of different diesel engines running on various blends of diesel fuel were measured. Similar to our previously published results, on logwood burning particles, a strong correlation between the organic fraction and the particle oxidative potential was observed. Sampling particles with the organic fraction removed resulted in a significant decrease in the measured redox activity. This indicates that the semi volatile organic fraction has an increased potency and redox activity and is most likely the major cause of oxidative stress.

Keywords: Reactive Oxygen Species, Diesel Exhaust, Particle Toxicity

The Study on Vertical and Temporal Variation of PM₁₀ of Yantaqu in Xi'an During Spring

Jingbo Zhao, Lan Yao, Na Xu, Zhenzhen Mu and Yuxia Li

College of Tourism and Environment, Shanxi Normal University, Xi'an, Shaanxi, China, 710062

Principal Contact: Jingbo Zhao, Professor, College of Tourism and Environment, Shanxi Normal University, Xi'an, Shaanxi, China, 710062.

Email: zhaojb104@126.com

Abstract

In order to ascertain vertical and temporal variation characteristics of PM₁₀ of Yanta area in Xi'an during spring, we observed the PM₁₀ mass concentration for 3 days of the four buildings near Changyanbao in Yanta area during Apr.3 to Apr.14 in 2010. The results showed that the PM₁₀ mass concentration was lower at the height of 1 and 51~54 meter; it was 0.029mg/m³ on average at the height of 1 meter and 0.045mg/m³ on average at the height of 51~54 meter, while PM₁₀ mass concentration was the highest at the height of 3~33 meter; it ranged from 0.089mg/m³ to 0.104mg/m³, 0.097mg/m³ on average. PM₁₀ mass concentration increased at the height of 54~81 meter, but it was lower than that at the height of 3~33 meter; it ranged from 0.042mg/m³ to 0.077mg/m³, 0.060mg/m³ on average. PM₁₀ mass concentration increased and decreased and finally increased with the increasing height. The trend was different from others' research, because this experiment was divided in height and time by more elaborates. PM₁₀ had a temporal variation with two peaks and two valleys in the day. It was the highest in the morning and lower in the afternoon and higher at night; In details, PM₁₀ mass concentration was lowest at about 06:00 and was low at about 18:00. The variation of PM₁₀ mass concentration was influenced by the stability of atmosphere, human activities, etc. Here we specially explain why PM₁₀ mass concentration was low at about 18:00. Although there are lots of human activities at about 18:00, the lower atmosphere is the most unstable at this time in one day and the wind speed is strong, which is beneficial to PM₁₀ diffusion, thus PM₁₀ mass concentration is low. The temperature at night is slightly higher than that in the morning and air convection is stronger, therefore, PM₁₀ mass concentration is higher in the morning. Due to the temperature at night is lower than the afternoon temperatures, PM₁₀ mass concentration at night is higher than that of the afternoon. In the observation period, The average value of PM₁₀ at the height of 1 to 81 meter were 0.110 mg/m³ below, all conformed to the national secondary standards. Just in terms of PM10 mass concentrations, air pollution is light and air quality is good.

Keywords: PM₁₀; Mass concentration; Vertical variation; Diurnal variation; Pollution level; Yantaqu in Xi'an

Emission and transport of carbonaceous aerosol in coastal and urban areas in China

Bing Chen¹, Ke Du², Yang Wang² and Jinsheng Chen²

1 Joint Research Unit to CSIC “Atmospheric Pollution”, University of Huelva, 21007 Huelva, Spain

2 Institute of Urban Environment, Chinese Academy of Sciences, 361021 Xiamen, China

Principal Contact: Dr. Bing Chen, Joint Research Unit to CSIC “Atmospheric Pollution”, University of Huelva, Campus EL Carmen, 21007 Huelva.

Tel: +34 959 219 811 E-mail: chenbin8976@yahoo.com.cn

Abstract

Organic and elemental carbon (OC and EC) of fine particulate matter ($PM_{2.5}$) was analyzed in the coastal urban and rural area of southeastern China, over which showed the increasing of aerosol burden. Carbonaceous matter made the average contribution to $PM_{2.5}$ about $27.7 \pm 7.1\%$ and $23.7 \pm 6.7\%$ in urban and rural areas, respectively, and the $PM_{2.5}$ concentration was bounded up with the increasing of the contribution. The intense loading of fine particulate matter was mostly accounted by the emission of carbonaceous aerosol. The annual average OC concentrations of $PM_{2.5}$ in urban and rural areas were 7.5 ± 4.4 and $7.2 \pm 4.0 \text{ g m}^{-3}$, respectively; annual average EC concentrations were 2.4 ± 0.9 and $1.3 \pm 0.6 \text{ g m}^{-3}$, respectively. The higher EC concentration in urban area than in rural area suggested significant anthropogenic emission to the urban atmosphere. OC and EC concentrations showed good positive correlation in samples from urban area during winter monsoon season, suggesting a dominant emission source (mostly traffic-related) in urban area. Comparison with previous literature reports showed the parallel spatial gradient of concentration of carbonaceous aerosol between urban and rural areas over world, suggesting the transport of air pollutants from urban atmosphere to the surrounding areas. The carbonaceous aerosol pollution in rural atmosphere can be attributed to in situ formation of secondary organic aerosol (SOA) and transport of air pollutants from urban atmosphere. The coastal urban hotspots associating with chemical transformation of gaseous organic precursors made the strong continental pollution outflow from China. The modern urban development associating

with intensive energy consumption in China should have an important role on the aerosol chemistry and physics, and ocean-continent-atmosphere carbon cycles.

Keywords: Organic carbon; Elemental carbon; PM_{2.5}; Urban; Coastal area.

Observational and modeling studies of the impacts of Indian summer monsoon circulation on spatiotemporal distributions of East Asian aerosols

Xiaodong Liu¹, Libin Yan¹, Ping Yang², Zhi-Yong Yin³, and Gerald R. North²

1 Institute of Earth Environment, Chinese Academy of Sciences, Xi'an, 710075, China

2 Texas A&M University, College Station, TX 77843, USA

3 University of San Diego, San Diego, CA 92110, USA

Principal Contact: Xiaodong Liu, Professor, 10 Fenghui south road, hi-tech Zone, Xi'an 710075, Shaanxi, China.

Email: liuxd@loess.llqg.ac.cn

Abstract

The spatial and temporal distributions of aerosol loading over East Asia are found to be closely related to variations of the Indian summer monsoon. The aerosol optical depth (AOD) at the 550 nm wavelength derived from the MODIS observations, gridded reanalysis and ground-based measurements are used. Two contrasting years, July 2002 and July 2003, which represent a weak summer monsoon year (WSMY) and an active Indian summer monsoon year (ASMY), are selected for the present study with a focus on an East Asian southern subregion (SR, 105°-120°E, 23°-32°N) and an East Asian northern subregion (NR, 115°-130°E, 35°-44°N). It is shown that the interannual variation of July mean wind intensity is a major driving factor in regulating the mid-summer spatial pattern of aerosols over East Asia, when the Indian monsoon index is anomalously large. The AOD anomalies in the NR and SR are positive and negative, respectively, during ASMY, whereas the opposite is observed during WSMY. Compared to WSMY, meridional winds and convection are stronger and more clouds and precipitation are observed in the NR subregion during ASMY. The opposite is observed in the SR subregion. We also use the regional coupled climate/aerosol model (RegCM3) and the global transport model (MOZART-4) to investigate the spatial distributions of AOD in ASMY and WSMY. The same aerosol emission inventory is used in the simulations for both cases, thus the variation in the simulated AOD distribution is primarily caused by the circulation pattern differences. The AOD over southern China is greater in WSMY, but the greater AOD is simulated over northern China and Korean Peninsula in ASMY. The above spatial-temporal variation pattern of aerosols over East Asia illustrates the non-negligible role of transport and dispersal mechanisms associated with the Indian summer monsoon in the region.

A significant contribution of aerosol and dust to Lake Qinghai, NE Tibetan Plateau

Zhangdong Jin and Fei Zhang

State Key Laboratory of Loess and Quaternary Geology, Institute of Earth Environment, Chinese Academy of Sciences, Xi'an 710075, China

Principal Contact: Zhangdong Jin, Prof., State Key Laboratory of Loess and Quaternary Geology, Institute of Earth Environment, Chinese Academy of Sciences, Xi'an 710075, China.

Tel: +86-29-88329660 Email: zhdjin@ieecas.cn

Abstract

Chemical composition of water and sediment is affected by various natural factors including the chemical composition of catchment rocks and soils, climatic variables, and aerosol and dust. The dust input to the rivers/lakes is likely important and its role in influencing the water and sediment chemistry needs to be quantified. However, little attention has been paid to the aerosol and dust contribution to the lake system. A series of our recent researches on Lake Qinghai indicate that the eolian dust has a significant contribution to both water and sediment.

Our data on recent lake sediments showed that part of potentially harmful elements were via the atmosphere. The average anthropogenic Pb flux in Lake Qinghai since the 1960s is approximately $12.2 \pm 3.5 \text{ mg/m}^2/\text{a}$. By analyzing water samples seasonally from the rivers and rain within the Lake Qinghai catchment, we found that dissolved compositions of the waters, in particular Cr, B, and Rb, were strongly influenced by eolian dust input. The results suggested that dry/wet atmospheric input contributes 36–57% of the total dissolved cations to the river waters. The eolian dust input was focused on the springtime, resulting in a higher flux of TDS and dissolved components during springtime than those during other seasons. Furthermore, an elemental input-output model showed that atmospheric input accounts for ~65% of the total inputs to the modern Lake Qinghai sediments.

Related papers

- Jin Z D, Han Y M, Chen L. Past atmospheric Pb deposition in Lake Qinghai, northeastern Tibetan Plateau. *Journal of Paleolimnology*, 2010, 43: 551-563
- Jin Z D, You C F, Yu J. Toward a geochemical mass balance of major elements in Lake Qinghai, NE Tibetan Plateau: A significant role of atmospheric deposition. *Applied Geochemistry*, 2009, 24: 1901-1907
- Jin Z D, You C F, Yu T L, et al. Sources and flux of trace elements in river water collected from the Lake Qinghai catchment, NE Tibetan Plateau. *Applied Geochemistry*, 2010, 25: 1536- 1546
- Zhang F, Jin Z D, Hu G, et al. Seasonally chemical weathering and CO₂ consumption flux of Lake Qinghai river system in the northeastern Tibetan Plateau. *Environmental Earth Sciences*, 2009, 59: 297-313

Parameters Influencing Analytical Reliability of Sulfur Speciations in Aerosol Samples Using Sulfur K-Edge X-Ray Absorption Near-Edge Structure (XANES)

Siwatt Pongpiachan^{1,2}, Warangkana Na Phatthalung³, Wantana Klysubun⁴, Kanjana Thumanu⁴, Kin Fai Ho², and Junji Cao²

1 School of Social and Environmental Development, National Institute of Development Administration (NIDA), 118 Moo 3, Sereethai Road, Klong-Chan, Bangkapi, Bangkok 10240, Thailand

2 SKLLQG, Institute of Earth Environment, Chinese Academy of Sciences (IEECAS), Xi'an 710075, China

3 Faculty of Environmental Management, Prince of Songkla University, Hat-Yai, Songkla 90120, Thailand

4 Synchrotron Light Research Institute (Public Organization), 111 University Ave. PO Box 93, Nakhon Ratchasima 30000, Thailand

Principal Contact: Dr. Siwatt Pongpiachan, Assist. Prof., School of Social and Environmental Development, National Institute of Development Administration (NIDA), 118 Moo3, Sereethai Road, Klong-Chan, Bangkapi, Bangkok 10240, Thailand.

Tel: +66-89637-2211, +66-27273113 E-mail: pongpiajun@gmail.com

Abstract

This paper aims to enhance the credibility of applying the sulfur K-edge XANES spectrum as an innovative “fingerprint” for characterizing environmental samples. The sensitivities of sulfur K-edge XANES spectra of aluminium sulfate ($\text{Al}(\text{SO}_4)_3$), manganese sulfate (MnSO_4), zinc sulfate ($\text{ZnSO}_4 \cdot 7\text{H}_2\text{O}$), potassium thiosulfate ($\text{K}_2\text{S}_2\text{O}_3$), chromic sulfate ($\text{Cr}_2(\text{SO}_4)_3 \cdot 15\text{H}_2\text{O}$), cobalt sulfate ($\text{CoSO}_4 \cdot 7\text{H}_2\text{O}$), nickel sulfate ($\text{NiSO}_4 \cdot 6\text{H}_2\text{O}$) and copper sulfate ($\text{CuSO}_4 \cdot 5\text{H}_2\text{O}$) detected by two different detectors, namely Lytle Detector (LyD) and Germanium Detector (GeD) were studied and compared. Further investigation on “self-absorption” effect revealed that the maximum sensitivities of sulfur K-edge XANES spectra were achieved when diluted eight sulfur compound standards with boron nitride (BN) at the mixing ratio of 50:50 coupled with GeD. The “particle-size” effect on sulfur K-edge XANES spectrum sensitivities was examined by comparing signal-to-noise ratios of total suspended particles (TSP) and PM_{10} collected at three major cities of Thailand, namely Chiang-Mai, Bangkok and Hat-Yai. The analytical results have demonstrated that the signal-to-noise ratios of sulfur K-edge XANES spectra were positively correlated with sulfate content in aerosols, and negatively connected with particle sizes.

Keywords: Sulfur K-edge XANES spectrum, Lytle Detector, Germanium Detector, Sulfur Speciation, TSP, PM_{10}

Carbonaceous and Ionic Components of Atmospheric Fine Particles in Beijing and its Impacts on Atmospheric Visibility

Jiamao Zhou¹, Renjian Zhang² and Junji Cao¹

1 SKLLQG, Institute of Earth Environment, Chinese Academy of Sciences, Xi'an, 710075 China

2 Institute of Atmospheric Physics, Chinese Academy of Sciences, Beijing, 100029 China

Principal Contact: Jiamao Zhou, Engineering, Institute of Earth Environment, Chinese Academy of Sciences, 10 Fenghui South Road, Hi-tech Zone, Xi'an, Shaanxi, 710075 China.
Tel: +86-29-88326128 Fax: +86-29-88320456 Email: zjm@ieecas.cn

Abstract

A ground-based observation of fine particles ($PM_{2.5}$) in Beijing was carried out continuously in 2006. The carbonaceous and ionic components as well as their distribution characteristics and seasonal variation were obtained. Annual mean mass concentration of $PM_{2.5}$ was $176.57 \pm 100.29 \mu\text{g}/\text{m}^3$. Remote dust and local dust by raised by strong wind in spring had considerable contribution to $PM_{2.5}$ mass concentration. Carbonaceous and water-soluble ionic components had significant seasonal variation, associated with diverse emission sources, different meteorological condition in different season and different formation mechanism of secondary aerosol ion. Comparing studies under different synoptic conditions suggested that the $PM_{2.5}$ pollution was mainly controlled by remove source transportation, but haze synoptic situation controlled by local pollution. The relationship between $PM_{2.5}$ and visibility was anti-correlation, Relationships of Concentrations of NH_4^+ , SO_4^{2-} , NO_3^- with $PM_{2.5}$ concentration in wither can be described using power function fitting.

Keywords: $PM_{2.5}$; OC; EC; Ion; Visibility

Contrastion and Investigation of Air quality in winter and summer in the portary storage-room of Museum of Terra-Cotta Army of Qin dynasty

Hua Li^{1,3,4}, Junji Cao^{1,2}, Yuan Gao⁵, and Bo Rong³

1 Institute of Earth Environment, Chinese Academic of Sciences, State Key Laboratory of Loess and Quaternary Geology, Xi'an 710075

2 Department of Environment Sciences and Engineering, Xi'an Jiaotong University, Xi'an 710049

3 Museum of terra-cotta army of Qin dynasty, Xi'an 710600

4 Graduate university of postgraduate, Chinese Academic of Sciences

5 Shaanxi History Museum

Principal Contact: Hua Li, Prof., Institute of Earth Environment, Chinese Academic of Sciences, Xi'an 710075, China.

Tel: 13772123777 Email: llhh669@sohu.com

Abstract

From Jan 30th to Mar 3rd (summer), Jul 28th to Aug 22nd (winter), 2008, A series of indoor air sample collection were conducted in the storage-room of museum of terra-cotta army of Qin dynasty to investigate air quality. Minivol portable aerosol sampler was used to collect PM_{2.5} samples, while passive Ogawa sampler was aimed to collect NH₃. Together with the mass concentration of SO₂ and NO₂ co-existed in air, The result shows that the average indoor PM_{2.5} mass concentration is 76.1 $\mu\text{g}/\text{m}^3$, outdoor PM_{2.5} mass concentration is 153.9 $\mu\text{g}/\text{m}^3$. in summer the average indoor PM_{2.5} mass concentration is 62.8 $\mu\text{g}/\text{m}^3$, outdoor PM_{2.5} mass concentration is 113.4 $\mu\text{g}/\text{m}^3$. Water-soluble ion of PM_{2.5} in the storage-room is mainly made up of SO₄²⁻, NO₃⁻ and NH₄⁺, there exist certain gases pollution Inside. Most of the content, by comparison, same fraction in winter is higher than that in summer. Outdoor is higher than indoor. Whereas in term of OC, outdoor is higher than indoor in winter, while indoor is higher than outdoor in summer, which indicated there still indoor OC source in summer.

Keywords: The Museum of Terra-Cotta Army of Qin dynasty, PM_{2.5}, water-soluble ion, gases pollution

Characterization of Carbonaceous aerosol and gaseous pollutants over urban air, India

S. Tiwari¹, D.S. Bisht¹, A.K. Srivastava¹, P. Pragya², and P.D. Safai¹

1 Indian Institute of Tropical Meteorology, Pune

2 S.C. P. G. College, Ballia, Uttar Pradesh -477001

Principal Contact: Suresh Tiwari, Dr. Indian Institute of Tropical Meteorology, New Delhi Branch, Prof. Ram Nath Vij Marg, R-Block, New Rajinder Nagar, New Delhi-110060.

E-mail: smbtiwari@tropmet.res.in

Abstract

Measurements of black carbon (BC), CO, NO_x and PM_{2.5} were conducted at five locations [Indian Institute of Tropical Meteorology (IITM) Delhi Branch, Delhi University (DU), Talkatora Stadium (TS), Jawahar Lal Nehru Stadium (JNS) and Major Dhyanchand Stadium (MS)] in National capital Territory of Delhi, India from 1st September 2010 to 21st January 2011. This is the first time spatial measurement was conducted at Delhi, a continental urban location in northern part of India. Spatial and temporal variability in the black carbon concentrations were explored by examining the diurnal, weekday/weekend, and day and night variations at these sites. The overall mean concentration of BC (Aethalometer) was very high, ranging from 0.6 to 61 $\mu\text{g}/\text{m}^3$, with a mean of 13.4±9.9 $\mu\text{g}/\text{m}^3$. Low concentration was observed at JNS (9.24 $\mu\text{g}/\text{m}^3$) however the highest was at DU (16.31 $\mu\text{g}/\text{m}^3$). The mean PM_{2.5} mass was 149.6 $\mu\text{g}/\text{m}^3$, and varied from 4.9 to 805 $\mu\text{g}/\text{m}^3$, far in excess of US proposed air quality standard and Indian air quality standards of annual average of 15 $\mu\text{g}/\text{m}^3$ and 40 $\mu\text{g}/\text{m}^3$ respectively. It was also observed that BC tracked PM_{2.5} and contributed about 9% to the fine particle mass measured at IITM site. High concentration (80.13 $\mu\text{g}/\text{m}^3$) of BC was observed at DU on 13.1.2011 due to increased soot particle concentrations, large emissions from biomass burning and also due to shallow and stable nature of the atmospheric boundary layer during winter. Diurnal BC behavior was observed during weekday as well as weekend consistent with traffic patterns and atmospheric mixing conditions. Associations of black carbon with gaseous pollutants such as CO, and NO_x are also explored to identify the temporal variations in their emissions. It was found that the concentrations of black carbon vary in response to the interplay of source activity, meteorological conditions, and spatial factors.

Keywords: Black carbon, diurnal variations, weekday/weekend, diurnal, Aethalometer, PM_{2.5}

Community composition and granularity distribution of airborne bacteria in summer in Guangzhou

Chaojie Song¹, Qiming Tan¹, Xianliang Chen¹, Rongjie Shi¹ and Xinyu Chen^{2,*}

1 Preventive Medicine Grade 2005, Guangzhou Medical College, Guangzhou 510182

2 Department of Pathogenic Biology, Guangzhou Medical College, Guangzhou 510182

Principal Contact: Chaojie Song, preventive medicine-majored student of Guangzhou

Medical College. E-mail: scj_0317@yahoo.com.cn;

Xinyu Chen, Tel/Fax: 86-20-81340200 E-mail: chenxinyu1357@163.com

Abstract

The study on community composition and granularity distribution of airborne bacteria was carried out in clean district and crowded district of Guangzhou. In haze weather period, the bacterium aerosol was tested on its category, particle size and count using particle impact collection. Results show that 15 species out of 8 genera were identified in clean district, among which 10 species from 4 genera were Gram-positive making up 66.5% and the rest 5 species of 4 genera were Gram-negative; and in crowded district 10 species of 4 genera were identified, with 9 species from 3 genera Gram-positive making up 88.9% and 1 from the rest 1 genus Gram-negative. The dominant bacteria groups in clean district are *S.lugdunensis*, *S.simulans* and *B.subtilis*. The dominant bacteria groups in crowded district are *S.hominis*, *S.lugdunensis* and *S.simulans*. In clean district and crowded district the granularity distribution of the bacterium aerosol remains consistent with 77.6%~93.7% bacterium aerosol settling in the 2~5 levels where this section of particle sizes is similar to the human lower respiratory tract. The bacteria concentrations in crowded district are much more than those in clean district and in both district the bacteria concentrations at 12:00 and 17:00 are much lower than those at 8:00 and 23:00.

Keywords: bacterium aerosol, bacteria community, granularity distribution, clean district, crowded district.

Emission of primary carbonaceous aerosol and formation pathways of secondary organic aerosol in the PRD

Nan Li¹, Tzung-May Fu², Junji Cao^{1,3}, Nanying Cao⁴, Shuncheng Lee⁴, and Junyu Zheng⁵

1 Division of Aerosol and Environment, Institute of Earth Environment, Chinese Academy of Sciences, No.10 Fenghui South Road, Xi'an, 710075

2 Department of Atmospheric and Oceanic Sciences, School of Physics, Peking University, No. 9 Chengfu Road, Haidian District, Beijing, 100871

3 Institute of Global Environmental Change, Xi'an Jiaotong University, No.28 Xianning West Road, Xi'an, 710049

4 Department of Civil and Structural Engineering, The Hong Kong Polytechnic University, Hung Hom, Kowloon, Hong Kong

5 College of Environment Science and Engineering, South China University of Technology, No.381 Wushan Road, Tianhe District, Guangzhou, 510641

Principal Contact: Tzung-May Fu, Professor, Peking University, No. 9 Chengfu Road, Haidian District, Beijing, China, 100871.

Tel: +86-10-62753221 Fax: +86-10-62751094 Email: tmfu@pku.edu.cn

Abstract

Carbonaceous aerosols, including elemental carbon aerosol (EC) and organic carbon aerosol (OC), are important components of atmospheric fine particulate matter (PM), particularly in the Pearl River Delta (PRD) region. Both EC and OC are emitted directly to the atmosphere by combustion. OC can also be formed in the atmosphere as part of secondary organic aerosol (SOA), which is produced by oxidation products of volatile organic compounds. We use the CMAQ regional chemical transport model to simulate seasonal EC and OC concentrations and compare model results to observations, with the goal of better quantifying the primary and secondary sources of carbonaceous aerosols in the PRD region. We include in the model current best “bottom-up” estimates of emissions from anthropogenic and biomass burning sources, as well as updated secondary formation mechanisms. In particular, we take into account the SOA production via irreversible uptake of dicarbonyls by aqueous particles. Our model results will be compared to observations to optimize emission inventories in the PRD region.

Keywords: Carbonaceous aerosol, secondary organic aerosol, emission, CMAQ

Elemental characteristics of fine-grained (<16 μ m) surficial samples from major Asian dust source regions

Feng Wu^{1*}, Youbin Sun¹, Ryuji Tada², Junji Cao¹, Yuko Isozaki², Hongyun Chen^{1,3}

1 State Key Laboratory of Loess and Quaternary Geology, Institute of Earth Environment, Chinese Academy of Science, Xi'an 710075, China

2 Department of Earth and Planetary Science, University of Tokyo, Tokyo 113-0033, Japan

3 Graduate University of Chinese Academy of Sciences, Beijing 100049

Principal Contact: Dr. Feng Wu, State Key Laboratory of Loess and Quaternary Geology, Institute of Earth Environment, Chinese Academy of Science, Xi'an 710075, China.

Tel: +86-29-88316017 Fax:+86-29-88320456 E-mail: kurt_wf@ieecas.cn

Abstract

Spatial difference in the elemental concentrations and/or their ratios of the surface samples in Asian dust source regions is the basis to determine their application in the source tracing of Asian dust. While several elemental ratios have been employed to distinguish the dusts from northern and western China, the approach was challenged recently because of the inclusion of grain-size sorting effect and limited sampling coverage in previous study. Here we carried out a systematic analysis of elemental geochemistry of fine-grained (< 16 μ m) fractions in the surface samples collected from arid and semi-arid regions of Northwestern China, including Taklimakan desert, Badain Juran Deserts and Qaidam Basin. The results showed that the ratios of most weathering-resistant elements to Al exhibit insignificant spatial difference among different source regions, implying that the Al-normalized elemental ratios cannot be used to distinguish fine dusts originated from these source regions. In contrast, Na/Al, Mg/Al, Ca/Al and Sr/Al showed large difference among these source regions, likely due to different pattern of modern temperature and precipitation in these regions. Since these four elemental ratios are sensitive to climatic changes and variable in different tempo-spatial scales, it is suggested that further research is needed to verify whether these ratios can be used as source tracers for paleo-dust cycling (i.e., Chinese loess).

Keywords: Asian inland, Arid and semi-arid regions, fine fractions of surface soil, elemental ratios.

Characterization and Conditioning of Fly Ashes Collected from Petroleum Coke Circulating Fluidized Bed Combustor

Li-Chi Liu¹, Hong-Ying Tseng¹, and Hsiu-Po Kuo^{1,2}

1 Department of Chemical and Materials Engineering, Chang Gung University, Tao-Yuan, Taiwan 333

2 Green Technology Research Center, Chang Gung University, Tao-Yuan, Taiwan 333

Principal Contact: Hsiu-Po Kuo, A/Professor, Department of Chemical and Materials Engineering, Chang Gung University, Tao-Yuan, Taiwan 333.

Tel: +886-3-2118800-5488 Fax: +886-3-2118700 Email: hpkuo@mail.cgu.edu.tw

Abstract

Low grade fossil fuels contain high percentage of sulfur and sulfur dioxides are often produced after combustion. To avoid the emission of sulfur dioxides, calcium carbonates are frequently acted as the in situ sulfur sorbent. In this work, the fly ashes collected from a commercial scale 125 MW petroleum coke circulating fluidized bed combustor are analyzed and conditioned for further applications. Since calcium carbonates are used as the desulphurization sorbent, fly ashes are mixtures of calcined calcium oxides, sulfated calcium sulfates, carbon coke, alumina oxide and silica dioxide. The complex composition of fly ashes makes further applications of the fly ashes difficult. Without appropriate conditioning, fly ash land disposal may cause environmental problems. In this study, fly ashes react with steam in varies conditions. Fly ashes are analyzed by BET, XRD, EDS and TGA before and after the hydration reaction. The wrapped calcium oxides transform to calcium hydroxide after the hydration reaction, causing an increasing of the specific surface area. With further granulation process caused by the cementitious calcium hydroxide, the produced hydrated fly ash granules can be recycled into the circulating fluidized bed combustor for desulphurization.

Keywords: Fly ash, Hydration reaction, Circulating fluidized bed

3-dimensional Simulation of Micro Virtual Impactor

Y.H. Joe¹ and J. Hwang^{1*}

(Affiliation, Times New Roman 12-pt., left-justified)

1 School of Mechanical Engineering, Yonsei University, Sinchon-dong, Seodaemun-gu, Seoul, Korea, 120-749

ABSTRACT

In this study, we examined the fluid flow and particle motion in the virtual impactor (VI) by 3-dimensional numerical simulation using computational fluid dynamics (CFD). Also, we calculated collection efficiency and wall loss of the MVI and compared with previous experimental results by other researcher. A commercial software, GAMBIT (2.3.16, Fluent Inc.) was used to generate geometry and mesh, and another commercial software, FLENT (6.3.26, Fluent Inc.) was used to calculate flow and particle motion. The Eulerian modeling approach and laminar, RNG k- ϵ viscous model was used to calculate flow motion. Discrete particle motion was calculated by the Lagrangian modeling approach. For calculate the collection efficiency, we took tracking each particle's final destination from their various initial positions, and calculated particle concentration distribution at the initial position, inlet, with Eulerian method. In conclusion, the calculated geometric cut-off diameter (GCD) of VI was 1.57 μm , and maximum wall loss (MWL) was 38.8%. These results were larger than experimental results (0.57 μm for GCD, 5%p. for MWL) of previous work, but shape of the collection efficiency curve are very similar to experiment result.

KEYWORDS

Virtual impactor, Simulation, Collection efficiency, Particle Concentration

Introduction

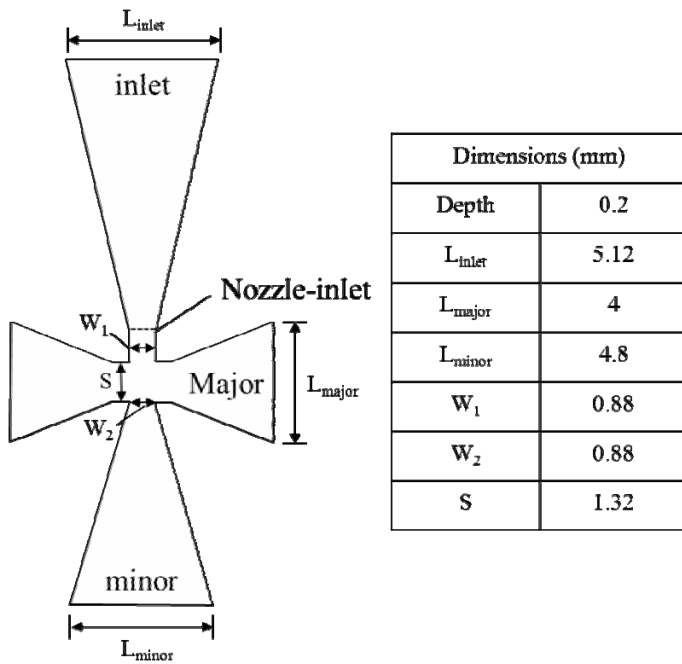
VI that function on the principle of inertial impaction for particle size classification has traditionally been used. Many researchers have carried out experiments or computational simulations in 2-dimensional to find characteristics and performances of VI [1][2][3]. In previous CFD study, the characteristics of VI are investigated by the particle motion equation and Lagrangian approach. Because they used the Lagrangian approach, the particle injection rate at the specific point in the inlet channel is assumed as a constant. However, the particle injection position at inlet channel is the significant factor for determining particle separation characteristics on the VI[4]

In this study, we examined the flow of the fluid and the behavior of particle motion in the VI by 3-dimensional numerical simulation with the CFD program. To calculate the collection efficiency, we took tracking the final destination of each particle with their various initial computation nodes, and calculated particle concentration distribution at the each initial node.

Experimental Methods

For CFD analysis, we used the commercial software, GAMBIT (2.3.16, Fluent Inc.), to construct geometry and mesh, and another commercial software, FLENT (6.3.26, Fluent Inc.) for calculating the flow and checking the particle motion. We took the geometry which the condition of Kim et. al.'s experimental research for simulation of the VI and compared with their experimental results (Fig. 1)[5]. Their experimental result is like below. The GCD is $0.95 \mu\text{m}$, and the MWL is 33.5% when the flow rates are $5.0 \times 10^{-6}\text{m}^3/\text{s}$, $4.5 \times 10^{-6}\text{m}^3/\text{s}$ (90% of inlet flow rate), $0.5 \times 10^{-6}\text{m}^3/\text{s}$ (10% of inlet flow rate) at inlet, major and minor channel, respectively. The mesh is gradually refined until grid-independent results are achieved; we select about 500,000 computational elements.

Figure 1. Geometry and dimensions of VI



We analyzed it with three steps. First, we calculated the flow motion in VI with continuity and Navier-Stokes equation, the Eulerian modeling approach. In addition, we applied laminar model and RNG k- ϵ viscous model on the simulation. The boundary condition of the inlet

channel was modeled as a velocity inlet ($v = 5.371$ m/s), velocity outlet ($v = 3.125$ m/s) at major channel, and no slip condition at each wall boundary. At minor channel, we assumed that the flow is exhausted at the atmosphere, so, we took the boundary condition of pressure outlet and set the static pressure as 101325pa on the minor channel (table 1). Second, particle concentration was calculated by UDS (user define scalar) method, eq.1 [6].

$$\frac{\partial C^*}{\partial t} + \frac{\partial}{\partial x_i} (\rho_p u_p C^* - \Gamma \frac{\partial C^*}{\partial x_i}) = 0 \quad (\text{Eq.1})$$

Where ρ_p is particle density, u_p is particle velocity, C^* is particle concentration ratio of inlet channel and each points, Γ is diffusivity, can be calculated by particle diffusivity equation, eq.2.

$$\Gamma = \frac{C_c K_B T}{3\pi\mu d_p} \quad (\text{Eq.2})$$

Where K_B is Boltzmann constant, C_c is Silp-correction factor, can be expressed by eq.3, T is Temperature of particle, μ is fluid viscosity, d_p is particle diameter, and λ is fluid mean free path.

$$C_c = 1 + 1.257 \frac{2\lambda}{d_p} + 0.40 \frac{2\lambda}{d_p} \exp[-1.10 \frac{d_p}{2\lambda}] \quad (\text{Eq.3})$$

The velocity profile of the result of the first step was used to the boundary condition of the velocity, $C^* = 1$, and $C^* = 0$ as the boundary conditions are used at inlet, and wall boundary for particle UDS equation. Particles ranging from 0.2 to 3 μm in size were used.

Finally, the motion of each discrete particle was calculated by the particle momentum equation, the Lagrangian modeling approach, in the eq.4.

$$\frac{du_p}{dt} = \frac{3\mu}{\rho_p d_p^2} \frac{C_D \text{Re}}{24} (u - u_p) \quad (\text{Eq.4})$$

Where C_D is particle drag coefficient, Re is relative Reynolds number, which is defined as eq. 5.

$$\text{Re} = \frac{\rho d_p |u_p - u|}{\mu} \quad (\text{Eq.5})$$

Brownian diffusion and Staffman lift force were neglected in the simulation. We calculated the efficiency (η) of the VI collection, and the wall loss (W.L.) by eq.6 and eq.7, and compared each conditions result with experimental data.

$$\eta = \frac{\sum (C_i^* V_i A_i)_{\text{minor}}}{\sum [(C_i^* V_i A_i)_{\text{major}} + (C_i^* V_i A_i)_{\text{minor}}]} \quad (\text{Eq.6})$$

$$W.L. = 1 - \frac{\sum [(C_i^* V_i A_i)_{\text{major}} + (C_i^* V_i A_i)_{\text{minor}}]}{\sum (C_i^* V_i A_i)_{\text{nozzle-inlet}}} \quad (\text{Eq.7})$$

Where V is velocity that is vertical component of nozzle-inlet surface, A is a face area, i means cells at each nozzle-inlet, and major, minor mean each value at nozzle-inlet, but throw out to major or minor channel, respectively.

Results and Discussion

In conclusion, the calculated GCD of VI was 1.46 μm , and MWL was 35.3% at case 1-1. In case of 1-2, GCD was 1.48 μm , MWL was 34.0%. In case of 1-3, GCD was 2.36 μm , MWL was 30% (Fig 2), and GCD was 1.56, 1.56, 1.82 μm , MWL was 38.4%, 38.4%, 38.8% was calculated in an order at case 2-1, 2-2, and 2-3(Fig 3). In the results (case 1) of the laminar viscosity model, GCD and MWL were closer to experimental results than RNG k- ϵ viscous model results (case 2). However, in the respect of the shape of the collection efficiency curve, RNG k- ϵ viscous model is more accurate than laminar viscosity model.

Figure 2. Particle collection efficiency and wall loss of VI at laminar viscosity model

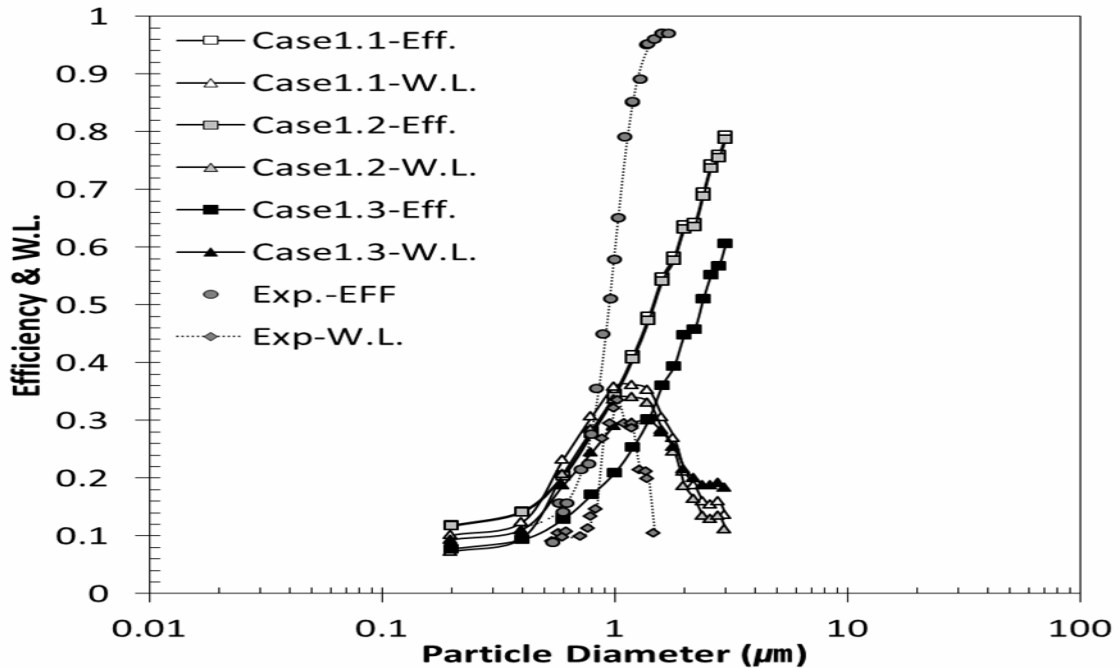
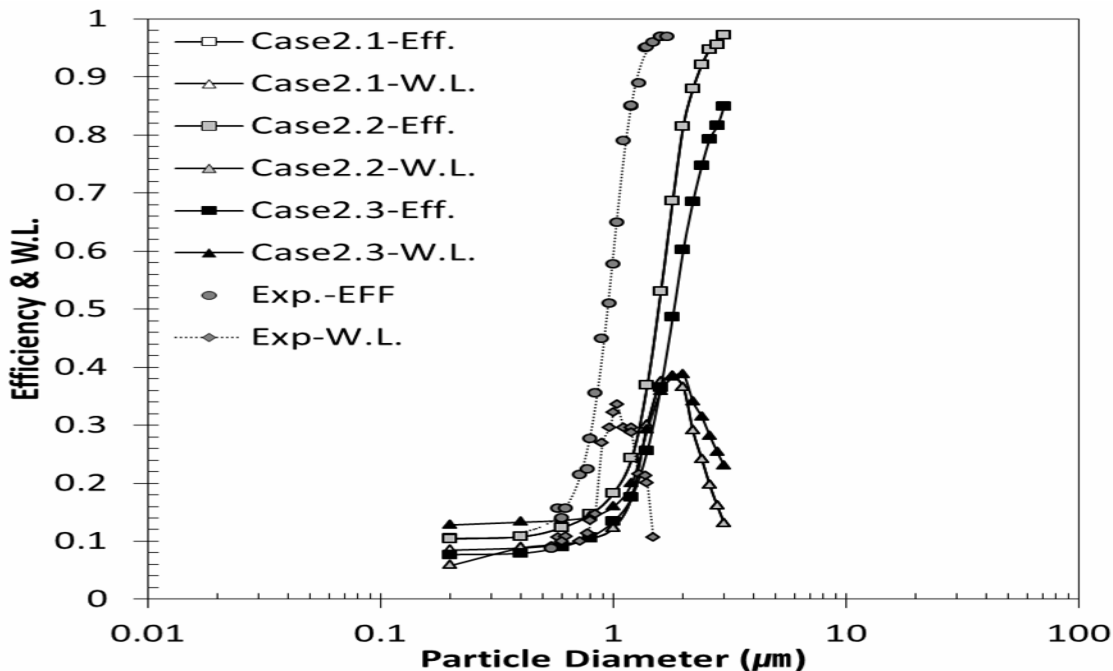


Figure 3. Particle collection efficiency and wall loss of VI at RNG κ - ϵ viscosity model



Errors of collection efficiency compared to experimental data at each particle diameter, shown around the error of 20~50% for all particle diameter in the case 1, but in the case 2, errors

of collection efficiency were 47~71% at the point that is near the experimental GCD, 1 μm , and less than 10% in the range of particle size that is more than 2.2 μm . When we considered flow rate, the collection efficiency was changed, but the particle concentration did not affect to result (Table 2).

Tables

Table 1. Simulation Conditions

	Model number						
	1-1	1-2	1-3	2-1	2-2	2-3	
Particle Concentration (C^*)	calculation	1	1	calculation	1	1	
Flow rate ($V_i A_i$)	calculation	calculation	1	calculation	calculation	1	
Viscosity Model	Laminar			RNG $\kappa-\epsilon$			
	Boundary Conditions						
Inlet	Velocity inlet $V = 5.371 \text{ m/s}$						
Major	Velocity outlet $V = 3.125 \text{ m/s}$						
Minor	Pressure outlet $P_{\text{static}} = 1 \text{ atm}$						

Table 2. Collection efficiency error with experimental data

	Model number					
	1-1	1-2	1-3	2-1	2-2	2-3
	Error (%)					
0.2	-	-	-	-	-	-
0.4	-	-	-	-	-	-
0.6	46.23	44.39	8.17	12.22	12.22	35.56
0.8	1.79	0.40	37.75	46.95	46.95	61.07
1	40.08	40.96	63.80	68.39	68.39	76.85
1.2	51.56	52.25	70.24	71.46	71.46	79.35
1.4	49.63	50.31	68.34	61.17	61.17	73.09
1.6	43.52	44.20	62.88	45.33	45.33	62.37
1.8	38.64	39.34	58.59	27.78	27.78	48.92
2	33.44	34.10	53.23	14.90	14.90	37.18
2.2	33.61	34.27	52.72	9.02	9.02	29.16
2.4	28.54	29.18	47.56	5.24	5.24	23.11
2.6	23.79	24.45	43.42	2.86	2.86	18.66
2.8	22.49	23.14	42.24	2.55	2.55	16.84
3	19.31	19.93	38.41	1.08	1.08	13.53

SUMMARY

The fluid flow and particle motion in the VI was investigated by novel 3-dimensional numerical simulation using CFD code. Also, we calculated collection efficiency and wall loss of the VI and compared with previous experimental results by other researchers. In conclusion, the calculated GCD of VI was about $1.46 \mu\text{m}$, and MWL was 35.3% in laminar viscosity case, and $1.56\mu\text{m}$, 38.4% in RNG k- ϵ viscosity case. When we applied laminar viscose model, the results of the VI property, GCD, MWL are closer to experimental data than RNG k- ϵ results. However, the shape of the collection efficiency curve was very similar to experimental results when viscosity model was RNG k- ϵ . In addition, there was not any reasonable change of calculated results of the VI collection efficiency property, when we considered initial particle concentration. However, when we considered the flow rate at each node, VI collection efficiency curves were left-shifted and had very high slope in efficiency curve without considered the flow rate. In this case, we selected the RNG k- ϵ viscosity model and considered the flow rate at each node, 45 ~ 71% of collection efficiency errors had occurred, but computational calculation results with other VI collection properties, curve shapes, GCD, and MWL were very similar to the experimental results.

ACKNOWLEDGMENTS

This work was supported by the National Research Foundation of Korea Grant funded by the Korean Government (MEST) (grant No. NRF-2010-0029297).

REFERENCES

- [1] Chen, B.T.; Yeh, H.C. *J. Aerosol Sci.* 1987, 18, 203–214.
- [2] Bergman, W.; Shinn, J.; Lochner, R.; Sawyer, S.; Milanovich, F.; Mariella, R. *J. Aerosol Sci.* 2005, 36, 619–638.
- [3] Loo, B. W.; Cork, C. P. *J. Aerosol Sci. Technol.* 1988, 9, 167–176.
- [4] Hari, S.; Hassan, Y. A. *J. Powder Technol.* 2008, 188, 13-22.
- [5] Kim, Y. H.; Park, D.; Hwang, J.; Kim, Y. H. *Lab Chip* 2009, 9, 2722-2728.
- [6] FLUENT 6.3 Documentation Hompage. See
<http://my.fit.edu/itresources/manuals/fluent6.3/help/index.htm>

Characteristics and cytotoxicity of coarse, fine and ultrafine particles exhausted from the stack gas of a municipal solid waste incinerator

Yu-Feng Kuo, Yuh-Jeen Huang, Ting-Shin Fan, and Yi-Siou Chen

Department of Biomedical Engineering and Environmental Sciences, National Tsing-Hua University, Hsinchu, 30013

Principal Contact: Yuh-Jeen Huang, Department of Biomedical Engineering and Environmental Sciences, National Tsing-Hua University, No. 101, Section 2, Kuang-Fu Road, Hsinchu, 30013, Taiwan.

Tel: +886-3-5715131 ext. 35496 Fax: +886-3-5718649 Email: yjhuang@mx.nthu.edu.tw

Abstract

In Taiwan, about 60% of municipal solid waste (MSW) is treated by incineration, 20% by landfill, and 17% by reuse and recycle. Twenty-four incinerators have been built and can be operated to burn 24,650 tons of MSW daily, and even the total incineration is approximately 6.2 million tons during 2010 in Taiwan¹. Many epidemiological and experimental studies have shown that particulate air pollution may induce and aggravate respiratory and cardiovascular diseases.

The intention of this study was to estimate the profile of metallic elements in coarse (diameters between 10-2.5 m, PM_{10-2.5}), fine (diameters between 2.5-1 m, PM_{2.5-1}) and ultrafine (diameters <1.0 m, PM₁) particles and investigate the viability and inflammation of A549 human alveolar epithelial cell exposed to these aerosol samples. These combustion aerosol samples were collected and real-time monitored at the sampling hole of a stack by using Electrical Low-Pressure cascade Impactor (ELPI) couple with a diluted system for the particles with the size range from 7 nm to 10 m. Furthermore, we also used BCR-176R (Standard Reference Sample of a City Waste Incineration Ash, Community Bureau Reference, No 176R) in our study. Heavy metal were analyzed by Laser ablation-inductively coupled plasma-mass spectrometry (LA-ICP-MS). Interesting, the results show the main elements contained in the particles with various diameters are not similar. The Na, Fe, Zn, and Pb were often founded in these three size range of particles, in which Na and Fe are crustal elements, whereas Zn and Pb are anthropogenic elements. Crustal elements were mainly distributed in coarse particles, and the anthropogenic elements were mainly found in fine and ultrafine particles. Moreover, the results of the cell viability assay indicated that ultrafine particles were more cytotoxic than fine and coarse particles, and the ultrafine particles exhibited a higher inflammatory potential.

Keywords: Municipal solid waste (MSW), Heavy metal, MTT assay, IL-8

¹ Taiwan Environmental Protection Agency (TEPA). Statistics Database. (2011).

Characteristics of Sized-resolved Anhydrosugars and Pollutants

Derived from Rice Straw Burning in Controlled Chamber

Chih-Jen Chuang¹, James J. Lee^{2*}, Jian-Li Lin²

1 Engineering Science and Technology, National Yunlin University of Science and Technology, Yunlin, Taiwan

2 Environmental Health and Safety Engineering, National Yunlin University of Science and Technology, Yunlin, Taiwan

Principal Contact: Chih-Jen Chuang, candidate for doctor's degree, National Yunlin

University of Science and Technology, 123 University Road, Section 3, Douliou, 640.

Tel: 05-5342601#4408 Fax 05-5312069 E-mail g9214711@yuntech.edu.tw.

Abstract

This study discusses the particle-sized emission characteristics in three combustion conditions (smoldering, flaming, and mixing conditions). The purpose of this paper is to investigate of characterize particle-sized profiles for the compositions of particulate mass, carbon species (OC and EC), three anhydrosugars (levoglucosan, mannosan, and galactosan) and water-soluble inorganic derived from rice straw burning in a controlled chamber. The results have shown that the smoldering smoke releases the highest particulate mass concentration in three combustion conditions. The particle-size emission of rice straw burning was concentrated in PM_{2.5} particles (66~77% of TSP). Levoglucosan constituent accounts 90% in three anhydrosugars from rice straw burning in the experiment. The ratio range of levoglucosan to mannosan (Levo/Mann) from rice straw burning was approximately 25-40 resulting from cracking cellulose composition in several burning conditions. The carbonaceous composition from rice straw burning was mainly consisted in organic carbon (OC>90%), indicated that rice straw burning belongs to incomplete combustion. Water-soluble ions of particles from rice straw burning significantly abound in splices of Cl⁻, F⁻, SO₄²⁻, K⁺, and NH₄⁺. The higher CO/CO₂ value (>11%) was belong to smoldering condition of rice straw burning. Therefore, the study indicated that levoglucosan might be assigned as a unique molecular tracer and very helpful to identify rice straw burning emission characteristics in the future.

Keywords: Biomass burning, Levoglucosan, Particle-size distribution, Ions, Carbon dioxide

Variation and key reactive species of ambient VOCs in the urban area of Shanghai, China

Leiyan Su^{1,2}, Hongli Wang², Changhong Chen^{2,1}, Cheng Huang², Li Li², Min Zhou¹,
Yuezhen Qiao¹, Yiran Chen²

1 The School of Resources and Environmental Engineering, East China University of
Science and Technology, Shanghai 200237

2 Shanghai Academy of Environmental Sciences, Shanghai 200233

Principal Contact: Leiyan Su, The School of Resources and Environmental
Engineering, East China University of Science and Technology, Shanghai 200237.

Email: suleiyan0126@163.com

Abstract

The ambient concentration of 56 VOCs species were measured continuously in the urban of Shanghai, China at Shanghai Academy of Environmental Sciences, from Jan. 1 to Dec. 31, 2010 by GC-FID instrument. The hourly mixing ratio of ambient VOCs in the urban of Shanghai is $(2.47\sim 301.48) \times 10^{-9}$, and the average mixing ratio is $(26.45\pm 23.36) \times 10^{-9}$. The major compositions of VOCs were alkane, alkene, aromatic, and acetylene, accounting for 46.72%, 33.18%, 11.33%, and 8.76% of the total VOCs, respectively. The ratios of T/B (toluene/benzene) was found at level of 3.51 ± 2.40 , indicating that vehicles are not the only source of ambient VOCs, but the others sources, e.g. solvent use, and evaporation of gasoline, and LPG, make large contribution to VOCs as well. And the ratio of E/E(ethane/ethyne) 0.98 ± 0.68 stating that the plume are aged. According to the ratio of E/C (ethyne/CO), the plume are fresh in spring and winter, and photochemical age are relatively long in summer and autumn. The constant of ambient VOCs radical loss rate (K^{OH}) is $8.05\times 10^{-12} \text{ cm}^3 \cdot \text{molecule}^{-1} \cdot \text{s}^{-1}$ and the maximum O₃ incremental reactivity (MIR) is 4.00 mol·mol⁻¹, which state the chemical reactivity of ambient air in urban Shanghai is correspond to ethylene. The mixing ratio and composition of VOCs vary with wind direction, since the different location of VOCs emission sources. To the OH radical loss rate (L^{OH}), the alkene and aromatic were the most important contributors, and accounted for 42.21% and 40.83%, respectively. In the case of ozone formation potential (OFP), the alkene and aromatic accounted for 21.70% and 62.75%, respectively. The key reactive species are xylene, toluene, ethylbenzene, ethylene, propylene, trans-2-butene, and isoprene.

Keywords: Volatile organic compounds; Concentration; Chemical reactivity; OH radical loss rate; Ozone formation potential

Real-time characterization of particle-bound polycyclic aromatic hydrocarbons at a heavily trafficked roadside site

Y. Cheng^{1,2,3}, K. F. Ho³, S. C. Lee³, Y. B. Peng¹, Y. M. Han², G. H. Wang², F. Wu², Y. Huang³, Y. W. Zhang¹, P. S. Yau³

1 Department of Environmental Science and Technology, School of Human Settlements and Civil Engineering, Xi'an Jiaotong University, No.28 Xianning West Road, Xi'an, Shaanxi, 710049, China

2 SKLLQG, Institute of Earth and Environment, CAS, Xi'an, Shaanxi, 710075, China

3 Department of Civil and Structural Engineering, Research Center for Environmental Technology and Management, The Hong Kong Polytechnic University, Hung Hom, Kowloon, Hong Kong

4 Division of Atmospheric Sciences, Desert Research Institute, Reno, Nevada, USA

Principal Contact: K.F. Ho, Prof., The Hong Kong Polytechnic University, Hung Hom, Kowloon, Hong Kong.

Tel: +852-27664811 E-mail: cehokf@polyu.edu.hk

Abstract

A continuous photo-electric aerosol sensor (PAS) was used along with other real-time instruments to characterize the particle-bound polycyclic aromatic hydrocarbons (p-PAHs) content at a heavily trafficked roadside site. The PAS output gave a good correlation ($R^2=0.8$) to the total concentration of the selected PAHs determined by gas chromatography/mass spectrometry (GC/MS). This technique was then employed to observe temporal variation of total p-PAHs. The measurements at roadside were performed for nine months during January through September 2005. The minimum of monthly average p-PAHs occurred in September 2005 and the maximum value occurred in June 2005. p-PAHs concentrations were highest at 09:00–11:00 a.m. in the workdays when the diesel-fueled vehicles are at a maximum level (3179 per hour for diesel vehicles, accounting for 50% of total on-road traffic counts), suggesting that during these period people living in that area are exposed to a higher number of diesel combustion particles enriched in p-PAHs coatings. In addition, the p-PAHs concentrations were found to depend upon the wind speed and wind direction. High p-PAHs concentrations observed at low wind speeds ($<0.1 \text{ m s}^{-1}$) and when the prevailing winds blow from the north west and south west, exceeding the values when winds blow from the rest direction sectors at high wind speeds ($>4.2 \text{ m s}^{-1}$).

Atmospheric Organic Carbon and Elemental Carbon in a Typical Semi-arid Area of Northeastern China in Spring

Renjian Zhang^{*1}, Jun Tao², K. F. Ho^{3,4}, Junji Cao³, Suixin Liu³ and Zhenxing Shen⁵

¹REC-TEA, Institute of Atmospheric Physics, Chinese Academy of Sciences, Beijing, China

²South China Institute of Environmental Sciences, Guangzhou 510655, China

³SKLLQG, Institute of Earth Environment, Chinese Academy of Sciences, Xi'an, China

⁴Department of Civil and Structural Engineering, The Hong Kong Polytechnic University, Hongkong, China

⁵Department of Environmental Science and Engineering, Xi'an Jiaotong University, Xi'an, China

ABSTRACT

We present the 24-hour PM_{2.5} observations that are associated with carbonaceous species at a typical site over a semi-arid region in the northern China during the spring of 2006. The objectives of this study are (1) to investigate the compositions and sources of carbonaceous aerosols in fine particles and evaluate the OC and EC fractions for Asian dust; (2) to investigate daily variations of highly absorbing aerosols (EC and dust) and OC; (3) to identify the transport pathways and possible sources for the carbonaceous aerosols; and, finally, (4) to estimate SOC with respect to transport time and direction in this region during the spring period. This study provides the spatial distribution of fine particles in northern China and evaluates the impact of this distribution on the regional environment.

The average concentrations of OC and EC in PM_{2.5} were 14.0 ± 8.3 and $2.1 \pm 1.3 \mu\text{gm}^{-3}$, respectively. The ratios of OC/EC in DS, NDS, and during the observational period in Tongyu are: 7.47 ± 1.83 , 7.53 ± 2.71 , and 7.51 ± 2.46 respectively. Strong correlations for OC and EC values were observed (with a high correlation coefficient) in Tongyu, which suggests that the emission of OC and EC at the Tongyu site was attributed to similar sources. A high $\Delta\text{K}^+/\Delta\text{OC}$ ratio of 12.3 in PM_{2.5} highlights the significant contributions of biomass-burning emissions. The average concentration of estimated SOC in PM_{2.5} at Tongyu was $5.9 \mu\text{gm}^{-3}$, which varied from $0 \mu\text{gm}^{-3}$ to $26.1 \mu\text{gm}^{-3}$. The percentages of the SOC concentrations in OC and PM_{2.5} concentrations were 42.0%, and 2.1%, respectively. The SOC concentrations during DS were higher than they were in NDS, suggesting that the chemical reaction process that is involved

* Corresponding author: ZHANG Renjian, zrj@mail.iap.ac.cn

in gas-particle conversation also occurred during the long-distance transportation of aerosol particles. The possible impact of biomass-burning and anthropogenic emissions on this region certainly deserves more scientific attention.

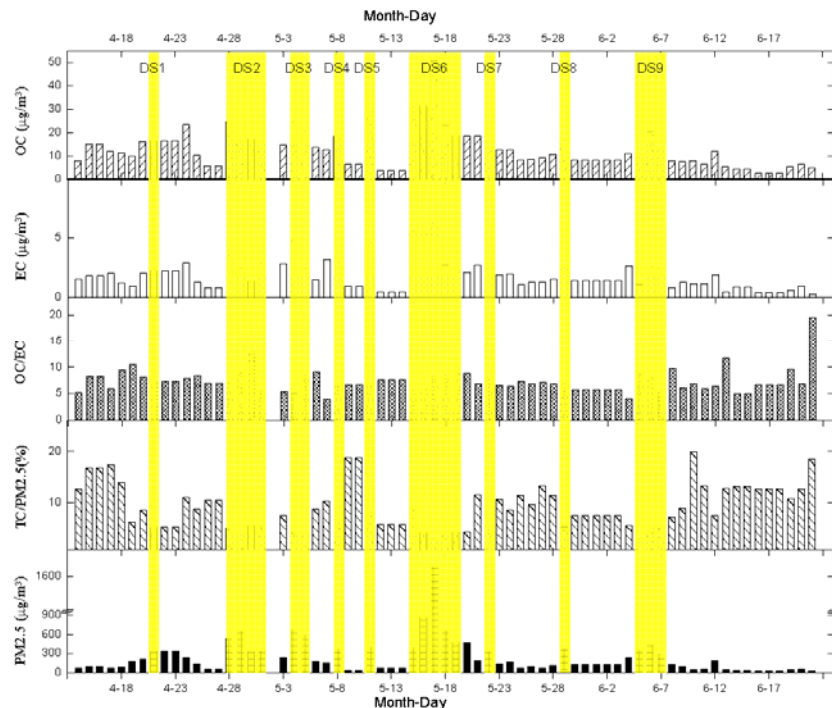


Figure 1. Time series of OC, EC, OC/EC, TC/PM_{2.5}, and PM_{2.5} in the spring in Tongyu (TC = OC + EC).

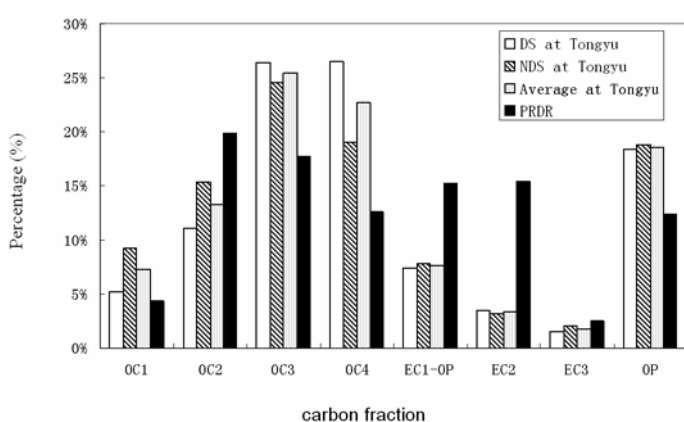


Figure 2. Percentage of total carbon contributed by eight carbon fractions at eight sampling sites in PM_{2.5} during the spring in Tongyu and PRDR (Cao et al., 2004).

REFERENCES

- Cao, J. J., S. C. Lee, K. F. Ho, S. C. Zou, K. K. Fung, Y. Li, J. G. Watson, and J. C. Chow, 2004: Spatial and seasonal variations of atmospheric organic carbon and elemental carbon in Pearl River Delta Region, China, *Atmos. Environ.*, **38**, 4447-4456.
- Chow, J. C., J. G. Watson, L. C. Pritchett, W. R. Pierson, C. A. Frazier, and R. G. Purcell, 1993: The DRI thermal/optical reflectance carbon analysis system: description, evaluation and applications in US air quality studies. *Atmos. Environ.*, **27A** (8), 1185–1201.

The observational characteristic of aerosol number concentration and size distribution at Shijiazhuang in spring season

Lianji Jin and Qingfei Zhai

Key Laboratory for Atmospheric Physics and Environment of CMA, Nanjing University of Information Science and Technology, No. 219 in the Ningliu Road, Nanjing, 210044

Principal Contact: Lianji Jin, Associate Professor, School of Atmospheric Physics, Nanjing University of Information Science and Technology , No. 219 in the Ningliu Road, Nanjing, 210044.

Tel: 13813923952 Email: jlj@nuist.edu.cn

Abstract

During May, 2010, number concentration of atmospheric aerosols near the ground at Shijiazhuang Meteorological Bureau, China were measured using WPS made by MSP Corporation in United States, combined with corresponding meteorological data, to study the characteristics of aerosol number concentration and size distribution in this observation and possible causes that lead to. The spectra of aerosol were mainly occupied by ultrafine particles($DP < 0.1\mu m$) in this observation. The average particle number concentration was high in all size scales. High emission of pollution gases and particles, weak wind condition and the transport effect when the dominant wind direction was southeast were the primary possible causes of this result; Obvious diurnal variation of aerosol concentration was observed in sunny days, which was mainly controlled by solar radiation, heat condition, the height of the boundary layer and construction, and that between different diameters had significant differences. Both total and ultrafine particles number concentration reached daily peak value at 7:00, 12:00 and 21:00, while coarse particles number concentration($DP > 0.1\mu m$) reached the peak value at 7:00 and 23:00.

Keywords: Shijiazhuang; atmospheric aerosol; number concentration; meteorological factors

Chemical Composition of TSP at Qinghai Lake Atmospheric Background Site in Summer, 2010

Zhuzi Zhao^{1,2}, Junji Cao¹, Suixin Liu¹ and Jiamao Zhou¹

1. SKLLQG, Institute of Earth Environment, Chinese Academy of Sciences, Xi'an, China

2. Graduate School of the Chinese Academy of Sciences, Beijing, China

ABSTRACT

We report chemical composition data for TSP from the Qinghai lake atmospheric background site, located at 3200m a.s.l.in the Easter Tibetan Plateau. The average TSP mass is $24.18\mu\text{g m}^{-3}$, ranging from 7.93 to $70.56\mu\text{g m}^{-3}$. The mean concentration levels are found to be $1.51 \pm 0.62\mu\text{g OC m}^{-3}$ and $0.30 \pm 0.13\mu\text{g EC m}^{-3}$. The OC/EC ratio can reach 5.24 in this site. SO_4^{2-} , NO_3^- , and Ca^{2+} were the dominant water-soluble species. The chemical composition suggests that the secondary inorganic aerosol(SIA) and organic matter(OM) account for nearly 30% of the TSP mass. The ratios of BC/TC, BC/OC, K^+/OC and K^+/EC suggest the aerosol pollution represents a mixture of biomass and fossil fuel combustion. The characteristic low abundances of OC and EC and their significant correlation with K^+ and SO_4^{2-} suggest contribution from long-range transport of anthropogenic species. Back-trajectories revealed that the air masses that originated inside China had higher concentrations than those that started western of China.

KEYWORDS

Background atmosphere, Chemical compositions, Back trajectory, Aerosol

Introduction

As a major component of atmospheric particulate matter (PM), carbonaceous material plays an important role in visibility reduction, radiative forcing, and adverse human health effects^[1~3]. Carbonaceous aerosols have received more attention recently because of their effects on regional climate, water resources, agriculture yields, air quality, visibility reduction, and public health, and it contributed 20-50% of aerosol in Chinese urban atmosphere from small-scale urban or regional atmosphere^[4~6]. Most of the atmospheric chemistry studies conducted on the Tibetan Plateau have focused on its southern edge^[7~8], however the data for other parts of the Plateau are limited. This paper presents a high time-resolved measurement in Xi'an at summer. The primary objectives of the study are to (1) to characterize the chemical compositions of the carbonaceous aerosol, (2) to investigate the transport of these substances to Qinghai Lake.

Experimental methods

The Qinghai Lake sampling station ($N36^{\circ} 58' 37''$, $E99^{\circ} 53' 56''$, 3200m asl) was selected to represent background site in Eastern Tibetan Plateau. In Qinghai Lake region yak dung was stored and air-dried outside the permanent Tibetan dwellings for cooking and heating in traditional Tibetan pastoralist society. The TSP samples were collected on 47mm quartz microfiber filters (Whatman Ltd, Maidstone, UK) using a RP2025 air sampler (Thermo, USA, 16.7 l/min) during summer, 2010. Total 16 samples were collected in this study. A 0.5 cm^2 punch from each Quartz-filter samples was analyzed for OC and EC with a DRI Model 2001 Thermal/optical Carbon Analyzer for carbon fractions following the Interagency Monitoring of Protected Visual Environments (IMPROVE) thermal/optical reflectance protocol. An ion chromatograph (Dionex, DX-300, USA) was used to measure ten ions (SO_4^{2-} , NO_3^- , F^- , Cl^- , NH_4^+ , Na^+ , K^+ , Ca^{2+} , Mg^{2+}). Ten elements (S, K, Ca, Fe, Cl, Ti, Zn, Ba, Pb, Mn) were measured by XRF(PanalyticalE5, Holland).

Results and Discussion

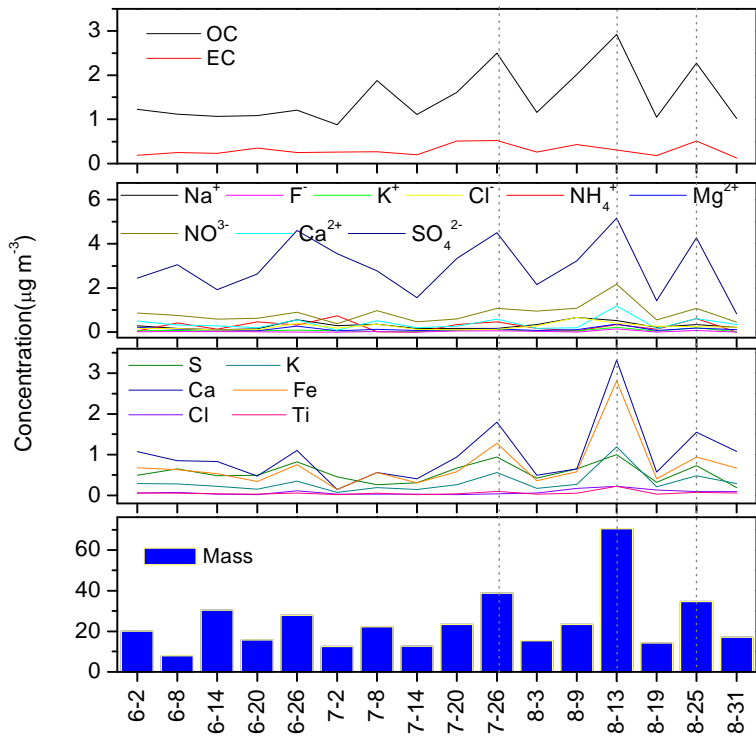
As shown in table 1, mean mass concentrations was $24.18\mu\text{g m}^{-3}$ (ranged from 7.93 to $70.56\mu\text{g m}^{-3}$). The dominant species of water-soluble were SO_4^{2-} , NO_3^- and Ca^{2+} .The increased photochemical activity was one of the important reasons for the high sulfate concentration during summer. Additionally, sea salt might contribute to the total sulfate concentration in TSP since the sampling site is situated quite close to the Qinghai Lake. Average OC and EC concentrations were 1.51 (0.88 - 2.92), 0.30 (0.13 - 0.52) $\mu\text{g m}^{-3}$, respectively. These background OC and EC concentrations are similar to 2 - $3\mu\text{g m}^{-3}$ for OC and 0.2 - $0.5\mu\text{g m}^{-3}$ for EC from CAWNET remote stations at Akdala and Shangri-La, Zhuzhang^[9]; to 0.13 - $0.30\mu\text{g m}^{-3}$ for EC from Mt. Waliguan^[10]; to 1.66 ± 0.79 OC from Nam Co region^[11]; 0.08 - $0.43\mu\text{g EC m}^{-3}$ from the Kosan marine GAW station of Korea^[12]; a litter lower than Manora Peak in North India^[13].The mean OC/EC ratio was about 5.24, which higher than the value of 2.0 used by Chow et al. to identify secondary aerosol formation.

The ratios (BC/TC BC/OC K+/OC and K+/EC) suggest the aerosol pollution represents a mixture of biomass and fossil fuel combustion^[14~16].

Table1. Average species concentrations ($\mu\text{g m}^{-3}$) of the TSP samples

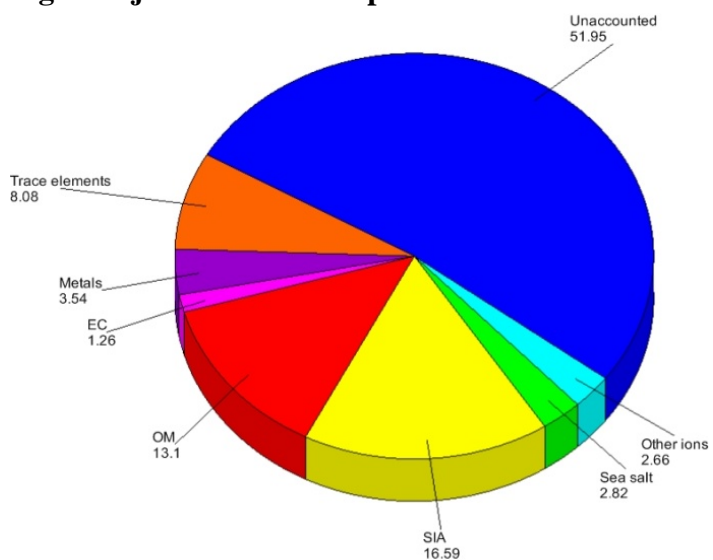
<i>Species</i>	<i>Mean</i>	<i>Standard deviation</i>	<i>Min</i>	<i>Min-Date</i>	<i>Max</i>	<i>Max-Date</i>
Mass	24.18	15.01	7.93	8-Jun	70.56	13-Aug
OC	1.51	0.62	0.88	2-Jul	2.92	13-Aug
EC	0.30	0.13	0.13	31-Aug	0.52	26-Jul
Na^+	0.30	0.16	0.12	14-Jun	0.66	9-Aug
NH_4^+	0.29	0.23	0.11	31-Aug	0.75	2-Jul
K^+	0.08	0.06	0.02	31-Aug	0.23	13-Aug
Mg^{2+}	0.14	0.08	0.06	20-Jun, 2-Jul	0.37	13-Aug
Ca^{2+}	0.39	0.27	0.09	2-Jul	1.19	13-Aug
F^-	0.04	0.04	0.01	26-Jun, 14-Jul, 19-Aug, 31-Aug;	0.15	13-Aug
Cl^-	0.25	0.15	0.10	14-Jun	0.67	9-Aug
NO_3^-	0.85	0.43	0.38	2-Jul	2.17	13-Aug
SO_4^{2-}	2.96	1.24	0.83	31-Aug	5.16	13-Aug
Fe	0.72	0.62	0.14	2-Jul	2.81	13-Aug
Ti	0.06	0.05	0.02	2-Jul	0.22	13-Aug
Zn	0.04	0.91	0.01	31-Aug	0.10	13-Aug
S	0.55	0.24	0.19	31-Aug	1.00	13-Aug
K	0.32	0.26	0.07	2-Jul	1.19	13-Aug
Ca	0.99	0.75	0.14	2-Jul	3.32	13-Aug
Cl	0.07	0.06	0.02	20-Jun, 20-Jul	0.22	13-Aug
OC/EC	5.24	1.69	3.09	20-Jun	9.29	13-Aug
BC(EC)/TC	0.17	0.04	0.10	13-Aug	0.24	20-Jun, 20-Jul
BC(EC)/OC	0.21	0.06	0.11	13-Aug	0.32	20-Jun, 20-Jul
K/OC	0.05	0.02	0.02	8-Jul;31-Aug	0.09	25-Aug
K/EC	0.25	0.15	0.11	8-Jul	0.73	13-Aug

Figure 1.The temporal variation of chemical species



As Shown in Fig.1, pollutants had three major peaks, on the Jul 26th, Aug 13th and Aug 25th.The major peaks in OC always coincided with the high values of ions(SO_4^{2-} , NO_3^- and Ca^{2+}), elements(Ca, Fe, S and K) and mass, which implies the same processes, including the effects of transport, caused these pollutants concentrations to co-vary.

Fig2. Major chemical compositions of TSP



*Organic matter(OM)=2.1OC

*Sea salt= $\text{Cl}^- + 1.45\text{Na}^+$

*Secondary inorganic aerosol(SIA)= nss- SO_4^{2-} $\text{NO}_3^- + \text{NH}_4^+$

* nss- SO_4^{2-} = $\text{SO}_4^{2-} - 0.231\text{Na}^+$

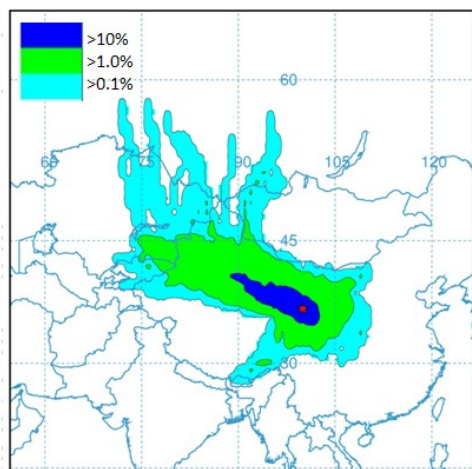
*Metals=Fe+ Ti+ Zn+ Pb+ Mn

*Trace elements=K+ Ca+ Cl+ S

*Trace ions= $\text{F}^- + \text{K}^+ + \text{Ca}^{2+} + \text{Mg}^{2+}$

Eight major constituents were used: organic matter, elemental carbon, sea salt, SIA, metals, trace ions, trace elements and unaccounted. The dominant components of the aerosol were SIA(16.59%), followed by organic matter (13.10%) and Trace elements(8.08%). The contributions of water, crustal elements (such as silicon, aluminum) might responsible for large amount of undefined mass stated as “others” in Fig.2.

Fig3. Frequency plot of 3-day back trajectories for the summer periods arriving at Qinghai Lake Station.



The trajectories fell into two major classes. Most of the air masses are rapidly moving and come from west, and others slow-moving air masses come from southwest and east. When the air mass coming from west and north, the Ca and Fe showed peaks. The pollutants concentrations for samples stratified by trajectory show that the air masses that originated inside China had higher concentrations than those that started western of China.

SUMMARY

The concentration of carbonaceous species and ions were relatively low , and had comparability with other high-altitude and remote sites. The TSP abundance at the high-altitude sit is dominated by biomass emission products around Qinghai Lake region as well as regional-scale fossil fuel

combustion and mineral dust source.Ca and Fe could be used as markers of northern and western aerosol coming to Qinghai Lake .The result suggested the emissions from inside China had little impact on the atmospheric environment here.

ACKNOWLEDGEMENTS

This work was supported by the National Key Technology R&D Program of China (No: 2007BAC30B01).

REFERENCES

- [1] Intergovernmental Panel on Climate Change (IPCC). Climate Change 1994: Radiative Forcing of Climate change and an evaluation of the IPCC IS92 Emission Scenarios; Cambridge University Press: New York, 1995.
- [2] Wilson, R.; Spengler, J. D. Particles in Our Air: Concentrations and Health Effects; Harvard University Press: Cambridge, MA.,1996.
- [3] He, K. B., F.M. Yang, et al.,*The characteristics of PM2.5 in Beijing,China*, Atmospheric Environment.2003. **35**, 4959– 4970.
- [4] Cao, J. J., S. C. Lee,et al., *Spatial and seasonal variations of atmospheric organic carbon and elemental carbon in Pearl River Delta Region, China*. Atmospheric Environment.2004. **38**, 4447– 4456.
- [5] Cao, J. J., et al.,*Characterization and source apportionment of atmospheric organic and elemental carbon during fall and winter of 2003 in Xi'an, China*, Atmos. Chem. Phys.2005. **5**, 3127– 3137.
- [6] Cao J.J., S.C.Lee.,et al. *Spatial and Seasonal Distributions of Carbonaceous Aerosols over China*.Journal of Geophysical Research, 2007. **112**. doi:10.1029/2006JD008205
- [7] Ming, J., Cachier, H.,et al. *Black carbon record based on a shallow Himalayan ice core and its climatic implications*. Atmos. Chem. Phys. 2008. **8** (5), 1343–1352.
- [8] Pant, P., Hegde, P.,et al. *Aerosol characteristics at a high-altitude location in central Himalayas: optical properties and radiative forcing*. J. Geophys. Res. 2006. **111**, D17206. doi:10.1029/2005JD006768.
- [9] Zhang X, W. Y., Zhang X, Guo W, Gong S, . *Journal of Geophysical Research*, **2008**,113, doi: 10.1029/2007JD009525.
- [10] Tang, J., et al. *Q. J. Appl. Meteorol.*, **1999**,10, 164-170(in chinese).
- [11] Ming, J., C. Xiao, J. Sun, S. Kang & P. Bonasoni. *Journal of Environmental Sciences*, **2010**, 22, 1748-1756.
- [12] Lee, H. S. & B.-W. Kang. *Atmospheric Environment*, **2001**, 35, 739-746.
- [13] Rengarajan, R., M. M. Sarin & A. K. Sudheer. *J. Geophys. Res.*, **2007**, 112, D21307.
- [14] Ferek, R.J., J.S. Reid, P.V. Hobbs, et al., *J. Geophys. Res.*, **1998**, 103, 32, 107-32, 118.

- [15] Ram, K. & M. M. Sarin *Atmospheric Environment*, **2011**, *45*, 460-468.
- [16] O. L. Mayol-Bracero, R. Gabriel, M. O. Andreae, et al., *J. Geophys. Res.*, **2002**, *107*, 19, 8030, doi:10.1029/2000JD000039.
- [17] Khan, M. F., Y. Shirasuna, et al. *Characterization of PM_{2.5}, PM_{2.5-10} and PM> 10 in ambient air, Yokohama, Japan*. *Atmospheric Research* 2010. **96**(1): 159-172.
- [18] Terzi, E., G. Argyropoulos, et al. *Chemical composition and mass closure of ambient PM₁₀ at urban sites*. *Atmospheric Environment*. 2010. **44**(18): 2231-2239.

Measurement of carbonyl compounds in PM_{2.5} in Xi'an, China

W.T. Dai¹, K.F. Ho¹, S.S.H. Ho^{1,2}, J.J. Cao¹

1 SKLLQG, Institute of Earth Environment, Chinese Academy of Sciences, Xi'an, 710075, China

2 Division of Atmospheric Sciences, Desert Research Institute, Reno, NV 89512, United States

Principal contact: Wenting Dai, SKLLQG, Institute of Earth Environment, Chinese Academy of Sciences, Xi'an, 710075, China.

Tel: 13720410370 Email: Daiwt@ieecas.cn

Abstract

Analytical method to detect carbonyls in particulate phase was developed by adopting derivatization agent DNPH-ACN-Pyridine followed by HPLC-UV quantification. The reproducibility and precision of the measurements are excellent. This method was used for measuring carbonyls in PM_{2.5} collected on quartz filter, sampled from 2008 to 2009. The results show that nonanaldehyde is the highest species in the high molecular weight carbonyls (C#≥6), followed by octanaldehyde, hexanaldehyde and heptaldehyde, accounting for 40%, 20%, 12% and 11% in total measured carbonyls. For dicarbonyls, the concentrations of methylglyoxal were much higher than the concentrations of glyoxal, and 10% higher in total carbonyls. The seasonal variation of high molecular weight carbonyls and dicarbonyls in PM_{2.5} are similar with the gas phase, namely winter > autumn > spring > summer (except C8). Strong correlation among carbonyls in winter was observed, due to low temperature, weakly photochemical reaction, and mainly primary emission sources. On the contrary, vehicle emission, cooking emission and photochemical reaction were the most important source in summer.

Keywords: Carbonyls, fine particle matter

Quantitive Role of INA Bacterial Aerosol in Initiating Heterogeneous Nucleation

Yaling Wang, Rui Du and Ziming Li

College of resources and environment, Graduate University of Chinese Academy of Science, Beijing 100049, China

ABSTRACT

This study examines the potential role of some strains of ice-nucleation active bacteria and sulfate aerosols, monocarboxylic acids (MCA) and dicarboxylic acids (DCA), which are considered the most effective ice nuclei. Freezing experiments using large numbers of small drops are performed using a modified version of the protocol described by Vali (1971) to compare the role of heterogeneous nucleation of Ice-Nucleation Active(INA) bacteria on freezing temperature in immerge mode, as well as of role of combined action INA bacteria with representative air pollutants. This paper deals with five typical INA bacteria strains: *P.syringae* pv. *panici*, *p.fluorescen*, *E.uredovora* and *X.campestris*, and *P.syringae* pv. *Lachrymans*. Methods for measurement of the cell mass for INA involved both direct plate counting and optical density (OD_{600nm}). Ice nucleation temperatures of individual bacterial strains were determined by counting threshold temperatures of no less than 200 droplets of bacterial suspension. Experiments shew that Composed with the INA bacteria *P.syringae* pv. *Lachrymans*, the other four strains show no nucleation activity, average freezing temperature of suspension of which are $-18.2\pm2.6 \sim -21.8\pm2.3^\circ C$ ($OD_{600}=0.4$ or 0.25 , all 10^8 CFU/ml except 10^6 CFU/ml for *P.syringae* pv. *panici*). *P.syringae* pv. *Lachrymans* had intermediate nucleation ability. As the concentration of suspension increased by 10 times from 10^2 to 10^9 CFU/ml (colony-forming units mL^{-1}), freezing temperature varied from $-21.7\pm2.7^\circ C$, similar to Milli-Q water, up to $-4.9\pm0.7^\circ C$. Nucleation temperatures increase with *P.syringae* pv. *Lachrymans*(*ps1-10*) bacterial population density, and finally approache the utmost. It indicated that nucleation ability of certain INA bacteria was clearly and closely dependent on bacteria number in suspension. Very little various substance facilitate freezing of *P.syringae* pv. *Lachrymans*.

KEYWORDS

Heterogeneous nucleation ,INA bacteria, Carboxylic acid, Freezing temperature

Introduction

As part of airborne particles, bioaerosol can impact the Earth's climate, directly by absorbing and scattering radiation and indirectly by forming or acting as cloud condensation nuclei (CCN) and ice-forming nuclei (IN), and then can strongly impact cloud dynamics, cloud radiative properties, precipitation formation and cloud chemistry^[1,2]. Bacteria have been observed in the boundary layer, in the upper troposphere^[3,4], and even in the stratosphere at altitudes up to 41 km above sea surface^[5]. The investigation of biologically generated freezing nuclei in the atmosphere has received renewed interests since Schnell and Vali (1972)^[6] first reported that a portion of the atmospheric freezing nuclei was of biogenic origin. During the past nearly half century, it is common knowledge that Bacteria are one of the many types of biogenic aerosol particles that are ubiquitous in the atmosphere^[7-10].

Biological ice nucleators can initiate heterogeneous nucleation and catalyzed for freezing of supercooled water drops. So-called ice-nucleation active(INA) bacteria, which function as catalysts for freezing at relatively warm temperatures (warmer than -10°C)^[11]. Bacteria have been regarded as effective ice nucleators. However, the process and properties of INA bacteria initializing nucleation remain further study and also quantitative research are needed for practical application in weather modification and scale-model simulation.

The objectives of this study were to determine quantitative relationship between INA bacteria number and freezing temperature, and how typical pollutants in atmosphere (carboxylic acid) effect freezing initiation.

Experimental Methods

The bacteria strains used in this study included *P.Syringae* pv. *Lachrymans*, *P.Syringae* pv.*panici*, *p. fluorescen*, *E.uredovora*, *X.campestris*.

Bacteria strains were inculcated for 24h at room temperature ,no more than 25°C in nutrient agar, and then kept in fridge of 4°C. Ice nucleation activity of bacteria was determined by automatically detecting droplet frozen instrument in Chinese Academy of Meteorological Science. For 10μl droplets of bacterial suspensions with certain OD600 or 10-fold dilution gradient magnitude, quantitative measurements of the number of freezing nuclei in bacteria and the temperature at which initiation of freezing takes place were accomplished using the freezing nucleus spectrometer describable by Vali(1971)^[12]. It is to be noted that results have statistical significance only when droplet number is no less than 200.

Results and Discussion

Nucleation activity of five stains

Table 1 showed that *P.syringae* pv. Panici, *E.uredovora*, *X.campestris* and *p.fluorescen* were non-active INA bacterias. The average freezing temperature of *P.syringae* pv. Lachrymans is -5.0°C and -5.4°C for OD₆₀₀=0.4 and OD₆₀₀=0.25, with the same order of magnitude concentration of bacteria suspension.

Quantitative relation between freezing temperature and cell concentration of *P.syringae* pv. *Lachrymans*(ps1-10)

The relationships between bacterial population density and nucleation temperatures are demonstrated in Figs 1. Mean populations of INA bacteria per ml for *P. syringae* was 10² with nucleation temperature of -21.7°C and 10⁸ at -4.9°C respectively. Nucleation temperatures increase with bacterial population density, and 10⁹ INA bacteria per ml almostly reached the peak and final utmost freezing temperature, the tendency of which agreed with P. Nejad's study, but P. Nejad^[13] suggested that per ml for *P. syringae* was 10² with nucleation temperature of -4.5°C and 10⁹ at -2.5°C respectively. These results show that nucleation temperature is highly dependent on bacterial cell density.

The air equivalent concentration of bacteria in clouds was estimated to be 5.9×10^3 cells/m³^[14]. Freezing temperatures of 10^3 - 10^5 INA bacteria per ml for *ps1-10* were -20.2—8.6 °C, which indicated some challenge of INA applying in weather modification as most effective nucleator.

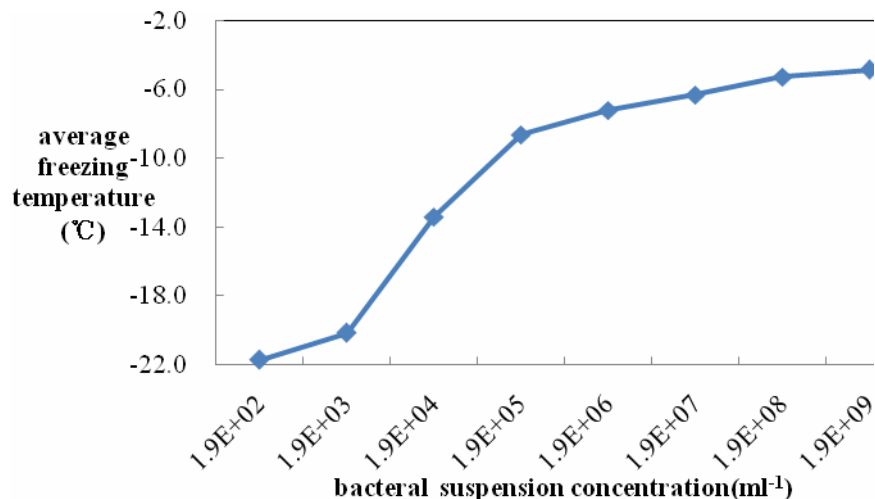
Tables

Table1. Nucleation temperatures of five stains ,OD600 is 0.25 and 0.4

strains	Suspensio n OD ₆₀₀	Suspension concentration(ml ⁻¹)	Average freezing temperatur e (°C)	Suspensio n OD ₆₀₀	Suspension concentration(ml ⁻¹)	Average freezing temperatur e (°C)
<i>P.syringae</i> pv. <i>Lachrymans</i>	0.409	4.5×10^8	-5.0(0.8)	0.249	2.9×10^8	-5.4 (0.7)
<i>P.syringae</i> pv. <i>panici</i>	0.407	7.2×10^6	-18.2(2.6)	0.250	1.4×10^6	-20.3(2.3)
<i>p.fluorescen</i>	0.400	3.43×10^8	-21.1(2.5)	0.255	1.2×10^8	-21.8(2.3)
<i>E.uredovora</i>	0.393	5.0×10^8	-21.5(2.3)	0.246	2.0×10^8	-19.7(2.5)
<i>X.campestris</i>	0.397	4.0×10^8	-20.6(3.1)	0.251	1.3×10^8	-19.9(3.3)

Figures

Fig. 1. Dependence of Ice Nucleation Activity (INA) on cell concentration of *P.syringae* pv. *Lachrymans*(ps1-10)



Combined action of ps1-10 and typical air pollutant(s)

Table2. Effect of combined action of ps1-10 and typical air pollutants on freezing temperature

Suspension concentration(ml^{-1})	10^6	10^5	10^4	10^3
ps1-10	-7.2(1.3)	-8.6(0.9)	-13.4(5.1)	-20.2(4.2)
with COOHCOOH	-8.4(0.7)		-19.3(4.5)	
with CH_3COONa	-8.2(0.9)		-14.1(5.9)	
with $(\text{NH}_4)_2\text{SO}_4$	-7.4(1.1)		-17.8(4.6)	
With dble-mix	-8.0(1.0)	-10.4(2.0)	-16.5(5.0)	-19.8(2.8)
with min-mix	-8.2(0.9)	-9.9(1.3)	-16.9(5.4)	-19.4(4.3)
With hlf-mix	-6.7(0.9)	-8.3(0.9)	-11.3(3.7)	-17.6(4.4)

In examined ps1-10 and typical air pollutant(s) mixture, for COOHCOOH, CH_3COONa , and $(\text{NH}_4)_2\text{SO}_4$, the concentration of single pollutant is $50\mu\text{mol/L}$, $50\mu\text{mol/L}$, $100\mu\text{mol/L}$; three pollutants were $(100+100+200)\mu\text{mol/L}$ for “dble-mix”, $(50+50+100)\mu\text{mol/L}$ for “min-mix”, $(25+25+50)$ for “hlf-mix”.

Table2. shows that combined action of ps1-10 and single air pollutant decreased freezing temperature, which is the same for double and min concentration-mixed pollutants, but when mixed pollutants halved, nucleation temperature increase, even higher than ps1-10 suspension with no adding any substance. Bacteria aerosol is actually a microscale system of various

inorganic and OC, and hence exhibit very complex physical properties (e.g., solubility, surface activity, hydrophobicity and morphology). The airborne microbial flora likely metabolizes chemical components of aerosols thereby potentially modifying atmosphere chemistry^[15], which complicate the combination action, not to speak of the mechanism and possibility of non-metabolic processes such as adsorption of molecules from biological surfaces^[16], chemical release due to cell lyses, and collision-coalescence processes^[17,18]. Thus, despite the relatively low mass concentration of DCA, their roles as CCN have been taken very seriously.

SUMMARY OR CONCLUSION

1. INA bacteria strains observed included: *Pseudomonas syringae*, *Erwinia herbicola*, *Pseudomonas viridiflava*, *Pseudomonas fluorescens*, *Erwinia ananas*, and *Xanthomonas campestris*, (Maki et al. 1974; Kozloff et al., 1983; Lindow 1983; Young 1987; Maki and Willoughby 1978; Warren et al. 1986; Abe et al. 1989; Orser et al. 1985; Hew and Yang, 1992). Some isolated varieties have no activity of catalyzing freezing.
2. Nucleation temperatures increase with *P.syringae* pv. *Lachrymans*(ps1-10) bacterial population density, and finally approach the utmost. Ice Nucleation of ps1-10 is moderately strong.
3. Combined action of ps1-10 and air pollutant is complicated and very little various substance facilitate freezing.

ACKNOWLEDGMENTS

This study was funded by The National Natural Science Fund. We thank my supervisor, Du Rui for her instruction and Shaozhong Yang for providing access to the equipment.

REFERENCES

- [1] Bauer H, Giebl H, Hitzenberger R, et al.. 2003. Airborne bacteria as cloud condensation nuclei[J]. Journal of Geophysical Research, 108: AAC2/1–AAC2/5.
- [2] Franc G D, Demott P J, 1998: Cloud activation of airborne *Erwinia carotovora* cells[J]. Journal of Applied Meteorology, 37: 1293- 1300.
- [3] Lindemann, J., Constantinidou H. A., Barchet W. R., and Upper C. D., 1982. Plants as sources of airborne bacteria including ice nucleation active bacteria. *Appl. Environ. Microbiol.* **44**, 1059–1063.
- [4] Lindow S.E., D.C. Arny, and C.D. Upper, 1983: Biological control of frost injury: establishment and effects of an isolate of *erwinia herbicola* antagonistic to ice nucleation active bacteria on corn in the field .*Phytopathology* 73:1102-1106

- [5]Wainwright, M., Wickramasinghe, N.C., Narlikar, J.V., Rajaratnam, P., 2003. Microorganisms cultured from stratospheric air samples obtained at 41 km. *FEMS Micro-biology Letters* 218, 161–165.
- [6]Schnell, R. C., and G. Vali, 1972: Atmospheric ice nuclei from decomposing vegetation. *Nature*, 236, 163–165.
- [7]Elbert, W., Taylor, P. E., Andreae, M. O., and Pöschl, U., 2007. Contribution of fungi to primary biogenic aerosols in the atmosphere: wet and dry discharged spores, carbohydrates, and inorganic ions. *Atmos. Chem. Phys.*, 7, 4569–4588.
- [8]Jaenicke, R., Matthias-Maser S., and Gruber S., 2007. Omnipresence of biological material in the atmosphere. *Environ. Chem.*, 4, 217-220.
- [9]Jaenicke, R., 2005. Abundance of cellular material and proteins in the atmosphere. *Science* 308, 73.
- [10]Burrows, S M, W Elbert, M G Lawrence, and U Pöschl, 2009: Bacteria in the global atmosphere part 1: review and synthesis of literature data for different ecosystems. *Atmos. Chem. Phys.*, 9, 9263-9280.
- [11]Maki L.R, Willoughby K.J., 1978. Bacteria as biogenic sources of freezing nuclei. *J. Appl. Microbiol.* 17: 1049–1053.
- [12]Vali, G. 1971: Quantitative evaluation of experimental results on the heterogeneous freezing nucleation of supercooled liquids. *J. Atmos. Sci.* 28, 402–409
- [13]Nejad, P., Granhall, U. and Ramstedt, M. ,2005: Factors influencing pathogenic Ice Nucleation Active (INA) bacteria isolated from Salix plants, soil and litter. *Journal of Agricultural Technology* 1(2): 207-222.
- [14]Bauer H, Giebl H, Hitzenberger R, et al.. 2003. Airborne bacteria as cloud condensation nuclei[J]. *Journal of Geophysical Research*, 108: AAC2/1–AAC2/5.
- [15]Morris, C.E., Georgakopoulos D.G., Sands, D.C., 2004. Ice nucleation active bacteria and their potential role in precipitation. *J. Phys.* 121, 87-103.
- [16]Co ^te ', V., G. Kos, R. Mortazavi, and P. A. Ariya. 2008. Microbial and “de novo” transformation of dicarboxylic acids by three airborne fungi. *Sci. TotalEnviron.* 390:530–537.
- [17]Sun J, Ariya P A. Atmospheric organic and bio-aerosols as cloud condensation nuclei (CCN): A review. *Atmos Environ*, 2006, 40: 795—820
- [18]Ariya P. A., Amyot M., 2004 *(invited)* The role of bioaerosols in atmospheric chemistry and physics. *Atmos. Environ.* 38: 1231-1232.

Analysis of the Diurnal Variation of Oxalic Acid in Aerosols by Desorption Electrospray Ionization Mass Spectrometry

Xiu Wu, Juntao Huo, Hong Chen and Xin Yang*

Principal Contact: Xin Yang, Professor, Department of Environmental Science & Engineering, Fudan University, 220 Handan Road, Shanghai 200433, China.

E-mail: 09210740012@fudan.edu.cn

Abstract

Dicarboxylic acids are an important group of water-soluble organic compounds (WSOC) in the atmospheric aerosols. They have received much attention because of their important roles in atmospheric chemistry. The most abundant diacid in the aerosol was oxalic acid (C₂) throughout the seasons. DESI-MS (Desorption Electrospray Ionization Mass Spectrometry) was applied for the first time to analysis the diurnal variation of oxalic acid (oxalate) in the ambient aerosols by using self-designed Time Resolved Aerosol Sampler (TRAS). TRAS can sample TSP or PM_{2.5} automatically with adjustable time resolution from 1 - 6 hours depending on the concentration of target compounds. Our 2-hr resolved data showed that the concentration of oxalate has a strong diurnal pattern with higher value during daytime. Peak concentration appeared in the morning from 6:30 am to 8:30 am and the lowest value occurred from 10:30 pm to 0:30 am. This daily variation may be attributed to the daytime photochemical reactions and/or direct emission from fossil fuel combustion. Standard samples of mixed dicarboxylic acids including oxalic acid, malonic acid and succinic acid were analyzed by DESI-MS under the common optimization parameters to confirm the validation of the above measurement. The limit of detection for each of the dicarboxylic acids is about 10 pg mm⁻². Calibrations for all the dicarboxylic acids showed linearity over a concentration range of 5 orders of magnitude with correlation coefficients R²>0.90.

Keywords: Desorption Electrospray Ionization Mass Spectrometry; oxalic acid; diurnal variation; Time Resolved Aerosol Sampler;

Comparison of Key Air Pollutant (PM_{2.5}) Sources and Their Source Strength over Two Consecutive Winter Seasons in Kanpur (India) Region

Soumabha Chakraborty¹, Anil Kumar Mandariya¹ and Tarun Gupta¹

1 Environmental Engineering and Management Program, IIT Kanpur, Kanpur 208016, UP, India

Principal Contact: Dr. Tarun Gupta, Associate Professor, Environmental Engineering and Management Program, IIT Kanpur, Kanpur 208016, UP, India.

Tel: 91 5122597128 Fax: 91 5122597395 E-mail: tarun@iitk.ac.in

Abstract

The main objective of this study was to compare the key air pollutant sources and their source strength over two consecutive years on the basis of PM_{2.5} measurement used for source apportionment via PMF (Positive Matrix Factorization) model. PM_{2.5} (particles having diameter < 2.5 μm) concentration has been measured in Kanpur, in the Indo-Gangetic Plain (IGP). Day time 8 hour integrated filter based samples were collected for two consecutive winter seasons (Nov'09 to Feb'10 and Nov'10 to Jan'11). The chemical analysis of these samples were carried out for anions (F⁻, Cl⁻, NO₃⁻, SO₄²⁻) and cation (NH₄⁺) using Ion Chromatography (IC) and 17 significant elements using ICP-OES. Water Soluble Organic Carbon (WSOC) present in PM_{2.5} was also determined using Total Organic Carbon Analyzer. The average PM_{2.5} concentration for the winter season 2009-2010 was found to be 172±60 μg/m³. The data set was used as an input for a source-receptor model (PMF). The PMF gave 8 source factors for the winter season of 2009-10. The analysis for 2010-11 data is ongoing.

Keywords: PM_{2.5}, Source apportionment; PMF; Ammonium; Anions; Elements.

Chemical Composition and Seasonal Variation of PM_{2.5} Aerosols at Hyderabad (India)

L.A.K. REDDY¹, J. SATYANARAYANA¹, MONIKA J KULSHRESRAH², R N RAO¹ and U C KULSHRESTHA^{3*},

¹ Indian Institute of Chemical Technology, Hyderabad 500007

² National Physical Laboratory, New Delhi 110012

³ Jawaharlal Nehru University, New Delhi 110067

Principal contact: Umesh Kulshrestha, Prof., Jawaharlal Nehru University, New Delhi 110067, Tel: 9717845703, umeshkulshrestha@yahoo.in

Abstract

The seasonal mean mass concentration of various ions in PM_{2.5} aerosols was estimated at an urban site in Hyderabad which lies in south central India. The study was carried out during January 2006 to August 2008 covering summer, monsoon and winter seasons. The results clearly showed the dominance of SO₄²⁻, NO₃⁻, Ca²⁺ and NH₄⁺ ions in PM_{2.5} aerosols. Concentration of SO₄²⁻, NO₃⁻ and NH₄⁺ ions was noticed highest during winter period while that of Ca²⁺ was highest during summer. At this site, moderate influence of sea salt was seen. Contribution of Cl⁻, which was 7 % during summer and winter periods, enhanced to 16% during the monsoon period. The major contribution to PM_{2.5} aerosols was observed due to SO₄²⁻ contributing 35%, 32% and 17% during winter, summer and monsoon seasons respectively. Ammonium contributed 15%, 12% and 0.5% during the winter, summer and monsoon seasons respectively. Mean contribution of NO₃⁻ was 24%, 20%, and 15% during winter, summer and monsoon seasons while calcium contributed 36%, 20% and 12% during monsoon, summer and winter seasons respectively. Apart from local crustal sources and transported through monsoon rains, it is likely that fine mode calcium may also be contributed by various industrial activities in the area. High correlation of SO₄²⁻ and NH₄⁺ indicated the existence of (NH₄)₂SO₄ or NH₄HSO₄. These fine aerosols are secondary aerosols formed by the oxidation of their precursor gases SO₂ and NH₃.

Keywords: PM_{2.5} aerosols, seasonal variation, anthropogenic sources, sulphate, secondary aerosol.

Direct & Indirect Radiative Forcing Simulation Study using WRF_Chem Model

Fenjuan WANG and Hua ZHANG

National Climate Centre, No. 46 Zhongguancun Nandajie Haidian District, Beijing, China,
100081

Principal Contact: Fenjuan WANG, PhD., National Climate Centre, No. 46 Zhongguancun
Nandajie Haidian District, Beijing, China, 100081, 010-58995365, 010-58998508,
wangfj@cma.gov.cn

Abstract

Atmospheric aerosol becomes climatically important, causes scattering and absorption of incoming solar radiation exerting the direct radiative forcing and contributes to the indirect radiative forcing by a series of proposed impacts that include increased cloud albedo due to increases in cloud droplet concentrations and size. We investigate direct and indirect effects of aerosols on the radiation budget and cloud microphysics by the Chemistry version of the Weather Research and Forecasting model (WRF-Chem). WRF-Chem includes MADE/SORGAM aerosol scheme, which divides aerosols into Aitken, accumulation, and coarse three modal distributions and assumes aerosols are internally mixed. The aerosol-radiation-microphysics interaction calculating aerosol number distribution and cloud droplet number from activated aerosol, providing aerosol optical properties over 4 wavelengths, cloud optical depth etc.. A coarse global emission inventory and a fine emission inventory in the region of China are implemented. The preliminary results show that aerosol radiation-cloud feedback reveals a significant sensitivity of the model to indirect effects. The insufficient emissions inventory over China used in the model is somehow infect the precise of the results.

Keywords : Atmospheric aerosol, Direct & Indirect Radiative Forcing, WRF-Chem

Climate Influences on Optical Characteristics of Aerosols Over The Arabian Gulf

Fatma Hasan¹, Hala K.Al-Jassar² and Kota S. Rao³

1 Kuwait University, physics department, Kuwait

2 Kuwait University, physics department, Kuwait

3 Kuwait University, physics department, Kuwait

Principal Contact: Fatma, Hasan, Kuwait University, physics department, P.O.Box 5969 Safat 13060 Kuwait.

Tel: + 965 66182666 Fax: + 965 24819374 E-mail: Fatma.Alkandri@gmail.com

Abstract

The aim of this study is to examine the optical characteristics of the transported particles via two consecutive wind regimes. The first one is a complex transition phase that occurs from 17 of April and ends on 31th of May . Wind velocities range from low to moderate speeds and come from different directions. The second wind regime is associated with dry hot North West winds (Al-Bowareh) that blow between first of June and ends on 17th of July under the influence of the seasonal Indian monsoon. The data records are obtained from Aerosol Robotic Network (AERONET) from three sites in Arabian Gulf, Kuwait, the Solar Village and Dhandah. Higher aerosols optical depths were recorded in the second phase due to temperatures raise. Coarse particles are dominant in both phases peaking at 2.24 μm at Kuwait and the Solar Village, 1.7 μm at Dhandah. The Single Scattering Albedo (SSA) in both phases increase slightly with the wave length. High absorption at 440 nm is found due to the presence of combustion aerosols. Our study shows that Kuwait and the Solar Village have higher soot concentrations than Dhandah. A strong correlation exist between the total absorption coefficient and the total volume concentration for particles with radius less than or equal 0.75 μm in Kuwait and the Solar village ($r = 0.62$, $r = 0.76$ respectively). Using aerosols optical data in conjunction with meteorological data allow us to build a statistical model for estimation of aerosol optical depth over the Arabian gulf.

Keywords: Aerosols, wind regime, optical depths, single scattering albedo, coarse particles, statistical model.

Sampling Method Evaluation for Measurement of Solid Particle Number Distributions from Marine Diesel Engines and Fuels

Jørgen B. Nielsen¹ and Sergey Ushakov²

¹ MARINTEK – Norwegian Marine Technology Research Institute, P.O. Box 4125 Valentinslyst, NO-7450 Trondheim, Norway

² Norwegian University of Science and Technology (NTNU), Department of Marine Technology, Otto Nielsens vei 10, NO-7491 Trondheim, Norway

Principal Contact: Sergey Ushakov, Norwegian University of Science and Technology (NTNU), Department of Marine Technology, Otto Nielsens vei 10, NO-7491 Trondheim, Norway, +47 97547380, sergey.ushakov@ntnu.no.

Abstract

The high content of impurities and sulfur in marine diesel fuels makes it challenging to separate volatile and solid components of emitted aerosols. The sampling methods for measurement of solid particulate matter (PM) number distribution developed for the automotive industry must be modified in order to measure the PM distributions in marine engines. This study evaluates sampling parameters and their effect on the formation of volatile particles. Different marine engines, both 2-stroke and 4-stroke, have been tested on typical marine fuels to identify the sampling system modifications, which are required to measure only solid particle number distributions. PM number distributions are obtained by a combined ELPI-SMPS instrument setup.

Keywords: particulate matter; MGO; HFO; marine diesel engine; ELPI; SMPS.

Characteristics of Ultrafine Particles Emitted from Compression Ignition Engines

Xinling Li, Wei Liu, and Zhen Huang

Key Laboratory of power Machinery and Engineering Education Ministry Shanghai Jiao Tong University

Principal Contact: Xinling Li, Doctor, Shanghai Jiao Tong University, 800 Dongchuan Road, Shanghai 200240, China.

Tel: 021-34206728 Fax: 021-34205949 Email: lxl@sjtu.edu.cn

Abstract

The measurements of effect of fuel properties and combustion mode on the ultrafine particle emission characteristics of compression ignition combustion engine were conducted. Three kinds of fuels: diesel (a baseline fuel), gas to liquid (GTL, with low sulfur and aromatic hydrocarbon) and dimethyl ether (DME, with oxygen content) were selected to test. Measurements of the ultrafine particle emission characteristics from a diesel engine fueled with diesel, GTL and DME under different engine loads and speeds were conducted respectively. The fuel sulfur and aromatic hydrocarbon and oxygen content show significant effect on the ultrafine particle number concentration and size distribution, in the meantime, the trade-off relationship between nucleation mode and accumulation mode particles in the exhaust was also observed. The effect of combustion modes (including compression ignition direct injection (CIDI), homogeneous charge compression ignition (HCCI) and compound charge compression ignition combustion (CCCI)) on ultrafine particles emitted from engines fuelled with n-heptane was studied. The results indicate that combustion modes significantly affect the ultrafine particle number concentration and size distribution. The number concentrations of nucleation mode particles and total particles have a significantly positive correlation with HC concentrations. The effect mechanism of fuel properties and combustion mode on the ultrafine particle emission characteristics was discussed in the paper.

Keywords: Compression Ignition Engines, ultrafine particle emission, fuel property, combustion mode

Source apportionment of ambient PM₁₀ using linear regression and chemical mass balance

Shamsh Pervez¹, Neha Dubey¹, and Yasmeen Pervez²

1 School of Studies in Chemistry, Pt. Ravishankar Shukla University, Raipur, CG, India

2 Department of Engineering Chemistry, CSIT, Kolihapuri, Durg, CG, India

Principal Contact: Shamsh Pervez, Professor, School of Studies in Chemistry, Pt. Ravishankar Shukla University, Raipur, CG, India.

Tel: +91-9425242455 Email: shamshp@yahoo.co.in

Abstract

Multi-complexity in location and type of sources in urban areas of India is the major challenge in quantifications of source contributions to air pollution mass in a specific atmospheric receptor. Various receptor models, especially provided by USEPA viz. Chemical Mass Balance (CMB), Positive Matrix Factorization (PMF) and UNMIX along with regression and simple factor analysis are being used in many source apportionment studies. Most of source apportionment studies of Indian origin are mainly based on regression and factor analysis method. The work being presented here is mainly focused on inter-comparison of results of source apportionment of ambient PM₁₀ using simple regression and CMB. The study area is Raipur City, Chhattisgarh, India. Four receptor sites belong to different environmentally defined zones and five sources (three major industrial complexes, road traffic emissions and local soils) have been selected for monitoring of PM₁₀ and development of their chemical profiles using 24 species. The PM₁₀ matrices of source and receptor sites have been used to assess the source-receptor relationship using linear regression analysis, while their chemical profiles have been used for source apportionment using chemical mass balance (CMB8). All the receptor sites have shown 3-5 fold higher PM₁₀ levels compared to Indian NAAQS standards (60 ug.m⁻³). Two major industrial complexes have shown dominating contributions to ambient PM₁₀ compared to other sources and similar results have been obtained from CMB, but with different relative contributions. Road-traffic emissions have shown different results of source-receptor relationship between both methods of source apportionment with more clarity of contributions using CMB.

Keywords: Source apportionment, ambient PM₁₀, regression analysis, CMB

Source Apportionment of Particulate Toxic load and their Biomarkers among Workers of Steel Re-rolling and Rice Mills

Yasmeen Pervez¹, James Methew², and Shamsh Pervez²

1 CSIT, Kolihapuri, Durg, CG 491, 010 India

2 Pt. Ravishankar Shukla University, Raipur, CG, 492010 India

Principal Contact: Shamsh Pervez, Professor, Pt. Ravishankar Shukla University, Raipur, CG, 492010 India.

Tel: +91-9425242455 Email: shamshp@yahoo.co.in

Abstract

Source apportionment of personal respirable particulate matter (RPM) of workers engaged in steel re-rolling and rice mills is needed due to the large number of workers engaged in these workshops located in central India. Source apportionment, using emission profiles of indoor sources in workshops and workers' residences, road-traffic, soils and ambient RPM has been carried out. Three workshops for each of two processes (re-rolling steel and rice milling) were selected within an urban-industrial region of central India. Five workers— were selected from each process type and across these categories using non-probability based representative sampling plan using longitudinal study design. RPM matrices have been analysed for inter-relation using linear regression initially. Chemical profiling of RPM for selected 17 species and CMB 8 execution has been carried out. Results have shown that indoor RPM of workshops and residences contributed more than half to personal RPM. Selected toxic species including carbon content have shown multiple source contribution with a quantitative significance more than 20%, especially residential-indoors, which mostly negligible in source-receptor relationship by simple regression. Higher presence of selected toxic metals has been observed in personal RPM levels which put forward the need to assess biomarkers of selected bio-fluids of workers.

Keywords: Workshop-indoors, fine particulate, source apportionment, chemical mass balance, personal exposure, biomarker

Characteristics, Sources and Long-range Transport of Heavy Metals of Aerosols over China

Rong Zhang Guoshun Zhuang* Juan Li Kan Huang Qiongzheng Wang Chang Xu

Yilun Jiang Ying Chen

(*Center for Atmospheric Chemistry Study, Department of Environmental Science
and Engineering, Fudan University, Shanghai, 200433, P. R. China*)

Abstract

China owns very serious pollution of heavy metals in atmospheric aerosol. Heavy metals with different type source shown different spatial distribution. Crustal element such as V, Co present much higher concentrations around the source areas of Asia Dust, like central Taklimakan desert, Yulin in northern Shaanxi, and Duolun in Inner-Mongolia; pollution elements like Cu, Pb, Zn, As, Cd, and Ni showed much higher concentration at urban areas such as Urumqi, Beijing, and Shanghai. When comparing with cities around the world, the concentration of major pollution elements like As, Cd, Pb, and Zn in aerosol of Chinese cities showed an order of magnitude higher. Heavy metals showed significant seasonal variation: concentrations of heavy metals in spring and winter were much higher than in summer and autumn of 2-7 folds for different elements.

Asia Dust and biomass burning was found to be an important source of heavy metals (As, Cd, Cu, Ni, Pb et al.) especially in summer. Under the control of air mass of dust or pollutants from biomass burning, concentrations of heavy metals in aerosol would rise sharply to several times higher.

The effect of the traffic ban and other related air-quality controlling measures in Beijing Olympic Games 2008 were evaluated and distinct decreases of heavy metals in the aerosol were observed. The controlling measures were effective in local air quality improvement, concerning the atmospheric heavy metal pollutants, suggesting that anthropogenic activities: industrial emission, coal combustion and traffic discharge, and architectural emissions could be main sources for heavy metals in aerosol. Regional emission and transport were also important factors to heavy metals of local aerosol.

Long-range transport of Asia Dust could be a very important process for transport and diffusion of heavy metals from local emission.

Key Words: **Aerosol; Heavy metals; Characteristics; Source; Long-range transport**

Vertical structures of PM₁₀ and PM_{2.5} and their dynamical characters in low atmosphere in Beijing urban area

DING Guoan¹, CHEN Zhenyu², GAO Zhiqiu¹, YAO Wenqing¹, CHENG Xinghong³,

1.Center of Atmospheric Watch and Service CMA, Chinese Academy of Meteorological Science, Beijing 100081, China

2.Civil Engineering Department, Hongkong Polytechnic University, Hongkong, China

3.National Meteorological Center, China Meteorological Administration, Beijing 100081, China

Principal Contact: DING Guoan, Prof., Center of Atmospheric Watch and Service CMA, Chinese Academy of Meteorological Science, Beijing 100081, China, Email: dingga@cams.cma.gov.cn

Abstract

The vertical structures and their dynamical characters of PM_{2.5} and PM₁₀ over Beijing urban area are revealed using the 1min mean continuous mass concentration data of PM_{2.5} and PM₁₀ at 8, 100, and 320 m heights of the meteorological observation tower of 325m at Institute of Atmospheric Physics, Chinese Academy of Sciences (IAP CAS tower hereafter) in 10-26 August 2003, as well as the daily mean mass concentration data of PM_{2.5} and PM₁₀ and the continuous data of CO and NO₂ at 8, 100 (low layer), 200 (middle layer), and 320 m (high layer) heights, in combination with the same period meteorological field observation data of the meteorological tower. The vertical distributions of aerosols observed on IAP CAS tower in Beijing can be roughly divided into two patterns: gradually and rapidly decreasing pattern, i.e. the vertical distribution of aerosols in calm weather or on pollution day belongs to the gradually decreasing pattern, while one on clean day or weak cold air day belongs to the rapidly decreasing pattern. The vertical distributive characters of aerosols were close related with the dynamical/ thermal structure and turbulence character of the atmosphere boundary layer. On the clean day, the low layer PM_{2.5} and PM₁₀ concentrations were close to those at 8 m height, while the concentrations rapidly decreased at the high layer, and their values were only one half of those at 8m, especially, the concentration of PM_{2.5} dropped even more. On the clean day, there existed stronger turbulence below 150m, aerosols were well mixed, but blocked by the more stronger inversion layer aloft, and meanwhile, at various heights, especially in the high layer, the horizontal wind speed was larger, resulting in the rapidly decrease of aerosol concentration, i.e. resulting in the obvious vertical difference of aerosol concentrations between the low and high layer. On the pollution day, the concentrations of PM_{2.5} and PM₁₀ at the low, middle, and high layers dropped successively by, on the average,

about 10% for each layer in comparison with those at 8 m height. On pollution days, in company with the low wind speed, there existed two shallow inversion layers in the boundary layer, but aerosols might be to some extent mixed below the inversion layer, therefore, on the pollution day the concentrations of PM_{2.5} and PM₁₀ dropped with height slowly; and the observational results also show that the concentrations at 320 m height were obvious high under SW and SE winds, but at other heights, the concentrations were not correlated with wind directions. The computational results of footprint analysis suggest that this was due to that the 320 m height was impacted by the pollutants transfer of southerly flow from the southern peripheral heavier polluted areas, such as Baoding, and Shijiazhuang of Hebei province, Tianjin, and Shandong province etc, while the low layer was only affected by Beijing's local pollution source. The computational results of power spectra and periods preliminarily reveal that under the condition of calm weather, the periods of PM₁₀ concentration at various heights of the tower were on the order of minutes, while in cases of larger wind speed, the concentrations of PM_{2.5} and PM₁₀ at 320 m height not only had the short periods of minute-order, but also the longer periods of hour order. In consistent with the conclusion previously drawn by Ding et al, that air pollutants at different heights and at different sites in Beijing had the character of "in-phase" variation, was also observed for the diurnal variation and mean diurnal variation of PM_{2.5} and PM₁₀ at various heights of the tower in this experiment, again confirming the "in-phase" temporal/spatial distributive character of air pollutants in the urban canopy of Beijing. The gentle double-peak character of the mean diurnal variation of PM_{2.5} and PM₁₀ was close related with the evident/similar diurnal variation of turbulent momentum fluxes, sensible heat fluxes, and turbulent kinetic energy at various heights in the urban canopy. Besides, under the condition of calm weather, the concentration of PM_{2.5} and PM₁₀ declined with height slowly, it was 90% of 8 m concentration at the low layer, a little lesser than 90% at the middle layer, and 80% at the high layer, respectively. Under the condition of weak cold air weather, the concentration remarkably dropped with height, it was 70% of 8 m concentration at the low layer, and 20-30% at the middle and high layers, especially the concentration of PM_{2.5} was even lower.

Keywords: PM₁₀, PM_{2.5}, mass concentration, vertical structure, dynamical character, footprint analysis

An overview of the measurements of the scattering, absorption and hygroscopic growth of aerosols in the rural areas of eastern China

Peng Yan and Xiuji Zhou

Chinese Academy of Meteorological Sciences, Zhongguancun Nandajie 46, Beijing, 100081

Principal Contact: Peng Yan, Professor, Chinese Academy of Meteorological Sciences, Zhongguancun Nandajie 46, Beijing, 100081, China.

Tel: 010-68406646 Email: yanpeng@cams.cma.gov.cn.

Abstract

Aerosol scattering and absorption coefficients and the hygroscopic growths are the key factors for direct radiative forcing and visibility impairment study. In this paper, the aerosol optical properties observed in the past years at the two GAW (Global Atmospheric Watch, WMO) regional background regions in the eastern China were characterized. The two sites are the regional background station in the northern plain of China (NPC), Shangdianzi station (SDZ), and the Lin'An station (LA) in the Yangtze river delta region (YRD), respectively. The main results are concluded as follow: The aerosol optical properties in the background region of NPC and YRD were much different, In general, the scattering and absorption coefficient of aerosols at LA were higher than those at SDZ, and the mean SSA at LA was much lower, indicating the strong light absorption of aerosols in Yangtze delta region. Compared with the previous measurement made at LA site in November 1999, the absorption coefficient nearly doubled while scattering coefficient decreased by about one third, which led to the significant reduction of SSA. These results indicated that the aerosols in that region were becoming more light-absorbing, and these changes would bring about a great impact on the regional climate in that region. The hygroscopic growth of aerosol measurements indicated that significant seasonal variations of $f(RH)$ are found at both sites with high $f(RH)$ in summer. On average, the mean $f(RH=80\%)$ at LA and SDZ were similar in the summer, while in winter the $f(RH=80\%)$ at LA is much higher than that at SDZ.

Keywords: aerosol optical properties, rural areas of eastern China, hygroscopic growth

An Aerosol Dipole Event over the Tropical Indian Ocean during 2006

P.R.C.Rahul^{*1}, P.S.Salvekar¹ and P.C.S.Devara¹

1Indian Institute of Tropical Meteorology, Pune, India

* Email: rcreddy@tropmet.res.in

Introduction

On a global scale, the natural sources of aerosols are more important than the anthropogenic aerosols but regionally, anthropogenic aerosols are more important. Aerosol plumes, the byproducts of biomass burning, have long been observed over large regions of the tropics with aircraft, balloons, and ground-based instrumentation . In the El Nino year 1997, Indonesia experienced abnormal drought conditions, and the number of land clearing fires by far exceeded the normal annual dry season's burning. During this very strong El Nino event of 1997–1998, Southeast Asia experienced severe drought, which caused large-scale forest fires. Indonesian Forest fires have been attributed predominantly to El Niño and IOD conditions , this led to the release of large amount of aerosols into the atmosphere, significantly affecting the regional aerosol distribution. The response of the AOD variability to the IOD event of 2006, is found to be different from that observed during 1997, which was associated with both El Nino and IOD. We also study the AOD variability along the equatorial western Indian Ocean and over Indonesia with the help of surface winds, OLR derived from NCEP/NCAR reanalysis data set and rainfall patterns obtained from TRMM in order to substantiate the findings.

Data

The region considered for study is the tropical Indian Ocean over the domain [10°S-10°N; 40°E-130°E]. Aerosol optical depths [at 550 nm] have been obtained using Level-3 MODIS gridded atmosphere monthly global product 'MOD08_M3'. Monthly average (AOD averaged over the full month) MOD08_M3 product files are available in Hierarchical Data Format (HDF-EOS) at spatial resolution of 1 degree by 1 degree. Monthly AOD anomalies of September, October and November 2006 were computed as departures from the 2000–2008 climatological mean for that month, i.e., we have extracted the September, October and November AOD (at 550 nm) anomalies from 9-year climatology (2000-2008). Similarly OLR and wind anomaly for September, October and November during 1997 and 2006 have been obtained from the NCEP 58-year climatology (1949-2008) and rainfall anomaly from the TRMM's 11-year climatology (1998-2008).

Results

Spatial distributions of the monthly AOD [550nm] anomalies are plotted in the Figure 1.a to c, for September, October and November 2006, respectively, over the

considered region, 10°S - 10°N ; 40°E - 130°E . Significant variability of the AOD anomalies is observed over the tropical Indian Ocean and Indonesia. From the anomaly plots it is clear that the aerosol plume originates over small domain over Indonesia during August [Figure not shown], and advects westward during September [Figure 1.a], by October [Figure 1.b] the plume is engulfing Indonesia, Sumatra and spreads into the east equatorial East Indian Ocean. The latitudinal extent of the plume with AODs $> +0.6$, is from 4°S - 8°N and longitudinally it covers 92°E - 125°E , i.e. covering over a massive $\sim 3,600\text{km}$ in October. The plume starts to wane in November [Figure 1.C], propagating into the East Indian Ocean and by December the plume diffuses.

The AOD anomalies over the central and western Arabian Sea are negative [-0.2] implying weaker plumes over a smaller domain as seen in Figure 1.a, during September 2006. These negative AOD anomalies enhance from -0.3 to -0.4 and spread over a larger spatial domain by November. Thus the anomalies observed during the September-November 2006 resemble a dipole-like structure of AOD variability over the Equatorial Indian Ocean, with positive AOD anomalies [+0.4 to +0.6] along the Eastern Indian Ocean and over Indonesia and negative AOD anomalies [-0.2 to -0.4] over the western and central Indian Ocean.

The spatial distribution of aerosols in the atmosphere is significantly influenced by the prevailing winds [1, 2]. The year 2006 being a dipole year, the wind fields are drastically different from those experienced during normal years as seen in the Figure 2. a-c. In a normal year (absence of IOD and El Nino), the southeast trade winds converge into the South Equatorial Trough [3] associated with the high-rainfall Ocean Tropical Convergence Zone, but during the IOD years, the surface wind field over the tropical Indian Ocean experiences large changes, especially in its zonal [east-west] component over the Equator. TRMM rainfall anomalies during September-November 2006 are also examined in Figure 3. a-c; there are negative anomalies [-400 mm] over the Eastern Indian Ocean and Indonesia during September-November, while positive anomalies [+400 to 500mm] exist over the western and central Arabian Sea. Shown in Figure 3. d-f are the plots of OLR anomalies derived from NCEP / NCAR reanalysis data sets. The regions of positive rainfall anomalies associate with the regions of negative OLR anomalies and vice-versa.

CONCLUSIONS

The large changes in the surface wind circulation over the tropical Indian Ocean and Indonesia affect both the Ocean and atmosphere – (i) In the Indian Ocean this effect is called the Indian Ocean Dipole and (ii) In the atmosphere, this effect is seen in the aerosol variability in the form of an Aerosol Dipole, as being reported in this study. This Aerosol Dipole is characterized by positive AOD anomalies [+0.4 to +0.6] in the eastern Indian Ocean and Indonesia, and negative AODs anomalies [-0.2 to -0.4] over the

western, northwestern and equatorial central Indian Ocean, during September-November 2006. The aerosol dipole variability has also been supported by the characteristic variability in the winds, OLR and rainfall anomalies.

REFERENCES

1. A.V. Smirnov, Y.Villevalde, N.T.O'Neill, A.Royer and A.Tarussov, Aerosol optical depth over the oceans: Analysis in terms of synoptic air mass types. *J. Geophys. Res.*, **100**, 16,639 –16,650 (1995).
2. K.K. Moorthy, S.K. Satheesh and B.V.Krishna Murthy., Investigations of marine aerosols over tropical Indian Ocean, *J Geophys Res* **102**, 18,827–18,842 (1997).
3. T. Yamagata, K. Mizuno and. Y. Masumoto., Seasonal Variations in the Equatorial Indian Ocean and their Impact on the Lombok Throughflow, *J. Geophys. Res.*, **101** [C5], 12465-12473 (1996).

Figure Captions:

Figure 1. a-c are the monthly-derived AOD anomalies from MODIS during September-November 2006.

Figure 2. a-c are the monthly-derived surface wind anomalies (m/s) during September-November 2006, while d-f represent the anomalies during September-November 1997.

Figure 3. a-c are the monthly-derived TRMM rainfall anomalies(mm) and d-f are the OLR anomalies(Watts/m²)during September-November 2006.

Figure 4. a-c are the monthly-derived AOD rainfall anomalies and d-f are the surface wind anomalies during September-November 2001.

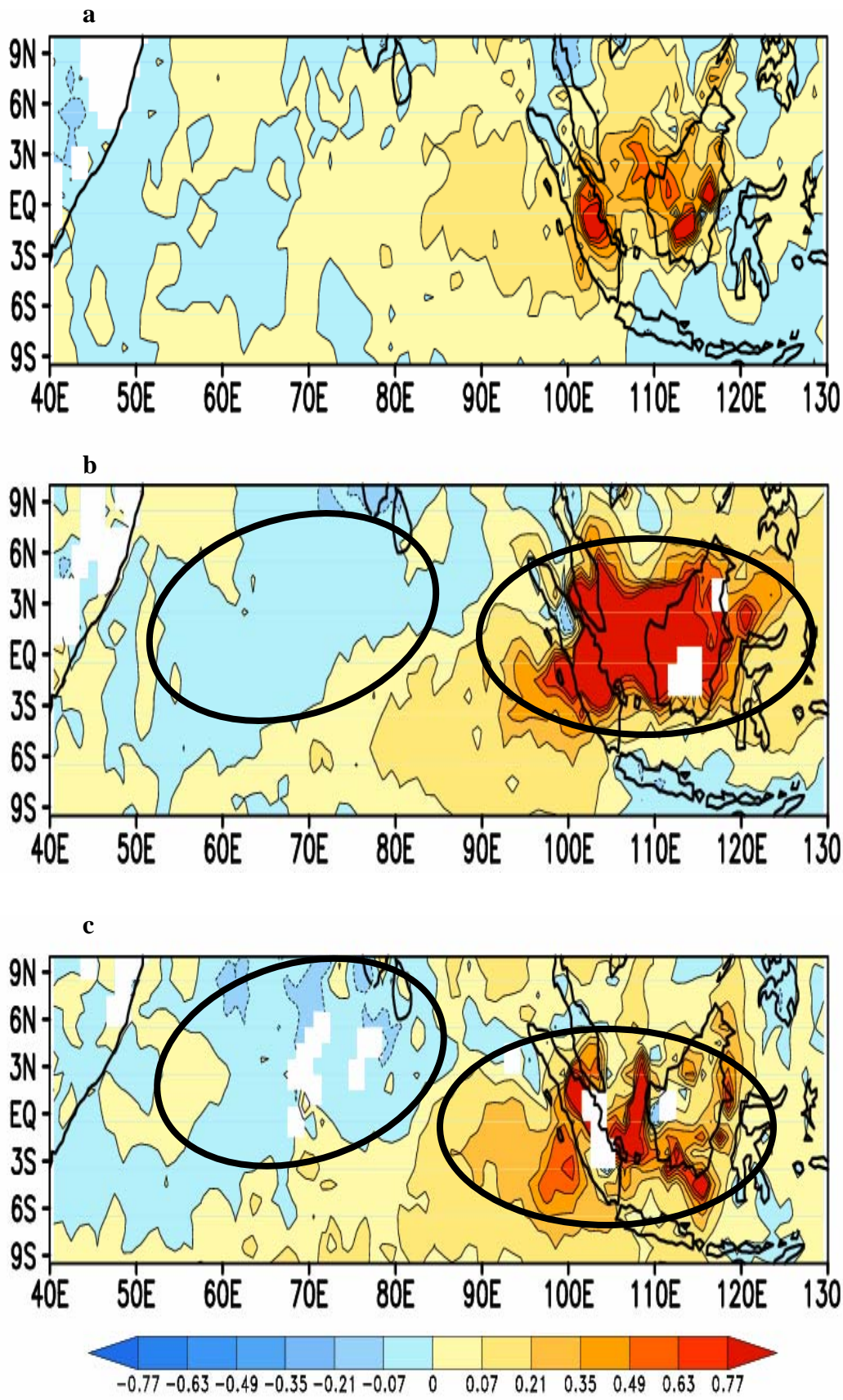
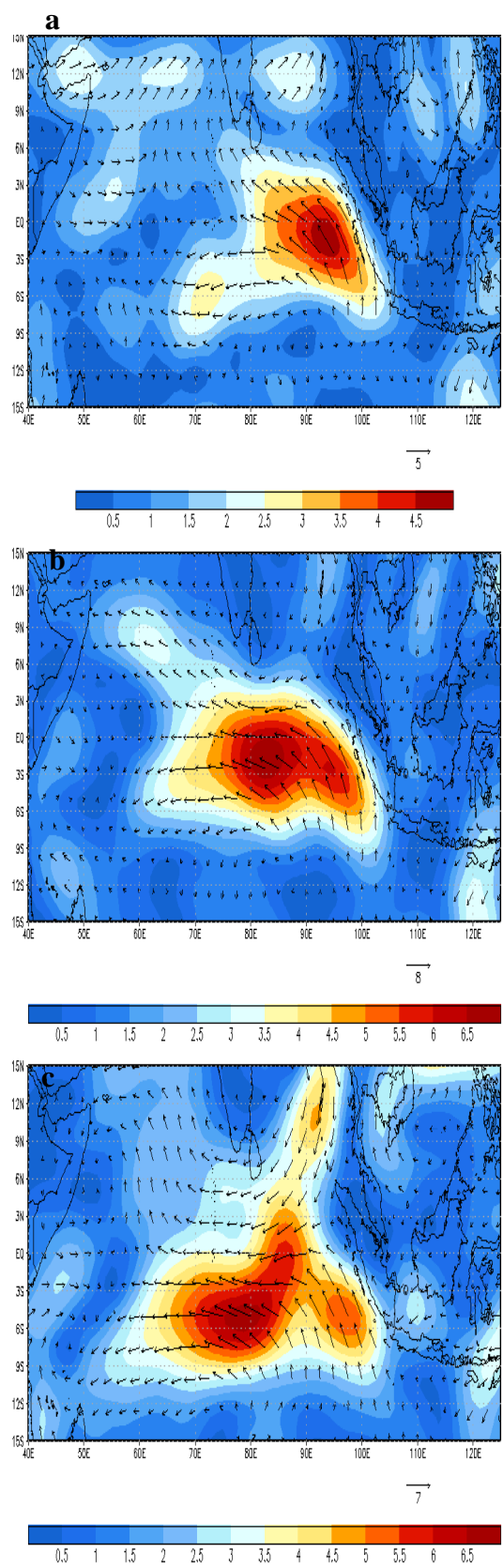


Figure 1

Monthly surface wind anomalies - 2006



Monthly surface wind anomalies - 1997

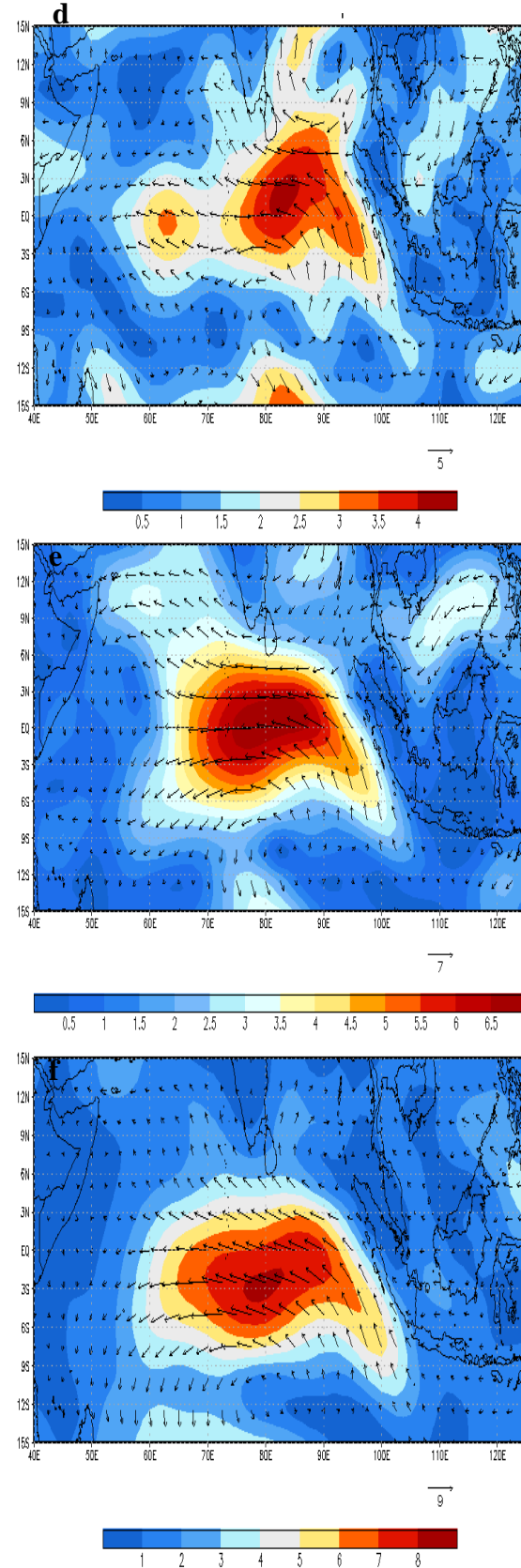


Figure 2

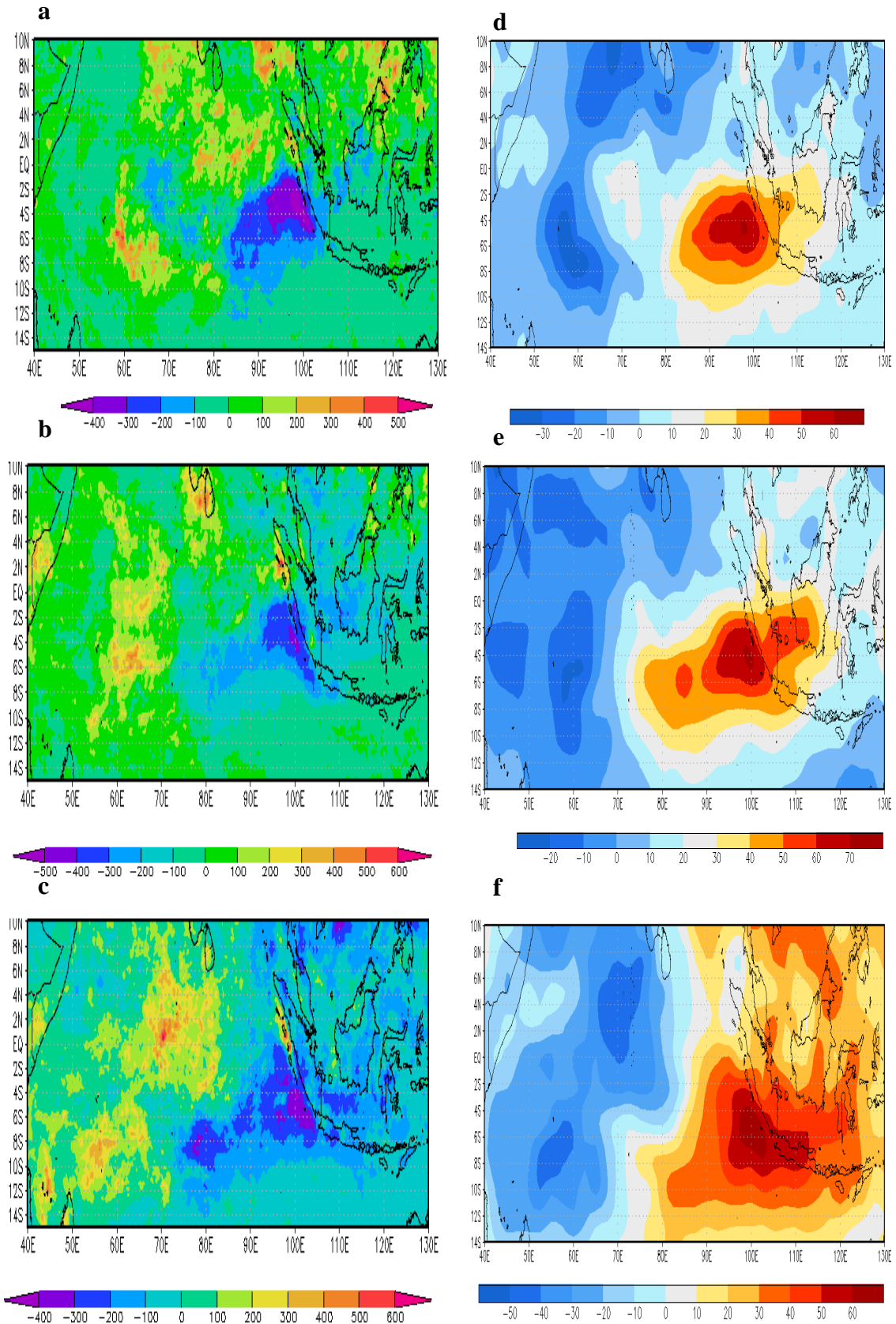
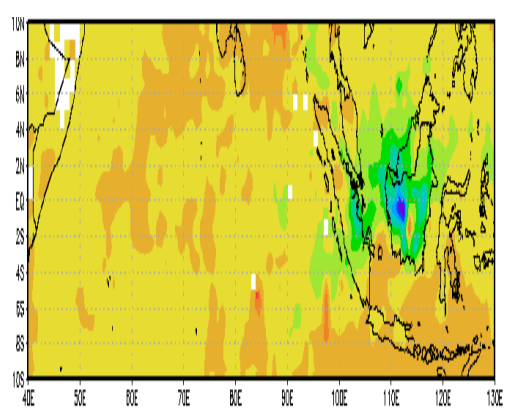
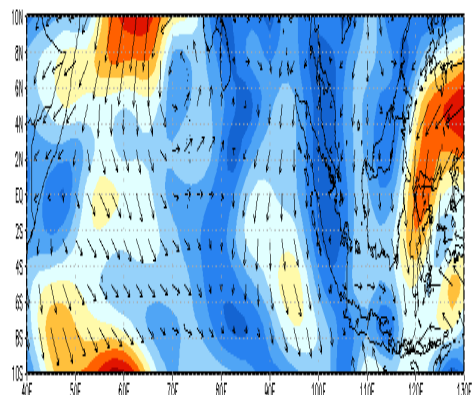
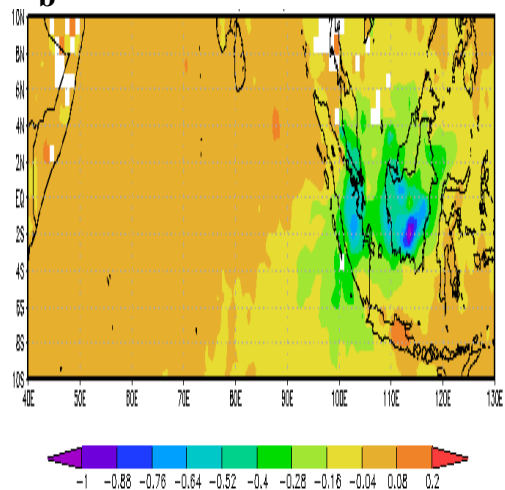
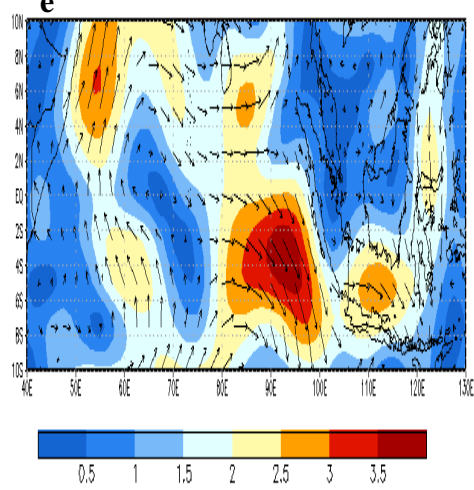
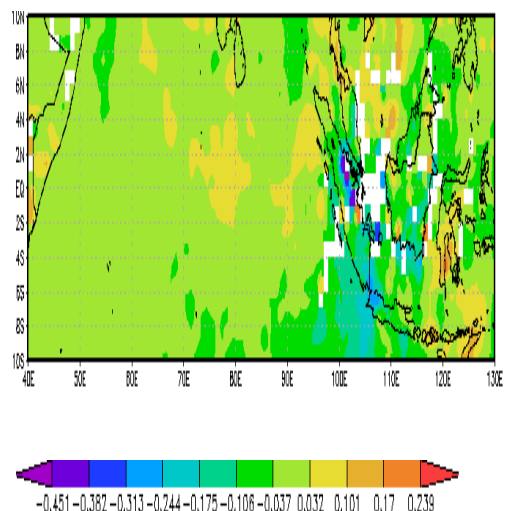
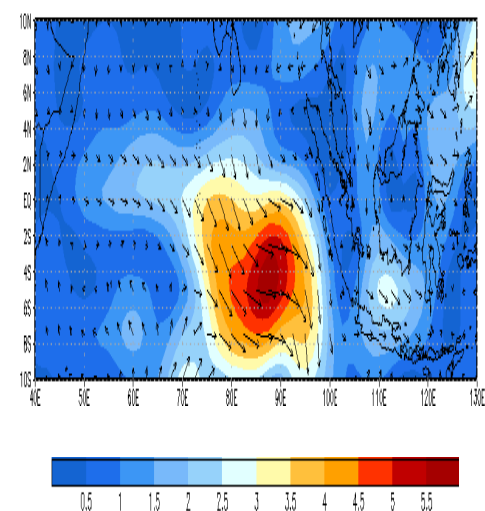


Figure 3

a**d****b****e****c****f****Figure 4**

Concentrations and composition of PAHs in urban environment of Hong Kong

Kin Fai Ho^{1,2}, Yan Cheng^{1,3}, Steven Sai Hang Ho¹, Shun Cheng Lee³, Linwei Tian²

1 SKLLQG, Institute of Earth Environment, Chinese Academy of Sciences,
Xi'an, 710075, China

2 School of Public Health and Primary Care, Chinese
University of Hong Kong, Hong Kong, China

3 Department of Civil and Structural Engineering,
Research Center for Environmental Technology and Management,

Principal Contact: K.F. Ho, Prof., The Hong Kong Polytechnic University, Hung Hom,
Kowloon, Hong Kong.

Tel: +852-27664811 E-mail: cehokf@polyu.edu.hk

Abstract

Vehicle emission (VE) is one of the important anthropogenic sources for airborne polycyclic aromatic hydrocarbons (PAHs) in urban cities. Roadside and five types of VE-dominated samples [(i) a gasoline-fueled private car park; (ii) a diesel-fueled minibus station; (iii) a whole food market entrance for diesel-fueled heavy goods vehicles; (iv) a diesel-fueled single-decked depot; and (v) a diesel-fueled double-decked bus depot] were collected at representative locations in Hong Kong. Seventeen gas and particulate PAHs in the samples were quantified during summer and winter 2003. Naphthalene, acenaphthylene, and acenaphthene were the most abundant gas PAHs while fluoranthene and pyrene were always the most abundant in the particle phase. Most of the gas PAHs consisted of two- and three-aromatic rings (~96%) whereas most of the particle-phase PAHs were in four-, five-, and six-ring (~60%) for fresh exhaust emissions. The concentrations of the total quantified gas- and particle PAHs at the three roadside locations were 820–3717 ng m⁻³ and 4.75–95.4 ng m⁻³, respectively. The highest concentrations of gaseous PAHs was determined in the samples collected at an entrance of a cross harbor tunnel in downtown area in summer. While the highest concentrations of particulate PAHs was determined in the samples collected at a main transportation gate for goods between Hong Kong and China in winter. Both regional and other anthropogenic sources affected the air qualities at the roadside locations as well. However, no seasonal variations were also observed for total quantified gas- and particle PAHs. Moreover, good correlations were found between diesel markers (fluoranthene and pyrene; 0.97) and gasoline markers (benzo[ghi]perylene and indeno[1,2,3-cd]pyrene; 0.84). And relatively high abundant of these markers were found in VE-dominated samples.

Keywords: PAHs, roadside, diesel, gasoline, vehicular emissions.

Relationship between PM concentrations and visibility at an urban area in southern Taiwan

Chien-Lung Chen¹, Feng-Chao Chung², San-Fu Lee³, Li-Ying Hsieh⁴, Su-Ching Kuo⁵ and Ying I. Tsai⁶

¹ Department of Industrial Engineering and Management, Fortune Institute of Technology, 1-10, Nwongchang Rd., Daliao, Kaohsiung 831, Taiwan.

² Department of General Education Center, Fortune Institute of Technology, 1-10, Nwongchang Rd., Daliao, Kaohsiung 831, Taiwan.

³ Department of Finance, Fortune Institute of Technology, 1-10, Nwongchang Rd., Daliao, Kaohsiung 831, Taiwan.

⁴ Department of Chemistry, National Cheng Kung University, 1, University Rd., Tainan 701, Taiwan.

⁵ Department of Medicinal Chemistry, Chia Nan University of Pharmacy and Science, 60, Sec. 1, Erh-Jen Rd., Jen-Te, Tainan 717, Taiwan.

⁶ Department of Environmental Engineering and Science, Chia Nan University of Pharmacy and Science, 60, Sec. 1, Erh-Jen Rd., Jen-Te, Tainan 717, Taiwan.

Principal Contact: Chien-Lung Chen, Assistant professor, Department of Industrial Engineering and Management, Fortune Institute of Technology, 1-10, Nwongchang Rd., Daliao, Kaohsiung 831, Taiwan, Tel: +886955343966, Fax: +88677889777, E-mail: clchen@center.fotech.edu.tw

Abstract

The airborne particulate matter (PM) can cause a decrease in the atmospheric visibility. Charlson et al. (1967) found the visibility could be shown as $L_v = k / M_c$, where L_v is the prevailing visibility (km), M_c is the PM concentrations (mg m^{-3}) and k is the concentration-visibility ratio (g m^{-2}). This study tries to establish the regression equation between particulate concentrations and atmospheric visibility at Kaohsiung, Taiwan. We used the average daily PM_{10} and $\text{PM}_{2.5}$ concentrations including nine air quality monitoring stations around Kaohsiung and average daily

visibility data at Kaohsiung weather station from 2005 to 2009. However, visibility distances can be reduced by precipitation effects. The concentrations and visibility data were screened for precipitation events. The time series plot for daily visibility, PM₁₀ and PM_{2.5} from 2005 to 2009 were shown in [Figure 1](#). PM₁₀ and PM_{2.5} concentrations show negative correlation with visibility ($R = -0.715$ and -0.747 , respectively). The results show that elevated PM concentrations impaired the atmospheric visibility. Then the data from 2005 to 2008 were applied as the regression period and the k values for PM₁₀ and PM_{2.5} are obtained as 0.3577 and 0.1959 shown in [Figure 2](#) ($R = 0.742$ and 0.749 , respectively). Finally the regressed k values are used to calculate the daily PM concentrations in 2009 as the verification period. [Figure 3](#) shows the plots of the observed versus calculated PM₁₀ and PM_{2.5} concentrations. The correlation coefficient and absolute bias between observed and calculated PM concentrations for PM₁₀ are 0.733 and 22.4%, similarly for PM_{2.5} are 0.803 and 24.4%. The calculated PM₁₀ and PM_{2.5} concentrations match well with the observed data at Kaohsiung weather station in 2009.

Keywords : visibility, particulate matter, regression equation

Reference

Charlson, R.J., H. Horvath and R. Pueschel, 1967, The Direct Measurement of Atmospheric Light Scattering Coefficient for Study Visibility and Pollution, *Atmospheric Environment*, Vol. 1, pp. 469-478.

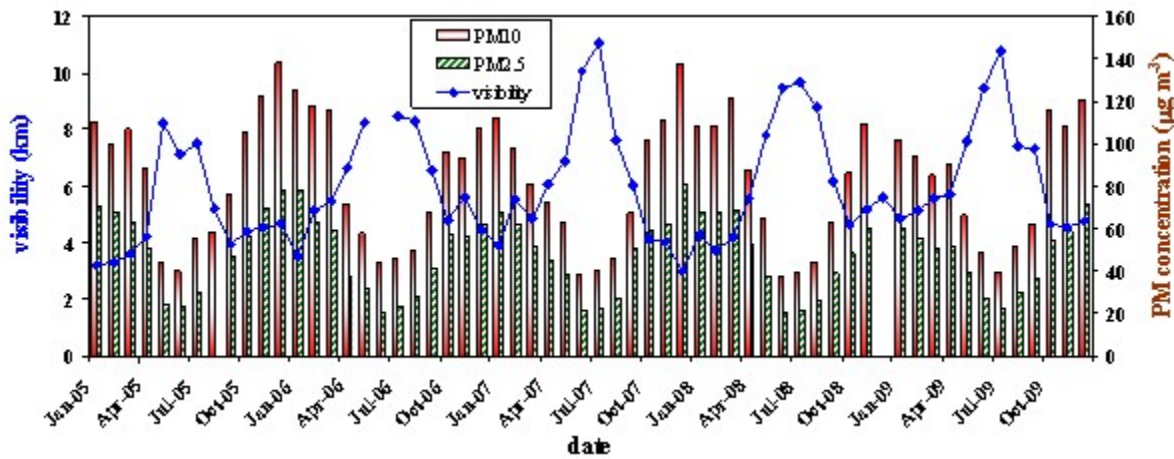


Figure 1. The time series plot of daily visibility, PM_{10} and $\text{PM}_{2.5}$ concentrations at Kaohsiung, Taiwan from 2005 to 2009.

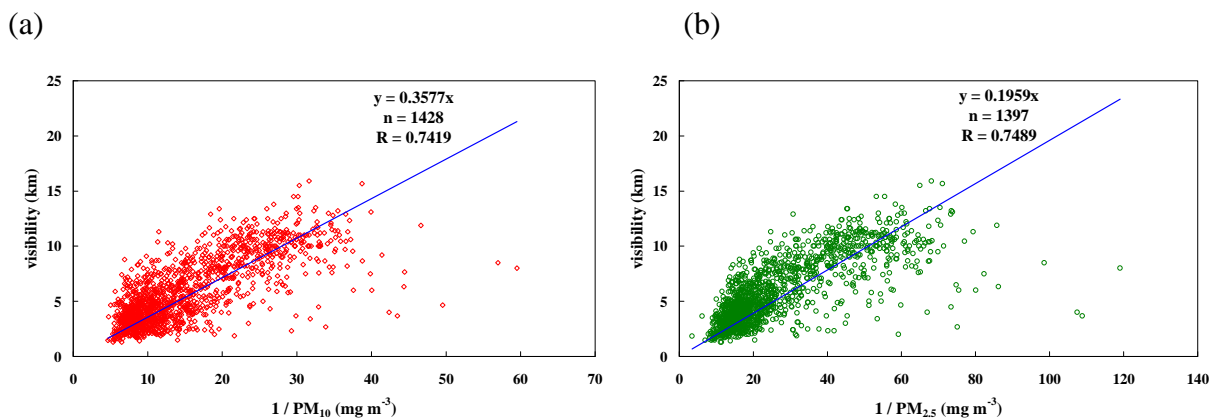


Figure 2. The regression equations and the k values for (a) PM_{10} and (b) $\text{PM}_{2.5}$ using the data from 2005 to 2008 as the regression period.

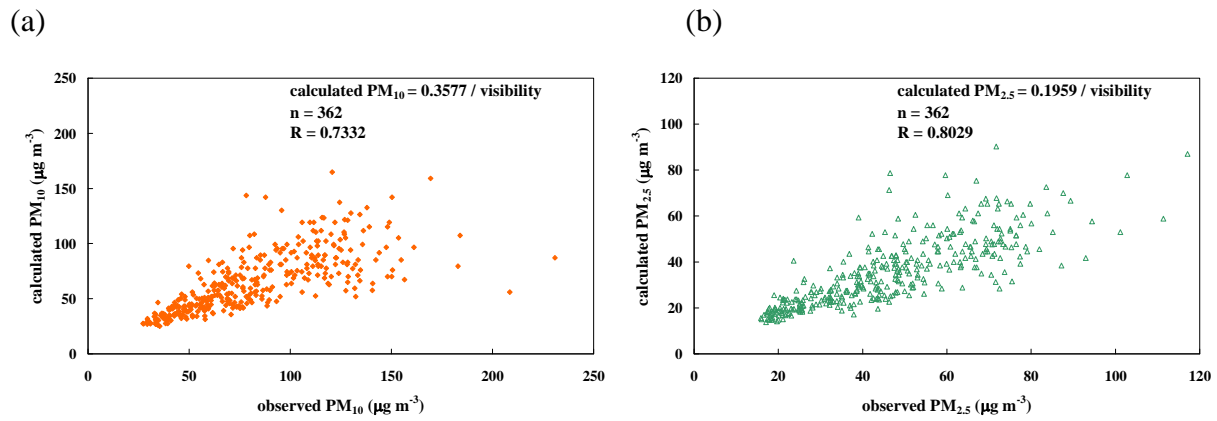


Figure 3. The observed versus calculated PM concentrations for (a) PM_{10} and (b) $\text{PM}_{2.5}$ using the data in 2009 as the verification period.

Particulate matter source apportionment based on a back trajectory model during episode days in central Taiwan

Chien-Lung Chen¹, San-Fu Lee², Feng-Chao Chung³, Su-Ching Kuo⁴, Jeng-Lin Tsai⁵, Pei-Hsuan Kuo⁵, Li-Ying Hsieh⁶ and Ying I. Tsai⁷

¹ Department of Industrial Engineering and Management, Fortune Institute of Technology, 1-10, Nwongchang Rd., Daliao, Kaohsiung 831, Taiwan

² Department of Finance, Fortune Institute of Technology, 1-10, Nwongchang Rd., Daliao, Kaohsiung 831, Taiwan.

³ Department of General Education Center, Fortune Institute of Technology, 1-10, Nwongchang Rd., Daliao, Kaohsiung 831, Taiwan

⁴ Department of Medicinal Chemistry, Chia Nan University of Pharmacy and Science, 60, Sec. 1, Erh-Jen Rd., Jen-Te, Tainan 717, Taiwan.

⁵ Department of Environmental Engineering, National Chung-Hsing University, 250, Kuokang Road, Taichung 402, Taiwan

⁶ Department of Chemistry, National Cheng Kung University, 1, University Rd., Tainan 701, Taiwan

⁷ Department of Environmental Engineering and Science, Chia Nan University of Pharmacy and Science, 60, Sec. 1, Erh-Jen Rd., Jen-Te, Tainan 717, Taiwan

Principal Contact: Chien-Lung Chen, Assistant professor, Department of Industrial Engineering and Management, Fortune Institute of Technology, 1-10, Nwongchang Rd., Daliao, Kaohsiung 831, Taiwan, Tel: +886955343966, Fax: +88677889777, E-mail: clchen@center.fotech.edu.tw

Abstract

It is important to realize the contribution of air pollutants emission sources to ambient concentrations to establish proper and effective strategies. We applied the Gaussian trajectory transfer-coefficient model (Tsuang, 2003; Tseng et al., 2003) to simulate the particulate matter (PM) concentrations and the source apportionments at Chungming Station in central Taiwan during PM episode days in 2008. The location of the receptor is shown in [Figure 1](#). Two kinds of

PM episode days are selected. One PM episode is during Asia dust storm period (2-4 March 2008) and the other PM episode is effected by ill-dispersion synoptic pattern (29 March 2008). The correlation coefficient (R) between the observed and calculated daily PM₁₀ concentrations from 28 February to 5 March 2008 including Asia dust storm is 0.716 ([Figure 2](#)). The source apportionments results indicated that the primary sources for PM₁₀ at Chungming Station were subsidence (31%) during dust storm period and upwind boundary concentration (26%) during non-dust storm period ([Figure 3](#)). The subsidence played an important role during the Asia dust storm. The subsidence increased 12% PM₁₀ apportionment during dust storm period than that during non-dust storm period. On the other hand, the correlation coefficient (R) between the observed and calculated daily PM₁₀ concentrations from 26 March to 1 April 2008 including one PM episode day is 0.965 ([Figure 4](#)). The primary sources for PM₁₀ at Chungming Station were upwind boundary concentration (24%) and point sources (23%) on the PM episode day ([Figure 5](#)). The synoptic system was high pressure circulation effected Taiwan which often causes the ambient in relatively stable condition. Not like the PM₁₀ source apportionment during dust storm period, the subsidence was less important and the long range secondary aerosol transport and local emissions seemed to have much influence on the PM₁₀ contribution to a receptor.

Keywords : source apportionment, trajectory model, PM episode

Reference

- B. J. Tsuang, “Quantification on the source/receptor relationship of primary pollutants and secondary aerosols by a Gaussian plume trajectory model: part I– theory,” *Atmospheric Environment*, vol. 37, pp.3981–3991, 2003.
- B. J. Tsuang, C. L. Chen, C. H. Lin, M. T. Cheng, Y. I. Tsai, C. P. Chio, R. C. Pan and P.H. Kuo, “Quantification on the source/receptor relationship of primary pollutants and secondary

aerosols by a Gaussian plume trajectory model: part II. Case study," *Atmospheric Environment*, vol. 37, pp.3993–4006, 2003.

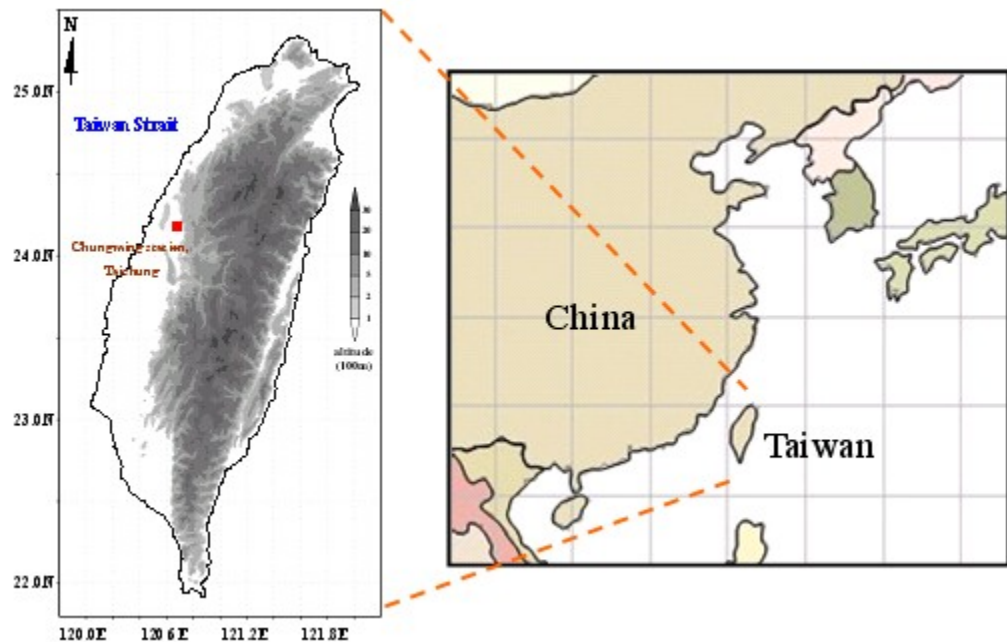


Figure 1. The location of Chungming station, Taichung, Taiwan.

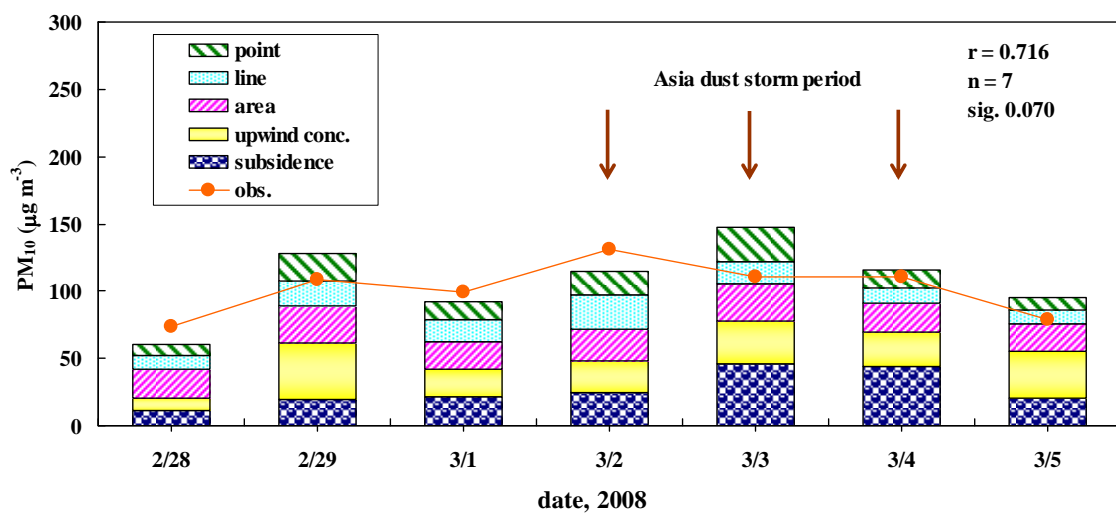


Figure 2. The observed and calculated PM₁₀ daily concentrations at Chungming station, Taichung, Taiwan from 28 February to 6 March 2008 including Asia dust storm.

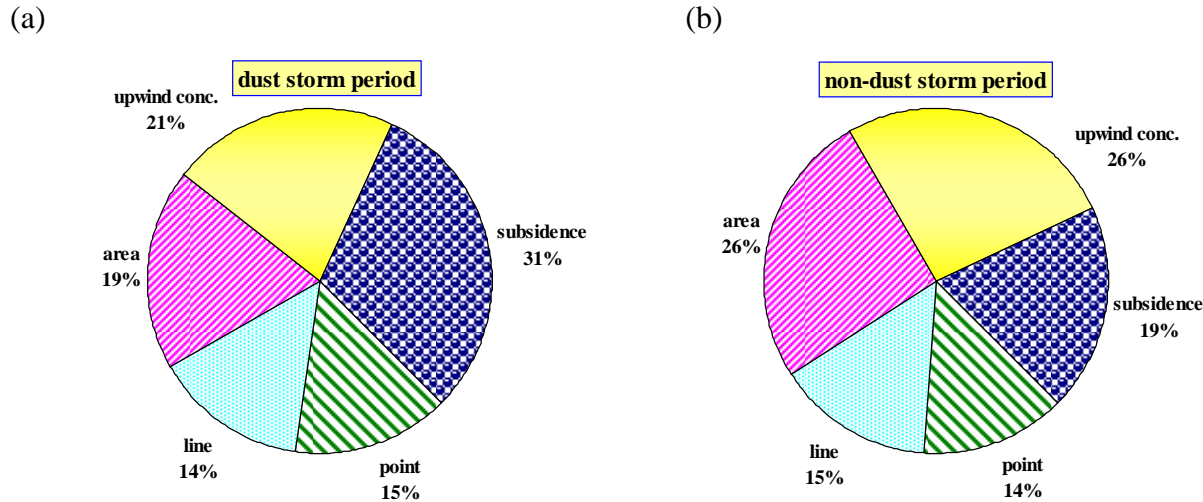


Figure 3. The PM₁₀ source apportionments at Chungming station, Taichung, Taiwan from 28 February to 6 March 2008. (a) dust storm period, (b) non-dust storm period

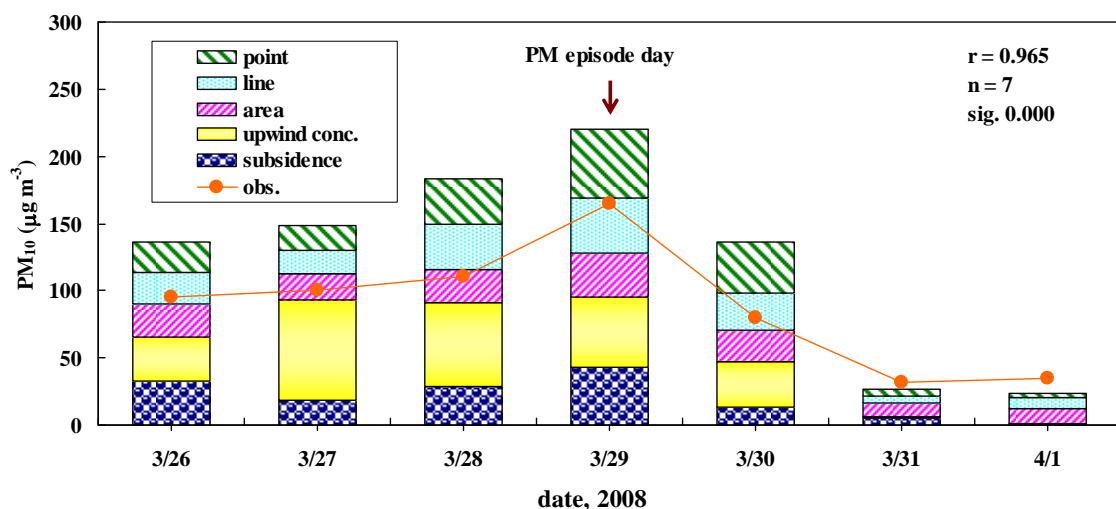


Figure 4. The observed and calculated PM₁₀ daily concentrations at Chungming station, Taichung, Taiwan from 26 March to 1 April 2008 including one PM episode day.

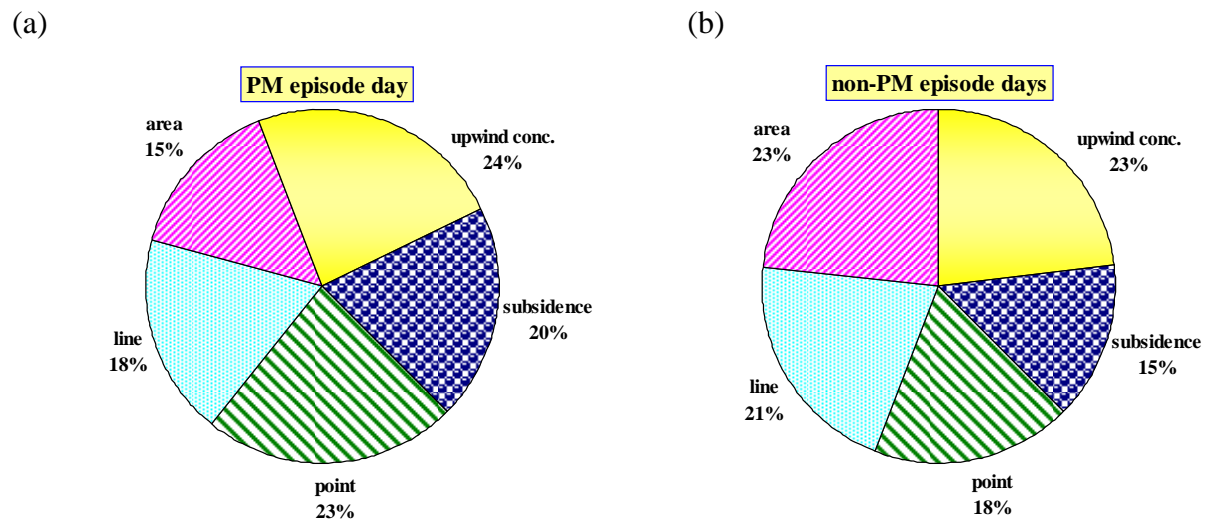


Figure 5. The PM_{10} source apportionments at Chungming station, Taichung, Taiwan from 26 March to 1 April 2008. (a) PM episode day, (b) non-PM episode days

Measurement of Near-road Black Carbon Emissions in an Urban Setting in Midwestern US

Jiangchuan Hu, Shuang Liang, Mingming Lu, Tim C. Keener, Zhuo Yao, and Heng Wei,
University of Cincinnati, Cincinnati, OH 45221, USA

Principal Contact: Mingming Lu, Dept. of Civil and Environ. Eng. Univ. of Cincinnati
Cincinnati, OH 45221, Phone: 513-556-0996, Fax: 513-556-2599, Email:
Mingming.lu@uc.edu

Abstract

Black carbon (BC) emissions have increasingly been studied due to its regional warming effects on climate change and adverse health effects. On-road transportation, especially truck laden traffic, is viewed as the predominant source of BC emissions in the US and other industrialized nations. While the graphite portion of the black carbon (the EC) contributes to global warming, the organic portion (OC) contributes to the cooling effect. The OC/EC distributions of BC tend to vary from location to location, and have some correlation with the traffic conditions. In Midwest UC, both industrial and traffic sources contribute to BC emissions. In order to better understand BC contribution from transportation, BC was collected at a busy intersection and a highway site. BC was collected from both direct reading (aethalometers) and filter based instruments, during rush hours, non-rush hours on both weekdays and weekends. Intersections tend to have stop-and-go traffic, which can potentially have high emissions, and pedestrians, which can be exposed to traffic generated pollutants. In the US, with more and more sustainable community redevelopment, bicycling and walking are increasingly incorporated into transportation planning to reduce pollutant emissions and save energy. Highways, on the other hand, will have more high speed traffic, especially more heavy duty trucks than local roads. Traffic data, such as traffic volume and vehicle types, were also collected. OC/EC analysis was performed on the filter based samples. The BC emission trends of peak, non-peak hours, local and highway sites will be presented and compared with ambient measurements. The OC/EC fractions will also be studied.

Keywords : black carbon, OC/EC, aethalometer, traffic

Pollutant Emissions from a non-road Source with a B20 Biodiesel Blend

Lora Monti ^a, Zifei Liu ^b and Mingming Lu ^b

^a Northwest high school, 10761 Pippin Road
Cincinnati, OH 45231

^b Department of Civil & Environmental Engineering, University of Cincinnati,
OH 45221-0071

Principal Contact: Mingming Lu, Dept. of Civil and Environ. Eng. Univ. of Cincinnati
Cincinnati, OH 45221, Phone: 513-556-0996, Fax: 513-556-2599, Email:
Mingming.lu@uc.edu

Abstract

Diesel particulate matter (DPM) has been regarded as carcinogenic by various agencies, such as the EPA, NIOSH (National Institute of Occupational Safety and Health), and WHO (World Health Organization), etc. In the recent decade, with the concern of fossil fuel shortage and climate change, various blends of biodiesel have been used in diesel powered machines world wide. Biodiesel reduce a country's dependence on imported petroleum and to lower pollutant emissions, as CO, HC and particulate matter according to some studies. Biodiesel can be derived from vegetable oil, recycled cooking oil and animal fat. In this study, two types of fuel were used, normal diesel (low sulfur diesel) and B20 (20% biodiesel with 80% normal diesel). Each fuel was tested at four load conditions with multiple measurements, *i.e.*, 0 (idle), 25, 50 and 75 kW with a non-road diesel generator. The EPA Method 5 (the Determination of Particulate Matter Emissions from Stationary Sources) was used to determine the amount of DPM generated from each fuel and the organic carbon and elemental carbon concentrations. The samples were collected on quartz filter instead of glass fiber filters in order to perform carbon speciation. The diesel particulate matter concentration was determined from the differential weight of the filter before and after running Method 5. After the filters were desiccated and weighed, the organic carbon and elemental carbon (OC/EC) was determined using the Thermal Optical Method 5040. A Testo Gas Analyzer was used to obtain the concentration of O₂, CO, CO₂, NO_x, and EA (extra air). The DPM from B20 is 10-15% lower than that of petro-diesel. The emissions of CO and NOx were close for the two fuels.

Keywords : Diesel particulate matter (DPM), OC/EC, B20

